Wind-Farm Parametrisations in Mesoscale Models

Volker, Patrick; Badger, Jake; Hahmann, Andrea N.; Hansen, Kurt Schaldemose

Published in:
Proceedings of the 2013 International Conference on aerodynamics of Offshore Wind Energy Systems and wakes (ICOWES2013)

Publication date:
2013

Document Version
Publisher's PDF, also known as Version of record

Proceedings of the:

2013 International Conference on Aerodynamics of Offshore Wind Energy Systems and Wakes (ICOWES2013)

Organized by:

DTU Wind Energy
Sino-Danish Consortium on Wind Turbine Aerodynamic Research
Center of Computational Wind Turbine Aerodynamics and Atmospheric Turbulence
Nordic Consortium on Optimization of Wind Farms

Editor: Wen Zhong Shen
Co-ordinator: Marianne Hjorthede Arbirk

Proceedings

ICOWES2013
Lyngby, Denmark
17 – 19 June 2013

Contents:

XI: Wind Conditions - 2

XII: Wind Farm Optimization & Aerodynamics

Preface

Offshore wind resource is vast and harvesting offshore wind energy is a fast growing industry. To reduce the cost of offshore wind energy, the size of the wind turbines has continuously increased and has today reached 6MW, and it is expected to increase even further in the years to come. Large wind turbines are more challenging with respect to aerodynamics, structures and wakes.

To promote opportunities of sharing the latest research results and accomplishments in offshore wind energy, the Technical University of Denmark (DTU) is hosting the 2013 **I**nternational **C**onference on Aerodynamics of **O**ffshore **W**ind **E**nergy **S**ystems and Wakes (ICOWES2013). Predecessors within the same fields are: the 2011 International Conference on Offshore Wind Energy and Ocean Energy (2011ICOWEOE) held in Beijing in October 2011 and the Wake Conference held in Gotland, Sweden in June 2011.

Various researchers and experts from Europe, America and Asia will discuss the latest results and developments in offshore wind energy and wakes at the conference.

I wish to express here my acknowledgements to all my colleagues and the scientific committee who greatly helped to make the ICOWES2013 conference as engaging, informative, and fruitful as possible. On behalf of the scientific committee, I wish everybody will have a very successful and exciting conference. On behalf of the organizing committee, I am pleased to welcome you all to Copenhagen and hope you will have a great time in the charming and wonderful city Copenhagen.

Wen Zhong Shen, PhD, Dr. Techn.
DTU Wind Energy

Chair of ICOWES2013

List of committee members:

Organizing committee:
Gunner Larsen, DTU Wind Energy, Denmark
Helge Aagaard Madsen, DTU Wind Energy, Denmark
Jens Nørkær Sørensen, DTU Wind Energy, Denmark
Kurt Schaldemose Hansen, DTU Wind Energy, Denmark
Stefan Ivanell, Gotland University, Sweden
Wen Zhong Shen, DTU Wind Energy, Denmark (Chair)

Scientific committee:
Antonio Crespo, UPM, Spain
Christian Masson, Ecole de Technologie Superieure, Canada
Dan Henningson, KTH, Sweden
Gerard Schepers, ECN, Netherlands
Gerard van Bussel, Deft University of Technology, Netherlands
Gijs van Kuik, Deft University of Technology, Netherlands
Javier Sanz Rodrigo, CENER, Spain
Jens Madsen, Vattenfall, Denmark
Jianzhong Xu, Chinese Academy of Sciences, China (Chair of the Scientific Committee)
Jin Chen, Chong Qing University, China
Mingming Zhang, Chinese Academy of Sciences, China
Niels N Sørensen, DTU Wind Energy, Denmark
Niels Troldborg, DTU Wind Energy, Denmark
Pat Moriarty, National Renewable Energy Laboratory, USA
Peter Eecen, ECN, Netherlands
Peter Schaffarczyk, University of Applied Sciences Kiel, Germany
Rebecca Barthelmie, Indiana University, USA
Spyros Voutsinas, NTUA, Greece
Takis Chaviaropoulos, CRES, Greece
Thomas Leweke, Institut de Recherche sur les Phénomènes Hors Equilibre, France
Tongguang Wang, Nanjing University of Aeronautics and Astronautics, China
Tonio Sant, University of Malta, Malta
Weijun Zhu, DTU Wind Energy, Denmark

Sponsor:

KEY Note Lecture:

Wind Turbine Wakes: Status and Challenges

Jens N. Sørensen

Department of Wind Energy
Technical University of Denmark

Wind turbines operating in clusters will always be subject to the influence wakes of neighboring turbines. The wake behind the wind turbines has a lower mean wind speed and an increased turbulence level compared to the undisturbed flow outside the farm, hence wake interaction leads to a decreased total production of power caused by lower kinetic energy in the wind. Furthermore, increased levels of fatigue loads are imposed on the turbines in the farm due to turbulent flow.
Wake modeling can be carried out using different models of varying levels of complexity. The simplest models assume linearly expanding wakes and are described by simple integral momentum equations, while the most complex models make use of computational fluid dynamics (CFD) and state of the art representations of the rotor blades. For an extensive list of different wake models, the reader is referred to Crespo et al. [1], Vermeer et al. [2] and Sørensen [3].
The wake behind a rotor consists essentially of a number of helical vortices that owing to roll-up effects mainly concentrates in tip and root vortices and which, under the influence of the ambient turbulence, breaks down into small scale turbulence. The wake can generally be divided into two distinct parts, the near wake and the far wake. Near wake features are related to the genesis of the vortex system, where the presence of the rotor is felt directly. The far wake is usually the downstream position where the wake dynamics no longer depends on the rotor characteristics.
In the past year wakes behind wind turbine blades have been studied both experimentally and numerically, using analytical tools as well as numerical simulations based on RANS or LES methodologies combined with actuator disc or line techniques. From these studies it has been shown that helical wakes are inherent unstable and that the flow inside a wind farm to a large extent is depending on the ambient turbulence and the stability properties of the atmospheric boundary layer.
In the presentation we give a status of state-or-the-art modeling of wind turbine wakes, including a general description of the challenges of wake modeling and a description of the various models in use today. Furthermore, we will present mechanisms for initial breakdown of the vortex pattern in the near wake as well as show results from studies of wake interaction and modeling of the interaction between wind farms and the atmospheric boundary layer.

References:

1. Crespo, A., Hernández, J. and Frandsen, S. (1999) 'Survey of modelling methods for wind turbine wakes and wind farms', ***Wind Energy***, vol. (1), pp. 1-24.
2. L.J. Vermeer, J.N. Sørensen and A. Crespo (2003), "*Wind Turbine Wake Aerodynamics*". ***Progress in Aerospace Sciences***, vol. 39, pp. 467-510.
3. Sørensen, J.N. (2011) 'Aerodynamic aspects of wind energy conversion'. ***Annual Review of Fluid Mechanics***, vol. 43, pp. 427-448.

IMPROVEMENTS IN ECN WAKE MODEL

H. Özdemir[1], M.C. Versteeg[2], A.J. Brand[1]

[1]ECN, P.O.Box 1, 1755 ZG Petten, NL, h.ozdemir@ecn.nl
[2]University of Twente, P.O.Box 217, 7500 AE Enschede, NL, m.c.versteeg@student.utwente.nl

INTRODUCTION

Wind turbines extract energy from the flow field so that the flow in the wake of a wind turbine contains less energy and more turbulence than the undisturbed flow, leading to less energy extraction for the downstream turbines. In large wind farms, most turbines are located in the wake of one or more turbines causing the flow characteristics felt by these turbines differ considerably from the free stream flow conditions. The most important wake effect is generally considered to be the lower wind speed behind the turbine(s) since this decreases the energy production and as such the economical performance of a wind farm. The overall loss of a wind farm is very much dependent on the conditions and the lay-out of the farm but it can be in the order of 5-10%. Apart from the loss in energy production an additional wake effect is formed by the increase in turbulence intensity, which leads to higher fatigue loads. In this sense it becomes important to understand the details of wake behavior to improve and/or optimize a wind farm layout. Within this study improvements are presented for the existing ECN wake model which constructs the fundamental basis of ECN's FarmFlow wind farm wake simulation tool [1].

The ECN wake model is called WakeFarm [2, 3, 4] and, based on the original UPMWAKE model proposed by Crespo *et al.* [5, 6], that simulates the wind turbine wakes by solving the steady parabolized Navier-Stokes equations in perturbation form in three-dimensions. The basic background flow is modeled by an atmospheric wind profile model based on Monin-Obukhov similarity theory [7]. The similarity relations suggested by Businger [8] *et al.* are used. Furthermore the perturbation variables are initialized by a near wake model where the parabolization is not justified since the axial-pressure gradient term is neglected.

Schepers [2] pointed out the problem in the near wake and used an empirical velocity-deficit profile as a boundary condition for the far wake. This approach depends on a data-fit with experimental data and the physics of the flow are not modeled explicitly. Schepers and Van der Pijl [4] proposed a model for the near wake based on the free-wake vortex method where the wind turbine is modeled by an actuator disc model and the wake is represented by discrete constant strength vortex rings. They obtained the solution with a panel method. A near wake model is presented here based on a free wake-vortex method as well, where the radius of the

wake and vorticity strength of discrete vortex rings are varied as suggested by Øye [9]. The induced velocities are obtained by a semi-analytical solution of the Biot-Savart law.

The diabatic wind profiles for the surface layer of the atmospheric boundary layer have been investigated extensively [8, 10]. The atmospheric stability model based on Monin-Obukhov [7] theory is only valid within the surface layer of the atmospheric boundary layer. Previous studies [11, 12, 13] show that boundary layer height varies typically between $50-200m$ under stable conditions and $500-1000m$ under unstable conditions. A need for a model that extends to the entire boundary layer height is obvious considering the sizes of modern wind turbines. Blackadar [14] and Lettau [15] studied a wind shear model covering the entire boundary layer height under neutral condition. Gryning *et al.* [16] extended this model to cover all stability conditions of the atmosphere based on measurements extending in to the mixing layer region where the surface layer scaling is connected with the geostrophic drag law. More recently similar work is done by Peña *et al.* [17]. Sathe *et al.* [18] showed that the loads are predicted smaller with the model proposed by Gryning when compared to models based only on surface layer wind profiles.

Within this study the ECN wake model is extended further based on the model proposed by Gryning *et al.* [16]. The numerical solution obtained by the ECN wake model using Gryning model is compared with the solution obtained by surface layer model and with the available data obtained by EWTW measurements.

The outline of this paper is as follows: First of all the governing equations of the ECN wake farm model are presented. Then the near wake modeling is discussed and the results compared with the original near wake modeling and EWTW data as well as the results obtained for various near wake implementation cases are shown. The details of the atmospheric stability model are given and the comparison with the solution obtained for the original surface layer model and with the available data obtained by EWTW measurements are presented. Finally the conclusions are summarized.

GOVERNING EQUATIONS

In the wake model originally proposed by Crespo *et al.* [5] the wind turbine is supposed to be immersed in a nonuniform basic flow corresponding to the surface layer of the atmospheric boundary layer. This surface layer which is modeled by the standard surface-layer scaling based on the Monin-Obukhov theory, is assumed to be perturbed by the wind turbine. The equations describing the perturbed flow are obtained by introducing the following perturbation variables in to the Navier-Stokes equations together with the conservation of mass and energy equations and two equations for turbulent kinetic energy and the dissipation rate of the turbulent kinetic energy:

$$u = u' + u_0, \quad v = v', \quad w = w', \quad p = p' + p_0, \quad \theta = \theta' + \theta_0, \quad k = k' + k_0, \quad \varepsilon = \varepsilon' + \varepsilon_0, \quad (1)$$

with u, v, and w are three components of the velocity vector, p is the pressure, θ is the potential temperature, k is the turbulent kinetic energy and ε is the turbulent dissipation rate. Furthermore, the subscript "0" refers to the undisturbed flow and the superscript $()'$ refers to a perturbation variable. This undisturbed flow does not vary in $x-$ and $y-$directions, but does vary in z direction.

For the wake flow behind a wind turbine the following assumptions are made: the streamwise pressure gradient is neglected in the far wake behind the wind turbine while the near wake is modeled by the free-vortex wake model as part of basic background flow. The streamwise diffusion is neglected leading to $\frac{\partial \tau_{ij}}{\partial x} = 0$ and $\nu_t \frac{\partial u_j}{\partial x} = 0$. The undisturbed flow in $y-$ and $z-$ directions is assumed to be zero meaning that the information is only traveling downstream. Furthermore the turbulent stresses can be modeled by Boussinesq's eddy viscosity approximation:

$$\tau_{ij} = \rho \nu_t \left[\frac{u_i}{x_j} + \frac{u_j}{x_i} \right] - \frac{2}{3} \rho k \delta_{ij}. \tag{2}$$

Under these assumption the Navier Stokes equations that describe the flow can be written in parabolized form where the elliptic terms are not present anymore. When the Navier-Stokes equations for the undisturbed flow are subtracted from those equations for the disturbed flow, the following relations can be derived. Please note that the superscript $()'$ is dropped for convenience.

Continuity equation:

$$\frac{\partial u}{\partial x} + \frac{\partial v}{\partial y} + \frac{\partial w}{\partial z} = 0. \tag{3}$$

Momentum equations (x, y and z directions):

$$\begin{aligned} (u_0+u)\frac{\partial u}{\partial x} + v\frac{\partial u}{\partial y} + w\frac{\partial (u_0+u)}{\partial z} &= (\nu_t + \nu_{t0})\frac{\partial^2 u}{\partial y^2} + \frac{\partial \nu_t}{\partial y}\frac{\partial u}{\partial y} \\ &+ (\nu_t + \nu_{t0})\frac{\partial^2 u}{\partial z^2} + \left(\frac{\partial \nu_t}{\partial z} + \frac{\partial \nu_{t0}}{\partial z} \right) \frac{\partial u}{\partial z} + \frac{\partial \nu_t}{\partial z}\frac{\partial u_0}{\partial z} + \nu_t \frac{\partial^2 u_0}{\partial z^2}, \end{aligned} \tag{4}$$

$$\begin{aligned} (u_0+u)\frac{\partial v}{\partial x} + v\frac{\partial v}{\partial y} + w\frac{\partial v}{\partial z} &= -\frac{2}{3}\frac{\partial k}{\partial y} - \frac{1}{\rho}\frac{\partial p}{\partial y} + 2(\nu_t + \nu_{t0})\frac{\partial^2 v}{\partial y^2} + 2\frac{\partial \nu_t}{\partial y}\frac{\partial v}{\partial y} \\ &+ (\nu_t + \nu_{t0})\frac{\partial^2 v}{\partial z^2} + \left(\frac{\partial \nu_t}{\partial z} + \frac{\partial \nu_{t0}}{\partial z} \right) \frac{\partial v}{\partial z} + \left(\frac{\partial \nu_t}{\partial z} + \frac{\partial \nu_{t0}}{\partial z} \right) \frac{\partial w}{\partial y}, \end{aligned} \tag{5}$$

$$\begin{aligned} (u_0+u)\frac{\partial w}{\partial x} + v\frac{\partial w}{\partial y} + w\frac{\partial w}{\partial z} &= -\frac{1}{\rho}\frac{\partial p}{\partial z} + (\nu_t + \nu_{t0})\frac{\partial^2 w}{\partial y^2} + \frac{\partial \nu_t}{\partial y}\frac{\partial w}{\partial y} \\ &+ 2(\nu_t + \nu_{t0})\frac{\partial^2 w}{\partial z^2} + 2\left(\frac{\partial \nu_t}{\partial z} + \frac{\partial \nu_{t0}}{\partial z} \right) \frac{\partial w}{\partial z} + \frac{\partial \nu_t}{\partial y}\frac{\partial v}{\partial z} - \frac{2}{3}\frac{\partial (k+k_0)}{\partial z} + \beta g \theta, \end{aligned} \tag{6}$$

with β is the expansion coefficient.

Energy equation:

$$\begin{aligned} (u_0+u)\frac{\partial \theta}{\partial x} + v\frac{\partial \theta}{\partial y} + \frac{\partial (\theta_0+\theta)}{\partial z} &= (\nu_\theta + \nu_{\theta 0})\frac{\partial^2 \theta}{\partial y^2} + w\frac{\partial \nu_\theta}{\partial y}\frac{\partial \theta}{\partial y} \\ &+ (\nu_\theta + \nu_{\theta 0})\frac{\partial^2 \theta}{\partial z^2} + \left(\frac{\partial \nu_\theta}{\partial z} + \frac{d\nu_{\theta 0}}{dz} \right) \frac{\partial \theta}{\partial z} + \frac{\partial \nu_\theta}{\partial z}\frac{\partial \theta_0}{\partial z} + \nu_\theta \frac{\partial^2 \theta_0}{\partial z^2}. \end{aligned} \tag{7}$$

Turbulent kinetic energy:

$$
\begin{aligned}
(u_0+u)\frac{\partial k}{\partial x}+v\frac{\partial k}{\partial y}+w\frac{\partial (k_0+k)}{\partial z} \quad &= \quad (\nu_k+\nu_{k0})\frac{\partial^2 k}{\partial y^2}+\frac{\partial \nu_k}{\partial y}\frac{\partial k}{\partial y}+(\nu_k+\nu_{k0})\frac{\partial^2 k}{\partial z^2} \\
&+\left(\frac{\partial \nu_k}{\partial z}+\frac{d\nu_{k0}}{dz}\right)\frac{\partial k}{\partial z}+\frac{\partial \nu_k}{\partial z}\frac{\partial k_0}{\partial z}+\nu_k\frac{\partial^2 k_0}{\partial z^2}+(\nu_t+\nu_{t0})\left[\left(\frac{\partial u}{\partial y}\right)^2+\left(\frac{\partial u}{\partial z}\right)^2+2\frac{\partial u}{\partial z}\frac{\partial u_0}{\partial z}\right] \\
&+\nu_t\left(\frac{du0}{dz}\right)^2-\beta g\nu_\theta\left(\frac{\partial \theta}{\partial z}+\frac{\partial \theta_0}{\partial z}\right)-\beta g\nu_{\theta 0}\frac{\partial \theta}{\partial z}-\varepsilon. \qquad (8)
\end{aligned}
$$

Dissipation rate of the turbulent kinetic energy:

$$
\begin{aligned}
&(u_0+u)\frac{\partial \varepsilon}{\partial x}+v\frac{\partial \varepsilon}{\partial y}+w\frac{\partial (\varepsilon_0+\varepsilon)}{\partial z} \quad = \\
&(\nu_\varepsilon+\nu_{\varepsilon 0})\frac{\partial^2 \varepsilon}{\partial y^2}+\frac{\partial \nu_\varepsilon}{\partial y}\frac{\partial \varepsilon}{\partial y}+(\nu_\varepsilon+\nu_{\varepsilon 0})\frac{\partial^2 \varepsilon}{\partial z^2}+\left(\frac{\partial \nu_\varepsilon}{\partial z}+\frac{d\nu_{\varepsilon 0}}{dz}\right)\frac{\partial \varepsilon}{\partial z}+\frac{\partial \nu_\varepsilon}{\partial z}\frac{\partial \varepsilon_0}{\partial z}+\nu_\varepsilon\frac{\partial^2 \varepsilon_0}{\partial z^2} \\
&+C_{\varepsilon_1}\frac{\varepsilon_0+\varepsilon}{k_0+k}(\nu_t+\nu_{t0})\left[\left(\frac{\partial u}{\partial y}\right)^2+\left(\frac{\partial u}{\partial z}\right)^2+\left(\frac{\partial u_0}{\partial z}\right)^2+2\frac{\partial u}{\partial z}\frac{\partial u_0}{\partial z}-(1-C_{\varepsilon_3})\beta g\frac{1}{\sigma_\theta}\frac{\partial(\theta+\theta_0)}{\partial z}\right] \\
&-C_{\varepsilon_1}\frac{\varepsilon_0}{k_0}\nu_{t0}\left[\left(\frac{\partial u_0}{\partial z}\right)^2-(1-C_{\varepsilon_3})\beta g\frac{1}{\sigma_\theta}\frac{\partial \theta_0}{\partial z}\right]-C_{\varepsilon_2}\frac{(\varepsilon+\varepsilon_0)^2}{k+k_0}+C_{\varepsilon_2}\frac{\varepsilon_0^2}{k_0}, \qquad (9)
\end{aligned}
$$

with,

$$
\nu_t=C_\mu\frac{(k+k_0)^2}{\varepsilon+\varepsilon_0}-\nu_{t0}, \quad \nu_\theta=\frac{\nu_t}{\sigma_\theta}, \quad \nu_k=\frac{\nu_t}{\sigma_k}, \quad \nu_\varepsilon=\frac{\nu_t}{\sigma_\varepsilon}. \qquad (10)
$$

where C_μ, C_{ε_1}, C_{ε_2}, C_{ε_3}, σ_θ, σ_k and σ_ε are the closure coefficients of the system. The system of equations given between equation (3) and (9) form a steady, three-dimensional parabolic set of equations. These equations are discretized with central differences and integrated employing the semi-implicit ADI scheme. The pressure is evaluated using the SIMPLE method [19].

Dirichlet and Neumann boundary conditions are applied at boundaries of the domain [6]. The numerical values are determined from the undisturbed flow in front of the wind turbine.

The solution domain size is chosen to be at least ten times the wind turbine diameter, D, along $x-$ direction (i.e., downstream wake direction) and six times the wind turbine diameter in $y-$ and $z-$directions. A grid stretching is applied along the $x-$direction within the near-wake region. For a typical simulation of a single turbine-single wake combination around $1 \cdot 10^6$ grid points are used.

NEAR WAKE MODEL

In the original ECN wake model the near wake is modeled by a free-wake vortex model where the vorticity strength of vortex rings are kept constant while the wake radius is varied. The solution is obtained by a panel method. In the current study the near-wake model is improved further as suggested by Øye [9]. The wind turbine rotor is modeled by an actuator disc model and the wake is represented by a thin vortex sheet which is described by vortex rings of variable

radius and variable vorticity strength leading to a variable transport velocity at infinity. Flow is assumed to be axisymmetric. Induced velocity profiles are obtained analytically using Biot-Savart law, where the elliptic integrals are evaluated numerically. The radii along the wake are calculated by making use of the continuity equation and the solution is iterated until convergence is reached between the local radius and the vorticity.

In figure (1) a comparison of various calculation methods that have been studied and the original panel method are presented. The wake radius is plotted against the distance from the turbine in downstream direction for constant vortex strength (Γ) and variable vortex strength cases for uniform and stretched grid distributions. All results are obtained for an axial induction factor of 0.28. The left-hand side of the figure is a close-up of the near-wake region while on the right-hand side the full domain is presented. In figure (2) the induced velocity just behind the rotor is

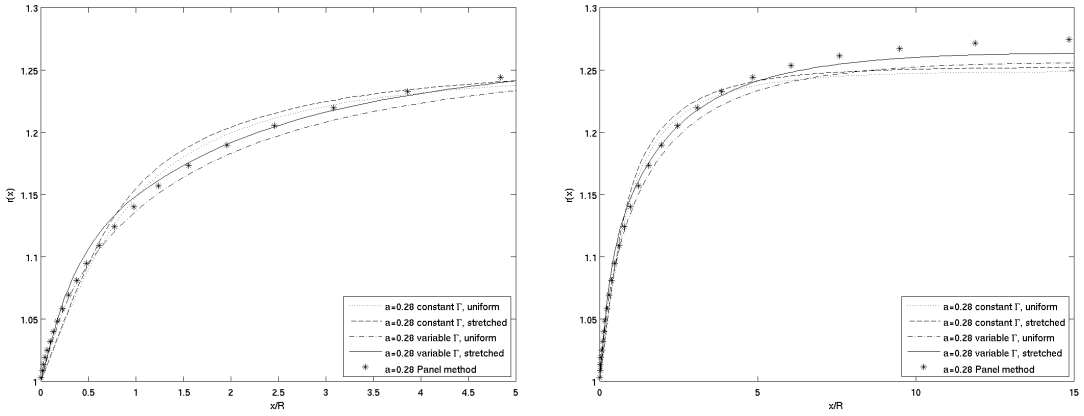

Figure 1: Comparison of the wake radius as a function of distance from the turbine up to $5R$ (left) and $15R$ (right) with $a = 0.28$, as simulated by the constant vorticity vortex ring model, the variable vorticity vortex ring model and the panel method. The new near wake models are simulated on uniform and stretched grids.

shown for the panel method and the variable vorticity vortex ring method for an axial induction factor of 0.28. It is clear that the models are comparable, but that inside the wake the induced velocity in downstream direction is higher in an absolute sense. According to actuator disc momentum theory the induced velocity just behind the rotor is $-aU_\infty$, so the variable vorticity vortex ring model agrees better with the theory. The results of both original and new wake models are compared with the experimental data obtained from the measurements at ECN Wind turbine Test field Wieringermeer, EWTW. The test site consists of five state of the art turbines in a row, a scaled wind farm with 10 wind turbines of 7.5 meter hight and 7.6 meter in diameter and 5 prototype spots for certification of industrial turbines. The five state of the art turbines, with a hub height and diameter of 80 meters, are situated in a row and a meteorological measurement mast is located in the proximity of T5 and T6, as can be seen on the left-hand side of figure (3) [20]. Since there is only one measured point in the field, multiple measurements are combined to get the horizontal wake profile behind a turbine on a certain distance. The right-hand side of

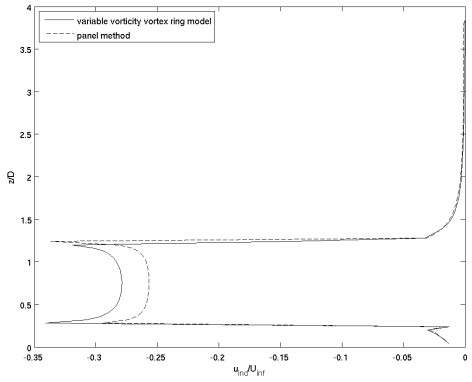

Figure 2: Comparison of velocity and force profiles just behind the rotor plane at the symmetry plane, as simulated by the variable vorticity vortex ring model (the new near wake model) and the panel method (the old near wake model).

figure (3) shows the distance S between the mast and the wind turbines: 2.5D and 3.5D. When the wind direction is 31 degrees or 315 degrees the velocity at the wake center is measured. When the wind comes from a different direction, the distance y to the wake center is calculated. The results of the numerical simulation obtained by the ECN wake model WakeFarm using the

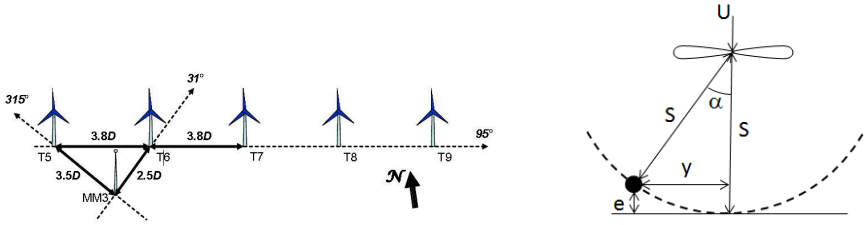

Figure 3: Location of wind turbines and meteorological measurement mast at EWTW (left). When the turbine yaws the meteorological mast moves along the dashed line with respect to the rotor (right).

original (panel method) and new near wake models are compared with the EWTW data and shown in figure (4). WakeFarm performs best at 2.5D, but for 3.5D the results deviate more from the experimental measurements. For the details of the experimental work one is referred to reference [20].

ATMOSPHERIC BOUNDARY LAYER STABILITY MODEL

In the original UPMWAKE model of Crespo *et al.* [5] a diabatic wind profile based on Monin-Obukhov [7] similarity theory and Businger *et al.* [8] formulation is used given as follows:

$$u = \frac{u_{*0}}{\kappa}\left[\ln\left(\frac{z}{z_0}\right) - \psi_m\left(z/L\right)\right], \tag{11}$$

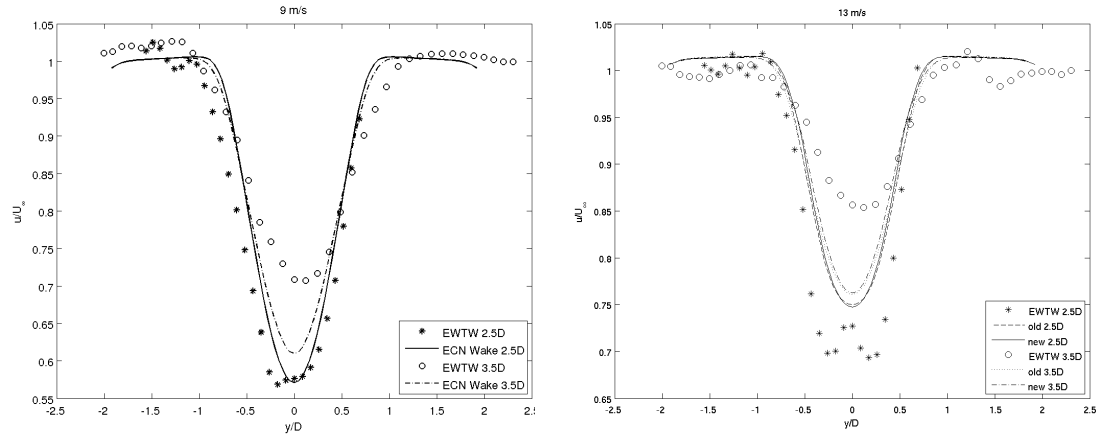

Figure 4: Comparison of EWTW experimental data with velocity profiles in wake direction, as simulated by ECN wake model using the original and the new near wake model, respectively.

where u_{*0} is the friction velocity near the ground, z is the height, z_0 is the aerodynamic roughness length, κ is the von Kármán constant, L is the Monin-Obukhov length and ψ_m is a universal stability function which is defined empirically. In the original ECN wake model the above wind profile is adopted whith the Bussinger *et al.* [8] form for stability function ψ_m where further details are given by Panofsky and Dutton [21]. The Monin-Obukhov length, L, is given by the following expression:

$$L = \frac{u_{*0}^3 T}{\kappa g \overline{\omega' \theta_0'}}, \tag{12}$$

where, T is the absolute temperature, θ_0 is the potential temperature and $\overline{\omega' \theta_0'}$ is the virtual kinematic heat flux.

The diabatic wind profile models using surface layer scaling of Monin-Obukhov [7] are valid only within the surface layer of the atmosphere. In the current study the extended wind profile model proposed by Gryning *et al.* [16] is used which is valid for the entire boundary layer. The model is given as follows:

For neutral conditions:

$$u = \frac{u_{*0}}{\kappa} \left[\ln\left(\frac{z}{z_0}\right) + \frac{z}{L_{MBL}} - \frac{z}{z_i}\left(\frac{z}{2L_{MBL}}\right) \right], \tag{13}$$

for unstable conditions:

$$u = \frac{u_{*0}}{\kappa} \left[\ln\left(\frac{z}{z_0}\right) - \psi_m\left(z/L\right) + \frac{z}{L_{MBL}} - \frac{z}{z_i}\left(\frac{z}{2L_{MBL}}\right) \right], \tag{14}$$

	Unstable	**Neutral**	**Stable**
L	-128 m	321 m	41 m
$\mathbf{z_i}$	117 m	205 m	49 m
$\mathbf{L_{MBL}}$	283 m	866 m	69 m

Table 1: Parameters used for figure (5)

for stable conditions:

$$u = \frac{u_{*0}}{\kappa}\left[\ln\left(\frac{z}{z_0}\right) - \psi_m\left(z/L\right)\left(1-\frac{z}{2z_i}\right) + \frac{z}{L_{MBL}} - \frac{z}{z_i}\left(\frac{z}{2L_{MBL}}\right)\right], \tag{15}$$

with z_i is the height of the atmospheric boundary layer and defined as follows for the neutral conditions [22]:

$$z_i = c\frac{u_{*0}}{|f|} \tag{16}$$

with c is a constant and f is the Coriolis parameter. The value of c is adopted from the works of Sathe *et al.* [18] and Peña *et al.* [23, 24] as 0.15 for neutral conditions, 0.14 for stable conditions and 0.13 for very stable conditions.

Stability function, ψ_m, is used from Businger *et al.* [8] for stable conditions and from Grachev *et al.* [10] for unstable conditions. An empirical fit suggested by Gryning *et al.* [16] for the scaling parameter, L_{MBL}, is in the following form:

$$\frac{u_{*0}}{fL_{MBL}} = \left(-2\ln\left(\frac{u_{*0}}{fz_0}\right) + 55\right) e^{\left(-\frac{\left(u_{*0}/fL\right)^2}{400}\right)}. \tag{17}$$

In figure (5) the influence of various models for an atmospheric boundary layer velocity profile is presented using the parameters listed in table (1). It can also be concluded from these figures that the choice for the atmospheric boundary layer stability model is most important for (very) stable conditions.

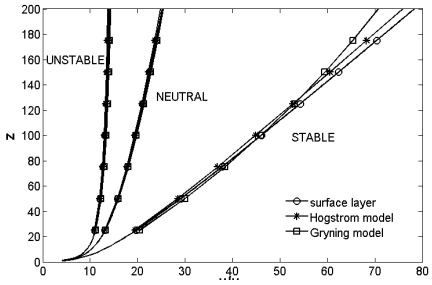

Figure 5: Influence of the atmospheric boundary-layer model on the velocity profile for unstable, neutral and stable conditions.

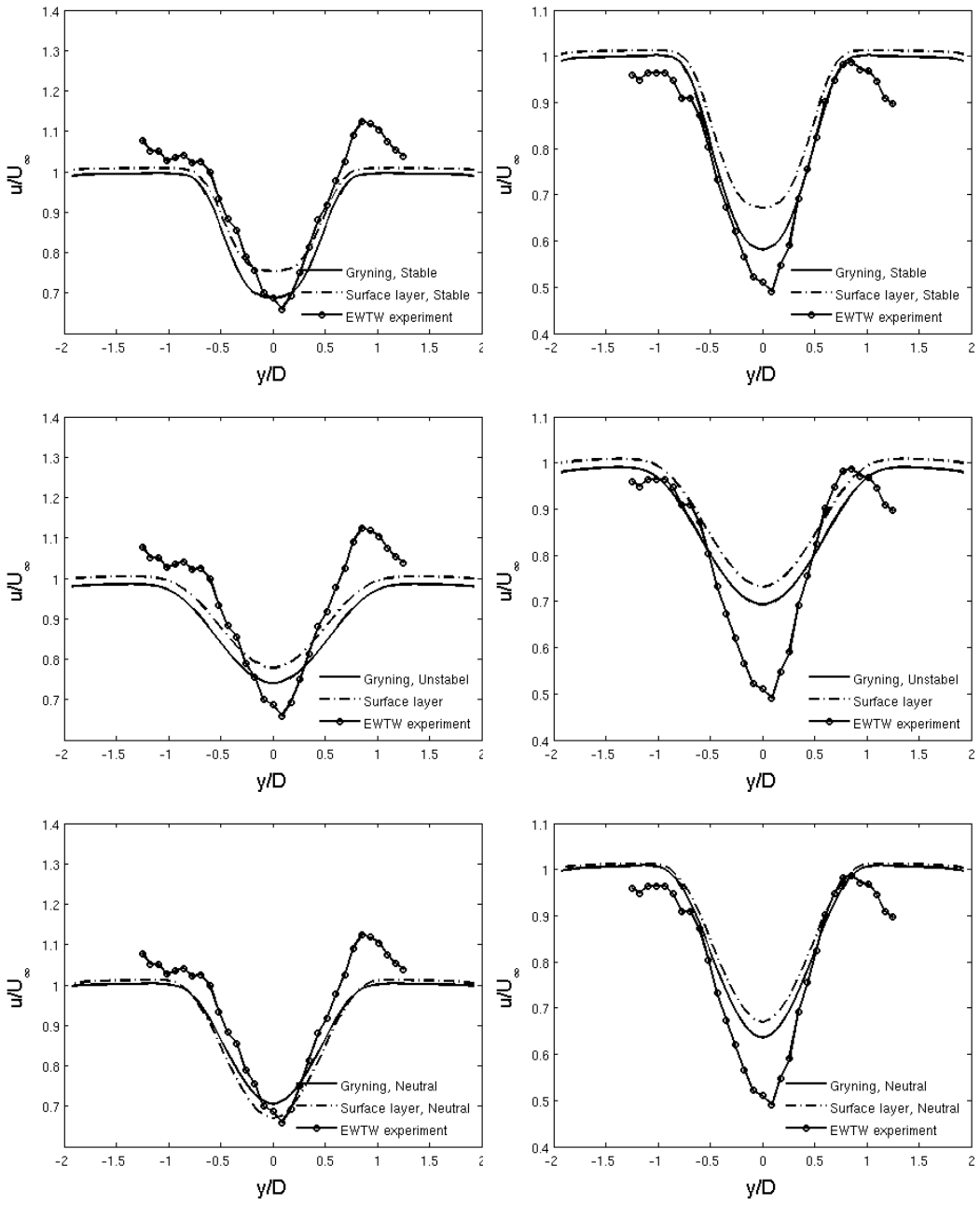

Figure 6: Comparison of numerical simulation using Gryning *et al.* [16] model for stable, neutral and unstable conditions with the surface layer model and the available data from EWTW measurements for $U_\infty = 8m/s$ (left) and $U_\infty = 10m/s$ (right).

Sathe *et al.* [18] showed the importance of using a diabatic wind profile for the entire boundary layer. They argued that using a surface layer model predicts the blade and rotor loads along the

wake direction much larger compared to a model for the entire boundary layer particularly for stable conditions, since in the surface-layer wind profile model under stable conditions, the wind profile length scale increases infinitely, leading to large wind gradients, while a wind profile for the entire boundary layer [16] limits the growth of this length scale using the boundary layer height, leading to smaller wind shear.

In figure (6) a comparison of numerical simulation using Gryning *et al.* [16] model valid for the entire boundary layer for stable, neutral and unstable conditions with the surface layer model and the available data from EWTW measurements for $U_\infty = 8m/s$ (left) and $U_\infty = 10m/s$ (right) is given. The EWTW data is evaluated as described in the previous section. The induced velocity is predicted lower compared to the surface layer model which is in agreement with Sathe *et al.* [18]. It should be noted here that a single EWTW data set is used for the entire stability region and the simulation results for each stability region are compared with this single data.

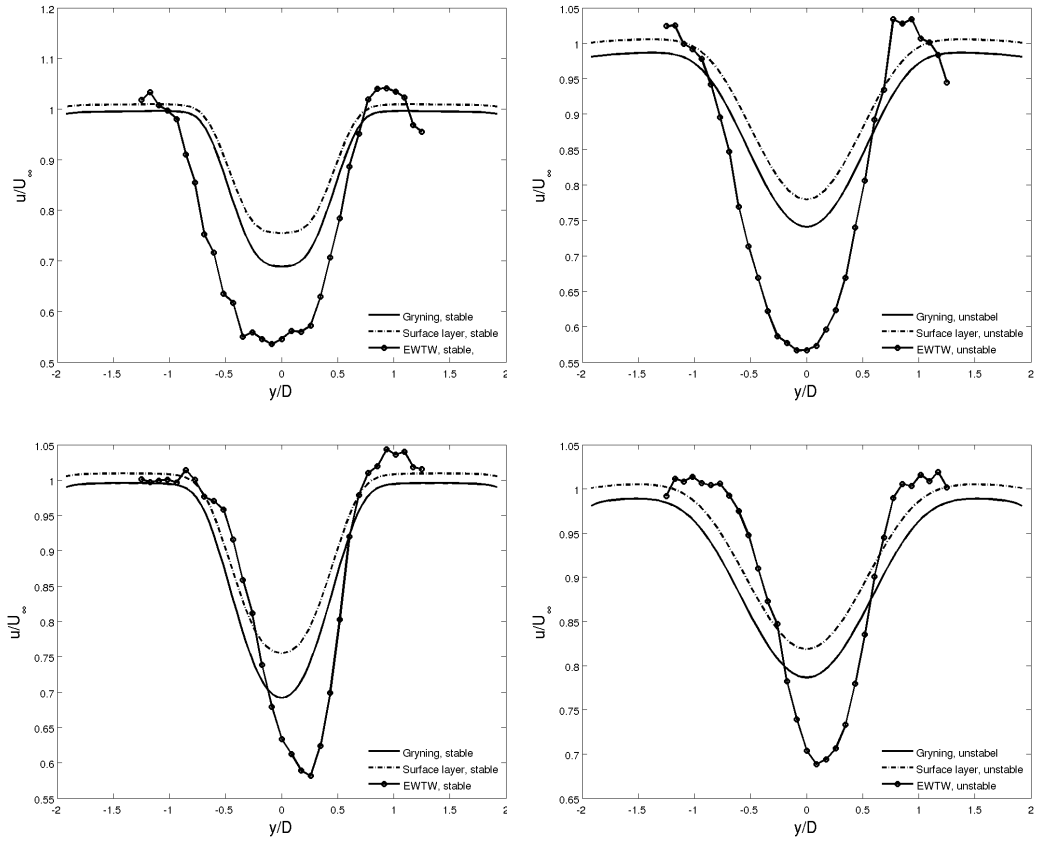

Figure 7: Comparison of numerical simulation using Gryning *et al.* [16] model with the surface layer model and the data from EWTW measurements for stable and unstable conditions for $U_\infty = 8m/s$, at $2.5D$ (left) and $3.5D$ (right).

There is a necessity of determination of the experimental data for various stability conditions.

The available EWTW data do not contain any information to categorize the stability of the atmosphere at the moment of the measurements. In the literature there are several rough estimates are given about the estimation of the stability condition of the atmosphere depending on the time of the day [22]. Based on these rough estimates the data measured between sunrise and sunset is assumed to be unstable and between sunset and sunrise is assumed to be stable. The comparison of the numerical simulation using Gryning *et al.* [16] model with the surface layer model and the data from EWTW measurements for stable and unstable conditions for $U_\infty = 8m/s$ is shown in figure (7) at $2.5D$ and $3.5D$ downstream of the turbine. Although the comparison is not conclusive because of the reliability of the data it is shown here for the demonstration purposes.

CONCLUSIONS

In this study improvements to ECN wake model, WakeFarm, are presented in two folds. First of all, an improved near wake model is shown where the wake is modeled by a thin vortex sheet represented by discrete vortex rings of variable strength. The solution is obtained analytically with the Biot-Savart law, where the elliptic integrals are evaluated numerically. It is shown that the induced velocity is lower than for the original near wake model, which is in accordance with the theory. Furthermore the diabatic wind profile model is improved by implementing a model valid for the entire boundary layer as suggested by Gryning *et al.* [16]. The results are compared with a diabatic wind model valid for the surface layer and with the data obtained from EWTW measurements. Although the results seem closer to the data, the EWTW data is a single data set representing all stability regions. An initial attempt to categorize the EWTW data in to two stability regions depending on the time of the day of the measured data did not lead to better conclusions. A need for a better data mining to distinguish the different stability regions and data from different sites is obvious. In addition, accurate temperature measurements should be standard for wake measurement campaigns.

ACKNOWLEDGMENTS

This work was performed in the framework of the EU funded project FP7-ENERGY-2011 283145 / Cluster Design.

REFERENCES

[1] FarmFlow, "http://www.ecn.nl/nl/units/wind/rd-programma/aerodynamica/windfarm-aerodynamics/farmflow/," 2013.

[2] J. G. Schepers, "Wakefarm: nabij zog model en ongestoord wind snelheidsveld," Tech. Rep. ECN-C–98-016, ECN, 1998.

[3] S. P. van der Pijl and J. G. Schepers, "Improvements of the wakefarm wake model," in *Workshop on wake modelling and benchmarking of models, Annex XXIII: Offshore wind energy technology and deployment*, (Billund), 2006.

[4] J. G. Schepers and S. P. van der Pijl, "Improved modelling of wake aerodynamics and assessment of new farm control strategies," in *The Science of Making Torque from Wind*, Journal of Physics: Conference series 75, 2007.

[5] A. Crespo, F. Manuel, D. Moreno, F. Fraga, and J. Hernáandez, "Numerical analysis of wind turbine wakes," in *Delphi Workshop on Wind turbine applications*, 1985.

[6] A. Crespo and J. Hernández, "Numerical modelling of the flow field in a wind turbine wake," in *3rd Joint ASCE/ASME Mechanics Conference*, 1989.

[7] A. S. Monin and A. M. Obukhov, "Basic laws of turbulent mixing in the surface layer of the atmosphere," *Tr. Akad. Nauk SSSR Geofiz. Inst.*, vol. 24, pp. 163–187, 1954. English translation by John Miller, 1959.

[8] J. A. Businger, J. C. Wjngaard, Y. Izumi, and E. F. Bradley, "Flux-profile relationships in the atmospheric surface layer," *Journal of the Atmospheric Sciences*, vol. 28, pp. 181–189, 1971.

[9] S. Øye, "A simple vortex model," in *3rd IEA Symposium on the Aerodynamics of Wind Turbines*, pp. 4.1–4.15.

[10] A. Grachev, C. Fairall, and E. Bradley, "Convective profile constants revisited," *Boundary-Layer Meteorology*, vol. 94, no. 3, pp. 495–515, 2000.

[11] P. Seibert, F. Beyrich, S. Gryning, S. Joffre, A. Rasmussen, and P. Tercier, "Review and intercomparison of operational methods for the determination of the mixing height," *Atmospheric Environment*, vol. 34, no. 7, pp. 1001 – 1027, 2000.

[12] M. A. Gárcia, M. L. Sánchez, B. de Torre, and I. A. Pérez, "Characterisation of the mixing height temporal evolution by means of a laser dial system in an urban area intercomparison results with a model application," *Ann. Geophys.*, vol. 25, p. 21192124, 2007.

[13] S. Emeisa, C. Münkelb, S. Vogtc, W. Müllerd, and K. Schäfera, "Atmospheric boundary-layer structure from simultaneous sodar, rass, and ceilometer measurements," *Atmospheric Environment*, vol. 38, no. 2, pp. 273–286, 2004.

[14] A. Blackadar, "The vertical distribution of wind and turbulent exchange in a neutral atmosphere," *Journal of Geophysical Research*, vol. 67, no. 8, pp. 3095–3102, 1962.

[15] H. Lettau, "Studies of the three-dimensional structure of the planetary boundary layer," Tech. Rep. AD-296160, University of Wisconsin, Department of Meteorology, 1962.

[16] S. E. Gryning, E. Batchvarova, B. Brümmer, H. Jørgensen, and S. Larsen, "On the extension of the wind profile over homogeneous terrain beyond the surface boundary layer," *Boundary-Layer Meteorology*, vol. 124, no. 2, pp. 251–268, 2007.

[17] A. Peña, S. E. Gryning, and C. B. Hasager, "Comparing mixing-length models of the diabatic wind profile over homogeneous terrain," *Theoretical and Applied Climatology*, 2010.

[18] A. Sathe, J. Mann, T. Barlas, W. A. A. M. Bierbooms, and G. J. W. van Bussel, "Influence of atmospheric stability on wind turbine loads," *Wind Energy Journal*, vol. DOI:10.1002/we.1528, 2012.

[19] S. V. Patankar and D. B. Spalding, "A calculation procedure for heat, mass and momentum transfer in three-dimensional parabolic flows," *Int. J. Heat Mass Transfer*, 1972.

[20] L. A. H. Machielse, P. J. Eecen, S. P. van der Pijl, and J. G. Schepers, "Ecn test farm measurements for validation of wake models," EWEC, 2007.

[21] H. Panofsky and J. Dutton, *Atmospheric Turbulence*. John Wiley and Sons, 1984.

[22] J. R. Garratt, *The atmospheric boundary layer*. Cambridge, 1992.

[23] A. Peña, S. E. Gryning, and C. B. Hasager, "Measurement and modelling of the wind speed profile in the marine atmospheric boundary layer," *Boundary-Layer Meteorology*, vol. 129, pp. 479–495, 2008.

[24] A. Peña, S. E. Gryning, J. Mann, and C. B. Hasager, "Length scales of the neutral wind profile over homogeneous terrain," *Journal of Applied Meteorology and Climatology*, vol. 49, pp. 792–806, 2010.

A New Analytical Model for Wind-Turbine Wakes

Majid Bastankhah[1], **Fernando Porté-Agel**[1]

[1]École Polytechnique Fédérale de Lausanne (EPFL),
Wind Engineering and Renewable Energy Laboratory (WIRE),
EPFL-ENAC-IIE-WIRE, CH-1015 Lausanne, fernando.porte-agel@epfl.ch

Abstract

A new analytical wake model is proposed and validated to predict the wind velocity distribution downwind of stand-alone wind turbines. The model is derived by applying conservation of mass and momentum to two different control volumes and assuming a Gaussian distribution for the velocity deficit in the wake. This simple model only requires one parameter to determine the velocity distribution in the wake. The results are compared to high-resolution wind-tunnel measurements and large-eddy simulation (LES) data. In general, it is found that the velocity deficit in the wake predicted by the proposed analytical model is in good agreement with the experimental and LES data. The results also show that the new model is more accurate than other common analytical models since they are based on inaccurate assumptions such as considering a top-hat distribution for the velocity deficit and not satisfying momentum conservation.

Key words: wind turbine, wakes, Gaussian distribution, top-hat models, velocity deficit

1 Introduction

Due to the drastic increase in the number of installed wind farms in the world, wind-turbine wakes have become important topics of study. As many wind turbines in a wind farms have to operate in the wakes of upwind turbines, they are exposed to incoming wind velocities that are smaller than those under unperturbed (no-wake) conditions. As a result, turbine wakes are responsible for important power losses in wind farms [1]. Extensive analytical, numerical and experimental efforts have been carried out to better understand and predict turbine wake flows. Although numerical and experimental techniques have become increasingly sophisticated and accurate in recent years, simple analytical models are still useful tools to predict wind-turbine wake flows and their effect on power production. They are widely used due to their simplicity and low computational cost [2]. Various analytical investigations have been conducted on wind-turbine wakes (e.g., [3-5]), but one of the pioneering models is the one proposed by Jensen [6]. His model assumes a top-hat shape for the velocity deficit in the wake (see fig. 1.a) and states:

$$\frac{\Delta U}{U_\infty} = \left(1-\sqrt{1-C_T}\right) / \left(1+\frac{2k_{wake}x}{d_0}\right)^2, \tag{1}$$

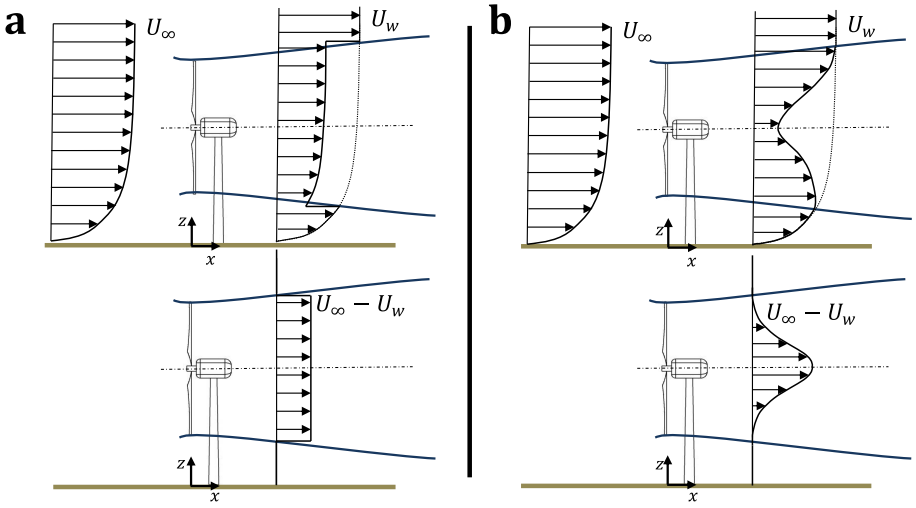

Figure 1: Schematic of the velocity and velocity-deficit profiles downwind of a wind turbine by assuming: (a) top-hat and (b) Gaussian distributions for the velocity deficit in the wake.

where C_T is the thrust coefficient of the turbine, k_{wake} the rate of wake expansion, d_0 the diameter of the wind turbine, x the downwind location and $\Delta U/U_\infty$ the normalized velocity deficit defined by:

$$\frac{\Delta U}{U_\infty} = \frac{U_\infty - U_w}{U_\infty}, \tag{2}$$

where U_∞ is the incoming wind velocity and U_w the wake velocity in the streamwise direction. Katić *et al.* [3] also used the top-hat model proposed by Jensen [6]. They claimed that the top-hat model is to give an estimate of the energy content rather than to describe the velocity field accurately, and hence they considered a top-hat shape for the velocity deficit in the wake because of its simplicity and low computational cost. Nevertheless, note that the energy available in the wind varies as the cube of the wind speed [7], therefore an improper evaluation of velocity field in a wind farm can lead to large errors in the prediction of the extracted energy output. Eq. 1 has been extensively used in the literature (e.g., [8]) and commercial softwares such as WAsP, WindPRO [9], WindSim [10] and OpenWind. However, there are two important limitations of this simple model that should be pointed out: (a) Even though Jensen [6] and Katić *et al.* [3] claimed using momentum conservation to derive Eq. 1, it will be shown in Sect. 2 that in reality they only used mass conservation to derive their model. (b) The assumption of a top-hat distribution of the velocity is expected to underestimate the velocity deficit in the center of the wake, and overestimate it near the edge of the wake [11].

Later, Larsen [12] applied Prandtl's mixing length to a self-similar velocity profile and proposed a model for the velocity deficit in the wake. Barthelmie *et al.* [13] proposed an empirical model based on sodar measurements, but their model has a non-negligible departure from the experimental measurements [11]. Frandsen *et al.* [14] applied momentum conservation to a cylindrical control volume around the turbine and proposed the following expression for the

velocity deficit in the wake:

$$\frac{\Delta U}{U_\infty} = \frac{1}{2}\left(1 - \sqrt{1 - 2\frac{A_0}{A_w}C_T}\right), \tag{3}$$

where A_0 is the rotor area (area swept by the wind-turbine blades) and A_w the cross-sectional area of the wake. Although they employed the momentum equation, their model still assumed a top-hat shape for the velocity deficit in the wake. Ishihara *et al.* [15], based on experimental measurements, proposed a wake model assuming a Gaussian distribution for the velocity deficit in the wake. However, it has been found to overestimate the velocity deficit in the wake [16].

Different growth rates have been proposed for wind-turbine wakes. For instance, Vermeulen [17] stated that the wake growth rate is given by the added effects of the ambient turbulence and the turbulence created by the shear in the wake as well as the turbine itself, and proposed an empirical model for the wake expansion. Jensen [6] assumed that the wake growth rate is constant for usual wakes and is approximately 0.1. Frandsen [5] empirically established the wake growth rate as $k_{wake} = 0.5/ln(z_h/z_0)$, where z_0 is the surface roughness and z_h the turbine hub height.

The intention of the work described in this paper is to propose and validate a simple and efficient analytical model for the prediction of the velocity downwind of a stand-alone wind turbine. For this purpose, the velocity deficit in the wake is first assumed to have a top-hat shape and momentum and mass conservations are then applied to two common control volumes which have been previously used in the context of the analytical models. The results are then improved by considering a Gaussian distribution for the velocity deficit in the wake. The results are also tested against wind-tunnel measurements [11] and LES data [18]. Chamorro and Porté-Agel [11] investigated the wake of miniature wind turbines in a turbulent boundary flow over the range of $2 < x/d_0 < 20$ using hot-wire anemometry. Wu and Porté-Agel [18] used LES to investigate the same wake region and validated their results by comparing them with the experimental measurements reported by Chamorro and Porté-Agel [11].

In Section 2, mass and momentum equations are applied to two different control volumes, and then the model is developed by considering a Gaussian distribution for the velocity deficit in Sect. 3. The results are then presented and compared with wind-tunnel measurements and the LES data in Sect. 4. The summary and final discussion are presented in Sect. 5.

2 Governing Equations

As mentioned earlier, to apply mass and momentum conservation, the velocity deficit in the wake is first assumed to have a top-hat shape. Two different control volumes: one is downwind of the wind turbine, and the other is around the turbine are also considered (see fig. 2).

2.1 The control volume downwind of a wind turbine

Figure 2.a shows a schematic of the considered conical control volume with the left cross-sectional area (side 1) equal to A_0, the right cross-sectional area (side 3) equal to A_w and the

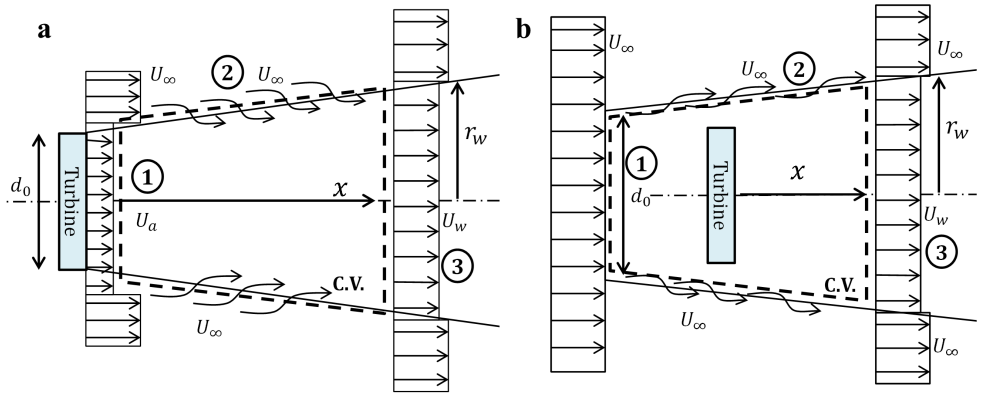

Figure 2: Schematic of the two considered control volumes: (a) downwind of the wind turbine, and (b) around the wind turbine.

horizontal axis in the streamwise direction. The incoming flow, U_∞, also enters through the lateral area of the control volume (side 2). According to mass conservation:

$$\dot{m}_2 = \rho U_w A_w - \rho U_a A_0, \tag{4}$$

where $\dot{m}_2$ is the mass flow rate through the lateral surface, ρ the density of the air and U_a the wind velocity just behind the wind turbine (see figure 2.a). Note that if $\dot{m}_2$ is replaced with $U_\infty(A_w - A_0)$ in mass conservation (Eq. 4), without considering momentum conservation, the basic equation that Jensen [6] used to establish his model will be obtained. It therefore implies that Jensen model can be derived by considering the mass conservation alone without any consideration of the balance of momentum.

Using the actuator disc concept, the wind velocity just behind the wind turbine can be written as: $U_a = U_\infty(1-a)$, where a is the induction factor defined as $a = (1/2)(1-\sqrt{1-C_T})$ [7]. Substituting U_a into Eq. 4 results in:

$$\dot{m}_2 = \rho U_w A_w - \rho U_\infty (1-a) A_0. \tag{5}$$

Balance of momentum in the streamwise direction gives:

$$\dot{m}_1 U_\infty (1-a) + \dot{m}_2 U_\infty = \dot{m}_3 U_w. \tag{6}$$

For sake of simplicity, the shear and pressure terms are neglected in the momentum equation. From Eqs. 5 and 6:

$$\rho A_w U_w (U_\infty - U_w) = \frac{1}{2} C_T \rho A_0 U_\infty^2. \tag{7}$$

It follows that:

$$\frac{\Delta U}{U_\infty} = 1 - \frac{U_w}{U_\infty} = \frac{1}{2}\left(1 - \sqrt{1 - \frac{2C_T}{(r_w/r_0)^2}}\right), \tag{8}$$

where r_0 is the radius of the turbine and r_w the wake radius. Eq. 8 states the normalized velocity

deficit as a function of C_T and the ratio of r_w/r_0. Although the considered control volume is similar to the one used by Jensen [6], the obtained formulation of the velocity deficit is different (compare Eq. 1 with Eq. 8). This difference is due to the fact that the Jensen's model derivation is based on mass conservation, unlike the new model that satisfies both mass and momentum conservations.

2.2 The control volume around a wind turbine

The control volume around the wind turbine is considered in this subsection (see fig. 2.b). The left cross-sectional area of this conical control volume is located upwind of the wind turbine (side 1) and is equal to A_0 and the right cross-sectional area (side 3) is equal to A_w. The incoming flow, U_∞, also exits through the lateral area (side 2). According to mass conservation:

$$\dot{m}_2 = \rho U_\infty A_0 - \rho U_w A_w. \tag{9}$$

Momentum conservation in the streamwise direction gives:

$$\dot{m}_1 U_\infty - \dot{m}_2 U_\infty - \dot{m}_3 U_w = T, \tag{10}$$

where T is the total force over the wind turbine which can be determined by [7]:

$$T = \frac{1}{2} C_T \rho A_0 U_\infty^2. \tag{11}$$

For this control volume, the shear and pressure terms in the momentum conservation equation are also neglected. Note that this assumption is less controversial for this control volume in comparison to the previous one because, in contrast to the previous one, the left and right borders of this control volume can be located far from the turbine. Eqs. 9, 10 and 11 result in:

$$\rho A_w U_w (U_\infty - U_w) = \frac{1}{2} C_T \rho A_0 U_\infty^2. \tag{12}$$

Note that the obtained equation for the velocity deficit in the control volume around the wind turbine (Eq. 12) is similar to the one for the control volume downwind of the wind turbine (Eq. 7). Therefore, it can be suggested that if the same governing equations are employed, the results will be the same and regardless of different considered control volumes. In addition, by applying mass and momentum conservation to two control volumes, we reach to the same formulation as that proposed by Frandsen *et al.* [14] (compare Eq. 8 with Eq. 3) whereas, as mentioned in subsection 2.1, it is different with the Jensen model (Eq. 1).

3 Gaussian velocity deficit of the wake

Gaussian axisymmetric shape of velocity profiles in wind-turbine wakes has been observed in free-stream flows (e.g., [19]). For turbulent boundary layers, Chamorro and Porté-Agel [20] found that, even though the velocity distribution in wind-turbine wakes does not show axisymmetric behavior, the velocity deficit in the wake has an approximately Gaussian axisymmetric

shape. Therefore, the Gaussian distribution can be considered for the velocity deficit, regardless of incoming conditions.

Using the formulation of the velocity deficit, with the top-hat assumption, derived in the previous section, the normalised total mass flow deficit rate $\dot{m}(x)$ defined by:

$$\dot{m}(x) = \int_{-\infty}^{+\infty} \frac{\Delta U}{U_\infty}(x) \mathrm{d}A, \tag{13}$$

can be determined at each downwind location. Then, the model is improved by considering the Gaussian distribution for the velocity deficit in the wake. Fig. 1 shows a two-dimensional schematic of the Gaussian distribution in comparison to the top-hat distribution for the velocity deficit at an arbitrary downwind location. The normalized Gaussian velocity deficit is defined by:

$$\frac{U_\infty(z) - U_w(x,y,z)}{U_\infty(z)} = \frac{\Delta U}{U_\infty} = C(x) \left\{ \frac{1}{\sigma\sqrt{2\pi}} e^{-\frac{(z-z_h)^2}{2\sigma^2}} \right\} \left\{ \frac{1}{\sigma\sqrt{2\pi}} e^{-\frac{y^2}{2\sigma^2}} \right\}, \tag{14}$$

where the coefficient of $C(x)$ is a function of x, σ the standard deviation of the normalized velocity deficit at each x, z and y are vertical and spanwise directions, respectively. Note that σ is not associated with *turbulent velocity fluctuation* in this paper. As mentioned earlier, the relation between the Gaussian and top-hat distribution is that $\dot{m}(x)$ at each downwind location should be identical. According to Eq. 13, $\dot{m}(x)$ for the top-hat distribution is:

$$\dot{m}(x) = \int_{-\infty}^{+\infty}\int_{-\infty}^{+\infty} \frac{\Delta U}{U_\infty}(x)_{top-hat} \mathrm{d}z\mathrm{d}y = \pi {r_w}^2 \frac{\Delta U}{U_\infty}(x)_{top-hat}, \tag{15}$$

and also for the Gaussian distribution,

$$\begin{aligned} \dot{m}(x) &= \int_{-\infty}^{+\infty}\int_{-\infty}^{+\infty} \frac{\Delta U}{U_\infty}(x)_{Gauss} \mathrm{d}z\mathrm{d}y \\ &= \int_{-\infty}^{+\infty}\int_{-\infty}^{+\infty} C(x) \left\{ \frac{1}{\sigma\sqrt{2\pi}} e^{-\frac{(z-z_h)^2}{2\sigma^2}} \right\} \left\{ \frac{1}{\sigma\sqrt{2\pi}} e^{-\frac{y^2}{2\sigma^2}} \right\} \mathrm{d}z\mathrm{d}y = C(x). \end{aligned} \tag{16}$$

By equating Eqs. 15 and 16, it is concluded that:

$$C(x) = \pi {r_w}^2 \frac{\Delta U}{U_\infty}(x)_{top-hat}. \tag{17}$$

Inserting Eqs. 8 and 17 into Eq. 14 and arranging, yields:

$$\begin{aligned} \frac{\Delta U}{U_\infty} &= \frac{1}{4}\left(\frac{r_w}{\sigma}\right)^2 \left(1 - \sqrt{1 - \frac{2C_T}{(1+2k_{wake}x/d_0)^2}}\right) \\ &\quad \times \exp\left(\frac{-2(r_w/\sigma)^2}{(1+2k_{wake}x/d_0)^2} \left\{ \left(\frac{z-z_h}{d_0}\right)^2 + \left(\frac{y}{d_0}\right)^2 \right\}\right). \end{aligned} \tag{18}$$

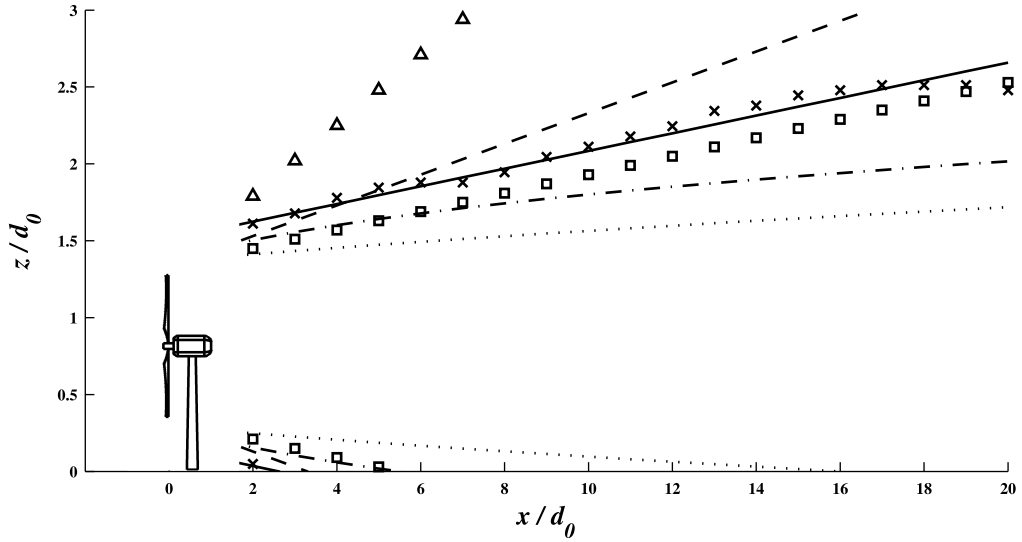

Figure 3: Normalized wake diameter versus normalized downwind distance: LES data [18] (*crosses*), fitted line for the LES data (*solid line*), Jensen model [6] (*dashed line*), Frandsen *et al.* (2006) model [14] (*dotted line*), Frandsen *et al.* (1992) model [5] (*square*), Vermeulen model [17] (*triangle*) and Larsen model [12] (*dashed-dotted line*).

Eq. 18 gives the normalized velocity deficit in the wake as a function of normalized coordinates ($x/d_0, y/d_0$ and z/d_0), C_T, r_w/r_0 and r_w/σ. In order to use the above equation, two unknown parameters: the wake expansion rate, $k_{wake} = \partial r_w/\partial x$, and the ratio of the wake radius over the standard deviation of the velocity deficit, r_w/σ, should be initially determined.

The following shows that the self-similarity of the wake implies that the ratio of r_w/σ is constant throughout the wake. As Johansson *et al.* [21] stated, there may be different levels of self-similarity in the wake, but this paper only corresponds to the self-similarity in mean velocities and is not related to the similarity in the turbulent fluctuation scales. The profile of the scaled velocity, $f(\xi)$, is defined by:

$$f(\xi) = \frac{U_\infty - U_w(x,r,0)}{U_\infty - U_w(x,0,0)}, \tag{19}$$

where $U(x,r,\theta)$ is the velocity in cylindrical coordinates and $\xi = r/r_w$. In self-similar wakes, this scaled velocity is believed to collapse to a single curve for different downwind locations. According to Eqs. 18 and 19, the scaled velocity corresponding to the proposed model is:

$$f(\xi) = e^{-0.5\xi^2(r_w/\sigma)^2}. \tag{20}$$

As mentioned above, $f(\xi)$ should be regardless of the downwind location in self-similar wakes. As a result, Eq. 20 points out that the ratio of r_w/σ should be constant over self-similar wakes. On the other hand, it is widely accepted that the majority of far wake regions satisfy the self-similarity in mean velocities [21], and thus, the ratio of r_w/σ, hereafter called β, can be assumed

to be constant for the wake region behind wind turbines. Comparison between the result obtained from Eq. 18 and the LES data reported by Wu and Porté-Agel [18] shows that $\beta = 2.5$ yields the best results.

It is important to note that it is not mathematically possible to define the wake radius, r_w, for a Gaussian distribution. One possibility is to define it as the radius at which the variation of the velocity along the radial direction becomes smaller than a certain threshold. Since the definition for r_w is not clear, the variation of σ instead of r_w will be used to evaluate k_{wake} in this paper. In a Gaussian distribution, σ can also be determined by:

$$\sigma^2 = \frac{1}{U_\infty - U_w(x,0,0)} \int_0^\infty (U_\infty - U_w) r dr. \tag{21}$$

In the literature, Eq. 21 has been used to determine the transverse length scale for bluff body wakes [21]. We define k^* as $k^* = \partial\sigma/\partial x$, and thus, with assuming self-similarity of the wake, $k_{wake} = \beta k^*$. In contrast to r_w, the magnitude of σ at each downwind location can be easily determined for Gaussian distributions.

In the following, the wake expansion behind the wind turbine for the different wake models as well as the LES data [18] is shown. As mentioned earlier, Wu and Porté-Agel [18] validated their LES results by comparing them with the experimental measurements reported by Chamorro and Porté-Agel [11]. The considered wind turbine has a hub height $z_h = 0.125$ m and a diameter $d_0 = 0.150$ m. The surface roughness length is $z_0 = 0.03$ mm and the ambient turbulence intensity at hub height approximately 0.07. If the inflow velocity at the hub height is 2.2 ms^{-1}, the thrust coefficient of the wind turbine, C_T, will be approximately 0.42. In order to find the value of the wake expansion rate $k_{wake} = \partial r_w/\partial x$ for the LES data, first $k^* = \partial\sigma/\partial x$ is determined by fitting Gaussian curves to the velocity-deficit profiles downwind the turbine, and then k_{wake} is estimated by multiplying k^* by β. As shown in the fig. 3, the wake approximately expands linearly in the considered range of x/d_0 for the LES data [18], and k_{wake} is approximately constant and equal to 0.058. The model proposed by Frandsen [5], $k_{wake} = 0.5/ln(z_h/z_0)$, is in acceptable agreement with the LES data, however, note that this model may not be useful for a large wind farm because in this case, the dominant factor in the wake expansion inside the wind farm is likely the turbulence produced by upwind turbines. The figure also shows that the Jensen model overestimates the wake growth rate. This error is probably due to the assumption of a constant value for the wake growth rate in Jensen model, whereas in the wake region, the turbulence created by the wind turbine, a function of C_T, seemingly increases mixing and the wake growth rate as a consequence. Thus, the wake growth rate for a miniature wind turbine, with a relatively small C_T compared with large scale wind turbines, is overestimated by Jensen model. Even though the empirical formulation established by Vermeulen [17], accounts for the effects of turbulence created by the wind turbine, it dramatically overestimates the wake growth rate. Finally, the models proposed by Larsen [12] and Frandsen *et al.* [14] underestimate the wake growth.

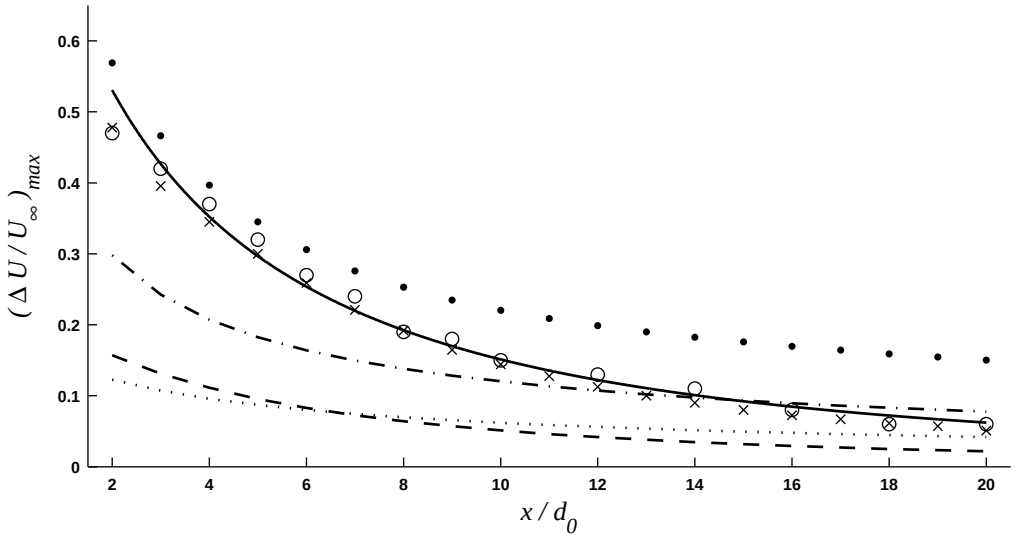

Figure 4: Normalized velocity deficit, at hub height, versus normalized downwind distance: wind-tunnel measurements [11] (*open circle*), LES data [18] (*crosses*), new proposed model (*solid line*), Jensen model [6] (*dashed line*), Frandsen *et al.* (2006) model [14] (*dotted line*), Larsen model [12] (*dashed-dotted line*) and Ishihara model [15] (*solid circle*).

4 Results

In this section, the results obtained by our proposed and previous models are compared with the high-resolution wind-tunnel measurements by Chamorro and Porté-Agel [11] and LES data by Wu and Porté-Agel [18]. The variation of normalized mean velocity, at turbine hub height, as a function of normalized downwind distance for different analytical models, the wind-tunnel measurements and LES data is displayed in fig. 4. The figure shows that there is a non-negligible difference between the model proposed by Jensen [6] and the measurements at distances $x/d_0 < 20$. This departure is arguably originated from: (a) assuming a uniform velocity distribution in the wake which leads to the observed underestimation at the center of the wake (where the maximum velocity deficit is found), and (b) not satisfying momentum conservation. The model proposed by Frandsen *et al.* [14] also underestimates the velocity deficit dramatically at turbine hub height. In addition to the top-hat assumption for the velocity deficit, the failure of their model could be partially attributed to assumed nonlinear expansion for the wake which is, as described in Sect. 3, not in agreement with the LES data at distances $x/d_0 < 20$. The model proposed by Larsen [12] also clearly underestimates the velocity deficit at distances $x/d_0 < 14$, and the model proposed by Ishihara *et al.* [15] slightly overpredicts the velocity deficit in the near-wake region ($x/d < 5$), but this overprediction increases with increasing downwind distance. This observed overprediction is in agreement with previously reported results [16]. Note that, as discussed earlier, a small difference in the velocity deficit between the predicted results and experimental measurements can lead to large errors in the power output predictions. On the other hand, the velocity deficit at hub height proposed by our model is in good agreement with the experimental and LES data at all distances.

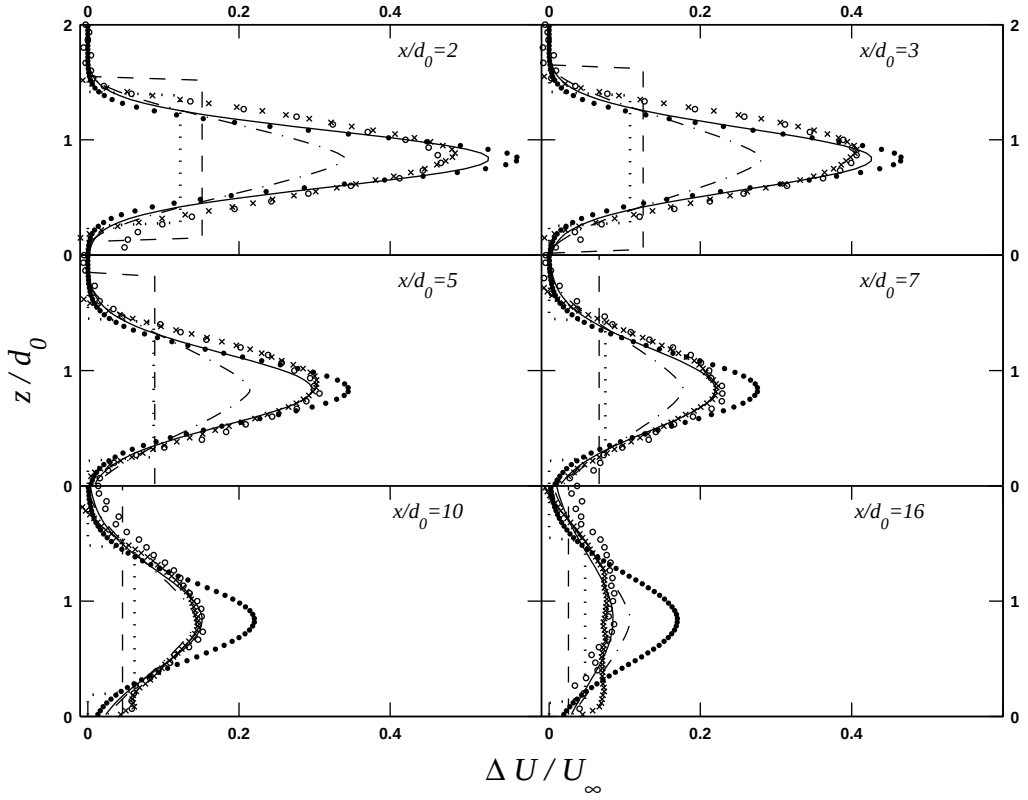

Figure 5: Comparison of vertical profiles of the streamwise velocity: wind-tunnel measurements [11] (*open circle*), LES data [18] (*crosses*), new proposed model (*solid line*), Jensen model [6] (*dashed line*), Frandsen *et al.* (2006) model [14] (*dotted line*), Larsen model [12] (*dashed-dotted line*) and Ishihara model [15] (*solid circle*).

The vertical profiles of streamwise velocity for the different models, the experimental measurements [11] and the LES data [18] on chosen downwind locations $(x/d = 2,3,5,7,10,16)$ are shown in fig. 5. The figure shows that the results obtained with our simple model for the velocity deficit in the wake (Eq. 18) are in acceptable agreement with both experimental and LES data. Figure 5 also shows that the model proposed by Larsen [12] clearly underestimates the velocity deficit and the empirical model proposed by Ishihara *et al.* [15] overepredicts it for $x/d = 5,7,10,16$. Furthermore, the top-hat models, proposed by Jensen [6] and Frandsen *et al.* [14], not only do clearly underestimate the velocity deficit at hub height but also overestimate it near the edge of the wake.

5 Summary

A new analytical model is proposed to model the deficit of the streamwise velocity in the wake of a stand-alone wind turbine. For this purpose, mass and momentum conservations are applied to two different control volumes: (a) downwind of the wind turbine, and (b) around the wind

turbine. A top-hat distribution for the velocity deficit in the wake is initially assumed to evaluate the total mass flow deficit rate downwind of the wind turbine, and then the analytical model is formulated by considering a Gaussian distribution for the velocity deficit. Finally, the velocity deficit in the wake can be computed as:

$$\frac{\Delta U}{U_\infty} = \frac{1}{4}\beta^2\left(1-\sqrt{1-\frac{2C_T}{(1+2\beta k^* x/d_0)^2}}\right) \times \exp\left(\frac{-2\beta^2}{(1+2\beta k^* x/d_0)^2}\left\{\left(\frac{z-z_h}{d_0}\right)^2+\left(\frac{y}{d_0}\right)^2\right\}\right), \quad (22)$$

where $\beta = 2.5$ and $k^* = \partial\sigma/\partial x$.

The comparison with the high-resolution wind-tunnel measurements [11] and LES data [18] shows that the velocity profiles obtained with the proposed model are in acceptable agreement with experimental and LES data. By contrast, the top-hat models, as expected, clearly underestimate the velocity deficit at the center of the wake and overestimate it near the edge of the wake. In addition, the model proposed by Ishihara *et al.* [15] typically overestimates the velocity deficit, and the one proposed by Larsen [12] clearly underestimates the velocity deficit at distances $x/d_0 < 14$. Our results also reveal that, although Jensen [6] and Katić *et al.* [3] claimed using momentum conservation to derive their well-known model, they only used mass conservation to derive their model.

Future research will consider the effect of inflow conditions such as incoming velocity profile and ambient turbulence intensity on the wake expansion parameter, k^*. For this purpose, other experimental and numerical datasets obtained for a range of surface cover types and atmospheric stabilities will be used. In addition, the proposed analytical model will be improved to evaluate velocity profiles inside wind farms for different farm layout configurations and inflow conditions.

REFERENCES

[1] L. Vermeer, J. Sørensen, and A. Crespo, "Wind turbine wake aerodynamics", Progress in Aerospace Sciences, vol.2 (1999) pp. 1-24.

[2] A. Crespo, J. Hernandez, and S. Frandsen, "Survey of modelling methods for wind turbine wakes and wind farms", Wind Energy, vol.136 (2010) pp. 515-533.

[3] I. Katić, J. Højstrup, and N. Jensen, "A simple model for cluster efficiency", in Proceedings of the European wind energy association conference and exhibition (1986) pp. 407-409.

[4] C. T. Kiranoudis and Z. B. Maroulis, "Effective short-cut modelling of wind park efciency", Renewable Energy, vol.11 (1997) pp. 439-457.

[5] S. Frandsen, "On the wind speed reduction in the center of large clusters of wind turbines", J. Wind Engng. Ind. Aerodyn., vol.39 (1992) pp. 251-256.

[6] N. Jensen, "A note on wind turbine interaction", Tech. Rep. Ris-M-2411, Risoe National Laboratory, Roskilde, Denmark, (1983) 16 pp.

[7] T. Burton, D. Sharpe, N. Jenkins, and E. Bossanyi, "Wind energy handbook", Wiley, 1st ed. (1995).

[8] G. Marmidis, S. Lazarou, and E. Pyrgioti, "Optimal placement of wind turbines in a wind park using monte carlo simulation", Renewable Energy, vol.33 (2008) pp. 1455-1460.

[9] M. L. Thøgersen, "Wind pro / park: Introduction to wind turbine wake modelling and wake generated turbulence", tech. rep., EMD International A/S, Niels Jernes Vej 10, DK-9220 Aalborg, Denmark (2010).

[10] G. Crastoa, A. Gravdahla, F. Castellanib, and E. Piccionib, "Wake modeling with the actuator disc concept", Energy Procedia., vol.24 (2012) pp. 385-392.

[11] L.P. Chamorro, F. Porté-Agel, "Effects of thermal stability and incoming boundary-layer flow characteristics on wind-turbine wakes: a wind-tunnel study", Boundary-Layer Meteorol, vol.136 (2010) pp. 515-533.

[12] G. C. Larsen, "A simple wake calculation procedure", tech. rep., Risø Natinal Laboratory, DK-4000 Roskilde, Denmark, December (1988).

[13] R. Barthelmie, G. Larsen, S. Pryor, H. Jorgensen, H. Bergstrom, W. Schlez, K. Rados, B. Lange, P. Volund, S. Neckelmann, S. Mogensen, G. Schepers, T. Hegberg, L. Folkerts, and M. Magnusson, "Endow (efcient development of offshore wind farms): modelling wake and boundary layer interactions", Wind Energy, vol.7 (2004) pp. 225-245.

[14] S. Frandsen, R. Barthelmie, S. Pryor, O. Rathmann, S. Larsen, J. Højstrup, and M. Thøgersen, "Analytical modelling of wind speed deficit in large offshore wind farms", Wind Energ, vol.9 (2006) pp. pp. 39-53.

[15] T. Ishihara, A. Yamaguchi, and Y. Fujino, "Development of a new wake model based on a wind tunnel experiment", in Global Wind Power (2004).

[16] A. R. Gravdahl, G. Crastoa, F. Castellani, and E. Piccioni, "Wake modeling with the actuator disc concept", tech. rep., WindSim (2012).

[17] P. E. J. Vermeulen, "An experimental analysis of wind turbine wakes", in 3rd Int. Symp. on Wind Energy Systems, (Lyngby) (1980) pp. 431-450.

[18] Y.T. Wu, F. Porté-Agel, "Large-eddy simulation of wind-turbine wakes: Evaluation of turbine parametrisations", Boundary-Layer Meteorol, vol.138 (2011) pp. 345-366.

[19] D. Medici and P. Alfredsson, "Measurement on a wind turbine wake: 3d effects and bluff body vortex shedding", Wind Energ., vol.9 (2006) pp. 219–236.

[20] L. Chamorro and F. Porté-Agel, "A wind-tunnel investigation of wind-turbine wakes: boundary-layer turbulence effects", Boundary-Layer Meteorol., vol.132 (2009) pp. 129–149.

[21] P. Johansson, W. George, and M. Gourlay, "Equilibrium similarity, effects of initial conditions and local Reynolds number on the axisymmetric wake", Phys. Fluids., vol.15 (2003) pp. 603-617.

CONSTRUCTION AND VALIDATION OF A NEW OFFSHORE WAKE MODEL

N. G. Nygaard, L. E. Jensen, R. Downey, M. Méchali

DONG Energy, Kraftværksvej 53, 7000 Fredericia, Denmark, nicny@dongenergy.dk

ABSTRACT

We present an empirical model for wakes in an offshore wind farm. By analyzing SCADA data from three wind farms we identify universal trends of isolated, single wakes. By incorporating a simple procedure for wake overlaps we construct a wind farm model. The predictive capability of our model is tested through blind validation studies of power ratios along transects and wind farm efficiency using data from three separate wind farms that were not used in deriving the model.

INTRODUCTION

Notwithstanding 20 years of offshore wind farming many aspects of wakes remain unresolved. Since wakes account for the single largest source of losses in an offshore wind farm, it is critical to accurately account for their influence on production. This becomes ever more prescient as wind farms increase in size and are clustered closely together. Models that accurately account for the wake effect are thus necessary to reduce the uncertainty of energy production estimates and optimize wind farm layouts. Several different wake models are presently used in the wind energy industry [1–13]. They can be roughly divided into two categories. One group of models attempt a faithful representation of the physical flow properties either based on the Reynolds-averaged Navier-Stokes equations [7,8] or Large-Eddy simulations [9,10]. While such models based on Computational Fluid Dynamics (CFD) are in principle very accurate, they are computationally intensive and may require significant effort to implement and use. The other class consists of engineering wake models based either on conservation laws coupled with assumptions about the wake expansion [3–6] or simplification of the fundamental flow equations [11,12]. Wake models that represent the wind farm as distributed roughness elements also fall in this category [5,13]. Engineering models are highly efficient in terms of computational resources, but since they do not include all of the physics, they are not guaranteed to be universally applicable. Both types of wake models are validated by comparing them with production data from operational wind farms [2,14–16].

In this work we construct a new model for offshore wakes based on a bottom-up approach of modeling single, isolated wakes. As offshore wind energy is becoming a mature industry, the amount of data gathered on wakes in offshore wind farms has reached a critical mass. We can now begin to compare wake characteristics across several wind farms with different sizes and turbine types, and in different locations. We base our model on more than 10 years of data from a range of DONG Energy's operational offshore wind farms, allowing us to identify the universal wake characteristics. To combine the effect of multiple wakes and thus model an entire wind farm we rely on the Kátic wake addition formula, which is of common use in the industry [4]. Our DONG Energy Wake Model (DEWaM) is subsequently validated against data from wind farms that have not been used in the model development.

MODEL INPUTS

The model we present here is based on analysis of 10 minute SCADA data from three offshore wind farms, see Figure 1. Barrow Offshore Wind Farm and Burbo Bank Offshore Wind Farm are located in the Irish Sea, while the third, Horns Rev 2, is off the Danish coast in the North Sea. To isolate production loses due to wakes the data are quality-filtered by excluding events where the turbine is unavailable or curtailed.

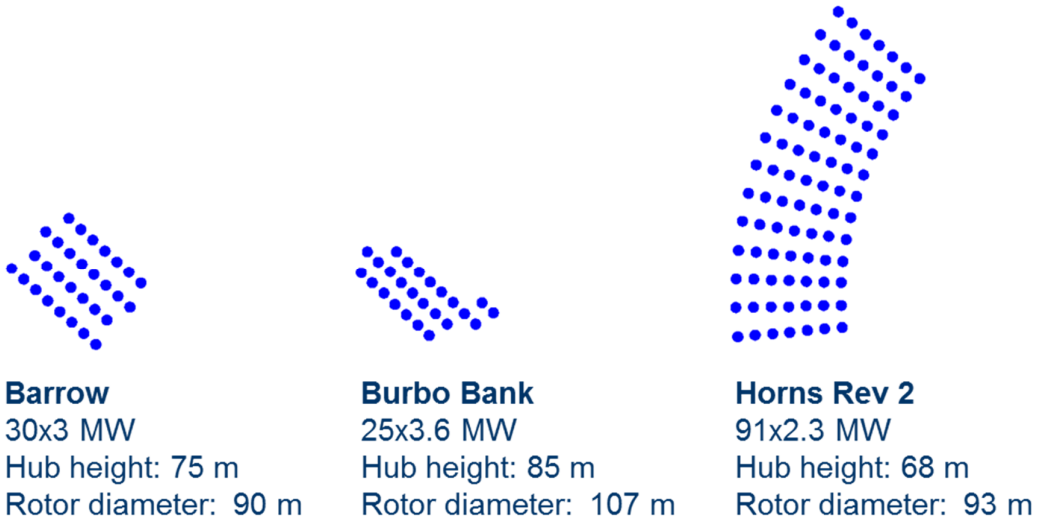

Figure 1: The three wind farms included in the modeling.

Due to the high cost of offshore meteorological masts onsite wind measurements are often not available. In that case, the meteorological variables that govern the wake behavior must be deduced from the turbine production data as discussed in the following. For consistency we have used this approach to specify the input parameters for the wake model in all the cases we consider in this paper. We have validated the methods presented below for cases with independent on-site wind measurements. From the analysis of the SCADA data we derive the free stream wind speed, the wind direction and the ambient turbulence intensity. This set of input parameters is not comprehensive and could neglect other environmental factors that influence the wakes.

Wind speed

The wind speed is derived from the turbine power production and the inverse power curve. The latter is corrected for non-standard air density, based on temperature measurements on the nacelle. However this procedure can only be used for wind speeds below the rated speed of the turbine, where a one-to one relation exists between wind speed and power. Results shown in this paper will therefore be limited to this range of wind speeds.

Wind direction

To derive the wind direction we calculate the mean yaw direction sensor signals of all the turbines in the wind farm. The turbine yaw signals exhibit significant scatter, since they are referenced to a point on the tower, which is set manually for each turbine. In addition, the yaw signals are affected by

turbine shut-down and start-up events. As a consequence the average yaw direction differs from the true wind direction by a time-dependent offset. To get a reliable wind direction we need to calibrate the mean yaw direction. Hence we consider the power deficit $\eta = 1 - P_2/P_1$ between two reference turbines on the edge of the wind farm [17]. The deficit profile as a function of the wind direction will be peaked at the direction between the two turbines. By fitting the deficit profile with a Gaussian we find the peak position offset angle, which is then used to correct the wind direction. To account for the time-dependence of the offset this calibration is performed in a moving time window. We have observed offsets ranging from -12° to 14°, which underscores the relevance of the wind direction calibration.

Turbulence intensity

The turbulence intensity is estimated from the approximate relation between the standard deviation of the power production σ_P, the 10-minute average wind speed u, and the 1st derivative of the power curve:

$$I \approx \frac{\sigma_P}{Bu\frac{dP}{dU}} \tag{1}$$

The constant B compensates for the averaging of the small scale fluctuations over the rotor area. In accordance with the recommendations in the literature we use a value of 0.8 for B [14,18]. This method relies on a Taylor expansion of the power curve and fails when the wind speed approaches the rated speed from below, since the derivative of the power curve approaches zero. In light of this limitation we have restricted the analysis to wind speeds between 4 m/s and 11 m/s. Of the three input variables derived from the turbine SCADA data the turbulence intensity is the least accurate, but we have confirmed that it has a reasonable correlation with the turbulence measured by a mast mounted anemometer.

Free stream turbines

For the best estimate of the undisturbed wind upstream of the wind farm we identify the turbines not affected by wakes. This is done for each wind direction by calculating the wake geometry assuming a linear wake expansion. To be conservative and reduce sensitivity to any calibration errors in the wind direction we use an extraordinarily large waked sector of 35° behind each turbine. Having identified the free stream turbines we find the free wind speed and ambient turbulence intensity by averaging their derived wind speeds and turbulence intensities, respectively. However, there is significant spatial variation of the wind speed among the free stream turbines, indicating that the presence of a large wind farm disturbs the inflow, making it heterogeneous. Similar results have been reported for the Nysted and Horns Rev 1 offshore wind farms [19,20].

METHODOLOGY

Our wake model is constructed in two steps. First we analyse and model the isolated, single wakes generated at the upstream edge of the wind farm. For each of the three analyzed wind farm we identify all single-wake pairs. These are pairs of turbines, where the downstream turbine is only in the wake of a single upstream partner facing the free wind. We use a conservative, linear wake expansion to calculate the wake geometry for all wind directions corresponding to distinct headings between pairs of turbines in the layout. For those directions we identify the downwind turbines that are only in the wake of a single upwind partner. The large value of the wake decay parameter ensures that the width

of the wakes is overestimated, and we assume that this allows us to single out pairs of turbines, where the wake profile is isolated and not overlapping with the wakes from other turbines (see below). Using this method we identify a total of 267 single-wake pairs across the three wind farms. These represent distances between the constituent turbines in the pairs ranging from $5.2D$ to $17D$, where D is the rotor diameter.

In the second step we model the complex flow of overlapping wakes in the interior of the wind farm by combining single wakes. Using the industry standard approach by Kátic *et al* [4], the wake deficits are calculated independently and subsequently added in quadrature.

Single-wake wind speed deficit profile

If the derived wind speed at the upwind turbine is u_1 and the wind speed at the waked turbine is u_2 the wind speed deficit is defined as

$$\delta = 1 - \frac{u_2}{u_1} \tag{2}$$

Note that the heterogeneity of the inflow is accounted for explicitly, as we define the wind speed deficit with respect to the wind speed at the upstream turbine initiating the wake, not the averaged free wind speed.

A typical plot of the wind speed deficit profile is shown in Figure 2, where the wind direction has been converted into the lateral displacement from the wake centerline. The isolated central peak demonstrates that our method has identified a single-wake pair, since the deficit profile is well separated from deficits originating from other upwind turbines, marked by the satellite peaks to the left and right. To smoothe the data we average them in a moving 5° window.

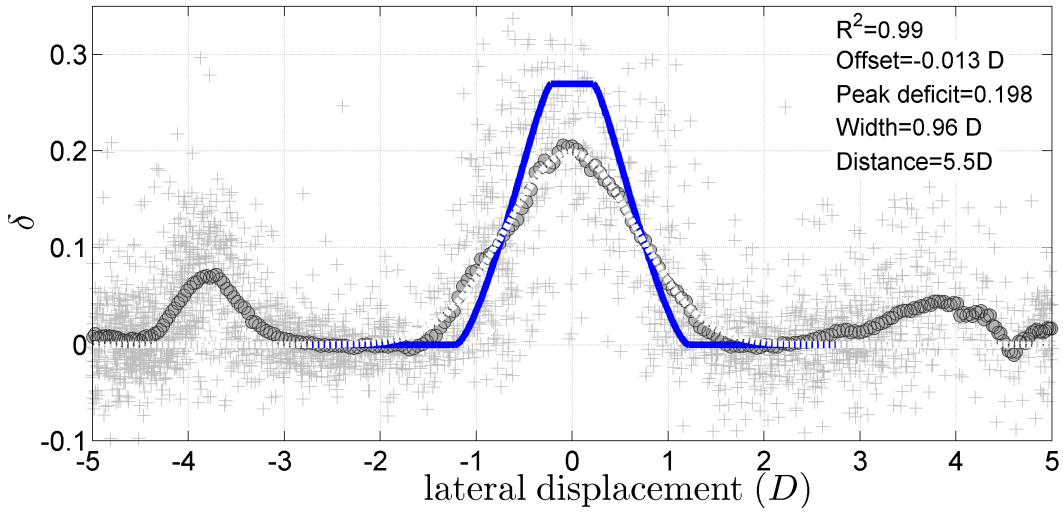

Figure 2: Wake profile for a pair of turbines in Barrow with a separation of $5.5D$. The faint grey plusses are the data, the filled circles indicated the averaged wind speed deficit, while the dashed line is a Gaussian fit. For comparison the Jensen model is plotted with the full line. The wind speed range is 7±0.5 m/s and the turbulence intensity lies between 4.5% and 9.5%. The fit parameters are given in the plot.

For each single-wake pair we assume a Gaussian profile for the wind speed deficit as a function of the wind direction, as predicted for a self-similar wake [21]:

$$\delta(x,y) = \delta_{\max} \exp\left[\frac{(y-y_0)^2}{\sigma^2}\right] \quad (3)$$

Here x and y are the separation of the turbines in the considered pair and the lateral displacement from the wake centerline, respectively. The wakes are then characterized by the height $\delta_{\max}$ and the width σ of the Gaussian fit, which represent the maximum wind speed deficit and a measure of the wake expansion, respectively. They both depend on the separation and on the flow case. The third parameter of the Gaussian fit is the offset of the peak position from zero y_0. Ideally, the offset of the deficit profile would be zero, but we find that a small residual offset remains even after the calibration of the wind direction. The size of this remaining offset is indicative of the uncertainty in our estimation of the wind direction. The expectation of a Gaussian profile for a self-similar wake in a free turbulent flow far from the wind turbine rotor is met by the generally high quality of the fits. For comparison the Jensen model profile (equation (8) in the appendix) is also plotted. The Jensen model overestimates the maximum deficit, while predicting a smaller wake width than supported by the data.

For each single-wake pair we analyze 91 different flow cases, representing different combinations of the free wind speed and the ambient turbulence intensity.

Single-wake model

Classic actuator disk theory predicts that the initial wind speed deficit directly behind the rotor is given by $1-\sqrt{1-C_T}$. To get the best possible description of the data it turns out to be useful to separate the dependence of the maximum deficit on the thrust coefficient from the direct dependence on the wind speed. Furthermore, similarity theory predicts that the relevant length scale for the variation of the maximum deficit is $\sqrt{C_T}D$ [21]. We thus consider a peak deficit of the form $\delta_{\max} = (1-\sqrt{1-C_T})F\left(u_\infty, x/\sqrt{C_T}D, I\right)$. Here F is a non-dimensional function of the free wind speed u_∞, the scaled position variable, and the ambient turbulence intensity. For the wake width the natural scaling parameter is the rotor diameter, since it determines the initial wake cross section.

We find that for all the flow cases considered the fundamental wake parameters exhibit universal behavior across the all three analyzed wind farms when properly scaled. This is illustrated in Figure 3 and demonstrates that the set of input parameters included here captures most of the natural variation of the wake properties.

The variation of the function F with distance on a log-log plot is nearly linear as illustrated in the top left panel in Figure 3, suggesting a power-law dependence of the maximum deficit on the downstream distance. The scaled peak deficit increases as the free wind speed is increased, see Figure 3 top right panel. The relationship is approximately linear. This observation is surprising, since in actuator disk theory the only influence of the wind speed is through the thrust coefficient and the size of the initial deficit. Specifically, the deficit increases in a wind speed range where the thrust coefficient is nearly constant.

The maximum wind speed deficit in the wake is observed to decrease slightly with increasing turbulence intensity (not shown). This reflects the more efficient mixing of the wake with the outside flow field as the turbulence level increases. The variation is consistent with the linear relationship found in previous offshore studies [19,22].

These observations lead us to investigate the following the model for the maximum wind speed deficit in the wake:

$$\delta_{\max}(x, u_\infty) = (1 - \sqrt{1 - C_T})\,(a u_\infty + b)\left(\frac{x}{\sqrt{C_T} D}\right)^c \tag{4}$$

We determine the three model parameter s a, b, and c by a two-dimensional nonlinear least squares fit of the model to the data for each value of the turbulence intensity. The parameters then become functions of the turbulence intensity. With an R^2-value around 0.9 the model captures the variation of the data very well.

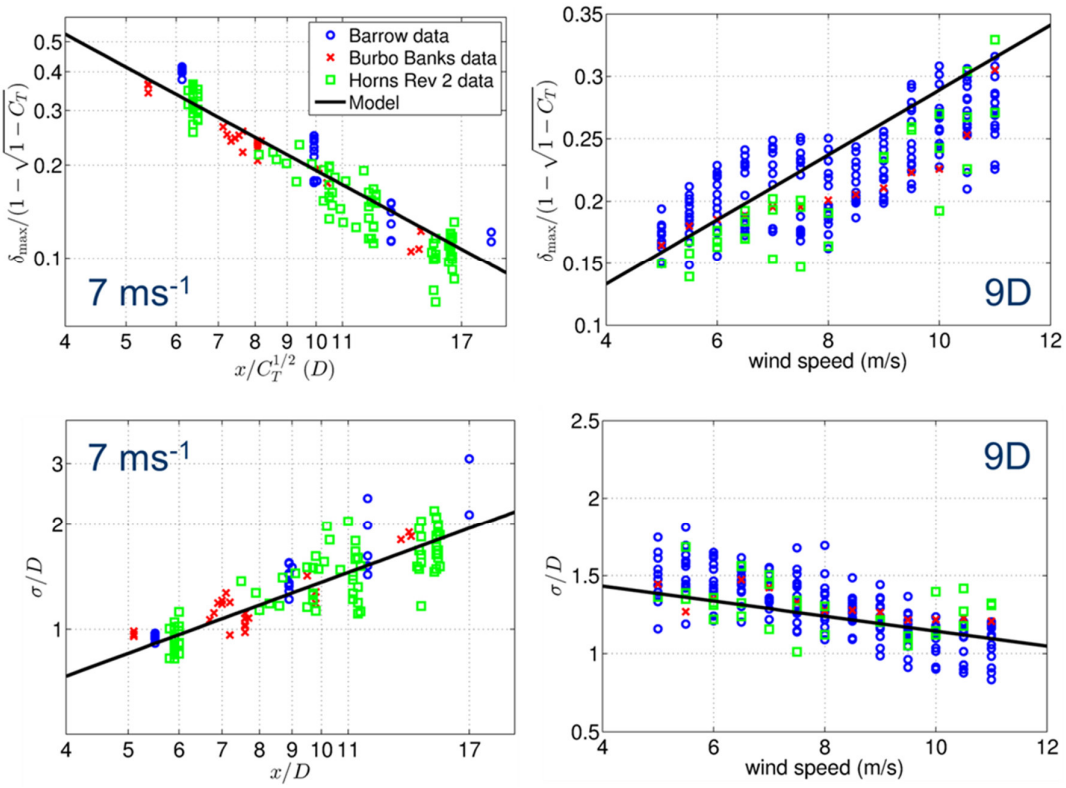

Figure 3: Scaled maximum deficit (top row) and wake width parameter (bottom row). The turbulence intensity is fixed at 5±2.5%. Left column: variation with separation at a fixed free wind speed of 7 m/s. Right column: variation with free stream wind speed for a fixed separation of 9*D*. The symbols represent data from the three analyzed wind farms, and the black solid line is the DEWaM single-wake model.

The width of the deficit profile scales roughly linearly with the distance on a log-log plot (Figure 3 bottom left panel). Hence the Gaussian width increases approximately as a power of the distance. On the other hand, the wake width decreases linearly with increasing wind speed (bottom right panel in Figure 3). We find that the turbulence intensity has very limited influence on the width of the wake.

With the behavior of the wake width parameter from the Gaussian fits we are led to a model description for the width of the form

$$\sigma(x, u_\infty) = (p + q u_\infty)\left(\frac{x}{D}\right)^s D \tag{5}$$

As for the maximum deficit the model parameters are determined by a surface fit at fixed ambient turbulence intensity. Due to a large variance of the wake width data, the quality of the model fit is

substantially smaller than for the maximum deficit. Hence there is a larger uncertainty associated with the three model parameters determining the width of the wake.

The resulting set of six parameters $\{a, b, c, p, q, s\}$ and their variation with turbulence intensity constitute our single-wake model DEWaM. In Figure 3 the DEWaM prediction is plotted with a solid line. Since the DEWaM parameters are derived from two-dimensional least squares fitting, they do not necessarily represent the optimal one-parametric regression in each of the four panels. Rather the model curves are cuts through the optimal fitting surfaces for the variation of the maximum deficit and the Gaussian wake width with distance and the free wind speed.

Wind farm model

The results presented above and the single-wake model derived from them characterizes the expansion of, and the wind speed recovery in, an isolated wake on the outskirts of the wind farm, in situations where interference from neighboring wakes is minimal. Inside the wind farm the flow is a complicated tangle of interacting wakes. The bottom-up philosophy behind a single-wake model is to treat the merging and overlapping wakes as independent, using a separate model for wake addition to derive the combined impact of multiple wakes on a turbine in the interior of the wind farm. In this work we adopt the wake addition procedure originally formulated by Kátic et al. [4]:

$$\delta_n = \sqrt{\sum_{k=1}^{n-1} \delta_{kn}^2} \tag{6}$$

For a given wind direction the turbines are sorted from the most upwind one to the one furthest downstream. At the nth downstream turbine the wind speed deficits δ_{kn} arising from all the $n-1$ turbines upstream are calculated *independently* with the single-wake model and combined in quadrature to produce the effective deficit.

VALIDATION OF DEWAM

The validation of a model against measured data is extremely important. A model is only useful insofar as its quality has been checked quantitatively and documented. Only then can we address the possible bias in the model and its inherent uncertainty.

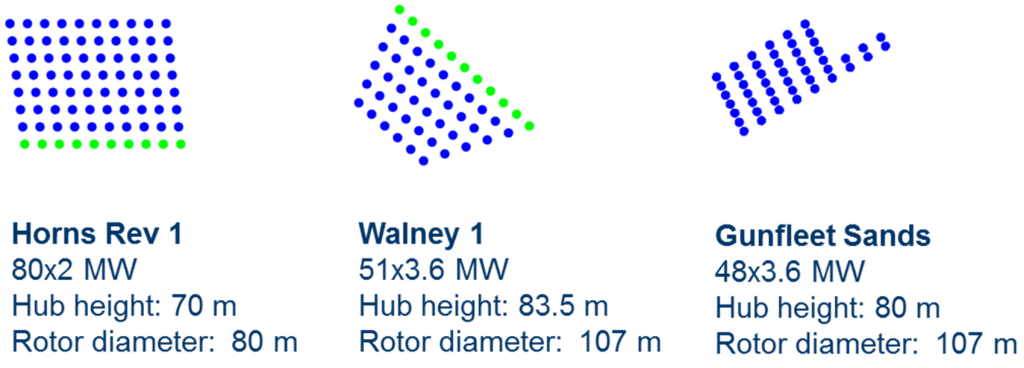

Figure 4: Wind farms used for the validation of DEWaM. The turbines used for the power ratio transect plots are marked in green.

The full validation of DEWaM is beyond the scope of this paper, and will be presented later. Here we merely illustrate the extent of the agreement between the model and data from three offshore wind farms. To ensure independence between the observations and our empirical model we use three wind farms that were not included in the modeling for this validation exercise. Horns Rev 1 is located west of Denmark in the North Sea, Walney 1 is in the Irish Sea, while Gunfleet Sands is situated in the Northern Thames Estuary.

When testing a model is important to align the validation procedure with the intended operational use of the model. Likewise the model evaluation should be set up to match as closely as possible the procedure used in preparing the data. These considerations inform the choices made when filtering the SCADA data and when running the model. In our case the intended use of DEWaM is energy yield calculations based on a statistical wind climate. Therefore the appropriate way to generate model results is to run the model for all wind directions with some resolution (here 1°) and average the results in wind direction sectors. The validation data are averaged using the same sectors. Since the eventual wind resource input to the model will include both periods with steady state flow conditions and events where the wind direction and/or the wind speed changes abruptly over the area of the prospective wind farm, no condition of flow stationarity has been imposed on the validation data.

For Horns Rev 1 and Walney 1 we present a comparison between the observed power ratio and model results from DEWaM for a transect corresponding to an exterior row of turbines in the wind farms. For wind directions along the transect line we anticipate that the turbines on the edge of the wind farm are the least affected by any errors in our wake addition approach, since the lateral merging with wakes from neighboring rows is less important here than in the interior of the wind farm. Hence we expect that the DEWaM prediction will be most accurate for the exterior turbines. The considered transects are marked in green in Figure 4.

For Horns Rev 1 the wind direction is 270°, in the case of Walney 1 the wind direction sector is centered on 132°. The sector size in both cases is 5°. We only include timestamps where all the turbines in the transect, and all turbines generating wakes affecting the transect, are fully operational, since turbines that are curtailed or shut down modify the wake experienced by the downstream in the transect. For the free wind speed we use the derived wind speed for front turbine in the row. The results presented in Figure 5 are for wind speeds between 8.5 m/s and 9.5 m/s. For each 10-minute timestamp the power ratio is calculated relative to the power of the first turbine in the transect. The results are then averaged in the chosen sector and wind speed bin. The error bars on the data indicate the 95% confidence interval on the mean values, meaning $1.96\sigma/\sqrt{M}$ where σ is the standard deviation of the M samples.

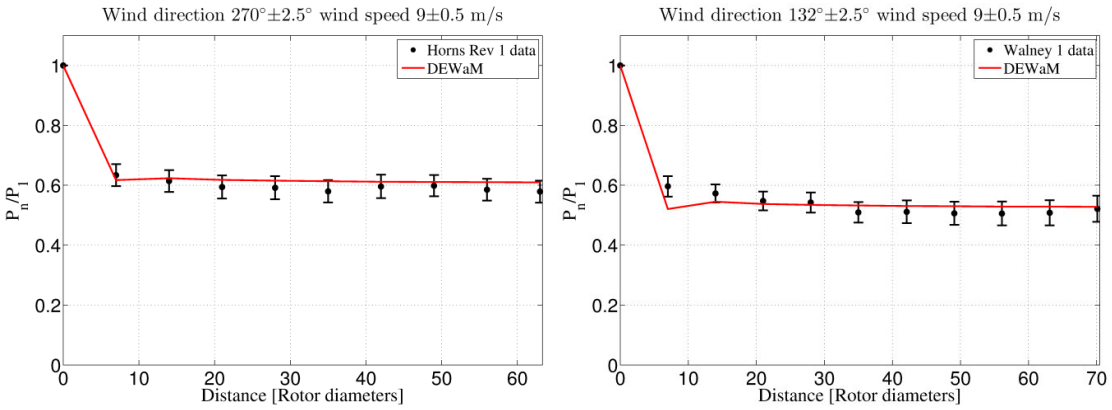

Figure 5: The power ratio along a transect. Left: Horns Rev 1 with the wind coming from the west. Right: Walney 1 with the wind direction from the south-east. The transects are highlighted in Figure 4.

DEWaM is run without any adjustable parameters with an input wind speed of 9 m/s for several wind directions in the chosen sector. The ambient turbulence intensity, which is an input to DEWaM, is found by averaging the derived turbulence at the first turbine in the transect. The predicted power ratios corresponding to the sampled wind directions are averaged for each turbine position.

The results for DEWaM are encouraging, especially since the wake addition has so far only been included in an ad-hoc manner.

The comparison for Gunfleet Sands is between the observed wind farm efficiency and that predicted by DEWaM. The wind farm efficiency is the ratio of the produced power to the free-stream power averaged over all the turbines:

$$e = \frac{1}{N}\sum_{n=1}^{N}\frac{P_n}{P_0} \tag{7}$$

For the measurements we allow up to 5% of the turbines to be unavailable to increase the data volume significantly. The number of turbines N is updated accordingly for each timestamp. Provided the unavailable turbines are distributed randomly through the wind farm the error introduced by this should not be large. To test our wake model we create an ensemble by calculating the predicted wind farm efficiency for every wind direction with a resolution of 1°. Both the measured and the modeled efficiencies are then averaged in wind direction sectors of 5°. Only data corresponding to a free wind speed of 9±0.5 m/s are included. In the modeling we assume a homogeneous inflow at 9 m/s and use the average measured ambient turbulence as input to DEWaM in each sector. The results are presented in Figure 6. DEWaM predicts the variations of the wind farm efficiency with wind direction with good accuracy.

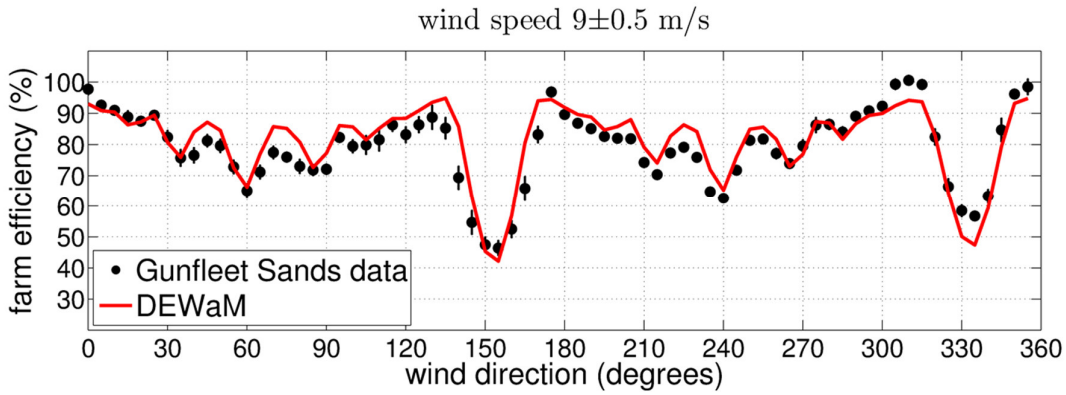

Figure 6: Wind farm efficiency for Gunfleet Sands. Data and model predictions are averaged in 5° wind direction sectors.

CONCLUSIONS

We have analyzed single-wake wind speed deficit profiles for a range of different flow cases and turbine separations. The deficit exhibits a universal dependence on the undisturbed wind speed upstream of the wind farm, the wind direction, and the ambient turbulence intensity. Based on this observation an empirical model for the propagation of single-wakes is possible, and the construction of our new wake model DEWaM is the main result of this paper. In DEWaM the wind speed deficit profile is Gaussian, and the wake width and centerline deficit are functions of the flow case and

distance the wake has travelled. To treat overlapping wakes we have implemented an industry standard approach for adding independent wakes. Our mathematical description of single-wakes together with a wake overlap method constitutes a model for the behavior of an entire wind farm.

We have tested the model in three validation cases based on datasets that were not included in the construction of the model. Both for power ratio along transects and for the wind farm efficiency as a function of the wind direction DEWaM shows promising results. A more extensive validation is underway.

DEWaM is still under development. As already mentioned wake addition has only been treated superficially by including a commonly used prescription for merging wakes. In future work we will analyze overlapping wakes in detail and extend the model to multiple-wake situations. Likewise, in its present form DEWaM neglects the influence of wake-added turbulence. An increased turbulence level accompanies the wind speed deficit in the wake, generated in the shear layer on the wake boundary. Increased turbulence intensity means a more efficient mixing with the high momentum air outside the wake and hence a faster decay of the wind speed deficit. At a later stage DEWaM will be extended to include this effect. The good agreement found between model predictions and observations at this stage is encouraging for future extensions of the model. Our results thus hold the potential to reduce the uncertainty of wind energy yield assessments. The implication for the planning and development of wind farm clusters is a reduced cost of energy.

REFERENCES

[1] Crespo A, Hernández J and Frandsen S 1999 Survey of Modelling Methods for Wind Turbine Wakes and Wind Farms *Wind Energy* **2** 1–24

[2] Barthelmie R J, Pryor S C, Frandsen S T, Hansen K S, Schepers J G, Rados K, Schlez W, Neubert A, Jensen L E and Neckelmann S 2010 Quantifying the Impact of Wind Turbine Wakes on Power Output at Offshore Wind Farms *Journal of Atmospheric and Oceanic Technology* **27** 1302–17

[3] Jensen N O 1983 *A Note on Wind Generator Interaction, Risø-M-2411*

[4] Kátic I, Højstrup J and Jensen N O 1986 A simple model for cluster efficiency *EWEA 1986*

[5] Frandsen S, Barthelmie R, Pryor S, Rathmann O and Larsen S 2006 Analytical Modelling of Wind Speed Deficit in Large Offshore Wind Farms *Wind Energy* **9** 39–53

[6] Rathmann O, Barthelmie R and Frandsen S Turbine Wake Model for Wind Resource Software *EWEC 2006*

[7] Westerhellweg A and Neumann T 2011 CFD simulations and measurements of wake effects at the alpha ventus offshore wind farm *EWEA Offshore* pp 1–9

[8] Montavon C, Hui S-Y, Graham J, Malins D, Housley P, Dahl E, De Villiers P and Gribben B 2011 OFFSHORE WIND ACCELERATOR: WAKE MODELLING USING CFD *EWEA* pp 1–10

[9] Calaf M, Meneveau C and Meyers J 2010 Large eddy simulation study of fully developed wind-turbine array boundary layers *Physics of Fluids* **22** 015110

[10] Wu Y-T and Porté-Agel F 2010 Large-Eddy Simulation of Wind-Turbine Wakes: Evaluation of Turbine Parametrisations *Boundary-Layer Meteorology* **138** 345–66

[11] Ainslie J F 1988 Calculating the flowfield in the wake of wind turbines *Journal of Wind Engineering and Industrial Aerodynamics* **27** 213–24

[12] Ott S 2011 Linearised CFD *Risø-I-3093(EN)* **3093**

[13] Emeis S 2010 A simple analytical wind park model considering atmospheric stability *Online* **13** 459–69

[14] Duckworth A and Barthelmie R J 2008 Investigation and Validation of Wind Turbine Wake Models *Wind Engineering* **32** 459–75

[15] Méchali M, Barthelmie R, Frandsen S, Jensen L and Réthoré P Wake effects at Horns Rev and their influence on energy pro- duction Data *EWEC 2006*

[16] Garza J, Blatt A and Gandoin R 2011 Evaluation of two novel wake models in offshore wind farms *EWEA Offshore*

[17] Réthoré P-E, Johansen N A, Frandsen S T, Barthelmie R, Hansen K S, Jensen L E and Bækgaard, Mikkel A.B. Kristoffersen J R 2009 Systematic wind farm measurement data reinforcement tool for wake model calibration *EOW Conference*

[18] Frandsen S, Chacón L, Crespo A, Enevoldsen P, Gómez-Elvira R, Hernández J, Manual F, Thomsen K and Sørensen P 1996 *Measurements and modelling offshore wind farms Risø-R-903 (EN)*

[19] Barthelmie R J and Jensen L E 2010 Evaluation of wind farm efficiency and wind turbine wakes at the Nysted offshore wind farm *Wind Energy* **13** 573–86

[20] Mitraszewski K, Nygaard N G, Hansen K S and Réthoré P-E 2012 Wall effects in offshore wind farms *The Science of Making Torque from Wind*

[21] Tennekes H and Lumley J L 1970 *A first course in turbulence* (Cambridge, Massachusetts: The MIT Press)

[22] Hansen K S, Barthelmie R J, Jensen L E and Sommer A 2012 The impact of turbulence intensity and atmospheric stability on power deficits due to wind turbine wakes at Horns Rev wind farm *Wind Energy* **15** 183–96

[23] Poulsen U V, Scholz J, Hedevang E, Cleve J and Greiner M 2012 Application of engineering wake models to data with high temporal resolution *submitted to Wind Energy*

APPENDIX: THE N. O. JENSEN MODEL

In the Jensen model a simple top-hat shape is adopted for the lateral wake profile. The wake diameter is assumed to increase linearly with the distance x from the upwind turbine: $D_w = D + 2kx$. Here k is the wake decay parameter, commonly set to 0.04 for offshore applications [2,19]. By balancing the momentum flowing into the wake at the rotor with that leaving through a vertical cross section at distance x, and using actuator disk theory to relate the initial deficit with the thrust coefficient, the wind speed deficit in the Jensen model becomes

$$\delta_{\mathrm{Jensen}}(x) = (1 - \sqrt{1 - C_T}) \left(\frac{1}{1 + 2k\frac{x}{D}} \right)^2 \frac{A_{\mathrm{overlap}}}{A_{\mathrm{rotor}}} \tag{8}$$

Our implementation the Jensen model includes a factor $A_{\mathrm{overlap}}/A_{\mathrm{rotor}}$ accounting for the partial overlap between the rotor area $A_{\mathrm{rotor}} = \pi D^2/4$ and the wake [6,23]. The area of overlap A_{overlap} decreases rapidly as the separation between the wake centerline and the center of the downstream rotor is increased by changing the wind direction.

BENCHMARKING OF WIND FARM SCALE WAKE MODELS IN THE EERA - DTOC PROJECT

P.-E. Réthoré[1], K.S. Hansen[1], R.J. Barthelmie[2], S.C. Pryor[2], G. Sieros[5], J. Prospathopoulos[5], J.M.L.M. Palma[4], V.C. Gomes[4], G. Schepers[3], P. Stuart[6], T. Young[6], J.S. Rodrigo[7], G.C. Larsen[1], T.J. Larsen[1], S. Ott[1], O. Rathmann[1], A. Peña[1], M. Gaumond[1] and C. B. Hasager[1]

[1]DTU, Wind Energy, Denmark, pire@dtu.dk
[2]Indiana University, Department of Geological Sciences, USA
[3]ECN, The Netherland, [4]University of Porto, Portugal
[5]CRES, Greece, [6]RES, United Kingdom, [7]CENER, Spain

ABSTRACT

Designing offshore wind farms next to existing or planned wind farm clusters has recently become a common practice in the North Sea. These types of projects face unprecedented challenges in term of wind energy siting. The currently ongoing European project FP7 EERA - DTOC (Design Tool for Offshore wind farm Clusters) is aiming at providing a new type of model work-flow to address this issue. The wake modeling part of the EERA - DTOC project is to improve the fundamental understanding of wind turbine wakes and modeling. One of these challenges is to create a new kind of wake modeling work-flow to combine wind farm (micro) and cluster (meso) scale wake models. For this purpose, a benchmark campaign is organized on the existing wind farm wake models available within the project, in order to identify which model would be the most appropriate for this coupling. A number of standardized wake cases for large offshore wind farms will be analyzed, which provide a reasonable range of conditions likely to be experienced in offshore wind farms. The systematic evaluation is based upon high - quality input data that is selected in the sister project IEA - Task 31 “WakeBench”.

INTRODUCTION

With the large offshore wind farms becoming common practice in Northern Europe, the need for reliable wind farm wake models has never been as critical as today. There exists many different

types of wind farm wake models that have been developed during the last three decades, some more complex than others. The wind industry is now to routinely calculating wind farms annual energy production (AEP) using more and more complex wind farm wake models. For instance, running non-linear Reynolds Averaged Navier-Stokes Computational Fluid Dynamics (CFD) actuator disc model has become practical for most medium size companies. In parallel, the amount data and understanding of the wind farm power production has increased significantly during the last 5 years.

The EERA-DTOC project (European Energy Research Alliance - Design Tool for Offshore wind farm Clusters) is focusing on providing a tool to design wind farm clusters, which is a combination of several offshore wind farms. An important element in this tool will be the wind farm annual production estimate, which will rely on one or several state of the art wind farm wake models. The different partners in the project have developed over the years many different offshore wind farm wake models that could be (one of) the potential candidate(s) to be implemented in the EERA-DTOC software. In order to select the right wake models a series of benchmarks are currently underway in collaboration with the IEA-Task 31 "WakeBench" project.

While previous offshore wind farm wake benchmark comparisons have been carried out during the past decade in the ENDOW project [19] and UpWind project [18], the new and refined models available for the industry combined with the better understanding and refined data of the wind farm SCADA make it relevant now to initiate a new benchmark based on the Horns Rev wind farm within the EERA-DTOC project.

This article will focus on presenting the different models with their specific sub-model assumptions, the Horns Rev wind farm, the challenges of creating a reliable reference dataset for the comparison with the wind farm wake models, the different test cases and finally a discussion of the results.

WAKE MODELS

The wind farm wake models present in the EERA-DTOC project are presented in tb. 1.

- **SCADA** is the processed wind farm data to be compared with the other wind farm wake models. Wind farm SCADA data are not usually referred in the literature as a model result. However, considering the amount of assumptions and processing methods that have to be applied in order to produce comparable results with a wind farm wake model, a processed SCADA data should in all fairness be treated as a model result. This point is further detailed in the following section.

- **Ainslie** is an eddy-viscosity wake model developed by RES-LTD [5-6] based on the original Ainslie model [8].

- **FarmFlow** is a parabolized k-ε actuator disc CFD model tailored for offshore wake simulation developed by ECN, based on the original UPM wind farm wake model from Crespo [9] combined with a vortex wake model in the close wake.

- **RANS** is an elliptic k-ε actuator disc CFD model tailored for offshore wake simulation developed by Porto University.
- **CRESflowNS** is an elliptic k-ω actuator disc CFD model tailored for offshore wake simulation developed by CRES [13-14].
- **WAsP/NOJ** is the PARK wake model of WAsP commercial software developed by DTU [10] and based on the original wake model from N.O. Jensen [11].
- **NOJ** is the original N.O Jensen model [11], using the mozaic tile methode of Rathmann [21].
- **DWM** is the Dynamic Wake Meandering model developed by DTU [16-17]. This model is the only dynamic model presented in this paper.
- **GCL** is the G.C. Larsen eddy-viscosity wake model v2009 developed by DTU [15].
- **FUGA** is a linearized actuator disc eddy-viscosity CFD model for offshore wind farm wake developed by DTU [12].

The wind farm wake models compared in this work can be categorized in different ways according to their sub-model assumptions. The sub-models considered in this analysis are:

- Inflow model: How the inflow wind speed is described
  - Log law: The log law is used to create the inflow condition, based on the sea roughness, the hub height and hub wind speed.
  - Homogeneous: The inflow is assumed to be homogeneous. Only the hub wind speed is needed.
  - TI: The turbulence intensity is needed.
  - Stability: The inflow conditions are dependent of atmospheric parameters
  - Mann: The inflow is generated through the Mann turbulence model. It can also be tuned to generate different inflow stability conditions and turbulence intensities.
- Hub wind speed model: How the wind speeds generated by the wake model are combined into an input to the wind turbine model. Here the number of points are indicated as a reference for how the turbines take into account the inflow partial wakes. The NOJ model is using a mosaic tile approach, weighting the wake wind speed with the intersectional area between the rotor and the upstream wake deficits.
- Wind turbine model: How the power and thrust are calculated:
  - HAWC2 is an aero-elastic model developed at DTU [7]
  - PTC: The Power and Thrust coefficient Curves, that takes the free-stream wind speed as a reference. Note that an additional method is required when used in combination with an elliptic CFD code in order to estimate this free-stream wind speed in wake conditions. This additional method is not considered in the present analysis.

Table 1: Sub-models assumptions

Institute	Model Name	Inflow	Hub WS	Turbine	Wake acc	Wake flow
DTU WE	SCADA	Processed wind farm SCADA measurements				
DTU WE	FUGA	Log law	7P	PTC	Linear	FUGA
DTU WE	GCL	Log law+TI	16P	PTC	Linear	GCL
DTU WE	DWM	Mann	$>$ 100P	HAWC2	Max.	DWM
DTU WE	NOJ	Homog.	Mosaic	PTC	RSS	NOJ
Indiana Uni	WAsP/NOJ	Homog.	Mosaic	PTC	RSS	NOJ+GPR
RES-LTD	Ainslie	Homog.+TI	1P	PTC	ARL	Ainslie+GPR
CRES	CRESflowNS	Log law	1P	PTC	Elliptic k-ω	
Porto Uni	RANS	Log law	1P	PTC	Elliptic k-ε	
ECN WE	FarmFlow	Stability	1P	PTC	Vortex + Parabolic k-ε	

- Wake accumulation model: How the wake contributions are accumulated
  - Linear: add the velocity deficits.
  - RSS: Root-Sum-Square (i.e. Quadratic).
  - k-ω or k-ε : The accumulation is done by solving the Reynolds Averaged Navier-Stokes equations.
  - Maximum: The maximum wake deficit is used.
  - ARL: Average RSS and Linear velocity deficits.
- Wake flow model: How the wake of one or several wind turbines is calculated. Each model has a different way to solve the momentum and mass flow conservation equation and to account for the inflow and wake generated turbulence. The CFD type models account directly for the ground plane through the Navier-Stokes equations (i.e. FUGA, RANS, CRESflowNS, FarmFlow); some use a Ground Plane Reflection (GPR) method (i.e. Ainslie, WAsP/NOJ); finally, some do not account for the ground surface (i.e. NOJ, GCL and DWM).

DATA PRESENTATION AND ANALYSIS

Horns Rev Wind Farm

The Horns Rev wind farm (HR) has a shared ownership by Vattenfall AB (60%) and DONG Energy AS (40%). It is located 14 km from the west coast of Denmark, with a water depth of 6-14 m. The wind farm has a rated capacity of 160 MW comprising 80 wind turbines, which

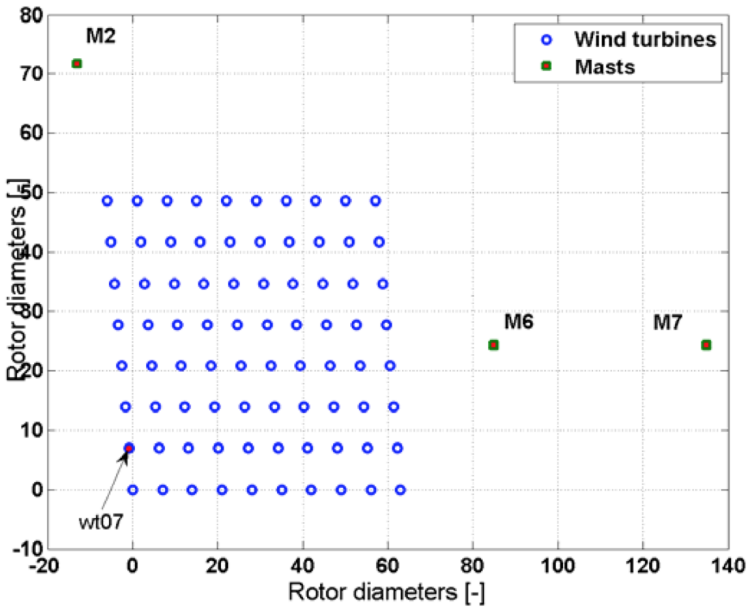

Figure 1: Horns Rev wind farm layout

are arranged in a regular array of 8 by 10 turbines, with a spacing of 560 m in both directions covering an area of 5x3.8 km2. The layout of the wind farm, fig. 1, is not completely rectangular, while the direction of the N-S columns is 353°. The wind turbines are installed with an internal spacing along the main directions of 7D. The diagonal wind turbine spacing is either 9.4 D or 10.4 D. Fig. 1 illustrates the location of the three offshore meteorological masts associated with the wind farm. Mast M2, with a height of 62m, was installed prior to the wind farm installation to document the wind conditions. Two identical masts M6 and M7 were installed as part of the Horns Rev wind farm wake measurements program with a height equal to the hub height of 70m. The wind farm comprises VESTAS V80 turbines, which are 2 MW pitch controlled, variable speed wind turbines with a diameter of 80 m and 70 m hub height. The wind farm has been in operation since 2004 and the SCADA statistics from 2005 – 2007 is available for the wake analysis [1].

The dataset for the current wake analysis was limited to three years, from 2005 to 2007, and includes the SCADA data from the 80 wind turbines and the two downstream wake masts (M6 & M7). Due to the local wind rose, the wake analysis shall be concentrated to westerly and easterly inflow sectors centered at 270° and 90° respectively. Because M6 & M7 are located inside the wind farm wake for the 270° sector, a flow reference has been establish based on wt07 (located in the most western row of the wind farm) in terms of wind speed derived from electrical power and wind direction derived from the calibrated wind turbine yaw position. For the western flow sector, the power curve of wt07 has been validated with wind speed measurements from M2, 62 m level [1]. None of the wind turbine yaw position sensors have been calibrated while these are not used in the wind turbine control, but the yaw position offset for wt07 has been calibrated

and found to be constant during the period, according to the guidelines in [2]. The estimated uncertainty of the wind direction is 5°. For the eastern flow sector, the measured wind speed and wind directions are recorded at 70 m level on either M6/M7.

Definition of power deficit

For westerly inflow, the power deficit is determined with respect to the reference wt07:

$$\text{Power Deficit} = \frac{P_{\text{wt07}} - P_{\text{wt}}}{P_{\text{wt07}}} \tag{1}$$

For easterly inflow, the power deficit is determined with respect to the reference wt95:

$$\text{Power Deficit} = \frac{P_{\text{wt95}} - P_{\text{wt}}}{P_{\text{wt95}}} \tag{2}$$

Definition of the error bars

In the plots presented in this article, the error bars on the SCADA plots are the standard uncertainty defined as

$$u = \frac{\sigma}{\sqrt{n}}, \tag{3}$$

with σ the standard deviation and n the number of 10-minute data points available for doing the averaging. Note that this value quantifies the level of confidence in the statistical representativity of the averaging, and not the amount of data spreading.

Data analysis

When looking at processed wind farm SCADA data it is quite important to keep in mind that it is the result of a number of assumptions and processing methods. For instance, fig. 2 illustrates the difference between three processing methods over the same test case: the single wake power deficit between two turbines (wt07 & wt17) in aligned in westerly inflow. All the curves are using the same data sample (2005-2009) but different wind direction sensors (the nacelle position of wind turbine wt07 (NP07) and the mast M7 wind vane), while the curve called we.512_ref is presenting the results using NP07 from another data sample, when the inflow wind was with stable stratification. The mast M7, as it can be seen in fig. 1 is located at more than 10km from the wind turbines wt07 and wt17. By using its wind vane as the sorting sensor, we make the assumption that the wind direction is the same over the distance of 10km. Because of the wind direction spatial/temporal variability, the further away the wind direction is measured, and the less likely this assumption is correct, which introduces an uncertainty in the wind direction correlated with the distance from the wind direction sensor to the wind turbine of interest. As discussed in [4], when considering ensemble average wake deficit data, an uncertainty in wind direction can have the same effect as introducing more partial wake and free wake cases into the ensemble average. So choosing M7 over a closer wind direction sensor, like NP07, gives an artificially lower wake maximum deficit.

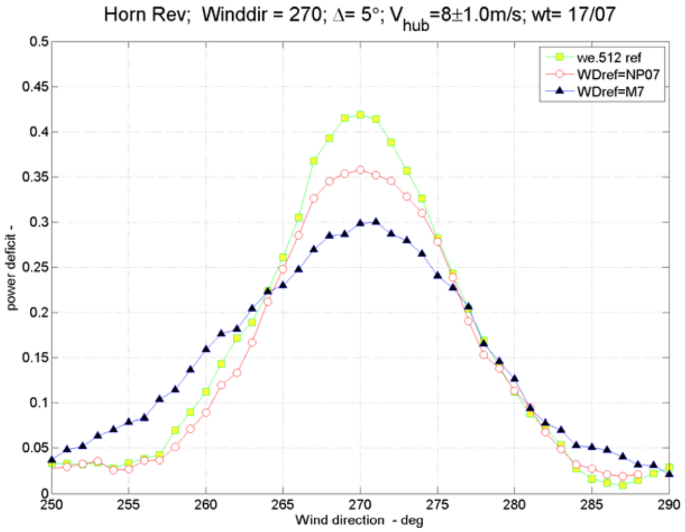

Figure 2: Wind turbine wake deficit using different inflow wind direction sensors (NP07 and M7). The single wakes are compared with a similar data presented in a reference article (we.512 ref).

The effect of wind direction spatial/temporal variability can also be seen by looking at the power deficit along different rows of wind turbines. In fig. 3, the wind direction is measured at the first turbine in the row 7. As the spatial/temporal variability is the lowest for the row 7, its power deficit is also the highest. The further away the rows are from the wind direction sensor, and the smaller the wake deficit appears to be. By taking the average of all the rows of wind turbines, the averaged line also have an artificially lower wake deficit compared with the row 7.

Even though the wind direction sensor is the closest possible, other sources of wind direction uncertainty can have a similar effect as the spatial/temporal variability over the processed wake data. Fig. 4 illustrates the probability density distribution of the power deficit along row 7 with a narrow wind direction angle bin. The results show that there is still a quite large spread of the power deficit, even though we saw previously that the results are better than in the other rows, or using another source of wind direction. Other unmeasured parameters, such as the large scale turbulence (with a time scale larger than the 10-minute averaging period) or the wind turbine yaw misalignment compared to the inflow wind direction, could introduce an uncertainty in wind direction that could cause these sort of spreading effects. Furthermore, the sub-10-minute inflow turbulence should cause a natural wake meandering of the wind turbines wake, which could also create this spreading effect. However, the wake meandering should be partially accounted for by the wake models, so it is quite difficult to dissociate the natural from the artificial spreading seen in the measurements.

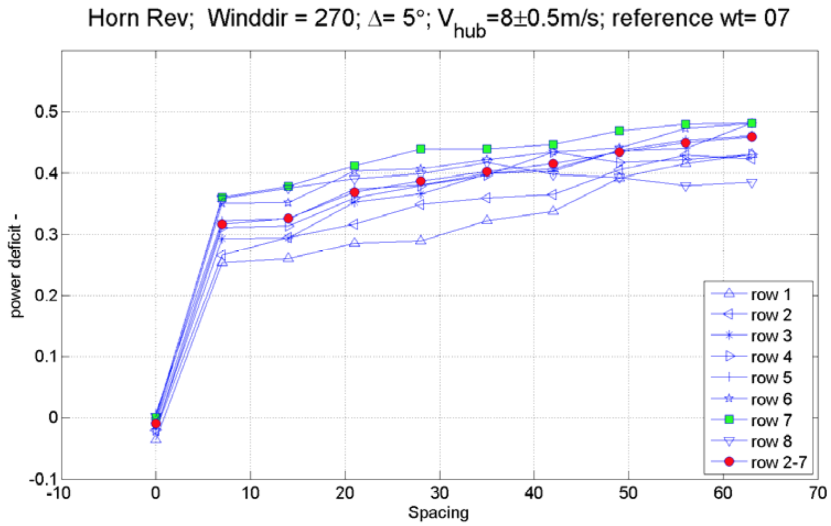

Figure 3: The power deficit along different lines of wind turbine in the westerly wind direction

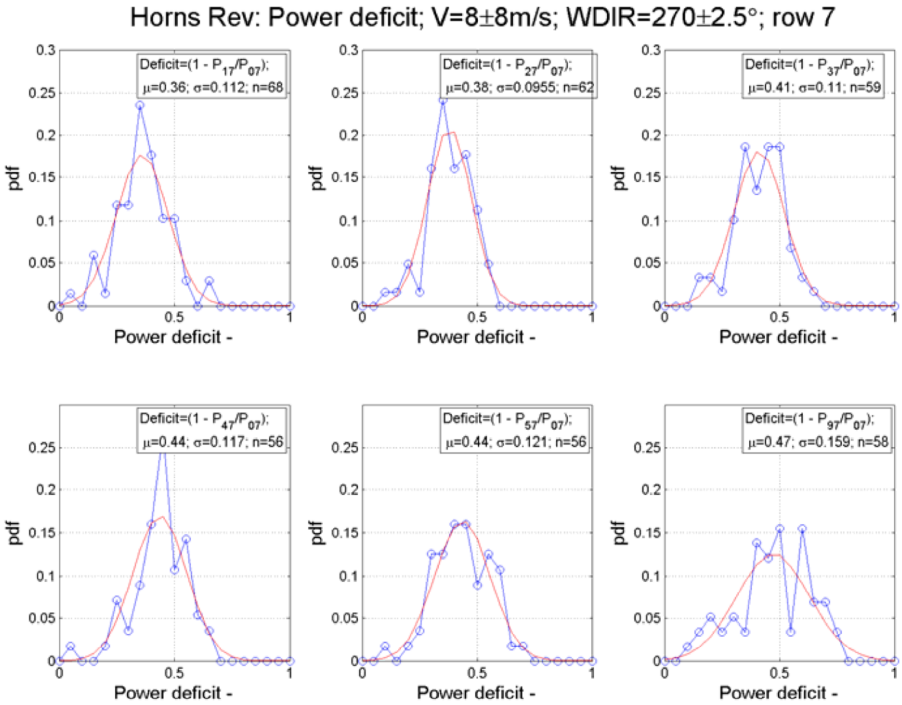

Figure 4: The probability distribution of the power deficit along the row 7.

RESULTS

This article focuses on three benchmark test cases analyzed in the EERA-DTOC and IEA-Task 31 WakeBench projects. The first one is the single wake power deficit test case, the second one is the power deficit along a row of wind turbines for different inflow wind direction bins and the third one is the maximum power deficit, between two turbines, at different downstream distance as a function of the inflow turbulence intensity.

Single wake power deficit test case

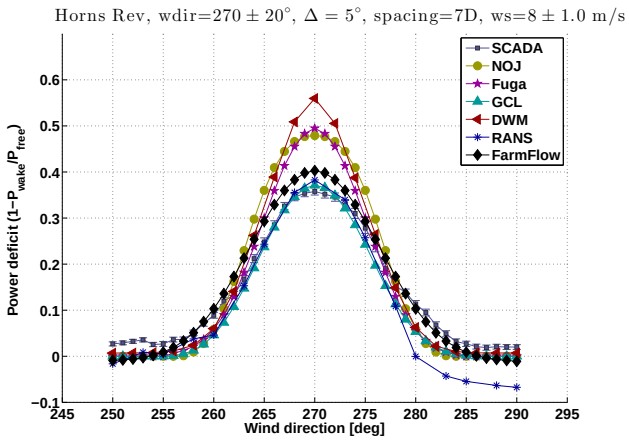

Figure 5: Single wake power deficit between pairs of wind turbines with a 5°averaging window.

The power deficit between wt17 and wt07 in the 270° wind direction, with an averaging window of 5° is illustrated in fig. 5. The wind direction is measured using the nacelle position of wt7 (NP07). The wind speed is measured using an inversed power curve using the power production of the first wind turbine in each row. When directly aligned in 270°, the wind turbines have a spacing of 7 rotor diameters.

GCL, RANS and FarmFlow seem to match the closest the SCADA wake deficit shape, while the other ones seem to over-predict the wake deficit. In the central part of the wake. The RANS model has an asymmetry on the right side that seems to indicate a speed up of the flow. This effect is not visible in the SCADA data.

Note that the SCADA point at 270° corresponds to the probability distribution data presented in top left fig. 4. This shows that even though the error bars are quite small (i.e the standard uncertainty is small), all the wake models are still within the SCADA measurement spreading.

Power deficit along a row of turbines

The power deficit between wt07 and the downstream turbines in row7 in the 270° wind direction, with an averaging window of $\Delta = 5°$, 15°, and 30° is illustrated in fig. 6, 7 and 8. The wind direction is measured using the nacelle position of wt07 (NP07). The wind speed is measured

using an inversed power curve using the power production of wt07. When directly aligned in 270°, the wind turbines have a spacing of 7 rotor diameters.

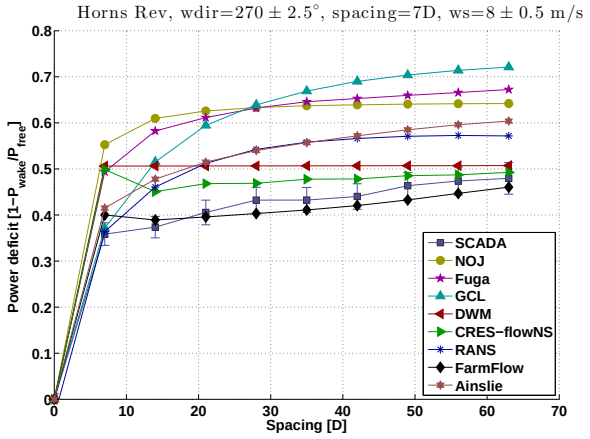

Figure 6: Power deficit along a row of turbine with and inflow wind direction bin of $\Delta = 5°$

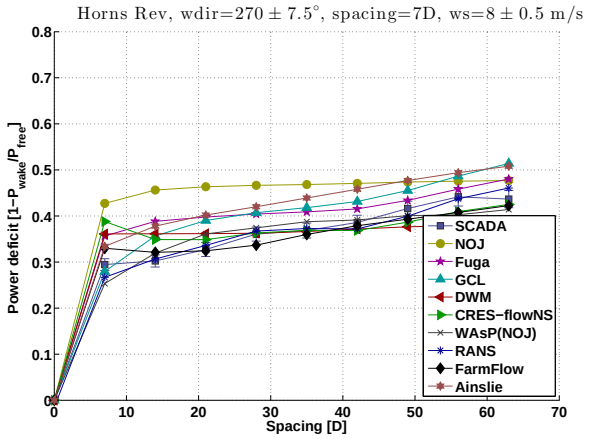

Figure 7: Power deficit along a row of turbine with and inflow wind direction bin of $\Delta = 15°$

As a general trend, most models seem to over-predict the wake deficit for small wind direction averaging window (Δ), and have a closer prediction to the largest Δ. Some of the models, like GCL and RANS have a close estimate of the first turbine downstream, and then seem to deviate gradually from the SCADA points for $\Delta = 5°$ (fig. 6). In the three Δs, FarmFlow seems to consistently match closely the shape of the SCADA points. Most models, except NOJ, WAsP/NOJ and DWM, seem to be very close to the SCADA point shape in $\Delta = 30°$ (fig. 8).

Note that the SCADA points with an averaging window of 5° fig. 6 corresponds to the

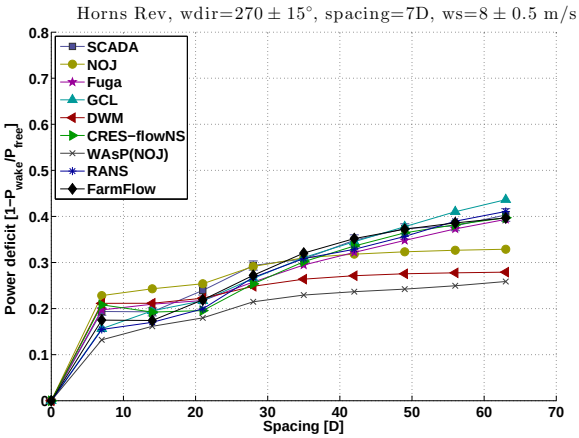

Figure 8: Power deficit along a row of turbine with and inflow wind direction bin of $\Delta = 30°$

probability distribution data plots in fig. 4. This shows that even though the error bars are quite small (i.e the standard uncertainty is small), all the wake models are still within the SCADA measurement spreading.

Maximum power deficit for different inflow turbulence intensity

The maximum power deficit between two turbines for different inflow turbulence intensity is illustrated at 7 rotor diameters (fig. 9) ad 10.4 rotor diameters (fig. 10).

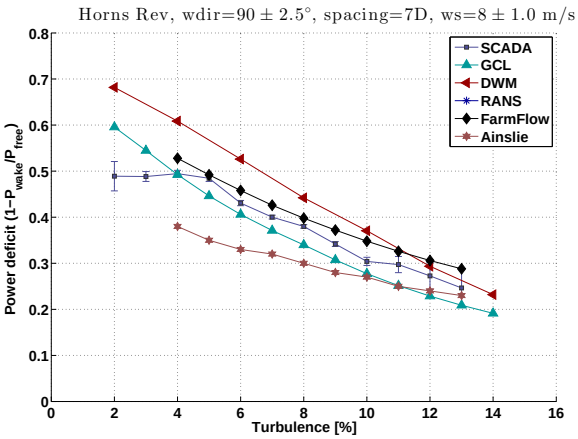

Figure 9: Maximum power deficit for different inflow turbulence intensity and a wind turbine spacing of 7 rotor diameters

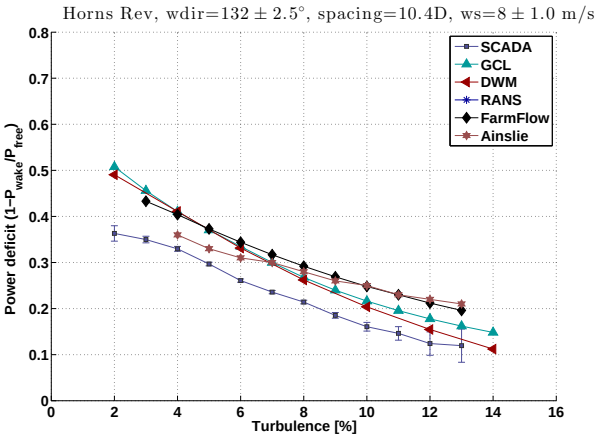

Figure 10: Maximum power deficit for different inflow turbulence intensity and a wind turbine spacing of 10.4 rotor diameters

Most models seem to capture the trend correctly.All the models have a tendency to over-predict the maximum wake deficit at 10.4D, even though some of the models (e.g. GCL and Ainslie) are under-predicting the wake deficit at 7D. There does not seem to be a model clearly better than the other ones in this benchmark.

DISCUSSION

As discussed in the data analysis section, the small wind direction sectors Δs are very sensitive to the wind direction uncertainty used to select the data. As the uncertainty in wind direction is still quite high because of the sensor used (the nacelle position sensor follows the yaw misalignment), the benchmarks based on the small Δs might not give a good representation of the accuracy of the wake models. The uncertainty in wind direction creates an artificially lower wake deficit during the ensemble averaging. In these smaller Δs the models seem in majority to over-predict the wake deficit, which might be because the SCADA is heavily influenced by the wind direction uncertainty. When looking at the probability distribution of the SCADA measurements, most of the models do seem to remain within the spreading of the data. With this in mind, it is quite difficult to pick one model performing better than the other one over the test castes $\Delta = 5^\circ$ and $\Delta = 15^\circ$.

For modeling more fairly the small Δs, it could be necessary to post-process the wake models to account for the effect of wind direction uncertainty in the measurement averaging as proposed by Gaumond et al. [4].

The wind direction sector $\Delta = 30^\circ$ is the Δ normally used for calculating the AEP. As estimating accurately the AEP is the main focus of the current EERA-DTOC project, it should be

here considered that $\Delta = 30^\circ$ is the more important benchmark compared with the two others Δs benchmarks. So even thought most models seem to over-estimate the wake deficit in the smaller Δs, many are still performing quite well in $\Delta = 30^\circ$ and could therefore still produce very accurate AEPs.

The results of fig. 6, 7 and 8 are very close to a previously published work on the same Horns Rev wind farm case in the UpWind project [18]. While since then the SCADA data have been refined (i.e the measurements points have a lower uncertainty), and some of the models have been re-factored for offshore conditions, the main conclusions stay the same. The wake model still over predict the narrow sectors, probably due to the wind direction uncertainty, while they perform satisfyingly for the larger sector.

Looking at the benchmark results, the wake accumulation method might have a strong influence the shape of the wake deficit along a row of turbine. The DWM (i.e. using the maximum) and NOJ flavors (i.e. using a RSS) seem to perform the least well to match the SCADA shape, even at large Δs. They both present flatter trends compared with the SCADA measurements, that seems to indicate that if the wind farm was larger their results would deviate even more strongly. This results are in agreement with previous studies [4,6].

It is somewhat difficult to judge the importance of the other sub-model assumptions as most models use quite different combinations. For instance, it is not clear how sensible the models are regarding the number of points needed to produce the hub wind speed. For answering this specific question, it would be more appropriate to carry out a sensitivity analysis on each specific model.

Similarly, only one model uses an advanced aero-elastic model with a controller for the wind turbine (DWM). It is not clear from the results that this would be giving a more realistic estimate of the wind farm annual energy production. Here again it would be interesting to test each model independently if they would benefit from a more sophisticated wind turbine model.

While they seem to perform satisfyingly in the first two test cases, the more computationally intensive non-linear CFD models such as RANS and CRESflowNS do not seem to show any more realistic behavior compared with the order of magnitude faster CFD models such as FarmFlow, FUGA or even the engineering models such as Ainslie or GCL.

CONCLUSIONS AND FUTURE WORK

This article presented the results of a benchmark campaign carried on within the EERA-DTOC project, in collaboration with the IEA-Task 31 ”WakeBench” project. A wide scope of different wake models have been compared on different types of test cases. Because of the complexity of dealing with large offshore wind farm SCADA data, it is very challenging to create comparable results to the wind farm wake models. Especially, the issue of wind direction uncertainty is found to create an artificially lower wake deficit. As the models are not directly taking into account this uncertainty it is important to take a step back from the benchmarking results and being pragmatic about the performance of the different models. For instance, the performance of

the wake models in small wind direction averaging windows are not so critical when estimating the annual energy production, which is the focus of EERA-DTOC.

Within the EERA-DTOC project another test case is planned on the Horns Rev benchmark. The wind farm efficiency polar distribution, should give a more quantifiable metric of the accuracy of the wind farm wake models to estimate AEPs. Another benchmark is also planned on the Lillgrund wind farm in collaboration with the IEA-Task 31 "WakeBench" and Vattenfall AB, the wind farm owner. The wind turbines are larger and more closely spaced, which should challenge the wake models in a different manner than the Horns Rev wind farm did.

ACKNOWLEDGEMENTS

This work is supported by the EU EERA-DTOC project nr. FP7-ENERGY-2011/n 282797, and of the Danish EUDP-WakeBench project nr. 64011-0308. The Horns Rev data was gratefully provided through previous projects by the wind farm owners Vattenfall AB and DONG Energy AS.

REFERENCES

[1] Hansen K., Barthelmie R.J., Jensen L., Sommer A., 2011a, The impact of turbulence intensity and atmospheric stability on power deficits due to wind turbine wakes at Horns Rev wind farm, Wind Energy, doi: 10.1002/we.512, 2001.
[2] Hansen K., et al., 2011b, Guideline to wind farm wake analysis. In UPWIND 1A2 Metrology, Final Report, Chapter 8, ECN-E–11-013, February 2011.
[3] Hansen K., et al., 2011c, Classification of atmospheric stability for offshore wind farms. In UPWIND 1A2 Metrology, Final Report, Chapter 10, ECN-E–11-013, February 2011.
[4] Gaumond M., et al., 2011c, Evaluation of the wind direction uncertainty and its impact on wake modelling at the Horns Rev offshore wind farm, Wind Energy, 2013.
[5] Anderson M., Simplified soultion to the eddy viscosity wake model, www.res-americas.com, 2009.
[6] Habenicht G. Offshore wake modelling, Presentation at Renewable UK Offshore Wind, www.res-group.com, 2011.
[7] Larsen T.J., Hansen A.M., How 2 HAWC2, the user's manual. Technical Report, Risø-R-1597, DTU-Wind Energy, Risø, Denmark 2007.
[8] Ainslie J.F., Calculating the flow field in the wake of wind turbines, Journal of Wind Engineering and Industrial Aerodynamics, 27: p 213-224, 1988.
[9] Crespo, A., Hernández, J., Fraga, E., Andreu, C., Experimental validation of the UPM computer code to calculate wind turbine wakes and comparison with other models. Journal of Wind

Engineering, 27, p 77–88, 1998.
[10] Mortensen N.G., Heathfield D.N., Rathmann O., Nielsen M., Wind Atlas Analysis and Application Program: WAsP 10 Help Facility. Technical report, Risø National Laboratory, Roskilde, Denmark, December 2011.
[11] N.O. Jensen. A note on wind generator interaction. Technical Report Risø-M- 2411, Risø National Laboratory, Roskilde, Denmark, 1983.
[12] Ott S., Berg J., Nielsen M., "Linearised CFD Models for Wakes". Technical Univ. of Denmark, Risoe National Lab. for Sustainable Energy. Wind Energy Div. Risoe-R-1772(EN) ISBN 978-87-550-3892-9. Available online.
[13] Prospathopoulos, J. M. and Chaviaropoulos, P.K., "Numerical simulation of offshore wind farm clusters", European Wind Energy Association, Conference proceedings 2013.
[14] Chaviaropoulos P. K. and Douvikas D. I., "Mean-flow-field Simulations over Complex Terrain Using a 3D Reynolds Averaged NavierStokes Solver," Proceedings of ECCOMAS 98, Vol. I, Part II, pp. 842-848. 1998.
[15] Larsen GC. A simple stationary semi-analytical wake model. Technical Report, Risø-R-1713(EN) August, Risø DTU 2009.
[16] Larsen GC, Madsen HA, Thomsen K, Larsen TJ. Wake meandering: a pragmatic approach. Wind Energy Jul 2008; 11(4):377–395, doi:10.1002/we.267.
[17] Madsen HA, Larsen GC, Larsen TJ, Troldborg N, Mikkelsen R. Calibration and Validation of the Dynamic Wake Meandering Model for Implementation in an Aeroelastic Code. Journal of Solar Energy Engineering 2010; 132(4):041 014, doi:10.1115/1.4002555.
[18] Barthelmie R.J., Hansen K., Frandsen S.T., Rathmann O., Schepers J.G., Schlez W., Phillips J., Rados K., Zervos A., Politis E.S., Chaviaropoulos P.K., Modelling and Measuring Flow and Wind Turbine Wakes in Large Wind Farms Offshore. Wind Energy, doi:10.1002/we.348, 2009.
[19] Barthelmie R.J., Barthelmie, Larsen G.C., Pryor S., Jørgensen H.E., Bergström H., Schlez W., Rados K., Lange B., Vølund P., Neckelmann S., Mogensen S., Schepers G., Hegberg T., Folkerts L., Magnusson M., ENDOW (efficient development of offshore wind farms): modelling wake and boundary layer interactions. Wind Energy. 2004. DOI: 10.1002/we.121.
[20] Réthoré P.-E., Wind Turbine Wake in Atmospheric Turbulence, PhD Thesis, Aalborg University, 2009.
[21] Rathmann O, Ott S & Kelly MC , 'Wind farm wake effects estimations by a mosaic tile wake model'. in: Proceedings. EWEA 2011.

Analysis of turbulent wake behind a wind turbine

N. Arjomand Kermani[1], S. Andersen[1], J. Sørensen[1], W. Shen[1]

[1]Technical University of Denmark, Department of Wind Energy, Nils Koppels Alle, Building 403, 2800, Lyngby, **nsarjomand@gmail.com, jns@mek.dtu.dk, wzs@mek.dtu.dk**

Abstract

The aim of this study is to improve the classical analytical model for estimation of the rate of wake expansion and the decay of wake velocity deficit in the far wake region behind a wind turbine. The relations for a fully turbulent axisymmetric far wake were derived by applying the mass and momentum conservations, the self-similarity of mean velocity profile and the eddy viscosity closure.

The theoretical approach is validated using the numerical results obtained from large eddy simulations with an actuator line technique at 0.1% and 3% ambient turbulence level and ambient wind velocity of 10 m/s, and 0.1% ambient turbulence level and ambient wind velocity of 7 m/s. The obtained results showed that neglecting the nonlinear term of velocity in the momentum equation in the far wake region cannot be a fair assumption, unlike what is generally assumed in most of text books of fluid mechanics. Therefore the theoretical determination of the power law for the wake expansion and the decay of the wake velocity deficit may not be valid in the case of the wake generated behind a wind turbine with low ambient turbulence and high thrust coefficient. Although at higher ambient turbulence levels or lower ambient wind velocities (higher thrust coefficients), this trend may be improved due to the faster recovery of the wake and therefore closer values to the theoretical approach may be obtained. In addition, the assumption of self-similarity behavior of the mean velocity profile, when scaled with center line velocity deficit, could be correct in the far wake region of a wind turbine and low ambient turbulence levels.

1. Introduction

Modeling of wind turbine wakes has been a hot research topic during the past few years. Due to the generation of the wakes behind upstream wind turbines, the annual power production of a downstream wind turbine is decreased but at the same time the fatigue load of the turbine is increased significantly, compared to the performance of a free standing wind turbine. Therefore, developing an effective mathematical model for precisely simulating the wake behavior behind the wind turbine is highly desirable. Such model can be useful for the estimation of energy production, and life time of wind turbines and finally for optimization purposes.

Today, all the wake models that are used to predict the performance of wind turbines are either CFD based models or kinematic wake models. The CFD based models are highly advanced which are able to predict the flow behaviors with a high degree of accuracy, but they are very time consuming and require massive computer resources. On the other hand, most of the kinematic wake models are mainly based on mass and momentum conservations. These models are basically calibrated with several empirical coefficients obtained from specific field measurements and therefore have limitations. Although the kinematic wake models use explicit representations of turbulence and its impact on the wake expansion, they have not been able to produce convincingly better predictions.

For many years it was imagined that the turbulence tends to forget its origin and in this context, the self-preserving state in the flow is obtained, when it becomes asymptotically independent of its initial conditions. Consequently, different types of flows, like wakes and other free turbulent shear flows can grow asymptotically at the same rate which is independent of their generators. This classical self-preservation approach was questioned for the first time in 1989 by George [1], who proposed a new methodology called "equilibrium similarity" analysis. In this new method, George [1] argued that the axisymmetric wake will reach a self-similarity state with respect to the mean velocity profile, if scaled with the centerline wake velocity deficit. Therefore, independent of how far downstream the wake moves or how large the Reynolds number is [1],the properly normalized mean velocity profiles with the centerline wake velocity deficit always collapse onto a unique curve, while the spreading rate and higher turbulence moments will appear differently, depending on their source. In 2003, Johansson et al. [2] validated the mentioned theory by using the experimental data for axisymmetric wake obtained by Johansson et al. [3, 4], the experimental data for axisymmetric wake behind five different generators obtained by Canon [5], and the direct numerical simulation obtained by Gourlay et al. [6].
In addition, by using kinetic energy equation and ad hoc assumptions about the dissipation, George [1] showed that the Reynolds number is the main factor in determining the rate of the axisymmetric wake width (either $\sim x^{\frac{1}{3}}$ or $\sim x^{\frac{1}{2}}$) which were always a doubt. By removing the ad hoc assumptions and using the Reynolds averaged equations, instead of kinetic energy Johansson et al. [2] revised this theory. Based on these studies, two different equilibrium similarity solutions were obtained for the two different cases of very high and low local Reynolds numbers in the axisymmetric wake.

Kinematic wake models are analytical models which gain a considerable attention for predicting the flow behavior behind the wind turbines due to their simplicity and low computational cost [7]. As reviewed in Vermeer et al. [8] and Crespo et al. [7] this approach was introduced for the first time by Lissama [9] and up to now a lot of researchers work on developing these models. N.O Jensen model [10, 11] is a single wake model based on the balance of momentum which describes the wake behind a wind turbine in terms of Guassian distribution of wake velocity deficit and the linear expansion of the wake. Larsen model [12, 13] is another kinematic model based on mass and momentum conservation together with the assumption of Prandtl's turbulent boundary layer equations and similarity. This model is described for two different levels of approaches where in the first order model, two power lows of 1/3 and -2/3 are obtained for the wake expansion and wake velocity deficit respectively while in the second order level these values changed to more complicated relations. In 2006, Frandsen [14] suggested a new analytical model based on the mass and momentum conservations, and the similarity assumption for prediction of the flow behavior in the wake for any size of wind farms. Compared to the previous models, this model is able to handle more condition close to the reality, but it is still required to be evaluated and calibrated based on the measurements. Most of the kinematic models that are used for predicting the wake behind wind turbine are based on self-similarity assumption of the mean velocity profile. However no one has shown the accuracy of this behavior in the far wake region of wind turbine and the possibility of having a unique profile independent of its source. In addition, these models are mainly based on the mass and momentum conservations, but none of them has considered the turbulent kinetic energy or the Reynolds stress equations, that may lead to more accuracy in prediction of the flow behaviors. Also there are still a lot of contradictory arguments regarding the spreading rate of the wake, and a lot of uncertainty about applying the initial conditions of the wake in these models.

The aim of the present study is to improve the classical analytical model for estimating the rate of wake expansion and the decay of wake velocity deficit in the far wake region behind a wind turbine. The asymptotic behavior of the far wake is investigated as well as a detailed theoretical approach is presented in the paper. The model has been developed by applying the mass and momentum conservations and Reynolds shear stress. Finally, a closed form solution is derived for centerline and radial wake velocity deficit, wake width, mean velocity profile, and relations for coefficients by adopting the self-similarity of mean velocity profile and utilizing the eddy viscosity closure scheme in the description of turbulent stresses.

The theoretical work is verified and validated against the results obtained from Navier-Stokes/Actuator Line simulations with large eddy simulation at 0.1% ambient turbulence and an ambient wind velocity of $U_\infty = 10\ m/s$. In addition, the effects of ambient turbulence level and thrust coefficient on the wake recovery and the flow behaviors are investigated by analyzing the flow parameters obtained from the numerical data at two different ambient turbulence levels of 3%, 6% and an ambient wind velocity of $U_\infty = 10\ m/s$ s, and 0.1% ambient turbulence level and an ambient wind velocity of $U_\infty = 7\ m/s$.

2. Methods

2.1 Theoretical approach

To make theoretical approach, the wake behind a wind turbine is assumed to be incompressible, steady and fully turbulent. However these assumptions may not be correct when looking at the instantaneous behavior of the wake flow; they will be acceptable if a relatively long time series of the data is considered. In addition the inflow is assumed to be uniform and stationary with time, and the ground effects and pressure gradient outside the wake are negligible.

2.1.1 Basic model equations

The wake is described in cylindrical coordinates (x, r) with the axial and radial velocity components (u, v) respectively. According to the above assumptions, the continuity equations for the mean and fluctuating velocity together with the stream-wise momentum equation can be rewritten as follows

$$\frac{\partial(\bar{u})}{\partial x} + \frac{1}{r}\frac{\partial(r\bar{v})}{\partial r} = 0 \quad ; \quad \frac{\partial(u')}{\partial x} + \frac{1}{r}\frac{\partial(rv')}{\partial r} = 0 \tag{1.}$$

$$\left(\bar{u}\frac{\partial\bar{u}}{\partial x} + \bar{v}\frac{\partial\bar{u}}{\partial r}\right) = -\frac{1}{r}\frac{\partial(r\overline{u'v'})}{\partial r} - \frac{\partial\left(\overline{u'^2}\right)}{\partial x} + \nu_s\left(\frac{\partial}{\partial x}\frac{\partial\bar{u}}{\partial x} + \frac{1}{r}\frac{\partial}{\partial r}\left(r\frac{\partial\bar{u}}{\partial r}\right)\right) - \frac{1}{\rho}\frac{\partial\bar{p}}{\partial x} \tag{2.}$$

where $u'$and v' are the fluctuating parts of u and v, and a bar over the quantities denotes time average. The third and fourth terms on the right hand side of Eq. 2 correspond to the viscous terms and the last term on the right hand side of the Eq. 2 is the pressure term. The equations of motion are simplified in the far wake region by analyzing the orders of magnitude and discarding many terms that are relatively small. In order to do so, two velocity scales (U_∞ and $\overline{u_s}$) and two length scales L and δ are used in the far wake, which stand for the ambient wind velocity, the cross sectional wake velocity deficit in the axial direction, and the stream-wise and cross-stream length scales, respectively. $\overline{u_s}$ is the cross sectional wake velocity deficit defined as the difference between U_∞ and the wake velocity in the axial direction $\overline{u}$, while $\overline{U_s}$ is the centerline wake velocity deficit. In addition, δ is equal to the perpendicular distance from the wake centerline to the wake edge (half of the wake width) and can be defined as two times of the distance from the centerline to where $U_\infty - \bar{u}$ is about $\frac{1}{2}\overline{U_s}$. For more information about the order of magnitude analysis the reader is referred to [15]. Consequently, for fully turbulent axisymmetric far wake Eq. 2 could be simplified as

$$(U_\infty)\frac{\partial}{\partial x}(\overline{u_s}) = -\frac{1}{r}\frac{\partial(r\overline{u'v'})}{\partial r} + \nu_s\frac{1}{r}\frac{\partial}{\partial r}(r\frac{\partial}{\partial r}\overline{u_s}) \tag{3.}$$

2.1.2 Momentum thickness and self-similarity analysis

An infinitely large cylindrical control volume surrounding the rotor is chosen with x-axis as the symmetry axis of the control volume. Therefore, using the previously defined assumptions, neglecting the shear forces acting on the control volume, and applying continuity equation the momentum theory applied to the chosen control volume can be simplified with respect to the mean velocity (neglecting the fluctuating terms) as follows,

$$2\pi\rho\int_0^\infty \bar{u}(U_\infty-\bar{u})rdr=\bar{T}\quad where\quad \bar{T}=\frac{1}{2}\rho C_T U_\infty^2 A=\frac{1}{2}\rho C_T U_\infty^2\frac{\pi}{4}D^2 \tag{4.}$$

where ρ, $\overline{T}$, C_T, A and D are the air density, thrust, thrust coefficient, rotor area and rotor diameter respectively. Therefore, based on the definition of momentum thickness (showed below) and Eq. 4, the relation between momentum thickness and thrust can be found as

$$\theta^2=\int_0^\infty\frac{\bar{u}}{U_\infty}\left(1-\frac{\bar{u}}{U_\infty}\right)rdr=\frac{\bar{T}}{2\pi\rho U_\infty^2}\ \rightarrow\ \theta^2=\frac{1}{4\pi}C_T A=\frac{1}{16}D^2C_T \tag{5.}$$

Considering the self-similarity assumption, the following relation can be written for the mean velocity profile and the Reynolds stress, where $u'v'$, $f(\eta)$, R_s, g and η are the Reynolds stress, the mean velocity deficit, the Reynolds shear-stress scaling function and profile, and the dimensionless similarity coordinates, respectively.

$$U_\infty-\bar{u}=\overline{U_s(x)}f(\eta)\ ;\ \ \overline{u_s(x)}=\overline{U_s(x)}f(\eta)\ ;\ \ -\overline{u'v'}=R_s(x)g(\eta)\ \ where\quad \eta=\frac{r}{\delta}\ \ and\ \ \delta=\delta(x) \tag{6.}$$

By substituting Eqs. 6 in Eq. 4 and neglecting the nonlinear term of the momentum equation (due to the far wake modelling) Eq. 4 can be simplified as follows, see also Johansson et al. [2]

$$2\pi\rho\int_0^\infty\left(U_\infty\overline{u_s(x)}-\overline{u_s(x)^2}\right)rdr=\bar{T}=2\pi\rho U_\infty^2\theta^2\quad\rightarrow\quad\overline{U_s}\delta^2\int_0^\infty\eta f(\eta)d\eta=\bar{T}=U_\infty\theta^2=Const \tag{7.}$$

By using Eq. 4 and Eqs. 6 in Eq. 3 and repeating similar analysis for Reynolds stress equations together with the elimination of viscous terms, Johansson et al. found the two power laws of 1/3 and -2/3 for the wake expansion and the decay of wake velocity deficit for high Reynolds solution in the far wake region, respectively as

$$\frac{\delta_*}{\theta}=a\left(\frac{x}{\theta}\right)^{\frac{1}{3}}\ ;\ \ \frac{\overline{U_s}}{U_\infty}=b\left(\frac{x}{\theta}\right)^{-\frac{2}{3}};\ and\quad x=x-x_0\ \ where\quad\delta_*^2=\lim_{R\to\infty}\frac{1}{U_s}\int_0^R(U_\infty-\bar{u})rdr \tag{8.}$$

where the coefficients (a and b) and the virtual origin of the far wake (x_0) are highly dependent on initial conditions. However, Eqs. 7 can be written based on δ (half of the wake width), where the coefficient (a) will have a different value compared to the case of δ_*(displacement thickness).

2.1.3 Mean and radial velocity profile

By using the relations in Eqs. 8 into Eq. 3, introducing the eddy viscosity in the form of $-\overline{u'v'}=\nu_T\frac{\partial\bar{u}}{\partial r}$, and employing the relations in Eqs. 7, the following equations were found for the mean velocity profile (f), and the relation between *a* and *b* coefficients, respectively.

$$f=\exp\left(-\frac{1}{6}\alpha\eta^2\right)\ \ where\ \alpha=\frac{aR_T}{b}\ \ ;\ \ and\ \ b=1/a^2 \tag{9.}$$

where $R_T = \frac{\overline{U_s}\delta}{\nu_T}$, is the turbulent Reynolds number which is assumed to be constant. By using Eqs. 6 and 8 in Eq. 1, the following relations will be obtained for the radial velocity profile. For more detailed information regarding the above calculation, the reader is referred to [15].

$$\overline{u_r} = \frac{\delta}{\eta}\, U_\infty \theta^{\frac{2}{3}} x^{-\frac{5}{3}} \left[\frac{b}{3}\eta^2 f(\eta)\right] \qquad (10.)$$

2.2 Numerical approach

The numerical model used here is a multi-block finite volume code combined with the Actuator Line technique. The Actuator Line model was developed by Sørensen and Shen [16] and later on implemented into the three dimensional Navier-Stokes solver EllipSys3D, developed by Michelsen [17, 18] and Sørensen [19]. In this code, the discretized incompressible Navier-Stokes equations, in general curvilinear coordinates, are solved by using the block structured finite volume approach [20]. In the actuator line model each blade is represented by a line and the loading is distributed radially along the lines representing the blade forces. The kinematics of the wake is determined by a fully three dimensional Navier-Stokes equations, whereas the loading on each blade, is determined by using tabulated airfoil data.

In addition, for Large Eddy simulation (LES), sub grid scale (SGS) models is used to model eddies of size smaller than the grid size. Therefore, the equations are obtained by filtering the time dependent Navier-Stokes equations in the physical space. The eddy-viscosity-based mixed scale model in [20] is used to model the small scales. In addition the Mann turbulence model [21] is used to produce the desired ambient turbulence for the simulations.

2.2.1 Computational domain and boundary conditions

The computations were carried out in a Cartesian computational mesh of about 14 million grid points (216×40^3) with dimensions 48R in the axial direction (x), 20R in the vertical direction (y) and 20R in the lateral direction (z). The actuator lines were rotating in the $y - z$ plane and located at 8R downstream of the inlet and the origin of rotation is the center of the plane. Therefore, the computational domain has covered the region extending from 8R before the rotor plane to 40R downstream of the rotor in the flow direction, and 10R from the rotor center in the y and z directions.

The grid points of the computational mesh are highly concentrated around and downstream of the rotor and distributed equally in order to resolve the strong gradients in the vicinity of the rotor and to maintain the generated flow structure in the wake simultaneously. While out of this region, they stretched away towards the outer boundaries. Note that in this simulation 16 grid cell is used to resolve a rotor radius in the equidistant region. The grid configuration is divided into 216 blocks (3×3 in cross-flow and 24 in flow direction) with 40^3 grid points in each block. Figure 1 shows the block configuration which is used in the simulations.

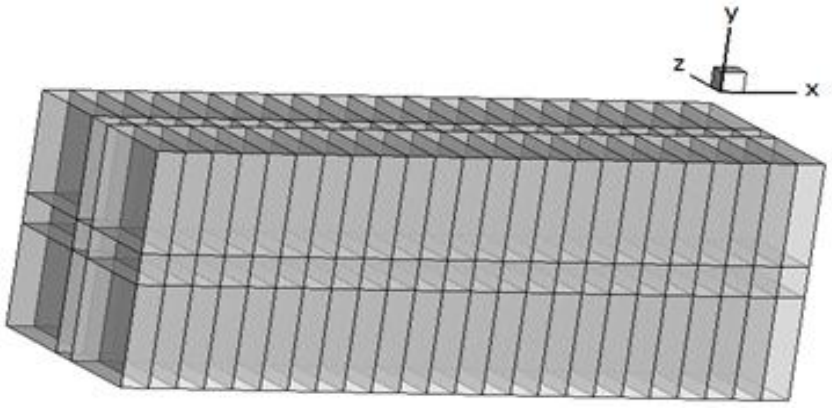

Figure 1: Grid configuration used in numerical simulation.

The boundary conditions used here are

Dirichlet boundary conditions with, constant and uniform flow velocity component (V_x) and zero velocity component in the y and z directions (V_y and V_Z) at the inlet ($x/R = 0$), a convective boundary condition at the outlet ($x/R = 48$), and periodic boundary condition at the lateral ($z/R = -10,\ z/R = 10$).

2.2.2 Wind turbine characteristics and flow parameters

The flow field past a 2.75 MW variable speed pitch regulated "NM80" stiff wind turbine equipped with three LM38.8 blades which are constructed with NACA634XX airfoils, is simulated. The rotor diameter of the wind turbine is equal to 80 m and it runs with the rated speed of 17.2 rpm. In addition, two different uniform inflow velocities of $U_\infty = 7 \text{ and } 10\ m/s$ with air density of $\rho = 1.22 \frac{kg}{m^3}$ are used in the presented work. Since the turbine's data is confidential, the detailed data are not allowed to be presented.

3. Results and discussions

The computation for 0.1% ambient turbulence and ambient wind velocity of 10 m/s (corresponding to $C_T = 0.75$ and a tip speed ratio of $\lambda = 7.78$) has been run first to examine the accuracy of the assumptions and then verify and validate the main characteristics of the flow predicted by the theoretical approach. Later on in the study, the simulations were repeated for 3 different conditions of (3%, and 6% ambient turbulence level and $U_\infty = 10\ m/s$) together with (0.1% ambient turbulence level and $U_\infty = 7\ m/s$ corresponding to $C_T = 0.86$ and a tip speed ratio of $\lambda = 11.42$) in order to evaluate the effects of ambient turbulence and wind turbine rotor aerodynamics on the flow behaviors.

The computations have run on a cluster where three component of dimensionless wake velocity deficit in axial, cross-sectional directions ($u/U_\infty, v/U_\infty, w/U_\infty$) are saved in $y-z$ planes, at the distances of $\frac{x}{D} = 1, 2, 3, 4, 5, 6, 7, 8, 9, 10, 11, 12, 13, 14, 15, 16, 17, 18, 19$ behind the wind turbine. All the data have been read and analyzed in Matlab software with time step duration of 0.5 seconds.

Figure 2 shows the dimensionless axial wake velocity deficit obtained from numerical simulation for 0.1% ambient turbulence level and $U_\infty = 10\ m/s$ averaged in time between 3.3 to 39 minutes in $y-z$ plane at four

different distances of $\frac{x}{D} = 3, 6, 11, 18$ behind the wind turbine. It can be seen from Figure 2, the decreasing and increasing trend of the centerline wake velocity deficit and the wake width as the wake evolves downstream. In addition, it is clear from the figure that the wake velocity deficit reaches the axisymmetric condition

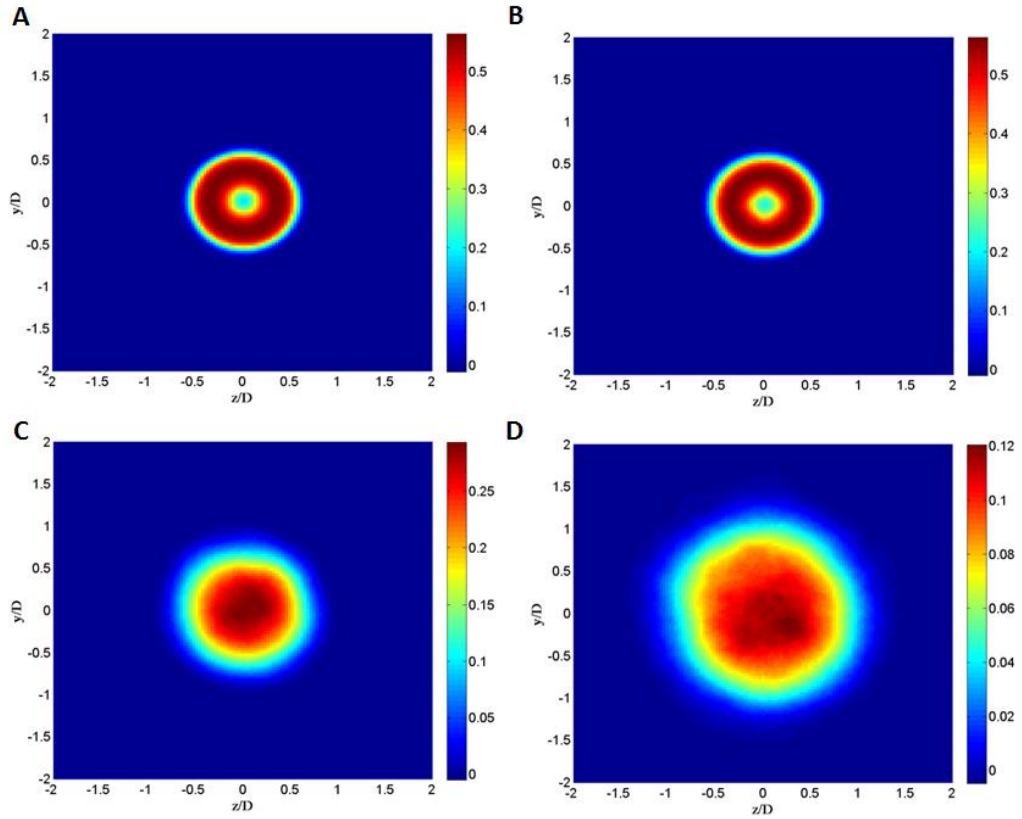

Figure 2: Dimensionless wake velocity deficit for 0.1% ambient turbulence and an ambient wind velocity of 10 m/s, at (A) x/D=3, (B) x/D=6, (C) x/D=11, (D) x/D=18 (obtained from numerical simulations)

3.1 Verification of steady state condition

Figure 3 shows the variation of the time-averaged dimensionless centerline wake velocity deficit ($\frac{\overline{U_s}}{U_\infty}$) by increasing the time interval of 0.25 min at each step, for 0.1% ambient turbulence level and $U_\infty = 10\ m/s$. The first point in Figure 3, corresponds to the value of centerline wake velocity deficit averaged by time between ($T_{avr} = 3.3\ to\ 30$ min). These relatively small variations of the time-averaged dimensionless wake velocity (less than 5%) shows the fact that the simulation time was large enough for the wake to reach the steady state conditions, and therefore satisfying the assumptions used in the theory.

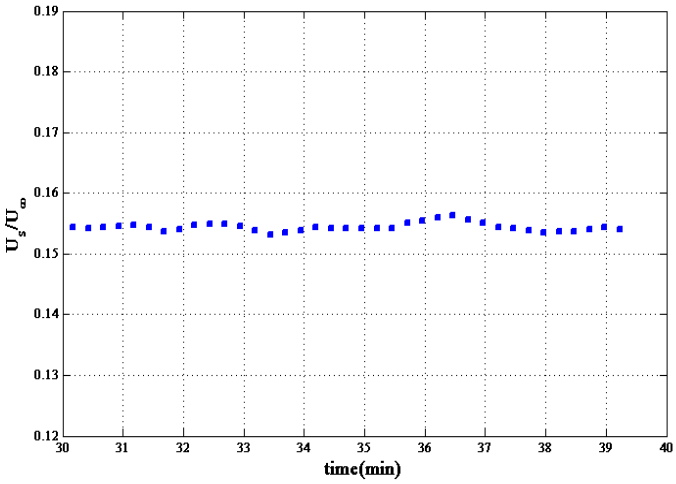

Figure 3: Variation of dimensionless centerline wake velocity deficit averaged in different time intervals, for 0.1% ambient turbulence and an ambient wind velocity of 10 m/s (obtained from numerical simulations)

3.2 Investigation of cross-sectional parameters

Figure 4 shows the cross-sectional profile of the dimensionless wake velocity deficit and the turbulence intensity at different distances behind the wind turbine for 0.1% ambient turbulence level and $U_\infty = 10\ m/s$. Note that the values shown for the dimensionless wake velocity deficit profile and turbulence intensity in Figure 4 correspond to the tangential averaged values between $\Delta\theta = 0$ to π ; and $-\pi$ to 0 of these quantities.

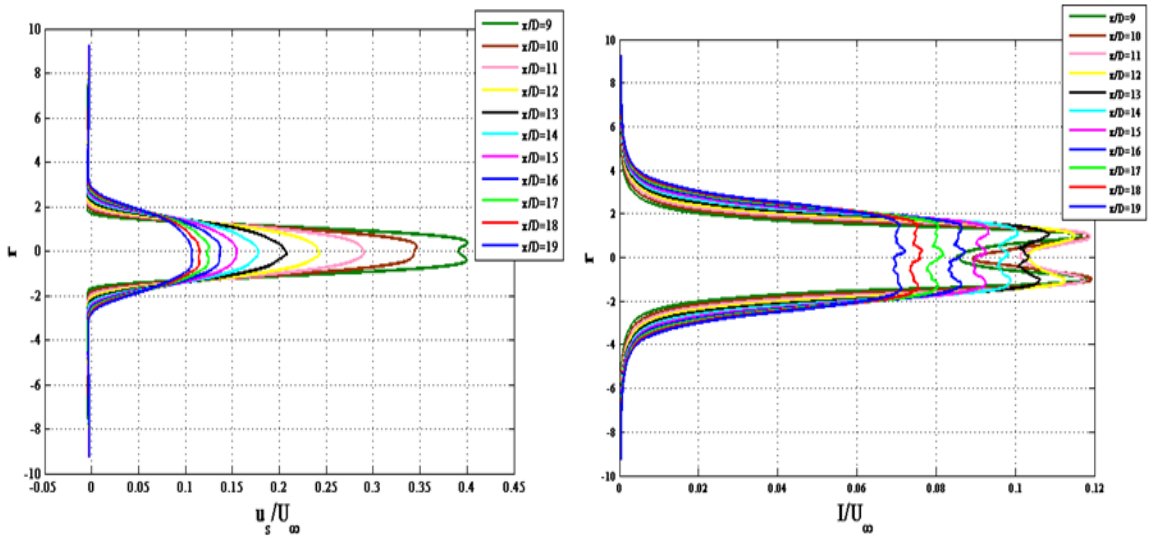

Figure 4: Cross-sectional dimensionless wake velocity deficit (left) turbulence intensity (right) at different distances behind the wind turbine for 0.1% ambient turbulence and an ambient wind velocity of 10 m/s (obtained from numerical simulations)

Figure 4 shows that both dimensionless cross-sectional profiles of wake velocity deficit and turbulence intensity are decreased as the wake evolves downstream. Figure 4 also shows that the dimensionless velocity deficit

profiles reach "a point of balance" and become approximately "bell-shaped with having a maximum approximately in the center of the wake". Since, in the transitional and far wake region the new turbulent fluctuations are generated by the radial shear flow, there is less generation of turbulence in the center of the wake. However, in this condition the turbulent diffusion is the dominant mechanism which transports the turbulent fluctuations to the center of the wake and therefore leads to fair approximation of the turbulence fluctuations with bell-shaped form.

3.3 Variation of flow parameters for different initial conditions

Comparing the figures of time-averaged wake velocity deficit profile shows that the transitional region (the region where the annular shear layer of the near wake is finished) for different ambient turbulence levels of 0.1%, 3% and 6% and $U_\infty = 10\ m/s$ is started at approximately $\frac{x}{D} \geq 9$, $\frac{x}{D} \geq 5, \frac{x}{D} \geq 3$ respectively, while for 0.1% ambient turbulence level and $U_\infty = 7\ m/s$ the transitional region will start at $\frac{x}{D} \geq 6$. Figure 5 shows the logarithmic behavior of dimensionless half of wake width and centerline wake velocity deficit in transitional and far wake region of wind turbine for 0.1%, 3%, 6% ambient turbulence levels and $U_\infty = 10\ m/s$, and 0.1% ambient turbulence level and $U_\infty = 7\ m/s$ corresponding to the time averaging of 35.7 min, 11.7 min, 11.7 min, and 35.2 min, respectively.

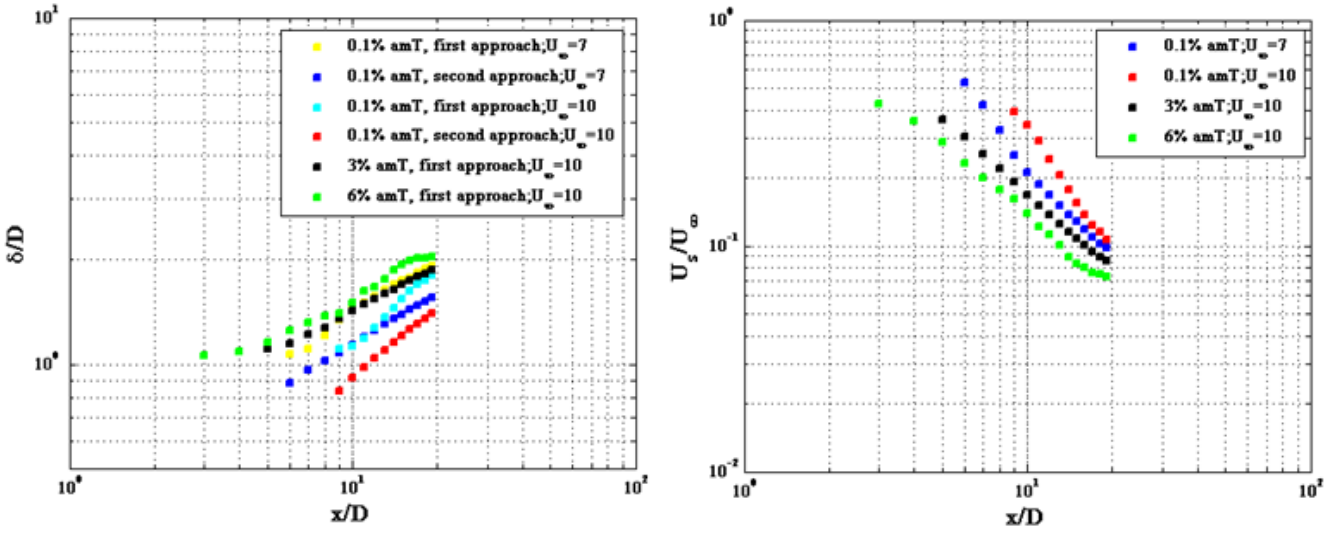

Figure 5: Log-log plot of dimensionless half of wake width (left) and the centerline wake velocity deficit (right) in transitional and far wake region, for different initial conditions

The wake width is calculated in two ways:

First approach (FA): Calculate δ to be two times of the distance from the wake centerline to which $\bar{u} - U_\infty$ is about $\frac{1}{2}\overline{U_s}$, where $\overline{U_s}$ is the time-averaged dimensionless wake velocity deficit at the center of y-z plane.

Second approach (SA): Calculate δ where $\frac{\bar{u}}{U_\infty} < 1$ and $\bar{u}$ stands for dimensionless wake velocity.

Comparing the values of dimensionless half of wake width for example at 0.1% and $U_\infty = 10\ m/s$ with Figure 2 seems that the estimations of $\frac{\delta}{D}$ based on the (first approach) is overestimated. Therefore, $\frac{\delta}{D}$ for 0.1% ambient

turbulence level is also calculated based on the second approach. Comparing the new values of $\frac{\delta}{D}$ with Figure 2 shows that the second approach might lead to more accurate results (for more details regarding calculation of $\frac{\delta}{D}$ the reader is referred to [15], however due to uncertainties at the edges of the wake , $\frac{\delta}{D}$ for ambient turbulence level larger than 0.1% is only calculated based on the second approach. In addition, the points related to x/D>17 may be effected by boundary conditions and therefore the last two points are not considered in further calculations in the study.

Comparing the amount of dimensionless half of wake width and centerline wake velocity deficit in Figure 5 shows that by increasing the ambient turbulence level, the decay of the centerline wake velocity deficit and the rate of wake width expansion will increase. Therefore, it can be concluded that increasing ambient turbulence level will lead to faster recovery of the wake. This could easily be explained by transferring of more momentum into the wake due to the larger gradient between the inside and outside of the flow, in the case of larger ambient turbulence levels. In addition, it can be seen from Figure 5 that for 0.1% ambient turbulence level by decreasing the ambient wind velocity (higher thrust coefficients), the wake recovery will be faster, but still slower than 3% ambient turbulence level.

In order to find the location where the far wake starts, the dimensionless centerline turbulence intensity ($\frac{I_s}{U_\infty}$) is plotted at different distances behind the wind turbine under different initial conditions, where I_s is defined as $\frac{I_s}{U_\infty} = \sqrt{\overline{u'^2}/U_\infty^2}$, and u' is the fluctuating wake velocity deficit.

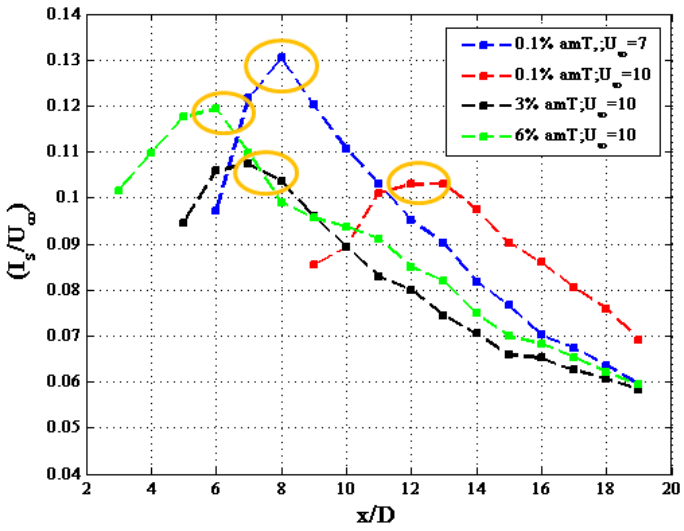

Figure 6: Centerline turbulence intensity at different distances behind the NM80 wind turbine under different initial conditions

It can be observed from Figure 6 that $\frac{I_s}{U_\infty}$ has increasing trend up to a certain level but after that it starts to decrease by increasing the distances. The main reason of that could be explained by the idea that in the near wake region, the turbulence level of the wake is mainly contributed from the ambient turbulence level in front of the turbine and the turbulence generated by the wind turbine rotors. From this region until the end of transitional region, the turbulence which is generated by the radial flow shear will start to affect the flow. Therefore,

dissipation starts to drain turbulent energy and the wake width increases while the velocity deficit is being reduced. This process may explain the gradual reduction of the increasing trend in both terms of $\frac{\overline{u'^2}}{U_\infty^2}$ as the wake evolves from the transitional region to the far wake, where the diffusion will be the dominant term and the turbulence will start to decrease considerably. Therefore, it is possible to find from Figure 6 that the end of the transitional region and therefore, beginning of the far wake will be at approximately $\frac{x}{D} \geq 13, \frac{x}{D} \geq 9, \frac{x}{D} \geq 8, \frac{x}{D} \geq 7$ for T=0.1% and $U_\infty = 10\ m/s$, T=0.1% and $U_\infty = 7 m/s$, T=3%and 6% ambient turbulence levels and $U_\infty = 10\ m/s$, respectively.

3.4 Power laws for centerline wake velocity deficit and half wake width

The accuracy of the two power laws of $\frac{1}{3}$ and $-\frac{2}{3}$ obtained in theoretical approach for the rate of wake expansion and decay of wake velocity deficit, are validated by numerical results. In order to do that these two powers ($\frac{1}{3}$ and $-\frac{2}{3}$) are also considered as two unknowns (α and β) in Eq. 8 as following,

$$\frac{\delta}{D} = A\left(\frac{x - x_0}{D}\right)^{\alpha} \quad ; \quad \frac{\overline{U_s}}{D} = B\left(\frac{x - x_0}{D}\right)^{\beta} \tag{11.}$$

It should be taken into consideration that the momentum thickness has decreasing trend in our data, due to the effect of pressure gradient, instead of a constant value which is required in Eqs. 8 (For more information, the reader is referred to [15]). Therefore, in order to obtain higher accuracy, Eqs. 8 are only non-dimensionalized based on the turbine diameter (D) in Eqs. 11 which means that he two coefficients *a* and *b* are now changed to A and B respectively. However, the relation between a, b in Eqs. 8 and A, B in Eqs, 11 could be easily found by using Eq. 5 as following.

$$A = 0.4\, C_T^{\frac{1}{3}} a \quad and \quad B = 0.4 C_T^{\frac{1}{3}} b \tag{12.}$$

In addition, it is also important to mention that in Eqs. 11, δ_* is substituted by δ which seems to give more accurate results. This means that the relation between a and b coefficients in Eqs. 9 ($b = 1/a^2$) is now changed to ($b = constant * 1/a^2$), since δ_* is the choice of δ, so that the integral in Eqs.7 ($\int_0^\infty \eta f(\eta) d\eta$) will be equal to unity.

However in Eq. 11 the system is not closed and the number of unknowns are different from the number of equations. Thus, in order to determine the unknowns, the problem is optimized and the best curve fitted with the numerical data based on the least square technique is found. The optimization process was down in Matlab by using "lsqcurvefit (f0, x00, xdata, Us)" and "lsqcurvefit (f0, x00, xdata, δ)" simultaneously, where f0 is defined as f0 = @(x,xdata)x(1)*(xdata-x0).^x(2), 'x','xd'; xdata corresponds the non-dimensionalized distances $\frac{x}{D}$ behind the rotor, and x0 and x00 are the virtual origin of the wake and initial value respectively. The previously mentioned "lsqcurvefit "will start at x00 and find the coefficient x to best fit the non-linear function f0 (x, xdata) to the data Us and δ ($ydata$) based on the least-square technique [22] as shown in Eq. 13.

$$\min_x \| F(x_i, xdata) - ydata \|_2^2 = \min_x \sum_i (F(x_i, xdata) - ydata_i)^2 \tag{13.}$$

Since X_0 is the joint term in both relations shown in Eq. 11, therefore it sets as an independent parameter in the non-linear function (f0), and consequently the problem is optimized based on this parameter for both quantities

of dimensionless centerline wake velocity deficit and half wake width at the same time. Moreover, optimization processes show that the problem is quite sensitive between the two distances where the transitional region is finished and the far wake is started. However it is not really possible to find the exact distance where the far wake starts. Therefore in order to have reliable results, which could be able to give close trend at both distances, the final solutions are chosen based on optimization of the average squared 2-norm of residuals of dimensionless centerline wake velocity deficit and half wake width between these two distances. Figure 7 shows the fitted curve with numerical data of dimensionless half wake width and centerline wake velocity deficit for different values of $\frac{x_0}{D} = 3$ to 8, 0.1% ambient turbulence level and $U_\infty = 10\ m/s$.

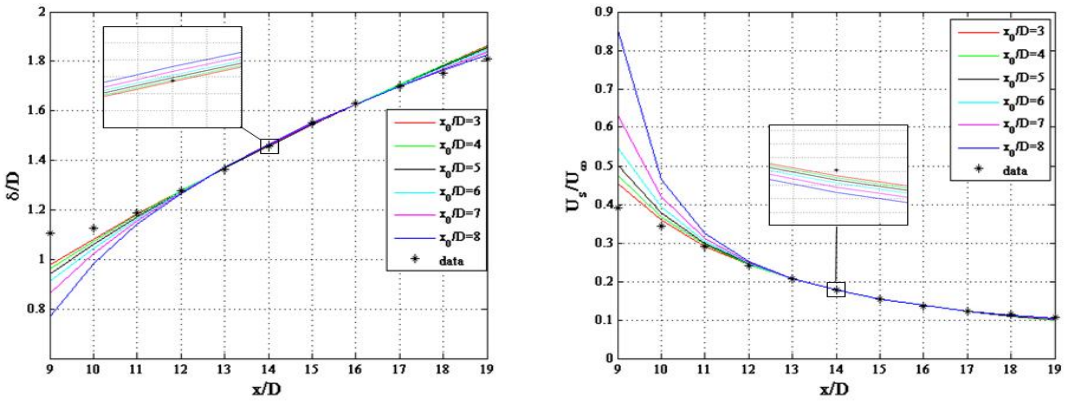

Figure 7: Fitted curve with numerical data of dimensionless half of wake width (left) and dimensionless centerline wake velocity deficit (right), for different x0/D values, 0.1% ambient turbulence level, and $U_\infty = 10\ m/s$

The results obtained from the optimization process for 0.1% and 3% ambient turbulence level and $U_\infty = 10\ m/s$ are as following. It should be taken into consideration that $\frac{\delta}{D}$ is calculated based on the second and first approach for ambient turbulence level of 0.1% and 3% respectively, in order to get the most reliable results.

***o*. 1%**: $\|residual\|_2^2 = 7.04E-06$; $\beta = -1.28$; $\alpha = 0.44$; $B = 3.06$; $A = 0.43$; $\frac{x_0}{D} = 4.84 \rightarrow \frac{\delta}{D} \sim \left(\frac{x}{D}\right)^{\frac{1}{2.27}}$; $\frac{U_s}{U_\infty} \sim \left(\frac{x}{D}\right)^{-\frac{2}{1.57}}$

3%: $\|residual\|_2^2 = 1.0674E-04$; $\beta = -1.01$; $\alpha = 0.39$; $B = 1.51$; $A = 0.6$; $\frac{x_0}{D} = 1.15 \rightarrow \frac{\delta}{D} \sim \left(\frac{x}{D}\right)^{\frac{1}{2.6}}$; $\frac{U_s}{U_\infty} \sim \left(\frac{x}{D}\right)^{-\frac{2}{1.98}}$

The above results show that the power which is obtained for the decay of centerline wake velocity deficit is far from the theoretical approach, while, the rate of wake expiation is a value between the two values which have been determined by Johansson et al. [2], for the two similarity equilibriums. However, for higher ambient turbulence the power laws become closer to the theoretical approach.

In addition, repeating the optimization processes for 0.1% ambient turbulence level and $U_\infty = 7\ m/s$ gave the following results

$\|residual\|_2^2 = 2.89E-04$; $\beta = -1.07$; $\alpha = 0.36$; $B = 1.78$; $A = 0.56$; $\frac{x_0}{D} = 2.97 \rightarrow \frac{\delta}{D} \sim \left(\frac{x}{D}\right)^{\frac{1}{2.8}}$; $\frac{U_s}{U_\infty} \sim \left(\frac{x}{D}\right)^{-\frac{2}{1.86}}$

Comparing the above results with the other two cases shows that the values obtained for the powers will become closer to the ones predicted by the theoretical approach as the wake recovers faster. However, comparing the rated of wake expansion for 0.1% ambient turbulence level and $U_\infty = 7\ m/s$ with 3% ambient turbulence level and $U_\infty = 10\ m/s$ shows a bit contradictory result. The main reason could be the fact of applying the first approach for estimation of the wake expansion at 3% ambient turbulence level and a relatively short time series of this simulation.

The difference between the results obtained from the optimization processes compared to theoretical approach might be due to the fact of neglecting of the nonlinear term of velocity deficit (the second term in the left side of Eq. 7). Figure 8 shows the percentage of the nonlinear term in the momentum integral in the transitional and far wake region behind the wind turbine for 0.1% and 3% ambient turbulence levels and $U_\infty = 10\ m/s$ and 0.1% ambient turbulence level and $U_\infty = 7 m/s$. As it is seen for 0.1% ambient turbulence, the percentage in the far wake region (x/D <12) is larger than 10, meaning that the theoretical approach might not be correct at this ambient turbulence level and wind speed. However, this trend improves by decreasing the ambient wind velocity or increasing the ambient turbulence level, due to the faster recovery of the wake.

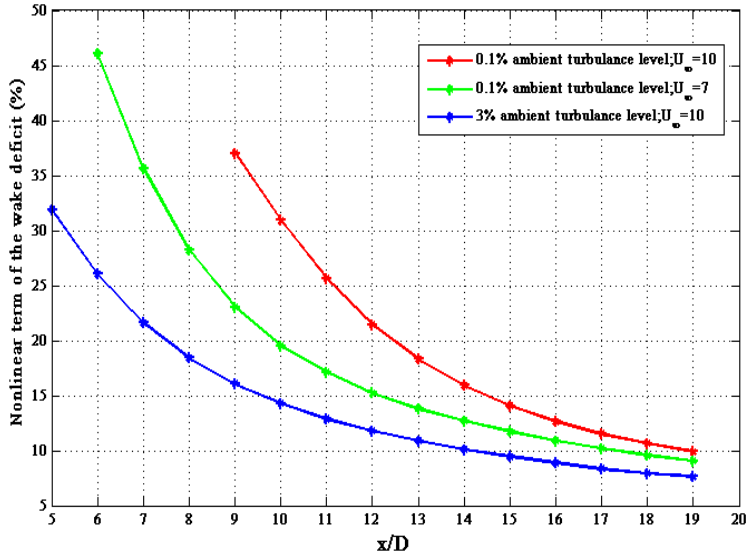

Figure 8: Estimation of the nonlinear term of the wake deficit in the momentum integral

To that end, it is also interesting to find the relations between β and α, as a function of thrust coefficient for 0.1% ambient turbulence level, Figure 9 shows these relations.

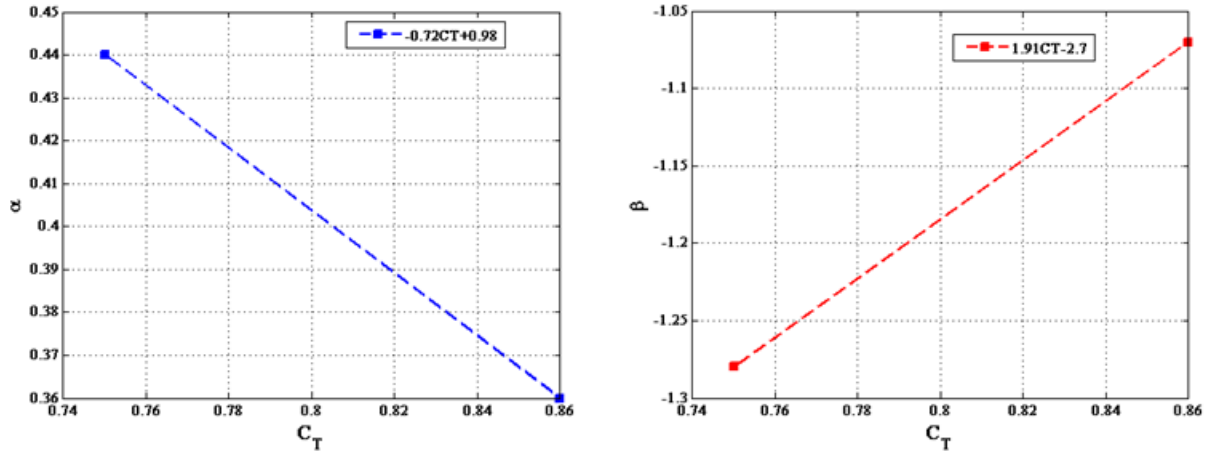

Figure 9, The relation between changes of β and α by the thrust coefficient, for 0.1% ambient turbulence level

3.5 Verification of the self-similarity behavior in the far wake

In order to verify the self-similarity behavior in the far wake of the wind turbine, the mean wake velocity profile scaled with centerline wake velocity deficit $\frac{\bar{u}-U_\infty}{\overline{U_s}}$ is plotted in self similarity coordinates $\eta = r/\delta$, for the case of 0.1% ambient turbulence level and $U_\infty = 10\ m/s$, in Figure 9.

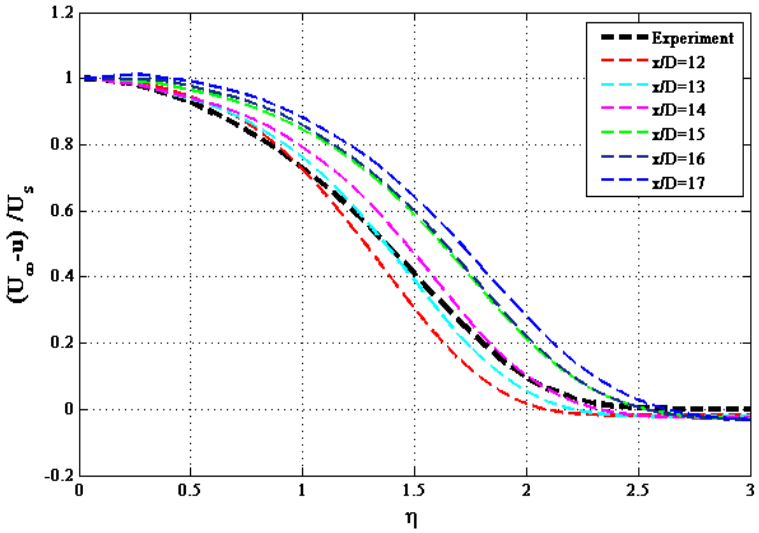

Figure 10: Mean wake velocity profile, scaled with centerline wake velocity deficit in self-preservation coordinate, (compared with the result shown in [2]).

In Figure 10, the numerical results are compared with a fitted curve to the experimental results which have been shown in [2] (black dashed line). However in the mentioned reference Johansson et al. argued that this trend is independent of the generator and should be similar for all cases. Figure 10 shows that the trends at different distances behind the wind turbine are in good agreement with the black dashed line. Therefore, it can be concluded that the mean velocity profile of the wake behind a wind turbine when scaled by centerline wake velocity deficit can reach the self-similarity state in the far wake region. However, the graphs do not collapse to a unique curve. This might be due to the presence of the pressure gradients even in the far wake which may lead to a small deviation of the above graphs, as the wake moves downstream.

4. Conclusion

The aim of this study was to improve the classical analytical model for estimating the rate of wake expansion and the decay of the wake velocity deficit in the far wake region behind a wind turbine. Therefore, in the theoretical approach, the flow parameters for a fully turbulent axisymmetric far wake were derived by applying the mass and momentum conservations, Reynolds shear stress, self- similarity assumption and utilizing the eddy viscosity closure. The theoretical approach was validated based on the results obtained from simulations that combine large eddy simulations with the actuator line technique for $0.1\%,\ 3\%, \text{and}\ 6\%$ ambient turbulence level and $U_\infty = 7 \text{ and } 10\ m/s$. The effect of ambient turbulence level and thrust coefficient on the wake recovery was investigated and the rate of wake expansion, and the decay of the wake velocity deficit was verified for 0.1%, 3% ambient turbulence level and $U_\infty = 10\ m/s$, and 0.1% ambient turbulence level and $U_\infty = 7\ m/s$. The results show that the time average of the wake velocity profile for a relatively long time domain will lead to axisymmetric and steady sate condition of the wake profile in a far wake region. The

nonlinear term of the velocity in the momentum equation in the far wake region cannot be neglected compared to the linear term, for low ambient turbulence level and high thrust coefficients. Therefore the theoretical determination of the powers for the wake expansion and the decay of the wake velocity deficit may not be valid in the case of the wake generated behind a wind turbine and low ambient turbulence level and high thrust coefficients. However, faster recovery of the wake by increasing the ambient turbulence level or decreasing the ambient wind velocity (higher thrust coefficients) will increase the differences between the linear and nonlinear terms of the momentum equations at certain distances behind the wind turbine, which will give closer powers for the decay of centerline wake velocity deficit and the expansion of half walk width, compared to the one predicted by the theoretical approach. In addition, the mean velocity profile of the wake behind a wind turbine, when scaled by the centerline wake velocity deficit, will reach the self-similarity state in a far wake region and low ambient turbulence level and high thrust coefficients.

Acknowledgement

This work was partly supported by the international project (DSF Sagsnr. 10-094544) under Danish Council for Strategic Research, Ministry of Science, Innovation and Higher Education, the Danish Council for Strategic Research for the project ' Center for Computational Wind Turbine Aerodynamics and Atmospheric Turbulence' (grant 2104-09-067216/DSF), (COMWIND) (http://www.comwind.mek.dtu.dk/Partners.aspx) , the Nordic Consortium on Optimization and Control of Wind Farms (http://picard.hgo.se/~nordwind/), which has provided access to the National Supercomputer Centre in Sweden (NSC), and Oticon Foundation.

References

[1] George, W.K., The self-preservation of turbulent flows and its relation to initial conditions and coherent structures. Advances in Turbulence, 1989: p. 39-73.

[2] Johansson, P.B.V., W.K. George, and M.J. Gourlay, Equilibrium similarity, effects of initial conditions and local Reynolds number on the axisymmetric wake. PHYSICS OF FLUIDS, 2003. 15(PART 3): p. 603-617.

[3] Johansson, P.B.V., The axisymmetric turbulent wake. 2002: Department of Thermo and Fluid Dynamics, Chalmers University of Technology.

[4] Johansson, P.B.V. and W.K. George, The far downstream evolution of the high-Reynolds-number axisymmetric wake behind a disk. Part 1. Single-point statistics. Journal of Fluid Mechanics, 2006. 555: p. 363-386.

[5] Cannon, S.C., Large-scale structures and the spatial evolution of wakes behind axisymmetric bluff bodies. 1991.

[6] Gourlay, M.J., et al., Numerical modeling of initially turbulent wakes with net momentum. PHYSICS OF FLUIDS, 2001. 13: p. 3783.

[7] Crespo, A., J. Hernandez, and S. Frandsen, Survey of modelling methods for wind turbine wakes and wind farms. Wind energy, 1999. 2(1): p. 1-24.

[8] Vermeer, L.J., J.N. Sørensen, and A. Crespo, Wind turbine wake aerodynamics. Progress in aerospace sciences, 2003. 39(6): p. 467-510.

[9] Lissaman PBS. Energy effectiveness of arbitrary arrays of wind turbine, in AIAA paper 79-0114, 1979. P.1-7

[10] Jensen, N.O., A note on wind generator interaction. 1983.

[11] Katic, I., et al., A Simple Model for Cluster Efficiency. EWEC'86. Proceedings. Vol. 1, 1987: p. 407-410.

[12] Larsen, G.C., A simple wake calculation procedure. 1988.

[13] Larsen, G.C., et al. Wind Fields in Wakes. in EWEC 1996 Proceedings. 1996. Goteborg (Sweden).

[14] Frandsen, S., et al., Analytical modelling of wind speed deficit in large offshore wind farms. Wind energy, 2006. 9: p. 39-53.

[15] Nasrin Arjomand Kermani, Analysis of turbulent wake behind a wind turbine, Master thesis, October 2012, Technical University of Denamk.

[16] Sørensen J. N., a.S.W.Z. Computation of wind tubine wakes using combined Novier Stokes/Actuator-Line Methodology. in the European Wind Energy Conferance EWEC 1999. Nice, Italy.

[17] Sørensen N.N, General Purpose Flow Solver Applied to flow over Hills in Risø, National labratory. 1995, Technical University of Denmark , Røskilde, Denmark.

[18] Michelsen, J.A., Basic 3D-A plat-Form for Development of multi block PDE solver. 1994, Department of luid mechanic, technical univerity of Denmark, DTU.

[19] Sørensen, N.N., General purpose flow solver applied to flow over hills. 1995: Risø¸ National Laboratory.

[20] Troldborg, N., J.N. Sørensen, and R. Mikkelsen. Actuator line simulation of wake of wind turbine operating in turbulent inflow. in Journal of Physics: Conference Series. 2007: IOP Publishing.

[21] Mann, J., Wind field simulation. Probabilistic engineering mechanics, 1998. 13(4): p. 269-282.

[22] MathWorks. [cited; Available , from: http://www.mathworks.se/help/optim/ug/lsqcurvefit.html.

DEVELOPMENT OF A THREE-DIMENSIONAL VISCOUS-INVISCID COUPLING METHOD FOR WIND TURBINE COMPUTATIONS

Néstor Ramos García , Jens Nørkær Sørensen and Wen Zhong Shen
Department of Wind Energy, Fluid Mechanics Section, Building 403,
Technical University of Denmark, DK-2800 Lyngby Denmark,
E-mail: nerga@dtu.dk

June 7, 2013

Abstract

$MIRAS$, a computational model for predicting the aerodynamic behavior of wind turbine blades and wakes subject to unsteady motions and viscous effects has been developed. The model is based on a three-dimensional panel method using a surface distribution of quadrilateral singularities with a Neumann no penetration condition. Viscous effects inside the boundary layer are taken into account through the coupling with the quasi-3D integral boundary layer solver Q^3UIC. A free-wake model is employed to simulate the vorticity released by the blades in the wake. In this paper simulations are presented in an effort to validate the code for three different rotor geometries, the MEXICO experiment rotor, the DELFT rotor and the NREL 5MW rotor.

1 Introduction

GPU and parallel computing, endless terabytes of memory, high speed connections, and other aspects of computer resources have become more powerful and accessible in recent years. However it is still behind our limits to use Navier-Stokes simulations for the design of wind turbines due to the large amount of computations involved in an optimization procedure. The free-wake vortex methods, extensively studied during the last four decades [1] [7] [2] [3], are now a mature tool with the potential to become the new generation of fast-tools for analysis and design of wind turbines. This type of code permits a direct interaction between the design procedure and the blade geometry (CAD) with a low computational cost. Unlike Navier-Stokes codes that need to solve the entire flow domain, panel methods can simulate the flow around a complex geometry by distributing singularity elements on the body surface. Panel methods become even more attractive by the possibility of solving the integral boundary layer equations and take into account the viscous effects using the transpiration velocity concept [4].

Wind turbine wake is a key element in the performance of rotor blade aerodynamics, having a strong influence in the rotor plane. From an engineering point of view, the free-wake vortex

approach is suitable to accurately model the inviscid phenomena that drives the general characteristics of the flow in the rotor wake, including the blade root and tip vortices, which are the most dominant structures in the wake. The basic free-wake vortex filament method consist of infinitely thin vortex filaments. To avoid numerical singularities, previous researchers have applied a viscous core model, modeling in this way a more physical distribution of the velocities induced by each one of the vortex filaments that forms the wake, desingularizing in this way the Biot-Savart law near the center of the filament, [8]. The diffusive time scales can be represented by changes in the vortex core radius as a function of the vortex age, using a turbulence eddy viscosity parameter [15]. Other improvements in the viscous core model include the introduction of changes in vortex strength due to filament stretching or squeezing, Ananthan and Leishman [9].

It is known that the viscous effects are important in the area surrounding the body surface, the boundary layer, playing a key role in the blade aerodynamics, especially at high angles of attack just before and after separation takes place. During the last decades simplified approaches to resolve the boundary layer equations have been developed by many researchers. In the two-dimensional case, panel methods have evolved to include viscous effects by solving the boundary layer in an integral manner, [10], [11] and [12] amongst others. Recently the Quasi-3D Unsteady Interactive Code Q^3UIC was developed by Ramos-García et al. [5] [6] to take into account the rotational effects arising from Coriolis and centrifugal forces. In the three-dimensional case, various researchers have previously implemented a viscous-inviscid coupling using the strip theory approach. Cebeci et al[20] combined a three-dimensional panel method with an inverse finite-difference boundary layer solver. Pesonen et al [21] and Lemmerman et al [22] coupled a three-dimensional panel method with an integral boundary layer solver. To the knowledge of the authors the present method has not yet been applied for the study of wind turbine aerodynamics and its wake dynamics.

In the present work a zonal viscous-inviscid coupling method is developed in which the inviscid part is composed by a three-dimensional panel method with a free-wake model, the viscous effects confined inside the boundary layer are computed with the integral boundary layer solver Q^3UIC. This viscous-inviscid interactive code will be referred as $MIRAS$, Method for viscous-inviscid Interactive Rotor Aerodynamic Simulations. In what follows $MIRAS$ is used to simulate the DELFT and MEXICO wind turbine model rotors and the NREL 5MW virtual rotor, simulated aerodynamic forces and wake velocities have been compared against experiments and Navier-Stokes simulations.

2 Governing equations

A wind turbine rotor is usually composed by two or three blades, their rotation generates a spiral vortex wake convected downstream. The rotor wake is formed by strong vortex structures and has a large impact in the aerodynamics of the rotor itself. To simulate the flow around a wind turbine rotor, we use a viscous-inviscid coupling method where the inviscid flow around the wind turbine rotor is solved using a panel method to simulate the blades, in which the viscous effects are taken into account by the Q^3UIC code. The wake is modeled by vortex filaments

released at the blades trailing edges in form of straight lines and convected downstream using the Biot-Savart law.

In the following paragraphs the theory behind this approach will be introduced briefly. For more detailed information about the model, the the reader is referred to Ramos-Garcia et al [5] [6].

For a potential flow around a solid body with surface S, the velocity at a point P in the flow domain can be expressed as a superposition of the undisturbed translating velocity, $\underline{U_\infty}$, and the disturbance velocity created by the solid body, $\underline{U_p}$, resulting in

$$\underline{U_I} = \underline{U_\infty} + \underline{U_p} \tag{1}$$

If the flow is considered to be incompressible, inviscid and irrotational, $\underline{U_p}$ can be expressed as

$$\underline{U_p} = -\nabla\phi \tag{2}$$

where ϕ is a potential function that satisfies the Laplace equation

$$\nabla^2\phi = 0 \tag{3}$$

As the solid body surface S is impermeable, the normal component of the velocity must be zero at the wall which gives a Neumann condition of no penetration across the body

$$\frac{\partial\phi}{\partial n} = \nabla\phi \cdot \underline{n} = \underline{U_\infty} \cdot \underline{n} \tag{4}$$

In practice, the problem is considered in two regions, the solid body and the downstream wake. The body is simulated by a distribution of quadrilateral surface dipoles, μ, and quadrilateral sources, σ. An extra source distribution, σ_{wT}, equal to the transpiration velocity computed with Q^3UIC, is introduced to account for viscous effects confined inside the boundary layer. The first row of wake elements is simulated using quadrilateral panel dipoles while further downstream the panels are converted into wake elements formed by straight line vortex filaments, Γ.

$$\nabla\Phi = \frac{-1}{4\pi}\int_b (\sigma + \sigma_{wT})\,\nabla\left(\frac{1}{r}\right) + \frac{1}{4\pi}\int_b \mu\nabla\left[\frac{\partial}{\partial n}\left(\frac{1}{r}\right)\right] + \frac{1}{4\pi}\int_w \Gamma\,\nabla\left[\frac{\partial}{\partial n}\left(\frac{1}{r}\right)\right] + \nabla\Phi_\infty \tag{5}$$

The vortex wake is released at the bodies trailing edges using the unsteady Kutta-Joukowsky condition of zero trailing edge loading. To satisfy this condition, at each time step a quadrilateral panel with a doublet distribution is created as the first wake panel for each one of the span-wise stations. The strength of these panels, $\underline{\Gamma_{fst}}$, is equal to the difference between the corresponding upper and lower trailing edge quadrilateral doublets

$$\underline{\Gamma_{fst}} = \underline{\mu_u} - \underline{\mu_l} \tag{6}$$

Following Katz and Plotkin [7] the first wake panel is convected downstream from the trailing edge with a 30% of the local undisturbed velocity. Downstream of the first row of wake panels the quadrilateral doublets are transformed into vortex filaments and clustered into vortex

elements. The strength of the vortex filaments remains constant in time with their motion represented by Lagrangian fluid markers placed at its end points which are convencted downstream with the total velocity $\underline{\mathbf{u}}$

$$\underline{\mathbf{u}} = \underline{\mathbf{u}}_{\infty} + \underline{\mathbf{u}}_{body} + \underline{\mathbf{u}}_{wake} \tag{7}$$

where $\underline{\mathbf{u}}_{\infty}$ is the freestream velocity, $\underline{\mathbf{u}}_{body}$ is the influence of the solid body and $\underline{\mathbf{u}}_{wake}$ is the induction created by the other wake elements.

The velocity induced by the wake vortex filaments is computed by applying the Biot-Savart law. In order to desingularize its behavior as $\mathbf{r}$ tends to zero the Biot-Savart formula is modified following Leishman et al. [13]. Where a viscous core is applied to all the released vortex filaments during the time updating procedure. Therefore, an approximation to viscous diffusion, vortex core growth and vortex straining is included modifying the Biot-Savart law as follows

$$\mathbf{u}_{wake} = K\frac{\Gamma}{4\pi}\frac{\underline{\mathbf{dl}} \times \underline{\mathbf{r}}}{|\underline{\mathbf{r}}|^3} \tag{8}$$

where K is the kernel parameter, which uses the Scully profile account for the vortex filament viscous core [14]. To include the core growth rate, Squire model is applied by introducing the turbulent eddy viscosity parameter [15]. Following Bhagwat and Leishman a straining model has been implemented to take into account the change in vortex filament radius due to its variations in length, stretching or squeezing [16].

Once the wake updating procedure is finalized, the new solution for the solid body singularities is calculated. Knowing the doublets, μ, the local inviscid perturbation velocities are calculated using a nodal interpolation of the doublets strength. Finally, the unsteady Bernoulli equation is used to compute the surface pressure on each one of the rotor blades,

$$\frac{\partial \underline{\phi}}{\partial t} + \frac{1}{2}|\underline{\mathbf{v}}|^2 + \frac{1}{\rho}\underline{p} = +\frac{1}{\rho}\underline{p}_{ref} \tag{9}$$

Viscous-inviscid coupling

The viscous boundary layer is solved by using the in-house Q^3UIC code. Q^3UIC is an aerodynamic tool developed to solve the quasi three-dimensional integral boundary layer equations, [5] [6]. The model is based on a viscous-inviscid interaction technique using strong coupling between the viscous and inviscid parts. In Q^3UIC, the inviscid part is solved using a two-dimensional potential flow panel method and the viscous effects are taken into account by solving the integral form of the boundary layer $r-$ and $\theta-$ momentum equations with extension for three-dimensional rotational effects created by Coriolis and centrifugal forces.

The r and θ integral momentum boundary layer equations can be written in terms of the boundary layer edge velocity, u_e, and the integral boundary layer parameters $\theta_1, \theta_2, \delta_1^*, \delta_2^*, \delta, \delta_3, H, C_f$ and β_w as:

$$\frac{\partial \theta_1}{\partial s} = -\frac{1}{u_e^2}\frac{d}{dt}\left(u_e \delta_1^*\right) - \frac{\partial \theta_1}{u_e}\frac{\partial u_e}{\partial s}\left(2+H\right) + \frac{C_f}{2} + s_w p_r \frac{2R_O l}{u_e c}\delta_2^* \tag{10}$$

$$\frac{\partial \theta_2}{\partial s} = -\frac{2\theta_2}{u_e}\frac{\partial u_e}{\partial s} + tan\beta_w \frac{C_f}{2} - \frac{1}{u_e}\frac{\partial u_e}{\partial r}\left(2\delta_3 + \delta\right) + \frac{l}{c}\left(\theta_1 + \delta_1^* - \delta - \delta_3 + s_w p_r \frac{2R_O}{u_e}\left(\delta - \delta_1^*\right)\right) \tag{11}$$

In the laminar flow region, the solution of the integral form of the $r-$ momentum Equation 10 is obtained using Twaites' method while in turbulent flow region, the solution of the integral form of the $r-$ and $\theta-$momentum Equations 10 and 11 is carried out using a set of three dimensional turbulent closure relations for the streamwise and spanwise boundary layer variables.

The coupling between the viscous and inviscid parts in $MIRAS$ is done locally for each of the spanwise stations through the transpiration function using the angle of attack calculated upstream the blades leading edge to set the viscous computations. Q^3UIC is used to compute the boundary layer parameters and obtain the chordwise distribution of the transpiration velocity at the center line of the discrete spanwise sections. Q^3UIC computations are performed for the given sectional airfoil geometry at the calculated angle of attack using the following non-dimensional parameters: Reynolds number, $Re = \sqrt{(\Omega r)^2 + (Q_w)^2}\, c/\nu$, ratio between rotational speed and relative velocity, $R_O = \Omega r / U_{rel}$ and ratio between chord length and radial position, $l = c/r$.

The transpiration velocity is computed using the following expression,

$$w_T = \frac{1}{\rho}\frac{\partial}{\partial s}\left(\rho u_e \delta_1^*\right) \tag{12}$$

w_T is introduced in the three dimensional panel method as a source distribution, which acts blowing outwards the limiting streamlines, mimicking the effect of a viscous boundary layer around the blade contour.

3 Results

In this section results obtained with the $MIRAS$ code for the DELFT model rotor, the MEXICO rotor and the virtual NREL 5MW rotor will be presented.

DELFT model rotor

In this section $MIRAS$ simulations of flows past the DELFT model rotor, Figure 1, are compared against hot-film measurements performed by Sant [17] in the open jet wind tunnel of Delft University of Technology. The two bladed DELFT rotor has a radius of $0.6\ m$. The blade has a constant chord of $0.08\ m$ and varying twist angle, constructed using NACA 0012 airfoil along the full blade span. The incoming wind speed in the presented simulations is $5.5\ ms^{-1}$ while

the blades are rotating at a constant angular velocity of $73.3\ s^{-1}$. A surface mesh consisting of 20 spanwise cells and 50 chordwise cells has been used for the $MIRAS$ simulations.

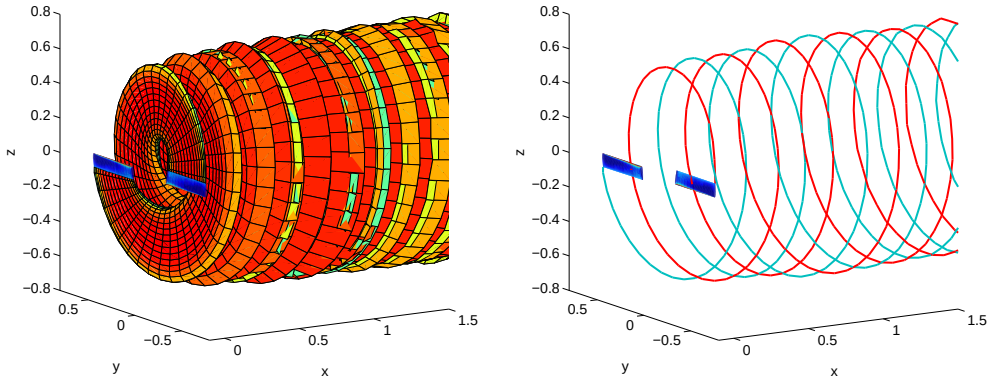

(a) (b)

Figure 1: The wake behind the DELFT rotor at $TSR = 7.96$ (a) full free wake (b) tip vortex filaments.

In Figure 2, the viscous and inviscid axial velocity predictions computed with $MIRAS$ are compared against measurements at distances of $3.5\ cm$ and $9\ cm$ downstream of the rotor plane at a radial location of $0.6R$ along the azimuthal direction from 0 to 360 degrees. Small differences arise between the viscous and inviscid simulations, and the viscous solution is closer to experimental data at the $3.5\ cm$ locations and vice versa at $9\ cm$. Simulations capture pretty well the axial velocity step created by the passage of the blade at the azimuthal positions of 180 and 360 degrees.

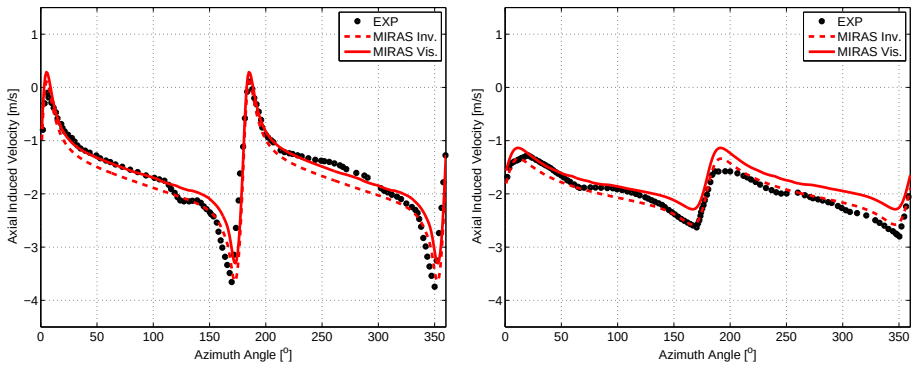

(a) (b)

Figure 2: Axial induced velocity along the azimuthal direction at (a) $3.5\ cm$ and (b) $9\ cm$ downstream of the rotor and a radial location of $0.6R$.

In Figure 3, $MIRAS$ predictions are compared against the measurements performed at a

radial location of $0.9R$ and two downstream positions. Calculated induced velocities are in good agreement with measurements at the $3.5\ cm$ location, implying therefore that the correct rotor loading was predicted. Larger differences can be appreciated at $9\,cm$, where inviscid simulations are closer to experiments. The more concentrated tip vortices computed in simulations and perhaps a deficient prediction of the wake filaments development near the tip region could give rise to such increasing mismatches between viscous, inviscid simulations and experiments with the downstream location. The use of a finer angular and spanwise discretization or even an adaptative mesh approach could improve the vortex roll-up characteristics.

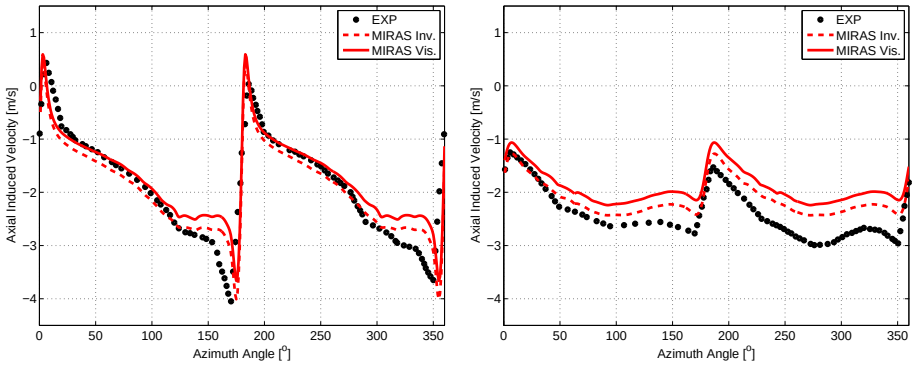

(a) (b)

Figure 3: Axial induced velocity along the azimuthal direction at (a) $3.5\ cm$ and (b) $9\ cm$ downstream of the rotor and a radial location of $0.9R$.

The calculated wake vortex filaments for the viscous simulations presented above are shown in Figure 4. The influence of the wake passage crossing through the hot-film sampling vicinity is clearly seen at the $0.9R$ locations around 180 and 360 degrees, although its influence diminish with the decreasing radial location due to the weaker vortices shed in that region.

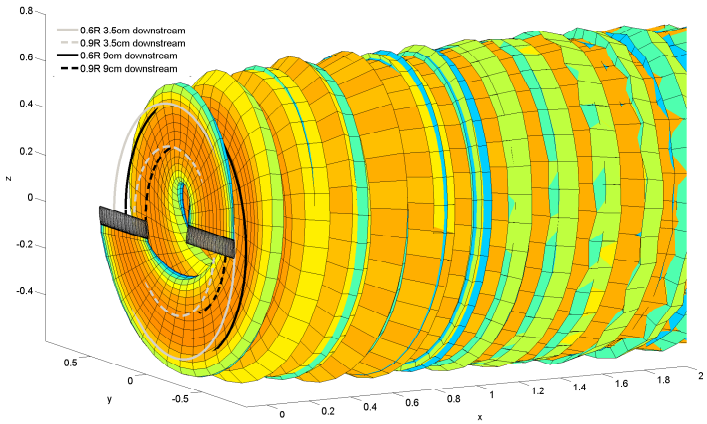

Figure 4: Calculated wake filaments for the DELFT rotor including hot-film location.

MEXICO model rotor

A further validation of the viscous and inviscid versions of the $MIRAS$ code is carried out for flows past the MEXICO rotor, Figure 5. In what follows the blade normal and tangential forces are compared against measurements and wake velocities are validated against PIV experimental data.

The MEXICO experiment was executed on a three-bladed wind turbine model with a diameter of $4.5\,m$ under controlled conditions in the Large Scale Low Speed Facility of the German-Dutch Wind tunnel Organization DNW with a $9.5\ X\ 9.5\ m^2$ open test section. The test cases considered here are the rotor rotating with a constant angular speed of $424.5\,rpm$ at wind speeds of 10, 15 and $24\ ms^{-1}$. The blades are subjected in all the three cases to a negative collective pitch of $\delta_0 = -2.3°$. Instantaneous velocities were extracted in a plane at 9 o'clock when looking downstream at the rotor when the first blade pointed upwards. For more detailed information about the MEXICO experiment campaign the reader is referred to Schepers and Snel [18].

A surface mesh consisting of 20 spanwise cells and 50 chordwise cells was used for $MIRAS$ simulations. Laminar to turbulent transition was forced at a 5% of the chord from the leading edge on both the upper and lower sides of the airfoil sections.

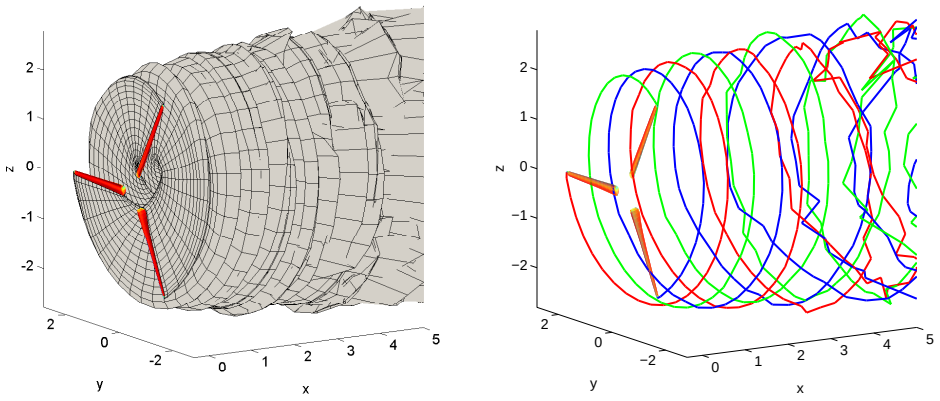

(a) (b)

Figure 5: MEXICO rotor at $TSR = 6.67$ (a) full free wake (b) Tip vortex filaments.

In Figure 6, the predictions of the normal an tangential blade forces are compared against experimental values for the wind speeds cases of 10, 15 and $24\ ms^{-1}$. As the wind speed increases the inviscid computations predict higher values of both normal and tangential forces while the viscous simulations are in much better agreement with experiments, except in the root region where rotational effects arising from Coriolis and centrifugal forces seem to be underpredicted. At $24\ ms^{-1}$ differences between the viscous and inviscid predictions are enormous, this is related to the existence of regions with trailing edge separation.

In Figures 7 and 8 $MIRAS$ viscous and inviscid predicted velocities are compared against PIV measurements in axial and radial traverses for a wind speed of $24ms^{-1}$. Viscous simulations

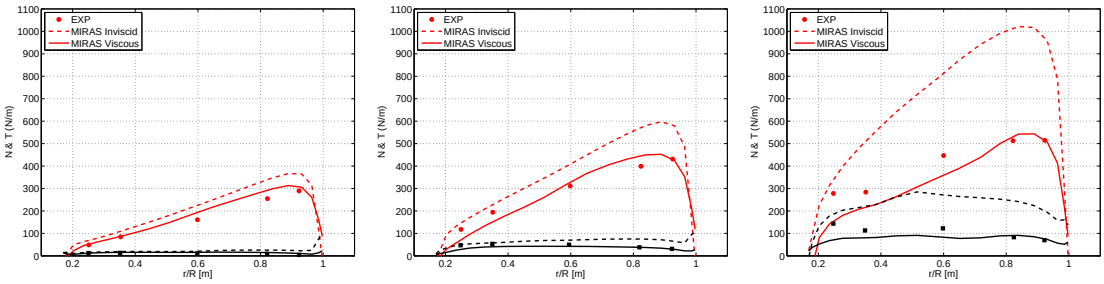

(a) (b) (c)

Figure 6: Blade normal and tangential forces at wind speeds of (a) 10, (b) 15 and (c) 24 ms^{-1}.

capture much better the axial velocities while the radial and tangential ones are more difficult to predict. Overall a good agreement was obtained against experiments in all the cases.

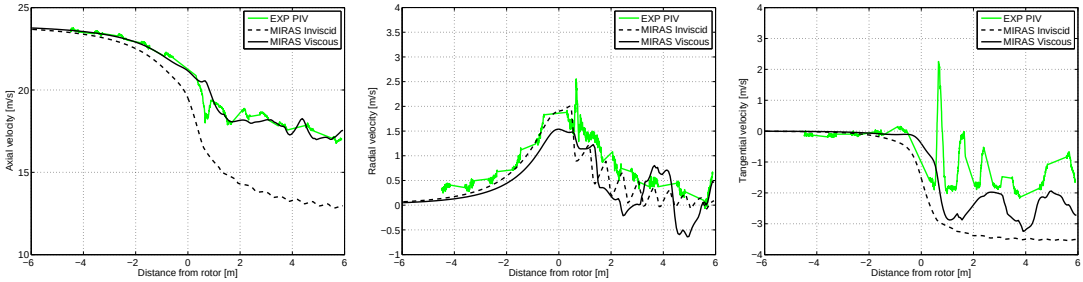

(a) (b) (c)

Figure 7: (a) Axial, (b) radial and (c) tangential velocities in an axial traverse of z = 1.38 m at a wind speed of 24 ms^{-1}.

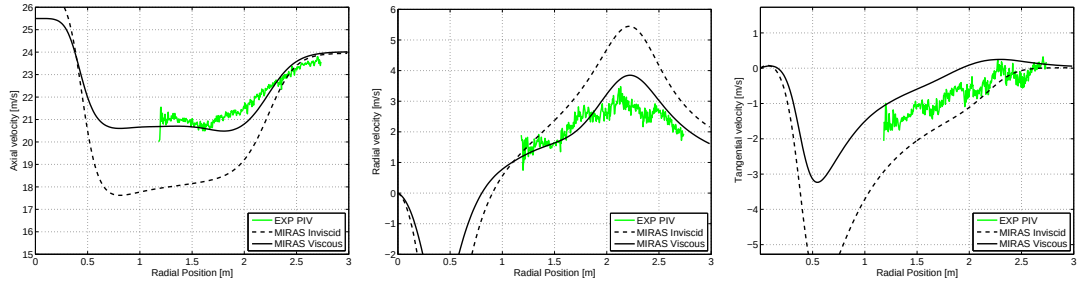

(a) (b) (c)

Figure 8: (a) Axial, (b) radial and (c) tangential velocities in a radial traverse of x = 0.30 m at a wind speed of 24 ms^{-1}.

NREL 5 MW virtual rotor

In this section $MIRAS$ simulations are compared against Navier-Stokes computations for the NREL 5 MW virtual wind turbine. The CFD computations were carried out using the $EllipSys3D$ code in fully turbulent mode with the $k-\omega$ SST turbulence model [19]. The mesh used by EllipSys3D is a cylindrical mesh of $4.2 \cdot 10^6$ mesh points which covers a domain with a radius of $245\ m$ and inlet and outlet located at $287\ m$ in front and behind the rotor. A surface mesh consisting of 20 spanwise cells and 50 chordwise cells has been used in this case and 14 wake revolutions were simulated with an angular discretization of $10°$.

The wake calculated in $MIRAS$ simulations, Figure 9, shows an important wake expansion and it can be appreciated how the interaction between the vortex sheets breaks the smooth shape of the wake as it moves downstream. This effect is clearly observed when following the vortex filaments released from the blades tip, Figure $9(b)$. After two wake revolutions the blade to blade filament interaction grows and generates a vortex pairing phenomena which makes the filaments tangle with each other as they move further downstream.

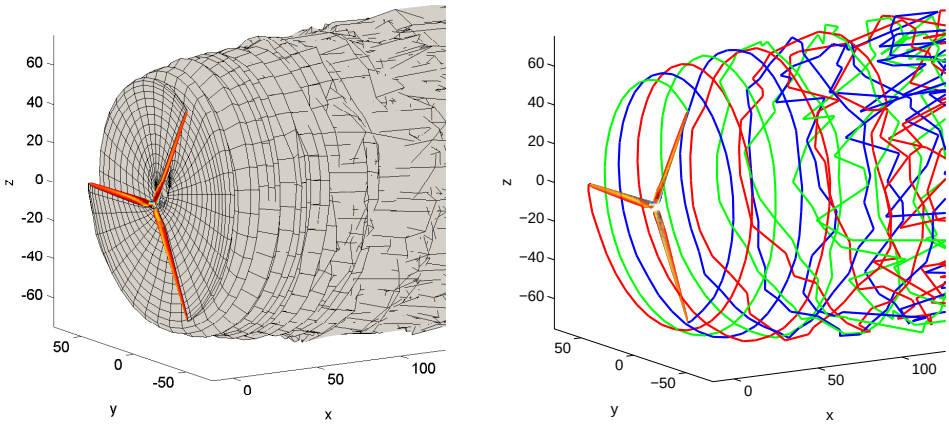

(a) (b)

Figure 9: (a) Full free wake (b) Tip vortex filaments of flows pass the NREL 5MW rotor at a $TSR = 6.65$.

Predicted normal and tangential forces are compared for the cases at wind speeds of $6\ ms^{-1}$ and $10\ ms^{-1}$, Figures 10 and 11. In terms of normal forces $MIRAS$ viscous predictions are in excellent agreement with CFD data, while the inviscid ones are overpredicted as expected. From the figures, it is seen that viscous simulations underpredict the tangential force near the blade tip region at the higher wind speed case, $10\ ms^{-1}$, although a better agreement is obtained at $6\ ms^{-1}$.

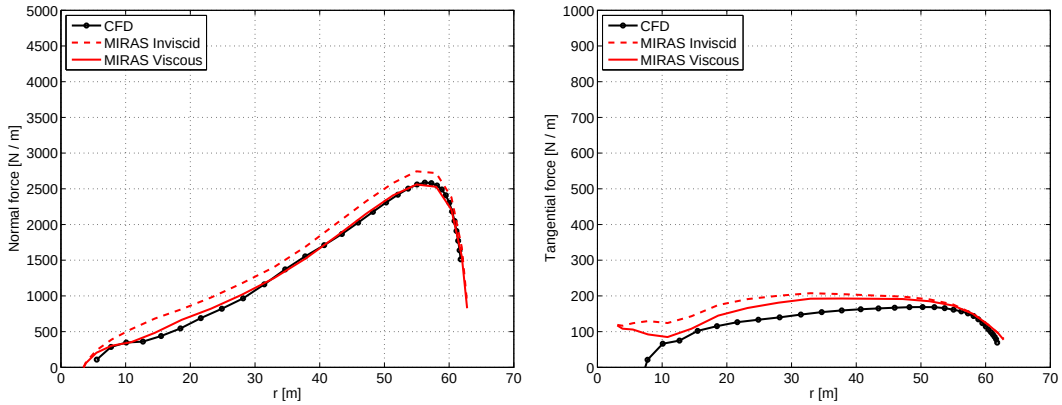

(a) (b)

Figure 10: (a) Normal and (b) tangential forces on the NREL 5MW blades. Viscous and inviscid $MIRAS$ and Navier-Stokes $EllipSys3D$ simulations for $6\,ms^{-1}$.

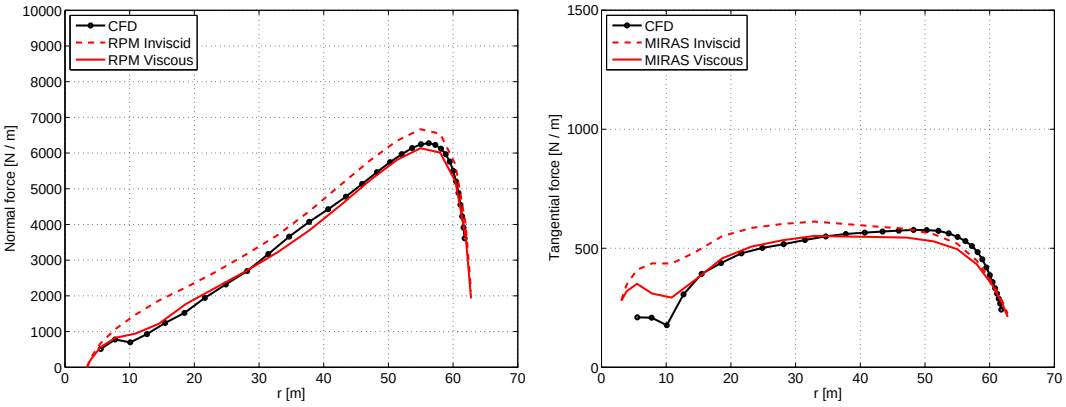

(a) (b)

Figure 11: (a) Normal and (b) tangential forces on the NREL 5MW blades. Viscous and inviscid $MIRAS$ and Navier-Stokes $EllipSys3D$ simulations for $10\,ms^{-1}$.

4 Conclusion

The $MIRAS$ code, an unsteady three-dimensional panel method coupled with the integral boundary layer solver Q^3UIC has been presented and validated against experiments and CFD simulations for three different wind turbine rotors.

Near wake axial velocities computed with $MIRAS$ have been compared with hot-film measurements for the DELFT model wind turbine obtaining a good agreement.

Computed axial, radial and tangential velocities have been validated against MEXICO PIV measurements, as well as normal and tangential blade forces.

To conclude the study, $MIRAS$ simulations of the virtual NREL 5 MW wind turbine have been compared against Navier-Stokes simulations in terms of blade forces, obtaining an excel-

lent agreement for the normal forces and a fairly good comparison for the tangential ones.

5 Acknowledgements

We gratefully acknowledge the support from the Danish Council for Strategic Research for the project 'Center for Computational Wind Turbine Aerodynamics and Atmospheric Turbulence' (2104-09-067216/DSF), the Energy Technology Development and Demonstration Program (EUDP-2011-64011-0094) and the Danish Energy Agency (EUDP-2012-64012-0146).

References

[1] J.L. Hess 1971 Numerical solution of inviscid subsonic flows *Von Karman Institute for Fluid Dynamics, Lecture Series,* ***34***

[2] J. Katz 1985 Calculation of the Aerodynamic Forces on Automotive Lifting Surfaces *Transactions of the ASME,* ***107****: 438–443*

[3] L. Morino, Z. Kaprielian and S.R. Sipcic 1985 Free Wake Analysis of Helicopter Rotors *Vertica,* ***9****: 127–140*

[4] M.J. Lighthill 1958 On displacement thickness *Journal of Fluid Mechanics, vol. 4, pp. 383-392*

[5] N. Ramos-García 2011 Unsteady viscous-inviscid interaction technique for wind turbine airfoils *PhD. Thesis, Technical University of Denmark, Department of Mechanical Engineering, ISBN 978-87-90416-53-9*

[6] N. Ramos-García, W.Z. Shen and J.N. Sørensen 2013 A Strong Viscous-Inviscid Interaction Model for Rotating Airfoils *Submitted to Wind energy*

[7] J. Katz and A. Plotkin 1977 Low speed aerodynamics *McGraw-Hill, second edition*

[8] J.G. Leishman 2000 Principles of Helicopter Aerodynamics *Cambridge University Press*

[9] S. Ananthan and J.G. Leishman 2004 Role of Filament Strain in the Free-Vortex Modeling of Rotor Wakes *Journal of the American Helicopter Society*

[10] T. Cebeci, M. F. Platzer, H. M. Jang and H. H. Chen 1993 An inviscid-viscous interaction approach to the calculation of dynamic stall initiation on airfoils *Journal of Turbomachinery,* ***115****: 714-723*

[11] J. N. Sørensen 1988 Prediction of Separated FLow Past Airfoil using Viscous-Inviscid Interaction Technique *La Recherche Aerosptatiale 1-11*

[12] M. Drela and M. B. Giles 1987 Viscous-inviscid analysis of transonic and low Reynolds number airfoil *AIAA journal **25**: 1347–1355*

[13] J.G. Leishman, M.J. Bhagwat and A. Bagai 2002 Free-Vortex Filament Methods for the Analysis of Helicopter Rotor Wakes *Journal of Aircraft **5**: 759–775*

[14] M.P. Scully 1975 Computation of Helicopter Rotor Wake Geometry and Its Influence on Rotor Harmonic Airloads *Ph.D. Thesis, Massachusetts Institute of Technology. Dept. of Aeronautics and Astronautics*

[15] H.B. Squire 1965 The growth of a vortex in turbulent flow *Aeronautical Quarterly **16**: 302–306*

[16] M.J. Bhagwat and J.G. Leishman 2001 Accuracy of Straight-Line Segmentation Applied to Curvilinear Vortex Filaments *Journal of the American Helicopter Society **46**:2:166-169*

[17] T. Sant 2007 Improving BEM-base Aerodynamic Models in Wind Turbine Design Codes *PhD Thesis, ISBN: 978-99932-0-483-1, Delft University Wind Energy Research Institute*

[18] J.G. Scheepers and H. Snel 2007 Model Experiments in Controlled Conditions Final Report *The Energy Research Center of the Netherlands The Energy Research Center of the Netherlands*

[19] W.Z. Shen, W.J. Zhu, J.N. Sørensen, N.N. Sørensen and P.E. Réthoré 2012 Study of tip loss corrections using CFD rotor computations *The Science of Making Torque from Wind, Oldenburg*

[20] T. Cebeci, D. Sedlock, K.C. Chang and R.W.Clark 1988 Analysis of Wings with Flow Separation *Journal of Aircraft, **26**:3:214-220*

[21] U.J. Pesonen, R.K. Agarwal and S. Laine 2000 Fast and Robust Viscous/Inviscid Interaction Code for Wing Flowfield Calculations *Journal of Aircraft, **37**:4:730-733*

[22] L.A. Lemmerman and V.R. Sonnad 1979 Three-Dimensional Viscous-Inviscid Coupling Using Surface Transpiration *Journal of Aircrfact, **16**:6:353-358*

ON THE GENERATION OF VORTICITY IN ROTOR- AND DISC FLOWS

Gijs van Kuik

DUWIND, Delft University of Technology, g.a.m.vankuik@tudelft.nl

ABSTRACT

Actuator disc and -line analyses as well as the momentum part of the Blade Element Momentum models use a given force field as input in flow field calculations. In most other aerodynamic analyses the force field is the output result instead of input. This is done by applying boundary conditions at the lifting surface with which the flow is solved and the pressure at the surface, so the load, is determined. In this respect both approaches are consistent, but appear to differ with respect to the generation of vorticity. In the lifting surface approach, usually Helmoltz's laws are used to show that bound and free vorticity is conserved, instead of being generated in the force field approach. Besides this, the question is discussed how a force field creates vorticity in an inviscid flow, since many papers consider viscosity as the vorticity generating mechanism. It is shown that both methods are consistent since Helmholtz's laws are incorrectly referred to. These laws have been derived in absence of non-conservative forces, while the surface pressure distribution is shown to the equivalent of such a force field. Furthermore a literature study reveals that not viscosity but a tangential pressure gradient is responsible for vorticity generation. This is consistent with the force field approach.

A comparison of the convection of vorticity in the wake of a disc, rotor blade and wing shows several characteristic differences. The linearised convection model for the wing, the horse shoe vortex, cannot be applied for wings with small aspect ratio since non-linear effects in the tip vortex creation and convection become dominant. The force field based methods used in rotor aerodynamics do not account for such an effect.

The paper provides some new findings but rather than being a research paper its character is mainly reviewing, resolving some questions on vorticity generation by force fields.

1 INTRODUCTION

Rotor aerodynamics is one of the few areas in aerodynamics where forces fields are used as input in flow calculations. In most other aerodynamic analyses the force field is the output instead of input. One of the reasons why force fields as input are not used anymore is that usually they are not known in advance. Furthermore the kinematical method for

which Lanchester, Prandtl and Joukowsky have laid the basis, has been shown to be very powerfull. However, particularly in rotor aerodynamics the use of force fields has some advantages. The force field approach allows for much easier physical interpretation of flow problems, since the thrust, being the integrated load, is the main parameter defining flow states. This holds for the classical actuator disc theory and the Blade Element Momentum (BEM) methods but also for actuator line analyses where blade properties are replaced by an assumed blade load in order to have a much lower computation time compared to full CFD solutions. The question how to know the force fields in advance is solved by either the definition of the problem (in actuator disc analyses: based on physical arguments a load distribution is assumed, e.g. Sørensen, Shen, Munduate [24]) or by iteration with other methods (in actuator line and momentum anlyses: for a given flow field the load is taken from a Blade Element calculation, which is used as force-input in the calculation of an updated flow field, etcetera, e.g. Shen, Zhu, Sørensen [23]).

The kinematical approach (no force field, boundary conditions at the lifting surface) and the dynamical approach (prescribed force fields) are compatible, as shown by Prandtl [20] for a wing and by van Kuik [11] for a rotor blade. However, a comparison of both methods with respect to the generation and convection of vorticity is not yet available while an important difference is observed, at first sight. A force field $\boldsymbol{f}$ is known to generate vorticity when $\boldsymbol{\nabla} \times \boldsymbol{f} \neq 0$ so when it is non-conservative. This is the case at the edge of an actuator disc or at the tip of an actuator line: at these positions vorticity is produced and trailed into the flow. In the kinematical method the blade is the carrier of bound vorticity, which continues as trailing vorticity. In other words: vorticity is conserved instead of generated which is sometimes explained by Helmholtz's laws for vorticity conservation. The consistency of both methods with respect to the generation of vorticity is the first topic of this paper. Moreover the question is addressed how a force field can produce vorticity in an inviscid flow, since many authors like Betz [3] mention viscosity as the main source of vorticity.

A second topic is to compare the vortex scheme of a wing (the horse shoe vortex) with the scheme of a rotating blade and an actuator disc. The horse shoe model is known to be valid for slender wings only since non-linear effects in the creation and convection of the tip vortex become larger for short wings. The question is whether similar effects are important in rotor flows.

The next section treats the equation of motion including force fields, after which the convection of the vorticity is discussed in section 3, followed by a concluding section.

2 GENERATION OF VORTICITY BY FORCE FIELDS

2.1 The equations of motion

The flow is assumed to be incompressible, homogeneous, inviscid and isentropic. Furthermore only steady flows are discussed here so the Euler equation

$$(\boldsymbol{v} \cdot \boldsymbol{\nabla})\, \boldsymbol{v} = \frac{1}{\rho} (\boldsymbol{f} - \boldsymbol{\nabla} p) \tag{1}$$

is valid, with $\boldsymbol{v}$ being the velocity vector, ρ the flow density and p the pressure, as well as the continuity equation

$$\boldsymbol{\nabla} \cdot \boldsymbol{v} = 0. \tag{2}$$

Rewriting (1) with the vector identity $(\boldsymbol{v} \cdot \boldsymbol{\nabla})\, \boldsymbol{v} = \nabla\, (\boldsymbol{v}.\boldsymbol{v})\, /2 - \boldsymbol{v} \times \boldsymbol{\omega}$ yields

$$\boldsymbol{f} = \boldsymbol{\nabla} H - \rho \boldsymbol{v} \times \boldsymbol{\omega} \tag{3}$$

where H is the Bernoulli constant $p + \rho/2 \boldsymbol{v} \cdot \boldsymbol{v}$ and $\boldsymbol{\omega}$ the vorticity.

The use of the force field $\boldsymbol{f}$ is discussed in old text books and papers, like von Kármán & Burgers [7]. Most modern textbooks pay some attention to the force term but at some moment assume that $\boldsymbol{f}$ is conservative, like the gravity force field. A conservative force field satisfies $\boldsymbol{\nabla} \times \boldsymbol{f} = 0$ or equivalently

$$\boldsymbol{f} = -\boldsymbol{\nabla} \mathcal{F} \tag{4}$$

where $\mathcal{F}$, being the potential of $\boldsymbol{f}$, can be considered as the associated potential energy, Batchelor [2] p. 138/157. If $\boldsymbol{\nabla} \mathcal{F}$ is supposed to be included in the pressure gradient $\boldsymbol{\nabla} p$, the force field term is removed from the equation of motion.

Here the force field term is retained explicitly. The force density $\boldsymbol{f}$ is confined to a limited volume V: force fields acting throughout space such as gravity fields are excluded. The relation between the force density $\boldsymbol{f}$, dimension Nm^{-3}, and the surface load $\boldsymbol{F}$, Nm^{-2}, is defined by integration of $\boldsymbol{f}$ across the thickness ϵ

$$\int_{\epsilon} \boldsymbol{f}\, dx = \boldsymbol{F}. \tag{5}$$

In general, the force field can have both components, non-conservative as well as a conservative. A non-conservative force field $\boldsymbol{f}$ is able to generate vorticity, as shown by the curl of (3), see Saffman [22] p. 10-11

$$(\boldsymbol{v} \cdot \boldsymbol{\nabla})\, \boldsymbol{\omega} = \frac{1}{\rho} \boldsymbol{\nabla} \times \boldsymbol{f} + (\boldsymbol{\omega} \cdot \boldsymbol{\nabla})\, \boldsymbol{v} \tag{6}$$

The right hand side gives the change of vorticity due to the action of a force field or due to tilting and stretching of already existing vorticity filament expressed by $(\boldsymbol{\omega} \cdot \boldsymbol{\nabla})\, \boldsymbol{v}$. If S is any closed surface encompassing the finite volume V at which $\boldsymbol{f}$ is distributed, so $\boldsymbol{f} = 0$ at S, then Stokes's theorem gives

$$\int_{V} \boldsymbol{\nabla} \times \boldsymbol{f}\, dV = \oint_{S} \boldsymbol{f} \cdot \boldsymbol{ds} = 0 \tag{7}$$

with $\boldsymbol{ds}$ being the tangential surface vector. This shows that the net generation of vorticity of any force field $\boldsymbol{f}$ distributed at a volume V is zero. Locally the production of vorticity can be non-zero since locally $\boldsymbol{\nabla} \times \boldsymbol{f} \neq 0$, but this is accompanied by production of an equal amount of vorticity with opposite sign somewhere else within V. This is

the force-field-based explanation of the fact that any lifting surface produces the same amount of positive and negative vorticity.

Creation of vorticity implies that angular momentum is added to the flow. The angular- or moment of momentum balance is satisfied automatically when the Euler equation is satisfied, as shown by Marshall [14] p. 50. However, an explicit relation between this balance and force fields is not found in literature. In the appendix it is shown that $\boldsymbol{\nabla} \times \boldsymbol{f}$ expresses, in differential form, the torque applied to a fluid element and similarly (6) the balance of angular momentum. The analysis is restricted to 2D- and 3D axisymmetric flows without swirl.

A second difference between conservative and non-conservative forces regards the conversion of power. For a steady flow Batchelor [2], eq. 3.5.1, gives the expression for the work done by a distribution of volume forces. Rewritten for inviscid isentropic flow this becomes

$$\boldsymbol{f} \cdot \boldsymbol{v} = (\boldsymbol{v}.\boldsymbol{\nabla})H. \tag{8}$$

The contribution of a conservative force field $\boldsymbol{f}_c$ is found by substitution of (4) in (8) resulting in $(\boldsymbol{v}.\boldsymbol{\nabla})(H + \mathcal{F}) = 0$ so $(H + \mathcal{F}) = \textit{constant}$. Batchelor [2], p. 158, interpretes this as the total energy of a material element being constant for inviscid, steady, isentropic flows. Subtracting the contribution by $\boldsymbol{f}_c$ from (8) gives for $\boldsymbol{f}_{nc}$, the non-conservative load: $\boldsymbol{f}_{nc} \cdot \boldsymbol{v} = (\boldsymbol{v}.\boldsymbol{\nabla})(H + \mathcal{F})$. Integration on V yields, using Gauss's theorem

$$\int_V \boldsymbol{f}_{nc} \cdot \boldsymbol{v} dV = \int_V \boldsymbol{\nabla} \cdot (H + \mathcal{F})\, \boldsymbol{v} dV = \oint_S (H + \mathcal{F})\, (\boldsymbol{v} \cdot \boldsymbol{e}_n)\, dS \tag{9}$$

with $\boldsymbol{e}_n$ as unit vector normal to S. It shows that the non-conservative force field does the work expressed as the flux of $H + \mathcal{F}$ through surface S.

Summarizing, force fields in the Euler equation of motion may be distinguished in:

- conservative force fields which do not create vorticity nor do work. They change the potential energy but conserve the total energy of fluid elements,
- non-conservative force fields which create vorticity and perform work.

2.2 Consistency of the force field- and lifting surface methods

Prandtl [20] showed that a distribution of normal forces acting on a translating lifting surface modeled as a bound vortex sheet $\boldsymbol{\gamma}$ is equivalent to a pressure distribution at that surface. In the appendix of van Kuik [11] a similar derivation is found for a rotating blade. Usually the space occupied by a body is excluded from the flow domain, with appropriate boundary conditions like zero normal velocity applied at the surface. The flow and pressure around it are determined by solving $\rho\, (\boldsymbol{v} \cdot \boldsymbol{\nabla})\, \boldsymbol{v} = -\boldsymbol{\nabla} p$ resulting in the pressure acting at the surface. In the force field approach this exclusion of the body volume is not made, but the surface is considered as the carrier of $\boldsymbol{f}$ that induces the flow field according to (1). The surface is considered as a layer of infinitely thin thickness ϵ, at which $\boldsymbol{f}$ is distributed. After integration of (1) across ϵ the force term becomes $\boldsymbol{F}$

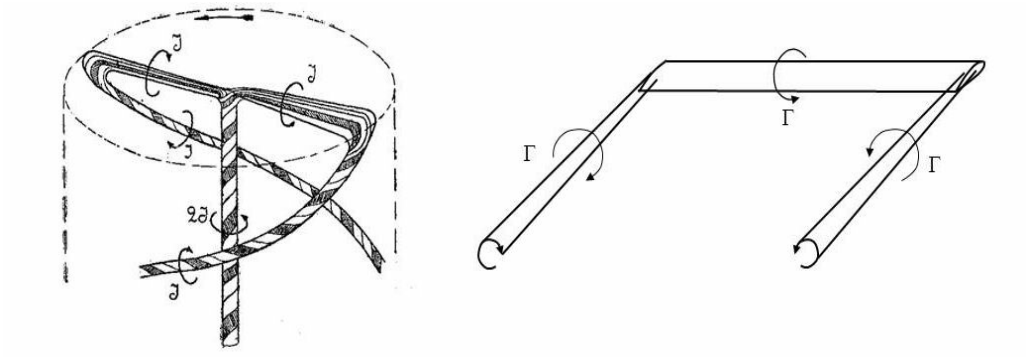

Figure 1: The rotor vortex model by Joukowski [6] and the wing model of Prandtl [20].

defined by (5) with $\boldsymbol{f}$ behaving as a Direc delta function. Integration of the other terms of (1) show that the convective term vanishes for $\epsilon \to 0$ and the pressure term becomes a pressure jump Δp. In case the surface covers a lifting body with thickness, the pressure p_0 at the inside is constant, so the result is

$$\boldsymbol{F} = \boldsymbol{e}_n \left(p - p_0\right) \tag{10}$$

and

$$\boldsymbol{\nabla} \times \boldsymbol{F} = \boldsymbol{\nabla} \times \boldsymbol{e}_n p. \tag{11}$$

This shows the equivalency of force field and kinematical approaches. However, the ability of force fields to generate vorticity seems to be in contrast to two observations often found in literature, on the conservation of vorticity and on the mechanisms that create vorticity.

2.3 The role of Helmholtz's conservation laws

The first observation regards the representation of a lifting surface by a bound vortex which is continued in the flow by two trailing vortices. For a rotor blade the combination of the root vortex, blade-bound vortex and the tip vortex constitute a continuous vortex system, as shown at the left of figure 1 copied from Joukowski [6]. This is to be considered as the equivalent of the 'horse-shoe' vortex of a wing as developed by Prandtl [20], displayed at the right of figure 1. When the bound vortex Γ (J in the left part of figure 1) is assumed to be constant, the models of Prandtl and Joukowsky show a continuous vortex line of uniform strength which is often explained by Helmholtz's laws on vorticity conservation, see e.g. Clancey [4], Katz & Plotkin [8] and Kundu [12]. However, Saffman [22], p. 10, shows that Helmholtz's vorticity conservation laws are not applicable, since these have been derived assuming only conservative forces. Consistent with this Meyer [17], p. 42, shows that Helmholtz's laws are not applicable to bound vorticity. In other words, Helmholtz's laws cannot be used to explain the continuation of bound vorticity in trailing vorticity. The correct kinematical explanation for the creation of

trailing vorticity is well described by Lighthill [13] who uses Stokes' theorem to show that $\gamma_{trailing} = d\Gamma_{bound}/ds$, s being the spanwise coordinate.

These considerations do not affect the validity of the horse-shoe models of Prandtl and Joukowsky but the physical explanation: these models should not be connected to *conservation* of vorticity. Similarly this holds for Kelvin's circulation theorem. The circulation around any closed contour enclosing the bound or free vortices equals Γ, so is conserved. However, this is not due to vorticity conservation since Kelvin's theorem is derived assuming only conservative forces with the contour being a material contour convected with the flow, see Saffman [22] §1.6. This is not the case for lifting surfaces, since a material contour around the tip vortex was a circulation-free contour when it was still upstream of the surface position. It is clear that the vorticity in the wake, once created, satisfies Helmholtz's laws or Kelvin's theorem.

The conclusion for this first observation is that a lifting surface generates vorticity corresponding to the force field approach. It satisfies the conservation of circulation, although this is not based on Helmholtz's laws or Kelvin's theorem.

2.4 Creating vorticity in inviscid flows

The second observation regards the role of viscosity in the generation of vorticity. Several authors, e.g. Betz [3], mention viscosity as the main source of vorticity while the force fields discussed here act in a non-viscous flow. This is brought up for discussion by some authors. Von Kármán & Burgers [7] and Saffman [22] treat the impulsive motion of respectively a force field and a body as a source of vorticity. With the equivalency of the kinematical and dynamical method, both impulsive actions become the same. Von Kármán & Burgers [7] also treat the continuous creation of vorticity for which $\boldsymbol{\nabla} \times \boldsymbol{F} \neq 0$ is shown to be the requirement. Prandtl [21] published a class of 2D vortex sheet spirals representing the vortex sheets emanating from a sharp trailing edge[1]. Batchelor [2], section 5.14, distinguishes the generation of vorticity at solid boundaries with a no-slip condition from the generation at a 'free surface', defined by the tangential surface tension being zero: *an impulsive moving solid boundary generates a sheet of (initially) infinite vorticity, a free surface requires a non-zero jump in velocity derivatives and generates a finite vorticity.* Morton [18] presents a comprehensive treatment on the generation of vorticity and the role of viscosity herein. He covers the mechanisms discussed above, concluding that viscosity is responsible for diffusion of vorticity but not for the generation of it. The tangential pressure gradient at the surface creates vorticity, by which this is possible in inviscid flows. This is in line with (11) showing that $\boldsymbol{\nabla} \times \boldsymbol{F} \neq 0$ is identical to $\boldsymbol{\nabla} \times \boldsymbol{e}_n p \neq 0$ being the necessary condition for the creation on new vorticity.

[1] Van Kuik [10] published a different interpretation of this class of spirals, showing that these are defined at a multi-valued Riemann surface and cannot represent a 2D vortex sheet.

3 CONVECTION OF VORTICITY

3.1 In actuator disc flows

For the actuator disc flow treated in this paper, the force and flow field are assumed to be axisymmetric, so all azimuthal derivatives are zero. The cylindrical coordinate system (x, r, φ) is used with the disc centreline coinciding with the positive x-axis and with $\boldsymbol{e}$ denoting the unit vector with an appropriate index, see figure 2. This gives the following expression for the vorticity $\boldsymbol{\omega}$

$$\boldsymbol{\omega} = \boldsymbol{e}_x \frac{\partial(r v_\varphi)}{r \partial r} - \boldsymbol{e}_r \frac{\partial v_\varphi}{\partial x} + \boldsymbol{e}_\varphi \left(\frac{\partial v_r}{\partial x} - \frac{\partial v_x}{\partial r} \right). \tag{12}$$

Once generated, vorticity is convected with the flow v and is subject to stretching and tilting, described by $(\boldsymbol{\omega} \cdot \boldsymbol{\nabla})\boldsymbol{v}$. In the wake $\boldsymbol{f} = 0$ so the azimuthal component of (6) becomes

$$(\boldsymbol{v} \cdot \boldsymbol{\nabla})\, \omega_\varphi = (\boldsymbol{\omega} \cdot \boldsymbol{\nabla})\, v_\varphi - \omega_r \frac{v_\varphi}{r} + \omega_\varphi \frac{v_r}{r} \tag{13}$$

By substitution of the axial and radial components of (12) $(\boldsymbol{\omega} \cdot \boldsymbol{\nabla})\, v_\varphi = \omega_x \partial v_\varphi / \partial x + \omega_r \partial v_\varphi / \partial r = -\omega_r v_\varphi / r$ is obtained, so

$$(\boldsymbol{v} \cdot \boldsymbol{\nabla})\, \omega_\varphi = -2\omega_r \frac{v_\varphi}{r} + \omega_\varphi \frac{v_r}{r}. \tag{14}$$

According to Darmofal [1] the first term at the right hand side describes the change of azimuthal vorticity due to tilting of radial vorticity. The second term describes the stretching of vorticity, also described by Saffman [22], p. 14. Further simplification of (14) is achieved by substitution of $v_r \omega_\varphi = (v_\varphi - \Omega r)\, \omega_r$ being the condition for a force free wake as shown by van Kuik [11]

$$(\boldsymbol{v} \cdot \boldsymbol{\nabla})\, \omega_\varphi = -\left(v_\varphi + \Omega r\right) \omega_r \tag{15}$$

Equation (15) shows that ω_r depends on the convection of ω_φ, so may be considered as a dependent component of $\boldsymbol{\omega}$. Both other components have a more characteristic role.

The role of ω_x becomes clear by considering the wake circulation $\Gamma = 2\pi r v_\varphi$. Using Stokes's theorem this becomes

$$\omega_x = \frac{1}{2\pi} \frac{\partial \Gamma}{r \partial r}. \tag{16}$$

Across the disc the azimuthal velocity increases by Δv_φ, so the disc contains bound vorticity $\gamma_{r,disc} = -\Delta v_\varphi$. Substitution in (16) gives

$$\omega_x = -\frac{d(r\gamma_{r,disc})}{r dr}. \tag{17}$$

If it is assumed that $r\gamma_{r,disc} = \textit{constant}$ for $0 \leq r \leq R_{disc}$, then the vorticity is concentrated in the root vortex and wake boundary. Integration of (16) and (17) then gives

$$\Gamma_{axis} = -2\pi r \gamma_{x,\ wake\ boundary} = -r\gamma_{r,disc}. \tag{18}$$

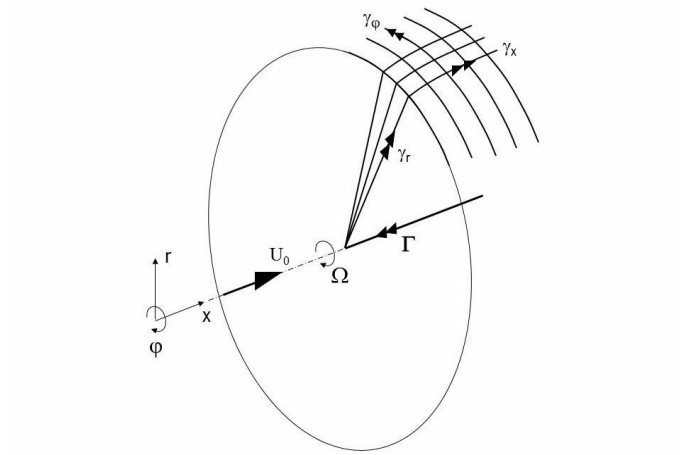

Figure 2: The vorticity system of an actuator disc with $r\gamma_{r,disc} = constant$ and finite Ω.

Figure 2 shows the decomposition of the wake vorticity. The centreline vorticity, the disc bound vorticity and the *axial* wake boundary vorticity constitute a system of connected vortex lines of equal (integrated) strength satisfying conservation of circulation. This vortex system induces the swirl in the wake, which is a measure for the work done by the force field as discussed by van Kuik [11].

The azimuthal vorticity is determined by the azimuthal component of the vorticity production and transport equation (6). The azimuthal vorticity may be considered to consist of a distribution of vortex rings. A vortex ring is a potential flow element: when added to a flow, the flow itself will change but all conservation laws are satisfied automatically. From a fluid dynamic point of view a consistent flow will result when azimuthal vorticity is added or removed, which is not possible for the axial and radial vorticity. For rotor flows, discussed in the next section, this property of the azimuthal wake vorticity is absent. A limit transition from rotor wake vorticity to disc wake vorticity, as done in van Kuik [11] for the force field itself, should give insight in this change of properties.

3.2 In rotor flows

Figure 1 shows the vortex models of Joukowsky for a two-bladed rotor and of Prandtl for a wing. Comparison with models as shown in figure 3 show the simplifications of the early models: Joukowsky kept the wake radius R as well as the pitch θ of the wake spirals constant, $\Delta r = 0$ and $\Delta x = R\varphi \tan\theta$, while Prandtl assumes zero inboard and downward movement of the tip vortices, $\Delta x = \Delta y = 0$. These assumptions generally have little impact, and make a linear analysis possible resulting in an easy calculation of the flow.

Several characteristic differences between the rotor- and wing model are observed. First is that $\Delta x \neq 0$ in the rotor model while $\Delta x = 0$ in the blade model. Converted

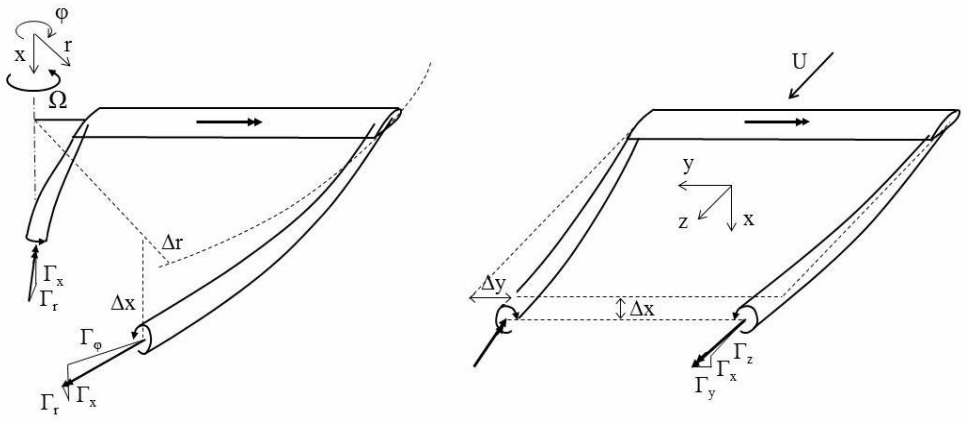

Figure 3: Details of the vortices trailing from a rotor blade in hover and a wing.

to the components of the vorticity, this implies that $\Gamma_{x,axis} = -\Gamma_{x,r=R} = \Gamma_{blade}$ for a rotor blade, while $\Gamma_{x,tipvortices} = 0$ for a wing. The axial vorticity in the rotor wake determines the swirl in the wake which in turn defines the converted power of rotors with finite rotational speed, see van Kuik [11]. In other words: the vorticity component that is least important for a wing is essential for a rotor. Another difference is the parameter that indicates when the linear models are not applicable any more. For the wing this is the aspect ratio $AR = span/chord$. Küchemann [9], section 4.6, shows that for very small AR the lift becomes quadratic in the angle of attack since the tipvortices affect the flow along the entire span instead as Δx and Δy become large at and immediately behind the wing. For rotor blades the definition of AR is not meaningful but the tip-effect is. The spanwise position of maximum blade circulation is close to the tip so knowledge on the creation and convection of the tip vortex may be necessary to accurately assess the blade load. Experiments have shown that the tip shape has impact on the load, see e.g. Gray e.a. [5]. Micallef, [15] and [16], measured at two wind turbine model rotors an inboard motion of the tip vortex before the wake expands. None of the force based methods take this phenomenon into account.

4 CONCLUSIONS

- The representation of a lifting surface by a force field is consistent with the more common method of applying boundary conditions at the surface after which the flow- and pressure field is solved. The disadvantage of the force field method is that the force field needs to be known in advance.
- The pressure distribution at any lifting surface of finite dimensions is, when represented as a force field, non-conservative.
- The non-conservative part of a force field generates vorticity. It is shown that this mechanism is identical to the local balance of moment of momentum, and is driven

by pressure gradients, not by viscosity.

- The apparent contradiction of a lifting surface that creates vorticity by its force field and the same surface that satisfies Helmholtz's laws for the conservation of vorticity by representing it as bound vorticity, is non-existent. The continuation of bound vorticity into trailing vorticity of equal strength finds no basis in Helmholtz's laws, since these have been derived in absence of non-conservative forces.
- The azimuthal vorticity in actuator disc flows has the property, not present in wing and rotor flows, that it does not depend on vorticity conservation in the wake.
- The force field based methods used in rotor aerodynamics do not account for non-linear effects in the tip vortex creation and convection.

REFERENCES

[1] Darmofal, D.L., 1993, The role of vorticity dynamics in vortex brakedown, AIAA 24th Fluid dynamics Conference, AIAA paper 93-3036.

[2] Batchelor, G.K., 1970, An introduction to fluid dynamics, Cambridge Univ. Press.

[3] Betz, A., 1950, Wie entsteht ein Wirbel in einer wenig zähen Flüssigkeit? Die Naturwissenschaften, Vol 37-9, p 193-196.

[4] Clancey, L.J., 1975, Aerodynamics, Pitman Publishing, London.

[5] Gray, R.B., McMahon, H.M., Shenoy, K.R., Hanimer, M.L., 1980, Surface pressure measurement at two tips of a model helicopter rotor in hover, *NACA CR-3281.*

[6] Joukowsky, N.E., 1912, Vortex theory of screw propeller, I. Trudy Otdeleniya Fizicheskikh Nauk Obshchestva Lubitelei Estestvoznaniya 16 (1), 1–31 (in Russian). In French: Joukowsky, N.E.: Théorie Tourbillonnaire de l'Hélice Propulsive, Gauthier-Villars et Cie, 1929, p 1-47.

[7] Kármán Th. von, Burgers, J.M., 1935, Motion of a perfect fluid produced by external forces, in Aerodynamic Theory Volume II division E, chapter IIIA, edited by W.F. Durand, Springer, Berlin Germany, Reprinted in 1963 as a Dover edition.

[8] Katz J., Plotkin A., 1991, Low-speed aerodynamics, McGraw-Hill, New York.

[9] Kűchemann, D., 1984, The aerodynamic design of aircraft, Pergamon Press, Oxford.

[10] Kuik, G.A.M. van, 2004, The flow induced by Prandtl's self-similar vortex sheet spirals at infinite distance from the spiral kernel European Journal of Mechanics B/Fluids 23 (2004) 607–616.

[11] Kuik, G.A.M. van, 2012, The relationship between loads and power of a rotor and an actuator disc, Proc. of the conference 'The Science of making Torque from Wind', to be published in the IOP Conference Series.

[12] Kundu, P.K., 1990, Fluid Mechanics, Academic Press Inc.

[13] Lighthill, J., 1986, An informal introduction to fluid mechanics, Clarendon Press.

[14] Marshall, J.S., 2001, Inviscid incompressible flow, John Wiley and Sons.

[15] Micallef D., van Bussel G., Simão Ferreira C., Sant T., 2012, An investigation of radial velocities for a horizontal axis wind turbine in axial and yawed flows, Wind Energ online, DOI: 10.1002/we.1503.

[16] Micallef D., Akay B., Simão Ferreira C., Sant T., van Bussel G., 2012, The origins of a wind turbine tip vortex, Proc. of the conference 'The Science of making Torque from Wind', to be published in the IOP Conference Series.
[17] Meyer, R.E., 1982, Introduction to mathematical fluid dynamics, Dover Publ.
[18] Morton, B.R., 1984, The generation and decay of vorticity, Geophys. Astrophys. Fluid Dynamics, 1984, Vol. 28, pp. 277-308.
[19] Okulov, V.L., Sørensen J.N., 2010, Maximum efficiency of wind turbine rotors using Joukowsky and Betz approaches, J. Fluid Mech. (2010), vol. 649, pp. 497–508.
[20] Prandtl, L., 1918, Tragflügeltheorie I Mitteilung, Nachrichten der Königlichem Gesellschaft der Wissenschaften zü Göttingen, Mathematisch-physikalische Klasse, page 451-477.
[21] Prandtl, L., 1922, Über die Entstehung von Wirbeln in der idealen Flüssigkeit, mit Anwendung auf die Tragflügeltheorie und andere Aufgaben. Vorträge aus dem Gebiete der Hydro- und Aerodynamik, ed. von Kármán und Levi-Cevita, Springer, Berlin.
[22] Saffman, P.G., 1992, Vortex Dynamics, Cambridge Monographs on Mechanics and Applied Mathematics, Cambridge University Press.
[23] Shen, W.Z., Zhu, W.J., Sørensen J.N., 2012, Actuator line/Navier–Stokes computations for the MEXICO rotor: comparison with detailed measurements, Wind Energ. 2012; 15:811–825.
[24] Sørensen, J.N., Shen, W.Z., Munduate, X., 1998, Analysis of wake states by a full-field actuator disc model, Wind Energy, 1, 73-88.

Appendix: Balance of angular momentum

This appendix is restricted to 2-D flows and 3-D axisymmetric flows without swirl. The curl of the Euler equation (3) gives

$$\frac{1}{\rho}\boldsymbol{\nabla}\times\boldsymbol{f} = -\boldsymbol{\nabla}\times(\boldsymbol{v}\times\boldsymbol{\omega})\,. \tag{19}$$

In the meridian plane a circle C is defined with polar coordinates (ξ,θ), enclosing area A. Integration of (19) on A shows, using Stokes' theorem

$$\frac{1}{\rho}\oint_C \boldsymbol{f}\cdot d\boldsymbol{c} = -\oint_C (\boldsymbol{v}\times\boldsymbol{\omega})\cdot d\boldsymbol{c} = \oint_C v_\xi \omega_\varphi \xi d\theta \tag{20}$$

where $d\boldsymbol{c}$ is tangent to C. Using $\omega_\varphi = \partial(\xi v_\theta)/(\xi\partial\xi) - \partial v_\xi/(\xi\partial\theta)$ and $\oint v_\xi \partial v_\xi = 0$ (20) becomes

$$\frac{1}{\rho}\oint_C \boldsymbol{f}\cdot d\boldsymbol{c} = \oint_C v_\xi \frac{\partial(\xi v_\theta)}{\partial\xi} d\theta \tag{21}$$

$$= \oint_C \left(\frac{\partial(\xi v_\theta v_\xi)}{\xi\partial\xi} - v_\theta\frac{\partial v_\xi}{\partial\xi}\right)\xi d\theta \tag{22}$$

Multiplication of (22) by ξ^* and integration for $0 \le \xi^* \le \xi$ gives the torque q about the centre of C exerted by the force field $\boldsymbol{f}$ within C

$$\begin{aligned}\frac{1}{\rho}q &= \int_0^{\xi} \xi^* \oint_C \boldsymbol{f}\cdot\boldsymbol{dc}\, d\xi^* = \int_0^{\xi}\oint_C \left(d\left(\xi^* v_\theta v_\xi\right) - v_\theta \xi^* dv_\xi\right)\xi^* d\theta \\ &= \int_0^{\xi}\oint_C d\left(\xi^{*2} v_\theta v_\xi\right) d\theta - \int_0^{\xi}\oint_C \xi^* v_\theta d\left(v_\xi \xi^*\right) d\theta \end{aligned} \tag{23}$$

The second integral is evaluated with the continuity equation (2) converted to the (ξ,θ) coordinate system

$$\begin{aligned}\frac{\partial v_x}{\partial x} + \frac{\partial\left(r v_r\right)}{r\partial r} &= \frac{\partial v_x}{\partial x} + \frac{\partial v_r}{\partial r} + \frac{v_r}{r} \\ &= \frac{\partial\left(\xi v_\xi\right)}{\xi^*\partial\xi^*} + \frac{\partial v_\theta}{\xi^*\partial\theta} + \frac{v_r}{r} = 0 \end{aligned} \tag{24}$$

by which

$$\begin{aligned}\int_0^{\xi}\oint_C \xi^* v_\theta d\left(v_\xi\xi^*\right) d\theta &= -\int_0^{\xi}\oint_C \xi^* v_\theta dv_\theta d\xi^* - \int_0^{\xi}\oint_C v_\theta \frac{v_r}{r}\xi^{*2} d\xi^* d\theta \\ &= -\int_0^{\xi}\oint_C v_\theta \frac{v_r}{r}\xi^{*2} d\xi^* d\theta \end{aligned} \tag{25}$$

so q is

$$\begin{aligned} q &= \rho\int_0^{\xi}\oint_C d\left(\xi^{*2} v_\theta v_\xi\right) d\theta + \rho\int_0^{\xi}\oint_C v_\theta\frac{v_r}{r}\xi^{*2} d\xi^* d\theta \\ &= \rho\oint_C \xi v_\theta v_\xi dC + \rho\iint_A \xi^* v_\theta \frac{v_r}{r} dA \end{aligned} \tag{26}$$

This is the balance of angular momentum with control surface C. The first term at the right hand side gives the 2-D balance in which the torque equals the increase of angular momentum, being the mass transport ρv_ξ having an angular momentum ξv_θ integrated along the contour C. The second term gives the change of angular momentum $\xi^* v_\theta$ as a consequence of the vorticity stretching (see the last term at the right hand side of (14).

This shows that (19) indeed is the balance of angular momentum in differential form.

LOCAL AND GLOBAL PAIRING IN HELICAL VORTEX SYSTEMS

T. Leweke, H. Bolnot, U. Quaranta, S. Le Dizès

IRPHE UMR 7342, CNRS, Aix-Marseille Université, 13013, Marseille, France
Thomas.Leweke@irphe.univ-mrs.fr

ABSTRACT

We present experimental results concerning the pairing instability in systems of one and two helical vortices. The vortices are generated in a water channel using carefully designed one- and two-bladed rotors. Different modes of local (along the azimuth of the helix) and uniform pairing are triggered by suitable modulations of the rotor motion. The resulting vortex deformations are visualized, and their growth rate is determined. Comparison with theoretical predictions for local and global pairing in spatially uniform helices shows very good agreement, indicating that the pairing dynamics of a given vortex segment involve only the nearest neighbours.

1. INTRODUCTION

The stability properties of helical vortices are of interest for applications such as wind turbine and helicopter wakes. In the former, they contribute to the transition from an organized vortex system to a turbulent wake behind the rotor, and in the latter they may be related to the inception of the so-called Vortex Ring State of the wake of a helicopter in steep descent [1,2]. In this work, we consider the particular instability that leads to vortex pairing, for which previous experimental [3,4] and numerical [5] studies have shown that it plays an important role in rotor wakes.

Vortex pairing is a process occurring in (infinite) arrays of identical concentrated vortices, whereby small perturbations of their initially equidistant positions are amplified in a way that neighbouring vortices approach each other and group in pairs. Lamb [6] has analysed the stability of single and double rows of point vortices in two dimensions, representing straight parallel vortex filaments in three dimensions. If one defines a non-dimensional growth rate $\sigma^* = \sigma\,(2h^2/\Gamma)$ of the pairing instability, where σ is the dimensional growth rate, and Γ and h the circulation and spacing of the vortices, one finds $\sigma^* = \pi/2$ for both cases. Two-dimensional pairing occurs, e.g., in shear layers, as a secondary instability of the Kelvin-Helmholtz instability [7]. It is distinct from merging of two vortex cores of like-signed vorticity into a single one, which happens when the two initial vortices come sufficiently close to each other (see, e.g., [8]). Merging may take place during the late stages of the pairing instability in arrays of real (distributed) vortices.

Systems of helical vortices, such as those found in the wake of a rotor, present locally arrays of identical curved (and slightly twisted) vortices, which are expected to exhibit the pairing instability. The simplest system consists in a single helical vortex filament, characterised by its circulation Γ and core radius a, as well as the helix radius R and pitch h (fig. 1a). In the frame of reference where the fluid at infinity has no velocity in the direction of the helix axis, the fluid inside the helix moves at a speed of the order of Γ/h, and the helix itself moves with a velocity of roughly half this value ($\Gamma/2h$). The latter velocity and h are used here for non-dimensionalisation, which leads to the expression for the non-dimensional growth rate σ^* given above.

For small pitch ($h \ll R$), the helix geometry is locally very similar to that of an array of axisymmetric vortex rings. Levy & Forsdyke [9] have treated analytically the stability of such a system with respect to pairing of neighbouring vortex rings. The growth rate now depends also on the core size a, since it influences the self-induced velocity of the curved vortices For small separation/pitch ($h \ll R$) and small core size ($a \ll R$), which includes most configurations relevant for applications, the growth rate approaches the value $\pi/2$.

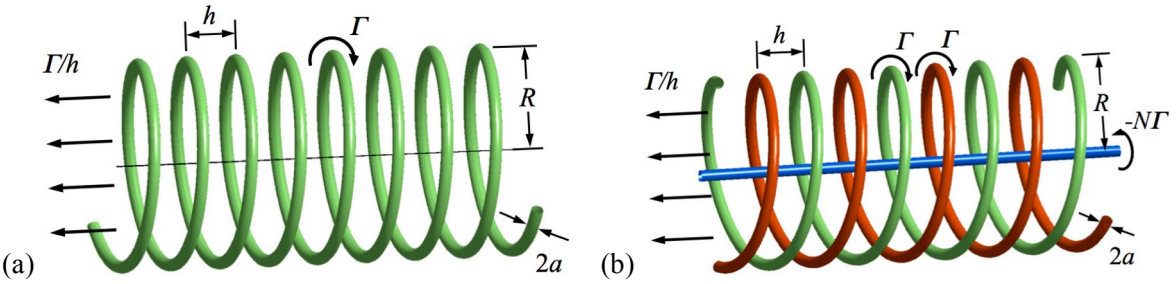

Fig. 1: Schematics of the vortex systems considered in this study, including the relevant parameters. (a) Single helical vortex; (b) double helix, showing also the central vortex (hub vortex) for the case of a rotor wake.

The stability of a genuinely helical vortex filament with respect to displacement perturbations was studied by Widnall [10] and subsequently by Fukumoto & Miyazaki [11] (a much earlier study by Levy & Forsdyke [12] of the same configuration was shown to be erroneous). For small h and a, various unstable modes are found at different wavelengths, all characterised by an out-of-phase displacement of successive helix turns leading to "local" vortex pairing, with growth rates again near $\sigma^* = \pi/2$.

Finally, Okulov & Sørensen [13] have considered systems of more than one helix, and including also a central "hub" vortex (see fig. 1b), which are more representative of realistic rotor wakes. Unstable perturbations involve azimuthally uniform displacements for each helix, leading therefore to a "global" pairing of the vortex filaments.

In the present study, we investigate experimentally, under carefully controlled conditions, the stability of single and double helical vortices with respect to the pairing mechanism. These vortex systems are spatially evolving, since they are generated by rotors in a water channel. The results concerning unstable modes and their growth rates will be compared to theoretical predictions, in particular those of Widnall [10] and Okulov & Sørensen [13], even though the latter concern spatially uniform, temporally evolving configurations.

2. EXPERIMENTAL DETAILS

Experiments were carried out in a recirculating free-surface water channel with a test section of dimensions 38 cm × 50 cm × 150 cm (length). The vortex system was generated near the test section entry by a single- or double-bladed rotor mounted on a shaft and driven by a computer-controlled stepper motor outside the test section using a belt (fig. 2a). The rotor blade geometry (fig. 2b) is based on the low-Reynolds number airfoil A18 by Selig *et al.* [14], with chord and twist distributions designed to operate in the wind turbine regime and produce a constant radial circulation distribution (Joukowsky rotor, see e.g. [15]) over the outer 75% of the span, in order to generate a highly concentrated tip vortex. The rotors have a radius $R_o = 80$ mm and a tip chord $c = 10$ mm. They are rotated at 5-6 Hz and placed in a uniform flow with a free stream velocity U ranging from 35 to 45 cm/s, which leads to tip speed ratios $\lambda = 2\pi f R_o/U$ in the range $5 < \lambda < 9$. The tip chord Reynolds number is of order 3×10^4, and the one based on the vortex circulation is $\mathrm{Re} = \Gamma/\nu \sim 10^4$ (ν: kinematic viscosity). The vortex structures are visualized using fluorescent dye illuminated by the light of an argon ion laser. The dye is either washed off the blade tip or injected at a fixed location near the blade tip trajectory. Quantitative measurements were carried out using two-component Particle Image Velocimetry [16] in planes containing the helix axes (e.g., fig. 4a). In the following, polar coordinates (r,θ,z) are used, with the origin at the centre of the rotor disk, and z pointing downstream.

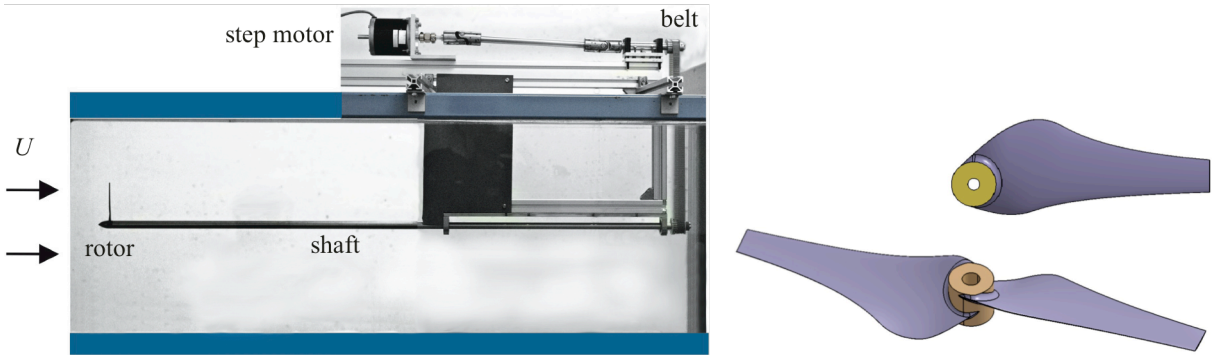

Fig. 2: (a) Side view of the water channel test section, showing the set-up used to generate a single helical vortex. (b) Geometries of the single- and double bladed rotors (R_o = 8 cm).

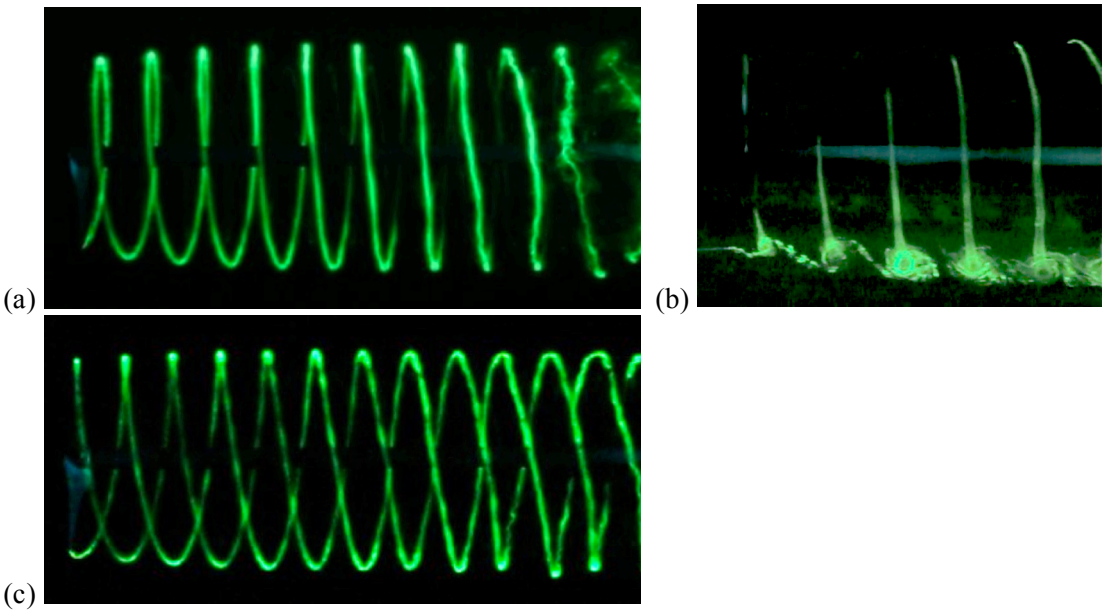

Fig. 3: Visualisation of the unperturbed helical vortices. The rotors are on the left; flow is from left to right. One-bladed rotor: (a) dye washed off the blade tip; (b) dye injected at a fixed position near the edge of the rotor disk. (c) Two-bladed rotor.

3. HELICAL VORTICES

Figs. 3(a) and 3(c) show the helical vortices produced by the one- and two-bladed rotors for the present set of conditions; they are regular and almost unperturbed for about 10 helix turns. The separation distance h between successive helix loops (equal to the helix pitch divided by the number of helices) is between 3 and 4 cm. Dye injection at a fixed location near the blade tip trajectory (fig. 3b) reveals the presence of a strong flow inside the core along the vortex axis. The dye pattern visualises the corresponding axial velocity profile and allows an estimate of the peak velocity V_a and the vortex core diameter $2a$ (width of the profile at 1/e of its maximum).

A typical distribution of azimuthal (with respect to the helix) vorticity in the r-z plane of the single-helix flow can be seen in fig. 4(a). It was obtained by averaging 100 instantaneous fields recorded at the same phase of the rotor motion. The cross sections of the helical blade tip vortex, as well as the

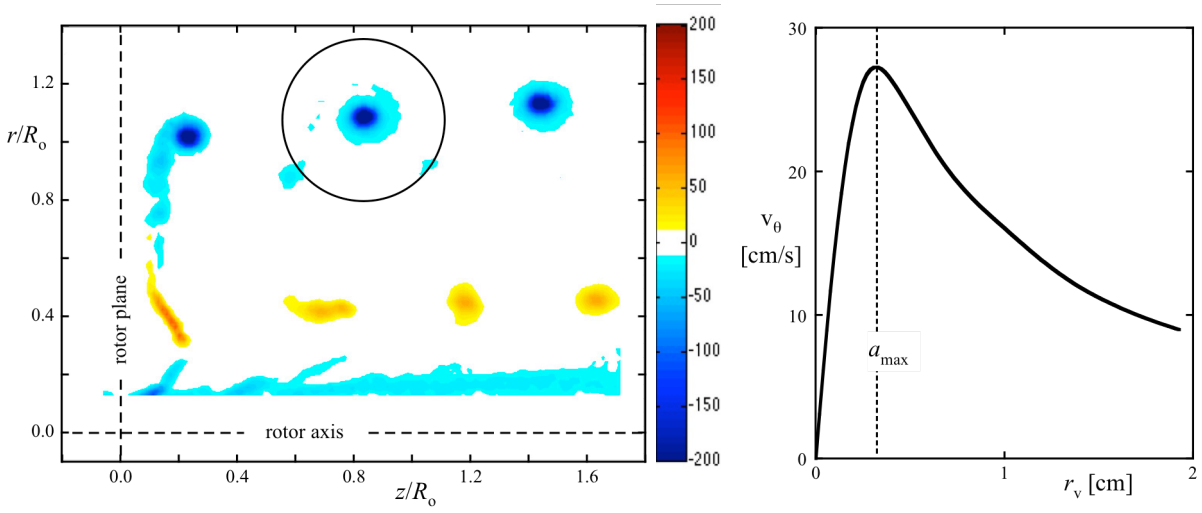

Fig. 4: Determination of vortex properties from PIV measurements. (a) Phase-averaged vorticity field in the *r*-*z* plane (Re = 10800; unit of vorticity: 1/s). (b) Mean azimuthal velocity of the vortex inside the circle in (a).

opposite-signed blade root (hub) vortex, are clearly seen. Due to the presence of the shaft, the root vortex takes on a helical shape as well. The shaft "boundary layer" can also be identified. Fig. 4(b) shows the azimuthally (with respect to the vortex) averaged velocity profile of the blade tip vortex, from which the core size parameter a_{max} can be found.

The combination of dye visualisations and PIV measurements allows a precise determination of the properties of the helical vortex systems. The parameter values for the two reference configurations considered in this paper (single and double helix) are summarised in table 1.

	R/a_{max}	h/a_{max}	Re	λ	$2\pi a_{max} V_a/\Gamma$
Single helix (1-bladed rotor)	27	15	10830	8.4	0.57
Double helix (2-bladed rotor)	37	17	9100	5.5	0.60

Table 1: Non-dimensional parameters characterising the reference configurations of the present study. $2\pi a_{max} V_a/\Gamma$ represents an inverse swirl parameter.

4. PAIRING INSTABILITY

Pairing of neighbouring helix loops was then induced in two ways. The first is a controlled variation of the blade rotation (details are given in [17]), leading to periodic streamwise displacement perturbations of the single helix. The modified helix geometry can be expressed as:

$$z/h = \theta/2\pi + A\cos(k\theta), \qquad (1)$$

with normalized azimuthal wave numbers k = 1/2, 3/2, 5/2, 7/2, and a relative displacement amplitude A. This choice results in an opposite streamwise displacement, varying in the azimuthal direction, of successive loops of the vortex. According to the stability analysis of Widnall [10], these perturbations are unstable. Experimental visualizations of these cases are shown in fig. 5. Maximum displacement occurs at $2k$ locations around the azimuth (always including the top), triggering local pairing there. A grouping and 'swapping' of successive loops is observed, as the helix moves downstream. The azimuthal variation of the pairing results in a complicated three-dimensional vortex structure, but no merging or breakdown to small-scale structures is seen. Fig. 6(a) shows local pairing for the double helix, obtained by a perturbation with k = 1.

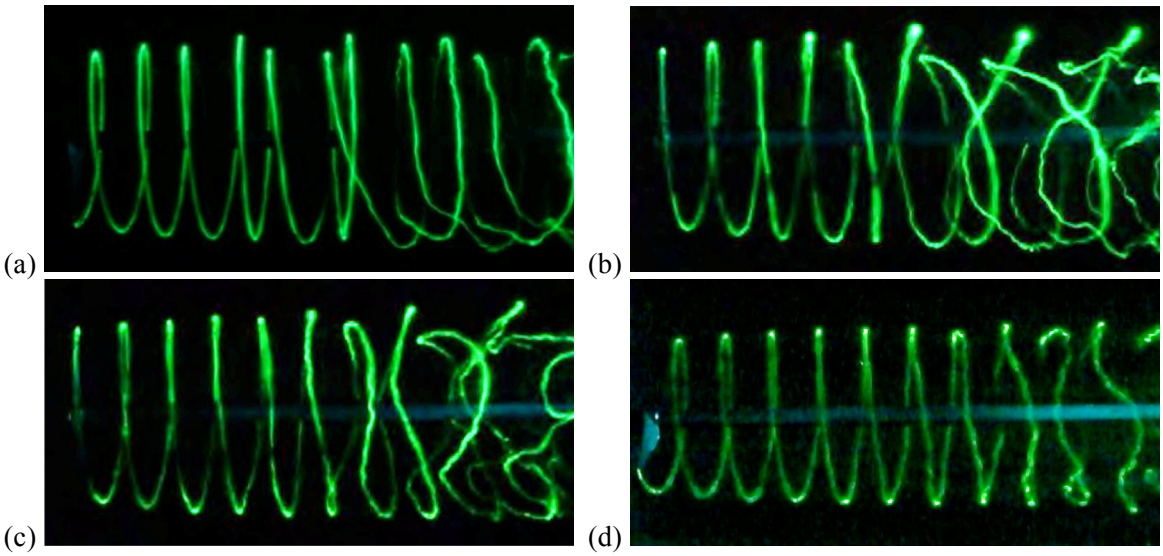

Fig. 5: Dye visualization of "local" pairing in a single helical vortex for various wavenumbers. (a) $k = 1/2$; (b) $k = 3/2$; (c) $k = 5/2$; (d) $k = 7/2$.

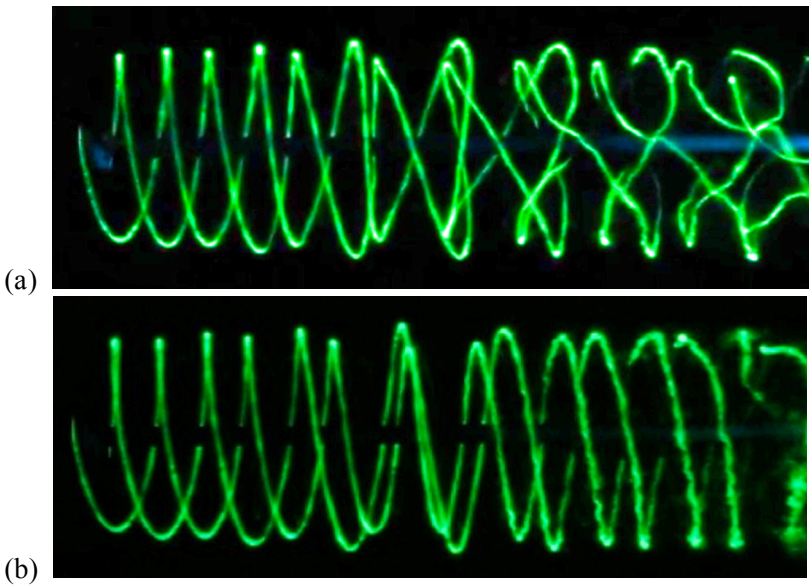

Fig. 6: (a) Local pairing with $k = 1$, and (b) uniform pairing in a double helix.

The second method of perturbation, applicable only to the double helix, consists in slightly off-centring the two-bladed rotor, which leads to a radial displacement of the two vortices in opposite directions. In this case, pairing develops uniformly at all azimuthal positions (fig. 6b), resulting again in a swapping of vortex loops at later stages, without merging or breakdown. The initial stages correspond qualitatively to the theoretical prediction that can be derived for this configuration from the stability analysis by Okulov & Sørensen [13].

It is possible to determine the growth rate of the deformations of the helical vortices leading to local or uniform pairing. A first method uses video recordings of dye visualizations which contain sequences of unperturbed and perturbed flow in the same run. Through a semi-automated process, one can measure the average unperturbed and perturbed positions of, e.g., the uppermost portions of the helix, and calculate their separation as function of downstream distance, which is equivalent to time. This is illustrated in the schematic in fig. 6(b), with an example measurement shown in fig. 7(a). One

observes indeed a certain time interval over which the increase in the displacement distance varies exponentially. A second method uses only visualisation sequences of perturbed vortex systems. It was found and confirmed by Direct Numerical Simulation [17] that a combination of separation distances between successive vortices in a perturbed helix (fig. 7c,d) also grows exponentially, with the linear growth rate of the pairing instability. This somewhat surprising feature allows a growth rate measurement without the necessity of correlating distinct video sequences, and in practice one also reaches much higher amplitudes, as illustrated in fig. 8. Both methods give essentially the same result. (The instability of a counter-rotating vortex pair, the Crow instability, is another example where a suitably chosen amplitude grows exponentially with the linear growth rate, well into the non-linear regime [18].)

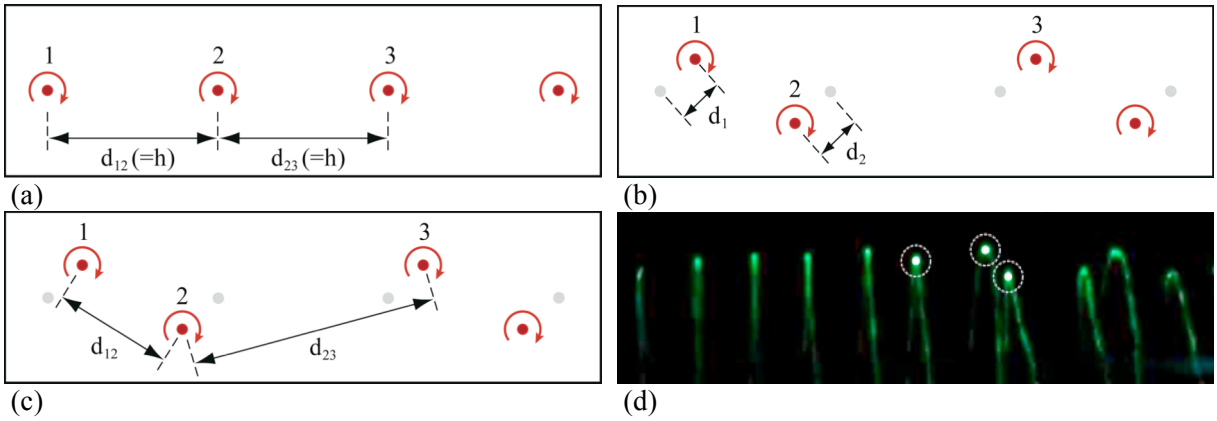

Fig. 7: Schematics and parameters used for the determination of the perturbation amplitude from dye visualization video sequences. (a) Unperturbed vortex array; (b) vortex displacements d_1 and d_2 from unperturbed positions; (3) distances d_{12} and d_{23} between consecutive vortices; (d) visualization example with a vortex triplet whose positions are tracked in time.

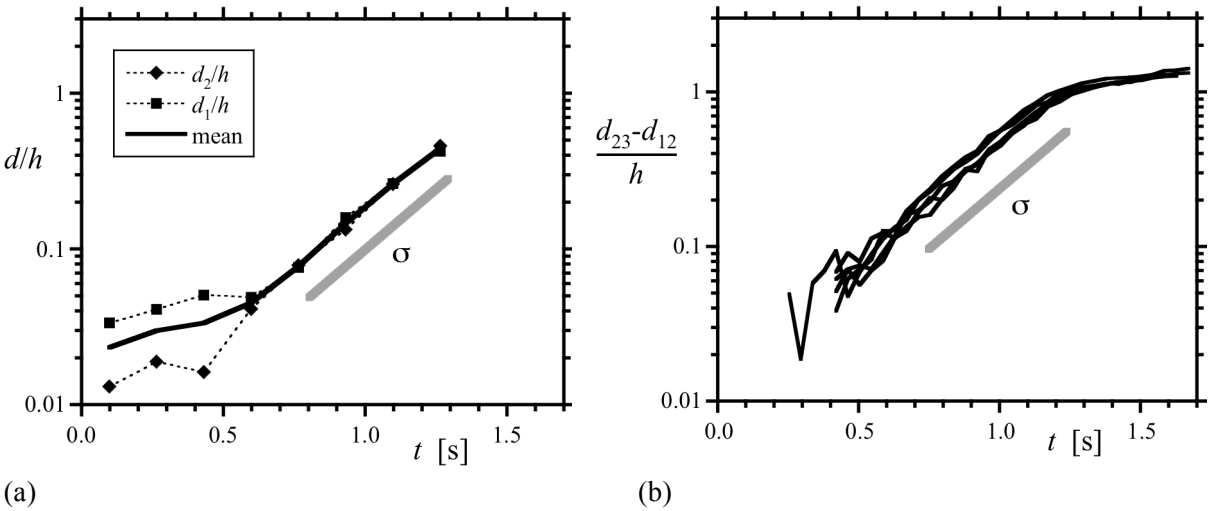

Fig. 8: Examples of growth rate measurements from the temporal evolution of the amplitudes defined in fig. 4, for the case of a singe helix and a perturbation with $k = 3/2$. (a) Method 1, using the distance between mean unperturbed and mean perturbed positions; (b) method 2, using the distances between successive vortex loops (results shown for 5 vortex triplets in the same run).

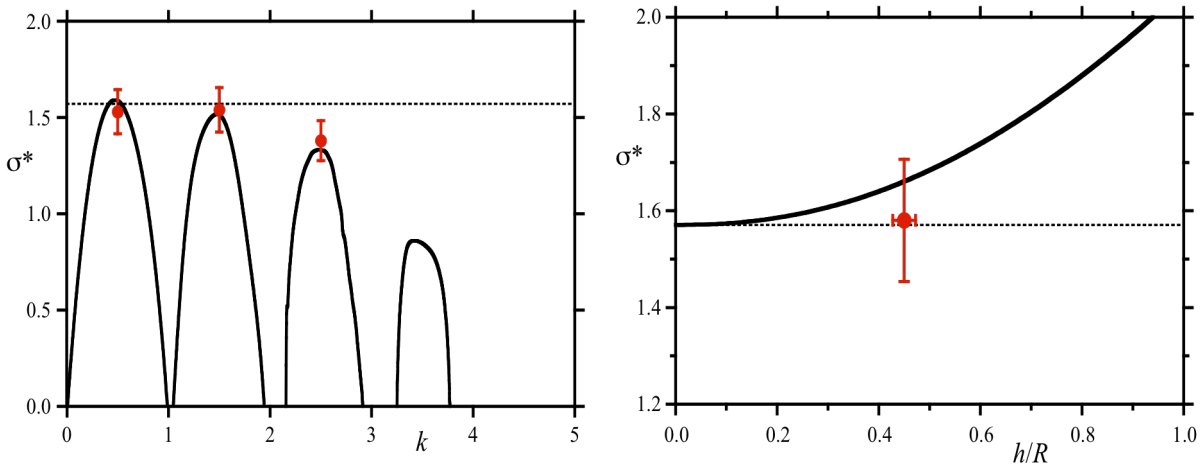

(a) (b)

Fig. 9: Growth rates of the pairing instability: comparison between experiment (symbols, Re=$O(10^4)$) and theory (lines, inviscid). (a) Local pairing of a single helix: experiment with $a_e/R = 0.06$ and $h/R = 0.56$; theoretical result by Widnall [10] for $a_e/R = 0.1$ and $h/R = 0.63$. (b) Uniform pairing of a double helix: experiment with $a_e/R = 0.07$ and; theoretical result by Okulov & Sørensen [13] for the same core size and perturbation mode. Dotted lines correspond to $\sigma^* = \pi/2$.

Growth rate measurements were carried out, using both methods, for the cases of local and uniform pairing shown in figs. 5 and 6. When comparing the experimental results to the corresponding theoretical predictions by Widnall [10] and Okulov & Sørensen [13], one has to keep in mind that the latter have considered helical vortex filaments of Rankine type (constant vorticity in the core) and without axial flow, whereas in the experiments, the vortices have a more distributed, smooth vorticity profile and a strong axial velocity inside the core (fig. 3b). We here use the concept of "equivalent core size", introduced by Widnall *et al.* [19], which allows to calculate, for a vortex with arbitrary (axisymmetric) velocity profiles, the radius a_e of a Rankine vortex without axial flow having the same self-induced dynamics. Fig. 9 shows the experimentally measured growth rates for local and uniform pairing, together with the relevant theoretical predictions. Although the parameters are not exactly the same for local pairing (fig. 9a), the values of the growth rates, as well as the wavenumber trend, are in excellent agreement. (It was not possible to determine any reliable growth rate experimentally for the very complex mode with $k = 7/2$.) The same agreement is found for uniform pairing (fig. 9b), for which a theoretical prediction with exactly the same parameters as in the experiment could be obtained.

5. CONCLUSION

The dynamics and stability of helical vortices represent an interesting fundamental topic in vortex dynamics, and they are also relevant for a number of practical applications, in particular those involving flow around rotors. One mechanism of instability comprises vortex pairing, a phenomenon known from shear layer dynamics. In this study we have experimentally observed and analysed in detail the pairing instability in the wake of one- and two-bladed rotors. In a single helical vortex, pairing can only occur locally along the azimuth, and a number of different instability wavelengths were seen. A double helix may exhibit uniform pairing, whereby each helix moves as a whole. The growth rates of the various instability modes were determined from dye visualisation sequences and compared to previous theoretical predictions, showing very good agreement. The fact that the experimental results for spatially evolving helical vortices agree so well with those predicted for spatially uniform vortices, seems to indicate that the pairing dynamics of a given vortex only involves a few nearest neighbours. It shows that the pairing instability in the wake of a rotor is indeed a

convective process, and that one can deduce the spatial evolution from the temporal one via the vortex convection speed.
Further work on this topic includes the experimental study of more general pairing scenarios: pairing of three or more successive loops, in-phase perturbations of neighbouring vortices, local pairing of multiple helices. On the theoretical side, predictions for local pairing of multiple helices, or for spatially evolving helical vortices, are not available so far.

Acknowledgements
This work is supported by EUROCOPTER S.A.S., under contract no. IPEC 0187N/2009, and by the French *Agence Nationale de la Recherche*, under contract no. ANR-12-BS09-0023-01.

REFERENCES

[1] J.G. Leishman, M.J. Bhagwat, S. Ananthan, "The vortex ring state as a spatially and temporally developing wake instability", Journal of the American Helicopter Society, vol. 49 (2004) pp. 160-175.
[2] H. Bolnot, S. Le Dizès, T. Leweke, "Spatio-temporal development of the pairing instability in helical vortices", AIAA Paper 2011-3927 (2011).
[3] P.H. Alfredsson, J.-Å. Dahlberg, "A preliminary wind tunnel study of windmill wake dispersion in various flow conditions", Technical Note AU-1499 (Part 7), The Aeronautical Research Institute of Sweden, Stockholm (1979).
[4] M. Felli, R. Camussi, F. Di Felice, "Mechanisms of evolution of the propeller wake in the transition and far fields", Journal of Fluid Mechanics, vol. 682 (2011) pp. 5-53.
[5] S. Ivanell, R. Mikkelsen, J.N. Sørensen, D. Henningson, "Stability analysis of the tip vortices of a wind turbine", Wind Energy, vol. 13 (2010) pp. 705-715.
[6] H. Lamb, *Hydrodynamics*, 6th edn., Cambridge University Press (1932).
[7] C.D. Winant, F.K. Browand, "Vortex pairing : the mechanism of turbulent mixing-layer growth at moderate Reynolds number", Journal of Fluid Mechanics, vol. 63 (1974) pp. 237-255.
[8] P. Meunier,S. Le Dizès, T. Leweke, "Physics of vortex merging", Comptes Rendus Physique, vol. 6 (2005), pp. 431-450.
[9] H. Levy, A.G. Forsdyke, "The stability of an infinite system of circular vortices", Proceedings of the Royal Society London A, vol. 114 (1927) pp. 594-604.
[10] S.E. Widnall, "The stability of a helical vortex filament", Journal of Fluid Mechanics, vol. 54 (1972) pp. 641-663.
[11] Y. Fukumoto, T. Miyazaki, "Three-dimensional distortions of a vortex filament with axial velocity"", Journal of Fluid Mechanics, vol. 222 (1991) pp. 369-416.
[12] H. Levy, A.G. Forsdyke, "The steady motion and stability of a helical vortex", Proceedings of the Royal Society London A, vol. 120 (1928) pp. 670-690.
[13] V.L. Okulov, J.N. Sørensen, "Stability of helical tip vortices in a rotor far wake", Journal of Fluid Mechanics, vol. 576 (2007) pp. 1-25.
[14] M.S. Selig, J.J. Guglielmo, A.P. Broeren, P. Giguere, *Summary of Low-Speed Airfoil Data, Volume 1*, SoarTech, Virginia Beach (1995).
[15] V.L. Okulov, J.N. Sørensen, "Maximum efficiency of wind turbine rotors using Joukowsky and Betz approaches", Journal of Fluid Mechanics, vol. 649 (2010) pp. 497-508.
[16] P. Meunier, T. Leweke, "Analysis and optimization of the error caused by high velocity gradients in particle image velocimetry", Experiments in Fluids, vol. 35 (2003) pp. 408-421.
[17] H. Bolnot, "Instabilités des tourbillons hélicoïdaux: application au sillage des rotors", Ph.D. Thesis, Aix-Marseille Université, Marseille, France (2012).
[18] D.W. Moore, "Finite amplitude waves on aircraft trailing vortices", Aeronautical Quarterly, vol. 23 (1972) pp. 307-314.
[19] S.E. Widnall, D.B. Bliss, A. Zalay, "Theoretical and experimental study of the instability of a vortex pair", in *Aircraft Wake Turbulence and Its Detection*, edited by J.H. Olsen, A. Goldberg, M. Rogers, Plenum, New York (1971) p. 305.

Load Alleviation Potential with Trailing Edge Flaps for Turbines in Wake Operation

Andreas Fischer[1], **Helge Aagaard Madsen**[1]

[1]Technical University of Denmark, Institute for Wind Energy, asfi@dtu.dk

ABSTRACT

We performed computations with the aeroelastic wind turbine code HAWC2 for the 2.3 NM80 wind turbine in free inflow conditions and in a full wake situation. The added turbulence in the wake flow is modelled with a dynamic wake meandering model. The computations were validated against measurements made during the DAN-AERO MW project. In this project a NM80 wind turbine situated in a small wind farm consisting of 8 turbines was equipped with inflow sensors and pressure tabs along the blade at 4 different radial sections. The inflow velocity and angle towards the blade as well as the normal force were in good agreement in measurement and computation. We applied an ideal flap control algorithm and investigated the fatigue load reduction potential for the blade normal force. The relative fatigue load reduction was the same in free flow condition and in wake operation, but the absolute value of the fatigue loads was higher in wake operation.

1 Introduction

Wind turbines placed in wind farms often operate in the wake of adjacent wind turbines. The wake flow creates turbulence which interacts with the atmospheric turbulence. Hence, the overall inflow turbulence level is increased. It is anticipated that such an operational condition leads also to an increase of the cyclic loads on the blade which cause fatigue damage. It is very much desired to decrease those loads.

In the DAN-AERO MW project [1] a 2.3MW NM80 wind turbine situated in a small wind farm consisting of 8 turbines was heavily equipped with sensors to measure inflow characteristics and blade loads. During the campaign the turbine operated in free inflow conditions as well as in wake situations. We evaluated the spectral characteristics of the inflow velocity and the blade normal force. The data set shows how those characteristics are changed by the wake. It is also used to validate the Dynamic Wake Meandering (DWM) [2], [3] model which was recently implemented in the aero-elastic code HAWC2 [4] and validated against full scale measurements [5]. This model describes in a simple and computationally effective way how the wake of a wind turbine increases the turbulence level of the atmospheric flow.

It was demonstrated that trailing edge flaps in combination with inflow measurements on the

blade are an effective measure to alleviate fatigue loads [6]. An ideal feed forward control algorithm using the measured relative velocity and angle of attack at a blade section to control the normal force was developed. In this paper the fatigue load reduction potential of trailing edge flaps for wind turbines operating in wake situations is demonstrated.

2 Methods

2.1 DAN AERO measurements

The measurements presented in this paper were carried out in the DAN-AERO MW project, funded by the Danish Energy Research programme EFP-2007 under contract Journal no. 33033-0074. The project was carried out in the period from March 2007 to December 2009 in corporation between Risø DTU, now DTU Wind Energy, and the companies LM Wind Power, Vestas Wind Systems, Siemens Wind Power and DONG Energy. More details of the experiment are presented in [1].
One blade of a NEG-Micon NM80 turbine was heavily equipped with measurement sensors. The three bladed turbine has a rotor diameter of 80m and the hub height is 57m, the rated power is 2.3MW. The blade contained among other sensors pressure tabs at radial position r=13m, 19m, 30m and 37m and four five-hole pitot tubes at radial position r=14.5m, 20.3m, 31m and 36m, figure 1.

Figure 1: The blade of the NM80 turbine equipped with measurement devices.

The turbine was placed in a small wind farm of 8 turbines at Tjæreborg Enge, about 1km away from the west coast of Jutland, Denmark, figure 2. The other turbines in the wind farm are of the same type. The nearest turbine was at a distance of 253m away from the NM80, the one furthest away at a distance of 884m. Calculations were made in [7] to predict for which wind directions the NM80 operates in the wake of another turbine and how much of the swept area of the rotor is influenced. The calculations were based on geometrical considerations and wake diameter variations depending on the induction. Our choice of free inflow and full wake cases

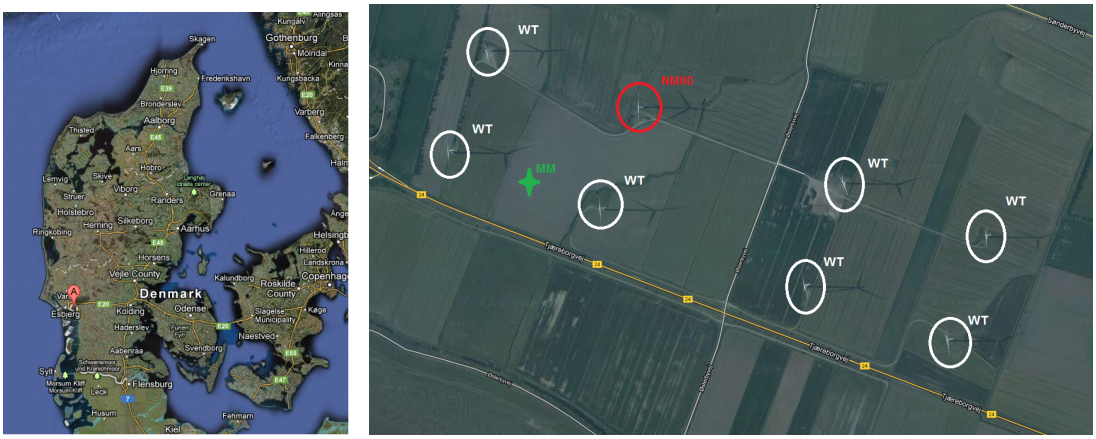

(a) Location in Denmark (b) Wind Farm

Figure 2: Map of the wind farm in Tjæreborg Enge. NM80: NM80 turbine, WT: wind turbine, MM: meteorological mast.

was based on those calculations.
A meteorological mast was situated about half way between the two turbines southwest of the NM80. The mast was equipped with cup anemometers and wind vanes at a height of 17m, 28.5m, 41m, 57m, 77m and 93m to provide wind speed and direction measurements. Additionally there were 3 sonic anemometers at altitude 17m, 57m and 93m. They provided measurements of the three components of the wind vector. Those sensors are suitable to provide the turbulence intensity of the inflow.

2.2 Aero-elastic model

The simulations in this work were performed with the aero-elastic code for horizontal axis wind turbines HAWC2 [4]. The code was developed at DTU wind energy over more than 10 years. The structural part of the code is based on a multibody formulation. Arbitrary large rotation of the bodies can be handled. The bodies are assembled of Timoshenko beam elements. The aerodynamic model is based on the classic blade element momentum theory. But the theory was extended to include the effects of dynamic, skewed and sheared inflow as well as large deflections and dynamic stall of the blades. The code can simulate trailing edge flaps on the blade.
The dynamic wake meandering model (DWM) is an essential part of this work. The theoretical background of this model is described in [2], the implementation in the HAWC2 code and tuning of the model parameters in [3]. The DWM adds the turbulence generated by the wake of another turbine linearly to the ambient inflow turbulence. The wake generated turbulence consists of two parts, the meandering of the velocity deficit driven by the large turbulence scales in the atmospheric flow and the small scale wake added turbulence generated by the sheared velocity profile in the wake and the shed blade bound vorticity.
The flow conditions as experienced during the measurements were described as closely as possible in the simulations, i.e. the wind velocity profile and the inflow turbulence intensity were

adjusted to match the measured ten minutes average. Inflow turbulence is described by the Mann turbulence model [8]. The structural model for HAWC2 of the NM80 turbine is described in [9]. The operational conditions of the NM80 turbine, i.e. the rotational speed of the rotor and the pitch angle setting, were monitored as well in the experiment and matched in the computations. Note that the turbine operated with constant rotational speed.

2.3 Fatigue Load Calculation

The equivalent fatigue load range number S_{eq} and the corresponding number of load range occurrences n_{eq} are defined according to the classical theory of Palmgren-Miner and Wöhler. It was derived in [10] and is given by

$$S_{eq} = \left(\frac{\sum n_i S_i^m}{n_{eq}} \right)^{1/m}. \tag{1}$$

The set of fatigue load ranges S_i and their number of occurrence n_i for a given load time trace are calculated with the Rainflow counting algorithm [11]. The Wöhler exponent m is a parameter describing the characteristic of the specific material. For wind turbine blades a value of $m = 10$ is normally used.
The equivalent fatigue load range number S_{eq} gives the range of a periodic load which causes the same fatigue damage as the set of fatigue load ranges S_i, n_i when occurring n_{eq} times. If we have a load time trace of of 600s duration and set $n_{eq} = 600$, the equivalent fatigue load range number can be interpreted as a sinusoidal load fluctuation with a frequency of 1Hz and we denote it with S_1.

3 Results

3.1 Inflow Conditions

The data base of the measurements in the DAN AERO project [1] contained two 10 minute measurement series with very similar inflow condition in terms of wind speed, shear and turbulence intensity, but the wind coming from very different direction, table 1. The flow conditions of

	wake situation 21/07/2009 13:10	free inflow situation 19/08/2009 12:30
wind speed at hub [m/s]	7.05	7.21
turbulence intensity at hub [%]	9	7
shear exponent [-]	0.09	0.15
wind direction at hub [deg]	256	161

Table 1: Wind conditions measured by the met mast.

the July measurement resulted in a situation where the NM80 turbine operates in the wake of turbine 1. The wake shadow coverage was estimated with the method described above, figure 3. According to the computation, 96% of the rotor area is in the wake shadow of the upstream

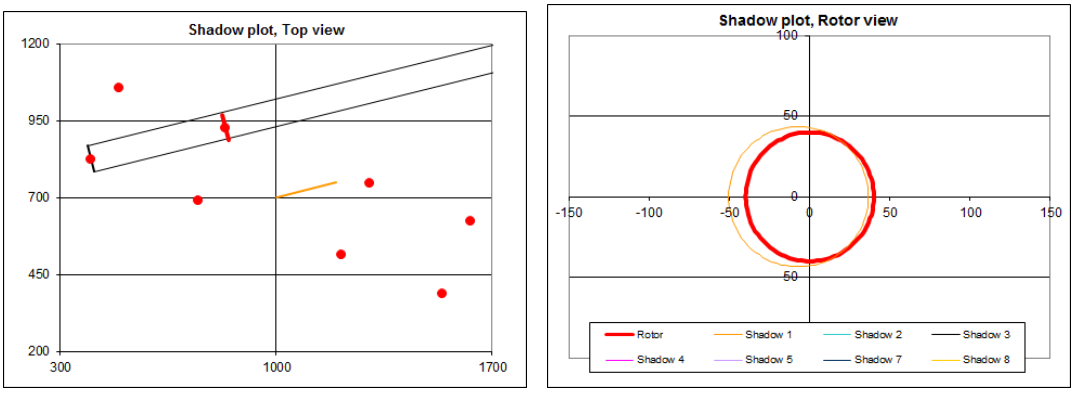

(a) Top view. (b) Rotor view.

Figure 3: Wake shadow for measurement on July 21st, 2009, 13:10.

turbine. Turbine 1 is at a distance of 448m away from the NM80 turbine. This corresponds to 5.6 times the rotor diameter.
In the august measurement the flow comes from a direction so that the turbine operates in free flow conditions, figure 4. The corridor for free flow conditions is very wide for this specific

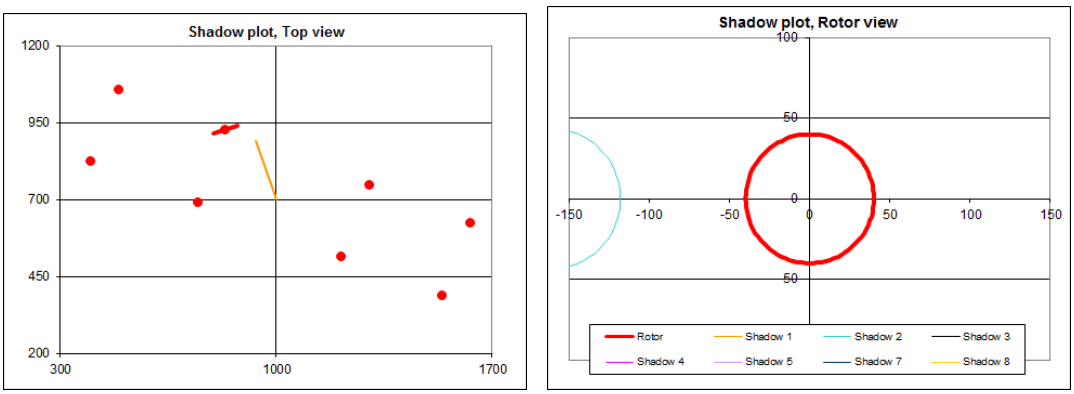

(a) Top view. (b) Rotor view.

Figure 4: Wake shadow for measurement on August 19th, 2009, 12:30.

range of wind directions. Even though there is an uncertainty in the wake prediction method, in this situation wake interaction is very unlikely.

3.2 Spectral Analysis of Inflow and Blade Normal Force

The spectral characteristics of the inflow to the blade is changed if the turbine operates in wake. We compare the measured and computed inflow characteristics for two blade sections, approximately r=20m and r=31m, in figure 5 and 6. Note that the exact measurement position and the computational node do not exactly coincide. All the spectra are characterized by peaks at

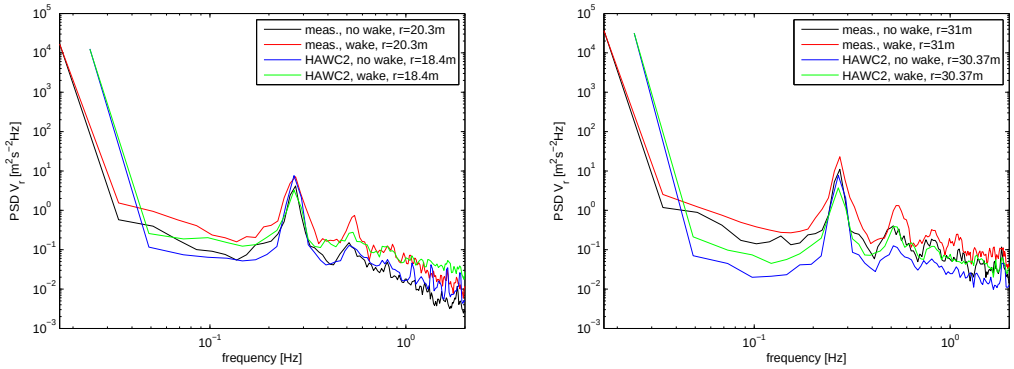

(a) radial position r=20m (b) radial position r=31m

Figure 5: PSD of the relative velocity.

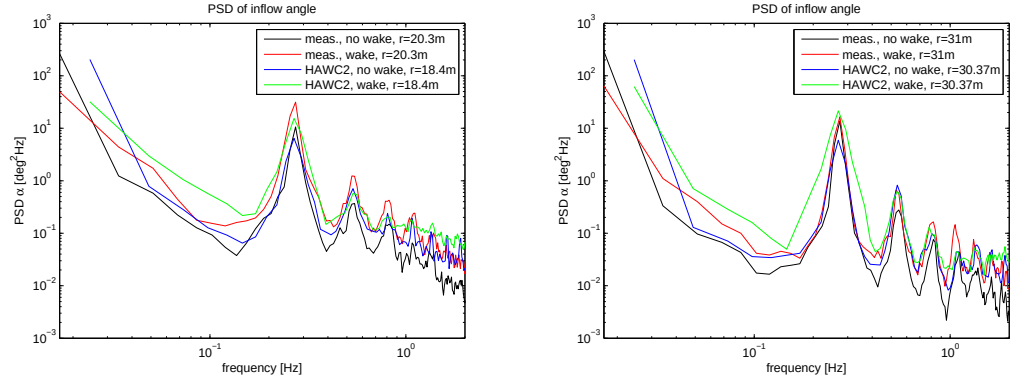

(a) radial position r=20m (b) radial position r=31m

Figure 6: PSD of the inflow angle.

multiples of the rotational frequency of the rotor. At the inner rotor position we observe higher spectral levels of the inflow velocity and inflow angle when the turbine operates in wake situation. For free inflow conditions the agreement between measured and computed inflow velocity spectrum is excellent. In full wake situation minor differences occur. The characteristic peak at 1 times the rotational frequency is broader in the measurement. For high frequencies the computation gives higher levels than the measurement. For the inflow angle the difference between measurement and computation are more significant. The size of the peak at a frequency equal to the rotational frequency is well predicted by the computation in both cases. But in the case of free inflow the spectral level of the computations is higher than the one of the measurements for higher frequencies. In wake situation the level for higher frequencies is overestimated, but the amplitude of the characteristic peaks is underestimated.

At the outer rotor position, the measured inflow velocity shows much higher turbulence levels as the computed one in both cases. In full wake situation the spectral peak corresponding to the

rotational frequency is broader in the measurement than in the computation. For the inflow angle the situation is reversed. The results of the computation have higher spectral levels. In full wake situation the width of the peak at the rotational frequency is broader in the computation than in the measurement.
The normal sectional blade force is displayed in figure 7. The agreement between measurement

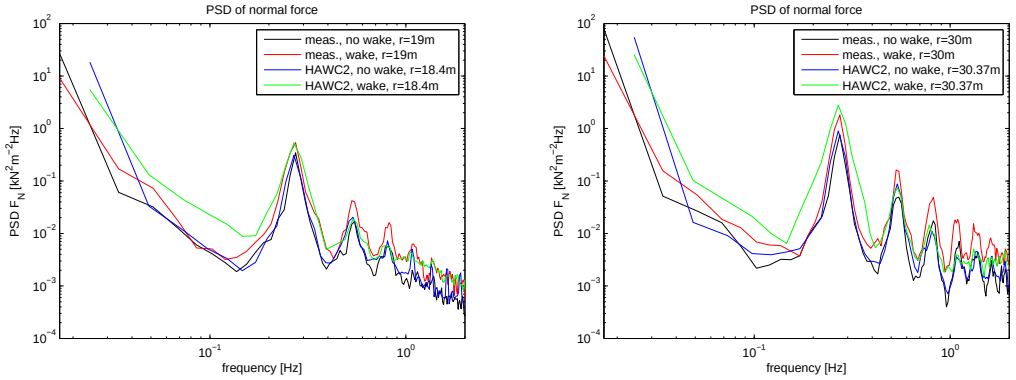

(a) radial position r=19m (b) radial position r=30m

Figure 7: PSD of the blade normal force.

and computation at both radial positions is excellent in free flow conditions. In full wake situation the level of the spectrum is higher than the level in free flow conditions. The computations give higher values than the measurements in the low frequency range and the peak at the rotational frequency is broader. The low frequency range is mainly influenced by the large scale movement of the turbine wake. The meandering turbulence level is normally the same as the one of the atmospheric turbulence. It can be reduced to give a better agreement with the measurement of the normal force. In the computations presented here the meandering turbulence level was slightly decreased to 7% instead of 9% (measured value of the atmospheric turbulence).
For higher frequencies the amplitude of the peaks corresponding to multiples of the rotational frequency are underestimated in level by the computation compared to the measurement. This regime is characterized by the small scale turbulence generated in the wake. The wake generated small scale turbulence might be underestimated be the DWM model.

3.3 Fatigue Load Analysis

Figure 8(a) shows the 1Hz equivalent fatigue load of the normal force at different blade positions. The fatigue loads were computed with a Wöhler exponent of $m = 10$. They are highly non-linear and due to some variation when computed for 10 minutes time series. In the regard of that the measurement and computation is in good agreement for the free inflow case. The computation overpredicts only slightly. The fatigue loads increase significantly if the turbine operates in the wake. The computation overpredicts also in this case, but the relative increase of the fatigue loads is well predicted, figure 8(b). This is due to the increased level of the blade normal force in the low frequency range in the computations. Low frequency fluctuations with high amplitude

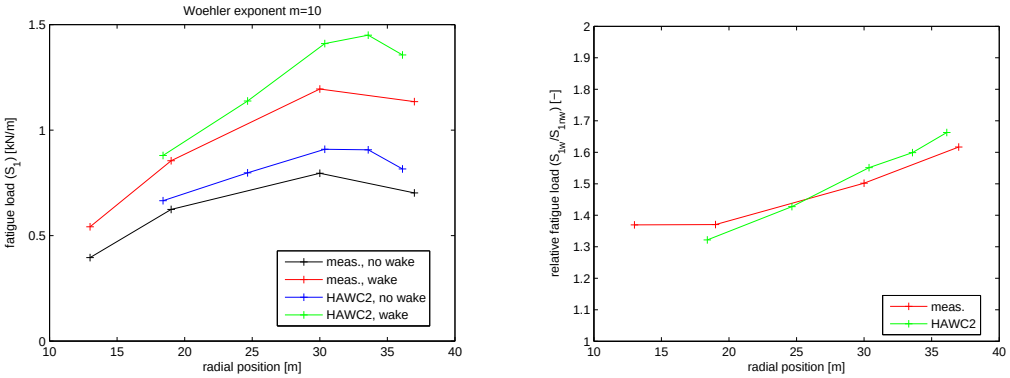

(a) absolute (b) normalized with free flow condition value

Figure 8: 1Hz equivalent fatigue loads of the normal force of the NM80 wind turbine.

count strongly to the equivalent fatigue load when a high Wöhler exponent is applied.
The spectrum of the fatigue load cycles at radial position r=19m and r=30m is shown in figure 9. The size of the second peak in the spectrum at high load ranges dictates mainly the value of the

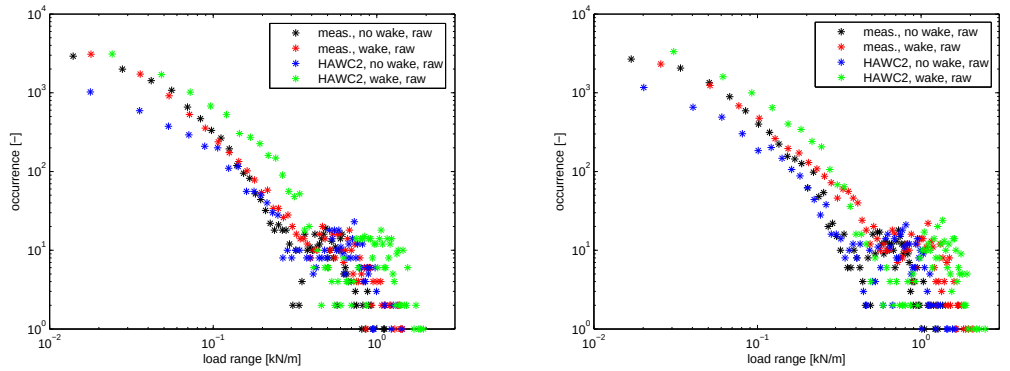

(a) r=19m (b) r=30m

Figure 9: Fatigue load cycle spectrum.

equivalent fatigue load because of the high Wöhler exponent. The behaviour of the spectrum in the low load range is of little importance. The computations show higher load ranges than the measurements.
To illustrate the load reduction potential of flaps we applied the control algorithm [6] to the time series of the blade normal forces by using the measured inflow velocity and angle at radial position 20.3m in the case of measurement data and at 18.4m in case of computations. This was the closest node in the BEM model to the measurement position. The equivalent fatigue load of the controlled normal force S_{1c} was computed and the absolute fatigue load reduction was quantified with $1 - S_{1c}/S_1$, figure 10(a). We applied an ideal filter to the blade normal force and computed the equivalent fatigue load S_{1f} for the filtered time series. The maximum obtainable

fatigue load reduction can then be quantified as $1 - S_{1f}/S_1$, the dashed lines in figure 10(a). The fatigue load reduction relative to the absolute maximum $(S_1 - S_{1c})/(S_1 - S_{1f})$ are shown in figure 10(b).

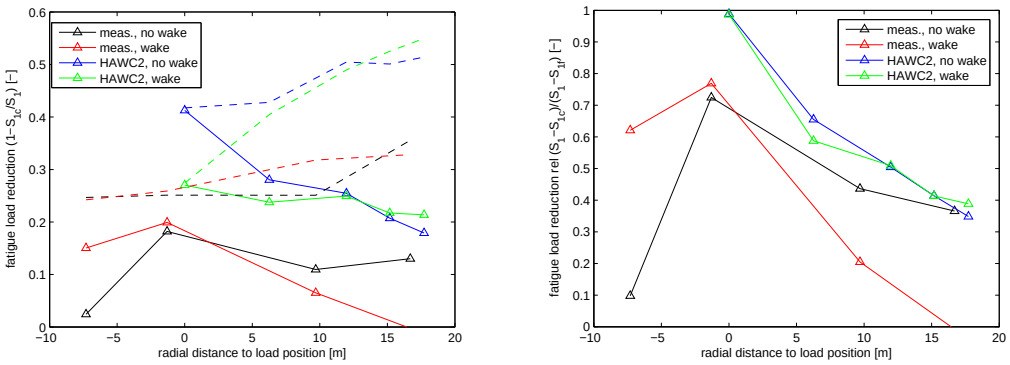

(a) absolute, dashed line: Maximum obtainable fatigue load reduction

(b) relative to maximum obtainable fatigue load reduction

Figure 10: Fatigue load reduction with ideal flap control.

The achieved fatigue load reduction is different for free inflow condition and full wake operation in the computations. But relative to the absolute maximum of the fatigue load reduction the achieved reductions are similar in both cases. The variation of the absolute values is due to the concrete time history of the inflow turbulence and is not influenced by wake operation. The fatigue loads were evaluated based on 10 min time series. It would be better to evaluate fatigue loads based on 1 hour time series. This was not possible in the case of the measurement and avoided in the computation in order to be consistent.
For the measured normal force a much lower fatigue load reduction was achieved compared to the computations. This could be due to added noise to the time series by the measurement system. However, the measurements show that a considerable fatigue load reduction is possible and the amount of reduction is the same in free flow conditions as in full wake operation.

4 Discussion

In the DAN AERO experiment a huge data set of full scale wind turbine aerodynamic and blade loading data was collected. The data set contained two measurements with similar wind conditions, but the NM80 wind turbine once operating in free inflow and once in a full wake situation. We investigated the spectral characteristics of the blade inflow velocity and angle as well as the blade normal force to evaluate the fatigue loads. The measured data was compared with computations with the HAWC2 aero-elastic code. The code includes a model describing the dynamic meandering of the wake (DWM).
The spectral level of the inflow velocity was in general slightly underpredicted by the HAWC2 code in both cases, except for high frequencies at the inboard part of the rotor. Here the level is higher than the one of the measurements. The spectral level of the inflow angle was in general

slightly overestimated, but in wake operation, the amplitude of the spectral peaks at multiples of the rotational frequency are underestimated.
For free flow condition the normal force spectra of computation and measurement were in excellent agreement. In wake operation, the normal force was overestimated in the low frequency range. Hence, we adjusted the turbulence level of the large scale movement of the wake. In the high frequency range the normal force level was underestimated by the computation. This domain is governed by the small turbulence scales in the wake.
The fatigue loads are much higher in wake operation compared to free inflow situation. This was confirmed both by measurement and computation, even though the computation overestimated the fatigue loads compared to the measurement. However, the relative increase of the fatigue loads due to wake operation was predicted correctly.
The fatigue load reduction potential by flaps is approximately the same in wake and free inflow situation. Due to the higher absolute value of the fatigue loads is the reduction more valuable in the case of wake operation. The fatigue load reduction potential predicted by the computations could not be obtained for the measured time series. Further investigation is necessary here.

References

[1] Madsen HA, Bak C, Paulsen US, Gaunaa M, Fuglsang P, Romblad J, Olesen NA, Enevoldsen P, Laursen J, Jensen L. The DAN-AERO MW Experiments: Final report. *Tech. Rep. Risø-R-1726(EN)*, Risø-DTU, Roskilde, Denmark September 2010.

[2] Larsen GC, Madsen HA, Thomsen K, Larsen TJ. Wake meandering - a pragmatic approach. *J. of Wind Energy* 2008; **11**:377–395.

[3] Madsen HA, Larsen GC, Larsen TJ, Troldborg N. Calibration and Validation of the Dynamic Wake Meandering Model for Implementation in an Aeroelastic Code. *J. Sol. Energy Eng.* 2010; **132**(4).

[4] Larsen TJ, Hansen AM. How to HAWC2, the users manual. *Tech. Rep. Risø-R-1597(ver.4-3)(EN)*, DTU Wind Energy, Roskilde, Denmark April 2012.

[5] Larsen TJ, Madsen HA, Larsen GC, Hansen KS. Validation of the dynamic wake meander model for loads and power production in the Egmond aan Zee wind farm. *J. Wind Energy* 2012; .

[6] Fischer A, Madsen HA. Investigation of the maximum load alleviation potential using trailing edge flaps controlled by inflow data. *The science of making torque from wind Conf. (EWEA)*, Oldenburg, GE, 2012.

[7] Bak C, Madsen HA, Hansen P, Rasmussen M, Fuglsang P, Romblad J, Olesen NA. DANAERO MW: Measurement campaigns on the NM80 2.3MW wind turbine at Tjæreborg 2009. *Tech. Rep. Risø-I-3046(EN)*, Risø-DTU, Roskilde, Denmark November 2010.

[8] Mann J. The spatial structure of neutral atmospheric surface-layer turbulence. *J. of Fluid Mech.* 1994; **273**:141–168.

[9] Hansen MH, Fuglsang P, Thomsen K. Aeroelastic modeling of the NM80 turbine with HAWC. *Tech. Rep. Risø-I-2017(EN)(Confidential)*, Risø-DTU, Roskilde, Denmark December 2004.

[10] Thomsen K. The Statistical Variation of Wind Turbine Fatigue Loads. *Tech. Rep. Risø-R-1063(EN)*, Risø National Laboratory, Roskilde, Denmark September 1998.

[11] Matsuishi M, Endo T. Fatigue of metals subjected to varying stress. Paper presented to Japan Soc Mech Engrs, Jukvoka, Japan 1968.

AERODYNAMIC PHYSICS OF SMART LOAD CONTROL FOR WIND TURBINE DUE TO EXTREME WIND SHEAR

M.M. Zhang*, W. Yu, J.Z. Xu

Institute of Engineering Thermophysics, Chinese Academy of Sciences, No. 11 Beisihuanxi Road, Beijing, China, 100190; Corresponding Author, e-mail: mmzhang@mail.etp.ac.cn

ABSTRACT

This paper presents a numerical investigation of the smart load control on an Upwind/NREL 5 MW reference wind turbine under the IEC extreme wind shear (EWS) condition utilizing newly develped aero-servo-elastic platform. The control action was implemented through the local perturbation of a deformable trailing edge flap (DTEF) per blade, which was driven by a smart rotor system, based on the FAST/Aerodyn and Matlab/Simulink codes. Resutls showed that, compared with the original collective pitch control method, the aerodynamic load in terms of blade flapwise root moment and tip deflection were effectively reduced. Furthermore, the smart rotor control also positively affected other components of the drive-chain as well as generator power and pitch system. It was found that the smart control effect altered the nature of the flow-blade interactions, changing the in-phased fluid-structure synchronization into much weaker couplings. As a result, the damping of the fluid-blade system was significantly enhanced, leading to great attenuation on the EWS load on both rotor and other drive-chain components.

I. Introduction

As we know, both fatigue and extreme loads contribute to the accrued damages in wind turbine components, eventually leading to failures. The former is often originated from turbulence, tower shadow, wind shear and yawed flow, etc, while the later is frequently induced by drastic wind velocity and/or direction changes. However, according to many previous investigations [1], if an effective active control method was properly introduced, not only the loadings on the turbine but the cost per kWh would be significantly decreased. Therefore, the active loading control has recently become a very hot research direction in the field of wind energy.

The controls of fatigue loads on turbines have been widely investigated before, among which the researches on the pitch control, including collective pitch control, cyclic pitch control and relatively advanced individual pitch control, are in the majority. Nevertheless, this method still suffers from several weaknesses [2], e.g. incapability to local fluctuating blades across the rotor disk, slow pitching of entire blade and premature wear on pitch components.

On the other hand, about one decade ago, the concept of “smart rotor control” emerged [3,4] and its basic idea was to drive local aerodynamic surfaces through a combination of sensors, actuators and controllers, and thus provides a higher load control capacity. Due to its inherent advantages over traditional pitch control, this concept has nowadays been regarded as a rather potential solution to reduce the loading on large-scale wind turbines. Furthermore, the “deformable trailing edge flap (DTEF)”, a flap that deforms in a flexible instead of traditional rigid shape, characterized by its positive performance, fast response, small size, wide controllable bandwidth and low flow disturbance, has been found to be the most efficient aerodynamic control method in contrast to other potential candidates [5], such as micro tab, morphing, active twist, suction/blowing, synthetic jet, and active vortex generator, *etc*, and a large amount of work on the fatigue load control has been conducted, which can be generally classified into numerical simulation and experimental test. For the former, based on the theoretical analysis of aerodynamic, structural dynamic and control in helicopter area,

together with the unique characteristics of wind turbine, most of research efforts had been made to build an efficient and accurate aero-servo-elastic simulation platform (e.g. GH Bladed, HAWC2, DU_SWAMP and Aerodyn/FAST) so that the fatigue loading could be effectively and optimally suppressed [6-11]. In respective of experiment, the smart rotor control system had been individually tested on 2D airfoil and small prototype turbine to verify this novel idea [12,13].

In contrast, to our knowledge, the smart control of the extreme loads was rarely studied except one paper concerned with load alleviation due to gust [14]. But the suppressions of extreme loads on turbines, especially on the blades, often play an even more important role in reliable O&M of turbines and this is particular true with the increasing size of offshore wind turbines. Additionally, the aerodynamic physics behind is still very lack, which may blockage further development of the technique in terms of improving numerical modeling, system optimal design and even evaluating control performance in the future. It is obvious that the targeted research work is urgently needed.

To this end, the present paper mainly focus on the control effectiveness of one typical extreme load on a large-scale wind turbine using smart rotor method with deformable trailing edge flap (DTEF) as well as the understanding of the corresponding aerodynamic physics. Specifically, deploying our newly developed aero-servo-elastic numerical platform [11], which was built by improving FAST/Aerodyn codes with the integration of external controller of deformable trailing edge flap into the Matlab/Simulink software, the smart blade control was conducted and assessed on the Upwind/NREL 5MW reference wind turbine under IEC extreme wind shear (EWS) condition [15]. To uncover the involved control physics, the coupling interactions among wind, blade and flap and the associated effect on other drive-train components were discussed in detail.

II. General Description of Aero-servo-elastic Simulation Platform

Recently, we have developed a new aero-servo-elastic platform, based on FAST/Aerodyn and Matlab/Simulink codes, to implement smart fatigue load control using DTEF [11], under which the maximum reductions in flapwise root moment and tip deflection of Upwind/NREL 5MW reference wind turbine [16], due to IEC Normal Turbulence Model (NTM) and Extreme Turbulence Model (ETM) turbulence, were effectively reduced up to 11% ~ 21%. Moreover, the load reduction on blades also showed positive effect on the loading of other drive-chain components, collective pitching action and power generation.

The previously developed simulation platform was still deployed in this paper. The lift coefficient, drag coefficient and pitching moment coefficient of each airfoil, i.e. C_l, C_d and C_m, were computed by RFOIL code, with more better characteristics in terms of numerical stability and boundary layer description [17] than XROIL code in previous investigations [8,14]. Specifically, C_l, C_d and C_m, as a function of α ranged from −20° to 23°, were first generated by RFOIL code, with flap deflection angles ranging from −10 degrees to 10 degrees in 1 degree increments. After that, airfoil tables were pre-processed using AirfoilPrep spreadsheets [18], which apply the Viterna method to expand performance to the α range of −180° ~ +180° required by the Aerodyn code. In addition, to further improve the airfoil aerodynamic, a semi-empirical Beddoes-Leishman dynamic stall model was utilized in Aerodyn/FAST code.

The control system of the wind turbine presently investigated can be separated into two systems, i.e. basic control system and DTEF control system. The former system of the reference 5 MW turbine, including generator-torque controller and collective pitch controller, was originally built by NREL using Aerodyn/FAST codes [16]. The control of the generator torque was conducted through adjusting the filtered generator speed, incorporating five regions: 1, 1½, 2, 2½, and 3, and the full-span collective blade pitch was manipulated using gain scheduled proportional-integral control based on the speed error between the filtered generator speed and the rated one in Region 3.

For the DTEF control system, the theory of multi-blade coordinate transformation was utilized. According to this, the action of the flap per blade could be independently controlled by a Linear Time Invariant (LTI) SISO feedback loop method. Normally, the LTI SISO systems are easily dealt with from a control perspective, as classical control techniques such as proportional-integral-derivative (PID) control can be employed. Presently, we used Matlab/Simulink codes to simulate the influence of the DTEF control system on all three blades. The main control architecture is shown in fig. 1. In

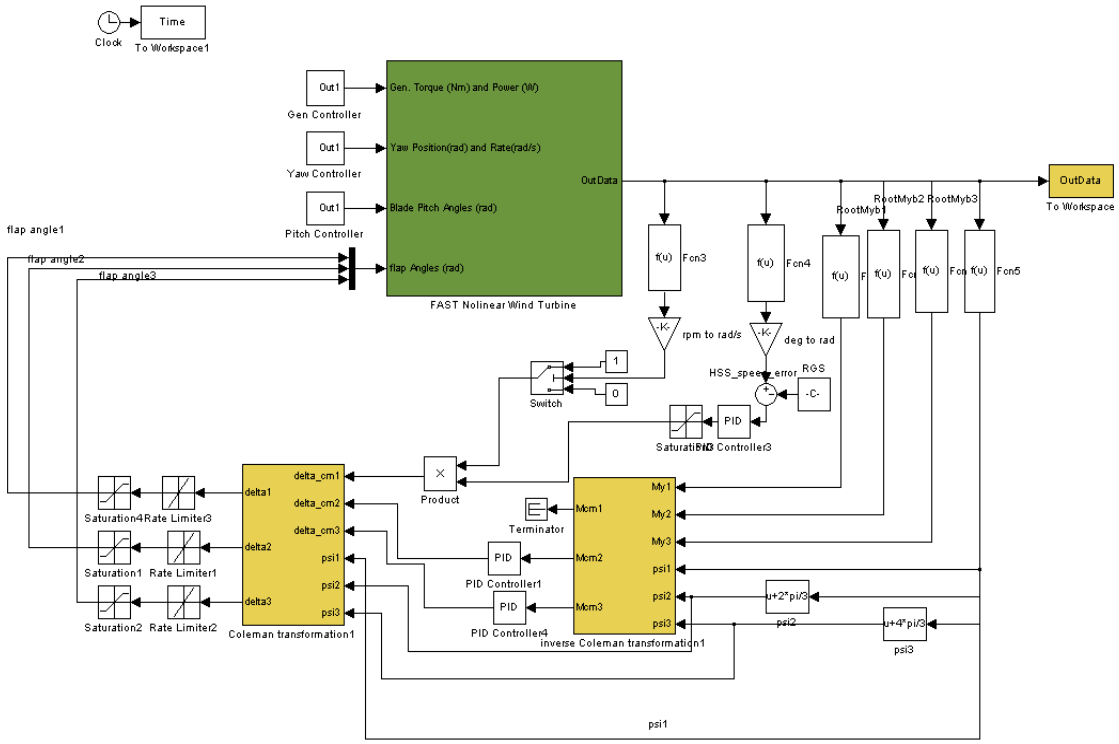

Figure1: Schematic of smart rotor control based on FAST/Aerodyn and Matlab/Simulink codes.

general, the root flapwise bending moments of the three blades, M_{By1}, M_{By2} and M_{By3}, are first transformed into the fixed frame of reference using the inverse Coleman transformation, yielding the hub yaw-wise and tilt-wise moments, respectively. Then these two moments are used as inputs to LTI PID controllers, and the control actions in the fixed frame are exerted through reasonably adjusting the proportional coefficient, the integration coefficient and the derivative coefficient. Finally, the resultant control is again transformed back into the rotating frame using the Coleman transformation to assign the proper flap angle to each blade for optimum control of M_{By1}, M_{By2} and M_{By3}. Here the deployment angle range of the individual DTEF, with a length of 10% chord and a distribution of 70% ~ 90% of each blade span, and the collective DTEF were limited to $\pm 10^{\circ}$ and $\pm 5^{\circ}$, respectively.

Using a similar analysis method as Lackner and Kuik [14] and our paper [11], the reduced frequency k, *i.e.*, $k = c\omega/U$, representing the degree of unsteadiness of an airfoil section subject to external disturbance, was examined to be about 0.0106, much less than 0.05, beyond which the aerodynamics of airfoil section could be considered to be unsteady. Based on this, we have confirmed that even though the aerodynamic of DTEF sections, which may influence the smart rotor simulations, are not entirely quasi-steady, it is indeed a safe assumption to do so. Here c, U and ω stand for the local chord length of the section, the local relative velocity at the section and the frequency of the disturbance in units of radians per second, respectively.

For more detailed information on the simulation platform, readers may go through the paper [11] for reference.

III. Performances of Smart Rotor Control on EWS Load

To exhibit and analyze the capability of the smart rotor control, focus was only put on the best results in this paper. Figs. 2-3 first show the typical results on the rotor in both time and frequency domain. Since it will take some time to stabilize the computation once it is executed, the time origin of abscissa is not 0s, but 20s. The typical 50s time histories of longitudinal wind speeds at the hub height (z_{hub}) and the tip of blade1 are displayed in fig. 2(a). The vertical transient EWS, abiding by the Eq. 1 [15], is imposed within the time range of 25s ~ 37s:

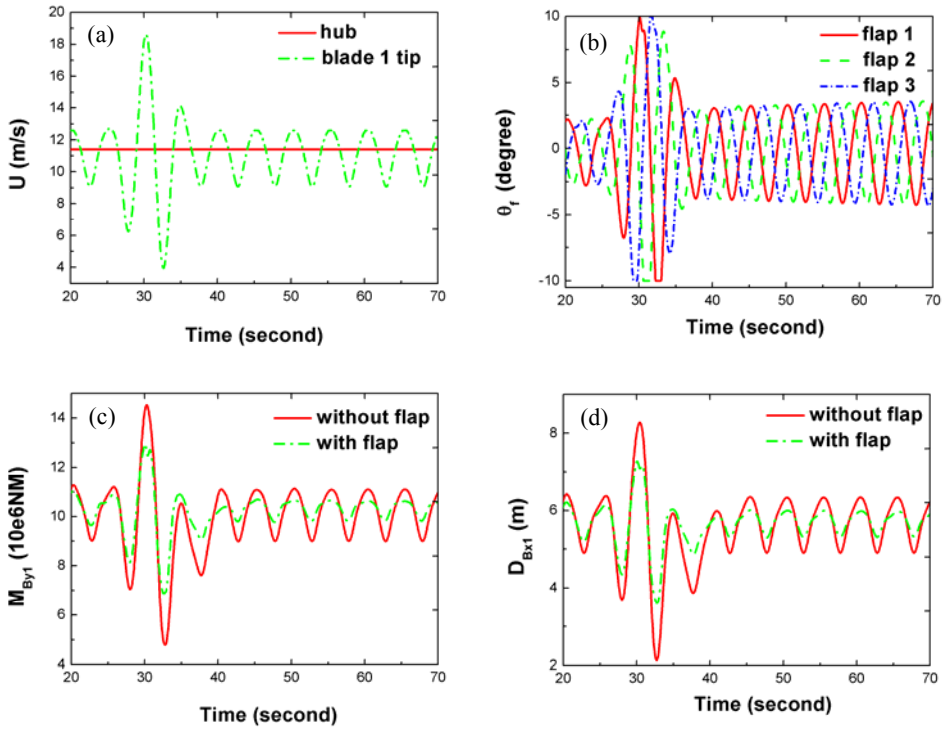

Figure 2: Typical time domain results: (a) longitudinal wind speed on blade 1; (b) deployment angles (θ_f) of three DTEFs; (c) blade1 flapwise root moment (M_{By1}); (d) blade 1 flapwise tip deflection (D_{Bx1}).

$$V(z,t)=\begin{cases} V_{hub}\left(\frac{z}{z_{hub}}\right)^{\alpha} \pm \left(\frac{z-z_{hub}}{D}\right)\left(2.5+0.2\beta\sigma_1\left(\frac{D}{\Lambda_1}\right)^{1/4}\right)(1-\cos(2\pi t/T)) & for\ 0\le t\le T \\ V_{hub}\left(\frac{z}{z_{hub}}\right)^{\alpha} \end{cases} . \quad (1)$$

where:

V_{hub} — wind speed at hub height, 11.4 m/s;

α — wind shear exponent, 0.2;

β — constant, 6.4;

D — rotor diameter, 126 m;

T — transient cycle of EWS, 12 s;

σ_1 — turbulence standard deviation, given using Eq. 2;

$$\sigma_1 = I_{ref}(0.75V_{hub} + b) \quad (2)$$

b — constant, 5.6 m/s;

I_{ref} — the expected value of the turbulence intensity at 15 m/s (= 0.14 for medium turbulence characteristics).

It is evident that the existence of strong wind shear greatly differentiates wind speed within the rotor plane [Fig. 2(a)]. From fig. 2(b), we can see that all three DTEFs take effect, but about 120° phase difference exists among them. Clearly, after the introduction of DTEF, fluctuations in the flapwise root moment (M_{By1}) and blade flapwise tip deflection (D_{Bx1}) were evidently suppressed, no matter in and out of the EWS process [Figs. 2(c)-(d)]. Correspondingly, the dominant spectral peaks at the 1st flapwise mode frequency of the blade1, i.e. f_{1P} = 0.2Hz [14], were significantly reduced up to 71.7% and 68.7% in the power spectral density of M_{By1} and D_{Bx1}, i.e. $E_{M_{By1}}$ and $E_{D_{Bx1}}$, while the peaks at the harmonic frequencies of 1P mode, i.e. f_{2P} and $f_{2.5P}$, and the 1st flapwise natural mode frequency ($f'_{M_{By1}} \approx$ 0.77 Hz [16]) were a little increased (Fig. 3), possibly related with the energy transfer among

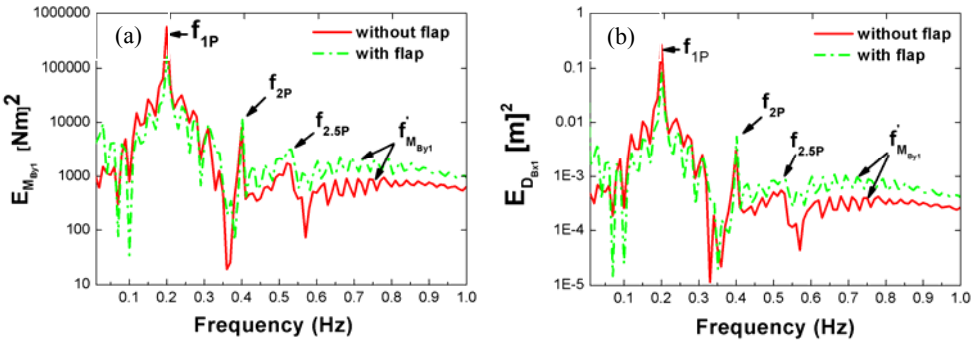

Figure 3: Typical PSD results of blade1 with and without DTEF: (a) flapwise root moment ($E_{M_{By1}}$); (b) flapwise tip deflection ($E_{D_{Bx1}}$).

these vibration modes. Note the small peaks at $f_{2.5P}$ were probably originated from the coupling of 1P mode and the 1st flapwise natural mode. Besides that, the PSD amplitude at about 0.1 Hz under the influence of DTEF is subject to huge reduction, related with the impaired EWS with a transit cycle of 12 s [Figs. 2(c)-(d)]. From another point of view, the energies of M_{By1} and D_{Bx1} associated with f_{1P} declined by 71.6% and 68.3%, respectively, which were calculated by integrating $E_{M_{By1}}$ and $E_{D_{Bx1}}$ over 3 dB bandwidth with respect to the peak value [19]. These results fully prove the smart control effectiveness on the extreme rotor load due to EWS.

In addition to the effect on blades, interests were also aroused to assess the function of the smart rotor control on other drive-chain components under EWS. Fig. 4 displays the typical time-series results of the bending moment of low speed shaft (M_{LSSy}), the yaw bearing moment (M_{Yawz}), the tower top deflection (D_{TTx}) and the tower root moment (M_{TBy}) with and without DTEF control. Obviously, all these four quantities were subject to very effective reduction, especially when EWS was introduced. This is reasonable since the decreased M_{By} at 1P mode is mainly responsible for the reduced loads on these components. Moreover, to see whether the basic collective pitch control was influenced as well, the variations of the representative time histories of two critical parameters, i.e. the rated generator power P_w and the collective pitch angle of blade1, are illustrated in fig. 5. It clearly shows that the deviation from the rated generator power (5 MW) is smaller and the amplitudes of pitch angles are

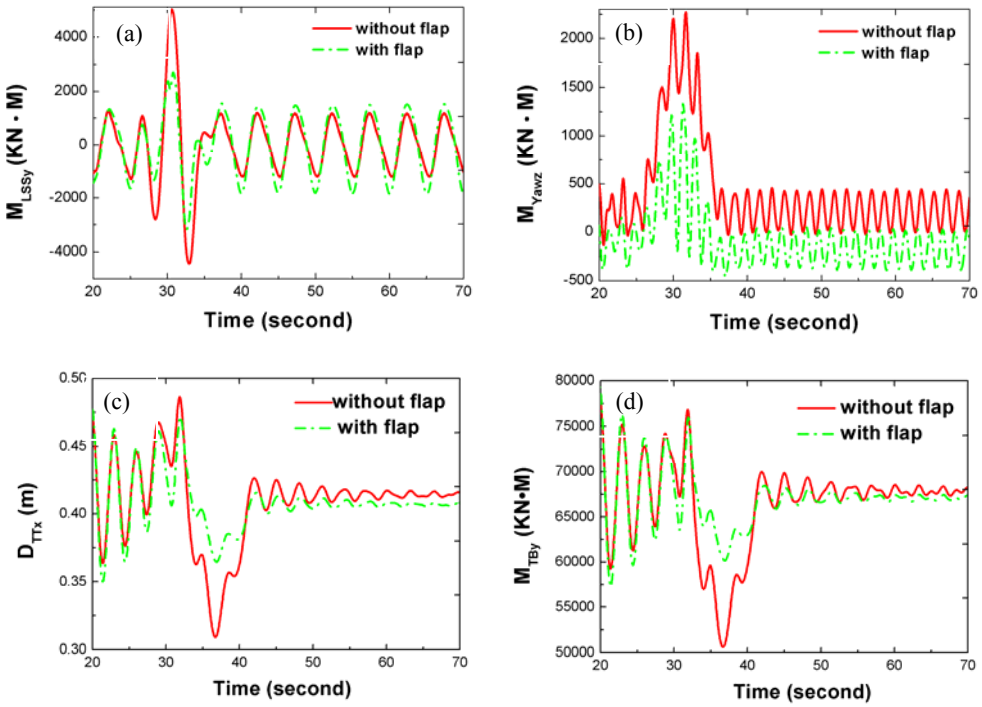

Figure 4: Typical time domain results with and without DTEF: (a) bending moment of low speed shaft (M_{LSSy}); (b) yaw bearing moment (M_{Yawz}); (c) tower top deflection (D_{TTx}); (d) tower root moment (M_{TBy}).

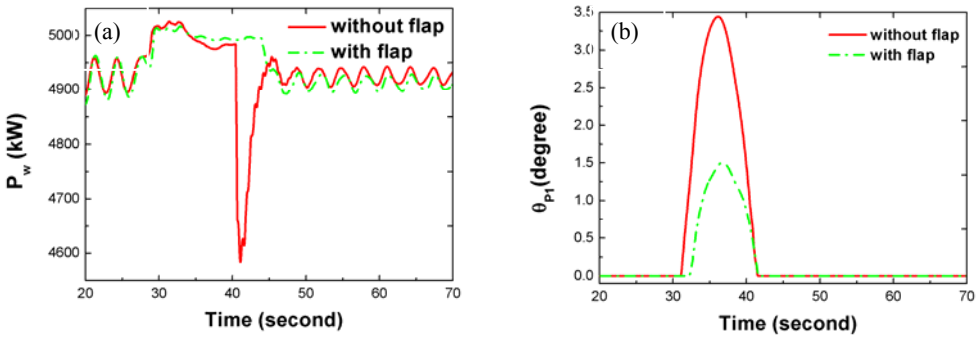

Figure 5: Typical time domains results with and without DTEF: (a) generator power (P_w); (b) collective pitch angle of blade1 (θ_{p1}).

much lessened for smart control. These results mean the deployment of flap angle may contribute to a smoother power output and less wear of the pitch control system.

The overall performances of the two control schemes, i.e. collective pitch control (CPC) and collective pitch control with flap control (CPC+FC), are summarized in table 1 for comparison. Here the data represent the change in the peak-to-peak value of all quantities under EWS. It can be seen that the smart control tends to much more outperform the traditional CPC case in every category, resulting in the maximum reduction percentage in M_{By} , D_{Bx} , M_{LSSy} , M_{Yawz} , D_{TTx} , M_{TBy} , P_w and θ_{p1} of 43.1%, 40.1%, 37.8%, 22.5%, 53.6%, 54.8%, 72.3% and 56.4%, respectively, totally agreeable with the trends shown in figs. 2-5.

Table 1 Summary of control performances of DTEF

	CPC	CPC+FC	Reduction/%		CPC	CPC+FC	Reduction/%
M_{By1} /MN·m	9.7363	6.095	37.4	D_{Bx1} / m	6.137	3.676	40.1
M_{By2} /MN·m	8.4039	6.1436	26.9	D_{Bx2} / m	5.215	3.664	29.7
M_{By3} /MN·m	9.2115	5.2369	43.1	D_{Bx3} / m	5.455	3.628	33.5
M_{LSSy} / KN·m	9473	5890	37.8	M_{Yawz} /KN·m	2306	1788	22.5
M_{TBy} / MN·m	22.228	10.039	54.8	P_w / kW	442.426	122.388	72.3
D_{TTx} /m	0.154	0.071	53.6	θ_{p1} / degree	3.444	1.503	56.4

IV. Discussions on Aerodynamic Physics of Smart Load Control

To uncover the physics behind the aforementioned aerodynamic control performances under EWS, the simultaneously sampled aerodynamic, structural dynamic and flap dynamic data of the blades were analyzed using the developed aero-servo-elastic platform. Specifically, the relationships among the normal force F_n, i.e. the aerodynamic force on the blade element normal to the local flapwise direction, the local flapwise acceleration a and the flap angle θ_f were interpreted. Since θ_f varies over a very small range ($\pm 10^{\circ}$), the flaps may be approximately thought to be activated in the local flapwise direction. For simplicity, the blade1 case was selected for a typical example. Figs. 6-9 indicate the spectral phase shift $\phi_{m1m2} = \tan^{-1}(Q_{m1m2} / Co_{m1m2})$ and coherence $Coh_{m1m2} = (Co_{m1m2}^2 + Q_{m1m2}^2) / E_{m1}E_{m2}$ among the three variables. Here Co_{m1m2} and Q_{m1m2} stand for the co-spectrum and quadrature spectrum of $m1$ and $m2$, respectively. Coh_{m1m2} provides a measure of the degree of correlation between the Fourier components of $m1$ and $m2$ and a fast Fourier transform (FFT) scheme is used for spectral calculation. All the analysis methods presented here have been successfully deployed during our previous investigations of fluid-structure-acoustic interaction control based on a novel perturbation technique [19-22].

Fig. 6 presents the typical spectral phase shift $\phi_{\theta_{f1}F_n}$ between θ_{f1} and F_n, which is computed near the central part location of DTEF (80.0% span location from the root of blade1). Evidently, under smart control, $\phi_{\theta_{f1}F_n}$ at f_{1P} is close to $-\pi$, suggesting that the perturbed flap activation and the nearby aerodynamic normal force on the blade are in anti-phase or opposite movement at primary 1P frequency. Correspondingly, the aerodynamic energy around the blade will be quickly dissipated, leading to an effective impairment in F_n and thus aero-elastic coupling of flow and blade. To further clarify this, the spectral phase of F_n and a near flap, i.e. $\phi_{F_n a}$, was also calculated with and without DTEF control, shown in fig. 7. Without control, $\phi_{F_n a}$ is around zero over a frequency range from 0.19 Hz to 0.81 Hz (covering f_{1P}, f_{2P}, $f_{2.5P}$ and $f'_{M_{By1}}$), indicating the strong synchronizing flow and structural vibration. Once perturbed using DTEF control, $\phi_{F_n a}$ at f_{1P}, f_{2P}, $f_{2.5P}$ and $f'_{M_{By1}}$ were all greatly deviated from 0. This implies a change in the nature of the flow-blade interaction near the flap location, that is, the synchronizing F_n and a turn into more disorder pattern, especially for 1P mode. As a result, $Coh_{F_n a}$ at f_{1P}, $f_{2.5P}$ and $f'_{M_{By1}}$ (Fig. 8) decrease by 96.2%, 97.1%, and 87.5%, respectively. For some reason, the peak at f_{2P} was invisible. Moreover, at another two typical spanwise locations of blade1 (16.7% and 56.7% span locations from the root of blade1), $Coh_{F_n a}$ are still subject to significant reductions at these mode frequencies [Figs. 9(a)-(b)]. Since the drastic reduction in $Coh_{F_n a}$ means a decoupled correlation between flow and the structural vibration of the whole blade,

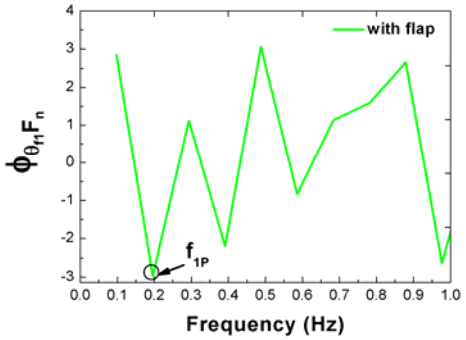

Figure 6: Typical spectral phase between θ_{f1} and normal force F_n on blade1 near flap1 with and without DTEF control.

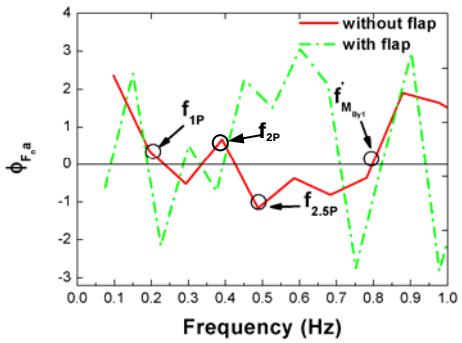

Figure 7: Typical spectral phase between F_n and a with and without DTEF control.

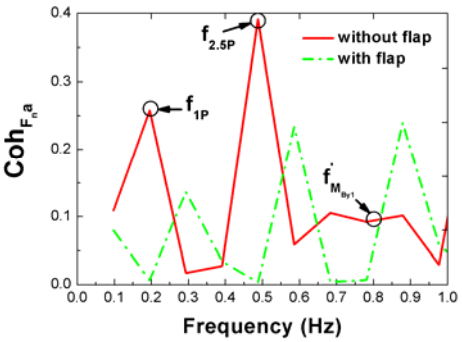

Figure 8: Typical spectral coherence between F_n and a with and without DTEF control.

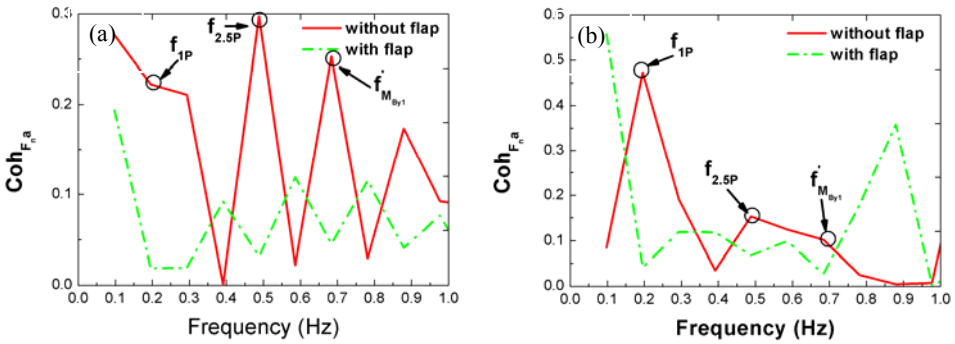

Figure 9: Typical spectral coherence between F_n and a at various spanwise locations with and without DTEF control: (a) 16.7% span location; (b) 56.7% span location.

the aerodynamic load and subsequent flapwise root moment on the blade will be greatly suppressed.

On the other hand, the variation in $\phi_{F_n a}$ and $Coh_{F_n a}$ may make one infer that the flow-blade system damping must be changed. As we know, damping models the energy dissipation of the system during structural vibration and plays an important role in the stability of a structure and its vibration amplitude. The synchronizing flow and blade vibration will be effectively attenuated if the damping ratio of the system is increased. It is therefore worthwhile examining how the system damping ratio has been altered due to the introduction of control. In this paper, we define the effective damping ratio ζ_e, representing the energy dissipation of a system, as the sum of structural damping ratio and fluid damping ratio. The former may be generated by material, friction, impacting, and the rubbing of two surfaces in contact, while the latter results from skin friction and viscous dissipation [23]. Similar with what we reported in [24], an autoregressive moving average (ARMA) technique with an order of 190 and 70000 data points was used to calculate ζ_e from the time series of blade displacement. It turned out that, compared with CPC case, an average increase in ζ_e by about 30.0% was obtained at 1P mode for smart control, consistent with the results in figs. 6-9.

V. Conclusions

Using our recent developed aero-servo-elastic platform, the smart blade control of the load on the rotor due to IEC extreme wind shear (EWS) was numerically investigated in this paper, with an aim to evaluate the control effectiveness and understand the associated aerodynamic physics behind. The investigation leads to the following conclusions.

(1) Compared with the original collective pitch control method, the extreme load on blades was effectively reduced under EWS condition. Maximum reduction in the flapwise root moment and the tip deflection of blades were up to 43.1% and 40.1%, respectively.
(2) Extreme load reduction on blades with the smart rotor control system was very helpful to suppress the corresponding loads on other drive-chain components of the wind turbine, e.g. low-speed shaft, yaw bearing and tower, as well as to decrease the power fluctuation and the wear on the pitch control system.
(3) The presently developed DTEF based smart control effectively turns the strong synchronized flow-blade interaction due to EWS turbulence into a much weaker one. This is associated with a significant increase in the effective damping ratio of the flow-blade system, implying an enhanced dissipation of flow and blade vibration energies and their diminished correlation. As a result, the rotor extreme load at the dominant 1P mode and subsequent those on drive-chain components are remarkably reduced.

Acknowledgments

This work was supported by the National Natural Science Foundation of China (Grant No. 51222606), "Hundred Talent Program" of Chinese Academy of Sciences and Sino-Denmark Collaboration Project (Grant No. 2010DFA62830).

REFERENCES

[1] P.S. Veers et al., "Trends in the design, manufacture and evaluation of wind turbine blades", Wind Energy, vol. 6 (2003), pp. 245-259.
[2] S.J. Johnson, C.P. Case van Dam, D.E. Berg, "Active load control techniques for wind turbines", SAND2008-4809.
[3] T.K. Barlas, G.A.M. van Kuik, "State of the art and prospectives of smart rotor control for wind turbines", Journal of Physics, vol. 75 (2007), pp. 1-20.
[4] S.S. Collis, R.D. Joslin, A. Seifert, V. Theofilis, "Issues in active flow control: Theory, control,

simulation and experiment", Progress in Aerospace Sciences, vol. 40 (2004), pp. 237-289.
[5] T.K. Barlas, G.A.M. van Kuik, "Review of state of the art rotor control research for wind turbines", Progress in Aerospace Sciences, vol. 46 (2010) pp. 1-27.
[6] N. Troldborg, "Computational study of the Riso-B1-18 airfoil equipped with actively controlled trailing edge flaps", M.Sc. Thesis Project, Technical University of Denmark, 2004.
[7] T. Buhl, M. Gaunaa, C. Bak, "Potential load reduction using airfoils with variable trailing edge geometry", Journal of Solar Energy Engineering, vol. 127 (2005), pp. 503-516.
[8] M.A. Lackner, G.A.M. van Kuik, "Comparison of smart rotor control approaches using trailing edge flaps and individual pitch control", Wind Energy, vol. 13(2010), pp. 117–134.
[9] B. Resor et al., "Impact of higher fidelity models on simulation of active aerodynamic load control for fatigue damage reduction", AIAA2010-253.
[10] P.B. Andersen, L. Henriksen, M. Gaunaa, C. Bak, T. Buhl, "Deformable trailing edge flaps for modern megawatt wind turbine controllers using strain gauge sensors", Wind Energy, vol. 13 (2010), pp. 193-206.
[11] W. Yu, M.M. Zhang, J.Z. Xu, " Effect of Smart Rotor Control Using a Deformable Trailing Edge Flap on Load Reduction under Normal and Extreme Turbulence", Energies, vol. 5 (2012), pp. 3608-3626.
[12] J.W. Wingerden et al., "On the proof of concept of a 'smart' wind turbine rotor blade for load alleviation", Wind Energy, vol. 11 (2008), pp. 265-280.
[13] A.W. Hulskamp et al., "Design of a scaled wind turbine with a smart rotor for dynamic load control experiments", Wind Energy, vol. 14(3) (2011), pp. 339-354.
[14] M.A. Lackner, G.A.M. van Kuik, "The performance of wind turbine smart rotor control approaches during extreme loads", Journal of Solar Energy Engineering, vol.132 (2010), pp. 011008-1-011008-8.
[15] Wind turbines-Part 1: Design requirements. International Electro-technical Commission (IEC), IEC 61400-1 Ed. 3, 2005.
[16] J. Jonkman, S. Butterfield, W. Musial, G. Scott, "Definition of a 5-MW Reference Wind Turbine for Offshore System Development", NREL/TP-500-38060; Technical Report, NREL, Golden, CO, USA, 2009.
[17] R.P.J.O.M. Van Rooij, "Modification of the Boundary Layer Calculation in RFOIL for Improved Airfoil Stall Prediction", Report IW-96087R; Technical Report; Delft University of Technology, Delft, The Netherland, 1996.
[18] National Renewable Energy Lab., NWTC Design Codes (AirfoilPrep); NREL: Golden, CO, USA, 2004. Available online: http://wind.nrel.gov/designcodes/preprocessors/airfoilprep/ (accessed on 11 November 2010).
[19] M.M. Zhang, L. Cheng, Y. Zhou, "Asynchronous control of vortex-induced acoustic cavity resonance using imbedded piezo-electric actuators", Journal of the Acoustical Society of America, vol. 126 (2009), pp. 36-45.
[20] M.M. Zhang, L. Cheng, Y. Zhou, "Closed-loop controlled vortex-airfoil interactions", Physics of Fluids, vol. 18 (2006), 046102.
[21] M.M. Zhang, L. Cheng, Y. Zhou, "Control of poststall airfoil aerodynamics based on surface perturbation", AIAA Journal, vol. 46 (2008), pp. 2510-2519.
[22] M.M. Zhang, J.Z. Xu, "Active control of fluctuating pressure induced by blade-vortex interaction", Science China Technological Sciences, vol. 54(4) (2011), pp.862-868.
[23] R.D. Blevins, Flow-Induced Vibration, Krieger, Malabar, FL, 1994.
[24] L. Cheng, Y. Zhou, M.M. Zhang, "Controlled vortex-induced vibration on a fix-supported flexible cylinder in cross-flow", Journal of Sound and Vibration, vol. 292 (2006), pp. 279-299.

WINDS OBSERVED IN THE NORTHERN EUROPEAN SEAS WITH WIND LIDARS, METEOROLOGICAL MASTS AND SATELLITE

C.B. Hasager[1], D. Stein[2], A. Peña[1], S Hagemann[3], T. Mikkelsen[1], M. Badger[1], A. Mouche[4], I. Karagali[1], M.L. Driesenaar[5], A. Stoffelsen[5], P. Astrup[1], F. Bingöl[1], M. Courtney[1], A. Oldroyd[6]

[1] DTU Wind Energy, Risø Campus, Roskilde (DK), **cbha@dtu.dk**, **aldi@dtu.dk**, **tomi@dtu.dk**, **mebc@dtu.dk**, **ioka@dtu.dk**, **poas@dtu.dk**, **febi@dtu.dk**, **mike@dtu.dk**
[2] GL Garrad Hassan, Hamburg (DE), **Detlef.stein@gl-group.com**
[3] IWES Fraunhofer, Kassel (DE), **Saskia.Hagemann@iwes.fraunhofer.de**
[4] CLS, Brest (FR), **amouche@cls.fr**
[5] KNMI, De Bilt (NL), **tilly.driesenaar@knmi.nl**, **ad.stoffelen@knmi.nl**
[6] Oldbaum Services, Stirling (UK), **andy@oldbaumservices.co.uk**

ABSTRACT

Ocean winds have been observed in the Baltic, Irish and North Seas from a combination of ground-based lidars, tall offshore meteorological masts and satellites remote sensing in recent years. In the FP7 project NORSEWInD (2008-2012) the project partners joined forces to ensure collection of these data. In particular, an array of wind profiling lidars was deployed at offshore platforms. All lidars were tested at the Høvsøre test site at DTU Wind Energy (former Risø DTU) prior to installation at the offshore platforms. The lidar operated in the harsh marine environment for several months, a few of them for up to two years when the project campaign ended.

The NORSEWInD database on lidar data in total contains around 11 years worth of observations (> 280.000 10 min data). The wind lidars were mounted such that winds were mapped at or very near 100 m above sea level. The lidars provide wind profile data and this has been used to characterize the vertical wind profile offshore. Also the data from the meteorological masts provide wind profile data. In addition, temperature profile observations are available at some of the meteorological masts. The temperature data were used to investigate the thermal effects on the wind profile. In conclusion, the parameters that influence the vertical wind profiles are found to be stability, surface roughness – the sea has changing roughness due to wind-wave interactions - , and boundary layer height, in this order of importance. However, it may be noted that for specific conditions, e.g. very stable atmosphere, the wind profiles can be heavily influenced by the boundary layer height at the 100 m level in the northern European seas. A very interesting part of the analysis includes the shear exponent (alpha) calculated during seasons, during 24-hours and for 12 wind directional bins. The latter resulted in so-called ‘alpha roses’, similar to wind roses but with the values of alpha given.

Satellite ocean surface winds were collected from synthetic aperture radar (SAR), scatterometer and passive microwave instruments. All satellite wind data provide winds at 10 m above sea level. Satellite winds from Envisat ASAR, QuikSCAT, ASCAT and SSM/I have been compared to offshore meteorological data. For the final satellite-based wind atlas 9,000 SAR scenes, collected by CLS and DTU, were reprocessed with the same algorithm in order to get an homogeneous data set. The number of overlapping SAR scenes varied from a few hundred to more than 1,400 in the study area. For QuikSCAT and ASCAT the available number of overlapping scenes is around 7000 and 600, respectively. The results are publically available in digital form from GIS, free of charge, through a link at www.norsewind.eu. The SSM/I wind maps from covering a period of 25 years were used to study temporal and seasonal trends in the power index.

Introduction

The EU FP7 project NORSEWInD (Northern Sea Wind Index Database) started in 2008 and ended in 2012 (www.norsewind.eu). One of the aims was to analyse the wind shear observed from the lidars.

Another aim was to produce a wind atlas based on satellite data. There were many more project aims such as developing a wind atlas based on numerical modeling using WRF (Weather Research and Forecasting model) [1,2], flow distortion modeling around the platform using wind tunnel measurements and CFD (Computational Fluid Dynamic) modeling [3], etc. In this article we focus on the analysis of the vertical wind shear observed from lidar and meteorological masts and the satellite data analysis.

Study site

The study area included the southern part of the Baltic Sea, the North Sea and the Irish Sea. The map in figure 1 shows the location of the offshore and near-shore (coastal) lidars.

Figure 1. Northern Seas with location of the offshore and near-shore lidars.

The lidars were installed on existing platforms. The names of the offshore installation spots are Babbage (BAB) in the UK, Beatrice (BEA) in the UK, Fino-3 (FN3) in Germany, Horns Rev-2 (HR2) in Denmark, Jacky (JAC) in the UK, ORP in Belgium, Schooner (SCO) in the UK, Siri (SIR) in Denmark and Taqa (P15) in Belgium. For the coastal sites the installations are in Latvia (LAT) and Utsira (UTS) in Norway.

Most of the lidars were pre-deployment tested near the Høvsøre, DTU Wind Energy meteorological mast for a short period of time. Most lidars passed or nearly passed the criteria that the slope of the linear regression should be within 0.98 and 1.01 and the linear correlation coefficient (R^2) should be > 0.98 for the wind speed range 4 -16 ms^{-1}. This is for comparison of wind speeds at 60, 80, 100 and 116m. Post-deployment tests for few lidars showed that these performed well also after six month to more than two years of offshore deployment.

Another part of work was to investigate the influence of flow distortion from the platforms to the observed winds. This work showed that the influence became insignificant around 2.4 times above the deck height of the platforms, thus the observations obtained at around 100 m were adequate for analysis of the wind shear at this height.

On the vertical wind shear observed from offshore lidars

The wind lidars were mounted on the deck of platforms such that winds were mapped at several levels at or very near 100 m above sea level. The lidars provide observations of the wind profile. Through analysis of the wind profile data, it is possible to characterize the vertical wind profile offshore. Temperature or other additional data were not available at the offshore lidar sites.

At the meteorological masts wind profile data were available and in several cases also temperature data. The temperature data were used to investigate the thermal effects on the wind profile. In conclusion, the vertical wind profiles were found to be dependent upon stability, surface roughness, and boundary layer height. The parameters are mention in their order of importance. However, it may be noted that for specific conditions, e.g. very stable atmosphere, the wind profiles can be heavily influenced by the boundary layer height at the 100 m level in the northern European seas [4].

A very interesting part of the lidar data analysis includes the shear exponent (alpha) calculated during seasons, during 24-hours and for 12 wind directional bins. The latter resulted in so-called ‘alpha roses’, similar to wind roses but with the values of alpha given. Finally, the frequency distribution of alpha for each node was calculated. Figure 2 shows an example of an alpha rose and distribution.

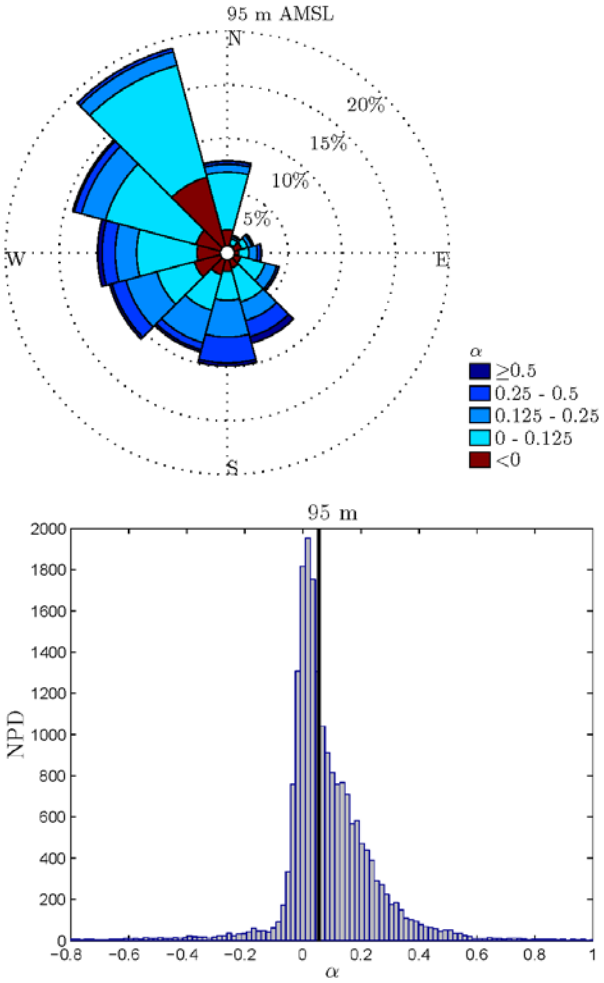

Fig. 2. Wind lidar data from platform Siri in the North Sea, upper panel the alpha rose and lower panel the distribution of alpha at 95 m above sea level. Courtesy data: DONG energy.

In figure 2 it is clear that the frequency of distribution of alpha vary in each of the 12 wind directional bins (sectors). Occasionally the shear is negative. This means that the winds are lower at the higher level. Possible reasons for this phenomenon are that the winds at the higher level not being in the lowest 10% of the surface boundary layer. This may occur when the boundary layer is shallow. Alternatively, the winds at the lowest level could be influenced by flow distortion (speed up) due to the platform, but this is not here thought to be the main reason as the investigation on flow distortion did not clearly identify this.

The data at Siri were observed between 2 February 2010 and 2 May 2011. The measurements are observed at 85 and 105 above mean sea level. From the data the wind shear at 95 m above mean sea level was estimated from the data. A total of 20243 10-minute observations are used. The WindCube was installed at 45 above mean sea level. There was lack of measurements until mid-June 2011, thus the result is based on more data from the summer months compared to winter months.

The frequency distribution of alpha for all sectors summed shows a wide spread of alpha values from around -0.8 to 1.0. The general assumption of alpha near 0.2 is close to the observed alpha median value whereas the most frequent alpha value observed is seen to be just above 0.

The advantage of the lidar observations is that they represent offshore winds at the height above mean sea level which is of main interest for the development of large scale offshore wind farms. The average size of turbines continues to grow. For the 3 to 6 MW rotors the vertical wind profile across the rotor is important for assessment of the wind energy resource. This information is provided by the wind profiling lidar network deployed in the NORSEWInD project.

On satellite surface wind observations

Several sources of satellite surface wind observations have been collected and analysed. One unique new satellite-derived wind atlas is based on Envisat ASAR scenes. The number of overlapping SAR scenes varied from a few hundred to more than 1,400 in the study area. For QuikSCAT and ASCAT the available number of overlapping scenes were around 7000 and 600, respectively. The results are publically available in digital form from GIS, free of charge, through a link at www.norsewind.eu. Also SSM/I passive microwave wind speed map have been analysed.

Envisat ASAR

An example of an Envisat ASAR surface wind map shows the surface winds at 10 m over the UK on 22 November 2011 at 21:41 UTC in Figure 3. The map is processed at DTU Wind Energy. Lee effect of the Scottish coast is seen in the North Sea. In the project surface wind maps were processed jointly by CLS and DTU Wind Energy. Investigation on the accuracy of different geophysical model functions (GMF) and input wind directions were tested and compared to selected offshore wind observations from meteorological masts. In the Baltic Sea observations from 10 offshore masts were collocated with Envisat ASAR winds in the period 2003 to 2010 [5]. The results compared to previous analysis from the North Sea [6, 7]. Generally, the linear regression results show root mean square error around 1.2 to 1.6 ms^{-1} and correlation coefficient (R^2) around 0.8 for wind speed. The differences between different GMF were not very large for this study area. It was decided to use one processing method for the entire archive of Envisat ASAR scenes, combined from CLS and DTU Wind Energy. CLS undertook this massive reprocessing of the full archive. Thereby a homogenous data set of surface wind maps were obtained.

The second part of the processing into satellite-based wind resource statistics was done at DTU Wind Energy using S-WAsP (Satellite- Wind Atlas and Application Program). As mentioned already the number of overlapping scenes was between a few hundred to more than 1,400. This ensured a unique new wind atlas for the study area. It is valid at 10 m above sea level and the spatial resolution is

around 2 km by 2 km. The resulting winds map, mean wind speed, Weibull scale and shape parameters and energy density are freely available at the web. In figure 4 the energy density map is shown. It may be noted that Yellow icons are placed in the map. It is possible to view a wind roses for each of these locations. As an example we show the wind roses from the Norwegian Sea near Norway and in the central southern Baltic Sea in Figure 5. Comparison of wind roses from the Horns Rev-1 in the North Sea and satellite SAR showed good results as reported in [8].

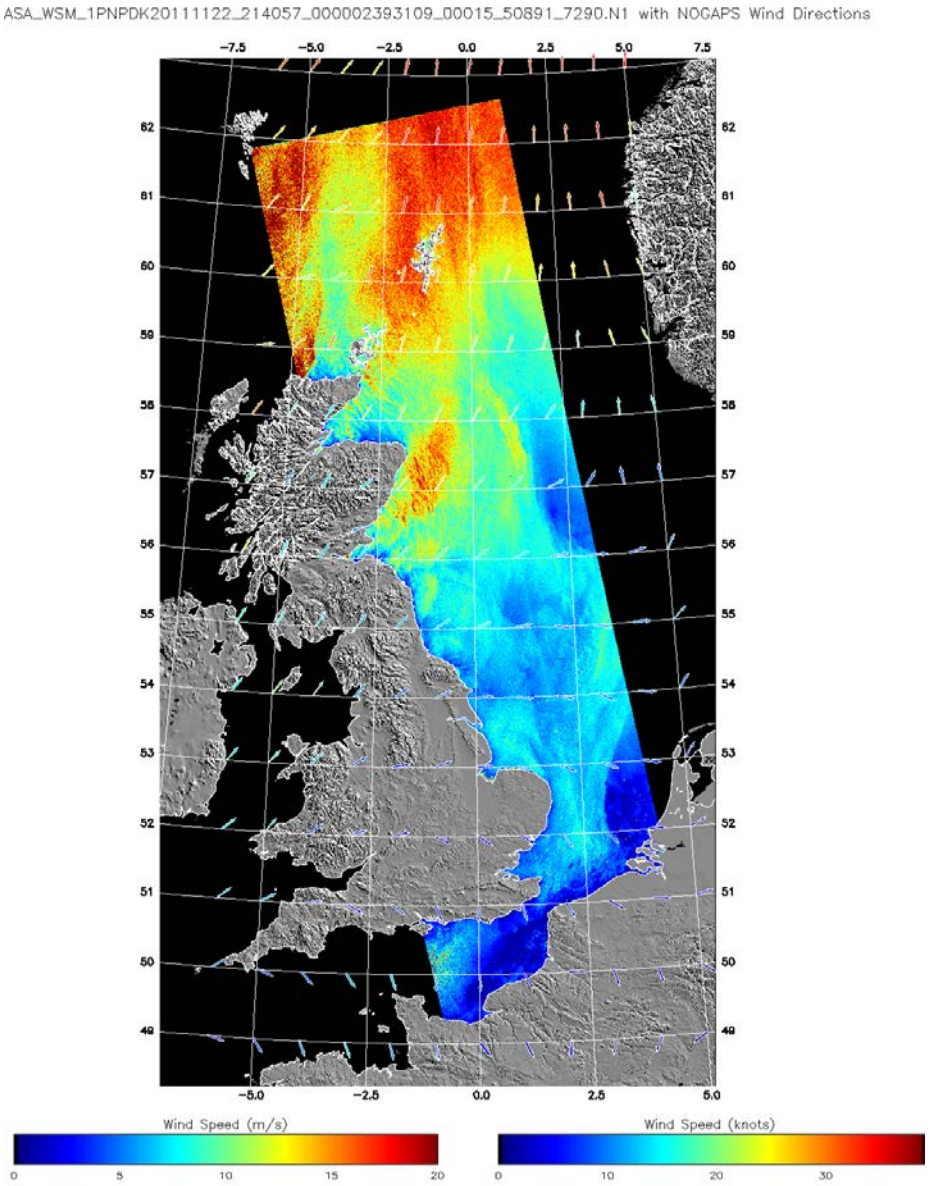

Figure 3. Ocean surface winds observed by Envisat ASAR on 22 November 2011 at 21.41 UTC around the UK. DTU Wind Energy and Johns Hopkins University, Applied Physics Laboratory.

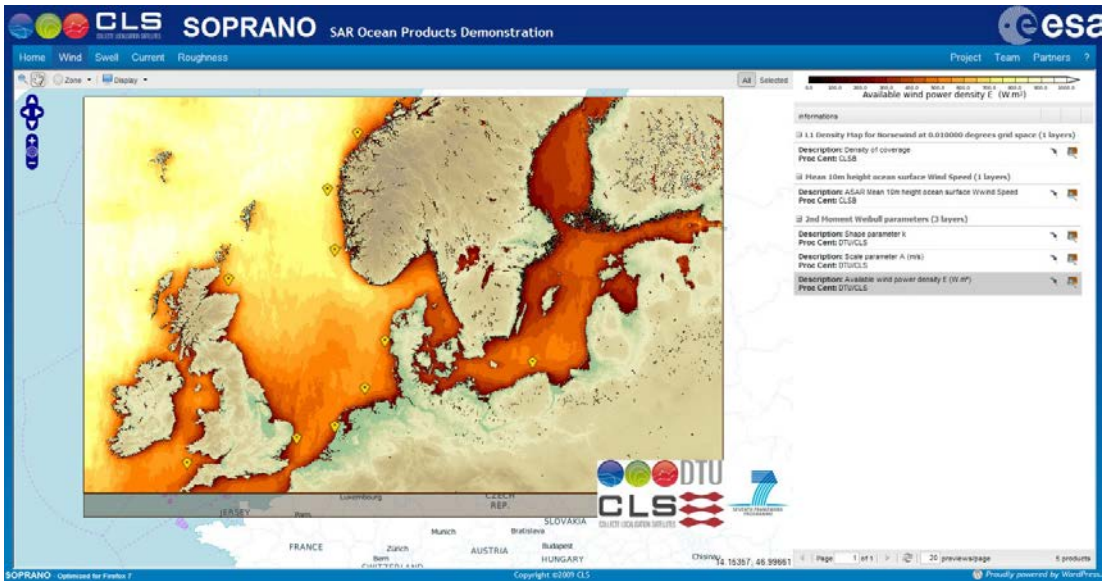

Fig. 4. Energy density maps based on 9,000 Envisat ASAR surface wind maps. The digital version is available at http://soprano.cls.fr /winds/statistics(L3) select Norsewind.

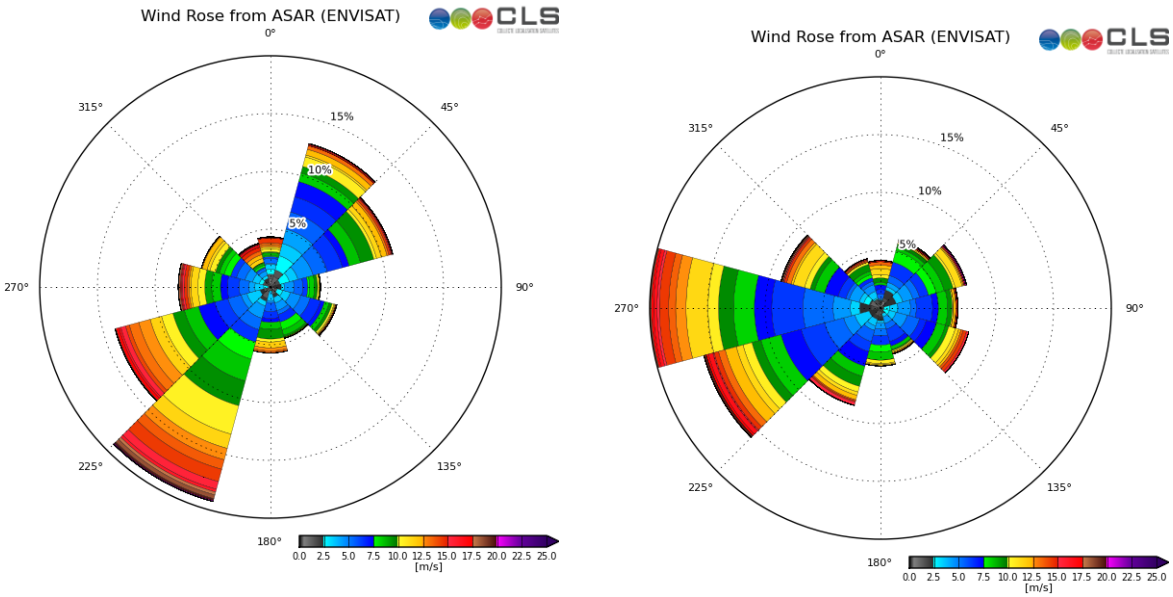

Figure 5. Wind roses observed in the Norwegian Sea near Norway and in the central southern Baltic Sea based on Envisat ASAR surface wind maps.

QuikSCAT and ASCAT

Surface vector wind observations from the scatterometers ASCAT and QuikSCAT have been analysed. The scatterometers were launched with the specific aim of observing surface ocean vector winds. QuikSCAT operated from 1999 to 2009 whereas ASCAT-1 was launched in 2006 and is in operation at present. The main advantage of scatterometer ocean winds as compared to SAR-based wind mapping is the more frequent observation cycles. For QuikSCAT it was twice per day in the study area while for ASCAT around every second day. The spatial resolution is around 25 km by 25 km. However, the new coastal ASCAT wind product is also available at 12.5 km by 12.5 km resolution.

The ASCAT and QuikSCAT mean surface wind speed climatology is presented in Figure 6. For ASCAT the data cover 2 years from 2006 to 2007 whereas for QuikSCAT the data cover 10 years from 1999 to 2009. The overall picture is rather similar with roughly the same wind speed levels in the study areas: the North Sea and the Irish Sea. The relatively lower mean winds east of the British Isles is clear in both maps. The ASCAT map is including more coastal regions, note e.g. the Danish inner waters. At the coast near the Netherlands some pixels show very high winds and we suspect this to be a spurious result due to the presence of many large container ships. When the microwave radiation is reflected from such hard targets it will be translated to too high winds.

The QuikSCAT 10-years data archieve has been used to study temporal and spatial variations. The result are presented in [9, 10]. The analysis include comparison to in-situ wind observations from several offshore meteorological masts.

SSM/I

The SSM/I wind maps from 25 years were used to study temporal and seasonal trends in the power index. [8]. The data from Remote Sensing Systems were used for the analysis.

Discussion

The overall aim of the NORSEWInD project was to observe ocean winds for wind resource assessment and to model the wind resource from mesoscale modeling in the Northern European Seas. The paper presents several new results based on observations from ground-based wind lidar and satellite SAR and scatterometer.

From the lidar observations, very interesting results on the variations of the shear exponent (alpha value) are presented. From the result it is seen that the often used value of 0.2 is not valid at all times. In fact, negative alpha values are observed occasionally which indicate that the typical assumption of a logarithmic wind profile is not always fulfilled offshore around hub-height of modern wind turbines. The results are shown from one lidar only, but in [4] the results from several more wind lidars and from some offshore meteorological masts are presented. At all locations, the distribution of alpha values has a wide range and includes negative values.

From satellite observations, the wind resource statistics provide a detailed view on the spatial variations across the study area. The maps are unique in providing spatial statistics based on homogeneous processing of observations. The satellite winds are valid at 10 meter above mean sea level. The next step is ongoing research on lifting the satellite wind statistics to hub-height using a combination of atmospheric stability information from mesoscale modeling [11].

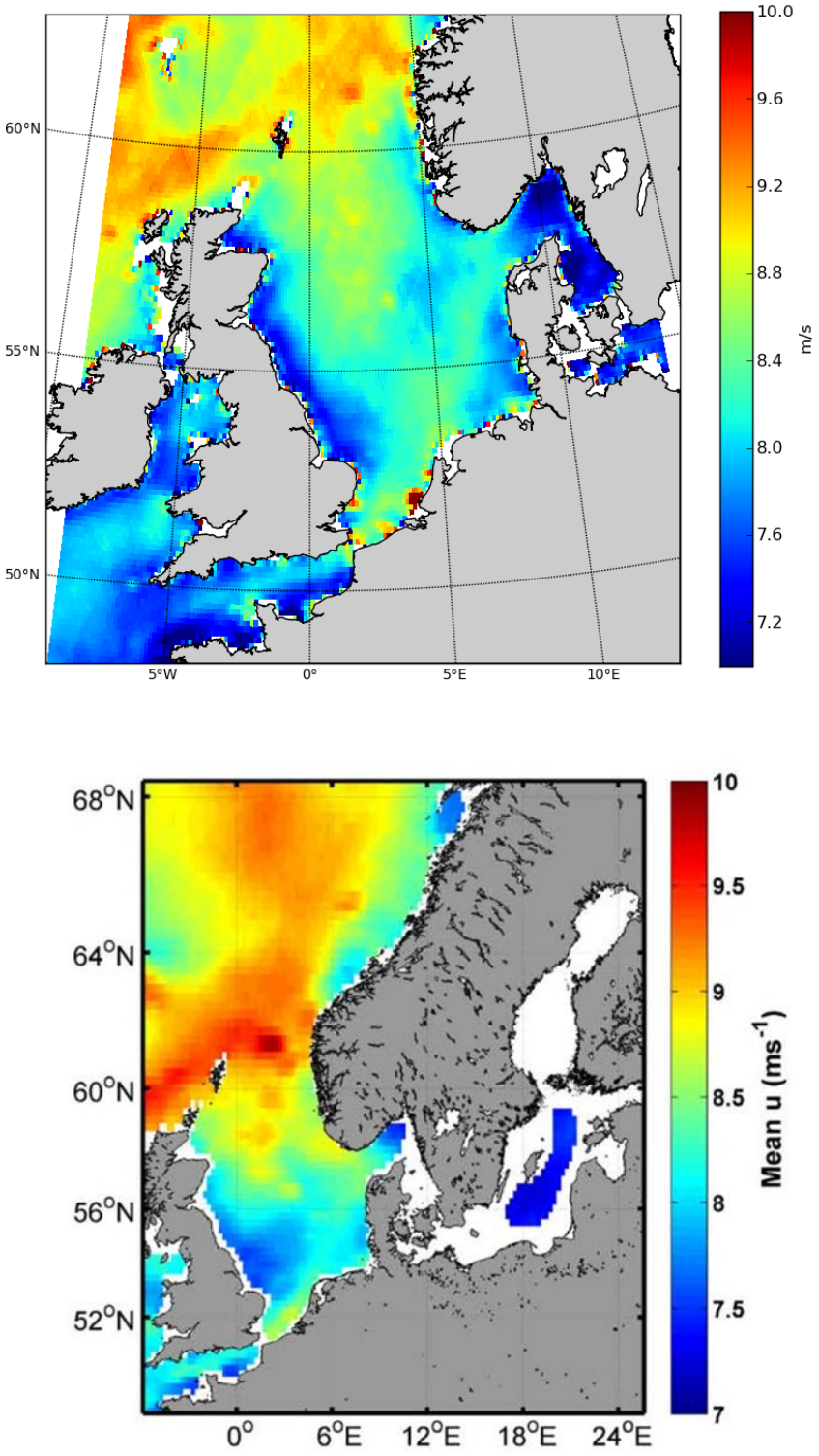

Figure 6. Mean wind speed maps observed from scatterometerin the Northern European Seas. Upper panel) ASCAT from 2006-2007. Lower panel) QuikSCAT from 1999-2009.

Conclusion

Offshore winds in the Northern European Seas vary both vertically and spatially. The observations from ground-based lidar provide new insight to the variation in the vertical shear, whereas the satellite SAR and scatterometer satellite observations provide maps with high spatial detail.

Acknowledgements
Funding from NORSEWInD TREN-FP7-219048 and satellite observations from the European Space Agency, EUMETSAT and Remote Sensing Systems and meteorological data from DONG energy.

REFERENCES

1. Berge, E., Hasager, C.B., Bredesen, R.E., Hahmann, A., Byrkjedal, Ø., Peña, A. Kravik, R., Harstveit, K., Costa, P., Oldroyd, A., 2013 NORSEWIND – Mesoscale model derived Wind Atlases for the Irish Sea, the North Sea and the Baltic Sea, EWEA2013, Vienna 4-7 Feb 2013, Conference proceedings, p.1-6
2. Hahmann, A. N., Lange, J., Pena Diaz, A., & Hasager, C. B. (2012). *The NORSEWInD numerical wind atlas for the South Baltic*. DTU Wind Energy. (DTU Wind Energy E; No. 0011(EN))
3. Stickland, M, Scanlon, T, Fabre, S, Oldroyd, A & Mikkelsen, T 2012, 'Measurement and simulation of the flow field around a triangular lattice meteorological mast' Paper presented at European Wind Energy Association Conference, EWEA 2012, Copenhagen, Denmark, 16/04/12 - 19/04/12
4. Peña, A.; Mikkelsen, T.; Gryning, S. E.; Hasager, C. B.; Hahmann, A.; Badger, M.; Karagali, I.; Courtney, M. *Offshore vertical wind shear*; DTU Wind Energy-E-0005(EN): 2012
5. Hasager, C.B., Badger, M., Peña, A, Larsén, X.G. 2010 SAR-based wind resource statistics in the Baltic Sea, *Remote Sens.* 2011, 3(1), 117-144 ; doi:10.3390/rs3010117
6. Christiansen, M.B.; Koch, W.; Horstmann, J.; Hasager, C.B.; Nielsen, *M.*. (2006), Wind resource assessment from C-band SAR. *Remote Sens. Environ.* v. 105 p. 68-81
7. Badger, M., Badger, J., Nielsen, M., Hasager, C.B., Peña, P. (2010) Wind class sampling of satellite SAR imagery for offshore wind resource mapping. J. of Applied Meteorology and Climatology, doi: 10.1175/2010JAMC2523.1
8. Hasager, C. B.; Badger, M.; Mouche, A.; Stoffelen, A.; Driesenaar, M. L.; Karagali, I.; Bingöl, F.; Peña, A.; Astrup, P.; Nielsen, M.; Hahmann, A. *Norsewind satellite wind climatology*;DTU Wind Energy -E-0007(EN); DTU Wind Energy, 2012.
9. Karagali I., Badger, M., Hahmann, A., Peña, A., Hasager. C., Sempreviva, A.M. 2013 Spatial and temporal variability in winds in the Northern European Seas, Renewable Energy, Vol. 57, p. 200-210, http://dx.doi.org/10.1016/j.renene.2013.01.017,
10. Karagali I., Peña, A., Badger, M., Hasager. C. 2012 Wind characteristics in the North and Baltic Seas from the QuikSCAT satellite, Wind Energy, DOI: 10.1002/we.1565
11. Badger, M., A. Peña, R. E. Bredesen, E. Berge, A. Hahmann, J. Badger, I. Karagali, C. B. Hasager and T. Mikkelsen, Bringing satellite winds to hub-height, paper presented at EWEA2012 Proceedings, 2012.

Great Lakes 3D Wind Experiment

SC Pryor, RJ Barthelmie, P Crippa, H Wang

Atmospheric Science Program, Department of Geological Sciences, Indiana University, Bloomington, IN 47405 Email: spryor@indiana.edu

D Valyou, P Marzocca, Clarkson University & D Matthiesen, Case Western Reserve University

1 Introduction

Many projects have sought to characterize offshore wind resources and flow conditions, but as wind farms increase in size, the scale and type of measurements has had to evolve. Some of the earlier work used solely meteorological masts [1], later experiments included more remote sensing such as sodar [2] and lidar [3], [4] and satellite remote sensing [5]. Here we focus on a model-measurement integration at a wind farm spatial scale.

The Great Lakes 3D wind experiment is designed to address four key objectives:

1. Evaluation of remote sensing technologies for applications to wind energy. This research is thus a component of efforts to better characterize the performance of the latest generation of ground-based remote sensing technologies relative to 'standard' meteorological instrumentation.
2. Evaluation of strategies to integrate data from a variety of different platforms and from numerical weather prediction models to provide a holistic understanding of flow across the scales of current generation wind farms.
3. Evaluation of the planetary boundary layer (PBL) as simulated using the Weather Research Forecasting model using uniquely detailed data sets.
4. Evaluation of coastal zone effects relevant to offshore (but fairly near coastline) wind farms.

An initial pilot field experiment was conducted at a northern Indiana wind farm in May 2012. The experiment was designed primarily to address objectives 1 and 2 (i.e. measurement intercomparison and develop an analysis framework suitable to quantify 3D wind characteristics over the area of a wind) (Figure 1). Data are also being integrated with simulations from the Weather Research and Forecasting model (WRF) which are in turn being conducted for a range of horizontal and vertical resolution and for a range of PBL schemes (objective 3).

A second experimental (and modeling) campaign will be conducted in May 2013 when all of the instrumentation will be deployed offshore in Lake Erie in 2013. That experiment will focus more specifically on objective 4 but will contribute to addressing the other three objectives.

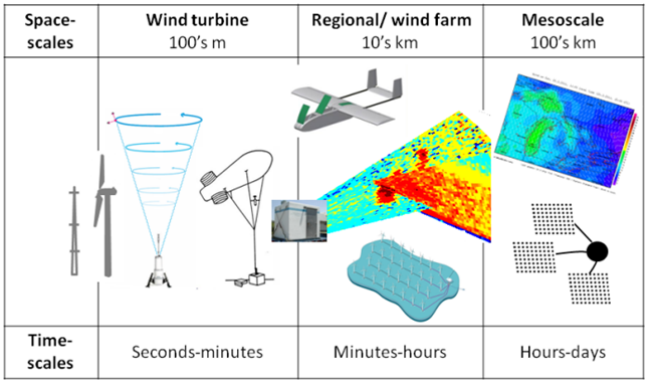

Figure 1. Overview of the Great Lakes 3D Wind Experiment in terms of the spatiotemporal scales considered and the link to wind industry relevant parameters

2 Experiment 1: Northern Indiana wind farm

The pilot experiment was conducted at a large wind farm in Northern Indiana. The terrain across the wind farm is relatively flat (change in elevation < 10 m), and the overall farm shape is roughly rectangular. The turbine layout is such that in the west-east direction the wind turbine spacing is ~ 5 rotor diameters (D) (where D = 80 m, and the range of spacing is 3.8-5.5 D), and in the south-north direction the turbine spacing is ~20 D (range; 18-22 D). The remote sensing instruments were deployed at 2 meteorological masts (▲) located on the southwest and northeast corners of the wind farm suite (Table 1 and Figure 2). Thus two ZephIR lidar systems and a Galion scanning lidar were deployed at the SW mast (Figure 2), while a single ZephIR was deployed at the NW mast. The distance between the sites is approximately 19 km. A tethersonde and Unmanned Aerial Vehicle (UAV) were operated from a private airstrip (✈) 2 km to the southwest of the SW mast (Figure 2).

Table 1. Instrument suite deployed

Instruments/Platform	Measurements
ZephIR lidars [6] Continuous wave laser (upward pointing)	Air temperature from mast Wind speed, wind direction and turbulence intensity at 40, 80, 120, 160 and 200 m
Galion lidar [7] Scanning pulsed lidar (range of scanning configurations)	Wind speed and direction Range gate = 30 m
Anasphere Tethersonde mounted anemometers Cup anemometers deployed as part of instrument package deployed on a tethered line below balloon	Wind speed, wind direction, air temperature, pressure and relative humidity (2 probes) at 40, 80, 120, 160 and 200 m
UAV mounted sonic anemometer	u, v and w components of the flow, plus sonic virtual temperature
Meteorological mast mounted cup anemometers and vanes (NRG)	Wind speed, wind direction at 80 m

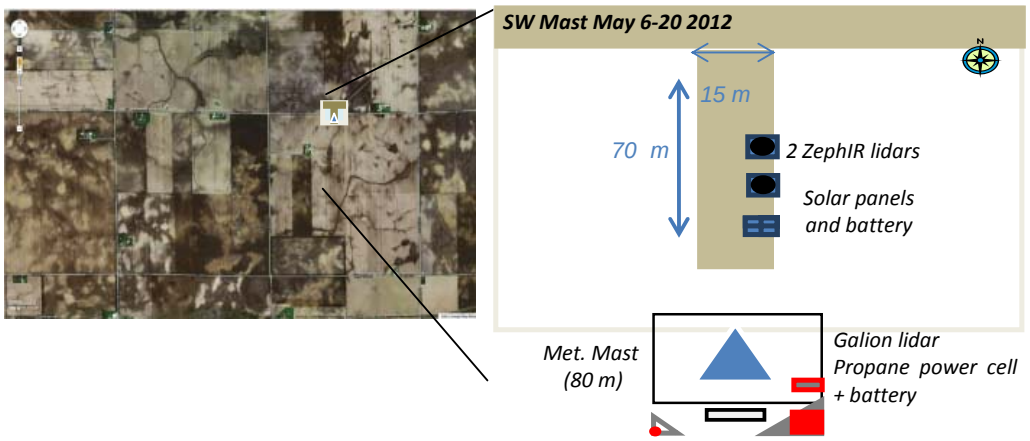

Figure 2. Overview of the site from Google maps (left) and showing the instrument layout at the SW corner of the wind farm (right).

The WRF simulations are conducted using a single nested grid. The outer grid has 324 x 274 cells of 9 km resolution (covering almost the entire eastern USA), while the inner nested grid (which was

centered on the wind farm) was 310 x 259 grid cells of 3 km. The simulations from which output is presented here were run with 35 vertical levels, the physics options selected include the Mellor-Yamada-Janjic PBL scheme, and the land cover was specified at a resolution of 0.7 km.

Pre-experiment testing focused on evaluation of (i) the independent power supplies (Midwest Portable Power: Figure 3) and (ii) wind speed measurements from the ZephIR lidars in comparison with the mast measurements. There were no power quality issues with the running of any of the lidars. The Galion scanning lidar needed 300 W of maximum power so a propane fuel cell was employed. Correlation coefficients for wind speed measurements from the mast-mounted cup anemometers and the ZephIR wind speeds during the pre-experiment period exceeded 0.98 and the intercept of a regression line was 0 ±0.05 m s^{-1}.

Figure 3. Solar panels used to power the 100 W ZephIR lidars.

For the main experiment there were three ZephIR lidars. These use a continuous wave laser to determine wind characteristics from the backscatter by atmospheric aerosols. They were operated to measure at five fixed heights (40, 80, 120, 160 and 200 m). The Galion scanning lidar also uses the Doppler shift of radiation backscatter to determine wind characteristics but with a pulse signal. The range-gate length was 30 m and azimuthal spacing between beam products < 3^{o} with range up to a maximum of 4 km distance/ 750 m height. A range of different scanning geometries used (Figure 4) to facilitate comparison of derived wind products from the various measurement configurations. Approximately 30 hours of tethersonde measurements were collected in 10-minute increments at 40-80-120-160 m heights using two sondes separated by ~40 m. These heights were selected to match the heights of the mast anemometers (40 and 80 m) and those selected for the operation of the ZephIRs. The UAV was operated with a nose-mounted sonic anemometer. Data from the sonic anemometer along with airspeed, components of acceleration and GPS position, heading, and ground speed were collected on the Golden Eagle during 9 flights of ~20-30 minutes duration.

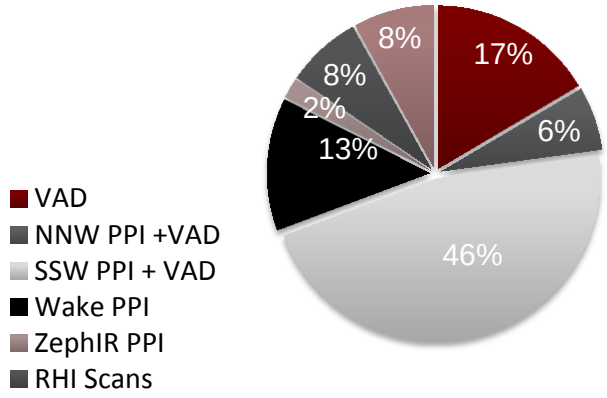

Figure 4. The percentage of the measurement period during which the Galion was operated in different scan modes. Where VAD = Vertical Azimuth Display, PPI = Plan Position Indicator and RHI =Range Height Indicator

Although this location was selected to represent homogeneous conditions (in terms of land cover and flat terrain), even at this site there are important spatial gradients of wind speed (of up to 1 ms^{-1}) over

the wind farm as indicated by the WRF simulations like due to small variations in land cover and importantly in soil moisture availability. These spatial gradients are typically largest overnight (Figure 5) and erode during the daytime as conditions become more convective.

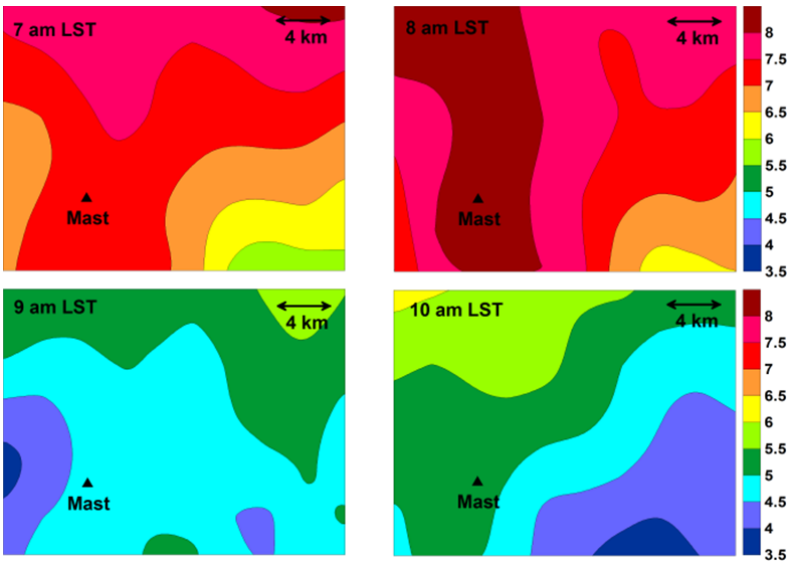

Figure 5. WRF simulations of 80 m height wind speeds (ms^{-1}) for the morning of May 18 2012

Data from the instrumentation operated continuously at the SW meteorological mast indicate a high degree of coherence and indicate relatively good agreement with the WRF simulated hub-height wind speeds (Figure 6). However, it is worthy of note that there are some discrepancies between the Galion when operated in PPI mode and the cup anemometer and the ZephIR lidars that are linked to the greater spatial aggregation of the Galion (i.e. in the PPI configuration used the volume over which wind speeds are sampled has an approximate depth of 20 m and depending on the elevation angle may be up to 300 m from the tower).

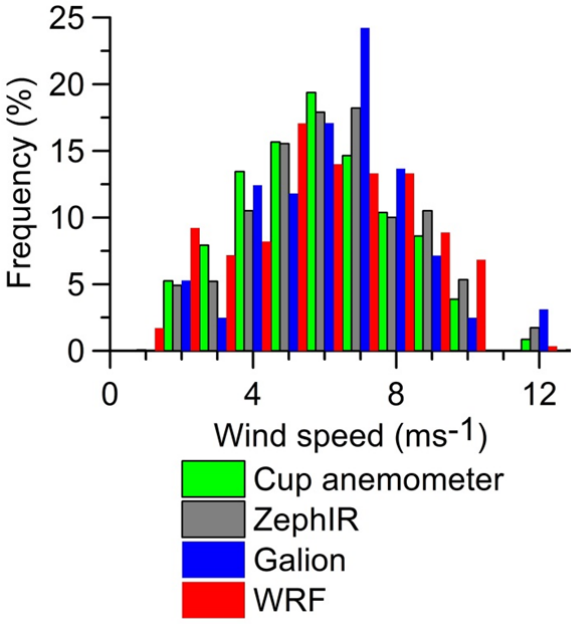

Figure 6. Frequency distribution of wind speeds at 80 m from the different instruments/platforms for the period May 10-17. Data are only included if valid measurements are available from all instruments, however the temporal averaging is not consistent for all platforms. Output from WRF is at an hourly interval but is 'instantaneous for a time step (in this case 10 seconds), while the measurements are 10 minute averages.

There is generally good agreement between the diurnal cycle and vertical profile of wind speed measured by the various instruments and simulated by WRF at 80 m height. However, as shown for

May 17 in Figure 7, WRF gives higher wind speeds overnight and is slower to simulate the development of convective conditions and breakdown of the shear layer than is implied by the observations. It is also worthy of note that the discrepancies between the Galion and other instruments overnight were only observed at 80 m, at the remaining heights at which wind speed comparisons were made there was much better agreement. The vertical wind speed profiles on May 18 (shown in Figure 8) also show an example of the transition from stable to unstable conditions, and in this example WRF and the various in situ measurements exhibit a higher degree of accord across all measurement heights.

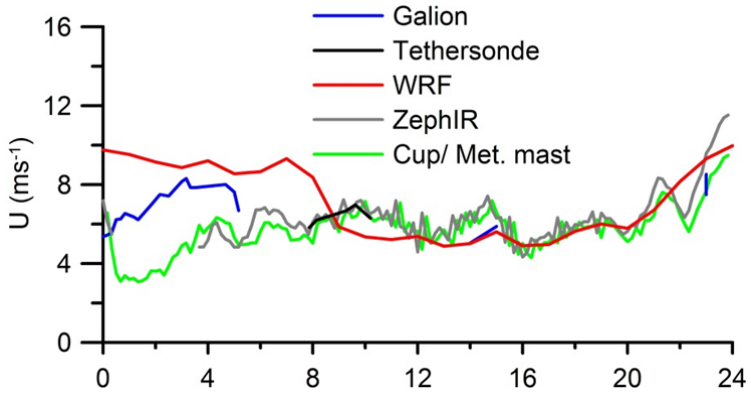

Figure 7. Wind speeds at 80 m height simulated by WRF and measured by the tethersonde anemometers, ZephIR lidar and the cup anemometers mounted on the meteorological during May 17 2012

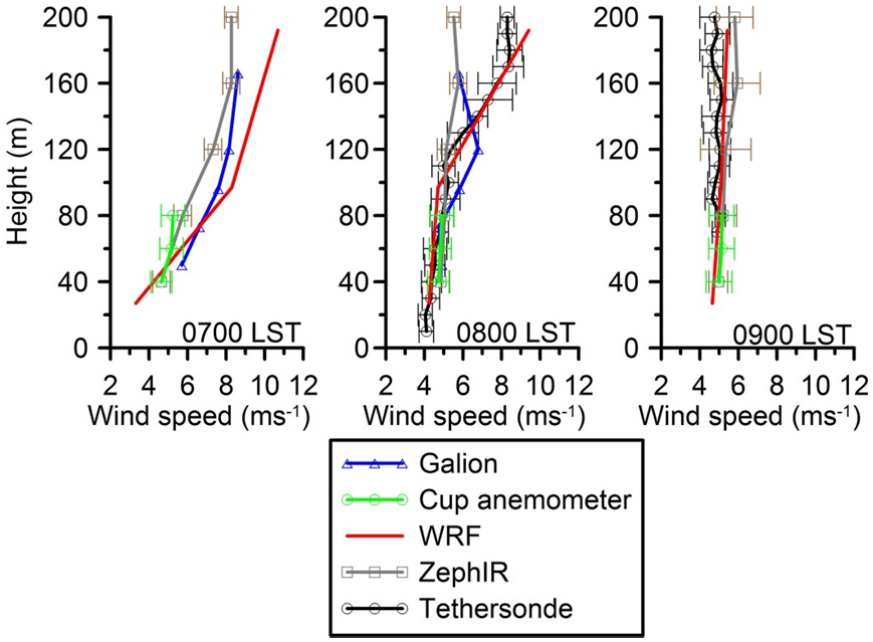

Figure 8. Wind speed profiles on May 18 2012.

3 Experiment 2: Lake Erie

The instrumentation deployed for the pilot experiment will shortly be redeployed in Lake Erie and will be supplemented by additional sonic anemometers. A sonic anemometer and one ZephIR lidar will be deployed on a water intake (Crib) located approximately 5 km offshore, while the Galion lidar and a second ZephIR lidar will be deployed close to the port at the water edge, along with a second sonic

anemometer on a crane (Figure 9). The third ZephIR lidar will be deployed further south along the shoreline. The UAV and tethersonde will be flown from close to a private airport, and the UAV will be flown along tracks out to the crib location. It is intended that this experimental design will allow detailed quantification of spatial gradients of wind speed and turbulence in the coastal zone and links to atmospheric stability.

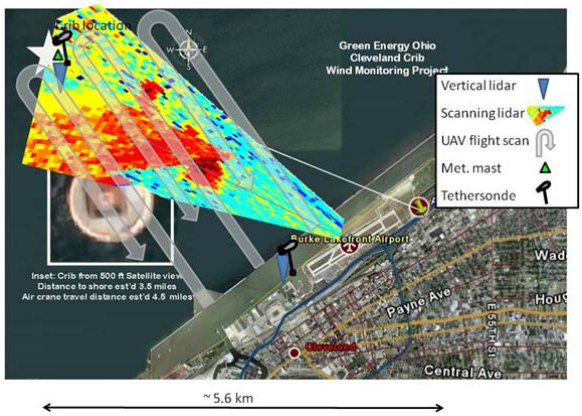

Figure 9. Overview of the planned experiment in Lake Erie May 2013

4 Summary

Data analysis for the 2012 experiment is ongoing, but initial results are very promising in terms of the instrument cross-calibration. 'Lessons learned' are being integrated into the planning for the 2013 Lake Erie experiment.

5 Acknowledgements

Many thanks to the two landowners and the owners of the private airstrip. This material is based upon work supported by the Department of Energy under Award Number #DE-EE0005379 and the National Science Foundation 1067007.

6 References

1. Barthelmie, R., O. Hansen, K. Enevoldsen, J. Højstrup, S. Larsen, S. Frandsen, S. Pryor, M. Motta, and P. Sanderhoff, *Ten years of meteorological measurements for offshore wind farms.* Journal of Solar Energy Engineering, 2005. **127(2)**: p. 170-176.
2. Coelingh, J., L. Folkerts, and E. van Zuylen. *Offshore sodar measurements - 1 year experience*. in *Offshore wind energy in Mediterranean and other European Seas*. 2003. Naples: ENEA.
3. Aitken, M.L., M.E. Rhodes, and J.K. Lundquist, *Performance of a Wind-Profiling Lidar in the Region of Wind Turbine Rotor Disks.* Journal of Atmospheric and Oceanic Technology, 2012. **29**(3): p. 347-355.
4. Iungo, G.V., Y.-T. Wu, and F. Porté-Agel, *Field measurements of wind turbine wakes with LiDARs.* Journal of Atmospheric and Oceanic Technology, 2012.
5. Hasager, C.B., A. Pena, M.B. Christiansen, P. Astrup, M. Nielsen, F. Monaldo, D. Thompson, and P. Nielsen, *Remote Sensing Observation Used in Offshore Wind Energy.* Ieee Journal of Selected Topics in Applied Earth Observations and Remote Sensing, 2008. **1**(1): p. 67-79.
6. Sathe, A., J. Mann, J. Gottschall, and M.S. Courtney, *Can Wind Lidars Measure Turbulence?* Journal of Atmospheric and Oceanic Technology, 2011. **28**(7): p. 853-868.
7. Clive, P.J.M. *Recent advances in Lidar wind measurement*. in *American Wind Energy Association*. 2008. Houston.

AN ANALYTICAL CANOPY-TYPE MODEL FOR WIND FARM-ATMOSPHERE INTERACTION

C.D. Markfort[1], W. Zhang[1], F. Porté-Agel[2]

[1]Saint Anthony Falls Laboratory, Department of Civil Engineering, University of Minneasota – Twin Cities, USA, mark0340@umn.edu and wzhang@umn.edu
[2]Wind Engineering and Renewable Energy (WIRE), École Polytechnique Fédérale de Lausanne (EPFL), Switzerland, fernando.porte-agel@epfl.ch

ABSTRACT

We present a new model for the interactions between large-scale wind farms and the atmospheric boundary layer (ABL) based on similarity to canopy flows. Wind farms capture momentum from the atmospheric boundary layer both at the leading edge and from above. Based on recent findings that turbulent flow in and above wind farms is similar to canopy-type flows, we examine this further with an analytical model that can predict the development length of the wind farm flow as well as vertical momentum absorption. Within the region of flow development, momentum is advected into the wind farm and wake turbulence draws excess momentum in from between turbines. This is characterized by large dispersive fluxes of momentum. Once the flow within the farm is developed, the area-averaged velocity profile exhibits an inflection point, characteristic of canopy-type flows. The inflected velocity profile is associated with the presence of a dominant characteristic turbulence scale, which may be responsible for a significant portion of the vertical momentum flux. Prediction of this scale is useful for determining the amount of available power for harvesting. The new model is tested with results from wind tunnel experiments, which characterize the turbulent flow in and above a model wind farms. The model is useful for representing wind farms in regional scale meteorological and wind resource assessment models, for the optimization of wind farms considering wind turbine spacing and layout, for assessing the impacts of upwind wind farms on nearby wind resources, and the environment.

INTRODUCTION

The prediction of the mean flow in wind farms is important for determining the mean momentum sink from the atmospheric boundary layer (ABL). This is needed for new parameterizations for the ABL in weather and climate models to account for the increasing presence of wind farms globally. Additionally, optimization of wind farm layouts can be improved with an adequate model for describing how the wind farm harvests wind energy from the ABL. Finally, turbulence in the ABL mediates transport of moisture, pollutants and climate controlling trace gases (e.g. CO_2 and CH_4). Prediction of scalar transport from the surface requires prediction of the surface shear stress and transport efficiency at the ground surface below the wind farm rotor level. For offshore wind farms, the surface shear stress is an important parameter needed to model the surface-layer dynamics in the ocean.

A wind farm can be classified as a type of penetrable roughness, a term first introduced by Brutsaert [1]. Commonly referred to as canopies, this includes forests and built-up urban areas. In such flows the momentum sink is not simply a skin drag as is assumed in surface layer schemes for the ABL, but includes vertically distributed drag due to the turbines as well. Depending on the efficiency of the wind farm at absorbing momentum from the ABL, shear stress may or may not be applied at the ground or water surface. The ABL in regions of tall roughness elements has three characteristic layers: a roughness sublayer (RSL), an inertial layer where the log-law applies and an outer layer. The RSL for a dense canopy is generally about twice the thickness of the layer occupied by the roughness elements ($2Z_H$), the log-layer region where Monin-Obukhov Similarity Theory (MOST) is applicable, resides between the RSL and the outer layer, or between about $2Z_H$ and about 15% of the total ABL thickness. Generally the ABL thickness is approximately 1000 m, and the height of wind farms is approximately 100 m. Therefore the log-layer would generally exist below 150 m. In the case of a wind farm however, the RSL may be 100 – 200 m deep, based on the above scaling, and therefore it is likely that the log-layer does not consistently form over large wind farms. This may mean that the approach of modeling the wind farm, as surface roughness is not applicable, as the concept of aerodynamic roughness is based on the zero-crossing elevation of the log-law. For mesoscale models, often the first grid level resides in the log-layer of the ABL (~10 – 100 m) and using the roughness parameterization for the surface is common. However because the wind farm layer intersects this region, it becomes necessary to model the drag of the wind farm within the lowest layers to better represent the effect of the wind farm on the structure of the ABL (e.g. [2]).

Recently the turbulence statistics for fully developed flow in and over a wind-farm were analyzed and it was found that the properties of the flow including the transport efficiencies for momentum and scalars are more similar to those of canopy-type flows than that of a surface layer [3]. However, unlike dense canopies (e.g. a forest), due to the relatively large spacing between wind turbines, the flow exhibits features that are unique to sparse canopies, namely large contributions of dispersive stresses and significant wake production of TKE. Additionally we studied the impact of wind farms on surface heat flux

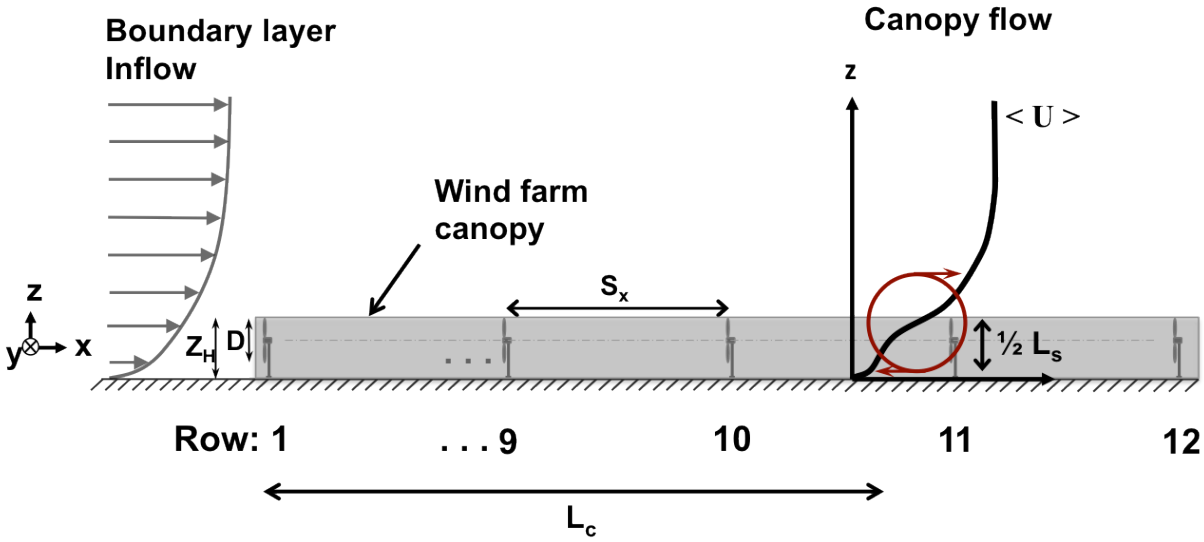

Figure 1: Schematic of a developing wind farm canopy flow. The distance required for the flow to develop L_c and the shear penetration L_s are directly related to the drag force on the canopy

and found a net reduction for a fully developed staggered wind farm [4]. From canopy-type flows we know there are two important characteristic length scales that can be used to characterize the interaction between canopies and the ABL. They include the canopy drag development length scale L_c and a shear length scale L_s ([5] and references therein). Figure 1 shows a schematic illustrating both length scales for an idealized wind farm canopy. L_c and L_s are the horizontal and vertical scales related to the absorption of momentum and are important quantities for understanding the overall efficiency of the wind farm. Both of these scales are derived from the dynamic interactions of the mean drag induced by the wind farm on the ABL flow. The vertically distributed drag in the RSL causes an inflected mean velocity profile, leading to the formation of Kelvin-Helmholtz type instability near the top of the wind farm. In order to determine these length scales we need a model for the mean wind profile through the wind farm.

Markfort et al. [3] found that the turbulent flow in wind farms is similar to that of canopy-type flows and the mean velocity across the rotor plane can be modeled using the classic model of Inoue [6]. We examine for the first time whether analytical canopy-type models can represent the turbulent flow within a fully developed wind farm. The assumptions of the models are examined, weaknesses investigated and improvements proposed. In Markfort et al. [3] we used the model from Inoue [6] to determine the thrust coefficient and estimate L_c based on the mean wind profiles. Here we compare those results against results from the spatially averaged, time mean momentum equations often used to represent canopy-type flows. A new model for sparse canopies is considered that can reproduce the effects of the wind farm drag on the flow as well as predict the surface shear stress at the ground or sea surface. Ultimately the goal of this work is to improve parameterization of mean wind and shear stress of wind-farm flow useful in weather, climate and wind farm optimization models.

THEORETICAL BACKGROUND

2.1 Formulation of the Wind Farm Canopy Model

To avoid having to model the details of individual wakes, the formulation incorporates averaging a unit volume of the flow that, for a uniform canopy, is defined based on the spacing and height of the canopy elements. We also assume neutral stratification of the ABL. Developing field averaged equations for the flow through a wind farm, $u = U + \bar{u}'' + u'$ where $U = \langle \bar{u} \rangle$ is the time and spatially averaged velocity signified by an overbar and angle brackets, respectively, $\bar{u}'' = \bar{u} - U$ is the spatial variation of the time mean flow around individual turbines, and $u' = u - U - \bar{u}''$ are the turbulent fluctuations. The spatially and temporally averaged momentum conservation equation takes the form:

$$-\frac{\partial \tau(z)}{\partial z} = \frac{1}{\rho}\frac{\partial P}{\partial x} + f_{\mathrm{wf}}(z), \tag{1}$$

where $\tau(z) = \langle \overline{u'w'} \rangle + \langle \bar{u}''\bar{w}'' \rangle$ is the total wall-normal shear stress, where $\langle \overline{u'w'} \rangle$ is the average kinematic turbulent shear stress, $\langle \bar{u}''\bar{w}'' \rangle$ is the dispersive flux of momentum, ρ is air density, P is mean pressure, and $f_{\mathrm{wf}}(z)$ represents the vertically distributed turbine induced force. The dispersive stress is the horizontally unresolved subgrid-scale quantity

that arises from horizontal spatial filtering of the momentum equation and represents the contribution to momentum transfer from correlations between spatial variations in the time-averaged flow.

2.2 Turbine Drag Parameterization

A standard parameterization for the turbine-induced force is employed, where

$$F_T = \frac{1}{2}\rho C_T A_r U^2. \tag{2}$$

The thrust coefficient is C_T and A_r is the rotor-swept area. The force, per unit mass, distributed over the unit volume occupied by turbines in a wind farm is

$$f_{\text{wf}} = \frac{F_T}{Z_H A_f} = \frac{U^2}{L_c}, \tag{3}$$

where Z_H is the top-tip height of the wind farm, and $A_f = S_x S_y D^2$ is the unit area of ground per turbine, D is the rotor diameter. S_x and S_y are the x (streamwise) and y (spanwise) spacing between wind turbines in multiples of D. f_{wf} can be simplified to the mean velocity squared divided by L_c. The drag development length scale L_c can be written in terms of the geometry of the wind farm as,

$$L_c = \frac{2Z_H A_f}{C_T A_r} = \frac{8Z_H S_x S_y}{\pi C_T}. \tag{4}$$

It approximately scales with the distance, from the front edge of the wind farm, required for the spatially averaged, time mean flow to develop within the wind farm. A numerical study of the ABL transition to urban canopies revealed that the flow development length scales as about $3L_c$, with a form that follows an exponential decay [7].

2.3 Reynolds Stress Parameterization

The Reynolds stresses can be parameterized using the mixing length formulation as,

$$-\langle\overline{u'w'}\rangle = l_m^2 \left(\frac{\partial U}{\partial z}\right)^2, \tag{5}$$

and rearranging allows for determining the mixing length based on measured turbulence profiles as

$$l_m = (-\langle\overline{\mathrm{u'w'}}\rangle)^{1/2} / \left(\frac{\partial \mathrm{U}}{\partial \mathrm{z}}\right). \tag{6}$$

For a surface layer, $l_m = l_{SL} = \kappa \mathrm{z}$, where κ is the von Karman coefficient (= 0.4). For dense canopy flows $l_m = l_C = 2\beta^3 L_c$, following [6], where $\beta = u_*/U_{Z_H}$. For sparse canopies where momentum is absorbed by roughness elements as well as the ground, it is likely that a combination of these two mixing lengths are important, with surface layer scaling being important near the ground and canopy scaling more important away from

the surface. Coceal and Belcher [7] proposed a model that smoothly varies between these two length scales following a harmonic interpolation function

$$\frac{1}{(l_m)^N} = \frac{1}{(l_{SL})^N} + \frac{1}{(l_C)^N} \tag{7}$$

where N can be used to adjust the weights of the contributions. This results in the mixing length being constrained by the smaller of the two length scales depending on height, and it is found that $N = 4$ best fits the measurements in this study. The dispersive stresses contribution is often small and therefore neglected as a first approximation.

EXPERIMENTS

3.1 Characterization of Fully Developed Wind-Farm Flow

Measurements of the fully developed wind-farm flow were obtained in a boundary-layer wind tunnel study, reported in Markfort et al. [3]. The experiments considered the development of a neutral boundary layer flow through and over an array of scaled, operating wind turbines. Two layouts were considered to investigate changes in wind direction. Perfectly aligned and perfectly staggered configurations provided insight on how the ABL develops over wind farms. The spacing of the turbines were $S_x = 5D$ and $S_y = 4D$ in both configurations. The diameter of the rotors were $D = 12.8$ cm and the top-tip height of the wind farm was $Z_H = 16.8$ cm. For the staggered case, the even numbered rows were shifted laterally by $y = 2D$. The area of the rotor-swept plane was $A_r = 0.013$ m^2 and the unit area of ground per turbine was $A_f = 0.34$ m^2. Figure 2 shows the vertical distribution of rotor area per unit ground area, normalized by A_r/A_f. To characterize the spatially averaged mean flow, profiles were collected downwind of the 12th and 11th rows of turbines at four selected locations for the aligned and staggered wind farms, respectively. The representativeness of the spatially-averaged flow by these profiles was confirmed by simulations of the wind farm using a validated research-level LES code [8].

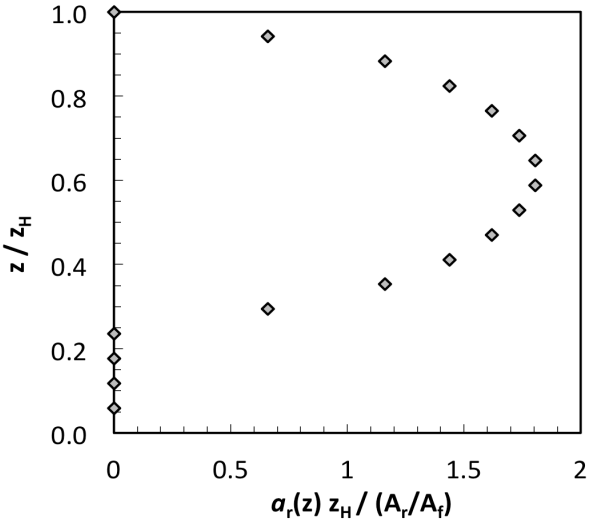

Figure 2: Vertical distribution of the normalized local rotor area per unit volume, $a_r(z)$

Figure 3 shows the mean velocity profiles for the aligned and staggered wind farm configurations, as well as total stress profiles and contributions of the dispersive stresses. The velocity exhibits an inflected mean wind profile, which is characteristic of canopy-type flows and leads to large-scale instability in the flow. Also unlike dense canopy-flows, the velocity does not go to zero within the canopy layer, but is significant near the surface. The inflection point and height of maximum shear stress occurs at $z \approx 0.9Z_H$. This point defines the top of a canopy flow from a dynamic perspective and provides the best estimate for the drag and shear penetration length scales. The shear stress is reduced with height due to the drag of the wind turbines. Approximately 20% of the maximum shear remains to be absorbed at the ground level. Dispersive stresses were found to be especially significant for the aligned wind farm at 40% of the maximum total stress. The maximum dispersive stress was 10% for the staggered case [3].

Due to the large dispersive stresses and indications that the flow through the aligned wind farm may not be fully developed, based on the estimate of L_c, we will only considering the flow in the staggered wind farm for this analysis. The aligned case may be generally considered a special case, occurring infrequently when the wind is perfectly aligned with the rows of turbines such that the direct upwind turbines wake turbines in adjacent rows. Based on measurements from Barthelmie et al. [9] this may be rare. The flows from non-aligned directions may be considered staggered. In general the wind-farm flow behaves closer to that of the staggered arrangement. As shown in [3], the flow development within a staggered wind farm requires less distance than an aligned wind farm due to more efficient lateral mixing of wakes evidenced by smaller dispersive stresses.

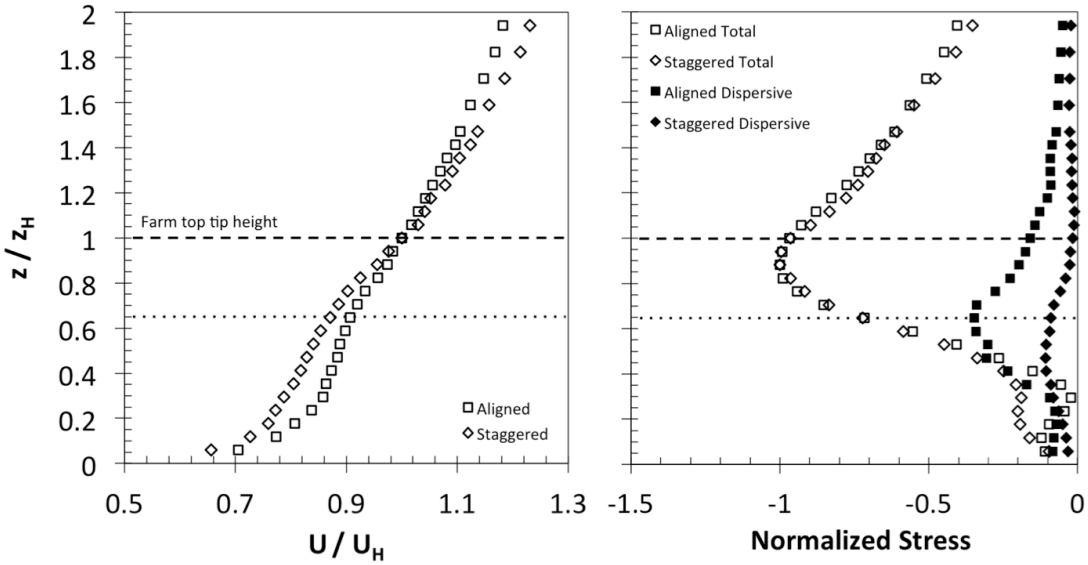

Figure 3: (Left) Mean, spanwise averaged velocity profiles measured within an aligned and staggered wind farm. (Right) Total stress and dispersive stress profiles normalized by u_*^2

3.2 Thrust Coefficient

The drag coefficient used in meteorological applications, e.g. flow in canopies, often incorporates the factor of ½ into C_D. However, here we use the engineering convention and maintain the factor separate from the estimate of the trust coefficient C_T. To estimate

C_T from the measured turbulence profiles using Eqn. 1, the turbine thrust parameterization defined above in Eqs. 3 and 4, is employed and rearranged to give

$$C_T = -2\left(\frac{\partial \tau(z)}{\partial z}\right)\left(\frac{8Z_H S_x S_y}{U^2 \pi}\right). \quad (8)$$

Figure 4 shows the distribution of C_T measured across the rotor-swept region of the wind farm. The distribution is well represented by a Gaussian function following

$$C_T = a\, exp\left[-\frac{\left(\frac{r}{R}-b\right)^2}{2c^2}\right], \quad (9)$$

where r/R is the distance form hub height normalized by the rotor radius and the coefficients a = 1.06, b = 0.086, c = 0.385. Calculating the depth averaged value for C_T we determine for the staggered configuration $C_T = 0.49$. This compares well with results based on large-eddy simulation (LES) for flow through a single turbine, modeled after the turbine used in these experiments, where C_T was determined to be 0.45 (Wu, pers. comm.). Using the experimentally determined value for C_T and the dynamic height of the canopy, we can determine L_c to be approximately 16 m, or $L_c/z_H \approx 100$ for the staggered wind farm. This agrees with the estimate presented in Markfort et al. [3].

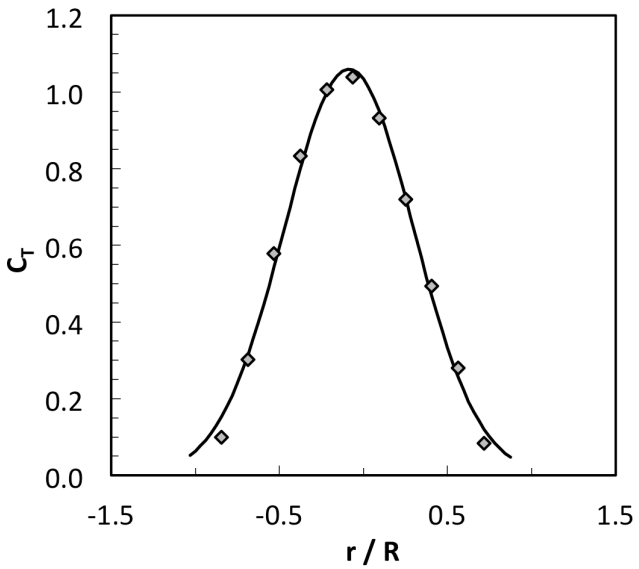

Figure 4: Plot of the distribution of the measured thrust coefficient in the fully developed staggered wind farm and a Gaussian fit

3.3 Momentum Penetration

The depth of the large scale eddies that carry momentum down into the wind farm from the ABL above is related to the shear instability caused by the inflection point in the mean velocity near the top of the wind farm. The shear instability scale can be approximated as

$$L_s = U_{0.9Z_H} / \left(\frac{\partial U}{\partial z}\right)_{z=0.9Z_H}. \quad (10)$$

The measured shear length scale for the experiment is $L_s/Z_H = 3.0$. For plane mixing layers it can be assumed that the distribution of large-scale vorticity is symmetric about the point of the velocity inflection and penetration is $\sim 1/2L_s$. However due to the presence of the drag elements that cause the shear flow in this case, it is likely that eddies penetrate a fraction less than half of L_s. Another measure of the shear scale, may be defined based on the mean velocity above the canopy and deep within the canopy. Here we define the scale of vorticity penetration as

$$\delta_\omega = \frac{U_{z=2Z_H} - U_{z=0.1Z_H}}{\left(\frac{\partial U}{\partial z}\right)_{z=0.9Z_H}}. \quad (11)$$

For the fully developed staggered wind farm, δ_ω/Z_H = 1.25 or about 40% of L_s. From Thom [10], the zero-plane displacement of the log-layer above the canopy can be defined as

$$\frac{d}{Z_H} = 1 - \frac{1}{2}\frac{\delta_\omega}{Z_H}. \quad (12)$$

This results in $d/Z_H = 0.37$ for the current experiment and is similar to the value $d/Z_H = 0.38$ determined in Markfort et al. [3] based on the velocity profiles above the wind farm.

ANALYTICAL CANOPY MODEL

4.1 Dense Canopy Model

Inoue [6] developed an analytical model for dense canopies that describes the mean wind profile in a fully developed canopy flow. The model essentially utilizes an assumption of constant mixing length to formulate an exponential decay relationship for $U(z)$ following,

$$U(z) = U_{Z_H} exp\left[\alpha\left(\frac{z}{Z_H} - 1\right)\right], \quad (13)$$

where α is an attenuation coefficient that increases with canopy density ($\alpha = \beta Z_H/l_C$). Results from Markfort et al. [3], compared with results from the previous section, indicate the model performs reasonable well for describing the mean wind across the rotor plane and is useful for determining the momentum absorbed by the wind farm.

One weakness of this model is that it does not faithfully capture the no-slip condition at the surface. Unlike dense canopies for which the model of Inoue was formulated, the mean wind near the surface may be significant in wind farms. The result is that wind farms behave more like sparse canopies where the turbines absorbs significant momentum but a non-negligible amount of momentum may be transferred to the ground as well. The assumptions for the dense canopy model, including the local density, drag coefficient and mixing length are all constant and the momentum is fully absorbed by the canopy, may not hold true when applied to wind farms. To develop a formulation useful for sparse wind-farm canopies, these assumptions must be relaxed to more accurately model the mean wind and shear stress, particularly near the surface.

4.2 Sparse Canopy Model

A sparse canopy is defined as a cluster of roughness elements that are tall enough to absorb significant momentum by form drag, however there remains significant momentum that is transferred to the surface and absorbed through skin friction. Similar flows have been addressed in the context of urban meteorology, as building density tends to vary significantly, leading to a need to depart from the simplified model in Eqn. 13. Generally the sparse canopy problem has been addressed using numerical models to solve the momentum conservation equation utilizing similar forms of the quadratic drag and mixing length parameterizations as presented above (e.g. [7]).

The requirement to handle the problem numerically arises from the nonlinear relationship between mean wind speed and the canopy drag force. Alternatively, Wang [11] proposed a linearization of the drag force equation. Here we employ this assumption for the turbine-induced force by relating the force to UU_{Z_H} instead of U^2. Employing the above parameterizations, Eqn. 3 and 5 are substituted into Eqn. 1, and assuming there is a negligible longitudinal pressure gradient results in

$$-\frac{\partial}{\partial z}\left(K\frac{\partial U}{\partial z}\right) = C_L \frac{A_r}{A_f z_H} U(z) U_{Z_H} \tag{14}$$

where $K = \kappa z s u_*$. This allows for an analytical solution with the form

$$U(z) = C_1 I_o(g(z)) + C_2 K_o(g(z)) \tag{15}$$

where the coefficients of integration are C_1 and C_2, and $I_o$and K_o are the modified Bessel functions of the first and second kind, respectively, of order 0. $I_o$and K_o depend on

$$g(z) = 2\sqrt{A\, z/z_H}, \tag{16}$$

where

$$A = C_L \frac{A_r}{A_f}(\kappa\beta s(\mathrm{z}))^{-1}. \tag{17}$$

Rewriting Eqn. 7 as

$$l_m = \kappa z s(z), \tag{18}$$

where

$$s(z) = \frac{l_c}{\left[(l_c)^N + (\kappa z)^N\right]^{1/N}} \tag{19}$$

provides the distribution of the mixing length, smoothly varying with height. In Eqn. 17, A can be interpreted as a dimensionless attenuation coefficient that characterizes the reduction of wind speed within the wind farm. The coefficient determines the shape of the velocity profile integrating the effects of turbine size and spacing, as well as the mixing length and C_T by way of the linearized drag coefficient, C_L.

The two integration coefficients are determined by solving Eqn. 15 for the no-slip condition at $z = z_0$ and for a known U_{Z_H}, as

$$C_1 = U(z_H)[I_o(g(z_H)) - I_o(g(z_0))K_o(g(z_H))/K_o(g(z_0))]^{-1}, \quad (20)$$

and

$$C_2 = C_1 I_o(g(z_0))/K_o(g(z_0)). \quad (21)$$

The linearized drag coefficient, C_L, can be solved by way of solving for A iteratively based on the boundary conditions. Alternatively, based on a number of model runs, varying the above controlling parameters, Wang [11] found that A could be well characterized based on the shear length scale L_s as expressed in Eqn. 10, and ultimately, was well represented with a simple quadratic relationship based on frontal area index, which for the wind farm is simply A_r/A_f. The relationship that best fits the results can be written in terms of the geometry of the wind farm as

$$A = 4.52\left(A_r/A_f\right) + 0.62\left(A_r/A_f\right)^2. \quad (22)$$

In this study we use Eqn. 22 to estimate C_L at $z = z_H$ and then allow A to vary with height following Eqn. 17.

Figure 5 shows the comparison between the measured mean velocity within the staggered wind farm (from Fig. 2) and the prediction of the sparse canopy model. Allowing A to vary vertically produced a result that is closer to the observed velocity profile across the rotor plane than if it is held constant based on Eqn. 22.

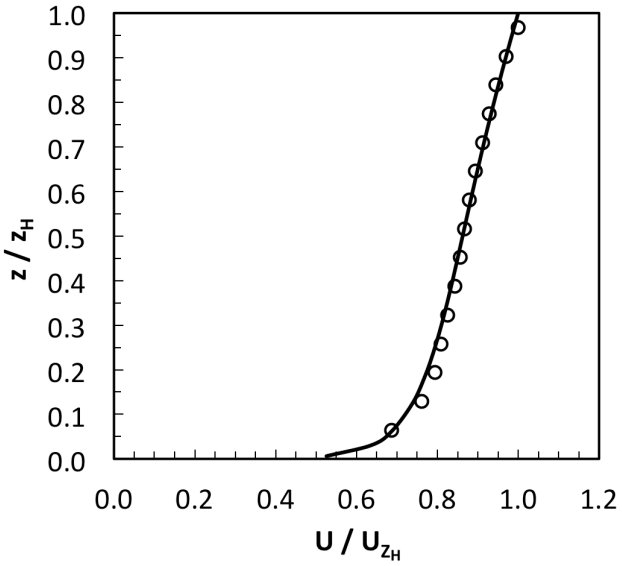

Figure 5: Plot comparing the normalized wind profile for the fully developed wind-farm flow in a staggered configuration with the prediction from the sparse canopy model

This also leads to a better approximation of the velocity gradient at $z/z_H = 1$ and therefore a better prediction of L_s. Two key features are captured by the model, first is the exponential attenuation of the velocity with height near the top of the wind farm and across the rotor-swept region, and second is the no-slip condition at the surface.

From Eqn. 6 the variation in mixing length is determined based on the measured profiles of mean velocity and shear stress. Using Eqs. 5, 15 and 18, we calculate the effective mixing length and the resulting shear stress based on the model. Figure 6 shows the results of the model compared with the data. The mixing length model reproduces the general features of the length scales of the flow with the values near the surface being weighted toward surface layer scaling while the mixing length approaches a constant value of l_c near the top of the wind farm. However, the measurement reveals a different behavior as the maximum measured value occurs near the center of the rotor plane and then decreases up to z_H. Then the measured mixing length approaches the inertial layer near the top of the wind farm that was identified in [3]. The mixing length model does not capture this behavior but is a good first approximation that is simple to implement, captures the average behavior and results in a reasonable profile for the shear stress. In particular the shear stress profile correctly partitions the amount of momentum absorbed by the wind farm and the shear stress near the surface. The result reveals the remaining stress absorbed by the ground or sea surface. In the present configuration the result is approximately 15 - 20% of the momentum absorbed by the wind farm remains at the surface.

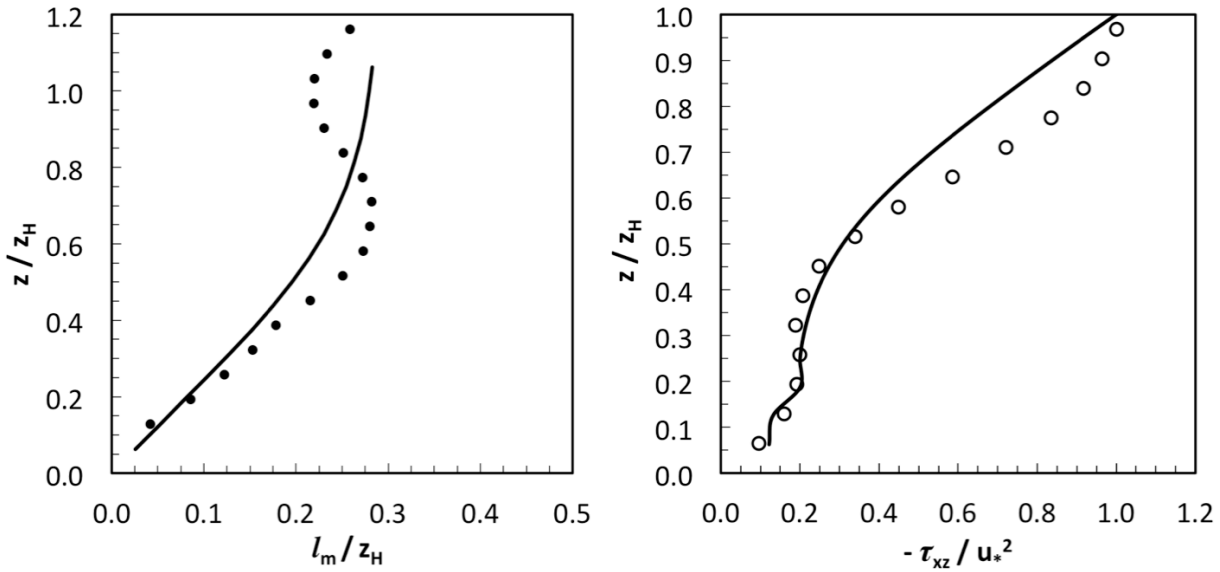

Figure 6: Plots comparing measurements with the results of the sparse canopy model for Left: mixing length, and Right: shear stress

SUMMARY AND DISCUSSION

We have shown that an analytical, sparse canopy model can reasonably represent the mean wind and non-negligible surface shear stress for flow through a wind farm. The model reproduces the no-slip condition at the surface and the surface shear stress by allowing the mixing length to vary with height inside the wind farm. The model can be

applied when the details of the flow around individual turbines are not required, and only overall spatially-averaged features of the wind-farm flow are of interest. This model can be solved using basic spreadsheet software, and can be cheaply employed into regional scale atmospheric flow models for weather prediction and wind farm development. Wind turbine spacing is an independent variable in the model and therefore the model can be used to optimize the design of wind farm layouts. The optimum turbine spacing can be estimated by minimizing the amount of momentum transferred to the surface. At the same time the shear penetration scale should be kept large to efficiently transfer momentum down from the ABL above the wind farm to the entire rotor-swept region. Given for example the wind farm layout studied here, with the same surface roughness, the turbines could be spaced closer together to capture the remaining momentum currently lost to the surface. For onshore installations, the model could be used to study the effect of changing land cover below the wind turbines to examine how a change in surface roughness may affect the partitioning of momentum between the wind farm and the surface. For offshore wind farms, the surface shear stress is an important boundary condition for sea-surface mixing. If a wind farm absorbs all the momentum, the mixing and temperature structure in the surface mixed layer of the ocean will be dramatically changed compared to before the wind farm was installed. The model should be tested for full-scale wind farms flows, using carefully measured, spatially representative wind profiles and in a validated LES framework. Although the main goals to represent the mean wind and shear stress within a wind farm are achieved with the current formulation, additional testing at full scale will provide the necessary data to improve the mixing length model and lead to a more robust formulation. Incorporation of dispersive stresses will allow for the consideration of the development region of the flow. Additionally, the mixing length model could be modified to account for atmospheric stability.

REFERENCES

[1] W. Brutsaert, “Evaporation into the atmosphere: Theory, history and applications”, Springer (1982) pp. 316.

[2] A.C. Fitch et al., “Local and mesoscale impacts of wind farms as parameterized in a mesoscale NWP model”, Monthly Weather Review, vol.140 (2012) pp. 3017-3038.

[3] C.D. Markfort, W. Zhang and F. Porté-Agel, “Turbulent flow and scalar transport through and over aligned and staggered wind farms”, Journal of Turbulence, vol.13 (2012) pp. 1-36.

[4] W. Zhang, C.D. Markfort and F. Porté-Agel, “Experimental study of the impact of large-scale wind farms on land-atmosphere exchanges”, vol.8 (2013) pp. 015002.

[5] S.E. Belcher, I.N. Harman, and J.J. Finnigan, “The wind in the willows: Flow in forest canopies in complex terrain”, Annual Review of Fluid Mechanics, vol.44 (2012) pp. 479-504.

[6] E. Inoue, “On the turbulent structure of airflow within crop canopies”, Journal of the Meteorology Society of Japan, vol.41 (1963) pp. 317-326.

[7] O. Coceal and S.E. Belcher, “A canopy model of mean winds through urban areas”, Q. J. Roy. Meteorol. Soc., vol.130 (2004) pp. 1349-1372.

[8] Y-T. Wu and F. Porté-Agel, “Simulation of turbulent flow inside and above wind farms: Model validations and layout effects”, vol.146 (2013) pp. 181-205.

[9] R.J. Barthelmie et al., “Modelling and measuring flow and wind turbine wakes in large wind farms offshore”, Wind Energy. vol.12 (2009) pp. 431-444.

[10] A.S.Thom, “Momentum absorption by vegetation”, Q. J. Roy. Meteorol. Soc., vol.97 (1971) pp. 414-428.

[11] W. Wang, “An analytical model for mean wind profiles in sparse canopies”, Boundary-Layer Meteorol., vol.142 (2012) pp. 383-399.

Can a Wind Turbine Survive in Tropical Cyclones?

T. Han[1], G. McCann[2], T. A. Mücke[3] and K. Freudenreich[3]

[1]GL Garrad Hassan, K.R. Poststraat 90, 8441 ER Heerenveen, the Netherlands, tao.han@gl-garradhassan.com
[2]GL Garrad Hassan, St Vincent's Works Silverthorne Lane, BS2 0QD, Bristol, UK
[3]Germanischer Lloyd Industrial Services GmbH, Renewables Certification, Brooktorkai 18, 20457 Hamburg, Germany

Abstract

This study presents the external wind conditions for the design and assessment of wind turbine loading in tropical cyclone regions, including physical constants, wind speed (cyclone classes), wind shear, turbulence intensity, turbulence length scale and turbulence spectral models. For the extreme condition, this study focuses on the wind characteristics of the cyclone eye-wall region that carries the strongest wind. For the dynamic response of wind turbine structures, it is worth the effort to characterize the size of eddies constituting turbulent wind. The turbulence integral length scale for cyclone wind is defined and validated with various measurements. Moreover, several turbulence spectral models are validated with field measurements and the ESDU von Karman model gives the best fit. Based on the external wind conditions, a new turbulent cyclone wind model is created with the associated load case(s). A state-of-the-art load analysis is performed using this new cyclone wind model and the results for the relevant turbine components are compared with the existing loads envelope. Finally, the question of whether a wind turbine could survive in a cyclone is addressed.

1. Introduction

The blooming of the wind energy industry has led to the desire for installing wind turbines in coastlines close to regions of high population density. Several of these areas are also prone to cyclones, such as the east coast of the U.S, the south-east coast of China, Taiwan, Japan and Korea. With respect to the extreme wind conditions, the current extreme load cases of the IEC 61400 standard [1] and the GL Guideline [2] may not be enough to predict the extreme loads in cyclones. It would be a very risky proposition to simply install an existing type of wind turbine in regions affected by tropical cyclones without taking into account the wind characteristics in the Cyclone Boundary Layer (CBL).

In the current IEC standard, a maximum 10-minute mean wind speed of up to 50 m/s at hub height for the extreme wind speed model is foreseen as the maximum standard wind class I. The turbines to be erected in tropical cyclone risk areas will have to be designed specifically to withstand higher wind speeds, depending on the cyclone class. In addition, analysis of wind loads on wind turbine components requires knowledge of the turbulence structures impinging upon them. The current definition of the parameters describing turbulence structures is aimed for normal ambient boundary layer, such as the definition of the velocity standard deviation and length scale in the IEC 61400-1 standard. For estimating the loads in cyclones, the characteristic features of the CBL need to be studied. Germanischer Lloyd is working on a Technical Note "Certification of Wind Turbines for Tropical Cyclone Conditions". This study may be considered an extension of this preparatory work with an emphasis on characterizing the turbulence to design wind turbines prevailing against cyclones.

2. Objective and Scope

The objective of this study is to present the external wind conditions for the design and assessment of a wind turbine in tropical cyclone conditions and to perform a state-of-the-art load analysis to address the question "Can a wind turbine survive in a tropical cyclone?" The loads of relevant turbine components will be reviewed and compared to the existing loads envelope. The turbine is assumed to be installed at an onshore location near the coastline in the cyclone region. The wind conditions in the CBL will be quantified to define a new cyclone wind model and the associated load case(s).

3. External conditions

3.1. Physical constants

The term 'tropical' refers to the geographical origin of the cyclone which is the region surrounding the Equator. A cyclone forms in oceanic regions where the sea-surface temperature (SST) is higher than 26.5 °C. It always has the most notable feature, the eye, which is a low-pressure centre surrounded by a circular rotating region called the eye-wall that carries extremely strong wind and heavy rain. As the storm is forming and being fuelled in the ocean, the air is characterized by high moisture content and the relative humidity (RH) is usually up to 80% [3]. As a consequence, the water vapour makes the air less dense than standard dry air because the molecular mass of vapour is less than the mass of dry air.

In the cross-section of a cyclone structure, the strongest horizontal wind is at the cyclone eye-wall and the wind speed drops abruptly either side of this region. In addition, the air pressure drops quickly and the temperature increases inside the eye-wall. This unique climatic condition can affect the integrity and safety of wind turbines. For cyclone load calculations, it is more meaningful to define physical constants of the tropical cyclone instead of using the values for normal climate in the IEC standard 61400-1. To be specific, the physical constants in the eye-wall are defined since this is the region that has most influence on the wind turbine extreme load analysis. A list of physical constants for a typical cyclone eye-wall region is summarized in Table 3-1.

Temperature [°C]	30
Pressure [hPa]	950
RH [%]	80
Moist air density [kg/m3]	1.094
Air viscosity [kg/ms]	1.82E-05

Table 3-1 Typical physical constants in a cyclone eye-wall

3.2. Cyclone class

Tropical cyclone classes are commonly categorized by the maximum sustained wind speed at the cyclone eye-wall region. For wind turbine loads assessment, Germanischer Lloyd (GL) refers to the well known Saffir-Simpson Hurricane Wind Scale (SSHWS), which is a 1 to 5 categorization according to the cyclone's maximum sustained wind speed (peak 1-min wind speed at the standard meteorological observation height 10m). The scale was developed by Herb Saffir and Bob Simpson in the 1970s. Its earlier versions incorporated central pressure and storm surge as components of the categories, known as the Saffir-Simpson Hurricane Scale. However, in order to provide a more scientifically defensible scale and reduce public confusion, the scale was revised removing the associated phenomena such as central pressure, flooding impact and storm surge. The latest version was released in 2012 and is shown in Table 3-2. The standard has been an excellent tool for alerting the general public to the possible damage of cyclones. [4] [5] [6]

One potential weakness of the SSHWS when used for wind turbine applications is that it is categorized by the 1 min sustained wind speed at 10m height while the wind energy industry

uses the 10-min averaged wind speed at hub height as the reference wind speed. This is due to the fact that the spectral gap for turbulent wind is in the region between 2 hours and 10 minutes, in which there is very little energy in the frequency spectrum. Thus any shorter time-scales may cause large variations in turbulence energy spectrum [7].

Tropical cyclone class	Sustained winds
1	119-153 km/h 33.1-42.4 m/s
2	154-177 km/h 42.5-49.1 m/s
3	178-208 km/h 49.2-57.8 m/s
4	209-251 km/h 57.9-70.2 m/s
5	>252 km/h >70.3 m/s

Table 3-2 Saffir-Simpson Hurricane Wind Scale (SSHWS) [5]

To convert these wind speeds to associated 10-min average values, the guideline from the World Meteorological Organization (WMO) [8] can be used. In this guideline, recommended factors are defined to convert so called sustained wind speeds to 10-min mean wind speeds in tropical cyclone conditions:

$$V_{10\text{min}} = K \cdot V_{\text{sustained}} \qquad \textbf{(3-1)}$$

Terrain category	A	B	C
Surface roughness z_0 [m]	~ 0.18	~ 0.07	~ 0.03
Conversion factor *K*	0.84	0.87	0.89

Table 3-3 Tropical cyclone terrain categories and their surface roughness length

The conversion factor K varies with terrain surface roughness. It is important to note that the terrain categories used in the WMO guideline are different from the IEC terrain categories for characterizing turbulence. The surface roughness and the conversion factor of the terrain type C have been slightly modified to match the existing turbulence classes A, B and C in the IEC standard.

3.3. Wind shear

To define the relevant wind speed at hub height for extreme load cases, the mean wind profile in the eye-wall region is required. Powell et al. [9] have measured mean wind profiles inside tropical cyclones using the Global Positioning System (GPS) since 1997. They have found that mean wind profiles generally follow the logarithmic law and the CBLs belong to the neutrally stable boundary layer with 500-700m above sea level depending on wind speed. For wind turbine engineering practice, it can be assumed that the mean wind profile follows the longitudinal shear profile:

$$V_z = \frac{u_*}{k}\ln\left(z/z_0\right) \qquad \textbf{(3-2)}$$

Where,

V_z = wind speed at hub height [m/s]
u_* = friction wind velocity [m/s]
k = von Karman constant = 0.41
z = height [m]
z_0 = surface roughness length [m]

The wind speed profile can be given in the power law as well:

$$V_z = V_{10} \cdot \left(z/z_{10}\right)^{\alpha} \qquad \textbf{(3-3)}$$

Where

V_{10} = wind speed at 10m height [m/s]
α = slope exponent $= 1/\ln\left(z_{10}/z_0\right)$
z_{10} = reference height = 10m

3.4. Turbulence

Essentially, the wind near ground is turbulent. A detailed understanding of the turbulence structure in the wind is important for designing

wind turbines to prevail against cyclones. In the wind industry, turbulent behaviours are often defined in term of the velocity standard deviation and the integral length scale.

3.4.1. Turbulence intensity

The Turbulence Intensity (TI) is a non-dimensional parameter *I* defined as:

$$I_i = \frac{\sigma_i}{V} \quad \textbf{(3-4)}$$

Where

V	=	longitude mean wind velocity [m/s]
σ_i	=	velocity standard deviation [m/s]
i	=	u, v, w for longitudinal, lateral and vertical directions

There are plenty of measurements of the turbulence intensity in cyclones published by Schroeder [10], Li [11], Wang [12] and An [13]. There is no evidence from these studies that the turbulence intensities in the CBL are any different from those in the normal ambient boundary layer. Therefore, the Normal Turbulence Model (NTM) in the IEC standard can be also used to calculate the representative value of the turbulence intensity in the CBL. Since the value for the TI does not vary much in the high wind speed region for a given terrain category, the TI can be assumed as a constant value across the cyclone wind speed categories and it only varies with surface roughness. The approximate expression of the longitudinal turbulence intensity is given in [8]:

$$I_u = \frac{1}{\ln(z_{10}/z_0)} \quad \textbf{(3-5)}$$

An et al. [13] have also analyzed the ratios between the turbulence intensities in the three wind directions from various references. According to their study, the components in the lateral and vertical directions have similar ratios as stated in the IEC standard:

$$I_v \geq 0.7 I_u \quad \textbf{(3-6)}$$

$$I_w \geq 0.5 I_u \quad \textbf{(3-7)}$$

3.4.2. Turbulence length scale

The second parameter required for modelling the turbulence spectrum in cyclones is an integral scale parameter called the turbulence length scale. This is used to characterize the size of the large eddies constituting turbulent flows. This scale is given by

$$L_i^x = V_z \int_0^\infty \rho_{ii} d\tau \quad \textbf{(3-8)}$$

Where

ρ_{ii}	=	corresponding autocorrelation function
τ	=	characteristic time [s]
i	=	u, v, w for longitudinal, lateral and vertical directions

From equation (3-8), the turbulence length scale can be calculated but it requires the autocorrelation function which is related to the spectral density function through the inverse Fourier transform [14]. This function needs to be derived from raw data of field measurements which makes the equation difficult to use for defining the length scale of the numerical spectral models.

However, there are other smart ways to find the length scale. The ESDU model [14] gives an equation for estimating the length scale in the high frequency region, where the well established spectral density equation due to Kolmogorov can be used to derive an expression for the spectral density which is dependent only on the mean wind speed profile parameters. If the von Karman spectral model is used for estimating the spectral density, the longitudinal length scale is given as

$$L_u^x = \frac{A^{3/2}(\sigma_u/u_*)^3 z}{2.5 K_z^{3/2}(1 - z/h)^2(1 + 5.75\, z/h)} \quad \textbf{(3-9)}$$

Where

A = $0.115[1 + 0.315(1 - z/h)^6]^{2/3}$

h = height of the boundary layer

K_z = Kolmogorov parameter

At the standard observation height (10 m), where z/h->0, the equation can be simplified as:

$$L_u^x = \frac{3.67}{K_z^{3/2}} \quad \textbf{(3-10)}$$

The only variable in equation (3-10) is the Kolmogorov parameter K_z. For isotropic turbulence, the ESDU model suggests that K_z is equal to 0.15 regardless of surface roughness. Following this assumption, L_u^x equals 63.5m at 10m height for all terrain categories.

However, a re-analysis of the data has been performed, incorporating more recent data obtained from measurements relatively close to the ground; which suggests that K_z varies with surface roughness and the height of the boundary layer [14]. For a tropical cyclone, the height of the boundary layer h is approximately from 400 to1000m as measured by Vickery et al. [15]. This boundary layer height may be a function of the inertial stability of the cyclone which is related to its radial distance from the centre of the storm. The height of the CBL will certainly be influenced by terrain roughness; however, it is hard to formulate a simple equation to calculate h according to the surface roughness length. Although there is an equation given in the ESDU 85020 report, it is not suitable for the CBL as the errors resulting from this equation are far too large compared with measurements.

For onshore turbine design, the height of the CBL is assumed as 700 meters for all terrain classes. The Kolmogorov parameter weakly depends on the roughness which is 0.134, 0.131 and 0.131 for the terrain category A, B and C, respectively. The turbulence length scale in equation (3-10) hardly varies with surface roughness. Therefore, for engineering purpose, it is suggested to use a single length scale 77m at 10m height instead of three.

In wind energy applications, the reference length scale for the spectral probability density models is defined at hub height instead of at 10m observation height. The length scale from equation (3-10) therefore has to be converted to the hub height of wind turbines. Several guidelines are presented here, defining conversion laws.

Eurocode 1 [16] quotes a converting equation from Couniham for wind engineering applications:

$$L_{u,EC}^x = L_t^x \left(\frac{z}{z_t}\right)^{\alpha(z_0)} = 300\left(\frac{z}{200}\right)^{0.67+0.05\ln(z_0)} \quad \textbf{(3-11)}$$

$$10\text{m} \le z \le 200\text{m}$$

The length scale $L_{u,EC}^x$ here is for the Kaimal model in Eurocode 1 which is slightly different from the length scale in equation (3-8). It can be converted to the integral length scale by multiplying by 0.73.

Dyrbe and Hansen [17] have also proposed a simple relationship between the longitudinal length scale and the height for structural design:

$$L_u^x = L_{10}^x \left(\frac{z}{z_{10}}\right)^{0.3} \quad \textbf{(3-12)}$$

Here, L_{10}^x= 100m and is independent of surface roughness.

Perhaps the most popular conversion law is equation (3-13) which comes from Edition 3 of the IEC 61400-1 international turbine design standard. This has been widely used for many years in wind turbine design and certification. However, according to this equation, the length scale becomes constant when the hub height reaches 60m. This does not agree with the results from cyclone field measurements.

$$L_k^x = 8.1\Lambda_1(\text{z}) = 8.1\begin{cases}0.7\text{z}, & \text{z} \le 60\text{ m} \\ 42, & \text{z} \ge 60\text{m}\end{cases} \quad \textbf{(3-13)}$$

The length scale L_k^x here is the Kaimal length scale which is equal to 2.33*L_u^x.

Equation (3-9) can be also used to convert length scale to a given height. However, if we assume the boundary layer height is 700m, the

length scale according to equation (3-9) increases linearly with height which doesn't match the measurements.

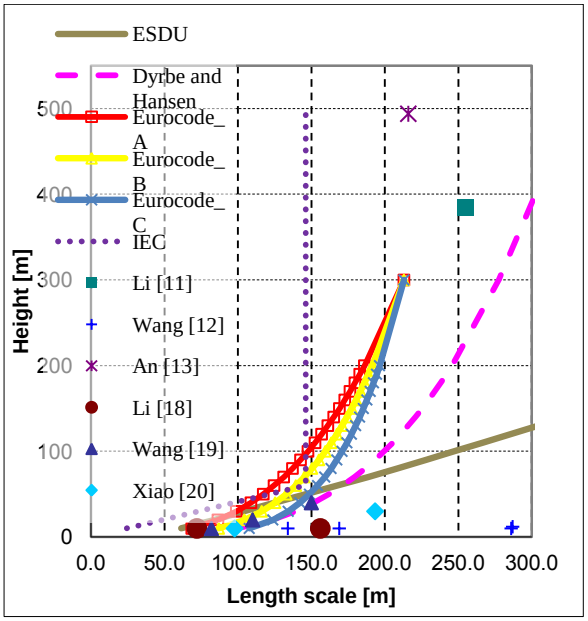

Figure 1 Longitudinal length scale versus height

Figure 1 shows the length scales according to the above conversion laws plotted alongside measured length scales from cyclones between 10m and 500m above the ground (taken from reference [11] [12] [13] [18] [19] [20]). It can be seen from this graph that none of the conversion laws shows good agreement with the measured length scales from cyclones. The Dyrbe and Hansen model described in equation (3-12) fits well with most of measurements below 40m height but fails to match the values measured at 400 and 500m. For wind turbine application, it is hard to conclude which converting law is the best due to the lack of data at the turbine hub height region (50-100m). Anyhow, measurements at 400 and 500m indicate the length scale is likely to follow a power law. The conversion law in the current IEC 61400-1 standard does not look reasonable in the CBL, perhaps because it was tuned for the normal atmospheric boundary layer. Hence, a converting law for length scales in the CBL needs to be specified. In this study, Dyrbe and Hansen model has been adapted, given by

$$L_u^x = L_{10}^x \left(\frac{z}{z_{10}}\right)^{0.3} \qquad \textbf{(3-14)}$$

With L_{10}^x = 77m and z_{10} =10m

Figure 2 shows the same graph but zoomed into the region near the wind turbine hub height (50~100m). The length scale from the adapted Dyrbe and Hansen model (3-14) is quite similar to the one for the length scale from Eurocode 1 category A model. Due to the lack of field measurements, it is not conclusive that equation (3-14) reflects the reality in the best way. Nevertheless it is on the conservative side for loading on wind turbine structures and has the advantage of being simple to use. Terrain category does not have to be considered in this model.

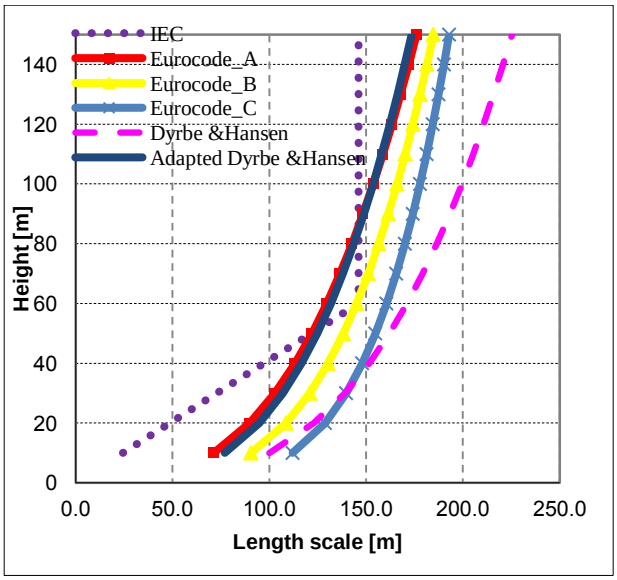

Figure 2 Longitudinal length scale versus height

3.4.3. Experimental validation of the turbulence length scale

The Florida Coastal Monitoring Program (FCMP) [21] focuses on full-scale experimental methods to quantify near-surface hurricane wind behaviour. The program collected tropical cyclone data from 10m-towers during the 1999-2003 Atlantic Hurricane Seasons. Figure 3 shows the 10-min length scales recorded during this measurement campaign binned by their associated roughness lengths and mean wind speeds. It can be seen from this graph that the length scales first decrease with increase of surface roughness length, then, they remain

constant when the roughness length increases above 0.07m. The length scales not only vary with roughness but also with wind speed. However, due to limited number of records in high wind speed, it can not be said with confidence that the length scale continues to decrease with increasing wind speed. The brown dashed line in Figure 3 is the 77m length scale from equation (3-10). The numerical value shows good agreement with experimental data for all three terrain categories defined in Section 3.2.

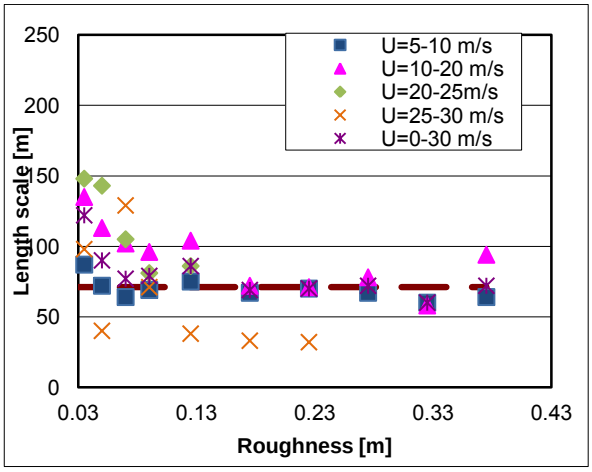

Figure 3 Length scales measured in the FCMP [21]

The equation (3-10) is also validated with two measured tropical cyclone time histories in reference [10] and [22]. Both measurements show that the longitudinal length scales have very large variances (roughly between 50 and 500m). As a result, it is hard to select one length to capture the entire cyclone life time. While the numerical length scales from equation (3-10) do predict the values near the maximum sustained wind inside cyclone eye-wall.

Wang [12] has analysed a series of high resolution data collected at 10m height in four typhoons (Washi, Damrey, Chanchu, and Prapiroon) in South China. In this study, the 10-min longitudinal integral length scale showed good agreement with the value from equation (3-10) .

3.4.4.Spectral analysis

There are four commonly used spectral models to characterize turbulence for wind turbine design. The Kaimal spectrum is an empirical model based on the measurements at 5.66m, 11.3m and 22.6m height over flat terrain [23]. The model was slightly adapted in the IEC standard and it is given as

$$\frac{nS_u(n)}{\sigma_u^2} = \frac{4nL_k^x/V_{hub}}{(1+6nL_k^x/V_{hub})^{5/3}} \qquad \textbf{(3-15)}$$

Here n is the frequency and $S_u(n)$ is the auto spectral density function for the longitudinal component. The only free parameter in both spectral models is the longitudinal length scale which shifts the spectral energy to higher or lower frequencies. In order to have the same high-frequency asymptotic limit for both models, the length scale of the Kaimal model is related to the integral length scale which is the length scale used in the von Karman model according to, $L_k^x = 2.33L_u^x$.

The von Karman spectrum addresses the spectral and correlation functions of a three dimensional homogeneous isotropic turbulent field. [24] The model is better defined than Kaimal's from a theoretical point of view. All the spectra and cross spectra functions in a turbulent flow field are well described and the assumptions involved are exactly formulated. For many years, it has been recognized as the best representation of turbulence spectra for strong winds [14]. However, one disadvantage is that this spectrum model is based on the assumption of isotropic turbulence. The ratios of the turbulence intensities in the three wind directions are always one which doesn't match the conclusion in Section 3.4.1. What is more, the turbulence spectrum shape seems to change with the height due to the shear effect. Harris [25] improved the Von Karman model for these disadvantages. The model is also quoted by the ESDU and well-known as the ESDU von Karman model.
Mann [26] also improved the isotropic von Karman spectral model by taking the shear effect into account. His model has one more adjustable parameter than the Kaimal and the von Karman model: the shear parameter Γ which controls the shape of the spectrum. If this parameter is zero, it means no shear effect on the spectrum and then the model becomes

the von Karman model. If it is 3.9, the Kaimal shape spectrum appears. One advantage of the Mann model is that all coherence functions are automatically generated for the given shear parameter and length scale [27]. However, one disadvantage of the Mann model is the TI ratios in the three directions are constrained by the shear parameter which is not easy to adapt to fit the measurements.

None of these spectral models exactly characterizes the turbulence in the CBL. Experimental verification and validation is needed to find the most suitable model for calculating loads in the CBL. To validate spectral models, two field measurements for the normalized longitudinal spectral probability density are presented here. Five spectral models are run with given length scale and velocity standard derivation, as follows:

von Karman	Using the von Karman spectral model
ESDU von Karman	Using the improved von Karman model from reference [14]
Kaimal	Using the Kaimal spectral model
IEC Mann	Using the Mann spectral model in IEC 61400-1 with shear parameter = 3.9
Mann:	Using the Mann spectral model and the integral length scale from equation (3-8), adapting the shear parameter in order to fit the measured spectrum.

Figure 4 shows the normalized longitudinal spectrum of the measured data (black line) from Typhoon Sally by Li et al. [11]. The data are measured at the height of approximately 384m. The mast was placed on Di Wang Tower in Shenzheng City. The data were measured in 1996 during the passage of Typhoon Sally. Unfortunately, the measured wind speeds were given in hourly mean values instead of 10-min averaged values. The spectral density of the wind speed shown here is for the whole period of 25 hours with the integral length scale of 255m. The mean turbulence intensity is 11.5% and the corresponding mean wind speed is 12.2 m/s.
Figure 5 shows the normalized longitudinal spectrum of Typhoon Muifa, measured by An et al [13]. The data were recorded at 492m on top of the Shanghai World Financial Center (SWFC) when Typhoon Muifa passed the city in August 2011. This measurement provided very detailed data of wind speeds, turbulence intensities and turbulence spectra which are 10 min averaged. The measured spectra are binned by wind speed which is very helpful for validating the turbulence spectra at the cyclone eye-wall region for the extreme load cases. The spectrum of mean wind 30.3 m/s (the purple line in Figure 5) has been chosen for validating the numerical models. The longitudinal turbulence intensity is 14% for the numerical models. The average observed value of the longitudinal length scale is 217.6m, however, it is not clear which value shall be used to generate the spectrum at mean wind speed 30.3 m/s. For the purposes of this study, a length scale of 247.8m is used, calculated from the equation (3-14) .

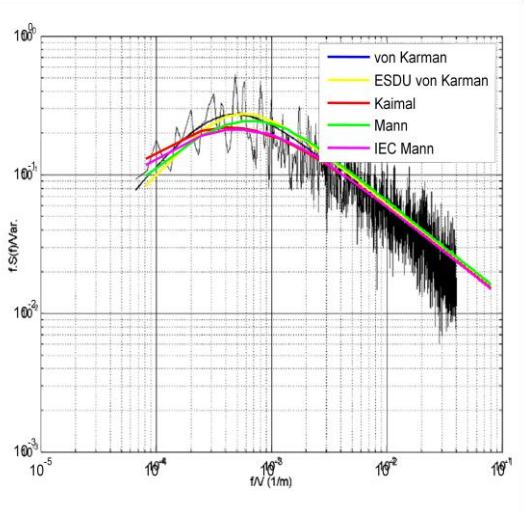

Figure 4 normalized u-spectrum on the basis of the measured data in Typhoon Sally [11]

The von Karman type spectral model shows the best representation of the measured spectral shapes in both figures. Within the low-frequency range, only the von Karman and ESDU von Karman spectrum fits well with the measurements, while the other spectral models overestimate the spectral probability density at this range. The Kaimal spectrum model and the IEC Mann model both underestimate the peak of the spectral probability density. The fit improves when a different shear parameter value is used for the Mann model. However, the TI ratios based on this shear parameter don't match the measured

values.

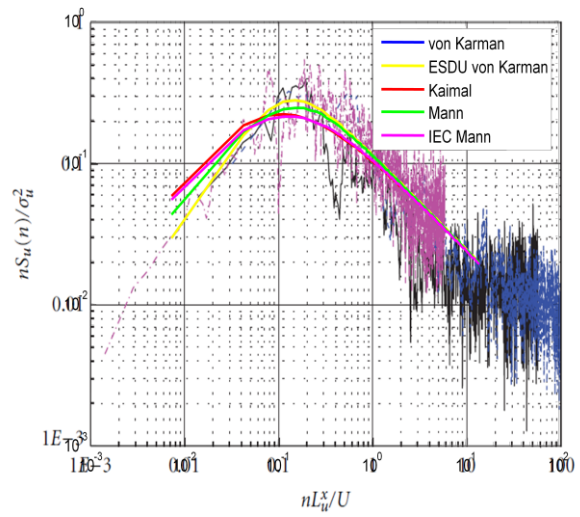

Figure 5 normalized u-spectrum on the basis of the measured data in Typhoon Muifa [13]

A similar conclusion was reach from a spectral comparison by Cao et al. in [28]. In their study, a measured spectrum at a 10-min mean wind speed of 30 m/s was compared with different spectral models, and it fits well with the shape of the von Karman spectrum model. Another study by Muecke et al. [29] comes to the same conclusion, although their work is not specially for cyclones. In their work, the measured wind spectra at the FINO1 mast in the Alpha Ventus wind farm is compared with various theoretical spectral models. The ESDU von Karman spectrum fits very well with the measured spectra at 61.5 and 81.5m, while the Kaimal spectrum does not give a good fit for any of the cases. Some significant differences in loading were also found for some key components of a wind turbine in the dynamic simulations using different theoretical spectral models. The same components are also selected in Section 4 for extreme loads comparison. Unfortunately, real load measurements have not been published yet and it is not possible to conclude which spectral model best predicts the real loads. Nevertheless, it can be said that the turbulence spectral model significantly affects turbine loading and it should be selected with caution.

4. Design situation and load case

Based on the defined external turbulent wind parameters, the Extreme Cyclone Wind Model (ECWM) is defined in this chapter for wind turbine loads analysis. A new Design Load Case (DLC) is defined here to use the ECWM for ultimate loads analysis.

4.1. Extreme cyclone wind model (ECWM)

For the ECWM, the basic parameters for wind modelling are listed in Table 4-1. Only the wind speeds of the SSHWS class 3, 4 and 5 are included as the class 1 and 2 wind speeds have already been covered by the reference wind speed in the IEC standard. The mean wind speeds at hub height which have been converted from the sustained values to the corresponding10-min mean values for each terrain class using equation (3-1). Since cyclones only occur in tropical climate, a value for air density of 1.094 kg/m3 is used instead of 1. 225 kg/m^3 as given in the IEC standard (see section 3.1).

The CBL is assumed as the neutral stable boundary layer with a wind profile defined as in equation (3-3). The turbulent wind inflow is defined with representative values of the turbulence intensities as given in equations (3-5) ~ (3-7). The integral turbulence length scale is defined in equation (3-14).

		Vhub [m/s]			Surface roughness [m]
Cyclone class		3	4	5	
Terrain class	A	41.2	48.6	59.1	0.18
	B	42.7	50.4	61.2	0.07
	C	43.7	51.5	62.6	0.03

Table 4-1 Basic parameters for the ECWM

On the basis of the above analysis in Section 3.4.4, the recommended turbulence spectral model for cyclone load calculations is the ESDU von Karman model in [14]. Once the longitudinal length scale is given, the other length scales required in the ESDU von Karman model can be automatically generated by the equations in [14].

Other spectral models should be used with great caution as the choice may significantly affect the loads. The length scales for other spectral models may also be defined differently from the integral length scale of turbulence in the ESDU von Karman model. In this case, the length scale from equation (3-14) needs to be converted to the appropriate value before using it. For instance, the length scale of the Kaimal model is $2.33L_u^x$.

4.2. Load case definition

Based on the ECWM, the DLC 6.x in the IEC 61400-1 standard has been adapted to create a new DLC for cyclone loading. It is very likely that wind turbines will lose electrical grid during cyclones. A grid failure will lead to yaw misalignment from all possible wind directions unless power back-up is provided for the control and the yaw system for the period of cyclone eye-wall passage. Since the grid failure is very likely to occur, the DLC shall be classified as normal (N) load cases for the ultimate load analysis (U). The associated safety factor is 1.35 for loads.

Design situation	Idling
Wind condition	ECWM
Other conditions	Loss of electrical network connection
Type of analysis	U
Partial safety factor	N

Table 4-2 Summary of the ECWM DLC

5. Cyclone loading

This section presents some simulation results showing loads from the cyclone DLC, and how this compares to the existing loads envelope. A set of simulations were carried out using the NREL 5MW wind turbine [30]. For illustration, the class 4 and class 5 cyclones over the terrain class B have been simulated according to the ECWM defined in the previous chapter. The wind fields are generated using the ESDU von Karman model, the Kaimal model and the Mann model. For each model, six stochastic turbulent wind fields are generated with random seeds.

Turbulence model	ESDU von Karman	Kaimal	Mann
Blade root Mxy	0.94	0.89	0.94
Tower base Mxy	0.89	0.82	0.92
Yaw bearing Mxy	0.33	0.33	0.34
Yaw bearing Fxy	0.97	0.87	0.98

Table 5-1 Extreme loads for cyclone class 4

In order to have a clear idea if the turbine can survive in cyclones, the extreme loads results for some key turbine components are normalized by the corresponding values in the loads envelope. If a value is greater than one, it means the turbine component is likely to fail in cyclones.

Turbulence model	ESDU von Karman	Kaimal	Mann
Blade root Mxy	1.46	1.41	1.44
Tower base Mxy	1.33	1.21	1.40
Yaw bearing Mxy	0.55	0.47	0.50
Yaw bearing Fxy	1.46	1.31	1.55

Table 5-2 Extreme loads for cyclone class 5

Table 5-1 shows the extreme loads from the three chosen turbulence spectral models for the class 4 cyclone. All normalized loads are less than one which means the NREL turbine can prevail against the class 4 cyclones. However, things look differently for the class 5 cyclone. Table 5-2 shows the extreme loads results from the three turbulence spectral models for the class 5 cyclone. The bending moments in the blade root, tower base and yaw bearing are almost 50% larger than their reference values. Most likely, the turbine will collapse in the class cyclone 5.

Notable differences with respect to turbulence model also appear in the load predictions. Table 5-3 shows the variations in percentages of the extreme loads from the Kaimal and Mann model for both cyclone cases in comparison with the baseline results from the ESDU von Karman model. The extreme loads of tower base and yaw bearing from the Kaimal model are significantly smaller than

the baseline results, while the Mann model predicts a similar level of loads to the ESDU von Karman model. Due to the lack of real loads measurements, it is hard to conclude which model is best for load prediction. Nevertheless, the ESDU von Karman and the Mann spectral model give more conservative results than the Kaimal model.

	Cyclone class 4		Cyclone class 5	
	Kaimal	Mann	Kaimal	Mann
Blade root Mxy	-5.8%	-0.7%	-3.0%	-0.8%
Tower base Mxy	-8.5%	3.1%	-8.9%	5.2%
Yaw bearing Mxy	-0.1%	2.4%	-13.7%	-9.3%
Yaw bearing Fxy	-11.0%	1.0%	-10.3%	6.6%

Table 5-3 Variation in percentages of the extreme loads

6. Conclusion

This paper presents the necessary parameters for the design and assessment of wind turbines in tropical cyclone conditions. The characteristics of the turbulence have been paid special attention. The turbulence longitudinal length scale at 10m observation height has been defined and shows fair agreement with length scales from various field measurements.

For turbulence spectral models, the ESDU von Karman spectrum model matches the measured cyclone spectra better than the other models. Although it is not possible to say with certainty which model is best for load predictions, the ESDU von Karman model does give conservative values of load and its spectral shape is closer to the measurements. This model is recommended to use for cyclone loading assessment. Thus, it is recommended using the ESDU von Karman model for cyclone loading assessment.

Finally, the question in the heading is answered here; the NREL turbine can not survive during the passage of the eye-wall of a class 5 cyclone. The loads are far beyond the envelope and the components need to be re-designed to prevail against a cyclone of this class. However, if the site only has cyclones below class 5, this turbine can survive during the cyclone passage.

Acknowledgement

The authors gratefully acknowledge the support of all the organizations and individuals who contributed to this study. In particular this is funded by GL Group. Special thanks go to Andy Cordle, James Nichols and Kimon Argyriadis for your valuable suggestions.

Reference

[1] "IEC 61400-1 Standard Ed.03," International Electrotechnical Commission, Geneva, 2005.

[2] "Guideline for the certification of wind turbines," Germanischer Lloyd Industrial Services GmbH, Hamburg, 2010.

[3] L. Wu, H. Su, R. G. Fovel, B. Wang, T. Shen and B. H. Kahn, "Relationship of environmental relative humidity with North Atlantic tropical cyclone intensity and intensification rate," *Geophysical research letters*, vol. 39, pp. 1-8, 2012.

[4] T. Schott, C. Landsea, G. Hafele, J. Lorens, A. Taylor, H. Thurm, B. Ward, M. Willis and W. Zaleski, "The Saffir-Simpson hurricane wind scale," National Hurricane Center, Miami, 2012.

[5] "Minor modification to Saffir-Simpson hurricane wind scale For the 2012 hurricane season," National Hurricane Center, Miami, 2012.

[6] "National Weather Service," National Hurricane Center, [Online]. Available: http://www.nhc.noaa.gov/aboutsshws.php.

[7] T. Burton, D. Sharpe, N. Jenkins and E. Bossanyi, Wind energy handbook, London: John Wiley&Sons Ltd., 2001.

[8] B. A. Harper, J. D. Kepert and J. D. Ginger, "Guidelines for converting between various wind

averaging periods in tropical cyclone conditions," World Meteorological Organization, Geneva, 2008.

[9] M. D. Powell, P. J. Vickery and T. A. Reinhold, "Reduced drag coefficient for high wind speeds in tropical cyclones," *Nature,* vol. 422, pp. 279-283, 2003.

[10] J. Schroeder and D. Smith, "Hurricane Bonnie wind flow characteristics as determined from WEMITE," *J. Wind Eng. Indust. Aerodyn,* vol. 91, pp. 767-789, 2003.

[11] Q. Li, Y. Xiao, C. Wong and A. Jeary, "Field measurements of typhoon effects on a super tall building," *Engineering structures,* vol. 26, p. 233–244, 2004.

[12] B. Wang, F. Hu and X. Cheng, "Wind gust and turbulence statistics of typhoons in South China," *Acta Meteorologica Sinica,* vol. 25, no. 1, pp. 113-127, 2011.

[13] Y.An, Y. Quan and M. Gu, "Field measurement of wind characteristics of Typhoon Muifa on the Shanghai World Financial Center," *International Journal of Distributed Sensor Networks,* vol. 2012, pp. 1-11, 2012.

[14] ESDU85020, "Characteristics of atmospheric turbulence near the ground Part II: single point data for strong winds (neutral atmosphere)," The Institution of Mechanical Engineers, 1985.

[15] P. J. Vickery, D. Wadhera, M.D.Powell and Y.Chen, "A hurricane boundary layer and wind field model for use in engineering applications," *J. Appl. Meteor. Climatol,* vol. 48, p. 381–405, 2009.

[16] "Eurocode 1: Actions on structures — General actions — Part 1-4: Wind actions," European Committee for Standardization, Brussels, 1994.

[17] C. Dyrbe and S. O. Hansen, Wind loads on structures, Chichester: John Wiley, 1997.

[18] L. Li, Y. Xiao, A. Kareem and L. Song, "A comparative study of wind characteristics in typhoons," in *13th International Conference on Wind Engineering,* Amsterdam, 2011.

[19] W. Xu, P. Huang and G. Ming, "Field measurements about integral scales of near-ground turbulence during Typhoon Muifa (in Chinese)," *Journal of Tongji university (natural science),* vol. 40, no. 10, pp. 1491-1497, 2012.

[20] L. Xiao, L. Li and L. Song, "Study on typhoon wind characteristics based on field measurements," in *The Seventh Asia-Pacific Conference on,* Taipei, 2009.

[21] F. Masters, "Measurement, modeling and simulation of ground-level tropical cyclone winds," University of Florida, Florida, 2004.

[22] J. Gao, R. Zhang and Y. Cai, "Analysis on boundary layer wind characteristics during super Typhoon Megi landfalls," in *13th International Conference on Wind Engineering,* Amsterdam, 2011.

[23] J. C. Kaimal, J. C. Wyngaard, Y. Izumi and O. R. Coté, "Spectral characteristics of surface-layer turbulence," *Quarterly Journal of the Royal Meteorological Society,* vol. 98, no. 417, p. 563–589, 1972.

[24] T. v. Kármán, "Progress in the statistical theory of turbulence," *Proceedings of the national academy of sciences of the United States of America,* vol. 34, no. 11, pp. 530-539, 1948.

[25] R. Harris, "Some Further thoughts on the spectrum of gustiness in strong winds," *J. Wind Eng. Indust. Aerodyn,* vol. 33, pp. 461-499, 1990.

[26] J. Mann, "The spatial structure of neutral atmospheric surfacelayer," *Journal of fluid mechanics,* vol. 273, pp. 141-168, 1994.

[27] J. Mann, "Wind field simulation," *Prob. Engng, Mech,* vol. 13, pp. 269-282, 1998.

[28] S.Cao, Y.Tamura, N.Kikuchi, M.Saito, I.kayama and Y. Matsuzaki, "Wind characteristics of a strong typhoon," *J. Wind Eng. Indust. Aerodyn,* vol. 97, pp. 11-21, 2009.

[29] T. Mücke, C. Harkness and K. Argyriadis, "Offshore wind turbulence model versus measurement," in *EWEA,* Copenhagen, 2102.

[30] J. Jonkman, S. Butterfield, W. Musial and G. Scott, "Definition of a 5-MW reference wind turbine for offshore system development," NREL, Golden, 2009.

RELATING HIGH-FREQUENCY OFFSHORE TURBULENCE STATISTICS TO BOUNDARY LAYER STABILITY

A. Jeromin[1] and A.P. Schaffarczyk[2]

[1]Forschungs- und Entwicklungszentrum FH Kiel GmbH, Schwentinestraße 24, 24149 Kiel, Germany, andreas.jeromin@fh-kiel-gmbh.de
[2]CEwind eG and University of Applied Sciences Kiel, Mech. Eng. Dept., Grenzstraße 3, 24149 Kiel, Germany, alois.schaffarczyk@fh-kiel.de

Abstract

To gain insight into the differences in onshore and offshore turbulence, pressure fluctuations were measured in offshore wind for different environmental conditions. A robust piezoelectric sensor was used to sample data at 50 kHz. Offshore measurements were performed at 100 m height on Germany's FINO3 offshore platform in the German Bight. Recent studies on various turbulence statistics were presented.

The statistical evaluation revealed that no dependency of simple turbulent properties like wind speed, wind direction or turbulence level (variance) on environmental conditions. Therefore, we relate higher statistical properties (described by the statistics of increments) to the stability state in the atmospheric boundary layer. Temperature data was provided by Deutscher Wetterdienst (DWD).

Special emphasis was given to the shape factor acording to Castaing's et al [4] superposition model.

Measurements for temperature and velocity are available at 100 m height and 10 m height. By estimating a gradient Richardson-number the boundary layer state is determined.

The statistics were sorted to be either within the unstable/neutral state or the stable state. The turbulence intensity is similar for unstable or neutral boundary layers, while at stable conditions the intensity is lower. This will also influence the statistical behavior of the turbulent pressure.

In case of unstable stratification the shape factor s_p^2 is close to zero, indicating that an unstable environment produces close-to gaussian distributions.

In addition a probabilistic approach to shape-factors-distribution is proposed.

1 Introduction

Site assessment for wind farms become more and more sophisticated even under off-shore conditions. In most cases turbulence is defined in the context of loads meaning that fluctuations with frequencies higher than few Hertz may be neglected.

In contrast to that it is well know from general turbulence theory that more structure may be contained which may be summarized with the term *intermittency*. In addtion aerodynamical

Figure 1: Locations of measurements on-shore at Kaiser-Wilhelm-Koog test site and off-shore at FINO3 platform 80 km behind the island of Sylt. ©FuE-Zentrum FH Kiel GmbH, Graphics: Bastian Barton

turbulence triggering early transition from the laminar to the turbulent state of the boundary layer on the blade lies in a much higher frequency range up to several kHz.

Therefore several measurement campaings were undertaken on- as well as off-shore to gain insight into the small-scale structure of atmospheric turbulence and possible differences of on- and off-shore wind.

2 Measurements

The measurements were done using a piezoelectric pressure sensor from PCB Piezotronics (fig. 2) that was connected to an imc Meßsysteme GmbH CS-1208 data logger. The diameter of the sensor was 15 mm for the sensing element. The minimal pressure resolution was 0.13 Pa and the possible temporal resolution ranged from 2.5 Hz to 80,000 Hz. In our measurements the pressure data was sampled at 50 kHz with a total length of 100 seconds. Wind speed and temperature were sampled at 1 Hz temporal resolution.

Before the field measurements began, the piezoelectric pressure sensor was verfied against a hot wire anemometer in a wind tunnel at University of Oldenbourg. The turbulent wind speed from the hot wire anemometer and the turbulent pressure variations had the same turbulent characteristical behavior [6].

The on-shore measurements were done in Kaiser-Wilhelm-Koog test site of GL/GH (see fig. 1). A lattice tower of 60 m height provided booms for mounting the pressure sensor and other measurement equipement. The pressure sensor was mounted at 55 m height. Wind speed and wind direction were recorded at 55 m height by calibrated cup anemometers and wind vanes, respectively. The temperature was recorded at 53 m height by a resistor-type thermometer.

The off-shore measurement platform FINO3 provided the location for the off-shore measurments. About 80 km behind the island of Sylt (see fig. 1) the platform was buildt near the future locations of the wind farms DanTysk and Sandbank 24. The tower is also a lattice tower with

booms for the measurement equipment. Two pressure sensors (fig. 3) were mounted at about 100 m height above mid sea level for parallel operation. The data acquisition for meteorological data was similar to the one on-shore. Wind speed and wind direction were available at 100 m height, temperature at 95 m height above mid sea level.

3 Analysis

The recorded data sets were categorized by wind speed classes of 6 m/s, 12 m/s and 16 m/s. An additional class at 10 m/s was used off-shore. For each measurement the statistical characteristics were analyzed with respect to power-spectral density, increment distributions, shape factor, structure functions, autocorrelation and taylor microscale. In this section the methods were explained, that were used in this study.

For a temporal quantity, like velocity or pressure, the increment can be defined as its difference between two times:

$$\Delta u = u(t+\Delta t) - u(t) \qquad \Leftrightarrow \qquad \Delta p = p(t+\Delta t) - p(t) \tag{1}$$

where u is the velocity, p the pressure, t the time and Δt a fixed increment delay. With the increment, the mean value is eliminated and the stochastic variation of the signal remains for a specific time scale Δt. The increments are the base for increment statistics as the structure functions or the shape parameter.

An ansatz from Castaing et al. [4] suggests that the distribution of increments was an overlay of normal distributions, but their variance was lognormal distributed. Here, the shape factor was a measure for the strength of intermittency and was computed by numerical integration. To be able to compute the shape factor s directly from the time series, Beck [2] superposed a normal distribution with a log-normal distribution. The combination of the flatness for both distributions

Figure 2: Pressure sensor after six month in off-shore service.

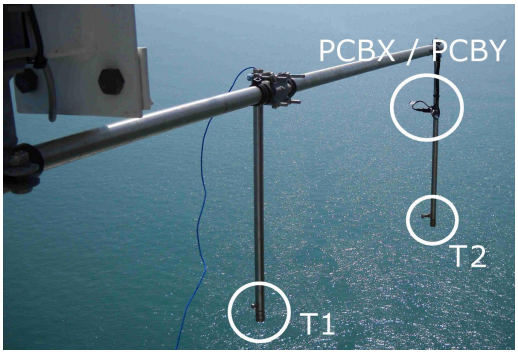

Figure 3: Installation of two parallel pressure sensors T1 and T2 on FINO3 platform.

results in the shape factor

$$s^2 = \ln\left(\frac{1}{3}\frac{\langle \Delta u^4 \rangle}{\langle \Delta u^2 \rangle^2}\right) \qquad \Rightarrow \qquad s_p^2 = \ln\left(\frac{1}{3}\frac{\langle \Delta p^4 \rangle}{\langle \Delta p^2 \rangle^2}\right). \tag{2}$$

where s^2 is the shape factor for the velocity and s_p^2 for the pressure, respectively. The brackets $\langle x \rangle$ define the mean value of a quantity x. An interpretation of this shape factor is given in [2]. A value of $s^2 \approx 0$ represents a normal distribution while for $s^2 \neq 0$ the distribution deviates from the normal distribution.

It is clear from the work of Batchelor [1] that turbulent velocities and pressure obey different scaling laws $\sim k^{-5/3}$ and $\sim k^{-7/5}$, resp. although seemingly related by $p \sim v^2$ according to Bernoulli's law. Direct comparison of hot-wire and piezo-electric pressure senor show comparable power-density spectra up to 4 kHz (unpublished, see [6]), however. Theoretical as well as experimental investigations [11] are still incomplete, so that there is no clear answer so far how $s_{(u)}^2$ and s_p^2 are related to each other exactly.

When heat transfer occurs, such as in the atmospheric boundary layer, stratification of the flow becomes important. In a stratified flow, the static stability of the boundary layer determines the characteristics of turbulence. As was shown by Sathe et al. in [9], turbulence intensity and power spectral density are different for a stable and an unstable flow.

The states of a stratified boundary layer exposed to heat transfer were defined by Obukhov [8] to be stable, neutral or unstable. Different methods allow to define the state of the atmospheric boundary layer [8] depending on the known variables. In our case the definition of the Richardson number is applicable. It is defined as:

$$Ri = \frac{g}{T}\frac{\partial\theta/\partial z}{(\partial v/\partial z)^2} \tag{3}$$

where g is the acceleration of gravity, T is the mean absolute temperature, z is the height normal to the surface and $\partial v/\partial z$ is the mean velocity gradient. The z-direction is orthogonal to the surface. The potential temperature θ is defined as

$$\theta = T\left(\frac{p_0}{p}\right)^{R/c_p} \tag{4}$$

where p is the pressure and $p_0 = 1000$ hPa the reference pressure, $R = 289\ \frac{\mathrm{J}}{\mathrm{kg\ K}}$ is the specific gas constant and $c_p = 1005\ \frac{\mathrm{J}}{\mathrm{kg\ K}}$ is the specific heat capacity of air.

In equation (3) the quantity $\frac{g}{T}\partial\theta/\partial z$ determines the forces introduced by heat transfer in the boundary layer. The term $(\partial v/\partial z)^2$ represents the momentum forces in the boundary layer. Now let us consider two points in the boundary layer at height z_1 and z_2 where $z_1 < z_2$ and $\Delta z = z_2 - z_1$. Ri from (3) can thus be rewritten with the differences between the two locations as

$$Ri = \frac{g}{T}\frac{\Delta\theta/\Delta z}{(\Delta v/\Delta z)^2} = \frac{g}{T}\frac{(\theta_2-\theta_1)/\Delta z}{((v_2-v_1)/\Delta z)^2} \tag{5}$$

We can assume that the boundary layer has a positive velocity gradient when $v_1 < v_2$ which is the case for a non-moving surface and a velocity $v >> 0$ for $z >> 0$. With this assumption only the convection part in eq. (5) remains. Three situations are possible to occure:

$\theta_2 > \theta_1$ The surface is colder than the fluid and the gradient becomes $\partial\theta/\partial z > 0$ and therefore $Ri > 0$. Heat is transported by conduction only, a convection flow does not occur. In this case the stratification is strong, turbulence gets damped. The boundary condition is STABLE for $Ri > 0$.

$\theta_2 = \theta_1$ The temperature gradient is zero and therefore $Ri = 0$. There is no temperature gradient and therefore no conduction nor convection. This condition is called NEUTRAL.

$\theta_2 < \theta_1$ The surface is warmer than the fluid and the gradient becomes $\partial\theta/\partial z < 0$ and therefore $Ri < 0$. Heat is transported by conduction and by convection from the surface to the fluid. The convection results in a vertical, upward component of the flow that interacts with the horizontal velocity component. This leads to production of turbulence in the boundary layer and therefore is called UNSTABLE.

From the measurements we obtained the values for p, T_{air} at 100 m height, wind speed v_{air} and wind direction as well as the sensor signal of the piezo electric microphone. Assuming the air to be a perfect gas, the density ρ can be calculated by the perfect gas law.

For the derivatives $\partial\theta/\partial z$ and $\partial v/\partial z$ the temperature and wind speed in a second height must be known. Unfortunately, this data was not available for most of the measurements. Therefore, these gradients had to be approximated in a different way.

The ground temperature T_{gnd} was estimated using data from the Deutscher Wetterdienst (DWD). For the onshore measurements the ground temperature at a nearby location was available at hourly samples. The temperature of the sea for the offshore measurements was interpolated from the measurement stations at Helgoland and in List (Sylt).

The sign of Ri is most dependent on the temperature gradient, so the velocity gradient can be assumed to be of lower importance. Therefore, a rough estimation was to use $v_{gnd} = 0$ for the computation of the velocity gradient. This effects most the absolute value of Ri but not the heat transfer conditions in the atmospheric boundary layer.

With this data an estimate for Ri was possible. The indentification of stable and unstable states were simple. However, the neutral state required a value of $Ri = 0$ which is hardly possible with our assumptions. To identify the neutral state, a bandwidth of $|Ri| < 0.02$ was defined for this condition.

4 Results

The computation of the shape parameter was straightforward and the results are shown in figure 4. The scale for the shape factor is shown on the left, colors indicate locations and symbols represent velocity classes. Time series, in which $s_p^2 < 2$ were greyed out and will not be considered in the following. For comparison reasons, the shape factor for the velocity measurements from Sreenivasan and Dhruva [10] at Brookhaven National Laboratory was included.

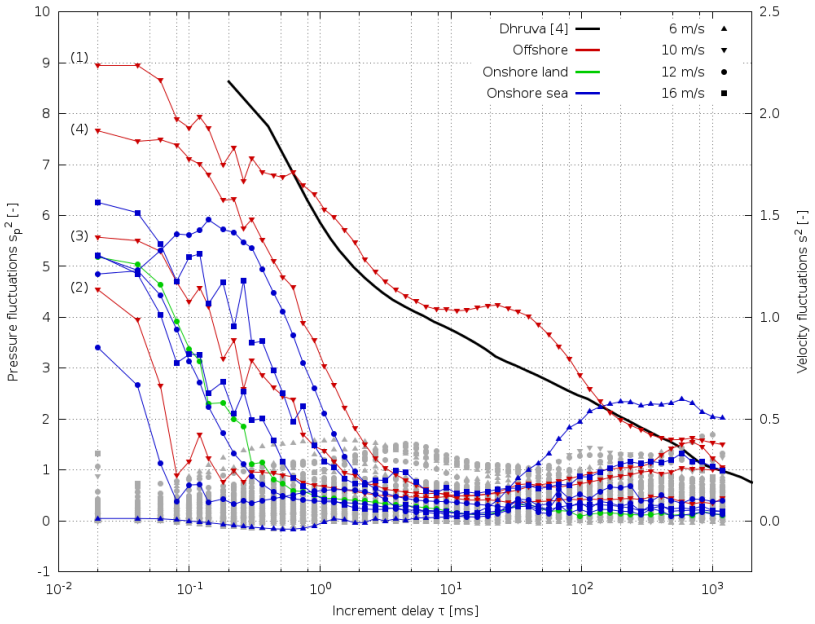

Figure 4: Shape paramters for all undertaken measurements. Colours represent locations: Offshore, Onshore land, Onshore closer to sea. Symbols represent the velocity classes for the wind speed. Measurements with $max(s_p^2) < 2$ are in grey.

The general behaviour of shape parameter functions for velocity and pressure agree, whereas absolute values may differ significanlty. This behavior was also observed in [7]. Surprizingly, most of the pressure measurements of s_p^2 close to zero. This was not reported for velocity measurements so far. So there might be a difference between turbulent velocity- and pressure-statistics.

One difference between the measurements of velocity and pressure were the different sample rates and the length of the time series. An increase of the sampling rate would only result in an extension to lower increment delay times and would therefore extend the curves to the left in figure 4. An increase of the length of the recorded time series would effect the curves of the shape parameter in a very different way.

In fig. 4 four offshore curves were marked with numbers in brackets. They were all recorded on the same day and almost at the same time:

(1) October 19, 2010, 8:44 a.m.

(2) October 19, 2010, 8:54 a.m.

(3) October 19, 2010, 8:55 a.m.

(4) October 19, 2010, 8:57 a.m.

Each time series was 100 s long. For (1) s_p^2 is high. But then the pressure data resulted in $s_p^2 \approx 0$ until the values increased eight minutes later at (2). The time series (2), (3) and (4) were

Table 1: Summary of ABL stability cases. Potential temperatures θ, wind speeds v_W and turbulence intensities Ti from cup anemometers, Ri numbers and estimated state of the boundary layer for some of our measurements.

Date & Time	Location	θ_{air} (K)	θ_{gnd} (K)	v_W (m/s)	Ti (%)	Ri (-)	Boundary layer state	
2010 Oct. 21, 7:56 a.m.	Offshore	279.3	285.0	6.6	8.2	-0.54	Unstable	
2008 Apr. 28, 9:35 a.m.	Onshore	287.6	290.0	6.1	11.9	-0.15	Unstable	
2010 Oct. 19, 8:57 a.m.	Offshore	283.1	286.8	10.8	2.2	-0.13	Unstable	*
2010 Oct. 19, 8:44 a.m.	Offshore	283.6	286.8	10.2	3.1	-0.12	Unstable	*
2010 Aug. 19, 8:13 a.m.	Offshore	288.8	291.3	12.7	2.8	-0.06	Unstable	
2008 Mar. 25, 2:55 p.m.	Onshore	274.2	276.0	11.3	10.8	-0.03	Unstable	*
2008 Mar. 29, 11:44 a.m.	Onshore	279.1	280.1	15.3	10.6	-0.01	Neutral	
2008 Mar. 30, 6:04 p.m.	Onshore	282.9	283.1	15.7	5.6	0.00	Neutral	*
2008 Apr. 28, 2:20 p.m.	Onshore	288.3	288.2	5.8	2.1	0.01	Neutral	*
2008 May 1, 2:55 a.m.	Onshore	284.7	283.3	6.0	6.0	0.10	Stable	
2008 Apr. 12, 7:24 p.m.	Onshore	282.7	279.6	5.2	11.0	0.28	Stable	

consecutive, so it can be said that the shape parameter for the turbulent pressure fluctuations varied in time. When the time series from 8:44 to 8:57 were concatenated and evaluated according to s_p^2, a curve similar to the one for the velocity fluctuations was seen. This was shown in [5].

This behavior was not reported for the velocity measurements at high sampling rates. But these measurements were very few until today, so it could be explained by different states of the atmospheric boundary layer. With the estimation of the Richardson number the state could be determined. A selection from our 119 measurements is shown in table 1. Measurements with $s_p^2 > 0$ were marked with a star behind the boundary layer state.

As can be seen in this table, conditions were found in the range from unstable to neutral and stable. However, for the occurance of high s_p^2 a correlation with the Richardson number, boundary layer state or the potential temperatures was not seen.

4.1 Transient behavior of a Sample Time-Serie

For the measurement on Oct. 19, 2010 the transient behavior of the shape factor was investigated in more detail. The information from that day are shown in table 2 in chronological order.

The measurement started at 8:44 a.m. when s_p^2 was high and the turbulence intensity from cup anemometers was low. In the following time series it was found that $s_p^2 \approx 0$, the mean velocity and the potential temperature of the air remained constant. Only the turbulence itensity was rising. Beginning with 8:50 a.m. the mean velocity began to fluctuate for the 100 seconds time series, while turbulence level and temperature remained constant. At 8:54 a.m. the shape factor began to rise (see also curve (2) in fig. 4). Promptly, the turbulence intensity dropped more than 5.5 points and also the potential temperature of the air decreased by 0.4 K with rising shape factor.

In our interpretation the unstable conditions of the boundary layer caused vertical transport

Table 2: Development of Time-Sereoi on Oct 19. Potential temperatures θ, wind speeds v_W and turbulence intensities Ti from cup anemometers, Ri numbers and estimated state for 2010, Oct. 19 measurements (offshore).

Time	θ_{air} **(K)**	θ_{gnd} **(K)**	v_W **(m/s)**	Ti **(%)**	Ri **(-)**	**Boundary layer state**	$s_p^2 \neq 0$
8:44 a.m.	283.6	286.8	10.2	3.1	-0.12	Unstable	*
8:45 a.m.	283.5	286.8	10.2	3.9	-0.13	Unstable	
8:47 a.m.	283.4	286.8	10.0	7.5	-0.14	Unstable	
8:49 a.m.	283.4	286.8	10.1	7.3	-0.13	Unstable	
8:50 a.m.	283.5	286.8	9.3	6.7	-0.16	Unstable	
8:52 a.m.	283.5	286.8	11.2	6.0	-0.11	Unstable	
8:54 a.m.	283.5	286.8	10.8	7.7	-0.11	Unstable	*
8:55 a.m.	283.2	286.8	11.2	4.2	-0.12	Unstable	*
8:57 a.m.	283.1	286.8	10.8	2.2	-0.13	Unstable	*

effects to occur. In the time from 8:45 to 8:49 the boundary layer was stratified, streamlines were horizontal and the cup anemometers were perfectly aligned. Also the turbulent fluctuations of the pressure were distributed normal. At 8:50 a.m. a cluster of warm air rised from the warm surface to the higher and colder regions of the boundary layer (θ_{air} ≈const., v_W fluctuating). In the wake of the warm cluster a second cluster with cold air sank from the higher levels towards the surface (θ_{air} dropped). This lead to strong vertical shear and disturbed the turbulent fluctuations of the pressure, their distribution began to deviate from the normal distribution ($s_p^2 > 0$ and increasing from 8:54). At the same time the turbulence intensity was sinking, too. Strong vertical flows somehow stratified the horizontal velocities that were seen by the cup anemometer. This interpretation is also illustrated in figure 5.

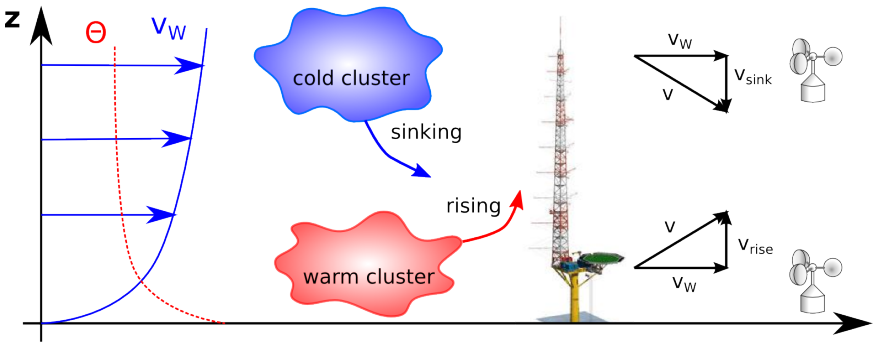

Figure 5: Sketch of boundary layer profiles at unstable conditions with warm and cold clusters of air that impact on the FINO3 platform.

Table 3: Correlation of Occurence-Probability of high shape-factor to boundary layer states for all 119 measurements

	Boundary layer state			
	Unstable	**Neutral**	**Stable**	**Total**
All	84	23	12	119
Offshore	65	0	0	65
Onshore	19	23	12	54
All $s_p^2 \neq 0$	7	4	0	11
Probability (%)	8	17	0	9
Offshore $s_p^2 \neq 0$	4	0	0	4
Probability (%)	6	-/-	-/-	-/-
Onshore $s_p^2 \neq 0$	3	4	0	7
Probability (%)	16	17	0	-/-

4.2 Probabilistic considerations

As was seen in the evaluation of boundary layer state and shape factor, the occurence of high shape factors (highly non-gaussian behaviour) is connected to turbulence as well. Therefore a probabilty for such an *intermittent* burst may be estimated. The counts and probabilities are listed in table 3.

In the first row the number of all measurements and their state are listed. Of a total of 119 measurements were 84 at unstable, 23 at neutral and 12 at stable conditions. The following two rows list the numbers for offshore and onshore locations with their states. In the fourth row the counts for high shape factor events were listed for all measurements. The probability for the occurence of a high-s_p^2 event at a specific boundary layer state was shown in the following line. The same was done for both locations off- and onshore.

One may notice that all measurements offshore were done at unstable conditions while for the onshore measurements all three states were covered. The cause could be found at the season when the experiments were done. The onshore measurements took place in spring 2008 during March to May. At this time of year the ground begins to warm up slowly while the air heatens up much faster. So the ground may be cooler than the air and stable states occur. Also the air might be chillier on a cloudy day or in the evening, and unstable conditions my occur. The offshore measurements were performed in late summer and autumn 2010. The sea was still warm from the summer season while the air began to chill down. Thus, only unstable conditions were covered by our measurements.

To relate boundary layer state and the occurence of high shape factors for the turbulent pressure fluctuations the focus was laid on the onshore measurements. With a probability of about 16 % a high-s_p^2 was found for unstable and neutral states (tab. 3). But at stable conditions high-s_p^2 was not observed. So it was concluded that the turbulent fluctuations of the pressure may deviate from a normal distribution at unstable or neutral boundary conditions but not at stable conditions.

4.3 Confidence considerations

To check our confidence in the above conclusion, possible errors were checked. Individual measurements at the onshore location were recorded at different hours and days, so they could be assumed to be random samples. The probability for the occurence of a high-s_p^2 event at unstable or neutral conditions was $\Phi_0 = 1/6$ and a binomial test was assumed.

Let us state the hypothesis that the probability for a high-s_p^2 event at stable state is the same as in unstable/neutral states. The hypothesis should be true, when one or more events occured, and false, when no events occured. For the twelve measurements at stable conditions this leads to a mean of 2 and the variance as $5/3$. The possibility for no events was $P = 0.112 = 11$ %. So we can reject the hypothesis of identical probabilities with a certainty of 89 %.

The confidence in the reliability of the assumed probability Φ_0 was checked. From the offshore measurements the probability for the occurence of high-s_p^2 was estimated to $\Phi_1 = 0.06$. Let us fomulate the hypothesis that the probability Φ_0 is correct. And we also state the alternative hypothesis that the probability is indeed lower than Φ_0 and the real probablility for the occurence of high-s_p^2 events is Φ_1. The 42 onshore measurements were used as the set of random samples, and the hypothesis would be rejected for less than four events. This assumptions lead to a probability of 6%, where $\Phi_0 = 1/6$ would be assumed to be true despite it was wrong. Also, the probability Φ_0 might be rejected despite it was true with a possibilty of 24

It could be concluded that onshore the probability for high-s_p^2 events was about 16 % with a confidence level of 96 %.

5 Conclusions

Highly resolved measurements of pressure and velocity for on- and offshore wind were investigated with respect to atmospheric boundary layer stability. It was found that high shape factors occur with about 10 % probability. Comparing on- and off-shore conditions the level of occurence seems to be almost doubled for the first case. All in all we notice the usefullness of the superposition-model of Castaing et al as was mentioned earlier by others [3].

Acknowledgements

We would like to thank the Germanischer Lloyd/Garrad Hassan (former WINDTEST) for their support in the measurements onshore and offshore. The Department of Physics at the University of Oldenbourg are thanked for their fruitful discussions and the testing of the sensors. Our thanks go also to the Deutscher Wetterdienst (DWD) for the provision of additional, local temperature data so that this study was possible. We thank the State of Schleswig-Holstein, Ministry for the Science, Economics and Transpoertation for funding this project with contract No. 122-09-023. The unknown referee gave valuable hints for improving the text.

REFERENCES

References

[1] G.K. Batchelor. Pressure fluctuations inisotropic turbulence. *Proc. Cam. Phil. Soc*, 47:359–374, 1951.

[2] C. Beck. Superstatistics in hydrodynamic turbulence. *Physica D*, 193:195–207, 2004.

[3] F. Böttcher, S. Barth, and J. Peinke. Small and large scale fluctuations in atmospheric wind speeds. *Stoch Environ Res Ris Asses*, 21(2):299 – 308, 2006.

[4] B Castaing, Y Gagne, and EJ Hopfinger. Velocity probability density functions of high reynolds number turbulence. *PHysica D*, 64(2):177–200, Jul 1990.

[5] A. Jeromin and A. P. Schaffarczyk. Advanced statistical analysis of high-frequency turbulent pressure fluctuations for on- and off-shore wind. In *EUROMECH Colloquium 528: Wind Energy and the impact of turbulence on the conversion process, Oldenburg, Germany*, 2012.

[6] A. Jeromin and A. P. Schaffarczyk. Statistische auswertungen turbulenter druckfluktuationen auf der off-shore messplattform fino3. Technical Report Report No. 78, in german, University of Applied Sciences Kiel, March 2012.

[7] A. Jeromin, A.P. Schaffarczyk, J. Puczylowski, J. Peinke, and M. Hoelling. Highy resolved measurements of atmospheric turbulence with the new 2d-atmospheric laser cantileaver anemometer. In *The Science of Making Torque from Wind 2012*, Oldenburg, Germany, October 9-11 2012.

[8] A. M. Obukhov. Turbulence in an atmosphere with a non-uniform temperature. *Boundary-Layer Metereology*, 2:7–29, 1971.

[9] M. Sathe, J. Mann, T. Barlas, W. Bierbooms, and G. van Bussel. Influence of atmospheric stability on wind turbine loads. In *The Science of Making Torque from Wind*, Oldenburg, Germany, 2012.

[10] K.R. Sreenivasan and B. Dhruva. Is there scaling in high-reynolds-number turbulence? *Pr. Theo.Phys. Supp.*, 130:103–120, 1998.

[11] H. Xu, T. Ouellette, D. Vincenzi, and B Bodenschatz. Accelleration correlations and pressure structure functions in high-reynolds number turbulence. *Phys. Rev. Lett.*, 99:204501,1–4, 2007.

WAKE MODEL EVALUATION METRICS AND THE VIRTUAL WAKES LABORATORY

RJ Barthelmie and SC Pryor
Atmospheric Science Program, Department of Geological Sciences, Indiana University
Email: rbarthel@indiana.edu

ABSTRACT
As evidenced by the recent development of IEA Wind Task 31 WAKEBENCH [1], there is a need to improve wake models for use in designing/operating large wind farms that are currently being built primarily offshore in Europe and on land in the USA. Establishing model credibility in a robust way is critically contingent on evaluation of model skill from a process-level perspective using appropriate, robust and reliable statistical metrics. Thus this paper will focus on providing:

1) A context for wake model evaluation that ensures models and measurements are being compared on an equivalent basis
2) A list of simple and readily quantifiable (robust) metrics to quantify discrepancies between measurements and models, and can diagnose model performance and serve to indicate whether model performance is improving
3) An open access resource of available/public data that can be used to develop and evaluate wake and wind farm models

1 Introduction

Challenges to evaluating wind turbine wake models are manifold. A number of potential approaches have been adopted in model evaluation studies including the use of case studies, and use of average composites, and any approach is likely a compromise between model type (statistical or prognostic), data availability and time constraints. Irrespective of the nature of the model evaluation exercise, model evaluation must be based on a quantitative metrics to objectively assess and diagnose model performance. Hence, in conjunction with the obvious need for robust frameworks under which to conduct model performance analyses, there is also a need for high quality data for use in model evaluation, such as are available from the open access on-line repository called the Virtual Wakes Laboratory. We describe this repository and provide example analyses based on these data with a focus on skill metrics and diagnostic analyses of wake models.

2 Observations

2.1 A context for wake model evaluation: Observational challenges

A major issue in quantifying wind turbine wakes and the physical controls on wake properties derive from challenges to making sufficiently precise and accurate measurements. Thus prior to discussing appropriate methods for wake model evaluation it is important to acknowledge some of the challenges to providing in situ measurements against which the models can be compared.
Given the velocity deficit in wakes is quantified by comparison with freestream conditions, one of the most important issues is correct characterization of the freestream wind and turbulence profile [2]. Additionally, the freestream flow will change over time or be non-homogeneous over the area of the wind farm [3]. Thus, despite the emphasis placed on accurate measurements of wind speed in wakes, the most important measurement by far is that of the freestream flow. Without an accurate freestream wind speed profile, all subsequent analysis will have uncertainties that are at least the equivalent of the uncertainty in the velocity deficit (except perhaps that of the near-wake under moderate wind speed conditions where the velocity deficit may be as much as 60% of the freestream wind speed at hub-

height [4]). Even in superficially homogeneous environments, given the scale of wind farms being built there is likely to be variability in the freestream wind speed across the wind farm. So in addition to capturing temporal variability that is introduced from situations such as the passage of fronts, spatial variability in the freestream wind speed must be incorporated into wake calculations. Gradients of wind speed in coastal areas [3] can introduce large-scale variability that is non-trivial and can even be of similar magnitude to more obvious inhomogeneities generated by complex terrain. Figure 1 illustrates the complexity of interpreting measurements from the first offshore wind farm located in Vindeby, Denmark. The mean wind speed distribution is mainly a function of the large scale synoptic flow with higher wind speeds from the southwest. The wind speed reduction at Sea Mast South (SMS) from wakes at 8.6 rotor diameters (D) from the single turbine 6E at 22º and from the row of turbines 1W to 5W at 320º is clear. However, in the absence of topography and impacts from wind turbine wakes it might be anticipated that the normalized wind speed would be equal to 1 in all wind directions. The large ratio of wind speeds at the SMS relative to the LM occurs for wind directions centered at approximately 85º and 220º which arise from the wind speed increase over the sea to SMS whereas the fetch to the land mast (LM) is over land. These kinds of gradients in wind speed at the coast can have an impact over much larger distances than the 2 km indicated here. Modeling and measurements from Nysted indicate gradients in hub-height wind speed extend and are detectable over at least 15 km, and further in stable conditions [3]. Thus over a large wind farm it is unlikely that even un-waked turbines (e.g. along the edge of an array) will experience a single inflow wind speed and turbulence profile. This issue is even more pronounced in complex terrain.

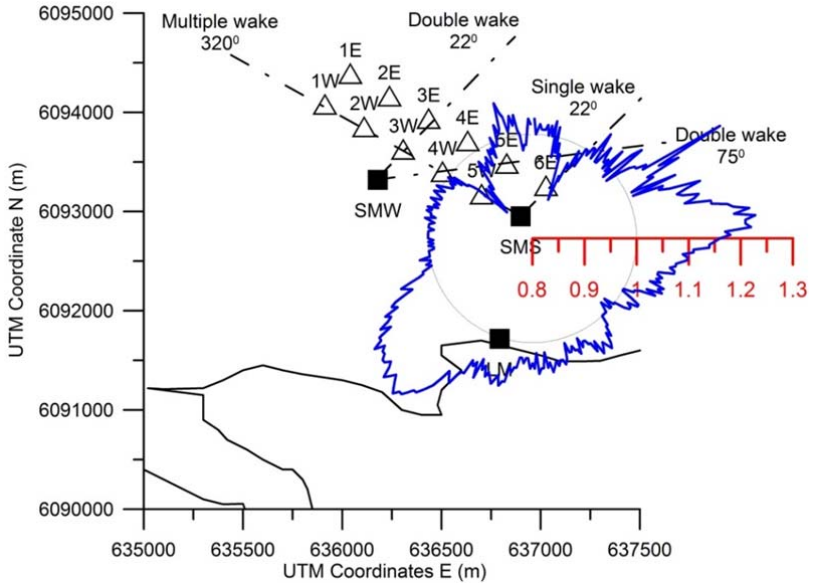

Figure 1. Hub-height (38 m) wind speed at Sea Mast South (SMS) normalized by wind speeds at the Land Mast for the period 1993-1996.

In addition to the freestream wind speed at turbine hub-height, wake behavior is also a function of the wind speed profile and turbulence intensity [5]. It has previously been demonstrated that vertical shear across the wind turbine blades not only influences the power production of a turbine [6] but the level of ambient turbulence is also a critical control on the transfer of momentum into the wake and thus the 'wake recovery' [5]. Recent improvements to remote sensing technologies have improved comparability of the resulting data to traditional anemometry for both wind speeds and turbulence [7-9], and offer the potential to obtain more vertical detail in profiles (of wind speed and turbulence) than can typically be obtained using instrumentation deployed on meteorological masts, and thus offer the potential for improved characterization of both freestream and wake conditions. However, there is need for further evaluation of these technologies to ensure data quality [10].

Given that the wind and turbulence characteristics in the wake are non-linear function of the wind turbine power and thrust coefficients (which are function of incident wind speed at turbine hub-height and the wind shear across the blades), for model evaluation exercises these must be known, bearing in mind that the onsite power curve may not be equivalent to the manufacturer's power curve. Realistically, the turbine power curve that is likely to be available to potential end users will likely be the manufacturer's power curve rather than the onsite power curve, although substantial deviations have been observed in the field [11] which may influence momentum extraction and turbine added turbulence intensity, and thus impact downstream wake behavior.
Further confounding issues to data interpretation and identification of appropriate initial and lateral boundary conditions for models arise from; (i) measurement errors in the wind direction (and thus the angle at which a wake impacts downstream turbines) or wind turbine yaw alignment errors and (ii) the role of atmospheric stability in dictating wake expansion and/or meandering. A frequent problem in use on in situ data for wake quantification is that wind direction measurements have bias issues (due to the difficulty of correctly aligning the direction measurement at installation on a meteorological mast), or that yaw measurements or the yaw control mechanism on individual turbines are imperfect. Alternatively the wind direction measurement (which typically derives from a wind vane) can drift over time, or under light wind speeds, the wind direction can change over the distance between the meteorological mast measurement and the turbine. As has been discussed previously [2] wake models typically assume one wind direction with no standard deviation of direction and hence overestimate wake losses because they focus on the wake center maximum velocity deficit, while the measurements contain directional variability due to stochastic effects in the atmosphere, and thus typically show a wider but shallower wake profile.

2.2 The Virtual Wakes Laboratory

A major bottle-neck confronting attempts to quantify the physical and dynamical controls on wind turbine wakes and to evaluate and improve wind turbine wake models (and wind farm models) is access to high quality observational data sets. The Virtual Wakes Laboratory (VWL) was designed to meet at least some of this need (Figure 2). The Virtual Wakes Laboratory is a freely accessible resource that currently contains wake and wind farm data that have been made available by a number of agencies. At present the VWL contains the data sets shown in Table 1 and can be accessed through: http://mypage.iu.edu/~rbarthel/Welcome.pdf. To gain access to the site potential users are required to register but there-after access to all data is provided.

Table 1. Data sets currently available in the Virtual Wake Laboratory

Type	Period	Site	Source	Reference
SCADA data for turbines with array presented as time series (2 data sets)	2001-2004	Middelgrunden	Middelgrunden Wind Turbine Cooperative	[11]
SCADA data for turbines with array presented as time series (2 data sets)	1996-2004	Vindeby	Originally from SEAS	[12, 13]
Case studies of wind and turbulence conditions in and out of wakes data collected with ship-mounted sodar	2001	Vindeby	ENDOW project	[14]
SCADA data for case studies of wake characteristics for specific wind direction and wind speed classes	2004-2006	Nysted	DONG/Vattenfall	[15]
SCADA data for case studies of wake characteristics for specific wind direction and wind speed classes	2005	Horns Rev	DONG/Vattenfall	[16]

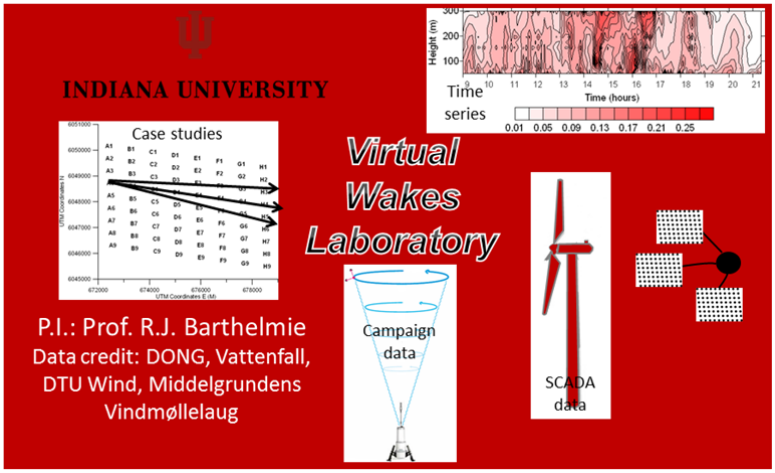

Figure 2. Interface for the Virtual Wakes Laboratory (http://mypage.iu.edu/~rbarthel/)

2.3 Model evaluation

Many previous wake model evaluation exercises have relied upon visual inspection of time series of velocity deficits downstream of wind turbines, but such analyses lack performance metrics and error attribution. A new approach is needed that addresses the following questions:

- What is the goal when comparing models with measurements?
- Which variables should agree, and to what level of precision and accuracy?
- What can or does the model simulate? Is this the same identical quantity under the same circumstances as is given in the measurements? If not, to what degree could they be expected to agree?
- Where models are shown to deviate from the observations, what types of model diagnostics can be undertaken to facilitate error attribution (and ultimately model improvement)?

In the following we present methods that can be applied to address at least some of the questions (see Table 2).

On the most fundamental level an individual wind turbine wake can be quantified using the following descriptors; the wake location (centerline), the wake magnitude (i.e. maximum velocity deficit at the centerline), and a wake width. Thus key evaluation metrics should include the wake depth (maximum velocity deficit for the wake center) at a given distance and the wake width (distance across the wake at which a reduction in the freestream wind speed can be detected) (Table 2 and Figure 3). Naturally, both metrics require that the freestream velocity profile is known. Since the normalized velocity will not be 1 in reality but might be lower or higher due to inhomogeneous in the flow or to wake 'shoulders' (over-speeding at the edges of wakes), it is necessary to set a threshold for recovery (that could be e.g. 95% of the freestream) that describes the 'wake edge'. A more systematic approach to determining wake metrics might be to assume a Gaussian distribution of velocity deficit and to determine the wake width and depth in terms of the standard deviation of distribution. If at a fixed point downstream from a turbine, one could define a wind direction associated with direct flow from the upstream wind turbine to the observational point. However, for slight variations in wind direction from this direction, the meteorological mast (or remote sensing volume) is impinged upon not by the centerline of the wake but a peripheral part of the wake, and thus by conditionally sampling the wind speed data for slight variations in the wind direction a picture such as that shown in Figure 3 can be developed. One standard deviation of wind direction around the centerline would contain 68% of observations inside the wake and correspond to a recovery of about 95% of the maximum velocity deficit at the center while two standard deviations would contain 95% of observations and about 0.99 of the maximum velocity deficit. Thus a robust estimate of true wake width can be derived.

Table 2. Wind turbine wake model evaluation. The first columns provides a summary of approaches for wind turbine wake model evaluation. The second column shows sample quantities that can be measured/modeled for comparison. The third columns summarizes statistical (skill) metrics to be used to quantify model-measurement agreement

Approaches	Quantities	Statistical Metric
Mean (time average)	Turbine power output	Standard deviation
Mean (statistics of similar cases)	Wind speed/turbulence intensity at hub-height	Root Mean Square Error
Case studies	Wake width and wake depth	Bias
Dynamic cases	Momentum deficits through the wind speed profile	Standard error

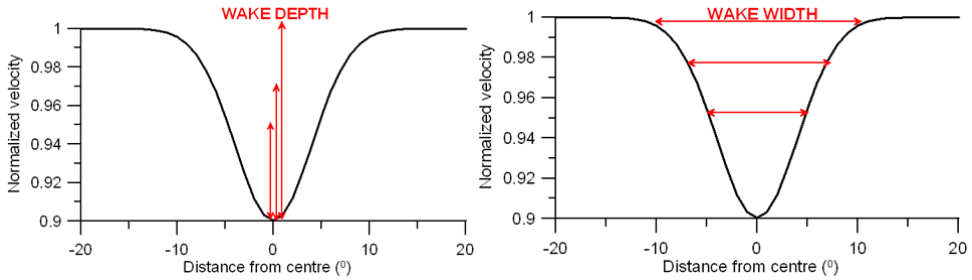

Figure 3. Possible wake model evaluation metrics - wake depth and wake width.

An alternative integrative metric for determining wake recovery is the momentum deficit at individual points across the wake or integrated across the wake (see example in Figure 4) [2].

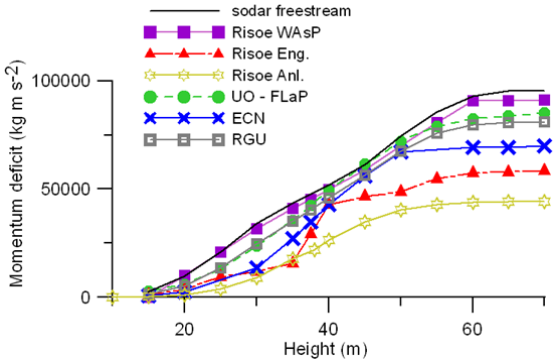

Figure 4. Comparison of the cumulative momentum deficit across the rotor plane for a single wake experiment (at 2.8 D downstream) in the Vindeby wind farm. In this analysis the freestream wind profile and the wake profile were measured using a boat-mounted sodar, and the models were initialized with the sodar derived freestream wind profile [2]. The measurements of the actual cumulative momentum deficit is shown by the curve denoted sodar freestream – where the same sodar was used to determine the freestream profile and the wake profile). The colored lines show momentum deficits computed from a variety of different wake models (with varying complexity). As shown, even at this short downstream distance some models under-predict the wake width and the momentum deficit, indicating too rapid wake recovery.

These types of evaluations provide a more systematic framework for wake model evaluation, are useful in terms of identifying model biases, and can be coupled with quantitative 'skill' metrics such as Root Mean Square Error if the comparisons can be undertaken across a range of – for example, wind speed classes, ambient turbulence intensity conditions etc. They can also be leveraged to more diagnostic approaches that can be used to attribute model error (or to diagnose the occurrence of

compensating errors). An example of this type of analysis is given below in the context of the components that contribute to an observed wake width and depth [17]. The actual wake width measured at some distance downstream from a turbine is comprised of contributions from; (i) the rotor diameter plus (ii) wake expansion (due to momentum transfer) plus (iii) meander (wind direction variability) (Figure 5). Quantifying these components rather than examining one wake width metric facilitates understanding of whether models are correctly parameterizing the components of wake width and therefore be more useful in terms of diagnosing the effectiveness of different parameterizations.

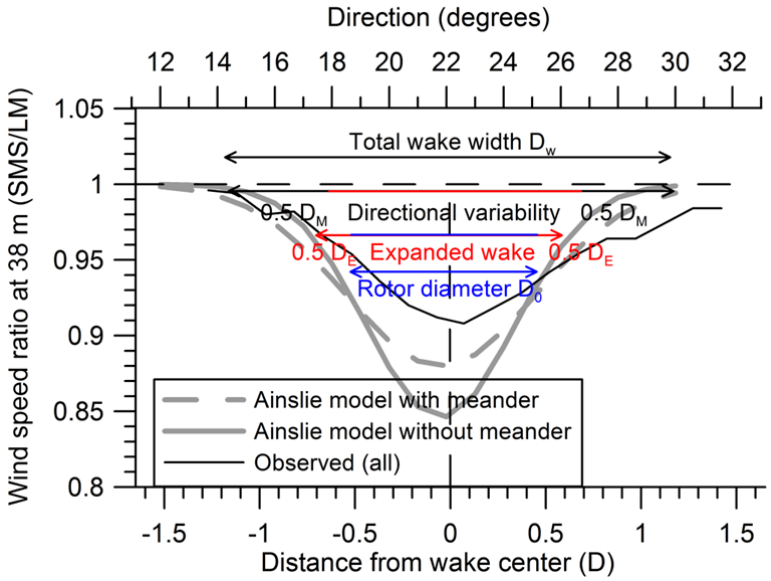

Figure 5. The ratio of wind speed at Vindeby mast SMS to mast LM by direction for the single wake (black line). Horizontal lines indicate the approximate contributions of the rotor diameter (D_0), wake expansion (D_E) and wake meandering (D_M) to the total wake width (D_W). The wake profiles of Ainslie [18] with and without wake meandering are shown in grey (Adapted from [17]).

The examples given above implicitly presume that the evaluation is cast in a framework where multiple case studies are conducted. That is each simulation is for conditions during a relatively short time window during which stationary can be assumed, and that these simulations are conducted for a realistic range of initial conditions (e.g. classes of wind speed, direction, ambient turbulence intensity, stability etc.). Obviously not all wake and wind farm models are suitable for this type of dynamic evaluation, for example some of the more parameterized models seek to describe the statistical properties of wakes rather than instantaneous realizations thereof, while some of the more computationally demanding models are more suited to a limited number of case studies than to producing large statistical ensembles. In either case we argue that a more quantitative approach is needed that does not simply compare, for example, the mean velocity deficit at the wake centerline, but includes some estimates of, for example, the standard deviation or the bias of model v. measurement agreement across a range of simulation conditions that can be objectively used to determine how closely models and measurements match.

When moving beyond evaluation of the simulations of individual wind turbine wakes, other approaches need to be adopted to evaluate wake models. Model complexes that take into account not only individual wakes, but wake-wake interactions and wind farm-atmosphere interactions are needed to fully capture the complexity of the flow fields [19]. Approaches to evaluating key aspects of models that capture wake-wake interactions include, but are not limited to:

(i) 'Down-a-row' (i.e. embedded wakes). In these analyses model-measurement comparisons have been conducted using a range of approaches to define the free-stream conditions, but then conditionally sampling by wind direction to select flow such that each turbine is in a direct wake of upstream turbine(s). The power output from each turbine is then normalized by the turbine that

experienced free-stream condition for comparison with wake models (e.g. [16]) compared with observations. Such comparisons are useful to assessing some aspects of wake-wake interactions, and represent a worst-case scenario in terms of wake related power-loss, but again are not trivial to interpret since the ambient data will always incorporate some directional variability within a wind speed class whereas most models assign zero directional variability.

(ii) Evaluation of overall wind farm efficiency [5]. In this approach the power produced over the entire wind farm can be integrated and compared to values from a wind farm model. This is useful in terms of perhaps best representing the apriori expectations for a given wind farm layout. However, in order to diagnose actual model performance it is necessary to disaggregate to individual turbines in order to determine whether the model is representing the actual power production gradients (and thus getting the right answer for the right reason). An example of the spatial variability of power output (normalized to the mean of all turbines within an array) is given in Figure 6 from Nysted, Denmark [20].

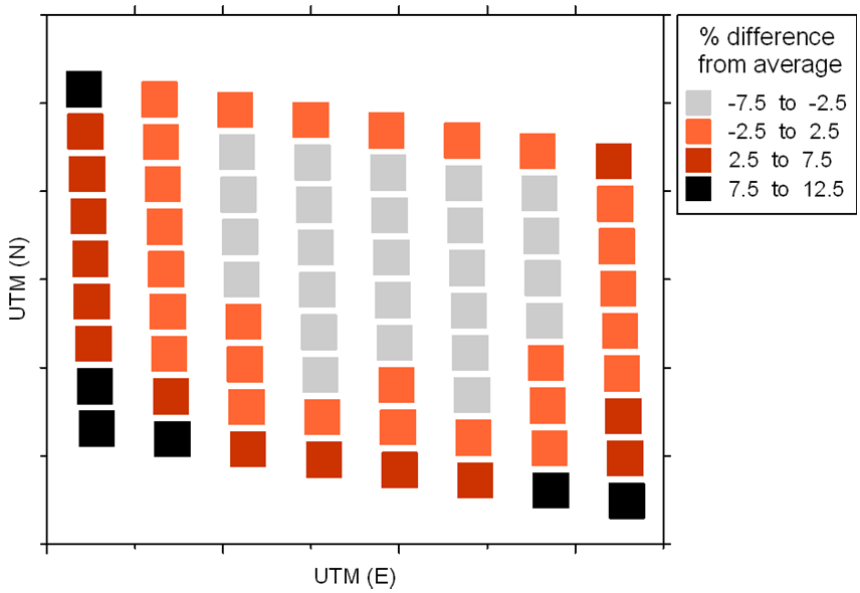

Figure 6. Example of the average wake losses by turbine from Nysted, Denmark, where the wake loss at each turbine is shown as the difference in power from the average for the whole wind farm (%) [20].

3 Summary

It is difficult at present to answer the question 'What is a successful outcome in terms of wake model evaluation?' or 'How much of the uncertainty is due to random noise rather than measurement or model error?' Until these questions can be addressed, wake modeling continues to be less quantitative than is needed to move forward in terms of optimization of wind farm layouts. This paper discusses the context for evaluating wake and wind farm models and measurements and focuses on moving away from visual inspection to defining a set of metrics that set out to describe and quantify model agreement with measurements based on a more systematic approach to the evaluation (e.g. as used in short-term forecasting). The paper advocates a greater focus on (i) dynamic studies, (ii) process-level experiments (and error attribution analyses) and (iii) quantitative metrics for model evaluation. As an aid to wake model evaluation the Virtual Wake Model Laboratory is described that is an open access resource that provides wake and wind farm data.

4 Acknowledgements

We would like to acknowledge funding from the National Science Foundation (#1067007), Dept. of Energy (#EE0005379), European Commission (EERA-DTOC 282797). Data in the Virtual Wakes Laboratory have been provided by DONG Energy, Vattenfall and Middelgrundens Vindmøllelaug.

5 References

1. Sanz Rodrigo, J. and P. Moriarty, *TASK 31. Benchmarking of wind farm flow models. Progress Report to ExCo 69. Trondheim May 22-24, 2012*, 2012.
2. Barthelmie, R.J., et al., *Comparison of wake model simulations with offshore wind turbine wake profiles measured by sodar.* Journal of Atmospheric and Oceanic Technology, 2006. **23(7)**: p. 888-901.
3. Barthelmie, R.J., et al., *Wind speed gradients in the coastal offshore environment: Issues pertaining to design and development of large offshore wind farms.* Wind Engineering, 2007. **31**(6): p. 369-382.
4. Whale, J., et al., *A study of the near wake structure of a wind turbine comparing measurements from a laboratory and full scale experiments.* Solar Energy, 1996. **56**: p. 621-633.
5. Barthelmie, R.J., K.S. Hansen, and S.C. Pryor, *Meteorological controls on wind turbine wakes.* Proceedings of the IEEE, 2012. **99**: p. 1-10. DOI: 10.1109/JPROC.2012.2204029
6. Wagner, R., et al., *Accounting for the speed shear in wind turbine power performance measurement.* Wind Energy, 2011. **14**(8): p. 993-1004.
7. Friedrich, K., et al., *Stability and turbulence in the atmospheric boundary layer: A comparison of remote sensing and tower observations.* Geophysical Research Letters, 2012. **VOL. 39, L03801**: p. doi:10.1029/2011GL050413, 2012.
8. Peña, A., et al., *Offshore Wind Profiling Using Light Detection and Ranging Measurements.* Wind Energy, 2009. **12**(2): p. 105-124.
9. Sathe, A., et al., *Can Wind Lidars Measure Turbulence?* Journal of Atmospheric and Oceanic Technology, 2011. **28**(7): p. 853-868.
10. Gottschall, J., et al., *Lidar profilers in the context of wind energy – A verification procedure for traceable measurements.* Wind Energy, 2012. **15**: p. 147-159.
11. Barthelmie, R.J., et al., *Modelling and measurements of power losses and turbulence intensity in wind turbine wakes at Middelgrunden offshore wind farm.* Wind Energy, 2007. **10**(DOI: 10.1002/we.238): p. 217-228.
12. Barthelmie, R.J., et al., *Meteorological aspects of offshore wind energy - observations from the Vindeby wind farm.* Journal of Wind Engineering and Industrial Aerodynamics, 1996. **62**(2-3): p. 191-211.
13. Frandsen, S., et al. *Measurements on and modelling of offshore wind farms*. 1996. 101 DOI: Risø-R-903(EN).
14. Barthelmie, R.J., et al., *Offshore wind turbine wakes measured by SODAR.* Journal of Atmospheric and Oceanic Technology, 2003. **30**: p. 466-477.
15. Barthelmie, R.J., et al., *Modelling and measuring flow and wind turbine wakes in large wind farms offshore.* Wind Energy, 2009. **12**(5): p. 431-444. DOI: 10.1002/we.348.
16. Barthelmie, R.J., et al., *Quantifying the impact of wind turbine wakes on power output at offshore wind farms.* Journal of Atmospheric and Oceanic Technology, 2010. **27**(8): p. 1302-1317.
17. Barthelmie, R.J. and S.C. Pryor, *Wake model evaluation using data from the Virtual Wakes Laboratory.* Applied Energy, 2013. **104**: p. 834-844.
18. Ainslie, J.F., *Calculating the flow field in the wake of wind turbines.* Journal of Wind Engineering and Industrial Aerodynamics, 1988. **27**: p. 213-224.

19. Frandsen, S., et al., *The making of a second-generation wind farm efficiency model-complex.* Wind Energy, 2009. **12**: p. 431-444.
20. Barthelmie, R.J. and L.E. Jensen, *Evaluation of power losses due to wind turbine wakes at the Nysted offshore wind farm.* Wind Energy, 2010. **13**: p. 573-586.

Wake modelling combining mesoscale and microscale models

J. Badger[1], P. J. H. Volker[1], J. Prospathospoulos[2], G. Sieros[2], S. Ott[1], P.-E. Rethore[1], A. N. Hahmann[1], C. Hasager[1]

[1]DTU Wind Energy, Frederiksborgvej 399, 4000 Roskilde, jaba@dtu.dk
[2]Centre for Renewable Energy Sources, 19th Km Marathonos Avenue, Athens, Greece

ABSTRACT

In this paper the basis for introducing thrust information from microscale wake models into mesocale model wake parameterizations will be described. A classification system for the different types of mesoscale wake parameterizations is suggested and outlined.
Four different mesoscale wake parameterizations are demonstrated in the Weather Research and Forecasting mesoscale model (WRF) in an idealized atmospheric flow. The model framework is the Horns Rev I wind farm experiencing an 7.97 m/s wind from 269.4^o. Three of the four parameterizations use thrust output from the CRESflow-NS microscale model.
The characteristics of the mesoscale wake that developed from the four parameterizations are examined. In addition the mesoscale model wakes are compared to measurement data from Horns Rev I. Overall it is seen as an advantage to incorporate microscale model data in mesocale model wake parameterizations.

INTRODUCTION

Presently there are two main types of turbine wake model. There are models which resolve individual wakes from a number of individual turbines, such as the wake model Fuga [1] and the CRESflow-NS model [2]. These models operate at rather fine resolution, on the order of metres, and thus are called microscale models. There are also models which model the collective impact of multiple wakes from several wind turbines. These are used in mesoscale models, and thus are called mesocale wake models, for example [3], and have resolution on the order of thousands of metres. Mesoscale models are used to calculate atmospheric flow and meteorological processes, they are routinely used in national and commerical weather centres for weather forecasting, and for wind resource assessment. Initially the two modelling approaches had little cross-over. In this paper however the cross-cover of information provided by the microscale to the mesoscale models is developed, demonstrated and evaluated.

The main objective of wake modelling in this paper is to capture correctly both the interaction of wakes on neighbouring downwind turbines, and the total wake effect of a wind farm, including the wake at long distances from the wind farm (the so-called mesoscale far wake).
For such a range of scales microscale and mesoscale models must be used together. The mesoscale model cannot explicitly model the individual turbines wakes, yet the microscale model alone cannot model influences of mesoscale circulations (at scales of several kilometres), such as coastal winds, convective systems, and orographic forced flow which may have a strong influence on the wake behaviour. The basic idea is that information from microscale wake models is passed in some form to the mesoscale models. Several strategies for how this can be done are set out in this paper.
The Weather and Forecast Research [4], WRF, a very widely used community mesoscale model, already has an implementation of a parameterization of wind turbine wakes [3]. This model applies a thrust, via the prognostic velocity tendency equation. The thrust is vertically distributed across model vertical levels proportional to the turbine rotor swept area over the model levels. In addition, turbines are parameterized as a turbulent kinetic energy source. The presence of wind turbines is expressed as a turbine number density per grid cell and rated power is prescribed. Exact turbine position is not needed and there is no interaction of one turbine wake on another turbine, within a grid cell, i.e. all turbines experience the same hub height wind speed. This parameterization will be denoted by WRF-WF.
A new wind turbine wake parameterization, called WRF-EWP [5], imposes a wind turbine wake velocity deficit which is vertically distributed according to a diffusion based model for wake expansion. The presence of wind turbines is determined by a turbine number per grid cell and power and thrust curves (i.e. power and thrust as funtion of hub-height wind speed) are employed. As in WRF-WF, exact turbine position is not needed and there is no interaction between turbines insider the same grid cell.
On the microscale side, for turbine wake modelling there are models such as CRESflow-NS [6][2], the amended GCL model [7], and FUGA [1]. These models work on actual wind turbine positions and account for wake impacts on downwind turbines. On the other hand, a spatially homogeneous and steady large scale wind forcing is assumed, i.e. the undistrubed flow surrounding the wind farm is uniform and constant.
By combining microscale wake models and mesocale models, the strengths of each can be complementing and the weaknesses of each mitigrating. In the next section, methods for combining microscale wake and mesoscale models will be described. This is followed by a section giving some results. The penultimate section discusses the results, future work and implications. The final section gives short conclusions.

METHOD

In this section four mesoscale model wake parameterizations will be compared. Three of the parameterizations use results from the microscale model CRESflow-NS [6][2]. The basis for including the microscale model results in the mesoscale parameterization is universal and thus can be used with any other microscale model.

The model simulations' set-up is designed to provide a simple way of comparing the behaviour of the different parameterizations. The WRF (v3.4) mesoscale simulations for all parameterizations are run using an idealized model set-up with wind speed of 7.97 m/s and direction 269.4^o at hub height (70 m above surface level). The details of this idealized WRF set-up can be found in [5]. The model horizontal grid spacing is 2240 m. The domain covers 180 x 65 km in the horizontal, from surface to 10 km in the vertical, using 40 model levels in the vertical. Near the surface the vertical spacing between levels is of order 10s of meters. The wind farm set-up that generates the wakes is that of Horns Rev I, off the west coast of Denmark. The wind farm contains 80 Vestas V80 wind turbines each with a rated capacity of 2 MW. The farm configuration is a slightly rhomboidal array with 10 rows from west to east and 8 rows from south to north. The turbine spacing is 560 m.

In general it is possible to classify the wake parameterization in two types according to where the thrust information, creating the wakes, comes from. For type I, the turbine thrusts come from the mesocale parameterization itself, i.e. from turbine thrust curves. For type II, the turbine thrusts come from a microscale model, precalculated and passed to the mesoscale parameterization in some way.

Within type II there are two ways the turbine thrusts can be expressed. For type IIA the thrust is given as a single turbine thrust value with no information about its distribution in space. For type IIB, the whole flow field is available and via momentum theory the effective distribution of thrust for a given volume can be obtained. Type IIB has some special issues which will be discussed in a later part of the paper.

Within Type IIA and IIB there are different ways to aggregate the turbine thrusts. It can be done either by summing up the thrusts on the basis of the mesoscale grid cells, type IIA/Bi, or by summing up thrusts on the basis of the whole wind farm, type IIA/Bii. The type IIA/Bii was used in Prospathopoulos and Chaviaropoulos [2].

Next, it is possible to consider how the sub-mesoscale-grid scale vertical wake expansion is handled. The horizontal resolution of the mesoscale model is 2240 m in this study. The wake will develop within this distance, however, there is no means within the mesoscale model, that this can be modelled, due to lack of resolution. Therefore, this sub-grid scale process needs to be parameterized or addressed in some way. In this paper, only two methods are examined. The first uses a diffusion based vertical wake expansion. It is written up in detail in [5]. The second method actually neglects sub-mesoscale-grid vertical expansion. In this case the turbine thrusts are distributed across mesoscale model levels according to the swept area of the turbine rotor on each model level, as in [2].

Table 1 describes the four wake parameterization compared in this paper. The first WRF-EWP has been described in full in [5]. It serves as a reference parameterization here. The other parameterizations feature the inclusion of the microscale model CRESflow-NS results. For WRF-CRES-EWP the turbine thrusts are aggregated on the basis of the mesoscale grid. It features the sub-mesoscale-grid vertical wake expansion used within WRF-EWP. For WRF-CRES-ROTOR the aggregation basis is the same as WRF-CRES-EWP, but no sub-mesoscale-grid wake expansion is included. For WRF-CRES-ROTOR-FA, there is no sub-mesoscale-grid wake expansion and the aggregation basis is the whole wind farm (along the wind direction axis).

In practice, all the parameterizations, except WRF-CRES-ROTOR-FA, impose a thrust on 6

Parameterization	thrust calculation	vertical thrust distribution	aggregation
WRF-EWP	turbine thrust curve	diffusive wake expansion	meso grid aggr.
WRF-CRES-EWP	CRES	diffusive wake expansion	meso grid aggr.
WRF-CRES-ROTOR	CRES	proportional to rotor swept area per level	meso grid aggr.
WRF-CRES-ROTOR-FA	CRES	proportional to rotor swept area per level	wind farm aggr.

Table 1: Table summarizing the different wake parameters tested in this paper.

mesoscale grid points (3 along wind direction x 2 normal to wind direction), covering the horizontal extent of the farm. Whereas for the WRF-CRES-ROTOR-FA parameterization thrust is imposed on 2 grid points (1 along wind direction x 2 normal to wind direction).
Figure 1a provides a schematic view of the how the parameterizations are constructed. The rectangular boxes represent a vertical slice of a mesoscale grid cell containing three wind turbines. The vertical extent of the rectangular box contains a number of vertical model levels. The microscale model explicitly models the wake from each turbine and the interaction of wakes on downstream turbines. Thus the turbine thrusts will not necessarily be the same. This is a departure from the wake parameterizations of type I, where the turbine thrusts within a single mesoscale grid cell will be the same.
Next, Fig. 1 shows that for the mesoscale parameterization each turbine is treated separately, the turbine is placed in the centre of the grid cell, and the thrust distribution across vertical model levels is calculated. The grid point total thrust is the sum of the individual vertically distributed thrusts.
Figures 1b and 1c shows the difference in the vertical distribution of the thrust using the rotor distribution and the diffusion based vertical wake expansion. Note that for the wake expansion, the wake length is always half the grid point spacing. In the wake expansion case, it can be seen that the thrust also determines the degree of vertical wake expansion. This is because the scale parameter for the vertical wake expansion is determined by a sub-grid scale wind velocity, as well as the horizontal grid size and the rotor diameter.
In Fig. 2 plan view of the same turbines as in Fig. 1 is shown. The square box represents a mesoscale grid cell. The microscale model explicitly models the horizontal expansion of the wake from the same three turbines. However, the evolution of the horizontal characteristics of the wake cannot be retained in the mesoscale model. A single value of thrust for each model level for each grid point must be reached in the parameterization.

RESULTS

In Figure 3 the wake characteristics in the horizontal and vertical can be seen for the different parameterizations. The two parameterizations using the diffusive vertical wake expansion, WRF-EWP and WRF-CRES-EWP (Figs. 3a and 3b) are rather similar. The minimum wind speed obtained is approximately 6.8 m/s in the downwind portion of the wind farm. The horizontal extent of the wake is slightly longer for WRF-EWP. The vertical profile of velocity deficit is also similar between WRF-EWP and WRF-CRES-EWP, with the 0.8 m/s deficit reaching

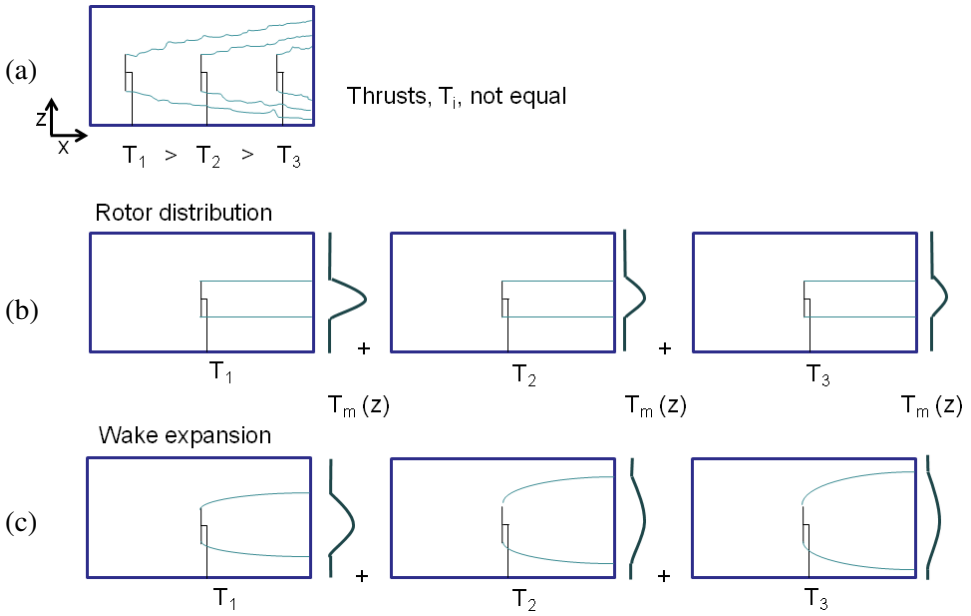

Figure 1: Schematic diagrams showing (a) the vertical expansion wake from three wind turbines of the same type calculated by a microscale model where the wind is blowing from the west (left) to east (right). Thrusts are calculated, and due to wakes effects on the downwind wind turbines, the thrust decreases as one moves eastwards. Schematic diagrams in (b) and (c) show how the microscale model calculated thrust can be used inside a mesoscale model. In (b) the thrust is distributed proportional to the swept area of the rotor on the mesoscale model vertical level. In (c) the thrust is distributed according to a vertical wake expansion contained in the wake parameterization scheme. In both cases there is no interaction between the turbines. It is as if the turbines were each in their own seperate mesoscale grid cell. The total thrust is the addition of the three separate vertical distributions of thrust.

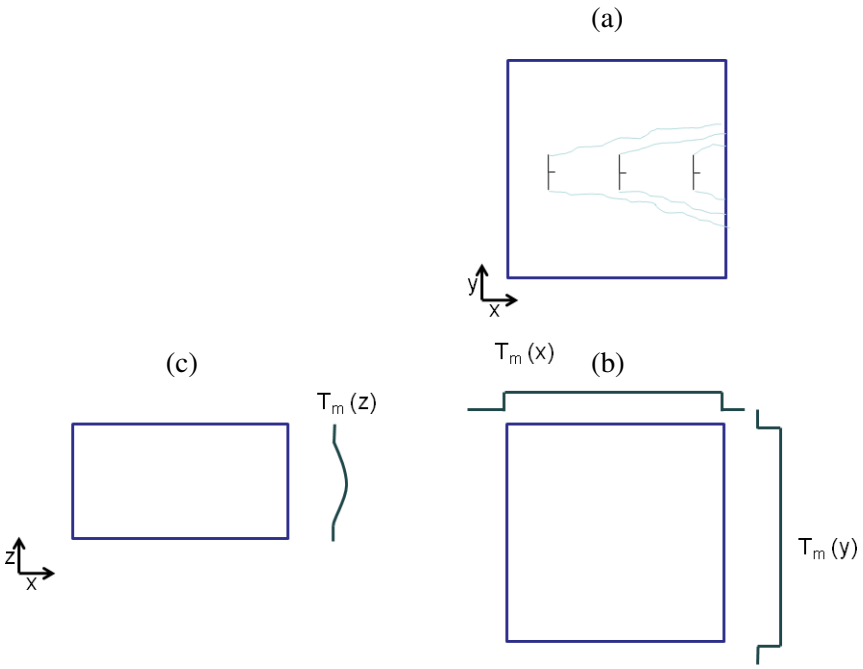

Figure 2: Schematic diagram showing (a) the horizontal expansion of wakes from the same 3 wind turbines shown in Fig. 1, calculated by a microscale model where the wind is blowing from the west (left) to east (right). The schematic diagrams in (b) and (c) illustrate that within the mesoscale grid cell the vertical distribution can be resolved (b), however the horizontal distibution cannot (c). Note: For mesoscale models, typical horizontal grid spacing is 1000s of metres, and vertical level spacing is 10s of metres near the surface.

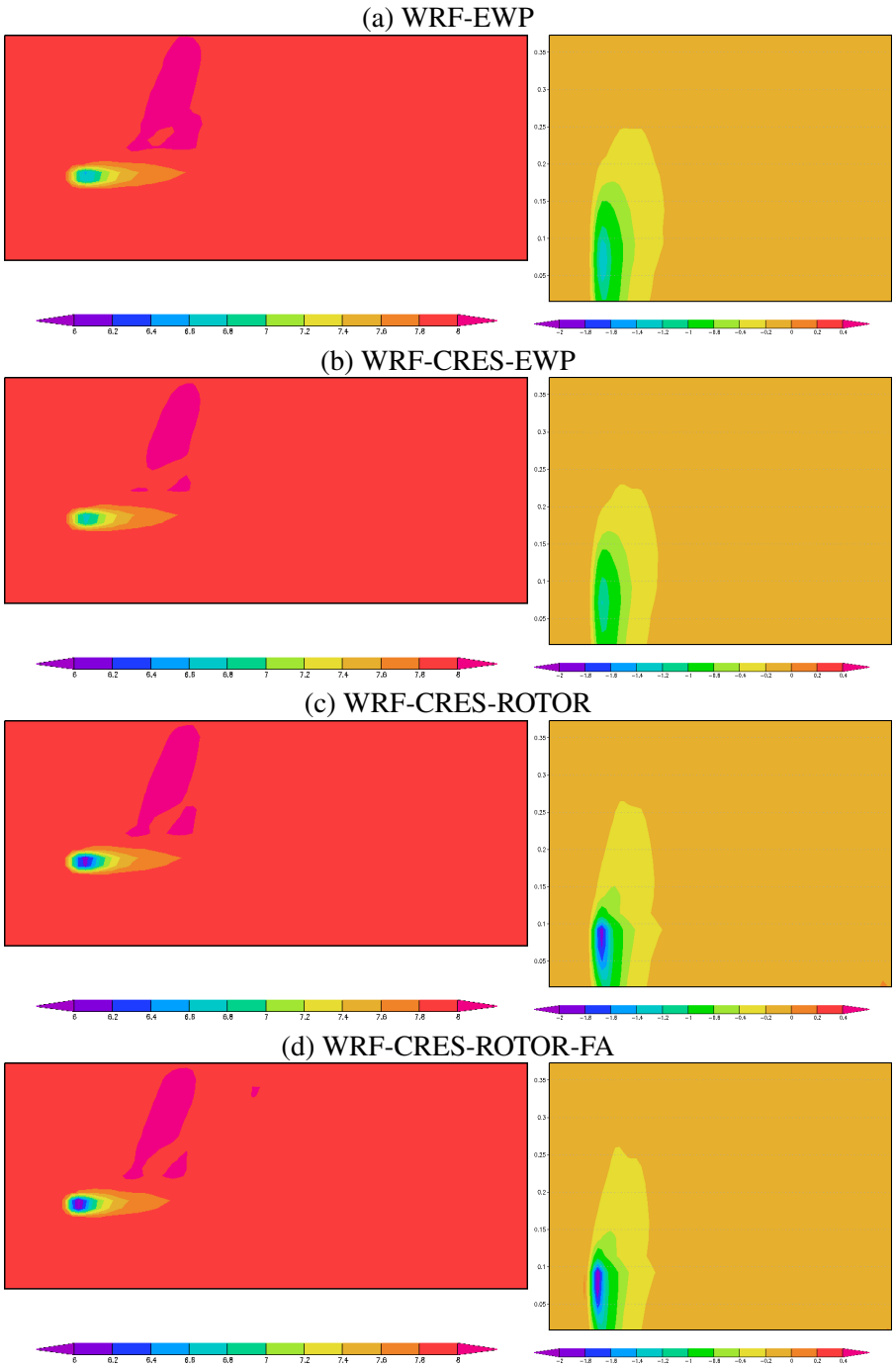

Figure 3: Plots giving maps of wake (left) and vertical sections of wake velocity deficit (right) for simulations having an inflow westerly surface wind of 8 m/s using different wake parameterizations, (a) WRF-EWP, (b) WRF-CRES-EWP, (c) WRF-CRES-ROTOR (d) WRF-CRES-ROTOR-FA. The wake maps (left) show the westerly component of wind speed at 70 m above surface level. The x-axis has 180 km extent and the y-axis has 65 km extent. The vertical sections of wake velocity deficit (right) are a slice through the wind farm. The x-axis extent is 180 km, the vertical extent is from 0 – 350 m above surface level.

approximately 150 m above surface level. However the WRF-EWP wake has a slightly large vertical extent.
For the two parameterizations using the vertical thrust distribution proportional to rotor swept area per level (i.e. no vertical wake expansion), WRF-CRES-ROTOR and WRF-CRES-ROTOR-FA, the minimum wind speed obtained is approximately 6.2 m/s and 6.0 m/s respectively. However the horizontal wake extent is shorter than for the diffusive vertical expansion parameterization. The shortest wake is for the WRF-CRES-ROTOR-FA parameterization. The vertical profile of velocity deficits are markedly different compared to WRF-EWP and WRF-CRES-EWP. The deficit exceeds 1.8 m/s in both cases, a little higher in the WRF-CRES-ROTOR-FA parameterization. However, the 0.8 m/s deficit reaches only 120 m above surface level. Consistent with the neglect of a sub-grid scale vertical wake expansion, it can be seen the deficit is more concentrated in the vertical in the WRF-CRES-ROTOR and WRF-CRES-ROTOR-FA parameterizations.
The difference between the mesoscale grid aggregation and wind farm aggregations parameterizations can be assessed by comparison of the WRF-CRES-ROTOR and WRF-CRES-ROTOR-FA results. The main differences are seen in the proximity of the wind farm, but further downwind the differences are reduced.
In Figure 4 the results from the mesoscale model parameterizations are compared with the measurements from the wind farm. The measurements are for wind speed within the range 7.5 – 8.5 m/s and wind direction within the range 255–285^o. The measurements are described in more depth in [8][5]. In Fig. 4 the wake wind speed deficit can be seen inside the farm at each turbine row and downstream of the wind farm at anemometers M6 and M7.
Considering WRF-EWP (Fig. 4a) as the reference [5], we can see that WRF-CRES-EWP (Fig. 4b) gives a slighly smaller wake deficit. Both parameterizations show good agreement with the measurement data, and lie well within the error bars. Considering next WRF-CRES-ROTOR (Fig. 4c), it can be seen that the wake deficit is large inside the wind farm, on the lower bounds of the error bars of the measurement data. Downwind of the wind farm, the difference compared to WRF-EWP is less pronounced, however the velocity deficits are still larger. Considering WRF-CRES-ROTOR-FA (Fig. 4d), it can be seen that inside the wind farm the deficit is very strong, below the lower bounds of the error bar. Downwind of the wind farm the difference is much reduced and agreement with measurement at masts M6 and M7 is good.

DISCUSSION

The differences in the wake simulations for the Horns Rev wind farm in this idealized set-up can be used to examine the characteristics of the various parameterizations.
The advantage of using turbine thrust information based on microscale modelling is that complex aspects of turbine interactions can be captured. For example, the difference in the behaviour between WRF-EWP and WRF-CRES-EWP is mainly due to the reduced turbine thrusts in the WRF-CRES-EWP parameterization.
The sub-mesoscale-grid vertical wake expansion is a necessary feature to capture the wake behaviour inside the wind farm and the near wind farm wake (c.f. WRF-CRES-EWP and WRF-

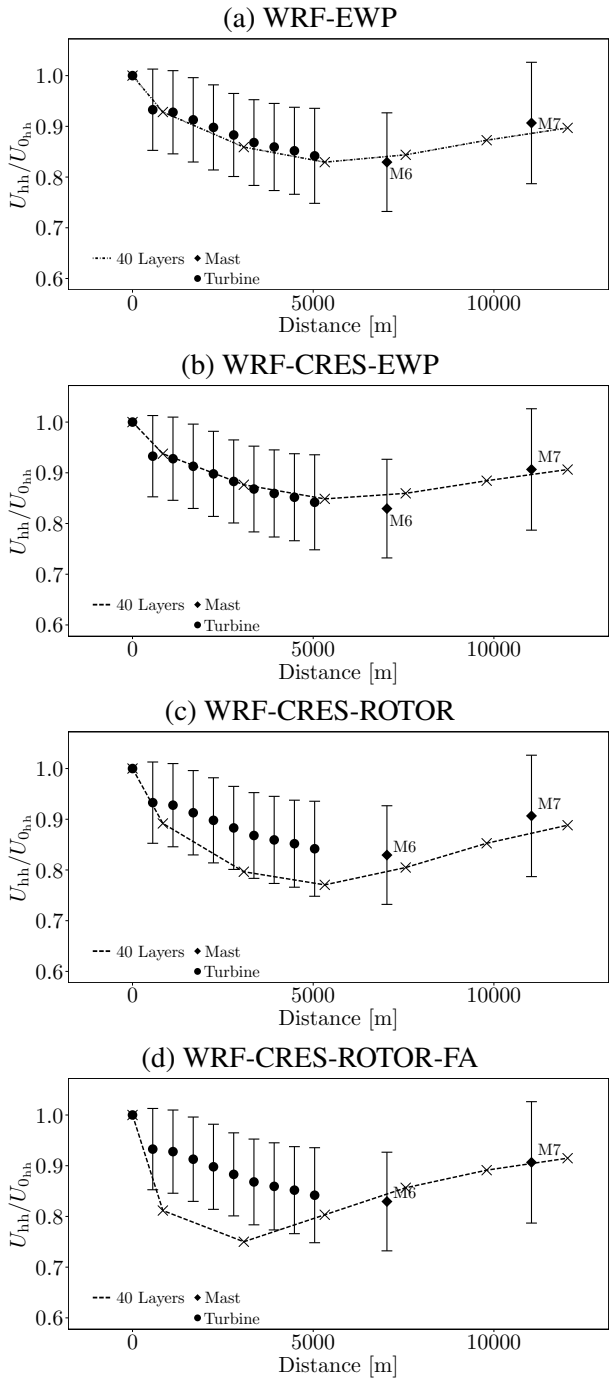

Figure 4: Recovery validation plots for different parameterizations used, (a) WRF-EWP, (b) WRF-CRES-EWP, (c) WRF-CRES and (d) WRF-CRES-FA. The x-axis is the distance in metres from the first turbine row, the y-axis is the wake horizontal wind speed expressed as a fraction of the inflow wind speed, both at 70 m above surface level, i.e. for first row turbines the value is 1. The black dots are measurements based on wind turbine power or from anemometers at mast 6 (M6) and mast (M7) downwind of the wind farm.

CRES-ROTOR). Without the vertical wake expansion the wake deficit tends to be too concentrated in the vertical, and associated with that, have too strong a deficit.
However, moving downwind of the wind farm into the far wake, the difference caused by including sub-mesoscale-grid vertical wake expansion, or not, becomes much less pronounced. In the far wake it is the mesoscale model that determines the wake and the initial vertical distribution of the wake becomes of less importance.
Aggregating the turbine thrusts according to the mesoscale grid or wind farm extent, has a large impact on the mesocale modelled wake within the wind farm. When imposing the thrust of the wind farm at 2 grid points rather than 6 grid points, the maximum wake deficit is too large compared to measurements. However, moving downwind of the wind farm, the model wake agrees well with measurement. It remains a question to what extent it is neccessary or beneficial to impose the wind farm thrust at few grid points.
Earlier in the paper it was stated that momentum theory can be used to determine the distribution of thrust associated with vertical wake expansion. This has the advantage that a model for the vertical wake expansion would no longer be required. However, there is a complication, if the wind farm covers several mesoscale grid cells. In that case, the inflow and outflow velocities of the grid cells, could be used to determine wake related thrust, but would include the effects of the continued expansion of wakes caused by turbines upwind of the grid cell in question. This is a problem, because the mesoscale wake parameterization should only address the representation of wakes caused by turbines in a single grid cell. The mesoscale model should thereafter alone deal with the developement of the wake downwind of the grid cell where the wakes originated.
It is for these reasons that a whole wind farm aggregation has some benefits, because in that case the application of momentum theory would be for a volume which envelops all turbines, and there would be no risk of double counting wakes by the microscale and mesoscale models.
A promising future development along these lines is the application of the FUGA microscale model [1]. In this model the application of momentum theory to determine wake thrust aggregated over mesoscale grid cells is possible because it is a linearized model, and a velocity deficit can be directly attributable to turbines in a single grid cell, even though there are developing wakes present from turbines in upwind grid cells.
In this paper only a single wind speed and wind direction is used, however the approach is readily extendable to any wind speed and direction by precalculating tables of turbine thrusts, for a number of wind speeds and directions. This data can be stored in a look-up table. Then within the parameterization the correct thrust data is retrieved depending on the mesoscale grid point wind speed and direction. However, a complication arises here. For unsteady mesoscale situations, the parameterization will be drawing from microscale model results, which assumed steady and unform flow situations. The impact of this mismatch needs to be addressed.
In the future, the mesoscale model also can provide upstream information such as wind speed (sheer), direction (veer or backing) and Richardson number for the microscale models. An extension of the cross-over between the two modelling scales is the application mesocale variability of conditions in the microscale models. For example, within a very large wind farm there may be significant variation of mesoscale wind conditions (speed and direction). This information, which can be provided by mesocale models, could be used in the microscale modelling of wakes, which at present assume a homogeneous mean wind speed and direction.

CONCLUSIONS

In this paper the basis for introducting thrust information from microscale wake models into mesocale model wake parameterizations was described. Different types of mesoscale wake parameterizations were outlined.
Four different mesoscale wake parameterizations were used in the mesoscale model WRF in an idealized atmospheric flow configutation. Three of the four parameterization used thrust output from the CRESflow-NS microscale model. The characteristics of the mesoscale wake that developed from the four parameterization was examined. In addition the mesoscale model wakes were compared to measurement data from Horns Rev. Overall it is seen as an advantage to incorporate microscale model data in mesocale model wake parameterizations.

ACKNOWLEDGMENTS

The authors wish to thank funding from the project EERA DTOC FP7-ENERGY-2011-1/ Number 282797, and from the WAUDIT programme (financed by Marie Curie ESR-FP7), which made this study and article possible. DONG Energy is thanked for providing the data for Horns Rev I. Kurt Hansen, DTU Wind Energy, is thanked for discussion and provision of analysed measurement data.

REFERENCES

[1] Ott, S., Berg, J., Nielsen, Morten, ”Linearised CFD Models for Wakes”. Technical Univ. of Denmark, Risoe National Lab. for Sustainable Energy. Wind Energy Div. Risoe-R-1772(EN) ISBN 978-87-550-3892-9. Available online.

[2] Prospathopoulos, J. M. and Chaviaropoulos, P.K., ”Numerical simulation of offshore wind farm clusters”, European Wind Energy Association, Conference proceedings 2013.

[3] Fitch, A., Olson, J., Lundquist, J., Dudhia, J., Gupta, A., Michalakes J., and Barstad, I.., ”Local and mesoscale impacts of wind farms as parameterized in a mesoscale NWP model”, Monthly Weather Review, 2012.

[4] Skamarock, W., Klemp J., Dudhia J., Gill, D., Barker, D., Duda M., Huang X., Wang W., and Powers, J,., ”A Description of the Advanced Research WRF Version 3”, NCAR Technical note, 2008.

[5] Volker P. J. H., Badger J., Hahmann A. N., Ott S. "Implementation and Evaluation of a Wind Farm Parametrisation in a Mesoscale Model", to be submitted to Boundary Layer Meteorology.

[6] Chaviaropoulos, P. K. and Douvikas, D. I., "Mean-flow-field Simulations over Complex Terrain Using a 3D Reynolds Averaged NavierStokes Solver," Proceedings of ECCOMAS 98, 1998, Vol. I, Part II, pp. 842-848

[7] J.W.M. Dekker, J.T.G. Pierik (Editors), "European Wind Standards II", ECN-C–99-73, 1999.

[8] Hansen, K. "WP1.1 Wake model performance validations Horns Rev offshore wind farm." Report: Eera-Dtoc, 2013.

High-fidelity simulation comparison of wake mitigation control strategies for a two-turbine case

P. Fleming[1], P. Gebraad[2], S. Lee[1], J.W. van Wingerden[2], K. Johnson[1], M. Churchfield[1], J. Michalakes[1], P. Spalart[3], P. Moriarty[1]

[1]National Renewable Energy Laboratory, Golden CO, USA, paul.fleming@nrel.gov
[2]Delft University of Technology, Delft, The Netherlands, J.W.vanWingerden@TUDelft.nl
[3]Boeing Commercial Airplanes, Seattle WA

Abstract

Wind turbines arranged in a wind plant impact each other through their wakes. Wind plant control is an active research field that attempts to improve wind plant performance by modifying individual turbine controllers to take into account these turbine-wake interactions. In this paper, we use high-fidelity simulations of a two-turbine fully-waked scenario to investigate the potential of several wake mitigation strategies. The strategies, including modification of yaw and tilt angle, as well as repositioning of the downstream turbine, represent a mix of known and novel approaches. The simulation results are compared through change relative to a baseline operation in terms of overall power capture and loading on the upstream and downstream turbine.

1 Introduction

Wind turbines influence nearby turbines aerodynamically as they extract energy from and enhance turbulence in the wind. Recently, wind turbine control systems researchers examined how these influences can be accounted for and adjusted such that increased wind power plant efficiency and reduced turbine loads can be obtained. Often in the literature, this is done by adapting the axial induction of individual turbines through pitch and torque control, [1, 2, 3]. In these methods, an axial induction factor is found that results in lower individual turbine power for an upstream tower, but higher plant power due to increased power capture by downstream turbines.

An alternative approach to wind plant control focuses instead on redirecting wakes around downstream turbines. One method of achieving this redirection that has been published in the literature is through intentional yaw misalignment in an upstream turbine. In [4] field-tests are carried out in a scaled wind plant test field, whereas in [5], computational fluid-dynamics (CFD) simulations are performed using actuator disk models of a wind turbine.

In this paper, we describe two-turbine simulation experiments of wake redirection based wind plant control using a high-fidelity wind plant simulator, the NREL SOWFA (Simulator for Off/Onshore Wind Farm Applications) tool [6]. SOWFA, described in Section 2, couples a computational fluid dynamics (CFD) solver with the aero-elastic turbine simulator FAST [7]. Using SOWFA, controllers can be compared in terms of their effects on power production and loading of upstream and downstream turbines. This is an important capability since a controller's effects on power production must be weighed against its effects on turbine loads.

In addition to evaluating the yaw misalignment method, we also introduce two additional concepts. First, we modify the tilt angle of an upstream turbine in order to redirect the wake vertically. The second method does not redirect the wake but instead repositions the downstream turbine (in the case of floating turbines), as proposed in [8]. Additional analysis of the yaw and tilt methods can be found in [9], which analyzes the ability of a single turbine to redirect the wake.

The control methods are evaluated using a simulation of two 5MW turbines, 7 rotor diameters apart, aligned in a turbulent inflow. For each method, the setpoint (yaw misalignment angle, tilt angle or downstream turbine position) is varied, and a 1000 second simulation is run. Additionally, because these techniques might move the downstream turbine from full wake to partial wake, which induces loading [10], we consider the cases where the downstream turbine is and isn't using independent pitch control (IPC) to mitigate uneven distribution of wind speed across the rotor plane. The results are compared in terms of total power output and key component loads on both the upstream and downstream turbine across all cases.

The contributions of the paper are: (1) the addition of a new method for wake-redirection wind plant control, using adaptation of the rotor tilt angle (with [9]), (2) an analysis and comparison of three methods of wind-plant wake mitigation using a high-fidelity simulator in terms of power and loading of an upstream and downstream turbine, and (3) an investigation into the use of IPC for mitigating the effects of partial wake on turbine loads.

The remainder of this paper is organized as follows. Section 2 provides an overview of the simulation tool SOWFA used in this work. Section 3 provides a description of the simulation scenario in terms of dimension, inflow properties, turbine properties and individual control laws. Section 4 presents and analyzes the results of the study. Section 5 provides some discussion points and considerations for future work. Finally, the conclusions are given in section 6.

2 SOWFA

In this work, a parametric study of the proposed control actuation methods is performed using a high-fidelity tool: Simulator for Off/Onshore Wind Farm Applications (SOWFA) [6] which is a large-eddy simulation (LES) framework coupled with NRELs aero-elastic turbine code [7] for studying wind turbines embedded in the atmospheric boundary layer (ABL). The kernel of the LES framework is based on open-source OpenFOAM libraries [11] which solves the in-

compressible Navier-Stokes equations augmented with a buoyancy term (based on Boussinesq approximation) and Coriolis acceleration to simulate atmospheric boundary layers under various conditions. The transport of potential temperature is solved in parallel to account for buoyancy. This set of governing equations are discretized over an unstructured finite volume mesh with second order central differencing scheme. The collocated formulation of the velocity and pressure variables is decoupled using the Rhie-Chow [12] interpolation method to avoid numerical instability. The time advancement method follows the predictor-corrector pressure-implicit splitting operation (PISO) of Issa [13] with three sub-step iteration to maintain second order accuracy. The Moeng model [14] is adapted to estimate the local time-varying shear stress. The sub-grid scale (SGS) turbulence closure employs the standard Smagorinsky [15] formulation with a constant of 0.135.

The turbine blades are represented by the actuator line (AL) method of Sørenesen and Shen [16], in which the blades are discritized along the radial line where the lift and drag forces are computed based on the incoming flow and the airfoil geometry at the actuator points. These force vectors are projected on to the computational domain space using a three-dimensional Gaussian filter which, as a collective whole, produce the wake structures similar to those from blade-geometry resolved simulations at significantly reduced computational cost. In SOWFA, the incoming flow velocity data at the actuator points from the flow solver are fed into FAST, from which the computed aerodynamic lift and drag forces and the shifted actuator points (caused by the blade deflections) are projected on to the momentum equation as a body force term completing the two-way coupling cycle. The structural loading responses induced by the aerodynamic forces are collected as FAST outputs which are later presented in this study. Further details on SOWFA can be found in [17].

With SOWFA, simulations of proposed wind plant control schemes can be analyzed. Because the simulation includes high-fidelity modeling of the atmosphere, and the turbine structure, it is possible to study simultaneously a controller's impact on power and turbine loads.

3 Experimental setup

As described in the introduction, the objective of the paper is to compare three strategies of wake mitigation (yaw-misalignment based, tilt-misalignment based and repositioning of the downstream turbine) using SOWFA. To this end, an "open-loop" two-turbine simulation study is performed in which the yaw, tilt, and position setpoints are swept and held fixed for separate 1000 second simulations with constant wind direction. Later research will develop active closed-loop control strategies for time-varying wind directions.

A scenario was developed to simulate two NREL 5-MW baseline turbines [18] in turbulent inflow. The turbulent scenario is that of a neutral boundary layer, selected based on a previously published study. [17] The inflow is generated in a precursor atmospheric LES on a domain that is 3 km by 3 km in the horizontal and 1 km in height. The horizontally-averaged wind speed is driven to 8 m/s at the turbine hub height and is controlled through a time-varying mean driving

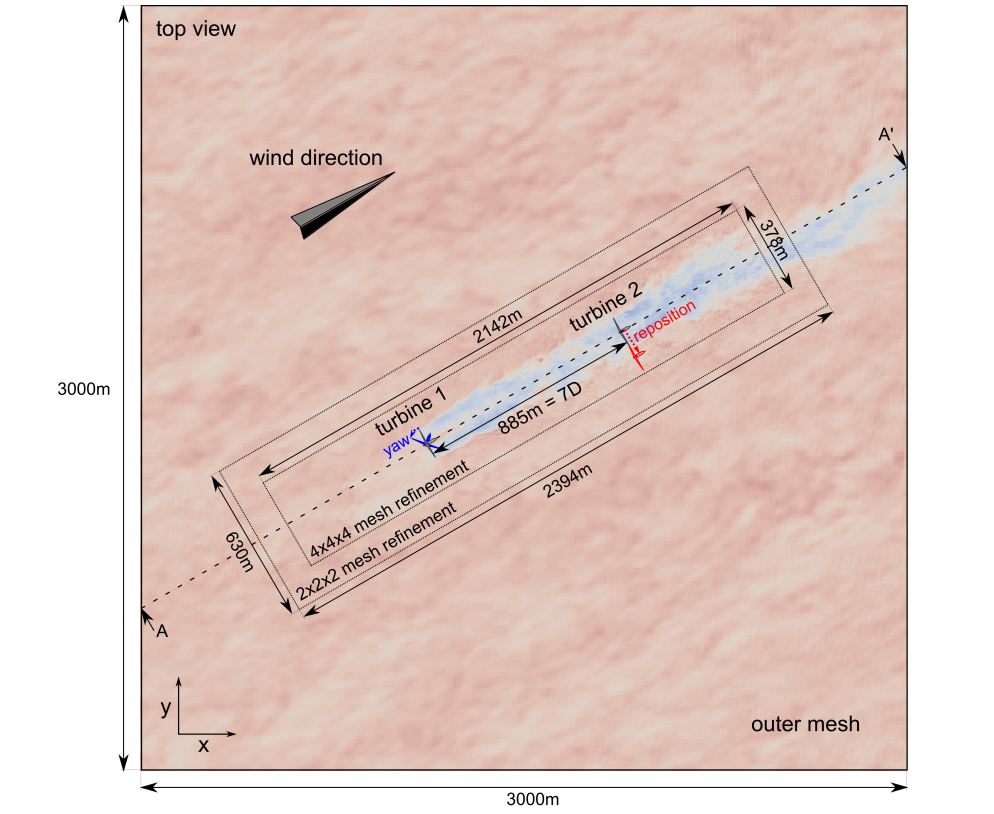

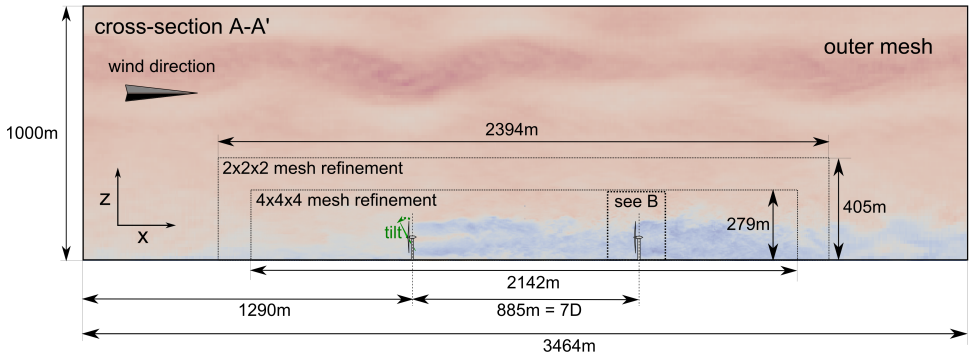

Block mesh generation for OpenFOAM CFD solver

	number of cells	size of cell
outer mesh:		
x-direction	250	12m
y-direction	250	12m
z-direction	83	12.05m

In a 2394 x 630 x 405 m box surrounding the turbines, the cell sizes are halved in x,y and z direction, and halved again in a 2142 x 378 x 279 m box, yielding:
- cell size in the inner mesh: 3m x 3m x 3m
- total number of cells: 14,921,616

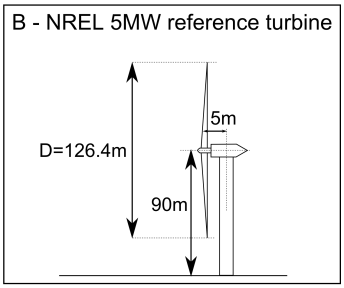

Figure 1: Overview of the experimental setup in the baseline case.

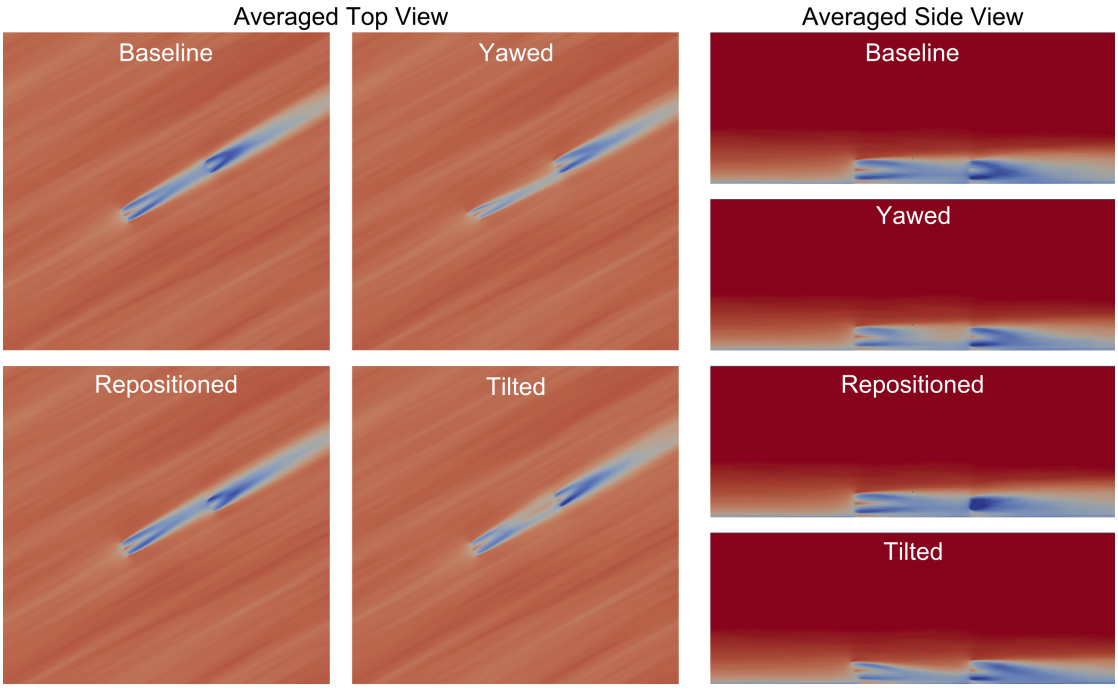

Figure 2: Example velocity fields for different wake redirection methods, generated by SOWFA.

pressure gradient. The wind comes from the southwest (300°) so that the elongated turbulent structures in the surface layer are not ”trapped” by the periodic boundaries, continually cycling through in the same location. In the baseline case, the turbine rotor axis is aligned with the wind direction. The surface temperature flux is set to zero, although a capping inversion initially at 750 m above the surface is used both to slow boundary layer growth and because it is a real feature of atmospheric boundary layers. The surface aerodynamic roughness is set to 0.001 m, which is typically of flow over water. Details on positioning of the turbines and meshing of the domain are given in fig. 1.

Screenshots from time averaged slices of the flow for the different control strategies is provided in fig. 2. SOWFA requires significant computational power in order to run high-fidelity simulations: using a sample time of 0.02s, the time steps take an average 2.5s to calculate on the Sandia/NREL Red Mesa supercomputer [19] using distributed computation with 256 processors. This yields an execution time of 34.4h for each simulation.

In each case, the turbines use the baseline controller defined in [18]) independently. Because wake redirection can move the downstream turbine from full wake to partial wake, inducing loads [10], we compare the use of IPC with the standard collective pitch control by switching on load-reducing IPC on the downstream turbine for the last 400s of the simulation. The IPC implementation is based on the design first presented in [20], using the parameters as specified in [21], with some adaptations to be able to use the load-reducing IPC in below-rated conditions.

A supervisory wind plant controller [22] collects the data from the individual turbines.

4 Results and Analysis

Following completion of the runs, the data was collected from each case and post-processed as follows. First the 1000s of time domain data for each was broken into segments. The first 200s of each run was discarded since the wake was not fully developed. The last 100s were also discarded due to system problems on the cluster leaving some files incomplete. Finally, the remaining time histories were divided into 200s-600s, in which the downstream turbine is not running IPC, and 700s-900s, when it is and the IPC startup transients have vanished. Although it should be possible to start IPC smoothly, since the transition was not our research focus we ramp it on rather abuptly. In the baseline case, IPC is never enabled, to provide a basis for comparison.

From these two blocks of time (200-600s and 700-900s), several metrics are computed. First, the average power is computed for each turbine. Next, loads are computed for blade out-of-plane (OOP) bending, drivetrain torsion, tower bending and yaw bearing moment. In the case of the tower load, a combined load is computed from the separate fore-aft and side-side loads using a root-sum-square combination. This is likewise done to combine the separate M_y and M_z loads on the yaw bearing. Individual loads are provided in the appendix. For each of these load signals, a damage equivalent load (DEL) is computed. The DEL is a standard metric of fatigue damage (see [23]). These results are summarized in figs. 3 and 4.

Fig. 3 shows the comparison of methods in the case where the downstream turbine does not use IPC. For each method, there is a sweep across possibles setpoint (yaw angle, tilt angle or reposition of downstream turbine position). The top row shows the total power output of each case, with the horizontal line indicating the baseline level and the numbers above each bar denoting percent change from the baseline case. The remaining rows of the figure indicate percent change in DEL for the components examined.

Starting with yaw-based control, in the best case the method shows an increase in power of 4.6%. Additionally, the simulation shows that for the upstream turbine with misaligned yaw, significant load reduction is observed for blade OOP bending, tower bending and yaw bearing moment. The downstream turbine however experiences a rise in blade OOP bending, drivetrain torsion and yaw bearing moment. This change is most likely due to the movement from full to partial wake overlap.

In the tilt case, a maximum power gain of 7.1% is observed. At this peak of power capture, it is seen that for the upstream turbine, the blade and yaw bearing loads have gone up while the drivetrain and tower loads have declined a small amount. As in the yaw case, the downstream turbine experiences an increase in blade loads, most likely due to partial-wake overlap. There is also a decrease in tower loads and increase in yaw bearing loads.

Tilt misalignment shows larger potential power production improvements than yaw when con-

Figure 3: Summary of results of two tubine simulation. The 3 columns are divided by control action. The top row shows the combined power output for each case, compared to the baseline case on the far left. The remaining rows indicate the percent change in load compared to the baseline.

sidering large positive tilt angles. With a positive tilt angle, the rotor would face downwards, and for conventional upstream turbine designs this would cause the blades to hit the tower. Therefore, a positive tilting mechanism is more suitable to downwind turbines [24]. Both negative and positive tilt angles will redirect the wake away from the downstream turbine rotor, but the positive tilting has the advantage that it will redirect the wake towards the ground, allowing high velocity air from higher altitudes to flow towards the upper part of the downstream rotor, resulting in a higher power production of the downstream turbine. Additional details on the wake displacements that can be achieved using yawing or tilting can be found in [9].

Repositioning of (floating) turbines produces the most substantial gains in power if the rotor of the downstream turbine is moved more than 25 meters out of the rotor axis of the upstream turbine (up to 41% improvement when the downstream turbine is moved a full rotor diameter). Observing the loads for the downstream turbine, there is little change for small changes in position, significant change for the discplacements yielding partial overlap, and then no change again when the turbine is moved a full rotor diameter.

Looking at the loads across experiments, the upstream turbine either sees an increase or decrease in blade OOP bending, depending on the angle chosen. Also, for the upstream turbine, yaw and tilt angle adjustments either decrease or minimally increase the drivetrain, tower and yaw load. A possible explanation for this effect is that these methods generally reduce the power capture of the upstream turbine, and derating can be considered as a load mitigation strategy. For the downstream turbine, all loads generally increase somewhat, and this is most likely due to moving from full to partial wake overlap.

Fig. 4 performs the same analysis, but now for the case where the downstream turbine is using IPC to mitigate the effect of partial wake overlap. Note that these results are based on 200s of simulation versus 400s in Fig. 3, and are from a different point in the simulation. The results are dramatic: the blade loads, tower loads and yaw bearing loads are consistently reduced when compared to the baseline case (which does not use IPC). The drivetrain loads are the exception, but the lack of a clear pattern indicates that perhaps this is a somewhat stochastic load. Missing from the current controller is a drivetrain damper, a very common element in industrial controllers that could be used to minimize the changes in drivetrain loads. Overall, the results indicates a very strong motivation for the use of IPC, in general, and as a way to eliminate the negative impacts of using wake-mitigation strategies.

The appendix provides the full results listed in absolute values (not relative to baseline).

5 Discussion

It is important to acknowledge the shortcomings of this current work. First, due to computational/time constraints, current results are based on simulations of only one inflow case. Future work will combine results from simulations using multiple wind inputs and better establish the robustness of these results. Additionally, the experiments are not of a closed-loop control, but

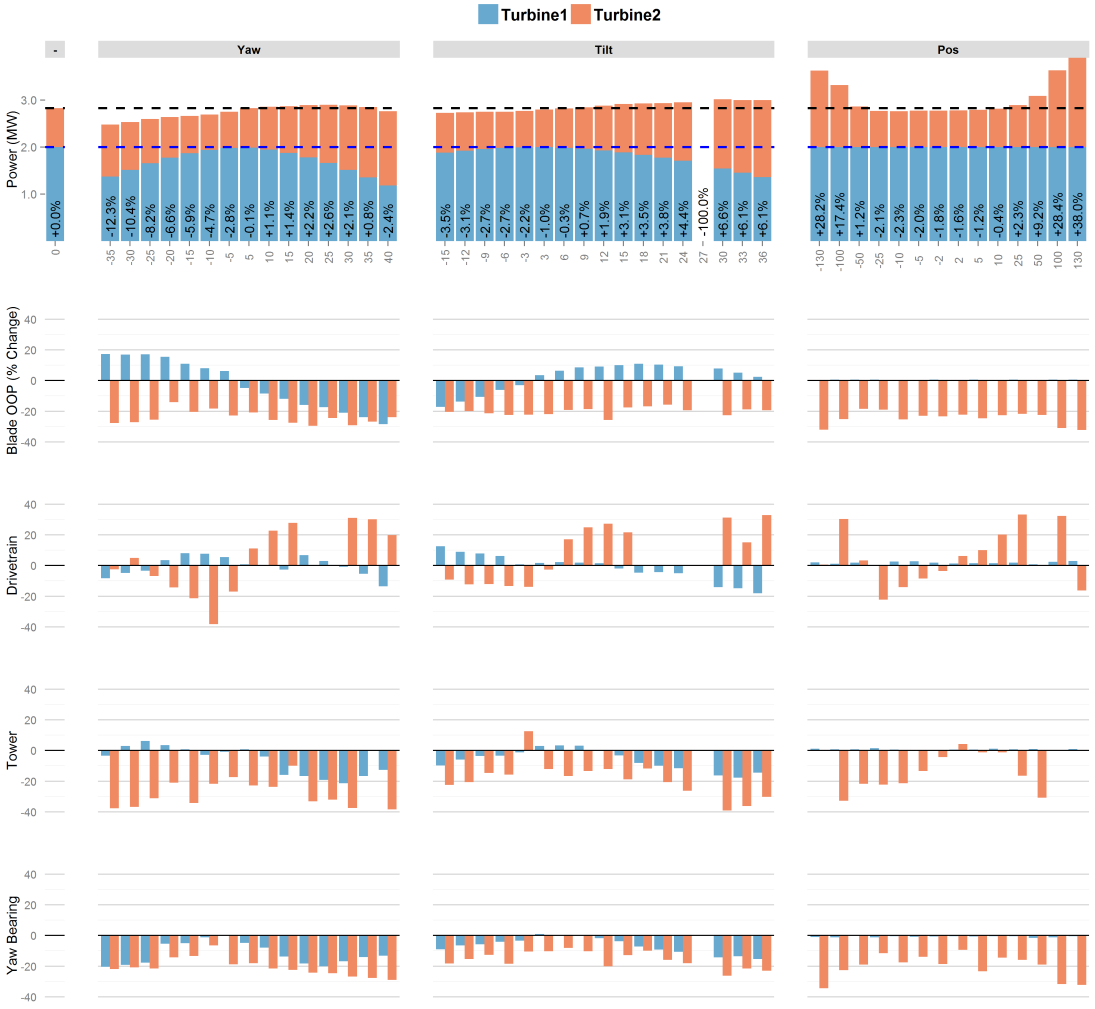

Figure 4: Comparison of data as in fig. 3, however with the downstream turbine operating with IPC in all cases except for the baseline. Note that due to system problems, one case is missing but will be present in final version.

of settings that take advantage of a stationary wind direction. This is a good first step, but in order to be applicable to real wind plants, future work must establish control loops which can accomplish similar results for changing wind direction conditions.

6 Conclusions

This report shows very good potential for all methods considered. For each case, operating points exist which couple improved power capture with, mostly, reduced loading. It is important to point out though that presently, the technology only exists to implement yaw misalignment. However, given that tilt and repositioning are capable of yielding more power capture, perhaps the effects could be considered in the design of future turbines. A second result of the paper is the very good potential of employing IPC to mitigate partial wake effects. This improves the benefit of the wake redirection or repositioning techniques by reducing the partial-wake-induced loads on the downstream turbine.

Acknowledgements

The authors are very grateful to Wesley Jones and the NREL High Performance Computing team for their crucial help and support in completing this simulation study.

This work was supported by the U.S. Department of Energy under Contract No. DE-AC36-08GO28308 with the National Renewable Energy Laboratory and by the NWO Veni Grant no. 11930 Reconfigurable floating wind farm.

References

[1] P.M.O. Gebraad, F.C. van Dam, and J.W. van Wingerden. A maximum power point tracking approach for wind farm control. In *Proceedings of The Science of Making Torque from Wind*, 2012.

[2] K.E. Johnson and G. Fritsch. Assessment of extremum seeking control for wind farm energy production. *Wind Engineering*, 36(6):701–716, 2012.

[3] J.R. Marden, S.D. Ruben, and L.Y. Pao. Surveying game theoretic approaches for wind farm optimization. In *Proceedings of the 50th IEEE Conference on Decision and Control*, volume 38, pages 584–596, 2012.

[4] J.W. Wagenaar, L.A.H. Machielse, and J.G. Schepers. Controlling wind in ECN's scaled wind farm. In *Proceedings of EWEA*, 2012.

[5] Á. Jiménez, A. Crespo, and E. Migoya. Application of a LES technique to characterize the wake deflection of a wind turbine in yaw. *Wind energy*, 13(6):559–572, 2010.

[6] M. Churchfield and S. Lee. NWTC design codes (SOWFA). `http://wind.nrel.gov/designcodes/simulators/SOWFA`, 2013.

[7] J. Jonkman. NWTC Design Codes (FAST). http://wind.nrel.gov/designcodes/simulators/fast, 2012.
[8] J.W. van Wingerden. Reconfigurable floating wind turbines, VENI project no. 11930, 2011.
[9] P. Fleming, P. Gebraad, S. Lee, J.W. van Wingerden, K. Johnson, M. Churchfield, J. Michalakes, P. Spalart, and P. Moriarty. Evaluating techniques for redirecting turbine wake using SOWFA. In *Proceedings of ICOWES*, 2013.
[10] Z. Yang, Y. Li, and Y.E. Seem. Improved individual pitch control for wind farm turbine load reduction via wake modeling. In *Proceedings of AIAA*, 2011.
[11] OpenFOAM, the open source CFD toolbox. http://www.openfoam.com/, 2013.
[12] C.M. Rhie and W.L. Chow. Numerical study of the turbulent flow past an airfoil with trailing edge separation. *AIAA Journal*, 21:1525–1532, 2012.
[13] R.I. Issa. Solution of the implicitly discretised fluid flow equations by operator-splitting. *Journal of computational physics*, 62(1):40–65, 1986.
[14] C.H. Moeng. A large-eddy simulation model for the study of planetary boundary layer turbulence. *Journal of the Atmospheric Sciences*, 41(13):2052–2062, 1984.
[15] J. Smagorinsky. General circulation experiments with the primitive equations. *Monthly Weather Review*, 91(3):99–164, 1963.
[16] J.N. Sørensen and W.Z. Shen. Numerical modeling of wind turbine wakes. *Journal of Fluids Engineering*, 124(2):393–399, 2002.
[17] M.J. Churchfield, S. Lee, J. Michalakes, and P.J. Moriarty. A numerical study of the effects of atmospheric and wake turbulence on wind turbine dynamics. *Journal of Turbulence*, 13(14):1–32, 2012.
[18] J. Jonkman, S. Butterfield, W. Musial, and G. Scott. Definition of a 5-MW reference wind turbine for offshore system development. Technical report, NREL/TP-500-38060, 2009.
[19] NREL's high-performance computing capabilities. http://www.nrel.gov/energysciences/csc/high_performance_computing_capabilities, 2009.
[20] E.A. Bossanyi. Controller for 5MW reference turbine. Technical report, Garrad Hassan and Partners Limited, 2009.
[21] I. Houtzager. *Towards Data-Driven Control for Modern Wind Turbines*. PhD thesis, Delft University of Technology, 2009.
[22] P. Fleming, P. Gebraad, J.W. van Wingerden, S. Lee, M. Churchfield, A. Scholbrock, J. Michalakes, K. Johnson, and P. Moriarty. The SOWFA super-controller: A high-fidelity tool for evaluating wind plant control approaches. In *Proceedings of EWEA*, 2013.
[23] M. Buhl Jr. MCrunch theory manual for version 1.00.
[24] Andrew Scholbrock. Private conversation.

Appendix

Table 1: Full results table

Case	Power (MW)			OOP Bending (kNm)		Drivetrain (kNm)		Fore-Aft (kNm)		Side-Side (kNm)		Yaw M_y (kNm)		Yaw M_z (kNm)	
	T1	T2	Total	T1	T2	T1	T2	T1	T2	T1	T2	T1	T2	T1	T2
Baseline	1.7	0.8	2.6	738.8	982.5	183.3	269.6	5382.3	11589.4	2529.5	5595.1	1083.6	1856.9	1121.6	1829.2
T1 yaw = -35°	1.2	1.2	2.4	913.3	1133.9	159.5	347.8	5247.1	10472.9	1964.4	4244.0	915.0	1519.2	913.8	1535.1
T1 yaw = -30°	1.3	1.1	2.4	905.8	1152.5	164.6	327.6	5412.3	9407.3	1347.3	5139.2	925.2	1484.6	949.8	1798.7
T1 yaw = -25°	1.4	1.0	2.5	886.7	1124.8	181.0	309.2	5504.9	11803.0	1264.3	5529.3	988.3	1812.6	982.3	1700.9
T1 yaw = -20°	1.5	0.9	2.5	873.2	1081.6	182.5	331.3	5446.8	14530.8	1465.8	6492.8	1021.6	1715.1	1005.2	1840.4
T1 yaw = -20°	0.9	2.5	848.4	1026.4	171.5	291.9	5323.0	12024.4	1411.8	5568.5	1036.9	1666.6	1041.4	2043.5	
T1 yaw = -10°	1.7	0.8	2.5	798.9	981.1	188.5	281.6	5221.8	11252.3	1758.0	5338.6	1062.4	1642.1	1079.8	1873.8
T1 yaw = -5°	1.7	0.8	2.5	781.1	1018.0	178.9	254.8	5192.6	15435.1	2145.4	7366.2	1072.9	1639.4	1107.4	1871.1
T1 yaw = 5°	1.7	0.9	2.6	705.8	1042.1	181.5	291.3	5425.9	13374.9	2927.8	7635.2	1050.7	1733.7	1134.4	1676.2
T1 yaw = 10°	1.7	1.0	2.6	678.6	1044.4	181.6	301.9	5360.1	11023.9	3435.5	5038.3	1039.3	1503.3	1120.4	1698.2
T1 yaw = 15°	1.6	1.0	2.6	649.3	1105.9	180.0	282.7	5146.6	11553.1	3679.8	4731.9	1013.6	1641.8	1121.8	1551.5
T1 yaw = 20°	1.5	1.1	2.7	642.1	1123.2	180.9	302.3	4677.1	11762.3	4174.0	5284.8	973.7	1533.6	1095.9	1675.3
T1 yaw = 25°	1.4	1.2	2.7	628.8	1136.9	177.4	344.2	5020.8	9839.3	4720.7	5275.7	928.8	1509.7	1046.0	1771.4
T1 yaw = 30°	1.3	1.3	2.7	607.6	1104.5	167.7	381.2	4327.6	11043.2	5120.2	5663.7	888.7	1608.3	980.6	1721.3
T1 yaw = 35°	1.2	1.4	2.6	609.6	1080.7	160.7	355.2	4097.8	10525.8	5183.9	5293.0	858.6	1396.3	947.2	1756.4
T1 yaw = 40°	1.0	1.5	2.5	598.9	1059.7	150.7	366.1	4965.4	10523.8	5989.8	5422.0	852.2	1470.8	899.2	1701.3
T1 tilt = -15°	1.6	0.9	2.5	620.2	908.4	197.3	244.5	5380.7	9632.7	2908.4	4557.4	1085.8	1548.4	1078.6	1829.6
T1 tilt = -12°	1.6	0.9	2.5	645.5	916.5	195.9	233.6	5404.2	11291.2	2702.8	4660.6	1063.0	1644.4	1089.3	1815.6
T1 tilt = -9°	1.7	0.9	2.5	657.5	967.0	190.1	232.9	5649.4	11467.2	2523.8	5328.9	1076.3	1761.2	1108.1	1789.5
T1 tilt = -6°	1.7	0.9	2.5	695.4	970.6	193.9	251.5	5454.0	10910.2	2446.4	5733.0	1082.2	1944.8	1130.6	1845.2
T1 tilt = -3°	1.7	0.8	2.5	722.1	979.9	186.4	252.7	5453.2	13100.4	2508.4	6115.3	1078.1	1804.4	1136.4	1701.6
T1 tilt = 3°	1.7	0.9	2.6	760.9	1032.6	178.1	286.8	5278.6	12021.9	2450.7	5834.5	1074.4	1766.1	1094.6	1814.5
T1 tilt = 6°	1.7	0.9	2.6	783.4	1043.4	174.1	294.2	5237.4	12492.4	2665.4	6288.1	1060.8	1571.3	1082.5	1667.6
T1 tilt = 9°	1.7	0.9	2.6	803.6	1137.3	175.7	328.4	5223.9	12350.6	2588.9	6018.5	1019.6	1704.2	1035.5	1655.4
T1 tilt = 12°	1.6	1.0	2.6	806.6	1203.6	176.0	339.3	5187.5	12808.0	2480.8	5902.0	993.1	1540.5	1000.2	1695.6
T1 tilt = 15°	1.6	1.0	2.7	817.8	1226.3	180.0	332.3	5311.1	12819.7	2506.9	5002.5	975.4	1466.2	966.0	1630.0
T1 tilt = 18°	1.6	1.1	2.7	827.2	1292.1	172.7	279.6	5597.0	11633.0	2688.8	4992.8	953.8	1489.2	922.6	1841.3
T1 tilt = 21°	1.5	1.2	2.7	822.3	1265.1	188.1	292.3	5383.3	13218.3	3143.5	4837.8	931.0	1443.2	895.0	1829.0
T1 tilt = 24°	1.5	1.2	2.7	838.8	1282.3	185.4	267.1	5224.5	10089.3	3315.6	5340.7	913.6	1466.6	859.5	1731.2
T1 tilt = 27°	1.4	1.3	2.7	831.3	1297.2	181.0	287.3	5121.4	9331.2	3703.5	4665.5	871.9	1533.3	826.3	1847.7
T1 tilt = 30°	1.3	1.4	2.7	812.2	1270.2	170.0	303.7	5149.2	9415.0	3569.6	4779.3	859.9	1443.1	778.9	1840.8
T1 tilt = 33°	1.3	1.5	2.7	811.3	1222.6	157.7	269.1	5121.8	9900.1	3587.1	4478.2	846.3	1485.5	755.0	1928.3
T1 tilt = 36°	1.2	1.6	2.7	785.1	1212.3	145.9	255.9	5105.4	9205.0	4157.1	3859.6	812.0	1519.0	704.6	1782.3
T1 moved -130m	1.7	1.7	3.4	738.0	1001.9	182.7	303.6	5406.1	8475.2	2511.4	3763.8	1082.3	1550.1	1114.0	1571.5
T1 moved -100m	1.7	1.5	3.2	739.5	1125.1	180.0	425.5	5404.8	10555.4	2517.2	5037.3	1080.8	1561.8	1116.0	1496.6
T1 moved -50m	1.7	1.0	2.7	739.1	1092.4	181.4	397.9	5410.4	11368.8	2543.7	5308.0	1082.9	1673.3	1115.8	2195.6
T1 moved -25m	1.7	0.9	2.6	740.6	1002.0	183.0	306.8	5365.5	12031.7	2557.7	6262.6	1081.3	1658.9	1117.7	1958.4
T1 moved -10m	1.7	0.8	2.5	738.2	994.1	183.2	265.3	5415.7	11915.1	2497.1	5360.0	1080.8	1757.8	1122.1	1865.8
T1 moved -5m	1.7	0.8	2.5	737.8	991.0	182.0	282.9	5391.1	11908.1	2510.4	5735.2	1081.7	1819.6	1123.2	1873.8
T1 moved -2m	1.7	0.8	2.6	738.2	982.3	182.0	278.8	5385.8	11446.8	2507.6	5476.8	1081.1	1820.1	1122.9	1875.7
T1 moved 2m	1.7	0.9	2.6	738.2	986.5	182.7	277.1	5392.9	11507.7	2508.5	5971.5	1081.9	1695.8	1123.0	1926.9
T1 moved 5m	1.7	0.9	2.6	737.5	984.8	181.8	294.0	5401.8	11354.7	2506.4	5387.4	1081.1	1649.8	1124.3	1893.5
T1 moved 10m	1.7	0.9	2.6	737.4	994.9	182.1	294.0	5381.3	12062.1	2522.2	5266.4	1079.2	1596.7	1122.0	1841.0
T1 moved 25m	1.7	1.0	2.7	737.4	1052.3	182.0	308.8	5392.2	12869.2	2460.7	5944.7	1081.0	1554.0	1110.8	1728.5
T1 moved 50m	1.7	1.2	2.9	739.3	1178.6	181.5	324.9	5367.7	10923.0	2540.4	5033.1	1081.0	1493.3	1117.6	1652.9
T1 moved 100m	1.7	1.7	3.4	740.1	1047.6	181.2	328.9	5377.1	7353.5	2508.2	4404.4	1079.5	1399.7	1115.4	1515.1
T1 moved 130m	1.7	1.9	3.6	739.6	868.8	182.4	308.5	5409.2	6724.1	2523.9	3333.5	1080.8	1147.4	1117.7	1386.9

Blind Test 2 calculations for two wind turbines in tandem arrangement

F. Pierella[1], L. Sætran[1], P.Å. Krogstad[1]

[1]Nowegian University of Science and Technology
fabio.pierella@ntnu.no

ABSTRACT

In this paper we report on the results of the Blind Test 2 challenge, a benchmark of calculation models for wind turbine wake and efficiency prediction applied to two machines in a tandem arrangement. Modelers with a suitable code were given boundary conditions and geometry of the test case, and invited to submit the calculation without knowing the experimental results a priori. The comparison showed that the performance calculation of the upstream turbine represented a challenge despite being a well known problem, while the performance and thrust of the downstream turbine was still in a preliminary phase and was affected by a large scatter. Models using 2D airfoil data suffered more than fully resolved methods, due to the higher complexity of the flow and to the importance of 3D effects in the downstream rotor flow. Mean flow calculations at $X = 1D$ from the downstream turbine showed that including the tower and the hub in the simulation improved the precision of the predictions, especially for what concerned asymmetries in the wake. Further from the rotor, $X = 4D$, the actuator line models perform very well and were able to capture the main features of the mean and turbulent flow, while actuator disc models showed their limitations especially for what concerned turbulent stresses prediction.

Introduction

The Blind Test 2 challenge had the purpose of validating the reliability of current turbine performance and wake calculations models, applied to a case where two turbines were positioned in a tandem with a downstream separation of $S = 3D$ The wake behind one turbine was addressed in a previous Blind Test challenge (hence referred to as BT1), held in Bergen in 2011. The results of the test can be found in Krogstad and Eriksen (2011, 2013). Other examples of Blind Test are present in literature, like the NREL Unsteady Aerodynamics Experiment, described by Simms et al. (2001), which addressed the same issue but on a larger rotor.

The results of these blind test and recent literature reviews, like Vermeer et al. (2003), highlighted the lack of well-documented experiments that facilitate the modelers when comparing their results with literature data. Key factors like free-flow turbulence levels, rotor and wind

tunnel geometry, experimental errors magnitude, tip speed ratio of the machines are usually not well documented and do not allow a precise benchmark of the modeled results.

In full scale experiments, inflow conditions are hard to monitor. Turbulence is rarely measured, and the effects of stability are difficult to take into account. Moreover, the complexity of the test rig adds additional uncertainties in the experimental results for which the comparison is often difficult, see Vermeer et al. (2003) and Krogstad and Eriksen (2013).

A major challenge for wind tunnel experiments is correctly scaling the experiment. Matching the tip speed ratio (λ) of a full scale turbine is not difficult, while it is more complicated to match the Reynolds number. A typical Reynolds number of a full scale turbine, based on the tangential velocity of the tip and on the blade tip chord, is in the order of 10^6, while for a wind tunnel experiment this number usually varies between 10^4 and 10^5, see e.g.Alfredsson and Dahlberg (1981); Smith (1990); Medici and Alfredsson (2006). Anyway, the scope of the current experiment is not to simulate a full scale case but rather to provide a well documented case for model benchmarking, and as other authors suggest the limitation can be neglected if the characteristics of the airfoil used are known, see Grant et al. (1997) and Vermeer et al. (2003).

Some early models are well described by Vermeer et al. (2003). The author divides between near and far wake models: nevertheless, far wake has the near wake as initial condition, so it is difficult to neatly separate the two. In most of the wind farms the downstream turbines work in the far wake of the upstream ones in the main wind direction, being the spacing $S \approx 10D$), but in cross wind and in some wind farms with a very tight spacing like Lillgund the downstream machine works in the near wake of the upstream ones, see Dahlberg and Thor (2009).

Ainslie (1988) presented a parabolic model called EVMOD which assumed axisymmetric and self-similar wakes and used an eddy viscosity model to close the turbulence equations. The model needs quite a few constants, and agrees well with wind tunnel experiments, but cannot handle complex features like turbulence enhancement on the top tip region and wake centerline downshift.

Crespo et al. (1988) takes the turbine into account as a perturbation inducing a velocity deficit and additional turbulence, which iss resolved by means of a $k-\varepsilon$ turbulence model. The model can include the effect of wind shear and turbulence and stability effects, and captures 3D effects like the maximum velocity deficit downshift. The model compares fairly well with wind tunnel experiments. An extension of this model from Crespo and Hernández (1989), applied to wind farms, showed a overestimaton of the velocity deficit when assuming linear superimposition of the velocity deficits of multiple turbines.

The same conclusion is drawn by Smith (1990) when elaborating a model to fit his wind tunnel experiments: the turbulence saturates after a few wind farm rows and reaches an equilibrium value. His model for the superposition of multiple wakes is based on a simplified version of the Reynolds averaged Navier-Stokes (N-S) equations coupled with an eddy viscosity model for turbulence closure, including shear on the incoming wind. The model agrees fairly well with the experiments, but needs to be calibrated on experiments.

More recently, with the increase of available computational power, full CFD models were employed in order to resolve the wake in more detail, using LES o RANS methods for turbulence modeling. In one example, Zahle and Sørensen (2007) shows how the wake grid size influences the rotor characteristics. The grid for the far wake has to be fine enough in order to to catch

(a): Wind Tunnel setup

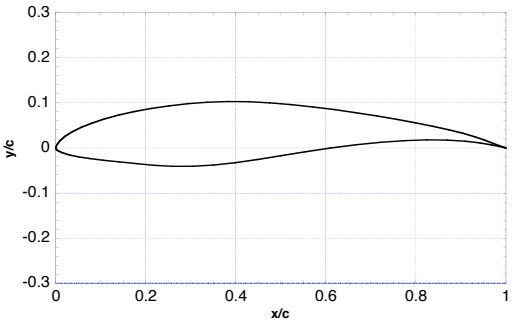

(b): Airfoil S826

Figure 1: Setup and airfoil geometry

the small vortical structures, while the near wake ($X/D < 0.5$) grid size is critical for a correct power and thrust prediction of the rotor.

The modeling of the rotor, nevertheless, remains the key issue. Fully resolving the rotor is computationally demanding, e.g.Zahle et al. (2009), but usually gives fairly good agreement.

When more than one turbine has to be simulated, other models become more convenient. In the actuator disc approach from Sørensen et al. (1998) the turbine is represented as an actuator disc, while in the actuator line modelTroldborg (2007); Troldborg et al. (2010) the turbine blades are represented as rotating point forces. Both models are coupled with a N-S solver using a LES approach, but RANS or U-RANS can be also used.

The model turbines in this study were designed in 2008, in order to be used as test cases. This is the reason for many of the design compromises achieved, very well argumented in Krogstad and Eriksen (2013).

Fig.1a depicts the two turbines object of this work positioned in the wind tunnel. T_1 is the upstream turbine, while T_2 is the downstream one. The two machines have the same bladeset, but slightly different hub size, which leads to different rotor diameter,: $D_1 = 0.894\ m$ while $D_2 = 0.944\ m$. The wind tunnel length is 12.4 turbine diameters, yielding a limited distance for wake measurements. The two three-bladed rotors have the same bladeset, based from root to tip on the s826 airfoil from NREL, see Somers (1999). The turbines had a maximum efficiency at $\lambda = 6$. We remark that a nominal diameter of ca. $D = 0.9\ m$ will be used for the non-dimensionalization of the parameters.

Scaling

As previously mentioned, wind tunnel experiments present scaling issues that limit the comparison to full scale turbines. The tip speed ratio similarity was easily achievable, notwithstanding the small diameter, since the rotational velocity could be easily adjusted via frequency converter controlled motors. The turbines were designed in order to be operated at a velocity of 10 m/s, and the were designed for an optimum performance at $\lambda = 6$. This means that for a reference

velocity of $U_{ref} = 10\ m/s$ the rotational speed of the turbines had to be set to $\omega \approx 1200\ rpm$. At $\omega \approx 2500\ rpm$ the turbine would reach the runaway point. When the flow is attached on the blades and the turbine is working at optimum, there is no spanwise flow. After stall, a significant amount of spanwise flow arises: in a separated bounday layer, in fact, the streamwise momentum is relatively small, so the centrifugal force starts pumping fluid towards the tip of the blade. The spanwise moving fluid is subject to a Coriolis force directed toward the trailing edge of the blade, which can significantly delay stall and alter the 2D characteristics of the airfoil, see Hansen (2008). This effect is supposed to be more pronounced in wind tunnel tests than in full scale turbine, due to the high rotational velocity involved.

The local Reynolds number based on the blade tip speed and the tip chord is $Re_c \approx 10^5$ for the upstream turbine at maximum performance, while for a full scale wind turbine this parameter is one order of magnitude higher. The deviation is even larger for the downstream wind turbine, which is operating at a lower λ. To make this difference as small as possible, the blade chord was designed to be 3 times larger than what would normally be used for such a rotor diameter. This implied larger local Reynolds number, a positive effect, but a quite low lift coefficient of the blade sections at turbine design condition, see also Krogstad and Eriksen (2013). The low Reynolds number is acceptable if the airfoil characteristics are known for the particular Reynolds range, and if the outer blade sections are above the critical Reynolds number, see also Grant et al. (1997) and Vermeer et al. (2003). The minimum U_{ref} that would guarantee Reynolds independency for the turbine rotors was investigated by Krogstad and Adaramola (2012), who found a critical velocity of $U_{ref} > 9\ m/s$.

The Reynolds number based on the diameter of the largest of the cylinders composing the tower of T_2, $D_T = 10.2\ cm$, and a freestream velocity of $U_{ref} = 10\ m/s$ was $Re_D^T \approx 7 \cdot 10^4$. For a similar Reynolds number the drag coefficient of a smooth cylinder would be $C_D = 1$, as from Delany and Sørensen (1953). For a full scale turbine tower the Reynolds number can be as high as $Re_D^T = 10 \cdot 10^6$, and the tower drag coefficient drops to $C_D = 0.4$. The wake of the tower is therefore much wider in the experiment than in a full scale case. In a typical $2.3MW$ Siemens wind turbine the ratio between the tower and the rotor diameters would be 0.05, with $D^T = 5\ m$ and $D = 93\ m$, while in the current experiment the ratio was 0.11, twice as big. For these reasons, we expect the velocity deficit caused by a full-scale turbine tower to be shallower and thus to recover at a shorter downstream distance from the rotor.

For a discussion on blockage effects please see the results from Blind Test 1 in Krogstad and Eriksen (2013).

Test Case

The experiments were carried out in the NTNU closed-loop wind tunnel facility. The wind tunnel dimensions at the inlet were $L = 11.15\ m$, $W = 2.72\ m$ and $H = 1.80\ m$. The height of the roof was adjusted in order to have a zero pressure gradient in the whole test section, therefore increasing at greater distances from the inlet.

The test case is well documented in an invitation document from Pierella et al. (2012) to which we refer to for more complex technical details. A detailed description of the wind tunnel is present in Krogstad and Adaramola (2012), Adaramola and Krogstad (2011) and Krogstad

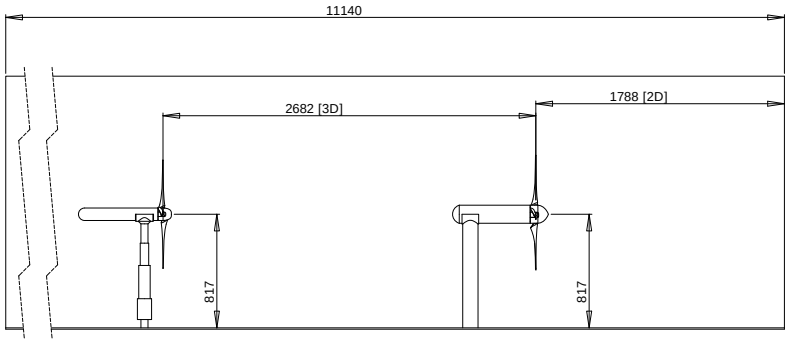

Figure 2: fig:Wind Tunnel setup, plan. Dimensions in $[mm]$

and Eriksen (2013).

The upstream turbine T_1 was positioned $2D$ from the wind tunnel inlet, in order to avoid perturbation of the incoming velocity profile. The downstream turbine T_2 was positioned at $S = 3D$ from the upstream turbine, and both turbines had the same hub height, $H^{hub} = 0.817\ m$ (fig. 1a). Both turbines were horizontally centered in the wind tunnel (fig. 2), and were alternatively positioned on an aerodynamic balance in order to measure the thrust on the rotor. The thrust of the tower and nacelle was measured and subtracted from the thrust of the turbine, to yield the trust of the rotor alone.

The invitation file for the Blind Test competition, see Pierella et al. (2012), included all the geometrical details of the turbines, which were made available to the modelers also under form of 3D CAD files.

Blade Geometry

As previously mentioned, the blades use the NREL S826 airfoil along the entire span. The profile was designed to have high lift coefficients, $C_L \approx 1.40$ for $Re_c = 2 \cdot 10^6$, low sensitivity to roughness, and docile stall characteristics, to be used on the tip of low solidity and highly tapered blades, as stated in Tangler and Somers (1996). The stall is controlled by a so-called separation ramp, a steep slope which confines the separation to a zone close to the trailing edge. In fig.1b the normalized airfoil coordinates are sketched; a complete description of the airfoil is given by Somers (1999).

A CAD file was provided to the participants, containing a 120 degrees segment of the nacelle of turbine T_2 with one blade mounted in the correct position.

Further references about the blade structure and design can be found in Krogstad and Eriksen (2013), Krogstad and Lund (2011), Adaramola and Krogstad (2011) and Pierella et al. (2012).

Required Output

The modelers were asked to provide predictions for performance and thrust coefficients and for wake mean and turbulent velocity in a set of three cases. The reference velocity of the wind tunnel was set to be constant, $U_{ref} = (10 \pm 0.1)\ m/s$. In all the setups, the upstream turbine T_1 was rotating at peak efficiency, or $\lambda_1 = 6$. The downstream turbine T_2, positioned at $S = 3D$, was running at three different tip speed ratios, one close to optimum efficiency in wake operation, one close to runaway conditions and one lower than optimum. All the tip speed ratios were calculated with respect to the reference velocity U_{ref}.

- **Setup A**: $\lambda_1 = 6$, $\lambda_2 = 4$ (Compulsory)
- **Setup B**: $\lambda_1 = 6$, $\lambda_2 = 7$ (Optional)
- **Setup C**: $\lambda_1 = 6$, $\lambda_2 = 2.5$ (Optional)

The required output was represented by the thrust and power coefficient for the upstream and downstream turbine, defined as:

$$C_P = \frac{2P}{\rho U_{ref}^3 A} \qquad (1) \qquad\qquad C_T = \frac{2P}{\rho U_{ref}^3 A} \qquad (2)$$

Velocity measurements were also part of the required output, in particular the non-dimensional streamwise mean velocity, $U^* = U/U_{ref}$, and the normalized streamwise reynolds stress, $u'^* = u'u'/U_{ref}^2$ along two perpendicular diagonals at three different downstream distances from the tandem, $X = [1D, 2.5D, 4D]$.

The compulsory output, necessary to be admitted to the competition, was represented by both performance and wake predictions for Setup A, while Setup B and C were optional.

Methods Description

We received data from 8 instutitions, which contributed with one simulation each, except GexCon which submitted two dataset. Most of them solved all the three Setups, while Uzol from METU only submitted the mandatory output.

The participants were asked to submit a method description in order to document the features of their models. Here follows a brief description of each of them.

Acona Flow technology

Manger from Acona Technology was the only participant who modeled the entire rotors and the wind tunnel, reproducing the whole test case as it was represented. The turbine structure and blades were finely meshed, and the total number of cells was $30 \cdot 10^6$. The flow was solved using *Fluent v. 14.0* and a $k-\omega$ turbulence closure model. The method performed quite well in the first Blind Test, also due to the choice of the modelers of including the hub, the nacelle and the walls in the simulation.

The results from Manger will be labeled as **Acona**.

CMR Prototech

The simulations were perfomed by Hallanger and Sand using a in-house CFD code called *Music*. The code was developed at CMR, and uses a standard steady state $k-\varepsilon$ model for turbulence closure, using the coefficients given in Launder and Spalding (1974).

A sub-grid turbulence model is also used to represent the turbulence generation by the wind turbines. The discretized equations are solved on a co-located grid with the SIMPLE algorithm as from Ferziger and Perić (1999).

The hubs are taken into account as a flow resistance, but the axial extent of the nacelles are not represented. The total number of grid points for the case was $3.9 \cdot 10^5$. The rotors were represented by a generalized BEM model with rotation, and the 2D airfoil data were produced by *Xfoil*, see Drela (1989). The walls were included in the simulations, while the tower of the turbines was not modeled.

The results from Hallanger and Sand will be labeled as **CMR**.

de Vaal - NTNU Marintek

De Vaal performed his calculations in *Fluent*, where a finite volume discretisation of incompressible N-S was implementd. The rotor wasmodeled as an axisymmetric actuator disc via BEM model, and the 2D airfoil data was calculated via the Q^3uick software implemented by García (2011), and were the same dataset used by the **DTU** contributors. The tower and the nacelle was not simulated by de Vaal, while the wind tunnel walls were taken into account. The turbulence closure model was Reynolds Stress modeling, whose implementation is included in the *Fluent* package.

The simulations from de Vaal will be marked as **DeVaal**.

DTU and Linné Flow Center

Mikkelsen and Sarmast performed a large eddy simulation using the *EllipSys3D* code developed by Risø and DTU. The computational domain is a regular cartesian grid, composed by a total of 42.46 million mesh points. The turbine rotor was represented by 43 points along each blade, on which the blade loads were calculated. The boundary conditions were constant inflow velocity and convective outflow, and the wind tunnel walls were included using no-slip boundary conditions. The wind tunnel turbulence was modeled by introducing synthetic turbulent fluctuations at $X = 1.5D$ upstream of the first wind turbine, following the method from Mann (1998). The 2D airfoil data were obtained from the in-house developed viscous-inviscid interactive code Q^3uick from García (2011).

The simulations from Mikkelsen and Sarmast will be labeled as **DTU-KTH**

GexCon

GexCon was the only modeler who submitted two simulations. The GexCon group, represented by Melheim, Slen and Khalil used a in-house the software package *FLACSeWind* developed by GexCon. This is a transient CFD solver which in this case used the standard $k-\varepsilon$ turbulence model. The computational domain was similar to the wind tunnel dimensions, but the increase in tunnel height to compensate for the growth of side wall boundary layers was not included. The rotor was represented as an actuator disk, and the turbine tower was not included in the simulation. The 2D airfoil data were obtained by Hansen via *XFoil*, see Drela (1989). The model used for the two simulations is the same, with the difference that in what is marked as **GexCon-sim1** the walls and the floor were taken into account as no-slip boundaries, while in **GexCon-sim2** they were represented as symmetry conditions.

University of Puerto Rico

Leonardi and Martinez Tossas, from the university of Puerto Rico, performed a LES simulation of the test case where the turbine rotors were simulated as actuator lines. The subgrid turbulence was taken into account via a standard Smagorinsky model. The walls, roof and floors were included in the simulation as no-slip conditions, but the towers and the nacelles of the turbines were not simulated. The tool *AirfoilPrep* from NREL was used to calculate the airfoil data.

The results from University of Puerto Rico will be labeled as **Leonardi**.

Meventus

The simulation from Meventus were performed by Lund and Bhutoria. The rotors were simulated as actuator lines, and the flow resolved via a LES simulation, with a Smagorinsky subgrid scale model. The code used was SOWFA, implemented by NREL in OpenFOAM, which included an actuator line model implementation together with other useful tools for simulating wind farm applications, see NWTC (2012). The 2D airfoil data were calculated via *XFoil*, see Krogstad and Lund (2011) for further details. While the walls were included in the simulation by setting a zero velocity at the tunnel boundaries, the effect of the nacelle and of the tower was not modeled.

The results from Meventus will be labeled as **Meventus**.

METU

The results from METU, the Middle East Technical University, were elaborated by Uzol and Sezek Uzol. The authors used the free-wake code *Aerosim*, a 3D unsteady free-wake vortex panel method. When simulating the turbine, the blades were discretized using quadrilateral panel elements, and vortex ring elements were placed within each element. During an unsteady run, at each time instant, the influence coefficients of surface panels are calculated using the induced velocity values from each vortex segment on the collocation points using Biot-Savart law. Then the blades are moved and a new solution is calculated for the new timestep. No tower and hub were modeled, while the walls of the wind tunnel were imposed as a zero velocity boundaries.

The results from METU will be labeled as **Uzol**.

Numerical and Experimental Uncertainties

The modelers were asked to provide proof of grid independency of their solution. As an example, the documentation from DTU-KTH showed that the calculations performed on a very fine grid with 2.4 times the number of cells than the grid for the submitted results, led to a change in the calculated C_P of 2%. The grid independency presented by CMR showed the same discrepancy between the C_P calculated on the finest grid and on the final grid used for calculations. The discretization schemes were at least second order in space and time.

The experimental uncertainty on the performance measurements was $\pm 2\%$ on the peak efficiency, while it was estimated to be lower than 5% on the mean velocity measurements.

Results

Performance and thrust

In fig. 3a, the calcluations for the upstream turbine showed a large scatter ($\pm 20\%$) around the experimental value. The experimental case presented a few challenges that made the prediction of the power coefficient of a free standing turbine, which in theory is a well known case, more complex. First of all, the performance curve of the upstream turbine showed a dip at $\lambda = 5$, which is most likely an indication that the flow on the rotor was not fully developed. Moreover, the characteristics of the airfoil *S*826 were not experimentally known for the relatively low local reynolds numbers, which means that every modeler had to produce his own 2D airfoil data for the relatively low local Reynolds number of the experiment.

Even when the same airfoil data was used in different models, like in the case of de Vaal and DTU-KTH, the predicted performances varied significantly. Acona's method, the only one which resolved the whole rotor surface and the turbine structure, performed quite well, as in the previous Blind Test 1 challenge. The actuator line (AL) methods performed averagely better than actuator disc (AD) models.

Fig. 3b shows a similar dispersion for what concerns the thrust coefficients. The free vortex from Uzol is far off, while all the other methods generally underpredicted the thrust on the rotor. Acona's results again had the best agreement, while the AD from de Vaal and CMR managed to match very closely the thrust of the rotor. All the actuator lines methods had a tendency to underpredict the thrust, similarly to what happened for the Blind Test 1, where Leonardi performed best. The only simulation which did not include the walls, GecCon-sim2, showed lower values than the relative one with walls, GexCon-sim1, showing, as expected, an enhancement of the thrust when the rotor is in a bounded flow Sørensen et al. (2006).

The efficiency calculations of T_2, fig. 3a, show an averagely larger relative scatter than for T_1. At $\lambda_2 = 4$ (Setup A) the downstream turbine had an optimum in the C_P curve, while in Setup B the turbine was close to the runaway point, reached for $\lambda_2 = 7.3$. In Setup C the performance of the turbine was less than optimum, where the root of the blades is stalled and the tip region is generating lift.

At $\lambda_2 = 4$, GexCon-sim1 performed best, matching the experimental results. The same simulation without the walls (GexCon-sim2) predicted a dramatically lower performance. The fully resolved simulation from Acona performed well, yielding to a slight overestimation of the power extraction. Despite using the same 2D airfoil data, DTU-KTH and DeVaal had markedly different results. The actuator line model was more precise in reproducing the turbine behavior when the incoming flow was characterized by strong shear and high turbulence levels. Also, DeVaal's method assumed axisymmetry, a too strong assumption in such a complicated flow. The free wake method from Uzol dramatically overestimated the turbine power production, like all the actuator line models. In this particular situation, the AD codes seemed to be averagely closer to the experiments, even though the scatter caused by the different 2D airfoil data used for the prediction makes the comparison between them quite complicated.

At $\lambda = 2.5$ the scatter between the different methods is smaller. The fully resolved rotor from Acona still gave a good agreement, together with GexCon-sim1. All the other methods overestimated the power production, except for the GexCon-sim2. At $\lambda_2 = 7$ the situation is more interesting: the power production is very close to zero, but most of the method did not catch the presence of the runaway point. Again Acona performed well, together with the AD method from CMR and GexCon-sim2. Acona's good results are not surprising: at this TSR the inner part of the rotor is working in propeller state, giving birth to strong spanwise flow which is very difficult to capture with methods based on 2D airfoil predictions.

All the simulations predicted the top performance at $\lambda_2 = 4$ except for DeVaal, while only a few methods found a lower efficiency for $\lambda_2 = 7$ than for $\lambda_2 = 2.5$. There seems to be no average trend for which AL is better than a AD model, which means that for performance calculations a more complex model does not give a better prediction than a relatively less complicated one. The incoming flow on the second turbine was not a required output for the current experiments, so it is not possible to state whether the errors in prediction come mostly from wrong calculations on the first wake or rather from wrong calculations on the second turbine rotor.

The thrust calculations for T_2, fig.3b, are equally scattered around the experimental values for low TSRs, while generally underpredict the thrust at high rotational regimes. The CMR method performs remarkably well throughout the whole span, reaching a close agreement with the experiments. At $\lambda = 4$ the GexCon simulations give low values, which happened for all the cases under exam, which may be rooted back to a wrong estimation of the 2D airfoil performance. At $\lambda = 7$ the thrust seems to be lower than expected for all the simulations, except the one from Leonardi. Amongst all the actuator line methods, the one from DTU-KTH is the one which agrees best with the data throughout the analyzed TSR range. Again, it is not possible to estimate a secure winner between Actuator Disc and Actuator Line methods: despite the relatively simpler model and the lower computational power demand (e.g. the total number of cells for CMR is $\approx 10^5$ while in DTU-KTH it is $34 \cdot 10^6$), the method outputted fairly good results.

In figure 4a the mean wake $X = 1D$ behind the turbine tandem in Setup A is depicted. The models who did not include the walls predicted a too high velocity outside of the wake. The only modelers who included the effect tower, directly as in the case of Acona, or indirectly, as CMR did, found a velocity profile closer to the experimental one. The overshoot which is visible in the other profiles was due to the fluid bypassing the center of the rotor where no energy extraction takes place. The experimental velocity profile is highly asymmetric, due to the perturbations of

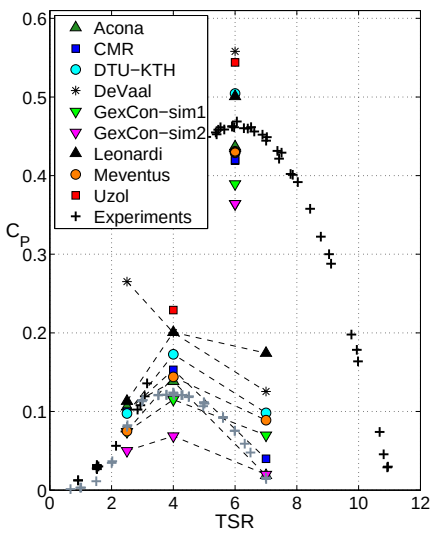

(a): Experimental C_P of T_1 (black) and T_2 (grey) vs. simulations

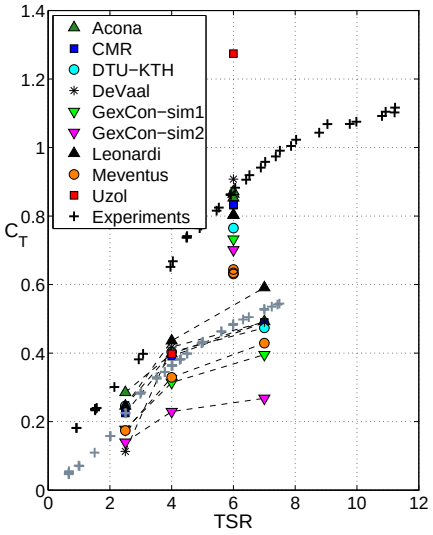

(b): Experimental C_T of T_1 (black) and T_2 (grey) vs. simulations

Figure 3: Performance and thrust coefficient of the upstream turbine T_1

the tower and of the nacelle, and only the Acona model managed to reproduce the non symmetry. The predictions from Uzol showed a too shallow wake and a very non-uniform velocity profile. The width of the turbine wake seems to be captured by mosto of the models, even though some of them predicted a too shallow velocity deficit, e.g. GexCon-sim1 and Leonardi.

For what concerns the streamwise Reynolds stress, fig, 4dalmost all the model predicted a turbulence intensity of the same order of magnitude of the measurements, contrarily to what emerged from BT1 where the difference was of some order of magnitude. The experimental profile was highly asymmetric, with one peak twice as strong as the other. The DTU-KTH model caught this non-symmetry but specular to the experimented one, and not as marked. The CMR model predicted an averagely too high turbulence intensity, especially inside the rotor span. The model from Meventus matched very well the turbulence peak value, but had no secondary peak at the center of the wake and showed no asymmetry. The model from Acona predicted very low turbulence levels, but it is unclear whether it was the strenght of the tip vortices or rather the turbulence production in the shear layer which was underestimated. One factor to note is that the models using a two equation closure for turbulence (Acona, CMR, GexCon) were invited to calculate the normal turbulent stress assuming turbulence isotropicity:

$$u'^2/U_{ref}^2 = \sqrt{2/3k} \tag{3}$$

This assumption is not appropriate, and cannot be confirmed by the current measurements.

The experimental vertical mean velocity profiles at $X = 1D$ for Setup A showed a somewhat different picture, in fig. 4c: the velocity on the negative Y axis does not recover to free stream value, due to the presence of the tower. This behavior could be captured only by the simulations

taking the tower into account, like Acona. CMR included the effect of the hub but not of the tower, hence their profiles look symmetric. The methods who have not included the hub experienced particularly high values of the velocity at $Y/D = 0$. The methods from Acona, Meventus and DTU-KTH actually matched the maximum velocity deficit of the $Y/D > 0$ side, but only the first managed to reproduce the asymmetry in the peak values of the velocity profile. The simulations confirmed that the wake of the tower has a great impact on the symmetry of the velocity profiles and on the different wake propagation rates in the vertical and horizontal direction, as previously highlighted by dedicated experiments.

The experimental values for the vertical stresses, in fig. 4d, showed two peaks of equal intensity, differently from the horizontal diagonal. Meventus and CMR predicted the maximum stress levels very accurately, while Acona's results were once more very low. The predictions from deVaal and DTU-KTH have the highest peak values both on the horizontal and vertical diagonal, a striking similarity considering that they use the same 2D airfoil data. GexCon predicted the turbulence values quite well, even though the turbulent stresses were too high inside the rotor span. KTH-DTU and GexCon were the only modeler who reproduced the turbulent peaks generated by the root vortices of the blades, even though their results show an additional dip which is most likely related to the absence of the hub in their simulations.

In Setup B the downstream turbine was running close to the runaway TSR, fig. 5a. The high values of the U/U_{ref} at the rotor center indicate that the inner part of the rotor is working as a propeller, transferring momentum into the wake. Acona's simulation closely matched the meak wake profile, and was the only one who correctly predicted the performance for the setup. CMR managed to reproduce the velocity deficit in the wake centerline, while all the other methods overestimated it, having neglected the presence of the hub. GexCon-sim2 performed well in Setup B, even though it failed outside of the wake. All the models predicted the width of the wake with acceptable accuracy.

The turbulence levels for Setup B, fig. 5b, showed peaks of different intensity in the positive and negative axes. The model from Acona caught this non-symmetry, even though the turbulent stresses were 4 times lower than expected. The predictions from DTU-KTH overpredicted the turbulent stresses, but reproduced the peaks in the turbulence profiles induced by the root vortices. Meventus performed very well on the tip region, but poor at the centerilne. The turbulent stresses in GexCon-sim1 agreed reasonably well across the rotor span.

$X/D = 4$

Farther from the rotor, $X = 4D$, the experimental mean velocity profile for Setup A looked much smoother than in figure 4, since the steep gradients were evened out by the turbulent transport and diffusion. The wake width was generally well caught, apart in the case of Uzol. The models that had predicted a low turbulence intensity inside the rotor disc at $X = 1D$, like DeVaal, Meventus and Leonardi, still featured a high velocity zone caused by the absence of the nacelle. Acona's model worked fine outside of the wake but predicted a slightly too high velocity deficit at the centerline. For what concerns the turbulent stresses, fig. 6b, the DTU-KTH model showed an almost perfect agreement with the experiments, together with the deVaal model. All the models, except Meventus, predicted markedly lower peak turbulent stresses at $X = 4D$ than at $X = 1D$,

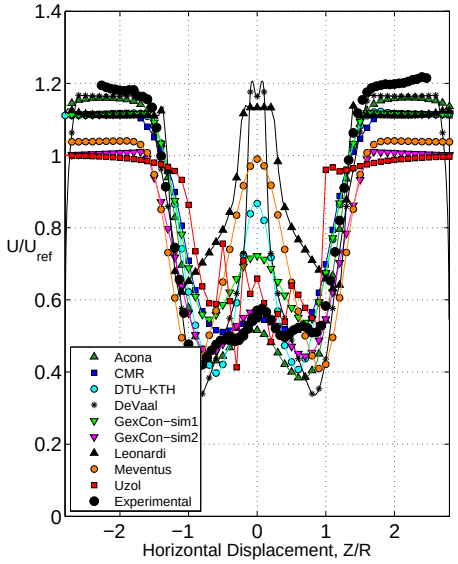

(a): U at $X = 1D$, Horizontal

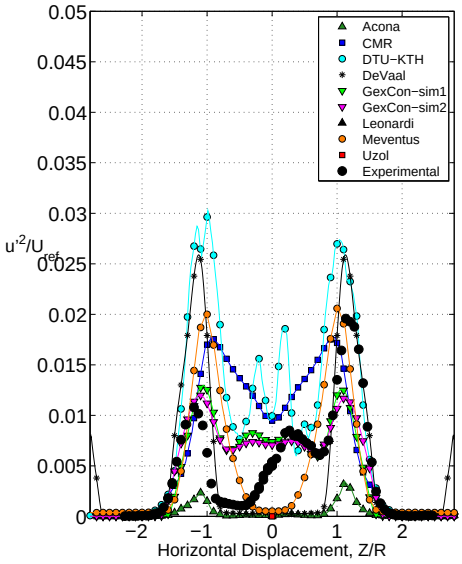

(b): u' at $X = 1D$, Horizontal

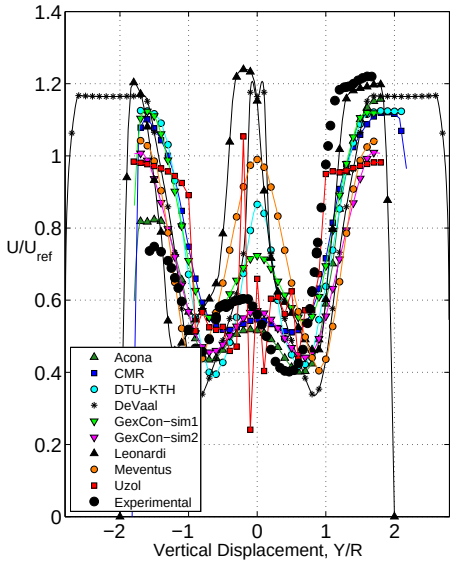

(c): U at $X = 1D$, Vertical

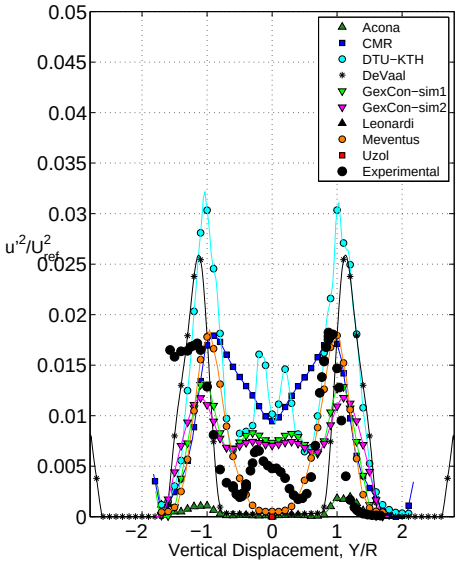

(d): u' at $X = 1D$, Vertical

Figure 4: Performance and thrust coefficient of the upstream turbine T_1, Setup A

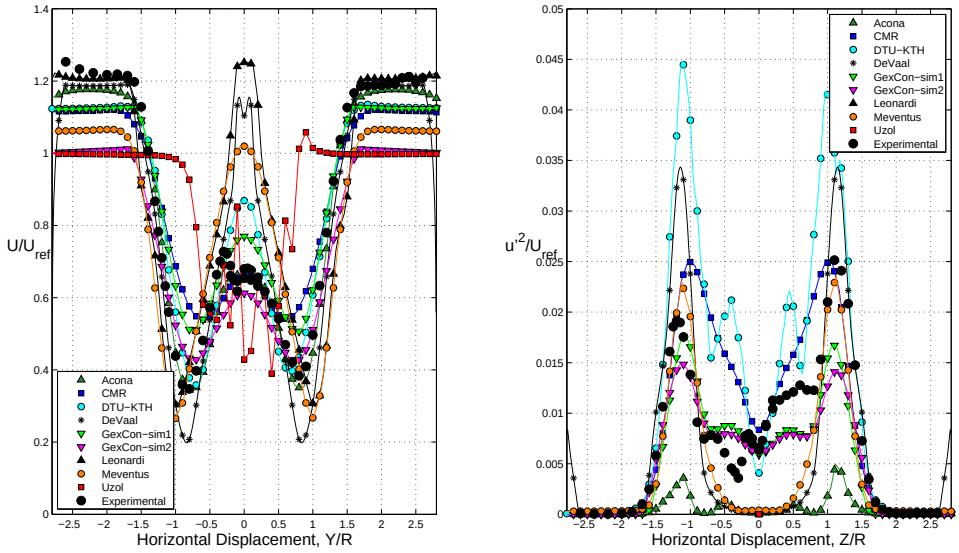

(a): U at $X = 1D$, Horizontal, Setup B (b): u' at $X = 1D$, Horizontal, Setup B

Figure 5: Wake predictions for the turbine tandem, Setup B

while in the experiments they were of the same magnitude, $u'^2/U_{ref}^2 = 0.02$. This means that the turbulent production happening in the shear layer was generally underestimated.

In Setup B, fig. 6c, the wake models predicted equally well the wake width, even though the best performance came from DTU-KTH. Again, models with a low turbulence intensity at the rotor centerline at $X = 1D$ failed to predict a smooth profile. AD methods like GexCon-sim1 and CMR performed reasonably well, but calculated too low turbulent stresses.

Fig. 6d shows that DTU-KTH performed very well, together with the BEM from deVaal. Acona's model again exhibited very low turbulent stresses, while Meventus predicted far too high turbulence levels.

Concluding remarks

This paper discussed the performance of numerical models for predicting the characteristic curves and the wake features of two wind turbines in tandem arrangement. The modelers were given boundary conditions and geometrical details of the test case, and had to predict the experimental results in a Blind Test challenge, i.e. perform the calculations without knowing the experimental results a priori.

For what concerns the performance of the upstream turbine, the models which fully resolve the flow around the turbine blades showed the best agreement. Simple AD models predicted the performance quite well, even though all the models generally underpredict the torque.

The relative scatter on the second turbine perfomance calculations was larger. The only

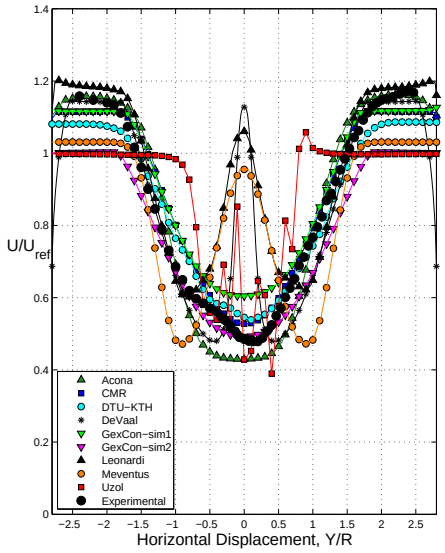

(a): U at $X = 4D$, Horizontal, Setup A

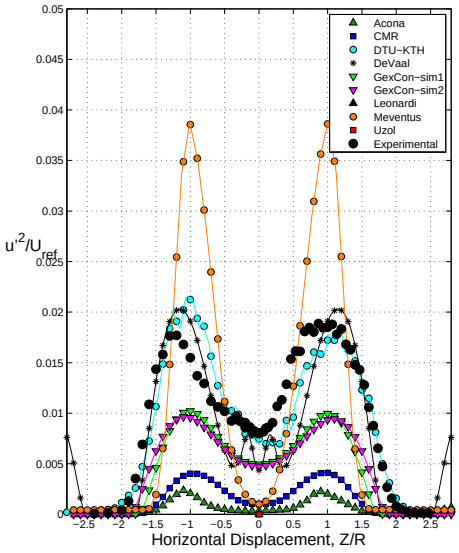

(b): u' at $X = 4D$, Horizontal, Setup A

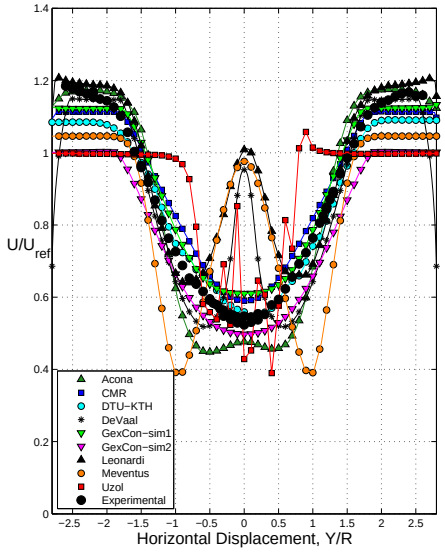

(c): U at $X = 4D$, Horizontal, Setup B

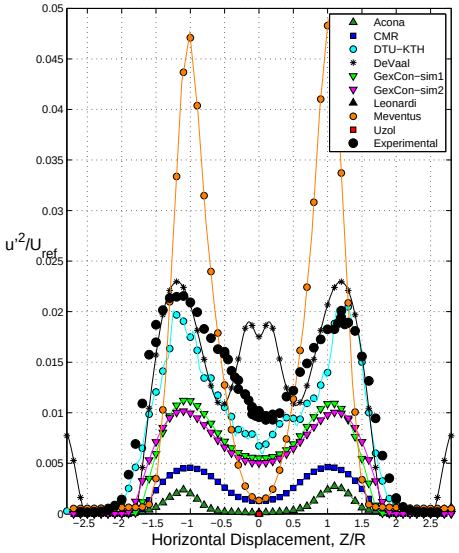

(d): u' at $X = 4D$, Horizontal, Setup B

Figure 6: Wake predictions for the turbine tandem, Setup B

model resolving the rotor geometry, from Acona, showed the best agreement, and correctly predicted the close to runaway point at $\lambda_2 = 7$. One AD code, from CMR, matched the experiments

quite well in all the TSR range, bur as a general tendency there was no secure winner among actuator discs and actuator line models, and more complex models did not yield significantly better results. The thrust was underpredicted by most of the models, especially for high TSR, where the inner part of the rotor works in propeller mode and represents a big challenge for models who base their predictions on 2D airfoil data.

Most of the models did not manage to capture the finer details of the near wake, especially the asymmetries in the profiles induced by the presence of the hub and of the turbine tower.

The predicted turbulence levels are generally of the same order of magnitude of the experimental values, with some exceptions. The fully resolved rotor simulation gave good results for the mean flow but showed poor agreement with the experimental turbulent stresses. Less detailed models, like actuator discs, generally overestimated the turbulence inside the rotor disc and underestimated the turbulence in the tip region.

Farther from the rotor, the actuator line models were the most accurate, with the DTU-KTH model showing very good agreement both in mean and turbulent flow, for what concerned Setup A.

In more complex working conditions, where the downstream turbine was close to runaway operation, the predictions of the fully resolved model have the best agreement on the mean flow near the rotor, while further downstream the AL models, when properly set, gave very reasonable estimates both for mean and turbulent flow.

REFERENCES

M.S. Adaramola, P.Å. Krogstad, Experimental investigation of wake effects on wind turbine performance, Renewable Energy 36 (2011) 2078–2086.

J. Ainslie, Calculating the flowfield in the wake of wind turbines, Journal of Wind Engineering and Industrial Aerodynamics 27 (1988) 213–224.

P. Alfredsson, J.Å. Dahlberg, Measurements of wake interaction effects on the power output from small wind turbine models, The Aeron. Int. of Sweden, Technical Note FFA HU 2181 (1981).

A. Crespo, J. Hernández, Numerical modelling of the flow field in a wind turbine wake, in: Proceedings of the 3rd Joint ASCE/ASME Mechanics Conference, pp. 121–127.

A. Crespo, J. Hernández, E. Fraga, C. Andreu, Experimental validation of the upm computer code to calculate wind turbine wakes and comparison with other models, Journal of Wind Engineering and Industrial Aerodynamics 27 (1988) 77–88.

J.Å. Dahlberg, S.E. Thor, Power performance and wake effects in the closely spaced lillgrund wind farm, Proceedings of the European Offshore Wind Energ (2009).

N. Delany, N. Sørensen, Low-speed drag of cylinders of various shapes (1953).

M. Drela, XFOIL: An Analysis and Design System for Low Reynolds Number Airfoils, Technical Report, NREL, 1989.

J.H. Ferziger, M. Perić, Computational methods for fluid dynamics, volume 2, Springer Berlin etc, 1999.

N.R. García, Unsteady viscous-inviscid interaction technique for wind turbine airfoils (2011).

I. Grant, P. Parkin, X. Wang, Optical vortex tracking studies of a horizontal axis wind turbine in yaw using laser-sheet, flow visualisation, Experiments in Fluids 23 (1997) 513–519.

M. Hansen, Aerodynamics of wind turbines, Earthscan/James & James, 2008.

P.Å. Krogstad, M.S. Adaramola, Performance and near wake measurements of a model horizontal axis wind turbine, Wind Energy 15 (2012) 743–756.

P.Å. Krogstad, P.E. Eriksen, "Blind Test" Workshop, Technical Report, NTNU, 2011.

P.Å. Krogstad, P.E. Eriksen, "blind test" calculations of the performance and wake development for a model wind turbine, Renewable Energy 50 (2013) 325 – 333.

P.Å. Krogstad, J.A. Lund, An experimental and numerical study of the performance of a model turbine, Wind Energy 15 (2011) 443–457.

B. Launder, D. Spalding, The numerical computation of turbulent flows, Computer Methods in Applied Mechanics and Engineering 3 (1974) 269 – 289.

J. Mann, Wind field simulation, Probabilistic Engineering Mechanics 13 (1998) 269 – 282.

D. Medici, P. Alfredsson, Measurements on a wind turbine wake: 3d effects and bluff body vortex shedding, WIND ENERGY-CHICHESTER- 9 (2006) 219.

NWTC, Sowfa - simulator for offshore wind farm applications, 2012.

F. Pierella, P.E. Eriksen, L. Sætran, P.Å. Krogstad, Invitation to the 2012 "Blind Test 2" Workshop - Calculations for two wind turbines in line, Invitation, Norwegian University of Science and Technology - NTNU, 2012.

D. Simms, S. Schreck, M. Hand, L. Fingersh, NREL Unsteady Aerodynamics Experiment in the NASA-Ames Wind Tunnel: A Comparison of Predictions to Measurements, Technical Report NREL/TP-500-29494; TRN: AH20012804:37:14 EST 2008NREL; EDB-01:070479English, 2001. Other Information: PBD: 22 Jun 2001.

D. Smith, Multiple wake measurements and analysis, in: Proceedings of the 12th BWEA Wind Energy.

D. Somers, Design and experimental results for the s825 airfoil, Airfoils, Inc., Port Matilda, Pennsylvania (1999).

J.N. Sørensen, W.Z. Shen, X. Munduate, Analysis of wake states by a full-field actuator disc model, Wind Energy 1 (1998) 73–88.

J.N. Sørensen, Z.S. Wen, R. Mikkelsen, Wall correction model for wind tunnels with open test section 44 (2006) 5.

J.L. Tangler, D.M. Somers, NREL airfoil families for HAWTs, National Renewable Energy Laboratory, 1996.

N. Troldborg, Actuator line simulation of wake of wind turbine operating in turbulent inflow, in: EWEC 2009, volume 75, IOP Publishing, 2007, p. 123.

N. Troldborg, J.N. Sørensen, R. Mikkelsen, Numerical simulations of wake characteristics of a wind turbine in uniform inflow, Wind Energy 13 (2010) 86–99.

L.J. Vermeer, J.N. Sørensen, A. Crespo, Wind turbine wake aerodynamics, Progress in aerospace sciences 39 (2003) 467–510.

F. Zahle, N.N. Sørensen, On the influence of far-wake resolution on wind turbine flow simulations, Journal of Physics: Conference Series 75 (2007) 012042.

F. Zahle, N.N. Sørensen, J. Johansen, Wind turbine rotor-tower interaction using an incompressible overset grid method, Wind Energy 12 (2009) 594–619.

Dynamics of the three helical vortex system and instability

I. Delbende[1,2], **M. Rossi**[1,3]

[1]UPMC, Université Pierre et Marie Curie-Paris 6
[2]LIMSI–CNRS, BP 133, 91403 Orsay Cedex, France, Ivan.Delbende@limsi.fr
[3]CNRS, d'Alembert–UPMC, 75232 Paris Cedex 05, France, Maurice.Rossi@upmc.fr

INTRODUCTION

Many systems develop helical vortices in their wake (propellers, wind turbines, helicopters). Such flows can be assumed, at least locally, to be helically symmetric, i.e invariant through combined axial translation of distance Δz and rotation of angle $\theta = \Delta z/L$ around the same z-axis, where $2\pi L$ is a constant called the helix pitch. Analytical [1] and numerical [2] works describing stationary vortices are mostly restricted to inviscid filaments and patches. Here, we present results from a direct numerical simulation (DNS) code with built-in helical symmetry [3]. This code is able to simulate the viscous dynamics of distributed vorticity profiles, it contains in a simple way the effects of 3D vortex curvature and torsion, and allows one to reach higher Reynolds numbers when compared to a full 3D DNS.

In this framework, the long-time (or equivalently far-wake) dynamics of regularly spaced helical vortices is investigated. In this article, we focus on the case of three identical vortices, and simulate their dynamics as their pitch and Reynolds number is varied. This fundamental work is indeed motivated by the case of wind turbine wakes, which are known to be dominated by helical tip and root vortices. At rated wind velocity, the reduced pitch L of tip vortices is related [4] to the rotor radius R and to the tip-speed ratio λ (which is the ratio between the tangential blade-tip velocity and the wind speed) by $L = \sqrt{2}R/(3\lambda)$: typical tip-speed ratios $\lambda = 5-10$ yield L/R values as low as $0.05-0.1$, but smaller as well as far larger values can be reached for other wind speeds. Typical Reynolds numbers $Re = \Gamma/\nu$ based on the circulation Γ of the vortices (ν denotes the kinematic viscosity) are of several million. In these systems, the real flow conditions are made far more complex because of the turbulent atmospheric boundary layer and of coherent structures possibly shed by an upstream turbine, especially in farms. Accurate modelling can be improved if the vortex dynamics and the transition in such complex flows is understood at a fundamental level, and this can be achieved only at the cost of severe simplifications. The present study is done in this spirit. Here, the Reynolds number does not exceed 10^4, the effects

of nonuniform incoming flow conditions are disregarded and, as a first step, the root vortices are not taken into account. This allows us to focus on basic helical vortex interactions occuring in this system. At large L/R, a "classical" three-vortex merging is shown to take place, which somewhat resembles the twodimensional two-vortex merging. When L/R is reduced, it takes more and more time for the vortices to merge, as their rotation speed around the system axis is slowed down by self-induced vorticity effects. This phenomenon is explained by following the interplay between vorticity and streamfunction in the co-rotating frame of reference [5], and tracking the locus of hyperbolic points of the streamfunction. At low L/R-values, typically less than 1, the exponential instability described by Okulov [6,7] is obtained, resulting in various grouping and merging scenarii at the nonlinear stage of evolution. At intermediate L/R-values of the order of 1, only viscous diffusion acts, resulting in a, slow, viscous type of merging.

Other types of instabilities which are fully threedimensional are not described within this helical framework. The helical code run on a short period of time allows one to generate a quasi-steady flow state which may then be used to investigate such instabilities.

NUMERICAL CODE WITH HELICAL SYMMETRY

Governing equations

A flow displays *helical symmetry* of *helix pitch* $2\pi L$ along a given axis if its velocity field is invariant under the combination of an axial translation of Δz and a rotation of angle $\Delta z/L$ around the same axis. The flow characteristics are identical along the helical lines $\theta - z/L = \text{const.}$ $L > 0$ corresponds to a right-handed helix and $L < 0$ to a left-handed helix. A scalar field is helically symmetric if it depends on only two space variables r and $\varphi \equiv \theta - z/L$. Helical symmetry for a vector field $\boldsymbol{u}$ can be expressed as follows:

$$\boldsymbol{u} = u_r(r,\varphi,t)\boldsymbol{e}_r(\theta) + u_\varphi(r,\varphi,t)\boldsymbol{e}_\varphi(r,\theta) + u_B(r,\varphi,t)\boldsymbol{e}_B(r,\theta) \tag{1}$$

where the orthonormal Beltrami basis (see fig. 1) is defined as

$$\boldsymbol{e}_B(r,\theta) = \alpha(r)\left[\boldsymbol{e}_z + \frac{r}{L}\boldsymbol{e}_\theta(\theta)\right], \quad \boldsymbol{e}_r(\theta), \quad \boldsymbol{e}_\varphi(r,\theta) = \boldsymbol{e}_B \times \boldsymbol{e}_r \tag{2}$$

with

$$\alpha(r) = \left(1 + \frac{r^2}{L^2}\right)^{-\frac{1}{2}}, \quad 0 \le \alpha(r) \le 1\,. \tag{3}$$

A general incompressible helical flow can be expressed with only two scalar fields as:

$$\boldsymbol{u} = u_B(r,\varphi,t)\,\boldsymbol{e}_B + \alpha(r)\nabla\psi(r,\varphi,t) \times \boldsymbol{e}_B \tag{4}$$

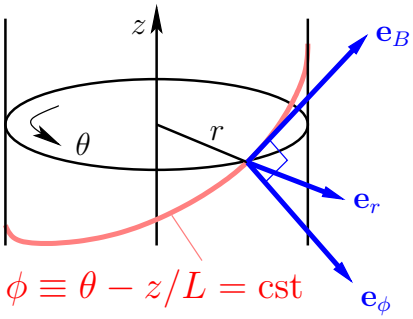

Figure 1: Local helical basis.

where $\psi(r,\varphi,t)$ is a streamfunction. Its vorticity field can be expressed as follows:

$$\boldsymbol{\omega} = \omega_B(r,\varphi,t)\,\boldsymbol{e}_B + \alpha\nabla\left(\frac{u_B(r,\varphi,t)}{\alpha}\right)\times\boldsymbol{e}_B\,. \tag{5}$$

The global field is given by the two scalar fields $\omega_B(r,\varphi,t)$ and $u_B(r,\varphi,t)$: indeed the streamfunction ψ is slaved to both the component of vorticity ω_B and of velocity u_B along the unit vector $\boldsymbol{e}_B$ by

$$\omega_B = -\mathbb{L}\psi + \frac{2\alpha^2}{L}u_B \tag{6}$$

where the linear operator $\mathbb{L}$ is a generalized Laplace operator:

$$\mathbb{L}(\cdot) = \frac{1}{r\alpha}\frac{\partial}{\partial r}\left(r\alpha^2\frac{\partial}{\partial r}(\cdot)\right) + \frac{1}{r^2\alpha}\frac{\partial^2}{\partial\varphi^2}(\cdot)\,. \tag{7}$$

The dynamical equations can be thus formulated within a generalization of the standard 2D ψ–ω method. The equation for u_B reads as

$$\partial_t u_B + NL_u = VT_u \tag{8}$$

where the nonlinear and viscous terms are given by

$$\begin{aligned} NL_u &\equiv \boldsymbol{e}_B\cdot[\boldsymbol{\omega}\times\boldsymbol{u}]\,, \\ VT_u &\equiv \nu\left[\mathbb{L}(\frac{u_B}{\alpha}) - \frac{2\alpha^2}{L}\omega_B\right]. \end{aligned} \tag{9}$$

The equation for ω_B reads

$$\partial_t\omega_B + NL_\omega = VT_\omega \tag{10}$$

where the nonlinear is given by

$$NL_\omega \equiv \boldsymbol{e}_B\cdot\nabla\times[\boldsymbol{\omega}\times\boldsymbol{u}]\,, \tag{11}$$

and the viscous term by

$$VT_\omega \equiv -\nu\, \boldsymbol{e}_B \cdot \nabla \times [\nabla \times \boldsymbol{\omega}] = \nu \left[\mathbb{L}(\frac{\omega_B}{\alpha}) - \left(\frac{2\alpha^2}{L}\right)^2 \omega_B + \frac{2\alpha^2}{L}\mathbb{L}(\frac{u_B}{\alpha}) \right] . \tag{12}$$

The boundary conditions are regularity conditions at the axis and potential flow conditions at the outer circular boundary. As variable $\varphi = \theta - z/L$ is 2π-periodic, the numerical code uses Fourier series along that direction, and second order finite differences in the radial direction. The time advance is performed using second order backward discretisation of the temporal derivative. Nonlinear terms appear explicitly through second order Adams–Bashforth extrapolation whereas the viscous terms are treated implicitly. More details can be found in [3].

Here we simulate the evolution of three identical helical vortices of circulation Γ. Their maximum vorticity is at distance R_0 from the axis, and are equally distributed along the azimuth. Each vortex has an initial small core size a_0 and a pitch $2\pi L$. It would be possible to make quantities dimensionless using the helix radius R_0 as space scale, quantity R_0^2/Γ as time scale. The physical problem would then depend on three dimensionless parameters, namely the Reynolds number $Re = \Gamma/\nu$, and the two ratios L/R_0 and a_0/R_0. However, the problem can be made generic and dependent only on two parameters if one considers the vortex dynamics starting from a *singular* helical vortex of radius $R_\star$, pitch L and core size $a_\star = 0$ at a certain time origin, say $t_\star$. Selecting different core sizes a_0 as initial conditions for the simulation at $t = 0$ then amounts to perform a shift of $t_\star$ to different points in the past. This procedure, common for rectilinear vortices in 2D vorticity dynamics, is extended here to helical vortices. In the following we thus adopt the quantities $R_\star$ and $R_\star^2/\Gamma$ as space and time scales. The dynamics is governed by the two parameters Re and the reduced pitch $\bar{L} \equiv L/R_\star$. The initial condition at $t = 0$ is arbitrarily chosen with core size $\bar{a_0} \equiv a_0/R_\star = 0.2$ and radius $\bar{R_0} \equiv R_0/R_\star = 1$. At the very beginning of the simulation, the radius abruptly increases by less than 1% as the initial condition is no equilibrium state. How the vorticity and velocity distributions are built and the time $t_\star$ computed is explained in the following section. Hereafter, all quantities are dimensionless, and, for sake of simplicity, we drop the bars above the corresponding variables.

Generic initial conditions for a set of helical vortices

When defining an initial condition with finite core size, it is thus important to ensure that this state results from the time evolution of an initial singular helical vortex line. First, within the helical symmetry, the conservation of vortex circulation Γ and axial momentum Π_z leads to

$$\int \omega_z \, \mathrm{d}S = \Gamma \, , \quad \int r\omega_\theta \, \mathrm{d}S = \frac{R_\star^2 \Gamma}{L} \, . \tag{13}$$

Let us choose the distribution $\tilde{\omega}_B$ in the (r, φ) plane, which corresponds to a Gaussian helical vorticity profile of size a_0 in a plane orthogonal to the singular filament. When $L \to \infty$ such a solution is an inviscid equilibrium which diffuses via diffusion from a singular filament. When L is finite it is an approximate inviscid equilibrium.

In order to fully determine the flow field, it is necessary to determine the helical velocity distribution u_B. A possible initial condition is such that $u_B/\alpha = \Gamma/(2\pi L)$. This is the case when the vorticity field is everywhere tangent to helical lines. In the inviscid framework, it is known that it remains so. When viscosity is present, this does not hold anymore, and it can be shown that a gradient of u_B/α is generated via viscous coupling between ω_B and u_B. Let us define the function f as

$$f(r,\phi) \equiv \frac{u_B}{\alpha} - \frac{\Gamma}{2\pi L}\,.$$

It can be established that in the limit of small f, the following relationship holds:

$$f(r,\varphi) = -\frac{2(t-t_\star)}{L\,Re}\alpha\omega_B(r,\varphi)\,.$$

For the generation of the initial condition, we hence assume f to be proportional to $\alpha\omega_B$. We then seek two normalisation constants C and D such that

$$\alpha\omega_B = C\alpha\tilde{\omega}_B \quad \text{and} \quad f = D\alpha\tilde{\omega}_B\,.$$

These constants are obtained using the conservation laws (13). In order to compute the time origin $t_\star$ corresponding to the singular vortex state, we use another conservation law linked to the angular momentum:

$$\int f\,\mathrm{d}S = -\frac{2(t-t_\star)}{L\,Re}\,,$$

that directly yields $t_\star$ when applied to the initial condition at $t = 0$.

The computation is done on dimensionless variables hence $\Gamma = 1$, $R_0 = 1$, $a_0 = 0.2$. The numerical domain is a disk of radius $R_{\text{ext}} = 3$, meshed by $N_r \times N_\theta$ grid points. For Reynolds number $Re = 5000$ and 10000, one choses $N_r = 512$ and $N_\theta = 384$. When $Re = 1000$, these values can be reduced to $N_r = 256$ and $N_\theta = 192$.

MERGING OF LARGE PITCH VORTICES

A typical case: $L = 2$, $Re = 5000$

In this section, we consider three helical vortices with large pitch, typically $L \geq 2$, and describe the merging process. Fig. 2 displays the helical vorticity ω_B and velocity u_B/α components in the $z = 0$ plane for several times during the simulation at $L = 2$ and $Re = 5000$. Also plotted are the streamlines in the frame rotating with the vortex system, obtained as isocontours of the co-rotating streamfunction ψ_R. These figures can be discussed in association to fig. 3a and 4a which characterize the motion in the $z = 0$ plane of the point with maximum helical vorticity ω_B, more specifically its radial position $r_{\max}(t)$ and its angular velocity $\Omega(t)$. In a first phase, the vortices rotate (see snapshots at $t - t_\star = 156$) counterclockwise and grow in size through viscous diffusion. Around a critical time $t_1 - t_\star = 363$, the vortices enter a second phase of

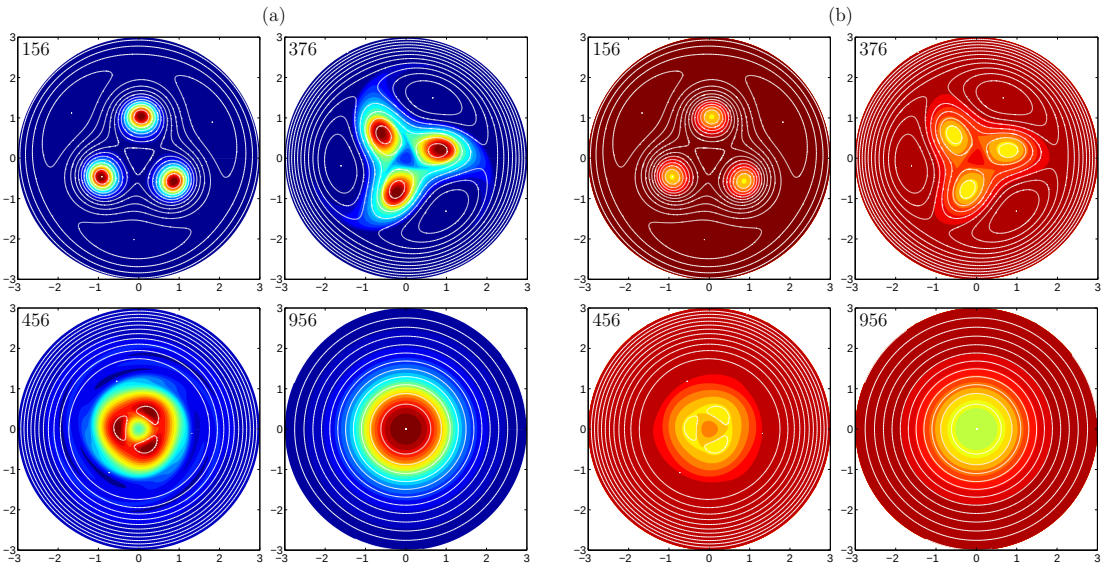

Figure 2: Isocontours of (a) ω_B (colored and filled) and ψ_R (white lines) and (b) u_B/α (colored and filled) and ψ_R, at $t-t_\star = 156, 376, 456, 956$. Simulation for $L = 2$ and $Re = 5000$.

the dynamics, namely a motion towards the center (see snapshots at $t-t_\star = 376$), while their angular velocity drastically increases. As there is a continuous shift from phase 1 to phase 2, we use the geometrical construction shown on fig. 3a to define t_1. As for the case of two-vortex merging, the second phase stops when the vortices are at a certain distance from the center, here for $t-t_\star \approx 400$. A third phase ($400 < t-t_\star < 600$) then begins with radial oscillations while the vortices keep on expanding (see snapshots at $t-t_\star = 456$). This expansion leads to an azimuthal overlap of the vortices and to an eventual axisymmetric corona of helical vorticity. This feature is absent for two-vortex merging where a single central vortex is formed. A fourth phase then begins ($600 < t-t_\star < 816$) where the maximum of vorticity inside the corona gently drifts towards the axis, as the asymptotic state is Gaussian (fifth phase). This phenomenon is seen in fig. 3a where a plateau without any oscillation is present as phase 4, which has no counterpart in the case of two-vortex merging.

Influence of the Reynolds number

The influence of the Reynolds number on the dynamics is shown on fig. 3b. Increasing the Reynolds number has several effects:

- Phase 1: the initial diffusion phase 1 is longer as viscous diffusion is diminished, and it is observed from the simulations that the duration of this phase $\Delta t_1 = t_1 - t_\star$ is proportional to Re at a fixed value of L.

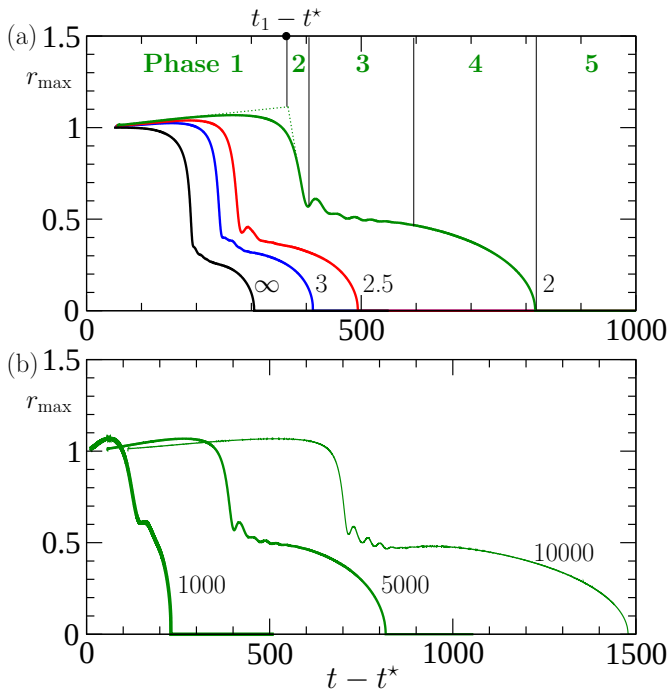

Figure 3: Radial position $r_{\max}$ of the vorticity maximum as a function of time $t - t_\star$ (a) for $L = \infty, 3, 2.5, 2$ and $Re = 5000$, (b) for $L = 2$ and $Re = 1000, 5000, 10000$.

- Phase 2: it is seen that the distance $r_{\max}(t_2)$ at the end of the radial compression phase 2 weakly depends on the Reynolds number, and this phase is shorter for higher Reynolds numbers.
- Phase 3: the frequency of the oscillations during phase 3 do not depend on the Reynolds number, and they are less damped at high *Re*.
- Phase 4: the duration of this purely diffusive phase is directly proportional to the Reynolds number.

Influence of the helical pitch

On fig. 3a, it can be seen that decreasing the pitch L from its infinite 2D value at constant Reynolds number *Re* has a marked slowdown effect on the merging process. One may be tempted to attribute this slowdown process to the fact that the vortices rotate at a weaker angular velocity as L is decreased, as depicted in fig. 4a. This reduced rotating speed comes from the increasing role of the self-induced velocity which tends to make vortices rotate clockwise. This effect is at the origin of the longer time scales observed as L is decreased, but not in a straightforward fashion, as explained below.

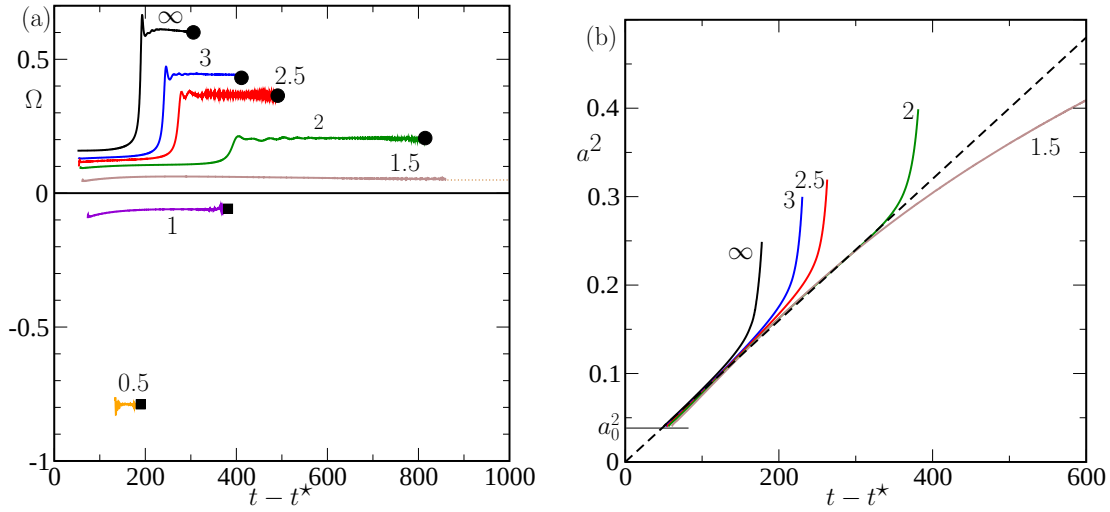

Figure 4: (a) Rotation rate Ω of the position of maximum vorticity with respect to time $t-t_\star$ for $L=\infty,3,2,1.5,1,0.5$ and $Re=5000$. The circle denotes a state for which the maximum vorticity is at this axis, a square denotes a symmetry breaking instability. (b) Squared core size of individual vortices a^2 as a function of time $t-t_\star$ for $L=\infty,3,2.5,2,1.5$ and $Re=5000$. The dashed-line shows the 2D diffusion law $a^2(t)=a_0^2+4\,t/Re$.

It should be first noticed that changing L has no significant effect on the time evolution of the vortex core size during phase 1 (see fig. 4b). The evolution law remains close to the 2D one $a^2(t)=a_0^2+4\,t/Re$. Yet, the critical core size $a(t_1)$ at which phase 2 begins increases as L is decreased. An explanation can be found by recalling the way the twodimensional vortex merging works in the two-vortex case: there, the convective merging phase 2 begins while a significant amount of vorticity has escaped the closed atmosphere of the two vortices, and begins to form filaments in the surrounding fluid. A similar scenario takes place here, as shown on fig. 5: at critical time t_1, vorticity has filled the atmosphere of the three vortices, and begins to escape into the peripheral rotating fluid through the hyperbolic points of the corotating streamfunction such as H_1, because of viscous diffusion. The subsequent formation of filaments is believed to be associated to the convective phase 2 whereby vortices are radially pushed towards the axis. It has been shown [8] that, for different values of L and Re, the pertinent parameter for convective merging is not the ratio $a/r_{\max}$, but rather the ratio between the core size a and the distance $d\equiv E_1H_1$ between the vortex center and the outer hyperbolic point (see fig. 5). Now, as L is decreased, the rotation speed decreases also, causing the hyperbolic points of the co-rotating streamfunction to move away from the axis, i.e. d increases. It is observed from the simulations that, at critical time, the ratio a/d remains near the value 0.54 ± 0.05 for all L and Re (this value is 0.36 for 2 helical vortices). Hence the critical core size increases together with d as L is decreased, which makes phase 1 last longer.

Fig. 5 also shows the topology of the flow in the vicinity of the axis: contrarily to the two-vortex case, a small central region is present, here of triangular shape. This structure seems

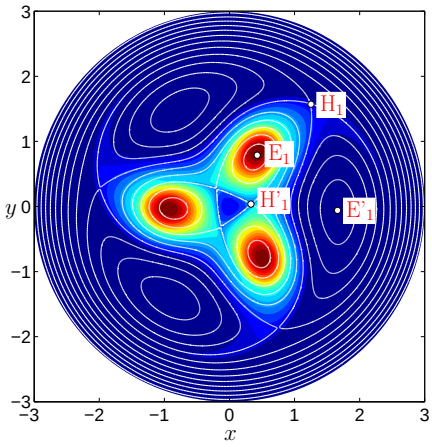

Figure 5: Isocontours of ω_B (colored and filled) and ψ_R (white lines) for $L = 2$ and $Re = 10000$ near critical time before the convective phase 2. The streamline pattern displays two types of hyperbolic points and two types of elliptic points.

robust — in the two-vortex case, we have here a single hyperbolic point [8] — since it prevents the merging of the vortices at the end of the oscillation phase 3 (see fig. 2 at $t - t_\star = 456$).

DIFFUSIVE MERGING AT INTERMEDIATE PITCH

At intermediate pitch $L \approx 1.5$, the rotation speed of the system is weak so that the hyperbolic points such as H_1 are situated far from the axis (typically at distance $r > 2$), so that neither filamentation, nor convective merging occurs. The behaviour of the system is thus dominated by viscous diffusion and successive vortices smoothly merge (fig. 6a), forming an axisymmetric corona of vorticity at a radial distance from the axis of order unity, since $r_{\max} \approx 1$.

INSTABILITY OF SMALL PITCH VORTICES

At small pitches, an array of helical vortices is known to be unstable [5,6] with respect to displacement modes, a phenomenon responsible for the destabilisation of propeller and wind turbine wakes. Okulov [6] showed that the critical pitch under which such instability occurs for the three vortex case with zero core size is $L_c = 1.132$. In the simulation at $L = 1.5$ of fig. 6a, the system is a priori stable with respect to Okulov's threshold. In order to check this, the simulation has been launched for the same parameter values, with an initial perturbation on the position of the 3 vortices (one of them has been radially pushed by 0.001, and one other azimuthally displaced by

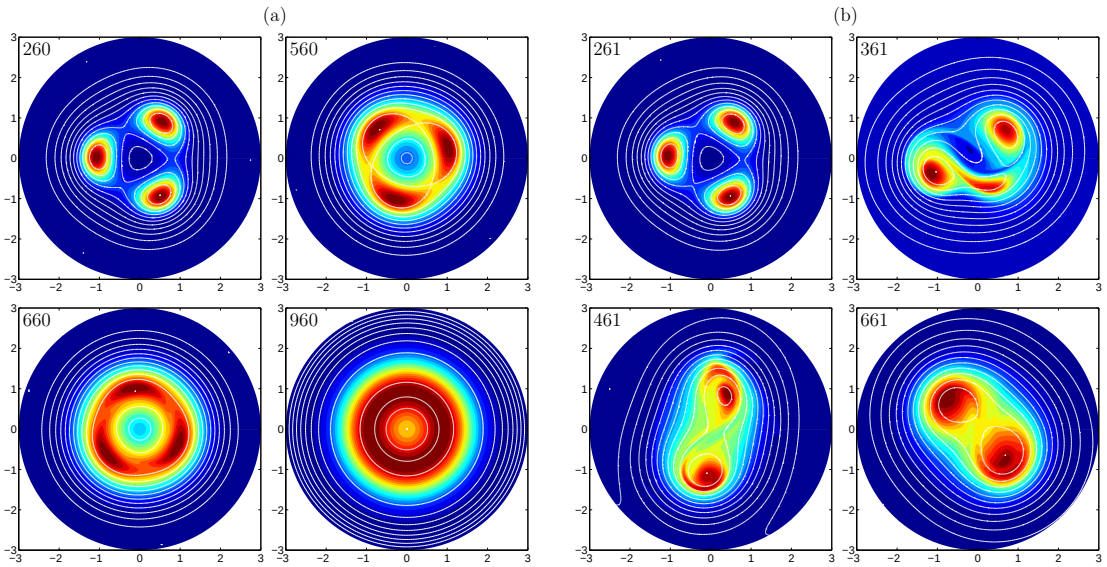

Figure 6: (a) Isocontours of ω_B and ψ_R at $t-t_\star = 260, 560, 660, 960$. Simulation for $L = 1.5$ and $Re = 5000$ without initial perturbation. (b) Isocontours of ω_B and ψ_R at $t-t_\star = 261, 361, 461, 661$. Simulation for $L = 1.5$ and $Re = 5000$, starting from a state in which the vortex positions have been perturbed by an amount 0.001.

0.001). The results are depicted in fig. 6b. It seems that an instability is active, and its effects are felt from $t-t_\star = 300$, causing two of the vortices to merge (see snapshot at $t-t_\star = 361$). After an exchange of vorticity (see snapshot at $t-t_\star = 461$), the system adopts a stable configuration with two thick-cored helices (see snapshot at $t-t_\star = 661$). One possibility is that the finite core size significantly alters the instability threshold, but this remains to be ascertained.

At the pitch value $L = 1$, the system should definitely be unstable. However, if no perturbation is initially set and the growth rate is small enough, the system may diffuse into an axisymmetric helical sheet before the Okulov instability develops significantly. This is illustrated on fig. 7, up to time $t-t_\star = 572$. It can be also observed that the newly formed sheet is unstable with respect to an azimuthal perturbation $m = 1$ (see at $t-t_\star = 402$). This leads to a destruction of the sheet (around $t-t_\star = 452$) and the system asymptotically converges towards one single helical vortex with a thick core (see at $t-t_\star = 852$). However, two reservations can be made: (a) at larger Reynolds numbers, the instability may become active before the sheet forms, (b) the restriction of the study to a helically symmetrical flow with fixed L presumably affects the way the sheet destabilizes: an instability mode is selected, but other waves with different pitches may be more unstable.

If a perturbation of small amplitude is initially set on the system for $L = 1$, then the instability is rapidly felt on the dynamics of the three vortices. This is illustrated on fig. 8, near time $t-t_\star = 122$. One of the helical vortices is then strongly stretched and merges with one of the others (see $t-t_\star = 142$ and $t = 162$.) This is reminiscent of the vortex grouping observed in some experiments [9]. The subsequent evolution is also interesting: the smaller vortex in turn

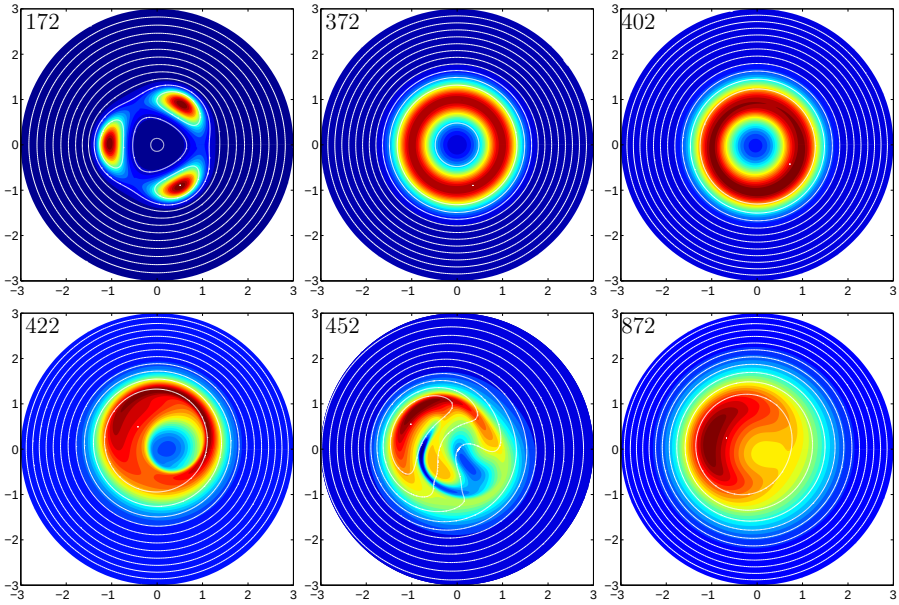

Figure 7: Isocontours of ω_B and ψ_R at $t-t_\star = 172, 372, 402, 422, 452, 872$. Simulation for $L = 1$ and $Re = 5000$ without initial perturbation.

gets stretched by the bigger one and they merge together (see $t - t_\star = 172$ and $t = 192$). This event yields one strong helical vortex with a very unsteady behaviour.

SUMMARY

In this paper, we investigate the dynamics of three helical vortices with respect to their helical pitch. At large pitch, vortex merging occurs that bears many analogies with the two-vortex system. The main difference lies in the structure of the axisymmetric state that is reached, namely a corona of vorticity that eventually diffuses smoothly towards a Gaussian vortex. At intermediate pitch $L \approx 1.5$, the system rotates slowly around the axis, and diffusive effects dominate the dynamics. However, a slight shift of the initial vortex positions is able to destabilize the system. At lower values of L, an axisymmetric sheet may also form, but it is found unstable with respect to a $m = 1$ mode. By contrast, shifting the initial vortex position leads to a rapid destabilisation of the system, and grouping and merging events are observed. This latter case is presumably relevant in real turbine wakes where the nondimensional helical pitch is rather small and large perturbations are due both to incoming flow and rotor geometry.

The three-vortex system can thus reach various asymptotic states either axisymmetric, or helical with one or two vortices depending on the Reynolds number and the pitch. Predicting precise frontiers between the various regimes is not an easy task, because the instability prop-

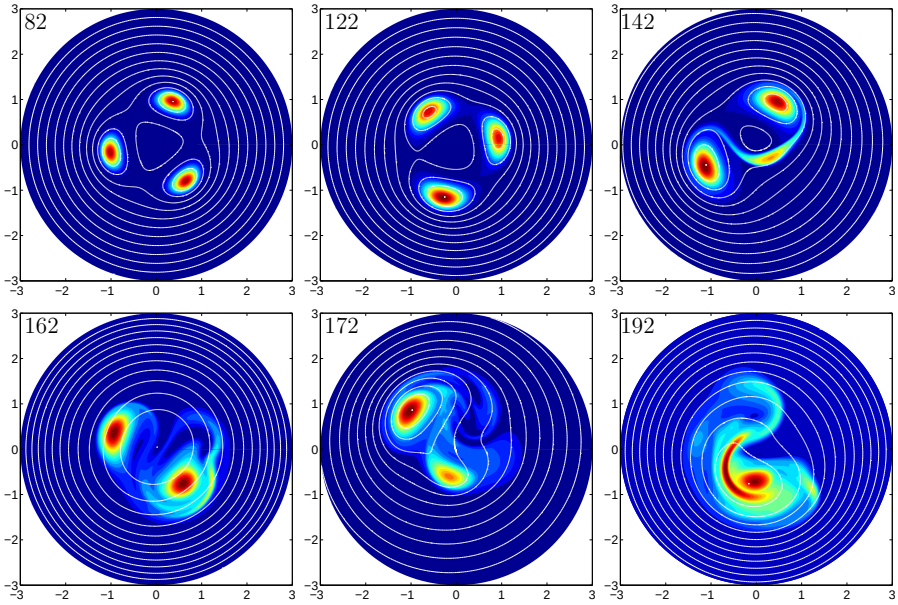

Figure 8: Isocontours of ω_B and ψ_R at $t - t_\star = 82, 122, 142, 162, 172, 192$. Simulation for $L = 1$ and $Re = 5000$, starting from a state in which the vortex positions have been perturbed by an amount 0.001.

erties at small pitch strongly depend on the vortex core size. Such sizes are not constant in the viscous regime, and the way they evolve in time is still an open question.

REFERENCES

[1] Kuibin and Okulov, *Phys. Fluids* **10**, 607 (1998).
[2] Lucas and Dritschel, *J. Fluid Mech.* **634**, 245 (2009).
[3] Delbende, Rossi and Daube, *Theoret. Comput. Fluid Dynamics* **26(1)**, 141 (2012).
[4] Wood and Boersma, *J. Fluid Mech.* **447**, 149 (2001).
[5] Melander, Zabusky and McWilliams, *J. Fluid Mech.* **195**, 305 (1988).
[6] Okulov, *J. Fluid Mech.* **521**, 319 (2004).
[7] Okulov and Sørensen, *J. Fluid Mech.* **576**, 1 (2007).
[8] Piton, *Ph.D thesis, UPMC* (2011).
[9] Felli, Camussi and di Felice, *J. Fluid Mech.* **682**, 5 (2011).

FULL PAPER
Helical vortex wake: How far is the infinity ?

Mohamed Ali[1], **Malek Abid**[1]

[1]IRPHE, U M R 7342 - CNRS et Université d'Aix-Marseille
49 rue Joliot Curie - BP 146 Technopôle de Château Gombert
13384 MARSEILLE Cedex 13
ali@irphe.univ-mrs.fr, abid@irphe.univ-mrs.fr

ABSTRACT

In this paper, we discuss the assumption that the helical vortex wake, such as the wind turbine wake, can be considered as an *infinite* vortex filament or tube. In the real life, vortices in helical wakes are of *finite* length. We compare the velocity field induced by an infinite helical vortex-filament and the velocity field induced by a finite length one. The analytical solution given by Fukumoto & Okulov is used for the infinite case and a Biot-Savart formulation is used for the finite case. A basic difference is found for the radial induced velocity due to the asymmetry of the finite helical vortex (near its boundaries). For the axial velocity field, the distance behind the rotor plane required to superimpose the two models is given and it is found weakly related to the pitch-radius ratio (h/R).
Keywords: Helical vortex tube/filament, Biot-Savart Formulation, rotor wake

INTRODUCTION

Helical vortices are observed in various types of flows. They are often created as tip vortices in rotating devices such as propellers, wind turbines, etc. This type of flow has been the subject of many theoretical, experimental and numerical studies. Many proposed analytical models, especially the Joukowsky model, assumed that the helical vortex wake can be modeled as an *infinite* vortex filament or tube (or N vortices in the case of a N-bladed rotor). This idealistic model was used for the stability analysis of helical vortex systems [2,6,8,9] and the design of rotor blade [1,7,10]. In this context, Hardin [3] developed in 1982 an exact solution for the velocity field, both interior and exterior, induced by an infinite helical vortex filament using Kepteyn's series. Recently, Fukumoto & Okulov [5] succeeded to represent this analytical solution in closed form using a singularity-separation technique. However, in the real life, vortices are of *finite* length (Figure 1).

In the present work, we study the influence of the geometric parameters of the vortex (pitch-radius ratio h/R and the number of coils N_c) on the validity of the above assumption. We calculate, for a finite-length vortex filament, the number of coils needed to consider that the induced velocity field coincides with that of an infinite filament ($N_c = \infty$) with the same circulation Γ, radius R and pitch h. So, we compare the induced velocities of an infinite filament $\vec{V}^I$, given by Fukumoto and Okulov solution [5], to those of a finite-length one $\vec{V}^F$, given by a Biot-Savart formulation [4]. Particular attention is given to the axial induced velocity knowing that it is the important component in wake modeling and blade design.

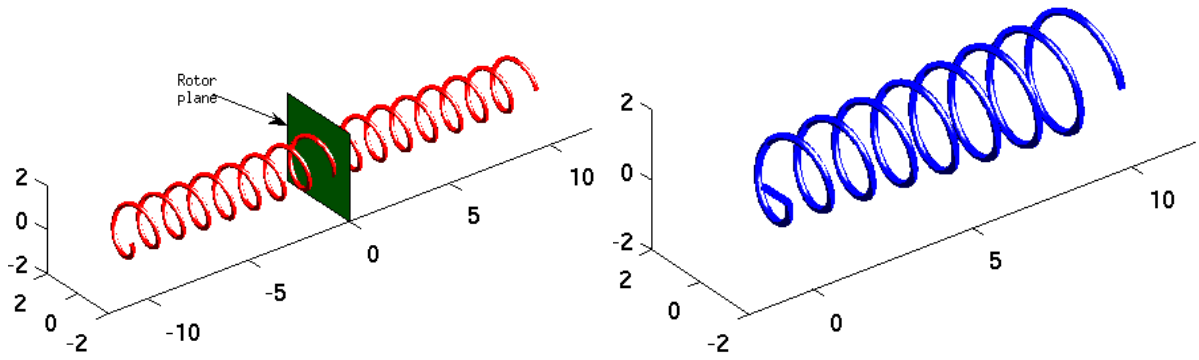

Figure 1: Helical vortex system: (left) an infinite helical vortex-tube, (right) a semi-infinite helical vortex-tube

FORMULATION

Velocity field induced by a finite helical vortex-filament

We consider a right-handed helical vortex-filament (figure 2) of circulation Γ and constant pitch h, with a finite length $L = 2\pi h N_c$, the axis of which is that of a cylinder with radius R. The position of the vortex filament is given, in a cylindrical coordinates system, (r, θ, z), z being the axial direction, by the following equation:

$$\overrightarrow{r}'(\theta') = R\overrightarrow{e_r}(\theta') + h\theta'\overrightarrow{e_z}. \tag{1}$$

The velocity induced by the finite filament on a point M ($\overrightarrow{r}(\theta) = R\overrightarrow{e_r}(\theta) + z\overrightarrow{e_z}$) is given by the Biot-Savart relation as follows:

$$\vec{V}^F(\vec{r}) = \frac{\Gamma}{4\pi}\int_{Helix}\frac{\vec{t}'(s')\wedge(\vec{r}-\vec{r}'(s'))}{\|\vec{r}-\vec{r}'(s')\|^3}ds', \quad \vec{r}\notin Helix \tag{2}$$

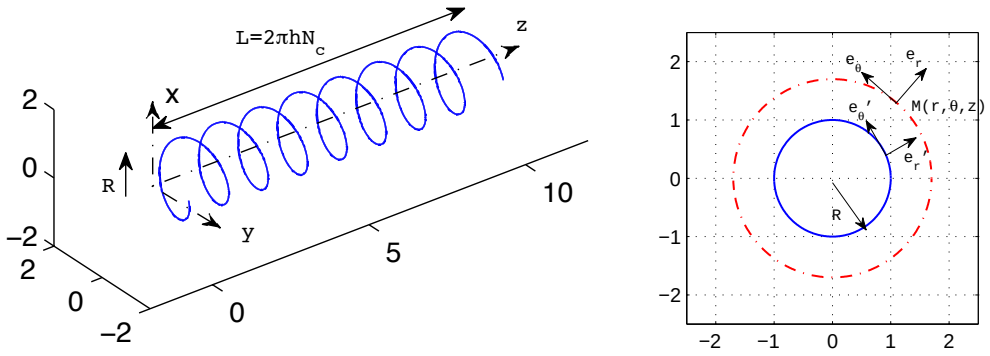

Figure 2: Geometry of the helical vortex filament

where $\vec{t}$ is the unit tangent vector to the helical vortex and s' is the (curvilinear) abscissa along $\vec{t}$ and is given by :

$$\vec{t}' = \frac{\frac{d\vec{r}'}{d\theta'}}{\|\frac{d\vec{r}'}{d\theta'}\|} = \frac{d\vec{r}'}{ds'} \tag{3}$$

$$\frac{ds'}{d\theta'} = \|\frac{d\vec{r}'}{d\theta'}\| \tag{4}$$

$$\vec{r}'(\theta') = R\vec{e}'_r(\theta') + k\theta'\vec{e}_z \tag{5}$$

$$\vec{r}(r,\theta,z) = r\vec{e}_r(\theta) + z\vec{e}_z \tag{6}$$

$$\tag{7}$$

with

$$\vec{e}'_r = \cos(\theta-\theta')\vec{e}_r + \sin(\theta-\theta')\vec{e}_\theta \tag{8}$$

$$\vec{e}'_\theta = \sin(\theta-\theta')\vec{e}_r + \cos(\theta-\theta')\vec{e}_\theta \tag{9}$$

This allows us to write :

$$ds' = \sqrt{R^2+k^2}\,d\theta' \tag{10}$$

$$\vec{t}' = \frac{1}{\sqrt{R^2+k^2}}(R\vec{e}'_\theta + k\vec{e}'_z) \tag{11}$$

and so,

$$\vec{t}' \wedge (\vec{r} - \vec{r}') = \frac{1}{\sqrt{R^2 + k^2}} \begin{pmatrix} R\sin(\theta - \theta') \\ R\cos(\theta - \theta') \\ k \end{pmatrix} \wedge \begin{pmatrix} r - R\cos(\theta - \theta') \\ R\sin(\theta - \theta') \\ z - k\theta' \end{pmatrix} \tag{12}$$

Finally, the velocity induced by the finite filament is given as follows:

$$\begin{aligned} \vec{V}^F(\vec{r}) &= \frac{\Gamma}{4\pi} \int_{[\theta']} \frac{1}{\left((r - R\cos(\theta - \theta'))^2 + R^2\sin^2(\theta - \theta') + (z - k\theta')^2\right)^3 / 2} \\ &\begin{pmatrix} R\cos(\theta - \theta')(z - k\theta') - Rk\sin(\theta - \theta') \\ k(r - R\cos(\theta - \theta')) - (z - k\theta')R\sin(\theta - \theta') \\ R^2 - rR\cos(\theta - \theta') \end{pmatrix} d\theta' \end{aligned} \tag{13}$$

Velocity field induced by an infinite helical vortex-filament

For the velocity induced by an infinite filament, $\vec{V}^I$, we consider the solution given by Fukumuto & Okulov [3]:

$$u_r(r,\chi) = -\frac{\Gamma}{2\pi rk} \sqrt[4]{(k^2 + r^2)(k^2 + R^2)}\, Im\left[\frac{e^{i\chi}}{e^{\mp\xi} - e^{i\chi}} \pm \frac{k}{24}\left(\frac{2k^2 + 9R^2}{(k^2 + R^2)^{3/2}} - \frac{2k^2 + 9r^2}{(k^2 + r^2)^{3/2}}\right) ln(1 - e^{\pm\xi + i\chi}\right] \tag{14}$$

$$u_\theta(r,\chi) = \frac{\Gamma}{2\pi r}\left(\begin{pmatrix} 0 \\ N_b \end{pmatrix} - \frac{\sqrt[4]{k^2 + R^2}}{\sqrt[4]{k^2 + r^2}} \sum_{n=1}^{N_b} Re\left[\frac{\pm e^{i\chi_n}}{e^{\mp\xi} - e^{i\chi_n}} + \frac{k}{24}\left(\frac{3r^2 - 2k^2}{(k^2 + r^2)^{3/2}} + \frac{9R^2 + 2k^2}{(k^2 + R^2)^{3/2}}\right) \ln(1 - e^{\pm\xi + i\chi})\right]\right) \tag{15}$$

$$u_z(r,\chi) = \frac{\Gamma}{2\pi r}\left(\begin{pmatrix} N_b \\ 0 \end{pmatrix} + \frac{\sqrt[4]{k^2 + R^2}}{\sqrt[4]{k^2 + r^2}} \sum_{n=1}^{N_b} Re\left[\frac{\pm e^{i\chi_n}}{e^{\mp\xi} - e^{i\chi_n}} + \frac{k}{24}\left(\frac{3r^2 - 2k^2}{(k^2 + r^2)^{3/2}} + \frac{9R^2 + 2k^2}{(k^2 + R^2)^{3/2}}\right) \ln(1 - e^{\pm\xi + i\chi})\right]\right) \tag{16}$$

where

$$\chi = \theta - z/k \tag{17}$$

$$\chi_n = \chi + \frac{2\pi(n-1)}{N_b} \tag{18}$$

$$e^{\xi} = \frac{r(1 + \sqrt{1 + R^2/kl^2})exp(\sqrt{1 + r^2/k^2})}{R(1 + \sqrt{1 + r^2/k^2})exp(1 + \sqrt{1 + R^2/k^2})} \tag{19}$$

where $Re[.]$ and $Im[.]$ indicate the real and imaginary parts of the complex expression, respectively. For the notations '$\pm$' and '(:)', the upper sign or symbol in parenthesis corresponds to $r < R$ and the lower to $r \geq R$.

RESULTS AND DISCUSSION

Radial induced velocity at the rotor plane

In what follows the induced axial flow-velocity of the infinite helical vortex is chosen as a velocity scale. One effect of breaking the symmetry of the wake is the creation of a radial velocity in the rotor plane. Figure 3 shows that the azimuth-averaged radial velocity in the rotor plane has a magnitude with same order as the axial induced velocity (only the $h/R = 1$ case is presented here, but the same behavior is found for different h/R). The presence of the radial velocity brings into question many theoretical approaches which neglect the radial velocity effect on the wind turbine wakes or does not consider it in the blade design process.
The non-zero radial velocity at the rotor plane is the most important difference between the two approaches considered here (infinite and finite vortex filament).

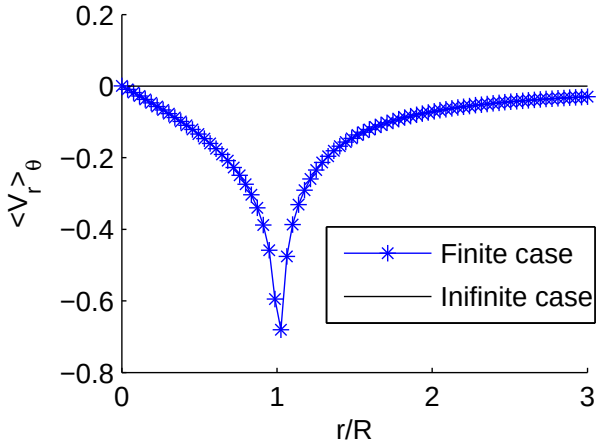

Figure 3: Radial induced velocity, averaged in the azimuthal direction, $\langle V_r \rangle_\theta$: comparison between velocity induced by the finite helical vortex and the infinite helical vortex at the rotor plane and for $h/R = 1$.

Axial induced velocity

As the axial induced velocity is the important component for the wake modeling and blade design, we discuss here its behavior for the two considered configurations.
As shown in Figure 4, the azimuth-averaged axial velocity induced by a finite helical vortex-filament depends on the pitch-radius ratio (h/R) and the number of coils which form the filament considered.
It's found that, for small h/R values, a high number of coils is needed to consider that $\vec{V}^F$ is equivalent to $\vec{V}^I$ (i.e., $||(\vec{V}^F - \vec{V}^I)/\vec{V}^I|| = \varepsilon,\ \varepsilon \ll 1$) , contrarily to the cases with high h/R where few coils are sufficient. In what follows, unless otherwise stated, $\vec{V}^F$ and $\vec{V}^I$ are evaluated at $r = 0$ and $z = L/2$, and only results for their axial components, V_z^F, and V_z^I are shown.
From an experimental point of view, the helical tip vortex generated during few rotor revolutions is equivalent to an infinite helical vortex with the same parameters (Γ, R, h) when $h/R \sim O(1)$

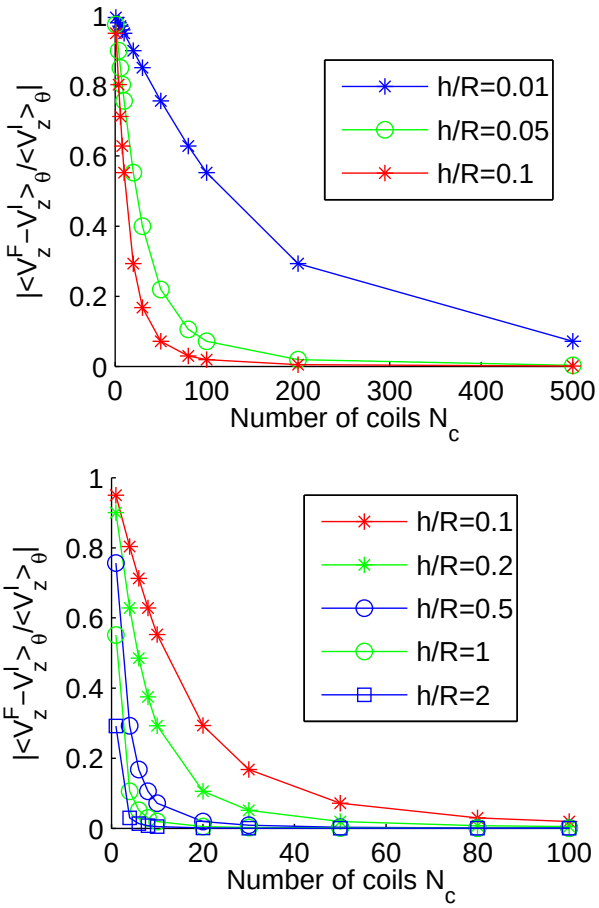

Figure 4: Comparison between a finite vortex filament (Biot-Savart formulation) and an infinite one (Fukumoto and Okulov analytical solution) for different h/R: the azimuthal average of the axial-velocity relative-difference is presented as a function of the number of coils N_c.

which is the case of wind turbine rotors. But for small h/R which is the case of helicopter rotors, the helical vortex generated can not be considered equivalent to an infinite helical vortex until it is formed by a large number of coils.
Based on our calculations, the relative difference between the two velocities V_z^I and V_z^F, for a given h/R, follows the following law:

$$\begin{aligned} \frac{|V_z^F - V_z^I|}{|V_z^I|} &= \exp(-N_c/N_c^*), \\ N_c^* &= \frac{\alpha}{\beta + h/R}. \end{aligned} \tag{20}$$

We find $\alpha \simeq 2$ and $\beta \simeq 2\ 10^{-3}$, two coefficients approximating the characteristic number

of coils N_c^*. Note that this law is the same (data not chown) for $r \neq 0$ if $\langle V_z^F \rangle_\theta$ and $\langle V_z^I \rangle_\theta$ are considered with $\langle . \rangle_\theta$ the average in the azimuthal direction θ.

It is interesting to note that, the number of coils can be transformed to a non-dimensional axial distance d, behind the rotor plane, given by:

$$d = N_c h/R \tag{21}$$

As shown in Figure 5, the difference between the two (azimuth-averaged) axial induced-velocities has a similarity behavior, i.e., all the curves collapse when the variable d is used, and

$$\begin{aligned} \frac{|V_z^F - V_z^I|}{|V_z^I|} &= \exp(d/d^*), \\ d^* &= N_c^* h/R = \frac{\alpha}{1+\beta R/h}, \end{aligned} \tag{22}$$

It is shown in Figure 6 that d^* converges quickly to a constant value equal to α ($i.e., d^* = 2$), it is weakly related to h/R, unlike N_c^*, ans so d is weakly related to the pitch-radius ratio. It is shown in the Figure 7 that the axial velocity field induced by the finite helical filament is equivalent to that given by an infinite helical filament for a nondimensional axial position $d \simeq 8$ from the rotor plane (with less than 1% relative difference). So the length, L, of the finite helical vortex-filament, that must be considered to ensure that the axial induced velocity coincides (near $L/2$) with that of an infinite vortex-filament prediction, is at least $L/R = 2d \simeq 16$ as sketched in Figure 8.

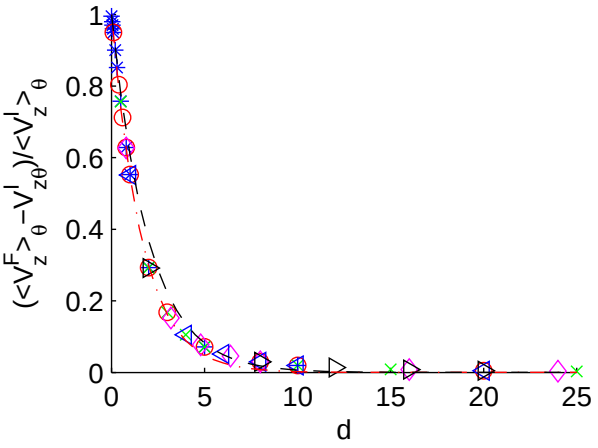

Figure 5: The comparison between the averaged axial velocity induced by the finite filament and that induced by the infinite filament at $r = 0$ as a function of the axial distance d, for different h/R : $*$ $h/R = 0.01$, $\circ$ $h/R = 0.1$, $\times$ $h/R = 0.5$, $\diamond$ $h/R = 0.8$, $\triangleleft$ $h/R = 1$, $\triangleright$ $h/R = 2$, $+$ $h/R = 10$, $-.-$ $\exp(-d/1.65)$, $--$ $\exp(-d/2)$.

Furthermore, this study justifies that the axial velocity induced by a finite helical vortex at

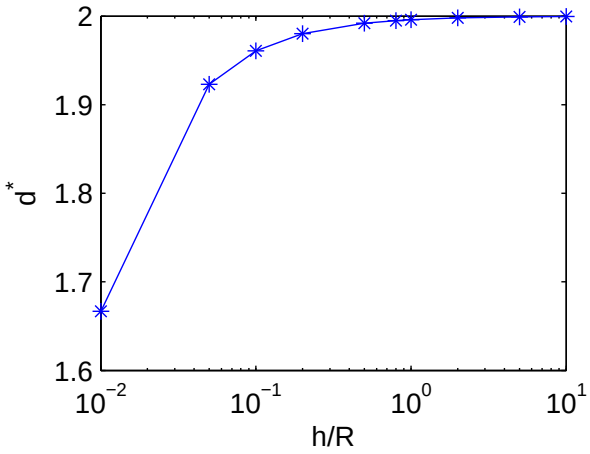

Figure 6: The characteristic distance d^* converge rapidly to $\alpha = 2$ for increasing pitch-radius ratio h/R

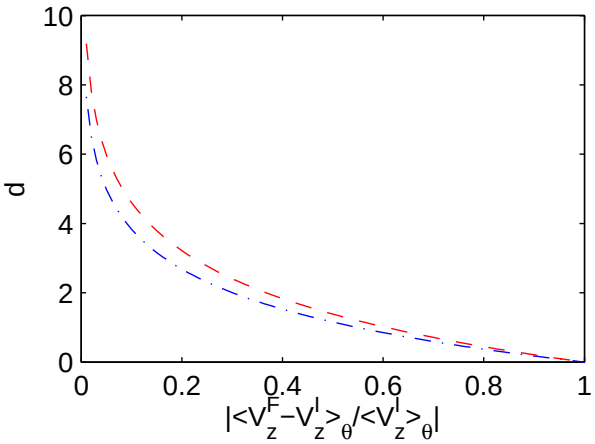

Figure 7: Axial distance behind the rotor plane as a function of $|\langle V_z^F - V_z^I\rangle_\theta / \langle V_z^I\rangle_\theta|$: $-.-$ $h/R = 0.01$, $--$ $h/R = 10$.

the rotor plane is the ***half*** of the velocity induced by an infinite helical vortex if $L \geq 16R$. Figure 9 shows the difference between the averaged axial velocities at the rotor plane ($d = 0$) and at axial position $d = 8$.

Comparison with a numerical simulation of a rotor wake

In this paragraph we present a comparison of azimuth averaged velocities, of infinite and finite helical (filament) vortices, with those of a finite helical vortex (with a core) in the wake of a rotating blade, obtained in a numerical simulation using the actuator line method [11]. A helical

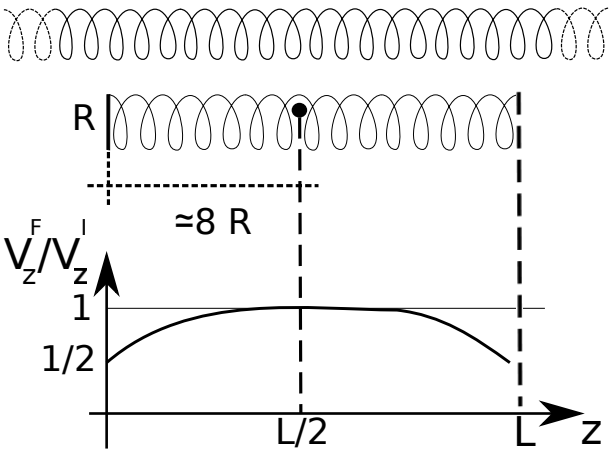

Figure 8: Sketch of the behavior of the axial velocity, V_z^F, induced by a finite helical vortex-filament of length $L/R = 2d = 16$. Near the central part, $L/2$, the velocity V_z^F is equal to that induced by an infinite helical vortex-filament V_z^I.

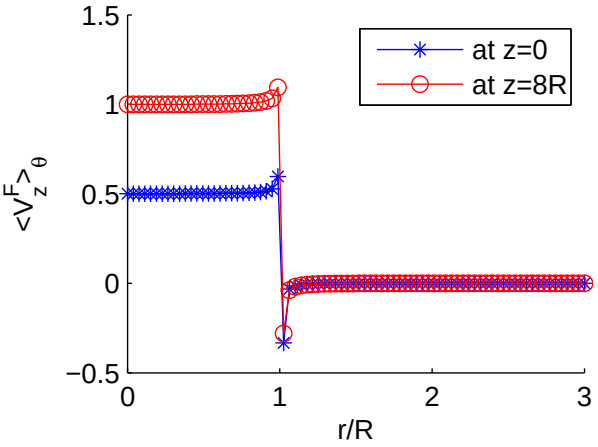

Figure 9: Axial induced velocity: $\langle V_z^F \rangle_\theta|_{d=0} = 1/2\langle V_z^F \rangle_\theta|_{d=8}$ for $h/R = 1$.

vortex filament, having the circulation and radius of the hub vortex, is also used in the finite and infinite computations of vortex filament velocities (see figure 10). The azimuth averaged velocities, in the rotor plane, are presented in figure 11. In the finite cases, the lengths of vortices are $L \simeq 16R$. It is shown that average velocities of finite length vortices are in good agreement, however they are different from those of the infinite case. Note, however, the factor two in magnitude between the finite and infinite cases for azimuthal and axial velocities.

CONCLUSION

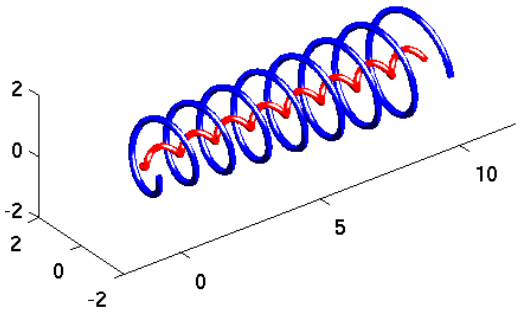

Figure 10: A sketch of the tip and hub vortices used to calculate velocities for comparison with those of the actuator line method.

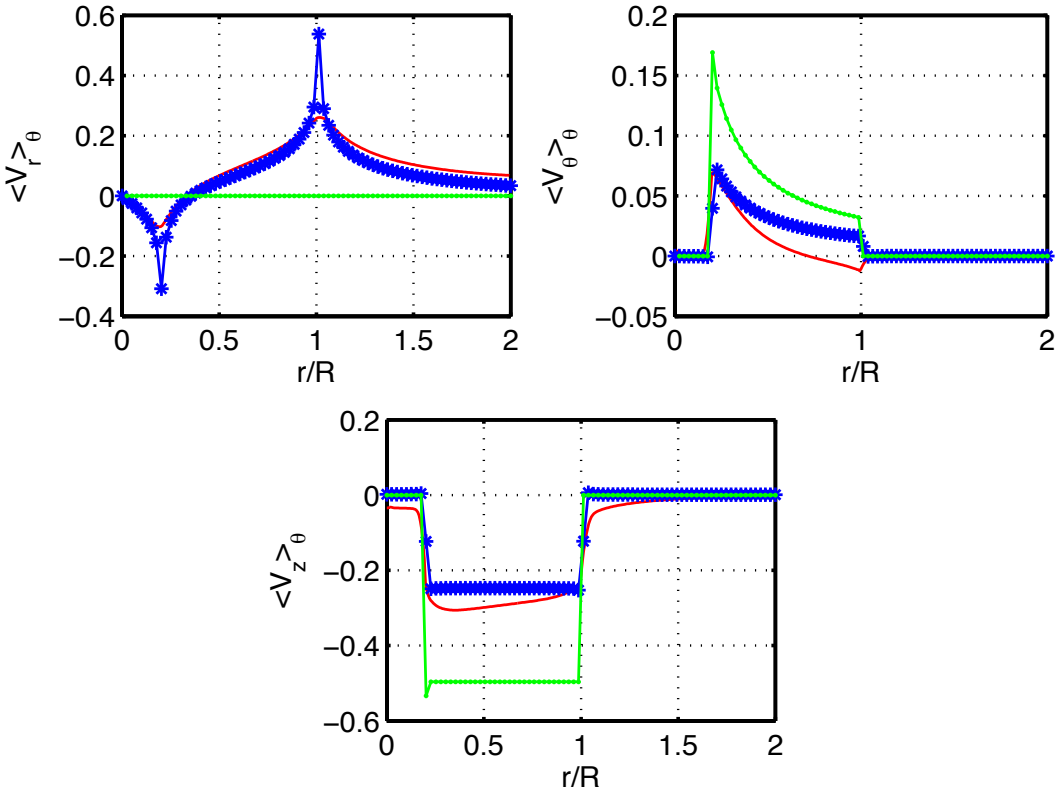

Figure 11: Azimuth averaged velocities at the rotor plane. Green color: infinite vortex; blue color: finite vortex with a length $L \simeq 16R$; red color: numerical simulation using the actuator line method in a computational box with an axial length $L \simeq 16R$.

A comparison between an infinite helical vortex-filament and a (realistic) finite helical vortex-filament has been done. The study allows to verify the validity of some approximations used to model wind turbine wakes and/or to design new blades. The main results of this study can be summarized as follows:

- 1. The symmetry of the infinite helical vortex-filament is broken when we consider a finite helical vortex-filament. Therefore, a not-negligible radial velocity appears at the rotor plan.
- 2. For a helical vortex-filament with a length $L \geq 16R$ (Figure 8), the axial induced velocity could be considered equivalent to that induced by an infinite helical vortex-filament near $L/2$, with a relative difference less than 1%. This length has been found to be independent of the pitch-radius ratio h/R.
- 3. The axial induced velocity at the rotor plane is found equal to the half of the velocity induced by the infinite vortex when $L \geq 16R$.

REFERENCES

[1] H. Glauert, "Airplane propellers", In: Durand, WF. (ed) Division in Aerodynamic Theory, Reprinted edition 1943, vol IV, pp. 169-360.
[2] S.E. Widnall, "The stability of helical vortex filament", J. Fluid Mech, vol 54 (1972) pp. 641-663.
[3] J.C. Hardin, "The velocity field induced by a helical vortex filament", Phys. Fluid, vol.25 (1982) pp. 1949-1952.
[4] P.G. Saffman, "Vortex Dynamics", Cambridge University Press 1992.
[5] Y. Fukumoto, V.L. Okulov, "The velocity field induced by a helical vortex tube", Phys. Fluid, vol.17 (2005) pp. 1-19.
[6] V.L. Okulov, J.N. Sørensen, "Stability of helical tip vortices in a rotor far wake", J. Fluid Mech, vol 576 (2007) pp. 1-25.
[7] V.L. Okulov, J.N. Sørensen, "Maximum efficiency of wind turbine rotors using Joukowsky and Betz approaches", J. Fluid Mech, vol 649 (2010) pp. 497-508.
[8] V.L. Okulov, J.N. Sørensen, "Applications of 2D helical vortex dynamics", Theor. Comput. Fluid Dyn., vol 24 (2010) pp. 395-401.
[9] I. Delbende, M. Rossi, O. Daube, "DNS of flows with helical symmetry", Theor. Comput. Fluid Dyn., (2011)
[10] H. Bolnot, "Instabilitées des tourbillons hélicoïdaux :application au sillage des rotors", PhD thesis, Aix-Marseille University, IRPHE, France 2012.
[11] Sorensen, J. N. and Shen, W. Z., "Numerical modeling of Wind Turbine Wakes," J. Fluids Eng., Vol. 124, 2002, pp. 393-399.

Evaluating techniques for redirecting turbine wake using SOWFA

P. Fleming[1], P. Gebraad[2], S. Lee[1], J.W. van Wingerden[2], K. Johnson[1], M. Churchfield[1], J. Michalakes[1], P. Spalart[3], P. Moriarty[1]

[1]National Renewable Energy Laboratory, Golden CO, USA, paul.fleming@nrel.gov
[2]Delft University of Technology, Delft, The Netherlands, J.W.vanWingerden@TUDelft.nl
[3]Boeing Commercial Airplanes, Seattle WA

Abstract

Wind plant control is an active field of research in which controllers seek to maximize overall wind-plant performance in terms of power production, loading, or both. Such control strategies are often different from those that are optimal for an individual turbine. One type of wind-plant control method is to redirect the wake of an upstream turbine in order to avoid downstream turbines. In this paper, we investigate several possible methods for redirecting a turbine's wake, including some existing and some novel approaches. The methods are compared in terms of their ability to redirect turbine wake, the effect on turbine power capture, and turbine loading using the high-fidelity wind plant simulation tool SOWFA.

1 Introduction

Wind turbine wakes are complex and difficult to model. When turbines are located together in wind power plants, wake interaction between turbines can decrease energy capture and increase turbine loads. Therefore, recent research has focused on the design of wind plant controllers to mitigate these effects. Often in the literature, the controllers are based on modifying an individual turbine's axial induction factor by adjusting pitch and torque. Example studies that use this approach to optimize the global wind plant power capture include [1, 2, 3].

An alternative approach to wind plant power optimization is to redirect the wake using yaw misalignment rather than to optimize induction. In this method, when two turbines are aligned in the wind direction, the upstream turbine intentionally misaligns its yaw angle so as to apply skew to the wake such that it avoids the downstream turbine. This method has been studied experimentally in [4] and in compuational fluid dynamics (CFD) simulation in [5] with encouraging results. In a similar way, vertical wake redirection obtained by changes in rotor tilt angle has been investated in [6] using a CFD model. Note that both [5] and [6] use an actuator disk model of the turbine and [6] assumes laminar flow.

In this paper, we examine the potential of turbine controllers to redirect the turbine wake. This study is done through experiments with the high-fidelity wind plant modeling tool SOWFA

(Simulator for Off/Onshore Wind Farm Applications) [7]. SOWFA allows simulations to be performed that return performance results in terms of effects on the turbine (for example, power and loading) as well as on the flow (wake redirection).

Wake redirection methods to be examined include both the yaw- and tilt-angle based methods discussed above. We further add an additional novel, to the best of our knowledge, approach. The method attempts to employ individual pitch control (IPC) to achieve a horizontal or vertical wake skew by intentionally inducing a yaw or tilt moment. IPC is typically used to remove these moments, but we use it in reverse to apply them. The four techniques to be evaluated are illustrated in fig. 1.

The contributions of this paper are: first, we introduce a novel approach to achieving wake redirection (IPC). Second, we use high-fidelity simulations to evaluate the methods both in terms of their capability to redirect wakes and in terms of the effect on turbine power and loads.

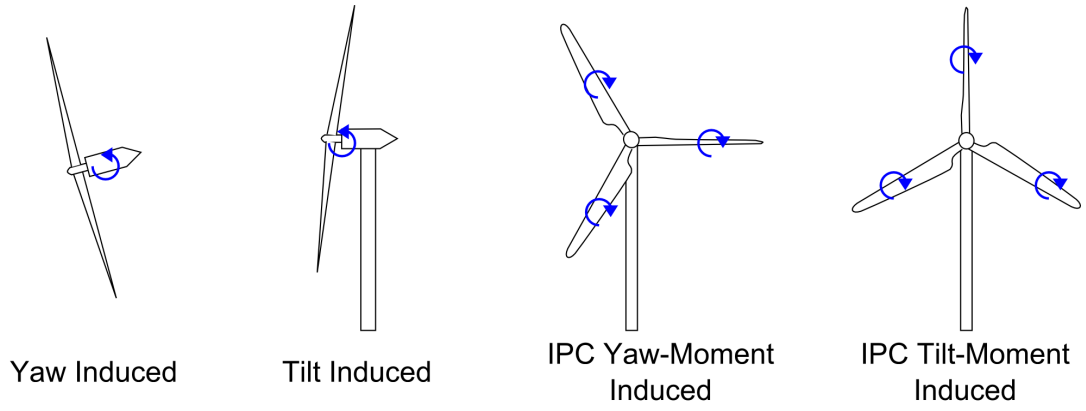

Figure 1: Techniques considered for redirecting the wake. Note that arrow directions in yaw and tilt case correspond to positive increases.

The remainder of this paper is organized as follows. Section 2 describes the high-fidelity wind plant simulation tool, SOWFA, used in this study. Section 3 provides details of the simulation experiment setup. Section 4 provides the results and analysis of the experiment. Conclusions are given in section 5.

2 SOWFA

SOWFA [7] is a CFD tool coupled with the National Renewable Energy Laboratory's (NREL's) FAST turbine simulator tool [8] for studying wind plant behavior. The CFD solver is based on the OpenFOAM CFD toolbox [9]. Specifically, a large-eddy simulation (LES) is used, which directly resolves the larger, energy-containing turbulent scales, to simulate the atmospheric boundary layer and the turbulence contained within it. Then, actuator line turbine models are placed

in the flow to create wakes that interact with one another, and the actuator lines are coupled with FAST. Extensive details are given by Churchfield et al. [10], and are summarized here.

The flow is computed using an unstructured, collocated, variable, finite-volume formulation that is second-order accurate in time and space. The filtered momentum equation is solved along with an elliptic equation for pressure that enforces continuity. Buoyancy effects are included through a Boussinesq term in the momentum equations necessitating the solution of a temperature transport equation. Velocity-pressure decoupling that would normally occur with a collocated incompressible method is avoided through Rhie-Chow [11] interpolation and the Pressure-Implicit Splitting Operation algorithm [12] is used solve the equation set. The linear systems that arise when discretizing the implicit equations are solved using preconditioned iterative solvers.

Coriolis forces account for the Earth's rotation. The lower surface boundary conditions based on Monin-Obuhkov [13] similarity theory is used, which is common practice in the atmospheric LES community. The upper boundary is a stress-free, rigid lid. First, a laterally periodic atmospheric boundary layer precursor simulation with no turbines is performed to generate the turbulent atmospheric boundary layer. Once that simulation has reached quasi-equilibrium, planes of inflow data are saved every time step. These data are then used as inflow boundary conditions for the non-periodic wind turbine simulation, and the downstream boundaries are outflow.

Sørensen and Shen's [14] actuator line method is used to model the interaction of the wind turbine blades with the wind. The basic idea is that each blade is represented as a line, and each line is discretized into segments. For each segment, the blade airfoil type, twist, and chord are known. The velocity vector experienced by that segment can be sampled from the LES flow field giving the velocity magnitude and angle of attack. Airfoil lift and drag tables are then used to compute the force vector at each actuator line segment. The forces are then projected, using a three-dimensional Gaussian at each actuator line segment, onto the flow field as volumetric body forces that enter the momentum equation. Large-scale structures like the rotor wake and blade tip, root, and bound vortices are resolved.

FAST is two-way loosely coupled to the actuator line model. The LES model samples the velocity along the actuator line segments and returns those values to FAST. FAST, which normally computes those velocities using blade element momentum theory, operates instead in blade-element mode because the LES solver computes induction caused by the rotor. The blade forces computed with FAST are returned to the LES solver and imposed as the body forces described above.

Validation of the SOWFA tool is an ongoing process. In [15], SOWFA was used to simulate the 48-turbine Liligrund wind plant, and the results were then compared with field data, with good agreement throughout the first five rows. Additionally, [10] includes documentation of experiments testing SOWFA's capability to simulate the inertial range in the turbulent energy spectra and the log-layer mean flow.

3 Simulation experiment

In this study, numerous simulations are run within SOWFA of a single turbine subject to the four proposed methods shown in fig. 1, which are applied in individual simulations with varying settings of yaw misalignment, tilt angle, or IPC moment set-point. The wind inflow is the same for all simulations. From the simulations, we extract the turbine's average power over the simulation, as well as the metrics of loading for several components. From the flow, we use a correlation method to idenitfy the wake-center at all locations downstream from the turbine. The results allow for a trade-off analysis of wake redirection potential vs. turbine effects.

Note that this study is limited to a single turbine and an examination of the flow behind it. However, an important consideration is the effect of changes made by an upstream turbine on a downstream turbine. Additionally, it is also important to learn if a reduction in the power output of the upstream turbine is compensated for by an increase in the power output of the downstream turbine. These issues are addressed in a related paper [16].

We simulate an NREL 5-MW baseline turbine [17] in turbulent inflow. The inflow, which is based on the study reported in [10], is that of a neutral atmospheric boundary layer. This inflow was selected because it had previously been validated and represents a realistic scenario. The inflow is generated in a precursor atmospheric LES on a domain that is 3 km by 3 km in the horizontal and 1 km in height. The horizontally averaged wind speed is driven to 8 m/s at the turbine hub height and is controlled through a time-varying mean driving pressure gradient. The wind comes from the southwest (300°) so that the elongated turbulent structures in the surface layer are not "trapped" by the periodic boundaries, continually cycling through in the same location. In the baseline case, the turbine rotor axis is aligned with the wind direction. The surface temperature flux is set to zero, although a capping inversion initially at 750 m above the surface is used both to slow boundary layer growth and because it is a real feature of atmospheric boundary layers. The surface aerodynamic roughness is set to 0.001 m, which is typical of flow over water. Details on the positioning of the turbine and meshing of the domain are given in fig. 2.

The yaw and tilt wake redirection strategies are tested for a range of settings. Each setting is tested in a simulation with 1,000s of simulated time. SOWFA requires significant computational power in order to run high-fidelity simulations: using a sample time of 0.02s, the time steps take an average 2.5s to calculate on the Sandia National Laboratories/NREL Red Mesa supercomputer [18], using distributed computation with 256 processors. This yields an execution time of 34.4h for each simulation.

In each case, the turbine uses the baseline controller defined in [17] for pitch and torque control. The IPC implementation is based on the design first presented in [19] using the parameters as specified in [20]. It is adapted so that IPC can be used in below-rated conditions and to induce an asymmetric moment, rather than remove one. Details on this IPC implementation are given in the Appendix.

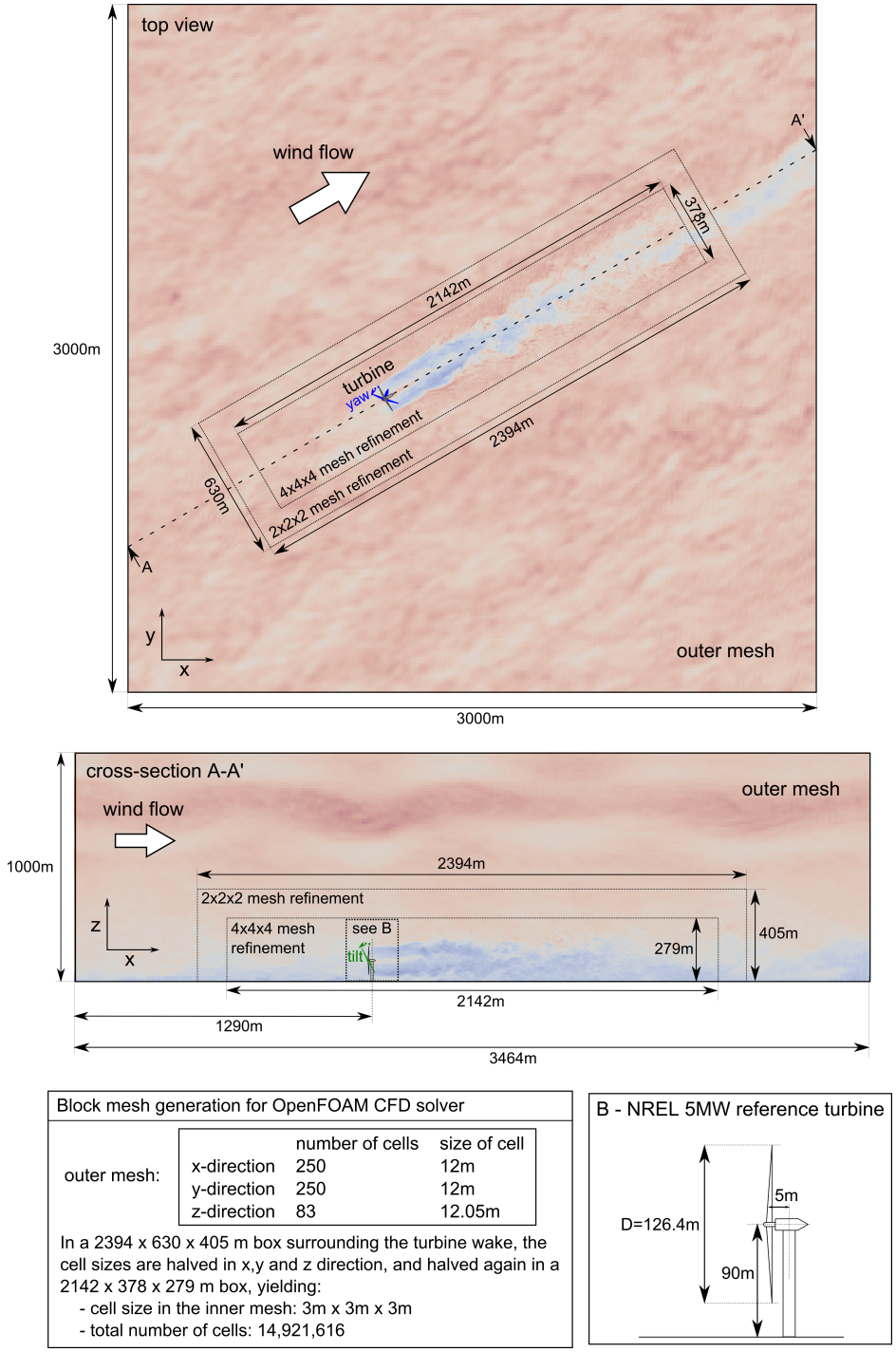

Block mesh generation for OpenFOAM CFD solver

	number of cells	size of cell
outer mesh: x-direction	250	12m
y-direction	250	12m
z-direction	83	12.05m

In a 2394 x 630 x 405 m box surrounding the turbine wake, the cell sizes are halved in x,y and z direction, and halved again in a 2142 x 378 x 279 m box, yielding:
- cell size in the inner mesh: 3m x 3m x 3m
- total number of cells: 14,921,616

Figure 2: Overview of the experimental setup in the baseline case.

4 Analysis and discussion

Following completion of the experiments, slices are extracted from the simulation outputs and a method is used to determine the mean wake center based on ideas of de Mare [21], which has been further developed at NREL. We take a horizontal slice of the mean velocity field at the turbine hub height and a vertical slice aligned with the mean wind and passing through the turbine centerline. From the horizontal slice, we take the mean velocity along lines within the slice plane and perpendicular to the flow at successive downstream locations. When plotted, the velocity along each line is a mean velocity profile. In the near wake, the velocity profiles are double-Gaussian in shape, and in the far wake, they resemble a normal Gaussian. The profiles at each downstream location are correlated with a Gaussian of similar width and depth. The point of maximum correlation is taken as the wake center position at each downstream location giving the lateral wake deflection. We follow the same process to find the vertical wake deflection using the vertical slice of mean velocity; however, we first subtract the vertical profile of mean velocity to remove the effect of vertical shear that is present in the atmospheric boundary layer. Fig. 3 shows the output of the wake center-line identification algorithm for several cases in the horizontal and vertical planes.

The cases shown in fig. 3 are representative of the collected results fully summarized in table 1. Wake center tracking results in the yaw and tilt simulations demostrate significant displacments of wake center, in agreement with the previous literature. The IPC methods produce some redirection. While it does not achieve as much redirection as yaw or tilt angle adjustments, the skew is in some cases significant. Also noted, that while the intention of the IPC algorithms were to approximate yaw misalignment through an IPC-induced yaw moment, or tilt via a tilt moment, the results show that the largest vertical skew is given when a yaw moment is targeted and the largest horizontal skew for a high tilt moment.

In addition to measurements of the wake, data were collected from the FAST turbine output. The data included time series of output power, blade out-of-plane (OOP) bending moment, drivetrain torsion, tower fore-aft and side-side bending, and the yawing and tilting moments experienced at the yaw bearing. Using a root-sum-square combination, the separate tower and yaw moments are combined into a single moment. An average power output is computed, as well as the damage equivalent load (DEL) for each load signal. The DEL is a standard metric of fatigue damage; see [22] for an example implementation. These results are summarized in table 1. Note that the measurement of wake displacement is taken at 7 rotor diameters from the turbine, which is a typical location for a downstream turbine.

Reviewing table 1, there is a positive result for yaw-based wake skew. One can see that when the turbine yaws in the positive direction, wake redirection and load reduction for all components are simultaneously achieved for a number of operating points. Using a yaw misalignment to reduce turbine loads has been studied in the literature and these results are consistent with those findings. [23] There is a loss of power, however the intention is that this reduction should be compensated for by a larger gain in a downstream turbine. [24]

Table 1: Full results of experiment. Turbine wake redirection is summarized by the wake center 7 rotor diameters downstream from the turbine, bold indicates the larger offset.

	Amount	Horizontal Wake-offset abs(x/D)	Vertical Wake-offset abs(x/D)	Power	Blade OOP	Drivetrain	Tower	Yaw Bearing
	Baseline	**0.08**	0.03	0.0%	+0.0%	+0.0%	+0.0%	+0.0%
Yaw-Based	-40^o	**0.33**	0.02	-39.4%	+5.6%	-17.3%	-20.3%	-13.9%
	-35^o	**0.32**	0.03	-31.2%	+8.9%	-10.7%	-17.7%	-0.7%
	-30^o	**0.27**	0.00	-23.8%	+9.5%	-6.1%	-15.2%	-6.7%
	-25^o	**0.24**	0.02	-16.8%	+14.2%	-0.8%	-14.9%	-8.0%
	-20^o	**0.17**	0.02	-11.2%	+11.7%	+2.3%	-7.7%	-9.8%
	-15^o	**0.10**	0.02	-6.0%	+7.2%	+1.5%	-10.5%	-3.5%
	-10^o	**0.05**	0.02	-2.6%	+8.6%	+1.0%	-10.3%	-2.8%
	-5^o	**0.03**	0.02	-0.4%	+5.3%	+0.8%	-5.9%	-3.1%
	5^o	**0.17**	0.05	-0.3%	-4.0%	-1.6%	-0.1%	-5.1%
	10^o	**0.24**	0.06	-2.6%	-5.2%	+1.3%	+0.1%	-9.7%
	15^o	**0.30**	0.06	-5.7%	-9.9%	-0.4%	-3.2%	-11.1%
	20^o	**0.35**	0.05	-10.6%	-13.3%	-1.0%	-6.0%	-14.4%
	25^o	**0.43**	0.08	-16.2%	-14.4%	-6.2%	-7.4%	-14.8%
	30^o	**0.49**	0.05	-23.3%	-17.1%	-10.2%	-12.7%	-8.1%
	35^o	**0.51**	0.05	-31.3%	-20.1%	-14.9%	-7.9%	-13.5%
	40^o	**0.54**	0.10	-40.1%	-24.4%	-22.2%	-7.1%	-1.5%
Tilt-Based	-15^o	0.05	**0.14**	-6.0%	-14.7%	+10.4%	-2.0%	-8.6%
	-12^o	0.10	**0.14**	-3.6%	-12.2%	+7.8%	-3.6%	-7.7%
	-9^o	0.08	**0.09**	-1.9%	-10.0%	+5.0%	-2.0%	+2.5%
	-3^o	**0.10**	0.02	0.1%	-0.6%	+0.7%	+5.5%	-3.2%
	3^o	**0.11**	0.10	-0.3%	+1.3%	+0.6%	-1.8%	-1.3%
	6^o	**0.11**	0.10	-0.5%	+4.1%	-2.0%	-3.3%	-4.9%
	9^o	0.13	**0.13**	-1.6%	+8.3%	-2.0%	-4.8%	-3.1%
	12^o	0.14	**0.16**	-3.2%	+5.8%	-2.8%	+3.0%	-0.9%
	15^o	0.11	**0.18**	-5.4%	+7.0%	-3.9%	-3.4%	+1.4%
IPC-Based	IPC-Yaw Max	0.05	**0.08**	-9.2%	+138.1%	+1.7%	+5.9%	+33.2%
	IPC-Yaw Min	**0.14**	0.08	-15.2%	+64.7%	+6.2%	+5.2%	+22.4%
	IPC-Tilt Max	**0.17**	0.03	-11.8%	+91.0%	+1.4%	+10.0%	+26.5%
	IPC-Tilt Min	0.05	**0.06**	-13.2%	+130.4%	+89.3%	+1.9%	+34.2%

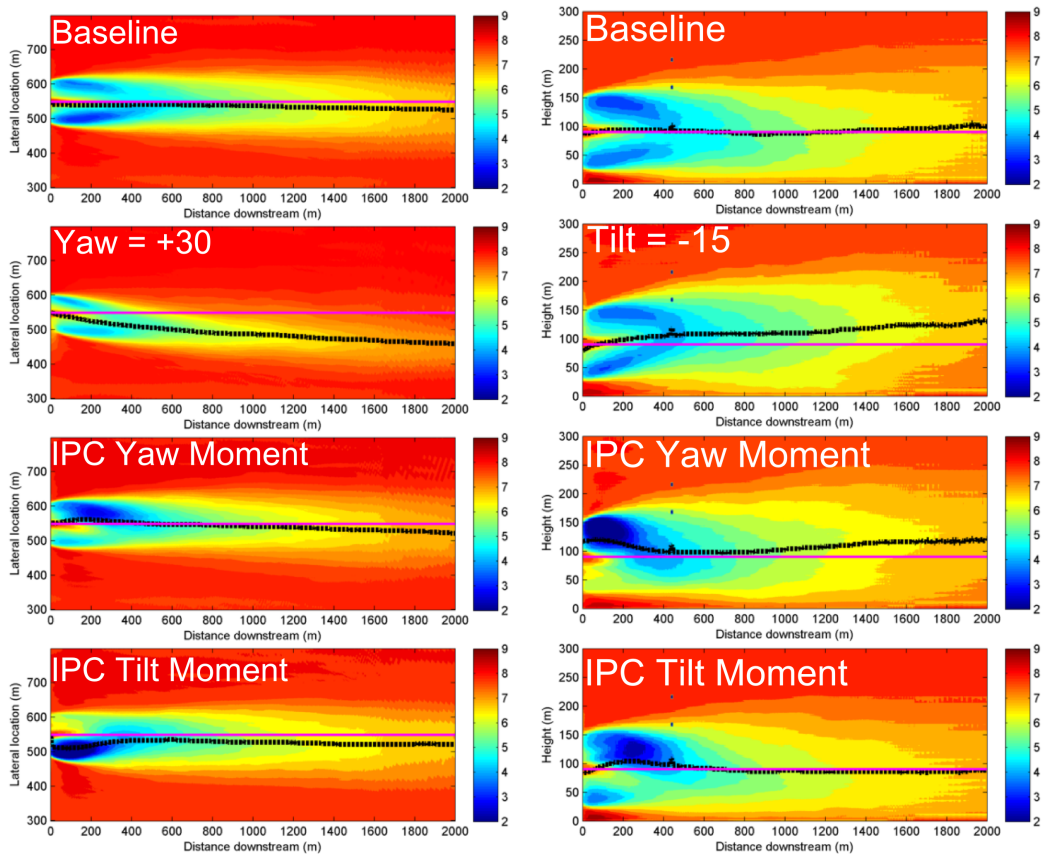

(a) Tracking wake center in horizontal slices

(b) Tracking wake center in vertical slices

Figure 3: Tracking the wake center using Gaussian correlation. The magneta lines pass through the turbine hub and are parallel to the inflow direction to indicate a zero skew base.

Tilt similarly demonstrates potential for wake redirection with, mostly, positive load impacts. Observing the loads in the 12 degree case, all are reduced with the exception of blade bending, which has gone up 10%. It should be pointed out that currently there is no means of modifying tilt angle in the field. However, the effect of causing the higher-speed higher-altitude winds to be pulled downward might be rewarding enough to justify further investigation, although given that positive tilt angles would cause the blades to come closer to the tower on upwind turbines, this is appropriate more for downwind machines. [25]

The results for the IPC-based methods are mixed. Signficant wake skew is achieved for some cases, however, because the method is maximizing an asymmetric rotor moment, the blade loads are substantially increased. This leads to the notion that while it may me possible to achieve wake redirection with IPC, this particular IPC algorithm is not a good method. Finding an IPC controller which achieves wake skew with reduced blade loads would be very useful because

IPC is already possible to implement on many existing turbines (unlike changes to tilt), and can be adjusted more quickly than yaw angle.

In considering the results, the authors now believe the initial concept for IPC-based wake redirection followed in this paper was fundamentally flawed. Specifically, while IPC can reproduce the rotor moments generated by yaw or tilt misalignment, this moment is not what can create skew. In the left of fig. 4, the conceptualization of yaw-misalignment induced wake redirection from [5] is redrawn. In it, the thrust force of the turbine is shown to act along the axis of the rotor shaft. When the wind inflow is at an angle to this direction, the thrust can be divided into components f_x and f_y. f_x is parallel to the flow and slows the wind, while f_y is perpendicular and applies the force which causes wake redirection. A moment produced in IPC is based on an uneven plane of thrust force. This yields a moment from the turbine's perspective, but no perpendicular force on the flow. However, IPC can cause a perpendicular net force on the flow. Observing the right section of fig. 4, when the blade torque through a rotor rotation is uneven (in the sense that rightward torque is not matched by leftward torque), a skew can result. This is because the reaction force on the flow is now also unbalanced, and a net perpendicular force is applied resulting in wake skew. Notice that the IPC configuration draw in fig. 4 will yield a tilt moment on the turbine (because the blade thrust is most different between the top and bottom azimuth positions) and a horizontal wake skew (because the flow reaction forces are most different in the horizontal force directions), which agrees with the results presented earlier.

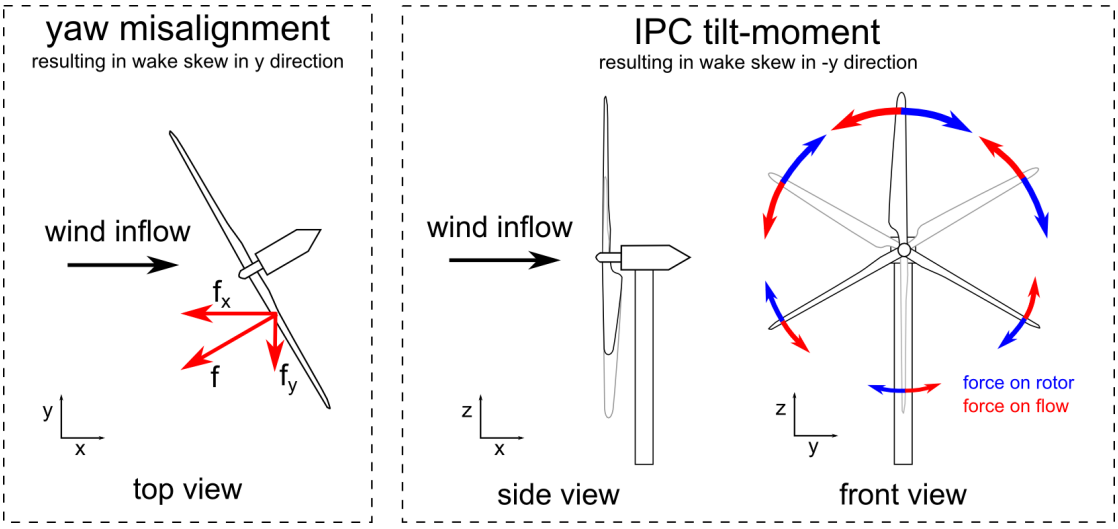

Figure 4: Demonstrating the difference between yaw/tilt and IPC-based methods for achieving wake skew. The figure on the left, based on the explanation given in [5], shows the thrust force decomposed into components. IPC, shown on the right, generates an asymetric rotor torque which can yield a force perpednciular to flow direciton.

This analysis hopefully indicates that while the IPC algorithm first developed, which seeks to

apply skew by maximizing yaw or tilt moment, is problematic, an alternative implementation may be possible. This implementation, the subject of future work, should attempt to maximize the wake skew through torque imbalance while minimizing rotor moments.

5 Conclusions

In this paper, the NREL wind plant simulation tool, SOWFA, was used to simulate and investigate several methods for wake redirection. Wake redirection is one proposed method for improving wind plant overall performance. For yaw misaligment, simulations showed significant redirection effects coupled with reductions in loading across measured components, a positive result. Tilt angle adjustment was shown to also achieve wake redirection while reducing all turbine loads except for blade OOP bending. Although modifying tilt angle is not currently a controllable feature of wind turbines, knowledge of the capability of this effect might be useful, especially if the effect of pulling in faster wind yields greater overall power gains.

IPC-based methods also demonstrated an ability to affect wake skew, however this was achieved with a substantial increase in blade loading. Analysis presented indicates that the IPC algorithm employed in this paper, while enough to prove the concept that IPC can redirect wake, it too simplistic for actual implementation and future work will focus on the determination of more optimal designs.

6 Acknowledgements

The authors are very grateful to Wesley Jones and the NREL High Performance Computing team for their crucial help and support in completing this simulation study. This work was supported by the U.S. Department of Energy under Contract No. DE-AC36-08GO28308 with the National Renewable Energy Laboratory.

References

[1] P.M.O. Gebraad, F.C. van Dam, and J.W. van Wingerden. A maximum power point tracking approach for wind farm control. In *Proceedings of The Science of Making Torque from Wind*, 2012.

[2] K.E. Johnson and G. Fritsch. Assessment of extremum seeking control for wind farm energy production. *Wind engineering*, 36(6):701–716, 2012.

[3] J.R. Marden, S.D. Ruben, and L.Y. Pao. Surveying game theoretic approaches for wind farm optimization. In *Proceedings of the 50th IEEE Conference on Decision and Control*, volume 38, pages 584–596, 2012.

[4] J.W. Wagenaar, L.A.H. Machielse, and J.G. Schepers. Controlling wind in ECN's scaled wind farm. In *Proceedings of EWEA*, 2012.

[5] Á. Jiménez, A. Crespo, and E. Migoya. Application of a LES technique to characterize the wake deflection of a wind turbine in yaw. *Wind energy*, 13(6):559–572, 2010.

[6] S. Guntur, N. Troldborg, and M. Gaunaa. Application of engineering models to predict wake deflection due to a tilted wind turbine. *EWEA, Denmark, Copenhagen*, 2012.

[7] M. Churchfield and S. Lee. NWTC design codes (SOWFA). `http://wind.nrel.gov/designcodes/simulators/SOWFA`, 2013.

[8] J. Jonkman. NWTC Design Codes (FAST). `http://wind.nrel.gov/designcodes/simulators/fast`, 2012.

[9] OpenFOAM, the open source CFD toolbox. `http://www.openfoam.com/`, 2013.

[10] M.J. Churchfield, S. Lee, J. Michalakes, and P.J. Moriarty. A numerical study of the effects of atmospheric and wake turbulence on wind turbine dynamics. *Journal of turbulence*, 13(14):1–32, 2012.

[11] C.M. Rhie and W.L. Chow. Numerical study of the turbulent flow past an airfoil with trailing edge separation. *AIAA journal*, 21(11):1525–1532, 1983.

[12] R.I. Issa. Solution of the implicitly discretised fluid flow equations by operator-splitting. *Journal of computational physics*, 62(1):40–65, 1986.

[13] A.S. Monin and A.M. Ohukhov. Basic laws of turbulent mixing in the surface layer of the atmosphere. *Tr. Akad. Nauk SSR Geophiz. Inst.*, 24(151):163–187, 1954.

[14] J.N. Sørensen and W.Z. Shen. Numerical modeling of wind turbine wakes. *Journal of fluids engineering*, 124:393–399, 2002.

[15] M.J. Churchfield, S. Lee, P.J. Moriarty, L.A. Martinez, S. Leonardi, G. Vijayakumar, and J.G. Brasseur. A large-eddy simulation of wind-plant aerodynamics. In *50th AIAA Aerospace Sciences Meeting including the New Horizons Forum and Aerospace Exposition, Nashville, TN*, 2012.

[16] P. Fleming, P. Gebraad, S. Lee, J.W. van Wingerden, K Johnson, M. Churchfield, J. Michalakes, P. Spalart, and P. Moriarty. High-fidelity simulation comparison of wake mitigation control strategies for a two-turbine case. In *International Conference on Aerodynamics of Offshore Wind Energy Systems and Wakes (ICOWES2013)*, 2013.

[17] J. Jonkman, S. Butterfield, W. Musial, and G. Scott. Definition of a 5-MW reference wind turbine for offshore system development. Technical report, NREL/TP-500-38060, 2009.

[18] NREL's high-performance computing capabilities. `http://www.nrel.gov/energysciences/csc/high_performance_computing_capabilities`, 2012.

[19] E.A. Bossanyi. Controller for 5MW reference turbine. Technical report, Garrad Hassan and Partners Limited, 2009.

[20] I. Houtzager. *Towards Data-Driven Control for Modern Wind Turbines*. PhD thesis, Delft University of Technology, 2009.

[21] M. de Maré. personal communication, 2012.

[22] M. Buhl Jr. MCrunch theory manual for version 1.00.

[23] K.A. Kragh and M.H. Hansen. Load alleviation of wind turbines by yaw misalignment. *Wind energy*, 2013.

[24] P. Fleming, P. Gebraad, S. Lee, J.W. van Wingerden, K. Johnson, M. Churchfield, J. Michalakes, P. Spalart, and P. Moriarty. High-fidelity simulation comparison of wake mitigation

control strategies for a two-turbine case. In *Proceedings of ICOWES*, 2013.
[25] Andrew Scholbrock. Private conversation.

Appendix

Appendix A: Implementation of IPC with induced yaw or tilt moments

This section explains how individual pitch control (IPC) was implemented to allow yaw and tilt moments to be induced by the IPC. The implementation also can be used in below-rated operation with varying rotor speeds. Let φ denote the rotor speed in rad/s, let $\{M_{y,i}\}_{i=1}^{3}$ denote blade root vibrations of each of the three blades, let $M_{r,yaw}$, $M_{r,tilt}$ denote setpoints for the induced yaw and tilt moments, and let s denote the Laplace operator. Then the 1P and 2P IPC additive adjustments to the pitch, $\left\{\delta\theta_{i,jP}\right\}_{i=1}^{3}$, are given by:

$$\begin{bmatrix} \delta\theta_{1,jP} \\ \delta\theta_{2,jP} \\ \delta\theta_{3,jP} \end{bmatrix} = \mathcal{L}(s) I_{3\times3} \mathcal{P}_{jP}(\varphi+\delta_{jP}) \begin{bmatrix} \frac{K_{i,jP,yaw}}{s} & 0 \\ 0 & \frac{K_{i,jP,tilt}}{s} \end{bmatrix} \times \left(\tfrac{2}{3} \mathcal{P}_{jP}^{T}(\varphi) \mathcal{N}_{jP}(s) I_{3\times3} \begin{bmatrix} M_{y,1} \\ M_{y,2} \\ M_{y,3} \end{bmatrix} - \begin{bmatrix} M_{r,yaw} \\ M_{r,tilt} \end{bmatrix} \right)$$

for $j = 1,2$, with Coleman transformation matrices:

$$P_{jP}(\varphi) = \begin{bmatrix} \cos(j\varphi) & \sin(j\varphi) \\ \cos(j(\varphi+2\pi/3)) & \sin(j(\varphi+2\pi/3)) \\ \cos(j(\varphi+4\pi/3)) & \sin(j(\varphi+4\pi/3)) \end{bmatrix},$$

and with inverse notch filters $\mathcal{N}_{jP}$, and low-pass filter $\mathcal{L}$:

$$\mathcal{N}_{jP}(s) = K_{jP} \frac{2\zeta_{jP}\omega_{jP}s}{s^2+2\zeta_{jP}\omega_{jP}s+\omega_{jP}^2}, \quad \mathcal{L}(s) = \frac{\omega_L^2}{s^2+2\zeta_L\omega_L s+\omega_L^2},$$

with $\omega_{jP} = j\varphi$, and parameters $K_\bullet$,$\zeta_\bullet$,ω_L,δ_{jP} as specified in [20]. The filters are used in a Tustin discretized form with a sample time of 0.02s. The pitch angles are saturated to a 5 degree amplitude, and the pitch rates are limited to 8 deg/s. In the IPC induced moment test cases, $M_{r,yaw}$ or $M_{r,tilt}$ are chosen large enough such that the pitch angles vary with maximum amplitude, in order to find the maximum effect of IPC action on the wake.

EXPERIMENTAL AND NUMERICAL AERODYNAMIC ANALYSIS OF VERTICAL AXIS WIND TURBINE WAKE

G. Tescione, D. Ragni, C. He, C.J. Simão Ferreira, G.J. van Bussel

DUWIND – Delft University Wind Energy Research Institute
Kluyverweg 1, 2629 HS, Delft, The Netherlands
G.Tescione@tudelft.nl (corresponding author)

ABSTRACT

The generation and evolution of the wake of a vertical axis wind turbine is investigated with an experimental and numerical approach. The experiments were conducted in an open-jet wind tunnel at $Re_c=80'000$ on a two straight blades turbine of 1 m diameter with a NACA0018 airfoil operating at a tip speed ratio of 4. Two-component particle image velocimetry measurements on the mid (symmetry) plane focused on the horizontal wake expansion and vorticity evolution, while three-component measurements based on a stereoscopic approach focused on the tip vortices dynamics on different vertical planes. The numerical simulations were performed with a 3D unsteady potential flow solver. The numerical model combines a panel method for the discretization of the blades and a free vortex wake method for the wake. Results from the 3D numerical simulations show a fast roll-up of the vortex filaments close to the blade tips which result in strong tip vortices. Such vortex structures undergo a vertical motion which causes a contraction of the wake in the inner part of the rotor area and an expansion on the boundaries. Results are consistent with previous simulations and the vertical contraction of the wake suggests a possible transport of energy by the tip vortices enhancing wake recovery.

Introduction

The direction where wind energy industry is going [1] (floating, large wind farms of multi-MW turbines) has made Vertical Axis Wind Turbines (VAWTs) recently gain new popularity in the wind energy community, as their use can potentially alleviate some of the new challenges posed by this trend. VAWTs are, mechanically speaking, simpler machines than HAWTs, having no yaw, and often no pitch, mechanisms. They show higher potentials of scalability, overcoming some of the limitations of HAWTs in this aspect [2],[3]. Moreover the possibility to place the generator under water helps stability and would decrease the size and cost of the floating support structure. Different research programmes in Europe and US are exploring the potentials of floating large VAWTs [4].
This renewed interest finds however a fragmented research field: after its peak during the 80's, VAWT research was discontinued for almost 15 years, during the 90's and early years of 2000. The commercial success of the Danish concept of horizontal axis turbines drove most of the research effort of the wind energy community, with few isolated researchers focusing on the vertical counterparts, and their use limited to small turbines for urban environment. VAWTs missed the extensive research characterizing HAWTs, resulting in a lack of knowledge about some basic aerodynamic behavior and an underdevelopment of proper models [5]. High order methods, namely CFD, need to face their inability to cope with high vorticity problems due to their inherent numerical dissipation. Accurate

wake dynamics is by these means hard to predict. Low order engineering models developed for HAWT have been adapted for VAWT design and analysis without considering the inherent differences, resulting in poor predictions. Also the experimental activity is poor compared to that of HAWTs, resulting in a lack of physical insight. This is the gap in VAWT aerodynamic research, the lack of a solid phenomenological background and proper tools to assist analysis and design.
The results presented in this paper are part of a research aimed at gaining a better understanding of the aerodynamics of the wake of a vertical axis wind turbine. This paper presents results from an experimental campaign on the flow inside the rotor and in the near wake of an H-VAWT and compares with results from a numerical analysis based on vortex theory.

Experimental setup

The experiments have been performed in the Open Jet Facility (OJF) of Delft University of Technology in March 2013[1], on a wind turbine model using Particle Image Velocimetry (PIV) technique.

Wind tunnel
The OJF is a closed-circuit open-jet wind tunnel driven by a *500 kW* electric motor. With an octagonal cross-section of *285x285 cm*, jet is free to expand in a *13.7x6.6x8.2 m* (LxWxH) test section. The flow velocity ranges from *3 m/s* to *34 m/s*, with a turbulence level of *0.24%* and a flow uniformity of *0.5%*. A *350 kW* radiator system is used for keeping a constant temperature of *20°C*.

Turbine model
The model is a 2-bladed, H-rotor type, VAWT with a rotor radius of *0.5 m*. A NACA0018 airfoil spans uniformly across the straight, un-tapered blades of *1 m* span and *6 cm* chord. The turbine has an aspect ratio of $AR = 1$ and a blade solidity of $\sigma = 0.11$. Each blade is supported by two struts, mounted at *0.2R* from the tips. The turbine is supported by a *3 m* steel shaft connected to a *200 W* DC brushless motor in order to drive the turbine at low wind speed and regulate rotational speed. An optical trigger mounted on the shaft is used to synchronize the PIV system for phased-lock acquisition. The turbine was operated at a tip speed ratio $\lambda = 4$ ($C_P = 0.4$ and $C_T = 0.8$, from the numerical simulations), with a rotational speed of *380 RPM* and a free stream velocity of *5 m/s*, reaching a chord-based Reynolds number of $Re_c = 80'000$.

PIV setup
The measurements were performed with Particle Image Velocimetry (PIV) system in two configurations: a 2C-PIV (planar) for horizontal plane measurements and a 3C-PIV (stereo) for vertical plane measurements.
Diethyl glycol-based seeding particles of *1 μm* diameter were produced by a SAFEX® twin fog generator located at the end of the open test section. A Quantel Evergreen® was used as the light source. The system consists of a double pulsed Nd:YAG laser, producing visible green light of wavelength *532 nm* with a *400 mJ* pulse energy. Two LaVision® Imager pro LX 16M were used for image capturing. The 12-bit camera has an image resolution of *4870x3246* pixels with a pixel size of *7.4 μm*. For the first configuration, measurements were taken in the horizontal plane at midspan position. Given the symmetry of the rotor and neglecting the presence of the tower, the flow was considered to be 2D, thus standard 2C-PIV set-up was used for this case. Two independent cameras

[1] A second set of measurements started in April 2013 (currently in progress) in the same facility with an improved turbine model and a smoother strut-blade connection. The Reynolds number was increased (from 80'000 to 180'000) and two different TSR (2.5 and 4.5) were measured. The flow around the blades at several azimuth positions was captured to determine the loads, and close-up analysis on blade vortex interaction was also performed. The data in the present version of this paper refer to the first experiment. Data from the second experiment will be presented at the conference and possibly included in the paper in the review phase.

were mounted on an horizontal beam, side by side at *1.3 m* from the horizontal laser sheet. Each camera is equipped with a *f = 105 mm* Nikon lens, with an aperture number *f# = 4*, resulting in a magnification factor of *M = 0.08*. The Field of View (FOV) of the combined window is *476x388 mm*, with short edge in the free stream direction. Image calibration showed a fit RMS of *0.30* and *0.52* for the two cameras, assuring a good data quality.
In the second configuration, measurements were taken in the vertical planes aligned with the free stream with stereoscopic PIV, obtaining all the components of the velocity vector in the planes. The two cameras were mounted on a vertical beam. The lower camera was placed at *1.7 m* from the measurement plane with a viewing angle of *41°*; a Nikon *f = 180 mm* lens gave a magnification factor of *M = 0.10*. The upper camera was placed at *1.4 m* with a viewing angle of *-11°*; a Nikon *f = 105 mm* lens resulted in a magnification factor of *M = 0.08*. The shared FOV is *366x280 mm*. From the calibration the fit RMS of two cameras are *0.40* and *0.28*.

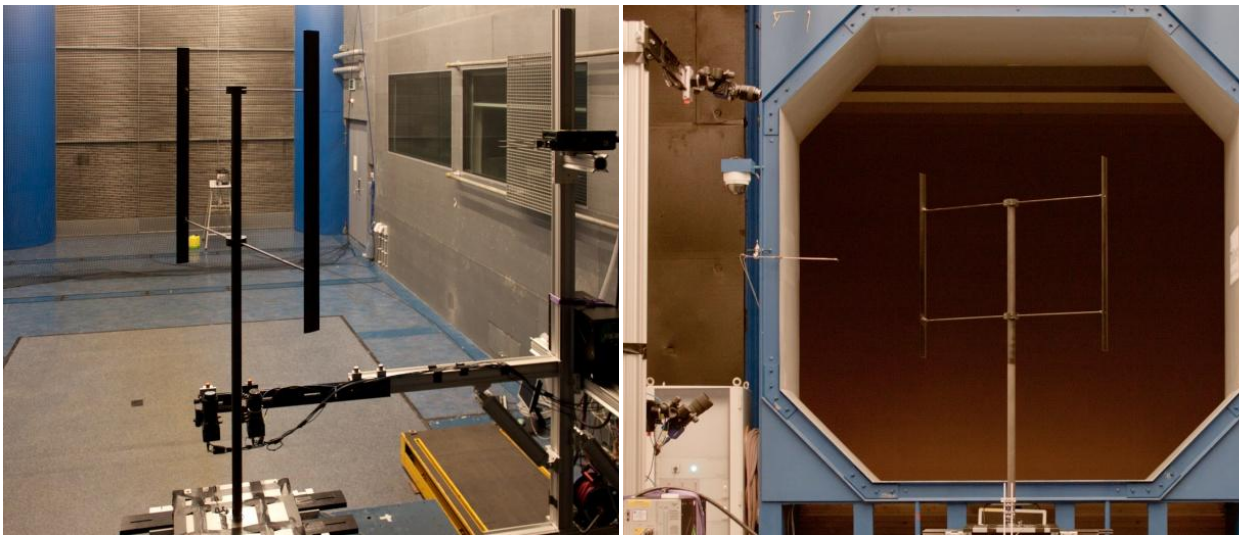

Figure 1: experimental setup for the measurement in the horizontal (*left*) and vertical (*right*) planes

System of reference and measurement windows
The origin of the coordinate system coincides with the turbine center, downwind direction is denoted as the positive x-direction, positive y-direction points to the windward side of the rotor (right if facing the wind) and positive z-direction points upwards. The $\theta = 0°$ position is with the two blades in the most upwind and downwind positions and a positive rotation is counter-clockwise seen from above. In both configurations a two degrees-of-freedom traversing system, with a stream-wise range of *1.5 m* and a cross-stream range of *1.0 m*, allowed synchronized motion of cameras and laser maintaining calibration. Due to its range limitation, the traversing system was placed in two x-positions: the first position spanned from *x/R = -1.33* to *x/R = 0.91* and the second position ranged from *x/R = 0.83* to *x/R = 3.90*. In y-direction the traversing system ranged from *y/R = 1.33* to *y/R = 0.49*. To cover the whole rotor area the turbine was mirrored (the blades flipped and the rotational direction inverted), allowing to measure the same half of the rotor area overcoming the obstruction of the supporting base and the central shaft without relocating the traverse system again.
For the horizontal measurements (first configuration) the whole rotor area was measured, except a region around the tower; the position of the measurement windows was determined by optical considerations to minimize blade shadows, which results in large overlap. In the wake region, measurements were limited to the central and boundary regions of the wake.
For the vertical measurements three cross-stream positions were used (*y/R = -0:8; 0; 0:8*) and the windows were center at *0.9H*, capturing the flow at the tip height.

Figure 2: System of reference and measurement windows for the horizontal (*centre*) and vertical (*right*) planes

Data acquisition and data processing

LaVision® Davis software was used for image acquisition and data processing. For each interrogation window, 200 image pairs were taken with a pulse separation of *320 μs*. Phased-lock data were acquired at two azimuth angles of *0°* and *90°*. The resulted raw data were pre-processed with a background noise removal; a sliding background removal and a 3x3 Gaussian filter to eliminate high frequency components. The smoothing process reduced the likelihood of peak-locking given the low magnification factors. The pre-processed images were processed using multi-pass correlation with final window size of *32x32* pixels and a 50% overlap ratio, resulting in a vector spacing of *1.2 mm*.

Experimental results

Results from the PIV measurements are shown in the present paragraph for the horizontal mid-plane (contours of the two velocity components U_x, U_y and of the vorticity ω_z) and for the vertical planes (contours of the three components of velocity and in-plane vorticity). All results are for $\lambda = 4$ and averaged over the phased-locked sampling at $\theta = 0°$; all velocities are normalized with U_∞ and vorticity with $c/\lambda U_\infty$. In the plots the wind direction is left to right, in-planes velocities are oriented accordingly to the plot axis, out-of-plane velocity and vorticity vectors are positive out of the paper.

Horizontal mid-plane

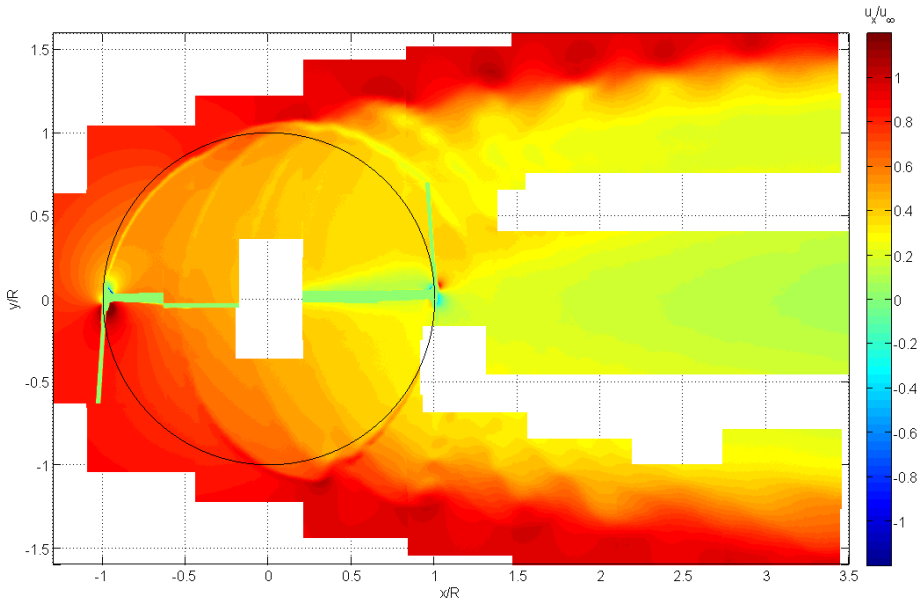

Figure 3: phased averaged normalized stream-wise velocity contours (U_x/U_∞, $\theta = 0°$, $\lambda = 4$)

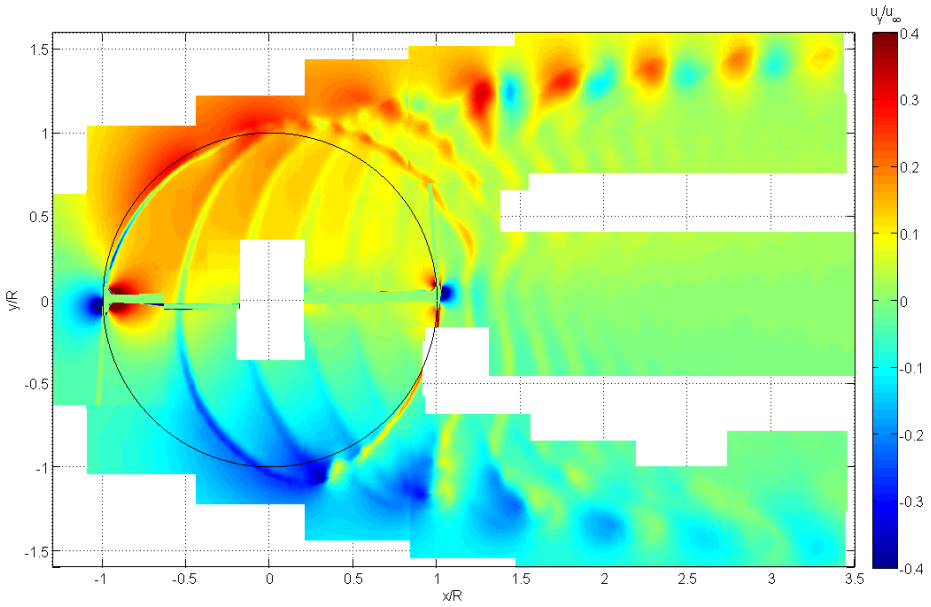

Figure 4: phased averaged normalized cross-stream velocity contours $(U_y/U_\infty, \theta = 0°, \lambda = 4)$

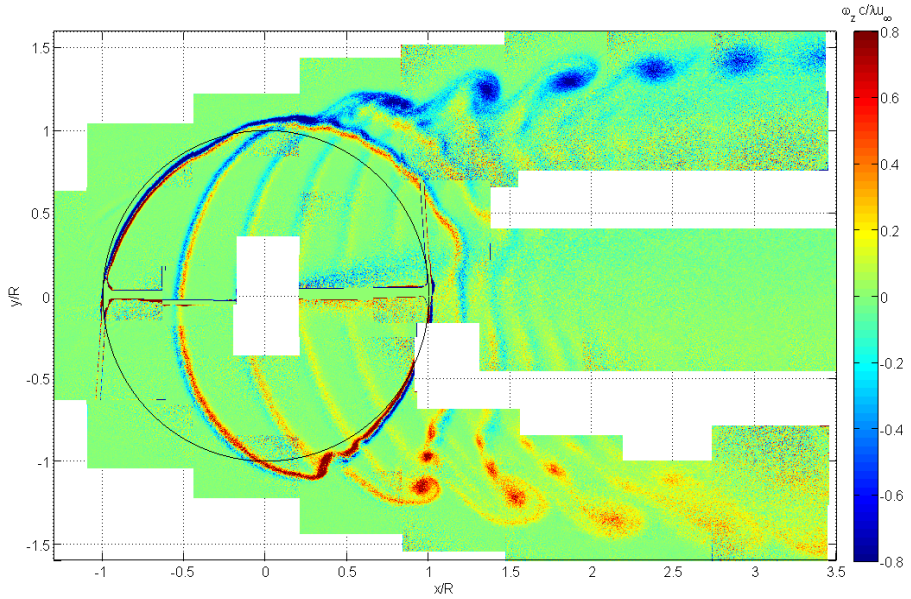

Figure 5: phased averaged normalized vorticity contours $(\omega_z c/\lambda U_\infty, \theta = 0°, \lambda = 4)$

Experimental results of the horizontal mid-plane clearly show the horizontal expansion and the velocity deficit in the near wake (Figure 3). The wake almost doubles its cross-stream extension 2 diameter downstream. The stream-wise velocity reaches a minimum of 10% of U_∞ in the centre of the wake at the most downwind measured distance with no sign of recovery. The distribution of stream-wise velocity in the cross-stream direction is not completely symmetric with respect to the centre, with a thinner shear layer in the windward half ($y > 0$). Figure 3 shows also the wake of the central shaft in the rotor area impinging the blade at *θ=180°* and its deflection to the windward side due to the upwash of the rotating shaft.

Figures 4 and 5 show the dynamics of the vortical structures in the shear layers and in the blades wakes. The vortex sheet shed by the blade during its rotation is crossed several times by the blades while moving downstream with the onset of instabilities which rapidly grow in a Kelvin-Helmothz fashion and roll up in bigger vortical structures. This is more visible (Figure 5) in the leeward region

($y < 0$) where the onset of the instabilities, the roll-up in three distinct vortical structures of different scales and the strechting and diffusion due to the shear layer is shown in five consecutive wake paths. The windward region presents a stronger roll-up and a single, bigger vortical structure is noticeable after the third wake path.

Vertical planes

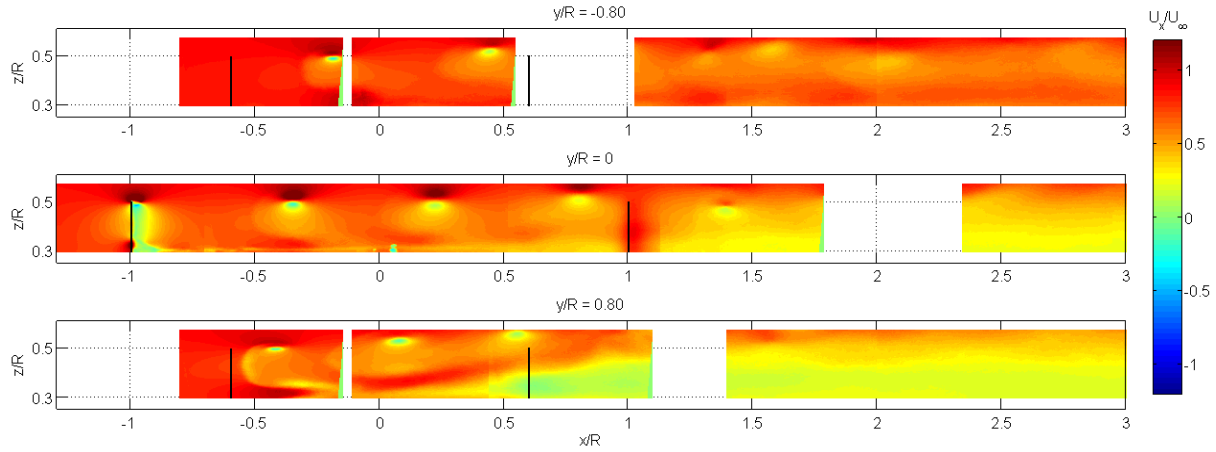

Figure 6: phased averaged normalized stream-wise velocity contours ($U_x/U_\infty, \theta = 0°, \lambda = 4$)

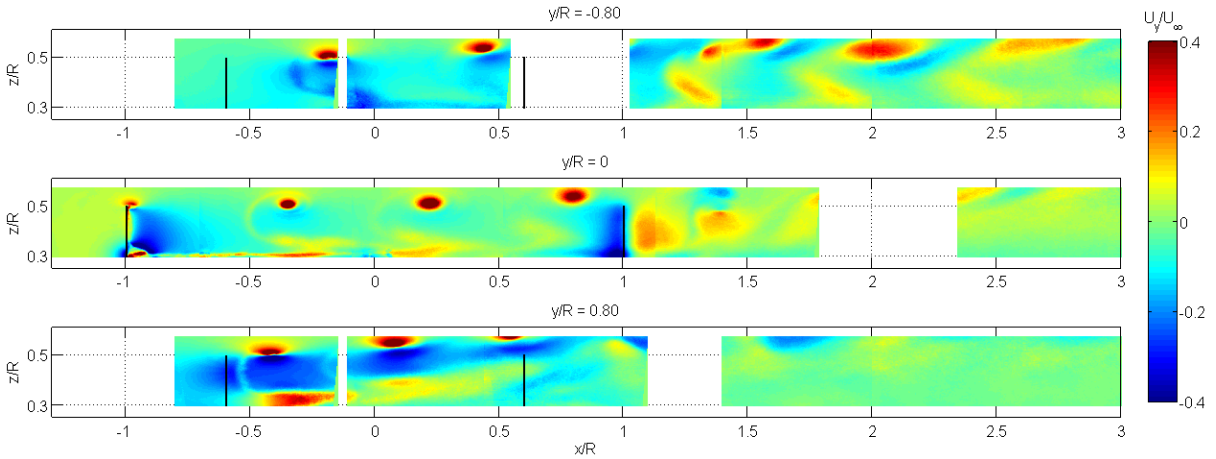

Figure 7: phased averaged normalized vertical velocity contours ($U_y/U_\infty, \theta = 0°, \lambda = 4$)

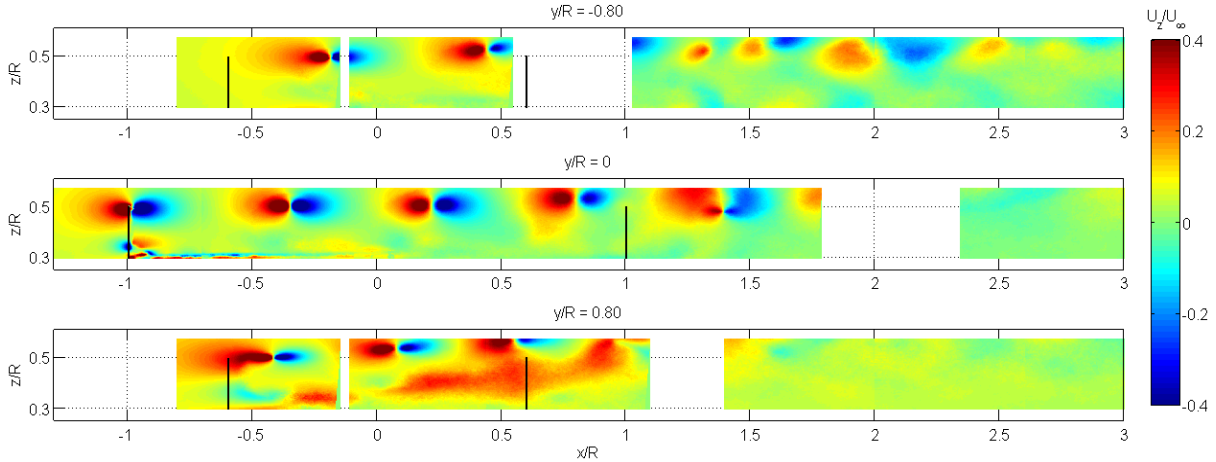

Figure 8: phased averaged normalized cross-stream velocity contours ($U_y/U_\infty, \theta = 0°, \lambda = 4$)

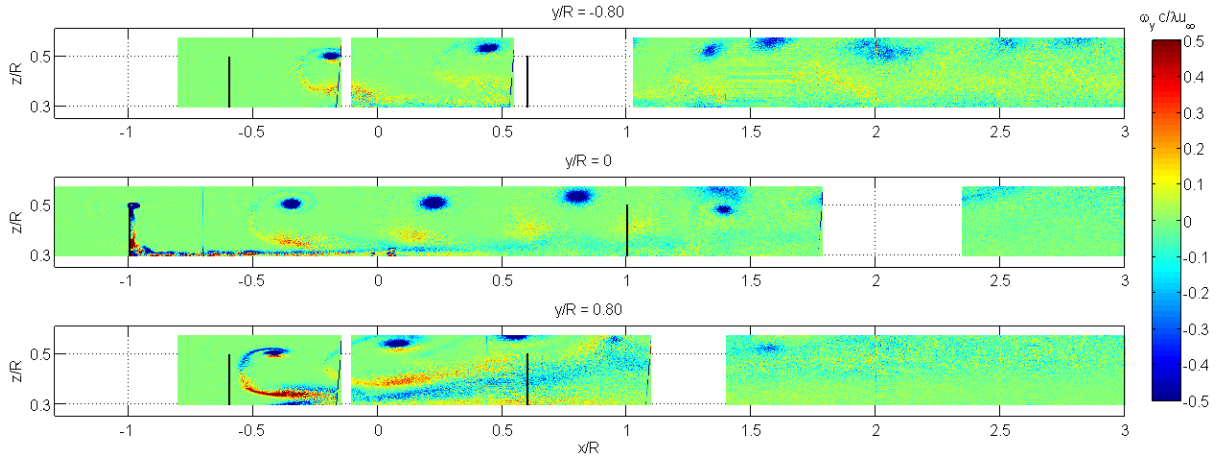

Figure 9: phased averaged normalized vorticity contours ($\omega_y c/\lambda U_\infty$, $\theta = 0°$, $\lambda = 4$)

Measurements in the vertical planes show the evolution of the tip vortex released from the upwind and downwind blade at different y-position. The difference in the vertical motion and in the strength of the vortex can be observed in figure 9. The strongest vortex is released by the tip of the upwind blade at $\theta=0°$, where the angle of attack and the bound vorticity of the blade is highest, in agreement with previous study [5]. The vortex moves then downwind at almost the same height before reaching the centre of the rotor and then starts moving slightly upward. The tip vortex released from the blade at $\theta=180°$ is of considerable lower strength and starts to move inboard to the middle of the wake. In the leeward region of the rotor ($y/R = -0.8$) the tip vortices have a similar behaviour while in the windward region ($y/R = 0.8$) the vortices move upward and quickly disappear from the measurement windows. These results are only partially in agreement with previous experimental works [6], where an inboard motion was observed for the tip vortex released at $\theta = 0°$ and an outboard motion approaching the edges of the wake. A possible explanation to this disagreement can be found in the high influence of the strut and of the blade-strut connection creating an opposite vortex structure which counteracts the tip vortex roll-up and consequent vertical motion. The high effect of the struts can be partially seen in Figure 9 as a sheet of positive vorticity at the lower boundary of the measurement window, starting at $y = 0$ and evolving at $y/R = 0.8$.

Figure 6 shows also a huge difference in the stream-wise velocity in the wake moving from the windward to the leeward region. In the vertical range of the measurement windows ($0.3 < z/H < 0.6$), the measurements show a narrow shear layer ($y/R = 0.8$) which decreases ($y/R = 0$) to disappear in a region of almost uniform flow at 80% of U_∞ ($y/R = -0.8$).

Numerical model

The model used for this numerical investigation is a free vortex wake method developed at TUDelft. The most computational expensive functions relative to the wake-to-wake and body-to-wake induction have been implemented in CUDA-C and run on parallel on GPU to speed up the calculations.

The blades are discretized with flat panels of constant source and doublets strengths, able to model thick lifting surfaces in attached flows. Source singularities ensure the non-entry boundary condition while doublets provide the circulation around the lifting body and their strength is established by the linearized Kutta condition at the trailing edge. The geometric discretization of 60 panels spanwise and 30 panels chordwise is clustered towards the leading and trailing edges and towards the tips of the blades to account for curvature and higher gradients. No deformation of the body is accounted for.

The wake is modeled as a lattice of straight vortex filaments: the spanwise filaments account for the spatial variation of circulation along the blade and represent trailed vorticity, while the chordwise filaments account for the temporal variation of circulation of the blade sections and represent shed vorticity. Wake elements are emitted only by the trailing edges, no wake elements are emitted in the

spanwise direction from the tip of the blades. For each time step the induction field of all the wake filaments and of the body panels is solved on the location of the wake markers (the filaments endpoints) and these are then free to evolve. The filaments have a viscous core with a Gaussian distribution to ensure desingularization. No viscous diffusion of the filament vorticity is currently included in the present results. As the endpoints of the filaments are used as markers, vortex stretching and tilting is automatically considered (the $\omega \cdot \nabla u$ term in the vorticity equation). The velocity recover is performed via direct integration of the Biot-Savart law, which leads to an exact solution with the exclusion of the viscous filament core.
A 2° azimuth step is used resulting in 180 time steps per rotation and an Adam-Bashforth second order time scheme is used. The solution is run till convergence of the integral values of C_T, for the case considered this is ensured after 15 rotations which corresponds to a wake extension of 12.5 diameters downstream. No wake cut-off is used: all wake elements are retained for the whole simulation, resulting in a final amount of 130K elements.
The model is able to catch the unsteady, 3D aerodynamics of the VAWT wake. Because of its completely lagrangian formulation it requires no grid creation and avoids numerical dissipation of the vorticity.
The simulation is run for further 15 rotations after convergence and location and strength of the vortex filaments and the panels are saved for every time step. The saved data are then post-processed and velocity fields are reconstructed from the vorticity distribution. Phased-lock averaged vector fields are obtained by averaging the last converged 15 rotations.

Numerical results

Results from the numerical simulation are shown in the present paragraph. To limit the number of plots presented, only results from the 3D model are presented for the horizontal mid-plane (contours of the two velocity components U_x,U_y) and for the vertical planes (contours of the three components of velocity). All results are for $\lambda = 4$ and averaged over 15 rotations at $\theta = 0°$. All contours plot have the same colorbar of the relative experimental results for easier comparison and all the same conventions on the vector direction apply.

Horizontal mid-plane

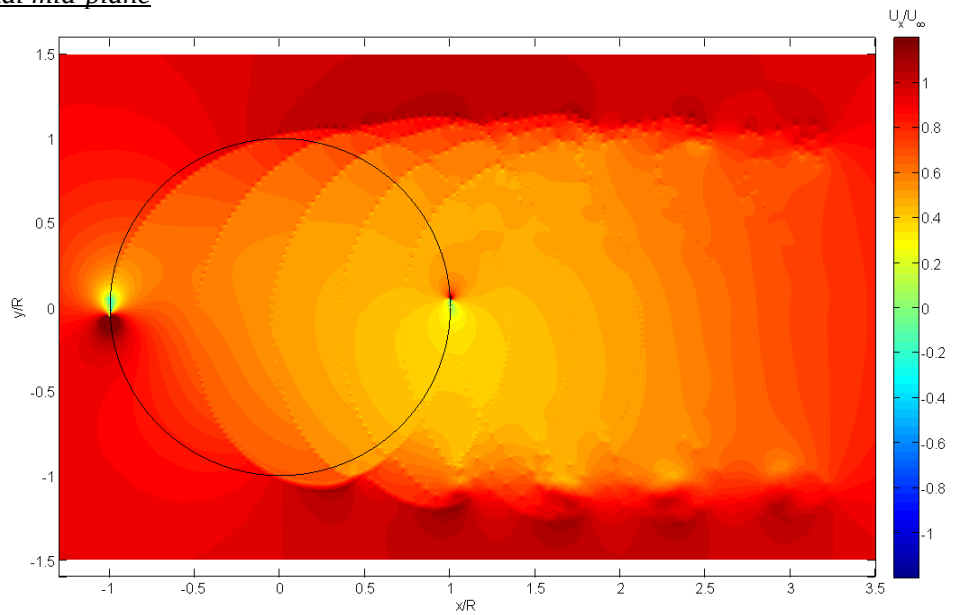

Figure 10: phased averaged normalized stream-wise velocity contours (U_x/U_∞, $\theta = 0°$, $\lambda = 4$)

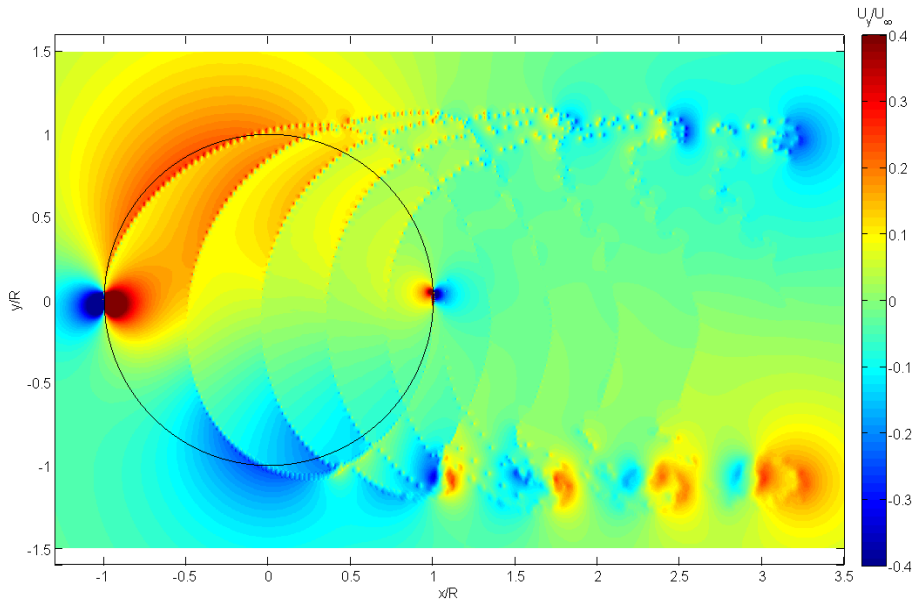

Figure 11: phased averaged normalized cross-stream velocity contours $(U_y/U_\infty, \theta = 0°, \lambda = 4)$

Results from the numerical simulation show a less pronounced expansion of the wake in the horizontal mid-plane, compared to the experimental results. The wake deficit is also considerably lessened (Figure 10) with a minimum stream-wise velocity of 30% of U_∞ right downwind the rotor area and a fast wake recovery with an almost uniform flow at $0.8U_\infty$ after only 2 diameter downwind. The simulation well captures the induction field in the upwind part of the rotor while the discrepancies increase in the downwind part and in the wake. Figure 11 shows the cross-stream velocity which again well compares with experimental results (Figure 4) in the upwind part of the rotor (except for the viscous regions in the blades wake) but not in the downwind part and in the rotor wake. Here after 1 diameter downstream there is an inversion in the shear layer evolution with a contraction of the wake and outer, more energetic flow, is transported inside the wake re-energising it.

Vertical planes

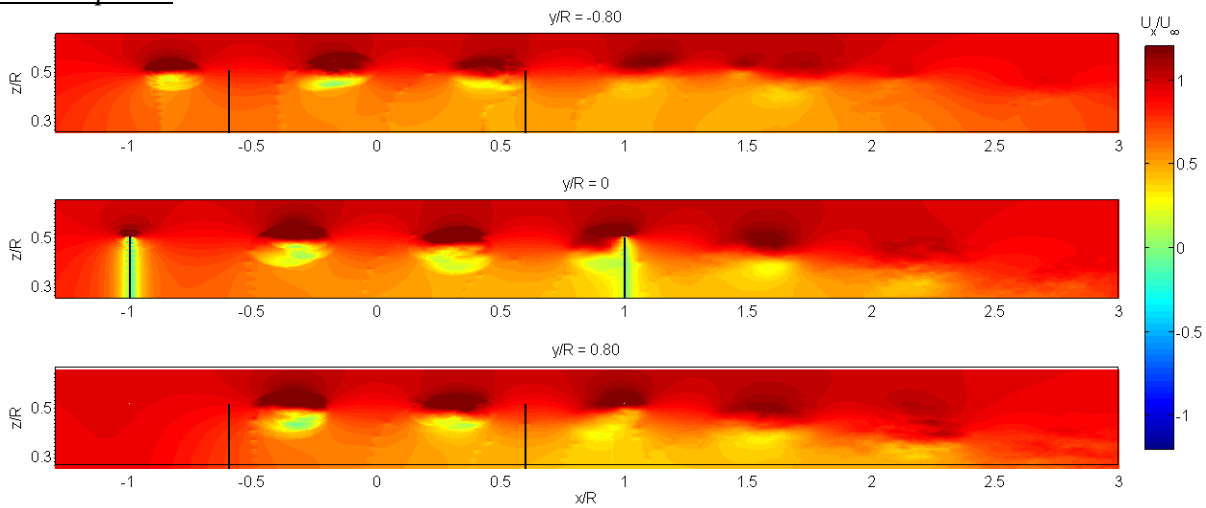

Figure 12: phased averaged normalized stream-wise velocity contours $(U_x/U_\infty, \theta = 0°, \lambda = 4)$

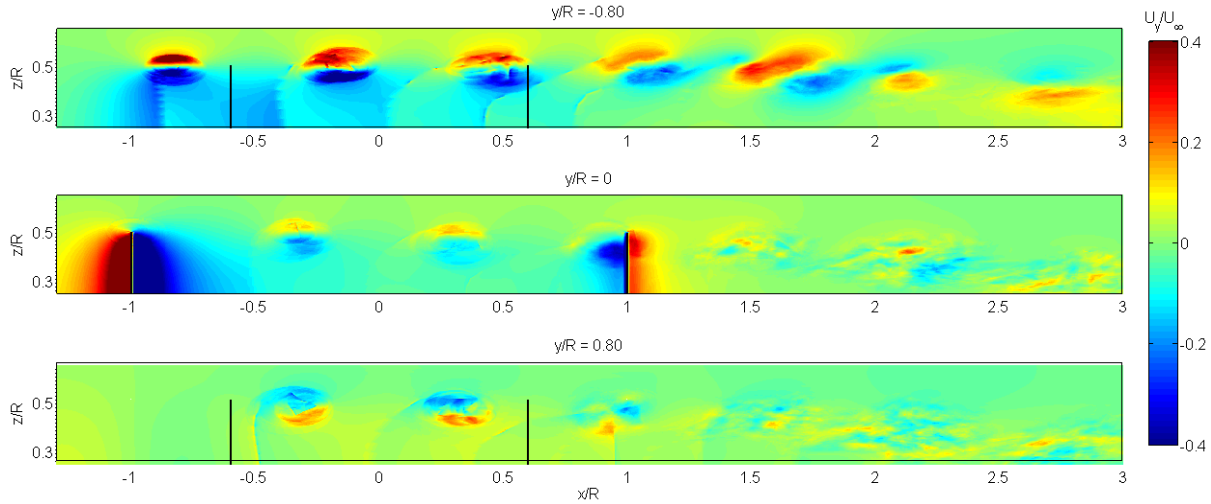

Figure 13: phased averaged normalized vertical velocity contours ($U_y/U_\infty, \theta = 0°, \lambda = 4$)

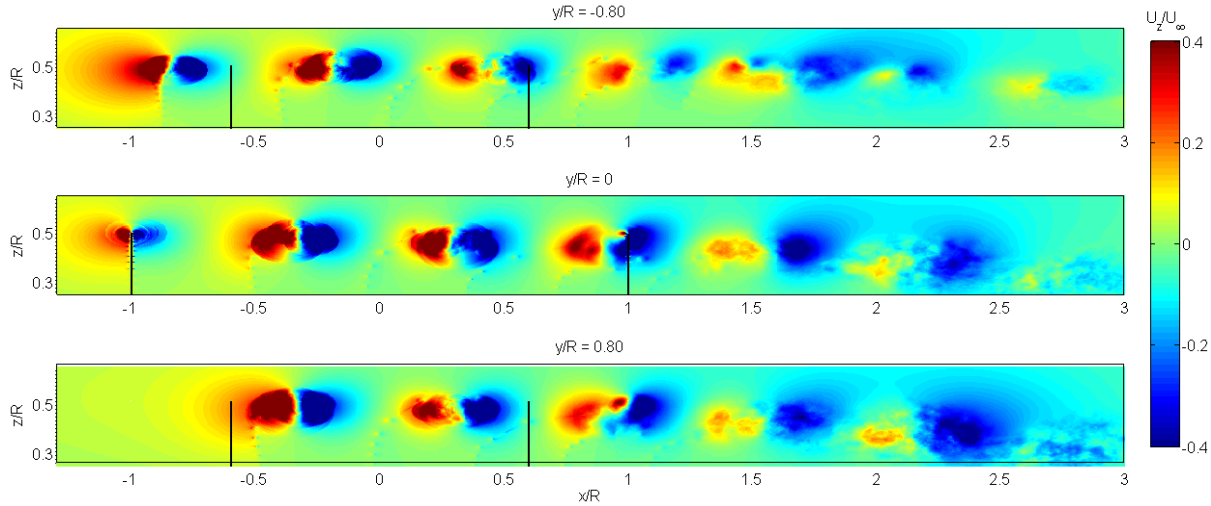

Figure 14: phased averaged normalized cross-stream velocity contours ($U_y/U_\infty, \theta = 0°, \lambda = 4$)

Numerical results for the flow in the vertical planes show a good agreement with experiments for the leeward region, except for an inboard motion of the tip vortices after 1D downstream, while the experiment showed a slight outboard motion. In the middle region of the wake similar results can be seen, with a pronounced inboard motion of the tip vortices which is not seen in the experiments. The greatest difference interests the windward region where the simulation shows a tip vortex inboard motion for *y/R = 0.8* (the motion will reverse direction only for greater values of *y/R*) while the experiments showed a quick upward motion. These numerical results are in agreement with previous numerical studies [7], where inboard motion of tip vortices was observed

Also the stream-wise velocity (Figure 12) shows a good comparison only for the leeward region, with a smaller induction and a more pronounced velocity recover in the rest of the wake. Results are in agreement with the ones for the horizontal mid-plane. Also in this case it has to be highlighted the absence of the shaft in the simulation, and for the tip vortex motion also the absence of the struts which have been identified as a possible cause of a reduced (or absent) inboard motion. Moreover it has to be considered that the numerical model doesn't have numerical dissipation and a diffusion model is not implemented, thus the strength of the vortices is conserved and a stronger roll-up is to be expected with respect to the experimental data.

Conclusions and further work

The near wake of a 2-bladed H-rotor VAWT has been investigated with PIV ($Re_c=80'000$) and with a free vortex wake, panel method. Measurements focused on the mid (symmetry) plane, where it was possible to capture the horizontal wake expansion, the generation and evolution of the cycloidal blade wake pattern and the onset of instabilities in the blade wake triggered by blade vortex interaction and evolved in coherent vortical structures. Stereoscopic measurements in the vertical planes aligned with the free stream captured the generation of the tip vortices and their vertical motion. Numerical results showed a less pronounced wake expansion in the mid-plane and a faster wake recovery with respect to the experiments. In the vertical planes a strong vertical inboard motion of the tip vortices is observed, in agreement with previous numerical works. The difference between experimental and numerical results have to be searched in the absence of the central shaft and supporting struts of the numerical model, and in the stronger roll-up of the vortices in the vortex method for which no diffusion is implemented.. A new experimental activity has already started on a modified version of the turbine model with a better blade-strut connection (with less interference in the flow and in the tip vortices motion) and allowing a higher Reynolds number ($Re_c=180'000$). This should allow having results more easily comparable with the numerical model.

REFERENCES

[1] "Wind in our Sails. The coming of Europe's offshore wind energy industry", European Wind Energy Association report. (2011)

[2] Peace S., "Another approach to wind.", Mech Eng; 126(6): 28–31. (2004)

[3] Musgrove P.J., " Wind energy conversion: recent progress and future prospects.", Sol Wind Technol; 4(1): 37–49. (1987)

[4] Vita L., Paulsen U.S., Pedersen T.F., Madsen H.A. Rasmussen F., "Deep Wind: A novel floating wind turbine concept.", Windtech International; 6(4): 29-31. (2010)

[5] C.J. Simão Ferreira., "The near wake of the VAWT, 2D and 3D views of the VAWT aerodynamics.", PhD thesis. Delft University of Technology. (2009)

[6] C. Hofemann, C.J. Simão Ferreira, K. Dixon, G.J. van Bussel, G. van Kuik, and F. Scarano., "3D stereo piv study of tip vortex evolution on a vawt.", Proceeding of EWEC, Brussels. (2008)

[7] F. Scheurich, T.M. Fletcher, and R.E. Brown., "Simulating the aerodynamic performance and wake dynamics of a vertical-axis wind turbine.", Wind Energy, 14(2): 159-177. (2011)

2D – CFD ANALYSIS OF TWO-BUCKET SAVONIUS ROTOR

K. Rogowski[1], R. Maroński[2]

[1]Warsaw University of Technology, Division of Mechanics, krogowski@meil.pw.edu.pl
[2] Warsaw University of Technology, Division of Mechanics, maron@meil.pw.edu.pl

ABSTRACT

CFD analysis of a two-dimensional two-bucket Savonius rotor was made using ANSYS FLUENT solver. Gaps between buckets in non-dimensional form were s/d=0.1 and s/d=0.2, where s was a width of the gap and d was a diameter of the Savonius bucket. Calculations were made for an inlet velocity of 7 m/s and a tip speed ratio in the range of 0.4 to 2.0. Computations of power characteristics for the Reynolds number corresponding to the inlet velocity of 14 m/s were made as well.

The computed power coefficients were compared with an experimental data coming from Sandia National Laboratories report.

Following turbulence models were used for simulation of a flow around the Savonius rotor: the Spalart-Allmaras, the k-epsilon, the RNG k-epsilon, the realizable k-epsilon and the k-omega. The Spalart-Allmaras and the RNG k-epsilon turbulence models gave a good agreement of the power coefficients with the experimental ones. A discrepancy of the experimental and CFD results was in the range of 2 to 8% for a tip speed ratio in the range of 0.4 to 1.2. Above a tip speed ratio of 1.2 the discrepancy was higher.

An impact of a side force and a downwind (drag) force acting on the Savonius rotor was also investigated. Calculations were made for four tip speed ratios: 0.4, 0.8, 1.2 and 1.6. It turned out that the downwind force and the side force were of the same order in magnitude.

From the point of view of a future three-dimensional analysis of the Savonius rotor and assumed short computation time, a mesh without a boundary layer mesh was used.

The impact of dimensions of a computational area (the area of a virtual wind tunnel) was tested. The Savonius rotor was put into the center of an area in the shape of a square. The minimum length of the side of the square was 20 meters for the Savonius rotor diameters of approximately 1 meter.

1. INTRODUCTION

A wind turbine with a Savonius rotor usually is a vertical axis wind turbine (VAWT). It is a drag-type machine but because of an airflow between buckets (the bent sheets of the Savonius rotor) an additional lift force appears on the buckets. The Savonius rotor was the biggest achievement of Finnish inventor Sigurd Johannes Savonius who patented it in 1926. The typical Savonius rotor is equipped with two buckets, but three or more buckets are possible. It usually has an S-shape cross-section. The wind turbine with such a rotor can achieve even 30% of the maximum power coefficient comparing with 60% following from Betz theory. However, this turbine needs 30 times greater surface

of the buckets comparing with a wing area of a conventional wind turbine to give the same output power. That is why the Savonius rotors are small and they are low energy devices. They can work as water pumps, drives for small electric generators, Flettner ventilators (developed by German aircraft engineer Anton Flettner in 1920s and still manufactured in the UK by Flettner Ventilator Limited). The Savonius wind turbines can provide water agitation to keep stock ponds ice-free during winter. Anemometres often are Savonius type turbines due to small costs and reliability. Because of a very small a starting torque of a Darrieus turbine, the Savonius rotor is sometimes used as a starter for these machines. Undoubtedly, one of the advantages of the Savonius rotor is a possibility of using it by residents of the Third World countries leaving without electricity. A worn out and empty oil barrel can be used as a low-power device.

In spite of very simple structure of the Savonius rotor its aerodynamics is very complicated for modeling. One can observe a lack of simplified aerodynamic methods for modeling of this type of wind turbines. One model (perhaps the only one) noticed by Paraschivoiu is a mathematical model proposed by Chauvin basing on the pressure drop on each side of the blades. It enables computing the power of the two-bucket Savonius rotor without a gap between the buckets. But the Savonius rotor without the gap is only a drag-type device and its maximum power coefficient is much less than that one for the rotor with the specific width of the gap. There are only two ways to possess the aerodynamic performances of the Savonius rotor: using Computational Fluid Dynamic methods (CFD) and/or via an experiment.

Numerical computations of the flow pattern around the rotor require integration of the Navier-Stokes equations. Direct integration of these equations (Direct Numerical Simulation – DNS) requires very small mesh and very efficient super computers. It gave the impulse for further development of the CFD methods. The CFD methods base on averaged in time Reynolds equations (Reynolds-averaged Navier-Stokes – RANS) or averaged in space equations (Large Eddy Simulation – LES). Using them one can solve the large scale problems and that is satisfactory for many practical applications.

The optimization of the geometry of the Savonius rotor is possible employing experimental or CFD methods. Many shapes and configurations of the Savonius rotor are used now. Some rotors are in the shape of a drill or the two-unit two-bucket Savonius rotors rotated 90˚ apart. It decreases the pulsation of the torque coefficient with the azimuth. Flat circular discs are attached at the ends of the Savonius rotor. Sometimes an additional shaft is used. It makes the structure more stiff. [1], [2], [6], [7]

2. PROBLEM FORMULATION

Power characteristics of the 2D two-bucket Savonius rotor were obtained using the computational fluid dynamic solver – ANSYS FLUENT. The power characteristics are expressed by a power coefficient as a function of a tip speed ratio. The power coefficient and a tip speed ratio are as follows:

$$Cp = Cm \cdot TSR, \tag{2.1}$$

$$TSR = \frac{\omega \cdot R}{V_{in}}, \tag{2.2}$$

where: ω – turbine rotational speed; R – rotor radius (see Figure 3.1); V_{in} – inlet velocity (velocity at the inlet of the wind tunnel); Cm – torque coefficient, which is defined as:

$$Cm = \frac{M}{1/2\,\rho \cdot V_{in}^2 \cdot A_s \cdot R}, \tag{2.3}$$

where: ρ – density of the air; A_s – turbine swept area; M – turbine torque.

The rotor swept area is defined as:

$$A_S = (4r - s) \cdot 1, \tag{2.4}$$

where: r – bucket radius (see Figure 3.1); s – bucket gap width; 1 – unit height of the Savonius rotor.

Moreover, a side force *Fy* and a downwind (drag) force *Fx* acting on the Savonius rotor as a function of azimuth position were investigated during the analysis (see Figure 2.1). They are given in non-dimensional form:

$$CFy = \frac{Fy}{1/2\,\rho \cdot V_{in}^2 \cdot A_S}, \tag{2.5}$$

$$CFy = \frac{Fy}{1/2\,\rho \cdot V_{in}^2 \cdot A_S}. \tag{2.6}$$

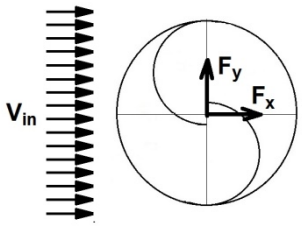

Figure 2.1: A side force *Fy,* and a downwind force *Fx*, exerted on a Savonius rotor.

3. GEOMETRICAL MODEL OF THE ROTOR

A two-dimensional geometrical model of the Savonius rotor necessary for numerical computations was created basing on Sandia's report. The model is given in Figure 3.1. A considered configuration of the Savonius rotor consists of two the same buckets (blades) of a radius *r* = 0.25m. The typical Savonius rotor has a gap between the buckets. Two non-dimensional widths of the gap were investigated: s/d=0.1 and s/d=0.2, where *d* is a diameter of the bucket and *d=2r*. Other symbols in the Figure 3.1 are: R – rotor radius; θ – bucket angular position (azimuth). Because of lack of the information about a thickness of the bucket wall, two millimeter thickness of the bucket has been assumed.

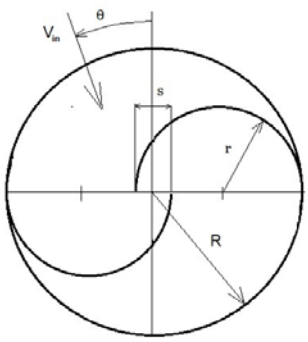

Figure 3.1: Two-dimensional model of the Savonius rotor.

The impact of dimensions of the wind tunnel on the power coefficient was tested (see Figure 3.2). Three dimensions of the wind tunnel were examined: W – width of the wind tunnel, Z – length between an inlet of the tunnel and the axis of rotation of the Savonius rotor, and T – length between the axis of the Savonius rotor and an outlet. An analysis of this chart has shown that the square work area of the wind tunnel with a side length of 20 meters was acceptable, but the length of 30 meters was used for better accuracy. The rotor radius R was 0.47m and 0.45m.

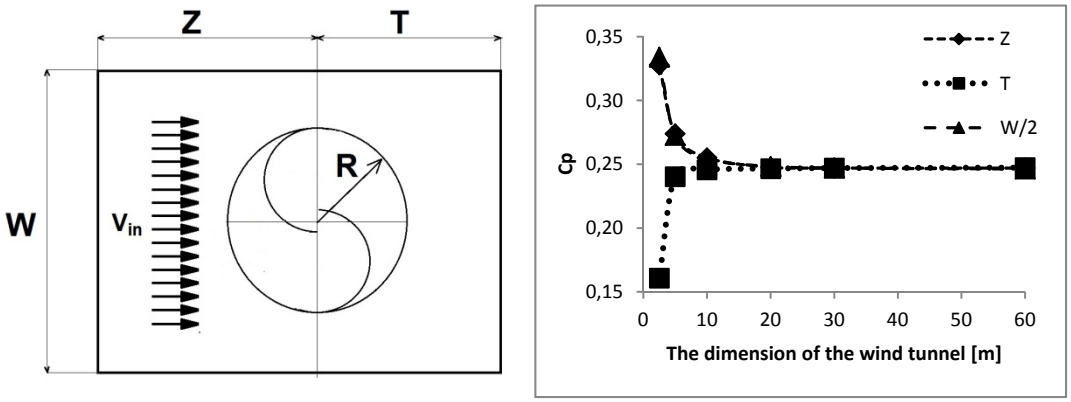

Figure 3.2: Influence of the dimensions of the computational area on the power coefficient.

4. MESH AND BOUNDARY CONDITIONS

The computational area around the Savonius rotor was approximated by finite elements. The flow around the buckets of the Savonius rotor may be in different directions for different azimuth position therefore triangle elements were used. Turbulence models available in ANSYS FLUENT allow users to choose the way of calculations. There are two possibilities depending on a non-dimensional length of the first layer of the mesh closest to walls of the buckets, so-called *wall y+*. It is very important to this parameter was in specific limitations for chosen way of calculations and for chosen turbulence model. A mesh (see Figure 4.1) reached a *wall y+* parameter in the range of 30 to 230 for a tip speed ratio in the range of 0.4 to 1.2 for every tested turbulence models. Above a tip speed ratio of 1.2, more and more values of *wall y+* were below limit of 30. That means that an uncertainty appeared for power coefficients obtained for tip speed ratios above 1.2. The number of elements of this mesh was 41 336. Edges of the buckets were divided into 90 elements. The mesh consists of two parts: a square of 30m

and a circle with a diameter of 1.8 m inside the square. The circular area can “rotate” during the simulation relatively to the motionless square area. The flow of the data between elements of these two areas was provided due to an interface condition.
Two types of boundary conditions were used: *velocity inlet* and *pressure outlet* at the inlet and the outlet of the wind tunnel respectively. Edges of the buckets were regarded as impermeable walls.

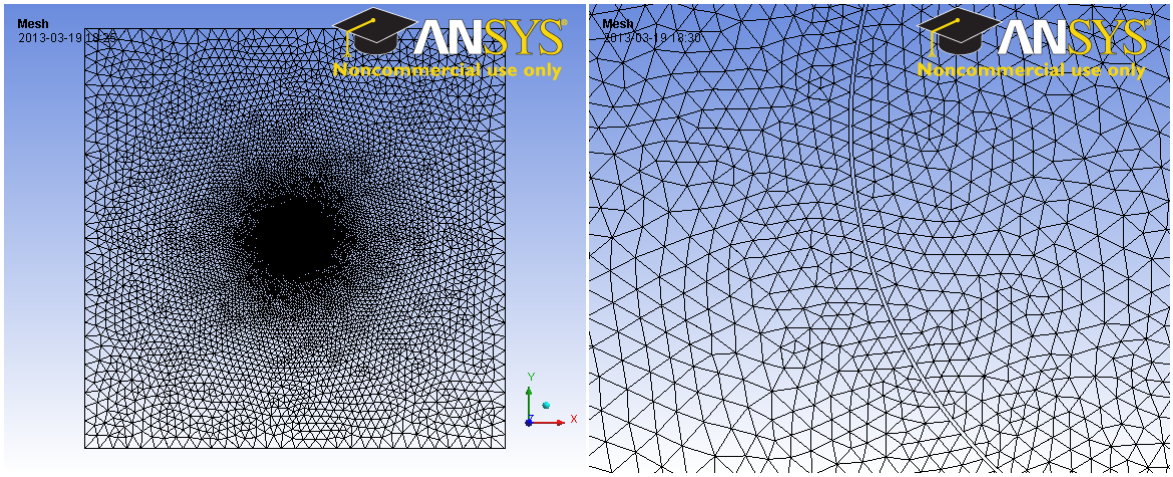

Figure 4.1: A mesh around a Savonius rotor without a boundary layer mesh.

5. TURBULENT MODELS

A choice of an appropriate turbulence model for CFD codes necessary to achieve satisfactory power characteristics is very important issue. There is no such turbulence model which gives good results for each class of flow. Generally, different turbulence models were developed for precise description of the specific classes of flows. Turbulence models differ each other in number of equations and a level of complexity. The models based on the Reynolds-averaged Navier-Stokes system of equations.
Following turbulence models were used for computations: the Spalart-Allamras, the k-epsilon, the realizable k-epsilon, the RNG k-epsilon and the k-omega.
The Spalart-Allmaras model is one-equation model, originally developed for aerospace applications (two-dimensional flows around an airfoil). It is also used in turbomachnery applications. The Spalart-Allmaras turbulence model solves a transport equation for the turbulent viscosity.
The k-epsilon model is one of the most popular, semi-empirical turbulence model which was created for low-speed incompressible flows. It was proposed by Launder and Spalding. The k-epsilon model has been modified many times and there are many specialized versions. The k-epsilon model solves two transport equations to calculate the kinetic turbulence energy – k and the dissipation rate – epsilon.
The RNG k-epsilon model is similar to the standard k-epsilon model but it has additional refinements. The RNG model was derived from the instantaneous Navier-Stokes equations using a statistical technique called renormalization group theory (RNG).
The realizable k-epsilon turbulence model is another specialized version of the standard k-epsilon model. It contains an alternative formulation of the turbulent viscosity and a modified transport equation for the dissipation rate, epsilon. It has been derived from an exact equation for the transport of the mean-square vorticity fluctuation.
The standard k-omega turbulence model is an empirical model which solves two transport equations for the turbulence kinetic energy – k, and the specific dissipation rate – omega. The k-omega model in

its standard form, available in ANSYS FLUENT, is based on Wilcox k-omega model. This model incorporates modifications for low-Reynolds number effects, compressibility and shear flow spreading. [4], [5]

6. VALIDATION OF THE ASSUMPTIONS AND THE RESULTS

There is a shortage of experimental data referring to performances of the Savonius rotor, therefore a report of Sandia Laboratories has been used in our investigations. This report is available on the Sandia's web page. It contains experimental results of fifteen configurations (two- and three-bucket) of the Savonius rotor wind turbine which were tested in the low speed wind tunnel. [2]

CFD computation of the flow around the Savonius rotor, which was presented in chapter 3 were made for following airflow parameters: inlet velocity, V_{in}, of 7 m/s, angular velocity (turbine rotational speed), ω, was in the range of 5.88 to 29.4 rad/s, tip speed ratio, TSR, was in the range of 0.4 to 2.0. Airflow velocities around the Savonius rotor were relatively low therefore an incompressible gas model was employed. Following parameters of the air were assumed: density of 1.225kg/m^3 and dynamic viscosity of $1.7894 \cdot 10^{-5}$ Pa·sec. Turbulence parameters of an airflow at the inlet were as follows: the turbulent intensity 5%, and the turbulent length scale 0.01 m. Such the value of the turbulent intensity corresponds to a high-turbulence case typical for turbines and compressors.

In Figures 6.1 and 6.2 the curves are given of a torque convergence as a function of simulation time for a tip speed ratios 0.4, 0.8, 1.2 and 1.6 and for three turbulence models: the Spalart-Allmaras, the RNG k-epsilon and the k-omega. Stability of the torque coefficients can be seen for a tip speed ratio in the range of 0.4 to 1.2÷1.4. Only 4 or 5 full revolutions of the Savonius rotor were necessary for minimizing the impact of the initial conditions. For a tip speed ratio above 1.2÷1.4 there were no stability of the torque coefficients for each used turbulence model, even after several dozen revolutions of the rotor.

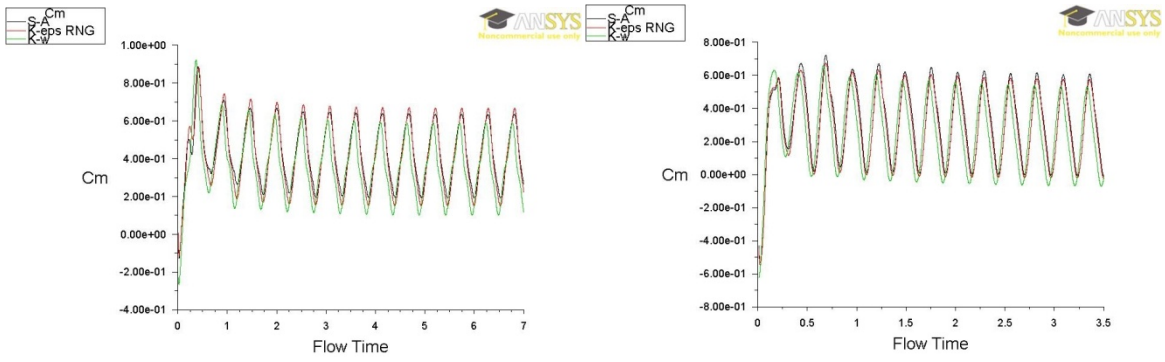

Figure 6.1: Torque convergence as a function of simulation time for TSR=0.4 (the left chart) and for TSR=0.8 (the right picture).

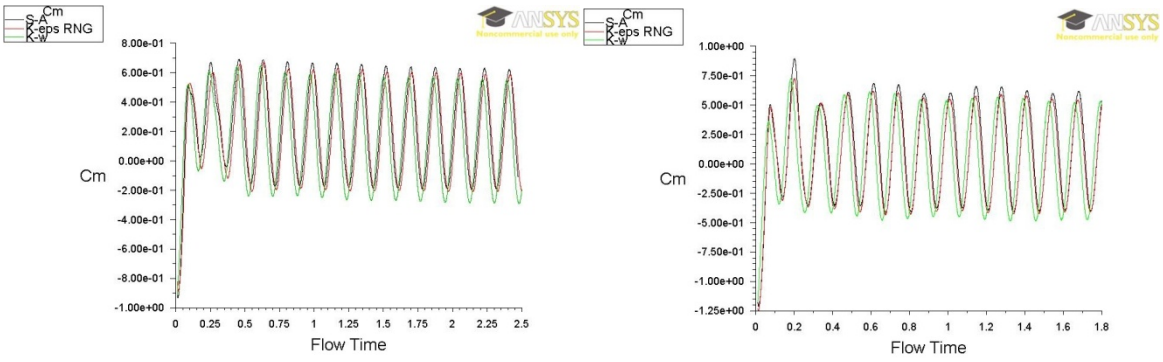

Figure 6.2: Torque convergence as a function of simulation time for TSR=1.2 (the left chart) and for TSR=1.6 (the right picture).

Differences between torque coefficients, Cm, as a function of azimuth position for one full revolution and for three sample turbulence models are more visible in the common graphs. These results are shown in Figures 6.3 and 6.4. As it can be seen, three turbulence models give quite considerable discrepancies of the torque coefficient.

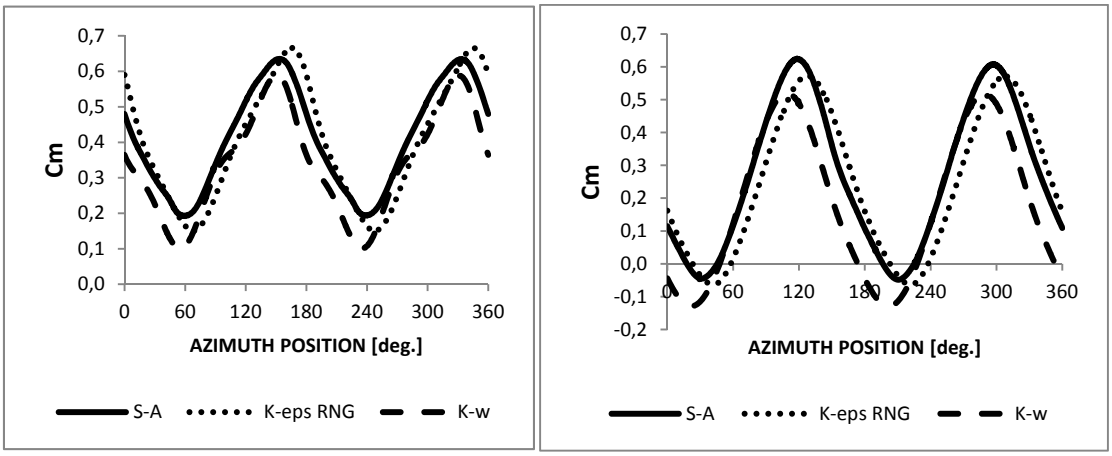

Figure 6.3: Torque coefficient as a function of azimuth position for one full revolution of the Savonius rotor for TSR=0.4 (on the left) and for TSR = 0.8 (on the right).

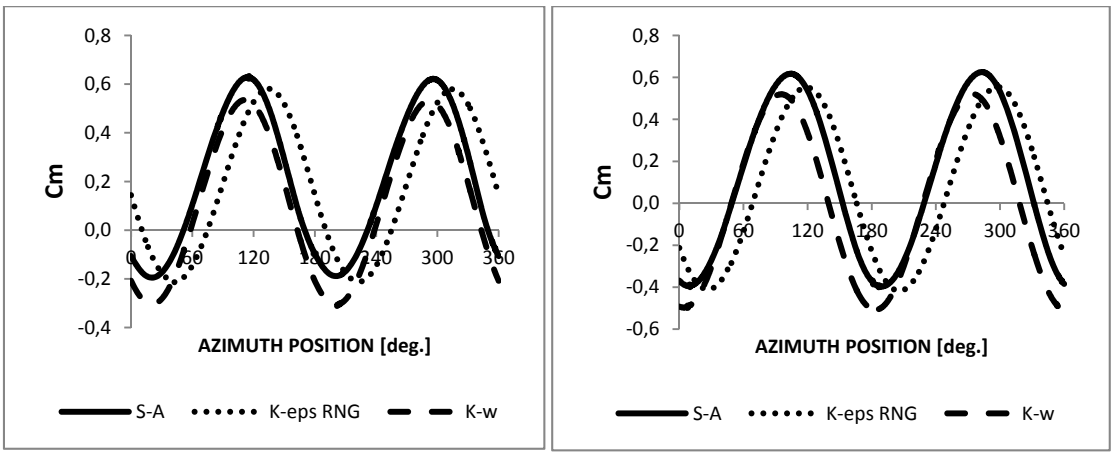

Figure 6.4: Torque coefficient as a function of azimuth position for one full revolution of the Savonius rotor for TSR=1.2 (on the left) and for TSR = 1.6 (on the right).

The torque coefficient as a function of azimuth position for a sample turbulence model of Spalart-Allmaras and for an usable range of a tip speed ratio from 0.6 to 1.2 is shown in the common graph in Figure 6.5. The obtained results show that up to a tip speed ratio of 1.1 the maxima of torque coefficient curves are at the same level. For increasing tip speed ratio, the minima of these curves reach smaller values up to -0.2.

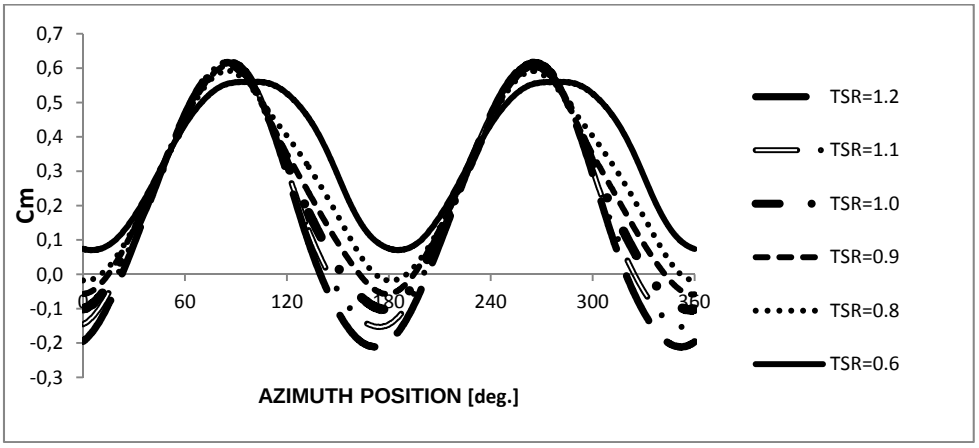

Figure 6.5: Torque coefficient as a function of azimuth position for six values of tip speed ratio and for sample turbulence model of Spalart-Allmaras.

Power characteristics of the Savonius rotor were obtained after averaging the torque coefficients corresponding to specific tip speed ratios and for each turbulence model. The results are shown in Figure 6.6. The obtained power characteristics were compared with the experimental results. Black dots correspond to the data from the Sandia's report. The curve corresponding to the RNG k-epsilon turbulence model coincides with the experimental data in the whole tested tip speed ratio range. The curve for the Spalart-Allmaras model gave overestimated results for the tip speed ratio above the value of 1.2. Other tested turbulence models gave unsatisfactory results.

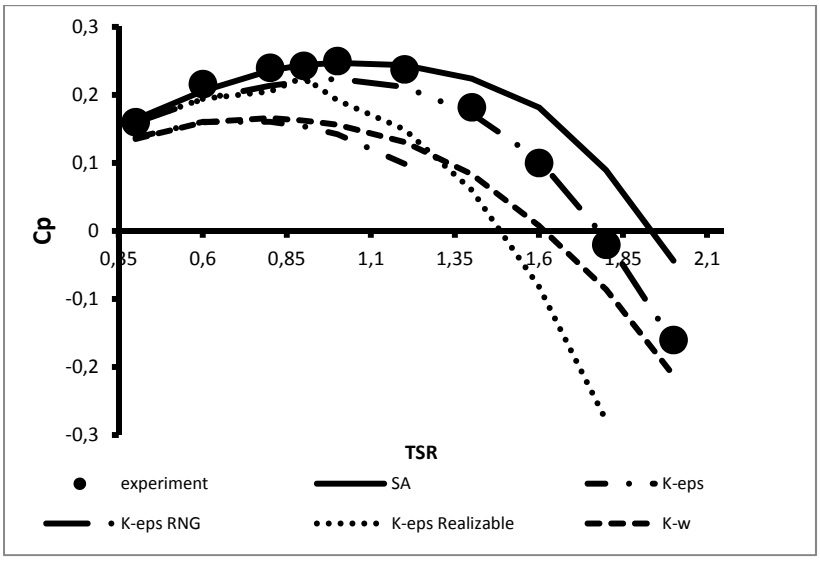

Figure 6.6: Power curve of the Savonius rotor for different turbulence models.

Basing on previous considerations, the Spalart-Allmaras and the RNG k-eps turbulence models were recognized as these giving satisfactory results especially for a tip speed ratio in the range of 0.4 to 1.2. Moreover, the Spalart-Allmaras turbulence model appeared less time-consuming in comparison with the RNG k-epsilon model. That is why the Spalart-Allmaras turbulence model was used for final analysis of the problem.

The power characteristics shown in Figure 6.7 concern two geometrical configurations of the Savonius rotor. In this test the influence of a width rate of the gap between two Savonius buckets was examined (s/d=0.1 and s/d=0.2). According to the Sandia's report, the Savonius configuration with the width rate of the gap of 0.1÷0.15 reached the best performance – maximum power coefficient was highest. The CFD results of the power coefficient confirmed conclusions from the experiment.

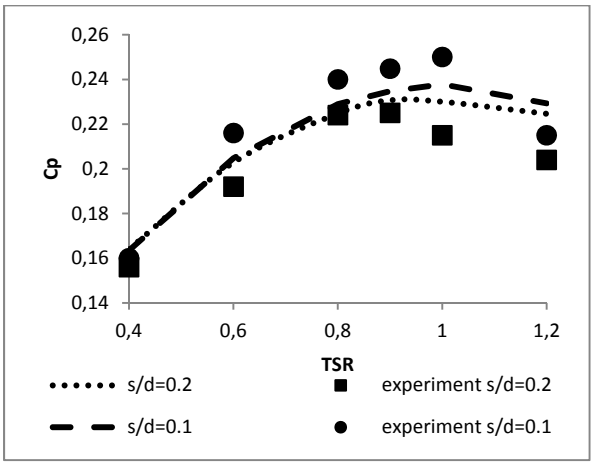

Figure 6.7: Power coefficient as a function of a tip speed ratio for two width ratios.

The tests of the influence of the inlet velocity Reynolds number confirmed another experimental conclusion - the maximum power coefficient slightly decreases with an increase of the inlet velocity. Power characteristics for two cases of the inlet velocity 7 m/s and 14 m/s are shown in Figure 6.8. The results were compared with the experimental ones.

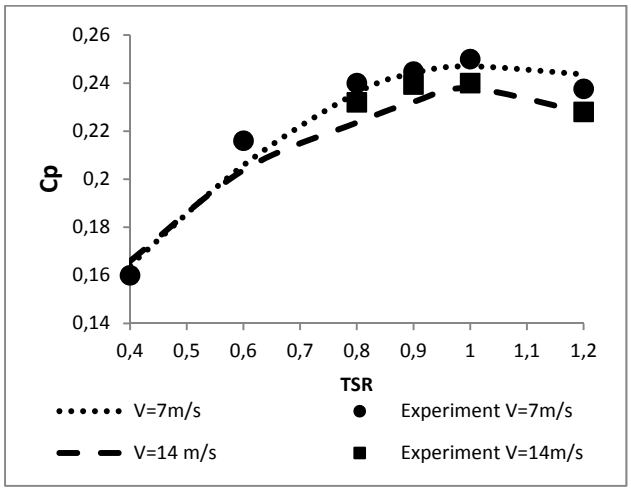

Figure 8.8: Influence of the Reynolds number on performances of the Savonius rotor.

Authors of the Sandia's report have written: *"Recent analytical studies, along with unpublished data of the authors, indicate that the Savonius rotor experiences side forces that are of the same order of magnitude as the downwind (drag) force"*[2]. It was decided to verify this thesis using ANSYS FLUENT solver and the Spalart-Allmaras turbulence model. Results of CFD computation of downwind force coefficients, CFx, and side force coefficients, CFy, as a function of azimuth position for tip speed ratios: 0.4, 0.8, 1.2 and 1.6 are shown in Figure 6.9. The force coefficients CFx and CFy corresponding to the same tip speed ratios are shown in Figures 6.10 and 6.11 on polar diagrams. It can be seen that the maximum values of the downwind force coefficient, CFx, increase with increase of a tip speed ratio. The maximum values of CFx for a tip speed ratio of 0.4 are higher than in the previously announced cases. However, the minimum values of the downside force are approximately at the same level. Values of the side force coefficients CFy are mostly negative. Minimum values of CFy curves decrease with increase of the tip speed ratio. Both forces are of the same order in magnitude.

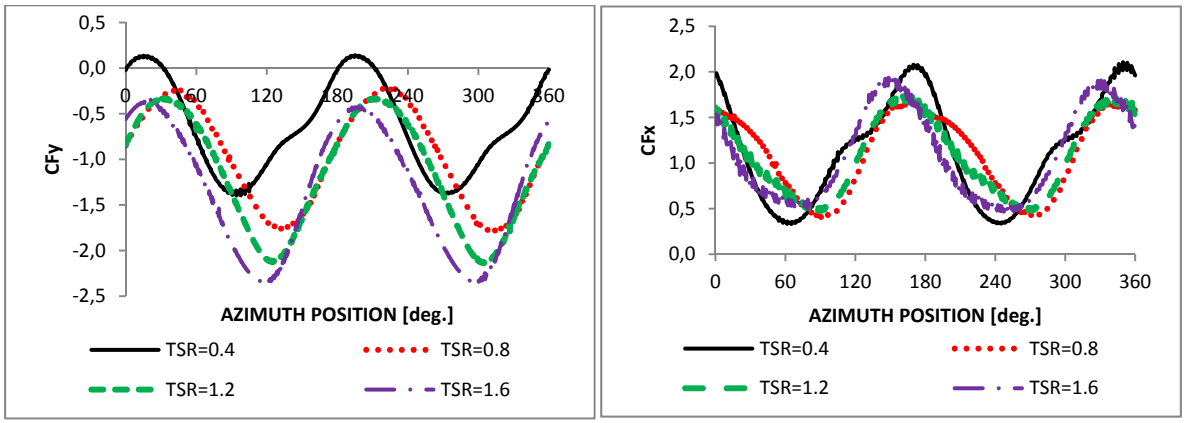

Figure 6.9: Side force coefficient (on the left) and downwind force coefficient (on the right) as a functions of azimuth position for four values of tip speed ratio.

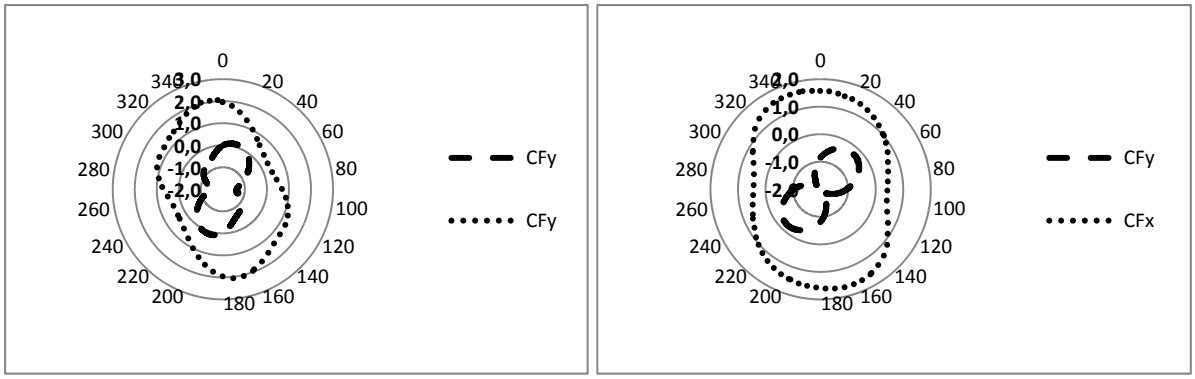

Figure 6.10: Polar graphs of force coefficients for TSR=0.4 (on the left) and for TSR=0.8 (on the right).

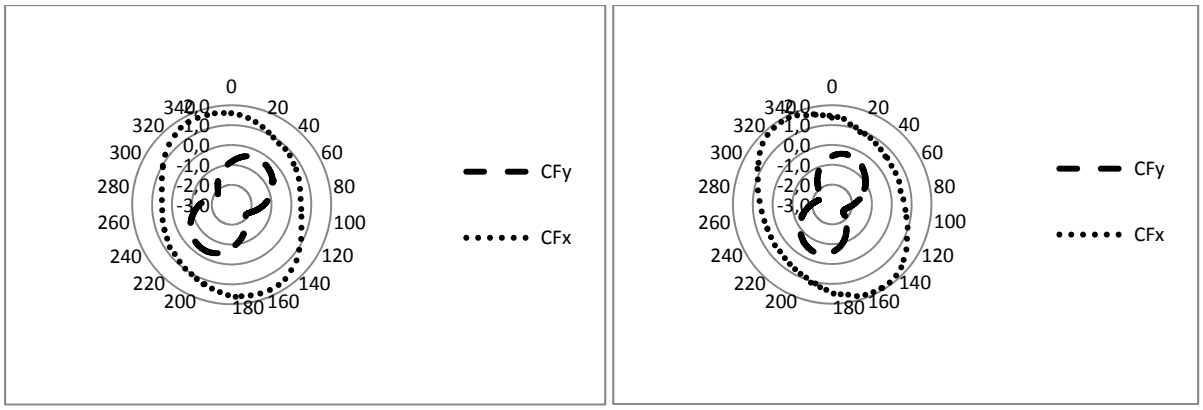

Figure 6.11: Polar graphs of force coefficients for TSR=1.2 (on the left) and for TSR=1.6 (on the right).

7. CONCLUSIONS

The purpose of this study was an assessment of power characteristics (the power coefficient as a function of a tip speed ratio) for a given Savonius rotor geometry using the CFD solver – ANSYS FLUENT. Moreover, the side force and the downwind force acting on the rotor were evaluated. The choice of an appropriate turbulence model was one of the most important issue for the problem solution.

The CFD study confirmed experimental results such as:

- the width ratio of the gap taken in the range of 0.1 to 0.15 gives the highest values of the power coefficient,
- with increase of the Reynolds number the maximum power coefficient slightly decreases.

From all studied turbulence models, two gave the best results: the Spalart-Allmeras and the RNG k-epsilon. The first one gave good convergence of the results with experimental ones for a tip speed ratio in the range of 0.4 to1.2. The second one was acceptable in the whole tested range of the tip speed ratios. But for each turbulence models the torque convergence was poorer for a tip speed ratio above 1.2, therefore results of the power coefficient above 1.2 appeared uncertain.

Analysis of the impact of the side force on the Savonius rotor confirmed a assumption that this force is of the same order in magnitude as the downside force. It should be taken during the design process of a such type of the wind turbine.

Dimension tests of the square-shape computing area showed that the minimum length of the square side should be 20 meters.

Experimental results of the velocity pattern around the Savonius rotor and wake vortex pattern behind the rotor are necessary for further analysis of the received CFD results.

Further studies of the mesh are also necessary. The choice of appropriate mesh seems to be an important issue. Rational using of the tools offered by ANSYS FLUENT solver is very important.

The presented method can be used for investigations of similar rotors. Computations for the mesh shown here may be executed using a standard personal computer.

8. REFERENCES

[1] I. Paraschivoiu, “Wind Turbine Design with Emphasis Darrieus Concept” (2009).

[2] B.E. Blackwell, R.E. Sheldahl, L.V. Feltz, “Wind Tunnel Performance Data for Two- and Three-Bucket Savonius Rotors”, SAND76-0131 (1977).

[3] W. Jagodziński, “Silniki wiatrowe” (1959) (in Polish).
[4] FLUENT Theory Guide (v. 13.0)
[5] A.Flaga, “Inżynieria wiatrowa. Podstawy i zastosowania” (2008) (in Polish).
[6] E. Hau, „Wind Turbines: Fundamentals, Technologies, Application, Economics (2005).
[7] T. Boczar, “Energetyka wiatrowa” (2008) (in Polish).

Noise Sources Investigation of A Commercial 1.5MW Wind Turbine

Bing Yang[1,2], Yue Wu[1,3], Shaohong Jia[1,3], Xiaolu Zhao[1,2], Jianzhong Xu[1,2]

[1]Institute of Engineering Thermophysics, No.11 Beisihuanxi Road, Haidian District, Beijing, China, 100190,yangbing@mail.etp.ac.cn
[2]National Research and Development Center of Wind Turbine Blade, No.11 Beisihuanxi Road, Haidian District, Beijing, China, 100190
[3]Graduate University of Chinese Academy of Sciences, No.19 Yuquan Road, Shijingshan District, Beijing, China, 100084

ABSTRACT

Series of noise measurements were carried out on a 1.5MW, direct drive, permanent magnet, horizontal axis wind turbine, with the rotor diameter of 88.2m and the hub height of 75.0m. A double-elliptic shape array consists of 32 microphones was positioned about one hub height upwind from the wind turbine. Conventional beamforming algorithm with diagonal removal and CLEAN-PSF, a deconvolution algorithm with higher resolution and lower side-lobe, were both used. To validate the algorithms, the measurement of a static noise - car horn by a circle shape microphone array was carried out in an anechoic chamber and the source map was correctly obtained. Distributions of noise sources on the rotor plane were mapped in frequency domain. Operation parameters of the turbine were recorded synchronously with the array signal acquisition by the control center inside the tower. The rotor speed dependence of the hub noise is investigated. It is obvious that noise generated near the blades tip is dominant. It is also revealed that the blade acoustic power level peak moves to the blade tip and decreases with increasing frequency. The trailing edge noise is the dominant noise source verified by the 5th power principle.

1. INTRODUCTION

As for wind turbines, the noise constitutes an important hindrance for widespread application. In order to reduce wind turbine noise, we must locate and reduce the dominant noises. Phased microphone arrays technique is the most advanced technique at present to locate noise sources of a wind turbine. Phased microphone arrays originated in fields of astronomy, sonar and seismology has been greatly developed in the past 2 decades[1] and nowadays more and more popular in use as a standard tool for locating acoustic sources of aircraft and wind turbine. A large number of researches using this technique were carried out around airfoils, blades and wind turbines. W. M. Humphreys developed a microphone directional array to obtain high resolution noise localization maps for locating the accurate sources on airfoils[2], L. Koop and K. Ehrenfried developed a method to consider background noise effects on source maps[3]. Stefan Oerlemans deeply described the algorithm of this technique and applied it on noise source detection in frequency domain on commercial wind turbines[4]. He then made similar efforts on two modified blades with trailing edge serrations and an optimized airfoil shape, respectively, showing trailing edge noise reductions and average overall noise reductions[5]. R. C. Ramachandran achieved broadband acoustic source maps on a wind turbine with a time-domain locating algorithm[6][7].

Conventional beamforming algorithm is the most commonly used algorithm for detecting noise sources in frequency domain for wind turbines. However, the resolution of conventional beamforming is not good enough because turbulent medium always causes the coherence loss that widens the main lobe of sound sources, and the main lobes of main sources may be covered by other sources and side lobes. “Diagonal Removal” processing can remove the self-noise contamination of microphones, which efficiently reduces the side lobe level and thus improves array resolution. In order to maintain “cleaner” source maps, advanced beamforming algorithms are developed. The CLEAN algorithm based on spatial coherence(CLEAN-SC) was developed by Sijtsmain， 2007, which uses the conventional beamforming map as the dirty map and subtracts out the dominant coherent source[8]. CLEAN-SC algorithm is relatively robust since it manually reduces or eliminates minor sources as well as the background noise and the side lobes.

In this paper, noise source measurements were carried out on 1.5MW commercial wind turbine at a wind farm. The initial purpose of these experiments is to locate the position of a tonal noise source that was detected when a noise measurement was carried out according to IEC 61400-11. The noise source maps in frequency domain were obtained by both conventional beamforming - Diagonal Removal and CLEAN-SC algorithm. Further investigations on the blade noise characters were made.

2. STATIC NOISE SOURCE MEASUREMENT IN ANECHOIC CHAMBER

A static noise source measurement was carried out in an anechoic chamber to validate the algorithms we used (Fig.1). A circle-shaped microphone array with a radius of 0.5 m consisting of 32 BSWA MPA416 microphones was positioned 2.5 m away from the static noise source-car horn. The car horn faced the array center. A waveform generator was connected to the horn to create tonal noise at 500Hz.The source distributions using conventional beamforming - Diagonal Removal and CLEAN-SC algorithm are showed in Fig.2. The algorithms could correctly fix the noise source position and prove its availability. It is shown that the main lobe of noise source is smaller and side lobes are mostly suppressed by using CLEAN-SC algorithm compared with the result of beamforming - Diagonal Removal.

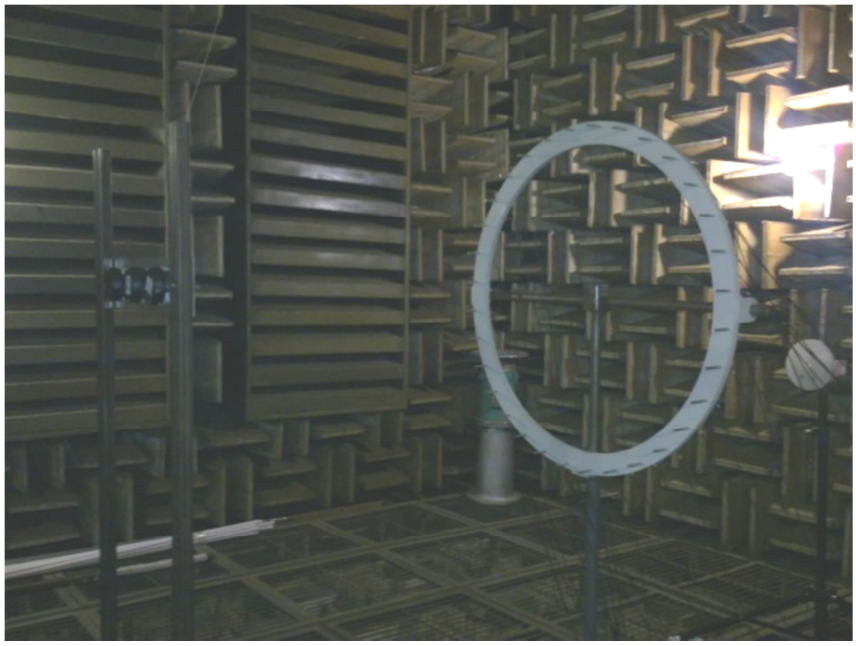

Fig.1 The static noise source measurement in an anechoic chamber

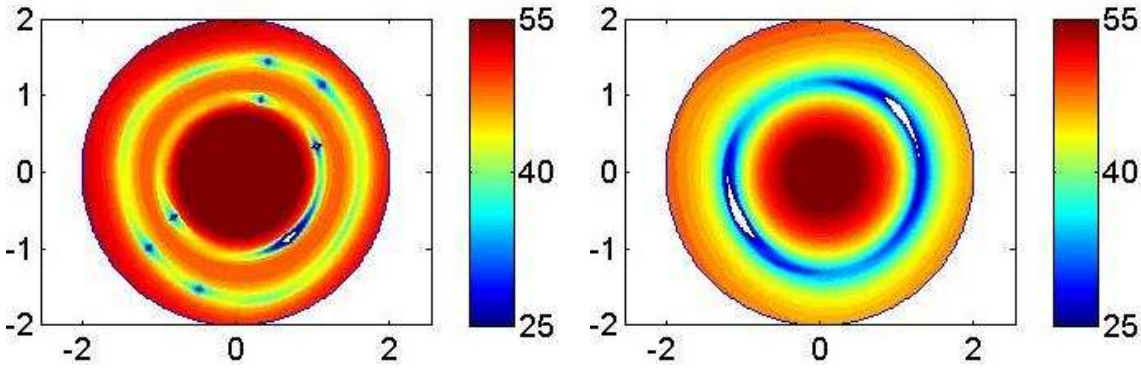

(a) (b)

Fig.2: Sound power level distributions of a static noise source using conventional beamforming (a) and CLEAN-SC (b)

3. WIND TURBINE NOISE MEASUREMENT

The experiment was carried out on a 1.5MW, direct drive, permanent magnet, horizontal axis wind turbine, with the rotor diameter of 88.2m and the hub height of 75.0m. The wind speed varies from 4.2 to 7.0 m/s during the experiments, which corresponds to variable rotor speed of 12.8 to 17.0 RPM. The microphone array was located at 75m upwind from the turbine, with its major axis directing to the tower (Fig.3).

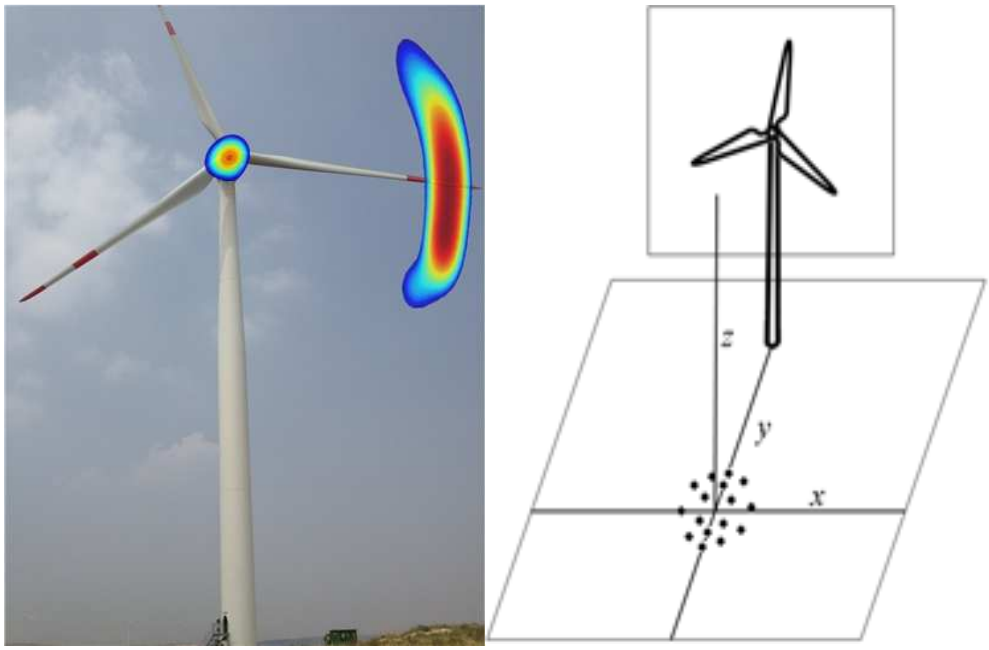

Fig.3 Test turbine and array set up

The array consists of 32 BSWA MPA416 microphones, each with a windscreen. Each microphone is tied up to a small stick and then mounted directly on the ground. A bubble level is used to make sure all the membranes of microphone are parallel to the horizontal ground and positioned at the same height. The array has a double-elliptic shape. The outer and inner ellipse respectively consists of 20 and 12 microphones and has a semi-minor axis length of 2m and 1m (Fig.4). An array in this shape can simultaneously ensure low side lobe levels at high frequencies and a good resolution at low frequencies. The semi-minor axis lengths are set half of the semi-major axis lengths, and the center of

the array is positioned about the same length of hub height upwind from the wind turbine, in order to obtain approximately the same array resolution in the horizontal and vertical direction of the rotor plane.

Fig.4 Microphone array set up

Sound pressure data from the microphones were synchronously measured by NI PXIe-4496 at a sample frequency of 50kHz and a total sampling time of 15s. The data were divided into 2500 sample blocks, each of which contains 0.5s sound pressure information, with a rectangular window and no overlap, yielding 300 averages and a narrowband frequency resolution of 20Hz. No filter was used since we would like to consider the sound pressure in all frequencies without weighting the signals.

The following turbine operation parameters were acquired at a sample rate of 1Hz synchronously with microphone measurement: wind speed at the rotor hub, rotor speed, blade pitch angel, yaw angle.

The test program lasted from Aug.5th to Aug.11th, 2012. A total number of 120 measurements were performed, corresponding to 120 data bases. By applying the following constrains, 8 most stable measurements were selected for further analysis:

1）Rotor speed within 1 RPM of average;

2）Wind speed within 1m/s

3）Yaw angle stable

Conventional beamforming and CLEAN-SC were respectively used to process the sound signals of each data base. The scanning grid is 50m in both x and z directions with a mesh size of 1 m in each direction. The effects of wind and blades movement were both considered. The acoustic sources of wind turbine were averaged over the complete sampling time of 15s.

The wind turbine noise source distributions of 1/3-octave center frequency are showed in Fig.5 and Fig.6. Sources are represented as the sound power level (SWL). Some of the frequencies are a little deviation from the 1/3-octave center frequency for the frequency resolution in these measurements is 20Hz. The turbine rotating speed is 17.0 RPM and the wind speed is 7.0m/s.

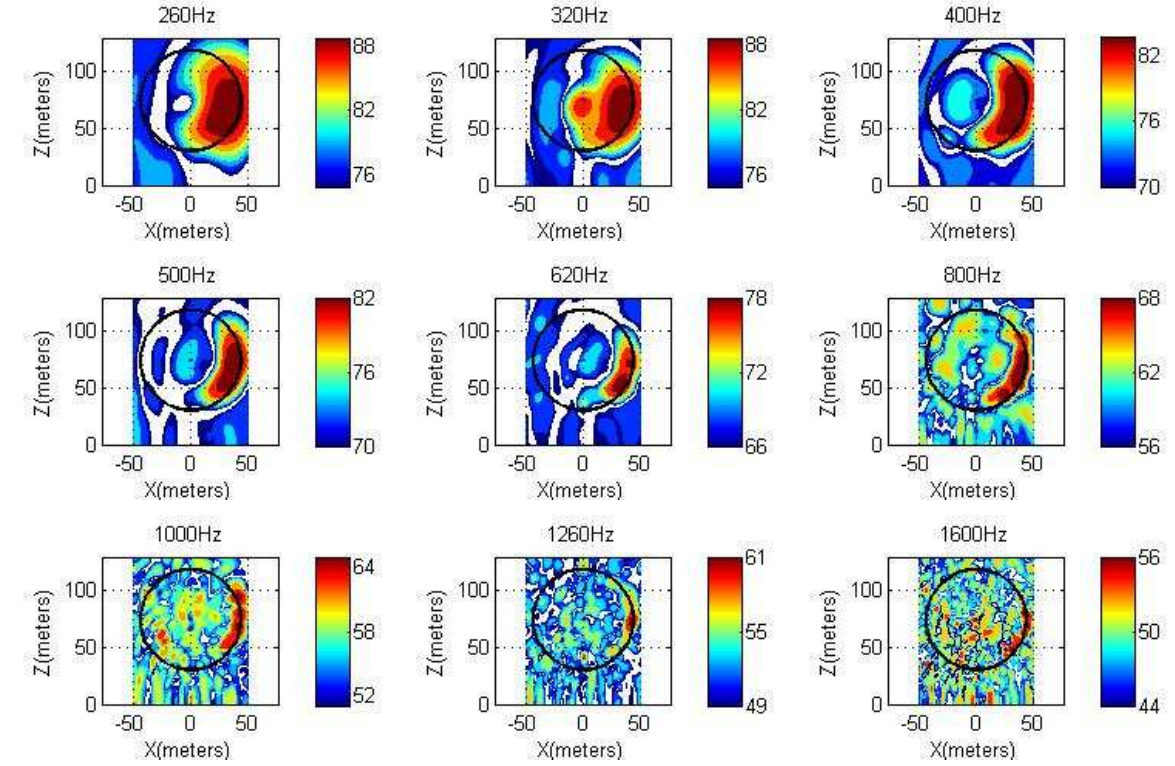

Fig.5 Average SWL distributions on the rotor plane using conventional beamforming
Rotor speed 17.0 RPM, wind speed 7.0m/s

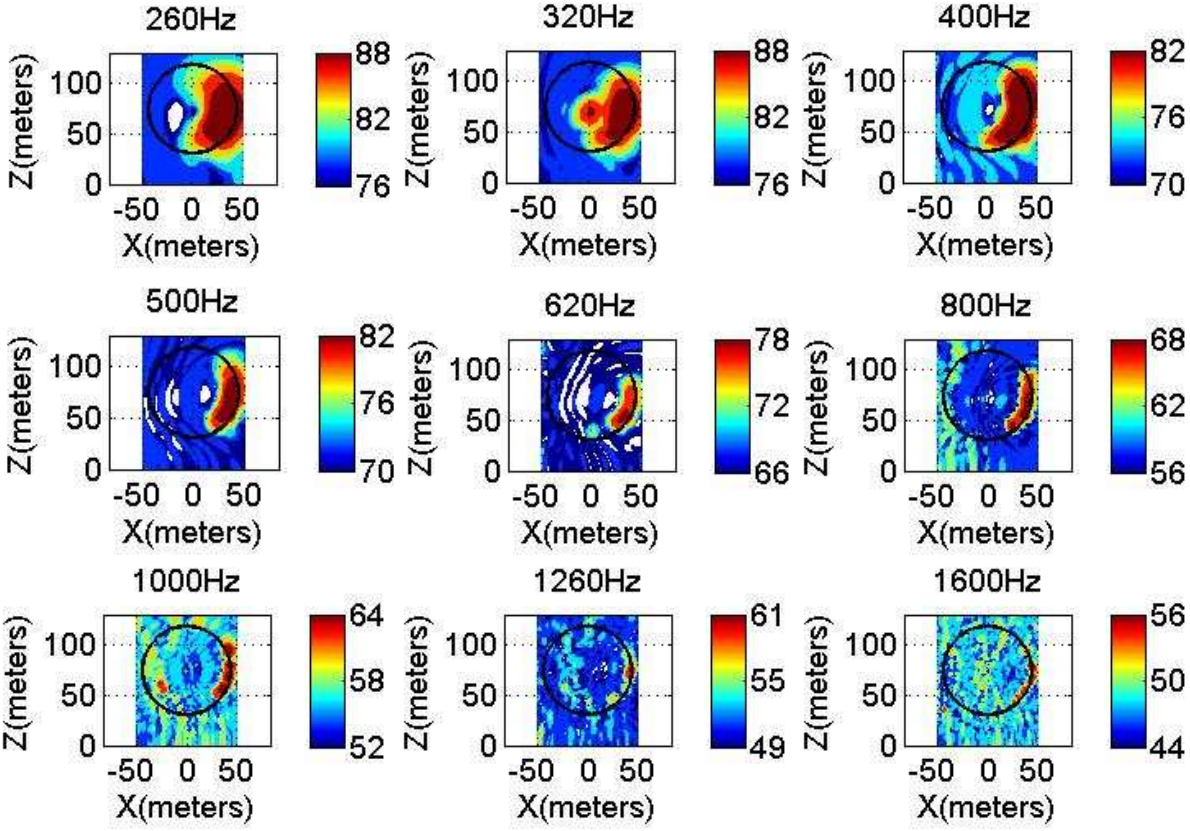

Fig.6 Average SWL distributions on the rotor plane using CLEAN-SC
Rotor speed 17.0 RPM, wind speed 7.0m/s

It is shown that the SWL of uncorrelated noise, side lobe and fake sources caused by coherence loss are decreased or eliminated by using the CLEAN-SC algorithm compared with the results of conventional beamforming –Diagonal Removal. Fig.6 provides much clearer source maps especially for high frequencies.

It is obvious that the dominant noises are produced during the downward movement of the blades, which is consistent with the experiment results of Oerlemans[4]. The dB scale range is set to 12dB for all frequencies in Fig.5 and Fig.6, which indicates that the SWL produced during the downward movement is at least 12dB more than during the upward movement for observers standing at the position of the microphone array. This phenomenon is observed not only for this operation condition but also for all the other measurements.

It is shown that the blade noise sources are not positioned at the very tip of the blades. The SWL peak location of the blade sources moves outwards with an increasing frequency, which is showed in Fig.7(a).The radius of noise peak position increases practically linearly under a frequency around 750Hz and then reaches the tip radius. It is revealed in Fig.7(b) that the SWL of blade source peak decreases with increasing frequency, and higher RPM and wind speed result in higher SWL at all frequencies.

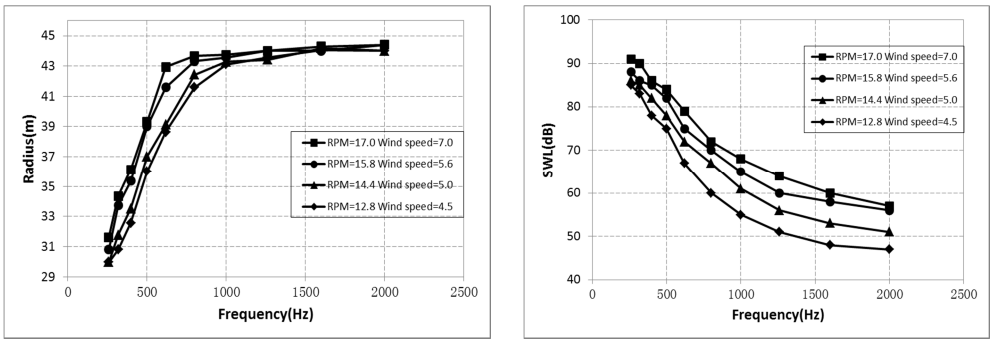

(a) (b)

Fig.7 Variations of the blade source peak radius (a) and SWL (b) with the frequency

The hub noise can be observed at a frequency about 320Hz in Fig.5-6. This phenomenon is confirmed by the frequency spectrums. Fig.8 is a typical spectrum processed within 1s SWL data from a specified working condition with the rotor speed of 13.9RPM and wind speed of 5.3m/s:

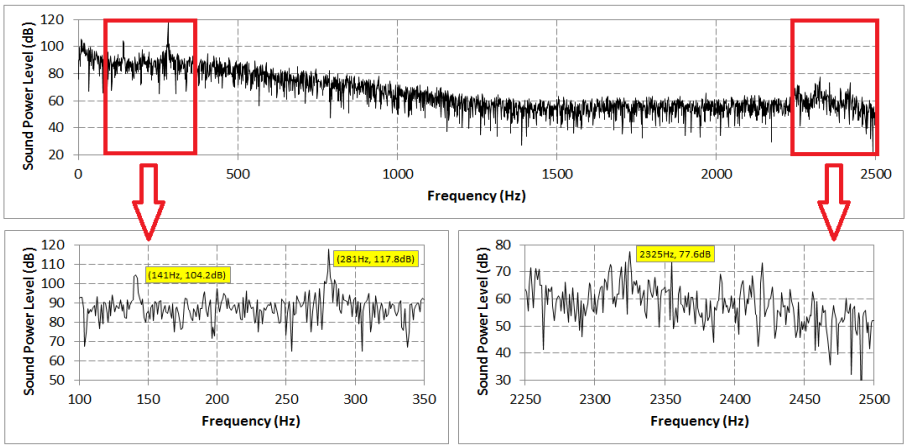

Fig.8 Overall noise spectrum, roter speed 13.9 rpm, wind speed 5.3m/s

It is showed that the tonal noise source is produced at about 280Hz. At the same time, several spectral lines with relatively high amplitude are observed around 2320Hz. The noise source distributions at both frequencies obtained using CLEAN-SC are shown in Fig.9:

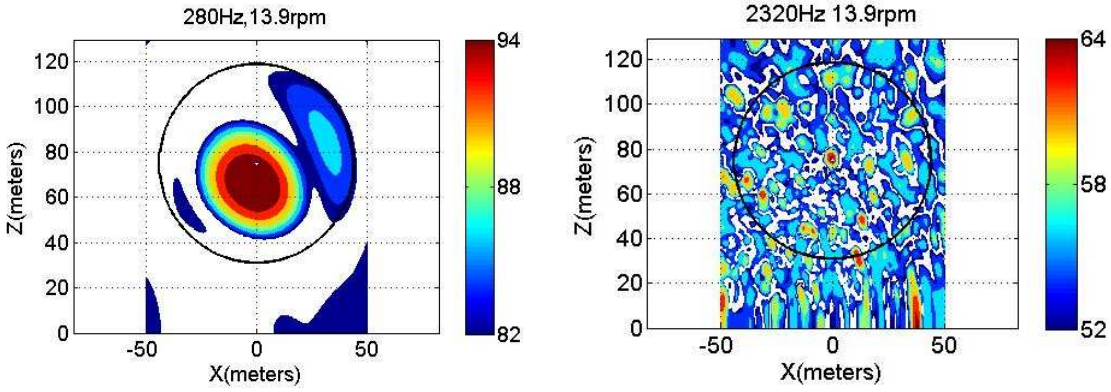

Fig.9: Tonal noise SWL on the rotor plane (rotor speed 13.9 rpm, wind speed 5.3m/s)

The conclusion can be made that the hub noise dominates blade noise at both these frequencies, which is abnormal since the noise from the blades appears to be the dominant sources at most frequencies. Similar results can be achieved when processing variety of turbine working conditions. The results confirm the observation that the frequency of the hub tonal noise at around 300Hz varies in direct proportion to the rotor speed (Fig.10), while the approximately 2320Hz tonal noise remains stable in all the measurements.

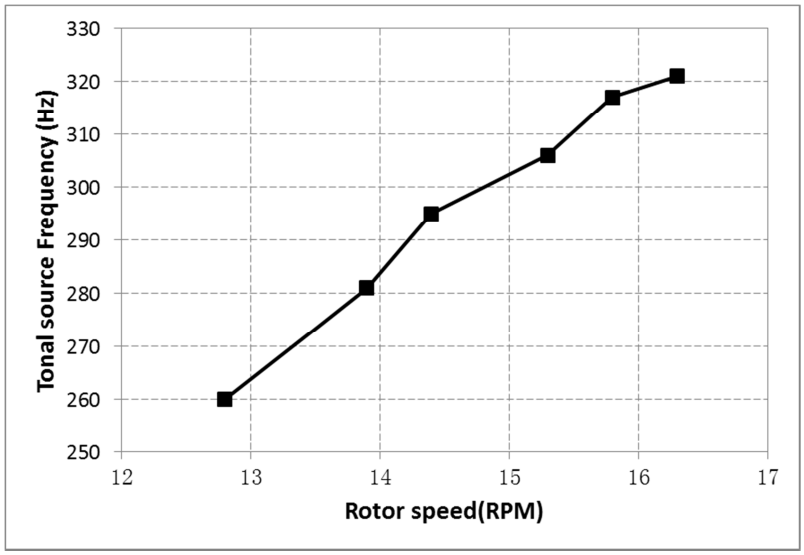

Fig.10: Variations of the hub tonal noise frequency with the rotor speed

Fig.11 shows that the SWL of the hub tonal noise initially increases and decreases quickly afterwards as the rotor speed and the wind speed increase. Moreover, the percentage of hub tonal noise contributions to the total SWL reveals the same tendency as the absolute tonal noise SWL.

It is also revealed in Fig.11 that the blade noise is indeed the dominant noise on the rotor plane. Comparing to the hub tonal noise, blade SWL is approximately linearly increasing with the rotor speed and the wind speed.

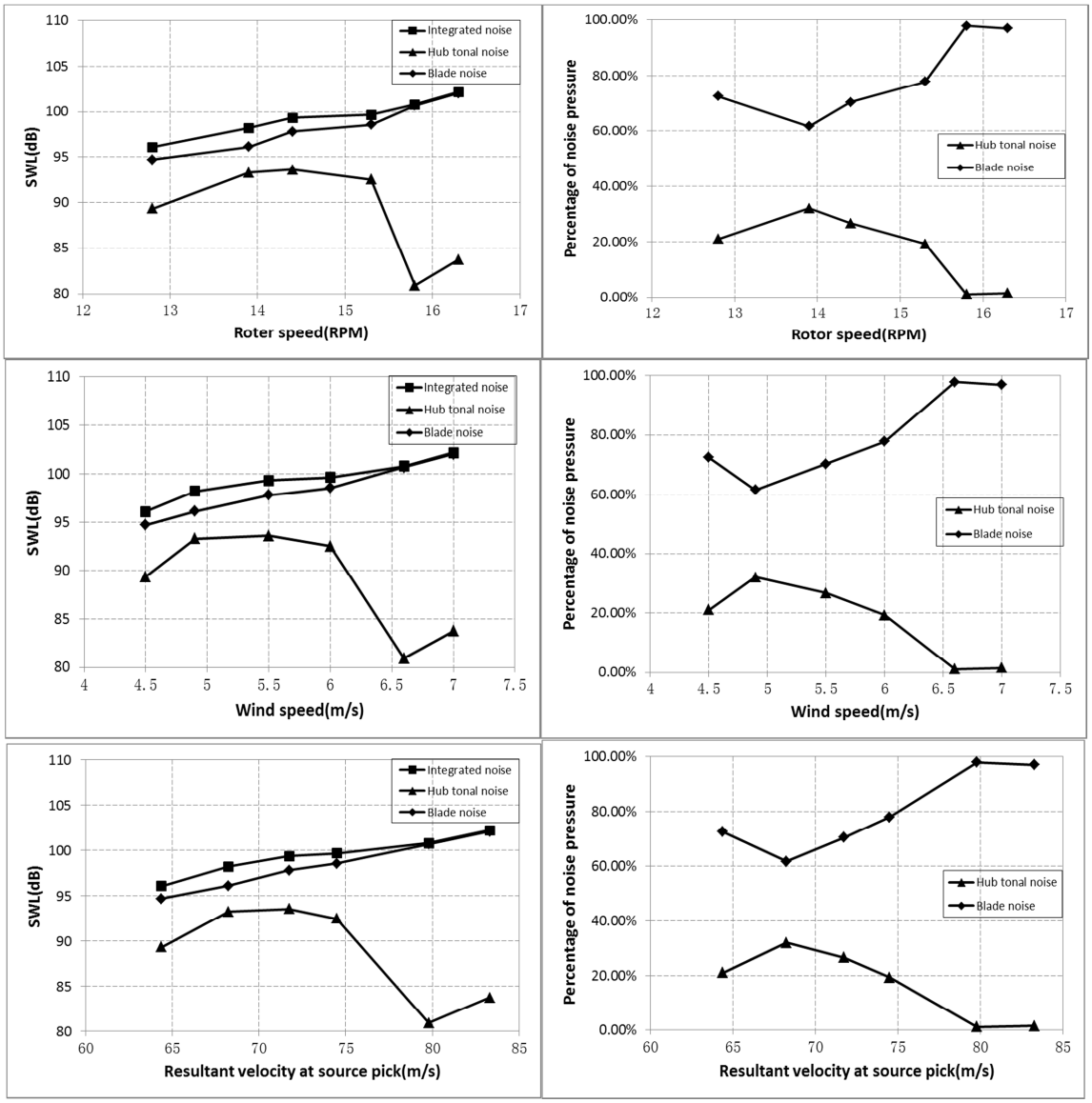

(a) (b)

Fig.11: Variations of the hub tonal noise, blade noise and integrated SWL (a) and the percentage of the hub tonal noise and blade noise (b) with the rotor speed, wind speed and resultant velocity

Furthermore, as we have known that trailing edge noise is commonly regarded as the prominent noise source for large wind turbine blade and the acoustic power of trailing edge noise is approximately proportional to the 5th power of the inflow velocity. So the relationship between the square of blades noise pressure and the 5th power of resultant velocity is shown as Fig.12. The Fig.12 shows the trailing edge noise source is the dominant noise source for the wind turbine blades used in our experiments.

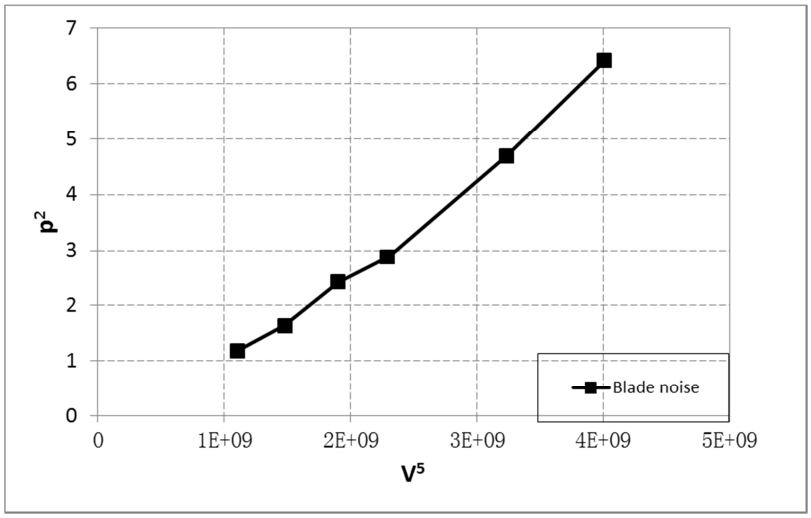

Fig.12: Variations of the square of blade noise with the 5th power of integrated blade speed

4. CONCLUSION

Wind turbine noise measurements were carried out on a three-bladed, 1.5 MW horizontal axis wind turbine. Conventional beamforming and CLEAN-SC were used to analyze the noise sources and the algorithms were validated by a static noise source experiment in an anechoic chamber. A double-ellipse shaped microphone array were positioned about one hub height upwind from the turbine to obtain the sound pressure signals from the wind turbine. The source distributions on rotor plane are shown in frequency domain. It is shown that blade noise emitted during the downward movement is the main source of the wind turbine rotor. The dominant blade noise sources locate near the blade tip and acoustic power level peak moves to the blade tip and decreases with increasing frequency. The trailing edge noise is the dominant noise source verified by the 5th power principle. Two tonal noise sources were located on the hub. The hub tonal noise decreased remarkably with increasing rotor speed and wind speed. On the contrary, the blade noise is approximately linearly increasing with the rotor speed and the wind speed.

ACKNOWLEDGEMENTS

Thank for the fund of National Natural Science Foundation of China (Grand No.51006107)，National High Technology Research and Development Program of China (863 Program) (Grant No. 2012AA051303）, Sino-Denmark Collaboration Project (Grant No. 2010DFA62830）

REFERENCES

[1]S. Oerlemans, Detection of Aeroacoustic Sound Sources on Aircraft and Wind Turbines, Thesis University of Twente, Enschede – With ref. – With summary in Dutch, ISBN 978-90-806343-9-8.

[2]W. M. Humphreys. Jr, T. F. Brooks, “Design and Use of Microphone Directional Arrays for Aeroacoustic Measurements”, 36st Aerospace Sciences Meeting & Exhibit, Reno, NV, Jan. 12-15, 1998.

[3]L. Koop and K. Ehrenfried, “Microphone-array processing for wind-tunnel measurements with strong background noise”, 14th AIAA/CEAS Aeroacoustics Conference (29th AIAA Aeroacoustics Conference), Vancouver, British Columbia Canada, 5 - 7 May 2008.

[4]S. Oerlemans, Acoustic Array Measurements on a Full Scale Wind Turbine, 11th AIAA/CEAS Aeroacoustics Conference (26th AIAA Aeroacoustics Conference), Monterey, California, 23 - 25 May 2005

[5]S. Oerlemans, M. Fisher, “Reduction of Wind Turbine Noise using Optimized Airfoils and Trailing-Edge Serrations”, 14th AIAA/CEAS Aeroacoustics Conference (29th AIAA Aeroacoustics Conference), Vancouver, British Columbia Canada, 5 - 7 May 2008.

[6]R. C. Ramachandran, H. Patel, “localization of wind turbine noise sources using a compact microphone array with advanced beamforming algorithms”, Berlin Beamforming conference, 2012.

[7]R. C. Ramachandran, G. Raman, “Noise Source Localization Using a Compact Phased Array: Studies on a Full Scale Wind Turbine in a Wind Farm”, wind engineering volume 36, NO. 5, 2012, pages 589-604.

[8]P. Sijtsma, “CLEAN based on spatial source coherence”, International journal of aeroacoustic volume 6, NO.4, 2007, pages 357–374.

Study on the Aerodynamic Performance of Swept-Blade Wind Turbine Using Free Wake Lifting Line Model

Q. Wang[a,c], Y. Xu[a,b], J.J. Song[a,c], C.F. Li[a,c], P.F. Ren[a,c], J.Z. Xu[a,b]

[a] *Institute of Engineering Thermophysics, Chinese Academy of Sciences, Beijing, China*
[b] *Key Laboratory of Wind Energy Utilization, Chinese Academy of Sciences, Beijing, China*
[c] *Graduate School of Chinese Academy of Sciences, Beijing, China*

For Horizontal Axis Wind Turbine (HAWT), the aerodynamic performance of the blade will become different when the geometry of the blade is bent backward in the rotor plane, which is usually called backward swept blade. In this paper the aerodynamic performance of backward swept blade rotor will be analyzed by Free Wake Lifting Line Model. In order to make it possible to apply lifting line method for analyzing swept blade, a proper 3D effect modification model is needed to be added in the computation. Firstly, a new 3D stall delay model is established, named Inviscid Stall Delay Model (ISDM), which is derived from the simplified Navier-Stocks (N-S) equations. In the model we treat the stall delay effects differently by the delay of the separation point on the airfoil, and aim to capture the further negative pressure reduction in the separation area due to the span wise flow. Secondly, a Free Wake Lifting Line Model is created and it is validated by the experimental results of NREL Phase VI wind turbine blade. Thirdly, based on the blade of the NREL Phase VI, two backward swept blades are constructed by different manners and their aerodynamic performance is explored by the lifting line code. From the results it can be concluded that due to the increased effective radius, the power captured by the backward swept blade is higher than that of the straight blade at lower wind speed condition. However, the performance of the backward swept blade is influenced by the local swept angle and the projected inflow speed.

Horizontal Axis Wind Turbine (HAWT), Back Swept Blade, Free Wake Lifting Line Model, Inviscid Stall Delay Model (ISDM), NREL Phase VI Wind Turbine

1. Introduction

With the development of the wind turbine technology, the advanced geometry of Horizontal Axis Wind Turbine (HAWT) blade is getting more and more attention. Among the different configurations, the backward swept blade rotor is considered to be able to decrease the aerodynamic loads and loads fluctuation acting on the blade, which is good for reducing the structural problems. Fig. 1 is the schematic diagram of backward swept blade and forward swept blade.

In the past few years, the aerodynamic performance of the backward swept blade is widely studied. However, there are different opinions about the aerodynamic performance of the backward swept blade.

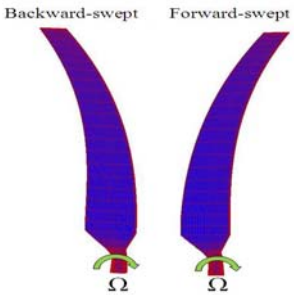

Fig. 1 The schematic diagram of backward swept blade and forward swept blade.

Some authors concluded that the backward swept blade can increase the output power and lower the loads. S. Larwood analyzed the dynamic behavior of the swept blade by the modified FAST code and the results showed a 5% annual energy production increase and a decrease in the flap-bending fatigue load over the straight blade [1]. R.S. Amano studied the backward swept blade rotor

* Corresponding author.
Email address: xuyu@etp.cn (Y. Xu).

by CFD method and found out that the span wise flow due to the swept edge geometry delays the stall point, which results in the power increase at higher wind speeds [2].

In contrast, there are some scholars who held different opinions. By using a hybrid Navier-Stocks/vortex panel solver, K. Suzuki et al studied the aerodynamic performance of the wind turbine blade influenced by different swept parameters. The results showed that the 10% backward sweep does not change the power and the bending momentum significantly [3]. T. Maggio et al analyzed the swept blade based on an aeroelastic model, which is a combination of a free wake lifting line code and a simplified structure model. He concluded that the backward sweep decreased the power and the thrust of the rotor [4]. Besides, Verelst et al [5] made an analysis of the different swept blade configurations by HAWC2 simulator. The results also showed a decrease in the energy production for the backward swept blade.

For engineering analysis of the swept blade, the lifting line and BEM methods are usually applied, which are 2D simulating tools. Due to the special 3D geometry characteristic of the backward swept blade, a proper 3D effect modification model is needed to be added in the computation of these models.

During the past decades, different 3D stall delay models have been developed. Snel et al. analyzed the 3D boundary layer on wind turbine blade by dimensional analysis and set up a stall delay model which has quadratic relationship with the local ratio between the chord length and the span wise position [6]. Based on his work, Chaviaropoulos and Hansen used a quasi-3D Navier-Stocks (N-S) solver to analyze the rotational effects of wind turbine blade and added the influence of the local twist angle to their stall delay model [7]. Snel' work was also developed by Du and Selig by assuming the velocity profile in the boundary layer to be Pohlhausen type [8]. Du's model is more comprehensive which contains the blade tip speed ratio etc. parameters. Corrigan and Shillings thought that the stall delay effects can be modeled by the delay of the stall angle of attack (AOA) of the airfoil and an additional portion of lift coefficient should be added to the 2D lift coefficient through the slope of the inviscid lift-incidence curve [9].

Different from the stall delay studies mentioned above, Lindenburg had made a deep analysis of the stall delay phenomenon based on the 'Centrifugal Pump' concept [10]. He proposed to add the ratio between the rotational speed at blade tip and the local relative speed to the model of Snel. Based on his analysis, Corten further developed the 'Centrifugal Pump' model and made a dimensional analysis of the N-S equations instead of boundary layer equations [11]. Based on the experimental study, Corten simplified the N-S equations and established the Inviscid Stall Model.

In this paper the Inviscid Stall Model will be further analyzed and its result will be involved in the computation of the lifting line code. The following content is mainly divided into four parts. In the first part, the Inviscid Stall Delay Model (ISDM) is derived step by step. After that, the free wake lifting line model will be developed and the validation is carried out based on the NREL Phase VI experimental results. In the third part, two different backward swept blades are constructed by different manners, and their aerodynamic performance will be computed by the lifting line model. At last, the conclusion will be given.

2. The Derivation of Inviscid Stall Delay Model

2.1 The Inviscid Stall Model

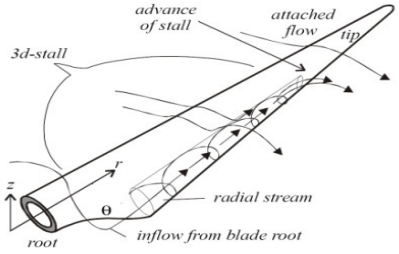

Fig. 2 The schematic diagram of Inviscid Stall Model [11].

As shown in Fig. 2, the Inviscid Stall Model proposed by Corten is aim to capture the mechanism of the stall delay effect influenced by the span wise flow in the separation area. Under the cylinder coordinate, the equations of the Inviscid Stall Model, which is derived from the N-S equations, are listed below.

$$\begin{aligned} &\frac{\partial V_\theta}{r\partial\theta}+\frac{\partial V_z}{\partial z}+\frac{\partial V_r}{\partial r}+\frac{V_r}{r}=0 \\ &\frac{\partial p}{\rho r\partial\theta}=2V_r\Omega \\ &V_r\frac{\partial V_r}{\partial r}=r\Omega^2-\frac{\partial p}{\rho\partial r} \\ &V_r\frac{\partial V_z}{\partial r}=0 \end{aligned} \tag{1}$$

2.2 The Analytical Solution and the Inviscid Stall Delay Modification Model

Assume the dimensionless span wise velocity has the following expression.

$$V_r^*=h(r^*)g(\theta);\ h=q(r^*)r^* \tag{2}$$

$$V_r^*=\frac{V_r}{U_\infty},\ r^*=\frac{r}{R} \tag{3}$$

where U_∞ is the inflow speed and R is the radius of the blade.

By separating the variables, the analytical solution of the Inviscid Stall Model can be derived in the following form,

$$V_r^* = \lambda(-1 \pm \sqrt{1+\frac{1}{\lambda}\frac{C_3}{r^{*2}}})r^*(\theta+\frac{C_2}{C_1}) \quad (4)$$

$$p^* = A(\lambda, r^*)[\frac{1}{2}(\theta-\theta_t)^2 + D_1(\theta-\theta_t) + D_2] \quad (5)$$

$$A(\lambda, r^*) = 4\lambda^2 r^{*2}(\sqrt{1+\frac{D_3}{\lambda r^{*2}}} - 1) \quad (6)$$

where C and D are constants, λ is the tip speed ratio (TSR), r^* and θ are the span wise and chord wise cylinder coordinates respectively.

Based on the analytical solution, 3D effects influenced by the span wise flow can be further analyzed. However, there is another problem needed to be solved that the span wise flow is the result of the overall 3D flow field while the local aerodynamic coefficient used in the lifting line model is just determined by the local 2D flow condition. So firstly, the following hypothesizes are needed to be introduced.

(a) Assume for 2D separation condition, the pressure distribution in the separation area is a constant, which is consistent with the analysis of Corten [11].

$$p_{2d}^* = D_4 \quad (7)$$

In this paper, the constant is approximately taken as -0.5.

(b) In Eq. (5), the pressure coefficient is nondimension alized by the inflow speed U_∞. At any span position, the local 2D flow condition is determined by the relative inflow velocity. As a result, U_∞ has to be replaced by the local relative inflow speed U_{rel}. So assume the 3D dimensionless pressure coefficient is

$$p_{3d}^* = p^* \frac{U_\infty^2}{U_\infty^2 + (\Omega r)^2} = p^* \frac{1}{1+\lambda^2 r^{*2}} \quad (8)$$

(c) Assume the pressure difference induced by the span wise flow in the separation area mainly affects the normal force of the local airfoil, which is defined by the normal direction of the chord. This is similar to the analysis of Lindenburg [10].

$$\Delta C_n \propto \left| \int_{\theta_t}^{\theta_s} \frac{1}{2}\rho U_{rel}^2 (p_{3d}^* - p_{2d}^*) r d\theta \right| \quad (9)$$

θ_s and θ_t are the cylinder coordinates of the separating position and trailing edge location respectively.

(d) The local AOA may have impact on the magnitude of the span wise flow (see Eq. (4)). From previous study, we found out that at primary stage of separation, the magnitude of the span wise flow is not as much as that in the condition when the flow completely separates from the surface. So we assume the pressure coefficient (Eq. (5)) has quadratic relationship with the AOA increase in the process of flow separation. This effect can be represented by the modification factor $g(\alpha)$ which will be discussed later.

According to these hypothesizes, the Inviscid Stall Delay modification can be created. Based on Eq. (5)-Eq. (9), the normal force coefficient can be written as

$$\Delta C_n \propto \left| \frac{r}{c}\{\frac{g(\alpha)}{1+\lambda^2 r^{*2}} A[\frac{1}{6}(\theta_s-\theta_t)^3 + \frac{D_1}{2}(\theta_s-\theta_t)^2 + D_2(\theta_s-\theta_t)] - D_4(\theta_s-\theta_t)\} \right| \quad (10)$$

In order to make a quantitative analysis, the area of the trailing edge separation (θ_s) is needed to be estimated.

Generally speaking, in the wind turbine flow field the trailing edge separation on the blade is a complex 3D unsteady problem, which is usually in association with the geometry of local airfoil, the TSR and the Reynolds number etc. In order to obtain the explicit formula of the trailing edge separation, the Kirchhoff-Helmholz model is used in this paper, which is based on the potential flow theory and is commonly used in the dynamic stall computation [12]. In the Kirchhoff-Helmholz model, the relationship between the trailing edge separation factor f and the normal force coefficient is

$$C_n = \frac{\partial C_{n,0}}{\partial \alpha}(\alpha - \alpha_0)(\frac{1+\sqrt{1-f}}{2})^2 \quad (11)$$

where α is the AOA, $\partial C_{n,0}/\partial\alpha$ is the slope of the $C_n - \alpha$ curve in the linear stage, α_0 is the AOA corresponding to the zero normal force coefficient and the trailing edge separation factor f is defined as

$$f = \frac{x_s - x_t}{c} \quad (12)$$

x_s and x_t are the positions the flow separating point and the trailing edge, and c is the chord length.

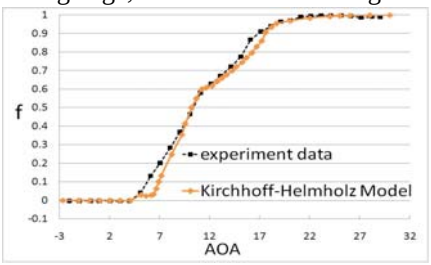

Fig. 3 The comparison between the results of Eq. (13) and the experiment.

Through the normal force coefficient, the trailing edge separation factor f can be computed by the following Equation.

$$f = 1 - (2\sqrt{\frac{C_n}{(\alpha-\alpha_0)\frac{\partial C_{n,0}}{\partial\alpha}}} - 1)^2 \quad (13)$$

To validate the result of Eq. (13), the trailing edge separation factor f of S809 airfoil is computed based on the lift and drag coefficients proposed in [10], and the result is compared with the experimental data [13] as shown in Fig. 3.

From the result of the separation factor, the modification factor $g(\alpha)$ can also be fixed. In the flow separation process, assume the flow separation begins at α_0 AOA and when the flow completely separates from the surface, the corresponding AOA is α_1. Then $g(\alpha)$

can be written as

$$g(\alpha)=\frac{(\alpha-\alpha_0)^2}{(\alpha_1-\alpha_0)^2},\ \alpha\in(\alpha_0,\alpha_1) \tag{14}$$

From Fig. 3 it can be seen that for S809 airfoil, α_0 and α_1 can be approximately taken as 5^o and 23^o.

According to the relationship between the normal force coefficient and the lift and drag coefficients,

$$\Delta C_l=\Delta C_n\cos(\alpha) \tag{15}$$

$$\Delta C_d=\Delta C_n\sin(\alpha) \tag{16}$$

and based on Eq. (4)-Eq. (16), the Invisid Stall Delay Model (ISDM) can be created and the lift and drag coefficients can be corrected as following,

$$C_{l3d}=C_{l2d}+H_1S\cos(\alpha) \tag{17}$$

$$C_{d3d}=C_{d2d}+H_2S\sin(\alpha) \tag{18}$$

$$S=\frac{r}{c}[\frac{g(\alpha)}{1+\lambda^2r^{*2}}A(\lambda,r^*)(\frac{1}{6}t^3+\frac{D_1}{2}t^2+D_2t)+\mathrm{D}_4t] \tag{19}$$

$$A(\lambda,r^*)=4\lambda^2r^{*2}(\sqrt{1+\frac{D_3}{\lambda r^{*2}}}-1) \tag{20}$$

$$t=\frac{fc}{r};\ r^*=\frac{r}{R};\ \lambda=\frac{\Omega R}{U_\infty} \tag{21}$$

where D_1, D_2, D_3, D_4 and H_1, H_2 are empirical parameters and *S* is named as the ISDM correction factor. In this paper these parameters are taken as $D_1=2$, $D_2=1$, $D_3=1.0$, $D_4=-0.5$, $H_1=0.5$ and $H_2=0.5$. The relationship between *S* and its dependent parameters under a typical condition of NREL Phase VI wind turbine is shown in Fig. 4.

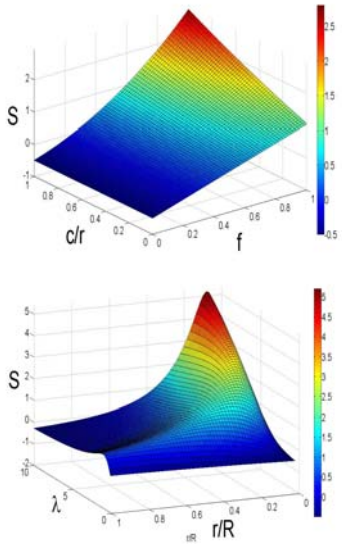

Fig. 4 The relationship between the correction factor S and its dependent variables

The Fig. 4 clearly shows the relationship between *S* and the chordlenth c, separation factor *f*, r^* and the TSR λ. *S* is significantly increased by the reduce of r^* and the increase of the λ.

2.3 Validation Case: NREL Phase VI Wind Turbine

In order to validate the ISDM, the model is applied to the blade of NREL phase VI wind turbine. For S809 airfoil, two commonly used experimental data are from the experiments of Ohio State University (OSU) wind tunnel and the Delft University of Technology (DUT) Low Speed Laboratory low-turbulence wind tunnel [14]. Lindenburg had made an analysis of the differences between these two experimental results and he proposed the lift coefficient of OSU should 'shift' of -0.53 degree, and the lift coefficient in the stall area should also be modified [10]. Fig. 5 shows the lift coefficients of OSU, DUT and data modified by Lindenburg. We can see that the lift coefficient seems to be averaged by the modification when the AOA is between 19 and 23 degrees. In this paper, the data of Lindenburg will be used.

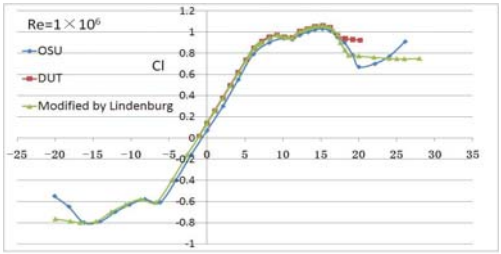

Fig. 5 The comparison of the lift coefficients from OSU, DUT experiments and that modified by Lindenburg.

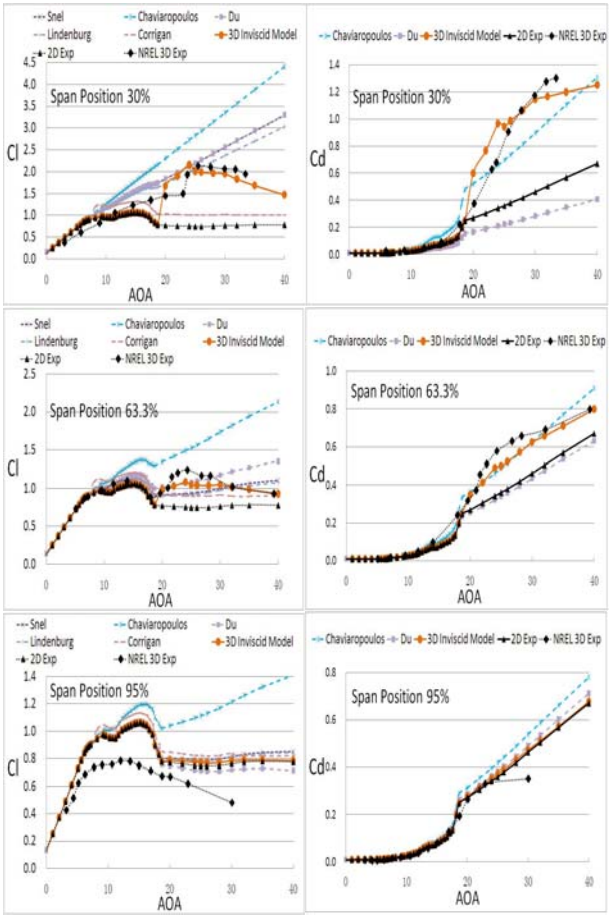

Fig. 6. The modified lift and drag coefficients comparison of NREL Phase VI rotor blade.

Fig. 6 shows the lift and drag coefficients modified by the ISDM and the comparison with the results of experiment and some other 3D stall delay correction models. From the figure, it can be seen that the 3D experimental data is significantly different with that of the 2D condition especially near the root of the blade. The 3D rotational effects improve both of the lift and drag coefficients in most of the span positions. At 30% span position, the ISDM is the only one that can predict the decrease trend of the lift coefficient. The sudden increase of the lift coefficient near 20° AOA is due to the effect of $g(\alpha)$. At 63.3% span position, the lift and the drag coefficients modified by ISDM are similar to the results of Du model. At 95% span position, all of the models failed to predict the low lift coefficients. Generally speaking, the ISDM has good predictions of the 3D stall delay effects of the airfoil coefficients, but the differences between the results of experiment and ISDM illustrates that the $g(\alpha)$ expression is needed to be further carefully studied.

3. The Free Wake Lifting Line Model

3.1 The Main Computational Process of Free Wake Lifting Line Model

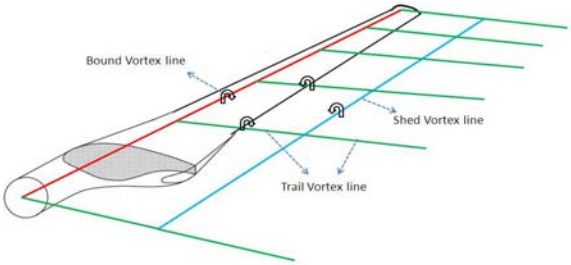

Fig. 7 The vortexes distribution in the Free Wake Lifting Line Model.

As shown in Fig. 7, the strength of the bound, trailing and shedding vortexes are the most important three quantities in the computation of the Free Wake Lifting Line Model which determine the accuracy of the final results. When all these three vortex strengths and the positions of the wake nodes are solved in the previous time step t_{j-1}, the velocity induced by all the wake vortex can be computed by Biot-Sarvart Law, shown in the following equation,

$$\vec{u} = \frac{\Gamma}{4\pi} \frac{(|\vec{r}_1| + |\vec{r}_2|)(\vec{r}_1 \times \vec{r}_2)}{|\vec{r}_1||\vec{r}_2|(|\vec{r}_1||\vec{r}_2| + \vec{r}_1 \square \vec{r}_2)} \qquad (22)$$

where $\vec{r}_1$ and $\vec{r}_2$ are the position vectors pointing from the endpoints of the straight vortex to the evaluation point and Γ is the vortex strength. After that, at any control point on the bound vortex line, the total relative incoming velocity and the corresponding AOA can be determined by adding the induced velocity, the free incoming velocity and the relative rotational velocity. Then based on the lift coefficients modified by ISDM, the strength of the new bound vortex can be iteratively computed by the Kutta-Joukowski Law, as shown in Eq. (23).

$$\Gamma_{bound}\big|_{ri,tj} = \frac{1}{2} U_{rel}\big|_{ri,tj} C_L(\alpha|_{ri,tj})\, c\big|_{ri,tj} \qquad (23)$$

Finally, the strength of the newly generated trail and shed vortexes are obtained by the differential of the bound vortex as shown in Eq. (24) and Eq. (25), and after that the time index moves to the next step. The detailed computational process is listed in Fig. 8.

$$\Gamma_{first\,shed}\big|_{ri,tj} = (\Gamma_{bound}\big|_{ri,tj} - \Gamma_{bound}\big|_{ri,tj-1}) / (t_j - t_{j-1}) \quad (24)$$

$$\Gamma_{first\,trail}\big|_{ri,tj} = (\Gamma_{bound}\big|_{ri,tj} - \Gamma_{bound}\big|_{ri-1,tj}) / (r_i - r_{i-1}) \quad (25)$$

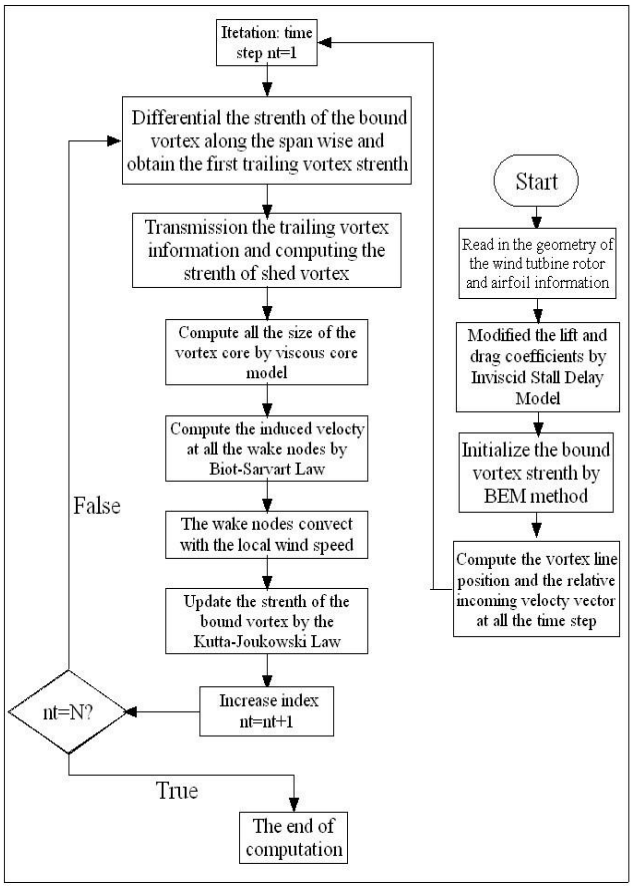

Fig. 8. The flow chart of the Free Wake Lifting Line Model computation.

3.2 The Viscous Vortex Core Model

The induced velocity computed by the Biot-Sarvart Law is singular when the evaluation point is just located on the vortex line. So in order to remove the singularity and involve the viscous effects, the Biot-Savart Law is needed to be modified by a viscous model. In this paper, the Leishman model is used, which is firstly proposed by Leishman in analyzing of the helicopter wake [15], as shown in the following,

$$K_v = \frac{\bar{r}^{-2}}{(1+\bar{r}^{-2n})^{\frac{1}{n}}} \tag{26}$$

$$\bar{r} = \frac{r}{r_e} \tag{27}$$

where r_e is the effective diameter of the vortex line and n is the empirical coefficient. As a result, the Biot-Sarvart formula changes into

$$\vec{u} = \frac{\Gamma}{4\pi} K_v \frac{(|\vec{r}_1| + |\vec{r}_2|)(\vec{r}_1 \times \vec{r}_2)}{|\vec{r}_1||\vec{r}_2|(|\vec{r}_1||\vec{r}_2| + \vec{r}_1 \cdot \vec{r}_2)} \tag{28}$$

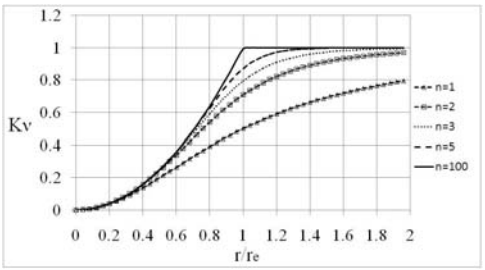

Fig. 9 The dependency of the viscous modification factor on the empirical factor *n*.

Fig. 9 shows the relationship between K_v and the empirical coefficient *n*. It has been demonstrated that when n=2 the model is similar to the Lamb-Oseen vortex model [15]. In the following computation n=2 is taken.

In Eq. (27) The effective diameter of the vortex line r_e can be used to simulate the growth of the vortex core due to the viscous effect. In this paper, the Ramasamy and Leishman vortex core model is utilized [16, 17].

$$r_e = r_c\left(\frac{l+\Delta l}{l}\right) \tag{29}$$

$$r_c = \sqrt{r_0 + 4a\nu(1 + a_1 \operatorname{Re}\nu)t} \tag{30}$$

l is length of the vortex line, a and a_1 are model parameters, they are taken as 1.25643 and 6.5×10^{-5} respectively.

3.3 The Validation of the Free Wake Lifting Line Model

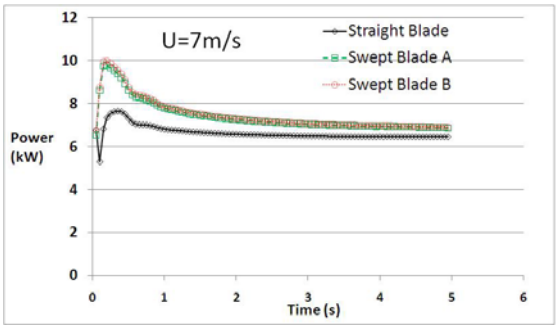

Fig. 10 The computational history at 7m/s wind speed condition.

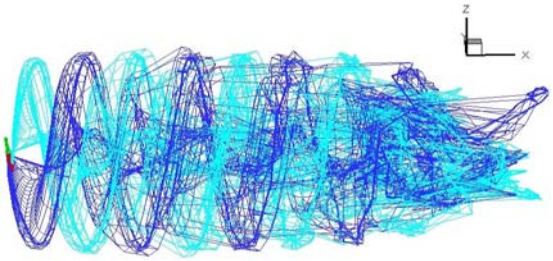

Fig. 11 The shape of the free wake at 7m/s wind speed condition.

Based on the established Inviscid Stall Delay Model and Free Wake Lifting Line Model, the output power and the thrust of NREL Phase VI wind turbine rotor are computed. Fig.10 shows the computational time history of the output power at 7m/s wind speed and Fig.11 shows the corresponding shape of the free wake after 4 revolutions. We can see that the helical wake vortex becomes more and more disorganized with the downstream development. So the viscous vortex core model is very necessary in the free wake lifting line computation.

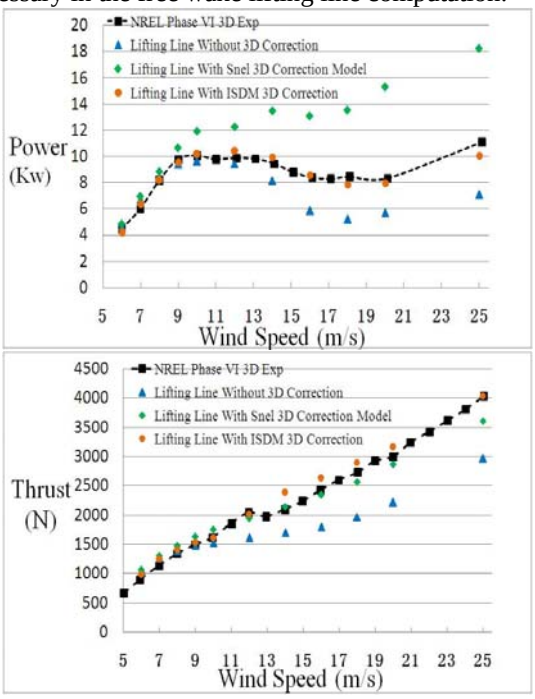

Fig. 12 The comparison of the power and thrust force between the NREL Phase VI experimental data and the results computed by Free Wake Lifting Model based on different 3D correction models.

The obtained results of the power and thrust force of the NREL Phase VI rotor are compared with the experimental data, as shown in Fig. 12. It is needed to be mentioned that the 3D correction model of Snel is used for comparison. It can be seen that by adding the ISDM, the results computed by the Free Wake Lifting Line Model show excellent agreement with the experimental data. In contrast, the results computed by the data of 2D and Snel are either underestimated or overestimated the power of the rotor, when the wind speed is greater than 13m/s. The results demonstrate that the Free Wake Lifting Line Model coupled with ISDM is capable of analyzing the aerodynamic performance of wind turbine rotor. In the following section, the backward swept blade rotor will

be analyzed.

4. The Performance Analysis of the Backward Swept Blade Rotor

4.1 The construction of different backward swept blades

Based on the blade of the NREL Phase VI wind turbine, the swept curve of the backward swept blade is created by the following exponential method, as proposed by reference [5],

$$x = a(\frac{z - z_0}{z_e - z_0})^b \tag{31}$$

where x is the sweeping distance compared with the straight blade, z is the span wise location, z_0 is the start point of the sweep, a and b are the geometry parameters. Assume the blade starts to sweep at the hub, the values of z_0 and z_e are taken as 0.508m and 5.029m respectively. Besides, the swept geometry parameters are selected as $a = 1, b = 3$. The comparison of the geometry curves between the swept and straight blades is plotted in Fig. 13, from which we can see that the effective radius (from the original point to the local span position) of the swept blade is obviously longer than that of the straight blade.

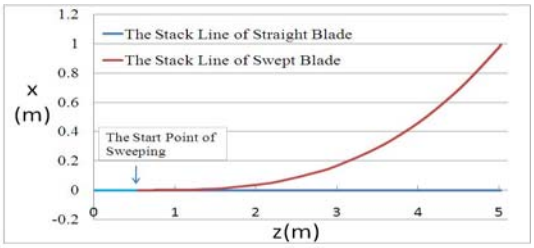

Fig. 13 The geometry curve comparison between the swept and the straight blades.

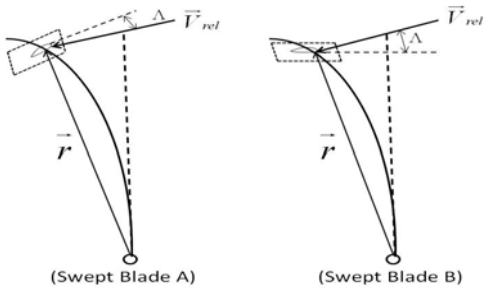

Fig. 14 Two different construction manners of swept blade: (A) the local airfoil plane is perpendicular to the swept curve; (B) the local airfoil plane is perpendicular to the original straight blade span wise.

Then considering the different construction methods may affect the aerodynamic performance of the swept blade, two different construction manners are used in this paper, as shown in Fig. 14, where Λ is the angle between the relative inflow vector and the plane in which the airfoil located, so that it is named as local swept angle. For swept blade A, the local airfoil plane is perpendicular to the swept curve, while the swept blade B is created by shear translating the airfoils in the plane of the original straight blade.

4.2 The output power and thrust force comparison of the backward swept blades

The aerodynamic performance of the swept blades is computed by the Free Wake Lifting Line Model and the results are compared with experimental data and that of the straight blade, as plotted in Fig. 15. It can be seen that the power of the backward swept blade rotor is higher than that of the straight blade when the wind speed is below 12m/s. This is mainly because of the increased effective radius. However, with the wind speed increasing, the power of the swept blade shows a decrease and becomes lower than that of the straight blade. Besides, we can see that the swept blade A captures more wind energy than B when the wind speed is between 12m/s to 17m/s. For the thrust aspect, both of the swept blades and the straight blade show a similar trend.

Besides, it should be noticed that there are differences between the results of the swept blade A and B. It means the construction manner of the swept blade has impact on its aerodynamic performance. In the future work, the created swept blade should be optimized, which has more practical meaning.

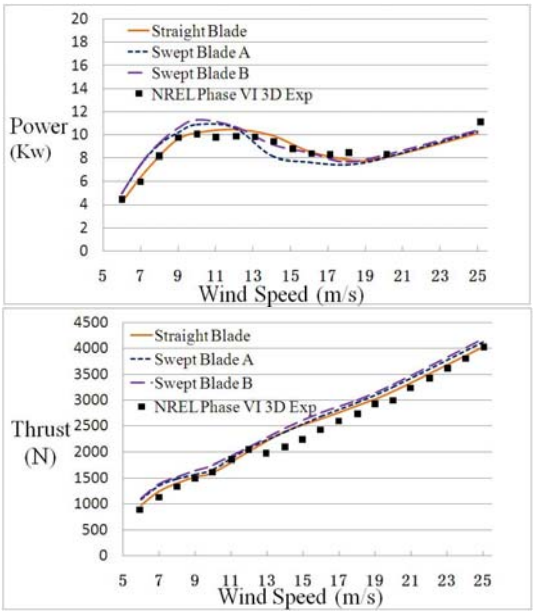

Fig. 15 The comparison of the power and thrust among the Swept Blades constructed by method A and B, the straight blade and the experimental data.

Fig. 16 shows the near wake vortex development of the different rotors after one revolution. It can be seen that for all these conditions the strength of the wake vortex are mainly concentrated at the tip and hub positions, forming the hub and tip vortexes respectively. Compared with the tip vortex, the hub vortex is more disorganized. Besides, we can see that the different span wise position of the backward swept and the straight blades result in different span wise shapes of the shedding vortex. Con-

sidering the induced velocity of these wake vortex, it may affect the subsequent development of the wake vortex system.

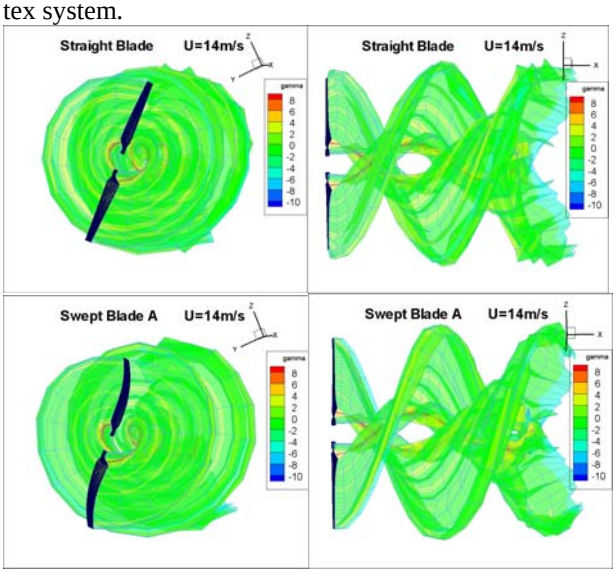

Fig. 16 The comparison of the power and thrust between the NREL Phase VI experimental data and the results computed by Free Wake Lifting Model based on different 3D correction model.

4.3 The influence of the local swept angle and the projected wind speed

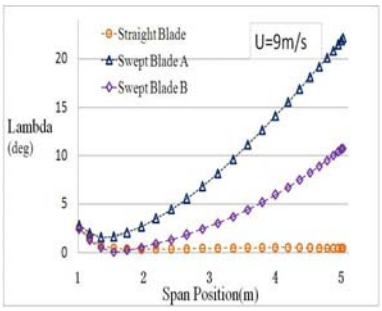

Fig. 17 The distribution of the local swept angle of the straight and swept blades constructed by method A and B, at 9m/s condition.

In the lifting line computation, the local swept angle determines the projected wind speed in the plane where the local airfoil located. This is another important factor that influences the power and trust force of the rotor.

Fig. 17 shows the span wise distribution of the local swept angle Λ of the swept and straight blades at 9 m/s wind speed condition. In the figure we can clearly see that Λ of the straight blade are nearly zero, but those of the swept blades are growing rapidly with the span wise position moving to the tip of the blade. It can be also seen that sweeping construction method A brings in larger Λ values than B.

Fig. 18 shows the comparison between the relative inflow speed and the corresponding projected speed. As we know, the longer a blade radius is the larger magnitude of the relative inflow speed it will bring in. From Fig. 18 we can see that although the relative inflow speed of the swept blade is larger than that of the straight blade, the condition of the projected speed is opposite. This is because of the projection effects of the local swept angle.

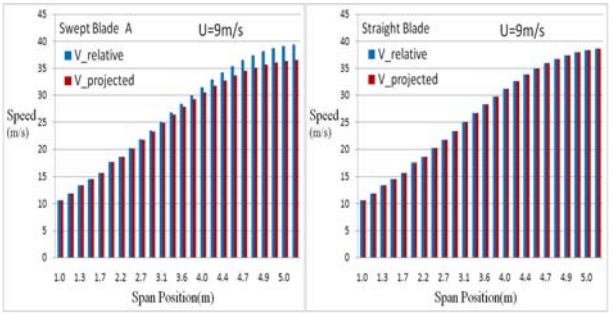

Fig. 18 The comparison of the relative and projected wind velocities for straight and swept blades at 10m/s condition.

Based on the analysis, it can be concluded that the increased effective radius of the backward swept blade is the main reason that lead to the increase of the output power at lower wind speed and the existence of local swept angel.

4.4 The comparison of the AOA and the bound vortex strength

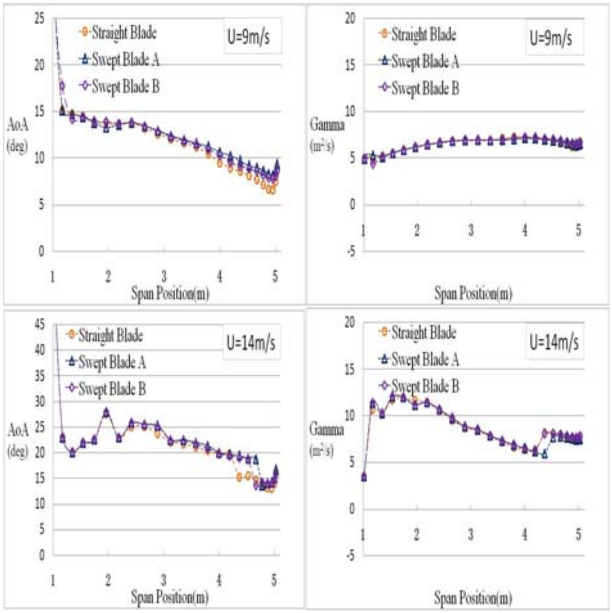

Fig. 19 The comparison of the AOA and the strength of the bound vortex distribution of the straight and the swept blades constructed by method A and B.

The distribution of the AOA and the strength of the bound vortex along the span are shown in Fig. 19. The difference of the AOA and the bound vortex strength between the swept and straight blades is not obvious except in the outboard region. At 9m/s wind speed, the AOA of the swept blade is about 8^o-10^o near the blade tip, which is larger than that of the straight blade. This is another reason that causes the higher output power of the swept blade at 9m/s wind speed. At 14m/s wind condition, the AOA of the swept blade is about 20^o, while that of the straight blade is about 15^o. From the lift and drag coefficients (Fig. 6), we can see that the corresponding lift coefficient of the swept blade is much lower than the straight blade. This is consistent with the output power result (Fig. 15).

5 Conclusion

In this paper, the aerodynamic performance of the swept-blade wind rotor is analyzed. In order to modify the wind turbine 3D effects resulted from the span wise flow, a new 3D stall delay model, ISDM is created, which is derived from a simplified N-S equations. The ISDM can capture the further negative pressure reduction in the separation area due to the span wise flow. The comparison between the results of the model and experimental data demonstrates the accuracy of the ISDM.

After that, based on the 3D correction model, a Free Wake Lifting Line Model is developed, which is validated by the NREL Phase VI experimental results.

Based on the lifting line model, the aerodynamic performance of the swept-blade wind turbine rotor is analyzed and it can be concluded that (i) the aerodynamic performance of the swept blade is closely related with the swept blade construction manner; (ii) the swept-blade rotor gains more wind energy at low wind speed condition, this is mainly because of the increased blade radius; (iii) although the sweep increases the radius of the blade, the local swept angles decrease the magnitude of the effective wind speed and limit the output power. In the future work, the 3D CFD computation about the backward swept blade will be carried out to further analyze the detailed 3D flow field.

Acknowledgments

This work was supported by the National Nature Sciences Foundation of China (Grant No. 50876105), the Sino-Denmark Collaboration Project (Grant No. 2010DFA62830), and the National High Technology Research and Development Program of China (863 Program) (Grant No. 2012AA051303)).

6 References

[1] S.M. Larwood, Dynamic analysis tool development for advanced geometry wind turbine blades, in, University of California, 2009.

[2] R. Amano, R. Malloy, CFD analysis on aerodynamic design optimization of wind turbine rotor blades, World Academy of Science, Engineering and Technology, 60 (2009) 71-75.

[3] K. Suzuki, S. Schmitz, J.-J. Chattot, Analysis of a Swept Wind Turbine Blade Using a Hybrid Navier–Stokes/Vortex-Panel Model, in: Computational Fluid Dynamics 2010, Springer, 2011, pp. 213-218.

[4] T. Maggio, F. Grasso, D. Coiro, Numerical Study on Performance of Innovative Wind Turbine Blade for Load Reduction, EWEA, EWEC2011, Bruxelles, (2011) 14-17.

[5] D.R. Verelst, T.J. Larsen, Load consequences when sweeping blades-A case study of a 5 MW pitch controlled wind turbine, in, Danmarks Tekniske Universitet, Risø Nationallaboratoriet for Bæredygtig Energi, 2010.

[6] H. Snel, R. Houwink, J. Bosschers, E.C. Nederland, Sectional prediction of lift coefficients on rotating wind turbine blades in stall, Netherlands Energy Research Foundation, 1994.

[7] P. Chaviaropoulos, M.O.L. Hansen, Investigating three-dimensional and rotational effects on wind turbine blades by means of a quasi-3D Navier-Stokes solver, Journal of Fluids Engineering, 122 (2000) 330-336.

[8] Z. Du, M. Selig, A 3-D stall-delay model for horizontal axis wind turbine performance prediction, in: AIAA-98-0021, 36th AIAA Aerospace Sciences Meeting and Exhibit, 1998 ASME Wind Energy Symposium Reno, NV, USA, 1998.

[9] J. Corrigan, J. Schillings, Empirical model for stall delay due to rotation, in: American Helicopter Society Aeromechanics Specialists Conf San Francisco, CA, 1994.

[10] C. Lindenburg, Investigation into rotor blade aerodynamics, Netherlands Society for Energy and the Environment, Paper ECN-C-03-025, (2003).

[11] G.P. Corten, E.C. Nederland, Inviscid stall model, in: Proceedings of the European Wind Energy Conference, Netherlands Energy Research Foundation, July 2001, pp. 466-469.

[12] J.G. Leishman, T.S. Beddoes, A generalised model for airfoil unsteady aerodynamic behaviour and dynamic stall using the indicial method, in: 42-th annual forum of the American Helicopter Society, Washington, 1986, pp. 243-265.

[13] W. Sheng, R.A.M.D. Galbraith, F.N. Coton, On the S809 airfoil's unsteady aerodynamic characteristics, Wind Energy, 12 (2009) 752-767.

[14] M.M. Hand, D. Simms, L. Fingersh, D. Jager, J. Cotrell, Unsteady aerodynamics experiment phase V: test configuration and available data campaigns, National Renewable Energy Laboratory, 2001.

[15] J.G. Leishman, Principles of helicopter aerodynamics, Cambridge University Press, 2006.

[16] M. Ramasamy, J.G. Leishman, A generalized model for transitional blade tip vortices, Journal of the American Helicopter Society, 51 (2006) 92-103.

[17] M. Ramasamy, J.G. Leishman, A reynolds number-based blade tip vortex model, Journal of the American Helicopter Society, 52 (2007) 214-223.

Predictions of unsteady aerodynamic loads on HAWT rotor in yawing and pitching using potential flow method

QIU Yong-Xing, WANG Xiao-Dong, KANG Shun

North China Electric Power University, Key Laboratory of CMCPPE Ministry of Education, Beijing 102206, China, kangs@ncepu.edu.cn

ABSTRACT

In order to study the unsteady aerodynamic loads on horizontal-axis wind turbine (HAWT) during the operation with yawing and pitching, an unsteady numerical simulation method is developed. It includes a nonlinear lifting line method for computing the aerodynamic loads on blades and a time-accurate free vortex method for simulating the wake. To improve the convergence property in the nonlinear lifting line method, an iterative algorithm based on the Newton-Raphson method is developed. For increasing the computational efficiency and the calculation accuracy, a new wake vortex model, consisting of a viscous vortex model, a vortex sheet model and a tip vortex model, is used. Wind turbines with different scale as, NREL Phase VI, TU Delft model turbine, and Tjæreborg wind turbine, are taken to validate the method for rotors operating in given yaw and/or pitch angles and in yawing and/or pitching process under different wind speeds. The results, including blade loads, rotor torque and location of tip vortex in the wake are in good agreement with the measured data and the data got with other methods. It is shown that the method developed could be well used for predicting the unsteady aerodynamic loads and the rotor wake in the operation process of blade pitching and/or rotor yawing.

Key words: HAWT, dynamic numerical simulation, unsteady, free vortex wake

1 Introduction

Horizontal-axis wind turbines (HAWT) operate in unsteady conditions with yaw wind, shear wind and gust wind, etc. Because of unsteady inflow conditions, fatigue and extreme loads on blades are generated, which affects the life time and security of wind turbines. Modern large scale wind turbines use the active control techniques (e.g. active pitch or yaw, etc.) to control the aerodynamic loads on blades. Researchers have shown that advanced active control techniques (e.g. individual pitch control) of HAWTs may play an important role in reducing the fatigue and extreme loads [1]. Therefore, it is necessary to undertake research to improve methods for the prediction of unsteady aerodynamic loads of HAWT's blades in the control process.

Due to its high cost and computing time, the Unsteady Reynolds-Averaged Navier-Stokes (URANS) equations are still difficult to use in dynamic simulation of HAWT in engineering applications. The conventional method, Blade-Element-Momentum (BEM) method, is still widely used. Liu *et al.* [2] applied the acceleration potential method to amend the BEM theory. The corrections considered the dynamic inflow effect. Juan [3] used the BEM method coupled with the controller to optimize the HAWT's control strategies. However, the BEM method is based on some empirical equations, which lacks correctly model the complex flow fields. As a result, the accuracy of BEM method is still unsatisfied for predictions of aerodynamic loads on HAWT in complex inflow conditions [4].

The Free-Vortex Method (FVM) is based on the assumption of the potential flow. In essence, the FVM method is made up of the blade aerodynamic model and the wake model. The blade aerodynamic model describes the flow fields around the blade and computes the circulation strength of the trailing and shed vortices released to the blade wake. It could be based on panel method, lifting

surface method or lifting line method. The model describes vorticity fields in wake through the use of vortex filaments. These vortex filaments are trailed by each blade and convected into the downstream wake. With the blade rotating, the spiral wake is generated. The free-vortex method simulates the unsteady flow fields around the blade more accurately than BEM method. Furthermore, its computational efficiency is also higher than CFD method.

Regarding to the blade aerodynamic model, the nonlinear lifting line methods are widely used in aerodynamic simulation for wind turbine blades. In this method, the airfoil aerodynamic data, which is usually obtained by experiments or CFD simulations, is coupled with the calculation of the vortex circulation strength. Therefore, not only the blade aerodynamic loads but also vortex circulation strengths have taken viscous effects into account. However, the widely used iterative method, called simple iterative method [7], may cause a poor convergence for the nonlinear lifting line method. In this method, the iterative process to solve the circulation is independent on each bound vortex filament. Thus, the relevance of the iterative process between different bound vortex filaments is not considered in this method.

With reference to the wake model, the vortex sheet model is made up of trailing and shed vortex filaments. Based on the Helmholtz and Kelvin law, this model is more accurate. However, there are too many vortex filaments in wake, and the computation efficiency decreased rapidly. Thus, a simplified wake model is needed.

Leishman *et al*. presented a time-accurate free wake method and used it in the aerodynamic simulations of the helicopter's rotor [5]. In this method, the blade was modeled by the lifting surface method, the wake model was simplified by the tip vortex filaments, which considered the trailing vortices, but the shed vortices are neglected. Xi Shen *et al*. used this method to research the aerodynamic loads on HAWT's blades under shear wind conditions [6]. Moreover, a FVM method has been already used for HAWT. It is made up of the nonlinear lifting line model and vortex sheet model. Sebastian *et al*. use this method for simulating the unsteady aerodynamic loads on offshore floating wind turbine [7].

In this paper, an improved free-vortex (IFVM) method is presented. The nonlinear lifting line method is used for the blade aerodynamic model. In order to improve the convergence of equations for the nonlinear lifting line method, the Newton-Raphson method is used. To increase the computation efficiency and keep the accuracy of the wake model, a hybrid wake model is presented. The wake near the rotor is modeled by the vortex sheet model, which consists of the trailing vortex filaments and the shed vortex filaments. In the far wake region, with the rolling up of the vortex sheets at the blade tip, the tip vortex filaments displaces the vortex sheet model. The viscous vortex core model is used for considering viscous effects in wake. Vortex filaments are numerically solved by the second-order backward difference (PC2B) method. The method is presented by Bagai and Leishman [8].

The paper is organized as follows. In the Methodology and Models section, the improved iterative algorithm for the nonlinear lifting line method, the hybrid wake model and the solution process are presented. In the Testing Models and Programs section, the testing wind turbines: NREL Phase VI, TU Delft model turbine and Tjæreborg wind turbine, and testing programs are introduced. In the Results and Discussions, the IFVM method is validated by being compared with the experiments, BEM method, FVM method [6] and GDW method [3]. The observed computed loads on the blades in pitching and yawing processes are analyzed.

2 Methodology and Models

2.1 Nonlinear lifting line method

The blade aerodynamic model is based on the nonlinear lifting line method. The blade is modeled by multiple bound vortex filaments, which are located at quarter-chord location (c/4). The bound vortex

filaments are discretized by the cosine segmentation and with refinement in blade tip and root. The trailing and shed vortices are modeled by trailing and shed straight-line vortex filaments (Fig.1). Each bound vortex filament has a circulation strength, which corresponds to the local aerodynamic load on the blade. On the basis of Helmholtz and Kelvin theorem, the trailing vortex circulation strength is the derivative of the bound vortex circulation strength with respect to the blade radius; the shed vortex circulation strength is the derivative of the bound vortex circulation strength with respect to the physical time.

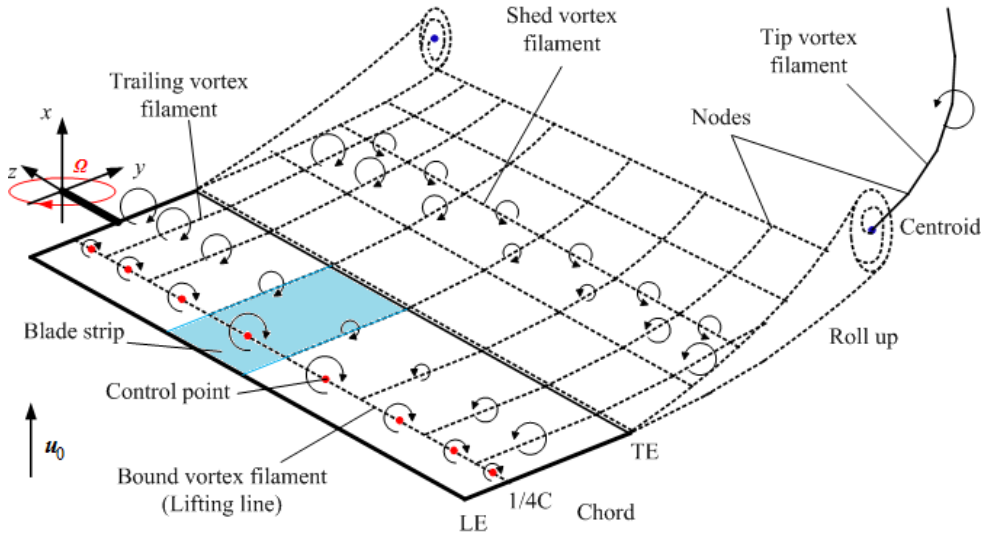

Figure 1Schematic of blade model and vortex wake model

Based on Kutta-Joukowski theorem, the lift force of a blade stripe obtained through

$$\Delta L_{\mathrm{P}} = \rho u \cdot \Gamma_{\mathrm{B}} \cdot l \tag{1}$$

where Γ_{B} is the circulation strength of the bound vortex filament.

The lift force may also be obtained from knowledge of the lift coefficient Cl of the blade strip,

$$\Delta L_{\mathrm{V}} = 1/2\,\rho u^2 \cdot c \cdot l \cdot Cl \tag{2}$$

where ρ is the air density, c is the local chord length of the blade, l is the width of a blade strip. The lift coefficient Cl of the blade is obtained using the airfoil aerodynamic data obtained by experiments or CFD methods. The viscous effects have been taken into account, such as the boundary layer on blade surface, the effects of separated flows. The relative velocity of the control point (located at middle point of a bound vortex filament) is u. It includes the inflow velocity $\boldsymbol{u}_0$, the rotation velocity $\boldsymbol{\Omega r}$, yawing velocity $\boldsymbol{u}_{\mathrm{m}}$ and induced velocity $\boldsymbol{u}_{\mathrm{I}}$.

$$u = \left| \boldsymbol{u}_0 + \boldsymbol{\Omega r} + \boldsymbol{u}_{\mathrm{m}} + \boldsymbol{u}_{\mathrm{I}} \right| \tag{3}$$

where the induced velocity $\boldsymbol{u}_{\mathrm{I}}$ at a given point is due to the bound, trailing and shed vortices from all rotor blades, and can be solved by Biot-Savart law [11].

On the basis of Kutta-Joukowski theorem, the equation of bound vortex circulation strength can be obtained by setting ΔL_{P} equals to ΔL_{V}. Solving the equation is an iterative process. The conventional method is the simple iterative method [7][12], which is simple but easily causes the problems of convergence.

For solving the problem, a new iterative algorithm is developed. The equation of the bound vortex circulation strength is

$$\left[\left(\Delta L_{\mathrm{P}} - \Delta L_{\mathrm{V}} \right)^2 \right] = 0 \tag{4}$$

In order to accelerate the convergence speed, the left hand side of the equation is set to the square of the difference between ΔL_P and ΔL_V. According to the Newton-Raphson method, in each iterative step, the difference f between ΔL_P and ΔL_V is defined by

$$[f]=\left[\left(\Delta L_P-\Delta L_V\right)^2\right] \tag{5}$$

Thus the iterative equation is obtain by

$$\begin{bmatrix} \frac{\partial f_1}{\partial \Gamma_{B1}} & \frac{\partial f_1}{\partial \Gamma_{B2}} & \cdots & \frac{\partial f_1}{\partial \Gamma_{Bn}} \\ \frac{\partial f_2}{\partial \Gamma_{B1}} & \frac{\partial f_2}{\partial \Gamma_{B2}} & \cdots & \frac{\partial f_2}{\partial \Gamma_{Bn}} \\ \vdots & \vdots & & \vdots \\ \frac{\partial f_n}{\partial \Gamma_{B1}} & \frac{\partial f_n}{\partial \Gamma_{B2}} & \cdots & \frac{\partial f_n}{\partial \Gamma_{Bn}} \end{bmatrix} \cdot \begin{bmatrix} \Delta\Gamma_{B1} \\ \Delta\Gamma_{B2} \\ \vdots \\ \Delta\Gamma_{Bn} \end{bmatrix} = -\begin{bmatrix} f_1 \\ f_2 \\ \vdots \\ f_n \end{bmatrix} \tag{6}$$

where n is the total number of the bound vortex filaments on blades, $\Delta\Gamma_B$ is the difference of Γ_B between two iterative steps. The iterative process is described as follows,

(i) Guess an initial circulation strength of bound, trailing and shed vortex filaments, and initial wake geometry

(ii) Calculate the relative velocity and the angle of attack (AOA) at each control point of the blade

(iii) Obtain the lift coefficient Cl of each control point at the angle of attack by interpolation in the corresponding airfoil aerodynamic data

(iv) Obtain for the 'f' with Equation (1), (2), and (5)

(v) Compute the Jacobi matrix in Equation (6)

(vi) Obtain for the $\Delta\Gamma_B$ with Equation (6) and convergence judgment with the equation:

$$\left[\Delta\Gamma_B\right]/\Gamma_{Bmax} \le 0.001 \tag{7}$$

If Equation (7) is satisfied, the iterative process of Γ_B has converged. Otherwise, the Γ_B will be updated with under relaxation factor ω:

$$\Gamma_B^{new} = \Gamma_B^{old} + \omega \cdot \Delta\Gamma_B \tag{8}$$

and then, go to step (ii).

In Equation (8), the recommended value of ω is 0.5. In Equation (5), the Jacobi matrix is solved by the numerical differentiation method.

If the bound vortex circulation strength is solved, the circulation strength of trailing and shed vortices filaments, which are located at the blade chord surface, can be computed in each time step [11]. At the same time, the blade aerodynamic loads are also obtained. Considering the effects of three-dimensional flows, the 3D stall delay model (Du-Selig stall delay model [13]) is used.

2.2 Algorithm of free vortex wake

2.2.1 Vortex wake model

With the blade rotating, the trailing and shed vortices are generated, and convected into the downstream wake. Since the trailing and shed vortex filaments model the vortices field, according to the Helmholtz and Kelvin law, these vortex filaments should be used in the whole wake region. However, the computation time increases rapidly with the increasing of the vortex filaments number. Thus, a simplified model is needed.

A hybrid wake model has been presented in Fig.1. The wake region can be divided into two regions: In region I which is behind the blade, the vortex sheet model is used, which is made up of trailing and shed vortex filaments; the tip vortex filament model is used in Region II, and connected to the centroid

point of the rolling up region of the vortex sheet. The hybrid wake model based on these assumptions can be summarized as follows:

(i) Because of the large strength of the tip and root vortices, the vortex sheets are rolled up into two concentrated vortices [9][10]. However, in the far wake (Region II) the tip vortices are dominant.
(ii) When the shed vortices convect into the far wake, they will dissipate gradually. Thus, the shed vortices are neglected in Region II.
(iii) The circulation strength of each vortex filament is constant. However, the vortex core radius of a vortex filament is variable in motion process.

To compute the circulation strength of the tip vortex filament (Γ_{tip}), the following method is used: at the last row of the vortex sheet, the trailing vortices circulations (Γ_{T}) are integrated from the radius (the radial position of the maximum bound circulation, r') to the blade tip. The integral value is the tip vortex circulation strength as follows.

$$\Gamma_{\text{tip}} = \int_{r'}^{r_{\text{tip}}} \Gamma_{\text{T}}(r)\mathrm{d}r \tag{9}$$

where r is the local radius on the blade.

In order to take the viscous effects in wake into account, and avoid the singularity of the velocity field around the vortex filament, the vortex core model (Lamb-Oseen model, Equation (10)) is used [11]

$$K_{\text{V}} = \frac{h^2}{\left(r_{\text{c}}^{\,4} + h^4\right)^{1/2}} \tag{10}$$

where the radius of the vortex core r_{c} is obtained by

$$r_{\text{c}} = \left[\frac{4a \cdot \delta_{\text{V}} \cdot \nu \cdot \left(t_{\text{w}} + S_{\text{c}}\right)}{1+\varepsilon}\right]^{1/2} \tag{11}$$

where a is a constant, which equals to 1.25643.ε is the strain rate of a vortex filament. δ_{V} is the turbulent viscosity coefficient. S_{c} is the time-offset parameter. ν is the kinematic viscosity.

2.2.2 Solution process

The governing equation used to describe the motion of vortex filaments in wake is as follows [8].

$$\frac{\partial \boldsymbol{r}_{\text{w}}}{\partial \psi} + \frac{\partial \boldsymbol{r}_{\text{w}}}{\partial \zeta} = \frac{\boldsymbol{u}_{\text{w}}}{\boldsymbol{\Omega}} \tag{12}$$

where $\boldsymbol{r}_{\text{w}}$ is the position vector of the node (fig.1)on the vortex filament. ψ is the azimuth angle of the blade in the absolute coordinate system. ζ is the azimuth angle of the node in the rotor coordinate system. $\boldsymbol{\Omega}$ is the angular speed of the blade. $\boldsymbol{u}_{\text{w}}$ is the velocity at the node in wake, which is the resultant velocity of the inflow velocity $\boldsymbol{u}_0$ and the induced velocity $\boldsymbol{u}_{\text{I}}$. Equation (12) is discretized with the second-order backward difference (PC2B) scheme:

$$\begin{aligned}\boldsymbol{r}_{\text{w}\,j+1,k+1} = {} & \frac{1}{7}\boldsymbol{r}_{\text{w}\,j+1,k} + \frac{5}{7}\boldsymbol{r}_{\text{w}\,j,k} - \frac{3}{7}\boldsymbol{r}_{\text{w}\,j,k+1} + \frac{3}{7}\boldsymbol{r}_{\text{w}\,j-1,k} + \frac{3}{7}\boldsymbol{r}_{\text{w}\,j-1,k+1} \\ & - \frac{1}{7}\boldsymbol{r}_{\text{w}\,j-2,k} - \frac{1}{7}\boldsymbol{r}_{\text{w}\,j-2,k+1} + \frac{8}{7}\boldsymbol{u}_{\text{w}\,j+\frac{1}{2},k+\frac{1}{2}} \cdot \frac{\Delta\psi}{\boldsymbol{\Omega}}\end{aligned} \tag{13}$$

where j is the number of the step of ψ. k is the number of the step of ζ. To solve Equation (13), the pseudo implicit algorithm [8] is used. The free-vortex method presented in this paper is a time-marching method. The solution process is illustrated by Fig. 2.

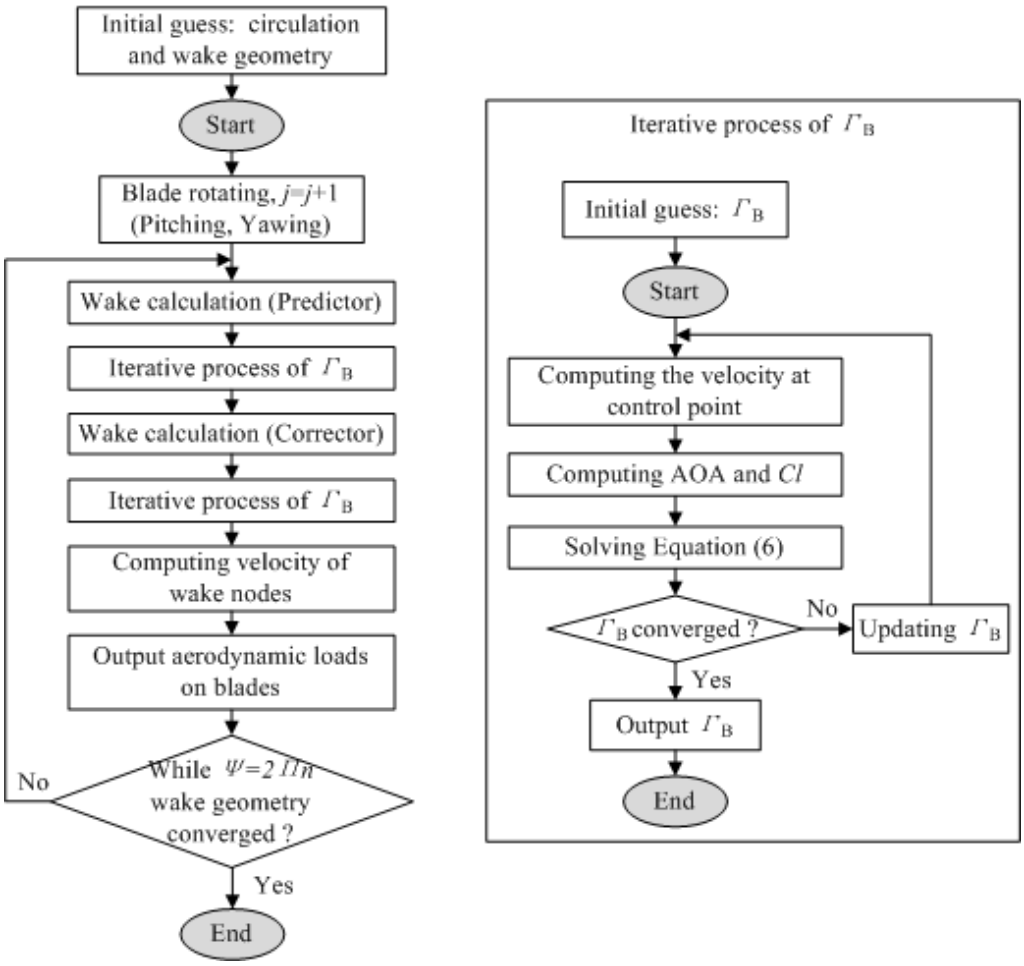

Figure 2 Flowchart describing the numerical solution process of IFVM method

3 Testing Models and Programs

For verification and validation of the method, three scales of wind turbines are used here as testing examples:

NREL Phase VI is a stall-regulated turbine and a power rating of 20 kW. It is designed by national renewable energy laboratory (NREL). The experiments were performed in the NASA Ames wind tunnel (24.4×36.6 m) [14], which have been considered a benchmark for evaluation of wind turbine aerodynamic methods [15].

TU Delft model turbine is designed for wind tunnel test and with a 1.5kW generator. The experiments were performed in the 2.24m-diameter open jet wind tunnel of Delft University of Technology. The experiments focus on the rotor wake measurements [16], which include the wake velocity field measurements and smoke visualization of tip vortex cores, etc., and can be considered an important reference for wake researches.

Tjæreborg wind turbine is a pitch-controlled wind turbine with a rotor diameter of 61.1m, a hub height of 60m and with a 2MW induction generator. It is built in Tjæreborg, a village on the west coast of Denmark, on 1987. The experiments were performed in the wind farm, and include the operating data in the control process [17]. These experimental data have become a valuable reference for the research on the dynamic process of wind turbines.

The geometric features of testing wind turbine rotors are given in Table 1.

Table 1 Rotors of testing wind turbine geometric features

Wind turbine	NREL Phase VI	TU Delft	Tjæreborg
Number of blades	2	2	3
Airfoil section	S809	NACA0012	NACA 4412-43
Diameter of rotor	10.046 m	1.2 m	61.1 m

The testing programs consist of four parts, as follows:

(i) Verifications of the wake model

Because the hybrid wake model (vortex sheet model and tip vortex model) is used, one should make sure that the vortex sheet extends far enough downstream. The distribution of induced velocity of the blade should be independent to the scale of vortex sheet model. Moreover, for the distribution of induced velocity at the blade, the hybrid wake model should approximate the vortex sheet model which is used in whole wake.

(ii) Case of given yaw angle and pitch angle

NREL Phase VI rotor is computed at wind speeds of 5 to 12m/s, the pitch angle of 3°, axial inflow condition. The power and thrust are computed and compared to the experiment [14]. Moreover, the wind turbine rotor is computed at multiple given yaw angles (10°, 30°, 45°and 60°)at the wind speed of 7m/s. The distributions of *Cn* and *Ct* at the blade are compared to the experiments, BEM method and FVM method [6]. The FVM method is made up of the lifting surface model and the tip vortex model.

The wake geometries of TU Delft rotor are computed in the conditions of multiple tip speed ratios (6, 8) and pitch angles (0°, 4°, 6°) and compared to the experiment [16].

(iii) Case of pitching process

Tjæreborg wind turbine is computed in two pitching processes: (1) at the wind speed of 7.4 m/s, the blade is pitching from 0.5°to 2.5°;after about 29 s, back to 0.5°; (2) at wind speed 10.6 m/s, the blade is pitching from 0.2°to 3.9°;after about 29 s, back to 0.2°. All of the computed results are compared to the experimental data. Moreover, for process (2), the IFVM method is compared to BEM method [3] and GDW (generalized dynamic wake) method [3].The generalized dynamic wake (GDW) method is presented by Suzuki[18].

(iv) Case of yawing process

NREL Phase VI rotor is simulated in yawing processes at yaw rates of 5°/s and 20°/s, at the wind speed of 7m/s. In these processes, the shaft torque of each blade is computed.

4 Results and Discussions

4.1 Verifications of the wake model

The scale of the vortex sheet model is defined by its number of revolutions ($nRev_{VS}$) or its relative length (l_{VS}/D, D is the rotor diameter) in rotor axial direction. The vortex sheet model includes most of vortex filaments, which are close to blades. Therefore, its scale affects the induced velocity of the blade, and dominates the computation efficiency. If the induced velocity at the blade is independent of the scale of vortex sheet model, the wake model is converged.

For the case of NREL Phase VI, the angle of attack (AOA) of the blade in 0.75R is computed at four positions (3, 6, 9 and 12 o'clock,) on the rotor plane at the wind speed of 7m/s, yaw angle of 30°. The research work of SANT [11] has shown that the numerical accuracy is satisfied while the azimuth angle for each time step is less than 10°, and the number of strip elements is between 21 and 31. In the following computation, the azimuth angle for each time step is 3.75°, and each blade includes 28 strip elements. Thus, the numerical accuracy is satisfied.

Because the AOA is a function of the induced velocity, it is used for the criteria of wake model convergence. The results show that if the $nRev_{VS}$ is more than about 1.33 (model III), the wake model is converged (Fig.3 (a)). Fig.3 shows the wake model III ($nRev_{VS}$=1.33) approximates the vortex sheet model that is used in whole wake region ($nRev_{VS}$>5) to compute the AOA of the blade. Therefore, in the following computations, the $nRev_{VS}$ of the vortex sheet model is between 1.0 and 1.33.

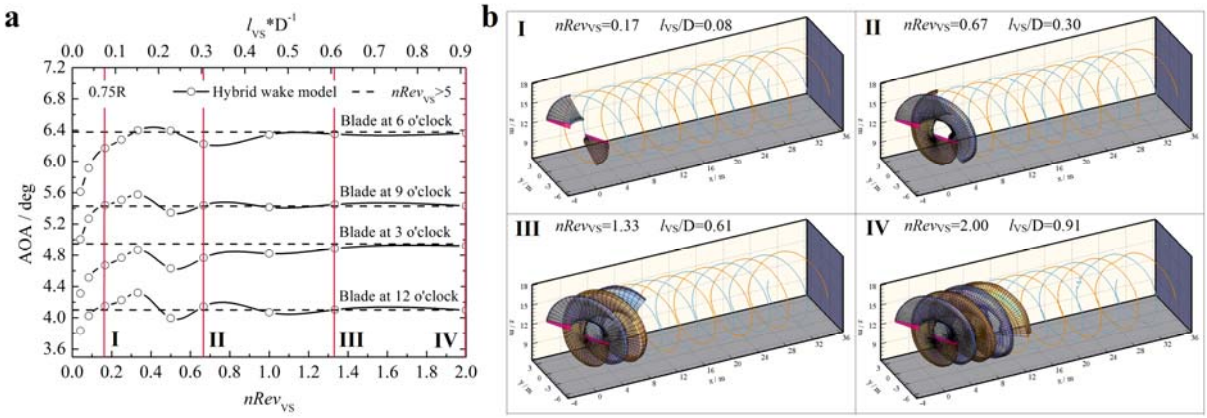

Figure 3 (a) AOA as a function of the $nRev_{VS}$ in 0.75R (b) four typical scales of wake models

4.2 Case of given yaw angle and pitch angle

Fig.4 presents the computed power and thrust of NREL Phase VI at the pitch angle of 3°and for axial inflow condition. The airfoil aerodynamic data of S809 is used. The three-dimensional effects are considered by the 3D stall-delayed model (Du-Selig model [13]). The results agree well with the experiment at wind speeds less than 10m/s. . However the computed power deviates away from the experimental curve when the wind speed is more than 10m/s. The main reason is that the blade has been stalled, and strong three dimensional separated flows occur on the suction surface of the blade [13]. However, the 3D stall-delayed model cannot represent this phenomenon correctly.

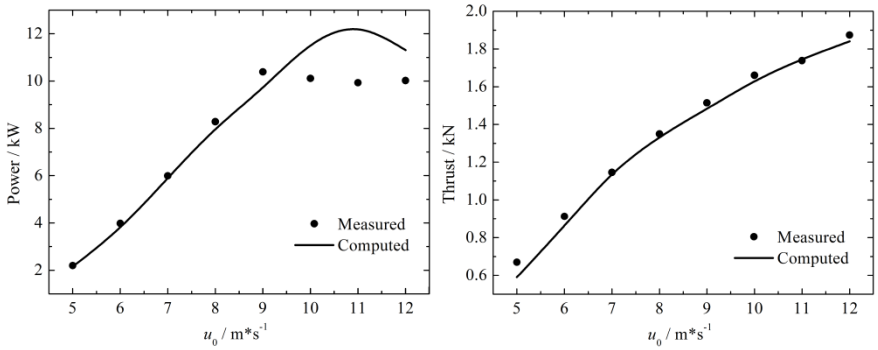

Figure 4 Comparison of the computed power and the thrust with respect to the wind speed, NREL Phase VI

In Fig.5, NREL Phase VI rotor is computed at multiple given yaw angles (10°, 30°, 45°and 60°), at the pitch angle of 3° and the wind speed of 7m/s. The tip speed ratio (TSR) is 5.41. The azimuth angle for each time step is 7.5°. Each blade is discretized by 28 strip elements. The distribution of normal and tangential force coefficients (*Cn*, *Ct* [14]) of the blade is computed by the improved free-vortex method (IFVM), the free-vortex (FVM) method [6] and BEM method. Fig.5 shows that the results of IFVM method are closest to the experiment. With the yaw angle increased, the *Ct* distribution, which is computed by BEM method, moves away from the experimental data in the root region of the blade. The reason is that the flow fields around the blade are very complex at large yaw angles. The BEM method cannot describe the complex flow fields correctly. Being compared to the experiment, the

results of the FVM method [6] are lower. One possible reason is that the scale of the vortex sheet is too short ($nRev_{VS} \leq 0.17$). And the shed vortices are neglected in this FVM method [6], which also has influence on the accuracy of the results.

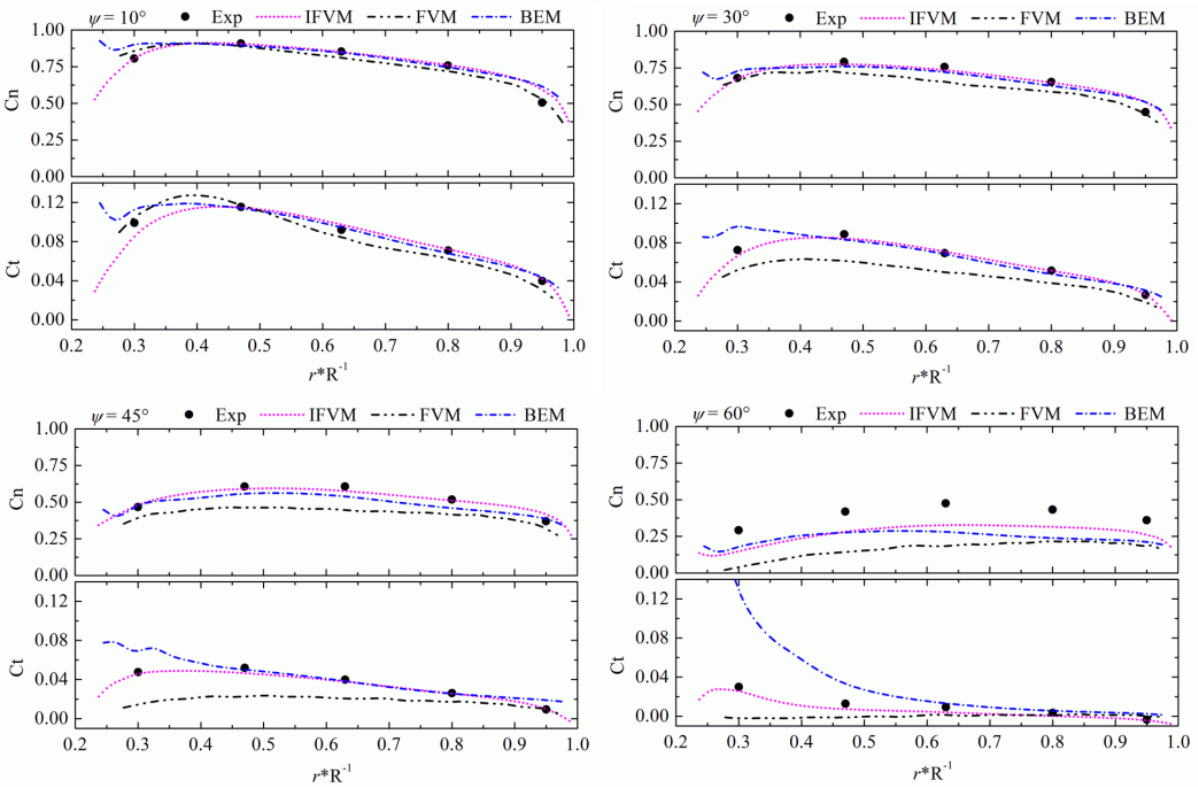

Figure 5 Comparison of the radial distributions of the computed normal and tangential force coefficients at multiple yaw angles, NREL Phase VI, TSR=5.41

For validation of the computed wake vortex geometry, TU Delft model turbine is computed under the axial inflow condition, and at multiple tip speed ratios (6, 8) and pitch angles (0°, 4°, 6°). The azimuth angle for each time step is 8.18°. Each blade is discretized by 21 strip elements. Fig.6 compares the computed wake geometries to the measured wakes [16]. The results show that in different inflow cases the IFVM method can simulate the rotor wake correctly.

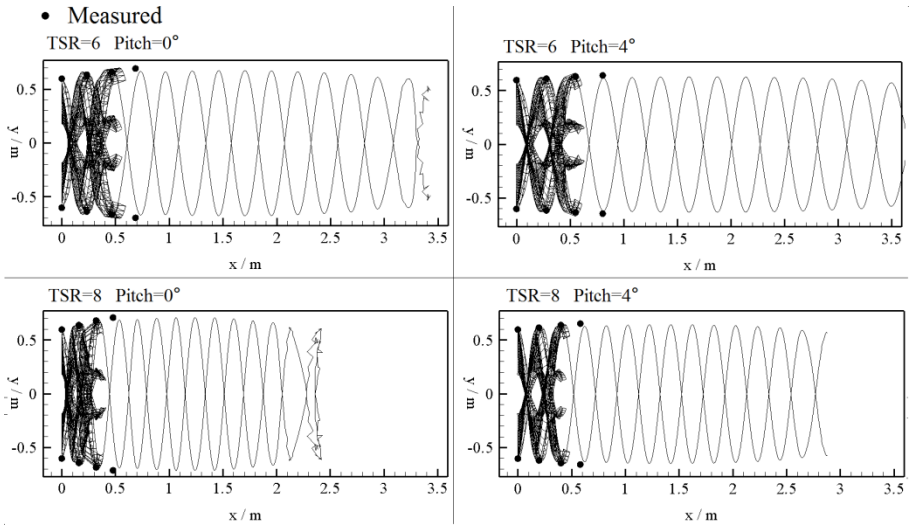

Figure 6 Comparison of the computed wake geometry, TU Delft model turbine

4.3 Case of pitching process

Fig.7 shows the comparison of the computed shaft torque and electrical power of Tjæreborg wind turbine to the results from experiment, BEM method [3] and GDW method [3]. In Fig.7 (a), the blade is pitching from 0.5°to 2.5°, after about 29 s, back to 0.5°, at the wind speed of 7.4m/s under the axial inflow condition. And the pitch rate is 1°/s. The azimuth angle for each time step is 7.5°. One time step is about 0.06 seconds. Each blade is discretized by 28 strip elements. Fig.7 (a) presents that the computed shaft torque by IFVM method agrees with measured data [19]. Because of the pitch control system, the curve of pitch angle is fluctuated slightly in pitching process, and the computed shaft torque takes corresponding fluctuations.

In Fig.7 (b), the blade is pitching from 0.2° to 3.9°, after about 29 s, back to 0.2°, at the wind speed of 10.6m/s under the axial inflow condition. The pitch rate is 3.7°/s. Compared to the computed electrical power computed from other three different methods, the results of IFVM method is more close to the measured data.

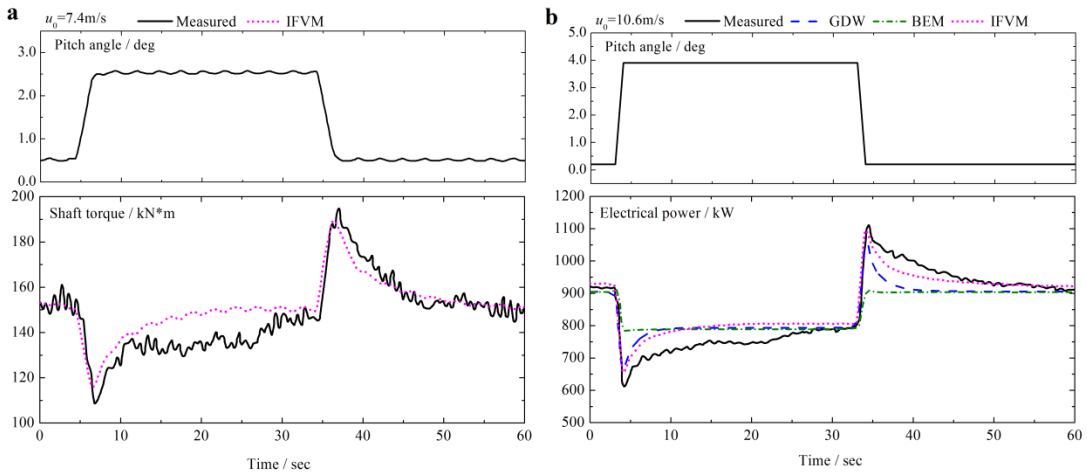

Figure 7 Comparison of the computed shaft torque and electrical power in pitching processes, Tjæreborg wind turbine,(a) pitching from 0.5°to 2.5°, after 29s return back to 0.5°, at wind speed of 7.4m/s, (b) pitching from 0.2°to 3.9°, after 29s return back to 0.2°, at wind speed of 10.6m/s

In Fig.7, when the pitching process is paused, the aerodynamic loads on blades will overshoot. One possible reason of the phenomenon is the unsteady characteristics of flow fields. And the delayed effects of the viscous flows around the blade could be another possible reason. On the other hand, according to the Helmholtz and Kelvin law, with the variations of the bound vortex circulation, the trailed and shed vortex circulations in wake have corresponding changes and affect the aerodynamic loads on blades. When the blade pitching is stopped, the vortex wake is tending towards stability. At the same time, it affects the blade more and more slightly. The aerodynamic loads on the blade will be stable.

4.4 Case of yawing process

In this section, NREL Phase VI wind turbine is computed in the yawing process from 60°to 0°, at the wind speed of 7m/s, at pitch angle of 3°. The azimuth angle for each time step is 7.5°. One time step is about 0.56 seconds. Each blade is discretized by 28 strip elements. In Fig.8, (a) the yaw rate is 5°/s, (b) the yaw rate is 20°/s. In the yawing process, the computed dynamic shaft torque of each blade is a function of the physical time as shown in fig.8. Moreover, the computed amplitude and mean values of shaft torques of Blade I at multiple given yaw angles (60°, 45°, 30°, 10°) are also presented in Fig. 8. As can be seen in this figure, there are three phases in the yawing process.

First of all, before rotor yawing, the yaw angle is fixed at 60°. In this phase, since the yaw angle is stable, the dynamic shaft torque of the blade is fluctuated periodically, and the amplitude is constant and equal to the case of the given yaw angle.

And then, the rotor is yawing from 60° to 0°. With the yaw angle decreasing, the shaft torque of the blade is dynamically increased. At the yaw rate of 5°/s, the amplitude of the dynamic shaft torque of the blade is close to that at given yaw angles. While at the yaw rate of 20°/s, the amplitude of the dynamic shaft torque is increased rapidly, and larger than the case of given yaw angles. The main reason is the relative velocity generated by the yawing affects the distribution of AOA at the blade dramatically.

At last, when the yaw angle is stable at 0°, the rotor stops yawing. At the yaw rate of 5°/s, the fluctuations of the shaft torque of the blade are disappeared rapidly. While at the yaw rate of 20°/s, the fluctuations only appears in a short time. The main reason is the delayed effects of the wake. Fig. 9 illustrates the variations of the wake at the yaw rate of 20°/s. In this figure, six instantaneous wake geometries correspond to six different time in Fig.8 (b).

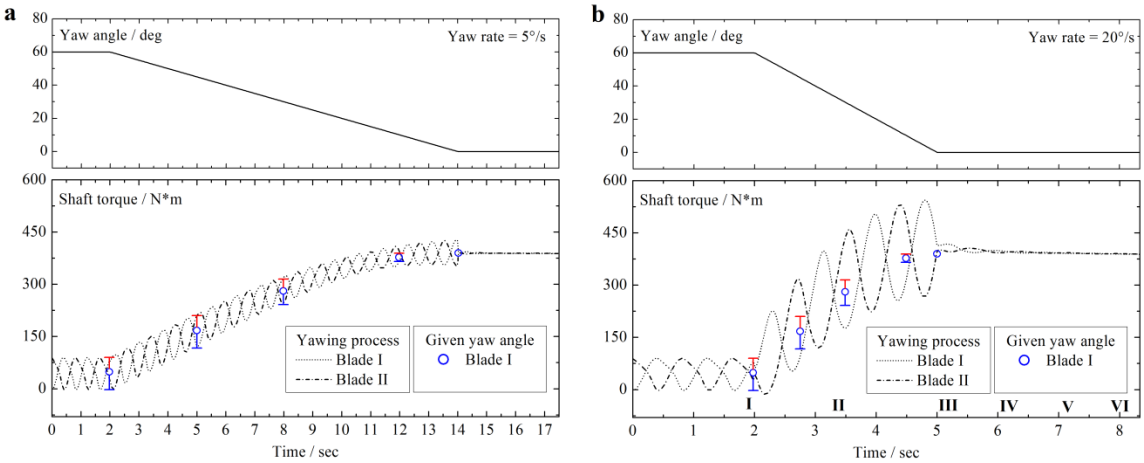

Figure 8 Computed shaft torque of the blade as the function of time at the different yaw rates, NREL Phase VI, (a) the yaw rate is 5°/s, (b) the yaw rate is 20°/s

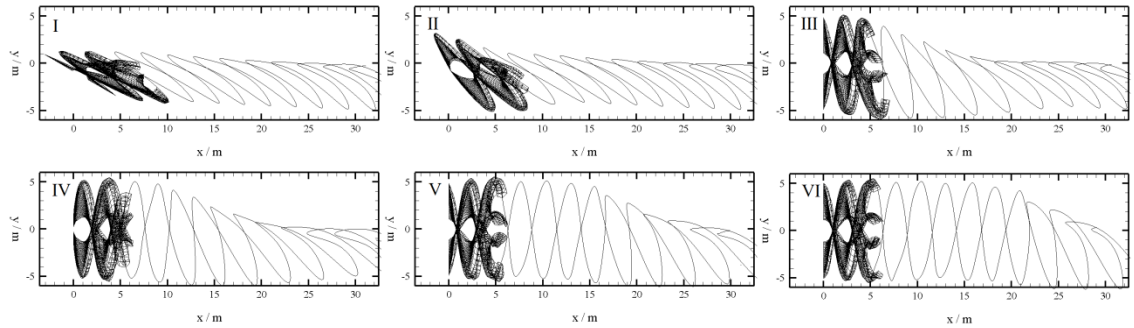

Figure 9 Computed instantaneous wakes of the rotor at the different time in the yawing process at the yaw rate of 20°/s, NREL Phase VI

5 Conclusions

A novel method for predictions of dynamic aerodynamic loads on HAWT's blades in yawing and pitching process is presented in this paper, which is based on the free-vortex method. Three scales of wind turbines are computed in the conditions of the given yaw and pitch angles and pitching or yawing process. The computed results are compared to the experimental data, as well as other methods. The variations of aerodynamic loads and wakes are analyzed.

The results show the method can predict the aerodynamic loads on blades accurately, and have higher computation efficiency. Compared to the experiment and other methods results, the method developed in this paper is more accurate. The analyses show the trailed and shed vortices affect the variations of aerodynamic loads in the pitching process; the yaw rate and dynamic wakes affect the shaft torque of the blade in yawing process.

REFERENCES

[1] Barlas T.K., van Kuik G.A.M., "Review of state of the art in smart rotor control research for wind turbines". Progress in Aerospace Science, vol.46 (2010) pp. 1-27

[2] Liu Xiong, Zhang Xianmin, Chen Yan, Ye Zhiquan, "Transient Aerodynamic Load Prediction Model for Horizontal Axis Wind Turbines based on Dynamic Inflow Theory". ACTA ENERGLAE SOLARIS SINICA, vol.4(2009) pp. 412-419

[3] Juan Jose Garcia Quirante, "Control of Wind Turbines for Power Regulation and Load Reduction". M.Sc. thesis, Technical University of Denmark, 2007

[4] Gupta Sandeep, Leishman J. Gordon, "COMPARISON OF MOMENTUM AND VORTEX METHODS FOR THE AERODYNAMIC ANALYSIS OF WIND TURBINES". Reno: 43rd AIAA Aerospace Sciences Meeting and Exhibit,2005

[5] Leishman J. Gordon, Bhagwat Mahendra J., Bagai Ashish, "Free-Vortex Filament Methods for the Analysis of Helicopter Rotor Wakes", Journal of aircraft, vol.39 (2002) pp. 759-775

[6] Shen Xin, Zhu Xiaocheng, Du Zhaohui, "Wind turbine aerodynamics and loads control in wind shear flow". Energy, vol.36 (2011)pp.1424-1434

[7] Sebastian T., Lackner M. A., "Development of a free vortex wake method code for offshore floating wind turbines". Renewable Energy, vol.46 (2012) pp.269-275

[8] Bagai A, Leishman J. Gordon, "Rotor Free-Wake Modeling Using a Pseudoimplicit Relaxation Algorithm". Journal of aircraft, vol.6 (1995) pp.1276-1285

[9] Landgrebe AJ. "The wake geometry of a hovering rotor and its influence on rotor performance". Journal of the American Helicopter Society, vol.17(4): 2-15

[10] Massouh F, Dobrev I. "Exploration of the vortex wake behind of wind turbine rotor". Journal of Physics: Conference Series 2007, 75: 012036

[11] SANT Tonio, "Improving BEM-based Aerodynamic Models in Wind Turbine Design Codes", PhD thesis, University of Malta, 2007

[12] Garrel A. van, "Development of A Wind Turbine Aerodynamics Simulation Module". ECN-C-03-079, 2003

[13] Yu Guohua, Shen Xin, Zhu Xiaocheng, Du Zhaohui, "An insight into the separate flow and stall delay for HAWT". Renewable Energy, vol.1 (2011) pp.69-76

[14] Hand M.M., Simms D.A., Fingersh L.J., Jager D.W., Cotrell J.R., Schreck S., Larwood S.M., "Unsteady aerodynamics experiment phase vi: Wind tunnel test configurations and available data campaign". Technical report NREL/TP-500-29955, NREL, 2001

[15] Simms D., Schreck S., Hand M., Fingersh L.J., "NREL Unsteady Aerodynamics Experiment in the NASA-Ames Wind Tunnel: A Comparison of Predictions to Measurements". Technical report NREL/TP-500-29494, NREL, 2001

[16] Haans Wouter, "Measurement and Modelling of Tip Vortex Paths in the Wake of a HAWT under Yawed Flow Conditions", J. Sol. Energy Eng, vol.456 (2005) pp. 127-135

[17] PF, BEP, KSH, "The Tjæreborg Wind Turbine Loads During Normal Operation Mode for CEC". Report EP94/456. 1994

[18] Suzuki A, "Application of dynamic inflow theory to wind turbine rotors". PhD thesis, The University of Utah, 2000

[19] "Tjæreborg Wind Turbine (Esbjerg) First dynamic inflow measurement", Department of Fluid Mechanics, DTH, DK-2800 Lyngby, 1991

Study of Blade Fence Effect on Wind Turbine Performance

J.J. Song[1,3], Y. Xu[1,3], Q. Wang[1,2], C.F. Li[1,2], J.Z. Xu[1,3]

[1]Institute of Engineering Thermophysics, Chinese Academy of Sciences, Beijing 100190, China, jjsong@iet.cn
[2]University of Chinese Academy of Sciences, Beijing 100049, China, jjsong@iet.cn
[3]Wind Energy Key Laboratory of Chinese Academy of Sciences, Beijing 100190, China, xuyu@iet.cn

Wind turbine blade is one of the most important components in wind power system. In order to meet the high power and large scale wind turbine development trend in China's low speed wind fields, the blade is designed longer and longer. To guarantee the structure strength requirement of the long blade, thick airfoil is adopted in inboard region, which can provide better structure rigidity, lower blade weight and fatigue load, as well as smaller production cost. However, thick airfoil is more prone to generate flow separation because of the large angles of attack. When separation occurs, the lift, which normally is rapidly increasing with the angle of attack, stops rising and the drag, which normally is very small, becomes comparable to the lift. These phenomena mentioned above will lead to wind energy absorption ability reduce[1] and are unfavorable to the power generation[2,3]. Sandia national laboratories[4] carried out 3D CFD simulation on rotor performance and loads, which refered to twist, fence and flatback.

In this paper, modeling and simulation of 1.5 MW wind turbine blade with and without a ring fence was made and analysed the fence effect on flow separation and power generation. We adopted SST k-ω turbulence model which is one of the most widely used eddy viscosity model, combining the advantages of k-ω model in near wall region with the advantages of the k - ε model in far field and have a good numerical stability. Besides, the pressure distribution and torque can be accurately forecast by the SST model.

1. Geometric model and grid generation

Because of the rotationally symmetric structure of the three-blade wind turbine, we just need study one of the blades, and the other two blades can be obtained by successively rotated 120 °. The computational domain – 1/3 cylindrical section – was set as follows: 6 times of blade length in radius, 10 times of blade length in upstream and downstream direction respectively (see fig. 1). The first layer grid thickness is 1e-5 and the total grid number is 3.5 million.

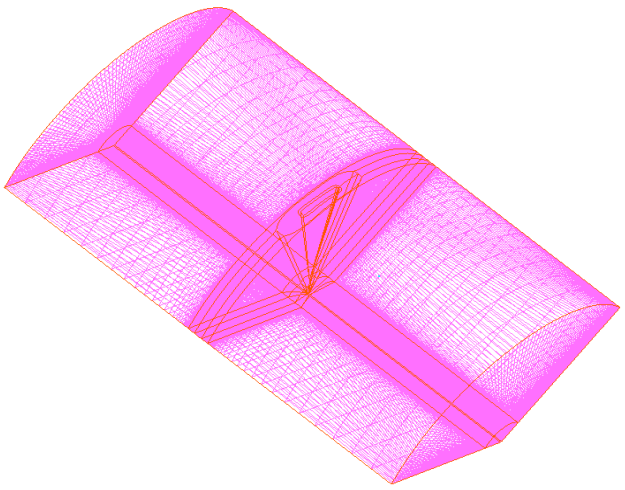

Figure 1: Computational domain and grid.

2. Flow field contrast at different wind speeds

We installed a ring fence (see fig. 2) that was 5% of the maximum chord length height and no thickness under the premise of not changing the blade structure characteristics. Under three different conditions: 7m/s, 11m/s and 15m/s wind speed, wind turbine blades with and without fence were made CFD calculation. Based on the original blade (that is blades without fence), flow separation was observed in inboard region, and the degree of separation aggravated along with the wind speed increase. We would analyze the fence's role that played on the blade through fig. 3. The fence could truncate the flow in spanwise direction and guide the flow along the string forward, which improved the blade surface flow separation condition. Separation area was obviously confined by the fence, and the flow field improved, output increased the most during the three conditions. When the wind speed was large enough, separation was more severe and the range of the fence influence was confined. If blade pitch was considered, the results at higher wind speeds would be better, due to the lower angles of attack and the slightly decreased separation region.

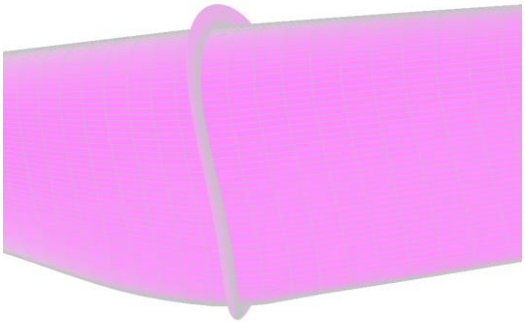

Figure 2: Fence at the maximum chord position.

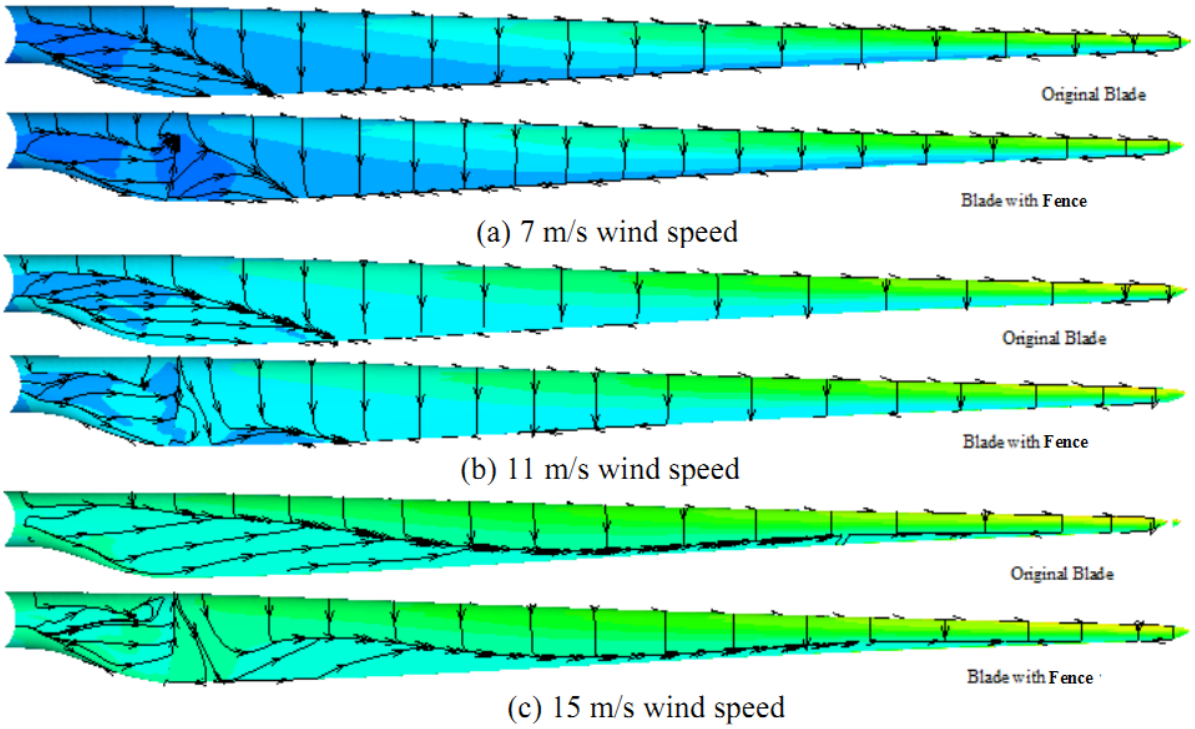

Figure 3: Limiting streamline of blade suction surface.

Took the 11m/s speed for example, we analysed the change of the flow field by the fence. After adding the fence, negative pressure peak value decrease and the adverse pressure gradient of the blade pressure surface at 13% and 15% length was smaller, which was benefit for the airflow attachment on the blade surface and the stall delay appeared. The fence made no effect on the pressure distribution at 30% and 40% length (see fig. 4). The influence on the

flow field (see fig. 5) at different section had similar regularity as the pressure distribution alteration.We would find that fence could indeed improve the flow condition on the blade surface and mitigate the adverse pressure gradient near the fence especially at 11m/s and 15 m/s. The influence on the flow field mainly concentrated in the nearby region behind the fence.

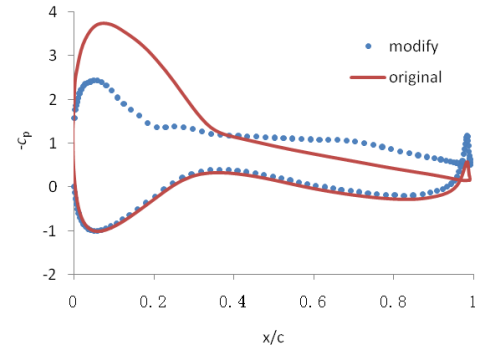

(a) 13% of the blade length

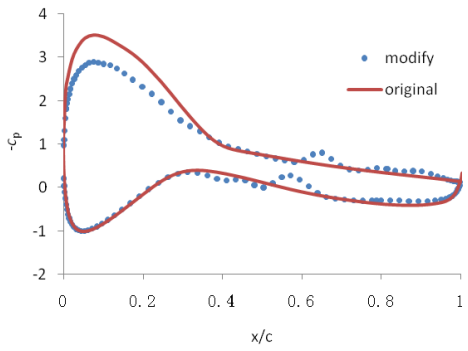

(b) 15% of the blade length

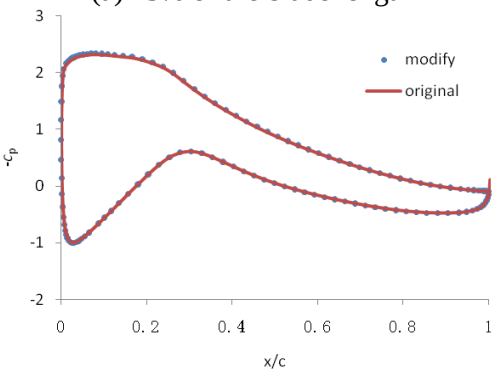

(c) 30% of the blade length

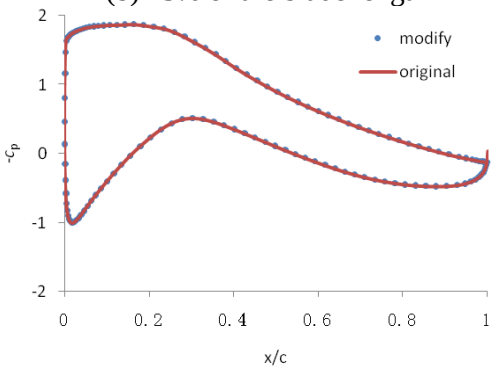

(d) 40% of the blade length

Figure 4: Pressure distribution at 11 m/s

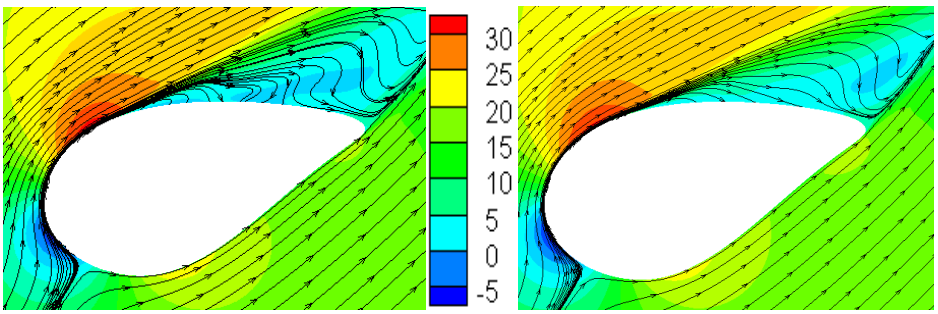

(a) 13% of the blade length

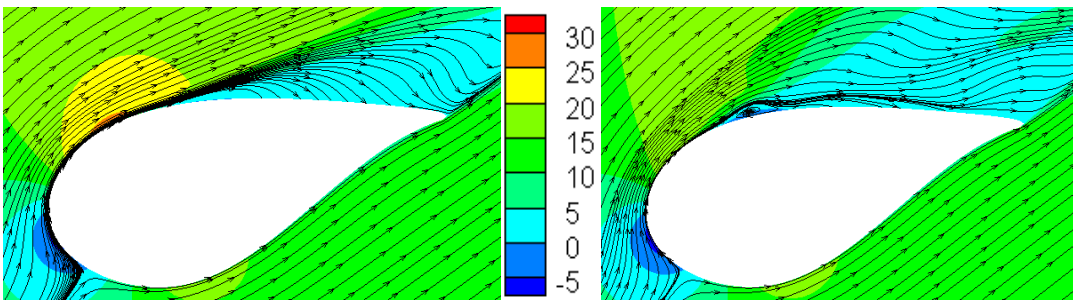

(b) 15% of the blade length

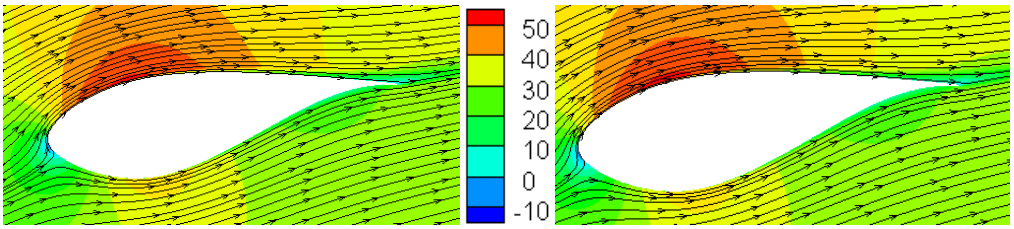

(c) 40% of the blade length

Figure 5: Streamline distribution at 11 m/s

3. Power generating capacity assessment

After verifying the fence's positive effect, more wind conditions from 3 m/s to 25 m/s were calculated. Combined with wind speed of the probability density distribution, we could get the annual energy output.

In spite of the interannual variability of annual average wind speed is difficult to predict, the wind speed changes of the year can still be described by a probability distribution. Formula (1) is the fraction of time for which the hourly mean wind speed exceeds U, while formula (2) is the fraction of time for which the hourly mean wind speed between U_i and U_{i+1}. The shape parameter K was preferred to 2, which was actually a fairly typical value for many locations. The scale parameter $A=\overline{U}\cdot\exp[-\Gamma(1+\frac{1}{K})]$, and chose the hub height of annual average wind speed U as 8.5 m/s (according to IEC international standard definition of IEC II medium wind), we could get the probability density distribution of different wind speeds (see fig.7).

$$f(U)=\exp[-(\frac{U}{A})^K] \quad (1)$$

$$f(U_i<U_o<U_{i+1})=\exp[-(\frac{U_i}{A})^K]-\exp[-(\frac{U_{i+1}}{A})^K] \quad (2)$$

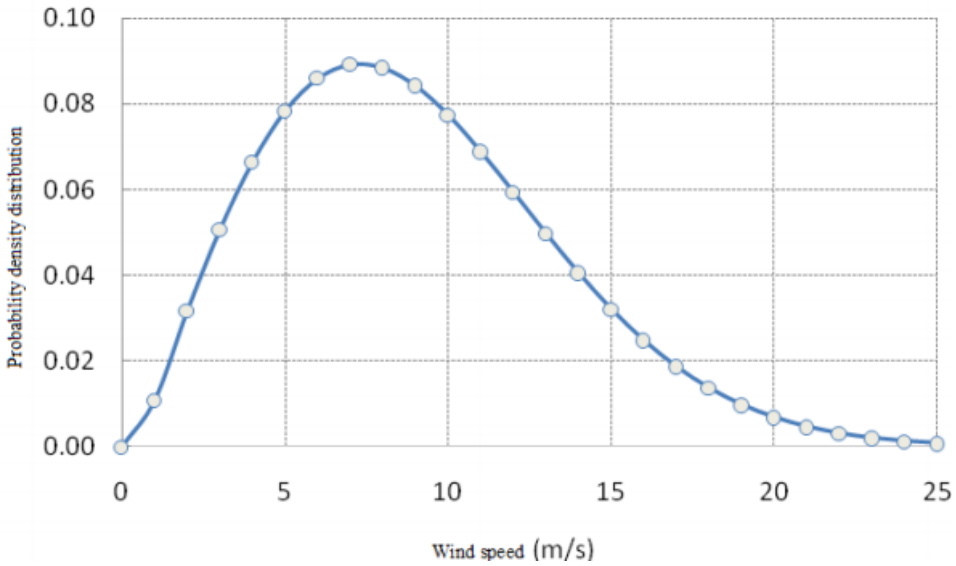

Figure 6: Probability density distribution of different wind speeds.

The annual power generation is the sum of power under different wind speeds, which can be gained by formula (3).

$$E=\sum c_p(U_o)\cdot\frac{1}{2}\rho U_o^3\cdot\frac{\pi D^2}{4}\cdot f(U_i<U_o<U_{i+1})\cdot 365\cdot 2 \quad (3)$$

Computations were made, and the original wind turbine annual power generation was 6.50667×10^6 kW/h, while the modified was 6.54442×10^6 kW/h. Comparing the results from blades with and without fence, fence brought the wind turbine annual generation in a 0.58% increase.

4. Conclusions

(1) From the calculation of original wind turbine blade, flow separation was observed in inboard region, and the degree of separation aggravated along with the wind speed increase.

(2) Fence could confine the separation region by truncating the flow in spanwise direction and guiding the flow along the string forward, which improved the blade surface flow separation condition.

(3) Fence could lead to negative pressure peak value decrease and the adverse pressure gradient of the blade pressure surface become smaller at 13% and 15% blade length, while less effect at 30% and 40% even farther of the blade length. The influence on flow field was similar like this.

(4) The fence brought the wind turbine annual generation in a 0.58% increase in IEC II medium wind.

Ackonwledgement

This paper is supported by Sino-Denmark Collaboration Project (Grant No. 2010 DFA 62830) and the National High Technology Research and Development Program of China (863 Program) (Grant No. 2012AA051303).

REFERENCES

[1] G.P. Corten, "Flow Separation on Wind Turbine Blades", Utrecht: Universiteit Utrecht (2001).

[2] A. Bruining, W.A. Timmer, "Airfoil Characteristics of Rotating Wind Turbine Blades", Journal of Wind Engineering and Industrial Aerodynamics, vol.39 (1992) pp. 35-39.

[3] Y.H. Li, Q.L. Zhang, "Numerical Simulation of Flow Field and Aerodynamic Performance of A Wind Turbine Blade", Acta Energiae Solaris Sinica, vol.29 (2008) pp. 1172-1176.

[4] C.P. van Dam, R. Chow, S. Saephan, "Insights into Rotor Performance and Loads through Three-Dimensional CFD", 2012 Wind Turbine Blade Workshop, May 30 – June 1 (2012).

Integrated airfoil and blade design method for large wind turbines

Wei Jun Zhu, Wen Zhong Shen
Department of Wind Energy, Technical University of Denmark,
DK-2800 Lyngby, Denmark, wjzh@dtu.dk, wzsh@dtu.dk

ABSTRACT

This paper presents an integrated method for designing airfoil families of large wind turbine blades. For a given rotor diameter and tip speed ratio, the optimal airfoils are designed based on the local speed ratios. To achieve high power performance at low cost, the airfoils are designed with an objective of high C_p and small chord length. When the airfoils are obtained, the optimum flow angle and rotor solidity are calculated which forms the basic input to the blade design. The new airfoils are designed based on the previous in-house airfoil family which were optimized at a Reynolds number of 3 million. A novel shape perturbation function is introduced to optimize the geometry on the existing airfoils and thus simplify the design procedure. The viscos/inviscid code Xfoil is used as the aerodynamic tool for airfoil optimization where the Reynolds number is set at 16 million with a free-stream Mach number of 0.25 at the blade tip. Results show that these new airfoils achieve high power coefficient in a wide range of angles of attack (AOA) and they are extremely insensitive to surface roughness.

1 Introduction

The earliest work on airfoil design began at 1900's where laminar airfoils were the main focus. Due to the development of computer technologies during the past century, flat plat theory was no longer popular for airfoil design, instead, numerical tools are mainly used for airfoil optimization. Hicks et al. [1] are one of the earliest aerodynamicists who made the airfoil design by numerical optimization. The design work of wind turbine airfoils were initiated by Tangler and Somers [2, 3] resulting in a family of NREL airfoils dedicated for wind turbine blades. More recently, researchers at DTU have made significant contributions in designing the wind turbine airfoils [4,5,6]. All these wind turbine airfoils meet the demand of high lift to drag ratio around design lift.

The state of art wind turbine airfoils generally have a high aerodynamic performance which provide the wind turbine blade to operate with high power performance. However, wind turbine blades designed with these airfoils do not necessarily operate in an optimum state because of the separated design of the airfoil and blade. More rigorous wind turbine blade design shall be integrated with specific airfoil design. The goal of maximizing annual energy product (AEP) can be better achieved by coupling an airfoil optimization routine together with the blade element momentum (BEM) theory or other similar tools. The integrated method increases the design complexity and addresses some other issues more than energy capture. The success of the integrated design work requires a sufficiently elaborated optimization tool. This paper provides a starting point for such an integrated design optimisation.

The core of the present optimization work is to develop large wind turbine blade with lower cost of energy (COE). To achieve this goal, new airfoils are designed and employed at specific blade radial positions. At every local blade station, the design objective of each airfoil is high power coefficient and small chord length. Beside this objective, various constrains are imposed, such as roughness insensitivity, maximum lift to drag ratio etc. The objective and constrains are different from each airfoil due to their different local flow condition. In the state of variable speed operation, the flow geometry over the rotor is preserved such that the flow angle is maintained at its optimum position. The blade platform designed in this paper ensures that the blade will have optimum flow geometry such that the axial induction factor approaches 1/3. The optimum flow geometry will not be guaranteed if the blade is constructed with other airfoils because these airfoils are not dedicated to such a blade. Ideally, a perfect rotor can be designed using the integrated method, i.e., construct the blade with airfoils specially designed and use the resulted optimal blade platform.

The paper is organized as following: Section 2 describes the integrated design method; Section 3 presents the airfoil design method and the results; Section 4 shows the platform of the optimum rotor; Conclusions are given in the final section.

2 The Integrated Design Method

The integrated design of airfoil family and blade can be started from the 2D-BEM analysis of an airfoil section at a given blade station. The core of the analysis is the iterative computation of the power coefficient of an airfoil. Because the power performance is an important measure of blade performance, it has often been used as a key reference number during design process [7]. With an aim of decreasing the cost, we introduce the rotor solidity as another parameter together with the power coefficient. In this analysis, we also involve the Prandtl's tip correction to the integrated design where the design of thin airfoils near tip might be affected.

According to the 1D-momentum theory, the solution of the power coefficient is maximized when the axial induction factor is *a=1/3*. With this condition being valid, it can be shown that the power coefficient of an airfoil section can be written as:

$$C_p = [(1-a)^2 + x(1+a')^2]xc_x\sigma \tag{1}$$

where the solidity is

$$\sigma = 2F\sin^2(\phi) \tag{2}$$

and *a*, *a'* are the axial and tangential induced velocity interference factors, respectively, *x* is the local speed ratio, c_x and c_y are the tangential and axial force coefficients, respectively, σ is the rotor solidity, ϕ is the local flow geometry and *F* is the Prandtl's tip loss function.

It is known that the Prandtl's tip loss function corrects the assumption of solid disk. Thus for rotors with a finite number of blades the correction has to be implemented to the blade design and well as airfoil design. Although various tip loss functions can be used for the design purpose [8], here we use one of the simplest corrections proposed by Prandtl which is written as:

$$F = 2\cos^{-1}(e^{-f})/\pi \tag{3}$$

where

$$f = B(R-r)/(2r\sin\phi) \tag{4}$$

In Eq. (1), not all of the variables have been explicitly given except for the axial induction factor that must equal to 1/3. The other parameters can be divided into two groups. Parameters in group 1 contain the values that will not enter into the BEM iterations. Such as the local speed ratio *x*, the length of the blade *R*, the number of the blades *B* and the airfoil normal and tangential force coefficients. To compute c_x and c_y, the lift and drag coefficients from the airfoils are needed during every step of airfoil optimization, such that

$$c_x = c_l(\sin\phi - c_d/c_l\cos\phi) \tag{5}$$

$$c_y = c_l(\cos\phi + c_d/c_l\sin\phi). \tag{6}$$

The other group of the variables will be iteratively solved due to their dependency. These parameters are the power coefficient C_p, the flow angle ϕ and the tangential induction factor *a'*. The values of C_p, ϕ and *a'* are initialized with zero before the first BEM iteration.

The geometric parameters in group 1 shall be fixed for a given blade design. In the present study, we take the 5MW reference wind turbine [9] as the reference rotor. This reference wind turbine has a maximum rotational speed of 12.1 RPM and the blade length of 63 m. In this task we are going to design a wind turbine rotor with a rated power about 20MW. Therefore the length of the new blade shall be approximately computed as

$$R = 63m\sqrt{20MW/5MW} = 128\,m. \tag{7}$$

According to the reference rotor, in the present work we fix the blade length at *R=130* m and the tip-speed-ratio (*TSR*) of 8.

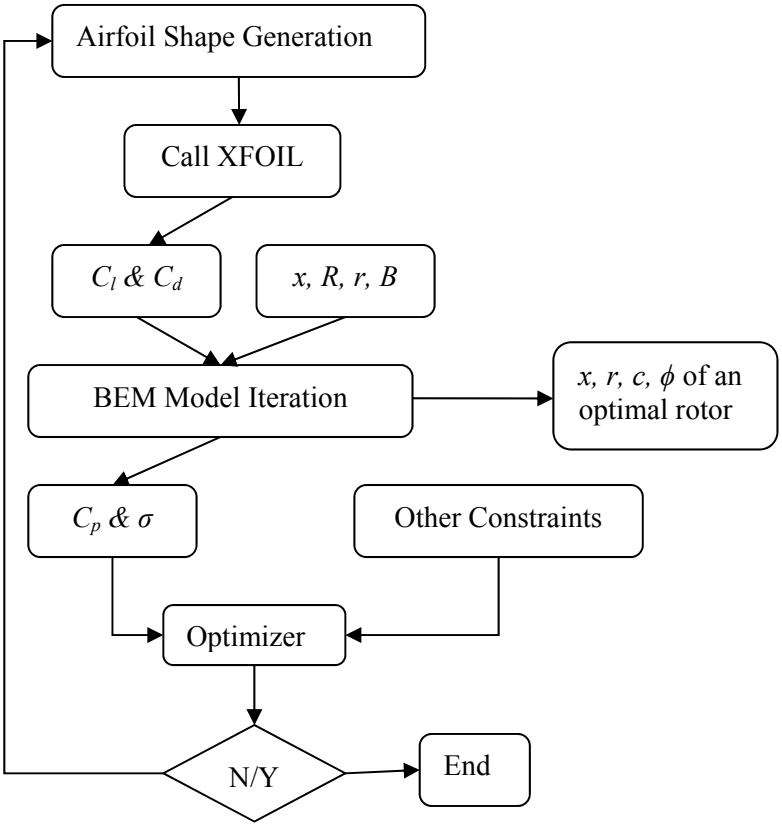

Figure 1. Flow chart of the integrated design.

The integrated design process is summarized in Figure 1. As seen in the flow chart, the main loop goes through the airfoil shape optimization and the 2D-BEM iteration is inside the main loop. The 2D-BEM calculation is an important part of the integrated design concept which links the airfoil optimization with the optimal blade design. The BEM iteration requires input from airfoil aerodynamics and blade local speed ratio etc. When the BEM converges, it forms an output to both the airfoil optimizer and the optimal rotor design. The final optimal rotor is found when the airfoil optimizer finds a converged solution.

3 Airfoil design and analysis

Before starting the design work, two key parameters are pre-defined for the blade: the rotor size and the *TSR*. As mentioned earlier the design *TSR* is 8 and the blade length is 130 m. This is considered as an upscaling case of the 5MW virtual wind turbine [9]. The local speed ratios, the local blade radius and the number of blades are the basic inputs to start the integrated design.

3.1 Design conditions

The design Reynolds number is estimated to be about Re=16x10^6 depending on the radial location. The Mach number at the blade tip is set to M_∞=*0.25*. The Mach number changes according to the local speed ratio. Design angle of attack is between 3^o and 10^o. Numerical computations go through each angle of attack between 3^o and 10^o. The wide range of angle of attack takes into account the off-design condition. Free transition simulation is based on the e^n model with *n=9*; forced transition simulation is carried out by fixing the upper and lower transition points at 5% and 10% chords measured from the leading edge, respectively. The numerical tool used for airfoil design is the Xfoil code developed by Drela [10]. The Xfoil code is iteratively used inside the optimization loop. All the above mentioned flow conditions are written as an input script that is recognized by Xfoil code.

3.2 Design variables

The choice of design variables is directly related to airfoil shape parameterization. Although lots of functions can be used to describe airfoil shapes, however, it is imperative to choose proper functions to represent airfoil geometry. In the

present study, instead of creating a new airfoil shape, a shape perturbation function is applied to modify an existing airfoil. The idea of using such function is to save computational time and inherit the shape from previous airfoils. The sum of the shape perturbation function used for the upper surface is

$$\Delta y_u(i) = \sum_{k=1}^{N} f_u(k) P_u(k,i) \tag{8}$$

and similar for the lower surface,

$$\Delta y_l(i) = \sum_{k=1}^{N} f_l(k) P_l(k,i). \tag{9}$$

In Eq. (8) and (9) the lower subscripts u, and l stand for the lower and upper airfoil surfaces, respectively, i is the index of the x and y coordinates, k is the index of the shape modes. The shape functions for each mode along the x-coordinate are

$$P_u(k,i) = \sin^{\xi}(\pi x_u(i)^{g(k)}) \tag{10}$$

$$P_l(k,i) = \sin^{\eta}(\pi x_l(i)^{g(k)}). \tag{11}$$

The amplitudes f_u and f_l in Eq. (8) and (9) are the design variables, and plus two more power factors of ξ, η, this gives a total number of design points $dofs=2*N+2$. g is a given vector which is the exponent of x. For example, the choice of g could be g=[0.1 0.2 0.3 0.5 1 3 5 8]. Because $x_{u,l} \in [0,1]$, functions (8) and (9) give zero value at leading edge and trailing edge points. Therefore leading edge and trailing edges are naturally fixed without being perturbed.

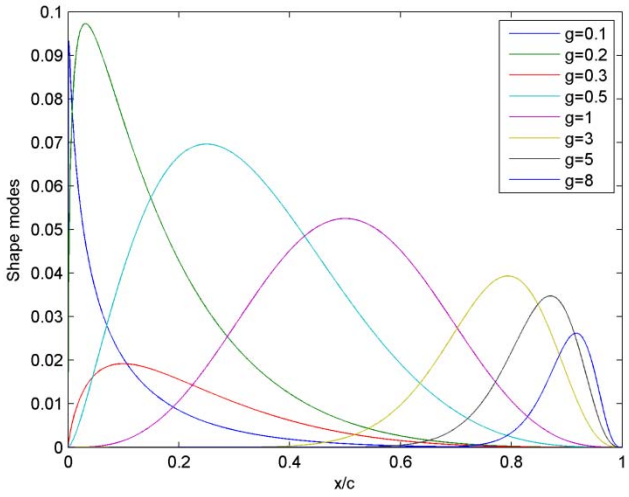

Figure 2. Example of the shape function.

Figure 2 shows an example of the shape perturbation function. The sum of the mode shapes will be added to the reference airfoil. One can add more shape modes to put more focus at any chord-wise location. For example, adding more values of $g<0.1$ leads to more detailed changes at leading edge. The amplitude coefficients f_u and f_l are updated after each iteration until the final airfoil shape is found.

3.3 Design objective

The design objective is the blending of power coefficient and the rotor solidity, such that

$$Obj = kC_p + (1-k)\sigma^{-1} \tag{12}$$

where k=0.5 for the middle part of the blade. The k value shall be modified along the blade station while the solidity changes.

To obtain good off-design property, the power coefficient is weighted between clean and rough conditions with the angle of attack ranging from $\alpha=3^o$ to $\alpha=10^o$.

$$C_p = 0.25 \sum_{\alpha=3}^{10} C_p^{clean} + 0.75 \sum_{\alpha=3}^{10} C_p^{rough} \quad (13)$$

If the converged solution can be found by the optimizer, Eq. (13) indicates that the resulted power coefficient will be insensitive to surface roughness and will keep high value over wide range of AOA.

3.4 Design constrains

The design constrains are: 1. thickness to chord ratio; 2. limited maximum lift; 3. limited difference in maximum lift for clean and rough cases to ensure less roughness sensitivity; 4. maximum thickness location x_{max}/c, for shape compatibility consideration; 5. Thickness constrain near the trailing edge, for structure consideration; 6. smooth surface curvature for surface structure consideration. The tolerance used for these constrains is between 10^{-4} and 10^{-3} depending on the type of constrains.

3.5 Optimization results

Since the new airfoils are optimized using our baseline DTU-LN2-xx airfoil family, for the purpose of this paper the resulting airfoil will be referred to as DTU-R130-xx airfoils. The designed airfoil family has five airfoils of thickness to chord ratio ranging from 18% to 30%. These geometries are plotted in Figure 3. To ensure less three dimensional effects due to curvature change along the blade span, the airfoils are designed to have smooth geometrical transition between each other. The shape compatibility is well controlled by the design constrains.

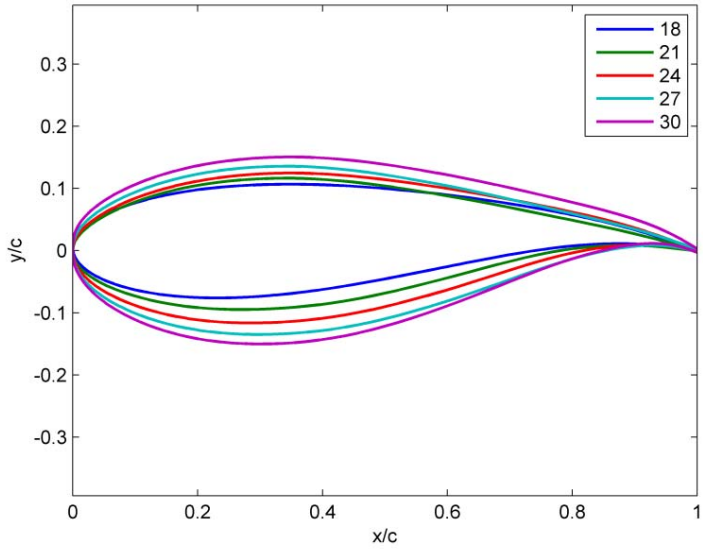

Figure 3. Airfoil shapes.

Some key design values are given in Table 1. The outer part (110-130m) of the blade is constructed with R130-18. The middle part (40-80m) contains R130-21, R130-24, R130-27 and R130-30. The inner part (0-40m) is interpolated between cylinder and R130-30. The corresponding local speed ratios are calculated in the table which are inputs to the optimization model. For sake of manufacturing, the resulting airfoils have increased trailing edge thickness along the blade. Considering the blade shape compatibility, the maximum thickness location also increases while thickness increases, it is referred to as x_{max}/c, the values are seen in the table as well. The design lift and maximum lift for the clean and rough cases are calculated for all the airfoils. According to the design constrains, the difference in C_l between clean and rough cases has to be small. For example of the R130-18 airfoil, the design lift coefficients C_{Lde} are 1.24 and 1.21 for clean and rough conditions, respectively. In general, all the designed airfoils have good characteristics of roughness insensitivity.

Thickness	18	18	18	21	24	27	30	50	100
Step1: Pre-define blade length and TSR									
r (m)	130	125	110	80	65	50	40	30	0
λ	8	7.69	6.77	4.92	4	3.08	2.46	1.54	-
Step2: Airfoil design based on the local TSR									

Bluntness	-	-	0.2	0.23	0.3	0.5	0.6	-	-
x_{max}/c	-	0.278	0.278	0.308	0.314	0.314	0.327	-	100
C_{Lde}	-	-	1.24/1.21	1.25/1.21	1.4/1.34	1.39/1.29	1.41/1.24	-	-
C_{Lmax}	-	-	2.04/2.03	1.97/1.96	1.97/1.95	1.89/1.86	1.89/1.85	-	-
$(C_L/C_D)_{max}$	-	-	146/137	160/130	150/ 119	151/108	132/84	-	-
Step3: Blade construction based on the optimal airfoils									
Chord(m)	0	2.4	3.57	4.91	5.37	6.99	8.67	10	7
β(º)	-	0.62	0.68	1.65	2.34	4.96	7.7	11	-
ϕ (º)	-	5.62	5.68	7.65	9.34	11.96	14.7	18	-
Solidity	-	0.009	0.015	0.029	0.039	0.668	0.10	-	-
Re ($\times 10^6$)	-	12.4	16.3	16.4	14.8	15.1	15.4	10	5

Table 1. Airfoil characteristics and blade parameters.

Figure 4 gives a closer look at the lift and drag characteristics of the R130-airfoils. A curve that weights between clean and rough flow conditions is shown in each sub-figure (solid line with triangles). The weighting coefficient is the same as used in Eq. (13). By looking at the horizontal axis, it is seen that the difference between maximum lift of clean and rough cases are small. The R130-18 and R130-21 airfoils have similar maximum lift and the other airfoils have less maximum lift due to increased thickness. The maximum lift has been limited at a certain level to keep maximum thrust under a certain level. By looking at the vertical axis, it is observed that the lift to drag ratio is kept at high level over wide range of lift which implies good off-design property. It is interesting to check the local power coefficients since it is an index that measures the quality of the optimization. The C_p values at different angles of attack are shown in Figure 5. It is found by numerical simulation that the C_p values are relatively high for all the airfoils. And more importantly the C_p curves are quite flat, i.e. between 5 to 9 degrees. These are the aerodynamic properties expected as the design objective.

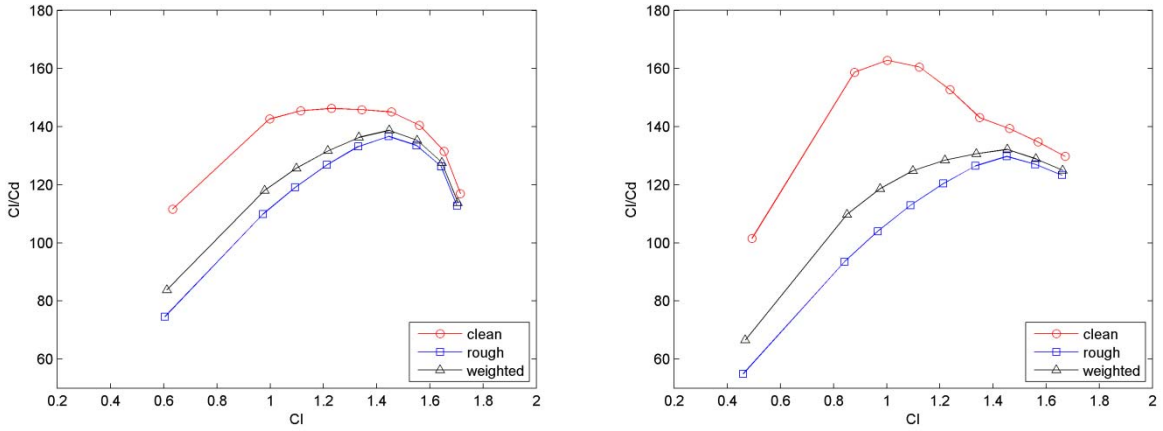

(a) (b)

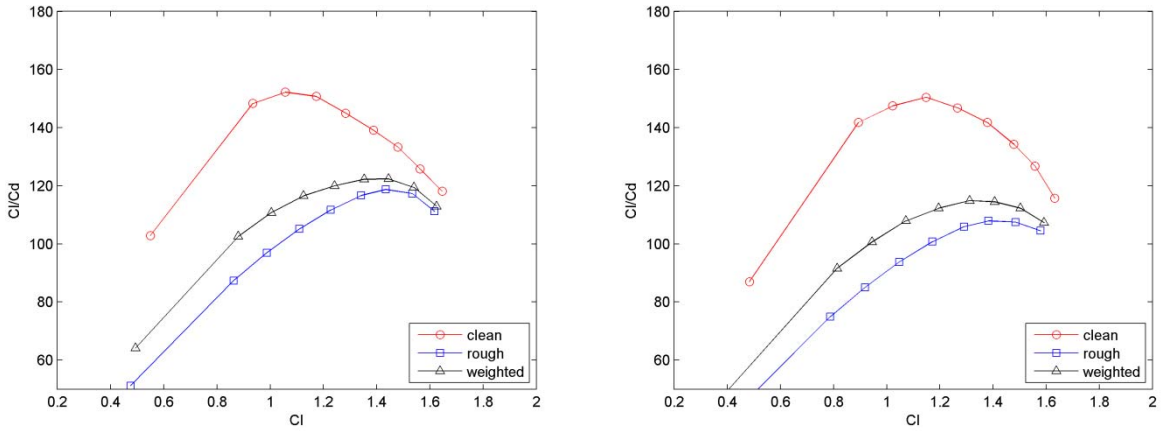

(c) (d)

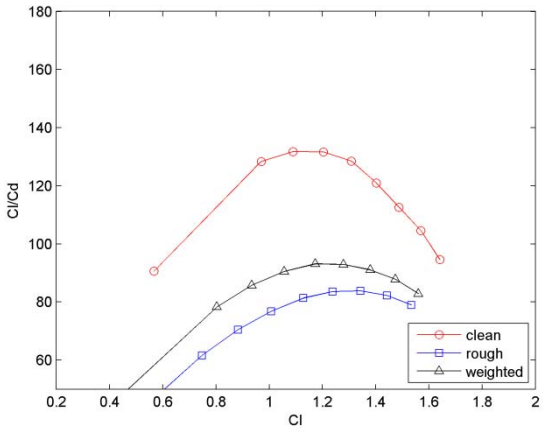

(e)

Figure 4. Lift against lift to drag ratios. (a) R130-18; (b) R130-21; (c) R130-24; (d) R130-27; (e) R130-30.

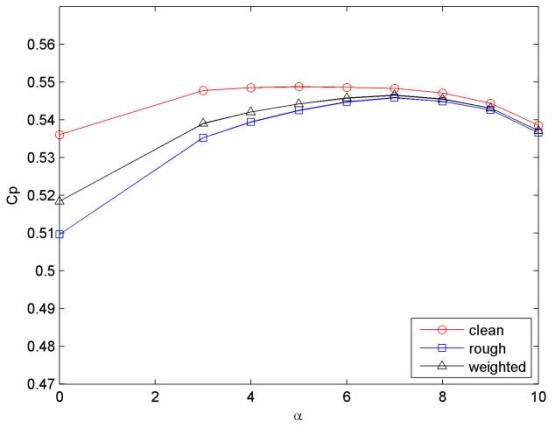

(a)

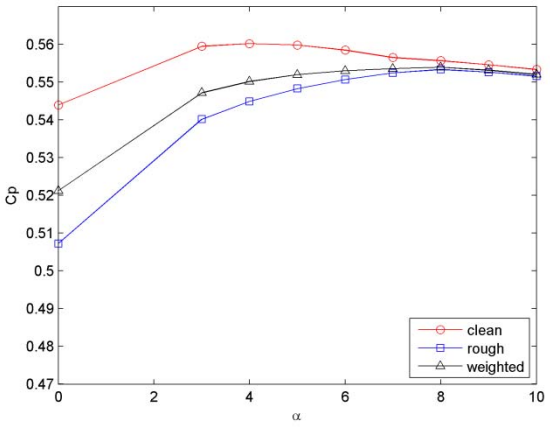

(b)

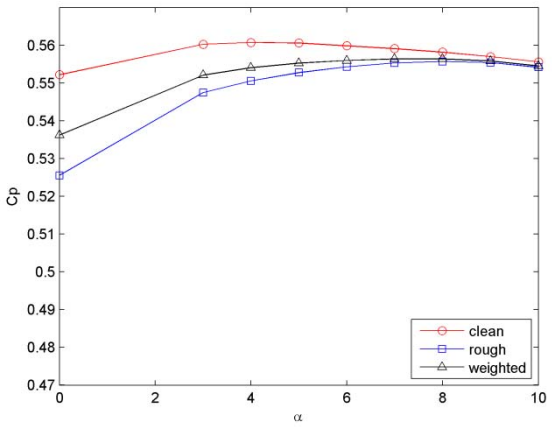

(c)

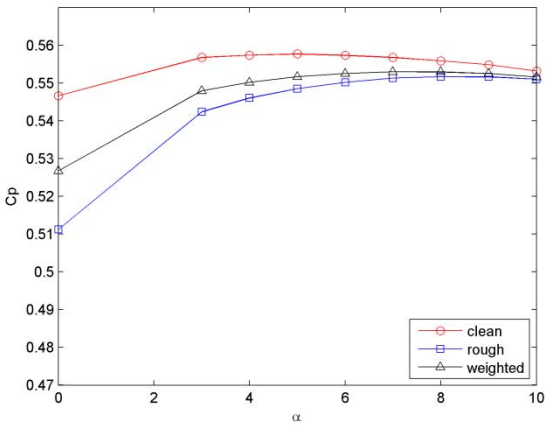

(d)

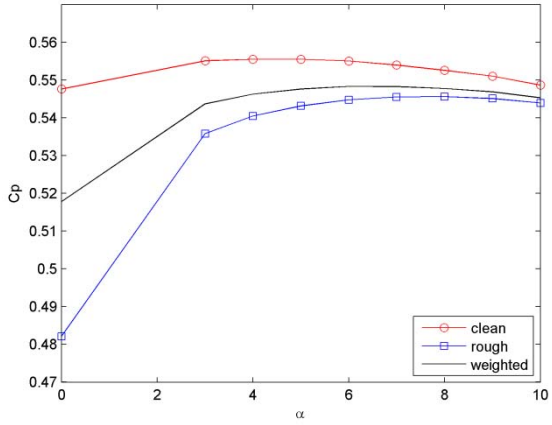

(e)

Figure 5. C_p at different AOA. (a) R130-18; (b) R130-21; (c) R130-24; (d) R130-27; (e) R130-30.

4 The platform of the optimal rotor

For each airfoil shown in Figure 1, according to Eq. (12), a local high C_p value can be obtained at a given blade radial position and it is the same for the local solidity. When such objective is achieved after some steps of airfoil optimization, the optimum values of chord length and flow angle are obtained. The chord and twist distributions form the basic platform of the optimum rotor, such distributions are shown in Figure 6 and Figure 7. These numbers are also seen in Table 1. Until now the whole process of the integrated design has been shown with a result of high C_p value and small solidity. However, these results are based on the assumption of an idealized normal induction factor 1/3. Further blade optimization shall be carried out based on the present baseline platform. The more detailed blade optimization must include the sophisticated BEM model which also calculates the induction factors. Beside this, the measured airfoil data are required as input to the BEM code.

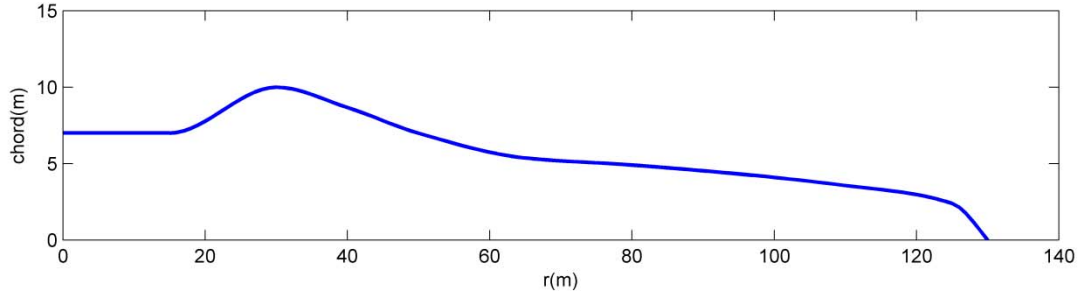

Figure 6. Chord distribution of the pre-designed blade. Platform envelop based on the designed airfoils.

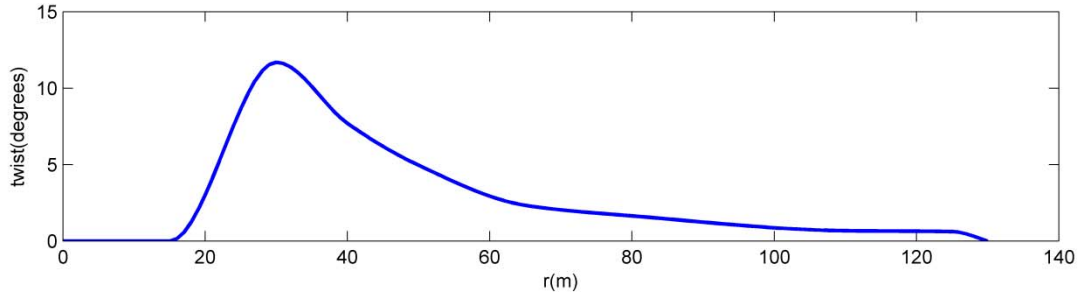

Figure 7. Twist distribution of the pre-designed blade.

5 Conclusions

An integrated method to design airfoils and rotor blade is introduced. The design procedure mainly includes three steps. The first step is to pre-define the TSR and the rotor size. These two parameters determine the output airfoils and the blade platform. Step two is the airfoil optimization based on the blade local speed ratio. 2D airfoil BEM computation is involved during airfoil optimization which provides values of local power coefficient and rotor solidity for the airfoil optimizer. In step three, results from BEM are collected at the final iteration of the airfoil optimization loop. Such results represent the condition of the optimal flow angle and chord length exists. Most of the computational effort has been put in step two where airfoils are optimized. The common characteristics of the resulted airfoils are high C_p over wide range of angle of attack. The airfoils are also very insensitive to roughness condition. As a result of the BEM computation, the optimal platform for the blade is obtained which can be regarded as the baseline shape for further optimization.

Acknowledgement

The research work is partially supported by two projects. The authors wish to express acknowledgement to the Danish Energy Agency (EUDP project j.nr. 64011-0094) and the Ministry of Science (DSF project Sagsnr. 12-130590).

References

[1] Hicks RM., Murman EM, and Vanderplaats GN. An assessment of airfoil design by numerical optimization. NASA TM X-3092, July 1974.
[2] Tangler JL, Somers DM. Status of the special purpose airfoil families. Proc. WINDPOWER'87, San Francisco, 1987.
[3] Tangle JL, Somers D M. NREL airfoil families for HAWT's. WINDPOWER'95, Washington D.C. Proc., 1995, 117-123.
[4] Fuglsang P, Bak C. Development of the RISØ wind turbine airfoils [J]. Wind Energy 2004; 7:145-162.
[5] Wang XD, Chen J, Shen WZ, Zhu WJ and Sørensen JN. Airfoils and methods for designing airfoils [P]. Application No. PCT/EP2010/056810, International patent application.
[6] Wang XD, Chen J, Shen WZ, Zhang S. Integration study on airfoil profile for wind turbines. *Journal of China Mechanical Engineering*. 2009, 20(2): 211-228.
[7] Bak C. Research in aeroelasticity EFP-2006: Key parameters in aerodynamic rotor design. RISØ National laboratory, Roskilde, Denmark.2007. RISØ-R-1611(EN).
[8] Shen WZ, Mikkelsen R and Sørensen JN. Tip Loss Corrections for Wind Turbine Computations. *Wind Energy* Wiley, 2005.
[9] Jonkman J, Butterfield S, Musial W and Scott G. Definition of a 5-MW reference wind turbine for offshore system development, *Technical Report NREL/TP-500-38060*, Golden, CO: National Renewable Energy Laboratory, February 2009.
[10] Drela M, XFOIL: An analysis and design system for low Reynolds number airfoils, Conference on Low Reynolds Number Aerodynamics, University of Notre Dame, 1989.

INTEGRATION OF AIRFOIL DESIGN DURING THE DESIGN OF NEW BLADES

L. Sartori[2], F. Grasso[1], C. Bottasso[2], A. Croce[2]

[1]Energy research Centre of the Netherlands (ECN), Westerduinweg 3, 1755LE, Petten, NL grasso@ecn.nl **(contact author)**
[2]Politecnico di Milano, Dip. Ing. Aerospaziale, Via La Masa 34, I-20156 Milano, Italy,
luca.sartori@polimi.it, carlo.bottasso@polimi.it, alessandro.croce@polimi.it

ABSTRACT

Despite the fact that the design of a new blade is a multidisciplinary task, often the different disciplines are combined together at later stage.
Looking at the aerodynamic design, it is common practice design/select the airfoils first and then design the blade in terms of chord and twist based on the initial selection of the airfoils. Although this approach is quite diffused, it limits the potentialities of obtaining optimal performance.
The present work is focused on investigating the benefits of designing the external shape of the blade including the airfoil shapes together with chord and twist.
To accomplish this, a design approach has been developed, where an advanced gradient based optimization algorithm is able to control the shape of the blade. The airfoils described in the work are the NACA 4 digits, while the chord distribution and the twist distribution are described through Bezier curves. In this way, the complexity of the problem is limited while a versatile geometrical description is kept.
After the details of the optimization scheme are illustrated, several numerical examples are shown, demonstrating the advantages in terms of performance and development time of integrating the design of the airfoils during the optimization of the blade.

INTRODUCTION

The design of a new rotor is a multidisciplinary task. The aerodynamics plays a crucial role, but of course an efficient structural design is also important to reduce the weight, while supporting the loads generated during the lifetime of the wind turbine. In regards of the general objective to decrease the cost of energy associated with the turbine, the aero-elastic behavior of the turbine cannot be neglected, as well as the role of the control strategies.
The present work is considering only of the aerodynamic side of this complex problem. Despite this, an important and innovative aspect is included, that is the integration of the airfoil design with the optimization of the chord and twist distributions.
Very often, the airfoils are selected in advance by using specific databases (i.e. ECN tool ATG), based on general requirements and experience of the designers. On one side this approach is convenient if the data related to the airfoils are experimental. This reduces also the uncertainties attached to the design. The airfoil aerodynamic characteristics play a fundamental role in designing the external shape of the blade, especially if a tool based on Blade Element Momentum (BEM) theory is used, where the 2D performance of the airfoils are a needed input that drives the optimization itself. The usage of existing, well known airfoils is also beneficial from structural point of view, since the internal layout should not reserve any surprise, once the shapes are investigated. The drawback of such approach is the limitation in terms of innovative solutions that can be obtained and design flexibility in regards of specific requirements.
In alternative, new airfoils can be designed depending on the actual requirements of the turbine. Starting from the middle 1980's, quite some work has been done to develop new airfoils specifically designed for wind turbines[1-4]. Specific studies[5-10] have been performed on airfoil design also at ECN. The main advantage of designing new airfoils is the possibility to address specific requirements in very effective way. On the other hand, extra expertise is required to develop new airfoils and ensure that the properties of the airfoils are gradually changing along the blade. From the design point of view, the right connection between airfoil performance and rotor performance is needed, since the design of new airfoils has the goal to improve the airfoil performance and , as consequence, the performance of the blade.

The novelty and the challenge of the present work is to explore the possibility of designing the external shape of the blade in just one design process that involves the design of the proper airfoils depending on the region of the blade and the optimization of chord and twist distribution. The main advantage is that the airfoils are designed directly based on rotor performance/requirements.
In the next paragraph the design approach, that is based on numerical optimization, is illustrated. Particular attention is paid in regards of the evaluation of the objective function and the geometrical parameterization; this is because the difficulty behind this integration is to combine the modeling of airfoils and blade.
Finally, some examples are presented to show the potentialities of this design scheme.

INTEGRATED DESIGN APPROACH

As mentioned in the introduction, the challenge of the present work is to be able to design an optimal blade including the 2D part (airfoils) and the 3D part (chord-twist distribution) at the same time. This implies a design approach that is robust, general and flexible.
The design scheme implemented in this work is based on multidisciplinary design optimization (MDO). In the most general sense, numerical optimization[11,12] solves the nonlinear, constrained problem to find the set of design variables, X_i, i=1, N, contained in vector $\boldsymbol{X}$, that will:

Minimize $F(X)$ (eq.1)

subject to:

$$g_j(X) \le 0,\ j = 1, M \quad \text{(eq.2)}$$

$$h_k(X) = 0,\ k = 1, L \quad \text{(eq. 3)}$$

$$X_i^L \le X_i \le X_i^U,\ i = 1, N \quad \text{(eq. 4)}$$

Equation 1 defines the objective function which depends on the values of the design variables, $\boldsymbol{X}$. Equations 2 and 3 are inequality and equality constraints respectively, while equation 4 defines the region of search for the minimum. The bounds defined for each degree of freedom by equation 4 are referred as side constraints. As it can be seen, the methodology is very general and able in principle to describe in a compact, efficient way problems with complex, interconnected sub components.
The FFSQP algorithm[13] has been implemented, that is a sequential quadratic programming (SQP) gradient based algorithm. The gradients have been approximated by finite differences.
Looking at the optimization process, different approaches are possible to combine the optimization of the airfoils with the optimization of the blade.
One option is to keep separate the design of the airfoils from the design of the blade. In this way, the design procedure is formed by two sub-optimization processes focused on airfoil and blade design. In practice, this would result in a complete optimization process of the airfoil(s) for each change in chord/twist.
Alternatively, the design process could be a so called “all in once” approach, where the optimization process is just one, including both the airfoils and the blade at the same time. From the implementation point of view, a single data structure is necessary in this case, containing degrees of freedom for both aspects of the design.
Decide in advance what is the best approach is hard. Depending on the specific problem, one procedure can be more convenient than the other one, in regards of quality of the optimal solution, computational time, robustness of the process. In this paper, the second approach has been preferred , mainly due to the interest of having a single design process dealing with the complete problem and trying to distinguish the roles/effects of the different sub-components.

Objective function evaluation

In order to evaluate the quality of the design produced by using this integrated approach, the performance of the rotor such the Cp_{max} and the annual energy production (AEP) have been used as objective functions.
The open source code WT_Perf[14] developed by NREL, has been implemented in the design procedure. WT_Perf is based on BEM theory, so the aerodynamic properties of the airfoils are a needed input. In the design scheme then, also a 2D solver is necessary to generate these input. XFOIL[15,16] panel code has been used, coupled with Viterna-Corrigan[17] analytical model to extend the numerical data between -180 and 180 degrees.

Geometrical parameterization

The selection of the most convenient degrees of freedom for the problem in exam, plays a crucial role in order to obtain an efficient and robust design scheme. In this case in particular, two parameterizations are needed: one for the airfoils and another for the blade. Looking at the design procedure from a computational point of view, it would be convenient to reduce as much as possible the total number of parameters to keep low the complexity of the problem. On the other hand, from the design perspective, being able to control the geometrical characteristics in details would be highly desirable.
Regarding chord and twist distributions these have been described through variable order Bezier curves. The main property of this approach is the fact that the shape of the curve is controlled by the position of few control points, as sketched in figure 1.

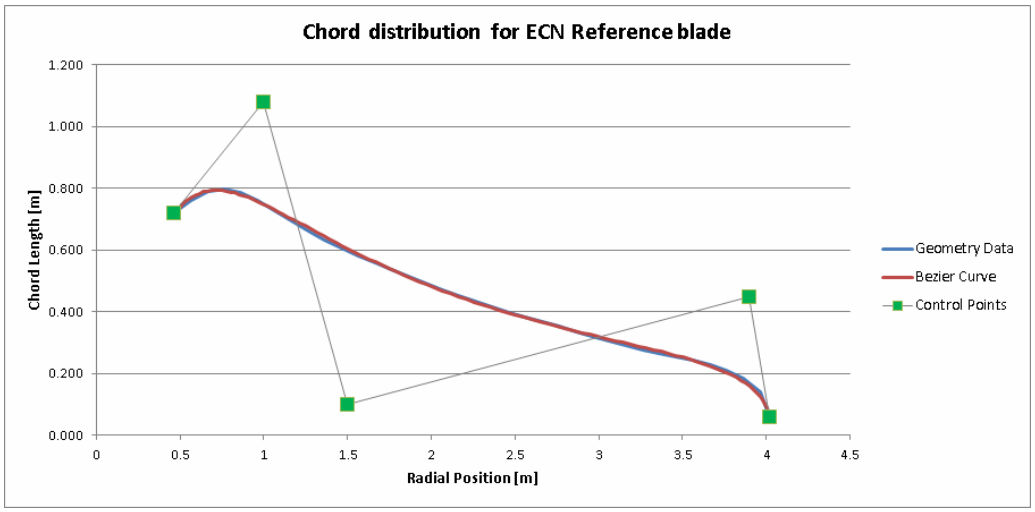

Figure 1 Example of chord distribution, by using fourth order Bezier curves.

The same approach could be conveniently used to describe the shape of the airfoils, as discussed by Samareh[18] and developed by Grasso[10]. However, a simplified approach has been preferred, that makes use of the geometrical parameterization of the NACA 4 digits airfoils. These geometries are described by a set of three equations related to the thickness distribution and the camber distribution.

$$y_t(x) = \frac{t}{0.2}c\left[0.2969\sqrt{\frac{x}{c}} - 0.1260\left(\frac{x}{c}\right) - 0.3516\left(\frac{x}{c}\right)^2 + 0.2843\left(\frac{x}{c}\right)^3 - 0.1015\left(\frac{x}{c}\right)^4\right] \quad \text{(eq. 5)}$$

$$y_c = \begin{cases} m\frac{x}{p^2}\left(2p - \frac{x}{c}\right) & for \quad 0 \le x \le pc \\ m\frac{c-x}{(1-p)^2}\left(1 + \frac{x}{c} - 2p\right) & for\ pc \le x \le c \end{cases} \quad \text{(eq. 6)}$$

The parameters that control the shape of the airfoils are the airfoil thickness (t), the maximum camber (m) and the chord wise location of the maximum camber (p). The complete description can be found in Abbott[19].
Although the usage of such class of airfoils limits the space of solutions that can be explored during the design, there are several advantages connected to this choice. It has been already mentioned the crucial role of the number of degrees of freedom in regards of the computational complexity of the design problem; for this parameterization, only three parameters are needed for each airfoil. The second and more important aspect is connected to the geometrical properties of the airfoils generated; due to the analytical description, any set of three parameters leads to a smooth shape. Especially in this first attempt to couple airfoil design and blade design, this fact allows to skip many checks on the regularity of the airfoil geometries, reducing the computational time and the number of trial unfeasible designs eliminated during the process.

NUMERICAL EXAMPLES

In this paragraph, several examples regarding the integrated airfoil/blade design are illustrated. The reference geometry has been a two blade rotor developed at ECN for marine applications, equipped with NACA 4418 airfoil (see table 1).

Table 1: Main characteristics of the reference blade.

Rotor radius [m]	4.022
Design water speed [m/s]	1.5
Rotor speed [RPM]	24.93
Pitch angle [deg]	-1.3
AEP [GWh/year]	0.018
Cp_{max} [-]	0.438

Also, for all the examples, a rectangular blade with zero twist, equipped with NACA 4418, airfoil has been used as baseline.
In terms of degrees of freedom, fourth order Bezier curves have been selected for the twist and chord distributions. Regarding the airfoils, the thickness has been kept constant to 18%. This is due to the absence in the current design scheme, of structural constraints; without these, very preliminary tests showed the tendency to reduce as much as possible the thickness of the airfoils in order to reduce the drag. The implementation of a simple structural model in further development, is expected to counter balance this trend and provide a more realistic solution.

Example 1: chord, twist and two airfoils to maximize the Cp

The objective of the test is to design a blade where the Cp_{max} is optimized, changing the chord and twist distributions and the camber characteristics of two airfoils installed along all the blade. Figures 2 and 3 show the optimal distributions for the chord and the twist.
Looking at the results, the Cp improves significantly compared to the baseline, but also in regards of the above mentioned reference blade, the Cp has larger value. It should be noticed that the baseline is a rectangular blade without any twist, so a very low Cp should be expected.
In figure 4, the comparison between the shapes of the airfoils is illustrated. As it can be seen, the optimal airfoils are quite different in terms of camber line, since they are more aft loaded. In figure 5 and 6, the aerodynamic characteristics of the airfoils, calculated with XFOIL, are shown. It should be noticed that both the new airfoils have better lift and efficiency performance.

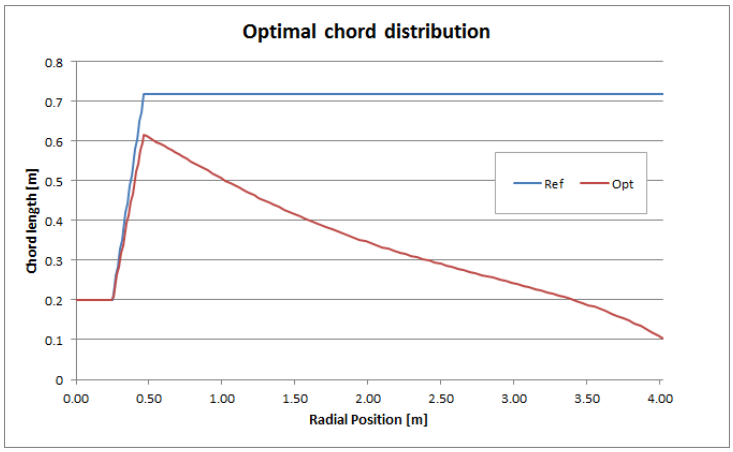

Figure 2 Optimal chord distribution.

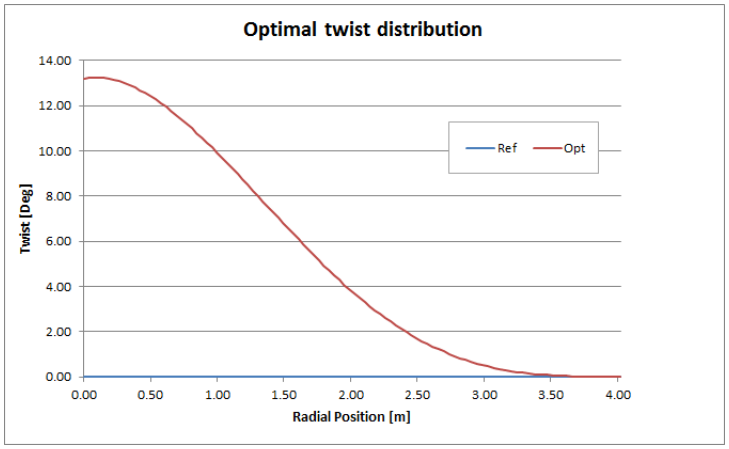

Figure 3 Optimal twist distribution.

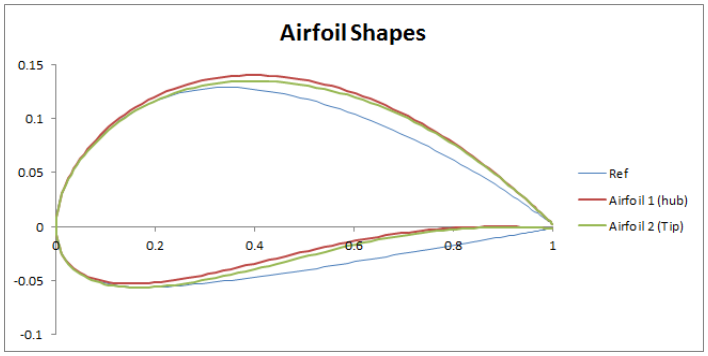

Figure 4 Optimal airfoil shapes.

Blade	Cp	Airfoil 1	Airfoil 2	Time [sec]
Baseline	0.2249	4418	4418	-
Opt	0.4531	6518	5518	8675.2

Table 2 Summary of the optimization process.

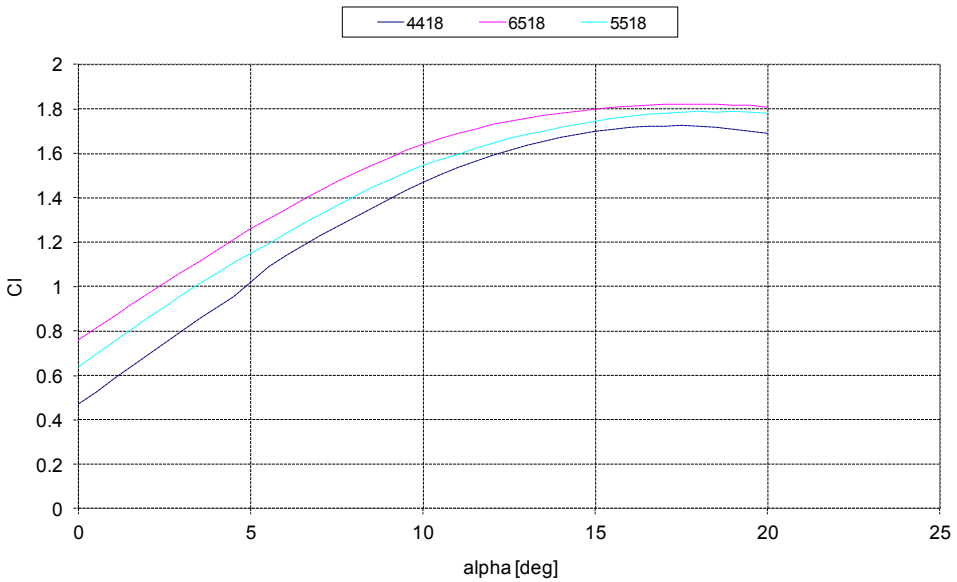

Figure 5 Lift curves of the airfoils involved during the design. XFOIL predictions. Free transition, 2 millions Reynolds number.

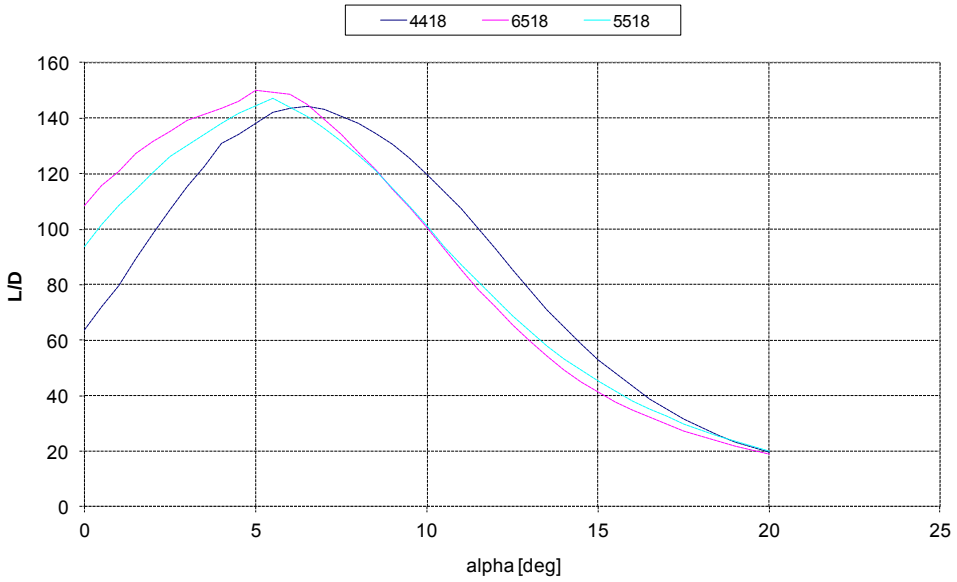

Figure 6 Efficiency curves of the airfoils involved during the optimization. XFOIL predictions. Free transition, 2 millions Reynolds number.

Example 2: chord, twist and three airfoils to maximize the Cp

The same test illustrated in the first example has been performed by increasing the number of airfoils along the blade, in order to check the robustness of the design procedure. As it can be observed, both the chord and twist distribution are still smooth, the airfoils are consistent with each other and the performance of the blade are improved.

Blade	Cp	Airfoil 1	Airfoil 2	Airfoil 3	Time [sec]
Baseline	0.2249	4418	4418	4418	-
Opt	0.4534	6518	5518	5518	19286

Table 3 Summary of the optimization process.

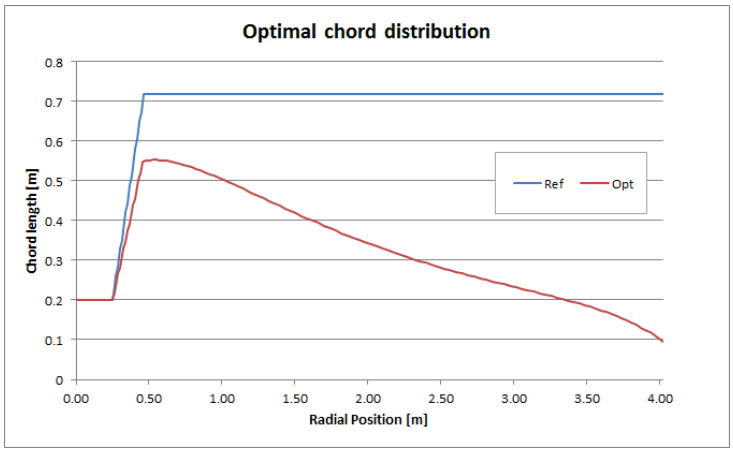

Figure 7 Optimal chord distribution.

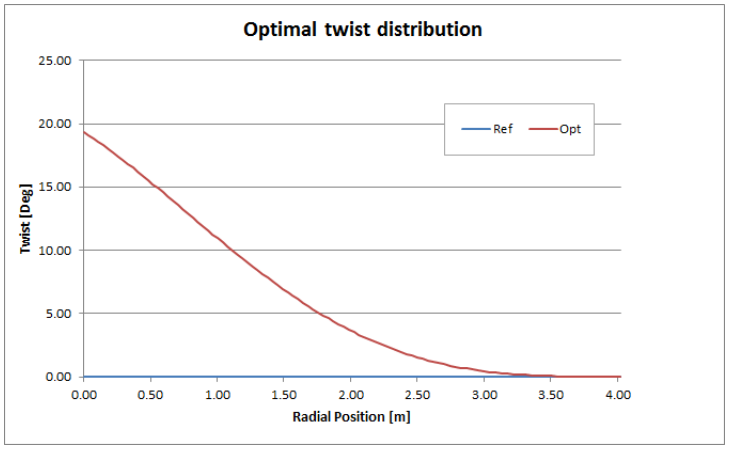

Figure 8 Optimal twist distribution.

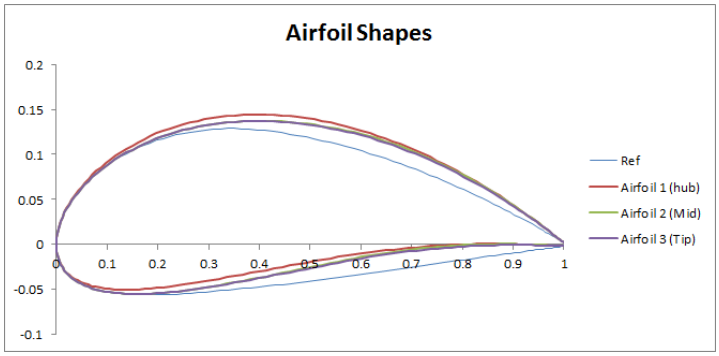

Figure 9 Optimal airfoil shapes.

Looking at the computational time, this increased in the second example, due to the increase of degrees of freedom and the amount of airfoil calculations for each iteration.

CONCLUSIONS

An investigation focused on the integration of airfoil design into blade design has been performed. In this first attempt, open source solvers have been used, coupled with an advanced optimization algorithm.
The first results proved that design the blades in combination with airfoil design, lead to better overall performance, including a fair distribution of airfoils along the blade.
In order to obtain more realistic results however, the description of the airfoils should be generalized by using for instance, Bezier curves also for the airfoil shapes.
Also, more accurate solvers, like RFOIL and Aeromodule, should be implemented. In the present work, the selection of the tools has been driven by the objective to focus the investigation on the basic aspects of such integration, more than on obtaining optimal solutions.
From this point of view, it cannot be neglected the importance of the structural model to work in multidisciplinary way with a complete design scheme. In the examples, the thickness has been prescribed; by adding a structural model, the thickness distribution along the blade could let be free to change and the optimal value would be a result of competing structural and aerodynamic tendencies. This will be the subject of future work.

ACKNOWLEDGMENTS

The present work has been carried out partially under the European Project INNWIND.EU (FP7 project no. 308974).

REFERENCES

[1] Tangler, J.L., Somers, D.M., "NREL Airfoil Families for HAWT's". Proc. WINDPOWER'95, Washington D.C., 1995; pp. 117–123.

[2] Björk, A., "Coordinates and Calculations for the FFA-W1-xxx, FFA-W2-xxx and FFA-W3-.xxx Series of Airfoils for Horizontal Axis Wind Turbines". FFA TN 1990-15, Stockholm, Sweden 1990.

[3] Timmer, W.,A., van Rooij, R.P.J.O.M., "Summary of the Delft University Wind Turbine Dedicated Airfoils". AIAA-2003-0352.

[4] Fuglsang, P., Bak, C., "Design and Verification of the new Risø-A1 Airfoil Family for Wind Turbines". AIAA-2001-0028.

[5] Grasso, F., "Hybrid Optimization for Wind Turbine Thick Airfoils", AIAA Proceedings, 9th AIAA Multidisciplinary Design Optimization Specialist Conference, 23-26 April 2012, Honolulu, HI, USA. AIAA 2012-1354.

[6] Grasso, F., "Development of Thick Airfoils for Wind Turbines", AIAA, Proceedings, 50th AIAA Aerospace Sciences Meeting, 9-12 January 2012, Nashville, TN, USA. AIAA 2012-0236.

[7] Grasso, F., "Design and optimization of Tidal Turbine Airfoils", Journal of Aircraft, AIAA, Vol.49, No.1, Jan.-Feb. 2012.

[8] Bizzarrini, N., Grasso, F., Coiro, D.P., "Numerical Optimization of High Efficiency, Low Noise Airfoils", AIAA, Proceedings, 29th AIAA Applied Aerodynamics Conference, 27-30 June 2011, Honolulu, HI, USA, AIAA 2011-3187.

[9] Bizzarrini, N., Grasso, F., Coiro, D.P., "Genetic Algorithms in Wind Turbine Airfoil Design", EWEA, EWEC2011, 14-17 March 2011, Bruxelles, Belgium.

[10] Grasso, F., "Usage of Numerical Optimization in Wind Turbine Airfoil Design", AIAA, Proceedings, 28th AIAA Applied Aerodynamics Conference, 28 june-1july 2010, Chicago, IL, USA, AIAA 2010-4404. Also Journal of Aircraft, AIAA, Vol.48, No.1, Jan.-Feb. 2011, DOI: 10.2514/1.C031089.

[11] Fletcher, R., "Practical Methods of Optimization", Wiley, 1987.

[12] Pedregal, P., "Introduction to Optimization", Springer, 2004, ISBN 0-387-40398-1.

[13] Zhou, T. L. , "User's Guide for FFSQP Version 3.7", April, 1997.

[14] Platt, A.D., Buhl Jr., M.L., "WT_Perf User guide for version 3.05.00", NREL, Tech. Report, Nov. 2012.

[15] Drela, M.,XFOIL: An Analysis and Design System for Low Reynolds Number Airfoils, Conference on Low Reynolds Number Airfoil Aerodynamics, University of Notre Dame, June 1989.

[16] Drela, M., "XFOIL 6.94 User Guide", MIT Aero & Astro, Dec 2001.

[17] Viterna L. A. and Corrigan R. D., "Fixed Pitch Rotor Performance of Large Horizontal Axis Wind Turbines", *DOE/NASA Workshop on Large Horizontal Axis Wind Turbines*, 28–30 July 1981, Cleveland, OH.

[18] Samareh, J., A., "Survey of Shape Parameterization Techniques for High-Fidelity Multidisciplinary Shape Optimization", AIAA Journal, Vol. 39, No. 5, May 2001, pp. 877-884.

[19] Abbott, I., Von Doenhoff, A., "Theory of Wing Sections", Dover Publications, Inc., Dover edition, 1958.

LIFT AND DRAG MEASUREMENTS OVER A WIND TURBINE BLADE WITH MICRO-FIBRILLAR STRUCTURES

V. Maldonado[1], F. Mehdi[1], N. Laal Dehghani[1], D. McKeon[1], B. Aksak[1], P. Glass[2], M. Sitti[2] J. Sheng[1], L. Castillo[1]

[1]Texas Tech University, Department of Mechanical Engineering, Lubbock TX 79409 USA
[2]Nanogrip, Pittsburg PA 15213 USA

ABSTRACT

The aerodynamic lift and drag of wind turbine blades covered with bio-inspired mushroom-like fibrillar structures is measured in order to demonstrate the lift enhancement and drag reduction potential of this novel structured surface. The micro-fibrillar structures forming the fiber array are composed of cylindrical stalks which gradually become larger close to their terminal end. The fibers are 100 μm in length, 50 μm in stalk diameter, and 100 μm in tip diameter. The micro-fibers are applied to the mid-section of an S809 airfoil wind turbine blade model and tested inside the Corssin Wind Tunnel at Johns Hopkins University. The blade was tested at a free-stream velocity of 10 m/s corresponding to a Reynolds number based on chord, Re_c of $2.08x10^5$ at a range of discrete angles of attack, α. Measurements of blade surface pressure and wake velocity deficit were made in order to compute the lift and drag coefficients. Preliminary results suggest that lift and drag are respectively significantly enhanced and reduced, where maximum drag reduction of about 38% occurred at $\alpha = 0^\circ$. These promising results motivated a more comprehensive study consisting of direct high-resolution load cell measurements on a similar S809 wind turbine blade model at Texas Tech University. Details of the blade design and experimental setup are presented in this paper, however the results are not included due to a conflict of interest pending journal publication.

INTRODUCTION

Bio-inspired structured surfaces have been the subject of considerable investigation over the last decade. The desire to employ the evolutionary design and functionality found in nature and bio-organisms to engineered man-made systems is of keen interest to the scientific community. The architecture of biological materials is highly organized from the molecular-scale to the macro-scale, which results in a material with a myriad of properties that provide multi-functionality. The properties of the materials and surfaces result from a complex interplay between the physical

and chemical surface structure and its interaction between a fluid or solid medium. Such bio-inspired surfaces can be utilized to develop multi-scale systems and devices that exhibit superior functional properties. This may be accomplished by understanding the surfaces' fluid/ structure phenomena and utilizing this knowledge to synthesize robust surfaces that can withstand real-world environmental conditions.

A variety of synthetic structured surfaces with unconventional topographical characteristics have been developed and analyzed to show a diverse set of functional attributes. Some of the more common properties include: superhydrophobicity, self-cleaning, selective adhesion, drag reduction in fluid flow, and energy harvesting/ conversion. Many times these surfaces display multi-functionality, as is the case with superhydrophobic surfaces [1] which also have the ability to self-clean [2] in the presence of a liquid or water. Such functional materials were inspired from nature after the famed lotus leaf [3] which repels water by forming it into droplets which roll off its surface. One bio-inspired surface in the form of tubercles was inspired from the humpback whales' flippers which give the whale enhanced maneuverability. Bio-inspired tubercles have already been implemented as a passive flow control technique to delay stall on flipper-like wind tunnel models [4]. Studies have shown that leading edge tubercles have the ability to delay stall at high angles of attack, and therefore increase turbine power when the blades operate in limited post-stall flow conditions [5].

A bio-inspired surface directly relevant to that of the current study is the synthetic shark skin [6]. The skin of fast-swimming sharks reduces the drag experienced by the shark as it swims through water. Tiny scales covering the skin are shaped like riblets and are aligned in the direction of fluid flow. Although shark-skin inspired surfaces have been shown to provide drag reduction of up to 9.9% [7], it is an incremental increase and not sufficient to have a significant impact in applications where this technology may be applied.

In the current investigation, a novel bio-inspired surface in the form of micro-fibrillar structures synthesized on a rubber substrate was applied on the smooth surface of an S809 airfoil wind turbine blade model. The geometric design and micro-fabrication of the fibrillar structures were inspired by the shape of mushrooms and is outlined in the study by Aksak *et al.* [8]. The functionality of these structures for aerodynamic performance enhancement (particularly drag reduction) was tested by measuring the lift and drag generated by the wind turbine blade. Prior research on the subject has demonstrated that by manipulating the surface characteristics, i.e. surface roughness, chemistry, wall compliance and by altering the near wall fluids properties such as effective viscosity, one can impact the genesis, growth and dissipation of near wall coherent structures which correlate strongly with high wall shear stress events that dominate viscous skin friction and drag Sheng *et al.* [9] and Hong and Katz [10].

Preliminary results obtained at Johns Hopkins University (limited by the use of indirect lift and drag measurement methods) are presented. These results represent a feasibility study for drag reduction and served as a motivation to perform accurate load cell measurements with a specially designed S809 wind turbine blade at Texas Tech University.

EXPERIMENTAL SETUP AND METHODS

Bio-inspired Micro-fibrillar Structures

Mushroom-tipped fibrillar structures are used as drag reduction surfaces in this study. The individual structures forming the fiber array are composed of cylindrical stalks which gradually get larger close to its terminal end. The fibers are 100 μm in length, 50 μm in stalk diameter, and 100 μm in tip diameter. The arrangement of the fibers is square packing with center-to-center distance of 120 μm. In addition, the alignment of the stalk and the tip can be controlled separately from 0 to 45 degrees which aids in creating surfaces with directional drag properties. Moreover, it is possible to create fiber arrays with heterogeneous fiber geometry such that the individual fibers forming the array have varying cross-sectional shape, diameter, and spacing. This tuning ability could provide optimal performance for transitional flows. For improved durability, fibers are made of a commercially available two-part polyurethane (ST-1085, BJB Enterprises). The manufacturing process starts with the fabrication of cylindrical fibers out of a photoresist (SU-8, Microchem) and then molding them with a silicone rubber to obtain a negative flexible mold Aksak *et al.* [8]. This flexible mold is then used to fabricate polyurethane microfibers. A post processing fabrication step based on dipping is performed to obtain the mushroom tipped fibers used in this study, Murphy *et al.* [11]. Finally, the cost of manufacturing and the scalability of the fabrication technique make this technology commercially viable.

Wind Tunnel Methods and S809 Wind Turbine Blade Model

The wind turbine experiments of the feasibility investigation were performed at the Corrsin Wind Tunnel at The Johns Hopkins University. This facility is a two-story closed-return wind tunnel with a 25:1 primary and a 1:1.27 secondary contraction. The test section contains a 1.22 m width, 0.91 m height, and a 10 m length where the background turbulence intensity is less than 0.1% at the end of the test section under normal operation. This unique facility is equipped with a removable active grid in order to generate free-stream turbulence. However, the experiments were conducted without the use of the active grid.

The wind turbine blade tested is designed with the S809 airfoil which is a 21% chord thickness airfoil utilized in horizontal-axis wind turbines. Figure 1(a) is a schematic of the S809 airfoil with the lift and drag forces representative of the experimental setup. The blade model is fabricated from an array of polycarbonate S809 airfoil ribs covered with a flexible plastic skin to retain its precise curvature. The 2-D blade spans the width of the wind tunnel test section (1.2 m) and has a constant chord of 0.25 m. The operating Reynolds number based on chord at the experimental free stream velocity of 10 m/s was $Re_c = 2.08\text{x}10^5$ which corresponds to the laminar flow regime. The blade was instrumented with an array of 36 static pressure ports

(18 each on the suction and pressure surfaces) at the mid-span location to acquire the pressure distribution for both the baseline surface and the micro-fiber film surface. Figure 1(b) is a photograph of the wind turbine blade mounted in the wind tunnel. Notice the micro-fibrillar film (white surface) around the blade and the pitot-tube directly behind it. The pressure taps were logarithmically distributed as a function of the chord, with a higher concentration of taps near the leading edge to capture a greater spatial resolution in the pressure readings in this region of the blade compared to the trailing edge. The blade pressure taps were individually connected to a pressure transducer capable of sampling the pressure differential, $P - P_\infty$ between the pressure tap on the surface of the blade and the reference free-stream pressure. A complication exists in the application of the micro-fibrillar film, which creates a small "step" between the baseline surface (which is flush with the pressure ports) and the film. This is expected to create a small error in the transducer reading of the surface pressure reading. The sample time was one minute at a sampling rate of 1000 Hz from which an average pressure differential reading was obtained. The blade is mounted inside the wind tunnel using two metal brackets which were adjusted to change the angle of attack to a range of angles of attack from 0 to 14 degrees.

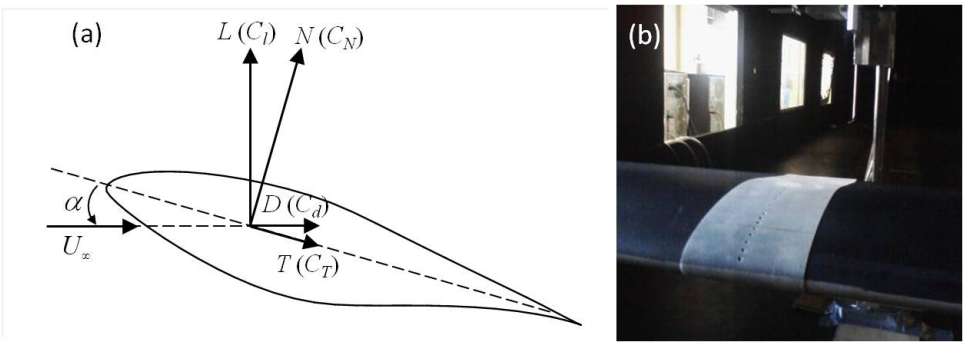

Figure 1: (a) Schematic of an S809 airfoil with lift and drag forces and (b) S809 wind turbine blade covered with micro-fibrillar structures on the center section

The velocity deficit in the wake of the blade was measured utilizing a minimally intrusive 2-mm diameter pitot-tube connected to the total (stagnation) pressure and static pressure ports of a pressure transducer sampled for one minute at a sampling rate of 1000 Hz. The pitot-tube was mounted on a traverse mechanism and traversed across the wake in 5 mm increments at a fixed downstream distance of one blade chord length, $1c$ (equal to 0.25 m) behind the blade trailing edge. A study has shown that this is an adequate downstream distance for valid wake velocity deficit measurements in airfoils at angles of attack below stall [12]. However, the accuracy of these measurements captured with a pitot-tube (as opposed to with hot-wire anemometry) decreases as the size of turbulent scales and intensity in the wake increases as the flow begins separating.

Integrated Load Cell S809 Wind Turbine Blade Model

An integrated load-cell S809 wind turbine blade model was specially designed for high-resolution lift and drag measurements in order to conclusively test the functionality of micro-fibrillar structures for aerodynamic enhancement of airfoils in an air-fluid medium. The results of this groundbreaking study are omitted for conflict of interest reasons, however some details of the blade design and fabrication are worth mentioning. The blade model consists of a metal skeleton with two outer "dummy" blade sections serving as a foundational ground (and to prevent wingtip vortices and ensure two-dimensionality of the flow) for the middle blade section which is mounted to two load cells (ATI Mini40-E with a resolution of $F_x, F_y = 1/100$N and $F_z = 1/50$N) on either side. This section is the portion of the blade where the aerodynamic loads are measured and is covered with micro-fibrillar structures on the top (suction) and bottom (pressure) surfaces. The blade contains a total span of 1.3 m and a constant chord (2-D) of 0.375 m. The center blade section spans 0.6 m and the outer dummy sections span 0.5 m each. A CAD assembly drawing of the wind turbine blade skeleton is shown in fig. 2(a) while a photograph of the fabricated blade is shown mounted inside the wind tunnel at Texas Tech University in fig. 2(b). Notice the the micro-fibrillar structures (white surface) applied to the mid-section of the blade. The relatively large area of synthesized micro-fibers (about 0.47 m^2) demonstrates the large scale manufacturing capability of this structured surface, which could otherwise become a barrier for practical application in medium to large-scale aerodynamic systems.

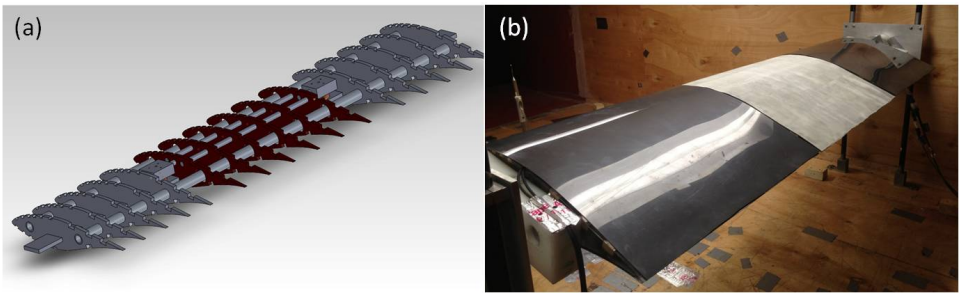

Figure 2: (a) CAD assembly drawing of the S809 wind turbine blade skeleton (b) Load-cell integrated S809 wind turbine blade covered with micro-fibrillar structures on the center section

RESULTS AND DISCUSSION

Blade Surface Pressure Measurements

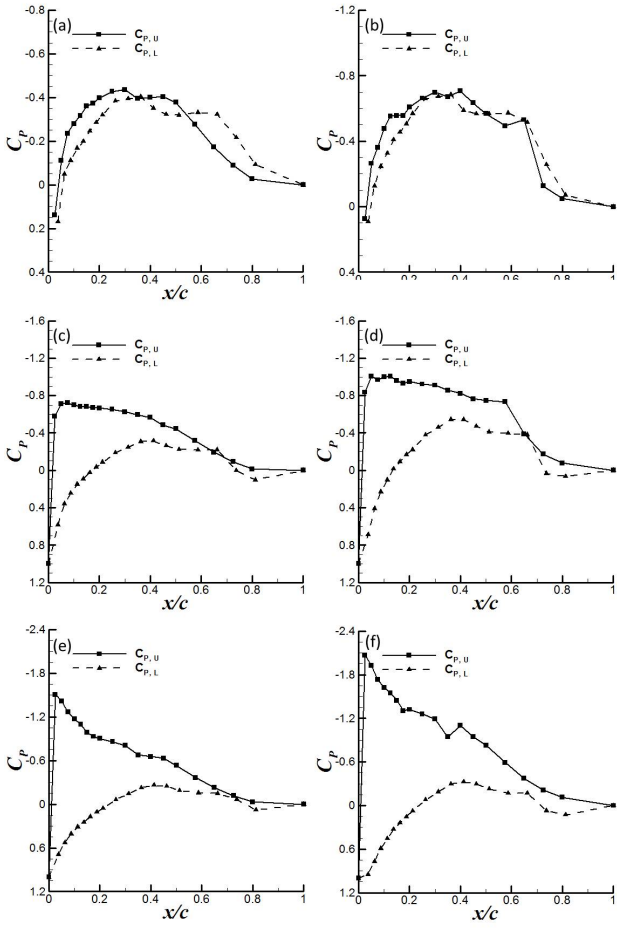

Figure 3: Blade pressure distributions for baseline (a), (c), (e) and micro-fiber (b), (d), (f) cases: (a) and (b) $\alpha = 0^\circ$, (c) and (d) $\alpha = 4^\circ$, (e) and (f) $\alpha = 8^\circ$

The blade surface pressure coefficient, C_P distributions as a function of the non-dimensional chord distance, x/c were acquired in order to compute the normal force coefficient, C_N (which is a significant component of the lift coefficient) for each case via numerical integration using Simpson's 1/3 Rule. The pressure coefficient at each pressure tap was acquired according to the

procedure described above and is equivalent to the static pressure at the pressure tap, P minus the reference free-stream pressure, P_∞ upstream of the wind turbine blade divided by the dynamic pressure, $1/2\rho U_\infty^2$.

Figure 3 are plots of the pressure distributions for the baseline fig. 3(a), (c), and (e) and micro-film fig. 3(b), (d), and (f) cases at angles of attack of 0°, 4°, and 8°. We observe that at $\alpha = 0°$, both the upper (suction) and lower (pressure) pressure coefficient curves, $C_{P,\,U}$ and $C_{P,\,L}$ respectively overlap each other. This suggest that when numerically integrated, the normal force coefficient (which is equivalent to the lift coefficient at $\alpha = 0°$) will be computed to a value close to $C_l = 0$. As the angle of attack is increased to $\alpha = 4°$, the suction peak of the micro-fiber case in fig. 3(d) reaches a higher negative value of $C_P \simeq -1.0$ compared to $C_P \simeq -0.72$. This translates to a higher numerically computed normal force coefficient (and thus lift) for the micro-fiber case, as will be shown later in the aerodynamics results. This trend of a higher suction peak and more negative upper pressure coefficient values for the micro-film cases continues as the angle of attack is increased further to $\alpha = 8°$, and $\alpha = 12°$ and 14° shown in fig. 4(a) and (b) and fig. 4(c) and (d). These results indicate that micro-fibrillar structures enhance lift at these angles of attack.

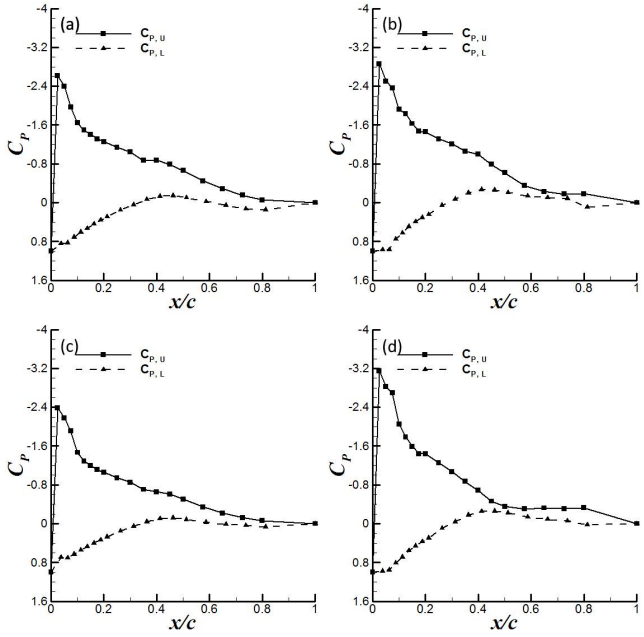

Figure 4: Blade pressure distributions for baseline (a), (c) and micro-fiber (b), (d) cases: (a) and (b) $\alpha = 12°$, (c) and (d) $\alpha = 14°$

Blade Wake Velocity Deficit Measurements

The velocity deficit in the wake of the wind turbine blade was measured utilizing a pitot-tube as described earlier. The purpose is to compute the total drag coefficient of the blade via numerical integration of the momentum deficit in the wake velocity distribution. The wake was measured for the angles of attack of 0, 4, 8, 12, and 14 degrees and are presented respectively in fig. 5(a) to (e).

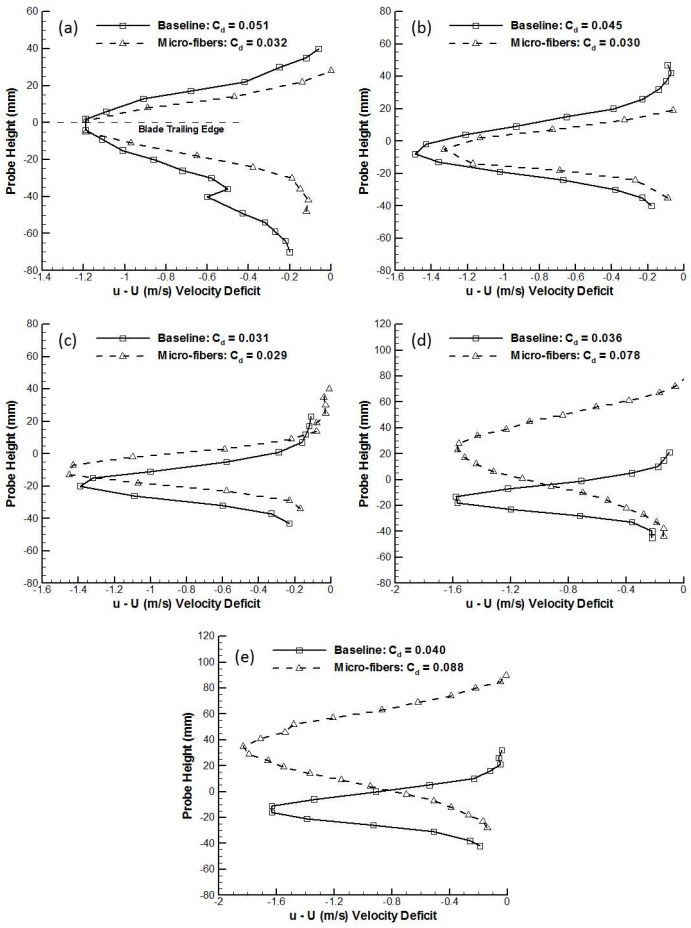

Figure 5: Wake velocity deficit distributions for the baseline and micro-fiber cases: (a) $\alpha = 0^\circ$, (b) $\alpha = 4^\circ$, (c) $\alpha = 8^\circ$, (d) $\alpha = 12^\circ$, and (e) $\alpha = 14^\circ$

The measured *Probe Height* on the vertical, y axis is relative to the blade trailing edge, i.e. a height of zero corresponds to a pitot-tube probe measurement at the same height as the trailing edge. Plotted on the horizontal, x axis is the wake *Velocity Deficit*, $(\bar{u} - U_\infty)$ defined as the pitot-tube measured stream-wise u component of velocity minus the free-stream velocity outside the wake, U_∞. The velocity deficit was measured 0.25 m (one chord length) downstream from the blade trailing edge. The resulting baseline and micro-fibers drag coefficient from numerical

integration of the wake distributions is also labeled in the plots. However, the drag coefficients will be discussed more details in the aerodynamics results of the next section. As shown in fig. 5(a) for the cases at $\alpha = 0^\circ$, the micro-fibers significantly reduce the momentum loss in the wake. The velocity deficit for a given probe height (particularly in the wake region below the blade) is lower than the baseline case. Due to the smaller wake profile, the integration from the bottom to the top of the wake results in a reduction of the baseline drag from $C_d = 0.051$ to $C_d = 0.032$ which represents a 37% drag reduction. As the angle of attack is increased to $\alpha = 4^\circ$ and 8° in fig. 5(b) and (c), the relative size of the baseline and micro-fibers wake distributions diminishes such that the drag coefficient of the blade with micro-fibers approaches that of the baseline case and the percentage of drag reduction decreases significantly. For angles of attack approaching stall at 12° and 14° in fig. 5(d) and (e), the role of the micro-fibers is drastically reversed where these cases create a larger momentum loss and thus drag compared to the baseline cases. It is important to note however, that the error associated in pitot-tube measurements increases with angle of attack; the pitot-tube can only measure the steady stream-wise u velocity component and not fluctuations in the vertical v component associated with turbulent wakes. These drag feasibility results, particularly at the higher angles of attack are intended only as estimations that motivated valid and direct load cell drag measurements of a similar S809 airfoil blade model as discussed.

Numerical Integration and Aerodynamic Lift and Drag

In this section, we examine how the aerodynamic lift and drag coefficients are obtained from the pressure coefficient and wake velocity deficit distributions presented earlier. Regression analysis was performed which consists of fitting 3th and 4th order polynomials to the experimental data resulting in negligible approximation errors (r-squared values close to one). For the pressure coefficient, C_P distributions, 20 discrete elements between a and b along the chord is given in Eq. 1 utilizing Simpson's 1/3 Rule. The variables a and b represent the non-dimensional chord-distance $x/c = 0$ and 1 respectively and n is the number of elements.

$$\int_a^b C_\mathrm{P} d\,(x/c) \approx \frac{(b-a)}{3n}\left[C_\mathrm{P}(x/c)_o + 4C_\mathrm{P}(x/c)_1 + 2C_\mathrm{P}(x/c)_2 + 4C_\mathrm{P}(x/c)_3 + \cdots + C_\mathrm{P}(x/c)_n\right] \quad (1)$$

Similarly for the wake profiles, the numerical integration of the velocity deficit, $(U_\infty - \bar{u})$ utilizing Simpson's 1/3 rule across the wake in the wall-normal direction, y is expressed as follows. The number of elements for each wake profile varies and is correlated to the number of pitot-tube measurements made across the wake in order to resolve it properly.

$$\begin{gathered}\int_a^b (U_\infty - \bar{u})\, d(y) \simeq \\ \frac{(b-a)}{3n}\left[(U_\infty - \bar{u})y_o + 4(U_\infty - \bar{u})y_1 + 2(U_\infty - \bar{u})y_2 + 4(U_\infty - \bar{u})y_3 + \cdots + (U_\infty - \bar{u})y_n\right]\end{gathered} \quad (2)$$

Where a and b are the lower and upper edge of the wake profile where the velocity deficit approaches zero. The normal force coefficient, C_N was computed by expanding Simpson's 1/3 rule on Eq. 1 to the integration of the lower minus upper pressure coefficient curves, $C_{\mathrm{P,\,L}}$and $C_{\mathrm{P,\,U}}$ shown below.

$$C_N = \int_{x/c=0}^{x/c=1} \left(C_{P,\,L} - C_{P,\,\mathrm{U}}\right)\, d\left(x/c\right) \tag{3}$$

The drag coefficient, C_d was computed by substituting the expression for the numerical integration of the velocity deficit in Eq. 2 into Eq. 4, where U_∞ and c is the free-stream velocity and wind turbine blade chord, with constant values of 10 m/s and 0.25 m

$$C_d = \frac{2}{U_\infty c} \int_{-\infty}^{+\infty} \left(U_\infty - \bar{u}\right)\, dy \tag{4}$$

Prior to calculating the lift coefficient, the tangential force coefficient, C_T was calculated according to the relation.

$$C_T = \frac{C_d}{\cos\alpha} - C_N \tan\alpha \tag{5}$$

Finally, the lift coefficient, C_l is found by substituting the normal and tangential coefficients into the expression below.

$$C_l = C_N \cos\alpha - C_T \sin\alpha \tag{6}$$

The lift and drag coefficients were computed and plotted as function of angle of attack in fig. 6(a) and (b) respectively. The plot of lift coefficient suggests that there is significant lift enhancement for all angles of attack except at α = 0° with micro-fibrillar structures. These results should be scrutinized in light of the small "step" that exists between the pressure taps and micro-film surface. Physically speaking, a higher lift coefficient caused by more negative pressure coefficient measurements via the pressure taps is a manifestation of higher speed flow over the pressure tap, U_P as considered by the equation, $C_P = 1 - \left(U_P/U_\infty\right)^2$. This suggest that the pressure transducer is measuring higher overall flow velocities with the micro-fibers surface, which may be due to the small circular cavity created by the micro-fiber surface and the actual blade surface. Such large enhancement in lift has not been shown in the literature with any other structured surface, hence these results are most likely erroneous and should be either validated or disproved with high resolution load cell measurements.

The drag coefficient plot of fig. 6(b) displays a peculiar behavior, namely there is a reversal in drag reduction at about α = 8°. The micro-fibrillar structures on the blade cause significant drag reduction at angles of attack below this angle, and equally adverse drag penalty at the higher angles of α = 12° and 14°. The baseline drag coefficient curve decreases from C_d values of 0.051, 0.045, and 0.031 respectively from α values of 0°, 4°, and 8°. For these same angles of attack, the micro-fiber cases yield C_d values of 0.032, 0.030, and 0.029. This represents decreasing drag reduction of 37%, 33% and 6%. However, at α = 12° and 14° the drag coefficient increases from 0.036 to 0.040 for the baseline case and from 0.078 and 0.088 for the micro-fibers case, which implies a very drastic drag penalty of 117% and 120%. Aside from a possibly sig-

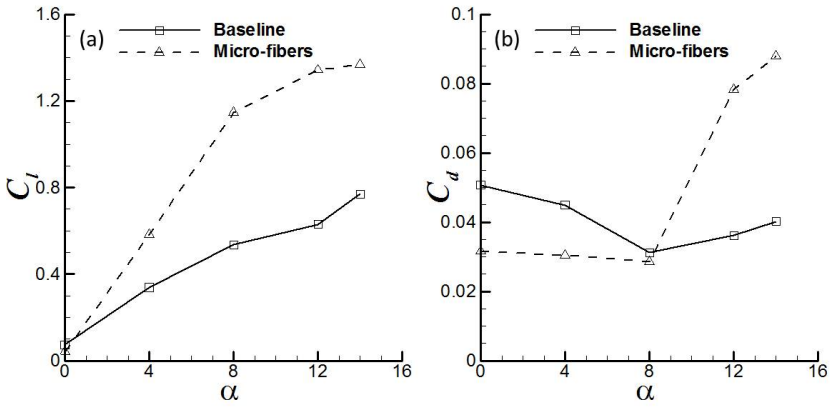

Figure 6: Aerodynamic coefficients: (a) C_l vs α and (b) C_d vs α

nificant error introduced by measuring the wake with a pitot-tube at the higher angles of attack, it is unclear what fluid/ boundary layer mechanisms are responsible for the drag reduction and penalties computed. Various structured surfaces in the literature have demonstrated the potential for modest drag reduction. It is believed that this is accomplished via a reduction in the wall shear stress (and thus skin friction) created by the existence of a slip velocity at the structure/ fluid boundary. The increase in the drag observed in the micro-fibers cases at $\alpha = 12^\circ$ and 14° would imply however that the micro-fibers may transition the fluid to turbulent flow due to the production of stream-wise vortices by the micro-fibers. More detailed experiments, particularly to analyze the structure of the boundary layer are necessary in order to understand and apply micro-fibrillar structures for aerodynamic systems.

CONCLUSIONS

Significant drag reduction of high-Reynolds number energy systems and transportation vehicles has enormous implications on the energy and sustainability of these systems, yet the development and application of a suitable structured surface has eluded science. In this feasibility study, we show that significant drag reduction may be possible with proposed micro-fibrillar structures. These structures were applied on a small section of an S809 wind turbine blade and the surface pressure distributions and wake velocity deficit was measured at a free-stream velocity of 10 m/s (resulting in a Reynolds number of $2.08x10^5$) and a range of angles of attack. It was shown via indirect and approximate drag coefficient computations that maximum drag reduction of 37% (compared to the baseline) occurs at zero degrees angle of attack. However, at angles of attack of 12° and 14° these results suggest a significant drag penalty.

Fundamental questions remain, of which most important is addressing the mechanism by which micro-fibers yield significant drag reduction, and how the inner and outer flow of the

boundary layer interact. Further studies are planned, which include high resolution load-cell measurements with the specially designed wind turbine blade discussed earlier. One of the main goals is to resolve the boundary layer and analyze its inner and outer flow structure utilizing laser-based flow techniques such as particle image velocimetry (PIV). Direct Numerical Simulations (DNS) will be performed in parallel in order to gain insight and complement the experiments. This will lead to an understanding of how to create optimum micro-fiber geometries in order to increase drag reduction and apply it to a wide range of multi-scale systems and Reynolds number flows.

REFERENCES

[1] M. Liu, S. Wang, Z. Wei, Y. Song, L. Jiang, "Bioinspired Design of a Superoleophobic and Low Adhesive Water/Solid Interface", Advanced Materials, vol.21 (2009) pp. 665-669.
[2] K. Liu, L. Jiang, "Bio-inspired Self-Cleaning Surfaces", Annual Review of Materials Research, vol.42 (2012) pp. 231-263.
[3] K. Balani, R.G. Batista, D. Lahiri, A. Agarwal, "The Hydrophobicity of a Lotus Leaf: A Nanomechanical and Computational Approach", Nanotechnology, vol.20 (2009) pp. 9.
[4] D.S. Miklosovic, M.M. Murray, L.E. Howle, F.E. Fish, "Leading-edge Tubercles Delay Stall on Humpback Whale (Megaptera Novaeangliae) Flippers", Physics of Fluids, vol.16 (2004).
[5] L.E. Howle, "WhalePower Wenvor Blade", Report, (2009).
[6] P. Ball, "Engineering Shark Skin and Other Solutions", Nature, vol.400 (1999) pp. 507-509.
[7] B. Bhushan, "Bioinspired Structures Surfaces", Langmuir, vol.28 (2012) pp. 1698-1714.
[8] B. Aksak, M.P. Murphy, M. Sitti, "Adhesion of Biologically Inspired Vertical and Angled Polymer Microfiber Arrays", Langmuir, vol.23 (2007) pp. 3322-3332.
[9] J. Sheng, E. Malkiel, J. Katz, "Buffer Layer Structures Associated with Extreme Wall Stress Events in a Smooth Wall Turbulent Boundary Layer", J. Fluid Mech., vol.633 (2009) pp. 17-60.
[10] J. Hong, J. Katz, C. Meneveau, M.P. Shultz, "Coherent Structures and Associated Subgrid-scale Energy Transfer in a Rough-wall Turbulent Channel Flow", J. Fluid Mech., (2012) pp.92-128.
[11] M. Murphy, B. Aksak, M. Sitti, "Gecko-inspired Directional and Controllable Adhesion", Small, vol.5 (2008) pp. 170-175.
[12] G. Karniadakis, A. Beskok, N. Aluru, "Microfluids and Nanofluidics, Springer (2005) New York.

PREDICTION OF THE AERODYNAMIC PERFORMANCE OF THE MEXICO ROTOR BY USING AIRFOIL DATA EXTRACTED FROM CFD

Hua Yang[1], Wenzhong Shen[2], Haoran Xu[3], Zedong Hong[1], Chao Liu[3]

[1]College of Power and Energy Engineering, Yangzhou University, Yangzhou, China, yanghua@yzu.edu.cn
[2]Department of Wind Energy, Technical University of Denmark, DK-2800 Lyngby, Denmark, wzsh@dtu.dk
[3]College of Water Conservancy Science and Engineering, Yangzhou University, Yangzhou, China, ydxuhaoran@163.com

ABSTRACT

Blade Element Momentum (BEM) theory is a widely used technique for prediction of wind turbine aerodynamics performance, but the reliability of airfoil data is an important factor to improve the prediction accuracy of aerodynamic loads and power using a BEM code. The airfoil characteristics used in BEM codes are mostly based on 2D wind tunnel measurements of airfoils with constant span. However, a BEM code using airfoil data obtained directly from 2D wind tunnel measurements will not yield the correct loading and power. As a consequence, 2D airfoil characteristics have to be corrected by using some models before they can be used in a BEM code. In this article, the airfoil data for the MEXICO (Model EXperiments in Controlled cOnditions) rotor are extracted from CFD (Computational Fluid Dynamics) results. The azimuthally averaged velocity is used as the sectional velocity to define the angle of attack and the coefficient of lift and drag is determined by the forces on the blade. The extracted airfoil data are put into a BEM code without corrections of rotational or tip effects, and the calculated axial and tangential forces are compared to both computations using BEM with Shen's tip loss correction models and experimental data. The comparisons show that the present method of determination of angle of attack is correct, and the re-calculated forces have good agreements with the experiment.

Key words: wind turbine, rotor aerodynamics, airfoil data

1 Introduction

BEM (Blade Element Momentum) theory is widely used to perform the aerodynamic prediction of horizontal axis wind turbines due to the requirement of less computational time. The load prediction accuracy of BEM depends on the reliability of the data of airfoil characteristics[1]. When wind turbine blade is rotating, the centrifugal force drives the air in the boundary layer flow to the blade tip. The Coriolis force produces an additional pressure gradient along the chordwise direction and drives the air flow to the trailing edge of the blade. All these make the boundary layer become thinner and the separation point of flow moves close to the trailing edge. So the stall angle of attack of airfoil at rotating condition is larger than at static condition, this phenomenon is so called stall delay. Because of the differences between the aerodynamic characteristics of blade in rotating and static condition, the two-dimensional airfoil characteristic data cannot be directly used in BEM to predict the performance of a rotating blade, and aerodynamic correction should be made for two-dimensional airfoil characteristic data. Some scholars have performed some research work on the correction for airfoil data by using of theoretical analysis and experiment. Various models have been developed by e.g. Snel *et al*.,[2] Du and Selig,[3] Chaviaropoulos and Hansen.[4] The airfoil characteristics can also be derived from experimental velocity and pressure data.[5]

With the development of computational technique, CFD (Computational Fluid Dynamics) method is widely used to perform research on predicting aerodynamic performance of wind turbines and developing new airfoils. Although CFD method takes a long time for calculation and has high requirement on computer hardware, CFD plays an important role on displaying detailed structure of flow (checking up and estimating the region of flow separation) and validating the empirical calculation model. Airfoil data can also be extracted directly from CFD rotor computations.[6]

In this article, CFD method is applied to perform numerical simulation on the MEXICO (Model EXperiments In Controlled cOnditions) rotor at three operational wind speeds. The data of airfoil characteristics extracted from the calculated result are applied in BEM to predict the performance of MEXICO rotor under other operational conditions, and the result calculated by BEM will be compared with experimental data to validate the prediction accuracy of CFD.

2 MEXICO rotor

The MEXICO project[7] was funded by the European Commission under FP5. The main objective was to create a database of detailed aerodynamic measurements on a wind turbine model to be used for model validation and improvement. The experiment was carried out at the Large Scale Low Speed Facility (LLF) of DNW German-Dutch wind tunnels, which is a high quality wind tunnel with a 9.5x9.5 m^2 open test section.

The rotor model has three blades with a diameter of 4.5 m. Three different airfoil sections were used in the design, DU91-W2-250 from 20% to 45% span, RISOE-A1-21 from 55% to 65% span and NACA 64-418 from 70% to 100% span. 148 dynamic pressured sensors were installed at five sections of 25%, 35%, 60%, 82% and 92% span to measure the blade surface pressure. Besides the pressure measurements, flow fields were also investigated by stereo PIV.

In the MEXICO experiment, various loads were measured using strain gauge techniques. These include the blade root flap moment, the edge moment and the low-speed shaft torque. Further details regarding the experiment can be found in Schepers *et al*.[7] The turbine was tested about 944 operational conditions, most of them under axial inflow conditions. Table 1 shows the operational axial-inflow conditions of the 9 cases used in the present study.

Table 1. Operational conditions used in the present study

Case number	Data file	Air density (kg m^{-3})	Wind speed (m s^{-1})	Rotational speed (rpm)	Tip speed ratio	Pitch angle (deg)
1	R011P0011D000111	1.188	10.00	423.5	10.0	0.7
2	R011P0011D000115	1.189	18.10	424.3	5.5	0.7
3	R011P0011D000117	1.188	24.00	424.4	4.2	0.7
4	R011P0011D000093	1.192	14.93	423.6	6.7	-2.3
5	R011P0011D000094	1.191	18.05	429.0	5.6	-2.3
6	R011P0011D000104	1.190	11.04	424.5	9.1	-2.3
7	R011P0011D000114	1.189	14.91	423.5	6.7	-5.3
8	R011P0011D000124	1.188	10.00	429.6	10.1	1.7
9	R011P0011D000127	1.188	14.96	424.4	6.7	-1.3

3 Numerical simulation

3.1 Numerical method

Steady numerical simulation method is employed to calculate the flow field of one blade passage under non-yawed condition. The size of the computational domain is shown in Figure 1(a). The inlet boundary is located at 4 times blade radius upstream and the outlet is located at 8 times bade radius downstream. The radius of computational domain is 4 times blade radius. The software of ICEM is used to generate the computational grid, the stationary domain is discretized by an unstructured tetrahedral mesh and the rotating domain is discretized by a structured hexahedral mesh. There are 3.6 $\times 10^6$ mesh elements in the one-third calculated domain as is shown in Figure 1(b). The hight of the first floor mesh element is about 3.6×10^{-5} m, which assures that y^+ is below 5 on the blade surface.

According to reference 8, the turbulence is modeled using Menter's *k-ω* SST turbulence model, which have the advantages of both $k-\omega$ and $k-\varepsilon$ models. At the same time, the cross-flow dissipation derivative integral is added into SST model, and the transport process of turbulence shear stress is taken into consideration in the definition of turbulent viscosity. So the SST model is more accurate of predicting the area of flow separation caused by adverse pressure gradient. SIMPLE algorithm is adopted to solve the full three-dimensional steady Reynolds time-averaged Navier-Stokes equations, and the convection terms are discretized with the second order upwind scheme.

Boundary conditions are as follows: prescribed axial velocity and static temperature at inlet; prescribed static pressure at outlet; non-slip flow is used on the surface of hub and blade; opening boundary conditions and circumferential periodic boundaries are used on outface and side surface respectively; the frozen technique is applied to dealing with the interface of rotational and stationary domains.

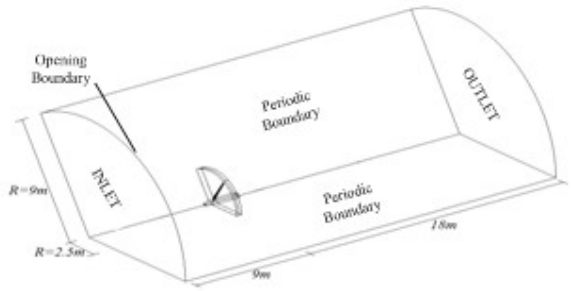

(a)

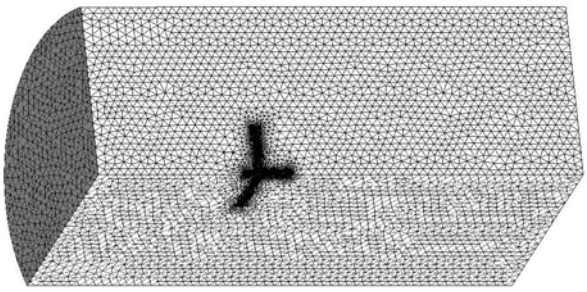

(b)

Fig. 1: Computational domain and mesh generation

3.2 Numerical simulation results

Numerical simulations are performed for case 1, 2, 3 in table 1. The distribution of pressure coefficient C_p at 60% span under three operating conditions is shown in Figure 2. From the figure it can be seen that the calculated C_p agrees well with experimental results when the tunnel velocity V_{tun} equals to 10 m/s and 18.1 m/s. When V_{tun} = 24 m/s, the calculated C_p on the pressure side agrees well with experimental results, while the C_p on the suction side is lower than experimental data, some pressure deviations exist between calculation and measurements, which may be caused by flow separation on the suction side. The limiting stream lines on the suction side are given in Figure 3. The figure shows that flow separation occurs at 60% span when the tunnel velocity is 24 m/s, while flow separation doesn't occur at the same blade when the inflow velocity is 10 m/s and 18.1 m/s. The separation flow area is increased with the increase of tunnel speed. The axial and tangential force can be calculated from the sectional pressure distribution. The comparison of axial and tangential force between calculations and measurements is shown in Figure 4. The figure indicates that the calculated force agrees well with the measured data. The axial force on the blade increases from hub to tip, while the

tangential force changes slightly along the radial direction. With the increase of tunnel velocity, the axial and tangential force at the same span increases.

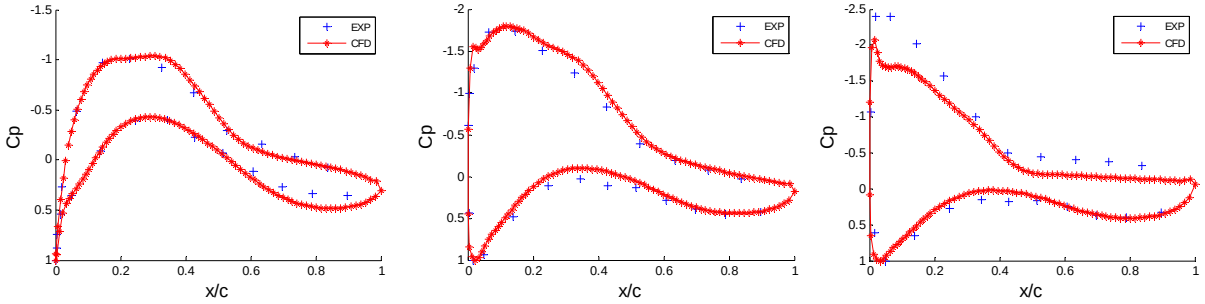

(a) V_{tun}=10m/s (b) V_{tun}= 18.1m/s (c) V_{tun}= 24m/s

Fig. 2: Pressure distributions at 60% span of the MEXICO blades threat the tunnel speeds of 10, 15 and 24 m/s.

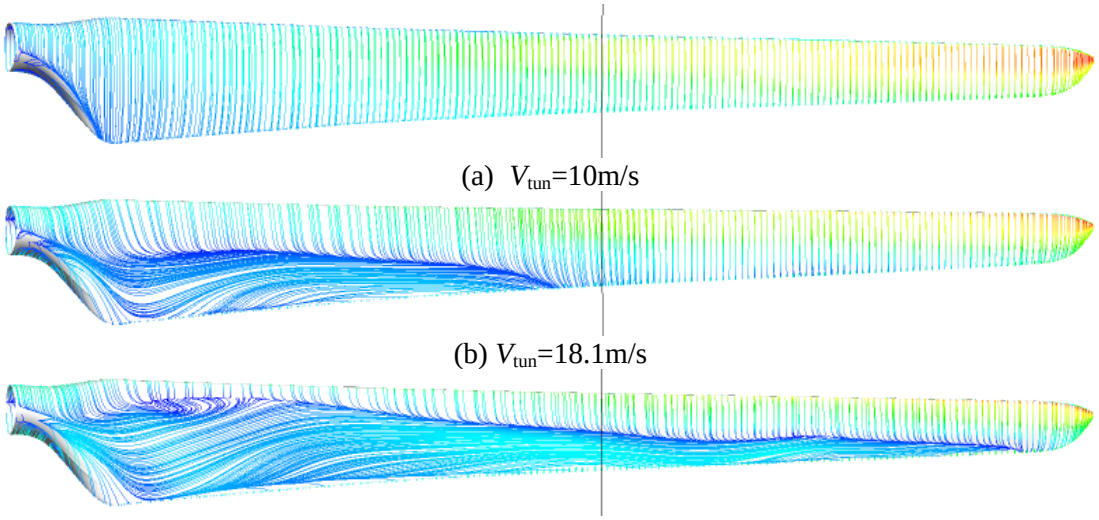

(a) V_{tun}=10m/s

(b) V_{tun}=18.1m/s

（c）V_{tun}=24m/s

Fig. 3: Limiting stream lines on the suction side of the MEXICO blades

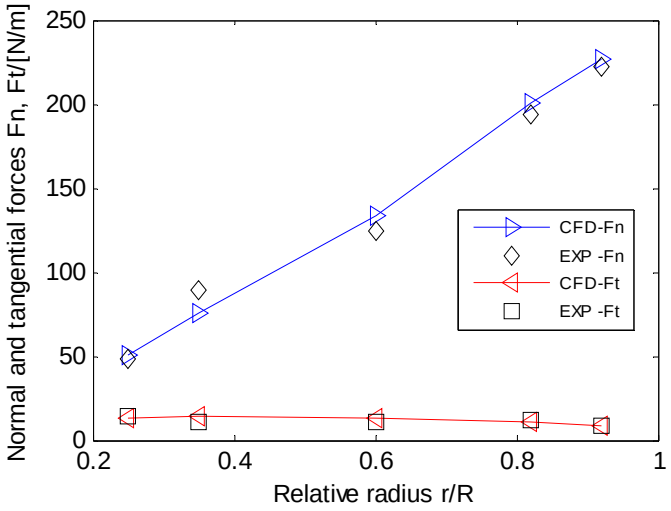

(a) V_{tun}= 10m/s

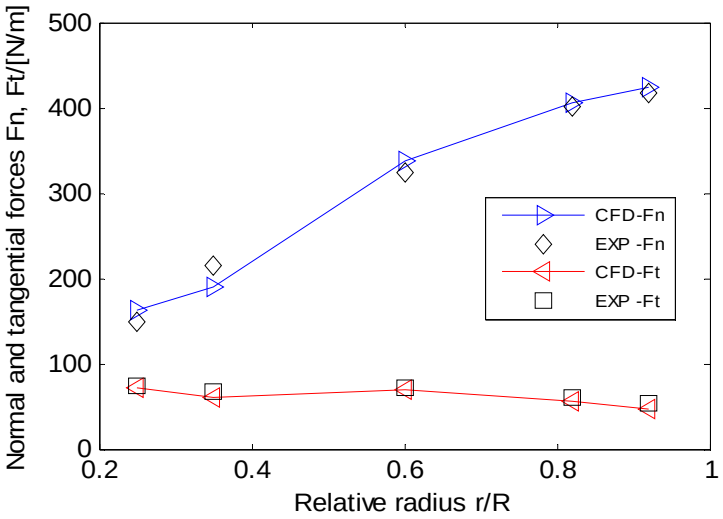

(b) V_{tun}=18.1m/s

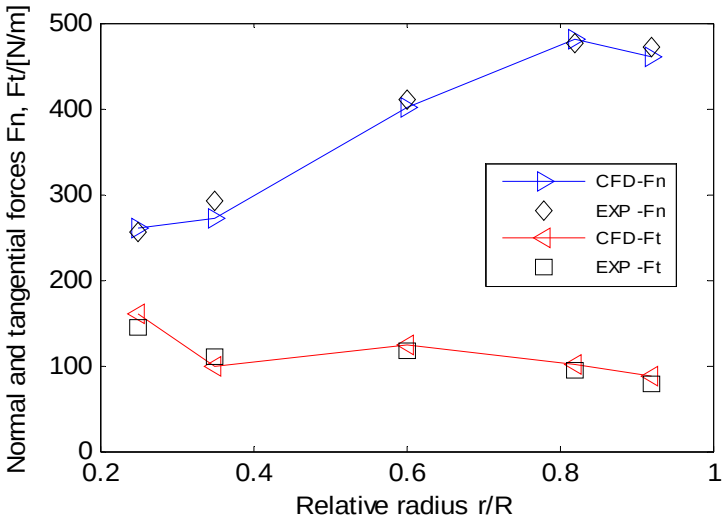

(c) V_{tun}= 24m/s

Fig. 4: Comparison of axial and tangential force distributions between experimental results and CFD results

4 Extraction of airfoil characteristics

4.1 Determination of the angle of attack

Because of the effect of centrifugal force and Coriolis force on the rotating blades, the airfoil characteristics have larger deviations between the static two-dimensional airfoil and the rotating three-dimensional airfoil. The flow field at the root part of blade is more complex, the two-dimensional airfoil data cannot be used by BEM directly and it should be corrected before it is used. In this article, the airfoil characteristics at the span of 25%, 35%, 55%, 60%, 65%, 75%, 82%, 85%, 92% is extracted from the numerical results.

The averaged azimuthally axial velocity V_{za} and tangential velocity V_{ta} on every section is calculated from the monitor points, shown in Figure 5, which are located in the circumferential direction every five degrees and in the rotating plane at a distance of one chord-length away from the leading edge. At last the relative velocity of a profile can be calculated according to the formula

$V_{rel} = \sqrt{V_{za}^2 + V_{ta}^2}$. As shown in Figure 6, the inflow angle can be defined as $\phi = \tan^{-1} \frac{V_{za}}{\Omega r + V_{ta}}$, and the angle of attack can be expressed as: $\alpha = \phi - \beta$, β can be determined according to the pitch angle and twist angle. The distribution of local pitch angle along the radial direction is given in Figure 7.

The distribution of angle of attack along the radial direction under three operating conditions is shown in Figure 8. It is obvious that, when the inflow velocity equals to 10 m/s, the angle of attack in the middle part is lower than that in the root and tip part of the blade. When the inflow velocity is equal to 18.1 m/s and 24 m/s, the angle of attack decreases monotone from the hub to the tip. Generally speaking, the variation amplitude of angle of attack under low inflow velocity is smaller than that under high inflow velocity.

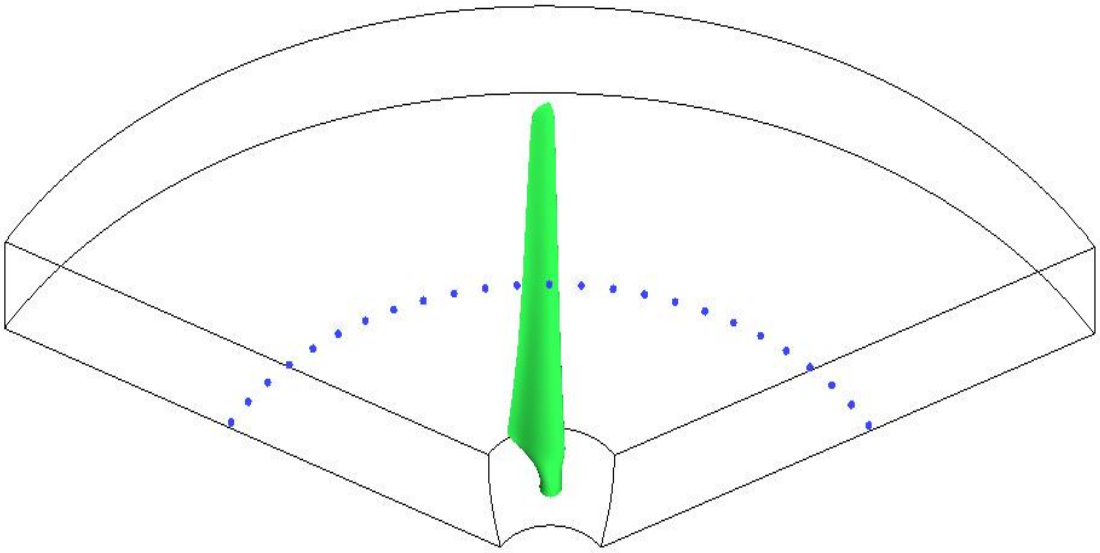

Fig. 5: Points for extraction velocity

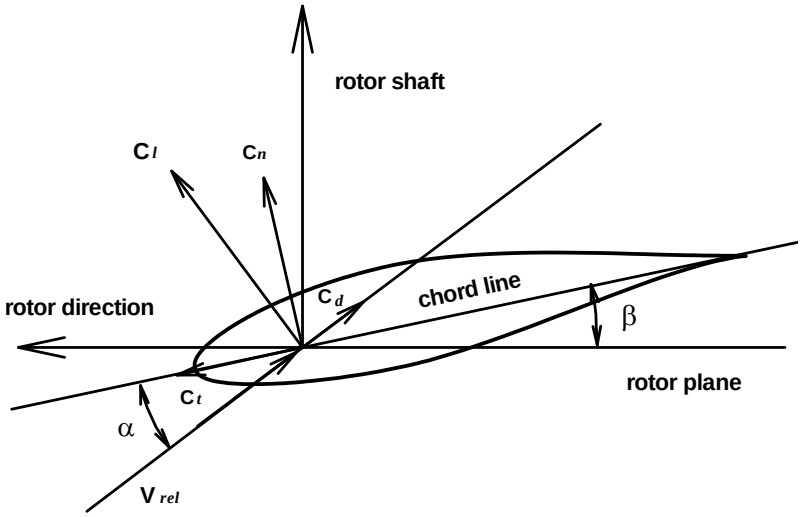

Fig. 6: Cross-section aerofoil element

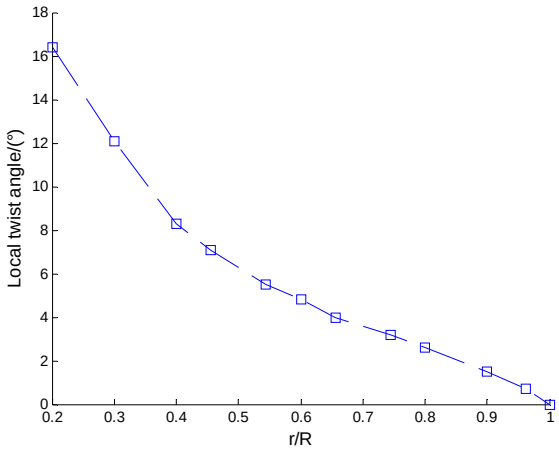

Fig. 7: Local twist angle along blade

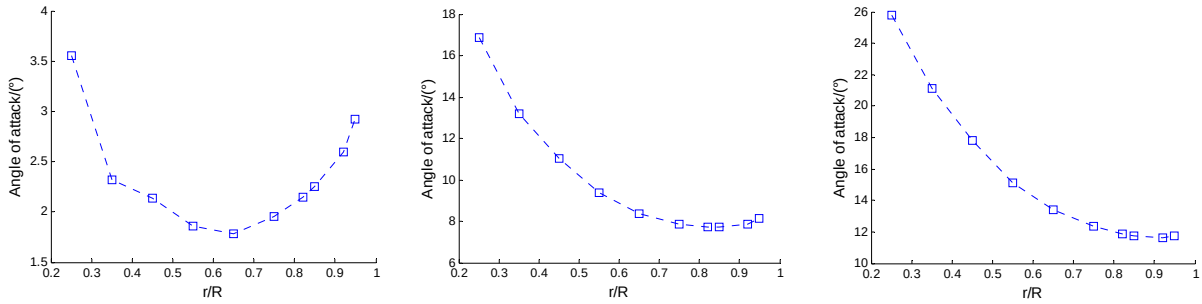

Fig. 8: Exacted angle of attack from CFD at three tunnel flow conditions

4.2 Determination of the lift and drag coefficient

From Figure 6, the local tangential force $C_t = \frac{F_t}{½\rho c V_{rel}^2}$ and normal force $C_n = \frac{F_n}{½\rho c V_{rel}^2}$ can be obtained from the computational pressure. When the local angle of attack and relative velocity are known, the lift and drag coefficients are calculated by formulae (1) and (2).

$$C_l = C_n \cos\alpha + C_t \sin\alpha \quad (1)$$

$$C_d = C_n \sin\alpha - C_t \cos\alpha \quad (2)$$

Where, ρ is the density of air, V_{rel} is the local velocity, c is chord length and α denotes the angle of attack.

4.3 Sectional airfoil characteristics

Three wind speeds are used to derive the airfoil characteristics in the present study, and the sectional airfoil data are fitted using spline interpolation functions. For comparison, 2D lift and drag coefficients are also plotted in Figure 9.

For the DU airfoil at the span of 25% and 35%, the stall angle of attack in the 2D case is about 10 degrees, which are less than the value of the rotating case. This phenomenon is called stall delay. When the angle of attack is less than 10 degrees, air is attached to the airfoil surface, the lift coefficient of the DU airfoil at both 25% and 35% span of the rotating blades is less than that in the 2D case and they are close to each other at the two spans. When the angle of attack is larger than 10 degrees, the lift coefficient of the DU airfoil at 25% span is larger than that in the 2D case, while at 35% span it is less than that of the 2D case. For the Risø airfoil at 55%, 60% and 65% span of the blades, the derived lift coefficient values are close to each other and less than that of the 2D case. With the increase of radius, the lift coefficient of the NACA airfoil in the outer part of blade decreases gradually.

The derived drag coefficient of the rotating DU airfoil is larger than that of the 2D case under the condition of both high and low angle of attack, while it is less than the 2D drag coefficient when the angle of attack is close to 15 degrees. For the Risø airfoil, the drag coefficient of 3D airfoil is less than

that of 2D airfoil. For the NACA airfoil, the 3D drag coefficient is larger than that of the 2D airfoil at high angle of attack, while the derived drag coefficient is less than that of the 2D airfoil at low angle of attack.

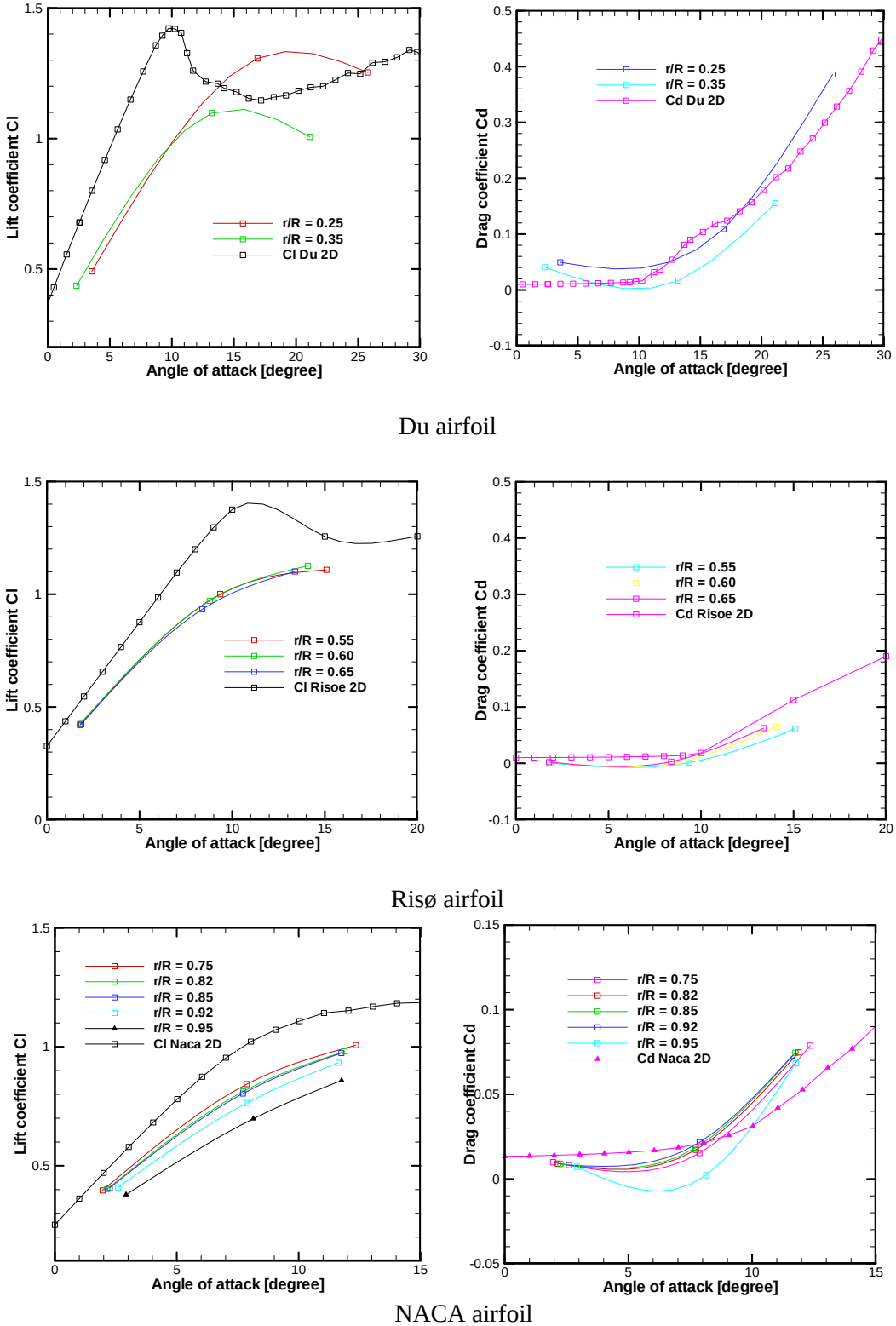

Fig.9. Airfoil characteristics of three airfoils extracted from CFD

5 Check on the extracted airfoil data using a BEM code

The BEM method is the most popular technique for computing loads and power of wind turbines. The method is a one-dimensional approach based on the actuator disc principle that corresponds to a rotor with an infinite number of blades. To account for the difference in circulation between an N-bladed rotor and an actuator disc, a tip loss factor was derived by Prandtl and introduced in the BEM technique by Glauert. In Glauert's method a correction factor, *F*, is introduced as follows,

$$F = \frac{2}{\pi}\cos^{-1}[\exp(-\frac{B(R-r)}{2r\sin\phi})], \tag{3}$$

where *B* denotes the number of blades and *(R-r)* is the distance from the tip to the local radial cross-section. Different tip loss correction models have been developed to calculate load and power of wind turbines. Shen *et al.* [9] analyzed a few existing tip loss correction models and found inconsistencies in the existing correction models, which results in incorrect predictions of the aerodynamic behaviour in the proximity of the tip. To remedy the inconsistencies, a new tip loss correction model was proposed:

$$F_1 = \frac{2}{\pi}\cos^{-1}[\exp(-g\frac{B(R-r)}{2r\sin\phi})], \tag{4}$$

Where
$$g = \exp[-0.125(B\lambda - 21)] + 0.1, \tag{5}$$

Where, λ is the tip speed ratio.

In order to validate the technique of determination of angle of attack, the obtained 10 sectional airfoil data are put into the BEM code without further correction. The same three cases where computation data were used for extracting airfoil data are first investigated. In Figure 10, the reproduced normal force distribution from the BEM with the derived airfoil data is compared with the original experimental data and BEM code using the Shen's tip loss correction model with 2D airfoil data. From the figure, the trend is consistent and small differences are seen at the blade root at the wind speed of 24 m/s. This is mainly due to the flow separation. It is worth noting that the load from BEM with 2D airfoil data is not smooth because the blade is consisted of different airfoils.

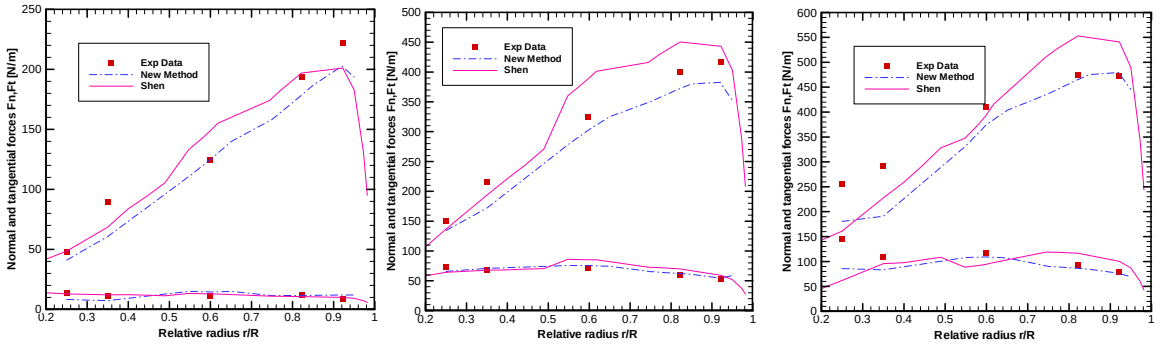

v_{tun} = 10 m/s v_{tun} = 15 m/s v_{tun} = 24 m/s

Fig. 10: Force distributions from experimental data, BEM using derived airfoil data and BEM using Shen's tip loss corrections for the MEXICO rotor at rotation speed of 424 rpm and a pitch angle of 0.7°.

To check whether the obtained airfoil characteristics can be used to predict the performance of the MEXICO rotor at other operating conditions, different tunnel speeds, pitch angles and rotor speeds are selected. Figure 11 show the axial and tangential forces at a rotor speed about of 424 rpm, different pitch angles and tunnel wind speeds. From the figure, very good agreements between the BEM code with extracted airfoil data and the experimental data are seen for both axial and tangential forces.

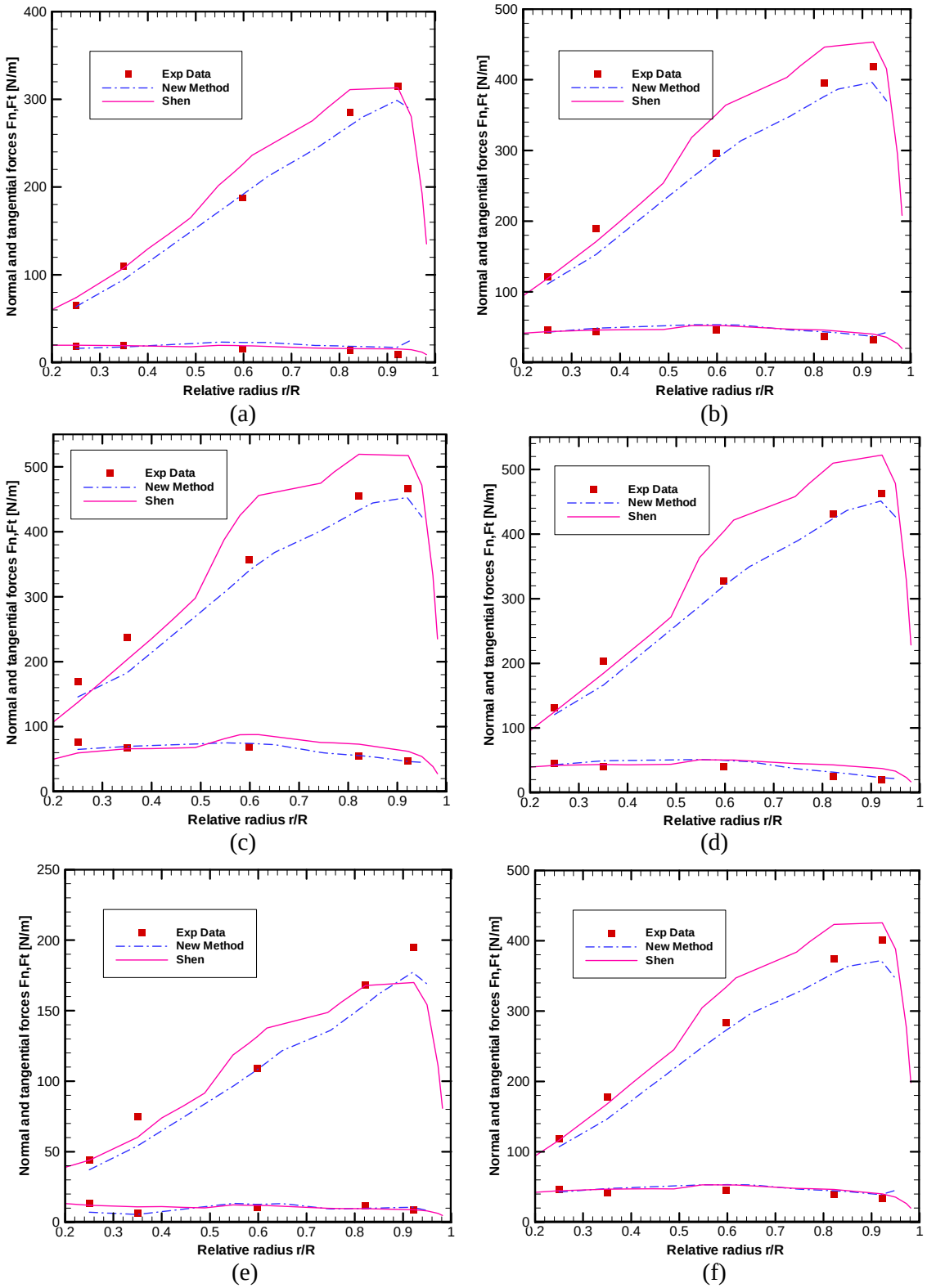

Fig. 11. Comparison of force distributions from experimental data and BEM using the derived airfoil data for the MEXICO rotor at rotation speed of 424.0 rpm.

(a) V_{tun}=11 m/s, θ_p=-2.3°; (b) V_{tun}=14.93 m/s, θ_p=-2.3°; (c) V_{tun}=18 m/s, θ_p=-2.3°;
(d) V_{tun}=14.91 m/s, θ_p= -5.3°; (e) V_{tun}=10 m/s, θ_p=1. 7°; (f) V_{tun}=15 m/s, θ_p=-1.3°;

6 Conclusions

In the present paper, the flow fields of the MEXICO rotor under three axial flow conditions are simulated by CFD with *k-ω* SST turbulence model. The local airfoil characteristics were derived from CFD computations using the azimuthally averaged velocity and the forces on the blade to extract lift and drag coefficients, C_l and C_d. The sectional airfoil data are fitted using spline interpolation functions and they are very different from the 2D airfoil data. The derived airfoil data are loaded into a BEM code without any correction model and checked by comparing the axial and tangential forces on the blade with experiments at the same operational conditions. Although the azimuthally averaged velocity is not exactly identical to the local velocity used for defining the angle of attack, there was a good agreement between the mechanical power predicted by BEM and experiment results. Because of the flow separation, the recalculated forces are lower than the experiment value near the root span at the wind speed of 24 m/s. The results from BEM with Shen's tip loss correction are also presented, and the calculated forces change suddenly on mid span. The reason may be that the MEXICO rotor constructed with three geometrically different airfoils. The derived airfoil data are also used to calculate the forces under the conditions of other pitch angles and tunnel wind speeds. Good agreements are also obtained in these results when compared with the measurements.

Acknowledgments

This paper is supported by Funds of International S&T Cooperation Program of China (Grant No. 2010DFA64660), the National Natural Science Foundation of China (Grant No. 50706041) and Danish Council for Strategic Research (Grant No. 12-130590).

REFERENCES

[1] HANSEN M O L, SØRENSEN J N, VOUTSINAS S, et al. "State of the art in wind turbine aerodynamics and aeroelasticity". *Progress in Aerospace Sciences*, 2006,42(4): 285-330.

[2] Snel H, Houwink R, Piers WJ, van Bussel GJW, Bruining A. "Sectional prediction of 3-D effects for stalled flow on rotating blades and comparison with measurements". *EWEC 1993*; 395-399.

[3] Du Z, Selig M. "A 3-D stall-delay model for horizontal axis wind turbine performance predictions". *AIAA-98-0021*, 1988.

[4] Chaviaropoulos PK, Hansen MOL. "Investigating three-dimensional and rotational effects on wind turbine blades by means of a quasi-3D Navier-Stokes solver". *Journal of Fluids Engineering 2000*, 122: 330-336.

[5] H Yang, WZ Shen, JN Sørensen, WJ Zhu, "Extraction of airfoil data using PIV and pressure measurements". *Wind Energy*, 2011, 14 (4): 539-556, DOI: 10.1002/we.441.

[6] JOHANSEN J and SØRENSEN N N. "Aerofoil characteristics from 3D CFD rotor computations". *Wind Energy*, 2004, 7(4): 283-294.

[7] SCHEPERS J G and SNEL H. "Model experiments in controlled conditions". *ECN Report*, ECN-E-07-042, 2007.

[8] Per-Åge Krogstad, Pål Egil Eriksen. "Blind test" calculations of the performance and wake development for a model wind turbine. Renewable Energy, 2013, 50: 325-333.

[9] SHEN W Z, MIKKELSEN R, SØRENSEN J N, et al. "Tip loss corrections for wind turbine computations". *Wind Energy*, 2005, 8(4): 457-475.

The aerodynamic analysis of large-scale offshore floating wind turbine using a free vortex wake model

Bofeng Xu, Tongguang Wang

Jiangsu Key Laboratory for Hi-Tech Research for Wind Turbine Design,
Nanjing University of Aeronautics and Astronautics
29 Yudao St., Nanjing 210016, China
bfxu1985@nuaa.edu.cn

ABSTRACT

A free vortex wake (FVW) model is developed to predict the aerodynamic performance and wake geometry of a large-scale offshore floating wind turbine (LOFWT). A new time-marching algorithm D3PC of third-order accuracy is applied in the FVW model. The representation of the additional degrees of freedom caused by the floating platform motions is introduced into the model. The FVW model is used to predict the steady performance in axial flow and the unsteady performance under different conditions including wind direction change and floating platform motions. The calculated rotor powers compare well with those from FAST codes for the majority of wind speeds. The FVW model can predict the overshoot before the next new equilibrium in an extreme wind direction change condition. The reorganising process of the wake geometry behind the wind turbine is observed. The platform kinematics results in the oscillation of electric power and the durative wake distortion.

KEYWORDS

Offshore floating wind turbine; free vortex wake; unsteady aerodynamic load; wake geometry; floating platform motion

1. INTRUDCTION

When the water is about more than 50 meters deep, the floating platform is a good choice for the tower foundation for the offshore wind turbine because of its economy and feasibility. The aerodynamic issue of the large-scale offshore floating wind turbine (LOFWT) is even more complex than that of the onshore wind turbine. The aerodynamic performance prediction is one of the most important bases for the design of wind turbine parts. Considering the accuracy and the economy, the free vortex wake (FVW) methods perhaps are the more suitable tools of simulations.

The FVW methods have been successfully applied in helicopters. Leishman [1], Bliss [2], Bagai [3], Bhagwat[4], et al have investigated the stability and convergence of the wake iterations in the FVW under different flight conditions, which can be introduced into wind turbine aerodynamic study due to the similarity between helicopter and wind turbine rotor flowfields. Garrel [5] introduced a non-linear vortex-line strength model into the FVW method incorporating the rotor wake rollup and the non-linear aerodynamic characteristics of blade. Sant et al used a FVW model to estimate the angles of attack from blade pressure measurements respectively in the axial conditions [6] and yawed conditions [7] providing better insight into how circulation formed at the blades. For steady conditions, the relaxation iterative algorithm can be used in the wake geometry resolution. However, for the unsteady conditions, a time-marching algorithm is needed to calculate the wake geometry which changes with time. Gupta developed a PC2B (Predictor-Corrector 2nd Backward) scheme [8] for wind turbine application and studied

the stability of PC2B [9], validating the Free-Vortex Model [10][11]. These works illustrate that the FVW method is efficient and reliable for wind turbine aerodynamic prediction and wake analysis.

The floating platform motions will result in additional aerodynamic unsteadiness compared to onshore systems. Sebastian et al [12] demonstrated that offshore floating wind turbines are different significantly from conventional offshore systems in terms of aerodynamics and characterized the aerodynamic unsteadiness. Sebastian et al [13] also developed a free vortex wake code for offshore floating wind turbines, but the validation calculation did not consider the effects of the floating platform motions. A new time-marching algorithm for the FVW method is presented in this study. The FVW model will be used to calculate the steady and unsteady aerodynamic performance of a 5-MW offshore floating wind turbine. The wake distortion and rotor power response due to unsteadiness will be analysed.

2. FREE VORTEX WAKE MODEL

2.1 Difference approximation of wake governing equation

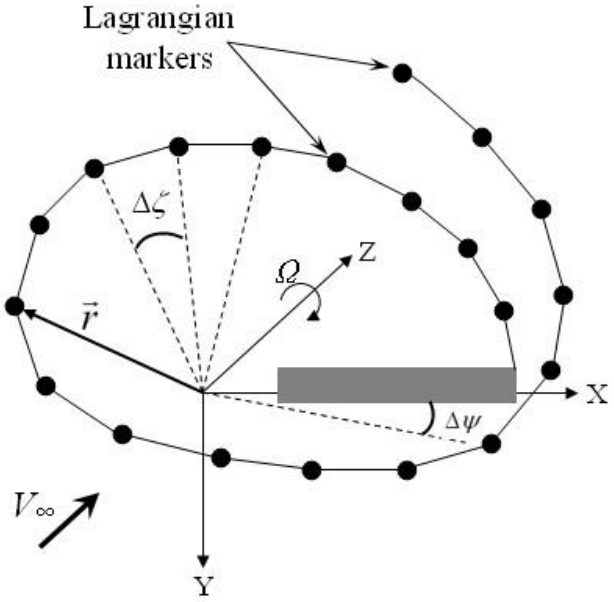

Figure 1. Schematic of the discretized tip vortex geometry

The FVW model assumes that the flow field is incompressible and potential. The blade is modeled as a series of elements, which are represented as a line of bound vorticity lying along the blade quarter chord line. The vortex filaments, extending downstream from the trailing edge of the blade element boundary, are allowed to freely distort under the influence of local velocity field. The governing equation of the vortex filaments is often written in the form of a partial differential equation as

$$\frac{\partial \vec{r}(\psi,\zeta)}{\partial \psi}+\frac{\partial \vec{r}(\psi,\zeta)}{\partial \zeta}=\frac{1}{\Omega}\left[\vec{V}_{\infty}+\vec{V}_{ind}\left(\vec{r}(\psi,\zeta),t\right)\right] \tag{1}$$

where the blade azimuth angle ψ is a temporal coordinate and the wake age angle ζ is a spatial coordinate. On the right hand side of Eq. 1, V_{ind} equals to the mean value of the values at the surrounding four grid points calculated by the Biot-Savart law. To solve the partial differential equation numerically, the finite difference approximations are used to approximate the derivatives on the left hand side. For the spatial (ζ) derivative, a five-point central difference approximation has been used in other algorithms like the PCC (Predictor-Corrector Central difference) [14] and the PC2B (Predictor-Corrector 2nd Backward) [15] and is also used in this paper. The accuracy of the temporal (ψ) derivative approximation is a significant part in a time-accurate free vortex method. The PCC algorithm still used a five-point central difference approximation,

whereas the PC2B algorithm used a second-order backward difference approximation. In the present work, a new time-accurate algorithm is developed. The Eq. 1 can be written in another form as

$$\frac{\partial \vec{r}(\psi,\zeta)}{\partial \psi} = -\frac{\partial \vec{r}(\psi,\zeta)}{\partial \zeta} + \frac{1}{\Omega}\left[\vec{V}_{\infty} + \vec{V}_{ind}\left(\vec{r}(\psi,\zeta),t\right)\right] \tag{2}$$

The Eq.2 can be written in a general form of ordinary difference equation as

$$\frac{dy}{dx} = f(x,y) \tag{3}$$

The predictor process in the predictor-corrector algorithm often adopts an explicit format, whereas the corrector process adopts an implicit format. Assuming the steps are equal, the general form of the linear multistep method for Eq.3 is written as

$$\sum_{j=0}^{k} \alpha_j y_{n+j} = h\sum_{j=0}^{k} \beta_i f_{n+j} \tag{4}$$

where $\alpha_j, \beta_j (j = 0,1,\cdots,k)$ are constants, y_{n+j} and f_{n+j} represent respectively the terms of $y\left(x_{n+j}\right)$ and $f\left(x_{n+j}, y_{n+j}\right)$. The values of α_j and β_j can be obtained by the method of undetermined coefficients.

An explicit three-step linear multistep method is given by

$$y_{n+3} = -\frac{1}{2}\left(3y_{n+2} - 6y_{n+1} + y_n\right) + 3hf_{n+2} \tag{5}$$

The local truncation error of Eq. 5 is

$$T_{n+3} = \frac{1}{2}h^4 y^{(4)}\left(x_n\right) + O\left(h^6\right) \tag{6}$$

An implicit three-step linear multistep method is given by

$$y_{n+3} = \frac{1}{11}\left(18y_{n+2} - 9y_{n+1} + 2y_n\right) + \frac{6}{11}hf_{n+3} \tag{7}$$

The local truncation error of Eq. 7 is

$$T_{n+3} = -\frac{3}{2}h^4 y^{(4)}\left(x_n\right) + O\left(h^6\right) \tag{8}$$

The explicit and implicit three-step linear multistep methods are used in the temporal (ψ) derivative approximation. A new predictor-corrector algorithm is developed as

Predictor

$$\begin{aligned}\tilde{r}_{i,j} = {} & \frac{1}{7}\left(9\tilde{r}_{i-1,j} - 12\tilde{r}_{i-2,j} + 2\tilde{r}_{i-3,j} + 3\tilde{r}_{i,j-1} + 3\tilde{r}_{i-1,j-1}\right) + \\ & \frac{6}{7}\frac{\Delta\psi}{\Omega}\left[V_{\infty} + \frac{1}{4}\left(V^{n-1}_{ind\,i,(j)} + V^{n-1}_{ind\,i-(1),j} + V^{n-1}_{ind\,i,(j-1)} + V^{n-1}_{ind\,i-(1),(j-1)}\right)\right]\end{aligned} \tag{9}$$

Corrector

$$\begin{aligned}r_{i,j} = {} & \frac{1}{14}\left(15r_{i-1,j} - 9r_{i-2,j} + 2r_{i-3,j} + 3\tilde{r}_{i,j-1} + 3\tilde{r}_{i-1,j-1}\right) + \\ & \frac{3}{7}\frac{\Delta\psi}{\Omega}\left[V_{\infty} + \frac{1}{8}\left(V^{n-1}_{ind\,i,(j)} + V^{n-1}_{ind\,i-(1),j} + V^{n-1}_{ind\,i,(j-1)} + V^{n-1}_{ind\,i-(1),(j-1)}\right)\right. \\ & \left. \frac{1}{8}\left(\tilde{V}_{ind\,i,j} + \tilde{V}_{ind\,(i),j-(1)} + \tilde{V}_{ind\,i-(1),(j)} + \tilde{V}_{ind\,i-(1),(j-1)}\right)\right]\end{aligned} \tag{10}$$

It is clear from the local truncation errors of Eq.5 and Eq.7 that the new predictor-corrector algorithm has third-order accuracy, so this algorithm is referred to as the D3PC (Three-step and Third-order Predictor-Corrector) algorithm. The PCC is a single-step algorithm and has second-order accuracy. The single-step algorithm is simple, but its numerical stability is not good enough. The multistep method has

been widely used recently because it has better stability and convergence. Although the PC3B algorithm is a three-step algorithm, it only achieves second-order accuracy, which results in low efficiency. The D3PC algorithm developed in this paper is also a three-step algorithm, and it has third-order accuracy.

2.2 Vortex core model

The induced velocity at the control node of vortex filaments is calculated using the Biot-Savart law. The velocity at point *P* (see figure 2) induced by a spatial straight-line vortex from point *A* to point *B* with constant strength is

$$\vec{V} = \frac{\Gamma}{4\pi h}\left(\cos\theta_A - \cos\theta_B\right)\vec{e} \tag{11}$$

where $\vec{e} = \dfrac{\vec{r}_{AB} \times \vec{r}_A}{\left|\vec{r}_{AB} \times \vec{r}_A\right|}$.

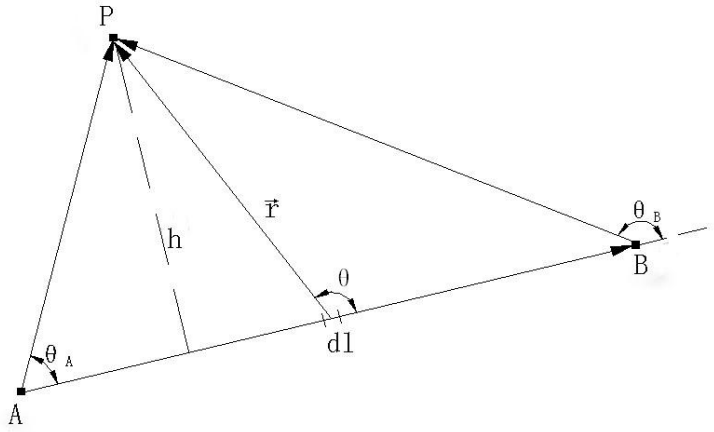

Figure 2. Schematic of a straight-line vortex and a point

However, when a collocation point is very close to the vortex line segment, a very high induced velocity will be obtained. In addition, the self-induced velocity has a logarithmic singularity. These two phenomena will cause convergence problems. To avoid the numerical problems, a viscous vortex core model is used in this paper. The core radius growth similar to the Lamb-Oseen [16] vortex model is used in the Biot-Savart law, and modified by an empirical viscous growth model [17]. The core radius model is given by

$$r_c(\zeta) = \sqrt{r_0^2 + \frac{4\alpha_L \delta \nu \zeta}{\Omega}} \tag{12}$$

where r_0 is the vortex core radius at zero wake age, α_L Lamb's constant ($\alpha_L = 1.25643$), ν the kinematic viscosity of air, δ a constant which is of the order of 10^4. Introducing the Leishman-Bagai [18] model, Eq. 11 can be modified as

$$\vec{V} = \frac{\Gamma}{4\pi}\frac{h}{\sqrt{r_c^4 + h^4}}\left(\cos\theta_A - \cos\theta_B\right)\vec{e} \tag{13}$$

Figure 3 shows the non-dimensional velocity, perpendicular to the vortex ring plane, induced by a vortex ring. When the point is very close to the radius position of vortex ring, the absolute values of induced velocities, which are calculated by the unmodified formula, increase rapidly. Moreover, a logarithmic singularity which is replaced by zero value is obtained at the radius position. Introducing the viscous vortex core in the induced velocity solution, the above numerical problems disappear and the values are continuous.

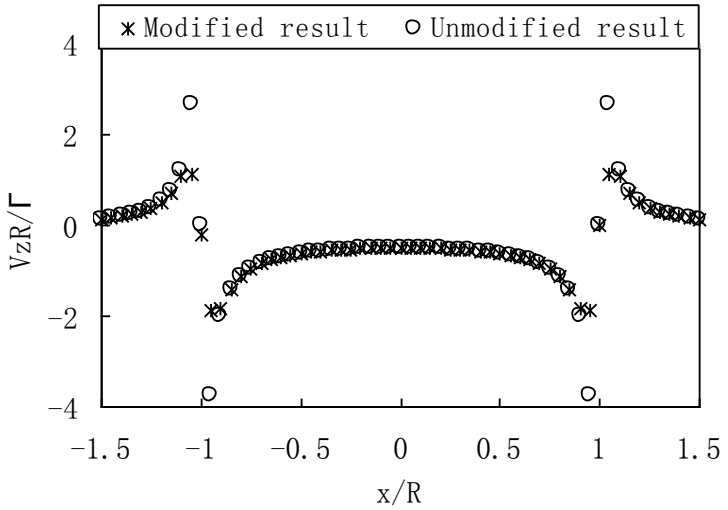

Figure 3. Non-dimensional induced velocity distribution in the vortex ring plane

3. NREL 5-MW WIND TURBINE

Table 1. Distributed blade aerodynamic properties

r(m)	Chord(m)	Twist(m)	Relative thickness	Airfoil
1.5000	3.542	13.308	100.00	Cylinder1
2.8667	3.542	13.308	100.00	Cylinder1
5.6000	3.854	13.308	90.04	Cylinder1
8.3333	4.167	13.308	75.59	Cylinder2
11.7500	4.557	13.308	59.25	DU40
15.8500	4.652	11.480	46.65	DU35
19.9500	4.458	10.162	39.03	DU35
24.0500	4.249	9.011	33.42	DU30
28.1500	4.007	7.795	28.45	DU25
32.2500	3.748	6.544	24.55	DU25
36.3500	3.502	5.361	21.42	DU21
40.4500	3.256	4.188	19.72	DU21
44.5500	3.01	3.125	18.00	NACA64
48.6500	2.764	2.319	18.00	NACA64
52.7500	2.518	1.526	18.00	NACA64
56.1667	2.313	0.863	18.00	NACA64
58.9000	2.086	0.370	18.00	NACA64
61.6333	1.419	0.106	18.00	NACA64
63.0000	0.800	0	18.00	NACA64

To assess offshore wind technology suitable in the shallow and deep waters of offshore sites, the US NREL designed the ‘NREL offshore 5-MW baseline wind turbine’ [19], which is now called the NREL 5-MW wind turbine and is studied as a calculation example in this paper. The radius of NREL 5-MW rotor is 63 m and the blade has a length of 61.5 m. Table 1 gives the aerodynamic properties at the blade sections. The airfoils used in the blade are DU40, DU35, DU30, DU25, DU21 and NACA64, respectively. The lift and drag coefficients of these airfoils used in the calculation model are chosen from the reference 19. The rotational stall delay has been applied in the lift and drag coefficients for 0 °to 90 °angles of attack. There is no data for the blade thickness, so the relative thickness distribution referring to the other blades is applied to this study.

Assuming the wind turbine is rigid. Six types of the platform motions considered in this study include

surge, sway, heave, pitch, roll and yaw, and the definitions of moving directions are showed in figure 4. The velocities of blade elements associated with the platform motions are calculated in the FVW model and the inflow conditions will be change transiently.

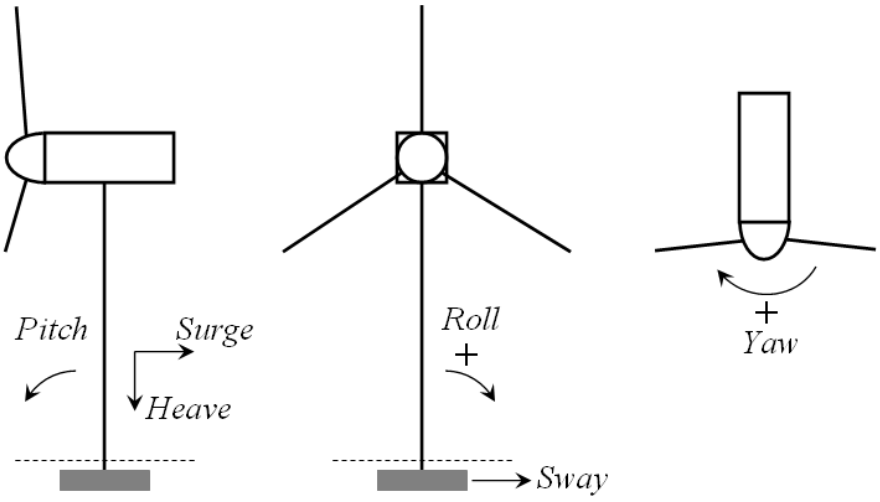

Figure 4. Schematic of platform motions

4. RESOLUTION PROCESS

The steady module of the FVW model is executed as follow:

1 Input the inflow condition and wind turbine parameters;

2 Calculate initial wake geometry;

3 Calculate blade condition and trailing vorticity;

4 Calculate induced velocities at control nodes of vortex filaments;

5 March the azimuth age. Predict the new wake geometry using Eq. 9;

6 Calculate induced velocities at blade element control points using the new wake geometry. Calculate blade condition and trailing vorticity;

7 Calculate induced velocities at control nodes of new vortex filaments using the new vorticity;

8 Correct the wake geometry using Eq. 10;

9 Calculate induced velocities at blade element control points;

10 If the azimuth age does not equal to 2π, return to step 3; If the azimuth age equals to 2π, calculate the RMS change between wake geometries of this moment and the last period. If the RMS change is less than a prescribed tolerance of 10^{-4}, convergence is achieved. Otherwise, return to step 3.

11 Calculate steady performance and export the results.

The unsteady module of the FVW model is executed as follow:

1 Execute the steady module;

2 March the azimuth age. Calculate the inflow condition of this moment;

3 Predict the new wake geometry using Eq. 9;

4 Calculate induced velocities at blade element control points using the new wake geometry. Calculate blade condition and trailing vorticity;

5 Calculate induced velocities at control nodes of new vortex filaments using the new vorticity;

6 Correct the wake geometry using Eq. 10;

7 Calculate induced velocities at blade element control points. Calculate the blade aerodynamic load and rotor performance.

8 Return to step 2. If the time course is completed, end the model.

The above whole process of the calculation can be showed in the figure 5.

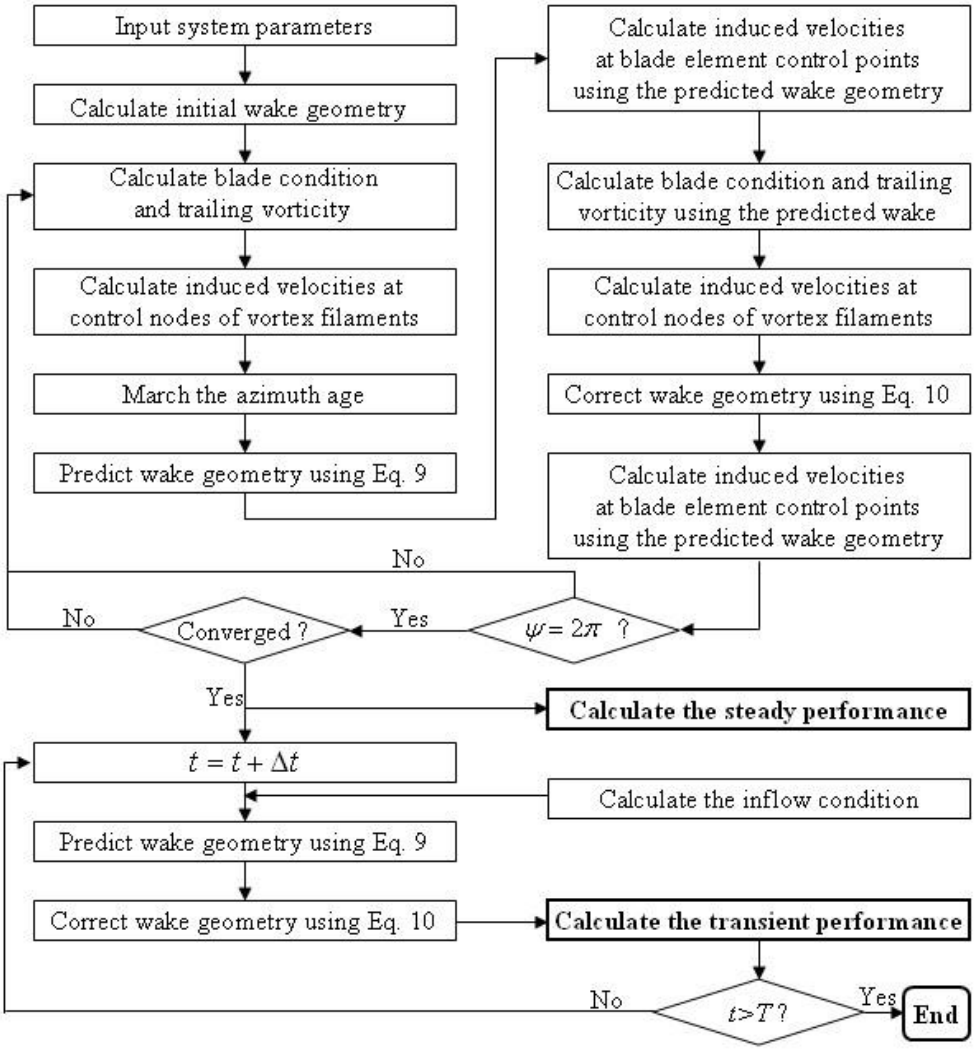

Figure 5. Flow chart of the free vortex wake model

5. RESULTS AND DISCUSSION

5.1 STEADY PERFORMANCE

The rotor power and rotor thrust of the NREL 5-MW wind turbine are calculated by the present FVW model at a number of given, steady, uniform wind speeds. The power production control strategy of this wind turbine is pitch-regulated and speed-variable. In the low wind speed regime, first the optimal tip speed ratio (TSR) is reached by changing the rotor speed. The optimal TSR is followed to maintain a maximum Cp by adjusting the rotor speed until the rated speed wind, above which the rated power and rated rotor speed are kept by adjusting blade pitch angle. The control curves of the pitch angle and the rotor speed (see figure 6) are from the NREL report [19], and are optimized by the FAST simulator in which BEM theory is used. Since there is no experimental data for the NREL 5-MW wind turbine, the results from FAST are used to compare with that of this study.

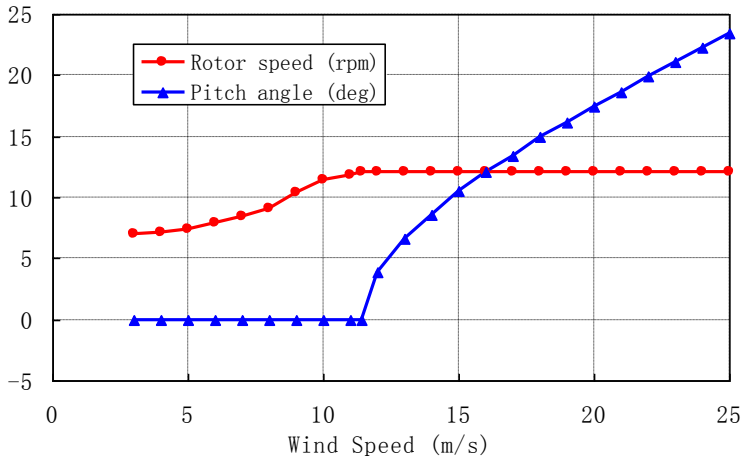

Figure 6. Control curves of the pitch angle and the rotor speed

Figure 7 shows the rotor power as a function of wind speed, in which the black curve is the FAST result [19] and the red one is the present FVW result. The rotor power increases cubically with wind speed before the rated wind speed. Above the rated wind speed, the rotor power remains at about 5300 kW. The agreement between the predicted powers from the FVW and FAST is noted to be very good for the vast majority of wind speeds. The pitch regulated curve is based on the BEM theory and is sensitive at the high wind speeds, so the rotor power fluctuates after the rated wind speed, and deviates from the FAST results. It shows that the pitch regulated curve optimized by the FVW model will be different from that in figure 6. Figure 8 shows the rotor thrust as a function of wind speed. The rotor thrust from the FVW model is lower than that from FAST in all wind speed region, although the trends of them are the same. The relative thickness distributions used in this paper and reference 19 may be different, so the results would not be consistent with each other. All of the rotor thrusts from the FVW are lower than those from FAST. This is reasonable because that the former only takes into account the viscosity in the vortex core but not in the whole flow fields.

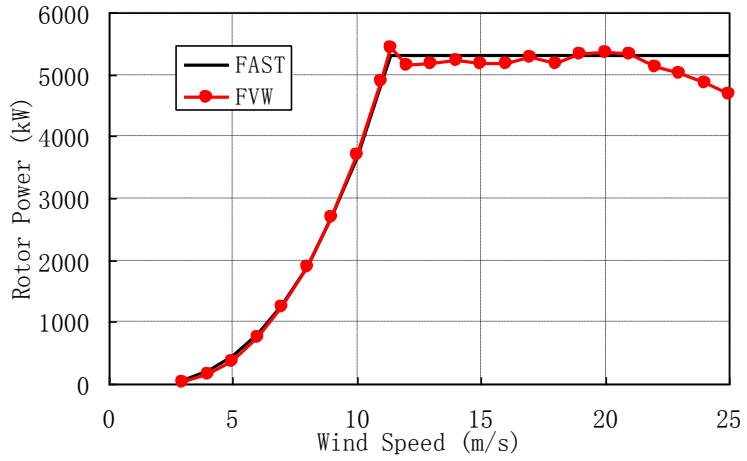

Figure 7. Rotor power as a function of wind speed

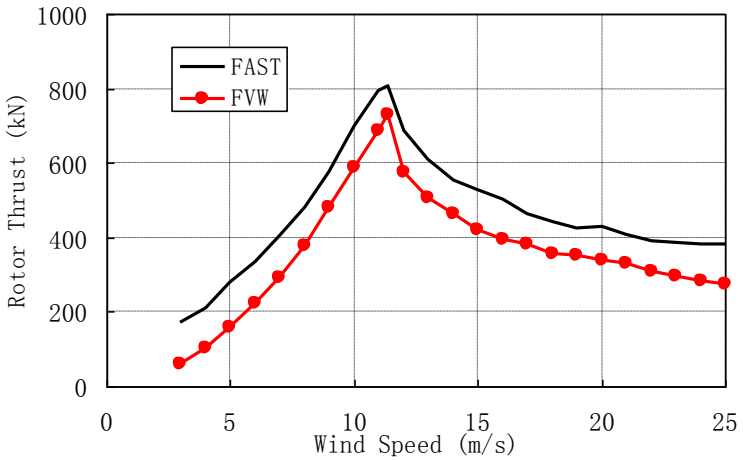

Figure 8. Rotor thrust as a function of wind speed

The comparisons above demonstrate that the FVW model in this paper has the capability of the steady aerodynamic calculation for large-scale wind turbines. It is pleasantly surprised that the convergence of present D3PC scheme is quite good. The wake geometry can be convergent in a wide range of tip speed ratios from 3 to 15.

5.2 UNSTEADY PERFORMANCE

Wind turbines operate at all times in an unsteady condition. Factors such as atmospheric turbulence, wind shear, and skewed flow, etc., all have significant effects on turbine blade inflow conditions. Additionally, the offshore floating wind turbines need consider the factors of floating platform motions. The cumulative effect of these phenomena results in the blade experiencing unsteady loading, which plays an important role in both the aerodynamic performance of the turbine and the fatigue life of its structure. Obviously, the unsteady aerodynamic performance must be well understood before the structural response can be accurately determined.

EXTREME DIRECTION CHANGE (EDC)

A condition of EDC is simulated at the rated wind speed 11.4m/s in this study. The EDC shall be given by

$$\gamma(t)=\begin{cases}0 & t<5\\ \frac{1}{2}\gamma_e\left(1-\cos\left(\pi\left(t-5\right)/T\right)\right) & 5\le t\le T+5\\ \gamma_e & t>T+5\end{cases} \tag{14}$$

where T is the duration of the EDC transient and $T=6\,\mathrm{s}$ here. γ_e is the amplitude of EDC. Figure 9 shows the EDC from 0 seconds to 60 seconds. Correspondingly, figure 10 shows the time-history of rotor power. It is clear that the power output drops rapidly with EDC. At $t=11\,\mathrm{s}$ the wind direction is increased to 30 degrees. First the power drops from 5350kW to 3725kW and approximately 15s later the power settles at a new periodic equilibrium.

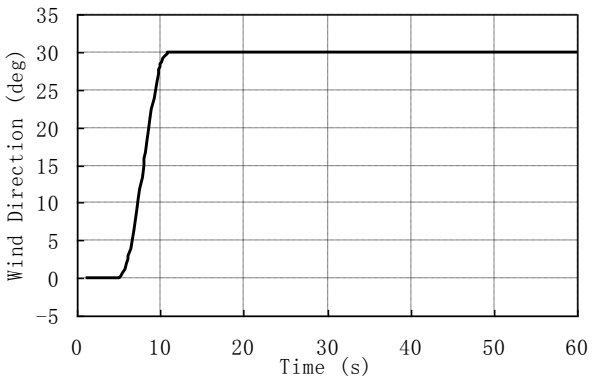

Figure 9. Time-history of EDC

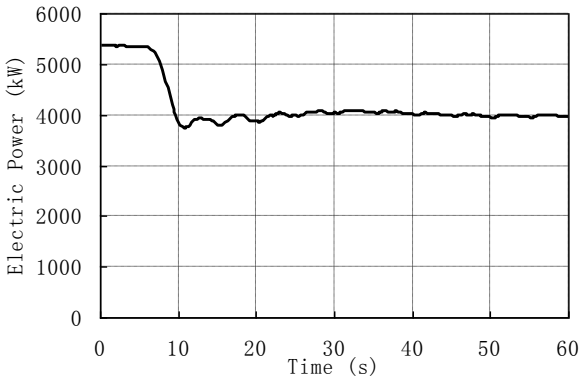

Figure 10. Time-history of rotor power

Figure 11 shows the top view of the blade tip vortex filaments behind the wind turbine at different times. Three vortex filaments from three different blades are denoted by different colours. When t = 0s, the wake geometry is regular. When the wind direction change starts, the wake moves into a new skewed wake. The induced effect between the old regular wake and the new skewed wake occurs, which causes highly unsteady loads on the blades. After about 15s, the wake is reorganised and becomes essentially periodic.

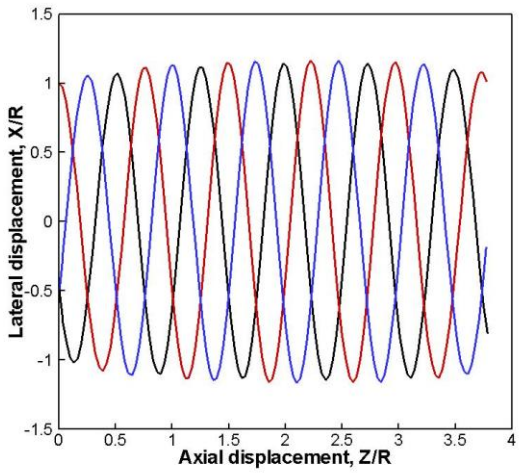

(a) t = 0s

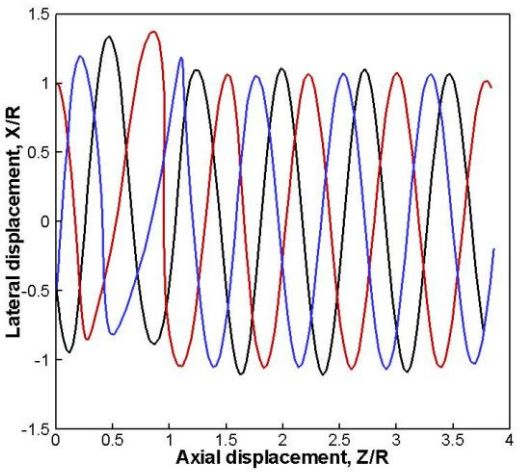

(b) t = 10s

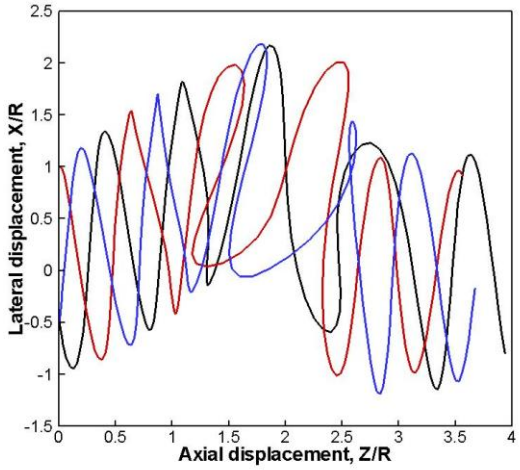

(c) t = 20s

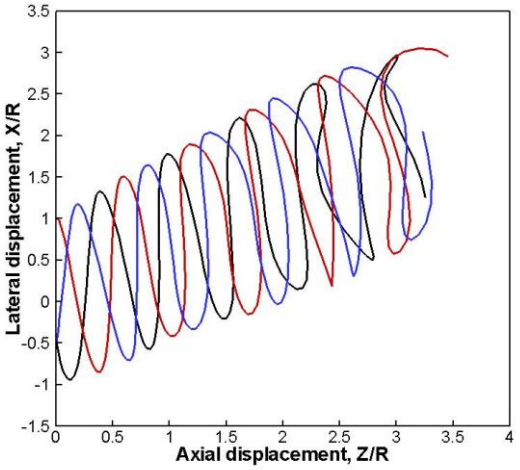

(d) t = 40s

Figure 11. Top view of the blade tip vortex filaments behind the wind turbine
(a) t = 0s; (b) t = 10s; (c) t = 20s; (d) t = 40s

FLOATING PLATFORM MOTIONS

The resulting FAST-simulated platform kinematics (see figure 12 [12]) of spar-buoy for the rated operating condition, lasting 200 s for simulation, was adopted in this study. The inflow condition change of each blade element was introduced in the FVW model to calculate the effects due to platform kinematics.

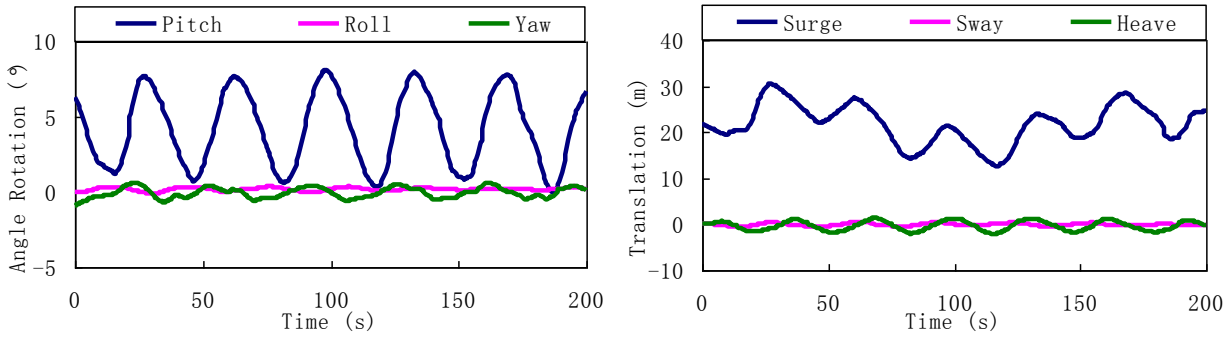

Figure 12. Time-history of platform motions of the NREL 5 MW turbine for rated operating condition

Figure 13 gives the rotor power responses corresponding to the platform kinematics. It is clear that the rotor power oscillates at the rated power 5300 kW without any rules. This is reasonable that the platform motions of six degrees of freedom (DOFs) are coupled with the inflow conditions.

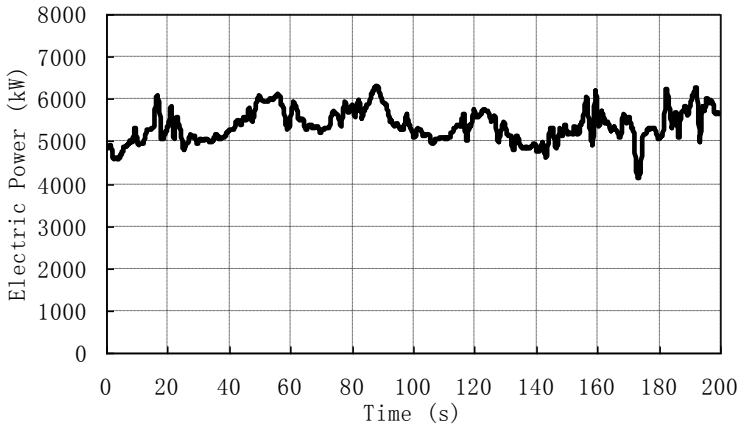

Figure 13. Rotor power response correspond to pitching motion

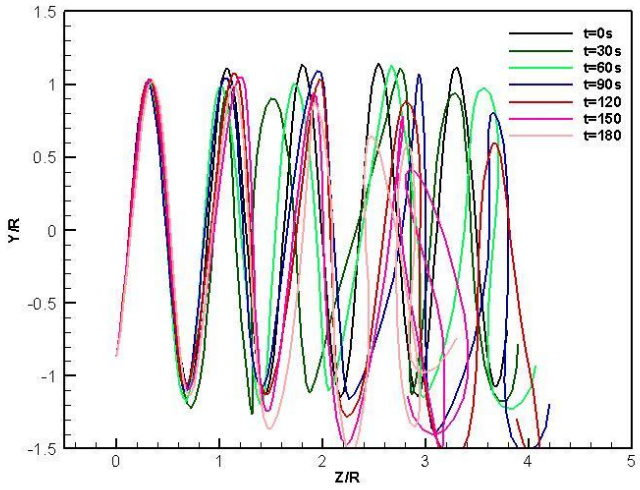

Figure 14. Lateral view of the blade tip vortex filaments behind the wind turbine at different simulating time

The tip vortex geometries constantly distort in the simulation process. The lateral view (figure 14) and top

view (figure 15) of the blade tip vortex filaments are exported at the time of 0, 30, 60, 90, 120, 150, 180 s. In the lateral view, the negative direction of the ordinate actually points upward. Because an average value of the angles of pitch DOF is about 5 °, the wakes are upward skewed. However, there is no skewed distortion in other two rotational DOFs.

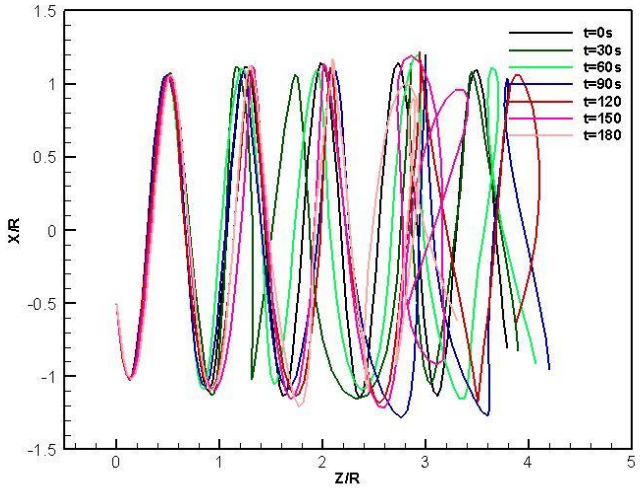

Figure 15. Top view of the blade tip vortex filaments behind the wind turbine at different simulating time

6. CONCLUSIONS

A new difference approximation, which is called D3PC algorithm, is developed for the FVW method in this paper. It is derived from the linear multistep method using the method of undetermined coefficients. The D3PC algorithm is a three-step algorithm of third-order accuracy.

The FVW model has been used to calculate the steady and unsteady aerodynamic characteristics of a large-scale offshore floating wind turbine, the NREL offshore 5-MW baseline wind turbine. The wake geometry can be convergent in a wide tip speed ratio region from 3 to 15. The steady results are compared with the FAST code results. The agreement of the predicted rotor powers between them is noted to be very good for the vast majority of wind speeds, while the rotor thrust from the FVW model is lower than that from FAST. A condition of EDC is simulated and an overshoot before the next new equilibrium can be observed. The wake geometries behind the wind turbine at different times are given and the wake reorganising process is observed. For a spar-buoy platform, six DOFs are taken account into the blade inflows. The rotor power oscillates at the rated power without any rules and the rotor wakes constantly distort.

REFERENCES

[1] Leishman JG, Bhagwat MJ, Bagai A. Free-Vortex Filament Methods for the Analysis of Helicopter Rotor Wakes. Journal of Aircraft. 2002, 39(5):759-775.

[2] Bliss DB, Miller WO. Efficient Free Wake Calculations Using Analytical/Numerical Matching and Far-Field Linearization. Journal of the American Helicopter Society. 1993, 38(2): 253- 263

[3] Bagai A., Leishman JG. Rotor Free-Wake Modeling using a Pseudoimplicit Relaxation Algorithm. Journal of Aircraft. 1995. 32(6):1276-1285

[4] Bhagwat MJ, Leishman JG. Stability, Consistency and Convergence of Time-Marching Free-Vortex Rotor Wake Algorithms. Journal of the American Helicopter Society. 2001, 46(1):59-71.

[5] Garrel AV. Development of a wind turbine aerodynamics simulation module[R]. ECN-C--03-079. Netherlands: Netherlands Energy Research Foundation, 2003.

[6] Sant T, Kuik GV, Bussel G. Estimating the Angle of Attack from Blade Pressure Measurements on the NREL Phase Ⅵ Rotor Using a Free Wake Vortex Model: Axial Conditions. Wind Energy. 2006,

9(6):549-577.

[7] Sant T, Kuik GV, Bussel G. Estimating the Angle of Attack from Blade Pressure Measurements on the National Renewable Energy Laboratory Phase Ⅵ Rotor Using a Free Wake Vortex Model: Yawed Conditions. Wind Energy. 2009, 12(1):1-32.

[8] Gupta S. Development of a time-accutate viscous lagrangian vortex wake model for wind turbine application. PhD thesis. University of Maryland, 2006.

[9] Gupta S, Leishman JG. Stability of Methods in the Free-Vortex Wake Analysis of Wind turbines. Collection of ASME Wind Energy Symposium Technical Papers AIAA Aerospace Sciences Meeting and Exhibit. 2004, p 339-353.

[10] Gupta S, Leishman JG. Validation of a Free-Vortex Model for Wind Turbines in Yawed Flow. Collection of Technical Papers-44th AIAA Aerospace Sciences Meeting. 2006. 7:4529-4543.

[11] Gupta S, Leishman JG. Performance Predictions of The NREL Phase Ⅵ Combined Experiment Rotor Using a Free-Vortex Wake Model. Collection of Technical Papers-44th AIAA Aerospace Sciences Meeting. 2006. 7:4544-4564.

[12] Sebastian T, Lackner MA. Characterization of the unsteady aerodynamics of offshore floating wind turbines. WIND ENERGY. Published online: 19 MAR, 2012.

[13] Sebastian T, Lackner MA. Development of a free vortex wake method code for offshore floating wind turbines. Renewable Energy. 2012, 46: 269-275.

[14] Bhagwat MJ, Leishman JG. Rotor Aerodynamics During Maneuvering Flight Using a Time-Accurate Free-vortex Wake , Journal of the American Helicopter Society, 2003, 48(3):143-158.

[15] Bhagwat MJ, Leishman JG. Time-accurate free vortex wake model for dynamic rotor response. American Helicopter Society Specialist Meeting. Atlanta, 2000.

[16] Lamb H. Hydrodynamics. Cambridge University Press,1932.

[17] Bhagwat MJ, Leishman JG. Correlation of helicopter tip vortex measurements. AIAA Journal, 2000, 38(2): 301-308.

[18] Bagai A, Leishman JG. Flow visualization of compressible vortex structures using density gradient techniques. Experiments in Fluids, 1993, 15: 431-442.

[19] Jonkman J, Butterfield S, Musial W, Scott G. Definition of a 5-MW reference wind turbine for offshore system development. NREL/TP-500-38060. Colorado: National Renewable Energy Laboratory, 2009.

INVESTIGATING THE AERODYNAMIC PERFORMANCE OF AN OFFSHORE FLOATING WIND TURBINE

R. Farrugia[1*], **T. Sant**[1], **D. Micallef**[1]

[*]Author for correspondence
[1]University of Malta, Department of Mechanical Eng., Msida, MSD 2080 Malta,
rfar0028@um.edu.mt

ABSTRACT

Understanding the impact of wave-induced dynamic effects on the aerodynamic performance of Offshore Floating Wind Turbines (OFWTs) is crucial towards developing cost-effective floating wind turbines to harness wind energy in deep water sites. The complexity of the wake of an OFWT has not yet been fully understood. Measurements and numerical simulations are essential. An experiment to investigate the aerodynamics of a model OFWT was undertaken at the University of Malta. Established experimental techniques used to analyse fixed HAWTs were applied and modified for the floating turbine condition. The effects of wave induced motions on the rotor aerodynamic variables were analysed in detail. An open source free wake vortex code was also used to examine whether certain phenomena observed in the experiments could be reproduced by the code when modelling a full-scale OFWT.

NOMENCLATURE

λ	[-]	Tip speed ratio
θ_{az}	[deg]	Blade azimuth angle
θ_{tip}	[deg]	Blade tip pitch angle
ω	[Hz]	Wave frequency
a_1	[-]	Axial induction factor
(r,θ,z)	[-]	Cylindrical coordinate system
v	[m/s]	Surge velocity
w_a	[m/s]	Hot wire derived axial velocity relative to the measurement plane
C_P	[-]	Power coefficient
C_Q	[-]	Torque coefficient
C_T	[-]	Thrust coefficient
R	[m]	Blade tip radius
RSD	[-]	Relative standard density (standard deviation/mean)
U_∞	[m/s]	Free stream velocity
U'_∞	[m/s]	Equivalent free stream velocity
V_{effx}	[m/s]	Velocity relative to the measurement plane measured by the hot-wire with orientation x

INTRODUCTION

Recently, there has been an increase in interest among industry and academia to develop and commercialise floating wind turbine technologies. It is believed that this technology would in the future offer enormous possibilities for harvesting wind energy in deep waters cost-effectively [1] [2]. Lowering the life cycle costs of offshore floating wind turbines (OFWTs) can solely be achieved if the entire system design is optimised [3]. However studies on the operating and failure design conditions which are unique to OFWTs have not yet been carried out with a high level of detail [4]. Such studies are crucial in determining whether conventional methods used in the modelling of fixed-bottom offshore and onshore wind turbines could be reliably adapted to model OFWTs.

A number of studies have been carried out on the hydrodynamic aspects namely the influence of the wave motion on the mooring-line and platform dynamics [5] [6] [7]. Design tools like FAST developed by NREL have been extended in order to enable the coupled time-domain dynamic analysis of OFWTs [8]. However the aerodynamics is still based on the Blade Element Momentum (BEM) theory with incorporated models to correct for hub and tip losses, dynamic inflow and dynamic stall. Sebastian [9] showed that the effect of the platform motion on the rotor's aerodynamic performance is not described by the BEM theory in a physically realistic manner. Due to the limited amount of knowledge available, comparable rotor conditions allow the advanced aerodynamic models used in the helicopter industry to be implemented in the analysis of the wake formation of a floating wind turbine. Potential flow methods, for instance, have been successfully applied by Sebastian and Lackner [10] developing a free wake code to simulate the wake development of a rotor oscillating under realistic platform motions.

Experimental measurements on both model and full-scale OFWTs are fundamental for validating numerical tools used to simulate floating rotor aerodynamics. A handful of projects such as WindFloat [11], Hywind [12] and Sway [13] have been commissioned where prototype OFWTs are being tested at sea. Similarly a small number of tests on model OFWTs have been carried out in wind and wave generating facilities [14] [15]. The focus of such experiments was mainly on the dynamic wind turbine motions and consequently rotor aerodynamic performance under floating conditions has not yet been investigated. To try and address this issue, recently the University of Malta (UoM) has carried out extensive power and flow measurements on a small-scale rigid wind turbine coupled with a tension leg platform (TLP) using a dedicated wind-wave generating facility.

OFWT WAKE AERODYNAMICS

The helical tip vortex structure is generally the predominant feature determining wind turbine wake behaviour. At the tip region, the rotor blades have very large pressure gradients resulting in the tip vortices having high circulation strength and swirl velocities. The result is a strong rolled-up tip vortex originating from each individual blade [16]. Therefore it is important to understand the physical development of the tip vortex and the impact that the velocity field in its vicinity has on the wake induced velocities at the rotor. In the case of OFWTs, the development of the tip vortices may differ from that of fixed-bottom wind turbines due to periodic changes in the wind relative to the rotor blades. Variations in the tip vortex pitch, rotor-to-wake and vortex-to-vortex interactions may lead to a higher uncertainty in determining the power developed by

the wind turbine rotor. This further emphasises the use of advanced models such as potential flow models and CFD to investigate these complex phenomena. This paper will therefore seek to address the following questions:

1. Is there a change in the power characteristics in the case of an OFWT compared to a fixed wind turbine?
2. Is there a difference in the wake features (tip vortex path, axial inductions) between floating and fixed wind turbines?
3. Do these wake characteristics vary with tip speed ratio thus suggesting that wave induced effects on the rotor performance are dependent on the latter's operating condition?

UOM OFWT EXPERIMENT

An experiment on an OFWT model was conducted at the Fluids Laboratory at the University of Malta. The first phase of the experiment consisted of power measurements while wake measurements were carried out in the second phase. A model floating wind turbine was attached to a TLP structure and installed in a wind tunnel and water tank respectively as shown in fig. 1. Details of the main components of the experimental set-up are listed in Table 1.

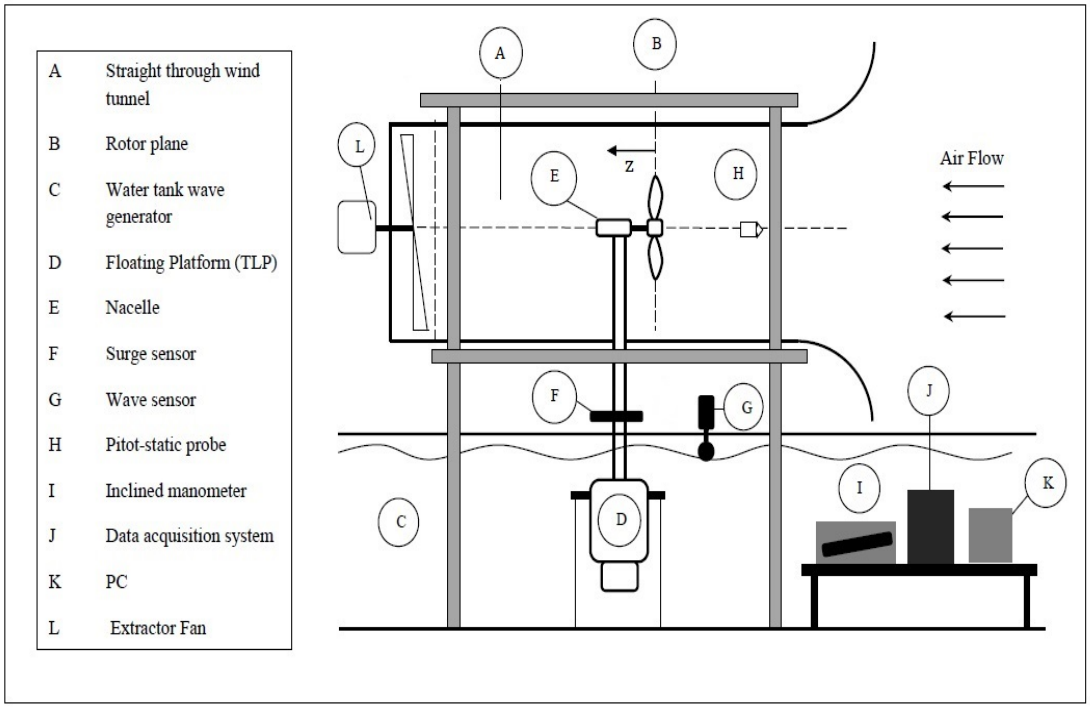

Figure 1: Schematic diagram of the UoM OFWT Experiment

Wind Turbine Properties

Blade length	0.2 m
Hub radius	0.03 m
Rotor diameter	0.46 m
Aerofoil type	S3034
Tower height	1.2 m
Chord type	constant
Chord length	0.04 m
Blade twist	1.2 °/cm

Platform Properties

Type	Tension-Leg Platform
Maximum diameter	0.26 m
Height	0.6 m

Wind Tunnel Properties

Configuration	Open-Jet Suction type
Test Section diameter	0.9 m
Maximum test section velocity	13 $\pm$ 0.1 m/s

Wave Generator Properties

Wave type	One dimensional intermediate/deep waves
Wave tank dimensions	8 x 0.75 m
Water depth	0.87 m

Sensory equipment

Platform surge	Multi-turn potentiometer
Wave height	Multi-turn potentiometer
Torque	Omega TQ513-012 electric torque meter
Wake velocity	Auspex U-Wire Probe (AHWU-100)
Rotor frequency	Incremental digital rotary encoder
Rotor frequency control	PID controller
Data acquisition device	SCC-68 I/O
Interfacing software	LabVIEW®

Table 1: Details of UoM OFWT experimental setup

PHASE I: POWER MEASUREMENTS

(a) METHODOLOGY

The first phase of the experiment was directed towards obtaining platform motion, rotor torque and frequency measurements under different wave and turbine operating conditions. This data was compared to the fixed platform condition. Blockage effects were assessed by applying the actuator disk method presented by Mikkelson [17]: for $U'_\infty/U_\infty < 1.02$, a θ_{tip} of greater than 6° together with a C_T of less than 0.6 had to be maintained. In fact for the fixed platform condition, good agreement in the C_P and C_Q curves was obtained between experimental measurements and simulations using GH Bladed. For all measurement runs, a sampling frequency of 100 Hz and a total of 1000 data samples were recorded. Four different one dimensional wave frequencies were considered: 0.36, 0.43, 0.67 and 0.83 Hz. The chosen frequencies were within the range of

the system natural frequency which was found to be around 0.51 Hz. These frequencies translate into peak surge velocities of 0.06, 0.17, 0.28 and 0.11 m/s respectively. With the tension leg platform, the most predominant degree of freedom was the translation in the wave direction (surge). The maximum translation normal to the wave direction (heave) was found to be only 1.2% of the peak-to-peak surge displacement while the remaining degrees of freedom (pitch, roll, yaw and sway) could be assumed to be negligible. In order to derive the OFWT performance characteristics for all wave conditions over a range of λ, the wind tunnel speed was kept constant at 8 m/s $\pm$5% while the rotor speed was varied over the range of 360 - 1800 rpm.

Wind turbine performance characteristics are determined by non-dimensional parameters such as C_P and C_Q. For fixed wind turbines the extracted power or torque is related to the available kinetic energy of the wind intersecting the wind turbine rotor. In the case of OFWT, the addition of the wave induced velocity component would technically contribute to the available kinetic energy relative to the turbine blades. Bayati et al [18] for instance analysed the power characteristics on an OFWT (with the use of a moving platform structure) with respect to the apparent wind. However in order to deduce the effect that different wave frequencies have on the aerodynamic power output at different λ the surge velocity was not included in the definitions of C_Q and C_P (see eqns. 1 and 2 respectively).

$$C_Q = \frac{Q}{\frac{1}{2}\rho A (U_\infty)^2 R} \tag{1}$$

$$C_P = \frac{Q\Omega}{\frac{1}{2}\rho A (U_\infty)^3} \tag{2}$$

(b) RESULTS

The relative standard deviation of the rotor frequency and the free stream velocity was kept below 1% and 3.5% respectively. Fig. 2 shows that there is no appreciable difference in the mean C_P and C_Q at the different wave conditions at low tip speed ratio. At high tip speed ratios where the rotor operates in attached flow, a slight difference in the mean C_P and C_Q among the test wave frequencies is evident.

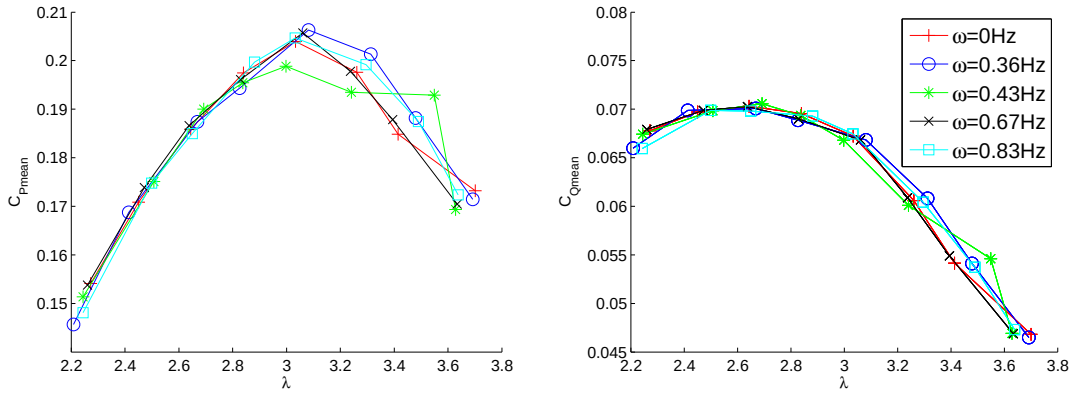

(a) C_P-λ (b) C_Q-λ

Figure 2: Measured power and torque characteristic curves for different wave frequencies ($0.16 < C_T < 0.32$)

The relative standard deviation in torque readings was examined to investigate whether the torque variations increase at high λ. Fig. 3 shows that the torque variations were not affected by changes in the surge frequency. Although an increase in torque fluctuations was to be expected for the floating platform compared to the fixed platform condition, variations in the aerodynamic loads could not be excluded. However the limited sensitivity of the torque sensor together with the inertia of the rotary system would have likely made it very difficult to measure the small variations in the aerodynamic torque as a result of surge frequency on such a small rotor.

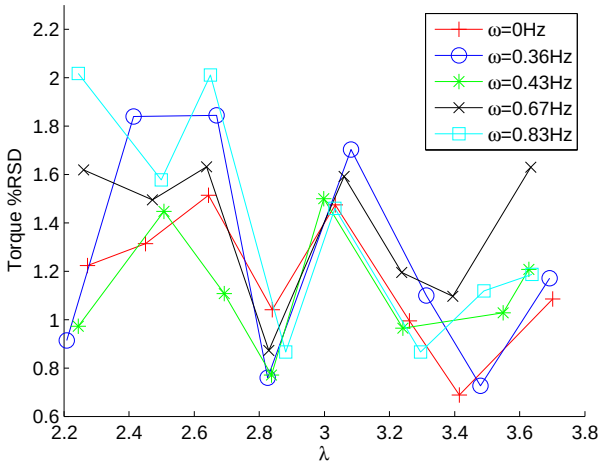

Figure 3: Relative standard deviation of torque against λ

PHASE II: WAKE MEASUREMENTS

(a) METHODOLOGY

In the second phase of the experiment, velocity measurements in the near wake of the rotor at different λ were carried out for both fixed and floating platform conditions. Wake velocity measurements using single probe hot wire anemometry were based on the traditional method applied in similar experiments conducted by Haans et al [19]. This involves measurements to be taken at three hot wire orientations for each spatial location. This method was implemented in the UoM OFWT experiment in order to obtain the three dimensional velocity components at intermittent radial locations within the range of $0.35 < r/R < 1.3$ along two measurement planes located downstream at $z/R = 0.17$ and 0.34. For this method speed and angular calibration of the single wire probe were required before readings at three different probe orientations at each spatial location could be obtained. For a given (r,θ,z) location a total of 36000 hot wire samples (1 sample every 1° of blade azimuth) were taken for the fixed platform condition while a 60 second measurement run was executed for the floating platform condition (ca. 50 surge cycles and 800 rotor revolutions).

The major constraint when using only a normal hot wire probe is the inability to simultaneously deduce the direction of the 3D velocity components. Furthermore during floating conditions, the surge displacement is introduced as an additional independent variable. Due to the fact that simultaneous measurements of the three hot wire orientations was not possible, the wake at any

position within the fluid stream was assumed to be periodic. However in order to deduce the 3D velocity components, both θ_{az} and the surge position have to be equal for the three hot wire signals, $V_{eff1,2,3}$. Zero-phase digital filtering was applied to the hot wire data using a second order Butterworth function, in order to eliminate the high frequency noise from the signal. The data was binned to obtain the $V_{eff1,2,3}$ measured by the hot wire to derive the instantaneous effective velocity for a given rotor frequency, *r/R*, *z/R*, surge position, surge direction, and θ_{az}. For each selected surge location a tolerance of $\pm$ 2 mm was used. It should also be noted that since surge is a vector the algorithm had to differentiate between different surge positions where the platform is either moving upstream and downstream.

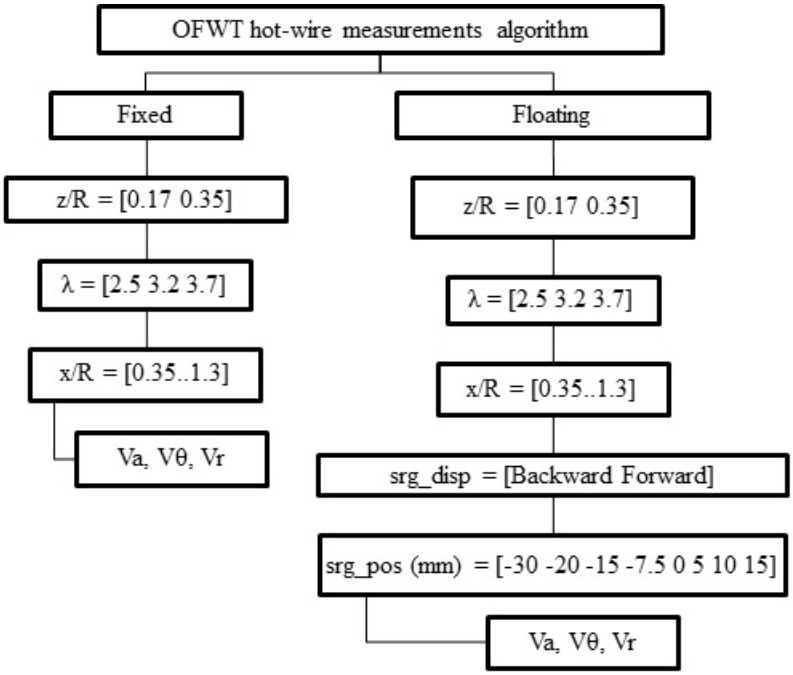

Figure 4: Flowchart of the hot-wire measurements algorithm

(b) RESULTS

With the algorithm discussed previously the velocity data measured in the three hot wire orientations was sorted according to θ_{az}, surge position and direction. Hence the magnitude of the axial, tangential and radial near-wake velocity components could be deduced. This could have only been achieved through a high repeatability (0.9 %RSD) in the peak-to-peak surge displacement. Due to the inability of the single hot wire to deduce changes in flow direction only the axial velocity was considered for the subsequent analysis.

The flow measurements were taken below, above and at the optimum tip speed ratio (λ = 2.5, 3.7, 3.2) for a θ_{tip} of 11° and U_∞ of 8 m/s. At these operating conditions, the measured C_T ranges from 0.3 to 0.32 when the platform is fixed. Furthermore the Reynolds Number of the rotor at the 0.7*R* location, as defined by Vermeer [20], reaches a maximum of 55600 at λ = 3.7. In the case of the floating platform condition a wave frequency of 0.83 Hz was considered. The limitations in rotor frequency and wind tunnel size, requiring a low C_T to be maintained to

minimize blockage effects, consequently constrained the operating $Re_{0.7R}$ to relatively low values. This may have provided for higher viscous effects compared to what is encountered during full-scale wind turbine conditions.

The axial velocity patterns obtained in this study are similar to other hot wire experiments carried out at TUDelft by Vermeer [20], Haans et al [19] and Sant [21]. The periodic fluctuations in the axial induction factor (see eqn. 3) brought about by the passage of the 2 blades are evident while the tip vortex path could be detected when the hot wire probe is traversed across the wake boundary (see fig. 5).

$$a_1 = 1 - \frac{w_a}{U_\infty} \tag{3}$$

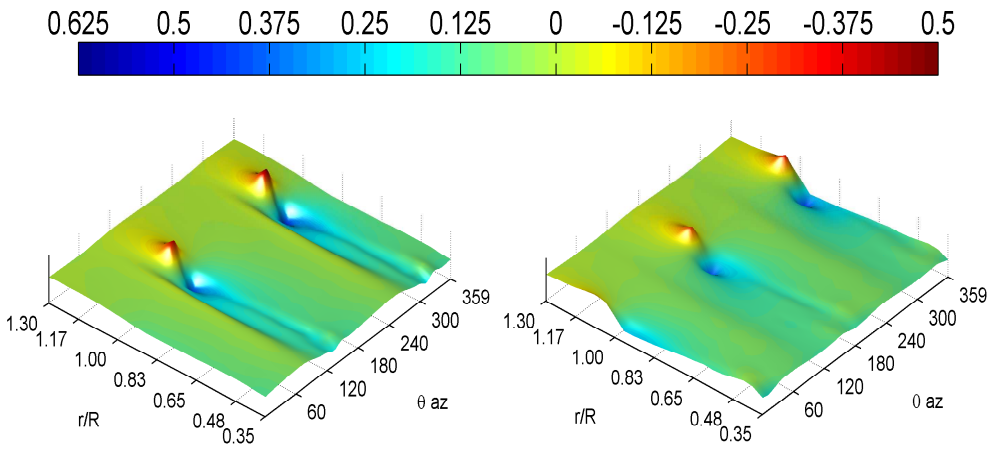

Figure 5: Surface plot of a_1 (see eqn. 3) against θ_{az} and r/R for λ = 3.2, ω = 0.83 Hz, surge position = 30 mm, and z/R = 0.17 and 0.35

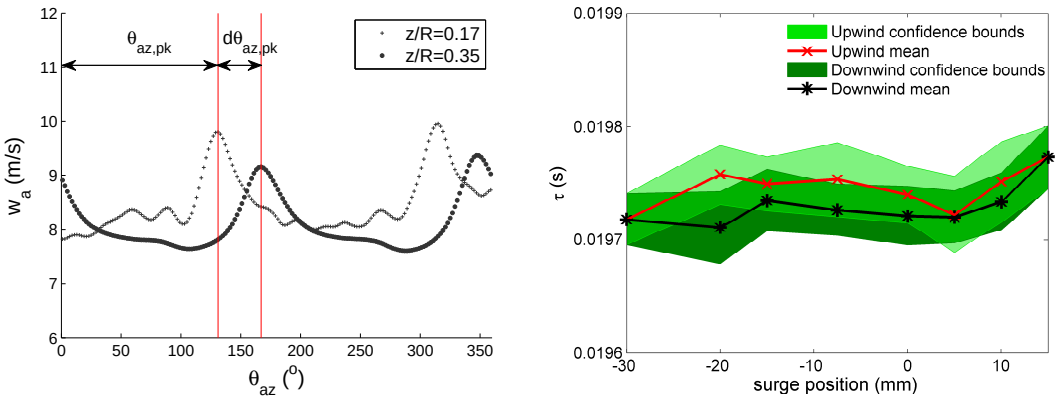

(a) w_a versus θ_{az} at λ =3.2 and r/R=1.1

(b) τ versus surge position for λ =3.2, z/R=0.17

Figure 6

Analysis of the tip vortex pitch was carried out by considering the parameter τ: the time taken for the detection of the tip vortex, shed by a particular blade, relative to the θ_{az} = 0 position of that same blade. The axial velocity signal outward of the tip vortex path (r/R=1.1) was used to determine the $\theta_{az,pk}$ at which a sharp peak in the velocity signal occurs (see fig. 6a). τ could thus be determined from the product of $\theta_{az,pk}$ and the sampling frequency. τ was analysed in order

to determine whether its distribution characteristics vary between the fixed and floating conditions. No difference was found in the skewness of the distribution however a higher kurtosis was observed at random surge locations for the floating condition compared to the fixed condition. This provides evidence that aperiodicity in the tip vortex passage axially downstream was not detected. The mean and deviations from the mean of τ for different surge positions and λ were also investigated as shown in fig. 6b. The difference in the mean of τ at the neutral surge location (-7.5mm) when the platform was moving upstream and downstream was found to be less than 1%. Moreover the 95% confidence limits do not vary substantially with both surge location and λ.

The time taken by the tip vortex to be detected by the hot wire from $z/R = 0.17$ to 0.35 was analysed by considering $d\tau$ deduced from $d\theta_{az,pk}$ shown in fig. 6a. A difference in the mean of $d\tau$ among the surge locations considered was less than 3%. Therefore no substantial information was found with regards to possible changes in the tip vortex path in a direction parallel to the oncoming wind. However from fig. 5 it should be noted that the tip vortex core itself was not detected and hence the peak in the velocity only signifies a certain position within the tip vortex outer radius.

Further investigation was directed towards the magnitude of the axial velocity induced by the tip vortex passage at $\theta_{az,pk}$. As shown in fig. 7a, for all λ investigated under floating conditions it was found that the peak axial velocity magnitude varied periodically with a frequency corresponding to the platform surge frequency and a maximum amplitude of 0.25 m/s. This effect may be linked to the addition of the surge velocity to the effective wind relative to both the OFWT and the hot wire. However it should be noted that a maximum amplitude of the surge velocity was only 0.11 m/s which may suggest the occurrence of indirect effects of the surge velocity on the wake aerodynamics. Therefore although temporal variations in the tip vortex transport velocity in the axial direction and hence the tip vortex pitch were not established from the hot wire measurements, platform oscillations may result in fluctuations in the strength of the trailing tip vortices. Moreover such fluctuations may also result from radial changes to the helical vortex path, that is, periodic compression and expansion of the path's diameter. Capturing such radial variations is practically not possible with a single hot wire probe.

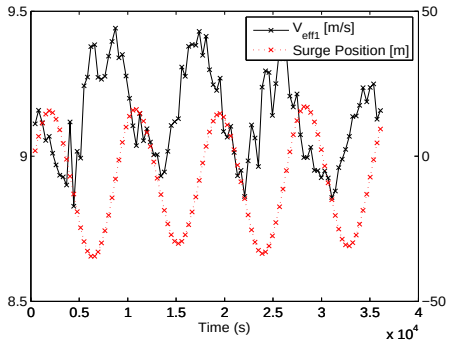

(a) Variations in the hot wire peak velocity (at $r/R = 1.1$ and $\lambda = 3.2$) and surge position signals with time

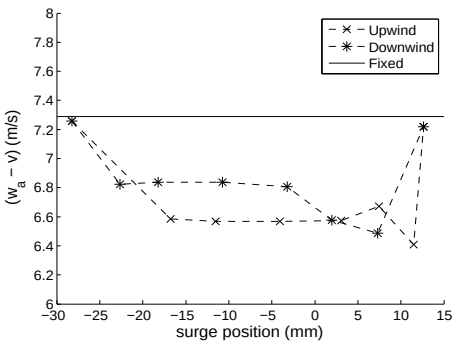

(b) Axial wake velocity versus surge position for $\lambda = 3.2$ and *r/R=0.7*

Figure 7

The effect of the surge velocity on the near-wake flow characteristics was also analysed by considering the variations in the axial wake velocity at (z/R = 0.17,0.35) against r/R and θ_{az}. In

order to describe the hot wire velocity measurements relative to the resultant wind intersecting the blade, the surge velocity vector was deducted from w_a as shown in fig. 7b.

Fig. 7b clearly shows that the axial wake velocity varies with surge location. This phenomenon was observed for all λ where an average difference in the axial wake velocity of 17% was obtained. Therefore despite of the fact that for each surge location the average surge velocity was deducted from w_a, a high variation in the axial wake velocity was still obtained. In fact the maximum surge velocity measured at the base of the tower (0.11 m/s) was only a small fraction of the relative wind speed. It has yet to be investigated whether such an occurrence is due to complex wake phenomena which are unable to be detected by a single probe hot wire.

FREE-WAKE VORTEX SIMULATIONS

An advanced numerical model was used to verify and obtain a better understanding about the physical observations obtained from the UoM OFWT experiment. The Wake Induced Dynamic Simulator (WinDS) developed at the University of Massachusetts and written by Sebastian and Lackner [10] [22] was used to analyse the wake formation of a full-size OFWT subjected to realistic platform oscillations. The free wake vortex code is based on the lifting line theory validated with the MEXICO and TUDelft experiments for fixed wind turbine rotors. The simulations were carried out by considering the NREL 5MW turbine with a TLP structure designed by MIT. To simplify the analysis, a flat plate aerofoil was used throughout the entire blade span. The platform surge motion was specified by fitting a 1D sinusoidal equation to the FAST simulated MIT TLP response [9]. This sinusoidal fit (frequency of 0.016 Hz and amplitude 0.435 m) for the surge displacement as function of time was prescribed to the free wake vortex model. Shaft tilt and turbine pre-coning were also neglected while the Scully viscous core model was used. The simulations were set at the rated velocity of 11 m/s while varying the rotor frequency and hence also λ. For the fixed platform conditions a number of time steps equivalent to 10 rotor revolutions were set while 1 surge cycle was simulated in the case of the floating condition. The simulations were run on Albert, a super-computing cluster situated at UoM.

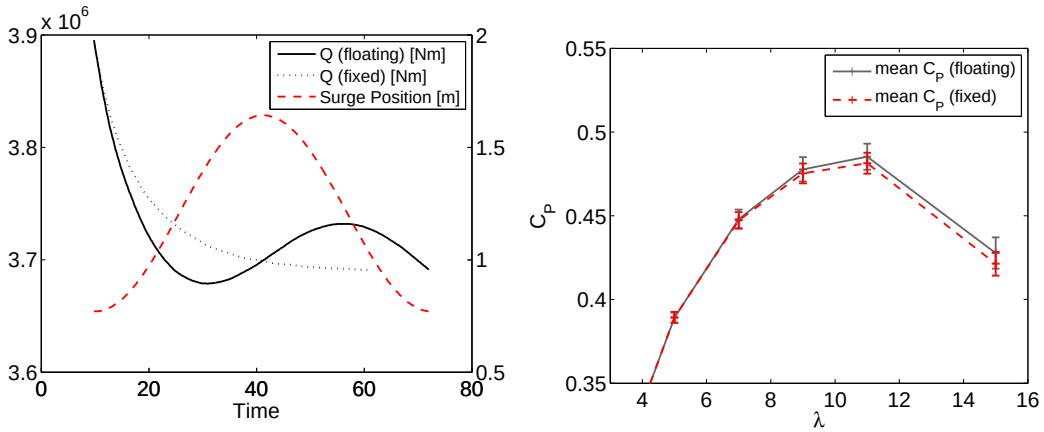

(a) Torque and surge position with time for $\lambda = 7$, $C_T = 0.55$

(b) C_P-λ

Figure 8: WinDS simulation results

From fig. 8a it can be seen that as opposed to the results of the UoM OFWT experiment, surge-induced fluctuations in the aerodynamic torque are evident and account to an RSD of 1% at

λ = 7. This further verifies the limitations mentioned in the results of Phase I. The time lag between the surge displacement and the torque also shows the importance of investigating the effect of stability on the OFWT performance. Fig. 8b shows that at high λ a difference in C_P emerges between the fixed and floating conditions. While this may suggest that the blade-wake interactions have a considerable effect on the wind turbine aerodynamics, the higher standard deviation in C_P shows that at high λ the accuracy of the chosen viscous core and vortex core growth models together with the numerical integration scheme needs to be analysed in detail.

CONCLUSIONS

From experimental results on a model OFWT evidence of wake-induced torque fluctuations was not found. This was likely due to the fact that the experiment was undertaken at low C_T and Re values. On the other hand numerical simulations on a full size OFWT under realistic conditions proved the existence of fluctuations in the aerodynamic torque under one dimensional platform surge motions. From the UoM OFWT experiment variations in the mean and distribution of the tip vortex path in a direction parallel to the oncoming wind between fixed and floating conditions were found to be minimal. However the wave-induced effects on a_1 were found to be substantial. Moreover higher variations in the mean C_P between the floating and fixed conditions at higher λ were observed in both the experiment and the numerical simulations. Further analysis on the wake development of an OFWT using free-wake vortex models will shed more light on the results presented in this paper.

ACKNOWLEDGEMENTS

The research work disclosed in this publication is partially funded by the Strategic Educational Pathways Scholarship (Malta). The scholarship is part-financed by the European Union - European Social Fund.

This research has been carried out using computational facilities procured through the European Regional Development Fund, Project ERDF-080 A Supercomputing Laboratory for the University of Malta (http://www.um.edu.mt/research/scienceeng/erdf_080).

REFERENCES

[1] S. Butterfield, W. Musial, J. Jonkman, and P. Sclavounos, "Engineering challenges for floating offshore wind turbines," in *Copenhagen Offshore Conference*, (Copenhagen, Denmark), 2005.

[2] W. Musial, S. Butterfield, and A. Boone, "Feasibilty of floating platform systems for wind turbines," in *23rd ASME Wind Energy Symposium*, (Reno, Nevada), 2004.

[3] A. Cordle, "State of the art design tools for floating offshore wind turbines," tech. rep., Project UpWind, March 2010.

[4] W. Matha, "Challenges in simulation of aerodynamics, hydrodynamics, and mooring-line dynamics of floating offshore wind turbines," in *21st Offshore and Polar Engineering Conference*, 2011.

[5] H. Bagbanci, "Dynamic analysis of offshore floating wind turbines," m.sc dissertation, Lisbon Technical University, Portugal, 2011.

[6] S. Shim, "Coupled dynamic analysis of floating offshore wind farms," m.sc dissertation, Texas A & M University, U.S.A, 2007.

[7] M. Karimirad and T. Moan, "A simplified method for coupled analysis of floating offshore wind turbines," *Marine Structures*, vol. 27, pp. 45–63, July 2012.

[8] J. Jonkman and P. Sclavonous, "Development of fully coupled aeroelastic models for offshore wind turbines," in *ASME Wind Energy Symposium*, (Reno, Nevada), January 2006.

[9] T. Sebastian, *The Aerodynamics and Near Wake of an Offshore Floating Horizontal Axis Wind Turbine*. Doctor of philosophy, Department of Mechanical & Industrial Engineering, University of Massachusetts, 2012.

[10] T. Sebastian, *Wake Induced Dynamic Simulator - WInDS*. Wind Energy Center, Department of Mechanical & Industrial Engineering, University of Massachusetts Amherst, December 2011.

[11] D. Roddier, C. Cermelli, A. Aubault, and A. Weinstein, "Windfloat: A floating foundation for offshore wind turbines," *Renewable and Sustainable Energy*, vol. 2, June 2010.

[12] "Hywind - the world's first full-scale floating wind turbine," 2009. Statoil press relaease.

[13] "Sway successfully deployed prototype," 2011. Sway press release.

[14] A. Naqvi, "Scale model experiments on floating offshore wind turbines," m.sc dissertation, Worcester Polytechnic Institute, U.K., 2012.

[15] H. Martin, "Development of a scale model wind turbine for testing of offshore floating wind turbine systems," m.sc dissertation, University of Maine, U.S.A, 2011.

[16] J. Leishman, *Principles of Helicopter Aerodynamics*. New York: Cambridge University Press, 2006.

[17] R. Mikkelsen, *Actuator Disc Methods Applied to Wind Turbines*. PhD thesis, Department of Mechanical Engineering, Technical University of Denmark, 2003.

[18] I. Bayati, M. Belloli, and S. Giappino, "An experimental test rig to simulate hydrodynamic forcing on floating offshore wind turbine platforms," in *Offshore Wind and other marine renewable Energy in Mediterranean and European Seas*, (Rome, Italy), pp. 45–53, 2012.

[19] W. Haans, T. Sant, G. van Kuik, and G. van Bussel, "Velocity measurements in the near wake of a horizontal axis wind turbine," in *31st European Rotorcraft Forum*, (Florence, Italy), 2005.

[20] L. Vermeer, J. Sorensen, and A. Crespo, "Wind turbine wake aerodynamics," *Progress in Aerospace Science*, vol. 39, pp. 467–510, 2003.

[21] T. Sant, *Improving BEM-based Aerodynamic Models in Wind Turbine Design Codes*. PhD thesis, University of Malta, Malta and Delft University of Technology, Netherlands, 2007.

[22] T. Sebastian and M. Lackner, "Development of a free vortex wake method code for offshore floating wind turbines,"

NUMERICAL MODELLING OF FLUID-STRUCTURE INTERACTIONS FOR FLOATING ACTUATOR DISCS

A. Viré[1], J. Xiang[1], M.D. Piggott[1,2], C.J. Cotter[3], C.C. Pain[1]

[1]Imperial College London, Earth Science & Engineering, SW7 2AZ London, UK, avire@imperial.ac.uk
[2]Imperial College London, Grantham Institute for Climate Change, SW7 2AZ London, UK
[3]Imperial College London, Dept. of Aeronautics, SW7 2AZ London, UK

ABSTRACT

This paper tackles the numerical modelling of fluid-structure interactions in the context of floating wind turbines. Two finite-element models are coupled in order to represent the mutual interactions between fluids and floating solids. The fluid-dynamics model 'Fluidity-ICOM' [15, 17] solves the Navier–Stokes equations on a fluid mesh covering the whole computational domain (containing both fluids and solids), whereas a super-imposed solid mesh represents the solid structures. The solid dynamics is solved using the finite-discrete element model (femdem) 'Y3D' [25]. The fluid and solid meshes are both unstructured. The fluid model can further refine dynamically the regions of high shear, through mesh adaptivity. The effect of the solid on the fluid dynamics, and vice-versa, is modelled through a volumetric penalty force added to the momentum balances of the fluids and solids. In order to satisfy the action-reaction principle at a discrete level, a supermesh [6] is constructed from the intersections between fluid and solid meshes. This enables: (i) arbitrarily-high orders of representation of the discrete fields, and (ii) different representations of the discrete fields on each mesh [23]. The present models are applied to two different cases. First, a fixed actuator-disc representing a wind turbine is subjected to a uniform flow. The numerical results obtained for different mesh resolutions and thrust coefficients are compared with a semi-analytical solution [4]. It is highlighted how adapting the mesh dynamically to the curvatures of the velocity and pressure fields predicts well the velocity deficit induced by the disc. Second, the dynamics of a buoyant pile is analysed when placed at the interface between air and water. It is qualitatively shown that the numerical solution provided by the coupled models satisfies Archimedes' principle. This work is a first-step towards the fully-coupled simulation of offshore wind turbines supported by a floating spar.

INTRODUCTION

The numerical modelling of fluid-structure interactions is important in the context of renewable energy production using offshore floating devices. This work targets floating wind turbines, where a floating pile supports the wind turbine and is moored to the seabed. Such devices are attractive in deep seas (typically deeper than 50 metres), where bottom-mounted foundations are too expensive. The numerical modelling of floating wind turbines is very challenging due to the dynamic interactions between the moving air-water and fluid-solid interfaces, and the presence of solid components of different physical properties. Numerical models are attractive in studying such coupled fluid-solid problems, because they can analyse different configurations while limiting expensive laboratory testing. A number of numerical methods exists to analyse the behaviour of fixed or floating structures, including: (i) linear radiation-diffraction codes, (ii) inviscid fully-nonlinear models (typically based on a velocity potential formulation), and (iii) viscous fully-nonlinear models (for solving the Navier–Stokes equations) [21]. The latter are particularly suitable for investigating extreme wind and wave conditions, for which the effects of fluid viscosity and air entrainment are important. In the case of floating bodies, the mutual interactions between fluids and solids further require the fluid- and solid- dynamics equations to be coupled [22]. The coupling can be achieved using either a single or multiple models. Two separate models, based on different spatial and temporal discretisations, are used in this work. On the one hand, the Navier–Stokes equations governing the fluid dynamics are solved using the open-source finite-element model 'Fluidity-ICOM' [15, 17]. The solution is computed on a *fluid mesh*, which covers the whole computational domain (containing both fluids and solids). In the regions covered by the solids, the effect of the solids on the fluid dynamics is accounted for as an additional force in the momentum equations. The volumetric force aims at relaxing the behaviours of the fluids and solids to one another in the regions covered by the solids. This methodology underpins the so-called immersed boundary method [8, 12, 14, 16]. On the other hand, the finite-discrete element model (femdem) 'Y3D' [25] solves the non-linear dynamics of solid structures. The latter are meshed separately using a so-called *solid mesh*. The fluid and solid meshes are both unstructured. The regions occupied by the solids are identified by mapping the solid mesh onto the fluid mesh. A solid-concentration field is thus defined on the fluid mesh. The volumetric force representing the effect of the solid on the fluid dynamics, and vice-versa, is also projected between both meshes. A novel algorithm was recently developed in order to ensure that the action-reaction principle is satisfied at a discrete level during the projections [23]. As opposed to other existing techniques, the algorithm enables: (i) arbitrarily high orders of representation of the discrete fields, and (ii) different representations of the discrete fields in each model. The present coupling algorithm presents further advantages. Firstly, the use of two meshes allows for the resolution to be tailored to the specific needs of the fluids and solids. Secondly, the present method does not yield ill-posed problems in the resolution of the Navier–Stokes equations, when multiple solids become arbitrarily close to one another. Lastly, the fluid mesh can be refined at the fluid-structure interfaces, which are tracked accurately as the solids move. The interactions between two fluids (e.g. air and water) are modelled by solving an advection-diffusion equation for a fluid-concentration field. The latter is represented by a piecewise-constant field over the finite elements. The present interface-tracking method [24] assumes that the fluid phases are immiscible.

NUMERICAL FORMULATION

Governing equations

Figure 1 illustrates the typical sequence of steps when modelling fluid-structure interactions in this study. The flow problem is solved over an extended domain $V = V_f \cup V_s$ (step 1 in Figure 1), where the fluid domain is V_f and the solid regions are denoted by V_s. As explained in the previous section, the Navier–Stokes equations are solved on a fluid mesh covering the extended domain V. However, in the regions covered by the solids, the behaviours of the fluids and solids are relaxed to one another. This requires modifying the equations in two ways. First, they are expressed in terms of a monolithic velocity field $u = \alpha_f u_f + \alpha_s u_s$, where u_f and u_s are the fluid and solid velocities, and $\alpha_i = V_i/V$ denotes the volume-fraction field (subscript f for the fluids and s for the solids). Second, a penalty force is added to the momentum balance, in order to relax the monolithic and solid velocities to one another in V_s. The governing continuity and momentum equations are

$$\nabla \cdot u = 0, \tag{1}$$

and

$$\rho \frac{\partial u}{\partial t} + \rho (u \cdot \nabla) u = -\nabla p + \nabla \cdot (2\mu S) + B + F_f, \tag{2}$$

where ρ is the fluid density, p is the pressure field, μ is the dynamic viscosity of the fluid, S is the deviatoric part of the strain-rate tensor, B represents external body forces (e.g. buoyancy), and F_f is the penalty force. The latter aims at discretely relaxing the velocities at the fluid-solid interfaces, and can be expressed as

$$F_f = \beta \alpha_s \alpha_f (u_s - u_f), \tag{3}$$

where $\beta = \rho/\Delta t$ is a factor that dictates how fast the fluid and solid velocities relax to one another, and Δt is the time step. At a discrete level, the product of volume fractions in Eq. (3) weakly enforces the relaxation condition at the fluid-solid interface. Since the fluid-dynamics equations are solved for the monolithic velocity u instead of u_f, Eq. (3) is written as

$$F_f = \beta (\alpha_s u_s - \alpha_s u), \tag{4}$$

by using the definition of the monolithic velocity. In this work, the open-source model 'Fluidity-ICOM' [15, 17] is used to solve the fluid-dynamics equations.

The solid-dynamics equations are solved using the finite-discrete element model (femdem) 'Y3D' [25] on a separate solid mesh covering solely the solid domain V_s (step 3 in Figure 1). The solid-dynamics equations are expressed as

$$\mathscr{L} d_s + F_{int} = F_{ext} + F_c + F_s, \tag{5}$$

where d_s denotes the solid displacement, $\mathscr{L}$ is an operator dependent on the velocity gradient, F_{int} stands for the internal forces, F_c is the contact force when multiple solids impact on each other, and F_{ext} is the external force including the surface traction force and the body forces. Details about these forces are given in [25]. The action-reaction force due to the surrounding fluid is denoted by F_s. Because fluids and solids interact, this force has to be exchanged between both models at every time interval (steps 2 and 4 in Figure 1). Importantly, certain conditions need to be ensured at the fluid-solid interface. For example, Newton's third law states that the total force acting on the fluids should equal the total force acting on the solids, the two forces being oriented in opposite directions, i.e.

$$\int_V F_f dV = -\int_{V_s} F_s dV_s. \tag{6}$$

The present algorithm ensures that this condition is satisfied at a discrete level. The force transfer is performed in two distinct steps, as illustrated in Fig. 2. The part of the force depending on the monolithic velocity, i.e. $F_1 = -\beta\alpha_s u$ in Eq. (3), is exchanged from fluid to solid model. It is first computed on a supermesh [6, 7], which is formed from the intersections between fluid and solid meshes, and then projected to the fluid and solid meshes using a Galerkin projection (Fig. 2). As shown in the literature [23], this ensures that the volume integral of F_1 is identical on both meshes, independently of: (i) the mesh resolutions, and (ii) the polynomial orders of the basis functions on each mesh. The part dependent on the solid velocity, i.e. $F_2 = \beta\alpha_s u_s$ in Eq. (3), is transferred from solid to fluid model. Because the solid mesh lies within the fluid mesh, a Galerkin projection of F_2 from solid to fluid mesh satisfies the same conservation property [23]. The number of solid time-steps per fluid time-step is usually greater than one, in order to resolve stresses propagating inside the solids. Thus, the force F_2 is averaged over the solid time-steps before being transferred to the fluid model.

Mesh adaptivity

The fluid model has the capability of optimising the mesh regularly in time, in order to refine the spatial resolution around certain flow features. In this work, mesh refinement tracks the small-scale dynamics developing in the turbine wake, while the mesh is coarsened far from the turbine. Details on the mesh-adaptivity procedure in 'Fluidity-ICOM' can be found in the literature [7, 10]. In this work, the mesh is adapted on two fields (i.e. velocity and pressure), as detailed in the next section. The desired geometric properties of the new mesh is described by a metric, which is a symmetric positive-definite tensor field. The metric is computed from the Hessian H of the solution field and a user-defined weight ε, i.e.

$$M = \det|H(x)|^{-\frac{1}{4+n}} \frac{|H(x)|}{\varepsilon(x)}, \tag{7}$$

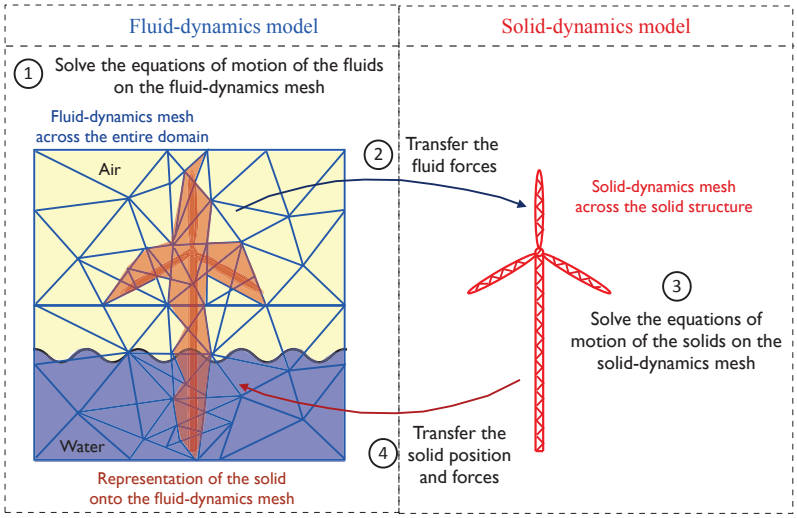

Figure 1: Typical sequence of steps (numbered from 1 to 4) required when modelling fluid-solid interactions using two distinct models.

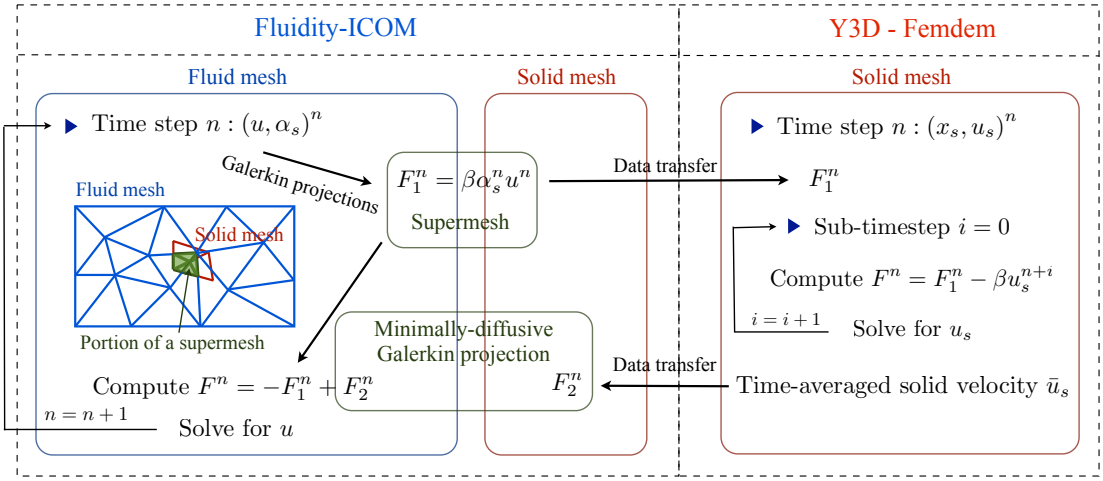

Figure 2: Coupling procedure between the finite-element models, with an illustration of a supermesh portion.

where n is the dimension of the space and the modified Hessian $|H|$ is

$$|H(x)| = Q(x)^T |\Lambda(x)| Q(x), \qquad |\Lambda(x)|_{ij} = \begin{cases} |\lambda_i(x)| & \text{if } i = j, \\ 0 & \text{if } i \neq j. \end{cases} \tag{8}$$

In Eq. (8), $\{\lambda_i\}$ are the eigenvalues of the Hessian, Q is the matrix of normalised eigenvectors, and the superscript T stands for the transpose. A metric is constructed for each of the fields on which adaptivity is performed, and the global metric is obtained from the superposition of each metric. The metrics provide a bound for the L_2 norm of the solution's interpolation error, whose target value is ε. The mesh is modified through optimisation, by minimising the error between the current size and shape of the elements and the values encoded in the global metric. The adaptivity procedure consists in generating a mesh $\mathscr{M}$, such that every edge v has unit edge length when measured with respect to the metric M, i.e.

$$\|v\|_M = \sqrt{v^T M v} = 1 \qquad \forall v \in \mathscr{M}. \tag{9}$$

According to Eq. (7), the mesh is refined for high curvatures in the chosen field (i.e. large eigenvalues) or small values of the field weight ε. Conversely, the mesh is coarsened in regions of low curvature in the field or if the field weight is increased. In this study, mesh adaptivity is controlled solely by the target value ε of the L_2 norm of the solution's interpolation error.

RESULTS

Uniform flow past a fixed actuator-disc

Wind turbines can be parameterised by thin discs, over which a thrust force is uniformly spread. The force acting on the fluid is derived from the actuator-disc theory [4], which assumes that the flow is homogeneous, incompressible, steady, friction-less and that no external force acts on the fluid up- or down-stream of the rotor. The thrust force is given by

$$T = \frac{1}{2}\rho u_0^2 A_d C_T, \tag{10}$$

where C_T is the thrust coefficient of the wind turbine, A_d is the frontal-area of the disc of diameter D, and u_0 is the far-upstream velocity. The disc area, thrust coefficient, and fluid density, are input parameters of the model. The far-upstream velocity u_0 is calculated at every iteration of the fluid-dynamics model, as

$$u_0 = \frac{u_d}{1-a}, \tag{11}$$

where u_d is the numerical velocity probed at the disc, and a is the axial-induction factor [4] defined as

$$a = \frac{1}{2}\left(1 - \sqrt{1-C_T}\right). \tag{12}$$

Existing studies on flows past actuator discs include: (i) semi-analytical solutions for the uniform potential flow past an infinitely-thin disc [4], (ii) computational fluid dynamics simulations of turbine wakes, for example [11, 19, 20], and (iii) experimental investigations in wind tunnels and wave tanks, e.g. [5, 9, 13]. The actuator-disc parameterisation of wind turbine however

presents certain limitations, including the absence of swirl and tip vortices induced in the flow. This representation is thus unsuitable for computing the aerodynamics and aero-elasticity of a three-bladed rotor under realistic conditions. However, it is often adopted when modelling farms of wind turbines, for which the intermediate- and far- wake regions are of interest, see for example [2, 3, 18]. The actuator-disc representation is chosen in this study for two reasons. First, the purpose is to validate the model on flows where a semi-analytical solution exists. At this stage, the aero-elasticity of realistic rotors is not discussed and is the subject of future work. Second, there is a rising interest for modelling farms of tidal turbines using 'Fluidity-ICOM', in which case coupling an actuator-disc model with a hydrodynamic model for the ocean is important. Because this paper considers a uniform flow without using turbulence model, the numerical results are solely compared with the semi-analytical solutions [4]. However, ongoing work focuses on non-uniform flows and high Reynolds numbers, to enable comparisons with experimental studies. In this paper, fixed turbines are considered in order to validate the model. Thus, the solid model does not solve the solid-dynamics equations. However, two meshes are used as described in the previous section: the fluid mesh covers the whole computational domain, while the solid mesh only discretises the disc. A solid-concentration field is defined on the fluid mesh, in order to identify the region occupied by the disc. The solid concentration is obtained by projecting a unitary field from solid to fluid mesh using a Galerkin projection. The thrust force acting on the fluid is spread uniformly across the disc. The disc centre is placed at $20D$ from the domain outlet, and $5D$ from the inlet and sides. The disc axis is aligned with the flow. The Reynolds number is set to $Re_D = \rho u_0 D/\mu = 10^3$, and three values of the thrust coefficients are considered ($C_T = 0.2; 0.45; 0.7$). Table 1 summarises the simulation parameters, where Δ is the disc thickness, N is the number of mesh nodes at steady state, l_e is the minimum length of the mesh edges, L_e is the maximum length of the mesh edges, and $\mathscr{E}_{\Delta p}$ indicates the relative error between the numerical and theoretical values of the pressure drop at the disc, when the steady state in reached. All the simulations are ran on 32 processing cores. The typical computational times, for running a non-dimensional time of $Tu_0/D = 50$, vary from 80 hours (non-adaptive cases) to 290 hours (adaptive cases). The higher run times are obtained at large thrust coefficients and small disc thickness. In all the simulations, the time step is such that the Courant number is fixed at 0.3. The velocity and pressure fields are further represented by continuous piecewise-linear functions over the elements (P1 finite elements). Simulations without dynamic re-meshing (i.e. non-adaptive) are labelled by NA in Tab. 1. In these cases, the mesh is generated by initially setting the interpolation error on the solid-concentration field to $\varepsilon_{\alpha_s} = 0.02$, and keeping the mesh unchanged throughout the simulations. By contrast, for the simulations with dynamic re-meshing (labelled by A), the fluid mesh is re-generated at a non-dimensional period of $Tu_0/D = 1$. The mesh modifications are such that the interpolation error on the pressure and velocity fields equals $\varepsilon_{p,u} = 0.05$. This yields mesh refinement around the disc and in its wake. Snapshots of the mesh in the $x-y$ plane (coloured by the streamwise velocity field) are shown in Fig. 3, without (top) and with (bottom) mesh adaptivity. The role of mesh adaptivity is particularly apparent in the disc wake.

Table 1 highlights that, for a given thrust coefficient, the magnitude of $\mathscr{E}_{\Delta p}$ systematically decreases when the disc thickness decreases. This is expected since the theoretical value of the pressure drop is derived in the limit of infinitely thin discs. Also, $\mathscr{E}_{\Delta p}$ is not significantly affected

Case	Adaptivity	Δ/D	C_T	$N \times 10^5$	l_e/D	L_e/D	$\mathscr{E}_{\Delta p}$ (%)
NA-T1	No	0.1	0.2	4.9	0.012	1.7	-8.6
NA-T1	No	0.1	0.4	4.9	0.012	1.7	-7.7
NA-T1	No	0.1	0.7	4.9	0.012	1.7	-5.8
NA-T05	No	0.05	0.2	4.9	0.012	1.7	-1.8
NA-T05	No	0.05	0.4	4.9	0.012	1.7	0
NA-T05	No	0.05	0.7	4.9	0.012	1.7	3.9
A-T1	Yes	0.1	0.2	7.2	0.022	0.72	-5.3
A-T1	Yes	0.1	0.4	11.1	0.015	0.71	-7.4
A-T1	Yes	0.1	0.7	13.7	0.01	0.69	-6.2
A-T05	Yes	0.05	0.2	7.4	0.016	0.71	-2.3
A-T05	Yes	0.05	0.4	8.6	0.01	0.68	-1
A-T05	Yes	0.05	0.7	12.7	0.01	0.69	-4

Table 1: Summary of the parameters and results when simulating flow past a fixed actuator-disc.

by mesh adaptivity, for a given thrust coefficient and disc thickness. This is explained by the fact that adaptivity mainly changes the mesh in the turbine wake, rather than in the disc vicinity (Fig. 3). The streamwise evolution of the streamwise velocity at the disc centreline $u_x(x, r = 0)$ is shown in Fig. 4, for $C_T = 0.2$ (top left), $C_T = 0.45$ (top right), and $C_T = 0.7$ (bottom left). The disc is located at $x/D = 0$. For each value of the thrust coefficient, results are shown without and with mesh adaptivity. Two values of the disc thickness are also considered: $\Delta/D = 0.1$ (labelled by T1) and $\Delta/D = 0.05$ (labelled by T05). The numerical results are compared with the corresponding semi-analytical solution [4], which is shown by a continuous line. In all cases, the numerical results agree well will the theoretical predictions in the near-wake ($x/D < 3$). Without mesh adaptivity, the streamwise velocity $u_x(x, r = 0)$ underestimates the theoretical solution for $3 < x/D < 10$, and overestimates the velocity deficit for $x/D > 10$. These discrepancies are due to an under-resolution of the flow field in the wake, when a fixed mesh is used. They disappear with mesh adaptivity. The numerical results obtained with mesh adaptivity exhibit the correct velocity deficit, which extends up to approximately $x/D \approx 10$. Further downstream, wake recovery occurs due to the effect of the fluid viscosity in the numerical simulations. No wake recovery is observed in the theoretical results, which are derived under the inviscid approximation. Furthermore, results are rather insensitive to the value of the disc thickness, for the range considered in this study. It is worth noting that this study focuses on the validation of the actuator-disc model using the present dual-mesh approach, rather than on the adequacy of the model to represent turbine wakes. Unlike flow past three-bladed rotors, the present parameterisation presents certain limitations, including the absence of swirl and tip vortices induced in the flow. The analysis of other turbine models accounting for these effects is beyond the scope of this study. Figure 4 (bottom right) shows the streamwise evolution of the streamwise velocity, $u_x(x, r = D)$, away from the disc centreline and using mesh adaptivity. The numerical value of the velocity peak, which occurs at $x/D \approx 1/2$, tends to overestimate the theoretical prediction, particularly at large thrust coefficients. This results from the entrainment of surrounding fluid, which is enhanced by

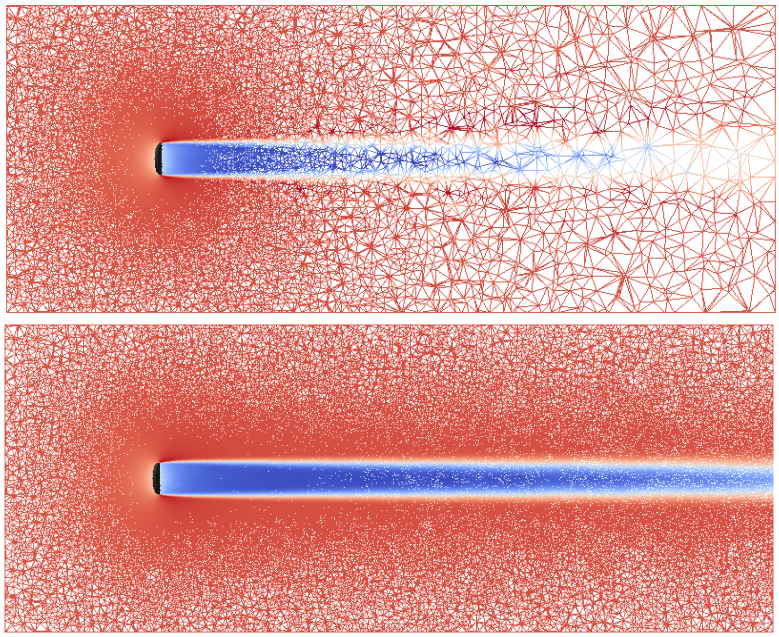

Figure 3: Numerical mesh, coloured by the streamwise velocity field, in the $x-y$ plane: non-adaptive (top), adaptive (bottom). The black area represents the disc.

the viscous nature of the fluid in the numerical simulations. Results without adaptivity are not shown for brevity and because the under-resolution of the shear layer developing at the disc tip causes spurious oscillations in the streamwise velocity in the wake at $r = D$. The extension to higher Reynolds numbers and other turbine models is the subject of future work.

Truncated pile floating at an air-water interface

The previous section demonstrated the applicability of the coupling algorithm to model fixed turbines using an actuator-disc parameterisation. In this section, the dynamic response of a floating pile is analysed when placed at the interface between two fluids of different physical properties. As discussed previously, a fluid mesh covers the whole computational domain and a solid mesh discretises the pile. In this case, the mutual interactions between fluids and solids further require to solve both the fluid- and solid- dynamics equations. The interface between the fluids is modelled using a tracking method. The fluid phases are assumed to be immiscible and a volume-fraction field α_f is associated with each fluid. The volume-fraction fields vary between 0 and 1, and they collectively sum to unity across the domain. The fluid interface is tracked in time by solving an advection-diffusion equation for α_f. A flux-limiting scheme is used to replace the need for interface reconstruction and particle tracking [24]. This greatly simplifies the interface-tracking method on unstructured meshes. Consistent discretisations for the momentum and material advection steps further ensure conservation of α_f. The advection-diffusion

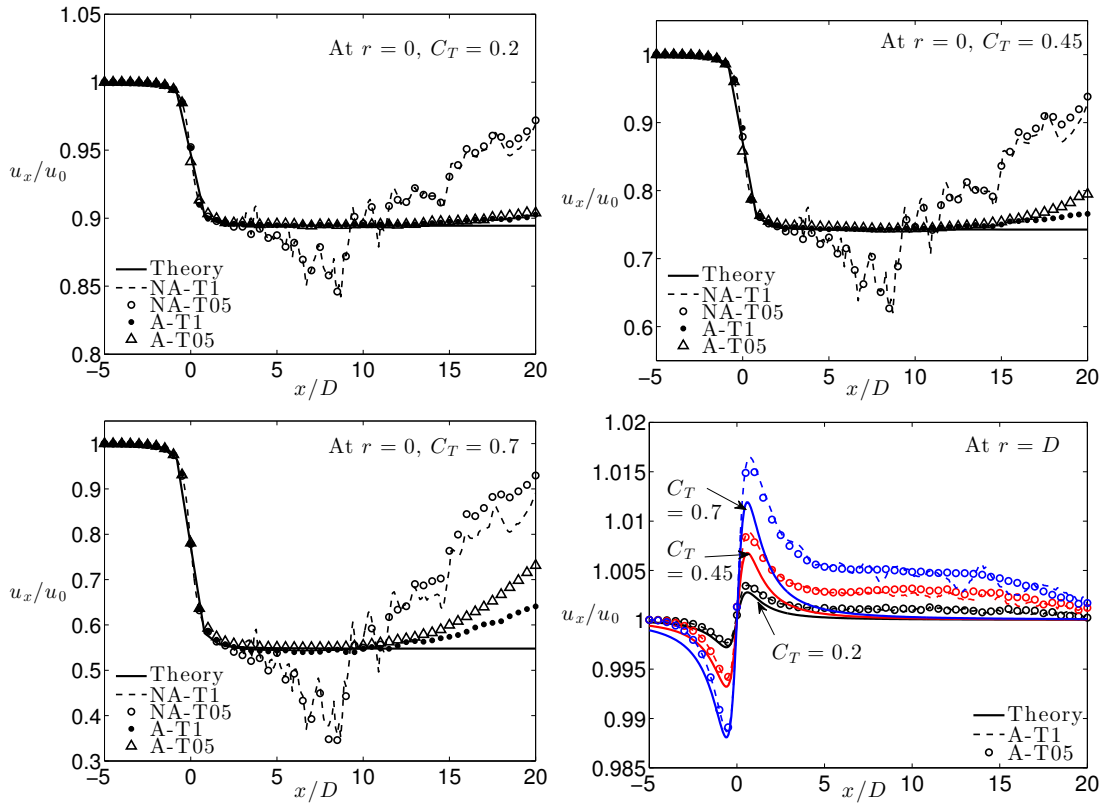

Figure 4: Streamwise evolution of the streamwise velocity $u_x(x)$: at $r = 0$ for $C_T = 0.2$ (top left), at $r = 0$ for $C_T = 0.45$ (top right), at $r = 0$ for $C_T = 0.7$ (bottom left), at $r = D$ for $C_T = 0.2; 0.45; 0.7$ (bottom right).

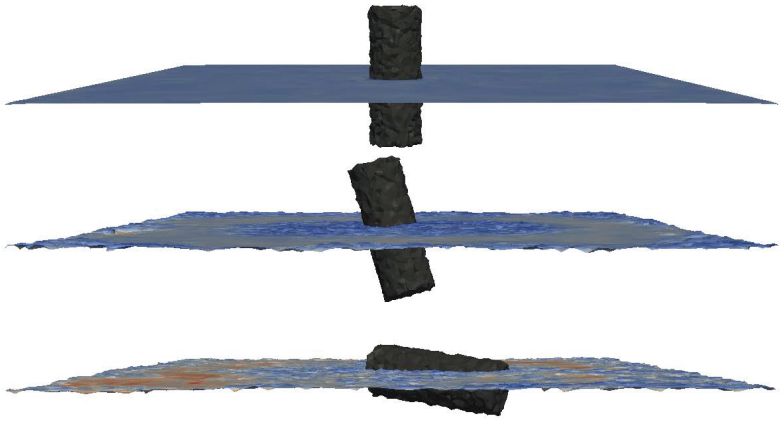

Figure 5: Dynamics of a truncated pile placed at an air-water interface: $t = 0s$ (top), $t = 2s$ (centre), $t = 10s$ (bottom).

equation is solved on a dual control-volume mesh, for a piecewise-constant representation of the volume-fraction fields. The advective fluxes are limited using the HyperC approach [24], and the Bassi-Rebay discretisation scheme is used for the diffusion term [1]. The velocity field is piecewise constant over the elements (P0 discretisation), while the pressure field varies linearly (P1 discretisation). The extension to higher-order finite-element pairs for velocity and pressure is the subject of future work.

The pile of diameter D and length $4D$ is centred in a box of edge length $20D$. The top half of the box is filled with air ($\rho_1 = 1.2\text{kg}\cdot\text{m}^{-3}$, $\mu_1 = 18.27\mu\text{Pa}\cdot\text{s}$) and the bottom half with water ($\rho_2 = 1000\text{kg}\cdot\text{m}^{-3}$, $\mu_2 = 1.002\text{mPa}\cdot\text{s}$). The pile density is uniform and equals half the water density. The simulation is ran on one CPU and requires approximately 15 hours of run time per second of physical time. The fluids are initially still and the pile lies vertically across the fluid interface (Figure 5, top). Because the pile position is not stable, it starts moving in heave before toppling over (Figure 5, centre). The pile eventually lies horizontally after approximately four seconds of physical time. It however continues to pitch slightly around the equilibrium position, which is horizontal and half submerged in water following Archimedes' principle (Fig. 5, bottom). This is possibly due to a low level of accuracy in the numerical representation of the interface, and is the subject of further investigation.

CONCLUSIONS

In this work, a novel coupling algorithm between two finite-element models is applied to the simulation of: (i) flow past a fixed turbine represented by an actuator disc, and (ii) a truncated pile floating at the interface between air and water. The coupling approach is novel in that spatial conservation is verified independently of the mesh resolution and the types of mesh used in both

models. To the authors' knowledge, previous studies enabling spatial conservation are limited in terms of mesh shape at the fluid-solid interface (e.g. coinciding meshes in both models) and/or level of representation of the discrete fields. The present method is also very versatile, since the use of two distinct models allows specific numerical requirements to be met for each material.

This paper shows the suitability of the present immersed-body approach, based on two separate meshes for the fluids and solids, to study flows past wind turbines. Good agreement between the theory and simulations was obtained for the velocity deficit induced by an actuator disc, when subjected to a uniform flow. It was also demonstrated how mesh adaptivity can be used in the fluid-dynamics model to accurately predict the turbine wake. Future work will focus on a wider range of turbine models and comparisons with experimental results. The present study also shows the capability of the coupled models to simulate the dynamics of a floating solid placed at an interface between two fluids, which are initially at rest. In the context of modelling multiple fluids, future work will focus on increasing the levels of representation of the velocity, pressure, and fluid-concentration fields in the interface-tracking method. This is required to accurately model wave propagation over long distances. This work is a first-step towards the fully-coupled numerical simulation of floating foundations for offshore renewables, using non-linear finite-element models.

This research is supported by the European Union Seventh Framework Programme (FP7/2007-2013) under grant agreement PIEF-GA-2010-272437.

REFERENCES

[1] F. Bassi, S. Rebay, J. Comput. Phys. 131, pp 267-279 (1997).
[2] M. Calaf, M.B. Parlange, C. Meneveau, Phys. Fluids 23, 126603 (2011).
[3] F. Castellani, A. Vignaroli, Applied Energy 101, 432-440 (2013).
[4] J.T. Conway, J. Fluid Mech. 297, 327-355 (1995).
[5] G. España, S. Aubrunn, S. Loyer, P. Devinant, J. Wind Eng. Ind. Aerodyn. 101, 24-33 (2012).
[6] P.E. Farrell, J.R. Maddison, Comput. Methods Appl. Mech. Eng. 200, 89-100 (2011).
[7] P.E. Farrell, PhD thesis, Imperial College London (2009).
[8] B. Griffith, R. Hornung, D. McQueen, C. Peskin, J. Comput. Phys. 223, 10-49 (2007).
[9] M.E. Harrison, W.M.J. Batten, L.E. Myers, A.S. Bahaj, IET Renew. Power Gener. 4, 613-627 (2010).
[10] H.R. Hiester, M.D. Piggott, P.A. Allison, Ocean Modelling 38, 1-11 (2011).
[11] H.A. Madsen, C. Bak, M. Døssing, R. Mikkelsen, S. Øye, Wind Energy 13, 373-389 (2010).
[12] A. Mark, B.G.M. van Wachem, J. Comput. Phys. 227, 6660-6680 (2008).
[13] L.E. Myers, A.S. Bahaj, Ocean Eng. 37, 218-227 (2010).
[14] R. Mittal, G. Iaccarino, Annu. Rev. Fluid Mech. 37, 239-261 (2005).

[15] C.C. Pain, A.P. Umpleby, C.R.E. de Oliveira, A.J.H. Goddard, Comput. Methods Appl. Mech. Engrg. 190, 3771-3796 (2001).
[16] C. Peskin, J Comput Phys. 10, 252-271 (1972).
[17] M.D. Piggott, G.J. Gorman, C.C. Pain, P.A. Allison, A.S. Candy, B.T. Martin, M.R. Wells, Int. J. Numer. Meth. Fluids 56, 1003-1015 (2008).
[18] P-E. Réthoré, A. Bechmann, J.N. Sørensen, S.T. Frandsen, J. Mann, H.E. Jørgensen, O. Rathmann, S.E. Larsen, J. Phys. Conf. Ser. 75, 012047 (2007).
[19] B. Sanderse, S.P. van der Pijl, B. Koren, Wind Energy 14, 799-819 (2011).
[20] J.N. Sørensen, W.Z. Shen, X. Munduate, Wind Energy 1, 73-88 (1998).
[21] J. Spinneken, V. Heller, S. Kramer, M. Piggott M, A. Viré, Int. J. Offshore and Polar Eng., ISOPE, Vol 3, 1043-1050 (2012).
[22] A. Viré, Rev. Environ. Sci. Biotechnol. 11(3), 223-226 (2012).
[23] A. Viré, J. Xiang, F. Milthaler, P.E. Farrell, M.D. Piggott, J.-P. Latham, D. Pavlidis, C.C. Pain, Ocean Dynamics 62, 1487-1501 (2012).
[24] C. Wilson, PhD thesis, Imperial College London (2009).
[25] J. Xiang, A. Munjiza, J-P. Latham, Int. J. Numer. Meth. Engng. 79, 946-978 (2009).

Kinetic Energy Entrainment Analysis for Variable Arrangement Wind Turbine Arrays via Proper Orthogonal Decomposition

Nicholas Hamilton[1], Murat Tutkun[2] and Raúl Bayoán Cal[1]

[1]Portland State University, Dept. Mechanical & Materials Engineering, Portland, OR, USA
[2]Institute for Energy Technology, Kjeller, Norway

ABSTRACT

A wind turbine array was created for the purpose of investigating wake interaction and atmospheric boundary layer recovery dynamics given standard cartesian and row-offset configurations. The snapshot proper orthogonal decomposition is applied to velocity measurements. Resulting POD modes are used in constructing low dimensional models of turbulent statistics including turbulence production and the flux of kinetic energy. Convergence for low-dimensional models determined by the absolute span of the streamwise average profile of the Reynolds stress $-\langle uv \rangle$. Models demonstrate that the flux of kinetic energy and turbulence production are accurately rebuilt with approximately 1% of the total resultant POD modes.

INTRODUCTION

The proper orthogonal decomposition (POD) has proven to be an effective means of identifying coherent structures in turbulent flows and the energy associated with such structures within the energy cascade of turbulence [1-4]. Further, because POD organizes the structures within turbulence according to energy content, low-dimensional models can be used to reconstruct flow statistics omitting the energy associated with high frequencies or small structures [5].

Performing POD analysis to a set of stochastic data measurements results in a set of ordered modes that correspond to the energy containing events in a flow field. POD can be applied to any multi-point measurements including rakes of hot-wire probes, usually done in the *classical* POD, or scalar visualization data, particle image velocimetry (PIV), or data resulting from numerical simulations, all of which are typically done in the form of *snapshot* POD. The POD has been applied to many flow configurations. Berkooz et al. provide a comprehensive survey of the early applications [2].

The POD is limited in its ability to organize structures, events, or patterns by the nature of input data as inherently stochastic as noted in [6]. A greater range of scales associated with any particular flow, such as high Reynolds number flows, will typically yield a greater number of

energy containing POD modes, whereas low Reynolds number data will exhibit a greater concentration of energy in fewer modes. The analysis may also neglect infrequent events, regardless of their dynamical importance [4]. Additionally, the POD applied to random data showing homogeneous behavior in any particular dimension or direction reduces to a Fourier decomposition. In such a case, Fourier transforms are typically applied in such a direction for numerical efficiency, but often lead to a poor description of local flow structures and must retain a large number of modes to describe the dynamics [7].

The POD has been applied to field measurements of wind turbine inflows by [8] in a grid of point-measurements spanning the rotor area. The results were used to formulate a low-dimensional representation of the inflow and subsequently fed into fatigue and loading simulations for the rotor blades. The result of this application of the classical POD yielded many results of the effects of turbulence on the loading and life cycles of a turbine. Because the outflow of the turbine was not investigated in this study, no correlations were made between the energetic POD modes and the power output of the turbine. The spanwise and vertical components of inflow velocity were omitted from the POD on the assumption that they were already in their principle components. Reconstructions of up to the first five modes were used in the bending fatigue load simulations.

Identifying the turbulent wake structures influencing the performance of turbines in an array is followed in the present research. It is currently understood that the large structures are responsible for a majority contribution to wake recovery by the entrainment of kinetic energy from above. An experiment was designed at Portland State University (PSU) to test the performance of wind turbine models in various configurations within an array. Coupled with measurements of power output are flow measurements in the form of stereographic particle image velocimetry (SPIV). Energy containing structures are distinguished and analyzed using snapshot proper orthogonal decomposition (POD) and reconstructions of the flow and quantities including the flux of kinetic energy are made using a low-dimensional model.

THEORY

Following the development of Pedesen [9], the method of snapshots, referred to from here as *snapshot* POD, is built on a basis of uncorrelated flow measurements in a field. Snapshot POD was introduced by Sirovich [10] and applied to scalar visual data with the intent to distinguish energetic structures on which flow fields are build. The stochastic flow filed can be written as,

$$\mathbf{u}_n = \mathbf{u}(\mathbf{x}, t^n) = \mathbf{u}(\mathbf{x}, n\tau), \qquad n \in [1, ..., N], \tag{1}$$

where x and t^n refer to the spatial coordinates and time at sample n, respectively, and τ is the typical time separation between measurements. The time separation, τ, is typically at least twice the integral time scale to ensure that measurements remain uncorrelated. Here, the velocity data is a collection of stochastic turbulent fluctuations. With a large number of samples, the two-point spatial correlation tensor can be approximated as,

$$\mathbf{R}(\mathbf{x},\mathbf{x}') = \frac{1}{N}\sum_{n=1}^{N}\mathbf{u}(\mathbf{x},t^n)\mathbf{u}^T(\mathbf{x}',t^n). \tag{2}$$

Above, the prime indicates a spatial shift of flow measurements.

The two-point spatial correlation tensor becomes the kernel of the POD eigenvalue problem solved numerically. It is then assumed that a basis of N modes can be written in terms of the original data as,

$$\Phi(\mathbf{x}) = \sum_{i=1}^{N} A(t^i)\mathbf{u}(\mathbf{x},t^n), \tag{3}$$

where $\Phi(\mathbf{x})$ is a deterministic field set sought by the POD. The POD modes $\Phi(\mathbf{x})$ can then be expressed as solutions to the eigenvalue problem

$$\mathbf{R}(\mathbf{x},\mathbf{x}')\Phi(\mathbf{x}') = \lambda\Phi(\mathbf{x}). \tag{4}$$

Solving the problem proposed by equation 4 yields a complete set of eigenfunctions and corresponding eigenvalues. The eigenfunctions can be used to then create a set of POD modes according to equation 3. The POD modes are typically normalized to obtain an orthonormal basis, the final expression of the POD basis:

$$\Phi^i(\mathbf{x}) = \frac{\sum_{i=1}^{N} A^i(t^n)\mathbf{u}(\mathbf{x},t^n)}{\|\sum_{i=1}^{N} A^i(t^n)\mathbf{u}(\mathbf{x},t^n)\|}. \tag{5}$$

The stochastic velocity fields can be reconstructed using the eigenfunctions of the POD,

$$\mathbf{u}(\mathbf{x},t^n) = \sum_{n=1}^{N} a_n\Phi^n(\mathbf{x}), \tag{6}$$

where a_n are a set of coefficients obtained by back-projecting the set of stochastic velocity fields onto the deterministic POD modes as,

$$a_n = \int_\Omega \mathbf{u}(\mathbf{x},t^n)\Phi^n(\mathbf{x})d\mathbf{x}'. \tag{7}$$

The cross correlation tensor, R_{ij}, can also be reconstructed using the eigenfunctions and eigenvalues obtained through the POD:

$$\mathbf{R}_{ij}(\mathbf{x},\mathbf{x}') = \lambda^n\Phi_i^n(\mathbf{x})\Phi_j^n(\mathbf{x}'). \tag{8}$$

Contraction of the reconstructed correlation tensor, R_{ij} shows that the total energy in the domain, Ω is equal to the summation of the eigenvalues, λ^n, as

$$E = \int_\Omega \langle \mathbf{u}_i(\mathbf{x})\mathbf{u}_i(\mathbf{x})\rangle = \sum_{n=1}^{N}\lambda^n. \tag{9}$$

Thus, the POD provides an optimal set of eigenfunctions that decompose the energy in the turbulence domain and the eigenvalue measures the energy associated with each mode. Fluctuating velocity measurements are reconstructed as in equation 6 and, as an extension, Reynolds stresses can be directly reconstructed as,

$$\left\langle u_i u_j(\mathbf{x}) \right\rangle = \left\langle \sum_{n=1}^{N} a_n \Phi_i^n \Phi_j^n(\mathbf{x}) \right\rangle . \tag{10}$$

EXPERIMENTAL SETUP

The snapshot POD detailed in the previous section was applied to stereographic particle image velocimetry (SPIV) data collected in a wind tunnel experiment conducted at Portland State University (PSU).

The wind tunnel experiment consisted of SPIV measurements taken directly upstream and downstream of entrance and exit row wind turbines in an array. Figure 1 provides an overview of the experimental arrangement including inflow conditioning in the form of a passive grid, vertical strakes and surface roughness. Wind turbine models were manufactured in-house and consisted of an electric motor for the nacelle and rotors formed of bent sheet steel.

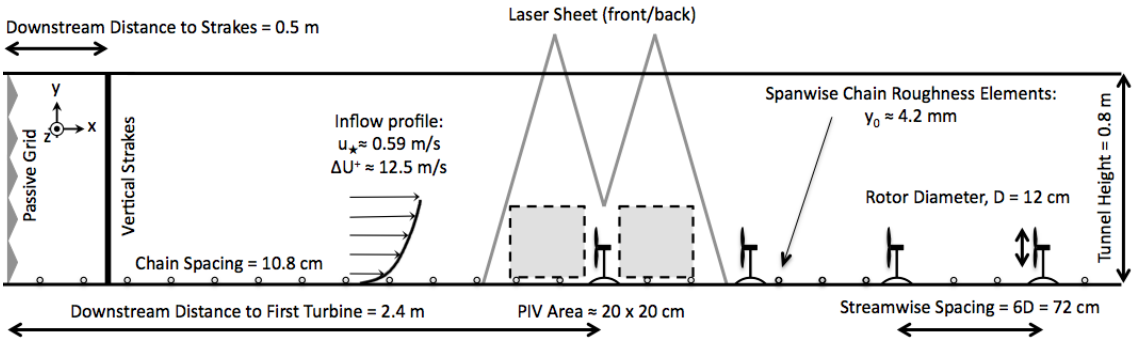

Figure 1: Schematic of experimental setup viewed from the user-side of the wind tunnel. Detail of PIV recording area and model wind turbine. Inflow parameters $u_\star$, ΔU^+, and y_0 were obtained by a logarithmic fit in the constant shear layer of the ABL. The schematic above is for reference only, dimensions are not to scale.

Measurements were made for different configurations of a wind turbine array shown in figure 2. A (4×3) cartesian arrangement formed the base case to which two different row-offset configurations were tested. In each of the offset cases, alternating rows of turbines were given a spanwise shift of 1.5 rotor diameters such that non-leading turbines were directly between turbines of preceding rows in a spanwise sense. The $(3-2-3-2)$ arrangement yielded an entrance row turbine whose particular inflow and dynamics are statistically identical to those of the base arrangement and the $(2-3-2-3)$ arrangement provided an empty position at the entrance row and an exit row turbine differing from that of the base arrangement.

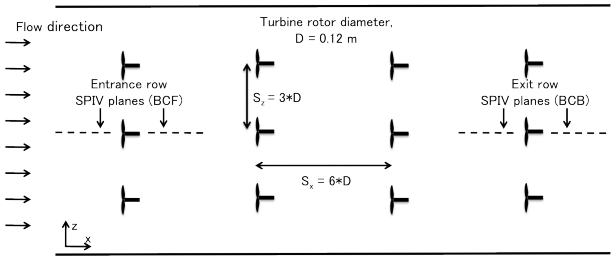

(a) Schematic of the base wind turbine configuration

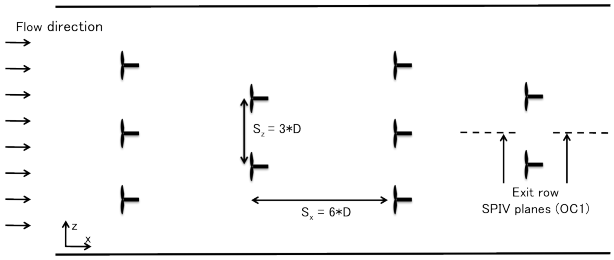

(b) Schematic of the first offset wind turbine configuration

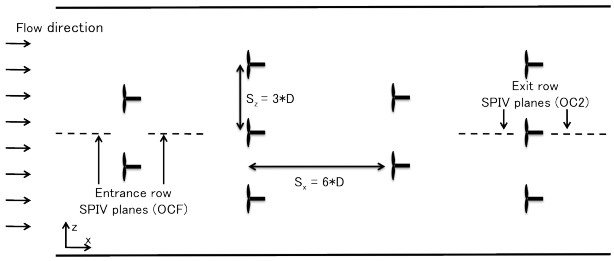

(c) Schematic of the second offset wind turbine configuration

Figure 2: In all cases, the streamwise spacing between rows is to six times the rotor diameter (0.72 m). The spanwise spacing between turbines is three rotor diameters (0.36 m).

RESULTS

Application of the snapshot POD to the SPIV data discussed above is detailed below. The eigenvalues, λ, yielded by equation 4 are discussed first regarding their relative content of the turbulent kinetic energy. Recalling that the sum of the eigenvalues is equal to the mean turbulent kinetic energy in each measurement location (equation 9), selecting a threshold of energy detailed by the eigenvalues is equivalent to selecting sets of turbulent structures containing the same level of turbulent energy.

For easy comparison of λ for each location, a successive sum is shown in figure 3. The successive sum, E_n, is,

$$E_n = \sum_{k=1}^{n} \lambda_k \tag{11}$$

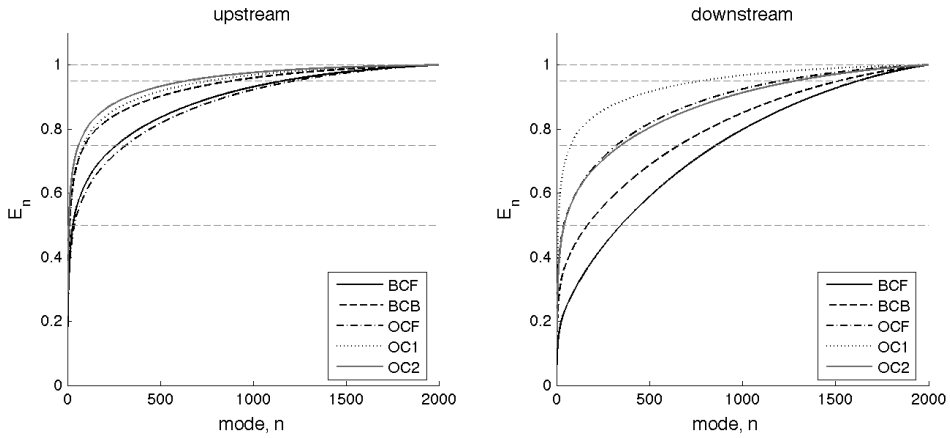

Figure 3: Successive summation of eigenvalues, λ_n. Locations where energy converges to the full turbulent kinetic energy faster demonstrate a sharper bend. A more even distribution of energy in eigenvalues show as slower convergence as in the downstream trends of BCF and BCB.

and describes the energy contained in the first n modes. Each case requires the full set of 2000 modes to rebuild the full turbulent kinetic energy as in equation 9. The figure also shows prescribed levels ($50, 75, 95$ and 100%) of energy as dashed horizontal lines. Points where the curves of E_n cross the horizontal thresholds correspond to the figures in table 1. Note that cases that converge to thresholds with fewer modes are those in which the difference in energy contained in large small scales is greater. Slow convergence to the full turbulent kinetic energy suggests that energy in the flow is more evenly distributed across a range of scales.

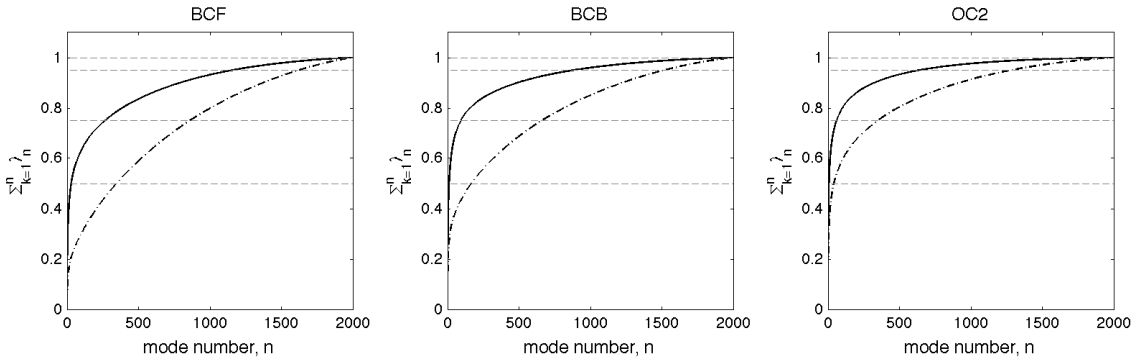

Figure 4: Side by side comparison of the successive sum of energy contained in modes, E_n, for wind turbine locations. From left, the subfigures correspond to the entrance row of the base arrangement, the exit row of the base arrangement, and the exit row of the $(2-3-2-3)$ row-offset case.

Figure 4 shows the successive summation of eigenvalues for the three turbine positions in the arrays. Each subfigure compares E_n for the upstream (solid line) and downstream (dashed

line) measurement locations. In every case, the upstream set of eigenvalues converges more quickly than the downstream position. For the measurement locations without turbines (OCF and OC1, not shown), the upstream and downstream trends are virtually identical as the turbulent kinetic energy is very similar in both positions. Without a turbine rotor to influence the relative content of energy in each scale, the turbulence is not expected to evolve significantly in a short downstream distance (approximately three rotor diameters). The slight differences seen in the two positions is due to the decay of turbulent structures at different downstream locations.

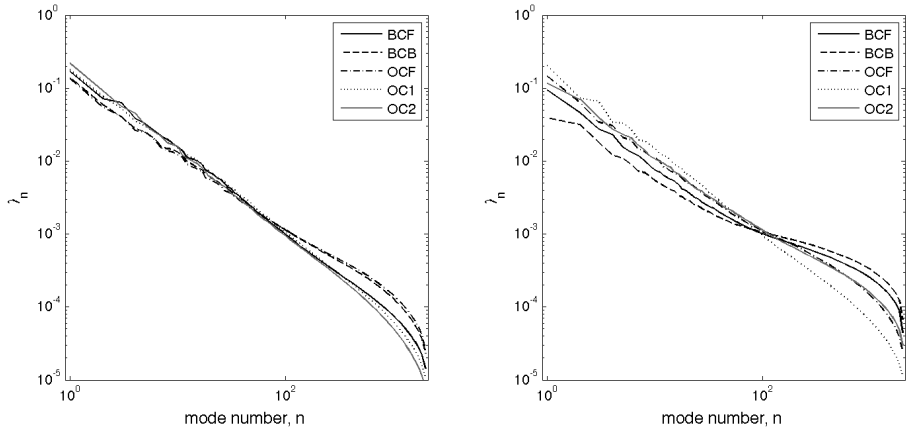

Figure 5: Comparison of λ values for each measurement position. The subplot on the left is the upstream location for each case and the right is downstream. Note that the first mode for all cases is higher downstream than upstream. Trends shown in log scale and show typical falloff according to $n^{-1.2}$ for large and intermediate scales (low mode number).

An alternate presentation of the distribution of energy contained in the eigenvalues of the POD is presented in figure 5. In the figure, the eigenvalues are self-normalized, such that for each case, $\sum \lambda_n = 1$. In the downstream measurement location (right subfigure) positions following wind turbines show a strong deviation from the $n^{-1.2}$ trend seen in the low mode numbers. The increase of energy contained in high mode numbers is attributed to the energy directed into smaller scales through the rotation of the turbine rotor.

The modes required to recover a specified threshold of the total turbulent kinetic energy are shown in table 1. These thresholds (with the exception of 90%) are shown as dashed horizontal lines in figures 3 and 4.

Table 1: Modes required to reconstruct a prescribed portion of turbulence energy (upstream–downstream)

	BCF	BCB	OCF	OC1	OC2
Modes for 50% energy	30 – 348	13 – 168	38 – 39	13 –10	8 – 42
Modes for 75% energy	266 – 860	94 – 661	317 – 324	85 – 77	61 – 349
Modes for 90% energy	789 – 1370	488 – 1222	857 – 845	404 – 410	323 – 918
Modes for 95% energy	1158 – 1621	883 – 1561	1219 – 1204	758 – 776	640 – 1282

The table details that the upstream position of each measurement location reaches the 50% threshold with fewer modes than the downstream position with the exception of the exit row position in the (3-2-3-2) offset arrangement. This agrees well with expected results as the turbulence coming into a turbine position is less than that of the outflow. In the case of OC1, the inflow requires more modes to rebuild 50% of the energy as energy is dissipated from the *small* scales of turbulence, leading to an apparent increase of energy in large scales. However, the information in the table is built on normalized sets of eigenvalues. That is, the energy is in fact decreasing in OC1 but the energy in the small scales decreases faster than the energy in the large scales.

To rebuild 50% of the energy in the inflow, between 0.4 (OC2) and 1.9 (OCF) of the modes are required. For the outflow up to 17.4 of the modes are required to reach the 50 threshold, as in BCF. The inflow of OC2, an exit row position *with* a turbine, has had between 10 and 12 rotor diameters to recover. This is also the position requiring the fewest modes to reconstruct a 50% of turbulent energy, approximately 20-30% of the modes required to reach he same energy level for inflow to the turbine array. This suggests that the relative amount of energy is more concentrated in larger scales for recovered wake positions than in the simulated ABL.

When the input data for the POD is homogenous, the resulting POD modes reduce to Fourier modes. In positions where there is at least a *weak* homogeneity, the POD modes demonstrate some Fourier-like behavior. This is evident in the low modes in upstream windows of the entrance row turbine locations as seen in figure 6. In such positions, the gradients in the streamwise direction are very small compared to the wall-normal direction. The POD modes of the entrance row of the base case (BCF) shown in figure 6 demonstrate some Fourier-type behavior in the streamwise direction. The color scale has been omitted from the figure as the modes alone have no physical meaning beyond the shapes of the structures they contain. It is only when they are multiplied by their respective coefficients a_n according to equation 6 that the magnitudes of the modes become representative of flow structures.

Also illustrated by the figure is the effect of the rotor blade on the POD modes of the flow. In figure 6(b) the upstream and downstream modes of Φ_u are nearly identical as the only physical change in the flow geometry is the mounting plate for the turbine models on the floor of the wind tunnel. This difference is seen most clearly as a distortion of the third and fourth downstream modes. Comparing these to the downstream modes corresponding to a turbine position in figure 6(a), there is much less homogeneity in the eigenfunctions. This effect is resultant of the motion of the rotor blade in the flow.

The POD modes shown in figure 6 are demonstrative of the orthogonal vector basis produced by the POD. The magnitudes of the modes have no physical relevance on their own. According to equation 7, the coefficients, a_n, are obtained by projecting the original stochastic velocity data onto the basis of deterministic POD modes and integrating over the measurement domain. Fluctuating velocity fields can then be reconstructed according to equation 6. By inference, one can use a subset of the POD modes to reconstruct velocity fluctuations with a portion of the total turbulent kinetic energy determined ahead of time.

Low-dimensional models in the following analysis are those comprised of a limited set of POD modes based on the ordered set of eigenvalues according to equation 9, above. Several approaches are taken in the creation of such models. The first approach to low-dimensional

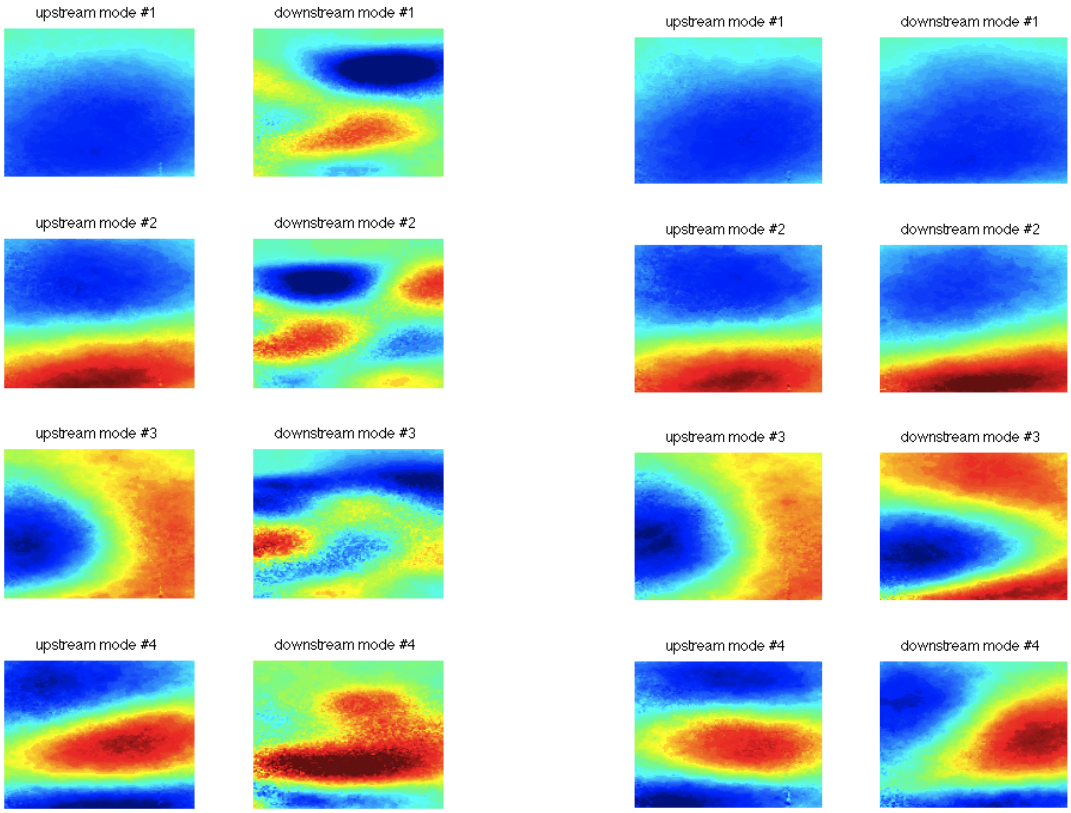

(a) First four modes of Φ_u from BCF

(b) First four modes of Φ_u from OCF

Figure 6: Comparison of upstream and downstream scalar POD modes corresponding to the streamwise direction for both entrance row measurement positions. Upstream modes in the left column of each subfigure are nearly identical between cases. Downstream modes vary greatly due to the presence of a wind turbine in BCF 6(a). Upstream and downstream modes for empty array position are very similar as flow has changed little between measurement locations.

modeling is considering a specific portion of the total turbulent kinetic energy according to the eigenvalues, λ_n. Most commonly, statistical quantities are reconstructed using only the POD modes required to assemble 50% of the total energy. Reconstructions in this sense can be to any prescribed percentage of the total energy in the measurements. Table 1 shows the number of modes required to reach several levels of the energy at each measurement location.

Figures 7 and 8 show the reconstructions of F_{12} using only 50% of the energy in the flow as detailed by the eigenvalues, λ_n, and shown in table 1. In the figures, the reconstructed flux of kinetic energy is nearly identical to the calculations shown resulting from statistics of measurements. This is demonstrative that the vertical entrainment of kinetic energy is reliant predominantly on the large structures of turbulence. Because turbulence is a three dimensional phenomenon and it tends to greatly increasing mixing rates and transport, an *increase* of turbulence kinetic energy in the near wake can lead to a shorter recovery length of the wake. The

increased energy of large structures in the upper wake area tends to increase the energy entrained from above into the turbine canopy.

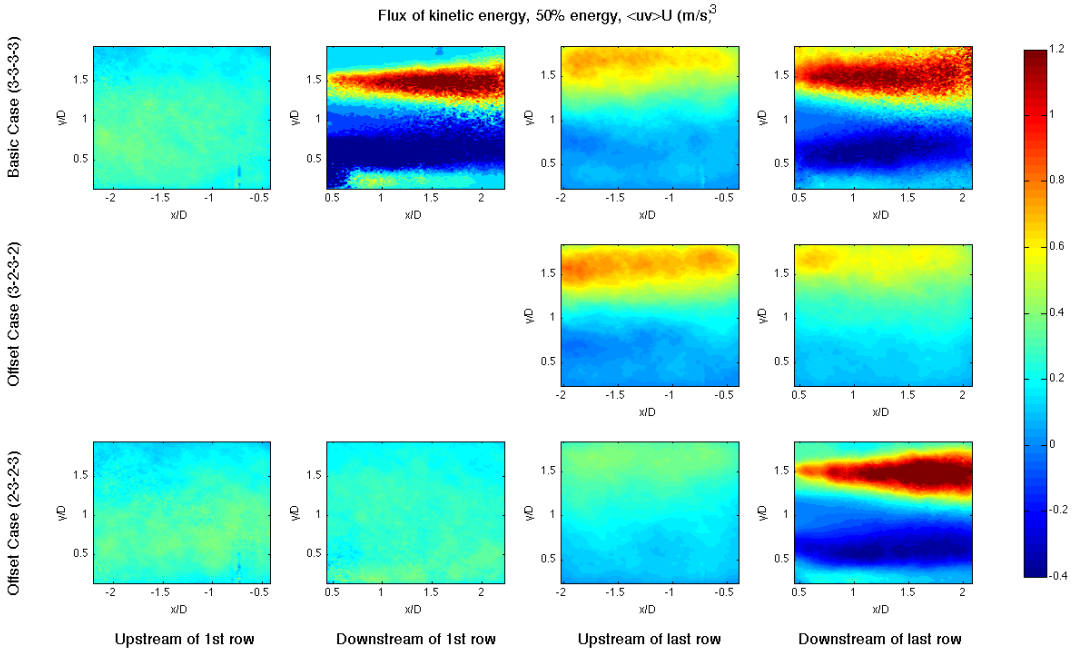

Figure 7: Reconstructions of the flux of kinetic energy F_{ij} for all measurement positions. Plotted data comprised of $-uv$ with only the modes containing the first 50% energy and the mean velocity field U from SPIV results.

Figure 8 shows the 50% reconstruction of F_{12} only in the near wakes of the the three wind turbine positions measured in the experiment, BCF, BCB, and OC2. Although each mode has a net positive contribution to the total turbulent kinetic energy in the field as denoted by λ_n and shown in figures 5 and 3, modes may make negative local contributions to stresses. The reconstructions shown in figure 8 show an overestimation of the flux of kinetic energy compared to the original statistical data. The implication of this is that the intermediate and small scales (associated with large mode numbers) make a contribution to F_{12} that is opposite the trend seen in the mean statistics.

CONCLUSIONS

The experiment conducted at PSU compares the turbulent dynamics of entrance and exit row wind turbines with cartesian and row-offset array configurations. Statistical fields of the flow measurements clearly show the difference of wakes and stresses produced in the interaction of wind turbines with the ABL.

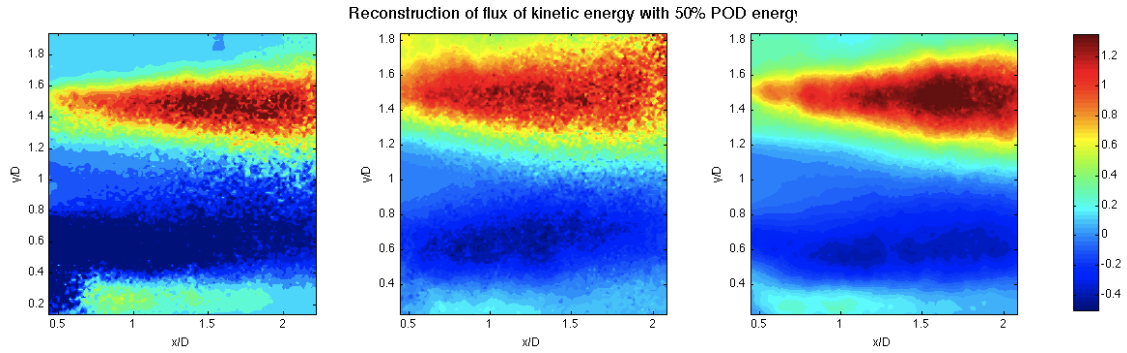

Figure 8: Reconstructions of the flux of kinetic energy F_{ij} for the immediate wake areas. Plotted data is the same as in figure 7 From left to right, the entrance and exit rows of the base arrangement, and the exit row of the second offset arrangement (2-3-2-3).

The snapshot POD was applied to the set of flow measurements collected in the experiment. From the resulting eigenvalues, it is observed that the energy contained in the POD modes varies considerably with measurement location and flow dynamics. The distribution of eigenvalues for each turbine demonstrate a similar trend for upstream measurements where energy falls off at approximately $n^{-1.2}$. The presence of wind turbines changes the distribution of energy amongst the modes greatly. Comparing the successive summation of eigenvalues λ_n shown in figure 3 to the power curves suggests a connection between the difference of upstream and downstream energy distributions and the power produced by wind turbine models.

According to theory, the POD modes demonstrate increasing complexity of structure as mode number grows. Vectorial modes in the upstream location associated with wind turbines show more homogeneity for a span of mode numbers whereas the downstream measurement location shows that the modes rapidly grow in complexity and structures decrease in size. Incoherent and transient structures are not typically associated with POD modes regardless of their dynamical importance.

Low-dimensional reconstructions of the flux of kinetic energy and turbulence production were approached through a convergence of the streamwise averaged profile of the reconstructed Reynolds stress, $-\langle uv \rangle$ to the profile obtained in the original statistics. It was shown that for turbines whose inflow is the undisturbed ABL (BCF) or a recovered wake (OC2), it requires approximately 0.6% of the total modes to reconstruct 95% of the span of $-\langle uv \rangle$. For the wind turbine with a greater momentum deficit in the inflow (BCB), the reconstruction requires approximately twice the number of modes to reach the convergence criterion.

REFERENCES

[1] R. J. Adrian, K. T. Christensen, and Z.-C. Liu. *Experiments in Fluids*, 29:275290, 2000.

[2] B. Berkooz, P. Holmes, and J. L. Lumley. *Annual Reviews of Fluid Mechanics,* 25:539 575, 1993.

[3] J. Borée. *Experiments in Fluids,* 35:188 192, 2003.

[4] J. Kostas, J Soria, and M. S. Chong. *Experiments in Fluids,* 38:146160, 2005.

[5] L. Cordier and M. Bergmann. *Lecture Series: von Karman Institute for Fluid Mechanics,* 2003-04.

[6] J. P. Bonnet, D. R. Cole, J. Delville, M. N. Glauser, and L. S. Ukeiley. *Experiments in Fluids,* 17:307 314, 1994.

[7] J. H. Citriniti and W. K. George. *Journal of Fluid Mechanics,* 418:137166, 2000.

[8] K. Saranyasoontorn and L. Manuel. *ASME Journal,* pages 110, 2005.

[9] J. M. Pedersen. *PhD thesis,* Technical University of Denmark, DK-2800 Lyngby, Denmark, February 2003.

[10] L. Sirovich. *Quarterly Applied Mathematics,* 45(3):561571, 1987.

Identification of Markov Processes within a Wind Turbine Array Boundary Layer

M. Melius[1], **M. Tutkun**[2], **R. Cal**[1]

[1] Mechanical Engineering Department, Portland State University,
Mechanical and Materials Engineering, P.O. Box 75
Portland, OR 97207-0751, meliusms@gmail.com, cal@me.pdx.edu
[2]Institute for Energy Technology (IFE),
Department of Process and Fluid Flow Technology,
P.O. Box 40, 2027 Kjeller, Norway, Murat.Tutkun@ife.no

1 Introduction

Wind energy has proven to be a significant source of renewable energy. Accurate projections of energy production are difficult to achieve because the wake of a wind turbine is highly intermittent and turbulent. It is well documented that the turbulent behavior within the internal boundary layer of a wind farm is influenced by turbine geometry, atmospheric conditions, and geographic features surrounding the farm. The interaction of these conditions creates an infinitely complex turbulent system which makes modeling the power production of a wind farm difficult. Among all of the values that can be measured, it has been shown that turbulence intensity within the internal boundary layer plays a significant role in the power output and mechanical fatigue of a wind turbine [1]. Therefore, effort is being put forth to predict the turbulence intensity throughout the internal boundary layer of a wind farm.

In observing Markovian processes, characteristics of the turbulence become evident within the wind turbine canopy. Markov chain theory of statistical development offers a valuable application to aid in the improved power production models. Markov theory states that if the development of a system can be determined, then the knowledge of the current state can provide enough information to determine the future state of the system. Markovian statistical prediction methods have been applied in many ways, including multi-scale reconstruction of time series [16], to provide a diagnostic tool for identifying patients with congestive heart failure [10], and financial models [12, 9, 14].

Fundamental experimental studies have been conducted to describe the development of turbulent flows. Among other methods and studies, the statistics of small-scale turbulence are analyzed, searching for the existence of Markov processes. Markov processes have been discovered in several turbulent flows, such as a high Reynolds number axisymmetric jet [17], within the wake behind a cylinder [18], and fractal-generated grid turbulence [19]. In each of these studies, the flows demonstrated Markov process behavior for scale differences larger than or equal to the Taylor microscale, λ. The Taylor microscale is considered to be the scale at which viscosity begins to play a role in the dynamics of the turbulent cascade, hence the dissipation

of turbulent kinetic energy becomes important and given by $\lambda^2 = \langle u(x)^2 \rangle / \langle (\frac{\partial u}{\partial x})^2 \rangle$, where the Taylor's frozen field hypothesis is recalled. Results from these studies also revealed that the extension of Markov process down to the Taylor micro scale was independent of Reynolds number when $100 < Re_\lambda < 1000$ [17].

For wind farm applications, Markov models have been used to represent the degradation pattern of wind turbine components, as repair times are stochastic and turbine access is limited by weather conditions [5]. The use of partially observed Markovian decision process has been suggested as a way to improve maintenance scheduling [5]. A Markov model for the performance of wind turbines that accounts for component reliability, the effect of wind speed, and turbine capacity was found to predict repair schedules with an accuracy of 10% or better when the number of turbines is greater than approximately 100 [2].

Application of Markovian theory to atmospheric turbulence was first addressed as a way to predict power production of a wind turbine by Anahua *et al.*[1]. From this study, it followed that even with different turbulence intensities, the characteristic of the wind turbine power performance can be properly reconstructed. The method was not only more accurate than the current standard procedure of ensemble averaging but it also allowed a faster and robust estimation of wind turbines power curves. This study addressed the turbulent fluctuations experienced by a wind turbine, which are not dealt with correctly by use of ensemble averaging [1].

Markov property analysis is applied to a model wind turbine array boundary layer. Hot-wire anemometry signals within the array are analyzed to determine the existence and limitations of Markov properties in the wake. The results are discussed in the context of turbulence theory and wind turbine wake development.

2 Theory

Kolmogorov defines turbulent flow as a combination of a wide range of scales, or so-called eddies, within the flow. The largest scales, also known as integral scales, are responsible for the injection of kinetic energy into the flow. The kinetic energy is then transferred through the turbulent cascade from large scales eddies to smaller scale eddies. At the smallest scales the kinetic energy is transferred into internal energy through viscous dissipation, thus these smaller scales are referred to as dissipative scales. This process is described in depth by Kolmogorov's turbulent cascade theory [11]. Kolmogorov suggests that in between the energy injecting scales and dissipative scales there exists a series of intermediate scales which are considered to be, at sufficiently high Reynolds numbers, independent of either end of the spectrum.

The interaction of scales is represented mathematically by the nonlinear term of the Navier-Stokes equation. Describing this interaction requires multipoint statistics in order to fully capture the behavior of the cascade. By analyzing the simultaneous interaction of all of the scales in a turbulent flow, it is theoretically possible to create a complete statistical description of the cascade. Through the application of Markov chain theory it becomes possible to evaluate the statistical behavior of the turbulent system as a diffusion process.

Statistics of velocity increments are used to characterize the turbulent cascade in physical space. The longitudinal velocity increments are considered for this analysis and are described as,

$$v(x,r) = u(x+r) - u(x) \tag{1}$$

where v and u represent velocity increment and velocity fluctuation respectively. The spatial distance between the two measurements is denoted by r, while x represents the origin. Kolmogorov [11] predicts n^{th} - order structure function, $\langle v(r)^n \rangle$ to be strictly a function of r and n, where $\langle v(r)^n \rangle \sim r^{n/3}$. Also, when $n = 2$, the second order structure function, $\langle v(r)^2 \rangle$ quantitatively describes the distribution of turbulent kinetic energy over different scales defined by the spatial separation, r [19].

One way of studying moments of velocity increments is to calculate the probability density function (pdf) of the velocity increments at different scales, $p(v,r)$. Since a complete description of the turbulence cascade is only possible by taking into account the interaction of all scales of motion, a multi-scale (N-point) joint pdf, $p(v_1,r_1;v_2,r_2;v_3,r_3;...;v_n,r_n)$ must be constructed. An essential quantity used in utilizing the theory of Markov processes is the conditional probability density functions. Given a joint pdf $p(v_1,r_1;v_2,r_2)$ used to find the probability of v_1 occurring at scale difference r_1 and v_2 occurring at scale difference r_2, where $r_1 < r_2$. One can find the conditional probability of v_1 occurring at scale difference r_1, given that velocity v_2 is occurring at scale difference r_2 by using the following equation:

$$p(v_1,r_1|v_2,r_2) = \frac{p(v_1,r_1;v_2,r_2)}{p(v_2,r_2)}. \tag{2}$$

This technique can be extended to all present velocity increments and scale differences within a respective system. For instance, to find the conditional pdf of v_1 at r_1 conditioned by all velocities and scales present, the conditional pdf is defined as $p(v_1,r_1|v_2,r_2;...;v_n,r_n)$. To find the conditional pdf for this case, joint pdfs can be used and given by,

$$p(v_1,r_1|v_2,r_2;...;v_n,r_n) = \frac{p(v_1,r_1;v_2,r_2;...;v_n,r_n)}{p(v_2,r_2;;v_n,r_n)}. \tag{3}$$

Obtaining an N-point conditional pdf provides a complete velocity increment - scale relation throughout the cascade. This is particularly difficult to do in practice, due to the large number of scales that exist in a turbulent flow field.

Applicability of Markov's theory offers a significant simplification in the calculation of the N-point conditional pdf. If the system is Markovian then the probability of the current state can be fully determined by the most recent state. Thus, the N-point conditional pdf of the velocity increments with Markovian properties can be simplified as follows:

$$p(v_1,r_1|v_2,r_2;...;v_n,r_n) = p(v_1,r_1|v_2,r_2). \tag{4}$$

From there, N-point joint pdf of the process can be constructed in terms of multiplication of the conditional pdfs as,

$$p(v_1,r_1;v_2,r_2;...;v_n,r_n) = \prod_{i=1}^{N-1} p(v_i,r_i|v_{i+1},r_{i+1}) p(v_n,r_n). \tag{5}$$

The implication of equation (5) is that knowledge of a conditional pdf $p(v_i,r_i|v_{i+1},r_{i+1})$ for any scale r_i and r_{i+1} is enough to reconstruct the complete statistical description of the velocity

increments embedded in the N-point pdf, $p(v_1, r_1; v_2, r_2; ...; v_n, r_n)$. In order for the process to be considered Markovian, equation (4) must be satisfied. It is clearly difficult to analyze all present scales of turbulence, however with a data set of $4x10^6$ measurements it is possible to examine the joint probabilities up to values of $n = 3$. Thus, equation (4) is transformed and expressed as:

$$p(v_1, r_1|v_2, r_2; v_3, r_3) = p(v_1, r_1|v_2, r_2). \tag{6}$$

A comparison of the two and three point conditional pdfs is conducted to evaluate the similarity between the two data sets in an effort to determine the Markovian nature of the process. The process of comparing overlapping conditional probabilities gives qualitative evidence to the existence of a Markov process. In order to create a quantitative understanding of the conditional pdfs equality, the Wilcoxon rank-sum test is employed. Departure from the outcome of the Wilcoxon test, denoted by ΔQ^*, from 1 indicates a departure of the process from being a Markovian one.

3 Experimental Setup

The experiment was conducted in the Corrsin Wind tunnel at The Johns Hopkins University. The test section of the wind tunnel is 10 *m* long, 0.9 *m* high, and 1.2 *m* wide. The wind tunnel is a closed-loop return type, with two contractions. To replicate the atmospheric boundary layer in which wind turbine arrays commonly encounter, strakes, an active grid as well as a rough surface composed of sandpaper were used to generate a mean shear profile and free-stream turbulence. A 3 $\times$ 3 array of model wind turbines with a rotor diameter, D, of 12 *cm* and tower height of 12 *cm* were placed in the turbulent boundary layer. A reference mean velocity of 9.4 ms^{-1} was selected as a characteristic wind velocity. Each turbine column was spaced $3D$ from the next in the cross-stream direction and each row was spaced 7D down stream from the preceding row. The wake statistics past the third row of turbines are representative of an infinite array. For more information on the experimental setup, see [6]. Using X-type hot wire anemometry to collect data, velocity measurements were taken at a sampling frequency of 40 kHz for 100 seconds at each location of the sample set. The sampling set includes one streamwise - wall-normal (XY) plane, behind the middle row wind turbine located in the last row of the array. The plane extends from the exit of the turbine to 8D downstream, measurements were taken 1 *cm* increments in wall-normal direction at 21 locations starting at 0.5 *cm* above floor at downstream increments of $1D$, as shown in Figure 1. Measurements were initially collected for wall-normal and streamwise velocities, then the probe was rotated to collect data for the cross-stream and downstream velocities. More detail on the hot-wire anemometer and accuracy of the data is provided in [6].

4 Results

In the absence of the ABL, a wind turbine wake is in itself a highly complicated system. Contained within the near-wake of a wind turbine wake, the flow is marred by complexity including tip vortices, stalled flow and three-dimensional effects caused by the rotating blades [20]. The standard is to space turbines 5-7 diameters downstream of each other to reduce the impact of these near-wake structures on the preceding turbines. More tightly arranged farms

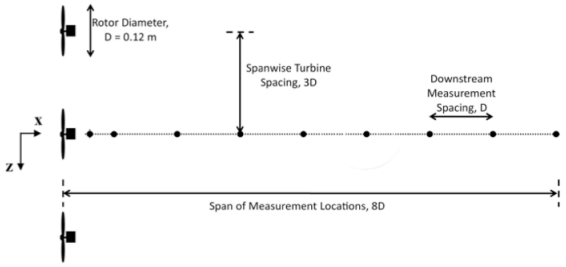

Figure 1: Schematic of streamwise and transverse measurement locations behind the middle turbine of the last row in model wind farm.

suffer from this close proximity spacing; leading to higher levels of turbulence intensity experienced by downstream turbines. In field measurements, it is important to note that most 'tracking/maintenance' measurements are done at the nacelle. Nevertheless, the characteristics of the wake are highly dependent upon the location of the probe, both in the longitudinal, x/D, and the vertical, y/D, locations.

To characterize the flow present behind a wind turbine within an array, the mean longitudinal velocity profiles are analyzed. The data plotted in Figure 2 contains the mean longitudinal velocity, U, which is normalized by the reference mean velocity of the wind tunnel, $U_o = 9.4\ m/s$. The figure presents nine wall-normal profiles, one for each x/D location. The dotted transversal lines represent the top and bottom tip of the turbine rotor. The results show that the velocity deficit is most pronounced in the near-wake region as expected. By $x/D = 5$, the velocity profile has recovered and increases uniformly, which indicates the existence of the far-wake region [15]. These results are similar to previous studies that addressed wind turbine wake recovery [7, 6, 21].

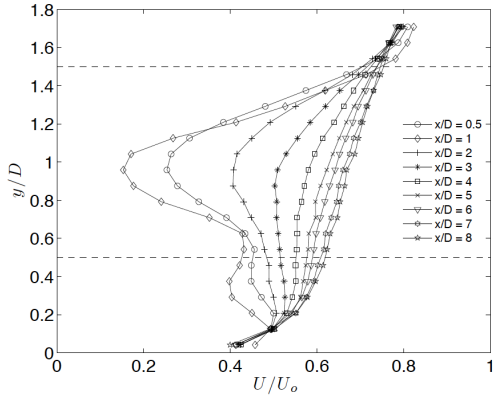

Figure 2: Mean longitudinal velocity profiles for each measurement location. Data are organized by downstream location. The horizontal dashed lines represent the locations of the top and bottom tip of the rotor blade.

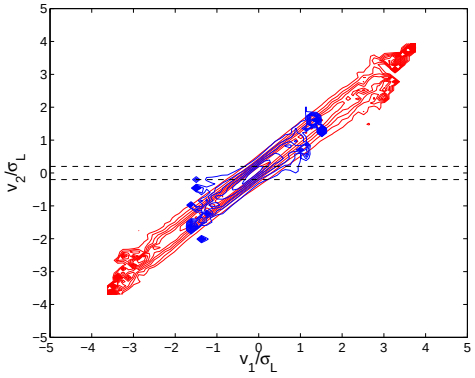

(a) Full conditional pdf comparison

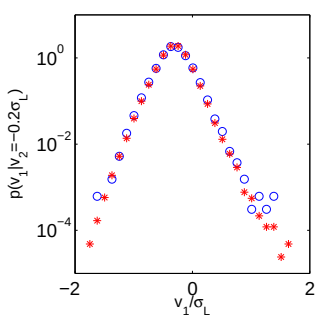

(b) Horizontal cut at $v_2/\sigma_L = -0.2$

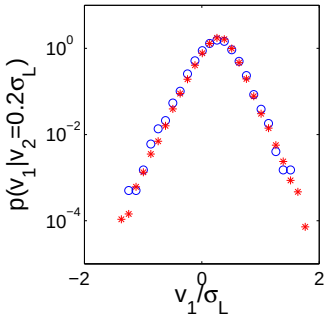

(c) Horizontal cut at $v_2/\sigma_L = 0.2$

Figure 3: One dimensional conditional pdfs, from $x/D = 3$, $p(v_1, r_1|v_2, r_2; v_3 = 0, r_3)$ [blue] and $p(v_1, r_1|v_2, r_2)$ [red], where $\Delta r = \lambda$ and v_3 is conditioned to 0.

4.1 2-point and 3-point conditional pdf comparison

To verify the existence of a Markovian behavior from equation (6), a comparison between the contour plots for $p(v_1, r_1|v_2, r_2; v_3 = 0, r_3)$, in blue, and $p(v_1, r_1|v_2, r_2)$, in red, is performed. Shown in Figure **??**, the velocity increment data was taken at $x/D = 3$ at hub height, broken into closer scales of $r_1 = L/2 - \lambda$, $r_2 = L/2$, and $r_3 = L/2 + \lambda$. v_1 and v_2 are overlaid in the contour plots as well as normalized by σ_L, the standard deviation. The close proximity of the contour lines indicates that equation (6) is satisfied and thus the flow is a Markov process for this specific velocity increment scale as figure 3(a) suggests. Furthermore, for scale differences larger than λ, the flow is Markovian at this location. Horizontal cuts at $v_2/\sigma_L = \pm 0.2$ are applied to the 3 dimensional pdfs to show the relative proximity of the two. It is clear that the pdfs for both cuts are in perfect agreement, thus again stating Markovianity of the flow at this particular location. This can be observed in figures 3(b) and 3(c), where $p(v_1, r_1|v_2, r_2; v_3 = 0, r_3)$, represented by blue circles, and $p(v_1, r_1|v_2, r_2)$, represented by red stars.

In stark contrast, if the scales of Δr are smaller than λ, then the conditional pdfs no longer satisfy equation (6), where $\Delta r = 0.3\lambda$. To be explicit, the velocity increment data is divided into $r_1 = L/2 - 0.3\lambda$, $r_2 = L/2$, and $r_3 = L/2 + 0.3\lambda$. As shown in Figure 4(a), the contours

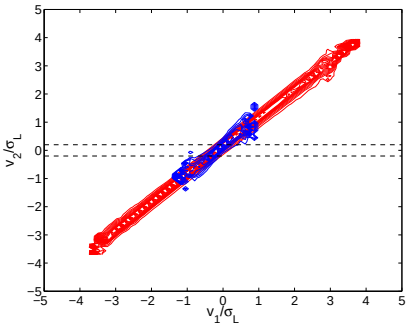

(a) Full conditional pdf comparison

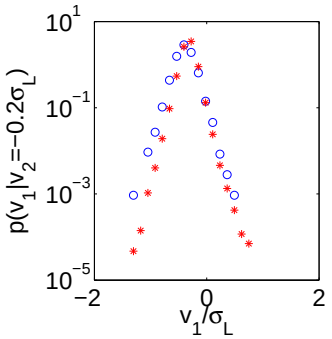

(b) Horizontal cut at $v_2/\sigma_L = -0.2$

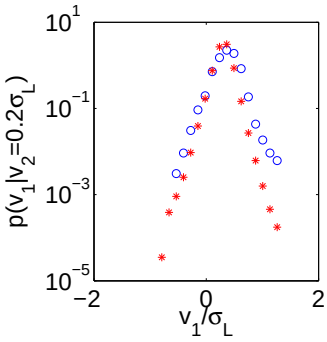

(c) Horizontal cut at $v_2/\sigma_L = 0.2$

Figure 4: One dimensional conditional pdfs, from $x/D = 3$, $p(v_1, r_1|v_2, r_2; v_3 = 0, r_3)$ [blue], and $p(v_1, r_1|v_2, r_2)$ [red], where $\Delta r = 0.3\lambda$ and v_3 is conditioned to 0.

for these smaller scale differences shows that the conditional pdfs are clearly different. There is a distinct difference between the skewness and kurtosis of the two pdfs, which is highlighted by the horizontal cuts through the pdfs shown in Figure 4(b) and 4(c). This indicates that the process is no longer Markovian at this smaller scale difference. This type of exploration of the small scale differences is helpful to visualize the scale dependence of the Markov property but does not give quantitative results. Therefore, to precisely determine the range of scales where Markovian properties hold at each location, a Wilcoxon test is performed.

4.2 Wilcoxon test

Wilcoxon rank-sum test is utilized to explore the range of scales where a Markov process exists. Subsequently, $\langle \Delta Q^* \rangle$ is a function of the physical separations r_1, r_2, and r_3. It is therefore possible to visualize the dependence of the Markovian behavior on r_n and the size of the scale differences, Δr. In order to get the full picture of the longitudinal velocity increments display of Markovian behavior, r_1 and Δr are varied in the following ranges: $1.5\lambda \leq r_1 \leq 20\lambda$ and $0 \leq \Delta r/\lambda \leq 5$. These variations are shown in figures 5 and **??**, where variations in the streamwise direction and vertical direction are assessed.

In the following figures, $\langle \Delta Q^* \rangle$ is plotted as a function of $\Delta r/\lambda$. Figure 5 shows the streamwise dependence of $\langle \Delta Q^* \rangle$ at hub height, $y/D = 1$. Figures 5(a) and 5(b) show $\langle \Delta Q^* \rangle$ from the near-wake for $x/D = 0.5$ and $x/D = 3$ respectively, while figures 5(c) and 5(d) reflect the

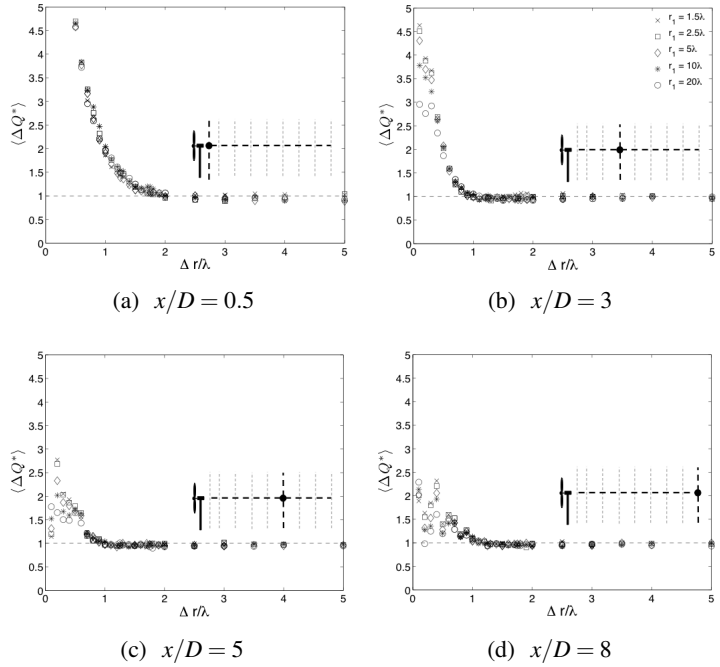

(a) $x/D = 0.5$ (b) $x/D = 3$

(c) $x/D = 5$ (d) $x/D = 8$

Figure 5: Wilcoxon test results showing downstream trend at hub height, $y/D = 1$.

results from the far-wake at $x/D = 5$ and $x/D = 8$. A cartoon has been included in each subfigure for reference in regards to the particular measurement location. In the location nearest to the hub at $x/D = 0.5$, the values of $\langle \Delta Q^* \rangle$ converge to 1 at $\Delta r = 5\lambda$ for all scales r_1, as shown in Figure 5(a). At this location it is seen that for scales below $\Delta r = 2\lambda$ the values for $\langle \Delta Q^* \rangle$ increase rapidly and the Markov behavior falls apart for these smaller scales of turbulence. The smallest initial scales, r_1, take the longest to reach 1 showing that near to the hub the flow is characterized by large scale intermittency. The level of departure from the small scale Markovian behavior may be an indication of why Barthelmie *et al.* found that despite differences in the measurement height and period, overall agreement is better between the turbulence intensity derived from power measurements and the meteorological mast than with those derived from data from the nacelle anemometers [3].

Further downstream in Figure 5(b) at $x/D = 3$, the Wilcoxon test results show that all values of r_1, $\langle \Delta Q^* \rangle = 1$ for scale differences of $\Delta r > 1.1\lambda$. At this location the rapid departure of $\langle \Delta Q^* \rangle$ from one is seen again, although this time the departure begins at scale differences of $\Delta r > 1.1\lambda$. A similar result is seen in Figure 5(c), where the value of $\langle \Delta Q^* \rangle = 1$ for scale differences of $\Delta r > \lambda$. This behavior is taken as an indication that the wake has begun to recover and that the large energy entrainment, present near the hub has decreased significantly. This result means that the conditional probability density functions are equivalent for these scales and thus over this range of scales the flow is a Markov process.

In Figure 5(b) and Figure 5(c) it is shown that for scales greater than, $\Delta r \geq \lambda$, the wake is a Markov process. It should be noted that once a $\langle \Delta Q^* \rangle$ value of one is reached, the Markov

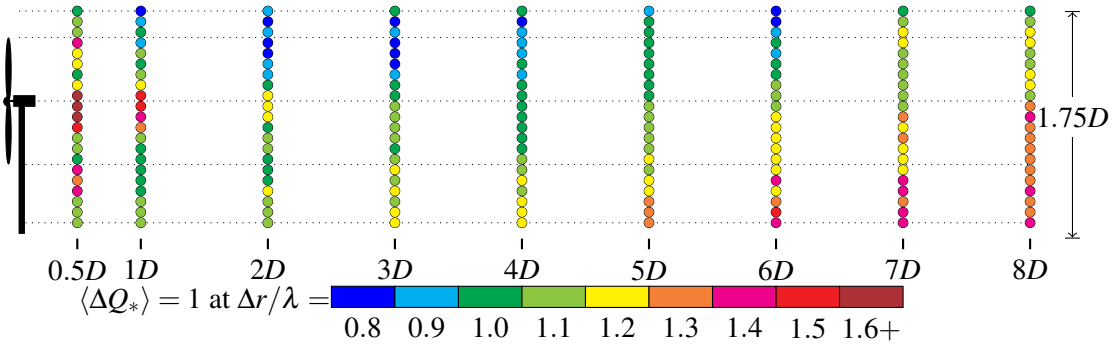

Figure 6: Spatial representation of Wilcoxon test results of streamwise and transverse measurement locations behind the middle turbine of the last row. Values of $\Delta r/\lambda$ are given as values where $\Delta Q^* = 1$

Figure 7: Spatial representation of Wilcoxon test results.

properties are not dependent upon the selection of r_1. This is a similar result to what has been shown to be the case for homogenous, isotropic turbulence in prior investigations [19, 17].

For $x/D = 8$, the values of Δr where $\langle \Delta Q^* \rangle = 1$ increase to 1.3λ as shown in Figure 5(d). At this location the wake of the turbine has remediated. These regions are characterized by low levels of shear. It is likely that at this point the level of shearing occurring is to low and there is a significant level of mixing between the ABL and the wake of the turbine.

As the flow moves downstream of the turbine, in Figures 5(b), 5(c), 5(d), the value of $\langle \Delta Q^* \rangle$ for scale differences $\Delta r/\lambda < 1$ approach unity. This behavior also demonstrates dependence upon the selection of the initial scale, r_1, where larger values of r_1 become closer to $\langle \Delta Q^* \rangle = 1$ relative to the smaller values of r_1, most clearly seen in Figure 5(d).

For the measurements of points located vertically at $x/D = 0.5$. Starting with locations just above the floor $\langle \Delta Q^* \rangle = 1$ at scales above the Taylor microscale. Within the lower (wall) boundary layer, these values vary from $\Delta r = 1.1\lambda$ to 1.4λ past the lower tip until just below hub height, $\langle \Delta Q^* \rangle$ increases to values of $\Delta r > 2\lambda$. This trend continues behind and just past the hub. The slight asymmetry between locations above and below the hub show that the turbine mast and the wall play a role in the flow characteristics. Where below the hub values of $\langle \Delta Q^* \rangle$ rarely converge to 1 at $\Delta r = \lambda$, while above hub height there are several locations where flow is Markovian for values of $\Delta r < 1$. Where starting at $x/d = 2$ $\langle \Delta Q^* \rangle$ values reach as low as 0.8λ.

Perhaps the most interesting results are found at $x/D = 4$ where the flow is showing Markovian properties down to the Taylor microscale at all locations above the bottom tip of the rotor. This location is often marked as the end of the near-wake and beginning of the far-wake region. It shows complete scale independence of the Markov property, as all scales of r_1 and subsequent Δr are Markovian at λ. It is also interesting to note that this location falls within the standard spacing of wind turbines, offering the possibility of usable information for more accurate power prediction and maintenance scheduling at these locations.

To further investigate the flow characteristics that affect the Markovian properties of the wake, a second look at the normalized energy spectra for specific locations of interest is taken. Previously, the spectra were presented in a traditional manner, but in order to identify the true

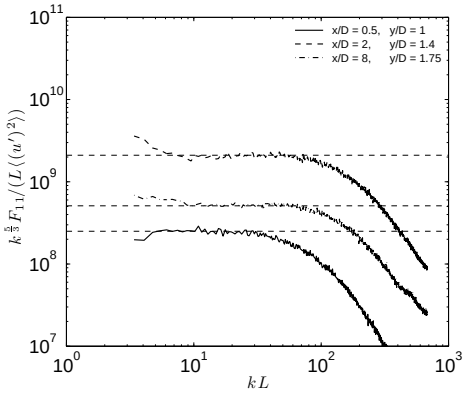

Figure 8: Flattened energy spectra have been shifted vertically to highlight the inertial sub-range at critical locations in the wake $x/D = 0.5$ at $y/D = 1$, $x/D = 2$ at $y/D = 1.4$, $x/D = 8$ at $y/D = 1.75$

length of the inertial sub-range, the spectra are multiplied by the wave number raised to the $5/3$ power, $k^{5/3}$. The effect of this manipulation is that for the range where the spectra have a $-5/3$ slope, the spectra will lay flat. From the results of the Wilcoxon test, it is found that the turbulence cascade $0.5D$ downstream of the hub is a Markov process for scale differences of $\Delta r = 5\lambda$. This value is reflected in Figure 8 where the inertial range is very short. This result is quite different from the Wilcoxon test result 2D downstream at the top tip, where $\langle \Delta Q^* \rangle = 1$ at $\Delta r = 0.8\lambda$. The energy spectra from this location shows a longer inertial sub-range of nearly a decade. This range is nearly the same length at the near free stream turbulence found at $8D$ location above the top tip. This figure leads to the conclusion that, for a larger inertial sub-range the process will be markovian for smaller scale differences, Δr.

5 Conclusions

Hot-wire anemometry data obtained in a wind tunnel experiment was used to evaluate the behavior of the turbulence statistics behind the center turbine in the exit row of a 3×3 wind turbine array. Profiles of mean velocity, turbulent kinetic energy production, and kinetic energy flux are used to characterize the wake. Furthermore, by comparing the conditional pdfs for $p(v1, r1|v2, r2; v3 = 0, r3)$ and $p(v1, r1|v2, r2)$, the wake is shown to demonstrate the presence of a Markov process for scale differences of $\Delta r \sim \lambda$. A Wilcoxon rank-sum test is preformed for numerous scale differences to investigate the equality of 2- and 3-point conditional pdfs for each measurement location. Results show that for hub height locations at $x/D = 0.5$ and $x/D = 1$, the flow is not a Markov process. Locations in the near-wake demonstrate incremental scale, r, dependence for the Markov process which is attributed to the geometric influence of the wind turbine and periodic structures caused by the rotation of the blades such as tip vortices. For other locations downstream of turbine array, the Wilcoxon test results show that the wind turbine wake is a Markov process for scales down to and occasionally below the Taylor microscale, λ. There is an apparent asymmetry between locations above and below hub height. Below hub height, $\langle \Delta Q^* \rangle$ equals unity at $\Delta r = 1.2\lambda$. For scales larger than this, the turbulent cascade is a Markov process at all measurement locations, but above hub height, $\langle \Delta Q^* \rangle = 1$ at $\Delta r = 1$ or less.

It is found that the presence of energy entrainment regions in the flow has a negative impact on the emergence of Markovian behavior at the scale differences smaller than λ, but does not eliminate the process altogether. At $x/D = 4$, most locations within the vertical profile that show Markovian behavior down to the Taylor microscale. This occurs at locations across the rotor diameter and above, an important implication for potential power prediction as the properties of the flow at these locations will serve as the inlet conditions for the next wind turbine. It is also shown that there is a correlation between the presence of an inertial sub-range and the Markovian process. Where a longer inertial sub-range leads to an extension of the range of the Markov process into smaller scales of turbulence.

As it is applied to wind energy, this holds great potential for improving maintenance schedules as well as improving the overall efficiency of the turbines. It has been shown in previous work [4, 8, 13] that prediction of power production becomes difficult with current techniques, where point measurements are taken upstream of a large scale wind farm. Once the wind enters the array, the complex interaction of the subsequent wind turbine wakes lead to poor estimation of power output. In this study, the downstream vertical locations that show the most consistent Markov properties are found to occur at four diameters downstream of a wind turbine within an array. With the experimental spacing of the turbines of $x/D = 7$ the resulting statistics are taken to represent the flow behavior found in an "infinite turbine array" [7]. This in combination with downstream spacing of turbines in a large wind farm is often larger than 4 diameters, offers a potential solution to the issues experienced by large scale arrays.

References

[1] E. Anahua, St. Barth, and J. Peinke. Markovian power curves for wind turbines. *Wind Energy*, 11(3):219–232, 2008.

[2] Sanjay R. Arwade, Matthew A. Lackner, and Mircea D. Grigoriu. Probabilistic models for wind turbine and wind farm performance. *Journal of Solar Energy Engineering*, 133(4):041006, 2011.

[3] R. J. Barthelmie, S. T. Frandsen, M. N. Nielsen, S. C. Pryor, P.-E. Rethore, and H. E. Jørgensen. Modelling and measurements of power losses and turbulence intensity in wind turbine wakes at middelgrunden offshore wind farm. *Wind Energy*, 10(6):517–528, 2007.

[4] R.J. Barthelmie, L. Folkerts, F.T. Ormel, P. Sanderhoff, P.J. Eecen, O. Stobbe, and N.M. Nielsen. Offshore wind turbine wakes measured by sodar. *J. Atmos. Ocean. Technol. (USA)*, 20(4):466 – 77, 2003.

[5] Eunshin Byon and Yu Ding. Season-dependent condition-based maintenance for a wind turbine using a partially observed markov decision process. *Power Systems, IEEE Transactions on*, 25(4):1823 –1834, nov. 2010.

[6] Raúl Bayoán Cal, José Lebrón, Luciano Castillo, Kang Hyung Suk, and Charles Meneveau. Experimental study of the horizontally averaged flow structure in a model wind-turbine array boundary layer. *Journal of Renewable and Sustainable Energy*, 2(1):013106, 2010.

[7] Leonardo P. Chamorro and Fernando Porté-Agel. Turbulent flow inside and above a wind farm: A wind-tunnel study. *Energies*, 4(11):1916–1936, 2011.

[8] A. Crespo, J. Hernandez, and S. Frandsen. Survey of modelling methods for wind turbine wakes and wind farms. *Wind Energy*, 2(1):1–24, 1999.

[9] W.H. Fleming. Controlled markov processes and mathematical finance. pages 407 – 46, Dordrecht, Netherlands, 1999.

[10] F. Ghasemi, M. Sahimi, J. Peinke, and M. Reza Rahimi Tabar. Analysis of non-stationary data for heart-rate fluctuations in terms of drift and diffusion coefficients. *J. Biol. Phys. (USA)*, 32(2):1117 – 28, 2006.

[11] A N Kolmogorov. Dissipation of energy in locally isotropic turbulence. *Doklady Akad. Nauk SSSR*, 32(16), 1941.

[12] T.S.-T. Leung. A markov-modulated stochastic control problem with optimal multiple stopping with application to finance. pages 559 – 66, Piscataway, NJ, USA, 2010.

[13] Y. Ma, T. Runolfsson, and J.N. Jiang. Cluster analysis of wind turbines of large wind farm with diffusion distance method. *Renewable Power Generation, IET*, 5(2):109 –116, March 2011.

[14] J.L. McCauley, K.E. Bassler, and G.H. Gunaratne. Markov processes, hurst exponents, and nonlinear diffusion equations: With application to finance. *Physica A (Netherlands)*, 369(2):343 – 53, 2006.

[15] C. Meneveau N. Hamilton, H. Suk Kang and R. Cal. Statistical analysis of kinetic energy entrainment in a model wind turbine array boundary layer. *Journal of Renewable and Sustainable Energy*, 4(6):063105, 2012.

[16] A.P. Nawroth and J. Peinke. Multiscale reconstruction of time series. *Physics Letters A*, 360(2):234 – 237, 2006.

[17] C. Renner, J. Peinke, and R. Friedrich. Experimental indications for markov properties of small-scale turbulence. *J. Fluid Mech. (UK)*, 433:383 – 409, 2001.

[18] M. Siefert and J. Peinke. Joint multi-scale statistics of longitudinal and transversal increments in small-scale wake turbulence. *Journal of Turbulence*, page N50, 2006.

[19] M Tutkun and L Mydlarski. Markovian properties of passive scalar increments in grid-generated turbulence. *New Journal of Physics*, 6(1):49, 2004.

[20] L.J. Vermeer, J.N. Sorensen, and A. Crespo. Wind turbine wake aerodynamics. *Progress in Aerospace Sciences*, 39(6-7):467 – 510, 2003.

[21] Wei Zhang, Corey Markfort, and Fernando Porté-Agel. Near-wake flow structure downwind of a wind turbine in a turbulent boundary layer. *Experiments in Fluids*, 52:1219–1235, 2012.

STUDY OF THE INFLUENCE OF ATMOSPHERIC TURBULENCE ON THE ASYMPTOTIC WAKE DEFICIT IN A VERY LONG LINE OF WIND TURBINES

S.-P. Breton[1], K. Nilsson[1], H. Olivares-Espinosa[2], C. Masson[2], L. Dufresne[2], S. Ivanell[1]
[1]Gotland University, Wind Energy Technology
Cramérgatan 3, 62165 Visby, Sweden, simon-philippe.breton@hgo.se
[2]École de technologie supérieure, Department of Mechanical Engineering
1100 Notre-Dame Ouest, Montréal, Québec, Canada, H3C 1K3

ABSTRACT

The influence of atmospheric turbulence on the development of the flow along a long row of wind turbines is studied, in search for an asymptotic wake deficit state. Calculations are performed using EllipSys3D, a CFD code that solves the Navier-Stokes equations in their incompressible form using a finite volume approach. In this code, the Large Eddy Simulation technique is used for modelling turbulence, and the wind turbine rotors are represented as actuator disks whose loading is determined through the use of tabulated airfoil data by applying the blade-element method.

Ten turbines are located along a row and separated from each other by seven rotor diameters, which is representative of the distance used in today's offshore wind farms. Turbulence is pre-generated with the Mann model, with imposed turbulent levels of 4.5 and 8.9%. The turbines are in this study isolated from their environment, as no effect from the ground is modeled. This makes the proposed study of the asymptotic wake state behavior easier. Analysis of the characteristics of the flow as a function of the position along the row of turbines is performed in terms of turbulence intensity, mean velocity, and power spectra of the velocity fluctuations. Power production along the row of turbines is also used as an indicator.

Calculations are performed below rated power, where a generator torque controller implemented in EllipSys3D renders it possible for the turbines to adapt to the inlet conditions in which they operate.

The results obtained for the turbulence intensity, power and mean velocity as a function of downstream distance show that an asymptotic wake state seems close to be reached near the end of the 10 turbine row. They also show a certain dependency on the imposed level of turbulence. Uncertainties obtained in the power spectra of the velocity fluctuations suggest that further investigation is necessary.

1 Introduction

Offshore conditions are normally associated with low turbulence levels and stable wind conditions. However, the flow situation deep inside a wind farm is highly turbulent. Since offshore farm are getting larger, it is of great importance to increase the understanding of the flow characteristics deep inside the farm since these will influence not only the performance of the farm but also the lifetime of the individual turbines.

The present work will study how the flow is behaving in a long line of turbines. The question then arises as to if a wake state can be achieved after a certain number of turbines for which the velocity deficit in the wake would reach an asymptotic behavior, and how this would depend on the level of atmospheric turbulence.

The work is performed using numerical computations with the large-eddy simulation (LES) technique and the EllipSys3D code, Michelsen [1][2] and Sørensen [3]. The wind turbines are parameterized using an actuator disc (ACD) method, Mikkelsen [4] and Troldborg et al. [5], which models the wind turbines using body forces determined from airfoil data. This method substantially reduces the computational costs since the boundary layer of the blades is no resolved compared to modeling the full geometry of the turbines. Pre-generated synthetic turbulence generated using the method of Mann, see Mann [6][7], is imposed in the domain. The simulations are performed using uniform inlet conditions and no shear is considered.

Similar simulations have been performed earlier by Troldborg et al. [8][9] which used an actuator line method in combination with LES to study the wake behavior of turbines in uniform and atmospheric boundary layer conditions. However, in these works, as the aim was not to study the asymptotic wake deficit state, a maximum of two turbines was modeled. Other work in the field field of wind turbine simulations using LES have been performed by Ivanell et al. [10], Ivanell [11], Porté-Agel et al, [12], Lu and Porté-Agel [13] among others. Furthermore, for an extensive list of different wake models, the reader is referred to Crespo et al. [14] and Vermeer et al. [15]. To the authors knowledge, however, no analysis such as the one suggested here, where a large number of aligned turbines are isolated from their environment and focus is put on the characteristics of the flow, has been performed with LES before.

As a first step, computations are performed with two different turbulence levels without the influence of wind turbines in order to study how the turbulence generated synthetically with the Mann method is developing as function of the downstream distance. In this case the turbulence intensity (TI) is determined for a number of downstrem postions. Furthermore, spectral analyses of the velocity fluctuations are performed at different downstream positions in an attempt to provide more information about the characteristics and evolution of the turbulence in the domain.

As a second step, computations are performed for three different turbulence levels with 10 aligned wind turbines. The mean streamwise velocity, TI and power production are determined as functions of the downstream distance. Spectral analyses are also performed as a function of the downstream position, in order to provide more information about the effect of the turbine rotors on the turbulence characteristics, and to help in determining if an asymptotic wake state is reached. Comparisons will also be performed in terms of production with experimental data obtained from two offshore wind farms.

2 Turbine specifications

A downscaled version of the conceptual NREL 5MW turbine is used in this study, see Jonkman et al. [16]. The used turbine has a radius of 46.5m and a nominal power of 2.3MW. The chord is downscaled linearly using the diameter ratio between the downscaled turbine and the full size NREL turbine as the scaling parameter. The twist together with C_L and C_D airfoil data for the different sections of the downscaled turbine blades are the same as presented in Jonkman et al. [16]. The power output of the turbine is actively controlled using the method described in Nilsson [18].

3 Numerical model

The simulations are performed with the EllipSys3D code developed at DTU / Risø. The EllipSys3D code is a general purpose 3D solver, originally developed by Michelsen [1][2] and Sørensen [3]. The code has been used and described in numerous studies and will hence not be described in detail here. The reader is referred to Mikkelsen [4], Troldborg et al. [5][8][9], Ivanell et al. [10][17] and Nilsson [18] among others for more information.

The computations are carried out as LES. With the LES technique large eddies are resolved explicitly and eddies smaller than a certain size are filtered out and modeled by an eddy-viscosity based sub-grid scale (SGS) model. For this work the mixed scale model developed by Ta Phuoc [19] is used. For more information about the LES technique and the SGS model, the reader is referred to Sagaut [20] and Ta Phuoc [19]. The code is formulated in primitive variables, i.e., pressure and velocity, in a collocated storage arrangement. The numerical method uses a blend of a third order Quadratic Upwind Interpolation for Convective Kinematics (QUICK) scheme (10%) and a fourth order Central Differences Scheme (CDS) (90%) for the convective terms, while it uses a second order CDS for the remaining terms. The use of the blend is a compromise between avoiding non-physical numerical wiggles and limiting numerical diffusion. The pressure correction equation is based on the Semi-Implicit Method for Pressure-Linked Equations (SIMPLE) algorithm.

3.1 Grid, boundary conditions, and simulation configuration

The grid used in this study has a resolution in the inner equidistant region of $0.1R$. This value is based on experience from previous studies, see Ivanell [11]. This is the region of interest where all turbines are placed and where the wake calculations are performed. In order to save grid points, the grid is stretched towards all boundaries as seen in Fig. 1 where the xy (left figure) and xz (right figure) planes of the grid are shown, respectively. The coordinate system is defined by (z,x,y), which refer respectively to the streamwise, vertical, and longitudinal directions. The grid measures totally $167\times20\times20R^3$. The equidistant region size is $150\times4\times4R^3$. It is centered in the xz plane, as seen in Fig. 1 (left), and it begins at a z value of $8R$.

For simulations where wind turbines are present, 10 wind turbines are placed at positions $(z,10R,10R)$. The first turbine is placed in position $z=17R$ and the remaining turbines are positioned just after each other with a spacing of $14R$.

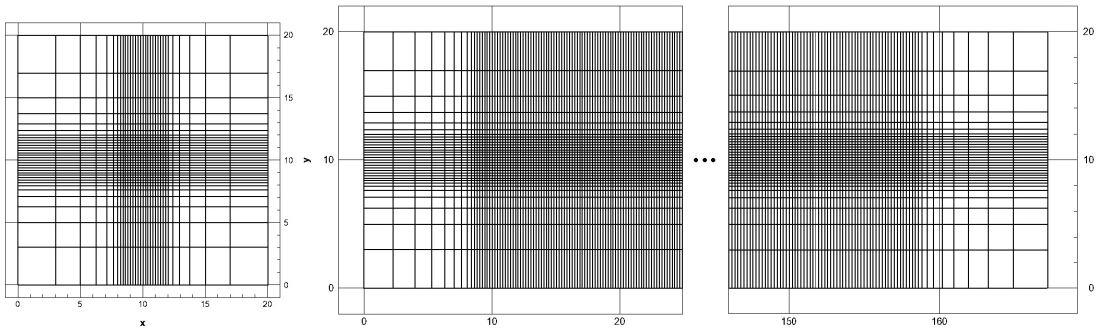

Figure 1: *xy* (left) and *xz* (right) planes plot of the grid. In the *xz* plane, only the inlet and outlet parts of the grid are shown and the remaining part of the grid is denoted by three dots.

Slip conditions are imposed at the bottom and at the top of the domain, cyclic conditions are imposed at the lateral boundaries and a convective condition is imposed at the outlet. Dirichlet conditions are employed for velocities and pressure at the inlet and a constant and uniform streamwise velocity component is applied at the upper and lower boundaries of the domain. 80000 timesteps are performed in each simulation, which corresponds to about 12 longitudinal flowtimes, with a flowtime referring to the time taken for the undisturbed flow to travel once through the domain in the axial direction.

3.2 Actuator disc method

The turbines are modeled in the simulations using the ACD method, see Mikkelsen [4] and Troldborg et al. [5]. In the ACD method the rotor is modeled as a disc on which body forces are imposed. The body forces are determined from local angles of attack and airfoil data (lift and drag coefficients as a function of the angle of attack). The velocities at the disc are computed by the flow solver in the global Cartesian grid. These velocities are being interpolated to a local polar grid. The rotor is initially given a rotational velocity, which is left to adapt to the conditions in which it operates through the use of a controller, as described in Nilsson [18]. The local angle of attack is determined by the local flow angle, the twist and the possible pitch of the blades. The forces acting on the disc are computed on the local polar grid by using the local angle of attack. In a last step the forces are interpolated back to the global Cartesian grid. It is emphasized that the disc loading is not uniform since the forces are computed using the local velocities determined for each grid point of the rotor disc. In order to avoid numerical problems, the body forces are regularized using a one-dimensional Gaussian approach. The regularization is performed using a standard deviation of $\varepsilon/\sqrt{2}$, where ε is the regularization parameter which set to $0.2R$. The local polar grid is defined using 21 grid points on the radius and 81 points in the azimuthal direction.

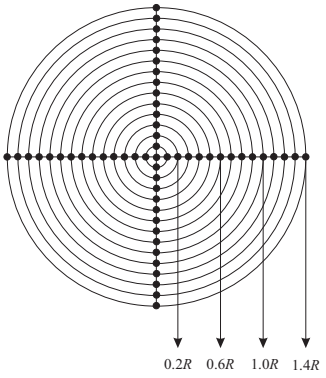

Figure 2: Schematical figure explaing how the time series of velocity are extracted.

3.3 Modeling turbulence

The modeling of the ambient turbulence is performed by introducing pre-generated synthetic ambient turbulence. The ambient turbulence is generated using the Mann model, [6][7]. The turbulent field computed by the model is homogeneous, Gaussian, anisotropic, and has the same second order statistics as the atmospheric turbulence. For the generation of ambient turbulence a box is defined measuring $333 \times 3.9 \times 3.9R^3$ with an equidistant resolution of approximately $0.16R$. The box consists of $2048 \times 32 \times 32$ grid points. As each position in the streamwise direction in the box corresponds to a timestep according to Taylor's frozen turbulence hypothesis, the box consists of 2048 timesteps. In order to impose the fluctuations in the CFD domain, the xy-planes at each z position are determined from the box. The fluctuations at these planes are recalculated into body forces and these are imposed using an analogy to the immersed boundary technique, Troldborg et al. [21]. The lower right corner of the planes of turbulence are at each timestep introduced at approximately $(z,x,y) = (13R, 8R, 8R)$ to ensure the entire plane to be within the equidistant region of the grid but upstream from the first turbine. The planes are then convected downstream by the flow solver. As the resolution and the timestep in the turbulence box differ from that of the LES, spatial and temporal interpolation are performed. The turbulence intensity (TI) is determined only by considering the streamwise component of the fluctuations. However, all three components are used in the computations. The input to the Mann model is a mean velocity of 8m/s and the roughness lengths $2.0 \cdot 10^{-5}$m and $3.5 \cdot 10^{-2}$m. The idea is to perform simulations with an imposed atmospheric TI equal to approximately 4 and 8%. Additionally, cases without atmospheric turbulence are simulated for comparison purposes.

3.4 Characterization of turbulence

In order to efficiently track time series of velocity at several points of interests, probe sheets are inserted at different z positions. The probe sheet at each z postion is distributed according to Fig. 2 and its center is placed at $(z, 10R, 10R)$. The first sheet is placed at $z = 17R$, the second sheet is placed at $24R$, and the remaining sheets are placed after each other with a spacing of $14R$, i.e., in-between each pair of turbines.

As mentioned above, the simulations are performed both without and with the influence of wind turbines. The former is used to analyze the TI and velocity fluctuations as a function of downstream distance, in an attempt to study the development of the synthetically generated turbulence throughout the domain, whereas the latter is used to analyze the impact of different TI levels on the wake flow, on the power production of the turbines, and on the eventual obtention of an asymptotic wake state.

The TI and mean streamwise velocity as functions of the downstream distance are determined as mean values over all the points starting from $0R$ to $1R$ in Fig. 2. They are averaged over the last 6 flow times of the simulations. In this paper, the ambient TI level, which corresponds to the imposed level of atmospheric turbulence in the simulations, will be referred to as $TI_{amb,0}$. We define it as the TI at the position of the first turbine ($17R$) when this turbine is not present. The TI at different axial positions in the absence and presence of wind turbines will be denoted respectively as TI_{NT} and TI_{WT}.

Power spectra of the velocity fluctuations are also calculated as a function of downstream position, radial position, and incoming turbulence intensity, in order to provide more information about the turbulence. This is done following the method outlined by George [22], at each position depicted in Fig. 2. In order to minimize fluctuations in the spectra, FFT's are performed on each of the last four 13336-timestep blocks of the 80000 timestep simulations, and are averaged together. Each block corresponds to the number of timesteps required for a Mann turbulence box to travel through the domain at the mean velocity (which also corresponds to two longitudinal flowtimes). Four flowtimes were then left for the flow to travel through the domain before starting to analyse the velocity fluctuations data. Results are finally presented as azimuthal averages of the spectra calculated at the four azimuthal positions around the circles shown in Fig. 2. Each resulting spectra, associated to a certain radial position, is in this way averaged over 16 13336-timestep blocks. Spectra were in this article only performed on the axial velocity fluctuations.

4 Results and discussion

4.1 In the absence of turbines

As a first step the $TI_{amb,0}$ is determined and it is found that the LES overestimates it with approximately 10% compared to values found directly by analyzing the Mann data set. $TI_{amb,0}$ in the LES are found to be 4.5% and 8.9%. In Fig. 3, TI_{NT} as a function of the downstream position is depicted for $TI_{amb,0} = 4.5\%$ and 8.9%. It is seen that the turbulence is dissipating significantly as the downstream distance increases. This behavior is expected since the turbulence is imposed only at one upstream position and since there is no other turbulence generated in the domain to sustain the $TI_{amb,0}$ value. The decay is however not very large at the positions of the two first turbines, making a study of the influence of $TI_{amb,0}$ on the first axial positions possible. Further downstream, it will be seen that the influence of $TI_{amb,0}$ on the wake development will decrease as the turbulence produced by the turbine rotors increases.

Fig. 4 shows the power spectra of the velocity fluctuations in the absence of turbines calculated at a radial distance of $1R$ as a function of the downstream distance, for the two studied

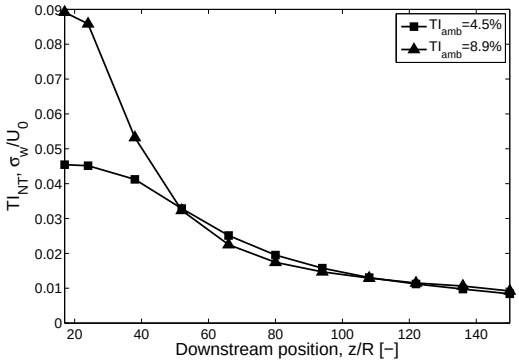

Figure 3: TI as a function of downstream distance in the absence of wind turbines.

levels of $TI_{amb,0}$. For the sake of clarity, some axial positions behind turbines were omitted in these graphs. Only one radial position is shown here for space considerations. The resulting figures are however enough to demonstrate the general behavior obtained.

The spectra are seen to consist in three distinct regions. In the low frequency region, the spectra are seen to follow the theoretical slope of -5/3 associated to the inertial range, where energy is transferred from large eddies to smaller ones. From a value of $f * R/V_0$ of about 1, the spectra depart from this slope, corresponding to the frequency at which energy dissipation starts to occur. In the present case where the grid spacing is 4.65m and incoming velocity is 8m/s, the time taken for non disturbed flow to travel one grid cell is 0.58s. This can be transferred into a Nyquist frequency of 0.86Hz, which is associated to a $f * R/V_0$ value of about 5, corresponding to the highest frequency of the structures that can be resolved in our calculations. After this, the eddies are modeled by the SGS model. In our spectra, energy dissipation starts to happen at a value of $f * R/V_0$ of about 1. The difference with the value of 5 calculated above might be explained by the fact that a certain number of cells might be needed to resolve a vortex structure. The last region at high frequencies is seen to have smaller fluctuations than the other regions, and a slope which goes back towards a value of -5/3. Such a behavior for the slope of the spectra at high frequencies is reported to have been seen in previous simulations performed with EllipSys3D with the blades modeled as actuator lines [23]. However, this does not appear to be the case with simulations performed in similar conditions using OpenFoam with the turbine rotors modeled as actuator discs (see [24] for a description of the setup used for these simulations). The different SGS model used in the LES simulations performed with OpenFoam (”classic Smagorinsky”) might explain the differences observed. A different convection scheme (QUICK in OpenFoam), related among other things to unequal levels of numerical diffusion, could also contribute to these distinct results. More work is however needed to be able to conclude on this matter.

The spectra associted to a $TI_{amb,0}$ of 8.9% depict a higher intensity than the ones associated to a $TI_{amb,0}$ of 4.5%, consistent with the fact that more energy is found in the wake for a higher level of turbulence. When looking at the two first regions described above, the spectra are seen to decrease in intensity as the downstream distance increases. This is consistent with the

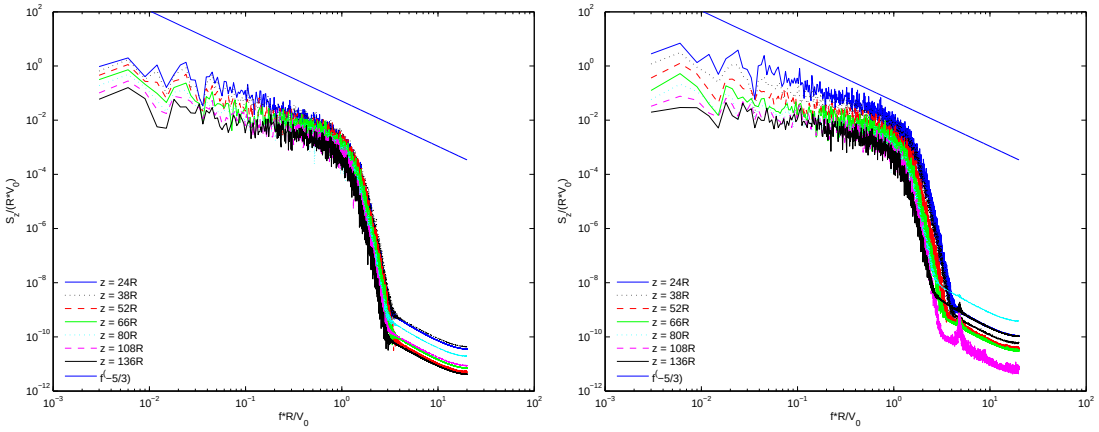

Figure 4: Power spectra of the velocity fluctuations in the absence of wind turbines, azimuthally averaged on a $1R$ circle centered at the position where the rotors will be located, for different downstream positions, with an $TI_{amb,0}$=4.5% (left) and 8.9% (right)

decrease of TI with increasing downstream distance seen in Fig. 3. This behavior is however not observed at high frequencies, where no clear trend can be found. Differences were actually also obtained at high frequencies when looking at different radial positions (not shown here), which was not the case at lower frequencies. A varying behavior is not expected for different radial positions, as flow properties are not awaited to change with radial position in the absence of turbines and influence from the ground. For this reason, and the fact that the results obtained at high frequencies are different from the ones predicted by Openfoam, the behavior of the spectra at high frequencies is deemed uncertain, and is currently under investigation.

The spectra seen in these figures however suggest that the turbulent fluctuations imposed with the Mann method, although decaying, remain significant along the region of interest, making the study suggested here possible. As mentioned above, in the presence of turbines, the level of turbulence will quickly be dominated by the turbine generated turbulence.

4.2 In the presence of turbines

TI_{WT} and the mean streamwise velocity are depicted in Fig. 5 as a function of axial position, in the presence of turbines. It is seen that the TI_{WT} (left figure) in the wake clearly depends on $TI_{amb,0}$, even at positions where TI_{NT} is more or less independent of $TI_{amb,0}$ (see Fig. 3 for comparison). A higher $TI_{amb,0}$ indeed results in a higher TI in the wake flow. This suggests that the wake structures somehow remember the initial turbulence conditions, as they are influenced by the initial flow conditions even far downstream.

The mean streamwise velocity determined at the same locations as the TI is shown in Fig. 5 (right). It is seen in this figure that the normalized velocity at position $z = 17R$ is just below 0.9, and is independent of $TI_{amb,0}$. Further downstream, the level of the mean velocity is dependent on $TI_{amb,0}$. It is also seen that the velocity is slowly decreasing with the downstream distance but is found to be more or less constant for the last 3 position for a given $TI_{amb,0}$. The impact of the imposed turbulence is also evident when comparing with the case where $TI_{amb,0} = 0\%$,

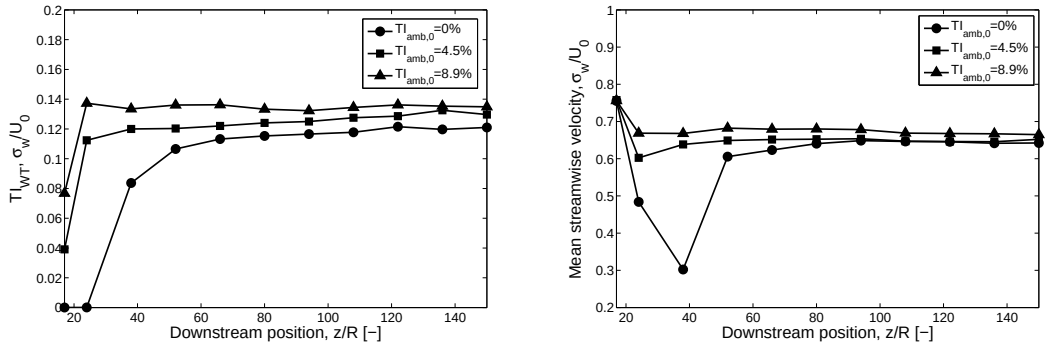

Figure 5: TI_{WT} (left) and mean streamwise velocity (right) as a function of downstream distance.

where a significant drop of the velocity is found at $z = 24R$ and $z = 38R$. After $z = 52R$ the wake flow has however recovered and the differences between the $TI_{amb,0} = 0\%$, $TI_{amb,0} = 4.5\%$ and $TI_{amb,0} = 8.9\%$ cases are minor. A higher $TI_{amb,0}$ is seen to result in a higher mean velocity. This is expected since a higher turbulence results in a higher level of mixing of the wake flow and the surrounding flow, allowing a quicker velocity recovery.

The trends show that all curves representing TI and mean velocities are aiming for an asymptotic value when the downstream distance increases. It is noted that this seems to happen faster with higher values of $TI_{amb,0}$.

The mean power output of the individual turbines as a function of streamwise position is depicted in Fig. 6. The power is normalized by the power of the first turbine in the line for each $TI_{amb,0}$ level. The trend for the production is found to follow a similar trend as that for the mean velocity (Fig. 5, right), which is expected. A higher $TI_{amb,0}$ results in a higher production. This can be seen earlier in studies, see e.g. Hansen et al. [25], and is expected since the mean velocity recovers faster when increasing $TI_{amb,0}$. It is noted that the power is extracted at the turbine positions while the mean velocity is extracted in between each pair of turbines. Also, to fit the measurement data the power curves are starting at $z = 0R$ while the velocity curves start at $z = 17R$. These aspects makes the velocity and power curves slightly shifted. The trends for the mean velocity and the production curves however follow each other as expected. For comparison purposes, the relative power measured at the Horns Rev and Lillgrund wind farms is plotted as a function of downstream distance, see Hansen et al. [25] and Nilsson et al.[26]. In the Horns Rev case the $TI_{amb,0}$ is equal to approximately 7% and in both the Lillgrund cases it is equal to approximately 5%. It is seen that there are large differences between the production in the Lillgrund cases and the the present simulations. This difference is believed mainly to be due to the spacing between the turbines which is much smaller in the Lillgrund case. Earlier comparisons between EllipSys3D simulations performed with a right spacing and the experimental data from Lillgrund have shown very good agreement, Nilsson et al.[26]. The results from the simulations performed here and the Horns Rev measured data show a similar trend. In this case, the same distance was used in the simulations between each turbine than in the real-life case. Obtaining the right trends from the simulations seem to be dependent on the use of a right distance between the simulated turbines. Let us note that the actual Horns Rev turbines have a nominal power of 2MW, compared to the 2.3MW nominal power used in

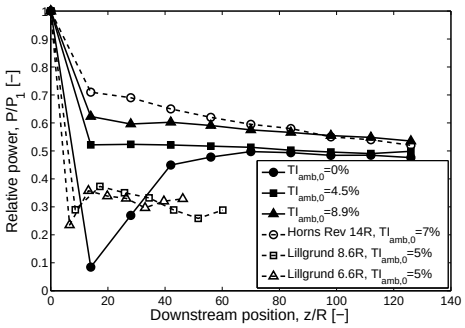

Figure 6: Relative power production for the different values of $TI_{amb,0}$. For comparison purposes also the measured production at the Horns Rev and Lillgrund wind farms are plotted.

the present simulations. In the experimental case, less kinetic energy is then extracted by each turbine, letting more energy pass to the following turbine. This should lead to higher production levels in the measured production, which is a likely explanation for the differences that can be seen between the simulations and experimental data for turbines 2-5 in the row.

Fig. 7 shows the power spectra of the velocity fluctuations corresponding to the ones showed in Fig. 4, but in the presence of turbines. In addition to spectra obtained with a $TI_{amb,0}$ of 4.5% and 8.9%, a spectrum is also shown for a $TI_{amb,0}$ of 0%. The same three regions that were described to make up the spectra in the absence of turbines in Fig. 4 can be observed here as well. In the case where $TI_{amb,0}$=0%, the intensity of the first spectrum (at 24R) is much smaller than at greater downstream distances. The wake takes in this case the form of a shear layer that appears to be very stable, and has not yet broken down. The velocity as a function of time inside this shear layer (not shown here) was seen to vary very little. The same phenomenon was observed for different radial positions around the 1R value. This can be related to the very low mean TI observed in Fig. 5. This changes drastically with increasing $TI_{amb,0}$, which causes the shear layer to break down and the wake to become unstable, resulting in a very large increase in the intensity of the spectra. The second turbine has a similar effect on the wake: it contributes to breaking down the shear layer that otherwise would remain stable over large distances, as seen in a previous work Breton et al [27].

At $TI_{amb,0}$=4.5 and 8.9%, an important difference in intensity is seen, in the whole frequency range shown, between the spectrum calculated at a distance of 24R and the ones corresponding to greater downstream distances. Indeed, in the first two regions, the intensity associated to this spectra is larger. In the third region, the opposite result is obtained, as the intensity is smaller for this spectra at high frequencies.

These differences suggest, as expected and seen above from looking for example at the turbulence intensity, that the turbulence characteristics of the wake are changing in an important way when going from behind the first turbine to behind the second turbine. Thereafter, it becomes however difficult, when looking at low frequencies, to differentiate between spectra obtained for distances greater than 24R. Indeed, from a distance of about 38R, the spectra become very close to each other and are hardly discernible, a behavior that can be related to the one observed in Fig.

5, where after a distance of 24R, the level of TI stays almost constant, except at 0% incoming TI, which shows a little variation that cannot be detected in the corresponding spectrum. The spectra differ somehow at high frequencies, but do not show a clear trend with increasing downstream distance. As explained when discussion Fig. 7, one should be careful with the results shown here at high frequencies, which require further investigation.

The spectra, in their current form, do not seem to make it possible to determine when an asymptotic state is reached. They become indeed too close together already from behind the second turbine to be discernable. It is hoped that a further investigation in the behavior of the spectra at high frequencies will allow to give more information in this regard.

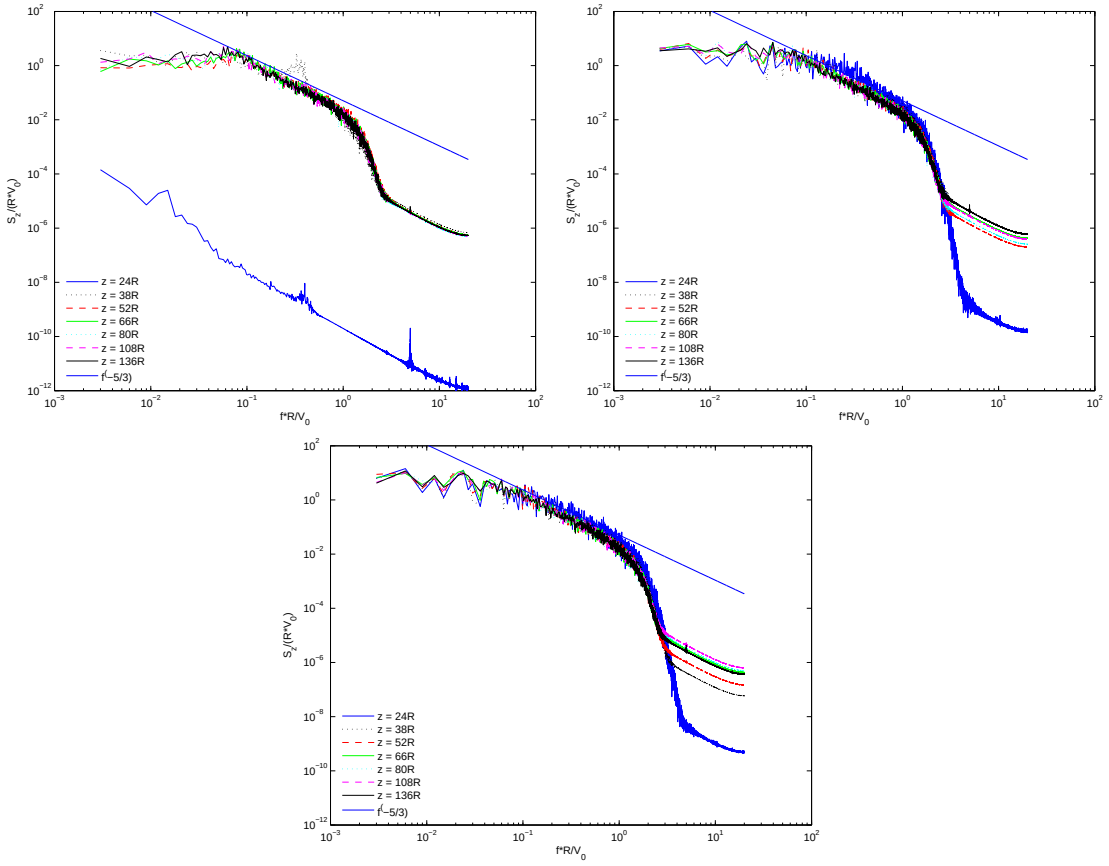

Figure 7: Power spectra of the velocity fluctuations in the presence of wind turbines, azimuthally averaged on a 1R circle centered at the rotor, for different downstream positions, with a $TI_{amb,0}$ of 0% (top left), 4.5% (top right) and 8.9% (bottom)

However, when considering the mean streamwise velocity, the TI and the power as functions of downstream distance for a given value of $TI_{amb,0}$, the conditions far downstream in the wake structure are believed to reach a near-asymptotic state since these mean quantities are considered as more or less independent of the downstream position. The dependency of this result on the imposed level of turbulence does not seem very strong, although imposing a certain level of

turbulence intensity seems to favor the obtention of this state, and accelerate its reach. A rather great uncertainty is however believed to be found in the dissipation of the imposed turbulence, and more work is needed to clearly conclude on the influence of the imposed level of turbulence on the obtention of an asymptotic wake state.

5 Conclusion

LES simulations were performed with EllipSys3D on a line of 10 wind turbines modeled as actuator discs, under different levels of imposed turbulence generated synthetically with the method of Mann, in search for an asymptotic wake deficit state. The characteristics of the turbulence were first studied in the absence of turbines. It was observed that the level of turbulence imposed in the simulations seems somehow to be remembered further downstream when looking at evolution of the turbulence intensity (TI), although it was observed to be decaying in the absence of wind turbines. The power spectra of the velocity fluctuations were observed to be in agreement (at least for a large part of the spectra), with what was expected, and provided interesting information about the characteristics of turbulence. However, the fact that their behavior was not fully understood at high frequencies and that no clear trends could be observed at these frequencies limited the amount of information available. Differences observed with similar simulations performed with OpenFoam in this frequency region also called for more investigations. An asymptotic wake deficit seemed very close to being obtained with 10 turbines when analyzing the mean velocity, power and turbulence intensity in the wake, and a higher level of imposed turbulence seemed to help reach this state. Comparisons in terms of power with experimental data from the Horns Rev offshore in which the turbines were separated by 7 rotor diameters as in the present case showed that similar trends were obtained

Future work will push this study further by considering a greater number of turbines, and a greater number of $TI_{amb,0}$, in hunt for a truly asymptotic wake state, and of its dependency on the imposed level of turbulence. This could be made easier by considering a finer grid, which should limit the decay of the imposed turbulence by numerical dissipation. It is also desired to study the effect from curtailment, where different turbines would be pitched, and the effect on the obtention or not of an asymptotic wake state will be studied. The effect from the distance between the turbines will also be investigated, along with the influence from the ground. Further comparisons between the results obtained with OpenFoam and EllipSys3D will be made in order to learn more about the differences obtained in the velocity fluctuations spectra at high frequencies. It is wished to perform simulations in very simple configurations aimed at isolating the effects from the different SGS model and convection scheme, in order to determine their impact on the results obtained, and she more light into the behavior of the spectra obtained at high frequencies, which could provide valuable information about the turbulence characteristics in the wake.

Acknowledgments

The computations were performed on resources provided by the Swedish National Infrastructure for Computing (SNIC) at the National Supercomputer Centre (NSC). The program Vindforsk from the Swedish Energy Agency is acknowleged for providing research funds for this work. Niels Troldborg from DTU is also greatly acknowledged for providing precious input into the analysis of the velocity fluctuations power spectra. Olivares-Espinosa wishes to thank the Consejo Nacional de Ciencia y Tecnologa (CONACYT-MEXICO) for their support.

REFERENCES

References

[1] Michelsen JA. Basis3D - A Platform for Development of Multiblock PDE Solvers. *Tech. rep. AFM 92-05* 1992; Technical University of Denmark

[2] Michelsen JA. Block Structured Multigrid Solution of 2D and 3D Elliptic PDE's. *Tech. rep. AFM 94-06* 1994; Technical University of Denmark

[3] Sørensen NN. General purpose flow solver applied to flow over hills. *PhD th. Risø-R-827-(EN)* 1995; Risø National Laboratory

[4] Mikkelsen R. Actuator Disc Methods Applied to Wind Turbines. *PhD th. MEK-FM-PHD 2003-02* 2003; Technical University of Denmark

[5] Troldborg N, Gaunaa M, Mikkelsen R. Actuator Disc Simulations of Influence of Wind Shear on Power Production of Wind Turbines. *Proc. of The science of making torque from wind* 2010; 271-297

[6] Mann J. The spatial structure of neutral atmospheric surface-layer turbulence. *J. Fluid Mech* 1994; **273**; 141-168

[7] Mann J. Wind field simulation. *Prob. Eng. Mech.* 1998; **13**; 269-282

[8] Troldborg N, Sørensen JN, Mikkelsen R. Numerical simulations of wake characteristics of a wind turbine in uniform inflow. *Wind Energy* 2010; **13**; 86-99

[9] Troldborg N, Larsen GC, Madsen HA, Hansen KS, Sørensen JN, Mikkelsen R. Numerical simulations of wake interaction between two wind turbines at various inflow conditions. *Wind Energy* 2011; **14**; 859-876

[10] Ivanell S, Mikkelsen R, Sørensen JN, Henningson D. Three-dimensional actuator disc modeling of wind farm wake interaction. *Proc. of the European Wind Energy Conference and Exhibition* 2008

[11] Ivanell S. Numerical Computations of Wind Turbine Wakes. *PhD th. TRITA-MEK 2009:01* 2009; KTH Engineering Sciences

[12] Porté-Agel F, Wu Y-T, Lu H, Conzemius RJ. Large-eddy simulation of atmospheric boundary layer flow through wind turbines and wind farms. *J. of Wind Eng. and Industrial Aerodynamics* 2011; **99**; 154-168

[13] Lu H, Porté-Agel. Large-eddy simulation of a very large wind farm in a stable atmospheric boundary layer. *Ph. of Fluids* 2011; **23**; 065101

[14] Crespo A, Hérnandez J, Frandsen S. Survey of Modeling Methods for Wind Turbine Wakes and Wind Farms. *Wind Energy* 1999; **2**; 1-24

[15] Vermeer LJ, Sørensen JN, Crespo A. Wind turbine wake aerodynamics. *Progress in Aerospace science* 2003; **39**; 467-510

[16] Jonkman J, Butterfield S, Musial W, Scott G. Definition of a 5-MW Reference Wind Turbine for Offshore System Development. *Tech. rep. NREL/TP-500-38060* 2009; National Renewable Energy Laboratory

[17] Ivanell S, Mikkelsen R, Sørensen JN, Henningson D. Validation of methods using EllipSys3D *Tech. rep. TRITA-MEK 2008:12* 2008; KTH Engineering Sciences

[18] Nilsson K. Numerical computations of wind turbine wakes and wake interaction. *Lic. th. TRITA-MEK 2012:18* 2012; KTH Engineering Sciences

[19] Ta Phuoc L. Modèles de sous maille appliqués aux écoulmements instationnaires décollés. *Tech. rep. LIMSI 93074* 1994; LIMSI France

[20] Sagaut P. *Large eddy simulation for incompressible flow* 2006; (Berlin Heidelberg: Springer)

[21] Troldborg N, Sørensen JN, Mikkelsen R. Actuator line simulation of wake of wind turbine operating in turbulent inflow. *Proc. of The science of making torque from wind* 2007; 012063

[22] George WK. Lectures in Turbulence for the 21st Century. *Lecture Notes* 1992; Chalmers University, Sweden, 2013.

[23] Private e-mail communication with Niels Troldborg, April 2013.

[24] Olivares-Espinosa H, Masson C, Dufresne L. Turbulence characteristics in a free wake of an AD: comparisons between a rotating and a non-rotating AD in uniform flow. *The Science of Making Torque from Wind.* Oldenburg, Germany, 2012

[25] Hansen KS, Barthelmie RJ, Jensen L, Sommer A. The impact of turbulence intensity and atmospheric stability on power deficits due to wind turbine wakes at Horns Rev wind farm. *Wind Energy* 2012; **15**; 183-196

[26] Nilsson K, Ivanell S, Hansen KS, Mikkelsen R, Sørensen JN, Breton S-P, Henningson D. Large-eddy simulations of the Lillgrund wind farm. *Submitted to Wind Energy* 2013

[27] Breton SP, Nilsson K, Ivanell S, Olivares-Espinosa H, Masson C, Dufresne L. Study of the effect of the presence of downstream turbines on upstream ones and use of a controller in CFD wind turbine simulation models. *The Science of Making Torque from Wind.* Oldenburg, Germany, 2012

Characterization of wind turbine wakes in a non-sheared turbulent flow

H. Olivares-Espinosa[1], S.-P. Breton[2], K. Nilsson[2]

C. Masson[1], L. Dufresne[1], and S. Ivanell[2]

[1] École de technologie supérieure, Department of Mechanical Engineering,
1100 rue Notre-Dame Ouest, Montréal, QC, H3C 1K3, Canada
Email: hugo.olivares-espinosa.1@ens.etsmtl.ca
[2]Gotland University, Wind Energy Technology
Cramergatan 3, 62167 Visby, Sweden

ABSTRACT

The characteristics of the turbulence field in wakes produced by horizontal-axis wind turbines under a uniform inflow are studied. To this aim, LES simulations of a rotor subjected to different types of inflow are performed with OpenFOAM®. Two different Actuator Disk (AD) models for the rotor are implemented with the goal of assessing their capabilities to reproduce the turbulence characteristics of the wake: a uniformly loaded rotor and an AD model based on the blade element theory that employs tabulated airfoil data to calculate the distribution of forces over the disk as well as the geometry and other physical parameters from a conceptual 5 MW offshore wind turbine. The latter AD implementation makes use of a control system to adjust the rotational velocity of the rotor to the conditions of the wind flow.

The turbulent wakes produced by the two AD models are analyzed over three different inflow conditions: laminar and two turbulent inflows of intensities 3.2 % and 6.7 % measured at the location of the rotor when the turbine is not present. The turbulence is pre-generated using the Mann model, that produces turbulent fields with the same second order statistics of the atmospheric turbulence. The turbulence is introduced in the computational domain at a position ahead of the rotor instead of at the inlet, to minimize its decay as it is convected downstream in the domain.

A study of the turbulence evolution in the absence of the rotor reveals a discrepancy between the values of the turbulence intensity of the pre-generated field when it is measured before and after it has been introduced in the computational domain. This in turn suggests a numerical issue caused by imposing a turbulent velocity field in the flow. However, once the turbulence is introduced, it is found to exhibit a very small decay as the flow moves downstream.

The simulations of the turbulent wake show differences in the turbulence characteristics of the near wake of each AD model. We also observe a dissimilar behaviour of the turbulence intensity along the wake for the different inflow conditions which difficult the task of determining

a conclusive trend. Nonetheless, the results show that the turbulence characteristics in the far wake are nearly independ of the AD model or the inflow turbulence characteristics.

This new implementation of the AD techniques and the use of the Mann method in OpenFOAM can be also proved useful in the future when comparing with the results of similar studies for which other CFD platforms are used.

1 Introduction

In the process of characterization of wind turbine wakes, one of the main elements consists of an adequate model of the turbine. One of the most recurred techniques to model the rotor is the Actuator Disk (AD) in which the rotor is represented as a permeable surface where a distribution of forces acts upon the flow. In its simplest formulation, the AD comprises a surface of uniform loading modelled by one-dimensional forces in the streamwise direction. This has been proved computationally affordable and sufficient to reproduce the turbulence characteristics of the wake [1],[2]. In spite of this, it has also been observed that the inclusion of non-uniform loading (which induces wake rotation) leads to a considerable improvement in the prediction of the mean velocity and turbulence intensity in the near wake [3],[4]. Similar studies have been performed with the Actuator Line (AL) model that permits a greater detail in the reproduction of the aerodynamic features of the rotor, overcoming the problem of the lack of tip vorticity reproduction of the AD [5],[6], [7]. Despite of these advantages, the AL (as well as the actuator surface) is still too computationally expensive to be used in the simulation of wind parks. Furthermore, turbulence features in the far wake are less affected by the precision of the aerodynamics of the rotor [8], making the AD a frequent choice for the simulation of wind turbines.

In the present work, we present a comparative study of the turbulence characteristics in the wake of a rotor modeled with an uniformly loaded AD and an AD where loading and torque are calculated using the blade-element theory [9] with a control system developed in [10] to regulate the rotational velocity. Furthermore, we include the comparison between the wake characteristics found using inflows of different turbulence intensities. The inflow turbulence has been generated using the Mann method [11], [12] in which a three-dimensional velocity field is generated by modelling the spectral tensor of the neutral atmosphere. In this way, the model is capable of producing turbulence fields with the same second-order statistics as the atmospheric turbulence. Moreover, following the technique applied in previous works [6], [7], we introduce this pre-generated turbulence in a plane ahead of the rotor instead of the inlet to minimize the effects of the turbulence decay. In addition to the comparative study, the decay of the turbulence in the absence of the rotor is also analyzed.

The studies are carried out using OpenFOAM 2.1.0 ®, a second-order finite-volume open-source CFD platform. The implementation of the techniques employed in this work in OpenFOAM represents a novel approach that, in addition, could be useful to perform comparisons with similar studies that use other CFD software.

2 Model description

2.1 Flow model

The simulations are performed using the Large-Eddy Simulations (LES) model, that allows to resolve the large (energy-containing) motions whereas the effects of the smaller eddies are modelled. More precisely, the Navier-Stokes equations are decomposed into a filtered (or resolved) component and a residual (or sub-grid scale, SGS) component. In the present simulations, the effect of the residual scales is parametrized following the classic Smagorinsky model. There, the subgrid viscosity is assumed to be proportional to the Smagorinsky coefficient C_s and the local cell length $\Delta = (\Delta_x \Delta_y \Delta_z)^{1/3}$. The value of C_S is set to 0.168.

2.2 Modelling of turbulence

In order to reproduce a turbulence field that resembles the characteristics of the atmospheric turbulence we employed the technique developed by Mann [11], [12] which provides a model for the spectral tensor of surface layer turbulence in a neutral atmosphere. More specifically, this technique employs Rapid Distortion Theory to estimate the anisotropy in the turbulence field (initially described by the von Kármán tensor) caused by wind shear, based on two fundamental assumptions: a) that shear is a linear function of the height above the surface and b) the concept and calculation of the eddy lifetime. The calculations performed by Mann result in a model with three adjustable parameters, which are in turn evaluated by comparing the model to different measurements of the ABL as well as analytical expressions of the spectrum, used in engineering applications. Finally, the three dimensional turbulent velocity field is determined from a decomposition of the spectral tensor, approximated by a Fourier transform. In this work, the formulation of the Mann model provided by recommendations of the IEC standard for wind turbine design [13] is employed.

The model of Mann is used to generate a stationary turbulence velocity field (a *turbulence box*), that is spatially homogeneous and has the same second-order statistics of the atmospheric turbulence. In our computations, a turbulence field is pre-generated in a spatially uniform domain. Assuming the Taylor hypothesis of equivalent spacial and temporal correlations, the streamwise axis of the turbulence box is assumed equivalent to time, so the cross-sectional planes of the box are introduced in the computational domain time step. In order to minimize the turbulence decay when introducing the turbulence in the inflow of the rotor, the turbulent velocity field is introduced at a plane ahead of the AD instead of the inlet.

2.3 Actuator disk

The rotor of a horizontal-axis wind turbine is modelled as an Actuator Disk (AD) [14], where the effect of the blades on the wind flow is reproduced by forces distributed over a disk. As the actual geometry of the blades is not reproduced, the load of the turbine is taken as an integrated quantity in the azimuthal direction.

Two different AD concepts are implemented in the course of our work with the goal of performing comparisons of the turbulence characteristics in their wakes. In the first case, it is

assumed that the forces over the AD are only in the axial direction and are distributed uniformly over the disk. If U_0 is the uniform inflow velocity, the force is calculated as

$$F_x = \frac{1}{2}\rho U_0 A C_T \tag{1}$$

where A is the area of the disk and C_T is the thrust coefficient. In the second approach, the forces are calculated following the blade element theory [9], where the lift and drag coefficients are obtained from tabulated airfoil data. This model is simply referred to as *AD with rotation* throughout this work. In this formulation, the forces per unit area acting on the AD are calculated from

$$d\mathbf{F} = \frac{1}{2}\rho U_{rel}^2 \frac{B}{2\pi r}(C_L \mathbf{e_l} + C_D \mathbf{e_d}) dA \tag{2}$$

where B is the number of blades and C_L, C_D are the lift and drag forces that are evaluated in function of the angle of attack, with $\mathbf{e_l}$ and $\mathbf{e_d}$ being the unit vectors pointing in the directions of lift and drag, respectively. The factor $B/2\pi r$ is commonly derived from spatially integrating over an annular element of area $dA = 2\pi r dr$ [9]. However, in this work such term is conceived as coming from a time averaging. In effect, as it was shown by [15] and [16], considering the time the blades spend over any given control volume during one rotation, the average force on the rotor is exactly equal to eq. (2). An interesting result of this formulation is that the force can be calculated with this expression independently from the shape of the control volume cells in the grid. As a result, the grid can be formed by squared cells which is highly desired in order to maintain a uniform grid-filter size in LES.

The introduction of the forces represents an abrupt discontinuity in the flow field, so large velocity gradients occur at the vicinity of the AD and oscillations (wiggles) on the velocity field appear. To avoid this effect, we distribute the forces that comprise the AD in the axysymmetric direction. This is done by taking the convolution of the forces and a Gaussian function $f(x) = \frac{1}{\sigma\sqrt{2\pi}} \exp\left[-\left(\frac{x}{2\sigma}\right)^2\right]$. In this manner, the value of the standard deviation σ (i.e. the distribution width) will define the thickness of the disk. The force distribution is defined between the limits $[-3\sigma, 3\sigma]$ so that it contains 99.7% of magnitude of the forces computed for the original —one cell thick— disk.

This AD implementation also includes the use of a control for the rotational velocity with respect to the inflow conditions, henceforth called *controller*. This system is designed to work below rated power, so the inflow velocity used is within that range. The model for this controller is described in [10].

2.4 Reference turbine model

Airfoil parameters are obtained from the conceptual 5 MW offshore wind turbine designed by the National Renewable Energy Laboratory (NREL) [17]. This is a conventional horizontal axis, three bladed (twisted and tapered), pitch-controlled and variable speed turbine created from design information of other turbines, mainly the REpower 5M. The radius of the rotor is 63 m with a peak power coefficient of $C_P = 0.482$, found when the tip-speed-ratio has a value of $\lambda = 7.55$ and the blade pitch angle is zero. Information regarding the torque vs. rotational speed

response of the turbine is also contained in that report and it was used to regulate the angular velocity of the turbine according to the method of [10].

3 Numerical model

Simulations are carried out using a uniform inflow of $U_\infty = 8$ m/s at the inlet. Within the computational domain, a central region where cells are equally spaced in the flow direction x is located at $L_x = 6.4\ R$ from the inlet and continues until the outlet. The region is separated from all the lateral boundaries by a distance of 6.9 R. Outside this region, the cells are stretched towards the boundaries. The side boundaries are set to periodic while the top and bottom are symmetry planes (the latter is chosen to relax the restrictions that periodic boundaries impose on the decomposition of the computational domain). At the outlet Neumann boundary conditions are imposed.

We performed a study to analyze the sensitivity of the solution, such as the computed power coefficient, to the changes in domain size, mesh and axial distribution of AD forces. In the study, the AD with rotation has a fixed rotational velocity of $\Omega = 9.16$ RPM which corresponds to the peak power coefficient for the given U_∞, as reported in [17]. We employed the domain size and mesh points from previous works [10],[18] as a reference.

	Ω [RPM]	C_P	C_T
Reference WT (at peak C_P)	9.16	0.482	$\sim$1.023
BEM calculation	9.16	0.489	0.863
Steady-state, laminar solver	9.16	0.508	0.808

Table 1: Performance values of the wind turbine obtained from a steady state, laminar solver compared to the ones provided by [17].

The results of the sensitivity studies indicated that the optimal computational domain consists of a rectangular mesh of size $L_x \times L_y \times L_z = 30.4\ R \times 20\ R \times 20\ R$, with a number of points equal to $N_x \times N_y \times N_z = 240 \times 136 \times 136$. The resolution of the central region is comprised by uniform cells of side length $\Delta = 0.05\ R$. The values for the performance of the turbine obtained with these parameters are shown in Table 1. These are compared to the reported values of the turbine designer [17], obtained by performing simulations using FAST at $\Omega = 9.16$, when the peak power coefficient is reported to be obtained. In addition, the values obtained using an in-house BEM code are also included. The agreement between the reported values of C_P from the designer and the steady-state simulation are generally good, being the largest difference that of the C_T, that is underestimated. The reasons of this are being currently investigated. The C_T of the designer report is calculated assuming that the total thrust is 500 kN, which is not exact as it is read from a curve.

LES simulations are performed using the domain size and mesh reported above. AD location, inflow and boundary conditions are the same as previously described. An adaptive time step solver is used where the CFL number is kept below 0.6. A QUICK interpolation scheme

is applied for the solution of convection terms. Simulations are run for three longitudinal flow-times (i.e. the time that takes to the freestream flow to cover the distance L_x) in order to allow stabilization of the turbulence in the flow and after this, measurements are taken during 10 flow-times. Computations are carried out for both AD implementations, uniformly loaded and AD with rotation. In the case of the latter, the controller is activated only after 0.5 flow-times have passed, as it was otherwise observed that since the rotational velocity and torque are not well-predicted at the beginning, the input values of the controller produce a rotational speed outside the range of our table. The starting value of Ω is 8 RPM. The load of the uniform AD is determined by the average C_T obtained from the AD with rotation under a non-turbulent inflow, which is found to be 0.8. Note that this allows a more direct comparison between results of the two rotor conceptions as equation (1) does not consider the load variations during the computations.

The ADs are exposed to three different inflow conditions: a non-turbulent inflow, a turbulent flow with a turbulence intensity (TI) of 3.2 % and another where TI is 6.7 %. The turbulent simulations are also referred to as the *low* and *high* turbulence cases. Turbulence intensities are measured at the location of the AD before it is placed in the domain. The turbulence is pre-generated according to the method outlined in Section 2.2 in a domain of $4096 \times 64 \times 64$ uniformly distributed cells. The planes of turbulence are introduced in the computational domain at 1.6 R upstream of the rotor. The cross-section area and number of points of the box coincide with that of the uniform region in the computational domain. Bearing the frozen turbulence hypothesis in mind, the cell spacing of the turbulence box is equivalent to the time it takes the flow, moving at CFL $= 1$. Therefore, since a plane needs to be introduced at each time step, linear interpolations are employed to calculate the value of the turbulence at the given time. The process continues by swapping the turbulence box along its length. When the complete box has been mapped into the domain, the process is repeated from the first plane so the turbulence is recycled. Lastly, we should make note that the length of the turbulence box is enough to cover almost the totality of the simulation, as it is desired to avoid the appearance of the recycling period of the box in the calculations of the spectra.

4 Results and discussion

4.1 Turbulence decay

As a first step we assess the properties of the turbulence field introduced in the computational domain in the absence of the rotor. It is evident that the introduction of a turbulent velocity field in a close location to the rotor represents a discontinuity in the flow and as such, it can be a source of numerical complications. For this analysis, we have chosen to record the velocity fluctuations at the location where the turbulence plane is introduced, at the position where the AD will be located and then downstream of it at 0, 2, 6, 10 and 20 R. This is done using a probe located along a line normal to the turbulence plane. As the turbulence is convected downstream, the flow field solution has to adapt to the imposed conditions, so differences in the turbulent velocity field with respect to the one generated in the box are to be expected. Certainly, when comparing the intensity of the turbulence of the box (spatially averaged) with respect to that of the turbulence introduced in the computational domain (temporally averaged),

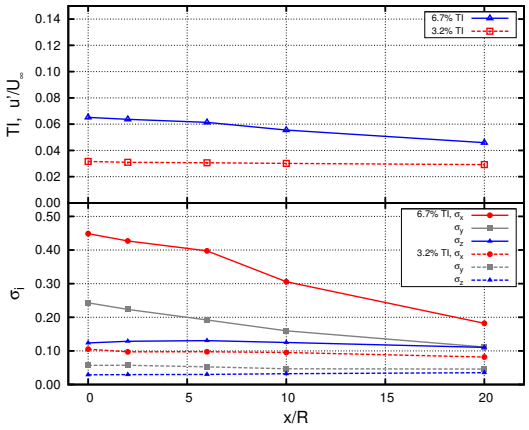

Figure 1: Turbulence decay in the absence of the rotor. *Top:* Average turbulence intensities at different positions along the domain. *Bottom:* Variances of the velocity fluctuation in each direction.

a relatively large difference is observed. The spaced average TIs measured in the box were 5.5 % and 11.7 % whereas the TIs measured in the computational domain using a probe were 3.2 % and 6.7 %, respectively. This is most likely the result of the numerical discontinuity resulting from the introduction of a turbulent velocity inside the flow field. This potential problem has been commented by authors of previous, similar studies [6], [7] where an alternative approach is implemented to avoid it. In summary, this method consists in producing the turbulent velocity in the computational domain by using source terms in the momentum equation, in analogy to the technique used to model the AD. We will explore this approach in the future. For the time being, we present our results by referring to the TIs calculated at the position where the rotor will be located once the wakes are simulated. Make note that results show averages of the recorded velocities at the probes during 10 flow-times.

Figure 1 shows the evolution of the TI downstream of the plane where turbulence is introduced. It is interesting to note that despite of the disagreement mentioned above, the decay is relatively low, especially for the low turbulence case. Also in the Figure 1 we can observe the evolution of the variances of the velocity fluctuations. While the low turbulence variances in all direction remain more or less stable, the high turbulence case show an appreciable decrease in the streamwise and vertical directions. On the other hand, the time-averaged Reynolds stresses show in Figure 2 a steady decrease, which is to be expected in the absence of shear. However, note that $\overline{uu}$ does not largely vary between 1 R ahead of the assumed rotor position until about 10 R downstream of it.

To complete the analysis of the turbulence decay in the absence of a rotor, the spectral characteristics of the velocity fluctuations in all directions are shown in the Figure 3 for different streamwise positions. The spectra are calculated from the values of the velocity fluctuations at each time step. For their calculation, a set equal to 2^{14} values is considered. For each case, the spectrum in the figure is calculated as the average of the spectra of subsets of 2^{11} values

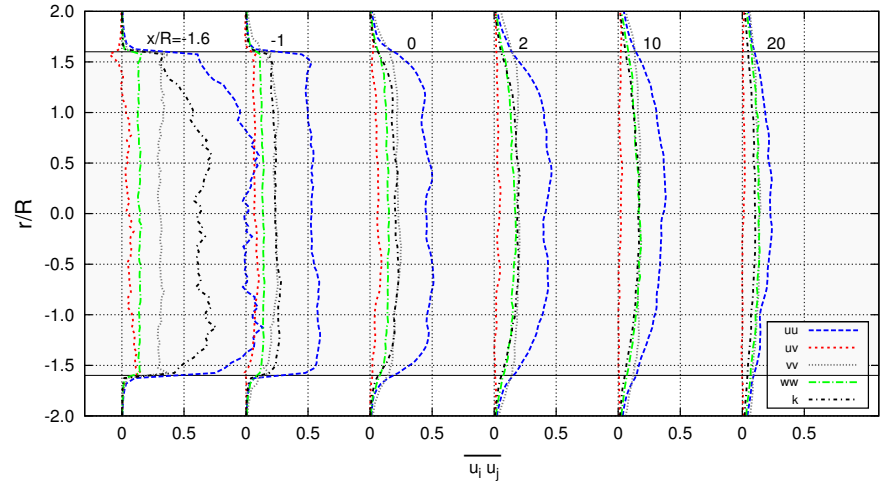

Figure 2: Evolution of the time-averaged Reynolds stresses at different downstream positions. The shaded region represents the side length of the plane where fluctuations are introduced into the computational domain, which coincides with the size of the uniform region of the domain. Negative values correspond to positions upstream of the rotor.

of the complete set. The spectra of the turbulence box is also shown, which is the result of a spacial average of subsets of 2^{12} values. At a first glance, we observe that for each direction, the spectra from the probes are shifted with respect to those of the Mann box. This is likely to be an indication of the variation of the magnitude of the velocity fluctuations when the turbulence planes are introduced in the computational domain. However, once the turbulent velocity field is being carried along the flow, there is little variation of the turbulence scales. In fact, there is a variation of dissipative scales for each position that does not follow a particular order. This is potentially due to the readjustment of the velocity field downstream of the plane where the turbulence is introduced. This feature has also been observed by [6] in a similar analysis.

4.2 Wake characteristics

After the assessment of the turbulence decay, we introduce the rotor in our computations to study the characteristics of the turbulence in the wake. In Figure 4 we can visualize some of the results from these simulations. There, the vorticity allows us to appreciate the development of the vorticity structures in the cases of laminar and turbulent inflows, for each rotor representation. In the case of laminar inflow, the structures develop earlier when using the AD with rotation than with the uniformly loaded technique. Yet, close to the outlet the turbulence field does not appear too different between these cases. The same comparison is not as evident in the case of turbulent inflow, the structures appear at about the same distance behind the rotor when using one or the other AD models. As expected, the incoming turbulence triggers the apparition of instabilities in the shear layer much sooner than in the laminar inflow cases. These observations are complemented by the features observed in Figure 5, where the vorticity contours illustrate the turbulence structures appearing in the case of the AD with rotation under a laminar and

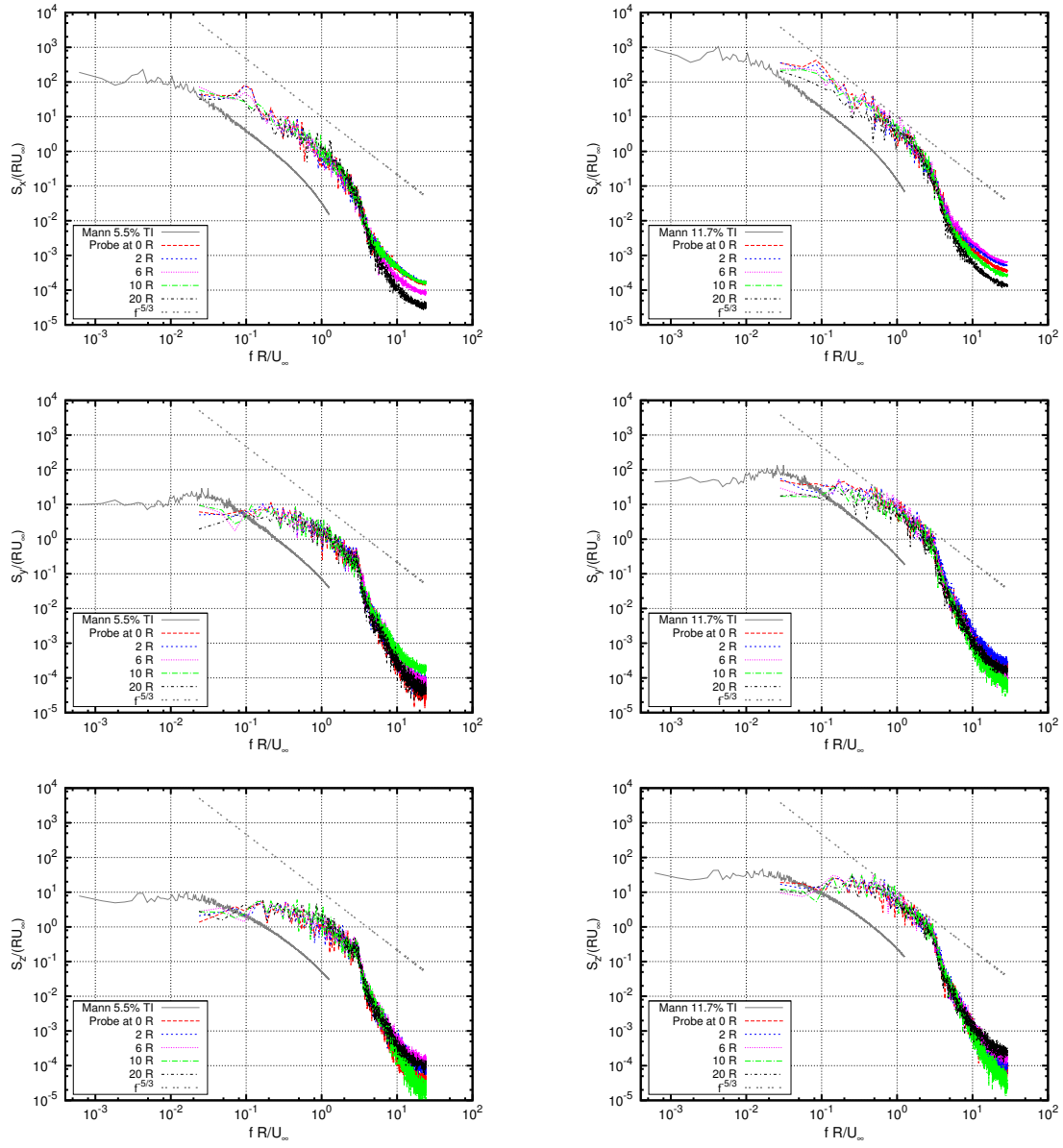

Figure 3: Spectral characteristics of the velocity fluctuations in the three spacewise directions at different downstream positions from the plane where synthetic turbulence is introduced. *Left column* low turbulence case, 3.2 % TI . *Right column:* high turbulence, 6.7 % TI. The spectra of each direction are presented row-wise.

a turbulent inflows. On the other hand, the velocity profiles in Figure 6 do not show a large difference in the estimation of the average velocity amongst the different rotor models in the cases of turbulent inflow, except for the first downstream positions where the AD with rotation reflects the fact that different loads are calculated radially. In contrast, the differences in the

velocity calculation between the two AD models are more noticeable for the laminar inflow case, where an appreciable difference remain even at 20 R behind the rotor.

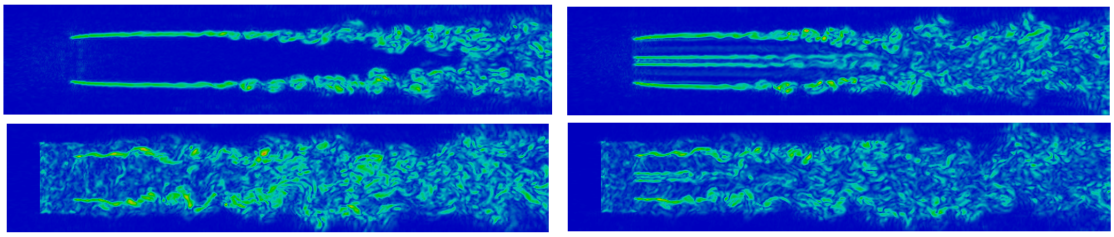

Figure 4: Visualization of the turbulence structures in the wakes with vorticity. *Left:* the wake of the uniformly loaded disk. *Right:* the wake of the AD with rotation. The images correspond to the cases of laminar inflow (top) and high turbulence inflow (bottom) at 13 flow-times from the start of the simulation.

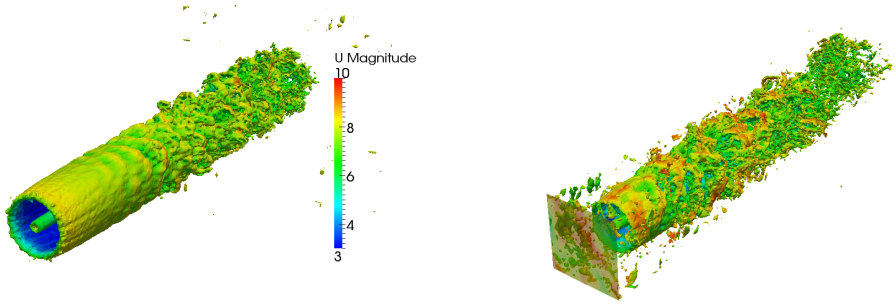

Figure 5: The wakes of the AD in uniform inflow (left) and high turbulence inflow (right) drawn using vorticity contours coloured with the velocity magnitude (in [m/s]) . In the latter, the plane where the turbulence velocity is introduced can be seen. Contours are calculated at 13 flow-times.

4.3 Turbulence characteristics in the wake flow

After having reviewed the turbulence evolution in the absence of turbines by means of the TI and the spectral characteristics of the velocity fluctuations, we perform a similar analysis in the wakes of the rotors for the different inflow conditions. Figure 7 shows the development of the TI at different streamwise positions. In order to observe the differences between the development of turbulence in different parts of the wake, two radial positions are monitored: the position at the rotational axis (as in the turbulence decay study) and the position y =R from the centreline within the area of the shear layer. The first feature that we can notice is that for the laminar inflow simulations, the turbulence increases both in the centre and at R in the uniform load model. On the contrary, in the AD with rotation, it increases at the centreline while at R it goes through a period of constant increase until about 10 R downstream, where it begins to drop. This trait exemplifies the importance that the rotating model of the disk has in the representation of the

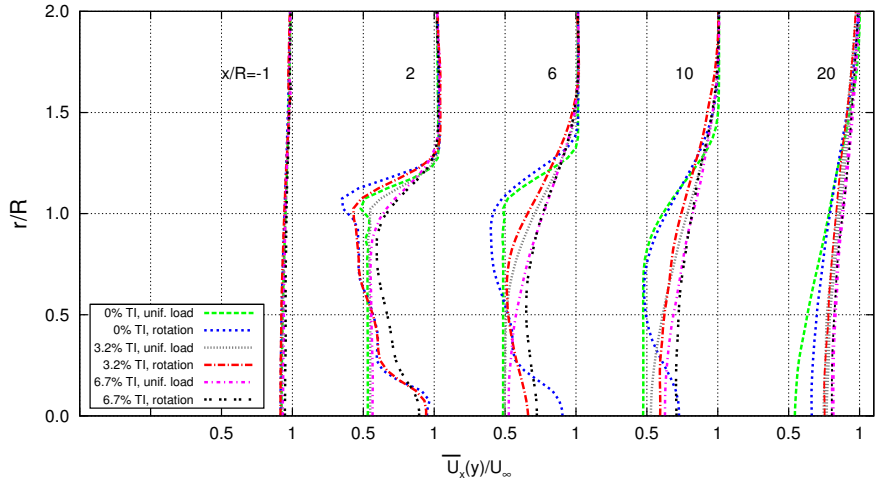

Figure 6: Averaged velocity profiles of the wake at different downstream positions.

turbulence field in the near wake. On the other hand, the results show a peculiar behaviour of the TI for the cases with inflow turbulence at the shear layer: for the low turbulence case, the turbulence rapidly increases until around 5 R, and from there it starts to decrease. In contrast, the high turbulence case shows a consistent reduction of TI downstream of the disk. The TIs in the low turbulence case starts at a lower value than the high turbulence case but at the next downstream position (5 R) it equals its value (for the uniformly loaded AD) and even overtakes it (AD with rotation). Thus, it appears as if the shear layer of the AD modelled with both techniques would not add up intensity to the velocity fluctuations when the incoming flow has the high TI. A similar behaviour is observed also at centreline positions in the case of the AD with rotation, although with a lower intensity. In spite of all this, the most remarkable feature is that in all cases, the value of TI at the last probes is almost the same, $\approx$8 %. This is consistent with previous observations, e.g. [3], that the turbulent velocity field in the far wake is relatively well represented by AD without rotation when comparing different models.

The spectral characteristics shown in Figure 8 complement this study. Here, we only present the spectra of the velocity fluctuations in the streamwise directions and for the probes located at R. The most visible difference amongst the different cases are seen in the spectra of the laminar inflow cases. There, we see that is not until the last downstream positions that the spectra takes the characteristic shape of a turbulent flow, in particular, the inertial sub-range with a slope of -5/3. Notice that the range of the spectra of the laminar flow, unlike all the other spectra shown in this work, goes down to 10^{-6}. Looking at the turbulent inflow cases, we can see that the low turbulence flow exhibits a tendency to increase the energy associated to the fluctuations downstream of the uniformly loaded disk (specially at the dissipation ranges) while for the AD with rotation the energies increase and then decrease with the downstream position. These features are consistent with the observations of the TI of Figure 7. Finally, spectra of the high turbulence case reveal little changes in the energy content of the fluctuations downstream of both AD representations. This tendency is also in agreement with what we can observe in the

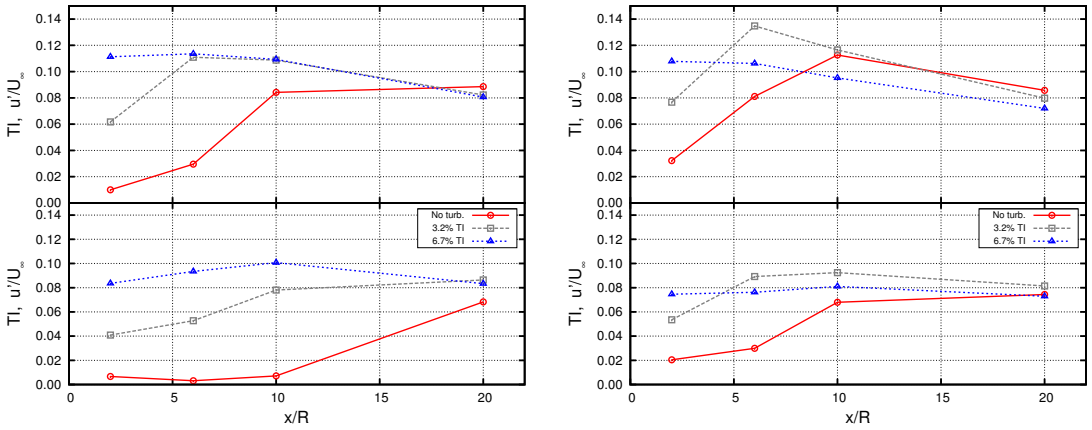

Figure 7: Turbulence intensity downstream of rotor modelled as an AD of uniform load (left) and as an AD with rotation (right). The upper graphs show the results from probes located at a distance R from the centreline of the domain whereas those at the bottom are extracted from probes along the centreline.

previous figure for the TI.

5 Conclusion

LES simulations of the turbulent wake of a rotor have been performed with the aim of characterizing the turbulence field produced therein. The rotor is modelled using two different Actuator Disk techniques, the uniformly loaded disk and a disk where the forces are calculated following the blade element theory, where the lift and drag are obtained from tabulated data. In addition to this, the rotating AD model includes the implementation of a rotational velocity controller. The purpose of employing two rotor representations was to examine the differences in the wake characteristics produced by each rotor model. As it has been pointed out in previous studies, the use of a non-uniform load in the AD that also considers the rotational velocity of the rotor leads to different estimations of the turbulence field, particularly in the near wake. Preliminar studies of the AD with rotation in laminar, steady-state flow show a good agreement of the power predicted for the rotor with respect to the values provided by the designer of the wind turbine that we model.

A study of the turbulence decay in the absence of a rotor reveals a discrepancy between the values of the turbulence intensity of the pre-generated turbulence when is measured in the box with respect to its value measured when the box is introduced in the computational domain. This suggests a numerical problem that shall be adressed in the future. Despite this issue, the turbulence is seen to decay very little as it is convected downstream.

Simulations under different inflow conditions with turbulence created using the Mann method showed that, when using the different rotor representations, differences in the turbulence characteristics are indeed observed just downstream from the rotor whereas they approach closely to

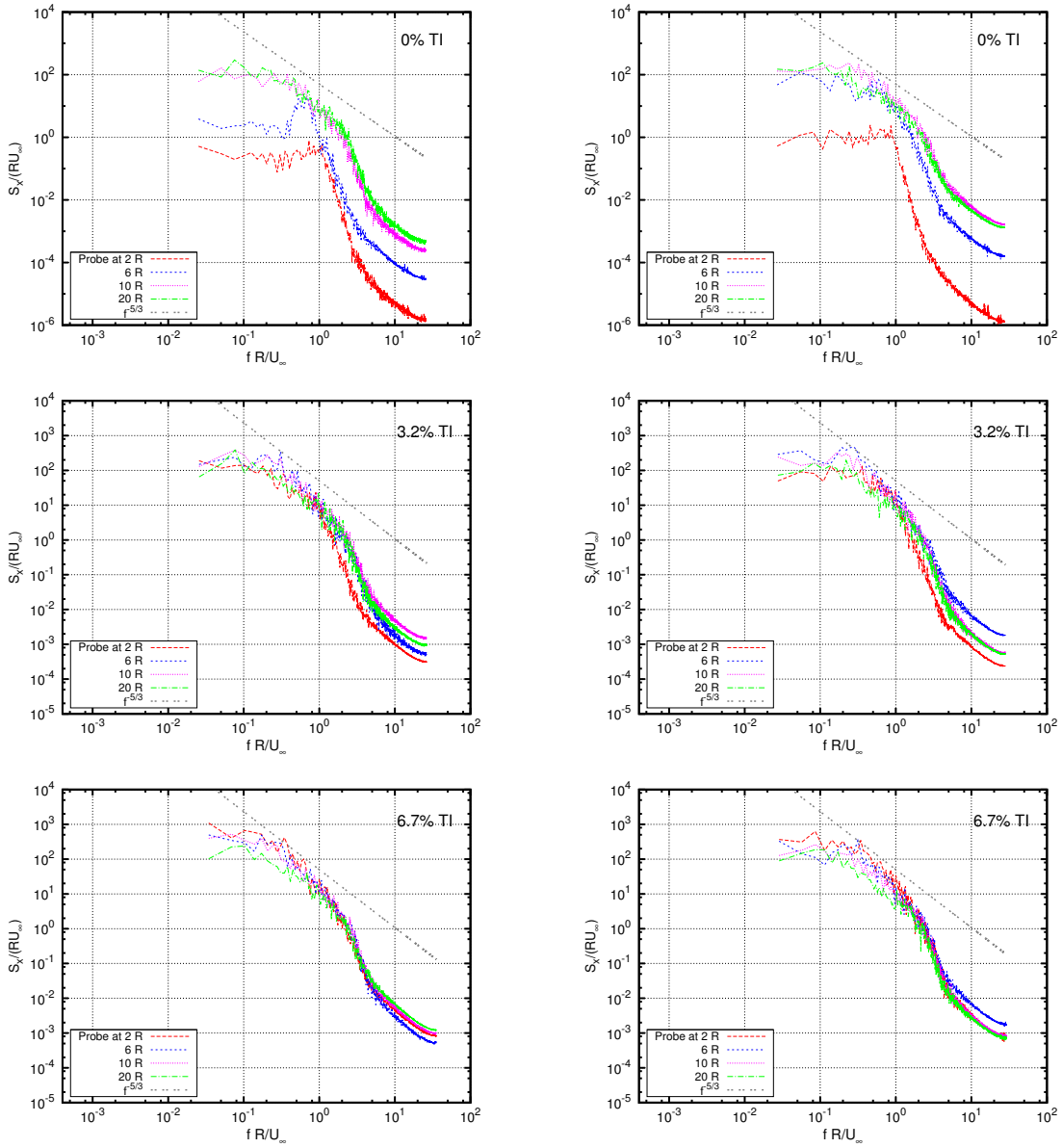

Figure 8: Energy spectra of the velocity fluctuations in the axial direction at different downstream positions from the plane where synthetic turbulence is introduced, for different types of inflow. *Left column:* uniformly loaded AD, *right column:* AD with rotation.

each other when moving further downstream, in the far wake region. The tendencies followed by the turbulence in the wake of the rotor are similar between both AD techniques when the inflow is non-turbulent. In contrast, the evolution of the turbulence characteristics when a turbulent inflow is employed is harder to qualify, which suggests that further studies are needed to achieve a proper characterization of the turbulence. Moreover, it is necessary to compare the results of our model with experimental results to better assess the validity of the techniques employed. Nevertheless, the implementation of the AD techniques and the use of the Mann method in OpenFOAM represents a novel approach that we expect can contribute to the study and characterization of the turbulence in the wakes of wind turbines. It will be of particular interes to compare the performance and accuracy of our implementation with other simulation platforms currently in use within the wind energy community.

Acknowledgements

The computations of this work were performed on the cluster Colosse of the Calcul Québec and Compute Canada research consortiums. We appreciate the support of the Laboratoire de recherche sur l'aérodynamic des éoliennes en milieu nordique (AEMN) of the École de technologie supérieure and the Consejo Nacional de Ciencia y Tecnología (CONACYT-Mexico). S.-P. Breton and K. Nilsson wish to thank the Swedish Energy Agency for supporting this research. We also thank the assistance of Mary Bautista and Jörn Nathan.

References

[1] Jimenez A, Crespo A, Migoya E and Garcia J. Large-eddy simulation of spectral coherence in a wind turbine wake. *Environ. Res. Lett.* 2008, **3**, 015004

[2] Sanderse B, Van Der Pijl and Koren S P. Review of computational fluid dynamics for wind turbine wake aerodynamics. *Wind Energy* 2011, **47(7)**, 779-820

[3] Porté-Agel F, Wu Y T, Lu H and Conzemius. Large-eddy simulation of atmospheric boundary layer flow through wind turbines and wind farms. *J. Wind Eng. Ind. Aerodyn.* 2011, **99**, 154-168

[4] Wu Y T and Porté-Agel F. Large-Eddy Simulation of Wind-Turbine Wakes: Evaluation of Turbine Parametrisations. *Boundary-Layer Meteorol.* 2011, **138** 345-366

[5] Sørensen J and Shen W. Numerical Modeling of Wind Turbine Wakes. *Journal of Fluid Engineering* 2002, **124** 393-399

[6] Troldborg N. Actuator Line Modeling of Wind Turbine Wakes PhD Thesis Technical University of Denmark, 2008

[7] Ivanell S. Numerical computations of wind turbine wakes PhD Thesis Royal Institute of Technology Stockholm, Sweden, 2009

[8] Vermeer L, Sørensen J and Crespo, A. Wind turbine wake aerodynamics. *Progress in Aerospace Sciences* 2003, **39** 467-510

[9] Manwell J, McGowan J and Rogers A. Wind Energy Explained, Wiley, 2008

[10] Breton S-P, Nilsson K, Ivanell S, Olivares-Espinosa H, Masson C and Dufresne L. Study of the effect of the presence of downstream turbines on upstream ones and use of a controller in CFD wind turbine simulation models. The Science of Making Torque from Wind, Oldenburg, Germany, October 2012.

[11] Mann J. Wind field simulation, *Prob. Engng. Mech.* 1998, **13**, 269-282.

[12] Mann J. Atmospheric turbulence. Technical University of Denmark, 2012

[13] International Standard. Wind turbines-part 1: Designed requirements. IEC 61400-1, 2005

[14] Sørensen, J. N. & Myken, A. Unsteady actuator disc model for horizontal axis wind turbine. Journal of Wind Engineering and Industry Aerodynamics 1992; **39**.

[15] Ammara I. Master's Thesis: Modélisation aérodynamique tridimensionnelle d'un parc d'éoliennes à axe horizontal (Ecole polytechnique de Montréal, Montréal, Canada), 1998

[16] Masson C, Smaïli A and Leclerc C. Aerodynamic analysis of HAWTs operating in unsteady conditions. *Wind Eng.* 2001, **4** 1-22

[17] Jonkman J, Butterfield S, Musial W and Scott G. Definition of a 5-MW reference wind turbine for offshore system development Tech. Rep. NREL/TP-500-38060 NREL, 2009

[18] H. Olivares-Espinosa, C. Masson and L. Dufresne, Turbulence characteristics in a free wake of an actuator disk: comparisons between a rotating and a non-rotating actuator disk in uniform inflow, The Science of Making Torque from Wind, Oldenburg, Germany, October 2012.

The nature of wind turbine fatigue loads in wind farms

G.C. Larsen, T.J. Larsen, H. Aa. Madsen, M.M. Pedersen

DTU, Department of Wind Energy, GULA@dtu.dk

ABSTRACT

The aim of the present paper is to further validate the predictive capability of the DWM/HAWC2 package for simulation of structural loadings in wind farms. The validation in particular focus on tower fatigue loading characteristics (i.e. equivalent moments) as function of turbine relative position, including turbine interspacing.
To accomplish this, comparative studies of predicted and measured fatigue load characteristics are performed. The involved data relates to full-scale measurements from the Danish Rødsand 2 offshore wind farm, where 6 turbines are instrumented with strain gauges providing tower top and bottom bending moments as well as tower the top torsion moment. The numerical predictions are based on a simulation package, where the Dynamic Wake Meandering model is interfaced with the in-house aeroelastic code HAWC2.
Comparing simulated and measured tower fatigue loading, good agreements were found between the extend of wake affected direction regimes. As for the magnitude of the (mean) wake loading, the tower top moments were under-estimated with of the order 15%, whereas the tower bottom moments were found to agree well with the measured results.

INTRODUCTION

Wind turbines located in wind farms experience inflow wind conditions that is substantially modified compared to the ambient wind field, which apply for stand-alone wind turbines. This drastic change of the environmental wind field conditions is caused by wakes emitted from upstream turbines, and it has significant implications not only for the power production of a wind farm, but also, and equally important, for the loading conditions of the individual turbines in the farm.
Recent research [1], [2], [3] has identified wake meandering as an important load driver for wind turbines operating in wind farms, and the Dynamic Wake Meandering (DWM) model [4] offers an efficient description of this intermittent flow field phenomenon. Compared to conventional methodologies for prediction of structural loads in wind farms, the DWM approach includes the effect from both modified turbulence *structure* and increased turbulence *intensity* of the wind farm flow field. This has interesting perspectives not only for the tower and foundation design loads, but certainly also for the optimal layout of a wind farm.
An interesting consequence of the intermittent type of wind farm turbulence field characteristics, predicted by the DWM model, is that, for turbines aligned with the mean wind direction, the imposed tower fatigue loading on downstream turbines depends in a non-monotonic way on the turbine interspacing. This is contrary to conventional approaches, where the fatigue loading increases monotonically with decreasing inter turbine spacing. The DWM method predicts tower/foundation fatigue loads that increases with the downstream spacing up to a certain point, after which they decrease as indicated in [5]. In the limit of infinite turbine interspacing, the imposed wind field loading asymptotically approaches that of a solitary turbine. The existence of a particular downstream distance, at which maximum tower/foundation fatigue loads are attained, is due to the meandering mechanism, and the downstream distance, at which maximum loading is experienced, corresponds to a situation where the lateral/(vertical) movements of the wake deficit causes the downstream turbine to

be exposed to frequent intermittent variations in the load pattern (i.e. changes in inflow characteristics between full wake situations, half wake situations and non-wake situations).
Whereas a detailed full-scale validation study has been made on the wake meandering mechanism as wind farm flow field phenomena [2], [6], a corresponding detailed validation study on the resulting wind turbine fatigue loads as function of downstream spacing has up to now not been possible, due to lack of suitable full-scale measurements. This has motivated a full-scale measuring campaign at the Danish Rødsand 2 offshore wind farm. Six turbines are instrumented with strain-gauges, providing tower top and tower bottom measurements for various loading conditions (i.e. mean wind speed; mean wind direction; ambient turbulence intensity; and ABL stability conditions).
The present paper deals with an analysis of these measurements and subsequent comparisons with numerical predictions. The analysis will in particular focus on tower fatigue loading characteristics (i.e. equivalent moments) as function of turbine interspacing. The numerical predictions are based on an integrated wake simulation package, combining the full non-linear aeroelastic code HAWC2 [7] with the Dynamic Wake Meandering (DWM) model [4], thus basically treating downstream advected wake deficits as passive tracers driven by the *large-scale* turbulent eddies in the ABL.
The paper is organized as follows. First, the numerical method used in the analysis is introduced. Next, the experimental setup and the involved flow cases are described. The selected flow cases are then analyzed and compared to analog numerical predictions and conclusions are given.

THE MODEL

The numerical model is based on two key elements – a *wind farm flow field model* and an *aeroelastic model*, where the former provides input to the latter.
In order to enable realistic load simulations of wind farm wind turbines, a detailed *in-stationary* modelling of the wind farm flow field is required. The DWM model [4] offers simulation of in-stationary wind farm flow fields with an acceptable computational effort and has therefore been used flow model in the present study. The DWM model describes the essential physics of the problem, and accounts for both the observed increased turbulence intensity (TI) of wake flow fields and the modified turbulence structure. The model has been successfully verified against both full-scale measurements [2] and against detailed CFD LES actuator line (ACL) computations [8]. The core of the model is a *split of scales* in the wake flow field, with large scales being responsible for stochastic *wake meandering*, and small scales being responsible for wake *attenuation* and *expansion* in the meandering frame of reference as caused by turbulent mixing. Thus, essentially the DWM model assumes that the transport of wakes in the atmospheric boundary layer (ABL) can be modeled by considering the wakes to act as passive tracers driven by a combination of large-scale turbulence structures and a mean downstream advection velocity, adopting the Taylor hypotheses.
Based on a simulated in-stationary wind farm flow field, the structural loading of each individual wind turbine (WT) in the wind farm can by predicted using the aeroelastic code HAWC2 [9]. HAWC2 is a finite element code with all essential non-linearities taken into account. The structural part of this code is based on a multi-body formulation as described in [10] using the floating frame of reference method. Each body includes its own coordinate system with calculation of internal inertia loads, when this coordinate system is moved in space, and hence large rotation and translation of the body motion are accounted for, thus providing a fully non-linear kinematic formulation. The aerodynamic part of the code is based on the Blade Element Momentum (BEM) theory, but extended from the classic approach to handle dynamic inflow, dynamic stall, skew inflow, shear effects on the aerodynamic induction and effects from large deflections to match the non-linear kinematic formulation of the structural part. In addition to structural elements and aerodynamics, the code includes modeling of generator, gear box and WT control system. Details on the interfacing of the DWM model with HAWC2 can be found in [8].
A crude heuristic estimate of the most critical turbine inter spacing for turbines aligned with the mean wind direction follows from a *conjecture* stating, that the most critical wake load situation is associated with wake meandering displacements centered around a half wake situation. In a statistical

framework, the *mean* wake lateral displacement, d_w, at a given down stream position, L, may be estimated as

$$d_w = \sigma_v t_w \ ,$$

where σ_v is the lateral wind speed standard deviation, and t_w is the wake transportation time from wake emission at the rotor plane to the down stream position defined by L. Adopting the Taylor hypothesis for the wake down stream transportation, with advection speed equal to the mean wind speed, we have

$$t_w = L/U \ ,$$

where U denotes the mean wind speed. Expressing σ_v as $3\sigma_u/4$ [11], where σ_u is the standard deviation of the longitudinal turbulence component, and introducing the turbulence intensity as $TI = \sigma_u/U$, the lateral *mean* wake displacement is finally given by

$$d_w = \frac{3L}{4} TI \ .$$

According to the conjecture, the critical turbine interspacing, L_c, for mean wind directions aligned along turbine rows is associated with $d_w = D/2$, whereby

$$L_c = \frac{2D}{3TI} \ .$$

THE MEASUREMENTS

An experimental campaign has been defined for the Danish Rødsand 2 offshore wind farm with the aim of providing full-scale data for a detailed analysis of tower and foundation loads. Six turbines are instrumented with strain-gauges based measuring systems that resolve selected structural loads in terms of tower top and tower bottom bending moments as well as the tower top torsion (i.e. yaw) moments. The locations of the instrumented turbines appear from figure 1.

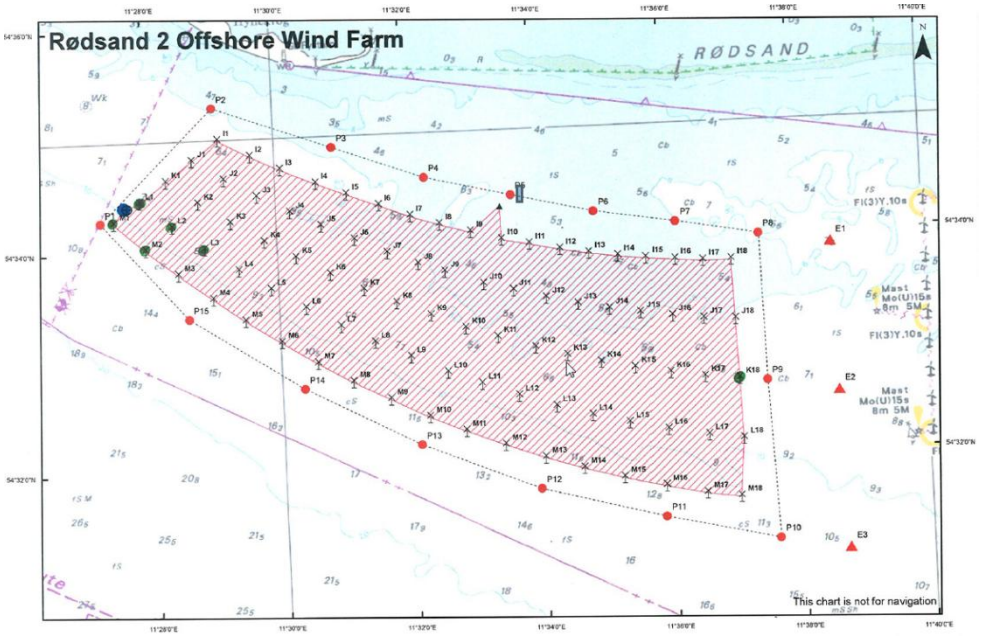

Figure 1: Overview of the the Rødsand 2 wind farm with the turbines selected for the measuring campaign (green rotors), and the offshore met. mast (blue circle between turbines M1 and L1).

Five of the turbines have primary been selected to support investigations of wind turbine structural loading as function of WT spacing for turbines located as the second turbine in a "row" (i.e. turbines

M1, M2, L1, L2 and L3 on Figure 1), whereas the sixth was chosen to illuminate the load conditions of a WT located deep inside a wind farm (i.e. turbine K18 on Figure 1). Furthermore, data from an already existing offshore meteorological mast, recording relevant atmospheric parameters as wind speed, wind direction and atmospheric stability conditions, are available for the analysis along with selected WT SCADA data (i.e. power production, rotational speed, nacelle wind speed and yaw position). However, for the available recording perod the wind speed sensors at the meteorological mast was dismounted for re-calibration, and consequently WT SCADA data for wind turbine M1 (in terms of yaw position and nacelle anamometer recordings) have been used to replace these in the present investigation.

The strain gauge recordings have initially been calibrated against closed form expressions for uniform prismatic Euler beams. A model based calibration is the only realistic possibility for offshore recorded tower torsion moments. As for the tower bending moments, however, these will at a later stage be subjected to a redundant calibration based on yawing the (known) nacelle/rotor mass 360° during a time span with wind speeds close to zero.

RESULTS AND DISCUSSIONS

The available structural measurements covers the period extending from January 11 to February 28 in 2013. The data are stored as 10-minute sequencies. To ensure a reasonable population of the data set – and to avoid wind speed regimes with very active WT blade pitching – the mean wind speed bin [7;9] m/s was chosen for the analysis. Depending on the mean wind direction, various single wake cases can be identified, of which 3 were selected for the present analysis. These represents WT inter spacings of 6.3D (direction 228°); 8.6D (direction 353°); and 10.5D (direction 273°), respectively.

To match the recorded data, simulations representing a mean wind speed of 8 m/s were performed with a 2° resolution of the inflow direction for each of the selected WT inter spacings. A simulation sequence represents a 30 minute period, and for each event, defined in terms of direction and spacing, 3 different turbulence seeds were used mimic the variability in the full scale data due to different realizations of the inflow stochastics. Neutral atmospheric conditions are assumed, and a representative inflow turbulence intensity of 7% was used, as based on a site characterization performed before construction of the wind farm.

Three tower bending moments were analysed – the magnitude of top and bottom bending moments and the tower top torsion moment. For each of these, the fatigue loading, quantified in terms of fatigue equivalent moments based on a Wöhler exponent equal to 4, were determined. Both measurements and simulations are normalized with respect to the free stream condition. However, especially for the measurements, the free stream conditions are challenging to identify and consequently associated with some uncertainty. The results are shown in figures 2-4 below.

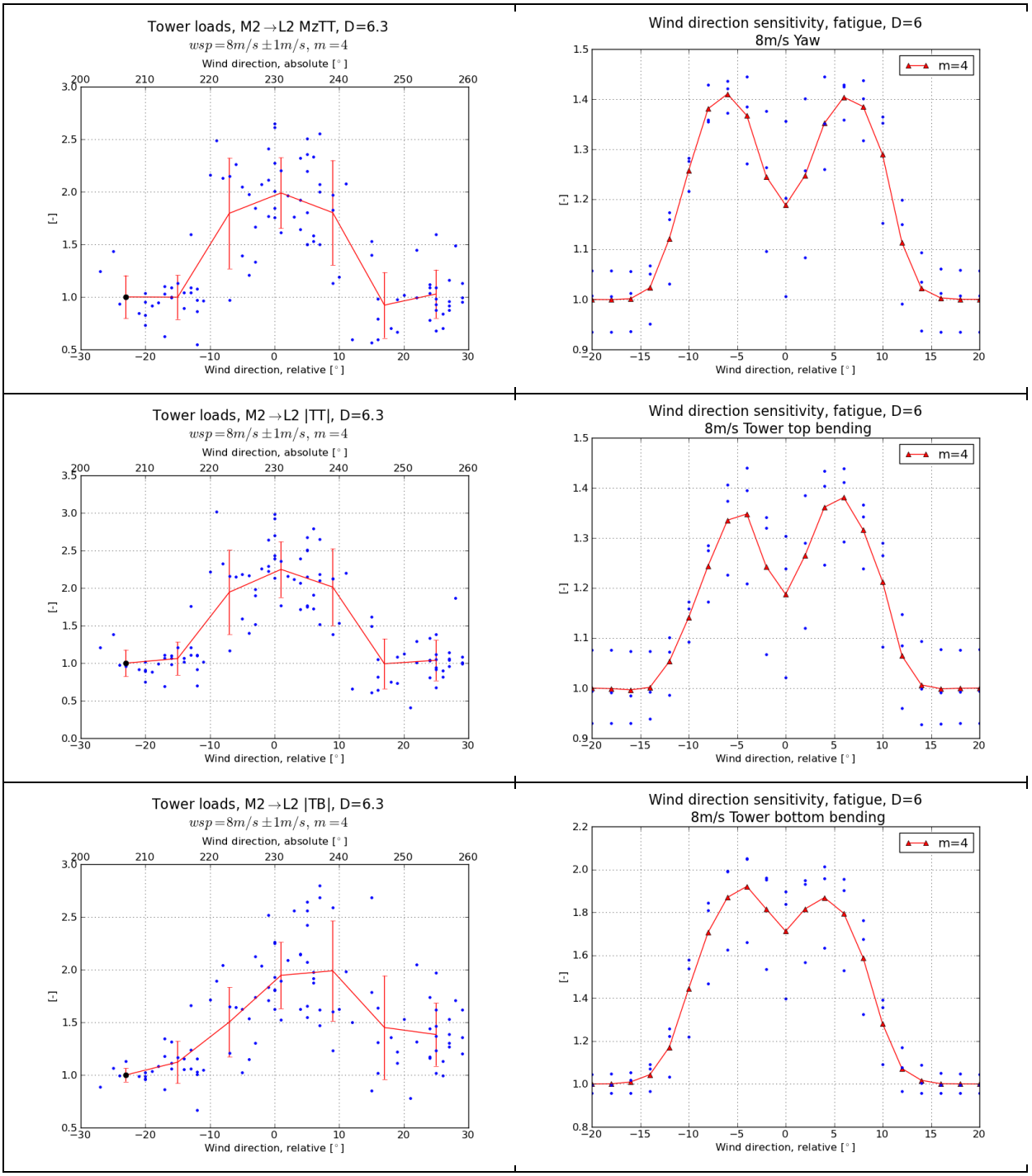

Figure 2: Measured (left) and simulated (right) tower equivalent moments associated with 6D spacing.

For all three investigated structural moments, the *measured* fatigue wake loading is approximately doubled compared to free inflow conditions. A significant scatter is observed on the data, reflecting both that fatigue equivalent moments are highly sensitive to different realizations of stochastics with same characteristics, but most likely also that the characteristics of the inflow stochastics change from sequence to sequence due to e.g. variations in atmospheric stability. The range of the wake affected regime can for the 6D case be identified to approximately ±15° around the wind direction defining this case. The same wake affected range is observed for the simulated results. The magnitude of the simulated fatigue loading corresponds well to the measurements for the tower bottom moment, but is under-estimated with approximately 30% for the tower top moments.

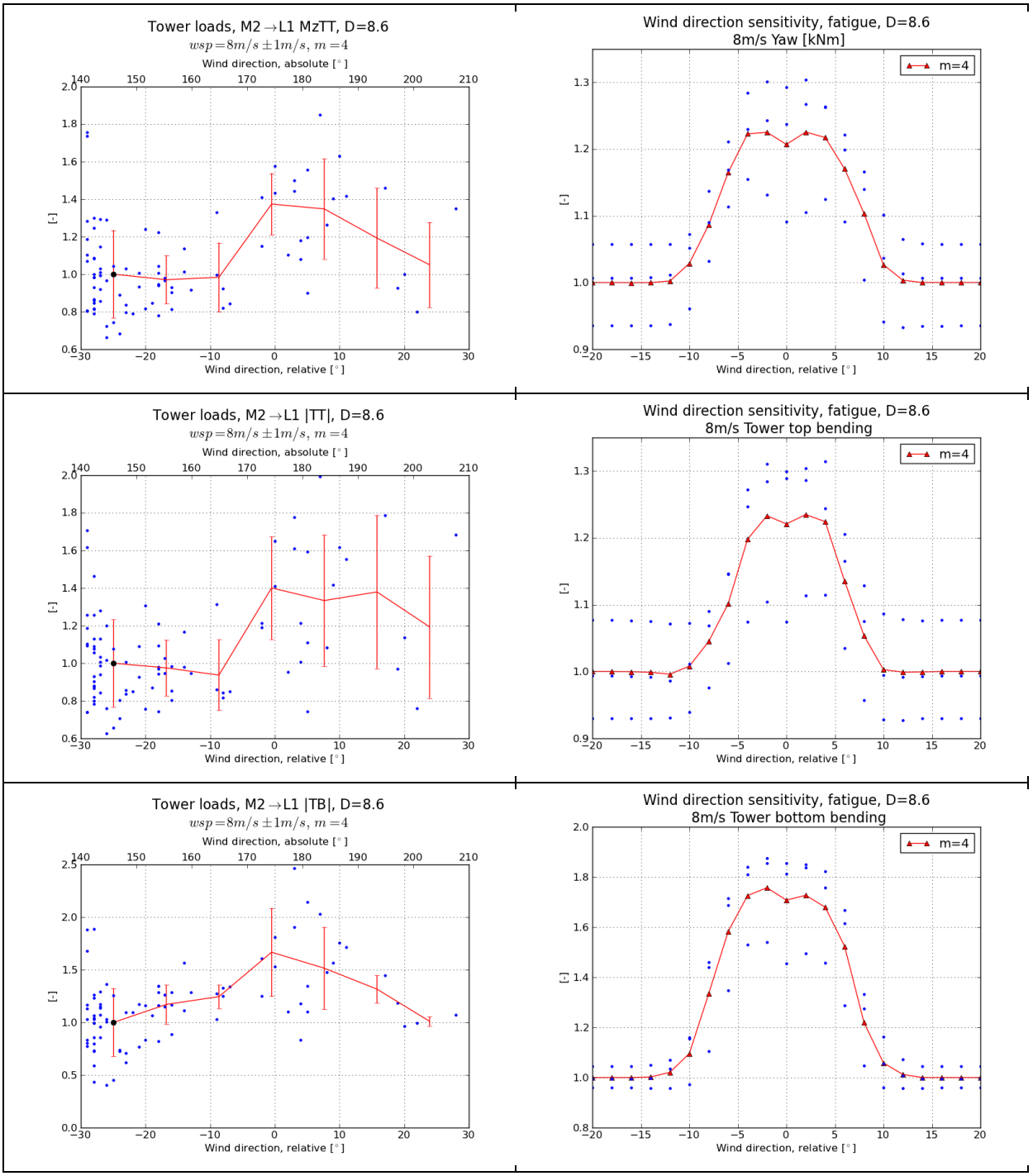

Figure 3: Measured (left) and simulated (right) tower equivalent momend ts associated with 8.6D spacing.

For the 8.6D case, the wake affected regime is narrowed down to approximately ±10° around the wind direction defining this case, which seems to agree with the measured results at least for the left hand wake regime boundary, corresponding to the most well populated part of this data set. As for the 6D case, good agreement is observed between measured and simulated tower bottom fatigue loading, whereas the tower top fatigue loading is under-estimated with approximately 15%. Compared to the 6D case, the wake loading is generally attenuated. For the simulations, however, the fatigue loading, corresponding to the direction defining the case, is slightly increased. Such an effect is not visible in the highly scattered measured results.

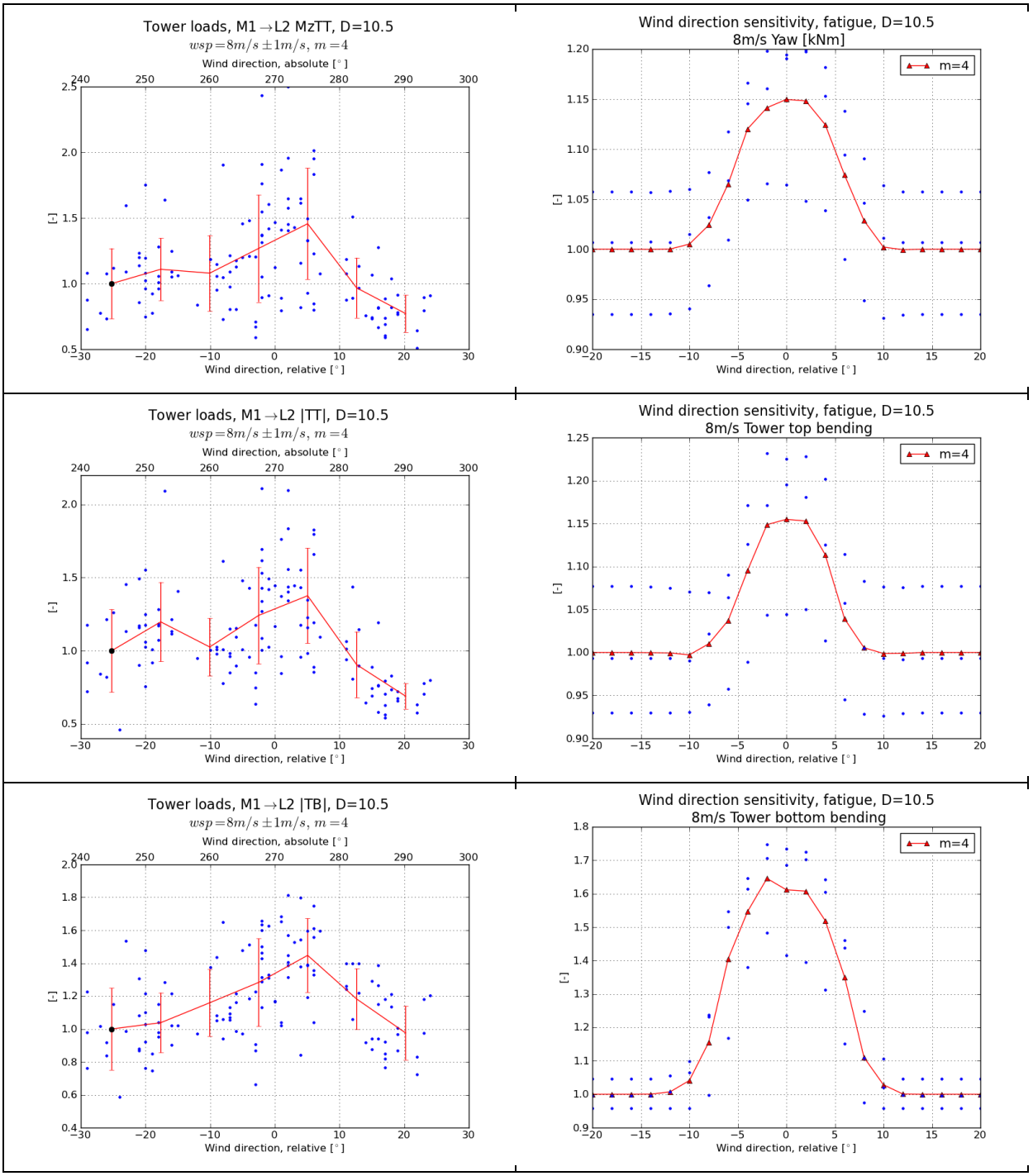

Figure 4: Measured (left) and simulated (right) tower equivalent moments associated with 10.5D spacing.

For the simulations, the wake affected regime associated with the 10.5D case is analog to the one observed for the 8.6D case; i.e. approximately ±10° around the wind direction defining the case. For the measurements, however, the large scatter in the data prevents a meaningful definition of the wake affected regime. The (mean) magnitude of the tower bottom moment is over-estimated of the order of 10% in the simulations, whereas the (mean) magnitude tower top fatigue equivalent moments are under-estimated of the order of 20%. Compared to the 8.6D case, the wake loading is slightly attenuated in the simulated results – a similar effect is difficult to identify in the measured data due to the large scatter.

In general, it is characteristic that the scatter in the measured results are massive and larger that observed in the simulated results. This is believer to be caused by: 1) The simulations being associated with one particular mean wind speed only (i.e. 8 m/s), whereas the measurements represents a range of mean wind speeds in the interval [7; 9] m/s with derived consequences for the turbine operational conditions; 2) Conventional measurement uncertainty; and 3) The simulations all refer to an ambient turbulence intensity of 7%. However, for the messurements, each 10 minute record will refer to individual turbulence intersities due to directional dependencies (i.e. upstream fetch characteristics) and variations in atmospheric stability conditions etc.
The directional dependence of the site turbulence intensity is substantial and is illustrated in figure 5, corresponding to a site characterization performed before construction of the wind farm.

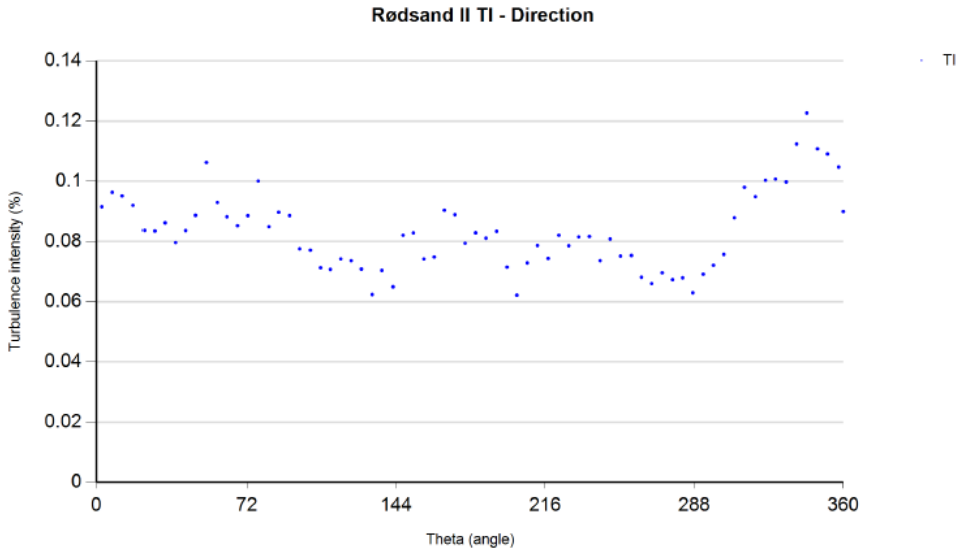

Figure 5: Turbulence intensity as function of mean wind direction for the Rødsand 2 site.

Unfortunately, the present data do not support identification of individual turbulence intersitues due to the preciously mentioned lack of wind speed recordings from the site meteorological mast during the recording period extending from January 11 to February 28 in 2013.
The load critical down stream distance, associated with the inflow direction aligned along turbine rows, is difficult to identify as based on the present data. However, with the available very crude spatial resolution, the simulations show maximum wake loading for this particular wind direction at the 8.6D spacing, which compares reasonable well with the crude engineering estimate, which suggests 9.5D as based on an ambient turbulence intensity level equal to 7%.

CONCLUSION

We have investigated measured wake affected fatigue loads for three different turbine inter spacings ranging from 6D to 10.5D and compared those with simulated results. A one-to-one mapping of the full-scale experimental data to analog numerical predicted results is in general difficult due to primary variations in inflow stochastics from time series to time series. For the presently available data set this mapping has been particularly difficult, due to lack of site meteorological recordings and thus especially individual turbulence intensity information associated with the investigated 10-minute time series. Further, even moderate WT yaw errors will impact the study more drastically that if site meteorological data were available.
Comparing simulated and measured tower fatigue loading, good agreements were found between the extend of wake affected direction regimes. As for the magnitude of the (mean) wake loading, the tower top moments were under-estimated with of the order 15%, whereas the tower bottom moments were found to agree well with the measured results.

In a future perspective much more data will be investigated, hopefully opening for a significantly more detailed comparison between measurements and simulations and also including more inter turbine spacing cases.

ACKNOWLEDGEMENTS

The PSO project “Wake affected offshore tower and foundation loads” under contract 2010-1-10546 is acknowledged for financial support and thus for making this study possible.

REFERENCES

[1] Larsen, T.J.; Madsen, H. A.; Larsen, G.C. and Hansen, K.S. (2012). Validation of the Dynamic Wake Meander Model for Loads and Power Production in the Egmond aan Zee Wind Farm. Wind Energy (ISSN: 1095-4244) (DOI: http://dx.doi.org/10.1002/we.1563).

[2] Bingöl, F.; Mann, J., and Larsen, G.C. (2010). Light detection and ranging measurements of wake dynamics Part I: One-dimensional Scanning. Wind Energy, **13(1)**, pp. 51–61.

[3] Espãna, G.; Aubrun, S.; Loyer, S. and Devinant, P. (2012). Wind tunnel study of the wake meandering downstream of a modeled wind turbine as an effect of large scale turbulent eddies. Journal of Wind Engineering and Industrial Aerodynamics, **101**, pp. 24–33.

[4] Larsen, G.C.; Madsen, H.Aa.; Thomsen, K. and Larsen, T.J. (2008). Wake Meandering - A Pragmatic Approach. Wind Energy, **11**, pp. 377–395.

[5] Larsen, T.J.; Larsen, G.C.; Aagaard Madsen, H. and Thomsen, K. (2008). Comparison of design methods for turbines in wake. 2008 European Wind Energy Conference and Exhibition, Brussels (BE), 31 Mar - 3 Apr.

[6] Trujillo, J.J.; Bingöl, F.; Larsen, G.C and Mann, J. (2010). Light detection and ranging measurements on wake dynamics; Part II: Two-dimensional Scanning. Wind Energy, **14**, 61-75.

[7] Larsen, T.J. and Hansen, A.M. (2007). How to HAWC2, the Users Manual, Risø-R-1597(EN), Risø National Laboratory - Technical University of Denmark.

[8] Madsen, H.Aa.; Larsen, G.C.; Larsen, T.J.; Troldborg, N. and Mikkelsen, R. (2010). Calibration and Validation of the Dynamic Wake Meandering Model for Implementation in an Aeroelastic Code. Journal of Solar Energy Engineering, Vol. 132 / 041014-1.

[9] Larsen, T.J. and Hansen A. (2007). How to HAWC2, the users manual. Technical Report Risø-R-1597(EN), Risø National Laboratory, Technical University of Denmark.

[10] Shabana, A. (1998). Dynamics of Multibody Systems, Cambridge University Press.

[11] Panofsky, H.A. and Dutton, J.A. (1984). Atmospheric Turbulence - Models and Methods for Engineering Applications. John Wiley & Sons.

Fast Multipole Accelerated Free-vortex Simulations of the Lillgrund Wind Farm

K.Brown[1], **C. Gundling**[1] **and J. Sitaraman**[1]

[1]University of Wyoming, Department of Mechanical Engineering
1000 E. University Ave, Laramie, WY, cgundlin@uwyo.edu

ABSTRACT

This article presents full wind farm simulations using a free-vortex wake method. The free-vortex wake code (UWAKE), developed at the University of Wyoming, has been coupled with the Weather Research and Forecasting model (WRF) and also the Mann model to allow accurate representation of the turbulent atmospheric inflow. Multi-level Fast Multipole Methods (MLFMM) are used to accelerate the computational speed of the simulations. The goal of this research is to develop a physics based method that, when coupled with precursor large eddy simulations (LES) or synthetic inflow turbulence, can provide fast and accurate wind farm simulations. The steps in validating the MLFMM implementation are first shown for single and two turbine simulations with both the HOLEC WPS-30 turbines at the Sexbierum wind farm and the Siemens 2.3 MW turbines at the offshore Lillgrund wind farm. The 48 wind turbines at the Lillgrund site are then simulated and power results are compared with field data and with past simulations using actuator line/disk with LES. The results with turbulent inflow show moderate differences depending on the method for producing the precursor inflow. The MLFMM free-vortex wake with both the WRF and Mann inflow produce similarly accurate results to prior actuator line/disk LES simulations, with the Mann simulations producing the closest match to the field data.

Introduction

At the University of Wyoming, we have developed and tested the full gamut of available computational fluid dynamics (CFD) models being used for wind farm simulations. One of the specific goals was to produce a lower complexity physics based model that could be developed, tested and cross-compared concurrently with the higher complexity methods such as LES and detached eddy simulations (DES). It has been shown in several articles [1, 2] that the tip and root vortices are the most dominant structures of a wind turbine near wake, therefore, the free-vortex wake model (UWAKE) simulates only these vortices. This method has shown promise in producing the same levels of accuracy as full-rotor computations with DES [3, 4]. This code is also currently part of the IEA Task 31 WAKEBENCH study.

A key step in the progression of UWAKE was the development of a new vortex core growth model [4] for use with turbulent inflow simulations. Free-vortex wake models are developed under the assumption of potential flow and have typically only been used to predict the near wake region. The near wake is usually defined as the region directly downstream the turbine in which the helical vortices from the turbine blades are distinct and stable. This near wake region can extend to several diameters downstream of the turbine depending on the turbine loading. In the free-vortex wake method diffusion is modeled empirically through the core growth of the tip and root vortices. The development of this new core growth method has broadened the potential application of free-vortex methods to both accurate prediction of the unstable far wake and prediction of wakes in atmospheric turbulent inflow.

An example of the solution produced by the free-vortex wake method is given in fig.1, where the vorticity iso-contours produced by the UWAKE method in steady and turbulent inflow (Mann model) for a single turbine are shown. The simulation was for the WPS-30 wind turbine at the Sexbierum wind farm. Both images are shown with an axial velocity of 8 $m\ s^{-1}$ and the turbine is rotating at 35 RPM. The version of UWAKE used for fig. 1 did not yet utilize Fast Multipole Method (FMM) for evaluation of mutually induced velocity contributions between vortex markers.

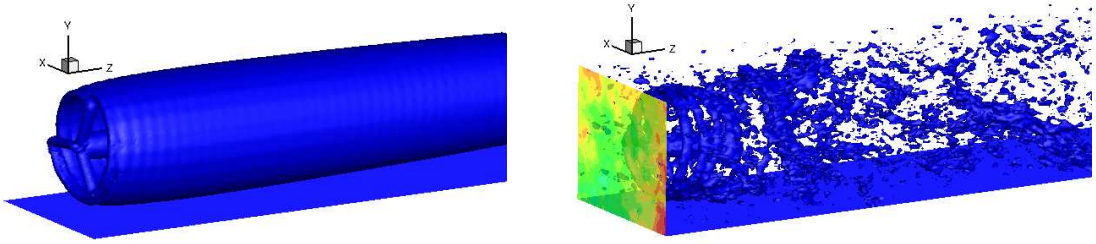

(a) Steady (b) Turbulent

Figure 1: Iso-vorticity contours for the Sexbierum turbine at 8 $m\ s^{-1}$ for a) steady and b) turbulent inflow

The objective of this paper is to accelerate UWAKE using the Multi-level Fast Multipole Method (MLFMM) and demonstrate success for wind farm computations. All computations are intended to be amenable to execution in massively parallel compute systems. Incremental validation and sensitivity studies are performed, first utilizing single turbines and then moving to higher complexity cases that involve two turbines and finally a wind farm scenario.

MLFMM [5] provides a computationally efficient way for computing interactions with multiple bodies (or vortex filaments as in the case of UWAKE). For a simulation of N bodies, the space is first divided into sub-domains, and then each body is assigned to the appropriate sub-domain. Within a given sub-domain, interactions between particles are calculated on an individual basis, while the forces acting between sub-domains are determined using a multipole expansion of the sub-domains. By using a multilevel tree scheme to divide the domain, interactions between bodies can be weighted as a function of the distance separating them, decreasing computation

time without introducing substantial error. While an N-body problem normally requires $\mathcal{O}(N^2)$ calculations, FMM with a multilevel tree can achieve similar accuracy with $\mathcal{O}$ (N) calculations.

Validation Data

The authors have previously tested the non-MLFMM version of UWAKE with several experimental cases including the data from the Sexbierum wind farm. While the turbines at the Sexbierum wind farm are outdated, this test study is continually used by researchers to test modeling methods due to extensive wake details that were measured and the data's availability to the public. In this study, the implementation of the MLFMM will first be verified by comparing to past results for the turbines at this site. Once the implementation is verified, the free-vortex method with MLFMM is used to predict the power of the turbines at the Lillgrund wind farm, so a brief description of the setup of the Lillgrund farm is given.

Sexbierum Wind Farm: The Dutch experimental wind farm at Sexbierum was utilized for a measurement campaign that took place between June and November of 1992 and concerned the measurement of wind speed, turbulence and shear in the turbine's wake, as well as measurements of the turbine's power[6]. The site contains 18 variable speed/variable pitch HOLEC WPS-30 turbines arranged in a 3 x 6 array as shown in fig. 2. These turbines have a rated power of 310 kW, a 30.1 meter (m) rotor diameter and use six different NACA 230XX airfoils along the span. The hub height of the tested turbine was 35 m. Meteorological masts were placed at 2.8 rotor diameters (D) upstream and 2.5, 5.5, and 8 D downstream of turbine T18 in order to measure inflow conditions and wind speed deficits in the wake. In fig. 2 the predominant wind direction is from turbine T18 to turbine T27.

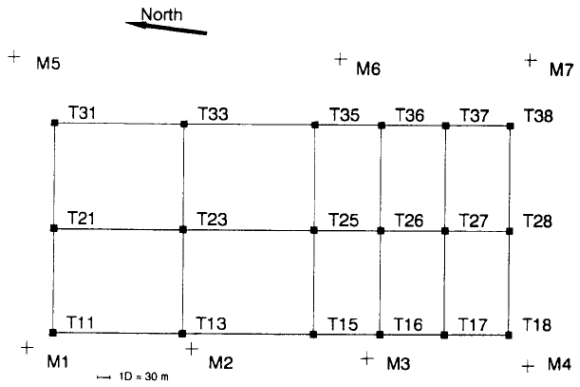

Figure 2: Layout of the 18 turbines at the Sexbierum wind farm

The specific conditions used to most closely model the site were recently defined as part of IEA Task 31 Wakebench study. The met-mast placed 2.8 D upstream of the tested turbine measured a range of hub height wind speeds from 5-10 $m\ s^{-1}$. It was shown by Cleijne[6] that the relative wind speed deficit results varied little between hub-height wind speeds of 6-10

$m\ s^{-1}$. The wind turbines operate at a constant tip speed ratio and the thrust coefficient is nearly constant in this wind speed range. A hub height velocity of 8 $m\ s^{-1}$ was used for all calculations in this study.

Lillgrund Wind Farm: Lillgrund is a operational offshore wind farm operated by Vattenfall Vindkraft AB and is located between Denmark and Sweden. The installed wind turbines in the farm were 48 Siemens SWT-2.3-93 three-bladed, upwind, horizontal-axis turbines. These turbines have a hub-height of 65 m. As the wind turbine blade information is not available to the public, an approximate method proposed by Churchfield[7] was used for generation of the aerodynamic information of the wind turbine blade, required for any blade element based models. Churchfield's method uses all the publicly available information about the turbine to construct a model of the turbine that produces similar performance to the actual turbine. The selected values of wind speed and turbulence intensity at hub-height used for simulations are 8.5 $m\ s^{-1}$ and 5% respectively, which closely match the site conditions[7].

The layout of the 48 turbines at the Lillgrund wind farm and the wind direction is shown in fig. 3. The available field data is comprised of time-averaged power production results for turbines in rows B-D. These results are taken from a database that includes more than a years worth of data. The entire wind farm is simulated, but in order to compare to the field data, the rows B-D, as shown in the figure, are analyzed in detail. This wind farm is ideal for studying the effects of turbine wakes as the turbines are closely spaced with 4.3 D between the turbines in the wind direction and 3.3 D in the direction perpendicular to the wind. Row D of the wind farm also includes a gap after the third turbine in the row, so there is 8.6 D spacing between the third and fourth turbines in the row.

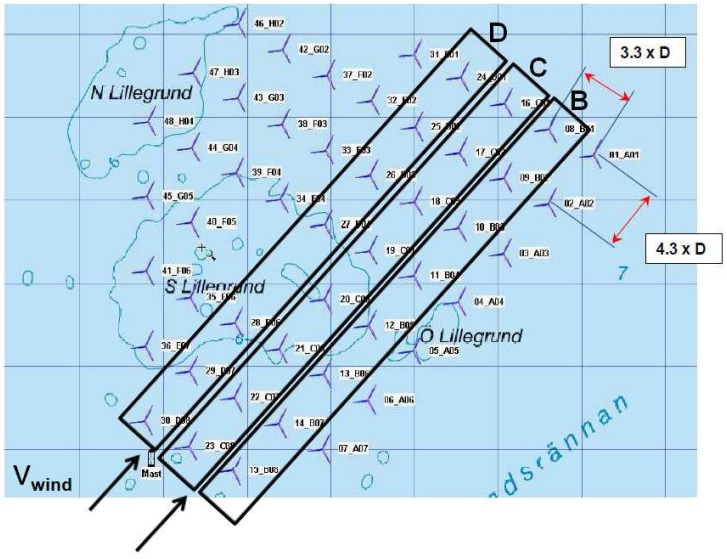

Figure 3: Layout of the 48 turbines at the Lillgrund wind farm

Numerical Methods

UWAKE Free-vortex Wake Method

In the free-vortex method, the vorticity transport equation can be written in partial differential form as

$$\frac{d\vec{r}(\psi,\zeta)}{d\psi} + \frac{d\vec{r}(\psi,\zeta)}{d\zeta} = \frac{1}{\Omega}\vec{V}(\vec{r}(\psi,\zeta)), \tag{1}$$

where $\vec{r}(\psi,\zeta)$ defines the position vector of a wake marker, located on a vortex filament that is trailed from a turbine blade located at an azimuth ψ, and wake age ζ. The turbine's rotational speed is given by Ω. The right hand side velocity, $\vec{V}(\vec{r}(\psi,\zeta))$ accounts for the instantaneous velocity field encountered by a marker on a vortex filament in the rotor wake. This includes the free-stream velocity, the induced velocities due to the vortex filaments present in the wake, and the induced contributions of the bound circulation representing the lifting turbine blades. The precursor inflow velocities are included as the free-stream velocity at the appropriate marker location and are then allowed to convect downstream. The vorticity transport equation is discretized into a set of finite difference equations that can then be numerically integrated. The time marching algorithm is a 2nd order backward predictor corrector algorithm and is based on the work by Bhagwat[8].

In the free-vortex method, viscous diffusion is modelled by the growth of the core radius given by Squire[9]

$$r_c(\zeta) = \sqrt{r_{initial}^2 + \frac{4\alpha\delta\nu\zeta}{\Omega}}, \tag{2}$$

where, $\alpha = 1.25643$, is an empirical factor, δ is the apparent viscosity coefficient, ν is the kinematic viscosity, $r_{initial}$ is the initial size of the vortex core and Ω is once again the rotational speed of the rotor. The δ parameter is formulated from the vortex Reynolds number Re_ν, where Re_ν is given by

$$Re_\nu = \frac{\Gamma_\nu}{\nu}, \tag{3}$$

where Γ_ν is the vortex circulation. δ is then defined as

$$\delta = 1 + a_1 Re_\nu. \tag{4}$$

The empirical factor a_1 has been determined in the past by Ramasamy[10] and the value of δ ranges between 10^1 and 10^6 depending on the scale of the turbine considered.

Modifications for Turbulent Inflow Simulations: The core model in UWAKE must be modified for use with precursor turbulent inflow to account for the added sub-grid scale (SGS) eddy viscosity. The new core growth model for turbulent inflow originates from Equation (2) and also uses the value of a_1 that was determined by Ramasamy. The use of turbulent inflow with a free-vortex wake method for wind turbine applications is a relatively new venture. The motivation for the coupling of inflow with a free-vortex wake code is that ideally it could lead to a faster, but equally accurate method to LES that incorporates a similar idea of resolving the large-scales and modeling the small-scales of turbulence. Velocity fluctuations from precursor

inflow simulations, when input to the free-vortex wake code, cause the wake to meander as previously shown by the authors[3]. Depending on the spatial/temporal resolution of the inflow, the inflow velocity fluctuations also cause varying levels of vortex filament stretching and instability/breakdown of the tip and root vortex structures. The additional modification now included in the free-vortex diffusion model is to account for the increased diffusion of the wake caused by the SGS eddy-viscosity in the precursor inflow. The full description of the modifications made to the core growth model for turbulent inflow are given in the author's prior work[4].

MLFMM Implementation: MLFMM was used to replace all direct vortex dynamics interactions within the existing version of UWAKE. MLFMM first divides the domain into boxes using an adaptive tree mesh, only subdividing boxes where either evaluation points or sources exist. A different tree was set up for each turbine, focusing primarily on the wake markers for that turbine but expanded to contain nearby evaluation points. An image of the wake markers after 100 timesteps and their containing boxes can be found in fig. 4. Note that there are additional evaluation points (sensor locations) where velocities are probed for postprocessing and evaluation. This is the reason for having refined meshes at regions where vortex markers are not present.

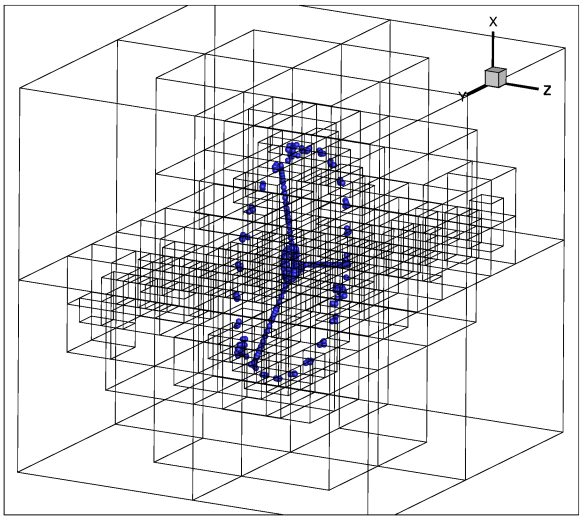

Figure 4: Adaptive mesh refinement after 100 timesteps

This implementation of MLFMM calculates velocities, $\vec{V}$, induced on wake markers due to vorticity, $\vec{\omega}$, using the Biot-Savart kernel. The code assumes that the length of a wake marker is small compared to the distance between markers, and that $\vec{\omega}$ is not a function of its position x. These assumptions yield Equation 5,

$$\vec{V}(x) = \frac{1}{4\pi}\nabla \times \frac{\omega}{|x-y|}. \tag{5}$$

From here, a vector potential $\vec{\phi}(x)$ is defined as $\vec{\phi}(x) = \frac{\vec{\omega}}{|x-y|}$, such that the velocity field can be calculated as $\vec{V}(x) = \nabla \times \vec{\phi}(x)$. The velocity induced at $\vec{x}$ by a group of N vortex filaments located at $\vec{y}_i (i = 1, N)$ is then given by:

$$\vec{V}(x) = \frac{1}{4\pi} \nabla \times \sum_{i=1}^{N} \frac{\vec{\omega}_i}{|x - y_i|}. \tag{6}$$

From Equation 6, it can be seen that the main task is to find the near- and far-field series expansions to the vector potential $\vec{\phi}(x)$ using a fast evaluation method.

Once a tree has been established, this algorithm finds expansion coefficients for the far field (S-expansion coefficients) on all boxes at every level. To start, these coefficients are computed about the origin,

$$\vec{\phi}(x) = \sum_{n=0}^{p} \sum_{m=-n}^{n} \frac{\vec{M}_n^m}{r^{n+1}} Y_n^m(\theta, \phi). \tag{7}$$

In Equation (7), $\vec{M}_n^m$ represents a moment of expansion that acts as a translation operator, and $\vec{Y}_n^m$ represents the spherical harmonic coefficients generated using associated Legendre polynomials. Next, the S-expansion coefficients are S-S translated, such that the S-expansion coefficients can be applied anywhere that is outside a given distance from the source box, as shown in Equation (8),

$$\vec{\phi}(x - x_2^*) = \sum_{j=0}^{p} \sum_{k=-j}^{j} \frac{\vec{M}_j^k}{r_1^{j+1}} Y_j^k(\theta_1, \phi_1). \tag{8}$$

This completes the *upward pass* of the routine, and now the *downward pass* starts, where the S-expansion coefficients are first translated into near-field expansion coefficients (R-expansion coefficients) in Equation (9),

$$\vec{\phi}(x - x_2^*) = \sum_{j=0}^{p} \sum_{k=-j}^{j} \vec{L}_j^k Y_n^m(\theta_1, \phi_1) r_1^j. \tag{9}$$

In Equation (9), $\vec{L}_j^k$ is the translation operator. Finally, R-expansion coefficients are translated such that they can apply on a shifted basis (i.e. not the origin),

$$\vec{\phi}(x - x_2^*) = \sum_{j=0}^{p} \sum_{k=-j}^{j} \vec{L}_j^k Y_j^k(\theta_1, \phi_1) r_1^j. \tag{10}$$

At this point, computation of the induced velocities can be performed by simply adding the exact solution for points within neighboring boxes and the curl of both R- and S- expansion terms to the wake markers.

Modifications to Parallelization Scheme: The operators that allow UWAKE to use many processors in parallel were modified to better work with MLFMM. UWAKE assigns one processor for each turbine in a farm simulation. For the direct evaluation method, UWAKE passed all wake markers for each individual turbine to every other turbine. Each turbine would then calculate

induced velocities on its own wake using the wake markers from every other turbine. If a similar strategy was employed when using MLFMM, the calculation would be inefficient. The box size for each turbine would be similar to the size of the wind farm and the MLFMM algorithm would require a large number of levels in order to resolve the local turbine's wake. Instead, a reverse calculation was employed where the locations of all wake markers are sent to each turbine, and each turbine then calculates its own contribution to the induced velocity at every marker. The velocity contributions at each marker can then be easily passed back to the appropriate turbine and the contributions from all turbines can be aggregated. The efficiency was improved using this reverse calculation method, as the contributions of a single rotor to far away wakes can be modeled as just the curl of the far-field expansion, leading to fewer performed calculations.

WRF LES

Version 3.3.3 of the WRF model has been used as the mesoscale solver for performing LES of the atmospheric boundary layer (ABL). The WRF dynamical core and its surrounding software framework and physics interfaces are well suited to application of atmospheric boundary layer flows, and the modeling system has been validated for numerical weather prediction. WRF contains a number of SGS stress models for calculation of the SGS stress tensor. The current study uses the nonlinear backscatter and anisotropy (NBA) model of Kosovic[11, 12] with a 1.5-order SGS TKE closure. The surface shear stress calculations were modified to specify the roughness length z_0 explicitly in the calculations. The surface heat flux was set to zero in all the WRF simulations while the friction velocity was calculated using the Monin-Obukhov theory. The default numerical schemes are used for spatial discretization and time marching.

For the Lillgrund wind farm simulations with WRF LES precursor inflow, the WRF simulations were performed on a domain size of $4096(x) \times 4096(y) \times 1024(z)$ m with a horizontal grid resolution of 16 m and a vertical grid resolution of 4 m. The turbulence intensity at hub height matched the site conditions of 5%. 256 seconds of data in 1 second time steps were saved for simulations with UWAKE. The WRF domain was chopped to half its original size for implementation with UWAKE. This gave a final horizontal and vertical dimensions of 2048 m and 512 m to help reduce the computational requirements. The horizontal dimension is slightly smaller than the expanse of the Lillgrund wind farm, which was strategic as only the inner rows of the farm were a focus in this study. At at wind speed of 8.5 $m\ s^{-1}$, it takes longer than 256 seconds to pass through the farm, so the data was padded to ensure periodicity.

Mann Synthetic Turbulence

The method of Mann[13, 14] was also used to generate inflow turbulence. The Mann method models the spectral tensor (three-dimensional (3-D) spectrum) using rapid distortion theory, combined with an assumption of linear shear and a model for eddy lifetime[2]. This model is used to simulate the 3-D velocity field and includes a coupling of the u-w velocities. The generated turbulence field is incompressible, homogeneous, stationary, Gaussian, anisotropic and has the same second order statistics as the atmosphere[2]. Once the Mann simulation is completed, the output is a spatial box of turbulent velocity fluctuations. The flow direction is inferred as the time axis using Taylor's frozen turbulence hypotheses. In order to create a

sheared boundary layer flow, the log-law profile in Equation (11) was added to the Mann velocity fluctuations in the streamwise direction.

$$U = \frac{u^*}{\kappa} \ln\left(\frac{z}{z_0}\right) \tag{11}$$

In Equation (11), U is the stream-wise velocity, u^* is the friction velocity, κ is the Von K*árm*á*n* constant, z is the height and z_0 is the roughness length.

For the Lillgrund farm simulations, the Mann inflow was generated to produce a hub height turbulence intensity of 5%. The Mann inflow varied slightly from the WRF inflow, as the horizontal spatial resolution was reduced from 16 m to 10 m. The time resolution was also halved to 0.5 seconds. The domain of the Mann inflow was to $2560(x) \times 2560(y) \times 512(z)$ m. The 2560 m in the flow (x) direction allowed for the extraction of 512 time steps or 256 seconds of data. Similar to the WRF inflow case, the Mann data was padded to ensure periodicity.

Results

0.1 Single Turbine MLFMM Verification

Verification of the MLFMM implementation is done by comparing to the non-MLFMM version of the code. The power of the Sexbierum turbine was first compared for the non-MLFMM and MLFMM versions of the code. The number of MLFMM levels (l) was varied as well as the truncation number (p) (the number of terms in far- and near-field MLFMM expansions). Figure 5 shows the power and thrust results plotted with the real or physical time on the horizontal axis. The outcome is that there are more fluctuations in the power when either l is increased or p is decreased. Increasing p leads to longer simulation times, but also more accurate calculations.

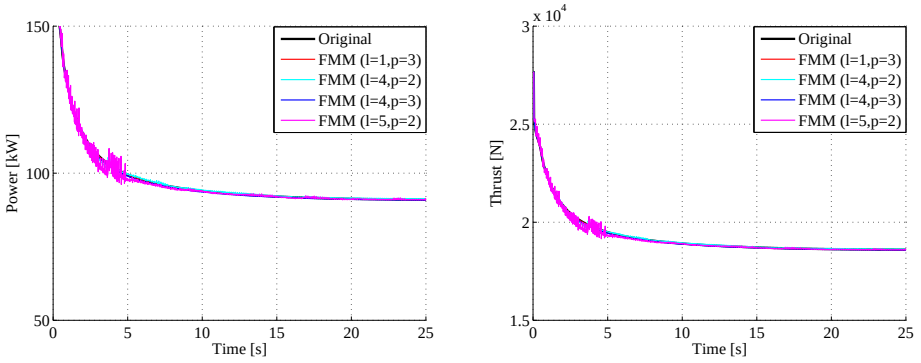

(a) Power (b) Thrust

Figure 5: Comparison of the a) power and b) thrust of the Sexbierum turbine with varying MLFMM parameters

The wake velocities were also considered for this single turbine Sexbierum case and the

results are shown in fig. 6, where l and p are once again varied. Only the $l = 5$ with $p = 2$ case shows any noticeable degradation of the solution.

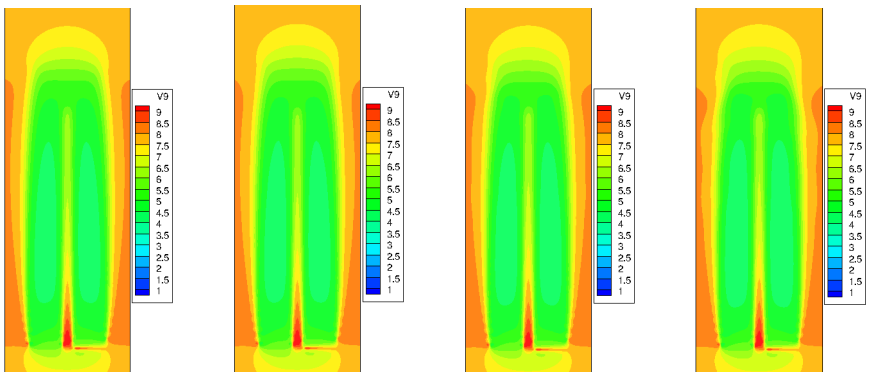

(a) Original (b) Level=4,p=3 (c) Level=4,p=2 (d) Level=5,p=2

Figure 6: Comparison of the wake velocities with varying MLFMM parameters, a) original code, b) level=4, p=3, c) level=4, p=2 and d) level=5, p=2

0.2 Two Turbine Parameter Sensitivity

A two turbine case was created for both the Sexbierum and Lillgrund turbines to test the effects of the adjustable parameters in UWAKE. The sensitivity of the forward and rear turbine's power due to the number of wake revolutions and the artificial viscosity (δ) were tested. In UWAKE, the number of wake revolutions that are modeled with wake markers is defined as an input. Each full rotation of a turbine blade creates a full wake revolution where the tip and root vortex are modeled.

In the presented sensitivity results, the MLFMM method with $l = 1$ and $p = 3$ is used, which gives a nearly identical solution to the non-MLFMM method. Only the power results are presented, but similar trends were also seen with the thrust. First for the Sexbierum turbine, fig. 7 shows the power variation for the forward and rear turbine due to the number of revolutions and fig. 8 shows the dependency of the power on the δ parameter. The rear turbine is placed at 5 D behind the forward turbine. The number of revolutions has little effect on the power of the forward turbine as long as a certain minumum ($revs \approx \quad > 10$) is met. On the other hand, the number of wake revolutions modeled has a significant effect on the rear turbine. It appears that near 25 revs the power of the second turbine begins to converge.

δ also has a minimal effect on the forward turbine's power, but greatly effects the downstream wake velocities of the forward turbine and therefore there are large differences in the power of the rear turbine when this parameter is varied.

The same study was then performed for the much larger Lillgrund turbine. The rear turbine was place at 4.3 D behind the forward turbine to mimic the row separation at the site. Figure 9 shows the power variation for the forward and rear turbine due to the number of revolutions modeled for the Lillgrund turbines. Similar to the Sexbierum case, the number of revolutions that are modeled barely changes the power of the forward turbine, but has a dramatic effect on

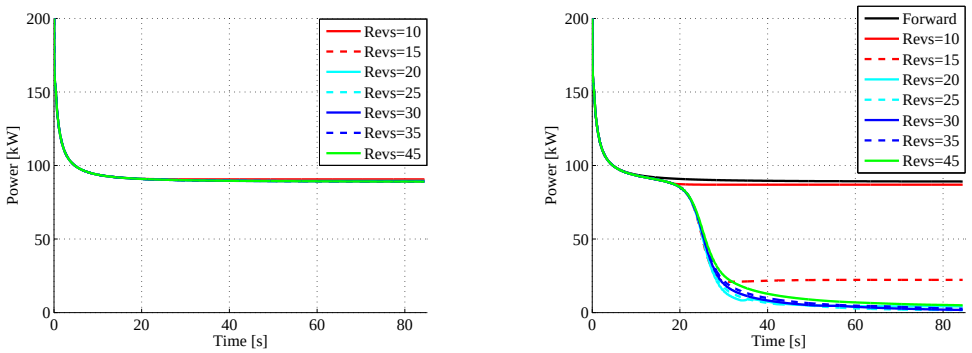

(a) Forward Turbine (b) Rear Turbine

Figure 7: Power of Sexbierum turbine with varying wake revolutions for a) forward and b) rear turbine

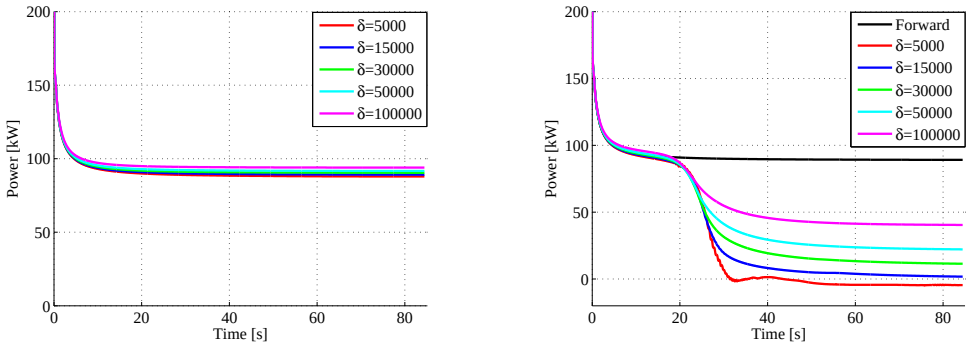

(a) Forward Turbine (b) Rear Turbine

Figure 8: Power of Sexbierum turbine with variation of δ for a) forward and b) rear turbine

the power of the rear turbine. Modeling 30-40 revs appears to converge the power of the rear turbine.

Figure 10 shows the dependency of the power of each turbine on the δ parameter. δ has a more pronounced effect on the power of both the forward and rear turbines for the Lillgrund case. For the forward turbine, increasing δ decreases the wake deficit which also leads to higher velocities near the rotor and therefore the power increases. For the rear turbine, δ needs to be increased drastically from the Sexbierum case to avoid overly large wake deficits. With δ too low, the large circulations produced at the wake markers actually cause instability in the wake.

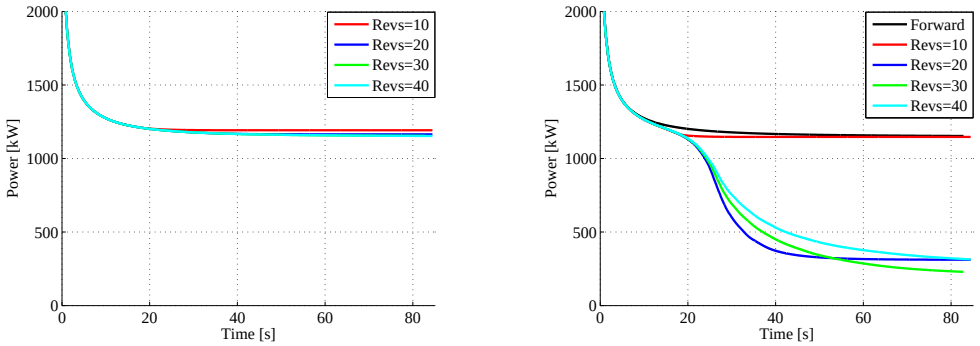

(a) Forward Turbine (b) Rear Turbine

Figure 9: Power of Lillgrund turbine with varying wake revolutions for a) forward and b) rear turbine

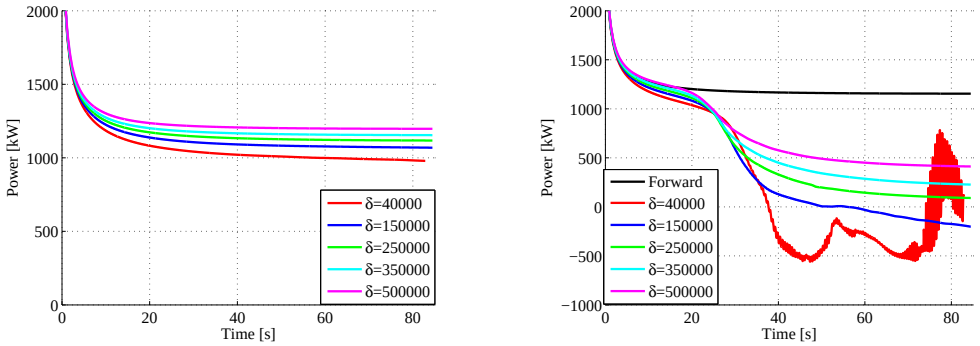

(a) Forward Turbine (b) Rear Turbine

Figure 10: Power of Lillgrund turbine with variation of δ for a) forward and b) rear turbine

0.3 Lillgrund Full Farm Simulations

Parametric Study of MLFMM Implementation: First, the number of wake markers used in a simulation was compared with the time needed to complete a given number of timesteps. This helps to establish at what point the algorithm becomes more efficient compared to the direct calculation. A typical MLFMM solver working on randomized points generally breaks even at around 16000 evaluation points. However, as fig. 11a shows, in the UWAKE implementation the break even point was not found for any number of wake markers. While a randomized point assortment tends to have source and evaluation points uniformly spread across the entire domain, the UWAKE implementation is mainly comprised of points that are a significant distance from one another. As a result, the interactions between wakes can be handled almost entirely with S-expansion coefficients, decreasing the time required for calculation.

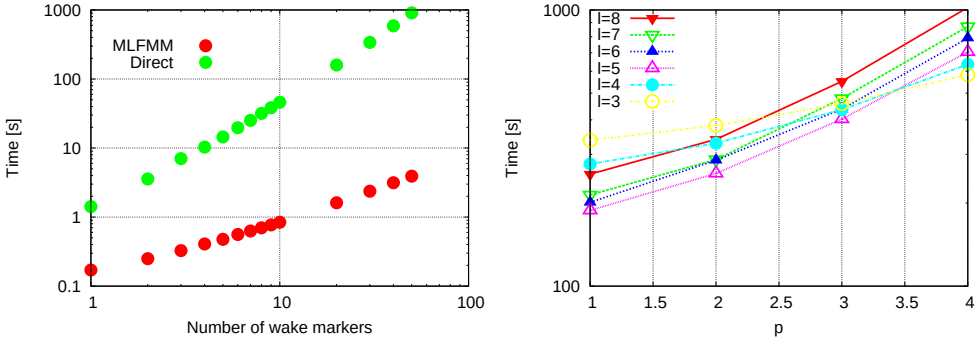

(a) Direct vs. MLFMM calculation

(b) Time to 100 steps

Figure 11: Comparison of MLFMM to direct calculation based on number of wake markers, and comparison of calculation time for different values of l and p to 100 timesteps

While the number of calculations required to perform MLFMM optimally goes to $\mathcal{O}$ (N), the actual number of calculations can vary significantly based on the parameters used. For this study, the effect of l and p was taken into account. As l goes to 1, the number of interactions that need to be calculated using an exact kernel increases dramatically, decreasing the efficiency of the algorithm. However, as l increases, the memory that needs to be allocated becomes more significant. The p term has a direct effect on the number of operations that need to be performed, with the current model performing $\mathcal{O}$ (p^4) operations. By allowing l to vary from 3 to 8 and p to vary from 1 to 4, the most accurate set of variables were found that still fall within acceptable time constraints. For all trials, the wake markers were modeled to 35 revolutions and the cases were simulated for 50 revolutions.

The dependency of calculation time on l and p can be seen in fig. 11b. For lower numbers of levels, the curve begins to level out as the solver approaches a direct solution. Above l=5 the curves take the same shape, with more time required for higher number of levels as the tree takes longer to generate. This would suggest that l=5 would be the most efficient for most simulations, and l=3 would be best for p above 3.

Results of the full parametric study show that the actual effects of p on accuracy are very much a function of l. Figure 12a shows results over Row B (defined in fig. 3) for l=3 and fig. 12b for l=4.

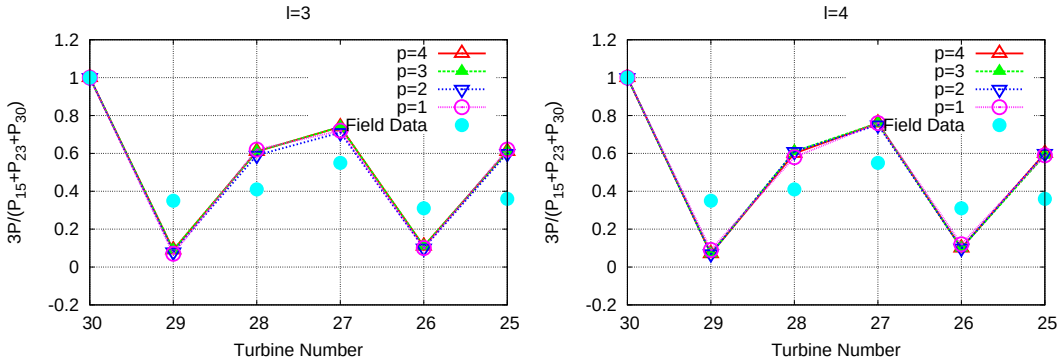

(a) l=3 (b) l=4

Figure 12: Comparison of relative turbine power for row D for the Lillgrund wind farm with MLFMM simulations run with l=3 and l=4 versus field data

Results were also compared for varying l with p held constant. Figure 13 shows the results for p=1 with l varying from 3 to 8.

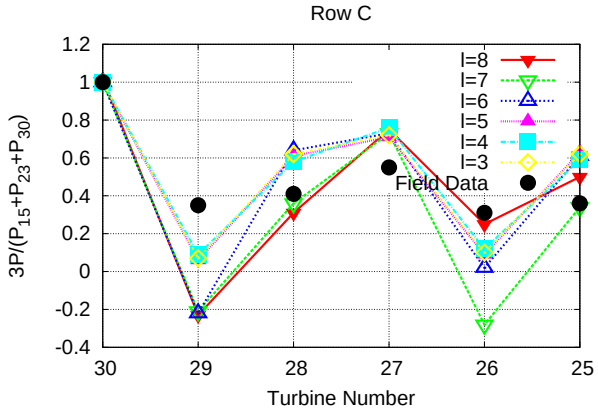

Figure 13: Relative turbine power for varying l

It is worth noting that since these results were collected with a low p value, it is expected that the truncation error will increase with l, as the number of translations that use p increase. From these results, it would seem that the ideal settings for MLFMM simulation of the Lillgrund wind farm would be with an l value of either 3 or 4, and p set to either 1 or 2, which should yield results in about 12 hours for 50 revolutions.

Power Results: The results for the UWAKE Lillgrund simulations of wind farm rows B, C and D using steady inflow, WRF turbulent inflow and Mann inflow are shown in fig. 14. These values

can be compared with the Lillgrund field data and the past actuator disk/line simulations from Churchfield and Gopalan[7, 15] in fig. 15. It should be noted that in comparing these power results from simulations to the field data, the field data has been averaged over much longer periods with varying atmospheric conditions, wind speed and wind direction. Contrastingly, simulations are performed for a single wind speed, direction and atmospheric conditions. In fig. 15 the data labeled 'Uniform Inflow' is Gopalan's simulation with the acuator disk, the data labeled 'Turbulent Inflow-C' and 'Turbulent Inflow-F' are Gopalan's simulations with WRF and the actuator disk and the data labeled 'Churchfield' is an actuator line simulation with OpenFOAM. The WRF inflow data used with UWAKE is identical to what was used in Gopalan's turbulent inflow results with the actuator disk.

First for the steady inflow case, there are significant differences in all three rows between UWAKE and Gopalan's actuator disk results. The UWAKE results appear to be more intuitive. There is a large drop in power for the second turbine in each row, as this row sees the undisturbed wake from the front turbine. Then moving down the row, the power recovers to higher levels since the interaction of each forward turbine's wake with each rear turbine creates more mixing and recovery of the wake wind speed deficits. These results suggest the UWAKE is producing significantly more wake generated turbulence than the actuator disk method.

Moving to the WRF simulation, in all three rows there is slightly less wind deficit when using UWAKE with WRF than when the actuator disk is used with WRF. The introduction of turbulent inflow reduces some of the discrepancy between UWAKE and the actuator disk as seen in the steady inflow case. The steady inflow cases showed that UWAKE is predicting more turbulence generated in the wake than the actuator disk, so it is consistent that the wake deficits are also less when using turbulent inflow. Compared to the experimental results, the UWAKE with WRF solution is slightly under predicting the wake effects which leads to more power at each turbine in the row.

Finally, for the UWAKE simulation with the Mann inflow, the results in general are closer to the actuator disk and line calculations, as well as the field data. The Mann inflow has a smaller spatial and temporal resolution compared to the WRF inflow and appears to be more appropriately modeling the inflow at the site. The under prediction of the wake effects in the WRF case compared to the Mann case is hypothesized to be a product of excessive meandering of the wake. This was seen in a previous study[4] and was because of the large spatial resolution of the WRF data and more energy contained in the larger scales of inflow turbulence. This will need to be verified in a future study by running a WRF simulation with finer spatial resolution. The largest difference between the Mann and WRF simulations is at turbine number 27 in row D. This is an interesting case, as there is double the spacing in front of this turbine, so the power jumps higher due to the reduced wake from turbine 28. UWAKE with the Mann model is very close to field data for this scenario, where as the WRF simulations over-predict the power at this turbine, which is once again expected to be an outcome of the excessive wake meandering.

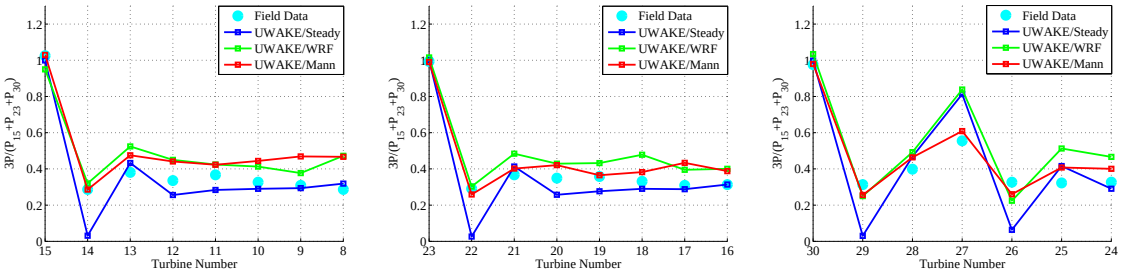

(a) Row B (b) Row C (c) Row D

Figure 14: UWAKE comparison of relative turbine power for rows B-D for the Lillgrund wind farm in steady inflow, WRF turbulent inflow and Mann turbulent inflow versus field data

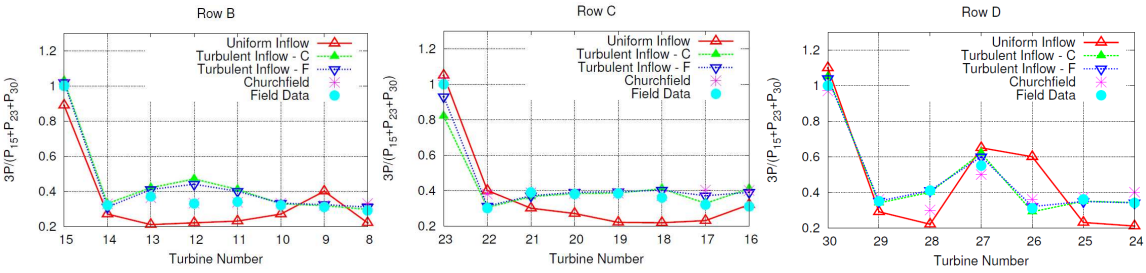

(a) Row B (b) Row C (c) Row D

Figure 15: Comparison of relative turbine power for rows B-D for the Lillgrund wind farm between actuator disk with steady inflow, coarse grid turbulent inflow (denoted by - C), fine grid, turbulent inflow (denoted by - F)[15], field data and simulations of Churchfield et. al[7]

Flow Visualization: The hub height velocity contours for the Lillgrund farm simulation for UWAKE in steady inflow, WRF turbulent inflow and Mann turbulent inflow can be seen in fig. 16. The B, C and D rows are labeled for each contour plot. In the visualization of the steady inflow, small amount of turbulence can be seen to be generated after the first turbine-wake interaction. The WRF inflow case shows large scales and associated meandering of the wake while the Mann inflow shows small scale structures and slightly increased wake dissipation rate.

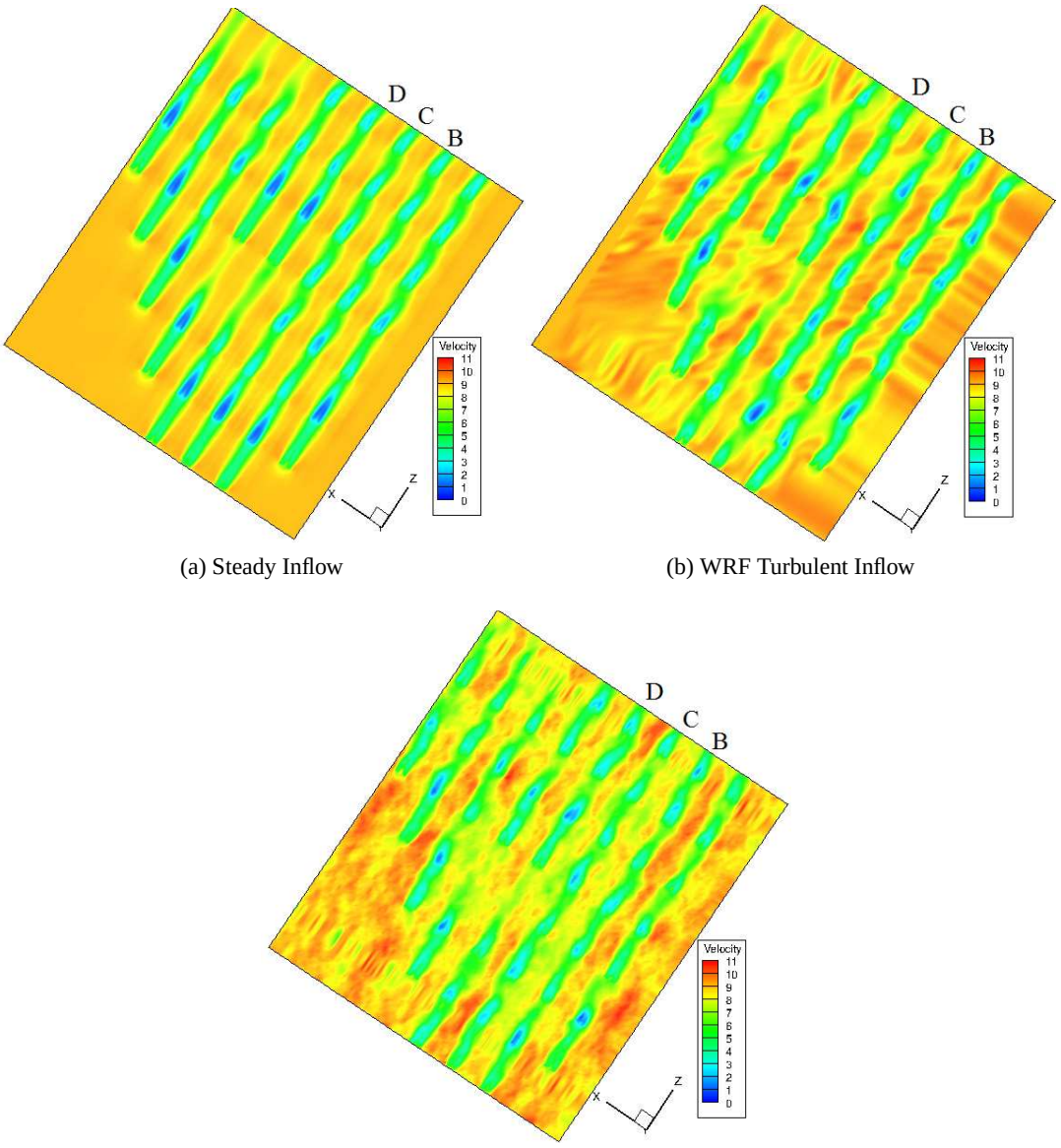

(a) Steady Inflow

(b) WRF Turbulent Inflow

(c) Mann Turbulent Inflow

Figure 16: Hub height velocity contours at 8.5 $m\,s^{-1}$ for UWAKE with a) steady inflow, b) WRF turbulent inflow and c) Mann turbulent inflow

Conclusions

The development and testing of MLFMM accelerated free-vortex wake full wind farm simulations have been presented. The results for the Lillgrund wind farm prove convincing with the free-vortex method producing comparable results to actuator line/disk LES simulations. The

key differentiator is that the free-vortex simulations were conducted with only a fraction of the computational resources and time of the LES – 6 hours on 48 CPUs for UWAKE compared to 6 days on 256 CPUs for LES.

The different methods for producing precursor inflow showed moderate effects on the solution. Simulations with the WRF inflow showed lesser wake deficits than the Mann inflow. This is because the WRF Inflow was generated with a larger spatial and temporal scale and there was more energy contained in the larger scale velocity fluctuations. This causes the wake to meander excessively. On the other hand, the Mann inflow has more energy contained in the smaller scale velocity fluctuations, and generated slightly lesser amounts of meandering. However, the energy in the smaller scales did increase the instability in the vortex wake. The smaller scale fluctuations appear to considerably effect the diffusion and stability of the wake. From these simulations the Mann inflow appears to more closely recreate the conditions that the turbine was experiencing during the experimental campaign. A finer spatial resolution simulation with WRF will need to be evaluated and compared with Mann inflow to further characterize the differences between precursor meso-scale simulations and synthetic turbulence.

Whenever simulations are compared to field data, such as presented in this article, there is always the issue that the field data has been averaged over much longer periods with varying atmospheric conditions, wind speed and wind direction. Contrastingly, simulations are performed for a single wind speed, direction and atmospheric conditions. One of the further advantages that this new free-vortex method provides is the ability to run several test cases with varying inflow conditions in the same amount of time as a single LES case. The simulations can also be run and averaged for anywhere from 10 minutes to an hour of physical time, rather than just a few minutes of physical time. Further investigation on this aspect is intended using this model.

References

[1] L. J. Vermeer, J. N. Sørenson, and A. S. Crespo, "Wind turbine wake aerodynamics," *Progress in Aerospace Science*, vol. 39, pp. 467–510, 2003.

[2] N. Troldborg, "Actuator line modeling of wind turbine wakes," Ph.D. dissertation, Technical University of Denmark, 2008.

[3] C. Gundling, B. Roget, J. Sitaraman, and R. Rai, "Comparison of wind turbine wakes in steady and turbulent inflow," in *50th AIAA Aerospace Sciences Meeting*, Nashville, TN, January 2012, pp. AIAA Paper 2012–0899.

[4] C. Gundling, H. Gopalan, B. Roget, and J. Sitaraman, "A free-vortex wake diffusion model for wind turbines in steady and turbulent atmospheric inflow," in *51st AIAA Aerospace Sciences Meeting*, Grapevine, TX, January 2013, pp. AIAA Paper 2013–1207.

[5] L. Greengard and V. Rokhlin, "A fast algorithm for particle simulations," *Journal of Computational Physics*, vol. 73, pp. 325–348, 1987.

[6] J. W. Cleijne, "Results of Sexbierum wind farm; single wake measurements," TNO Institute of Environmental and Energy Technology, Apeldoorn, Netherlands, Tech. Rep. 93-082, 112324-22420, 1993.

[7] M. J. Churchfield, P. J. M. S. Lee, L. A. Martinez, S. Leonardi, G. Vijayakumar, and J. G. Brasseur, "Large-eddy simulations of wind-plant aerodynamics," in *50th AIAA Aerospace Sciences Meeting and Exhibit*, Nashville, TN, January 2012, pp. AIAA Paper 2012–537.

[8] M. Bhagwat and J. G. Leishman, "Stability, consistency and convergence of time-marching free-vortex rotor wake algorithms," *Journal of American Helicopter Society*, vol. 46, pp. 59–71, 2001.

[9] H. B. Squire, "The growth of a vortex in turbulent flow," *Aeronautical Quarterly*, vol. 16, pp. 302–306, 1965.

[10] M. Ramasamy, "Contributions to the measurement and analysis of helicopter blade tip vortices," Ph.D. dissertation, University of Maryland, 2004.

[11] B. Kosovic, "Subgrid-scale modelling for the large-eddy simulation of high-reynolds-number boundary layers," *Journal of Fluid Mechanics*, vol. 336, no. 1, pp. 151–182, 1997.

[12] J. D. Mirocha, J. K. Lundquist, and B. Kosovic, "Implementation of a nonlinear subfilter turbulence stress model for large-eddy simulation in the advanced research WRF model," *Monthly Weather Review*, vol. 138, no. 11, pp. 4212–4228, 2010.

[13] J. Mann, "The spatial structure of neutral atmospheric surface-layer turbulence," *Journal of Fluid Mechanics*, vol. 273, pp. 141–168, 1994.

[14] ——, "Wind field simulation," *Probalistic Engineering Mechanics*, vol. 13, pp. 269–282, 1998.

[15] H. Gopalan, C. Gundling, and J. Sitaraman, "Coupled mesoscale microscale model for wind resource estimation and turbine aerodynamics using an overset approach," in *51st AIAA Aerospace Sciences Meeting*, Grapevine, TX, January 2013, pp. AIAA Paper 2013–392.

Wind-Farm Parametrisations in Mesoscale Models

P.J.H. Volker, J. Badger, A.N. Hahmann and K.S. Hansen

Wind Energy Department, Technical University of Denmark, pvol@dtu.dk

Abstract

In this paper we compare three wind-farm parametrisations for mesoscale models against measurement data from the Horns Rev I offshore wind-farm. The parametrisations vary from a simple rotor drag method, to more sophisticated models. Additional to (4) we investigated the horizontal resolution dependency of the considered approaches.

1 Introduction

The offshore wind-farm (WF) technology has matured significantly in the past decade. Currently the largest installed WF (London array phase I) with a nominal capacity of 630 MW, is almost four times larger then the Horns Rev I (160 MW) WF, which began to operate in 2005. The North Sea area, which is at the moment the most lucrative region for offshore WFs, is however limited. Therefore it will become increasingly important to study the effect of large WFs on the atmosphere from an economical (WF efficiency, WF interaction), as well as from an ecological point of view.

We use in this study the mesoscale model for it's ability to take atmospheric conditions into account, which can influence the wake extension. Its drawback is the lack in resolution compared to Computational Fluid Dynamics (CFD) models, implying that it is not possible to simulate single turbine wakes. Instead a WF parametrisation should model the average effects of wind turbines inside a mesoscale grid cell.

Three WF schemes will be analysed. The first approach, hereafter Rotor Drag, adds only a drag force to the flow, which proportional to the turbine blade area intersection with the model grid level. The second parametrisation, hereafter WRF-WF, is included in the Weather Research and Forecast Model (WRF) (3), a publicly available open source model written in fortran. It applies a drag and a turbulence kinetic energy source term to the flow at each rotor intersecting vertical grid level and adds turbulence kinetic energy (TKE) to the flow. The third WF scheme, Explicit Wake Parametrisation (EWP) (4) has been developed at DTU Wind Energy and adds a drag force based on similarity principles. It models the wind turbines by effecting the vertical distribution of the horizontal velocity field with a Gaussian distributed deceleration. The approximately Gaussian form could be confirmed by wind tunnel experiments (1). The parametrisation has been implemented in at WRF model.

In a previous study (4) we analysed the WRF-WF and EWP approach against long term measurements from the offshore WF Horns Rev I. We found that the additional TKE in the WRF-WF approach caused a intensive mixing zone, leading to a too fast velocity deficit recovery close to the WF. The additional TKE caused, furthermore, the scheme to be vertical resolution dependent, consequently the energy extracted from the flow will vary with vertical resolution. In this article we extend the previous study by analysing the horizontal dependency of both parametrisations. This is done by simulating the same WF size with a 1.12 km, 1.68 km and 2.24 km horizontal resolution. We will verify the WF parametrisations against long term in-situ measurements from the Horns Rev I WF. The mesoscale model was run in the idealised case mode with 40 vertical layers. The vertical resolution was in the planetary boundary layer (PBL) in the order of 10 m (the five lowest layers were on 10, 30, 50 ,71 and 92 meter respectively). Unlike CFD models, mesoscale models are not expected to be horizontal resolution independent.

2 Mesoscale Model

Mesoscale models are designed to forecast weather phenomena with typical length scales down to 5 km. Therefore, to limit computational costs, a coarse horizontal resolution in the order of kilometres is required. The vertical resolution is in the Planetary Boundary Layer (PBL) typically in the order of decametres to allow the vertical temperature and moisture structure to be resolved sufficiently. Mesoscale models are intended to resolve, similar to Reynolds Averaged Navier-Stokes (RANS) models, only the mean flow, whereas the turbulence part of the spectrum is completely modelled. The basic assumption is the scale separation of the resolved mesoscale processes and the unresolved turbulent ones, since no explicit filtering is applied. This means that the solution will not converge to the expected value with horizontal grid refinement, since from a certain horizontal scale onwards double counting will take place. Mesocale models are generally non hydrostatic and fully compressible. This means that they contain a prognostic equations for all three wind velocity components and a complete continuity equation. Furthermore, they contain a prognostic equation for the temperature as well as for all moisture components. Finally, the pressure is obtained via the equation of state. The time step used in the prognostic equations is determined by the Courant number, which is a function of the advection velocity and the horizontal grid size. The lower boundary values, are over land provided by soil (diffusion) models and over water they are generally obtained from reanalysis data.

2.1 Parametrisation of Wind Turbines

All unresolved processes need to be parametrised. Examples are local and non-local (convection) turbulent transport, turbulent surface fluxes, moisture phase changes and radiation. Since $D_0 << \Delta x$, where D_0 is the wind turbine diameter and Δx the horizontal grid spacing, the effect of wind turbines are also unresolved. On the other hand, since $D_0 > \Delta z$, where Δz is the vertical grid spacing, the vertical turbine wake structure can be described. Due to the coarse horizontal resolution we will typically find several turbines in one mesoscale grid cell. It is therefore not possible to resolve single turbine wakes and hence to take into account single turbine interaction explicitly by the model. Instead the parametrisation should apply a grid cell averaged

deceleration, accounting for the average impact of all the grid cell containing turbines. Then the mesoscale model is intended to simulate the WF wake. We should aim to describe the grid cell average deceleration as accurately as possible, since the near WF wake is sensitive to the amount of energy extracted by the wind turbines. The energy extracted from a single turbine can be modelled by adding an additional force (in the opposite flow direction) to the velocity balance equation. For a compressible fluid, neglecting viscous effects, the most general form of the Reynolds averaged Navier-Stokes reads

$$\frac{\partial U_i}{\partial t} + U_j \frac{\partial U_i}{\partial x_j} + \frac{\partial \overline{u_i u_j}}{\partial x_j} = F_i. \tag{1}$$

Here, we use capital letters for mean quantities and lower-case letters for the fluctuations. The index i is equal to x, y and z. All the forcing contributions are incorporated in the force (per mass) term F_i on the right hand side, such as the pressure gradient force or coriolis force. Also the turbine induced drag force is be part of the forcing term F_i.

2.2 Rotor Drag

A simple way to take turbine effects into account, is to apply a thrust force at every turbine blade intersecting model level k to the horizontal components of the Reynolds averaged Navier-Stokes equation. The additional thrust force reads

$$F_{i,k} = \frac{C_T N_{n,m} A_k U_{i,k} |U_k|}{2 (\Delta x)^2 \Delta z_k}, \tag{2}$$

where C_T is the thrust coefficient, $N_{n,m}$ the number of turbines located in grid cell (n,m), A_k the turbine blade area intersecting with model level k, $U_{i,k}$ the horizontal wind velocity component in the direction $i = x, y$. The absolute horizontal velocity on level k is $|U_k| = \sqrt{U_k^2 + V_k^2}$, where U_k and V_k are the horizontal velocity components in the x and y direction, respectively. Δx and Δz_k are the horizontal and vertical grid spacing at level k. In this way the subgrid velocity deficit expansion in the vertical direction is neglected, since the vertical velocity deficit is restricted to the turbine blade extension.

2.3 WRF-WF

The WRF-WF scheme is from version 3.2.1 included in the WRF model. This parametrisation applies a drag force eq.(2), as well as an additional source term of turbulence kinetic energy (TKE), to the flow. The total TKE applied to the model level k reads

$$\frac{\overline{u_{i,k} u_{i,k}}}{2} = \left(\frac{\overline{u_{i,k} u_{i,k}}}{2} \right)_m + C_{\mathrm{TKE}} \frac{N_{n,m} A_k |U_k^3| \Delta t}{2 (\Delta x) \Delta z_k}, \tag{3}$$

where the subscript m stands for the model TKE. The factor of proportionality C_{TKE} is equal to $C_T - C_p$, where C_P is the power coefficient and Δt the model time-step. The second term on the right hand side represents the wind turbine induced TKE. The additional TKE will lead to an

increased turbulence (diffusion) coefficient for momentum $K_m = qlS(m)$, where $q = \sqrt{2TKE}$ is the turbulence velocity, l the turbulence length scale (obtained from a diagnostic relationship) and $S(m)$ a stability correction. In this way the vertical sub grid scale wake expansion is obtained implicitly.

2.4 Explicit Wake Parametrisation

In the Explicit Wake Parametrisation (EWP) (4), it has been assumed that inside a turbine containing grid cell the additional turbine caused turbulence will be balanced by its dissipation. This is justified by the large ratio between the horizontal grid spacing and the turbine blade diameter. The downstream sub-grid scale velocity deficit development is described explicitly via a turbulence diffusion process.

The velocity deficit is assumed to be approximately Gaussian shaped and it is described by a characteristic length and velocity scale. From an one dimensional diffusion equation we obtain the characteristic length scale,

$$\ell^2 = \left(\frac{2K_m}{U_0}\right) x + \ell_0^2, \tag{4}$$

where ℓ_0 is the initial length scale and U_0 the hub height velocity. The one dimensional diffusion has a Gaussian distribution as analytical solution. If this is used, we obtain for the velocity deficit

$$\Delta U(z) = U_s e^{-\frac{1}{2}\left(\frac{z-h}{\ell}\right)^2} = U_s f(z,\ell)\,, \text{ consequently } U = U_0 - U_s f(z,\ell), \tag{5}$$

where h is the turbine hub height and U_s the maximum velocity deficit. The function $f(z,\ell) \equiv f$ expresses the velocity deficit distribution. The maximum velocity deficit U_s can be obtained from the total thrust equation. This gives

$$\frac{1}{2}\rho\, C_T\, \pi\, R_0^2 U_0^2 = W\rho \int_0^{z_{\max}} U_0\,(U_0 - U)\, dz, \tag{6}$$

where ρ is the atmospheric density, R_0 the turbine blade radius and W the horizontal wake width. Combining eq. (5) and eq. (6), integrating over the domain height $z_{\max}$ gives for the maximum velocity deficit

$$U_s = \sqrt{\frac{\pi}{2}}\, \frac{C_T\, R_0^2\, U_0}{W\, \ell}. \tag{7}$$

We obtained finally a full set of equations, which describe the velocity deficit completely. We notice that the final thrust equation is independent of the width W of the wake.

3 Measurements Data

For the evaluation of the different WF description, we used the measurements from the Horns Rev I WF, see fig.(1). The Horns Rev I WF consists of 80 2 MW wind turbines, each with a diameter of 80 m and a hub height of 70 m. The turbines are arranged in 10 columns from east

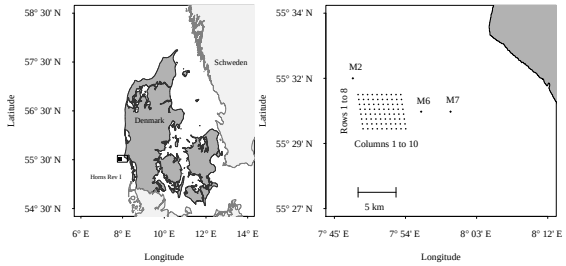

Figure 1: Location of the Horns Rev I WF and the meteorological masts.

to west and 8 rows from south to north as described in (5). The turbine spacing is 560 m in the west to east direction. For the model validation only measurements from 2005 to 2009 in the upstream wind sector of $255^\circ \leq \theta \leq 285^\circ$ 30° has been used for a wind speed interval 7.5 m s^{-1} to 8.5 m s^{-1} in neutral conditions have been selected. In this case the northerly wind direction is defined to be at 0° and the rotation is in the clockwise direction. The inflow conditions are determined with reference to a) wind speed based on mean power for wind turbine 07 (seventh turbine from the north in the first column) in combination with the official power curve; b) wind direction from M7 at level 68 m. The neutral conditions are defined for Monin-Obukhov lengths $|L| > 500$ m, but all observations have been included without filtering. The wind speed along the west-east row of turbines is derived from the mean power level in combination with the official power curve. The uncertainty of the mean wind speed (U) along the row of turbines is determined as the standard uncertainty σ.

4 Model Set-Up

We used the WRF model in idealised case mode with open boundaries and no surface fluxes. The model is initialised with a constant geostropic wind, which converge to $U = 7.97$ m s^{-1} and $V = 0.09$ m s^{-1} ($\theta = 269.4^\circ$) at hub height. In this model configuration the Coriolis force acts on the velocity perturbation from the initial condition. The dry atmosphere converges to a neutral temperature profile with an inversion height at around 700 m. The surface fluxes were set to zero. The cloud microphysics, as well as the convection scheme, were turned off. For all simulations the MYNN (1.5) PBL turbulence diffusion scheme (2) was used as required for the WRF-WF parametrisation. The model was set up with 80×30 grid cells in the horizontal direction. In the vertical direction we used 40 layers (the lowest layers were on 10, 30, 50 ,71 and 92 m respectively). To study the horizontal dependency of the three WF parametrisations, we have run the WRF model with a horizontal grid spacing of 1120 m (R1120), 1680 m (R1680) and 2240 m (R2240) respectively. The model set-up is summarised in table (4).

Table 1: WRFV3.4 simulation set up

	(R1120)	(R1680)	(R2240)
Domain (x,y,z):	80 × 30 × 40	80 × 30 × 40	80 × 30 × 40
Top (m):	10000	10000	10000
Horizontal grid spacing:	1120 m	1680 m	2240 m
Boundary condition:	OPEN	OPEN	OPEN
PBL scheme:	MYNN (1.5)	MYNN (1.5)	MYNN (1.5)
Coriolis:	TRUE	TRUE	TRUE

4.1 Wind-Farm Layout

The WF layout for the three runs is depicted in fig.(2). The WF contains in all simulations 8 rows and 10 columns. We use the dotted lines for the grid cells in which the turbine density does not change.

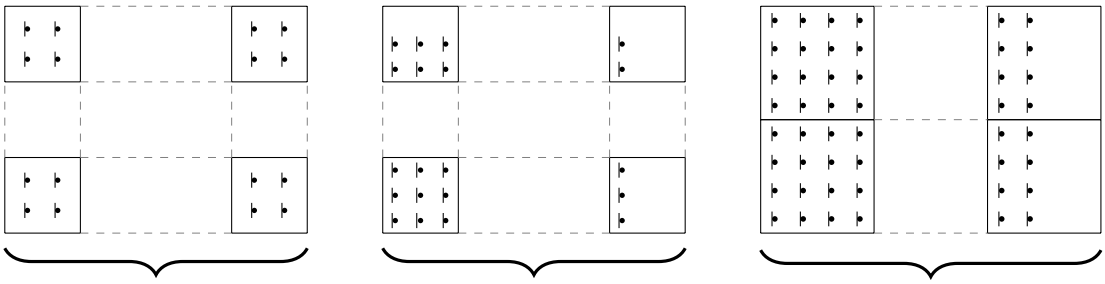

Figure 2: On the left side the WF layout for the R1120 simulation has been plotted, in the centre the WF layout for the R1680 simulation and on the right side the WF layout of the R2240.

We notice that the number of turbines per grid cell is not constant in the R1680 and R2240 simulation.

4.2 Wind-Farm Scheme Adjustments

WRF-WF scheme

The WRF-WF scheme uses per default an empirical power curve to obtain the power coefficient C_P. The thrust coefficient is then derived by a empirical relationship $C_T = \min(7C_p/4, 0.9)$. To guarantee the same applied thrust in all simulations, we used the thrust coefficient from the Vestas V80 thrust curve as in the EWP scheme. Afterwards the inverse relationship from above is applied to obtain the power coefficient ($C_p = C_T/1.75$). In this way the ratio between the thurst and power coefficient remains unchanged in the WRF-WF parametrisation.

EWP scheme

The initial length scale has been set to $\ell_0 = 1.5R_0$. Here we included vertical meandering and viscous effects to the inviscid fluid solution $\ell_0 = R_0$.

5 Evaluation

In this study we use the near and far WF wake for a 10% and 5% velocity, respectively. This definition was made for terminology convenience only.

Near Wind-Farm Wake

In fig.(3) we plotted the normalised velocity deficit for the three approaches. We used U_h for the downstream grid cell averaged hub height velocity and U_{0_h} for the WF upstream velocity at

hub height. The upstream velocity is obtained from the reference run without WF. The velocity

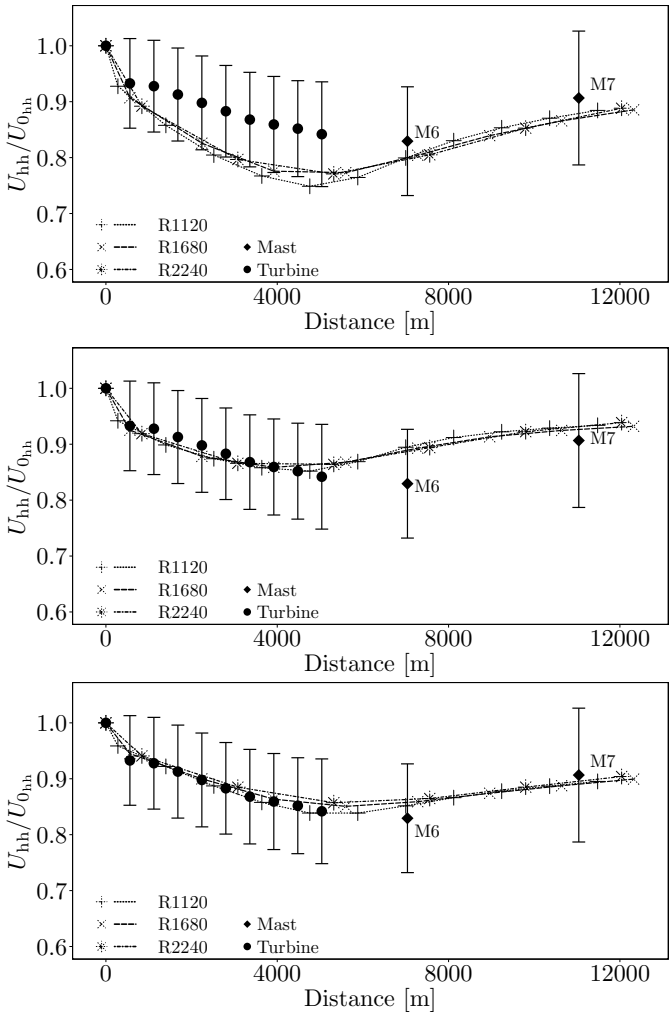

Figure 3: Velocity deficit recovery plot for the Rotor Drag, WRF-WF and EWP scheme respectively. The measurements are represented by dots and diamonds. The dots are the derived velocity deficits from the power measurements, whereas the diamonds are directly derived from cup anemometer measurements. Top: Rotor Drag , centre WRF-WF and bottom EWP approach. The error bars represent the standard deviation σ of the measurements.

deficit for every downstream grid cell has been obtained by averaging over the complete WF extension in the cross-stream direction, i.e. for the R1120 simulation over 4 rows, for the R1680 simulation over 3 rows and for the R2240 run over 2 rows (see fig.(2)). The figure on the top shows the results from the Rotor Drag approach, the one on the centre shows the results from the WRF-WF approach and the bottom one the results from the EWP scheme. From fig.(3a) we can conclude that the modelled velocity deficit, inside the WF and in the near WF wake, is deeper then the measured one. This is expected since no sub grid scale wake expansion in the vertical direction is taken into account, consequently the wake impact at hub height is too strong.

Furthermore, we find a horizontal grid size dependency. The maximum difference in velocity deficit is 3% at the end of the WF, at mast 7 the difference is reduced to less then 1%. From the WRF-WF simulation, fig.(3b), we can conclude that the hub height velocity deficit is in line with the measurements. However the recovery is faster then observed. The scheme is almost horizontal grid independent (less then 1%). From fig.(3c) we notice that the velocity deficit is well described by the EWP approach. The difference between the R1120 run and the R2240 one is slightly higher then 1% at the end of the WF, after M6 the velocity deficit differences converge.

Wind-Farm Wake

In fig.(4), fig.(5) and fig.(6), we plotted the normalised velocity deficits for the Rotor Drag, WRF-WF and EWP approaches respectively. The plot on the top panel shows always the velocity deficit from the R1120 simulation, the one on the centre that from the R1680 simulation and the one on the bottom that from the R2240 simulation.

Rotor Drag Approach

a)

b)

c)

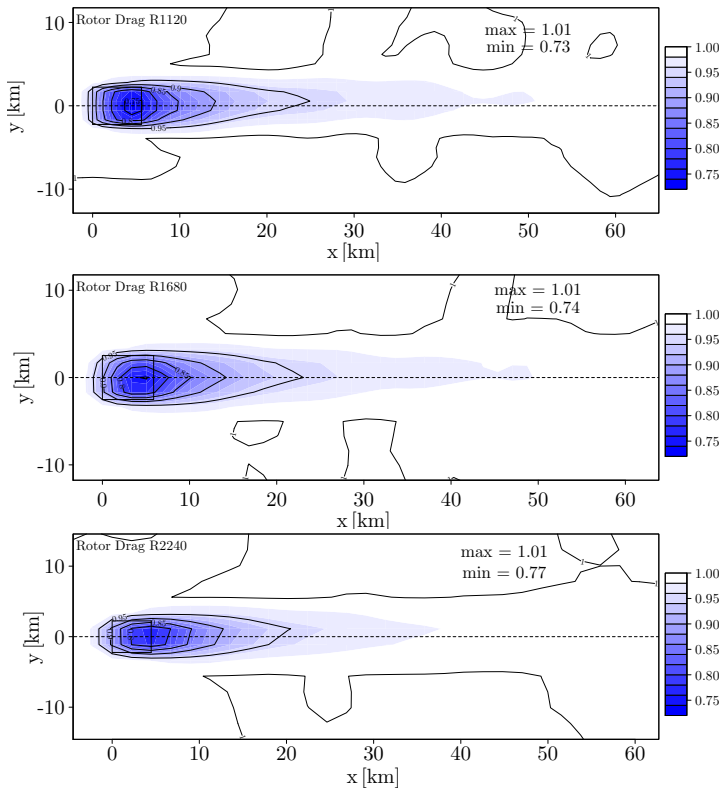

Figure 4: Velocity deficit recovery plot for the Rotor Drag approach. For the R1120, R1680 and R2240 simulation respectively.

From fig.(4) we find that the 10% velocity deficit recovery is reached at around 8 km downstream in all simulations. The far WF wake with a 5% velocity deficit, is not wide enough anymore to be resolved in the R2240 simulation.

WRF-WF Scheme

From fig.(5), where the velocity deficit for the WRF-WF has been plotted we find that the 10% velocity deficit varies almost 40% (∼1.7 km in the R1680 run and ∼2.8 km in the R2240 simulation). Although the maximum velocity deficit in the WRF-WF approach is around 15%, which is around 10% less then with the Rotor Drag approach, we find that the WF wake extension is similar in both approaches.

a)

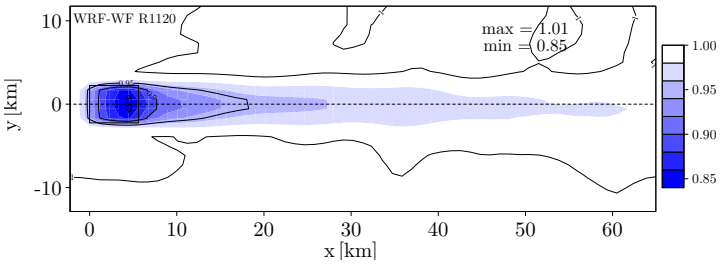

b)

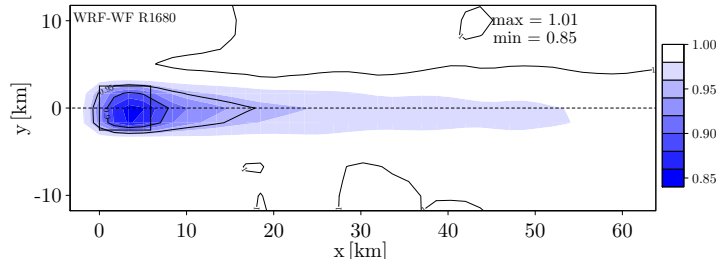

c)

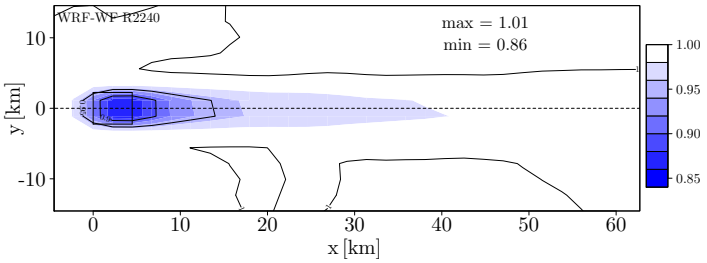

Figure 5: Identical to fig.(4), this time for the WRF-WF approach

EWP Scheme

We find from fig.(6) that the extension of the 10% velocity deficit level varies by circa 6% between the R1120 and R2240 simulation (∼8.0 km in the R1120 compared to ∼ 7.5,km in the R2240).

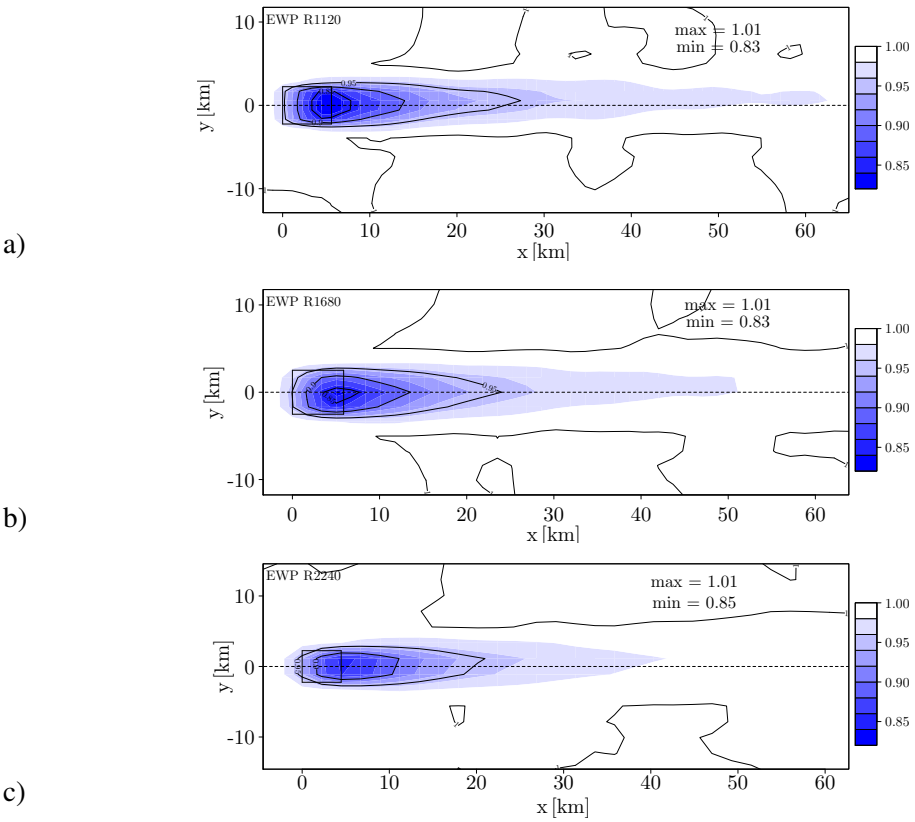

Figure 6: Identical to fig.(4), this time for the EWP scheme

Discussion and Conclusion

We analysed three WF approaches (Rotor Drag, WRF-WF and EWP) against long term averaged measurements from Horns Rev I.

For the near WF wake, fig.(3), we found that the velocity deficit was overestimated in the Rotor Drag approach, while in the WRF-WF approach it was too fast. The velocity deficit from the EWP scheme fitted the measurements well. Furthermore, we found that the Rotor Drag approach was the most sensitive to the horizontal resolution variation. The EWP scheme is shown to be sensitive to the horizontal resolution variation within the WF (1% difference), whereas the velocity deficits for the different resolutions converged already 2 km after the the WF. The horizontal resolution sensitivity within the WF was smaller for the WRF-WF. However, in the WF wake a slight sensitivity to the horizontal resolution was found. We have to remind ourselves that the turbine density per grid cell in this analysis was not constant in the R1680 and R2240 simulation.

Furthermore, we investigated also the horizontal resolution dependency of the WF wake extension. We found that the mesoscale model is not able to simulate the narrow (in cross-stream

direction) far WF wake velocity deficit. This leads to a shorter WF wake extension in the R2240 simulation for all the schemes. The near WF wake extension was less sensitive to the horizontal resolution in the Rotor Drag approach, followed by the EWP scheme (6%). In the WRF-WF the near WF wake extension varied around 40%.

Acknowledgements

Research has been funded in by EERA-DTOC FP7-ENERGY-2011-1/no 282797 and we would like to acknowledge Vattenfall AB and DONG Energy A/S for using data from the Horns Rev offshore wind-farm.

References

[1] Chamorro, L. P., Porté-Agel, F. *A Wind-Tunnel Investigation of Wind-Turbine Wakes: Boundary-Layer Turbulence Effects*. Boundary Layer Meteorology, 132:129-149, 2009.

[2] Nakanishi, M., and Niino, H.. *Development of an improved turbulence closure model for the atmospheric boundary layer*. Journal of the meteorological Society of Japan, 87:895-912, 2009.

[3] Skamarock, W., Klemp J., Dudhia J., Gill, D., Barker, D., Duda M., Huang X., Wang W., and Powers, J,. *A Description of the Advanced Research WRF Version 3*. NCAR Technical note, 2008.

[4] Volker, P. J. H., Badger, J., Hahmann, A. N., Ott S. *Implementation and Evaluation of a Wind Farm Parametrisation in a Mesoscale Model*. submitted.

[5] Hansen, K.S., et al., *The impact of turbulence intensity and atmospheric stability on power deficits due to wind turbine wakes at Horns Rev wind farm*. Wind Energy, 2012. 15(1):183-196, 2012.

LARGE-EDDY SIMULATION BASED STUDY OF OFFSHORE WIND TURBINE ARRAY BOUNDARY LAYERS

D. Yang[1], C. Meneveau[1], L. Shen[2]†

[1]Johns Hopkins University, Department of Mechanical Engineering,
Baltimore, MD 21218, USA, di_yang@jhu.edu, meneveau@jhu.edu
[2]University of Minnesota, Department of Mechanical Engineering and
St. Anthony Falls Laboratory, Minneapolis, MN 55455, USA, shen@umn.edu

ABSTRACT

A hybrid numerical model is developed for the simulation of offshore wind farms. In the model, the wind turbulence is simulated using the large-eddy simulation technique; the ocean wave field is simulated using a potential-flow based method; and the wind and wave simulations are coupled through a two-way feedback scheme. The effect of wind turbines on the wind field is represented by an actuator disk model. Using this numerical model, the effect of ocean waves on the wind farm dynamics is studied by considering a variety of fully-developed and fetch-limited wind-sea conditions. The simulation results indicate that the offshore wind farm obtains a higher wind power extraction rate under the fully-developed wind-sea condition compared with the fetch-limited condition.

INTRODUCTION

Having larger available space, higher wind energy, and relatively less visual impact and noise, offshore wind power has become a new frontier of wind energy study. Unlike their land-based counterparts, offshore wind farms are operated in a complex environment in which the sea surface is covered by progressive surface waves of various sizes that interact with the wind over a wide range of scales. Thus, better understanding of the offshore wind farm dynamics and accurate predictions of offshore wind farm performance require consideration of turbine–wind–wave coupling dynamics.

In recent years, advancements in large-eddy simulation (LES) of atmospheric flows combined with wind turbine models have made LES a useful tool for wind energy research (e.g., Jimenez *et al.* [1, 2]; Troldborg *et al.* [3]; and Wu and Porté-Agel [4]). By performing LES of a wind turbine array with periodic lateral boundary conditions, Calaf *et al.* [5] were able to capture the complex interaction of wind turbine wakes as well as the large-scale interaction between the wind farms and the atmospheric boundary layer. Particularly, their statistical analyses of the LES results revealed that for a fully developed wind turbine array boundary layer, the wind at

†Author to whom correspondence should be addressed.

the turbine rotor height obtains kinetic energy mainly through the vertical flux of energy from the atmosphere above, rather than from horizontal energy flux.

While wind power on land is being actively explored, there is a lack of LES tools for the simulation of offshore wind farms. In this study, a hybrid numerical capability is developed for the simulation of large-scale offshore wind farms. The numerical framework consists of: (i) a LES of wind turbulence on a curvilinear coordinate that follows the wave surface motion [6]; (ii) a spectral simulation of nonlinear sea-surface waves with high resolution, which is dynamically coupled with the wind LES [7]; and (iii) an actuator-disk model for the wind turbines. For the first time, these modeling tools are coupled in the simulation to capture the complex flow physics of the offshore wind farms.

Following Calaf *et al.* [5], in our simulation, a very large wind farm is modeled with an "infinite" turbine array (by means of periodic boundary conditions in the horizontal directions). The turbine array boundary layer is considered to be fully developed. The sea surface is covered by wind-generated wave field, with both fetch-limited condition and fully-developed condition being considered. For the wind farm configuration, various streamwise spacing (i.e. $s_x = 10.5$, 7, and 5.25, with s_x being the ratio of streamwise turbine spacing to the turbine diameter) are investigated. Based on the simulation data, the characteristics of offshore wind turbine array boundary layer are studied.

This paper is organized as follows. First, the numerical method used in our hybrid model is introduced, followed by the validation of the model. Next, the problem setup and the parameters for the simulation cases are discussed. The results of these cases are then analyzed to study the effect of ocean waves on wind farm dynamics. Finally, conclusions are given.

NUMERICAL METHOD

For the wind field, we consider a neutrally stratified atmospheric boundary layer flow in a horizontally periodic domain. The coordinate system is denoted as $x_i(i = 1,2,3) = (x,y,z)$, where x and y are the horizontal coordinates and z is the vertical coordinate, with $z = 0$ being the mean sea surface. The velocity components in x-, y-, and z-directions are denoted as $u_i(i = 1,2,3) = (u,v,w)$, respectively.

In LES, the motion of wind turbulence is described by the filtered Navier–Stokes equations for incompressible flows,

$$\frac{\partial \widetilde{u}_i}{\partial t} + \widetilde{u}_j \frac{\partial \widetilde{u}_i}{\partial x_j} = -\frac{1}{\rho_a}\frac{\partial \widetilde{p}^*}{\partial x_i} - \frac{\partial \tau^d_{ij}}{\partial x_j} - \frac{1}{\rho}\frac{\partial p_\infty}{\partial x}\delta_{i1} + f_T \delta_{i1} \,, \tag{1}$$

$$\frac{\partial \widetilde{u}_i}{\partial x_i} = 0 \,. \tag{2}$$

Here, $(\widetilde{...})$ indicates filtering at the grid scale Δ; ρ_a is the density of air; $\tau_{ij} = \widetilde{u_i u_j} - \widetilde{u}_i \widetilde{u}_j$ is the subgrid-scale (SGS) stress tensor, and τ^d_{ij} is its trace-free part; and $\widetilde{p}^* = \widetilde{p} + \tau_{kk}/3 - p_\infty$ is the filtered modified pressure. In this study, we consider the condition of mean wind being perpendicular to the wind turbine rotor plane, i.e. along the $+x$-direction. The imposed pressure gradient $\partial p_\infty/\partial x$ models the effect of geostrophic wind forcing [5]. The friction velocity for the

wind above the turbine array is thus $u_* = \sqrt{-\overline{H}(\partial p_\infty/\partial x)/\rho_a}$, where $\overline{H}$ is the height of the top boundary of the simulation domain with respect to the mean sea surface.

In this study, we consider the sea surface being covered by pure wind-generated waves. Under such conditions, the floating offshore wind turbine platforms from many of the practical designs, e.g., the MIT/NREL TLP [8] and the WindFloat [9], result in only small motions in response to the wind and waves. Therefore, in this study, we neglect the motions of the platform and assume the wind turbines to be fixed in space. The turbine-induced force in Eq. (1), f_T, is calculated by the actuator-disk model originally applied in LES by Jimenez *et al.* [1, 2]. In the present study, we use the modified version proposed by Meyers and Meneveau [10]. In this model, the turbine induced force per unit mass in the streamwise direction is given by

$$f_T(x_i,y_j,z_k) = -\frac{1}{2}\frac{C_T}{(1-a)^2}\langle u^T\rangle_d^2\frac{\gamma_{j,k}}{\Delta x}\,. \tag{3}$$

Here, (x_i,y_j,z_k) denotes the position of a given grid point with index (i,j,k); $C_T = 3/4$ is the thrust coefficient and $a = 1/4$ is the induction factor [1, 5]; $\langle u^T\rangle_d$ is the local reference wind velocity evaluated by spatial averaging over all grid points within the turbine disk; $\gamma_{j,k}$ is the fraction of area overlap between the grid cell (j,k) and the turbine rotor circle; and Δx is the streamwise grid size.

In Eq. (1), the SGS stress tensor is modeled using the Lagrangian-averaged scale-dependent dynamic Smagorinsky model, as described in Bou-Zeid *et al.* [11]. On the other hand, the molecular viscous term is neglected because the Reynolds number for the flows considered in this study is very high. This also prevents the resolving of the turbulence boundary layer near the wave surface. Consequently, in the simulation, a surface-layer model is employed to impose proper sea-surface stress to the wind turbulence, which is expressed as [11]

$$\tau_{i3}^{SGS}(x,y,t) \;=\; -\left[\frac{\kappa}{\ln(d_2/z_0)}\right]^2\widehat{\widetilde{U}}_r(x,y,t)\widehat{\widetilde{u}}_{r,i}(x,y,t)\,,\quad i=1,2\,. \tag{4}$$

Here, $\kappa = 0.4$ is the von Kármán constant; $\widehat{\widetilde{(...)}}$ indicates filtering at the test-filter scale 2Δ; z_0 is the sea-surface roughness associated with the SGS waves; $\widehat{\widetilde{u}}_{r,i}$ are the filtered horizontal wind velocities relative to the water surface at the first off-surface grid-point (i.e., in the LES code, at height d_2 above the sea surface),

$$\widehat{\widetilde{u}}_{r,i}(x,y,t) = \widehat{\widetilde{u}}_i(x,y,d_2,t) - \widehat{\widetilde{u}}_{s,i}(x,y,t)\,,\quad i=1,2\,. \tag{5}$$

Here, the values of $\widehat{\widetilde{u}}_{s,i}$ are obtained by the test-filtering of the sea surface velocities $u_{s,i}$; and

$$\widehat{\widetilde{U}}_r(x,y,t) = \sqrt{\left[\widehat{\widetilde{u}}_r(x,y,t)\right]^2 + \left[\widehat{\widetilde{v}}_r(x,y,t)\right]^2} \tag{6}$$

is the magnitude of horizontal wind velocity relative to the wave surface.

In the simulations, the streamwise and spanwise boundaries are treated as periodic, so that the finite number of wind turbines in the simulation domain represent a subset of an infinitely large wind farm [5]. The top of the simulation domain is considered to be rigid and slip-free.

The bottom is bounded by the wave surface, with von Neumann condition for the velocity field given by Eq. (4). A time-dependent boundary-fitted grid is used to follow the curvature of the wave surface. The irregular wave surface-bounded domain in the physical space is transformed to a right rectangular prism in the computational space using an algebraic mapping [6].

For spatial discretization, we use a Fourier-series-based pseudo-spectral method on a collocated grid in the horizontal directions, and a second-order finite-difference method on a staggered grid in the vertical direction. The governing equations are integrated in time with a fractional-step method. First, the momentum equations without the pressure terms are advanced in time with a second-order Adams–Bashforth scheme. Then, a Poisson equation is solved for the pressure to provide correction for the velocity field so that the incompressibility constraint is satisfied. The effect of resolved-scale sea-surface waves on the wind field, i.e. the form drag, is captured by this wave-correlated pressure field. The details and validations of the numerical scheme are provided in Yang and Shen [6].

The motion of the sea-surface waves is simulated using a high-order spectral method (HOSM) [12]. The HOSM simulates nonlinear waves using the Zakharov formulation [13], in which the wave motion is described by the surface elevation η and the surface potential Φ^s. Here, $\Phi^s = \Phi(x,y,z=\eta(x,y,t),t)$ with Φ being the velocity potential. With a perturbation series of Φ with respect to the wave steepness to the order of M and Taylor series expansion about the mean water level $z=0$,

$$\Phi^s(x,y,t) = \sum_{m=1}^{M} \sum_{\ell=0}^{M-m} \frac{\eta^\ell}{\ell!} \frac{\partial^\ell}{\partial z^\ell} \Phi^{(m)}(x,y,z,t)\bigg|_{z=0} , \tag{7}$$

and an eigenfunction expansion of each $\Phi^{(m)}$ with N modes,

$$\Phi^{(m)}(x,y,z,t) = \sum_{k=1}^{N} \Phi_k^{(m)}(t) \Psi_k(x,y,z) , \tag{8}$$

the kinematic and dynamic free surface boundary conditions are written as [12]

$$\frac{\partial \eta}{\partial t} = -\nabla_h \eta \cdot \nabla_h \Phi^s + \left(1+|\nabla_h \eta|^2\right) \left[\sum_{m=1}^{M} \sum_{\ell=0}^{M-m} \frac{\eta^\ell}{\ell!} \sum_{k=1}^{N} \Phi_k^{(m)} \frac{\partial^{\ell+1} \Psi_k}{\partial z^{\ell+1}}\bigg|_{z=0} \right] , \tag{9}$$

$$\frac{\partial \Phi^s}{\partial t} = -g\eta - \frac{|\nabla_h \Phi^s|^2}{2} - \frac{p_a(x,y,t)}{\rho_w} + \frac{1+|\nabla_h \eta|^2}{2} \left[\sum_{m=1}^{M} \sum_{\ell=0}^{M-m} \frac{\eta^\ell}{\ell!} \sum_{k=1}^{N} \Phi_k^{(m)} \frac{\partial^{\ell+1} \Psi_k}{\partial z^{\ell+1}}\bigg|_{z=0} \right]^2 . \tag{10}$$

In this paper, we consider deep water waves, for which the eigenfunctions Ψ_k are

$$\Psi_k(x,y,z) = \exp\left(|\mathbf{k}| z + \mathrm{i}\mathbf{k}\cdot\mathbf{x}\right) . \tag{11}$$

Here $\mathrm{i} = \sqrt{-1}$; and $\mathbf{k} = (k_x, k_y)$ is the wavenumber vector, which is related to the scalar wavenumber k through $k = |\mathbf{k}| = \sqrt{k_x^2 + k_y^2}$. In HOSM, Eqs. (9) and (10) are advanced in time by a fourth-order Runge–Kutta scheme. The equations are discretized in space by a Fourier-series-based pseudo-spectral method. The quadratic terms are de-aliased with the $3/2$ rule. The HOSM simulation of sea-surface wave field is coupled with the LES of wind turbulence through a

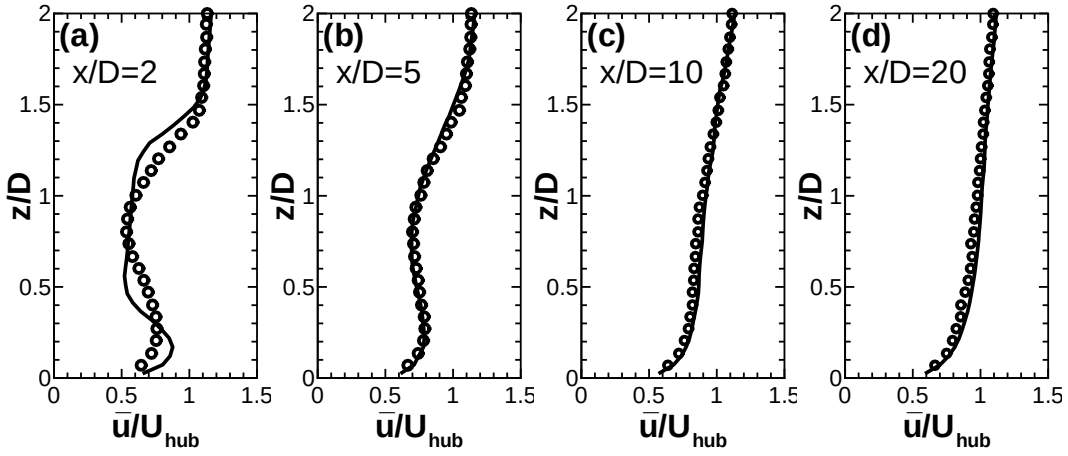

Figure 1: Vertical profiles of time-averaged velocity $\bar{u}$ at the central cross-section of the wake behind a single turbine at four downstream locations: (*a*) $x/D = 2$; (*b*) $x/D = 5$; (*c*) $x/D = 10$; and (*d*) $x/D = 20$. Here, D is the diameter of the turbine rotor, and U_{hub} is the mean inflow wind velocity measured at $1D$ upstream of wind turbine hub. The wind tunnel measurement data of Chamorro and Porté-Agel [16] is denoted by ∘, and the current LES result is denoted by ——.

fractional-step scheme. Details and validations of the coupling scheme are given in Yang and Shen [7].

VALIDATION

The current turbulence flow solver has been tested extensively for various wind–wave problems [14, 15, 6, 7]. Therefore, the validation of wind–wave interaction simulation is not taken up in this paper. Here, we focus on the validation of wind turbine modeling by comparing the current LES result with existing experimental data in the literature.

We perform a LES of air flow past a single wind turbine, with the parameters matching those in the laboratory measurement of Chamorro and Porté-Agel [16]. The wind turbine has a diameter of $D = 0.15\,\text{m}$ and a hub height of $H_{\text{hub}} = 0.125\,\text{m}$. The mean inflow velocity (measured at $1D$ upstream of wind turbine hub) is $U_{\text{hub}} = 2.2\,\text{m/s}$. The wind friction velocity is $u_* = 0.102\,\text{m/s}$. The bottom boundary is flat and has a surface roughness of $0.03\,\text{mm}$. The simulation domain has a size of $(L_x, L_y, \overline{H}) = (4.32, 0.72, 0.46)\,\text{m}$. The domain is sufficiently long in the streamwise direction ($L_x/D = 28.8$), so that the effect of periodic boundary condition on the statistics of the inflow wind towards the turbine rotor is negligibly small. The grid resolution is $N_x \times N_y \times N_z = 256 \times 48 \times 64$, with evenly distributed grid points in all of the three directions.

Figure 1 shows the vertical profiles of time-averaged streamwise velocity $\bar{u}$ at the central cross-section of the turbine wake. LES results at $x/D = 2$, 5, 10, and 20 are shown. The wind-tunnel measurement data from Chamorro and Porté-Agel [16] are plotted for comparison. Using an actuator-disk model of the wind turbine, the current LES captures the velocity deficit in the wake behind the turbine rotor ($0.33 < z/D < 1.33$, with the center of turbine rotor at $z/D =$

Table 1: Parameters of wave spectra for the HOSM simulations. Here, U_{10} is the mean wind velocity at the height of 10 m above the mean water level; and F is the distance over which the wind has been blowing the water surface. At the peak of the wave spectra (denoted by the subscript 'p'), k_p is the wavenumber; and c_p is the wave phase speed.

wave spectrum	U_{10} (m/s)	F (km)	k_p (m^{-1})	c_p (m/s)
JONSWAP	12.5	80.0	0.1	9.7
P–M	12.5	∞	0.04	15.3

$H_{\text{hub}}/D = 0.83$). The magnitude of velocity deficit obtained by the current LES agrees with the measurement data. In the near-turbine region (figure 1*a*), the LES result shows a relatively flat velocity profile within the turbine rotor region. This flattening is caused by the use of the disk-averaged reference velocity in the actuator-disk model when calculating the turbine-induced force (Eq. 3). Similar LES results have also been reported by Wu and Porté-Agel [4]. At the further downstream locations (Fig. 1*b*), the mean wind velocity profiles obtained by the LES agrees very well with the wind-tunnel measurement data. Due to the turbulent mixing, the mean velocity at hub height recovers and increases to $0.70\,U_{\text{hub}}$ at $x/D = 5$, compared with $0.56\,U_{\text{hub}}$ at $x/D = 2$.

PROBLEM SETUP

For the simulation of offshore wind farms, we consider a turbulent wind turbine array boundary layer over an open sea area. For the sea-surface wave field, we consider both fetch-limited and fully-developed sea conditions. For a wind-sea with limited fetch (defined as the distance of waves being blown by wind, and denoted by F), we use the wave spectrum obtained during the Joint North Sea Wave Observation Project (JONSWAP) [17]. For a fully developed sea, its surface wave field satisfies the Pierson–Moskowitz (P–M) spectrum [18]. In this study, we consider an environmental wind field (before encountering the wind farm) with a mean wind velocity of $U_{10} = 12.5$ m/s at the height of 10 m above the mean water level. The key parameters of the corresponding wave fields for the given wind condition are listed in Table 1.

For the LES of offshore wind farms, we consider an $N_{\text{row}} \times 3$ wind turbine array within the simulation domain, which is a periodic representation of a large wind farm under fully developed condition. Here, N_{row} is the number of turbine rows (in the streamwise direction) in the simulation domain, and three values of $N_{\text{row}} = 2$, 3, and 4 are considered in this study. For these three values of N_{row}, the cases for JONSWAP wave condition are named as J2, J3, and J4, respectively; the cases for P–M wave condition are named as PM2, PM3, and PM4, respectively. The wind turbines have a hub height of $H_{\text{hub}} = 100$ m and a rotor diameter of $D = 100$ m. The computational domain of the LES has a size of $(L_x, L_y, \overline{H}) = (2.1, 1.5, 1.0)$ km, so that the streamwise wind turbine spacing parameter is $s_x = (L_x/N_{\text{row}})/D = 10.5$, 7.0, and 5.25 for $N_{\text{row}} = 2$, 3, and 4, respectively; and the spanwise spacing parameter has a fixed value of $s_y = (L_y/3)/D = 5.0$. The bottom of the wind field is bounded by sea-surface waves and has a prescribed value of 2.0×10^{-4} m for the subgrid-scale sea-surface roughness z_0, consistent with typical observed values [19, 20].

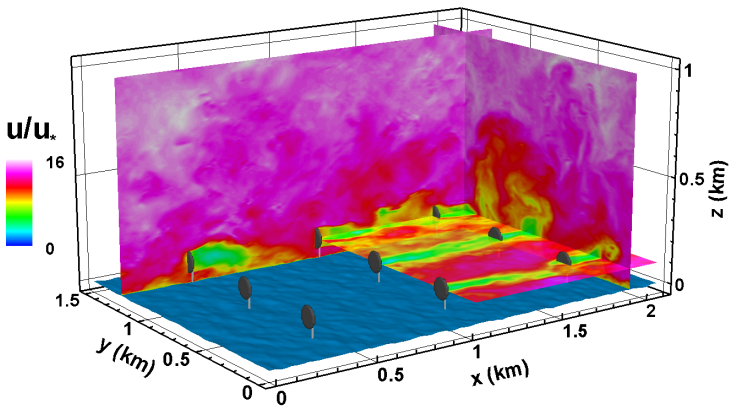

Figure 2: Illustration of three-dimensional flow field in the fully developed wind turbine array boundary layer over water waves for case PM3. Contours of instantaneous streamwise velocity u (normalized by u_*) are plotted on the three representative (x,y)-, (x,z)-, and (y,z)-planes. For the visualization of sea-surface waves, only half of the (x,y)-plane is shown.

For the LES, we use a grid resolution of $N_x \times N_y \times N_z = 192 \times 128 \times 192$, with evenly spaced grid in all of the three directions. For the HOSM, a higher horizontal grid resolution of $N_x \times N_y = 512 \times 384$ is used to resolve the energy-containing wave modes in the spectra. During the early stage of each simulation, the imposed pressure gradient Π in Eq. (1) is fine-tuned to approach a steady-state constant value so that the mean velocity at the top boundary U_{top} remains the same constant value among different cases. As a result, the wind turbine array boundary layer satisfies the desired geostrophic wind condition [5]. An example of the results of case PM3 is shown in Fig. 2.

We note that after the dynamically coupled wind and waves encounter the offshore wind farm, the wind speed near the sea surface is reduced and the waves near the spectrum peak propagate a bit faster than the wind. Therefore, within the wind farm region, the sea-surface wave field is effectively in a "fully developed" condition for both JONSWAP and P–M cases [18]. Under such condition, the wave field is able to maintain its basic spectral form without significant growth or decay. Thus the horizontally periodic boundary condition for both the wind farm and the wave field serves as a reasonable assumption in the current LES.

RESULTS

For wind blowing over waves, the total streamwise stress acting on the wind at the sea surface consists of two components, i.e.

$$\tau_{\text{total}} = \underbrace{-\frac{\rho}{A}\iint_A \tau_{xz}^{SGS}\,\mathrm{d}x\mathrm{d}y}_{\tau_s} + \underbrace{\frac{1}{A}\iint_A \widetilde{p}_s\frac{\partial\widetilde{\eta}}{\partial x}\,\mathrm{d}x\mathrm{d}y}_{\tau_p}\,. \tag{12}$$

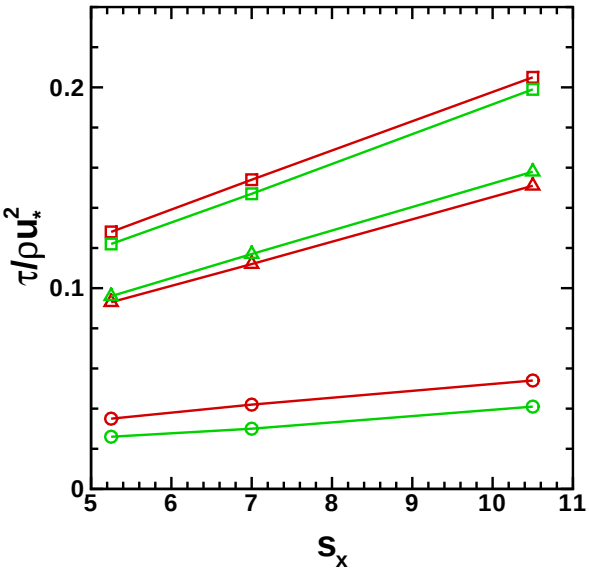

Figure 3: Budget of sea-surface stress as a function of streamwise turbine spacing s_x: △, surface shear stress τ_s; ○, wave form drag τ_p; and □, total surface stress τ_{total}. Results for JONSWAP wave condition are denoted by red color; results for P–M wave condition are denoted by green color.

Here, τ_s is the surface shear stress, with τ_{xz}^{SGS} given by Eq. (4); τ_p is the wave form drag, with $\widetilde{p}_s$ being the air pressure acting on the wave surface; and A is the total horizontal sea-surface area in the simulation domain.

Figure 3 shows the sea-surface stress budget for the various LES cases (represented as a function of s_x). Compared with the corresponding P–M wave cases, the JONSWAP wave cases have slightly smaller shear stress but larger wave form drag and total surface stress. Note that the dominant waves in the P–M cases are longer than those in the JONSWAP cases. Based on the dispersion relation of water waves, the dominant waves in the P–M cases are faster. Faster waves have smaller relative velocity with respective to the wind above. As a result, P–M cases have less wave form drag than JONSWAP cases. The current LES result is consistent with the results of previous studies on wind–wave interaction, which showed that faster waves induce smaller resistance to the wind [21]. Moreover, for a given wave condition, the turbine number per unit surface area increases as the streamwise turbine spacing s_x decreases. This results in an increase of turbine-induced stress and consequently a decrease of total surface stress τ_{total} (when normalized by the external wind friction velocity u_* above the turbine layer).

For the study of offshore wind farm dynamics, a key quantity to investigate is the power extraction rate of the wind farm. Based on the LES results, the power extracted by the wind turbines can be calculated directly based on the turbine induced force and wind velocity. Following

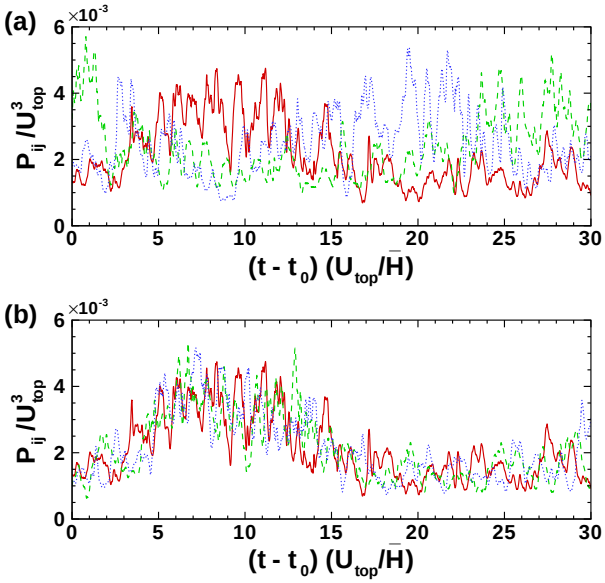

Figure 4: Extracted wind power density for wind turbines at different columns (denoted by 'c') and rows (denoted by 'r') for case J3. In (a), the three wind turbines in the first row are shown: red solid line, $(c1, r1)$; green dashed line, $(c2, r1)$; and blue dotted line, $(c3, r1)$. In (b), the three wind turbines in the first column are shown: red solid line, $(c1, r1)$; green dashed line, $(c1, r2)$; and blue dotted line, $(c1, r3)$. Here, U_{top} is the mean wind velocity at the top of the simulation domain; and t_0 is the time when statistical sampling starts.

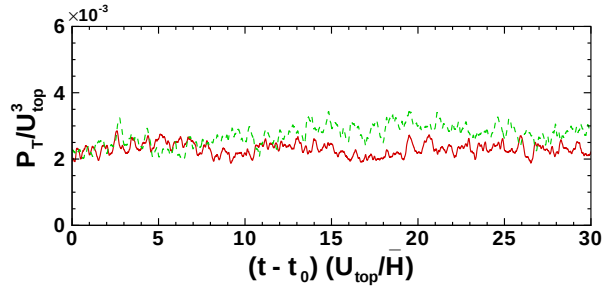

Figure 5: Averaged extracted power density of the wind farm for two different wave conditions: red solid line, J3; and green dashed line, PM3. Here, U_{top} is the mean wind velocity at the top of the simulation domain; and t_0 is the time that statistical sampling starts.

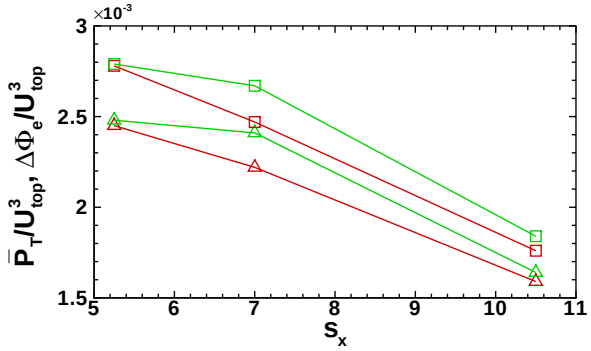

Figure 6: Time-averaged extracted power density of the wind farm and vertical flux of kinetic energy into the wind farm: △, $\overline{P}_T$; and □, $\Delta\Phi_e$. Results for JONSWAP wave condition are denoted by red color; results for P–M wave condition are denoted by green color.

Calaf *et al.* [5], the extracted power density by an individual wind turbine is defined as [5]

$$P_{ij} = \frac{\left(\frac{1}{2}C_T\frac{\pi}{4}D^2\langle u^T\rangle_d^3\right)_{ij}}{s_x s_y D^2}\,, \tag{13}$$

where the subscript 'ij' denotes the turbine at the i-th row and j-th column. The averaged extracted wind power density over the entire wind farm is then calculated as

$$P_T = \frac{1}{N_{\rm row}N_{\rm col}}\sum_{i=1}^{N_{\rm row}}\sum_{j=1}^{N_{\rm col}} P_{ij}\,. \tag{14}$$

As illustrated in Fig. 2, there exists large spatial variation for the instantaneous wind field around different wind turbines, caused by the complex interactions among the turbines within the turbine array as well as their interactions with the atmospheric boundary layer. Consequently, the extracted power densities P_{ij} by different turbines exhibit appreciable variation, as shown in Fig. 4. Particularly, the variation of P_{ij} among turbines in different columns is significant in both long and short terms (Fig. 4*a*); the variation of P_{ij} among turbines in different rows is mainly in short term, and the long term variation is relatively small (Fig. 4*b*). Figure 5 shows the averaged power extraction rate P_T of the entire wind farm for cases J3 and PM3. The averaged performance of the entire wind farm has much less temporal variation than those of the individual turbines shown in Fig. 4.

The time-averaged values of P_T for various cases are calculated and plotted in Fig. 6. For a given turbine spacing, a wind farm above P–M waves extracts more power than that above JONSWAP waves. This increase of wind farm performance is caused by the stronger wave motion in the P–M wave cases compared with the JONSWAP wave cases. In the wake region behind each wind turbine, the strong deficit of wind speed causes waves to feed momentum back to wind. As shown in Table 1, under the same wind forcing, the fully-developed (P–M) wave field has larger peak wave phase speed than the fetch-limited (JONSWAP) wave field. As a result, within the turbine wake regions, the P–M waves have relatively stronger capability to help

recover the wind speed; out of the wake regions, the wind field experiences less wave resistance in the P–M wave cases than in the corresponding JONSWAP wave cases, resulting in slightly larger wind velocity near the wave surface as well as at the turbine rotor height. The turbines above the P–M waves thus have larger incident wind energy and achieve higher performance than the turbines above the JONSWAP waves.

When the streamwise turbine spacing decreases from $s_x = 10.5$ to $s_x = 7$, the near-surface wind velocity decreases and the long waves in the wave field become faster relative to the wind, resulting in an enhancement of the wave effect. Therefore, the difference of P_T between cases J3 and PM3 is larger than the difference between cases J2 and PM2. As the turbine spacing further decreases to $s_x = 5.25$, the distance between turbines is too small so that the waves in neither the P–M nor the JONSWAP cases have sufficient time to help recover the wind speed deficit in the turbine wake regions, thus resulting in insignificant difference between cases J4 and PM4.

Calaf *et al.* [5] showed that a large wind farm gains energy supplement mainly by the vertical flux of kinetic energy from the wind above it. The net kinetic energy flux into the wind farm can be calculated by

$$\Delta\Phi_e = \left[\left(-\langle\overline{u'w'}\rangle - \langle\overline{u}''\overline{w}''\rangle\right)\langle\overline{u}\rangle\right]\Big|_{z=H_{\rm hub}+D/2}^{z=H_{\rm hub}-D/2} . \tag{15}$$

Here, the overbar $\overline{u}_i$ denotes the time averaging; the brackets $\langle u_i\rangle$ denotes the horizontal averaging; $u_i' = u_i - \overline{u}_i$ denotes the fluctuating velocity due to temporal variation; and $u_i'' = u_i - \langle\overline{u}_i\rangle$ denotes the fluctuating velocity due to both temporal and spatial variations. The values of $\Delta\Phi_e$ for various cases are also plotted in Fig. 6, which show consistent trend as $\overline{P}_T$ when s_x changes. For all the cases, the values of $\overline{P}_T$ and $\Delta\Phi_e$ are close, indicating the balance between the vertical energy flux and the turbine power extraction. The difference among them is caused mainly by kinetic energy dissipation through turbulence.

CONCLUSIONS

Offshore wind energy has become an important frontier of sustainable energy research. In this study, LES of wind turbulence coupled with potential flow simulation of ocean waves is performed for offshore wind farms. LES of the lower atmospheric boundary layer over ocean waves is performed using a boundary-fitted grid that follows the wave motion. The nonlinear evolution of the wave field is simulated using a high-order spectral method. Large wind farms are modeled as periodic wind turbine arrays, with the effect of turbines on the wind modeled using an actuator disc method. Statistical analysis of the wind farm dynamics shows that the wind field is influenced by the sea-surface waves due to the effect of wave-induced form drag. As a result, the energy extraction rate of the wind turbines varies with wave condition, with a higher extraction rate being obtained over fully-developed wind-sea conditions than over fetch-limited, developing wind-sea conditions.

ACKNOWLEDGEMENT

DY and LS acknowledge the support of NSF-CBET-1133700 and ONR-N00014-09-1-0395. CM acknowledges the support of NSF-AGS-1045189 and NSF-OISE-1243482.

REFERENCES

[1] A. Jimenez, A. Crespo, E. Migoya, and J. Garcia, "Advances in large-eddy simulation of a wind turbine wake," Journal of Physics: Conference Series **75**, 012041 (2007).

[2] A. Jimenez, A. Crespo, E. Migoya, and J. Garcia, "Large-eddy simulation of spectral coherence in a wind turbine wake," Environmental Research Letters **3**, 015004 (2008).

[3] N. Troldborg, J. N. Sorensen, and R. Mikkelsen, "Numerical simulations of wake characteristics of a wind turbine in uniform inflow," Wind Energy **13**, 86 (2010).

[4] Y.-T. Wu and F. Porté-Agel, "Large-eddy simulation of wind-turbine wakes: evaluation of turbine parametrisations," Boundary-Layer Meteorol. **138**, 345 (2011).

[5] M. Calaf, C. Meneveau, and J. Meyers, "Large eddy simulation study of fully developed wind-turbine array boundary layers," Phys. Fluids **22**, 015110 (2010).

[6] D. Yang and L. Shen, "Simulation of viscous flows with undulatory boundaries. Part I: Basic solver," J. Comput. Phys. **230** 5488 (2011).

[7] D. Yang and L. Shen, "Simulation of viscous flows with undulatory boundaries. Part II: Coupling with other solvers for two-fluid computations," J. Comput. Phys. **230** 5510 (2011).

[8] E. N. Wayman, P. D. Sclavounos, S. Butterfield, J. Jonkman, and W. Musial, "Coupled dynamic modeling of floating wind turbine systems," Proceedings of the offshore technology conference, Houston, Texas, 1–4 May 2006.

[9] D. Roddier, C. Cermelli, A. Aubault, and A. Weinstein, "WindFloat: A floating foundation for offshore wind turbines," J. Renewable Sustainable Energy **2**, 033104 (2010).

[10] J. Meyers and C. Meneveau, "Large eddy simulation of large wind-turbine arrays in the atmospheric boundary layer," Proceedings of the 48th AIAA Aerospace Sciences Meeting Including the New Horizons Forum and Aerospace Exposition, AIAA 2010–827 (2010).

[11] E. Bou-Zeid, C. Meneveau, and M. Parlange, "A scale-dependent lagrangian dynamic model for large eddy simulation of complex turbulent flows," Phys. Fluids **17**, 025105 (2005).

[12] D. G. Dommermuth and D. K. P. Yue, "A high-order spectral method for the study of nonlinear gravity waves," J. Fluid Mech. **184**, 267 (1987).

[13] V. E. Zakharov, "Stability of periodic wave of finite amplitude on the surface of a deep fluid," J. Appl. Mech. Tech. Phys. **2** 190 (1968).

[14] D. Yang and L. Shen, "Characteristics of coherent vortical structures in turbulent flows over progressive surface waves," Phys. Fluids **21** 125106 (2009).

[15] D. Yang and L. Shen, "Direct-simulation-based sutdy of turbulent flow over various waving boundaries," J. Fluid Mech. **650** 131 (2010).

[16] L. P. Chamorro and F. Porté-Agel, "Effects of thermal stability and incoming boundary-layer flow characteristics on wind-turbine wakes: a wind-tunnel study," Boundary-Layer Meteorol. **136**, 515 (2010).

[17] K. Hasselmann, T. P. Barnett, E. Bouws, H. Carlson, D. E. Cartwright, K. Enke, J. A. Ewing, H. Gienapp, D. E. Hasselmann, P. Kruseman, A. Meerburg, P. Müller, D. J. Olbers, K. Richter, W. Sell, and H. Walden, "Measurements of wind-wave growth and swell decay during the Joint North Sea Wave Project (JONSWAP)," Dtsch. Hydrogr. Z. Suppl. **8**, N12 (1973).

[18] W. J. Pierson and L. Moskowitz, "A proposed spectral form for fully developed wind seas based on the similarity theory of S. A. Kitaigordskii," J. Geophys. Res. **69**, 5181 (1964).

[19] P. P. Sullivan, J. E. Edson, T. Hristov, and J. C. McWilliams, "Large-eddy simulations and observations of atmospheric marine boundary layers above nonequilibrium surface waves," J. Atmos. Sci. **65**, 1225 (2008).

[20] P. P. Sullivan and J. C. McWilliams, "Dynamics of winds and currents coupled to surface waves," Annu. Rev. Fluid Mech. **42**, 19 (2010).

[21] S. E. Belcher and J. C. R. Hunt, "Turbulent flow over hills and waves," Annu. Rev. Fluid Mech. **30**, 507 (1998).

COMPARISON OF ENERGY FLUXES IN TWO-BLADED AND THREE-BLADED MODEL WIND TURBINE ARRAYS

D. McKeon[1], A. Newman[1], E. Camp[2], M. Melius[2], R. Cal[2], L. Castillo[1]

[1]Texas Tech University, Department of Mechanical Engineering, Box 41021, Lubbock, TX, 79409, dalton.mckeon@ttu.edu
[2]Portland State University, Department of Mechanical and Materials Engineering, P.O. Box 751, Portland, OR, 97207-0751

ABSTRACT

Understanding the interactions of wind turbine arrays with the atmospheric boundary layer is necessary for many issues involved, including turbine siting and array power prediction. Although three-bladed turbines dominate the onshore market, two-bladed wind turbines continue to be viable, especially in offshore applications. Understanding the influence of the number of rotor blades on the flow field through a wind turbine array is vital to wind turbine siting and increasing the installed capacity of wind energy. The goal of this study is to compare fluxes of turbulent kinetic energy in two arrays with the same spacing, where one utilizes two-bladed turbines and the other utilizes three-bladed turbines, in a wind tunnel. This wind tunnel study was performed at the Wind Energy and Turbulence laboratory at Portland State University. Both arrays have three turbines in the spanwise direction and four turbines in the streamwise direction; the spanwise spacing was 3D and the streamwise spacing was 6D. A particle image velocimetry (PIV) system is used to generate data planes along the centerline of the array. Contours of mean velocity, Reynolds stresses, energy flux, and energy dissipation are generated. In each array, the integrated flux gives consistent results through the array and similar patterns in the streamwise direction are seen in both arrays. These similar patterns may indicate that some scaling exists for the turbulent kinetic energy flux, but none is presented in this paper.

Introduction

As wind turbines are deployed in increasingly larger arrays, a greater understanding of the interactions between turbines and the atmospheric boundary layer is necessary. These interactions influence the transport of energy from upper to lower levels of the altered boundary layer. These interactions are even less understood when comparing two-bladed and three-bladed wind turbines operating in an array. This paper presents results from a wind tunnel study comparing the effects of two-bladed and three-bladed rotors on the fluxes of kinetic energy in an array. In previous works, three-bladed wind turbine arrays have been studied extensively, while several recent works have begun to investigate the role of fluxes of kinetic energy in energy recovery within the array.

In (Chamorro & Porté-Agel, 2011), a wind tunnel study of two wind turbine array layouts was performed. Both arrays were 3 X 10 and had spanwise spacing of 4D; one array had streamwise spacing of 5D while the other had streamwise spacing of 7D. Although energy fluxes were not investigated, the flow was found to be characterized by two regions above and below the top tip height. The region above top tip height was then found broken into an inner and outer layer, resulting in the prescription of a roughness length to the wind turbine array.

In order to investigate energy recovery between turbines, experiments were performed on arrays of model wind turbines. In (Cal, Lebrón, Castillo, Kang, & Meneveau, 2010) and (Lebron, Castillo, & Meneveau, 2012), PIV measurements of the volume surrounding the middle wind turbine in the last row of a 3 X 3 array were investigated with 7D spacing in the streamwise direction and 3D spacing in the spanwise direction. Flow characteristics were averaged on horizontal planes to compare with

analytical models. By integrating contributing terms in front and behind of the turbine, it was shown that turbulent kinetic energy flux was on the same order as the power produced by the turbine, illustrating the importance of vertical entrainment of energy from the atmosphere above.

Multiple large eddy simulations were performed in (Calaf, Meneveau, & Meyers, 2010), investigating multiple turbine layouts. Each simulation was run using periodic boundary conditions such that "fully developed" conditions were generated. For one layout, whose dimensions were 7.85D in the streamwise direction and 5.23D in the spanwise direction, an analysis similar to that performed in (Cal, Lebrón, Castillo, Kang, & Meneveau, 2010) was used to find contributing terms in the simulated data. It was again concluded that the main mechanism of energy recovery in the array was turbulent kinetic energy flux.

Although these studies have illustrated the importance of turbulent kinetic energy flux in an array, the effect on these fluxes of the number of blades on the rotor has not been quantified. Therefore, the goal of this paper is to demonstrate the differences in mean kinetic energy fluxes in model wind turbine arrays with two bladed and three bladed rotors.

Conservation Equations

Relevant terms for flow development are found through analysis of the Reynolds-averaged Navier-Stokes equation in the streamwise direction with atmospheric boundary layer assumptions included. In this case, x, y, and z are the streamwise, vertical, and spanwise directions, respectively, and u, v, and w are their corresponding velocities; velocities are separated into time-averaged and time-varying terms (eg $u = \overline{u} + u'$). Thrust forces from the turbine are included in the body force term, $\bar{f}_x$; because no analysis is carried out across a wind turbine, this term is effectively zero. Viscous terms are neglected as no analysis is performed near the wall.

$$\bar{u}\frac{\partial \bar{u}}{\partial x} + \bar{v}\frac{\partial \bar{u}}{\partial y} = -\frac{1}{\rho}\frac{d\bar{p}}{dx} - \frac{\partial}{\partial y}\overline{u'v'} + \bar{f}_x \tag{1}$$

When the momentum equation is multiplied by the mean streamwise velocity, the mechanical energy equation is produced. This is shown in Equation (2) where $\frac{1}{2}\bar{u}^2$ is the kinetic energy. In large arrays, the developing terms are expected to be small, and the important terms are expected to be those in Equation (3). $\overline{P_x}$ indicates the product of the streamwise velocity and the thrust force from the turbine; again, this term is zero when away from a wind turbine.

$$\bar{u}\frac{\partial \frac{1}{2}\bar{u}^2}{\partial x} + \bar{v}\frac{\partial \frac{1}{2}\bar{u}^2}{\partial y} = -\frac{\bar{u}}{\rho}\frac{d\bar{p}}{dx} - \frac{\partial}{\partial y}\left(\left(\overline{u'v'}\right)\bar{u}\right) + \overline{u'v'}\frac{\partial \bar{u}}{\partial y} + \overline{P_x} \tag{2}$$

$$0 \cong -\frac{\partial}{\partial y}\left(\bar{u}\left(\overline{u'v'}\right)\right) + \frac{\partial \bar{u}}{\partial y}\overline{u'v'} + \overline{P_x} \tag{3}$$

The quantities which will be measured and compared between two arrays are the mean velocity, $\bar{u}$, Reynolds shear stresses, $\overline{u'v'}$, turbulent kinetic energy flux, $\bar{u}(\overline{u'v'})$, and turbulent kinetic energy production, $\frac{\partial \bar{u}}{\partial y}(\overline{u'v'})$. These terms are shown to be significant to energy exchange by (Cal, Lebrón, Castillo, Kang, & Meneveau, 2010), (Lebron, Castillo, & Meneveau, 2012), and (Calaf, Meneveau, & Meyers, 2010). Because the focus of this paper is on vertical fluxes of mean kinetic energy, the pressure gradient is neglected, though it is noted that this term can contribute significantly in the energy transport in the streamwise direction. In the context of comparing number of blades, all terms

from Equation (3) will be evaluated. Further, due to the lack of spatial averaging in the spanwise direction, no dispersive stresses or fluxes are calculated.

Experimental Setup and Data Analysis

Measurements were performed at the Wind Energy and Turbulence Laboratory at Portland State University. A scaled atmospheric boundary layer was generated for both arrays. 2D PIV measurements were then performed along the centerline in the two-bladed and three-bladed arrays to characterize the flow field within the arrays, as in Figure 1. The experiment was performed in a closed loop wind tunnel with a 0.8 meter high, 1.2 meter wide, and 5 meter long test section. A boundary layer representing an atmospheric boundary layer was created using a passive grid, strakes, and surface roughness elements.

The turbines were arranged in a 3 X 4 array, with four turbines in the streamwise direction. Both arrays utilized 6D spacing in the streamwise direction and 3D spacing in the spanwise direction. The passive grid created turbulence through the flow profile, while strakes were utilized to generate a flow profile modeled on a neutrally-stratified atmospheric boundary layer. Nine strakes were cut from 12.7 mm thick acrylic plastic and distributed uniformly through the cross-section of the test section. Each strake has a higher blockage ratio near the floor, creating more shear. This allows for less upstream distance to develop an appropriate profile. Chains placed every 10.7 cm on the floor of the wind tunnel produced the desired surface roughness, each with a height of approximately 4 mm. Coriolis forces are neglected in this experiment.

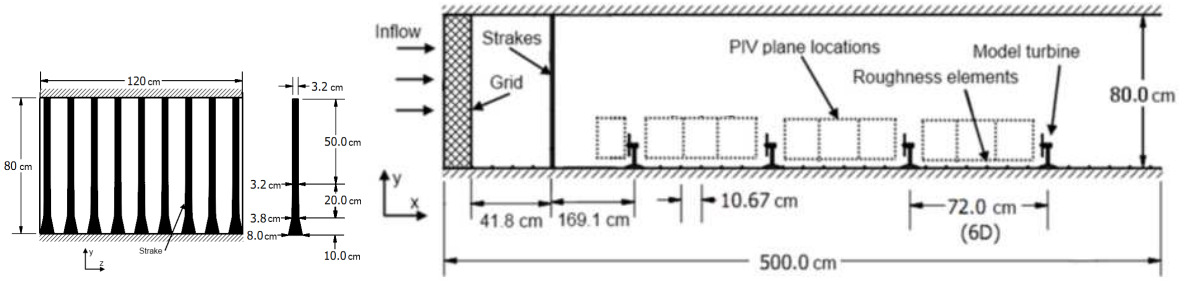

Figure 1. Experimental Layout

The model wind turbines for both cases were 12 cm diameter and 12 cm hub height. For both two-bladed and three-bladed rotors, the blade chord and twist profiles were held constant. Blades were twisted sheet metal, with 20º twist at the root and 15º twist at the tip. Only the number of blades was different between the two rotors, as seen in Figure 2.

The model wind turbines have been scaled down approximately 833 times when compared to a full scale wind turbine of 100 meter height and 100 meter diameter. The Reynolds number with respect to incoming wind speed and rotor diameter will not be matched between the model and full scale, so full dynamic similarity is not achieved; however, Reynolds number effects are known to be less significant when investigating large scale properties of turbulent flow rather than individual turbine performance.

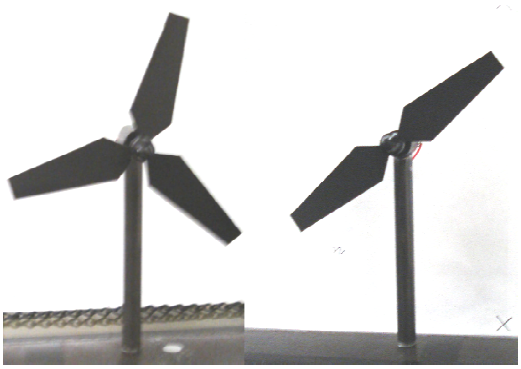

Figure 2. Two- and Three-Bladed Turbines

The coefficient of power, Cp, is defined in Equation (4); it is the ratio of power produced by the turbine to the mechanical power in the wind. To compare the effect of the number of blades in a rotor on flow development within an array, Cp is matched between the two rotors at each row. It was hypothesized that, if the power extracted from the flow was matched non-dimensionally, a scale could be found to match the power entrained in the array from the upper levels of the boundary layer.

In order to measure Cp, a torque sensor similar to that in (Kang & Meneveau, 2010) was used to measure the torque of the turbine, while the rotor frequency was measured using an optical sensor. A range of power levels were produced by varying the electrical load on the motor, while the incoming flow was held constant. This operation was performed first at the first row, after which a Cp was chosen for the first row. With the Cp fixed for the first row, power data was then collected at the second row. This allowed for constant inflow at each row.

$$C_P = \frac{P_{turbine}}{\frac{1}{2}\rho A u^3} = f\left(\lambda, \frac{h}{D}, \frac{1}{Re_D}, N\right) \tag{4}$$

Using dimensional analysis, it is found that Cp is a function of tip speed ratio λ (ie ratio of tip speed to inlet speed), ratio of height to diameter h/d, the Reynolds number based on diameter and inlet velocity Re_D, and the number of blades N. Matching Cp at each row resulted in Cp ranging from .13 to .15 throughout both arrays. Holding a constant Cp between two rotors with differing numbers of blades resulted in a different tip speed ratio for each.

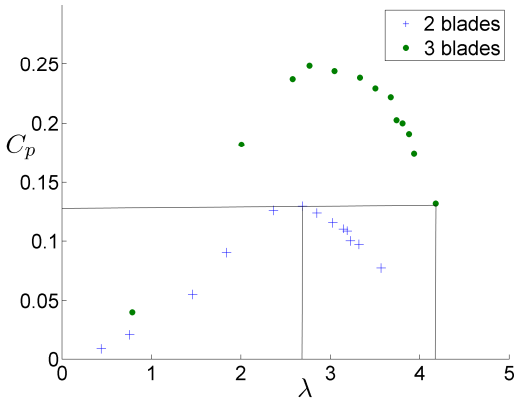

Figure 3. Cp Curve from Third Row, Illustrating Difference in Tip Speed Ratio

	P (W)	Cp	ω (hz)	λ
Row 1 2b	0.09	0.15	221	3
Row 1 3b	0.1	0.15	288	4
Row 2 2b	0.07	0.15	176	2.6
Row 2 3b	0.06	0.15	262	2.8
Row 3 2b	0.05	0.13	167	2.7
Row 3 3b	0.04	0.13	247	3.3
Row 4 2b	0.05	0.15	175	2.6
Row 4 3b	0.05	0.15	243	3.4

Table 1. Power and Cp Measurements through the Array

Although Cp is matched at each row, the characteristic drop in power is seen between each subsequent row in the streamwise direction, with power output reduced by ½ in the fourth row for both arrays. In both arrays, the frequency varies between each row. In the three bladed array, the frequency ranges from 243 to 288 hz, while in the two bladed array it ranges from 167 to 221 hz. The larger frequencies in the three bladed array are due to choosing to match Cp on the right hand side of the curve. Because $\lambda = \frac{\omega R}{u_{inlet}}$, choosing Cp values from the right hand side of the curve implies allowing the turbine to spin faster, thus torqueing the shaft less. This is a more feasible scenario than over-loading the turbine.

In order to calculate values for the flow characteristics and their development throughout the array, PIV measurements were taken along the centerline of the array. A LaVision PIV system was used with a laser sheet thickness between 1 and 1.5 mm. Time between laser pulses 100 μs. 2000 samples were taken at each plane and time averaged. A total of 10 planes were collected for each array.

Inlet conditions were calculated 1D upstream of the first row using PIV measurements. The velocity averaged over the rotor area was calculated to be approximately 4.5 m/s. The inlet velocity profile and Reynolds stresses are given below in Figure 4 and Figure 5. The inlet velocity conditions were nearly consistent with a scaled atmospheric boundary layer. There is some difference in the Reynolds shear stress values at the inlet; this is likely due to the higher blockage ratio of the three bladed rotors affecting the upstream flow.

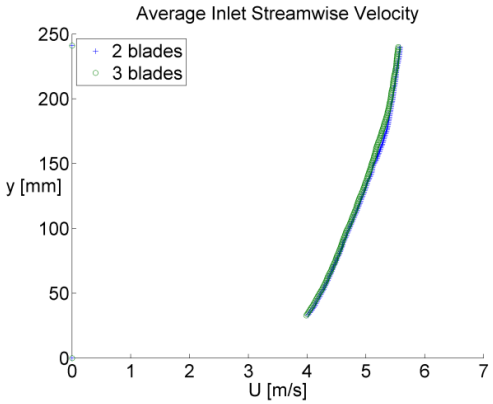

Figure 4. Inlet Streamwise Velocity

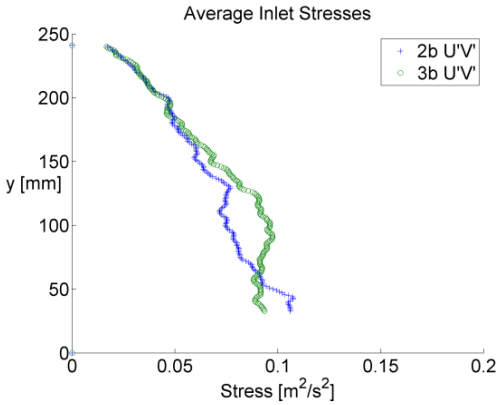

Figure 5. Inlet Shear Stresses

Results

Isocontours of streamwise and vertical velocity are shown in Figure 6 and Figure 7, while contours of Reynolds shear stress are shown in Figure 8. In all contour plots, the flow direction is from left to right. For each field between turbine rows, a 4th order polynomial interpolation in the streamwise direction was applied for each quantity.

Figure 6 shows the streamwise velocity field for the two-bladed array in the upper part of the figure and the three bladed array in the lower part of the figure. Data was not collected in the regions near the turbines due to potentially damaging laser reflections. In both fields, the wake is clearly visible, as is the slowdown effect as the flow approaches a turbine. It is clear that the velocity deficit is much greater in the three-bladed array than in the two-bladed array. The larger slowdown effect in the three-bladed array is also evident.

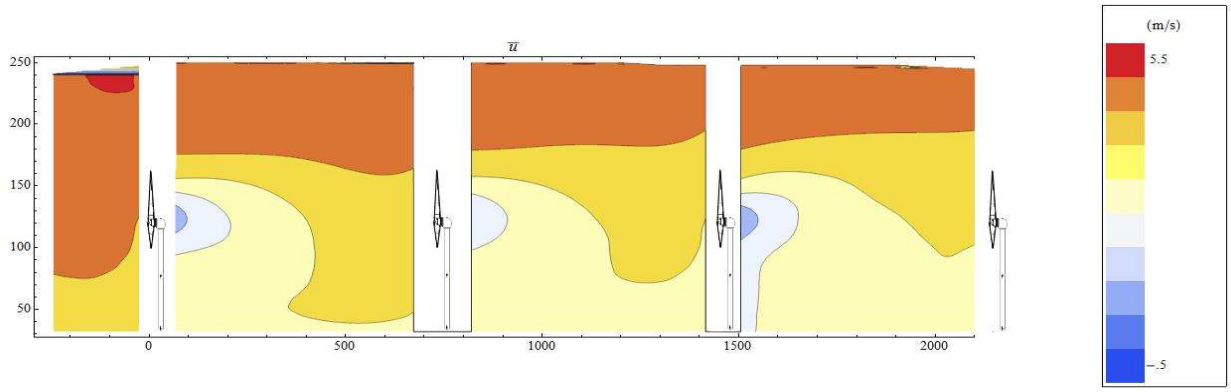

Figure 6(a) Two-Bladed Array

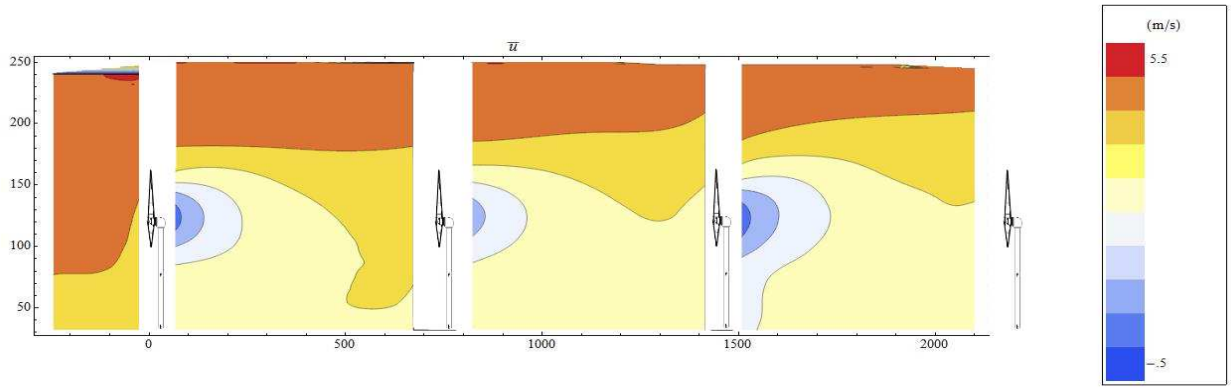

Figure 6(b) Three-Bladed Array

Figure 6 – Average Streamwise Velocity Field

Figure 7 shows the vertical velocity fields for the two arrays. In both, the effect of the rotor on the incoming flow is apparent, causing a distinct vertical speed-up in order for the air to move around the blockage. These effects are also seen after the rotor, where a small area of negative vertical velocity is seen at the bottom tip of the rotor.

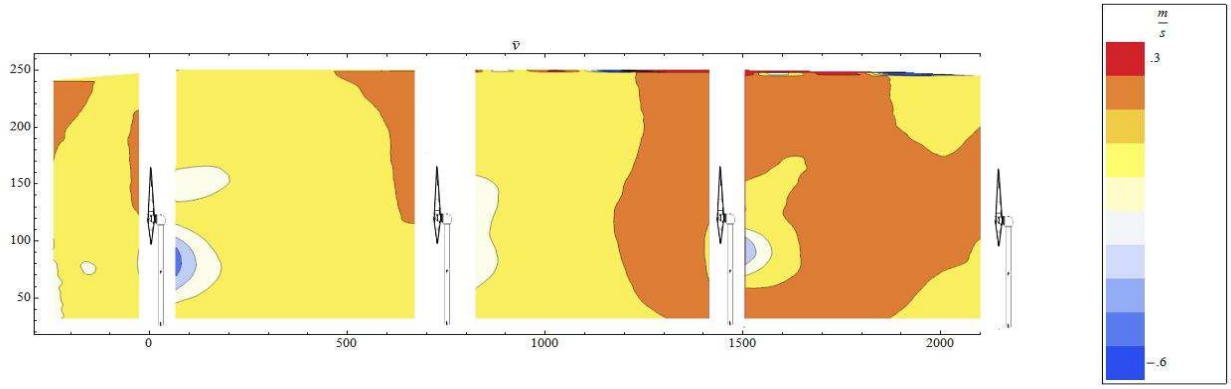

Figure 7(a) Two-Bladed Array

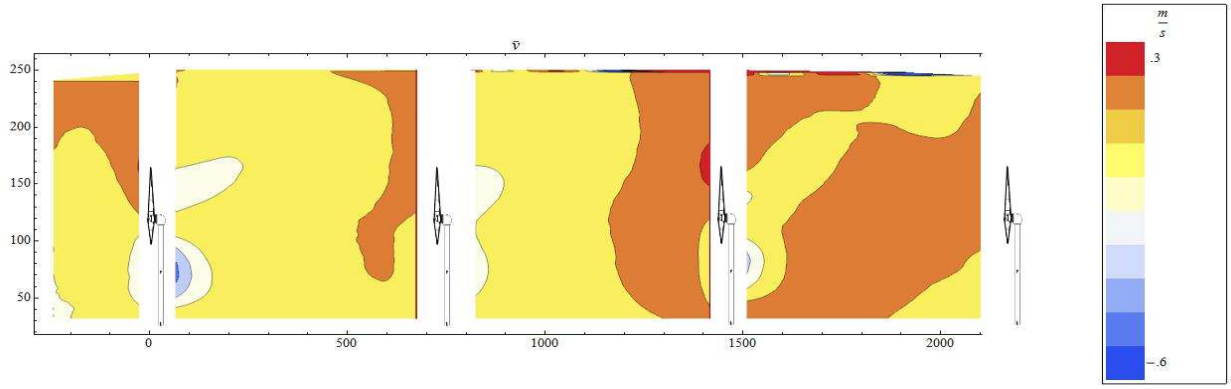

Figure 7(b) Three-Bladed Array

Figure 7 – Average Vertical Velocity Field

Time averaged Reynolds shear stress fields were also generated, as seen in Figure 8. Here the effect of the wake is seen to extend all the way from one row of turbines to the next. Additionally the Reynolds shear stresses at the top of the wake and the bottom of the wake have opposite signs, indicating that energy may be re-entering the array through the top and the bottom of the array.

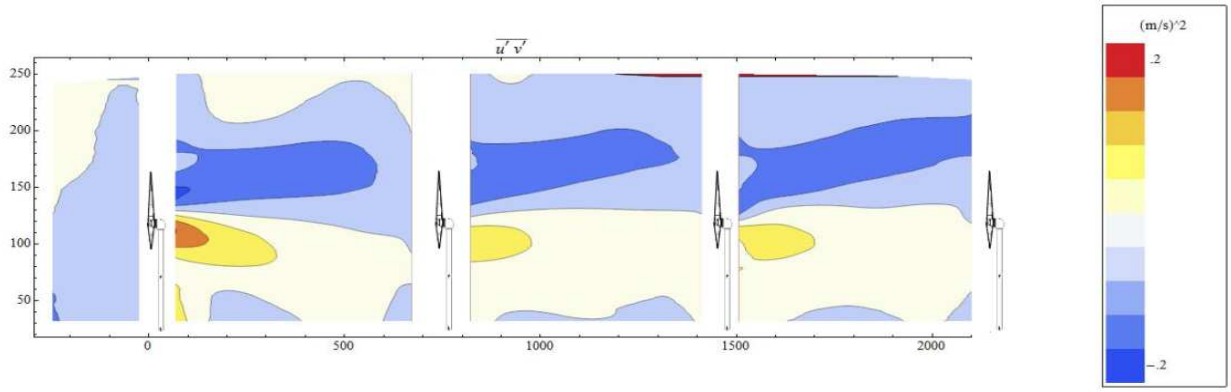

Figure 8(a) Two-Bladed Array

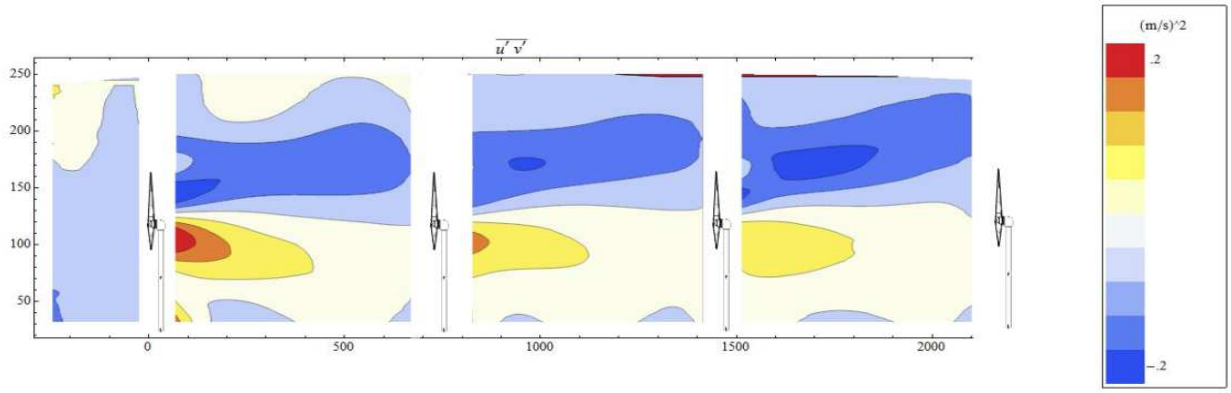

Figure 8(b) Three-Bladed Array

Figure 8 – Average Reynolds Shear Stress Field

Analysis

As previously identified, turbulent kinetic energy flux is the primary mechanism by which energy is vertically entrained into the array from upper levels of the boundary layer. This flux is assumed to operate over a rectangle just behind a turbine whose area is spanwise and streamwise spacing of the array. Further, this area is considered at the top and bottom tip height.

Rather than consider only one value of flux to represent the entire area, the flux is averaged over lengths of one diameter in the streamwise direction. These fluxes are then integrated to calculate the flux for the entire area. The contribution to the power in the wind can then be calculated as below.

$$P_{flux} = \left(\left(\bar{u}\,\overline{u'v'}\right)_{toptip} - \left(\bar{u}\,\overline{u'v'}\right)_{bottip}\right) \rho_{air} s_x\, s_z\, D^2 \tag{5}$$

Below are the averaged fluxes at one diameter increments downstream. Various values, such as power output from the turbine and power in the wind at the inlet, were investigated as scales for the values of the turbulent kinetic energy fluxes, but none was able to collapse the data. The similar patterns of the

fluxes between the arrays, however, may indicate that there is some scaling relationship that is more complicated than a single scaling value.

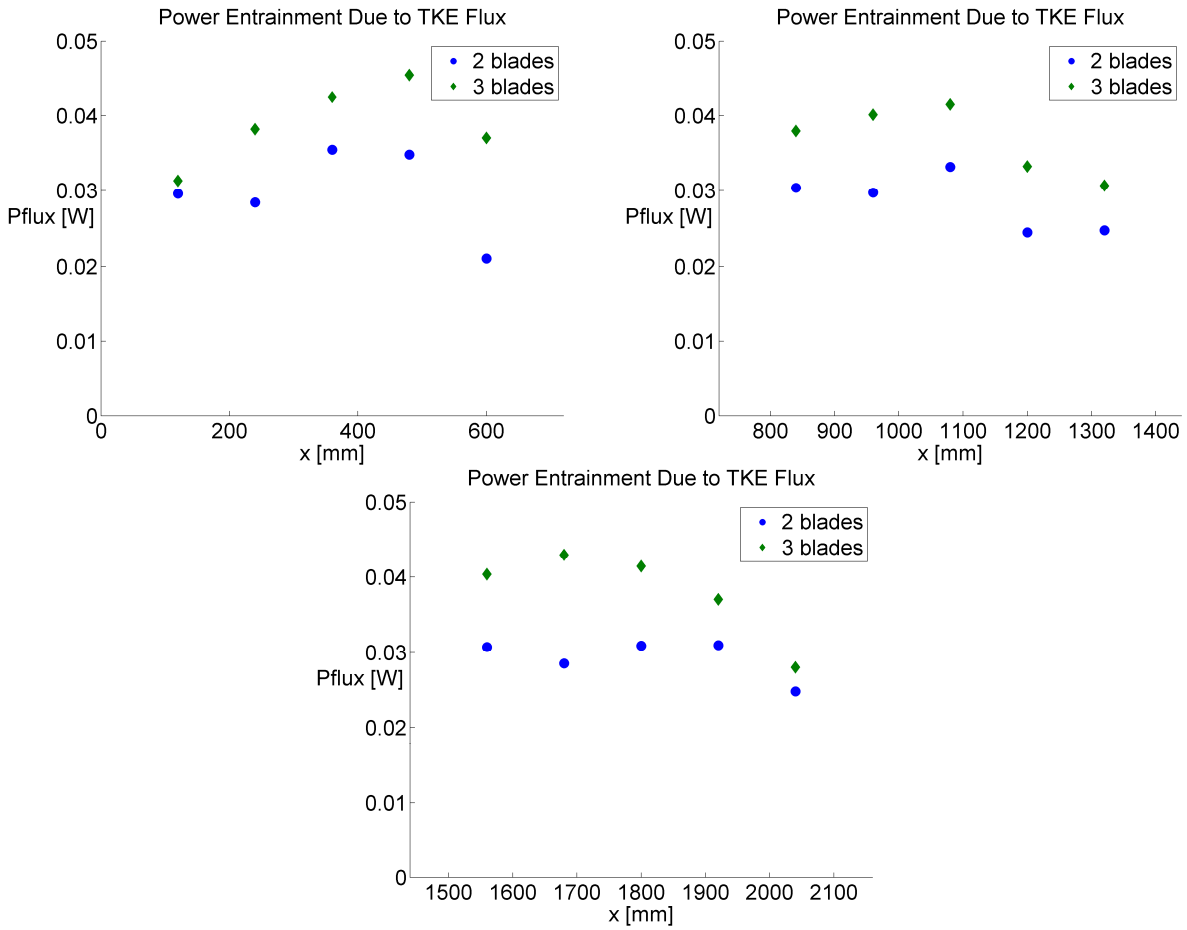

Figure 9. Turbulent Kinetic Energy Flux into Array

The energy loss due to turbulent kinetic energy production was also calculated. The production term, $\frac{\partial \bar{u}}{\partial y}(\overline{u'v'})$, was integrated through the same control volume as the flux term. This resulted in a quantification of the energy lost to production of turbulence. Again, no consistent scaling was found between the two arrays.

$$P_{production} = \rho_{air} s_x s_z D^2 \int_{bottip}^{toptip} \overline{u'v'} \frac{\partial \bar{u}}{\partial y} \, dy \tag{6}$$

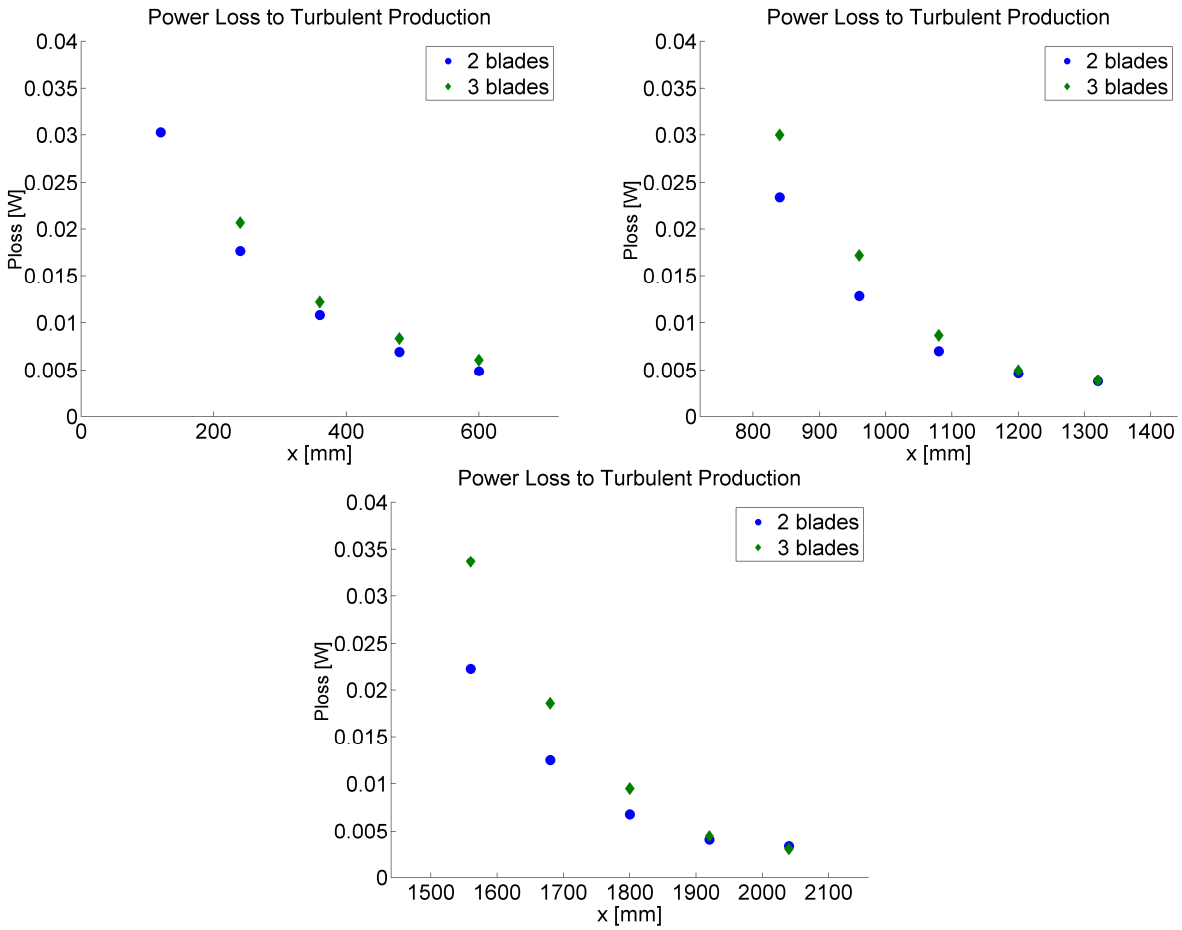

Figure 10. Turbulent Kinetic Energy Production inside Array

In Table 2, a summary of the above quantities is given as well as the turbine power output for comparison. Note that the integrated power values of production are significantly lower than integrated power values of the flux.

	2 Bladed Array			**3 Bladed Array**		
	$P_{turbine}$ [W]	P_{flux} [W]	$P_{production}$ [W]	$P_{turbine}$ [W]	P_{flux} [W]	$P_{production}$ [W]
Behind Row 1	0.09	0.15	0.07	0.1	0.19	0.09
Behind Row 2	0.07	0.14	0.05	0.06	0.18	0.06
Behind Row 3	0.05	0.15	0.05	0.04	0.19	0.07

Table 2. Summary of Results

Conclusion

Results comparing the vertical energy entrainment in a two-bladed and three-bladed model wind turbine array have been presented. Although power produced by the turbines was matched non-dimensionally through the power coefficient, C_p, no scale was found to match the vertical energy entrainment. This difference can not be explained by the difference in energy loss due to production, indicating that the scaling relationship between the two arrays, if it exists, may be more complicated

than a dependence on one quantity such as power produced by the turbine. This idea is reinforced by the similar patterns between the fluxes as the flow progresses in the streamwise direction.

An interesting feature of the flux of turbulent kinetic energy into the array is the consistent power contribution to the flow when integrated over top-tip and bottom-tip areas. In both the two and three-bladed arrays, the integrated flux between rows stays approximately the same: approximately 0.15 W for the two-bladed array and approximately 0.19 W for the three-bladed array. This result is unexpected, as the power extracted at each row in both arrays is different at each row. Further investigation may indicate reasons for this consistent pattern.

References

Cal, R., Lebrón, J., Castillo, L., Kang, H., & Meneveau, C. (2010). Experimental study of the horizontally averaged flow structure in a model wind-turbine array boundary layer. *Journal of Renewable and Sustainable Energy , 2,* 013106.

Calaf, M., Meneveau, C., & Meyers, J. (2010). Large eddy simulation study of fully developed wind-turbine array boundary layers. *Physics of Fluids , 22,* 015110.

Chamorro, L., & Porté-Agel, F. (2011). Turbulent Flow Inside and Above a Wind Farm: A Wind-Tunnel Study. *Energies , 4* (11), 1916--1936.

Kang, H., & Meneveau, C. (2010). Direct mechanical torque sensor for model wind turbines. *Measurement Science and Technology , 21,* 105206.

Lebron, J., Castillo, L., & Meneveau, C. (2012). Experimental study of the kinetic energy budget in a wind turbine streamtube. *Journal of Turbulence* (13).

Lebron-Bosques, J. (2011). *PIV Measurements of a Scaled-Down Wind Farm Subject to Atmospheric Boundary Layer Conditions.* Troy, NY: Rensselaer Polytechnic Institute.

Nonlinear Eddy Viscosity Models applied to Wind Turbine Wakes

M.P. van der Laan[1], N. N. Sørensen[1], P.-E. Réthoré[1], J. Mann[1], M.C. Kelly[1], J.G. Schepers[2]

[1]Technical University of Denmark, DTU Wind Energy, Risø Campus, Building 114, Frederiksborgvej 399, 4000 Roskilde, Denmark, plaa@dtu.dk
[2]Energy Research Centre of the Netherlands (ECN), Wind Energy, Petten, 1755ZG, The Netherlands

27 March 2013

ABSTRACT

The linear $k-\varepsilon$ eddy viscosity model and modified versions of two existing nonlinear eddy viscosity models are applied to single wind turbine wake simulations using a Reynolds Averaged Navier-Stokes code. Results are compared with field wake measurements. The nonlinear models give better results compared to the linear model, however, high turbulence levels can produce numerical instabilities.

1 INTRODUCTION

The energy losses in a wind farm due to interaction of wakes can often range between 10% to 20% [1]. Therefore, reliable and practical modeling of the influence of wind turbine wakes in wind farms is necessary in order to estimate the wind farm annual energy production. Computational Fluid Dynamics (CFD) methods as Large Eddy Simulation (LES) or Reynolds Average Navier-Stokes (RANS) can be employed to simulate wake effects. Results of LES has proven to compare well with results of wake measurements [2] but the computational costs are still high. RANS is roughly two orders of computational effort cheaper than LES, however, previous studies have shown that the most widely used turbulence models in RANS, e.g. the linear $k-\varepsilon$ eddy viscosity model (EVM), fail to predict the wake deficit and the Reynolds-stresses in a wake [3]. The basis of a linear EVM is the eddy viscosity hypothesis of Boussinesq that linearly relates the Reynolds-stresses to the symmetrical part of the velocity gradients (i.e. the strain rate tensor $S_{ij} = 1/2\,(U_{i,j} + U_{j,i})$) [4]. As a result, the linear EVM cannot represent effects caused by the anti symmetric part of the velocity gradients (i.e. the vorticity tensor $\Omega_{ij} = 1/2\,(U_{i,j} - U_{j,i})$) and effects caused by products of the velocity gradients, e.g.: normal Reynolds-stress anisotropy, swirl and stream line curvature. A turbulence model that can include all these effects is the nonlinear eddy viscosity model (NLEVM) of Apsley and Leschziner [5], which is based on an extended eddy viscosity hypothesis where nonlinear terms of products of S_{ij} and Ω_{ij} are present up to the third order. The cubic NLEVM is used in this research with minor modifications such that the user can control the (undisturbed) turbulence intensity. In addition to the cubic NLEVM of Apsley and Leschziner, the quartic NLEVM of Taulbee [6] is investigated, which was previously studied by Crespo et al. [7]. The background, definition and modifications of the cubic NLEVM and the quartic NLEVM are given in Sec. 2. In Sec. 3 both NLEVMs are tested and compared with field measurements of two single wind turbine wake cases.

In this paper tensors are written with bold symbols and index notation: $\mathbf{a} \equiv a_{ij}$. Traces of tensors are written as: $\{\mathbf{a}\} \equiv a_{ii}$. Summation is only done with roman indices. Greek indices are not summed up. In addition, a tensor product is written as: $\mathbf{as} \equiv a_{ik}s_{kj}$ and $\{\mathbf{as}\} \equiv a_{kl}s_{lk}$.

2 NONLINEAR EDDY VISCOSITY MODELS

The background and definition of the cubic and the quartic NLEVM are discussed in Sec. 2.1. The calibration of the model constants is addressed in Sec. 2.2 and Sec. 2.3. Limiter functions for guaranteeing positive, bounded eddy viscosity are presented in Sec. 2.4 and Sec. 2.5, respectively. Sec. 2.6 provides details about the implementation.

2.1 Background and definition

The foundations of the nonlinear stress-strain relationship used in the NLEVMs is based on algebraic Reynolds-stress models (ARSMs) where the Reynolds-stress is calculated via an implicit algebraic set of equations. The ARSMs are derived from differential Reynolds-stress models by using Rodi's weak assumption [8]. In addition, the pressure-strain model of Launder et al. [9] is used to obtain the full algebraic set of equations:

$$\mathbf{a} \quad = \quad -\alpha\mathbf{s} - \beta\left(\mathbf{sa} - \mathbf{as} - \frac{2}{3}\{\mathbf{as}\}\mathbf{I}\right) + \gamma(\mathbf{a}\omega - \omega\mathbf{a}), \tag{1}$$

where $\mathbf{a} \equiv a_{ij} \equiv \frac{\overline{u_i'u_j'}}{k} - \frac{2}{3}\delta_{ij}$ is the normalized anisotropic Reynolds-stress tensor, with k as the turbulent kinetic energy, $\overline{u_i'u_j'}$ as the Reynolds-stress tensor and $\mathbf{I} \equiv \delta_{ij}$ as the Kronecker delta. The tensors $\mathbf{s} \equiv s_{ij} \equiv \frac{1}{2}\frac{k}{\varepsilon}(U_{i,j} + U_{i,j})$ and $\omega \equiv \omega_{ij} \equiv \frac{1}{2}\frac{k}{\varepsilon}(U_{i,j} - U_{i,j})$ are the normalized strain-rate tensor and the normalized vorticity tensor, respectively, with $U_{i,j}$ as the mean velocity gradient and ε as the dissipation. In addition, three parameters are present in Eq. 1: α, β and γ, which are a function of the ratio of turbulent production and dissipation: $\mathscr{P}/\varepsilon$, and two constants: C_1 and C_2 that originate from the pressure-strain model of Launder et al. The implicit algebraic equations of Eq. 1 often behave numerically stiffly. Therefore, Pope [10] proposed a method to derive an exact explicit solution which has been adopted by Gatski and Speziale [11] to obtain the full explicit solution in three dimensional space. However, this solution has singularities and is not useful for practical applications. Taulbee [6] made the assumption that $\beta = 0$ to obtain a simplified ARSM and used the method of Pope to derive the corresponding NLEVM. (Note that in the literature these explicit solutions are also referred to as explicit algebraic Reynolds-stress models, however, the term NLEVM will be used in this research.) Apsley and Leschziner [5] used a different approach to obtain an explicit solution. Instead of using the method of Pope, a formal iteration procedure is employed to approximate the full explicit solution.

In the notation of Pope, the explicit solution of Eq. 1 can be written as:

$$\mathbf{a} = \sum_{\lambda=1}^{10} G^{(\lambda)}(\eta_i)\mathbf{T}^{(\lambda)}(\mathbf{s},\omega), \tag{2}$$

with ten linearly independent tensors $T^{(\lambda)}$:

$$\begin{array}{lcllcl}
\mathbf{T}^{(1)} & = & \mathbf{s}, & \mathbf{T}^{(6)} & = & \omega^2\mathbf{s} + \mathbf{s}\omega^2 - \frac{2}{3}\{\mathbf{s}\omega^2\}\mathbf{I}, \\
\mathbf{T}^{(2)} & = & \mathbf{s}\omega - \omega\mathbf{s}, & \mathbf{T}^{(7)} & = & \omega\mathbf{s}\omega^2 - \omega^2\mathbf{s}\omega, \\
\mathbf{T}^{(3)} & = & \mathbf{s}^2 - \frac{1}{3}\{\mathbf{s}^2\}\mathbf{I}, & \mathbf{T}^{(8)} & = & \mathbf{s}\omega\mathbf{s}^2 - \mathbf{s}^2\omega\mathbf{s}, \\
\mathbf{T}^{(4)} & = & \omega^2 - \frac{1}{3}\{\omega^2\}\mathbf{I}, & \mathbf{T}^{(9)} & = & \omega^2\mathbf{s}^2 + \mathbf{s}^2\omega^2 - \frac{2}{3}\{\omega^2\mathbf{s}^2\}\mathbf{I}, \\
\mathbf{T}^{(5)} & = & \omega\mathbf{s}^2 - \mathbf{s}^2\omega, & \mathbf{T}^{(10)} & = & \omega\mathbf{s}^2\omega^2 - \omega^2\mathbf{s}^2\omega,
\end{array} \tag{3}$$

$G^{(\lambda)}(\eta_i)$ are scalar functions of invariants η_i. There is a finite number of linearly independent tensor groups because any other higher order tensor, e.q. $\omega\mathbf{s}^3\omega^2 - \omega^2\mathbf{s}^3\omega$, can be written as a linear combination of $T^{(\lambda)}$ employing the Cayley-Hamilton theorem [10]. Any rewritten higher order tensor group will break up into lower order tensors multiplied by invariants which are stored in the scalar functions $G^{(\lambda)}$. In total five linearly independent invariants exist:

$$\eta_1 = \{\mathbf{s}^2\},\ \eta_2 = \{\omega^2\},\ \eta_3 = \{\mathbf{s}^3\},\ \eta_4 = \{\mathbf{s}\omega^2\},\ \eta_5 = \{\mathbf{s}^2\omega^2\}. \tag{4}$$

Due to the linear independence, all tensor groups $T^{(\lambda)}$ must share the properties of **a**, hence, each $T^{(\lambda)}$ is a second order symmetric deviatoric tensor.

The nonlinear stress-strain relationships in the NLEVM of Taulbee and the NLEVM of Apsley and Leschziner can be written in the form of Eq. 2. The corresponding scalar functions are given in Table 1.

$G^{(\lambda)}$	linear EVM	cubic NLEVM	quartic NLEVM
$G^{(1)}$	$-\alpha$	$-\alpha\left(1+\frac{2}{3}\beta^2\eta_1+2\gamma^2\eta_2\right)$	$-\alpha\left(1-\frac{1}{2}\eta_2\gamma^2\right)/Q$
$G^{(2)}$	0	$\alpha\gamma$	$\alpha\gamma\left(1-2\eta_2\gamma^2\right)/Q$
$G^{(3)}$	0	$2\alpha\beta$	0
$G^{(4)}$	0	0	$-6\alpha\gamma^4\eta_4/Q$
$G^{(5)}$	0	$-3\alpha\beta\gamma$	0
$G^{(6)}$	0	$-3\alpha\gamma^2$	$-3\alpha\gamma^2/Q$
$G^{(7)}$	0	0	$3\alpha\gamma^3/Q$

Table 1: Scalar functions of stress-strain relation of linear EVM and NLEVMs. $G^{(8-10)} = 0$. $Q \equiv \left(1-2\eta_2\gamma^2\right)\left(1-\frac{1}{2}\eta_2\gamma^2\right)$.

2.2 Calibration

The NLEVMs given in Sec. 2.1 include two or three parameters, namely α, β and γ. In theory, the parental ARSM of Eq. 1 defines the parameters. However, the logarithmic region of a boundary layer is not properly described when the same parameters in the NLEVMs are used because the NLEVMs are approximated explicit solutions of the ARSM. Therefore, α, β and γ are determined from calibration. Apsley and Leschziner determined α, β and γ by a calibration with a simple shear flow in which the only non zero components of the strain-rate tensor and the vorticity tensor are: $s_{13} = s_{31} = \frac{1}{2}\tilde{\sigma}$ and $\omega_{13} = -\omega_{31} = \frac{1}{2}\tilde{\sigma}$, respectively. Note that the shear parameter is defined as $\sigma \equiv \frac{k}{\varepsilon}\sqrt{(U_{i,j})^2}$ and the $\sim$ symbol denotes calibration parameters. In addition, the standard atmospheric Cartesian system is used in which the flow direction is *x*- or 1-axis and the wall normal direction is *z*- or 3-axis. The normalized anisotropic Reynolds-stress in simple shear flow is defined as:

$$a_{ij} = \begin{bmatrix} \tilde{a}_{11} & 0 & \tilde{a}_{13} \\ 0 & -\tilde{a}_{11}-\tilde{a}_{33} & 0 \\ \tilde{a}_{13} & 0 & \tilde{a}_{33} \end{bmatrix}. \tag{5}$$

Substituting s_{ij}, ω_{ij} and a_{ij}, belonging to the simple shear flow, into Eq. 2 leads to three linearly independent equations for the cubic NLEVM. The solution is derived by Apsley and Leschziner [5] and it is given in Table 2. The same procedure is carried out for the quartic NLEVM of Taulbee. The resulting two linearly independent equations are:

$$\tilde{a}_{11} = \frac{(\alpha\tilde{\sigma})(\gamma\tilde{\sigma})}{\tilde{Q}}\left(1+\frac{1}{4}(\gamma\tilde{\sigma})^2\right), \qquad \tilde{a}_{13} = -\frac{(\alpha\tilde{\sigma})}{\tilde{Q}}\left(1+\frac{1}{4}(\gamma\tilde{\sigma})^2\right), \tag{6}$$

with

$$\tilde{Q} \equiv \left(1+(\gamma\tilde{\sigma})^2\right)\left(1+\frac{1}{4}(\gamma\tilde{\sigma})^2\right), \tag{7}$$

and the solution is also given in Table 2.

	cubic NLEVM	quartic NLEVM
$\alpha\tilde{\sigma}$	$-\tilde{a}_{13}+\sqrt{\tilde{a}_{13}^2+(\tilde{a}_{11}-\tilde{a}_{33})^2-3(\tilde{a}_{11}+\tilde{a}_{33})^2}$	$-2\tilde{a}_{13}\left(1+\left(\frac{\tilde{a}_{11}}{\tilde{a}_{13}}\right)^2\right)$
$\beta\tilde{\sigma}$	$\frac{3(\tilde{a}_{11}+\tilde{a}_{33})}{\alpha\tilde{\sigma}}$	0
$\gamma\tilde{\sigma}$	$\frac{(\tilde{a}_{11}-\tilde{a}_{33})}{\alpha\tilde{\sigma}}$	$-\frac{\tilde{a}_{11}}{\tilde{a}_{13}}$

Table 2: Definition of NLEVM parameters α,β and γ determined by calibration.

2.3 Choice of calibration parameters $\tilde{a}_{11},\tilde{a}_{33},\tilde{a}_{13}$ and $\tilde{\sigma}$

In the previous section the two NLEVMs are calibrated with a simple shear flow. The simple shear flow is characterized by the anisotropic Reynolds-stress components $\tilde{a}_{11},\tilde{a}_{33},\tilde{a}_{13}$ and the shear parameter $\tilde{\sigma}$. The choice of these four constants will determine the scalar functions $G^{(\lambda)}$ in Eq. 2, hence, the model performance of the NLEVM is directly related to $\tilde{a}_{11},\tilde{a}_{33},\tilde{a}_{13}$ and $\tilde{\sigma}$.

For atmospheric flows describing a simple shear flow with $\widetilde{\mathscr{P}/\varepsilon}=1$, it is desired to be able to set the turbulence intensity I_{ref} at the inlet boundary for a certain reference height $z=z_{ref}$. Using the linear $(k-\varepsilon)$ EVM, the turbulence intensity is determined by setting $\tilde{C}_\mu$. Since the solution of the linear $k-\varepsilon$ EVM for the logarithmic region of a simple shear flow for a rough wall is [12]:

$$\frac{U}{u^*}=\frac{1}{\kappa}\ln\left(\frac{z}{z_0}\right),\ k=\frac{u^{*2}}{\sqrt{\tilde{C}_\mu}},\ \varepsilon=\frac{u^{*3}}{\kappa z}, \tag{8}$$

using $U=U_{ref}$ and $z=z_{ref}$, then:

$$I_{ref} \equiv \frac{\sqrt{\frac{2}{3}k}}{U_{ref}}=\tilde{C}_\mu^{-\frac{1}{4}}\sqrt{\frac{2}{3}}\frac{\kappa}{\ln\left(\frac{z_{ref}}{z_0}\right)}. \tag{9}$$

Note that U is the stream-wise mean velocity, u^* is the friction velocity, κ is the Von Karman constant, z is the distance from the wall and z_0 is the wall roughness. In addition, $\tilde{C}_\mu$ is used to distinguish from the (non constant) C_μ present in the NLEVMs. The value of $\tilde{\sigma}$ and $\tilde{a}_{13}$ can be related to $\tilde{C}_\mu$ by using Eq. 8:

$$\tilde{\sigma}=\frac{k}{\varepsilon}\left\|\frac{\partial U}{\partial z}\right\|=\frac{u^*}{\kappa z}=\frac{1}{\sqrt{\tilde{C}_\mu}}, \tag{10}$$

and

$$\left.\begin{aligned}\widetilde{\mathscr{P}/\varepsilon} &\equiv -\{\tilde{\mathbf{a}}\tilde{\mathbf{s}}\}=1\\ &=-2\tilde{a}_{13}\tilde{s}_{13}=-\tilde{a}_{13}\tilde{\sigma}=-\tilde{a}_{13}\tfrac{1}{\sqrt{\tilde{C}_\mu}}\end{aligned}\right\}\Rightarrow \tilde{a}_{13}=-\sqrt{\tilde{C}_\mu}. \tag{11}$$

The other two calibration parameters $\tilde{a}_{11},\tilde{a}_{33}$ cannot be related to $\tilde{C}_\mu$. Instead, either measurements or computation can determine the values of $\tilde{a}_{11},\tilde{a}_{33}$ in simple shear flow with a rough wall. Apsley and Leschziner used a direct numerical simulation of channel flow to obtain wall functions for all four calibration parameters. In this research the asymptotic value (normal wall distance

$\rightarrow \infty$) of $\tilde{a}_{11}, \tilde{a}_{33}$ of the same direct numerical simulation is used [5]: $\tilde{a}_{11} = 0.333,\ \tilde{a}_{33} = -0.263$. In the work of Crespo et al. [7] the NLEVM of Taulbee was calibrated with atmospheric measurements in which $\tilde{a}_{11} = -\tilde{a}_{33} = 0.38$. However, in the current work it is preferred to use the direct numerical simulation data. A consequence of using the calculated calibration parameters with $\tilde{a}_{11} \neq -\tilde{a}_{33}$ for the quartic NLEVM is that the resulting a_{11} and a_{33} for a simple shear flow are not equal to the intended value of the calibration parameters. Instead $a_{11} = \frac{1}{2}(\tilde{a}_{11} - \tilde{a}_{22}) = 0.298$ and $a_{33} = -\frac{1}{2}(\tilde{a}_{11} - \tilde{a}_{22}) = -0.298$.

2.4 Boundedness

The scalar function $G^{(1)}$ of the cubic NLEVM is not bounded. Apsley and Leschziner proposed to use a limiter function $f_P(\sigma)$ for all scalar functions which has been adopted in the present research. Except for $G^{(4)}$, all scalar functions $G^{(\lambda)}$ of the quartic NLEVM are all bounded by the invariant η_2 in the denominator:

$$\begin{aligned} \lim_{\eta_2 \to 0}, G^{(1)} &= -\alpha,\ \lim_{\eta_2 \to 0}, G^{(2)} = \alpha\gamma,\ \lim_{\eta_2 \to 0}, G^{(6)} = -3\alpha\gamma^2\ \lim_{\eta_2 \to 0}, G^{(7)} = 3\alpha\gamma^3, \quad (12) \\ \lim_{\eta_2 \to -\infty} G^{(1,2,6,7)} &= 0. \end{aligned}$$

The boundedness of the scalar function $G^{(4)}$ is not obvious since it has the invariant η_4 in the numerator, which could hypothetically grow faster than its denominator. $\eta_4 = \{\mathbf{s}\omega^2\}$ is a function of all nine velocity derivatives $U_{i,j}$, however, $\eta_2 = \{\omega^2\}$ is only a function of the off-diagonal velocity derivatives. As a result, the derivatives $U_{\alpha,\alpha}$, present in the nominator of $G^{(4)}$, are not bounded by the denominator. In the flow around a wind turbine, the derivative $\partial U/\partial x$ is large in vicinity of the rotor which might cause unstable behavior of the NLEVM because of $G^{(4)}$. In the test case of Sec. 3 a bounding function for η_4 is found to be redundant. In addition, the limiter function $f_P(\sigma)$ that is used for the cubic NLEVM is not applied to the quartic NLEVM.

2.5 Effective C_μ

The NLEVMs of Sec. 2.1 include a flow-dependent C_μ that is used to define the eddy viscosity: $\mu_T = \rho C_\mu \frac{k^2}{\varepsilon}$. In the notation of Pope the NLEVM can be written as:

$$\mathbf{a} = -2C_\mu \mathbf{s} + \sum_{\lambda=2}^{10} G^{(\lambda)}(\eta_i)\,\mathbf{T}^{(\lambda)}(\mathbf{s},\omega), \quad (13)$$

where $-2C_\mu\mathbf{s}$ is the linear part of the NLEVMs with an effective C_μ:

$$C_\mu = -\frac{1}{2}G^{(1)} = \begin{cases} \frac{1}{2}\alpha\left(1 + \frac{2}{3}\beta^2\{\mathbf{s}^2\} + 2\gamma^2\{\omega^2\}\right) & \text{(cubic)} \\ \frac{\frac{1}{2}\alpha\left(1 - \frac{1}{2}\{\omega^2\}\gamma^2\right)}{(1 - 2\{\omega^2\}\gamma^2)(2 - \{\omega^2\}\gamma^2)} & \text{(quartic)} \end{cases} \quad (14)$$

The calibration parameters α, β and γ and the first invariant $\{\mathbf{s}^2\}$ are always positive, however, the second invariant is always negative: $\{\omega^2\}$. This means that effective C_μ in the cubic NLEVM is not unconditionally positive. The effective C_μ in the quartic NLEVM is always positive but can still become zero. Apsley and Leschziner made the same observation about their cubic NLEVM and proposed to use a different C_μ in the eddy viscosity relation: $C_\mu = \tilde{C}_\mu f_P$ where f_P is the limiter function used to keep the scalar functions bounded. However, omitting the complete flow-dependent C_μ reduces the model performance. In present research the definition of Eq. 14 is used for both NLEVMs and an unconditional positive and nonzero C_μ is forced by a maximum limiter:

$$C_\mu = \max\left(-\frac{1}{2}G^{(1)}, a\tilde{C}_\mu\right), \quad (15)$$

where a is a positive small number such that $C_\mu \neq 0$, i.e. 1×10^{-4}.

2.6 Implementation

The NLEVMs are implemented as an extension of the linear $k-\varepsilon$ EVM. The nonlinear part of the stress-strain relationship of the NLEVMs is implemented as a momentum source term. The effective C_μ is used to define the eddy viscosity and the transport equations for k and ε used in the linear EVM are also employed for the NLEVMs.

3 WIERINGERMEER TEST CASE

The cubic and quartic NLEVMs are used to simulate the wake of a single wind turbine. Wake measurements from the Wind Turbine Test Site Wieringermeer (EWTW), owned by the Energy Research Centre of the Netherlands (ECN), are used to compare with the numerical simulations. The results of almost 5 years of measurements have been published by Schepers [13]. In addition, the 10 minute averaged data was made available for this research. In the two subsequent sections, a brief overview of the site is presented and the choice of input parameters for the numerical simulations are motivated. The single wake simulations are discussed in Sec. 3.3.

3.1 Site overview

EWTW is located in the North West of the Netherlands. The landscape mainly consist of flat farmland. 2 km East from the meteorological mast a large lake (IJsselmeer) is present. The land and the lake are separated by a dike which is 8 m and 3 m tall with respect to the land and the lake, respectively.

The meteorological mast is located South of five 2.5 MW wind turbines with a 80 m rotor diameter and hub height. The layout of the five wind turbines is given in Fig. 1. Two single wake cases are measured for wind directions around 31°and 315°with a corresponding downstream distance of 2.5D and 3.5D, respectively.

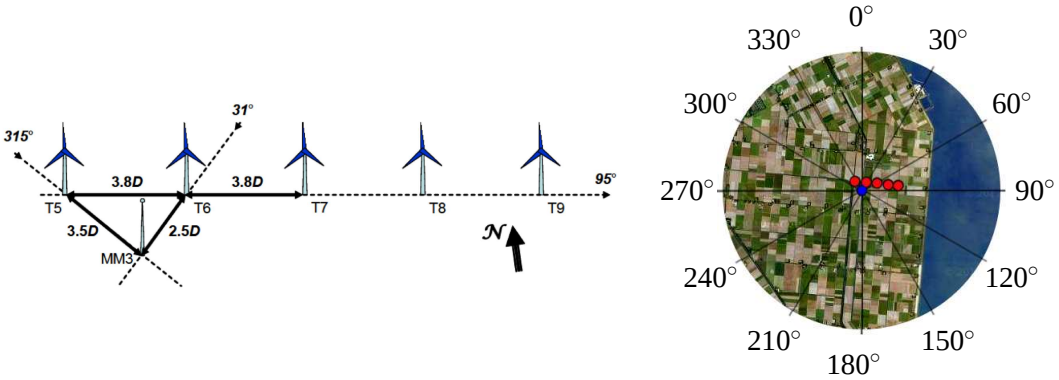

Figure 1: Research wind turbines at EWTW site. Left: geometrical sketch, source: [13]. Right: satellite image of 4 km radius around meteorological mast MM3 (blue dot), five red dots: research wind turbines, source: Google Earth.

3.2 Input parameters for numerical simulations

In order to compare the measurements with the numerical simulations the following input parameters for the numerical simulations are necessary: the undisturbed stream-wise wind speed at hub height $U_{H,\infty}$, the undisturbed friction velocity u^*, the thrust coefficient C_T, the undisturbed turbulence intensity at hub height $I_{H,\infty}$ and the roughness height z_0. The estimated input parameters are listed in Table 3 and are motivated in subsequent sections.

wake case	2.5D													3.5D
$U_{H,\infty}$ [m/s]	10.9													10.7
C_T [-]	0.63													0.63
dir. [°]	1	6	11	16	21	26	31	36	41	46	51	56	61	285-345
z_0 [cm]	13	11	9.1	7.0	5.5	4.3	3.4	2.8	2.4	2.1	1.9	1.2	0.94	3.0
u^* [m/s]	0.68	0.66	0.64	0.62	0.60	0.58	0.56	0.55	0.54	0.53	0.52	0.50	0.48	0.54
$I_{H,\infty}$ [%]	7.8	7.5	7.3	7.1	7.0	6.9	6.8	6.7	6.7	6.6	6.6	6.5	6.4	10

Table 3: Summary of input parameters for numerical computations of the two single wake cases.

Undisturbed velocity
The meteorological mast is instrumented with sonic anemometers, cups and vanes at 80 m. Unfortunately, upstream measurements are not carried out. Therefore, the upstream undisturbed wind speed at hub height is estimated from power measurements of wind turbine T5 (3.5D case) and wind turbine T6 (2.5D case). Only data with undisturbed wind speeds between 10-12 m/s are selected. The average of the wind speed between 1-61°and 285-345°, corresponding to the two single wake cases, are 10.9 m/s and 10.7 m/s, respectively.

Friction velocity
The friction velocity is calculated with the log law: $u^* = U_{H,\infty}\kappa/\ln(z_H/z_0)$.

Atmospheric stability
The lack of upstream measurements makes it impossible to identify and disregard non-neutral atmospheric measurements. However, the probability of a near neutral atmospheric boundary layer increases with high wind speeds, i.e. 10-12 m/s.

Thrust coefficient
The thrust coefficient curve is measured and calculated by Schepers [14]. The measurements are based on the tower bending moment and the calculations are carried out with PHATAS [15]. Both methods estimate at thrust coefficient of 0.63 for the averaged undisturbed wind speeds of 10.7 m/s and 10.9 m/s.

Turbulence intensity
Since there is a the lack of upstream measurements an estimation of the undisturbed inflow turbulence intensity for the 3.5D case is made by averaging the corresponding closest 'undisturbed' sector. Between 250°and 280°the average turbulence intensity is equal to 10%. Note that only undisturbed wind speeds between 10-12 m/s are considered. The turbulence intensities for North Eastern winds are calculated by a number of precursor simulations, as discussed in the following section.

Roughness height
For Western winds the roughness is dictated by flat farmland with sparse larger vegetation, as shown in Fig. 1. By physical inspection the roughness height is estimated to be 0.03 m. For Eastern winds the roughness height is affected by the lake and the farmland. Therefore, the streamwise velocity profile at the location of wind turbine T6 is calculated with a RANS precursor simulation of the most important terrain features: the water to land roughness change, the height difference between the land and the water and a Gaussian shaped dike. EllipSys3D is used as flow solver [16]. In total thirteen different wind directions are investigated between 1-61°with equidistant intervals. At the inflow a loglaw profile is prescribed where the friction velocity is set such that the hub height velocity at the original wind turbine location is approximately equal

to the measured average of 10.9 m/s (deviations are within 0.3%). The linear $k-\varepsilon$ turbulence model is used with constants that are applicable for atmospheric terrain flows, i.e. $C_\mu = 0.03$ and $C_{\varepsilon 1} = 1.21$ [16].

All precursor simulations show that the wind turbine rotor is operating in the transition zone between the inner boundary layer, caused by the roughness change and the outer boundary layer. The velocity profile in the mixing layer is approximated by a logarithmic profile based on linear curve fit between 60 m and 100 m in the $ln(z)-u$ domain. From the curve fit the effective friction velocity and the effective roughness height are calculated. The results for all thirteen wind direction are listed in Table 3 and will be used in the wake simulations. Note that the non-equilibrium profile could also be used directly as an input for the wake simulations, however, the NLEVMs show numerically unstable behavior when the non-equilibrium profile is prescribed at the inlet. Therefore, only the fitted logarithmic profile belonging to the mixing layer will be used as inlet condition.

3.3 Numerical simulations

The two measured wake cases (2.5D and 3.5D) are simulated with RANS using three different turbulence models: the linear $k-\varepsilon$ EVM and the two NLEVMs from Sec. 2.

Method

The in-house incompressible finite volume code EllipSys3D is used as flow solver [16].

The wind turbine is modeled as an Actuator Disk (AD) [17] on which the blade forces are distributed in the radial direction and constant in the circumferential direction. The real blade forces of the research wind turbines of EWTW are not available. Therefore, the force distribution of the NREL 5 MW reference wind turbine blade, calculated with a detached eddy simulation, is used in which the total thrust force is scaled with C_T.

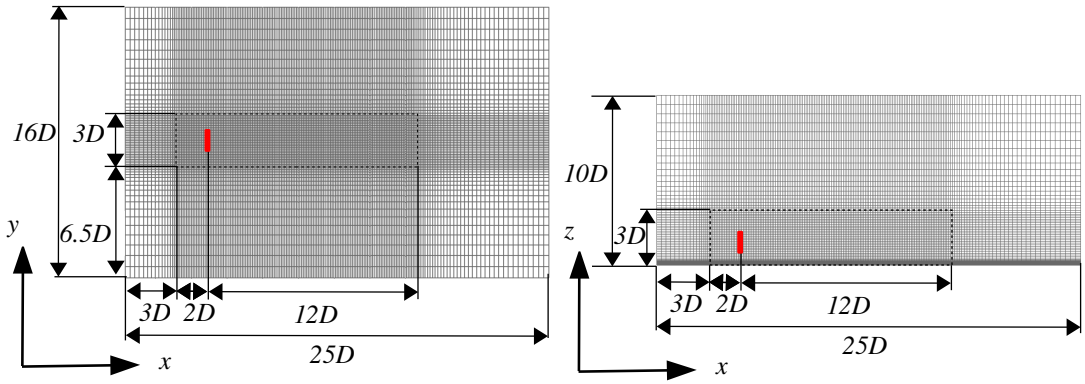

Figure 2: Computational domain. Left: top view. Right: side view. Dotted black box marks the wake domain. Actuator disk is illustrated as a red filled box. One in every two nodes is shown.

The AD is placed in a box shaped domain of dimensions: 25D $\times$ 16D $\times$ 10D, as shown in Fig. 2. In total $192 \times 64 \times 96 = 1.18$ million cells are used to discretize the domain. The wall at $z = 0$ is modeled as a rough wall where the first cell height is in the order of the roughness height. The boundaries at $x = 0$ and $x = 25$D is an inlet and an outlet, respectively. At the inlet a stream-wise logarithmic profile is specified. The top boundary at $z = 10$D and the side boundaries at $y = 0$ and $y = 16$D are modeled as symmetric walls. Around the AD a wake domain of dimensions: 14D $\times$ 3D $\times$ 3D is defined where uniform spacing of ten cells per diameter is applied in all directions. (Below $z = \frac{1}{2}z_H$ the cells in the wall normal direction are refined due to the presence of the wall.) A mesh study has shown that ten cells per diameter is sufficient [17]. Outside the wake domain stretching is allowed with a maximum edge growth ratio of 1.2.

The input parameters from Table 3 are used in the AD simulations. However, the NLEVMs show numerically unstable behavior for a turbulence intensity of 10%. (Note that the instabilities are also seen when the AD is switched off and they are not related to the unboundedness of $G^{(4)}$ of the quartic NLEVM.) Therefore, the 3.5D wake case is simulated with a turbulence intensity of 8% such that a comparison between the turbulence models can be made. The 2.5D wake case is performed with thirteen simulations corresponding to wind directions between 1-61°with uniform intervals. One AD simulation is conducted for the 3.5D wake case.

The turbulence intensity is set through C_μ by using Eq. 9 and the logarithmic solution is preserved by adapting $C_{\varepsilon,1}$ as: $C_{\varepsilon,1} = C_{\varepsilon,2} - \kappa^2/\left(\sqrt{C_\mu}\sigma_\varepsilon\right)$. The other turbulence constants in the transport equations for k and ε are chosen to be: $C_{\varepsilon,2} = 1.92$, $\kappa = 0.40$, $\sigma_\varepsilon = 1.30$ and $\sigma_k = 1.00$.

Standard values for the density and the dynamic fluid viscosity are used: $\rho = 1.225$ kg/m^3 and $\mu = 1.784 \times 10^{-5}$ kg/(m.s).

Results

The results of the numerical simulations are plotted with the results of the measurements in Fig. 3. For each wake case, three quantities at hub height are plotted against the relative wind direction, namely: the stream-wise velocity $U/U_{H,\infty}$, the stream-wise Reynolds-stress $\sqrt{\overline{u'u'}}/U_{H,\infty}$ and the vertical Reynolds-stress $\sqrt{\overline{w'w'}}/U_{H,\infty}$.

2.5D case

For the 2.5D case the linear EVM under predicts the measured wake deficit by 20% as shown in Fig. 3a. The NLEVMs calculate a much deeper wake deficit compared to the linear EVM but still under predicted the measured one by 5-10%. The reason for the improved performance is further explained in the paragraph: *Influence of effective* C_μ.

The wake at 2.5D is slightly asymmetric. Schepers [13] hypothesized that as this site the asymmetry of wake is caused by terrain effects. The hypothesis is confirmed by all three turbulence models in which a similar wake asymmetry is seen. Thus, the directional dependency of the wind profile and the turbulence intensities, calculated by the precursor field simulations, are capturing the dominant terrain effects.

The Reynolds-stresses calculated by the NLEVMs are closer to the measured Reynolds-stresses compared the ones calculated by the linear EVM. The vertical Reynolds-stress $\sqrt{\overline{w'w'}}/U_{H,\infty}$ from Fig. 3e calculated by the linear EVM is roughly 25% higher than the measured ones, also outside the wake. The main reason for the offset is coming from the fact that the linear EVM is isotropic ($a_{\alpha\alpha} = 0$ in simple shear) and can only be tuned for the undisturbed turbulent kinetic energy. The NLEVMs match the measurements better because the NLEVMs include normal Reynolds-stresses anisotropy. The stream-wise Reynolds-stress $\sqrt{\overline{u'u'}}/U_{H,\infty}$ from Fig. 3c calculated by the NLEVM simulations still unpredicted the magnitude of the measured Reynold-stresses.

3.5D case

As mentioned before, the NLEVMs show numerically unstable behavior in the 3.5D wake case when the measured turbulence intensity of 10% is used. Therefore, the numerical simulations cannot directly be compared with the measurements. Compared to the wake deficit of the 2.5D case, the results of the linear EVM are even more different from the results of the NLEVMs, as seen in Fig. 3b. The wake deficit calculated by the NLEVMs is 15% larger then the one calculated by the linear EVM. Similar observations can be made about the Reynolds-stress as done for the 2.5D case. The asymmetry of the measured wake deficit are not induced by terrain effects [13]. Zahle and Sørensen concluded that the combination of shear and wake rotation can cause wake asymmetry [18]. However, a similar effect is not seen in the current simulations even though rotational forces are applied on the AD.

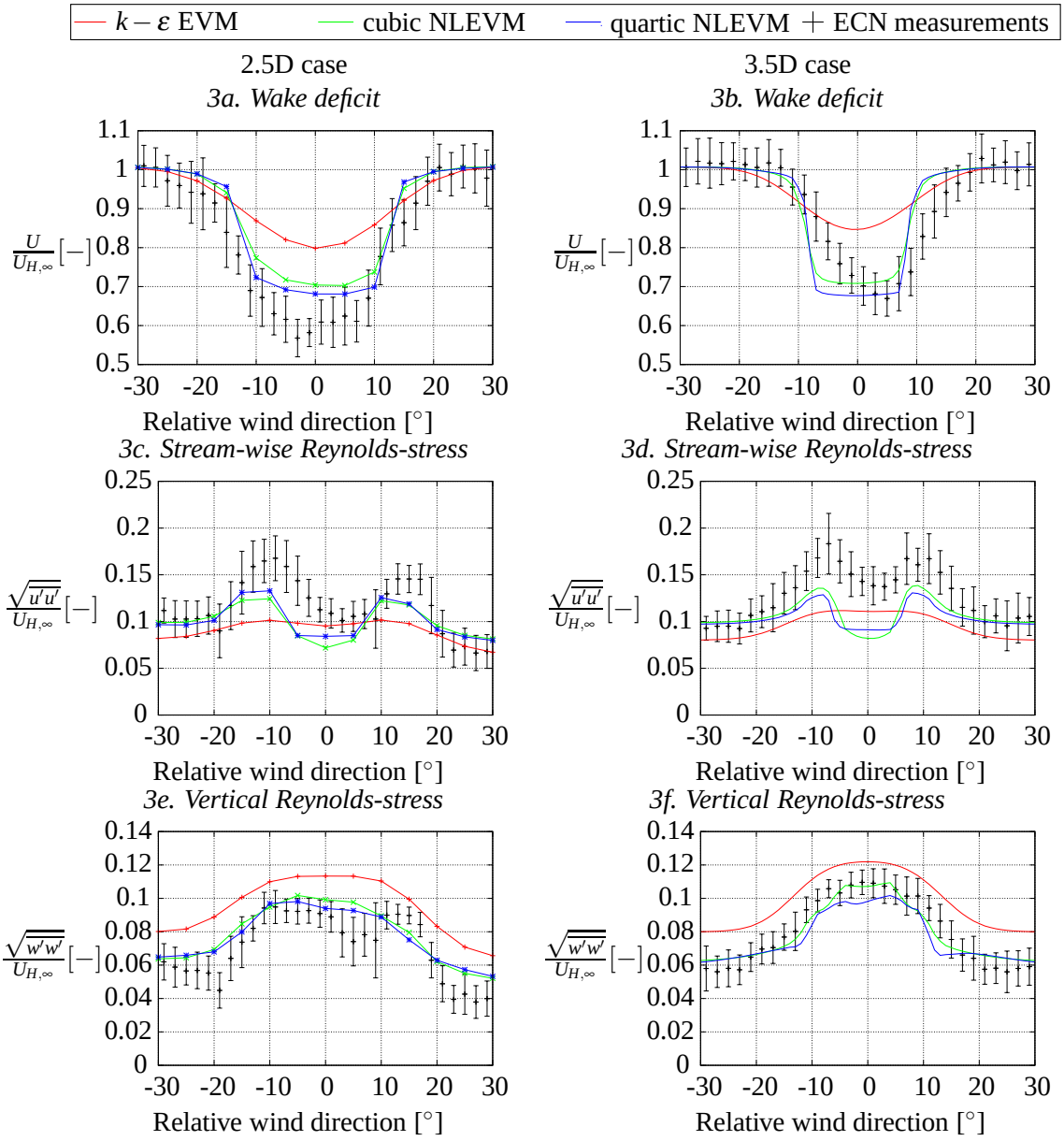

Figure 3: Wake deficit and Reynolds-stresses at hub height for relative wind directions. Left: 2.5D case with $U_{H,\infty} = 10.9$ m/s, right: 3.5D case with $U_{H,\infty} = 10.7$ m/s. The measurements include error bars of one standard deviation. For 3.5D case: measured: $I_{H,\infty} = 10\%$ and the simulation are carried out with $I_{H,\infty} = 8\%$.

Influence of effective C_μ

The wake deficit calculated by the NLEVMs is much larger compared to the linear EVM. The main reason for the difference is the effective, flow-dependent C_μ of Eq. 14. Within 1D downstream of the at $z = z_H + 0.5D$, a large positive peak of normalized mean velocity gradient $k/\varepsilon \partial u/\partial z$ is present. This gradient is the dominant term in the two invariants $\eta_1 \approx -\eta_2 \approx 1/2\,(k/\varepsilon \partial u/\partial z)^2$. Without the limiter function of Eq. 15, the effective C_μ in the cubic model for the 2.5D wake case at 31°becomes negative:

$$C_\mu \approx \frac{1}{2}\alpha\left(1 + \left(\frac{k}{\varepsilon}\frac{\partial u}{\partial z}\right)^2\left(\frac{1}{3}\beta^2 - \gamma^2\right)\right) \approx -6. \tag{16}$$

Hence, the limiter function is active and the effective C_μ is equal to $1\times10^{-4}\tilde{C}_\mu$. As a result, the turbulent eddy viscosity $\mu_T=\rho C_\mu\frac{k^2}{\varepsilon}$ in the cubic NLEVM, is decreased downstream of the AD and the NLEVM behaves less dissipative compared to the linear EVM. A similar conclusion can be made about the quartic NLEVM in which the lowest effective C_μ is equal to $\approx 1\times10^{-3}$.

Using the proposed C_μ formulation of Apsley and Leschziner, in which C_μ is flow-dependent: $C_\mu=\tilde{C}_\mu f_P(\sigma)$ through the limiter function $f_P(\sigma)$, the eddy viscosity is also lowered downstream of the AD, since the shear parameter is large: $\sigma^2\approx(k/\varepsilon\partial u/\partial z)^2$. However, the decrease of eddy viscosity is less compared to using the true effective C_μ of Eq. 14.

Wake recovery

In Fig. 4 the stream-wise velocity $U/U_{H,\infty}$ at hub height at a relative wind direction of 0°is plotted against the stream-wise downstream distance $(x-x_{AD})/D$ for all three turbulence models and both wake cases. Except for undisturbed turbulence intensity at hub height, the simulation parameters used in the two wake cases are similar, as listed in Table 3 (31°and 285-245°). Hence, the influence of $I_{H,\infty}$ on performance of the turbulence models can be investigated. The wake recovery calculated by the linear $k-\varepsilon$ EVM is faster with increasing turbulence intensity, however, the opposite is observed for the NLEVMs. Higher turbulence levels should enhance mixing which accelerates the wake recovery. Therefore, the NLEVMs show unphysical behavior towards changes of $I_{H,\infty}$. The unphysical behavior is caused by the flow-dependent C_μ. For higher undisturbed turbulence intensities, the largest derivative $k/\varepsilon\partial u/\partial z$ increases, which lowers the flow-dependent C_μ, as discussed in the previous paragraph. As a result, the eddy viscosity decreases with increasing undisturbed turbulence intensity and the wake recovery is delayed.

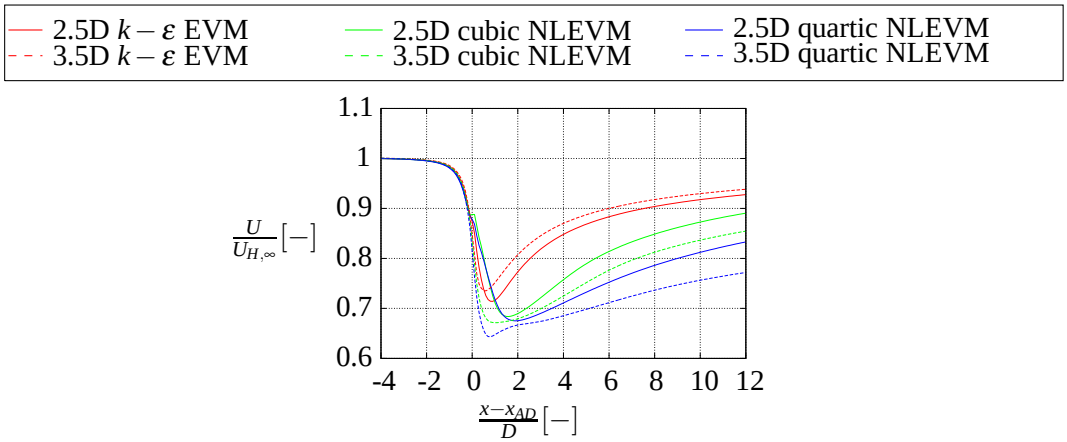

Figure 4: Wake deficit recovery at hub height at a relative wind direction of 0°. 2.5D case: $I_{H,\infty}=6.8\%$ and 3.5D case: $I_{H,\infty}=8\%$.

4 CONCLUSION

The linear $k-\varepsilon$ EVM and modified versions of the cubic NLEVM of Apsley and Leschziner and the quartic NLEVM of Taulbee are tested and compared with wake measurements from Wieringermeer for two single wake cases: 2.5D and 3.5D at different wind directions. In the 2.5D case the performance of the NLEVMs is much better compared to the linear EVM, however, the wake deficit and the stream-wise Reynolds-stress are still under predicted compared to the measurements. The numerically unstable behavior of the NLEVMs at high turbulence intensities makes it impossible to simulate the 3.5D case with the observed-based undisturbed turbulence intensity of 10%. Not having the full flexibility of setting the undisturbed turbulence intensity is a major drawback of the NLEVMs. The 3.5D case is simulated by all three turbulence models with a turbulence intensity of 8%. In terms of wake deficit and Reynolds-stresses, the difference between

the linear EVM and the two NLEVMs is even larger compared to the 2.5D case.

The performance increase of the NLEVMs is caused by the flow-dependent C_μ which lowers the eddy viscosity downstream of the AD. Unfortunately, the flow-dependent C_μ is also responsible for predicting a faster wake recovery for lower undisturbed turbulence intensities, which is unphysical behavior.

REFERENCES

[1] R. J. Barthelmie, S. T. Frandsen, N. M. Nielsen, S. C. Pryor, P.-E. Réthoré, and H. E. Jørgensen, "Modelling and measurements of power losses and turbulence intensity in wind turbine wakes at middelgrunden offshore wind farm," *Wind Energy*, vol. 10, pp. 217–228, 2007.

[2] N. Troldborg, G. C. Larsen, H. A. Madsen, K. S. Hansen, J. N. Sørensen, and R. Mikkelsen, "Numerical simulations of wake interaction between two wind turbines at various inflow conditions," *Wind Energy*, vol. 14, p. 859876, 2011.

[3] P.-E. Réthoré, *Wind Turbine Wake in Atmospheric Turbulence*. PhD thesis, Risø, 2009.

[4] M. J. Boussinesq, *Théorie de l'écoulement tourbillonnant et tumultueux des liquides*. Gauthier-Villars et fils, 1897.

[5] D. D. Apsley and M. A. Leschziner, "A new low-reynolds-number nonlinear two-equation turbulence model for complex flows," *International Journal of Heat and Fuid Flow*, vol. 19, pp. 209–222, 1998.

[6] D. B. Taulbee, "An improved algebraic reynolds stress model and corresponding nonlinear stress model," *Physics of Fluids*, vol. A4 11, pp. 2555–2561, 1992.

[7] A. Crespo, R. Gómez-Elvira, E. Migoya, F. Manuel, and H. J., "Anisotropy of turbulence in wind turbine wakes," *Journal of Wind Engineering and Industrial Aerodynamics*, vol. 93, pp. 797–814, 2005.

[8] W. Rodi, "A new algebraic relation for calculating the reynolds stress," *Zeitschrift for angewandte mathematik und mechanik*, vol. 56, pp. 227–238, 1976.

[9] B. E. Launder, G. J. Reece, and W. Rodi, "Progress in the development of a reynolds-stress turbulence closure," *Jounal of Fluid Mechanics*, vol. 68, pp. 537–566, 1975.

[10] S. B. Pope, "A more general effective-viscosity hypothesis," *Jounal of Fluid Mechanics*, vol. 72, pp. 331–440, 1975.

[11] T. B. Gatski and C. G. Speziale, "On explicit algebraic models for complex turbulent flows," *Jounal of Fluid Mechanics*, vol. 254, pp. 59–78, 1993.

[12] P. J. Richards and R. P. Hoxey, "Appropriate boundary conditions for computational wind engineering models using the $k-\varepsilon$ turbulence model," *Journal of Wind Engineering and Industrial Aerodynamics*, vol. 46,47, pp. 145–153, 1993.

[13] J. G. Schepers, "Analysis of wake measurements from the ECN wind turbine test site wieringermeer, EWTW," *Wind Energy*, vol. 15, p. 575591, 2012.

[14] J. G. Schepers, "Personal communication," 2012.

[15] C. Lindenburg and H. Snel, "PHATAS-II: program for horizontal axis wind turbine analysis and simulation version II," tech. rep., ECN-C–93-038, 1993.

[16] N. N. Sørensen, *General purpose flow solver applied to flow over hills*. PhD thesis, Technical University of Denmark, 1994.

[17] P.-E. Réthoré, M. P. van der Laan, N. Troldborg, F. Zahle, and N. N. Sørensen, "Verification and validation of an actuator disc model," *Wind Energy*, 2013.

[18] F. Zahle and N. N. Sørensen, "Overset grid flow simulation on a modern wind turbine," in *AIAA-2008-6727*, 2008.

Experimental analysis of the kinetic energy transport and turbulence production in the wake of a model wind turbine

L.E.M. Lignarolo[1], D.Ragni[1], C. Krishnaswami[1], Q.Chen[1,2], C.J. Simao Ferreira[1], G.J.W. van Bussel[1]

[1]Delft University of Technology, Wind Energy, l.e.m.lignarolo@tudelft.nl
[2]Wuhan University, State Key Laboratory of Water Resources and Hydropower Engineering Science

ABSTRACT

The mixing properties of the self-induced flow in a wind turbine wake are studied. The wake of a model horizontal axis wind turbine is analysed with the Particle Image Velocimetry technique and a triple decomposition of the flow. The process of wake re-energising is studied and its dependency on the wake flow structures and stability is shown. The streamwise development of the wake velocity is presented, as well as its clear dependency on the onset of the pairwise instability of the tip-vortices. The mean flow kinetic energy transport and turbulence production is calculated for different regions of the wake. The main conclusion is that the stability of the tip-vortex helix has a strong influence on the mixing of the wake with the outer flow and its re-energising. A thorough estimation of the energy transport at wake scale and the modelling of its dependency on the turbine characteristics would be a first step towards a rotor design process which does not only take into account the aerodynamic and power optimisation of the rotor itself, but also the re-energising properties of the wake, namely the "design of the wake".

Introduction

The wake of a horizontal axis wind turbine (HAWT) is a complex three-dimensional turbulent flow. Its physics has been studied in depth with experiments and field measurements and modelled with numerical analysis. The large inaccuracy in the prediction of loads and energy yields of a wind turbine in a wind farm encountered in the current numerical codes is largely due to the poor modelling of the wake [1], still based on the actuator disc assumption, which does not allow for a correct prediction of the kinetic energy transport and turbulence creation in the flow of a turbine's wake, as shown in [9] . These factors are of paramount importance, because turbulent mixing governs the re-energising process of the wake. In a large wind farm, the energy is provided mainly by the entrainment of high kinetic energy air from the flow above the wind farm itself, apart from the front rows, as demonstrated in previous studies [2]. This phenomenon happens at two different levels: at the atmospheric turbulent flow level and at the wake-induced level. The second one is of particular interest because it concerns the mixing process owing to the presence of the tip vortex helix, its instability and its breakdown, namely parameters which are directly depending on the turbine design and its operation. This becomes even more important for off-shore wind farms, where the role of atmospheric turbulence is much lower than on-shore. However, currently there is no model which allows to quantify the wake induced mixing, nor there is a detailed set of experimental observations in controlled conditions for understanding the physics of this phenomenon and validating a possible model.
Previous studies focussed on the self-induced mixing properties of the wake can be found in [3], [6] and [11], who demonstrate how different turbine parameters affect the wake development in terms of wake stability. [7] makes the hypothesis that the near wake tip vortices prevent the wake to mix with the outer air, but the quantification of the effect of the vortices and their break-down in terms of energy transport is not in his focus; also, this assumption seems to be in contradiction with previous statements of [5], who says that the tip vortices are contributing to the entrainment of air in the wake. [4] demonstrates the importance of vertical transport of kinetic energy to replenish the wakes and to enable the power extraction in the array. This inspiring study is focussed on analysing the mixing

process due to the large scale atmospheric turbulence and its effect on the smaller scale flow structures within a wind farm. In the present project, the environment turbulence is not taken into consideration, in order to study the mixing properties of the wake *per se*, solely caused by the wake induced flow. To the authors knowledge, there is no available study on the effect of the different wake flow structures on the kinetic energy balance of the wake itself and that shows what is their dependency on the turbine characteristics.

The aim of this project is to visualise the dependency of the wake re-energising on the tip vortex helix instability and breakdown. An experimental study is conducted to characterise the evolution of the vortex structures in the wake of a 60 centimetres-diameter two-bladed HAWT model. The measurements are performed in the Open Jet Facility (OJF) wind tunnel of Delft University of Technology and a high-resolution Stereo Particle Image Velocimetry (SPIV) system is used to achieve detailed flow measurements. The wake is measured up to 4 diameters downstream. The zone of interest in the present paper however is up to 2.7 diameters. The wake recovery is estimated in terms of wake velocity and its clear dependency on the onset of wake instability is shown. The wake mixing is determined in terms of mean flow kinetic energy transport. The turbine's wake velocity field u_i is decomposed according to [8] as $u_i = \overline{u_\iota} + \widetilde{u_\iota} + u'_i$ .The terms in the right hand side indicate respectively the mean flow, the periodically fluctuating coherent structures (tip vortices) and a random fluctuating component (turbulence). The phase-locked mean flow kinetic energy transport equation for inviscid flow is:

$$\left(\overline{u_\jmath} + \widetilde{u_\jmath}\right)\frac{\partial \overline{KE}}{\partial x_j} = -\left(\frac{\partial \overline{p u_\iota}}{\partial x_i}\right) - \overline{u_\iota}\frac{\partial \overline{u_\iota}}{\partial t} - \overline{u_\iota}\overline{u_\jmath}\frac{\partial \overline{u_\iota}}{\partial x_j} - \left(-< u_i{'}u'_j > -\widetilde{u_\iota}\widetilde{u_\jmath}\right)\frac{\partial \overline{u_\iota}}{\partial x_j} - \frac{\partial}{\partial x_j}\left[\overline{u_\iota} < u_i{'}u'_j > + \overline{u_\iota}\left(\widetilde{u_\iota}\widetilde{u_\jmath}\right)\right]. \quad \text{Eq. 1}$$

where <-> indicates the phase-locked average of the quantity, the kinetic energy is $\overline{KE} = \frac{1}{2}\overline{u_\iota}\overline{u_\iota}$, p is the barometric pressure and $\widetilde{u_\iota}\widetilde{u_\jmath}$ and $u_i{'}u'_j$ are respectively the Reynolds stresses due to coherent and incoherent fluctuations. The most important terms to be calculated are the fourth and the fifth term of Eq.1's right-hand side, which represent respectively the mean flow kinetic energy loss into turbulence and vortices and the kinetic energy transport due to the periodic vortices and the turbulence. the latter is represented by a gradient of kinetic energy fluxes. The fourth term can also be written substituting the mean velocity with the phase-locked average velocity and discarding the periodic contribution, obtaining the equation of the turbulence kinetic energy production in one phase. This is shown in Equation 2 in the x-y plane:

$$\langle Pe \rangle = -u'^2\frac{\partial \langle u \rangle}{\partial x} - v'^2\frac{\partial \langle v \rangle}{\partial y} - u'v'\left(\frac{\partial \langle u \rangle}{\partial y} + \frac{\partial \langle v \rangle}{\partial x}\right). \quad \text{Eq. 2}$$

In this paper it will be shown how the kinetic energy transport is strongly dominated by the disruption of coherence of the vortical structures in the wake. The objective for the near future is to quantify these terms for both a wind turbine rotor's and a porous disc's wake (simulating the actuator disc used in numerical models) and to show the differences in the process of kinetic energy entrainment and destruction (turbulence production) along the two wake's shear layers. This will help understanding the limitations in the current wake models, based on the actuator disc assumption, and will help researchers to understand what level of accuracy (and at what flow scale) the future improved models must have for correctly simulating the wake effect in large wind farms. Ultimately, this will extend the knowledge on the wake re-energising properties for exploiting them in the future wind turbine and wind farm design.

Experimental setup

Wind tunnel and measurement conditions

Experiments have been conducted in the closed-loop open jet wind-tunnel of Delft University of Technology. The wind-tunnel has an octagonal nozzle with an equivalent diameter of 3 m and a contraction ratio of 4:1. Powered by a 500 kW motor, the wind tunnel can achieve a maximum velocity of 34m/s (120kmph). It provides a uniform flow with 0.5% turbulent intensity. The uniform velocity area contracts with a 4.8° semi-angle, due to the shear layer at the boundary of the jet. The flow temperature is kept constant through a heat exchanger which provides up to 350 kW of cooling power. In a previous experimental campaign, aimed analysing the wind tunnel flow oscillations, the stable jet length has been establish as long as 3m from the exit, corresponding to 5 turbine diameters.

Tip Speed Ratio [-]	Frequency of wind turbine [Hz]	Wind speed [m/s]	Thrust coefficient [-]
4.8	9.67	3.8	0.82
6	18.00	5.7	0.89

Table 1: test cases

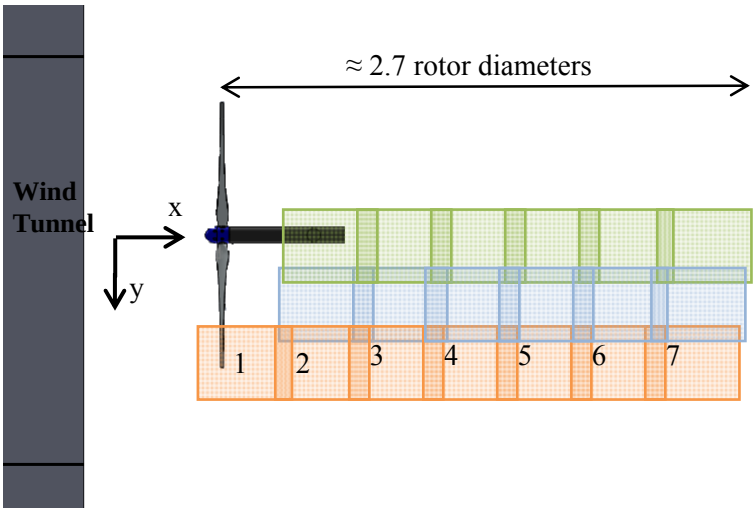

Figure 1: measurement matrix

The measurements were performed on the wake of the wind turbine up to 4 rotor diameters. In this paper the results up to 2.7D are presented as shown in Figure 1. Each window represents a field of view (FOV) in a plane parallel to the ground at the hub height; the darker shade between the windows shows the overlap between two adjacent FOV, which varies from 97 mm to 147 mm in the x direction. The flow was also captured at two inboard positions A and B with an overlap of 102 mm to 98 mm respectively. The measurements were performed in unconditioned sampling and in phase-locked for different azimuthal positions of the blades (-5, 0 and 5 degrees), using an optical trigger positioned inside the nacelle. The device provides one pulse for each rotation and triggers the laser and the cameras. By changing the trigger delay, different phases can be captured. The distance between the turbine and the wind tunnel exit is approximately 0.5 rotor diameters.

Wind turbine model

The wind turbine used in the experiment is a 2-bladed wind turbine with a design tip speed ratio of 6. The rotor radius is 30cm (which provides a low model to tunnel area ratio of 0.04) with a maximum twist of about 18.0 degrees at the root and a minimum twist of 4.4 degrees at the tip. The maximum chord of the blade is 7.4 cm which occurs at a distance of 5.5 cm from the axis. An Eppler E387 [10] airfoil with a thickness to chord ratio of 9.06% is used along the blade span. The Reynolds number at the tip region is about 100,000 at TSR=6. The twist and chord distribution are shown in Figure 2. The nacelle is designed in order to be compact, so that its effect on the flow is minimal. The nacelle which occupies about 6% of the total diameter, houses a DC brushless motor, a gearbox, a hall encoder and the optical trigger. The turbine is mounted on a tower which is 3m tall.

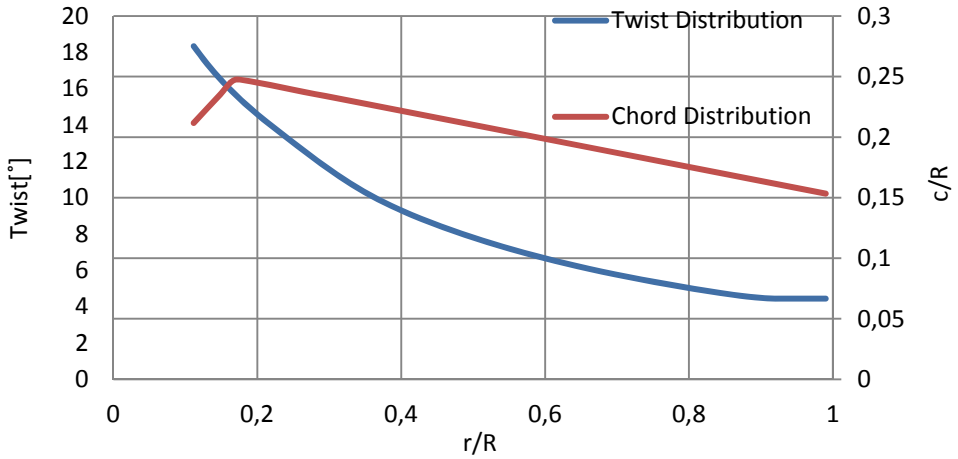

Figure 2: Blade Characteristics

Stereo Particle Image Velocimetry

A stereoscopic PIV setup has been installed in a traversing system able to scan the flow field in the wake of the horizontal-axis wind-turbine wake. The required illumination is provided by a Quantel Evergreen Nd:YAG laser system with 200 mJ/pulse energy at a max frequency of 15 Hz (527 nm wavelength). The laser light is conveyed to form a 2 mm laser sheet of about 35 cm width at the field of view, by combination of a spherical lens of focal f = -50 mm and two cylindrical lenses of f = +80 mm and f = -40 mm. Two LaVision Imager Pro LX 16 Mpix (4870 × 3246 px^2, 12 bits) with pixel pitch of 7.4 µm/px are used to image a field of view of 357 × 253 mm^2, obtained with two Nikon lenses of f = 180 mm and aperture $f\#$ = 2.8 - 4, at a magnification M of 0.10 The focusing plane has been slightly offset with respect to the laser plane (defocusing), to obtain an image of the particle of about 2-3 px, to mitigate the bias errors associated with peak locking [13]. Seeding was provided in the test section by a SAFEX smoke generator with SAFEX MIX, able to produce liquid droplets of less than 1 µm. The entire setup was mounted on a traversing system able to translate in two directions. Ensemble of 400 (phase-locked), 720 (unconditioned) double-frame recordings have been acquired and processed by LaVision Davis 8.1.4. Interrogation windows of 24 × 24 px^2 with 50% overlap allows to have a vector resolution of 1.76 mm, and a vector pitch of 0.88 mm.

The laser control, camera synchronization, and image acquisition are triggered by an opto-coupler TCST 2103, together with a disc perforated at a specific azimuthal position and rotating with the

turbine's shaft providing a one-pulse digital signal for each rotation. The cameras and the laser are mounted on the same structure which in turn is mounted on a traversing system, thus guaranteeing the same setup while the traversing systems travels.

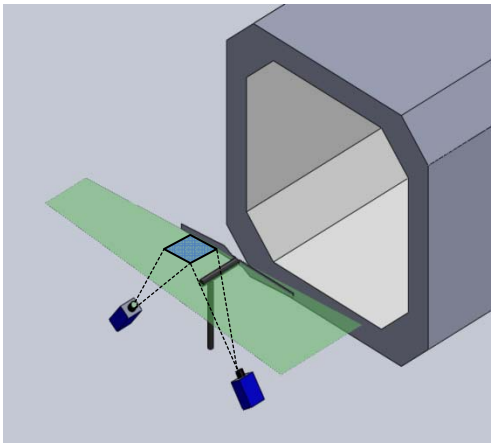

Figure 3: Setup for wake location

Separation Time between the images	200μs
Final interrogation window size	24 x 24
Number of Images	For phase locked sampling: 400 For unconditioned sampling: 720
Pixel size	0.0074 mm/px

Table 2: PIV parameters

Experimental results

In this section, the near- and transition- wake velocity fields till ~2.7 diameters downstream are shown for two different tip-speed ratios. Results are both for phase–locked and unconditioned sampling, namely representing the phase-locked average velocity field and its unconditioned average on all phases. Figure 4 depicts the normalised axial velocity field in the shear layer between the wake and the outer flow till about 1.6 metres (~2.7 diameters) downstream averaged on all phases. The most evident feature in these plots is the location of the wake breakdown, where vortices start a pairwise interaction, the so-called leapfrogging, as shown also in [3,11] and presented later in this paper. In the average field, this appears as a sudden enlargement of the shear layer, starting at ~1 diameter downstream for TSR=6 and ~1.3 diameters downstream for TSR=4 and reaching its maximum at ~1.4 diameters for TSR=6 and at ~1.7 diameters for TSR=4.8. The onset of wake instability is therefore clearly depending on the TSR as shown in [5]. Figure 5 shows the phase-locked velocity field of the shear layer and the inboard region till the hub centreline. The evolution of the tip vortex is shown and the pairwise interaction is now evident. In this picture the nacelle's wake is visible in the inboard region. It is also evident how the tip-vortex has almost completely diffused after the first leapfrogging. This would suggest a strong influence of the large scale wake instability on the tip-vortex diffusion. This hypothesis will be addressed in future studies. Figure 6, depicting the streamwise profiles of axial velocity at different radial locations, shows that the re-energising process starts right after the instability around locations ~1.4 diameters for TSR=6 and at ~1.7 diameters for TSR=4.8. Comparing Figure 6 and Figure 5, it is clear that the onset of the re-energising process coincides with the location of the leapfrogging event. After reaching a minimum at the maximum wake expansion, the axial

velocity intakes a process of re-energising, starting from the outer regions where the turbulent mixing with the external flows happens as evident in Figure 7.

In Figure 8 and 9 the terms $\overline{u_i}\left(\widetilde{u_i}\widetilde{u_j}\right)$ and $\overline{u_i}\langle u_i{}'u_j'\rangle$ of Equation 1 in the x-y plane (namely $\bar{u}(\tilde{u}\tilde{v})$ and $\bar{u}\langle u'u_j'\rangle$) are estimated. These represent the fluxes of mean-flow kinetic energy by means of the periodic vortices and the turbulence respectively. Positive values mean downward fluxes of kinetic energy. Two zones can be identified. The first zone, where the wake expansion occurs, shows the tip-vortices structures to be the only structures determining a mean flow kinetic energy transport across the wake layer, although with a zero net value. The second zone, after the onset of the wake instability, is characterised by a downward net entrainment of kinetic energy, i.e. towards the inner region of the wake., signifying a dominant role of incoherent structures in the mean flow kinetic energy transport and therefore in the re-energising process. The finding is in accordance with the hypothesis of Medici (2005) who stated that the near wake tip-vortices are acting as a shield preventing the wake to mix with the outer flow. Figure 10 shows the production of turbulent kinetic energy, which constitutes a sink of mean flow kinetic energy. Equation 2 describes the process of destruction of the phase averaged flow kinetic energy by mean of the turbulent fluctuations. Again, it is possible to see how the generation of turbulence becomes more violent in the downstream regions after the instability.

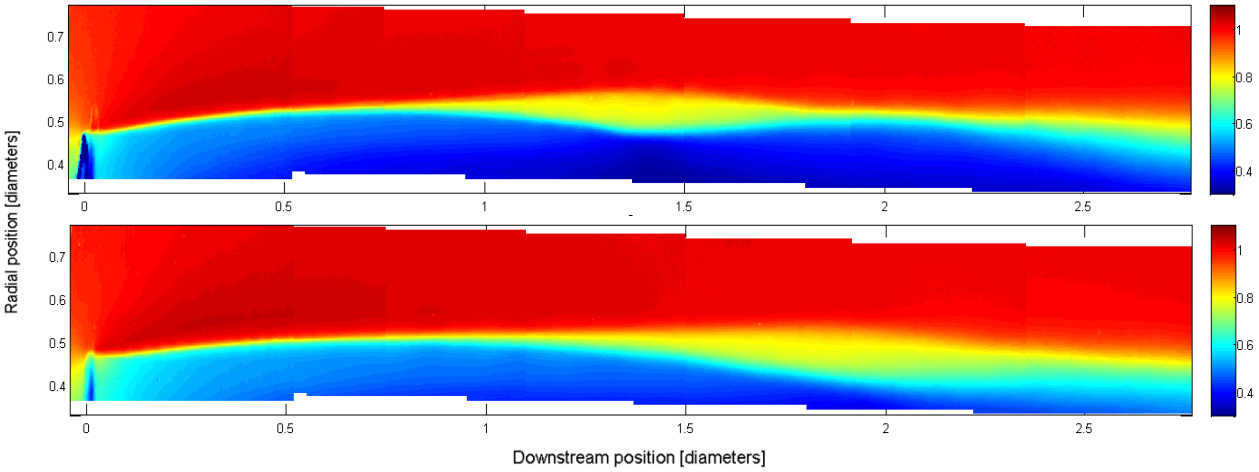

Figure 4: normalised average axial velocity field $\bar{u}/U_{inf}$ in the wake shear layer till 2.7 diameters downstream at two different tip-speed ratios; (up)TSR=6; (down)TSR=4.8

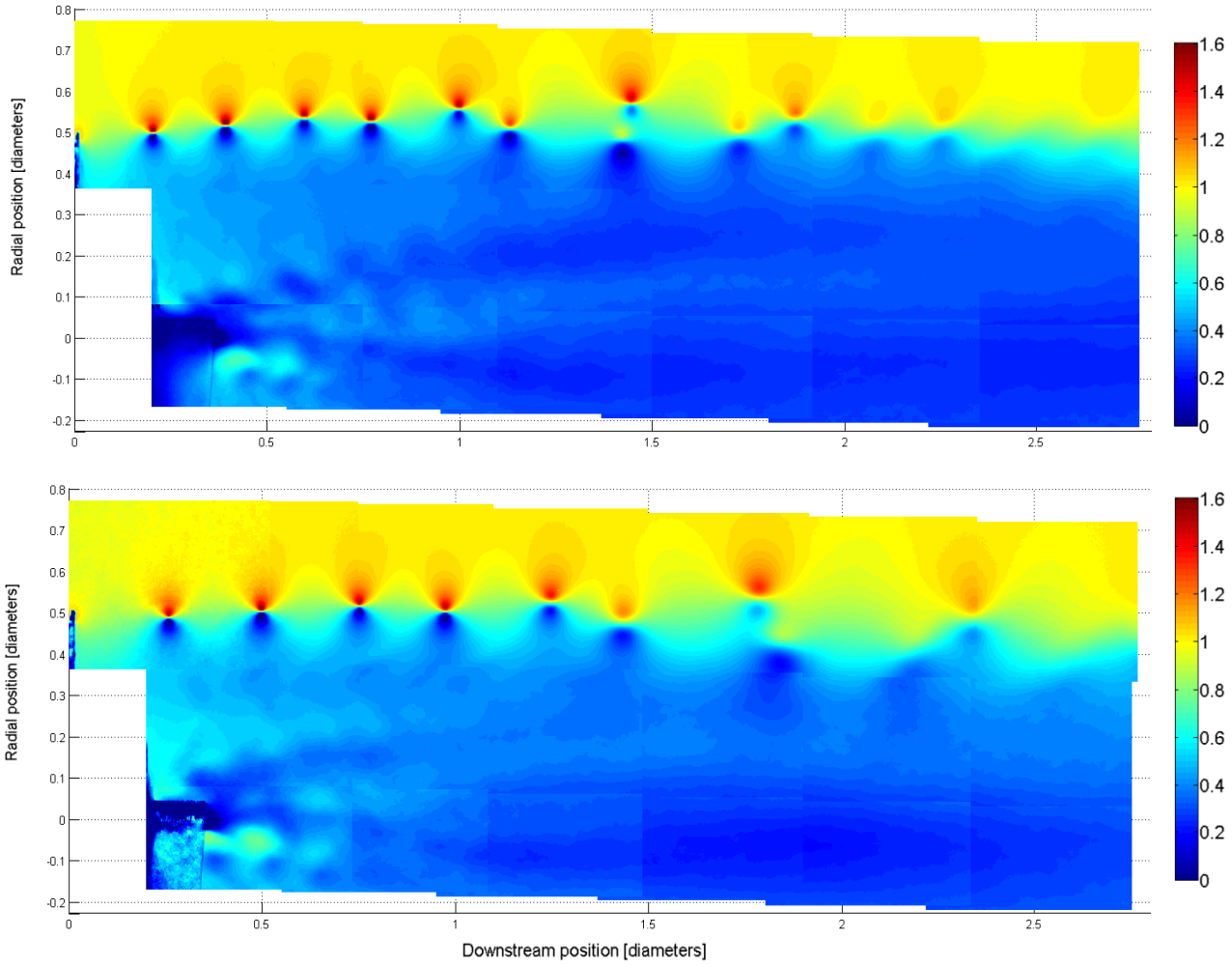

Figure 5: phase-locked averaged normalized axial velocity field $\langle u \rangle / U_{inf}$ for TSR=6 (up) and TSR=4 (down)

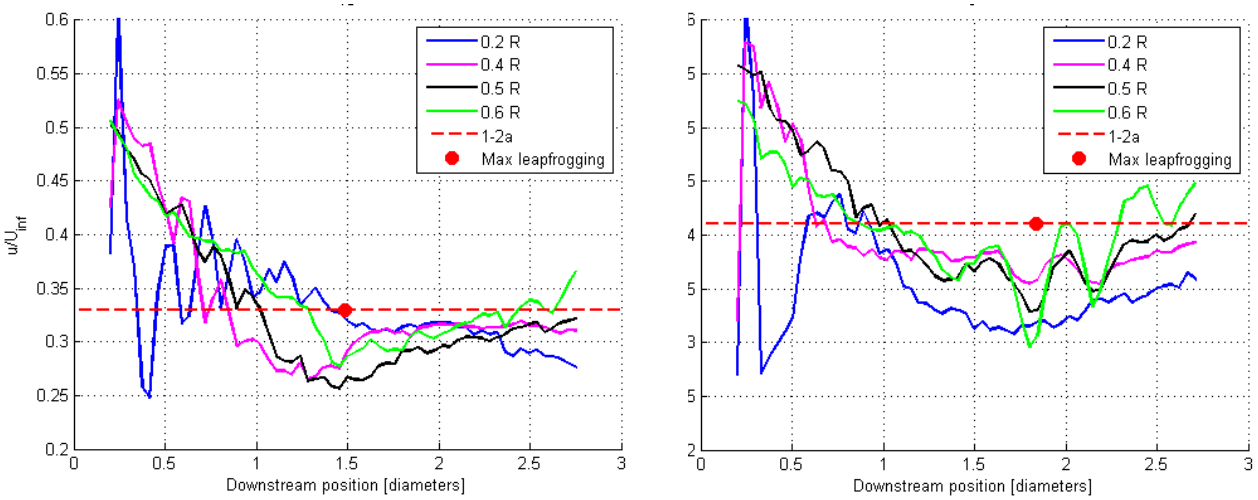

Figure 6: streamwise profiles of normalized phase locked axial velocity field $\langle u \rangle / U_{inf}$ at 4 different radial locations compared with the momentum theory value at the maximum wake expansion $U_{wake} = U_{inf}(1-a)$ at two different tip-speed ratios; (left)TSR=6; (right)TSR=4.8. The red dot indicates the location of the "maximum leapfrogging" in that phase, when the vortex filaments are one on top of each other.

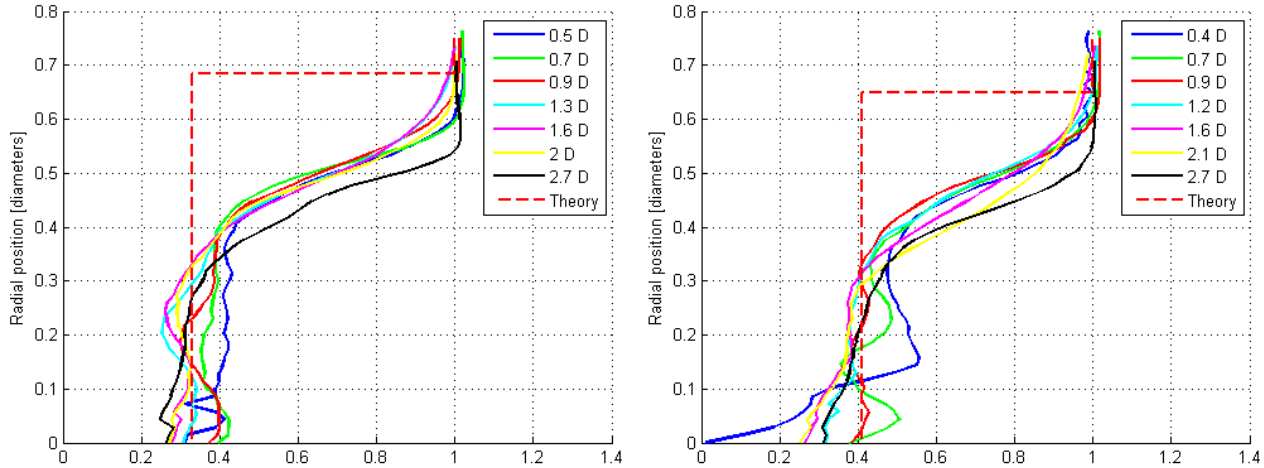

Figure 7: vertical profiles of normalized phase locked axial velocity field $\langle u \rangle / U_{inf}$ at 7 different downstream locations compared with the momentum theory profile at two different tip-speed ratios; (left)TSR=6; (right)TSR=4.8.

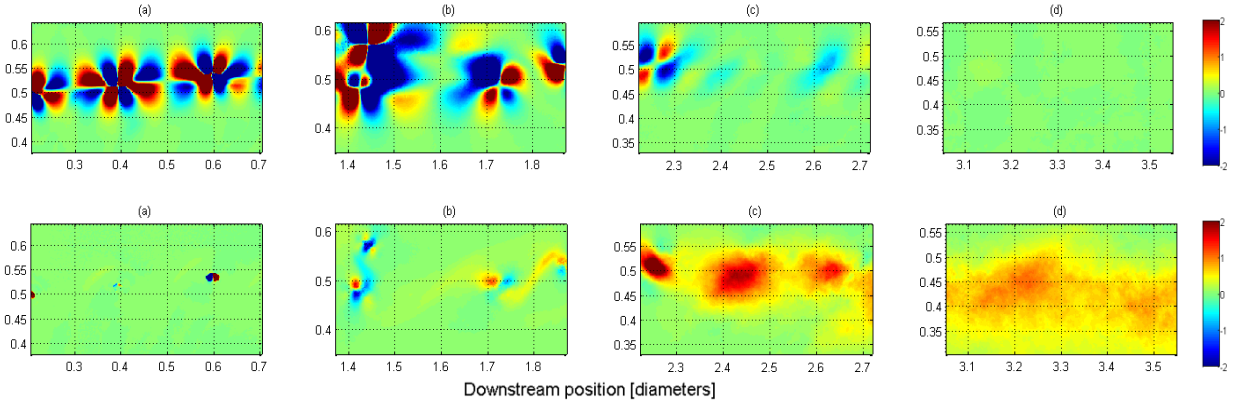

Figure 8:flux of mean flow kinetic energy [m^3/s^3] $\bar{u}\langle u'v'\rangle$ in one phase at 4 different downstream locations at TSR=6; (up) flux due to periodic (coherent) fluctuations; (down) flux due to random (incoherent) fluctuations

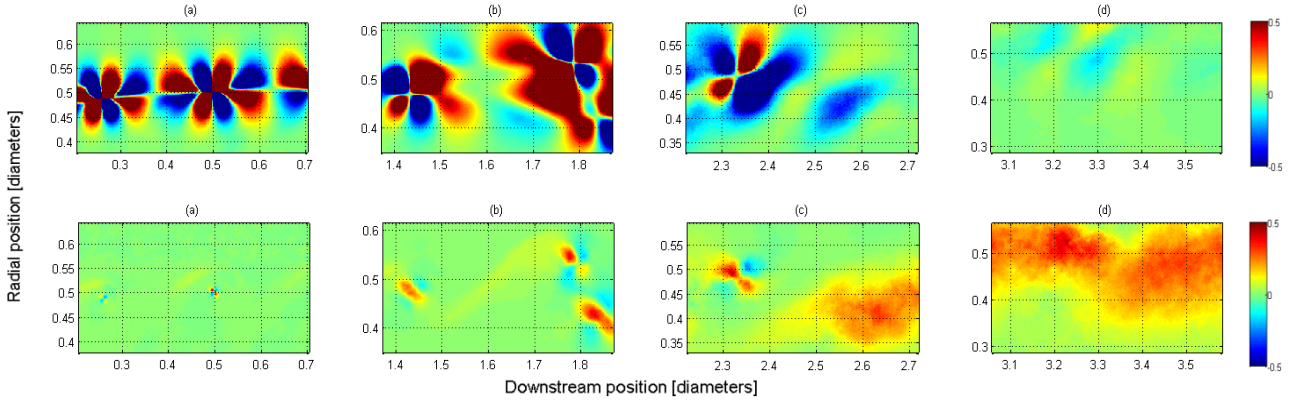

Figure 9: flux of mean flow kinetic energy [m^3/s^3] $\bar{u}\langle u'v'\rangle$ in one phase at 4 different downstream locations at TSR=4.8; (up) flux due to periodic (coherent) fluctuations; (down) flux due to random (incoherent) fluctuations

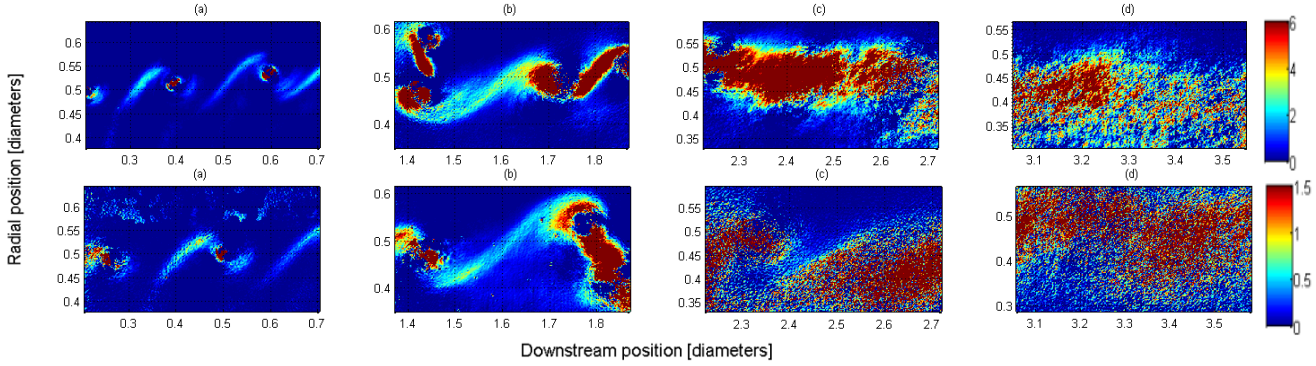

Figure 10: production of turbulent kinetic energy $\langle Pe\rangle = -u'^2\frac{\partial\langle u\rangle}{\partial x} - v'^2\frac{\partial\langle v\rangle}{\partial y} - u'v'\left(\frac{\partial\langle u\rangle}{\partial y} + \frac{\partial\langle v\rangle}{\partial x}\right)$ in one phase at 4 different downstream locations at two different tip-speed ratios; (up)TSR=6; (down)TSR=4.8

Conclusions and future work

The wake of a 60-centimetres HAWT has been measured with SPIV and analysed in order to investigate a relationship between the wake recovery and the evolution and instability of the tip-vortex helix. Unconditioned and phase-locked sampling of the velocity field have been conducted up to 2.7 diameters downstream in order to show the average field as well as the evolution of the tip vortices and their pairwise interaction. The main observation is a clear dependency of the onset of the instability on the value of TSR according to [3] and a strong influence of the leapfrogging event on the re-energising process of the wake. The finding is in accordance with the hypothesis of [7] who stated that the near wake tip-vortices are acting as a shield preventing the wake to mix with the outer flow. As last it is shown how the transport of the mean flow kinetic energy in the wake shear layer changes after the wake breakdown. The study suggests the possibility of a rotor design process which does not only take into account the aerodynamic and power optimisation of the rotor, but also the re-energising properties of the wake, in order to obtain more unstable and faster re-energising wakes. In the near future, the same experiment will be performed with a porous disc for simulating the actuator disc case and to show the differences in the process of kinetic energy entrainment and destruction along the two wake's in order to cast more light on the limitations in the current wake models based on the actuator disc assumption.

REFERENCES

[1] Barthelmie, R.J., Rathmann, O., Frandsen, S.T., Hansen, K.S., Politis, E., Prospathopoulos, J., Rados, K., Cabezón, D., Schlez, W., Phillips, J., Neubert, A., Schepers, J.G., van der Pijl, S.P., 2007. Modelling and measurements of wakes in large wind farms. Journal of Physics: Conference Series 75, 012049.

[2] Cal, R.B., Lebrón, J., Castillo, L., Kang , H.S., Meneveau, C., 2010. Experimental study of the horizontally averaged flow structure in a model wind-turbine array boundary layer. Journal of Renewable and Sustainable Energy 2.

[3] Felli, M., Camussi, R., Di Felice, F., 2011. Mechanisms of evolution of the propeller wake in the transition and far fields. Journal of Fluid Mechanics 682, 5-53.

[4] Hamilton, N., Kang, H.S., Meneveau, C., Cal, R.B., 2012. Statistical analysis of kinetic energy entrainment in a model wind turbine array boundary layer. Journal of Renewable and Sustainable Energy 4, 063105-063119.

[5] Hütter, U., 1977. Optimum Wind-Energy Conversion Systems. Annual Review of Fluid Mechanics 9, 399-419.

[6] Ivanell, S., Mikkelsen, R., Sørensen, J.N., Henningson, D., 2010. Stability analysis of the tip vortices of a wind turbine. WIND ENERGY 13, 705-715.

[7] Medici, D., 2005. Experimental Studies of Wind Turbine Wakes – Power Optimisation and Meandering, Mechanics. Royal Institute of Technology (KTH), Stockholm.

[8] Reynolds, W.C., Hussain, A.K.M.F., 1972. The mechanics of an organized wave in turbulent shear flow. Part 3. Theoretical models and comparisons with experiments. Journal of Fluid Mechanics 54, 263-288.

[9] Schepers, J.G., 2012. Engineering models in wind energy aerodynamics, Aerospace Engineering. Delft University of Technology.

[10] Selig, M.S., Guglielmo, J.J., Broeren, A.P., Giguère, P., 1995. Summary of Low-Speed Airfoil Data, in: Beach, V. (Ed.), Virginia Beach, VA, p. 292.
[11] Sorensen, J.N., 2011. Instability of helical tip vortices in rotor wakes. Journal of Fluid Mechanics.
[12] Westerweel, J., 1997 Fundamentals of digital particle image velocimetry. Measurement Science and Technology 8, 1379–1392.

Modeling turbine wakes and power losses within a wind farm using LES: An application to the Horns Rev offshore wind farm

Y.T. Wu[1], **F. Porté-Agel**[1]

[1] École Polytechnique Fédérale de Lausanne (EPFL)
Wind Engineering and Renewable Energy Laboratory (WIRE)
EPFL-ENAC-IIE-WIRE, Lausanne CH-1015, Switzerland
yu-ting.wu@epfl.ch
fernando.porte-agel@epfl.ch

ABSTRACT

A large-eddy simulation (LES) framework is used to model multiple wake flows and associated power losses within the Horns Rev offshore wind farm under conditions of near-neutral stability. A tuning-free Lagrangian scale-dependent dynamic model is used for the parameterization of the subgrid-scale stresses. The turbine-generated power outputs and the turbine-induced forces (e.g. thrust, lift, drag) are parameterized using two models: (a) the traditional actuator-disk model without rotation (ADM-NR), which uses 1D momentum theory to relate the power output and the thrust force with a representative velocity over the rotor (e.g., the disk-averaged velocity); and (b) the actuator-disk model with rotation (ADM-R), which adopts blade element theory to calculate the lift and drag forces (which produce thrust, rotor shaft torque and power) based on the local blade and flow characteristics. The ADM-NR and the ADM-R require dynamic specifications of the thrust coefficient and the blade angular speed, respectively, in wind farm simulations. Here the ADM-R turbine model is coupled with a new dynamic procedure to predict the blade angular speed (and the power) based on a turbine-model-specific relationship between shaft torque and rotational speed. This relationship, which is unique for a given turbine model, is derived from simulations of a stand-alone wind turbine in conditions for which the thrust coefficient can be validated. Comparison with observed power data shows that better agreement with the predicted power outputs is obtained with the ADM-R than with the ADM-NR, which ignores the torque effect on the turbine wakes and rotor power. Besides, simulations using different inflow conditions show that the mean wind direction has a strong effect on the spatial distributions of the time-averaged velocity and the turbulence intensity within the farm. These, in turn, affect the power outputs and the fatigue loads on the turbines. When the prevailing wind direction is parallel to the turbine rows, the velocity deficit and the power losses are greatest, and the turbulence intensity levels are highest and have a symmetric pattern (dual-peak at hub height) on both sides of the turbine wakes.

Keywords : Actuator-disk models; Atmospheric boundary layer; Blade element theory; Horns Rev offshore wind farm; Large-eddy simulation; Power deficit; Wind-farm wakes

1 Introduction

When wind turbines are clustered together in a finite area, power losses due to turbine wakes are inevitable and vary with their arrangement and the incoming wind conditions. In large offshore wind farms (e.g., Horns Rev, Lillgrund, Middelgrunden, and Nysted), average power losses are in the order of 10%

to 23% of the total power output [1; 2]. These power losses are associated with the wind velocity distribution inside the wind farms, which is modulated by complex interactions between the atmospheric boundary layer (ABL) turbulence and multiple wind-turbine wakes. This ABL-wind-farm interaction is multiscale and fully coupled, and is in turn affected by several factors such as atmospheric stability, land-/sea-surface characteristics, wind-farm layout and wind direction. Accurate numerical prediction of the ABL flow and its interaction with wind turbines and wind farms, as well as of power losses due to wakes and loads, is necessary for designing wind energy projects (wind-turbine siting) in order to minimize the impact of upstream wakes on the productivity of downstream turbines.

Some wind-farm design tools that include different wind-turbine wake models have been developed and implemented in predictions of power losses in operational wind farms [3; 1; 4]. These wake models can be grouped into analytical wake models [5; 6; 7] and numerical wake models [8; 9; 10]. In general, analytical wake models are simplified such that they are fairly straightforward and require less computational time to estimate the wind-farm wind resources and power losses due to wakes. These models involve algebraic models for turbine-induced wake velocities and superimpositions of multiple turbine wakes. Some analytical wake models, such as the Park Model [11], have been implemented in 'industry-standard' softwares (e.g., Wind Atlas Analysis and Application Program (WAsP), WindPro and WindFarmer) for the assessment of wind resources and the micro-siting of wind turbines and wind farms. Another alternative for predicting turbine power output is the use of numerical wake models, which parameterize the turbine-induced forces using 1D momentum theory or blade-element theory. Numerical wake models are incorporated in steady/unsteady computational-fluid-dynamics (CFD) models. In particular, unsteady CFD models can provide detailed information on wind-turbine-induced wakes and turbulence over a wide range of spatial and temporal scales, as well as turbine-generated power outputs. Note that computers are getting more powerful and promote the use of CFD modeling as a design tool for large wind farms in industry. Accuracy of the modeling technique, in both the turbine wakes and power outputs, still needs to be further validated.

In [1], both analytical and numerical wake models are used to predict the turbine power losses at Horns Rev for different wind directions and different wind sectors. The predicted power output results are in disagreement with the observed data for a wind sector of less than 10 degrees. In particular, the predicted power outputs are underestimated by up to 55% in the full-wake conditions, in which the incoming wind direction is parallel to the turbine rows. This discrepancy reflects the need for improvements in both turbulence modeling and turbine parameterization in the wind-farm design tools.

In previous studies, both Reynolds-averaged NavierStokes (RANS) and large-eddy simulation (LES) models, coupled with actuator disk-/line-based models for turbine rotor parameterization, have been used for the modeling of the turbulence in ABL flows through wind turbines [e.g., 12; 13; 14; 15]. In particular, the actuator-disk model without rotation (ADM-NR), the actuator-disk model with rotation (ADM), or both have been increasingly used in the wind farm simulations [16; 17; 18]. Until recently, rigorous validation studies [19; 20; 18] have shown that using LES, coupled with the Lagrangian scale-dependent dynamic model for the subgrid-scale (SGS) stress and the ADM-R for turbine-induced lift and drag forces, is able to reproduce the magnitude and spatial distribution of the most relevant turbulence statistics (e.g. mean velocity, turbulence kinetic energy and turbulent stresses) of turbine wakes in turbulent boundary layer flows.

Some recent studies [21; 22] have examined the power losses from large wind farms using LES coupled with actuator-disk/actuator-line models and a designed controller. However, these studies retain uncertainties, in both the turbulence modeling and the turbine parameterization, which may strongly affect the characteristics of multiple turbine wakes and the estimation of associated power losses in large wind farm simulations.

In this study, we adopt the LES framework to investigate the effect of multiple turbine wakes on power losses in a large wind farm. A Lagrangian scale-dependent dynamic model is used to model the sub-grid-scale (SGS) stress [23]. Two actuator-disk type models for turbine parameterization are used:

the traditional actuator-disk model (ADM-NR) and the actuator-disk model with rotation (ADM-R). Numerical simulations are carried out to examine the effect of different incoming wind directions on the power losses in the Horns Rev wind farm under near-neutral conditions. A short description of the LES framework is given in Section 2. The Horns Rev wind farm and turbines are specified in Section 3. The numerical set-up is presented in Section 4. The predicted power losses as well as the spatial distribution of the mean velocity and the turbulence intensity obtained from the turbulence statistics are shown and discussed in Section 5. Finally conclusions are given in Section 6.

2 Large-Eddy Simulation Framework

2.1 Governing equations of the flow

We use a modified version of the LES code developed by [24; 25; 26; 23; 20; 18]. The code solves the conservation of mass and the conservation of momentum written in rotation form:

$$\frac{\partial \widetilde{u}_i}{\partial x_i} = 0 \,, \tag{1}$$

and

$$\frac{\partial \widetilde{u}_i}{\partial t} + \widetilde{u}_j \left(\frac{\partial \widetilde{u}_i}{\partial x_j} - \frac{\partial \widetilde{u}_j}{\partial x_i} \right) = -\frac{1}{\rho}\frac{\partial \widetilde{p}^*}{\partial x_i} - \frac{\partial \tau_{ij}^d}{\partial x_j} + \nu \frac{\partial^2 \widetilde{u}_i}{\partial x_j^2} - \frac{f_i}{\rho} + \mathscr{F}_i, \tag{2}$$

where the tilde represents a three-dimensional spatial filtering operation at scale Δ, $\widetilde{u}_i$ is the resolved velocity in the i-th direction (with $i = 1,2,3$ corresponding to the streamwise (x), spanwise (y) and vertical (z) directions in a Cartesian coordinate system), ρ is the air density, $\widetilde{p}^*$is the modified pressure, τ_{ij}^d is the deviatoric part of the SGS momentum flux, ν is the kinematic viscosity of air, f_i is an immersed force (per unit volume) for modeling the effect of wind turbines on the flow, and $\mathscr{F}_i$ is a forcing term (e.g., a mean pressure gradient). The SGS momentum flux is modeled using a Lagrangian scale-dependent dynamic model [23]. An immersed force (per unit volume) f_i is parameterized using the two actuator-disk type models (i.e. ADM-R and ADM-NR) [20; 18] for modeling the effect of wind turbines on the flow. MoninObukhov similarity theory is applied to compute the instantaneous (filtered) surface shear stress as a function of the velocity field at the lowest vertical grid point. More details on the numerical method of the LES code can be found in [25; 26; 23].

2.2 Actuator-disk model without rotation (ADM-NR)

The actuator-disk model without rotation (ADM-NR), also called the traditional/Rankine-Froude actuator-disk model, is a popular numerical wind turbine model implemented in both in-house CFD codes [13; 14] and commercial software (e.g., WindSim) [4]. The ADM-NR only considers a uniform thrust load over the circular rotor disk and neglects the effect of wake rotation. Suggested by [16], it is more natural that the axial normal (thrust) force acting on the actuator disk is modeled as

$$F_x^{ADM-NR} = \frac{\rho}{2} \langle \widetilde{u}_0 \rangle^2 C_T \cdot A_e = \frac{\rho}{2} \frac{\langle V_x \rangle^2}{(1-a)^2} C_T \cdot A_e, \tag{3}$$

where the angle bracket denotes a spatial average within the rotor disk, $\widetilde{u}_0$ is the unperturbed streamwise velocity of the incident flow, V_x is the velocity at the rotor, and C_T is the thrust coefficient. For turbines whose thrust and power coefficients are known, the ADM-NR can be used to predict the power output of a wind farm. For simplicity, we compute the power output of a wind turbine based on its power curve and the unperturbed velocity corrected with the disk-averaged velocity and axial induction factor (i.e., $\langle \widetilde{u}_0 \rangle = \langle V_x \rangle / (1-a)$). The axial induction factor a is calculated using $a = 0.5\left(1 - \sqrt{1 - C_T}\right)$ derived

from 1D momentum theory.

2.3 Actuator-disk model with rotation (ADM-R)

A common parameterization strategy in turbine models consists of computing the turbine-induced lift and drag forces with the blade element approach. In this approach, both lift and drag forces acting on each blade element (see Figure 1a) are parameterized based on the relative wind velocity, the geometry of a blade airfoil, and tabulated airfoil data. The decomposition of the resultant force $\boldsymbol{F}$ as well as the relative wind triangle are shown in Figure 1a and their relationships are formulated as follows:

$$\text{Lift force: } L = 0.5\rho V_{rel}^2\, c\Delta r\, C_L \tag{4}$$

$$\text{Drag force: } D = 0.5\rho V_{rel}^2\, c\Delta r\, C_D \tag{5}$$

$$\text{Relative wind velocity : } V_{rel} = \sqrt{V_x^2 + (\Omega r + V_\theta)^2} \tag{6}$$

$$\text{Angle of relative wind : } \phi = \tan^{-1}\left[V_x/(\Omega r - V_\theta)\right] = \theta_p + \gamma + \alpha \tag{7}$$

$$\text{Normal force : } F_x = L\cos\phi + D\sin\phi \tag{8}$$

$$\text{Tangential force : } F_\theta = L\sin\phi - D\cos\phi \tag{9}$$

where c is the local chord length, Δr is the radial length of the airfoil element, V_x is the axial velocity on the rotor, V_θ is the tangential velocity on the rotor, Ω is the blade angular velocity, θ_p is the pitch angle, γ is the twist angle, and α is the angle of attack. C_L and C_D are the lift and drag coefficients obtained from tabulated airfoil data, respectively. It should be noted that the above-mentioned forces are modeled for each blade element, and therefore a method that distributes the forces on the computational mesh is needed.

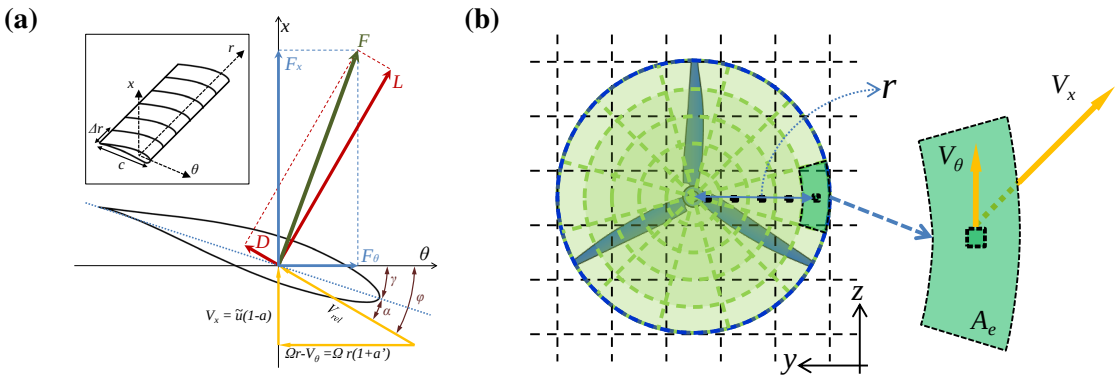

Figure 1: Schematic of a cross-sectional airfoil element (a) and a cylindrical mesh for actuator-disk approaches (b)

A computationally efficient way to distribute the blade-induced forces in large wind farm simulations is using the rotating actuator-disk concept. In this model, the rotor-swept area is represented by an actuator disk on which both normal and tangential forces act upon the incoming flow at a rate that coincides with the period-averaged mechanical work extracted from the flow. The normal force slows down the speed of the flow passing through a rotor, while the tangential force induces the wake rotation behind a turbine. Hence this approach has been referred to as the actuator-disk model with rotation (ADM-R). In the ADM-R, the normal and tangential forces are computed on a cylindrical mesh in order to represent the circular disk shape. The equations for power, shaft torque, and the forces are written as

follows:

$$\text{Power output: } P_O = P_R \cdot \eta \tag{10}$$

$$\text{Rotor power: } P_R = Q \cdot \Omega \tag{11}$$

$$\text{Total (shaft) torque: } Q = \Sigma r \cdot F_\theta^{ADM-R} \tag{12}$$

$$\text{Normal force : } F_x^{ADM-R} = \frac{\rho V_{rel}^2}{2} \frac{Bc}{2\pi r} \left(C_L \cos\phi + C_D \sin\phi\right) \cdot A_e \tag{13}$$

$$\text{Tangential force : } F_\theta^{ADM-R} = \frac{\rho V_{rel}^2}{2} \frac{Bc}{2\pi r} \left(C_L \sin\phi - C_D \cos\phi\right) \cdot A_e \tag{14}$$

where η is the mechanical efficiency of a wind turbine, B is the number of blades, and A_e is the frontal area of each element on a cylindrical mesh system (see Figure 1b). In order to avoid singular behavior and numerical instability, both normal and tangential forces are distributed smoothly in a three-dimensional Gaussian manner by taking the convolution of the local load and a regularization kernel. Besides, note that the ADM-R has no capability to dynamically specify the blade angular velocity based on the incoming wind velocity. Therefore, a new dynamic procedure for the ADM-R to predict the angular speed (and the power) is introduced next.

2.4 Dynamic calculation of a blade angular speed for the ADM-R

To predict the mechanical power of a rotor, we have to know shaft torque and its relationship to the rotating speed. In general, this relationship, which is unique for a given wind turbine, implies a one-to-one relation between the shaft torque and the blade angular speed regardless of incoming wind conditions. The torque-speed relationship can be derived from a series of single wind turbine simulations in which the blade angular speed corresponding to the undisturbed incoming wind velocity is specified a priori. In these simulations, the results also can be used to validate the ADM-R through comparison with rotor thrust coefficient if available from the turbine manufacturer. In the present study, both the thrust coefficient comparison and the torque-speed relationship for a chosen wind turbine (i.e., Vestas V80) are presented in the next section.

As mentioned earlier, the ADM-R adopts blade element theory to parameterize the turbine-generated power output and the turbine-induced forces. However, it is known that the ADM-R is unable to predict the angular velocity of a rotor and thus the power. To overcome this limitation, here we couple the ADM-R with a new dynamic procedure to predict the angular speed based on the torque-speed relationship. In the 'dynamic' ADM-R, the important numerical operations, in the order of their execution, are detailed below:

- Step 1: Interpolate V_x and V_θ on the cylindrical mesh based on the resolved velocity components ($\widetilde{u}$, $\widetilde{v}$, $\widetilde{w}$) at the rotor plane, and then calculate V_{rel} using Equation 6;
- Step 2: Guess an initial value for Ω^o;
- Step 3: Calculate the total (shaft) torque Q;
- Step 4: Calculate the new Ω^n based on the computed Q and the torque-speed relationship;
- Step 5: Calculate $\varepsilon_{tol} = |1 - \Omega^o/\Omega^n|$ and then replace Ω^o with Ω^n;
- Step 6: Return to Step 3 until ε_{tol} is less than a given tolerance value (e.g., 0.001);
- Step 7: Calculate F_x^{ADM-R}, F_θ^{ADM-R}, and P_O.

3 The Horns Rev wind farm and the turbine characteristics

The Horns Rev offshore wind farm is located in the eastern North Sea, around 15 km off the westernmost point of Denmark. It consists of eighty Vestas V-80 2MW wind turbines within an area of about 20 km^2. Each turbine has a hub height H_{hub} = 70 m (above sea level) and a rotor diameter d = 80 m. The wind farm layout has a rhomboid shape with a minimum spacing of 7 rotor diameters between two consecutive turbines in both the 10 rows (approximately 7 degrees turned from North-South) and 8 columns (see Figure 2). Due to the effect of the farm layout, the variation in incoming wind direction causes a spatial change in the wake region behind each turbine. For example, in full-wake conditions the turbine separation distances are 7.0d, 9.3d, and 10.4d for θ_{wind}=270.0^o, 221.5^o, and 311.5^o, respectively (see Figure 2). These different separation distances lead to a strong effect on the power outputs of the turbines located downstream [27]. In this wind farm, the operational records of the turbines (i.e. power output, pitch angle, and rotor angular velocity) were extracted from the Supervisory Control And Data Acquisition (SCADA) system with a reference period of 10 minutes, and corrected with meteorological data measured by the cup anemometers on three nearby masts (M2, M6 and M7) [3; 1; 28]. Based on the analysis of meteorological data [3; 1; 21], the incoming flow to the wind farm is characterized by 10 min turbulence intensity $\approx 7\%$ for a mean wind speed of 8$\pm$0.5 m s^{-1} at hub height and in near-neutral stability conditions (i.e., $|z/L| < 0.1$, where z is the height and L is the Monin$-$Obukhov length).

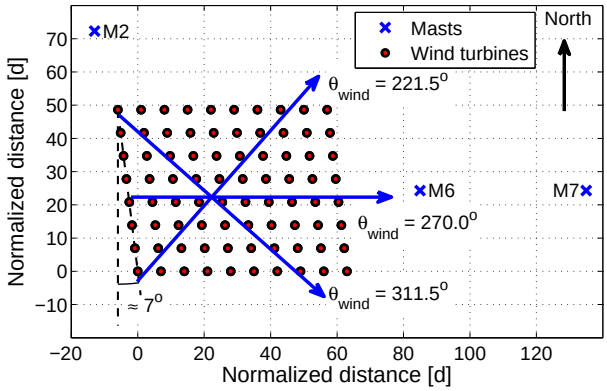

Figure 2: Layout of Horns Rev wind farm and three surrounding masts (M2, M6 and M7)

Even though the detailed geometry of the V80 turbine blades is unknown, some key parameters have been disclosed in the literature. For example, the chord length at the blade root and tip positions is 3.52 m and 0.48 m, respectively. The twist angle decreases from 13 (root) to 0 (tip). The V80 blade is composed of a NACA 63-xxx airfoil between the blade tip and its center, and an FFA W3-xxx airfoil between the center of the blade and the hub [29]. Here we use the above-mentioned parameters in the blade-element momentum (BEM) approach [30] and create the radial distribution of the twist angle and the chord length based on the aerodynamic characteristics of NACA 63-415 and the FFA W3-241 airfoils. The distribution of both lift and drag coefficients versus the angle of attack can be found in [31] for the NACA 63-415 airfoil and in [32] for the FFA W3-241 airfoil.

The blade geometry (i.e. chord length and twist angle) has been tested in a series of LESs of the ABL flows through a stand-alone V80 turbine. In these simulations, the range of hub-height mean wind speeds varies from 5 to 20 m s^{-1}. The rotor angular velocity is specified a priori in the ADM-R to compute the rotor thrust coefficient, shaft torque, and rotor power. In particular, the computed total rotor thrust coefficient values show acceptable agreement with the manufacturers thrust coefficient curve (Figure 3a). This comparison can serve as the ADM-R model validation. The shaft torque and the corresponding rotor angular velocity provide a significant relationship (Figure 3b) that is used to predict the rotating speed of each turbine in the LES of the Horns Rev wind farm. Besides, the mechanical efficiency of the Vestas V80 wind turbine is determined based on the computed rotor power and its power output curve, and has a value of about 0.93.

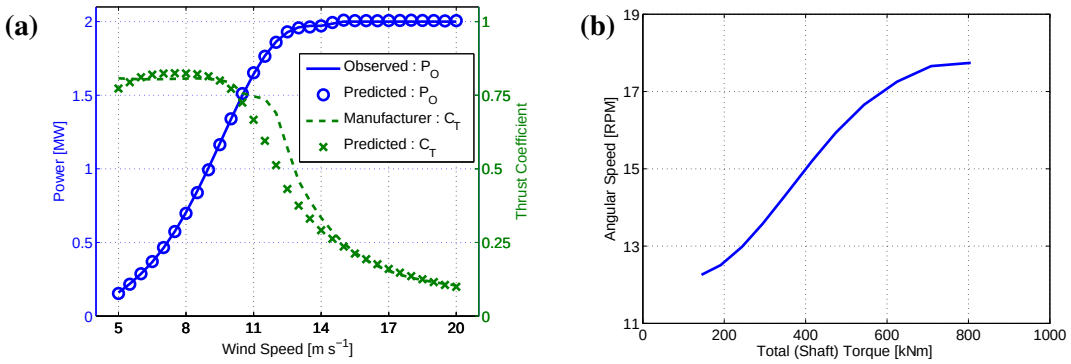

Figure 3: (a) Power curves and thrust coefficient curves with respect to a range of wind speeds for Vestas V80-2MW turbines; (b) relationship between the total shaft torque and the rotor angular velocity

Table 1: Numerical set-up for neutral ABL simulations with different incoming wind directions

Case	Wind angle [deg]	S_x [d]	S_y [d]	L_x [m]	L_y [m]	L_z [m]	Δ_x [m]	Δ_y [m]	Δ_z [m]
HR-266	266.0	-	-	14896.96	8333.57	500	23.28	13.02	7.94
HR-268	268.0	-	-	14924.24	6253.99	500	23.32	9.77	7.94
HR-270	270.0	7.00	6.95	14933.33	9881.58	500	23.33	15.44	7.94
HR-272	272.0	-	-	14924.24	6253.99	500	23.32	9.77	7.94
HR-274	274.0	-	-	14896.96	8333.57	500	23.28	13.02	7.94
HR-218	217.5	-	-	12126.65	10152.19	500	18.95	15.86	7.94
HR-220	219.5	-	-	12670.40	9873.94	500	19.80	15.43	7.94
HR-222	221.5	9.28	5.24	13198.73	9583.66	500	20.62	14.97	7.94
HR-224	223.5	-	-	13710.97	9281.70	500	21.42	14.50	7.94
HR-226	225.5	-	-	14206.50	8968.44	500	22.20	14.01	7.94
HR-308	307.5	-	-	17766.33	8395.38	500	27.76	13.12	7.94
HR-310	309.5	-	-	17279.40	8771.82	500	27.00	13.71	7.94
HR-312	311.5	10.48	4.64	16771.40	9137.58	500	26.21	14.28	7.94
HR-314	313.5	-	-	16242.98	9492.21	500	25.38	14.83	7.94
HR-316	315.5	-	-	15694.77	9835.27	500	24.52	15.37	7.94

4 Numerical set-up

The LES framework, coupled with the ADM-R and the ADM-NR, is used to model the multiple turbine wakes and the associated power losses in the Horns Rev wind farm. In particular we focus on cases in which observed power data are available under near-neutral stability conditions for a hub-height wind speed of 8 ± 0.5 m s^{-1} and with wind direction sectors of $\theta_{wind} = 270.0\pm1^o$, 270.0 ± 5^o, 221.5 ± 1^o, 221.5 ± 5^o, 311.5 ± 1^o, and 311.5 ± 5^o. To systemically investigate the power losses in these cases, we perform a series of LESs with different simulation domain sizes (L_x, L_y, L_z), as shown in Table 1. The height of the computational domain is set to $L_z = 500$ m, corresponding to the boundary-layer depth δ. This height is close to the boundary-layer depth observed by [33] at Horns Rev. A constant streamwise pressure gradient is used to drive the flow within the boundary layer. The domain is divided uniformly into $N_x \times N_y \times N_z = 640\times640\times64$ grid points, with a grid resolution (Δ_x, Δ_y, Δ_z). As a result, the turbine rotor diameter is covered by at least 5 points in the spanwise direction and 10 points in the vertical direction. Based on previous resolution sensitivity results [34; 18], the grid resolution over the rotor is well suited for the LES framework to account for the most significant characteristics of wind-turbine wakes.

The simulations are carried out by employing an incoming flow condition that has a mean wind speed of 8 m s^{-1} and a 10-min turbulence intensity of 7% at hub height level. In the surface layer of the incoming flow (around 20% of the boundary layer depth), the mean velocity profile is characterized by a log law with a friction velocity of 0.287 m s^{-1} and an aerodynamic roughness length equal to 0.001 m. The turbulence intensity is computed in 10-minute intervals based on the instantaneous (filtered) velocity components $\widetilde{u}$ and $\widetilde{v}$, since the Horns Rev meteorological data were measured by cup anemometers and

analyzed using 10-minute intervals.

In the simulations using the ADM-NR, the thrust coefficient C_T is dynamically specified based on the manufacturers thrust coefficient curve (shown in Figure 3b) and the incoming wind velocity. The incoming wind velocity is estimated from a disk-averaged velocity (at rotor) corrected with the axial induction factor (i.e., $\langle \widetilde{u_0} \rangle = \langle V_x \rangle / (1-a)$). For all the turbines, the thrust force and the power output are modeled based on the thrust coefficient curve and power curve (shown in Figure 3b), respectively. It should be pointed out that these two curves are applicable to V80 turbines operating in unperturbed inflow conditions.

All the simulations using the ADM-R and the ADM-NR were run for a period (physical time) of 100 min, and the flow statistics were computed during the last 60 min, which guarantees quasi-steady flow conditions as well as the statistical convergence of the results presented in the next section.

5 Results

Both the ADM-R and the ADM-NR are used to model the turbine power outputs in the Horns Rev wind farm with a range of inflow wind directions from 265^o to 275^o, which corresponds to five cases of HR-266 to HR-274 (see Table 1). In order to compare the observed and simulated power outputs for the 10^o wake sector, we average the simulated power results obtained from the five cases (i.e., HR-266 to HR-274). Figure 4 shows the comparison of observed and simulated power outputs for the two wake sectors of $\theta_{wind} = 270.0 \pm 1^o$ and 270.0 ± 5^o. The simulated power outputs obtained using the ADM-R show acceptable agreement with the observed power data from the Horns Rev wind farm. The ADM-NR tends to underestimate the power output, with greater discrepancy on downstream turbines located between the second row and fifth row. The largest discrepancy between observed and simulated power outputs is in the second row of turbines, where the simulations underpredict the power by 17% and 6% for the ADM-NR and ADM-R, respectively. In the ADM-NR results the obvious underestimation is attributed to two reasons: first, the ADM-NR only considers a uniform distribution of the thrust force and ignores the wake rotation effect; second, both the thrust and power coefficients, which are applicable for the turbines in undisturbed inflow conditions, are used for the downstream turbines operating in the wakes of upstream turbines.

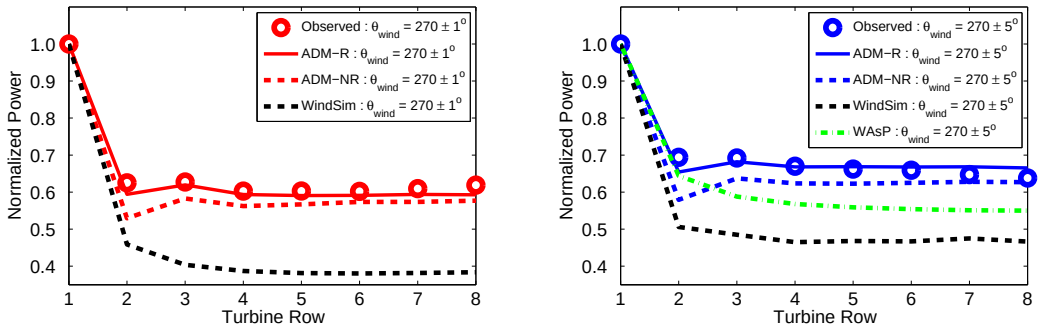

Figure 4: Comparison of the observed and simulated power output data for the wake sectors of $\theta_{wind} = 270.0 \pm 1^o$ (left) and 270.0 ± 5^o (right)

In this study, we also use two wind-farm design tools, WindSim and WAsP, for the turbine power comparison and focus on the two cases with a wake sector of $\theta_{wind} = 270.0 \pm 1^o$ and 270.0 ± 5^o. In simulations performed by WindSim, a uniform actuator-disk model (similar to the ADM-NR) built in a steady RANS flow solver with the standard κ-ε turbulence model is used to predict the turbine power output. To calculate the power output for the wake sector of $\theta_{wind} = 270.0 \pm 5^o$, the simulations corresponding to five different incoming mean wind directions (i.e, $\theta_{wind} = 266^o$, 268^o, 270^o, 272^o, 274^o) are carried out. Besides, unlike WindSim that can evaluate the turbine power within a narrow wake sector, WAsP has the minimum allowable wind sector of 10^o and, therefore, is used only for the larger wake sector

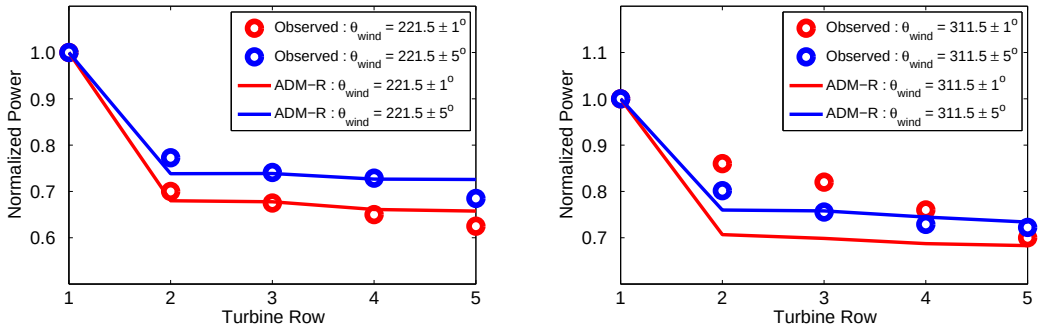

Figure 5: Comparison of the observed and simulated power output data for the wake sectors of θ_{wind} = 221.5±1^o and 221.5±5^o (left) as well as θ_{wind} = 311.5±1^o and 311.5±5^o (right)

case. In WAsP, the turbine-generated wakes and power output are calculated by a linearized wake model using the inflow data following a two-parameter Weibull distribution. The power outputs predicted using WindSim and WAsP are shown in Figure 4. From this figure it is obvious that these two wind-farm design tools predict power outputs that are far below the observed data and the simulated results obtained from the LES framework with the ADM-NR and the ADM-R. This comparison, particularly the results obtained using the ADM-NR and WindSim, highlights the importance of turbulence modeling on turbine power prediction.

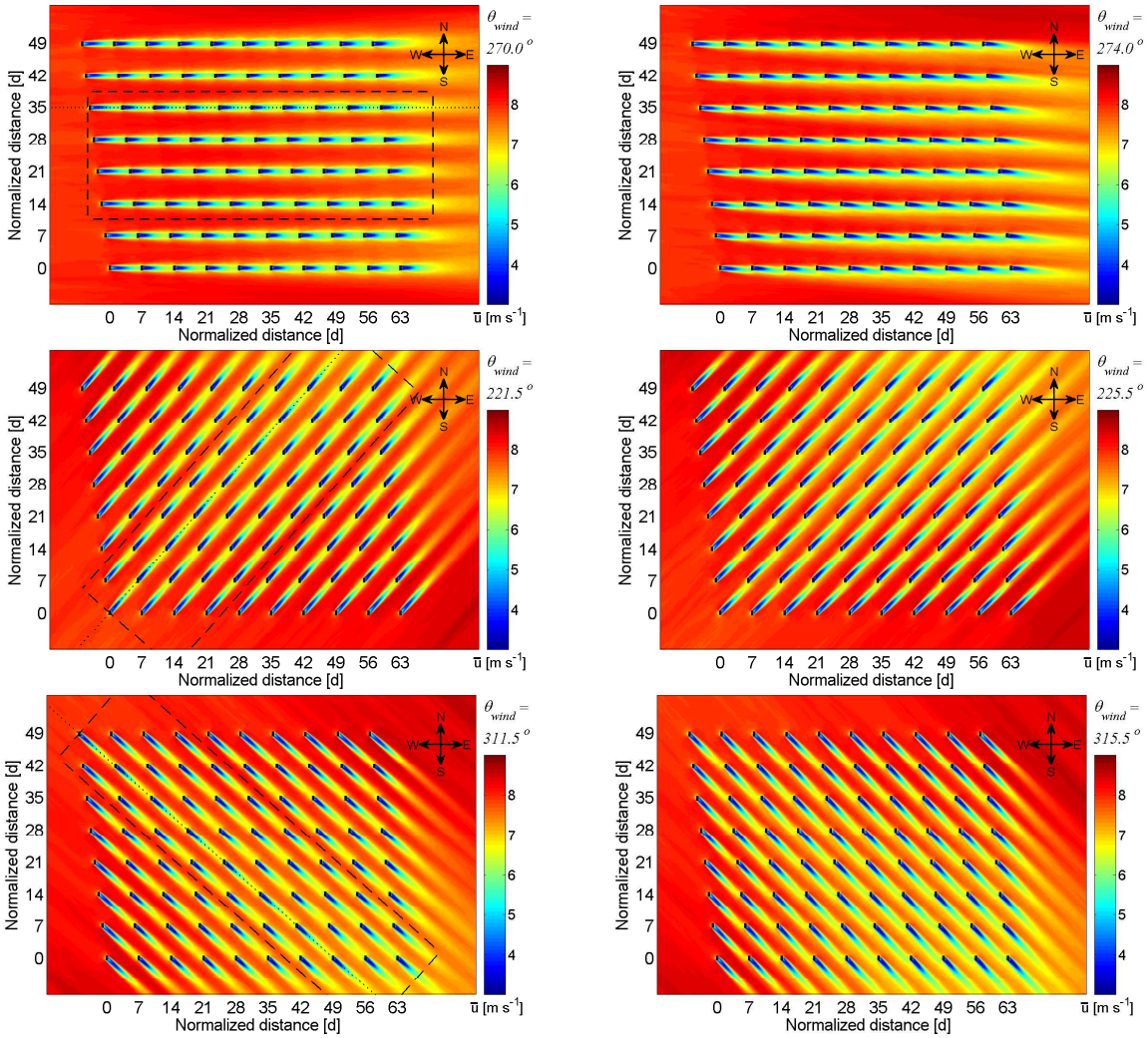

Figure 6: Contours of the time-averaged streamwise velocity on a horizontal plane at hub level for different incoming wind directions

In this study, the ADM-R is used to predict the power losses in the Horns Rev wind farm for different wake sectors around three different mean wind directions. These wind directions are θ_{wind} = 270.0^o, 221.5^o and 311.5^o, corresponding to a turbine separation of 7d, 9.4d and 10.4d (along the prevailing wind direction) respectively. Figure 5 shows the comparison of observed and simulated power outputs for the wake sectors of θ_{wind} = 221.5$\pm$1^o and 221.5$\pm$5^o as well as θ_{wind} = 311.5$\pm$1^o and 311.5$\pm$5^o. The simulated power outputs for the wake sectors of θ_{wind} = 270.0$\pm$1^o and 270.0$\pm$5^o are shown in Figure 4. From these two figures, we find that the simulated power outputs using the ADM-R show acceptable agreement with the observed data except for the θ_{wind} = 311.5$\pm$1^o wake sector case. It should be noted that the observed power data on the downstream turbines, particularly in the second and third rows, is larger for the wake sector of θ_{wind} = 311.5$\pm$1^o rather than θ_{wind}=311.5$\pm$5^o. This is in apparent contradiction with the expected consequences of power data analysis (i.e., the wider wake sector the larger power output) for large wind farms [1; 2].

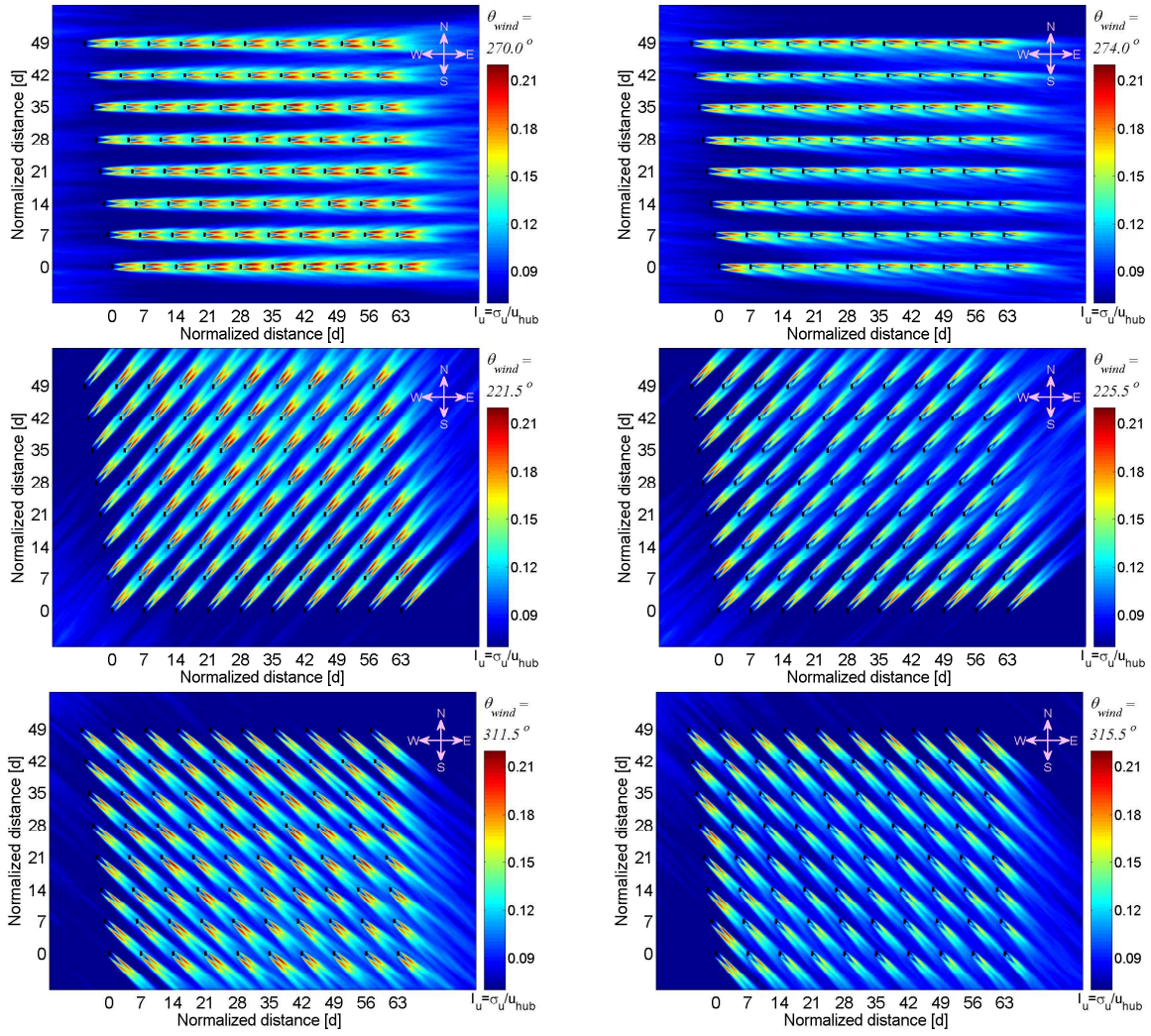

Figure 7: Contours of the 10 minute streamwise turbulence intensity on a horizontal plane at hub level for different incoming wind directions

In order to better understand turbine power degradation, here we focus on the structure and characteristics of the multiple turbine wakes and their variability with incoming wind directions inside the wind farm. Figures 6 and 7 show contours of the time-averaged streamwise velocity and the (resolved) streamwise turbulence intensity (obtained with the ADM-R), respectively, on a horizontal plane at hub level for different mean wind directions. From these figures, it is clear that the power degradation is associated

with a strong wake effect. In particular, in full-wake conditions (i.e., HR-270, HR-222, and HR-312) the turbines located downstream are exposed to an inflow with a lower velocity (Figure 6) and higher turbulence (Figure 7), which leads to a larger wind power reduction compared with other partial-wake conditions. Besides, the simulation results show that the inflow wind direction causes a strong effect on the spatial distributions of the time-averaged streamwise velocity and the streamwise turbulence intensity within the farm. These are associated with the variation in turbine separation distances (in the direction of the wind) under different incoming wind directions and, in turn, affect the fatigue loads and the power output on the turbines. Due to the effect of full wake interactions in the cases of HR-270, HR-222, and HR-312, the turbulence intensity levels are strongly enhanced and have a symmetric pattern (dual-peak at hub height) on both sides of the turbine wakes.

6 Conclusions

A recently-developed LES framework is used to investigate the effect of multiple wake flows and associated power losses in a large wind farm. The SGS stresses are parameterized using a Lagrangian scale-dependent dynamic SGS model. The turbine-generated power output and the forces (e.g. thrust, lift, drag) are modeled using two approaches: (a) the traditional actuator-disk model without rotation (ADM-NR) and (b) the actuator-disk model with rotation (ADM-R). In order to predict power output from wind farms, the turbine models require dynamic specifications of some important parameters, such as the power coefficient for the ADM-NR and the blade angular speed for the ADM-R. In this study, we propose a new dynamic procedure coupled with the ADM-R to predict the turbine power output based on a turbine-model-specific relationship between the shaft torque and the blade angular speed. This torque-speed relationship is specific for a given wind turbine model regardless of inflow conditions. This is unlike the turbine thrust and power coefficients, which are different for different inflow conditions (e.g., undisturbed inflow vs. wake inflow).

We choose the Horns Rev wind farm as a case study since data were available for a range of inflow conditions. The wind farm consists of eighty Vestas V80 2MW wind turbines. The torque-speed relationship for the V80 turbines is obtained from a series of stand-alone turbine simulations in which the blade angular speed is specified a priori and the computed thrust coefficient is compared with data from the turbine manufacturer. This comparison shows an acceptable agreement, which provides confidence in the blade geometry and the torque-speed relationship that are used in the wind farm simulations.

The simulations results show that the predicted power outputs obtained using the ADM-R are in good agreement with observed power data from the Horns Rev wind farm. The ADM-NR tends to underestimate the power output due to two reasons. First, the ADM-NR only considers a uniform distribution of the thrust force and ignores the wake rotation effect, which cannot accurately account for the turbine wakes. Second, both the thrust and power coefficients, which are suitable for the turbines in undisturbed inflow conditions, are used for the turbines operating in the wakes of upstream turbines. Besides, two commercial wind-farm design tools, WindSim and WAsP, are used to model the turbine power losses. The turbine power outputs obtained using WindSim and WAsP together with the two actuator disk models are compared. The results show that these two design tools substantially under-predict the turbine power outputs since they cannot accurately model turbulence in the complex turbine wake flow within the wind farm.

Simulations using different inflow conditions show that the mean wind direction has a strong effect on the spatial distributions of the time-averaged velocity and the turbulence intensity within the farm. These, in turn, affect the power output and the fatigue loads on the turbines. When the prevailing wind direction is parallel to the turbine rows, the velocity deficit and the power losses are greatest, and the turbulence intensity levels are highest and have a symmetrical pattern (dual-peak at hub height) on both sides of the turbine wakes.

References

[1] R. J. Barthelmie, K. Hansen, S. T. Frandsen, O. Rathmann, J. G. Schepers, W. Schlez, J. Phillips, K. Rados, A. Zervos, E. S. Politis, and P. K. Chaviaropoulos, "Modelling and measuring flow and wind turbine wakes in large wind farms offshore," *Wind Energy*, vol. 12, no. 5, pp. 431–444, 2009.

[2] R. J. Barthelmie, S. C. Pryor, S. T. Frandsen, K. S. Hansen, J. G. Schepers, K. Rados, W. Schlez, A. Neubert, L. E. Jensen, and S. Neckelmann, "Quantifying the impact of wind turbine wakes on power output at offshore wind farms," *J Atmos Oceanic Technol*, vol. 27, pp. 1302–1317, 2010.

[3] D. R. VanLuvanee, "Investigation of observed and modeled wake effects at Horns Rev using WindPRO," Master's thesis, Technical University of Denmark, 2006.

[4] G. Crasto, F. Castellani, A. R. Gravdahl, and E. Piccioni, "Offshore wind power prediction through CFD simulation and the actuator disc model," in *EWEA, Brussels, Belgium: Europes Premier Wind Energy Event*, 2011.

[5] I. Katic, J. Højstrup, and N. Jensen, *A Simple Model for Cluster Efficiency*, pp. 407–410. A. Raguzzi, 1987.

[6] G. Larsen, *A simple wake calculation procedure*. Risø-M, Risø National Laboratory, 1988.

[7] T. Ishihara, A. Yamaguchi, and Y. Fujino, "Development of a new wake model based on a wind tunnel experiment," in *Global Wind Power*, 2004.

[8] J. Ainslie, "Calculating the flowfield in the wake of wind turbines," *J Wind Eng Ind Aerodyn*, vol. 27, no. 13, pp. 213 – 224, 1988.

[9] A. Crespo, J. Hernandez, E. Fraga, and C. Andreu, "Experimental validation of the UPM computer code to calculate wind turbine wakes and comparison with other models," *J Wind Eng Ind Aerodyn*, vol. 27, no. 13, pp. 77–88, 1988.

[10] K. Rados, G. Larsen, R. Barthelmie, W. Schlez, B. Lange, G. Schepers, T. Hegberg, and M. Magnisson, "Comparison of wake models with data for offshore windfarms," *Wind Eng*, vol. 25, pp. 271–280, 2001.

[11] N. O. Jensen, "A note on wind generator interaction," in *Risø-M-2411, Risø National Laboratory, Roskilde,*, 1984.

[12] R. Gómez-Elvira, A. Crespo, E. Migoya, and J. Manuel F. Hernández, "Anisotropy of turbulence in wind turbine wakes," *J Wind Eng Ind Aerodyn*, vol. 93, pp. 797–814, 2005.

[13] A. Jimenez, A. Crespo, E. Migoya, and J. Garcia, "Advances in large-eddy simulation of a wind turbine wake," *J Phys: Conf Ser*, vol. 75, 2007. 012041.

[14] A. Jimenez, A. Crespo, E. Migoya, and J. Garcia, "Large-eddy simulation of spectral coherence in a wind turbine wake," *Environ Res Lett*, vol. 3, 2008. 015004.

[15] H. Lu and F. Porté-Agel, "Large-eddy simulation of a very large wind farm in a stable atmospheric boundary layer," *Phys Fluids*, vol. 23, p. 065101, 2011.

[16] M. Calaf, C. Meneveau, and J. Meyers, "Large eddy simulation study of fully developed wind-turbine array boundary layers," *Phys Fluids*, vol. 22, no. 1, 2010. 015110.

[17] M. Calaf, M. B. Parlange, and C. Meneveau, "Large eddy simulation study of scalar transport in fully developed wind-turbine array boundary layers," *Phys Fluids*, vol. 23, no. 12, p. 126603, 2011.

[18] Y. T. Wu and F. Porté-Agel, "Simulation of turbulent flow inside and above wind farms: Model validation and layout effects," *Boundary-Layer Meteorol*, vol. 146, no. 2, pp. 181–205, 2013.

[19] F. Porté-Agel, Y. T. Wu, H. Lu, and R. J. Conzemius, "Large-eddy simulation of atmospheric boundary layer flow through wind turbines and wind farms," *J Wind Eng Ind Aerodyn*, vol. 99, pp. 154–168, 2011.

[20] Y. T. Wu and F. Porté-Agel, "Large-eddy simulation of wind-turbine wakes: Evaluation of turbine parametrisations," *Boundary-Layer Meteorol*, vol. 138, no. 3, pp. 345–366, 2011.

[21] S. Ivanell, R. F. Mikkelsen, J. N. Sørensen, K. S. Hansen, and D. Henningson, *The impact of wind direction in atmospheric BL on interacting wakes at Horns Rev wind farm*, pp. 407–426. 2010. Torque 2010.

[22] M. J. Churchfield, S. Lee, P. J. Moriarty, L. A. Martinez, S. Leonardi, G. Vijayakumar, and J. G. Brasseur, "A large-eddy simulation of wind-plant aerodynamics: Preprint," in *50th AIAA Aerospace Sciences Meeting, Nashville, Tennessee*, 2012.

[23] R. Stoll and F. Porté-Agel, "Dynamic subgrid-scale models for momentum and scalar fluxes in large-eddy simulations of neutrally stratified atmospheric boundary layers over heterogeneous terrain," *Water Resour Res*, vol. 42, 2006. W01409.

[24] J. D. Albertson, A. V. Johansson, J. H. Haritonidis, and H. Eckelmann, "The fluctuating wall-shear stress and the velocity field in the viscous sublayer," *Phys Fluids*, vol. 31, pp. 1026–1033, 1988.

[25] F. Porté-Agel, C. Meneveau, and M. B. Parlange, "A scale-dependent dynamic model for large-eddy simulation: Application to a neutral atmospheric boundary layer," *J Fluid Mech*, vol. 415, pp. 261–284, 2000.

[26] F. Porté-Agel, "A scale-dependent dynamic model for scalar transport in large-eddy simulations of the atmospheric boundary layer," *Boundary-Layer Meteorol*, vol. 112, pp. 81–105, 2004.

[27] R. J. Barthelmie, O. Rathmann, S. T. Frandsen, K. Hansen, E. Politis, J. Prospathopoulos, P. K. Chaviaropoulos, K. Rados, D. Cabezón, W. Schlez, J. Phillips, A. Neubert, J. Schepers, and S. van der Pijl, "Modelling and measurements of wakes in large wind farms," *J Phys: Conf Ser*, vol. 75, 2007. 012049.

[28] K. S. Hansen, R. J. Barthelmie, L. E. Jensen, and A. Sommer, "The impact of turbulence intensity and atmospheric stability on power deficits due to wind turbine wakes at Horns Rev wind farm," *Wind Energy*, vol. 15, pp. 183–196, 2012.

[29] A. Ilinca, "Analysis and mitigation of icing effects on wind turbines," *Wind Turbines, Ibrahim Al-Bahadly (Ed.), ISBN: 978-953-307-221-0, InTech*, 2011. Available from: http://www.intechopen.com/books/wind-turbines/analysis-and-mitigation-of-icing-effects-on-wind-turbines.

[30] J. F. Manwell, J. G. McGowan, and A. L. Rogers, *Wind Energy Explained: Theory, Design and Application*. John Wiley & Sons, second ed., 2009.

[31] C. Bak, P. Fuglsang, J. Johansen, and I. Antoniou, "Wind tunnel tests of the naca 63-415 and a modified naca 63-415 airfoil," *Risø National Laboratory*, vol. Risø-R-1193, pp. 1–108, 2000.

[32] P. Fuglsang, I. Antoniou, K. S. Dahl, and M. H. A., "Wind tunnel tests of the ffa-w3-241, ffa-w3-301 and naca 63-430 airfoils," *Risø National Laboratory*, vol. Risø-R-1041, pp. 1–163, 1998.

[33] A. Peña and S.-E. Gryning, "Charnock's Roughness Length Model and Non-dimensional Wind Profiles Over the Sea," *Boundary-Layer Meteorol*, vol. 128, pp. 191–203, 2008.

[34] Y. Wu and F. Porté-Agel, "Atmospheric turbulence effects on wind-turbine wakes: An les study," *Energies*, vol. 5, no. 12, pp. 5340–5362, 2012.

Prediction of Wind Energy Distribution in Complex Terrain using CFD

Chang Xu [1], Chenqi Li[1], Jianchuan Yang[1], Wenzhong Shen[2], Yuan Zheng[1], Deyou Liu[1]

[1]Hohai University, College of Energy and Electrical Engineering, Nanjing, Jiangsu Province, 211100, China, zhuifengxu@hhu.edu.cn ,0702020122@hhu.edu.cn

[2]Technical University of Denmark, Department of Wind Energy, Nils Koppels Alle, Building 403, 2800 Lyngby, Denmark, wzsh@dtu.dk

ABSTRACT

Based on linear models, WAsP software predicts wind energy distribution, with a good accuracy for flat terrain, but with a large error under complicated topography. In this paper, numerical simulations are carried out using the FLUENT software on a mesh generated by the GAMBIT and ARGIS software to predict wind speed distribution in complex terrain. TECPLOT software post-processing is used to get the whole wind flow field, the wind speed distribution characteristics and distribution of wind energy. The obtained results are compared with the results of WAsP software and are also more accordance with the actual conditions.

Keywords: wind farm, complex terrain, wind energy resources evaluation, CFD numerical simulation

0 INTRODUCTION

In recent years, wind energy has become the fastest growing renewable energy [1-3]. Wind energy resource assessment is a basic work for the construction of wind farms. Power calculation of a wind farm is directly related to economic factor and wind power grid connection. Currently, wind energy resource and power capacity are usually calculated by WAsP software developed by Danish RisΦ laboratory. The linear model was adopted in the software.Wind energy resource assessment and wind power output are often accurate for the flat terrain and would be higher error for the complex terrain. The software should be further improved for increasing the prediction accuracy [4-5]. With the wind energy resource exploitation further development, wind farm site is transferring from flat terrain of wind speed stability and good construction conditions to complex terrain of high turbulence and bad construction conditions [6-8]. So it is essential to develop a novel method or code to estimate the wind energy distribution or the wind farm layout.

Due to the complex topography, wind energy distribution and turbine output calculations are difficult currently because of the aerodynamic detouring flow and the turbine wake models, and the former is usually the key point. At present wind mast data are very too limited to estimate the whole wind farm energy distribution accurately. With rapid development of CFD technology in recent years, many researchers tried to apply the technology to estimate the wind energy for the wind farm [9-13]. This paper tried to develop a numerical calculation method by combining the topography data process, CFD model and calculation, post-processing. Through the calculation analysis of wind speed and wind energy distribution of a wind farm, the results obtained are compared to the results of WAsP software and it could show the more accordance with the actual conditions. At the same time the method developed by the paper is easy to apply to the actual engineering.

1 TERRAIN DIGITAL PROCESSING

Complex terrain of a wind farm is usually depicted by Autocad isohypse contour, But when calculating aerodynamic field by CFD, it needs to digitize the complex terrain for developing the physical model. Argis is a powerful software which can analysis geographic information system, digital map, geographic information acquisition, and is also the most powerful and the most widely used in geographic information system industry. This paper uses the Argis to get tin file by

separating contour figure of Autocad file, and the tin file can be turned into dem file of coordinates by discretization. In this paper, the wind farm calculated is from north China. The original Autocad isohypse contour is shown in figure 1, and the terrain discreted is shown in figure 2 by the Argis software. Figure 3 is the wind farm contour map, which is fitted to the results obtained by Argis at height. By the comparison and analysis, the topographic map discreted by ARGIS software is in accordance with the original digital topographic map with very high accuracy.

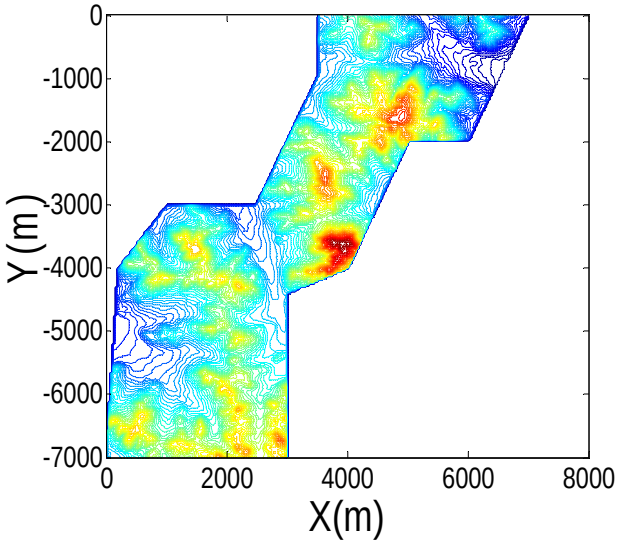

Figure 1: Two-dimensional Autocad terrain isohypse contour

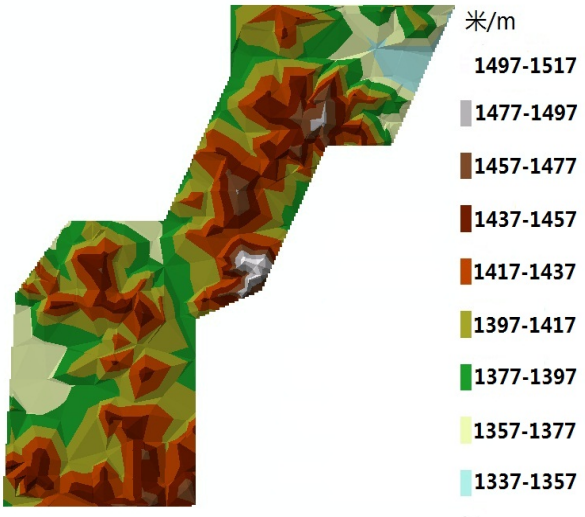

Figure 2: Argis map

According to the complex topography and discreted digital files, develop the physical model of topography in the Gambit software. According to the topographic data, the selection of calculation area is 7000 m * 7000 m * 500 m, the blank terrain in original map complemented by surrounding terrain ,as shown in figure 4, The height is 500 m, choose the unstructured grid, ground surface grid for 30 m by 30 m, In the vertical direction on the surface to mesh with 500 m height is divided into three layers, 0 to 50 m, 50-200 m, 200-500 m respectively, and the grid interval is 5 m, 10 m and 30 m respectively .

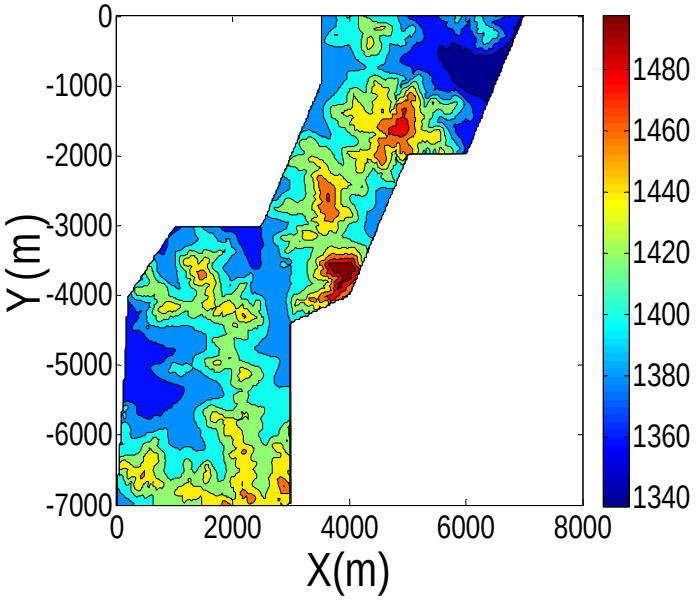

Figure 3: Wind farms contour map

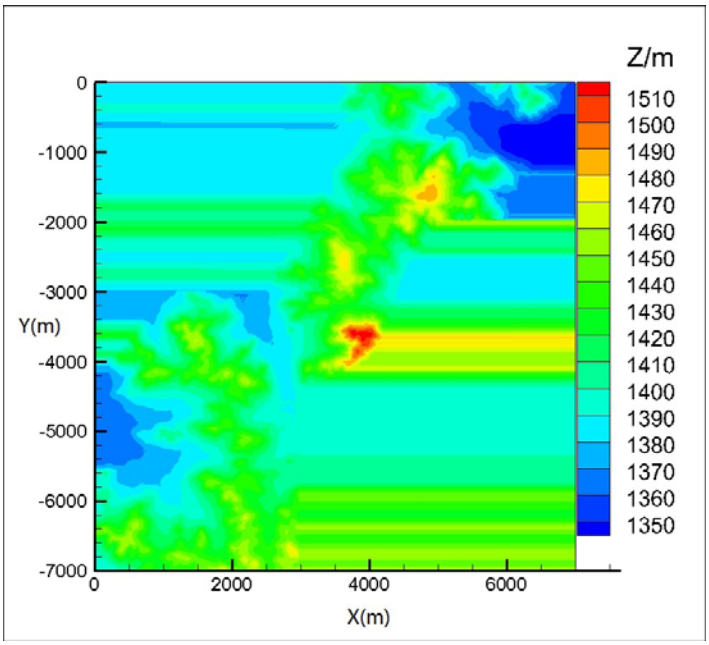

Figure 4: Wind farm calculation zone

2 MATHEMATICAL MODEL AND CALCULATION

Standard Navier - Stokes equations (cartesian coordinate system) are expressed as equations (1)-(4) [14]:

$$\frac{\partial \rho}{\partial t} + div(\rho \vec{u}) = 0 \quad (1)$$

$$\rho \frac{\partial u}{\partial t} + div(\rho u \vec{u}) = div(\mu \, grad \, u) - \frac{\partial p}{\partial x} \quad (2)$$

$$\rho \frac{\partial v}{\partial t} + div(\rho v \vec{u}) = div(\mu \, grad \, v) - \frac{\partial p}{\partial y} \quad (3)$$

$$\rho \frac{\partial w}{\partial t} + div(\rho w \vec{u}) = div(\mu \, grad \, w) - \frac{\partial p}{\partial z} \quad (4)$$

This article chooses the steady, constant physical property control equations and the standard k - ε turbulence models are used [15]：

$$\frac{\partial \rho k}{\partial t} + div(\rho k \vec{u}) = div(\Gamma_k \, grad \, k) + G - \rho\varepsilon \tag{5}$$

$$\frac{\partial \rho k}{\partial t} + div(\rho \varepsilon \vec{u}) = div(\Gamma_k \, grad \, \varepsilon) + \frac{C_{1\varepsilon}}{k} G - C_{2\varepsilon} \rho \frac{\varepsilon^2}{k} \tag{6}$$

ρ is the density of air, and u , v the horizontal wind speeds respectively, w the vertical wind speed, p the air pressure, μ the turbulence viscosity, Γ_k diffusion coefficient of k , G the turbulent energy generation rate or the kinetic energy dissipation rate, $G - \rho\varepsilon$ the net source term and the model constant. Equation parameters are set as: second order discretization form of the upper wind method，bottom boundary conditions are processed with the wall function method, entrance is velocity inlet, outlet is outflow, others are all symmetry conditions. Equations are solved by the simplic algorithm. According to the wind speeds from the wind masts in the wind farm. Wind rose diagram is divided by 12 sections, the average wind speeds of each section are calculated. And the boundary condition is used by equation (7):

$$u(z) = \frac{u_*}{\kappa} \ln\left(\frac{z}{z_0}\right) \tag{7}$$

u_* is speed of surface friction coefficient, κ is the von Karman constant (0.4), z_0 is surface roughness length . Inlet boundary condition is coupled by Fluent UDF editor. Wind velocity inlet of 0 to 30^0 direction is shown as Figure 5, it can be seen the trend of velocity inlet increases along the height direction. The ground wind speed is close to zero.

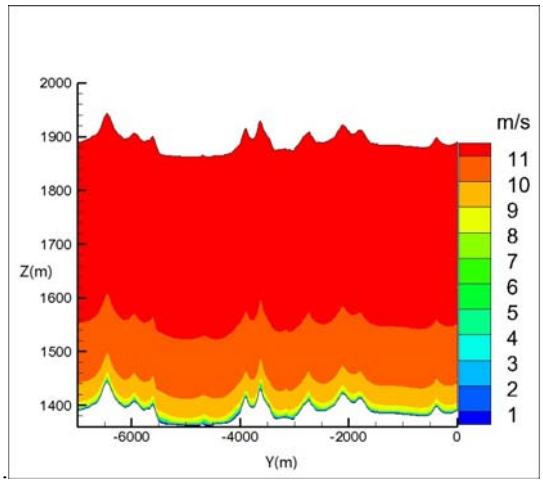

Figure 5: speed inlet condition from 0 to 30 degree

3 RESULT ANALYSIS

3.1 Wind calculation results

Wind energy density is defined as wind energy power per area [16], Thus wind energy density formula, also called wind power density formula is expressed as:

$$w = \frac{1}{2} \rho v^3 \tag{8}$$

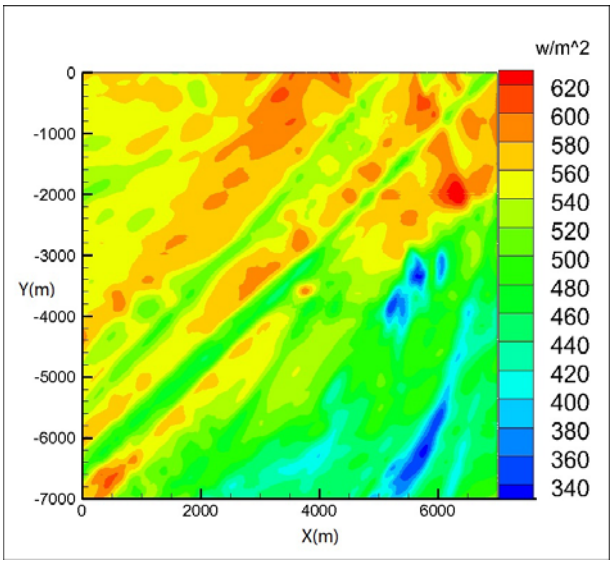

Figure 6: Wind energy distribution (z=1600m)

Aerodynamic field computations are carried out by FLUENT software in 12 directions. Wind energy distributions are summerized according to wind speed probability distribution of each direction by TECPLOT software. Wind energy distribution is shown as from Figure 6 to Figure 8 at different heights. Wind energy distribution will increase with height increasing. But there is very big difference at the same height level because of different height and detouring flow. Figure 9 and Figure 10 show the local wind energy distribution and velocity distribution at the position of the topographic map, which the specific scope of coordinates is x = 2500-5000 m and y = - 3000 m. In Figure 9, the wind energy distribution is obtained from 12 wind speeds due to probability distribution, Figure 10 is the wind velocity distribution when the wind blowing hillside at the wind direction of 0 to 30 degree zone, which can be seen from the figure leeward slope wind velocity is smaller than windward slope wind velocity, the wind speed decreases caused by slope block as a result of the energy loss.

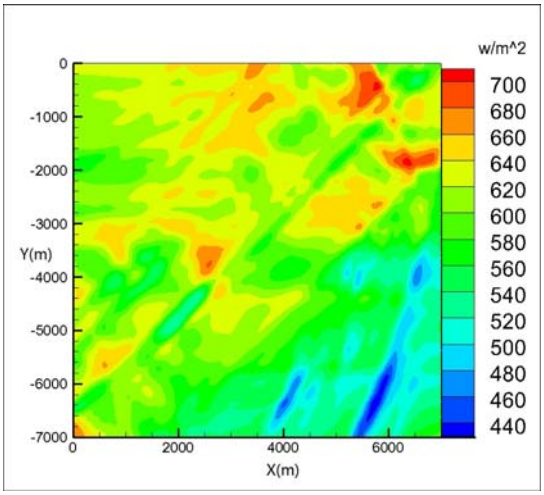

Figure 7: Wind energy distribution (z=1700m)

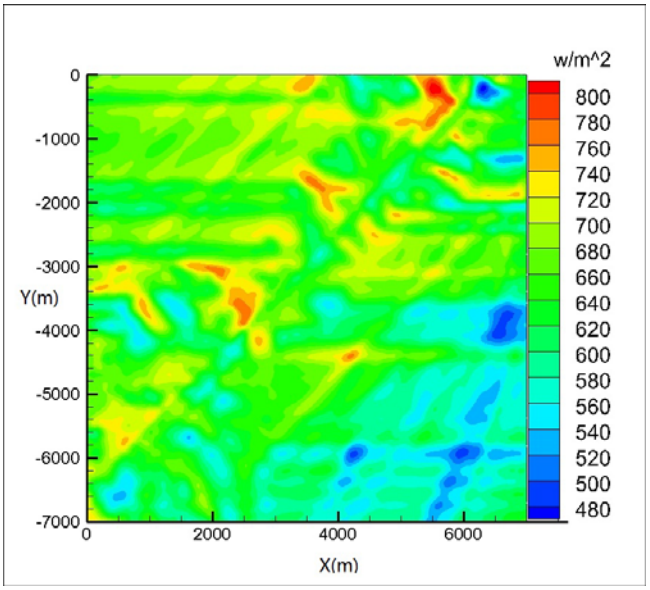

Figure 8: Wind energy distribution (z=1800m)

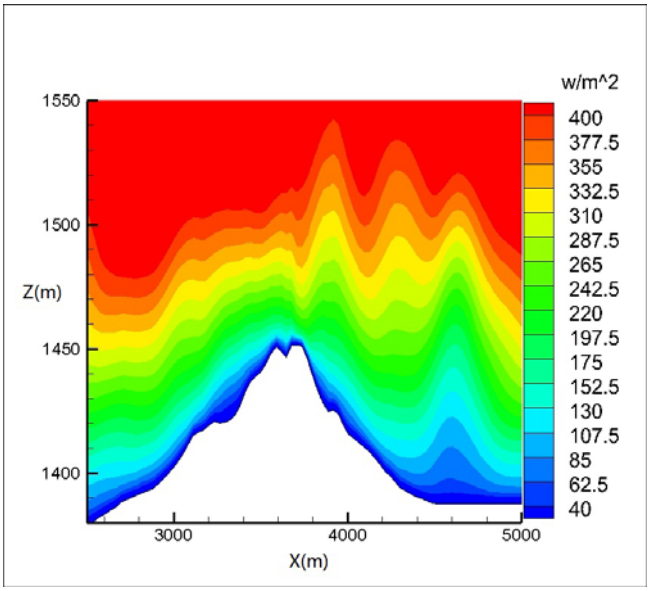

Figure 9: Local wind energy distribution

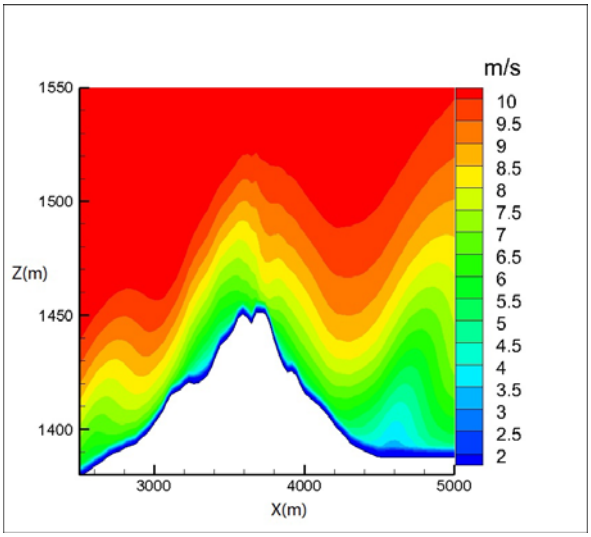

Figure 10: Local wind velocity distribution

3.2 Comparison between numerical simulation and WAsP software

In the CFD calculation result of the wind farm, along the prevailing wind direction, 20 evenly distribution points are checked by the results of the CFD numerical simulation and the WAsP software respectively. Results show that there are some differences between these two methods. In the Tab.1, points from 6 to 20 , CFD results are smaller around 100-200 w/m^2 than the results of the WAsP, and the first five points is close to the edge of the terrain, the result of range is bigger. From Figure 11,we can intuitively see, just the second calculation point in the distribution of wind energy outweighs the WAsP. The other CFD calculation results are less than the WAsP calculation results. The calculation results are consistent with the engineering results, which wind distribution calculated in complex terrain using WAsP is often bigger than the measurement from the wind farm at present. This is because the WAsP is just taking consideration of the height influence on the wind speed by Lissaman model, while ignoring the detouring flow of the terrain. Otherwise, CFD numerical simulation method takes the terrain height and detouring flow effect on wind speed distribution, thus more accord with the actual wind power distribution results obtained.

Tab.1 distribution of wind energy in 20 calculated point by CFD and WAsP

Points	X/m	Ym/	Z/m	CFD/ (w/m^2)	WAsP/ (w/m^2)	Difference/ (w/m^2)
1	150.8621	−6849.14	1428.775	352.0798	378.3076	26.2278
2	452.5862	−6547.41	1487.5	568.931	432.9725	−135.9585
3	754.3103	−6245.69	1459.047	394.0908	412.5912	18.5004
4	1056.034	−5943.97	1415.502	214.5136	354.0609	139.5473
5	1357.759	−5642.24	1428.367	319.9514	377.6848	57.7334
6	1659.483	−5340.52	1419.449	215.2356	362.272	147.0364
7	1961.207	−5038.79	1447.859	270.9516	402.0661	131.1145
8	2262.931	−4737.07	1434.054	195.2646	385.8512	190.5866
9	2564.655	−4435.34	1438.466	246.8089	391.5182	144.7093
10	2866.379	−4133.62	1419.913	149.0633	363.1724	214.1091
11	3168.103	−3831.9	1435.779	163.1859	388.1296	224.9437
12	3469.828	−3530.17	1480.485	271.2416	428.591	157.3494
13	3771.552	−3228.45	1455.358	220.3219	409.3249	189.003
14	4073.276	−2926.72	1452.328	235.1058	406.4986	171.3928
15	4375	−2625	1441.018	205.4146	394.5711	189.1565
16	4676.724	−2323.28	1459.547	265.2732	413.0201	147.7469
17	4978.448	−2021.55	1482.582	293.8114	429.9375	136.1261
18	5280.172	−1719.83	1477.5	316.9961	426.6165	109.6204
19	5581.897	−1418.1	1433.579	194.8793	385.2088	190.3295
20	5883.621	−1116.38	1415.281	254.5544	353.5692	99.0148

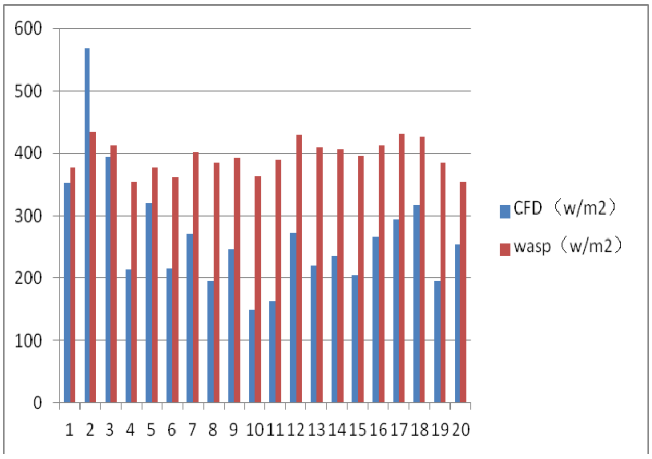

Figure 11: Wind energy diagram in calculation 20 points by CFD and WAsP

4 CONCLUSIONS

(1) In the complex terrain, it was compared that the wind power distribution calculation results of the CFD and the WAsP software, and CFD calculation method calculates more accurately the wind flow over the complicated topography and the distribution of wind energy.

(2) WAsP is a traditional wind resource evaluation software based on the linear wake model and Lissaman model. Calculation error is often a little big for complex terrain. CFD numerical simulation method for complex terrain can take the effects of wind speed change with height by detouring flow accurately, the wind energy calculation results are often smaller than the results of WAsP. This matches the fact that WAsP calculation results are often over-estimated in complex terrain.

REFERENCES

[1] HAN Chun-fu. Wind energy resources evaluation method analysis and application [J]. Energy Conservation, Vol.322,No.5 (2009)pp.22-24.

[2] HU Yi, ZHANG Jian. Research on wind speed of wind resources evaluation [J]. Inner Mongolia Science Technology & Economy, No.21 (2011) pp.76-78.

[3] Liang Si-chao, ZHANG Xiao-dong, KANG Shun, KANG Yalan, ZHAO Yongfeng. A method of wind farm wind resources evaluation in complex terrain Based on numerical simulation [J]. ACTA AERODYNAMICA SINICA , Vol.21,No.3 (2012) pp. 415-421.

[4] LAI Yong-lun, WU Qing. Analysis on application of WAsP to wind energy resource assessment for Sige Wind Farm in Guizhou [J]. HongShui River, Vol.28,No.4 (2009) pp. 106-108

[5] YANG Zhen-bin, XUE Heng, SANG Jian-guo. A trial research on complex terrain wind energy resources evaluation[J]. Acta Energiae Solaris Sinica, Vol.25,No.6 (2004) pp.744-749.

[6] Yang X-Y, Xiao Y, Chen S-Y. Wind Speed and Generated Power Forecasting in Wind Farm[J]. Proceedings- Chinese Socity of Electrical Engineering. Vol.25,No.11 (2005) pp.1.

[7] Berge Erik, Nyhammer Finn,Tallhaug Lars, Jacobsen Øystein. An evaluation of the WAsP model at a coastal mountainous site in Norway[J]. Wind Energy. Vol.9,No.1 (2006) pp.131-140.

[8] Kusiak Andrew,Zheng Haiyang. Optimization of wind turbine energy and power factor with an evolutionary computation algorithm[J]. Renewable Energy. Vol.35,No.3 (2010) pp. 1324-1332

[9] FENG Chang-qing, DU Yan-jun, BAO Zi-guang, XUAN Ji-xin. The applicability between Wind energy resources evaluation software WAsP and WT [J]. Electric Power, Vol.43,No.1 (2010) pp. 61-65.

[10] H. A. Madsen, G. C. Larsen and T. J. Larsen. Calibration. validation of the dynamic wake meandering model for implementation in an aeroelastic code[J]. Journal of Solar Energy Engineering, Vol.132,No.4 (2010) pp. 41-71.

[11] J. Berg,J. Mann, A. Bechmann,H. E. Jørgensen. The Bolund Experiment, Part I： Flow Over a Steep, Three-Dimensional Hill[J].Boundary-Layer Meteorology. Vol.142,No.2 (2011) pp.219

[12] Bingöl Ferhat,Mann Jakob,Foussekis Dimitri. Conically scanning lidar error in complex terrain [J]. Meteorologische Zeitschrift. Vol.18,No.2 (2009) pp. 189-196.

[13] Kindler Detlef,Oldroyd Andrew,MacAskill Allan,Finch Danny. An eight month test campaign of the Qinetiq ZephIR system： Preliminary results[J]. Meteorologische Zeitschrift. Vol.16,No.5 (2007) pp.479

[14] WANG Mei-ling, LUO Yong, ZHOU Rong-wei. Application of WindSim to Wind Energy Resources Assessment of Complex Terrain in china [J]. Meteorological Monthly, Vol.36,No.2 (2010) pp. 113-119.

[15] WANG Fu-Jun. Computational fluid dynamics analysis[M]. Bei Jing: Tsinghua university press,(2004)pp.113-119

[16] TIAN Zi-Chan, YANG Yong-Ping, LIU Yong-Qian. Complex terrain of wind resources evaluation research[D]. Bei Jing: North China electric power university,2009.

Evaluation of SKIRON mesoscale model at FINO-1 as a function atmospheric stability.

S. Lozano[1], J. Sanz[1], P. Correia[1], E. Cantero[1]

[1]CENER, Wind Energy Department, Spain, slozano@cener.com

Abstract

Wind resource assessment from mesoscale models has traditionaly focused on the mean wind speed over a region of interest. Detailed characterization of wind speed and direction at hub height, wind shear and atmospheric stability, are also important aspects to consider in order to meet the very demanding accuracy required by wind energy projects.

With this paper our purpose is to present a validation of Skiron mesoscale model used for offshore wind resource characterization. A year-long wind simulation is carried out to determinate whether it can reliably estimate the mean vertical profile, wind direction distribution and the wind speed magnitude at FINO-I offshore tower.
The FINO-1 offshore platform is a good site for validation since it offers a rather complete dataset that includs flux-profile measurements. Hence, it is possible to produce a characterization of atmospheric stability and classify the vertical structure of the marine boundary layer.

Our results indicate that SKIRON model is able to capture the essential wind characteristics: with an mean bias of the 90 m annual wind speed of just -0.041 m/s and a correlation coefficient of 0.898.

]

1. Introduction

Wind resource assessment from mesoscale models has traditionaly focused on the mean wind speed over a region of interest. Detailed characterization of wind speed and direction

at hub height, wind shear and atmospheric stability, are also important aspects to consider in order to meet the very demanding accuracy required by wind energy projects. Mesoscale models are tipicaly used to obtain a preliminary coarse wind map in order to identify suitable areas for wind energy deployment. Long term mesoscale model simulation provide a very useful information to locate regions suitable for wind measurement campaigns. In the offshore environment, industry is very keen at substituting measurements with virtual met masts from mesoscale models in order to reduce the high costs of installing and maintaining a real met mast. We explore the possibility of using long term meteorological simulations to extract the relevant information for wind resource characterization.

2. Methodolgy

Skiron, as other numerical weather prediction (NWP) models, exhibits skill in predicting the synoptic weather for conventional forecasting purposes. However, the parameters critical for wind resource assessment, such as near-surface wind speeds, wind directions, vertical wind shears between the surface and turbine blade tip, and turbulence, have less impact on routine weather forecasts, and so have not received as much attention as other weather phenomena (precipitation, thunderstorms, hurricanes). Large errors in boundary-layer parameters, significantly impact wind energy projects, contributing to costly errors in wind farm siting and energy forecasting. An extended validation beyond the mean wind speed is required in order to provide improved knowledge about the provide a full picture of other relevant parameters in wind energy assessment.

2.1. The NWP model

The model used by CENER for long term simulation is SKIRON. The regional weather forecasting system SKIRON was developed for operational use at the Hellenic National Meteorological Service. The entire system is fully parallelized and requires Unix computational environment. Its central component is the Eta limited area weather forecasting model. The atmospheric model used is the Eta model. It uses a specific *'step mountain'* vertical coordinate. Partial differential equations are represented by finite-difference schemes in the model. In the horizontal, the model is discretized over a semi-staggered E grid.

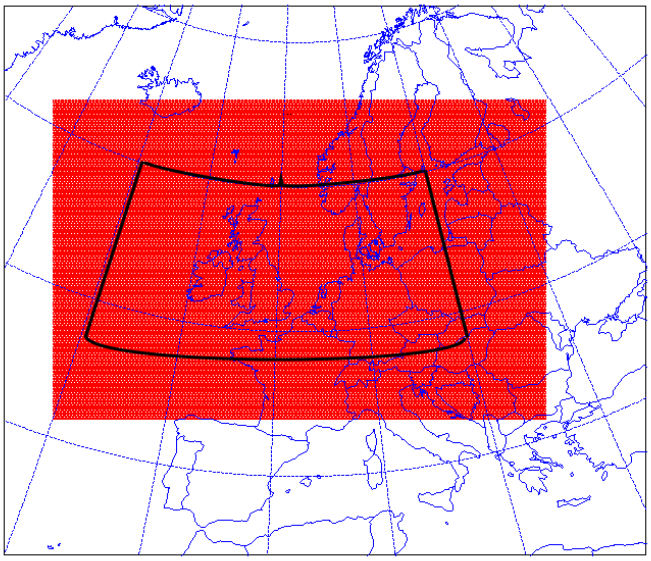

Figure 1: Computational domain including the North Sea and the UK offshore areas

Year 2006 has been simulated with SKIRON for the area shown in Figure 1. The model configuration corresponds to the standard settings used by CENER for routinely day-ahead wind power forecasting, which has been optimized after years of experience.
The genaral model setting is as follow:
Global Forecasting System (GFS, from NCAR/NCEP) from the 12 UTC cycle provide initial and boundary conditions. Horizontal Resolution: 0.05°x0.05° latitude/longitude. Vertical Resolutions: 50 Eta vertical levels. Temporal resolution: output frequency = 1h (52h horizon) and model time step = 15 sec. No nesting technique is used. A unique domain able to capture the synoptic patterns governing the meteorology of the region of interest is configurated.

Model physics packages:

Convection schemes: Betts-Miller-Janjic (Janjic 1994);

Cloud mycrophysics: Ferrier scheme (Ferrier et al. 2002);

Radiation scheme: SW - Lacis and Hansen (1974); LW â Fels and Schwarzkopf (1975);

Land surface scheme: Noah (Chen et al. 1997) with 12 types of vegetation and 7 types of soil texture, 4 soil layers;

Turbulence and PBL: Mellor-Yamada 2.5, and Monin-Obukhov similarity theory in the surface layer, with Paulson stability functions.

Only wind simulated on the four lowest Eta levels are used in this study. The hight of this levels are 9.99m, 34.03m, 68.61m and 116.47m.

2.2. Observational data

Flux-profile data for 2006 from the FINO-1 offshore platform has been used for validation. Fino-1 is a 100-m mast, fully equipped for the characterization of the marine boundary layer. Measurements of cup-anemometer wind speed at 8 levels (33, 40, 50, 60, 70, 80, 90 and 100m), temperature and relative humidity at 5 levels (33, 40, 50, 70 and 100m) and 3D turbulent flux measurements from sonic anemometers located at 40, 60 and 80m have been used. A data quality check has been applied. Only profiles with good data in all the levels have been used. Although the main quality filer applied in this study is realted with mast shadow effects. The direction sectors affected by mast shadow effects are not taken into account at this point. The large structure of the mast is responsible for a large flow distortion on the instruments, which results in 5% reduction of the annual wind speed if the data from the shadowed sector is included. So, in this study only correct wind direction sector (225°±67.5°) is considered for the analysis.

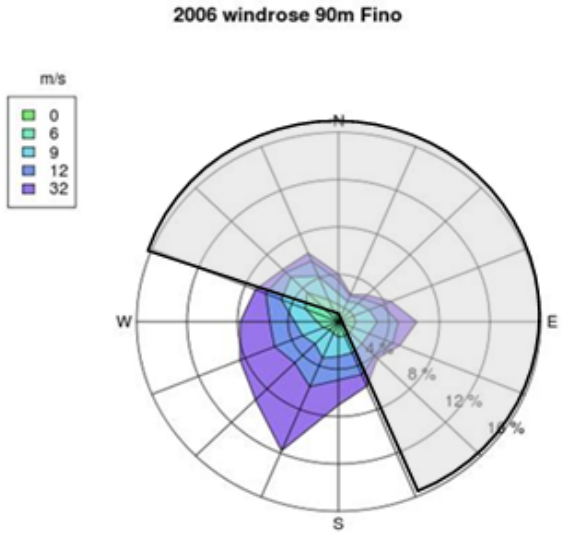

Figure 2: Prevaling wind direction in Fino mast

As expected when only the South-West sector is considered, the mean velocity measured at Fino mast increases on average from 9.25m/s to 10.5m/s.

As a result, a unified dataset is obtained with synchronized measured and simulated data for all levels. Atmospheric thermal stratification dominates the offshore ABL at Fino1 in the wind turbine operational range [1]. Atmospheric stability is here defined in terms of

the Obukhov length L, a measure of the length aboth the sea level where mechanical shear-generated turbulence dominates over thermal-driven turbulence.

$$L = -\frac{{u_*}^3}{\kappa \frac{g}{\Theta_0} \overline{w\theta}} \quad (1)$$

where $\kappa = 0.4$ is the von Karman constant, g the acceleration due to gravity, Θ_0 is a reference temperature, $\overline{w\theta}$ is the local kinematic heat flux and u_* the local friction velocity.
The Obukhov length is used to classify the wind conditions according to the following classes: N=neutral |L|>1000m, SU=slightly unstable -1000m<L<- 200m, VU=very unstable -200m<L<0, SS=slightly stable 200m<L<1000m, VS=very stable 0< L <200m.

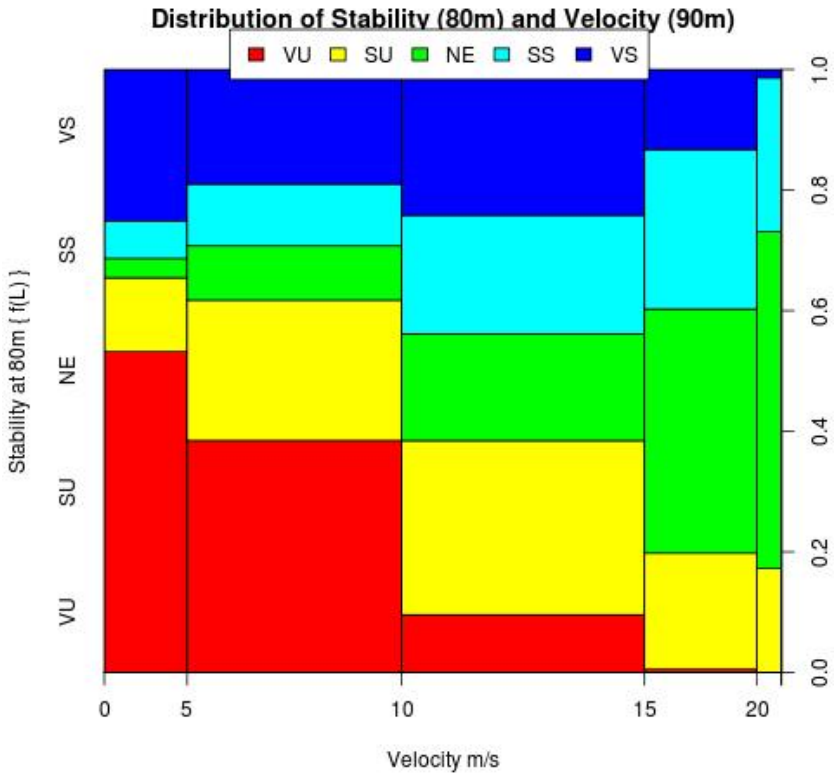

Figure 3: stability at 80m level and velocity at 90m (N=neutral |L|>1000m, SU=slightly unstable -1000m<L<- 200m, VU=very unstable -200m<L<0, SS=slightly stable 200m<L<1000m, VS=very stable 0< L <200m)

3. Wind shear

The study uses the shear exponent α (alpha) from the power law equation between two vertical levels:

$$\frac{U_2}{U_1} = (\frac{z_2}{z_1})^{\alpha} \quad (2)$$

where U is the horizontal wind speed and z is the height above the sea surface. There are several approaches to calculate α from a wind time series. For instance, to use mean wind speeds at two heights to calculate an overall mean shear parameter. Or to use 1-hour wind speeds at two heights to calculate a hourly shear parameter [8]. Wind shear values were calculated by averaging hourly alpha values from individual values between levels for this study.

4. Results

While the selected evaluation period is of one year duration, we are confident that the results can be generalized for longer periods.
A comparison between each level of Fino mast data and the nearest grid point of the model has been made. Simulated and measured hourly time series of wind speed, direction and wind shear have been compared.

4.1. Annual Wind Characteristics

Looking at the annual wind direction measured at differents levels no significant wind direction shear is appreciated. The main direction corresponds with open water conditions. Skiron shows very good skill at predicting the wind rose at any level (Figure 4). Here we only show 90m wind rose because the wind rose at other leves are almost the same.

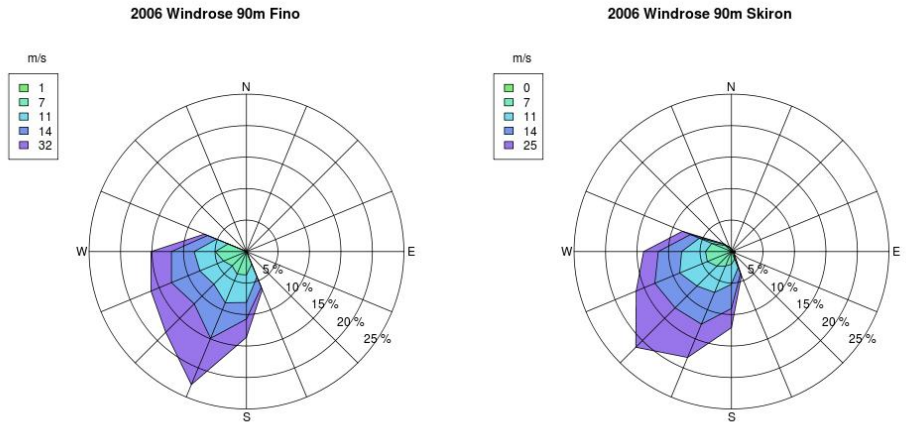

Figure 4: Wind rose measured and simulated at 90m, excluding the sector affected by mast shadow effects

The offshore daily cycle in open-sea conditions, i.e. resulting from a long fetch from the coast, is characterized by its weak amplitude compared with onshore conditions. In effect, the sea surface temperature has considerably more inertia than the land and the temperature differences between day and night are less pronounced. Skiron model fits perfectly this fact. Simulated diurnal wind is almost identical to observational pattern (Figure 5) : lowest winds at midday increasing during the evening.

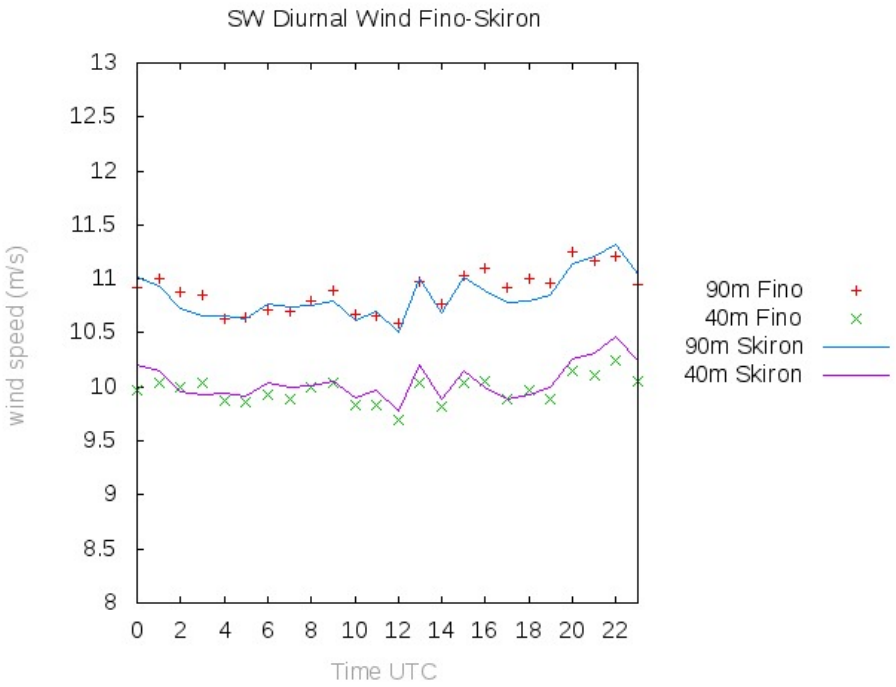

Figure 5: Diurnal variation of wind speed at two heights (90m and 40m) from the model and measurement

Figure 6 presents the mean profiles at 00UTC and 12UTC. The differences between the

measured and simulated vertical wind shear are not significant.

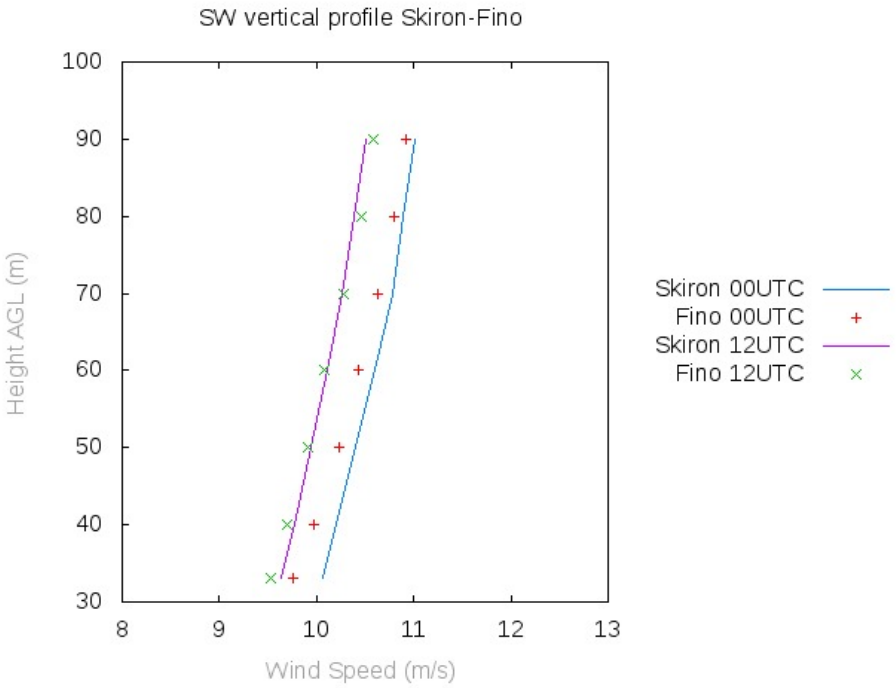

Figure 6: Diurnal variation of vertical wind profile. Model (lines) and measurements (dots)

Figure 7 shows the annual diurnal pattern of *alpha* values. Skiron predicts lower values of alpha, although the daily pattern is quite similar: highest wind shear during evening hours (around 0,12) and lower values early in the morning, with a minimum wind shear around 0,07.

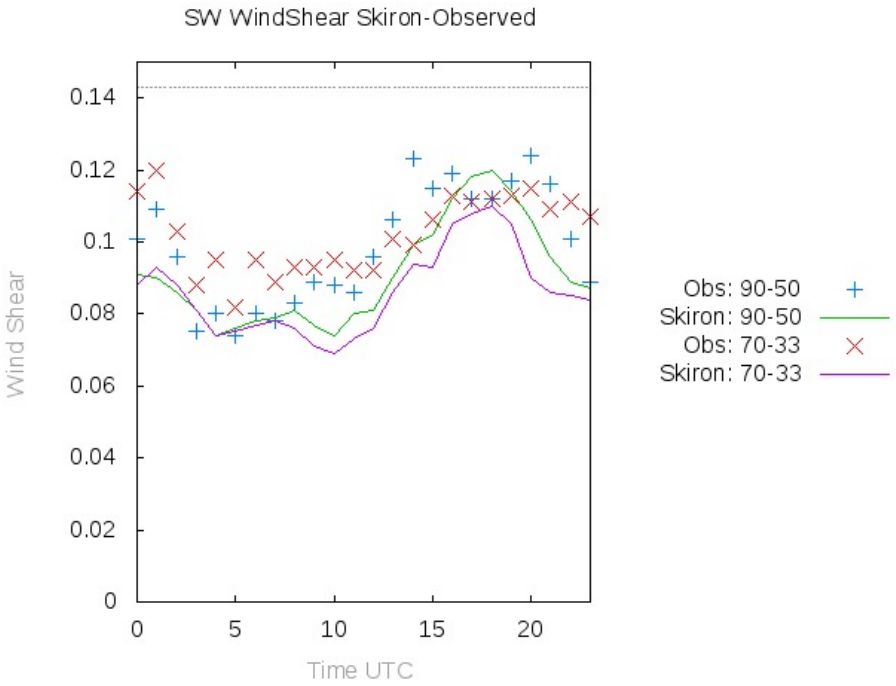

Figure 7: Wind Shear between 90m-50m and 70m-33m levels for prevaling wind direction. Lines corresponds to Skiron wind shear and crosses to the observational wind shear

Wind shear values from measurements for different levels show a typical diurnal behavior, with highest values during evening hours, and the lowest wind shear close to sunrise time (Figure 7). Skiron simulates very well this diurnal pattern although doesn't shows the intra-levels variability observed on the measurements (Figure 7).

4.2. Classification of Wind Characteristics by Stability

The observed stability, in terms of the Obukhov length, is used to classify the wind conditions. Regardless of the level used to define the stability, the distribution of the stability versus wind speed is quite similar. The higher the wind speed the more numerous neutral cases and the lower the wind speed the more frequent the stable and unstable situations (Figure 8).

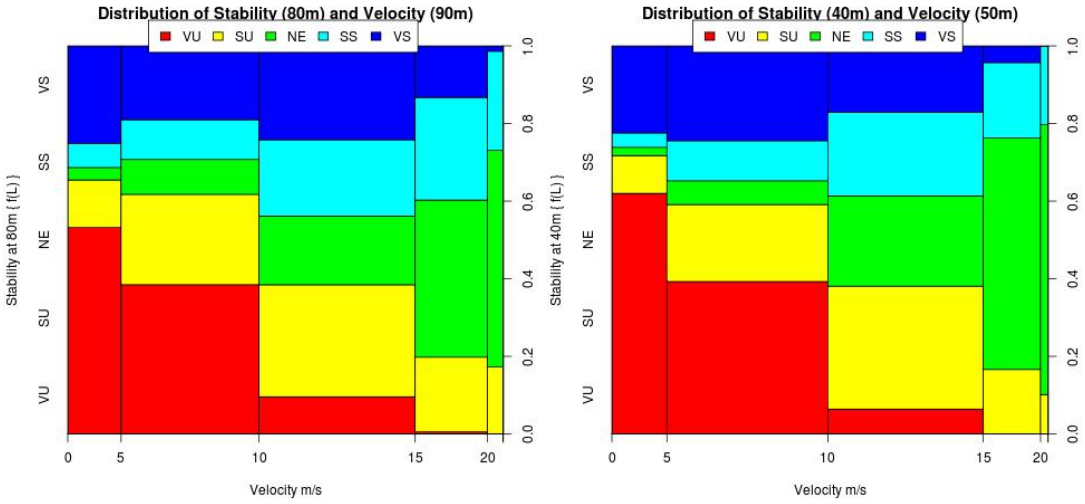

Figure 8: Left: stability at 80m level and velocity at 90m; Right: stability at 40m level and velocity at 50m; (N=neutral |L|>1000m, SU=slightly unstable -1000m<L<- 200m, VU=very unstable -200m<L<0, SS=slightly stable 200m<L<1000m, VS=very stable 0< L <200m)

It is worth analysing the wind rose for different stability classes. When only stable or very stable conditions are selected, the wind rose shows prevailing winds from South-West (Figure 9). The same happens under neutral conditions. The prevailing wind sector is the South-SouthWest (Figure 10). On the other hand, unstable and very unstable conditions are more predominant in the West and North-West sectors (Figure 11). Skiron shows good agreement in predicting the prevailing winds under the various stability classes.

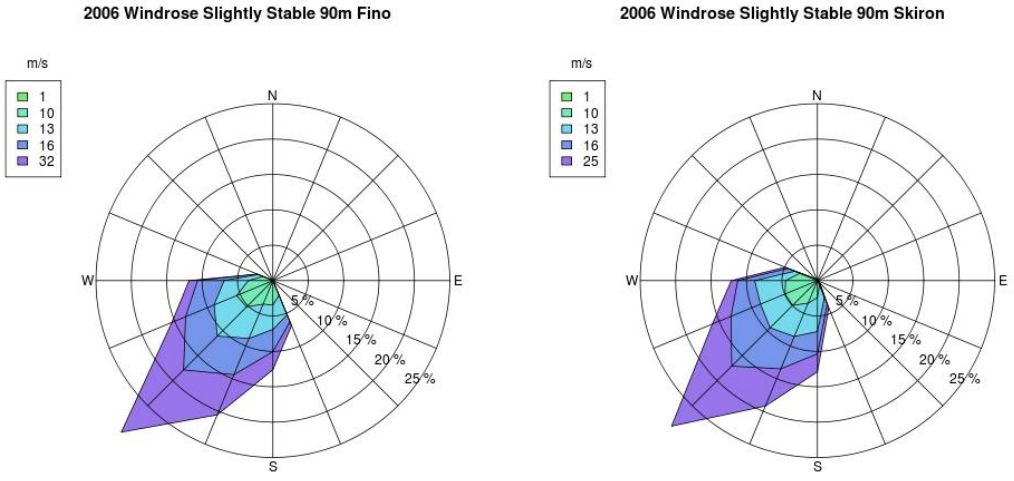

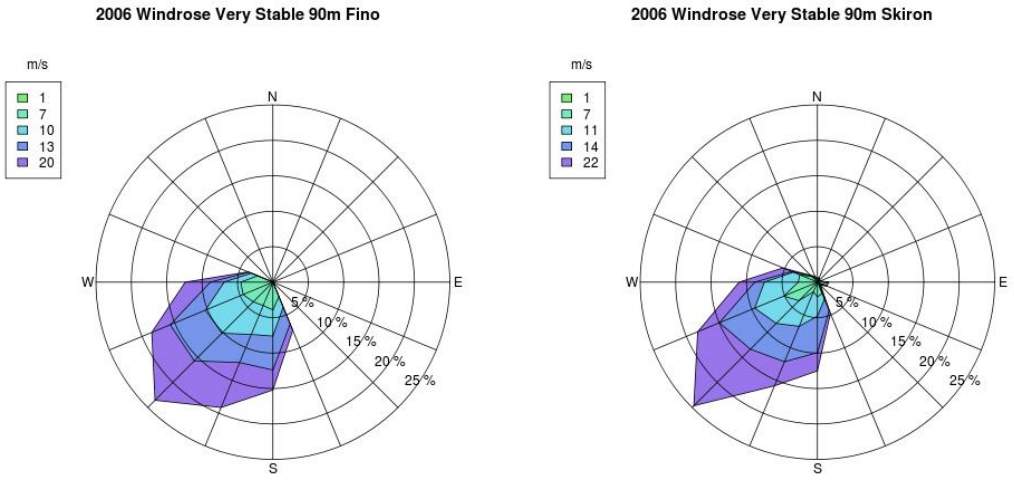

Figure 9: Wind roses under Slightly Stable (up) and Very Stable (down) conditions. Excluding the sector affected by mast shadow effects.

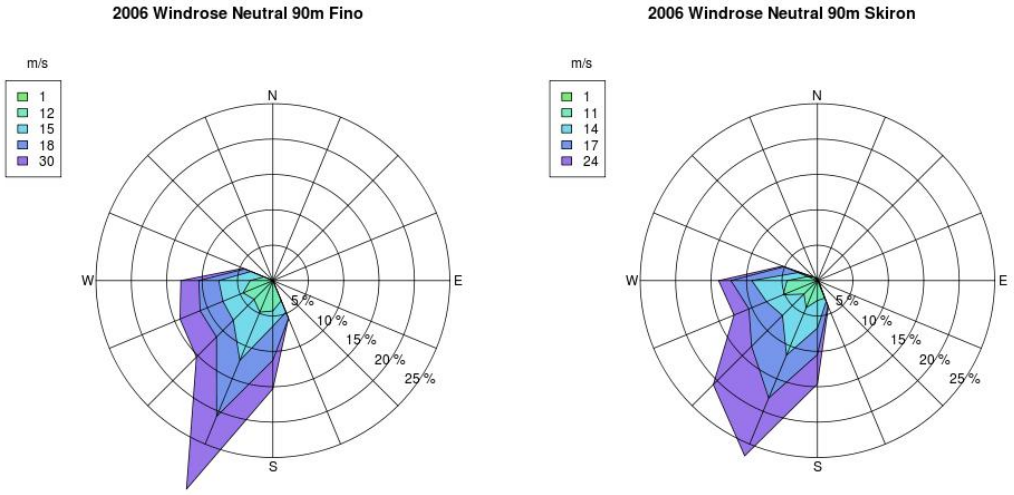

Figure 10: Wind roses under neutral conditions. Excluding the sector affected by mast shadow effects

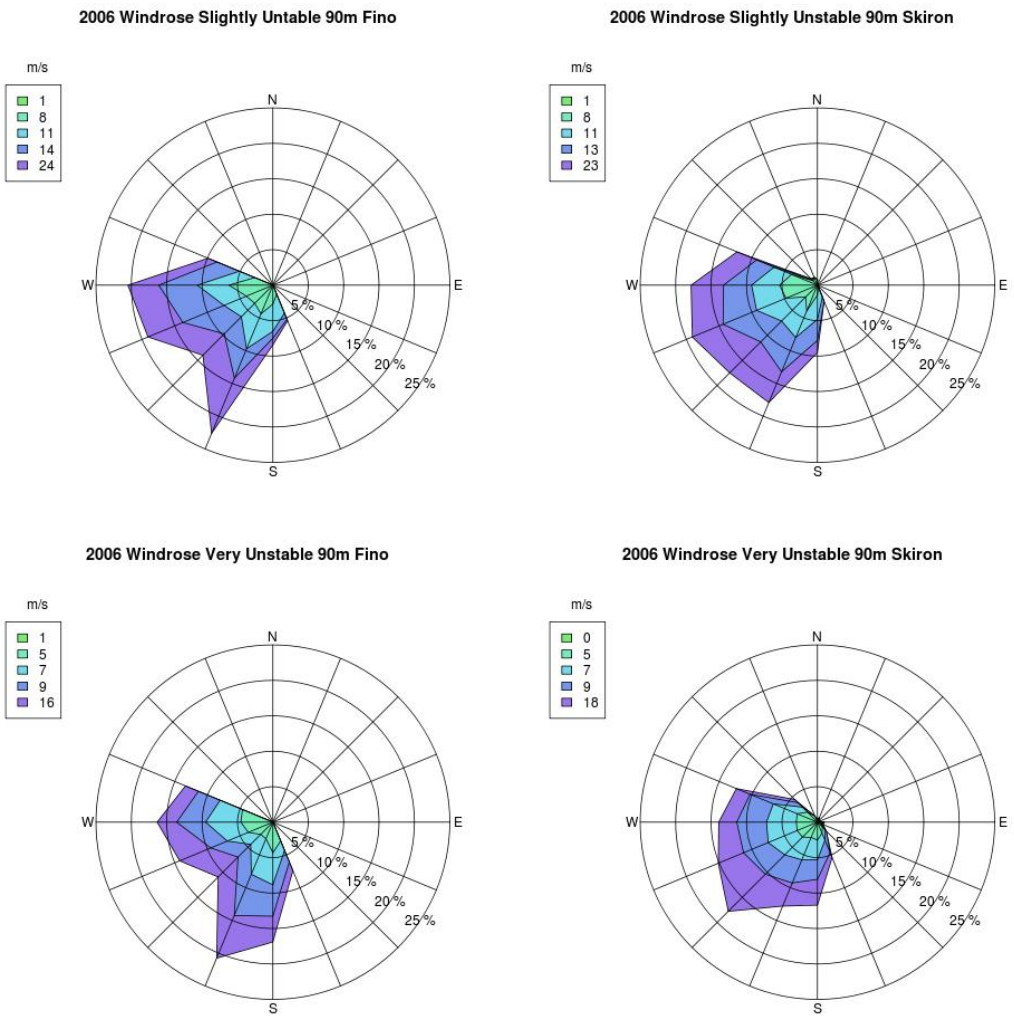

Figure 11: Wind roses under Slightly Unstable (up) and Very Unstable (down) conditions. Excluding the sector affected by mast shadow effects.

The vertical wind profile is a strong function of the atmospheric stability. For very stable or very unstable conditions wind speed is quite lower than for neutral conditions (Figure 12 and 13). Skiron simulates this fact. But for very stable and slightly stable conditions the wind is not well stimated by the model. Although Skiron shows similar wind vertical profile shape.

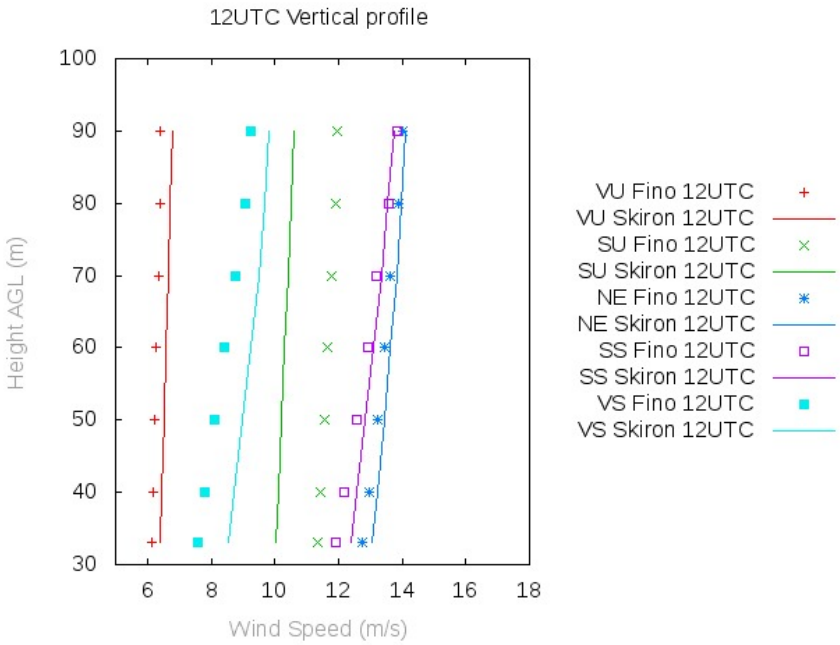

Figure 12: Vertical wind profile under diferent stability conditions at 12UTC. Points: observations. Lines: Skiron model

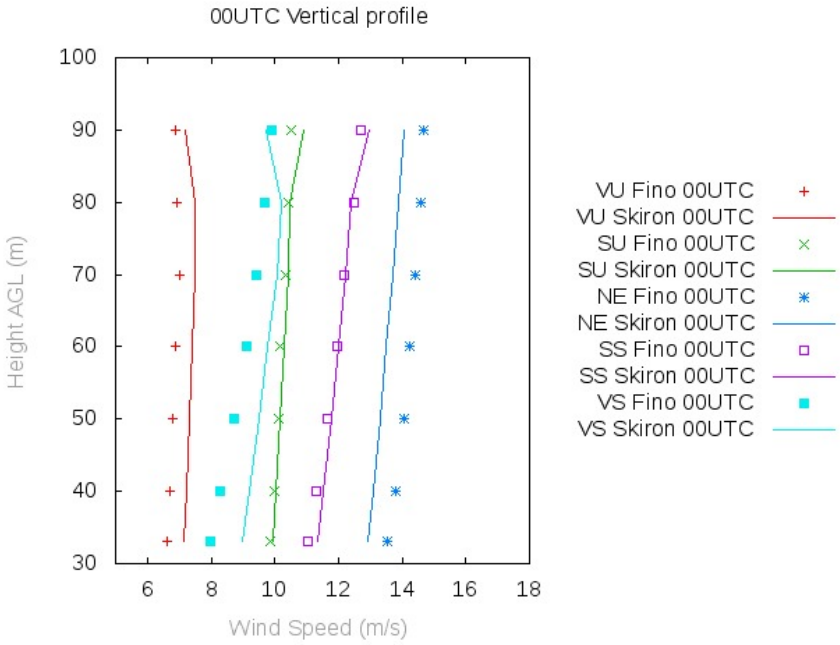

Figure 13: Vertical wind profile under diferent stability conditions at 00UTC. Points: observations. Lines: Skiron model

It is well know that α strongly varies with atmospheric stability (intimately related to thermal stratification and wind shear), as well as surface roughness [2]. This is noticed at Fino 1 observing the wind shear behavior by stability (Table 1). The shear exponent shows

	VU	SU	NE	SS	VS
V90 Fino	6.922	11.135	14.50	12.97	10.030
V90 Skiron	6.975	10.836	14.07	13.05	10.405
Error (%)	1%	3%	3%	1%	4%
Wind Shear Fino 90m-50m	0.036	0.049	0.086	0.145	0.1960
Wind Shear Skiron 90m-50m	0.056	0.066	0.084	0.121	0.1379
Error (%)	54%	35%	2%	16%	30%

Table 1: Wind Speed and Wind Shear values and errors (only wind shear between 90m and 50m is show here)

a wide variability, with low shear values associated with unstable conditions, as shown by the measurements and simulations.

Nevertheless, while wind speed error remains constant with stability, the error on the stimated wind shear shows a hard dependency on the stability. Wins Shear is clearly overstimated and understimated under very unstable and very stable conditions respectively. In the other hand, for neutral conditon the error of wind shear is negligible, increasing this error as the stability goes far from the neutral conditions.

5. Conclusions

In this study SKIRON model was evaluated to determinate its capability to represent offshore site specific wind characteristics. Wind direction, diurnal wind pattern and vertical profiles from one year SKIRON's simulation were compared to observational data from Fino1 tower. The overall performance of Skiron is very good at predicting the wind speed and direction distributions. The diurnal wind pattern and mean vertical profile are practically equal. When the wind conditions are classified according to the atmospheric stability, the model still shows good performance at predicting the stability-dependent wind rose, showing quite important differences between the stable and unstable regimes. Wind shear is predicted fairly well by Skiron in the unstable and neutral regimes while some underestimation of the shear exponent is observed in the stable regime. In the stable regime the boundary layer becomes shallower and it is neccesary to increase the number of vertical levels in the lower part of the atmosphere.

References

[1] J. Sanz Rodrigo *Flux-profile characterization of the offshore ABL ofr the parameterization of CFD models*. EWAE Offoshre, November 2011, Amsterdam.

[2] Brandon Storm and Sukanta Basu *The WRF model forecast-derived low-level wind shear climatology over the United States Great Plains*. Energies 2010, 3, 258-276.

[3] M.Gastón, E.Pascal, U.Irigoyen, E.Cantero, Y.Loureiro, L.Frías, S.Lozano, I.Martí *Wind resources map of Spain at mesoscale. Methodology and validation*. Proceedings of the European Wind Energy conference 2008.

[4] Kallos G *The Regional weather forecasting system SKIRON*.Proceedings, Symposium on Regional Weather Prediction on Parallel Computer Environments, 15-17 October 1997, Athens, Greece, 9 pp

[5] P. Louka1, G. Kallos, G. Galanis1, P. Katsafados1, and I. Pytharoulis. *Resolution issues on NWPs for wind power applications - Downscaling*.

[6] Katsafados P. *Factors and parameterizations that determine the performance of limited area models in longrange forecasts*. PhD thesis 2003, School of Physics, Univ. of Athens, Greece, pp. 257

[7] M. Schwartz and D. Elliot *Wind Shear Characteristics at Central Plains Tall Towers*. American Wind Energy Association, Wind Power 2006 Conference. Pittsburgh, Pennsylvania. June 2006.

[8] M.L. Ray, A.L. Rogers, and J.G. McGowan *Analysis fo wind shear models and trends in different terrains*. AWEA 2006.

[9] Kasemsan Manomaiphiboon *Investigation of Wind Shear Characteristics at Five 100-m Meteorological Towers in Thailand*. The 5^{th} Eco-energy and Materials Science and Engineerind Symposium, November 2007, Pattaya, Thailand.

Effect of different sea surface dynamical roughness parameterization on wind speed simulation on offshore area

Zhou Rongwei He Xiaofeng Zhu Rong
CMA Public Meteorological Service Center

Abstract: Wind field offshore area and coastal area was affected by the scheme of sea surface dynamical roughness parameterization greatly. Three methods were selected to simulation the wind field with WRF model in Hangzhou Bay such as: constant value of 0.0001, scheme of WRF model, scheme of Yelland and Taylor. The simulation period was January, April, July and October, 2010. The following conclusions were drawn by comparison between simulation results and observation data: the simulation results of the scheme that sea surface dynamical roughness was parameterized by friction velocity were better than that of the scheme that the dynamical roughness was constant, and the results of Yelland and Taylor scheme was in more agreement with observational data than that of WRF scheme. During sea wind, the improvement was more obvious in the scheme considering variation ofd dynamical roughness as friction velocity. It was found out by relative error of each wind speed segment by 1m/s: the relative error of three scheme was all decrease with the increase of wind speed when the observational wind speed was less than 8m/s, and the results of Yelland and Taylor method was best, that of constant value was worst. While the relative error of all three scheme was increase with the increase of wind speed when it was greater than 8m/s, and the relative error of scheme of Yelland and Taylor was greatest, while that of constant value was least.

Key Words: sea surface dynamical roughness, wind speed, numerical simulation

1. Introduction

With the development and utilization of wind energy resource, offshore wind energy resource was more and more getting attention. Besides observation by wind mast, the simulation results were also adopted to assess offshore wind resource. At present, the methods commonly adopted were wind energy resource assessment software based on computational fluid dynamics(CFD) such as WindSim, Meteodyn WT and so on, mesoscale meteorological model such as MM5, WRF and so on, and combined method on mesoscale model and microscale model such as MM5/Calmet, WRF/Calmet and so on.

Besides synoptic background, wind field of sea surface was also effected by dynamical condition of sea surface. The dynamical parameter that could influence wind field in the height focused by wind power industry was dynamical effect of sea surface wave such as dynamical roughness. Sea surface dynamical roughness was considered as constant such as 0.0001 that not varied as wind speed in CFD software, while in mesoscale meteorological model it was parameterized by other meteorological parameter such as wind speed, friction speed, and so on. The sea

surface dynamical roughness was parameterized with friction speed by Charnock(1955) firstly as $z_0 = \alpha u_*^2 / g$. z_0 was sea surface dynamical roughness. α was empirical constant. u_* was friction speed. g was acceleration of gravity. And then Charnock scheme was developed by adding effect of smooth flow as $z_0 = \alpha u_*^2 / g + 0.11\nu / u_*$, and υ was viscosity constant. The empirical constant was considered by different wind speed segment respectively by Yelland and Taylor(1996). Taylor and Yelland(2001) parameterized dynamical roughness by effect wave height and wave steepness other than friction speed. Oost(2002) considered mainly effect of wave age. The scheme of Taylor and Yelland(2001) and Oost(2002) were based on wave parameters that were not involved in meteorological model.

In this paper, the developed scheme based on friction speed by Charnock was adopted to study effect of sea surface dynamical roughness to wind speed, influence of different schemes of sea surface dynamical roughness to simulation results of offshore wind speed, and applicability of different schemes was analyzed.

2. Method and numerical settings

The wind field of China offshore area was simulated with three parameterization schemes of sea surface dynamical roughness such as constant value as 0.0001(scheme P03), parameterization scheme in WRF model(scheme P04)(MMMD, NCAR, 2010), and Yelland and Taylor(1996) parameterization method(scheme P05).

WRF parameterization scheme: $$z_0 = \frac{0.0185 u_*^2}{g} + 1.59 e^{-5}$$

Yelland and Taylor parameterization scheme: $$z_0 = \frac{z_{ch} u_*^2}{g} + 0.11 \frac{\upsilon}{u_*}$$

$$z_{ch} = \begin{cases} 0.011, & U \le 10 m/s \\ 0.011 + \dfrac{0.007(U - 10)}{8}, & 10 m/s < U \le 18 m/s \\ 0.018, & U > 18 m/s \end{cases}$$

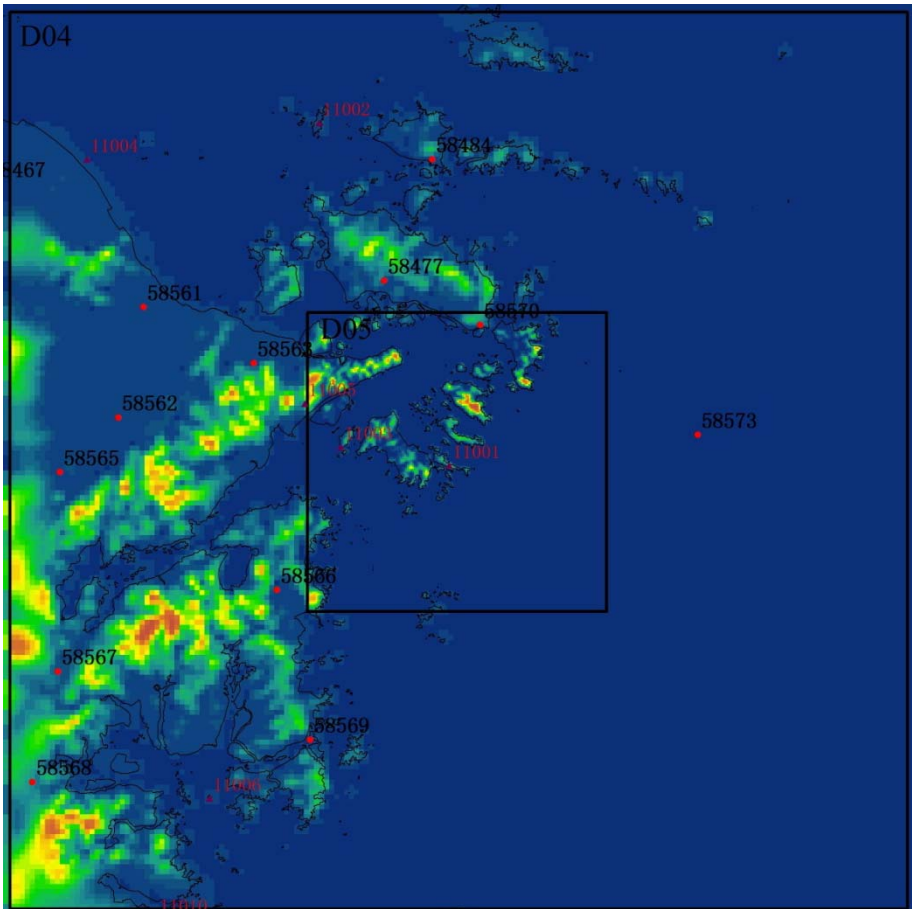

Fig. 1 simulation domain of D04 and D05

The simulation area was around Hangzhou Bay, Zhejiang province with 5 domains in WRF model. The horizontal resolution of each domain was 27km(D01), 9km(D02), 3km(D03), 1km(D04) and 0.333km(D05) respectively. Horizontal grid number was 121×91, 91×91, 121×121, 181×181 and 181×181, and vertical grid number was 30. Except that SRTM3 data that was terrain data with horizontal resolution of 3 second(about 90m) in domain D05 and D04, while WRF terrain data with 30 second resolution was used in domain D01, D02 and D03. Fig. 1 showed area and terrain of domain D04 and D05. As shown in fig.1, the horizontal resolution of terrain data in domain D05 was 333.333m, while it was 1km in domain D04. And the dots in fig. 1 described automatic weather stations and wind masts that observation . A day was a simulation case from UTC 18 on last day for 30 simulation hours. The simulation results from UTC 00 to UTC 23 on the simulation day were used to analyze. Table 1 described the adopted parameterization schemes of physical process. NCEP reanalysis data with 0.5°×0.5°resolution was used as initial and boundary condition. The offshore wind field around Hangzhou Bay was simulation in January, April, July and October 2010.

Table 1 Physical parameterization scheme in WRF model

physical option	parameterization scheme
microphysics option	Ferrier (new Eta) microphysics
longwave radiation option	Rrtm scheme
shortwave radiation option	Dudhia scheme
surface-layer option	Monin-Obukhov scheme
land-surface option	Unified Noah land-surface model
boundary-layer option	YSU scheme

3. Verification of simulation results

The simulation results were verified with observation data of automatic weather stations and wind masts. As there were only three observation dots in domain D05, all verification results concerned D05 was average results of the three dots, while that concerned D04 and D03 was average results of all 18 dots. The verification parameters were correlation coefficient, relative error and root-mean-square error. The monthly verification results of each observation station were obtained firstly, then monthly average results were got by mean of 18 or 3 stations, and annual average results were the mean value of four month results. The average verification results of 18 stations were obtained by comparison between observations and simulation results of domain D03 with 3km horizontal resolution, that of domain D04 with 1km resolution. As described in table 1, except correlation coefficient, the results of relative error and root-mean-square error indicated that scheme P05 of Yelland and Taylor was best, followed by scheme P04 of WRF model, and scheme P03 of constant dynamical roughness was worst. The verification results of all 3 scheme also indicated that the simulation results were basically equal with 3km and 1km horizontal resolution. There were 3 observation stations in domain D05. The mean verification results of these 3 stations in domain D03 with 3km resolution, domain D04 with 1km resolution and domain D05 in 333.333m resolution indicated that the simulation results of scheme P03 with constant dynamical roughness was worst, and that of scheme P05 was best with all 3 horizontal resolution. And with the same dynamical roughness scheme, the results of domain D04 with 1km resolution was best, followed by that of domain D05 with 333.333m resolution, and that of domain D03 with 3km resolution was worst. The following conclusion was drawn as that the simulation results were not developed only by increasing horizontal resolution. Although with the same parameterization scheme simulation results with 333.333m resolution were worse than that with 1km resolution, the results with 333.333m

resolution by Yelland and Taylor scheme were better than that with 1km resolution by WRF model scheme and constant value scheme.

To further analyze the improvement of wind speed simulation results in offshore and coastal areas by Yelland and Taylor scheme, table 3 indicated verification results of all 18 observation stations with 1km horizontal resolution by 3 different parameterization schemes.

Table 2 Verification results of different parameterization schemes

domain	mast number	correlation coefficient			relative error			RMSE		
		P03	P04	P05	P03	P04	P05	P03	P04	P05
D03	18	0.57	0.57	0.56	0.56	0.54	0.50	2.81	2.71	2.58
D04	18	0.56	0.56	0.55	0.56	0.53	0.50	2.82	2.73	2.59
D03	3	0.52	0.52	0.49	0.39	0.37	0.31	2.77	2.68	2.49
D04	3	0.52	0.51	0.49	0.32	0.30	0.25	2.54	2.47	2.34
D05	3	0.51	0.51	0.48	0.35	0.33	0.28	2.65	2.59	2.46

Table 3 Verification results of each station in domain D04

station	correlation			relative error			RMSE		
	P03	P04	P05	P03	P04	P05	P03	P04	P05
58477	0.61	0.61	0.59	0.89	0.87	0.82	2.92	2.86	2.71
58484	0.66	0.65	0.64	0.35	0.34	0.29	2.36	2.30	2.16
58561	0.56	0.54	0.55	0.99	0.95	0.92	3.25	3.12	2.96
58562	0.50	0.50	0.50	0.55	0.53	0.53	2.13	2.08	2.04
58563	0.45	0.45	0.43	1.35	1.32	1.22	4.28	4.13	3.82
58565	0.59	0.59	0.58	0.40	0.39	0.42	2.13	2.10	2.12
58566	0.47	0.47	0.48	1.54	1.51	1.48	3.53	3.46	3.36
58567	0.63	0.61	0.62	0.56	0.53	0.55	2.49	2.45	2.41
58568	0.42	0.41	0.41	0.79	0.77	0.77	2.37	2.35	2.36
58569	0.55	0.56	0.54	0.48	0.45	0.36	3.66	3.45	3.06
58570	0.57	0.56	0.53	0.29	0.27	0.22	2.42	2.33	2.19
58573	0.88	0.87	0.86	0.12	0.07	0.03	2.18	2.00	2.04
11001	0.33	0.33	0.29	0.42	0.41	0.35	2.99	2.90	2.77
11002	0.63	0.63	0.63	0.11	0.09	0.04	2.52	2.36	2.19
11003	0.65	0.65	0.64	0.24	0.23	0.18	2.23	2.19	2.07
11004	0.61	0.61	0.59	0.32	0.29	0.22	2.76	2.62	2.38
11005	0.51	0.49	0.48	0.10	0.11	0.10	3.06	3.07	3.07

11006	0.51	0.51	0.50	0.53	0.51	0.44	3.46	3.33	2.99
average	0.56	0.56	0.55	0.56	0.53	0.50	2.82	2.73	2.59

There were 12 automatic weather stations and 6 wind masts in domain D04 with 1km horizontal resolution. As indicted by mean results of all observation stations by different parameterization schemes that correlation coefficient results were basically the same, relative error and root-mean-square error of scheme P04 of WRF model and scheme P05 of Yelland and Taylor were better than that of scheme P03 of constant dynamical roughness, and the results of P05 was better than that of P04. But the verification results of each stations by scheme P05 was not all better than that by scheme P04. As indicated in table 3, there were 2 stations that results of WRF model was best. Except these 2 stations, the results of all the other 16 stations by Yelland and Taylor scheme were best. The main reason was that the parameterization scheme only changed the dynamical roughness on sea area and improved wind speed results of offshore and coastal areas obviously, while it was weaker in relatively distant areas away from coastline. Therefore the following conclusion was drawn as that: the result with considering the parameterization scheme of dynamical roughness was better than that of constant value, and Yelland and Taylor scheme was more suitable than WRF model scheme.

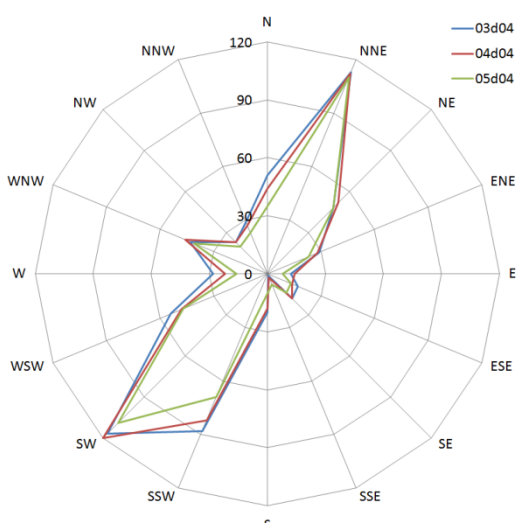

(a)58570

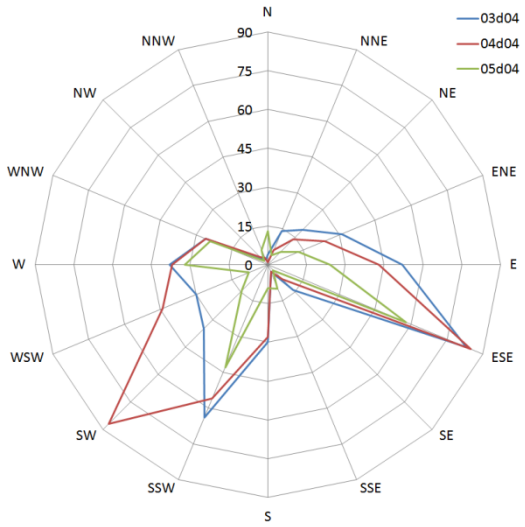

(b)58573

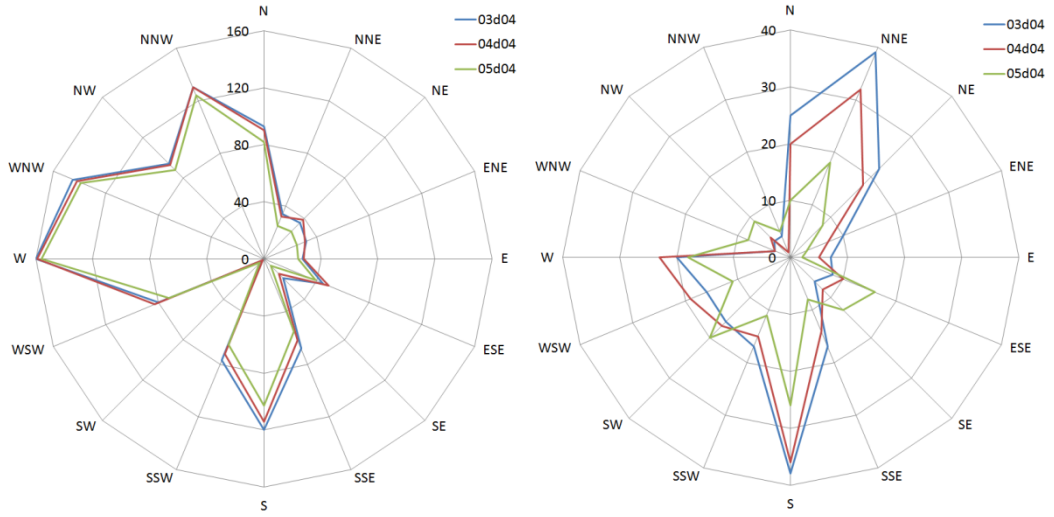

(c)11001 (d)11002

Fig 2 Relative error of wind speed in different wind direction

Figure 2 showed the relative error of mean wind speed in different wind direction with 3 parameterization schemes in automatics weather station 58570, 58573 and mast 11001, 11002. All simulation results in figure 2 were that of domain D04 with 1km horizontal resolution. As indicated in figure 2 that the results of scheme P04 and P05 were better that that of P03 with constant value, and the improvement of P05 with Yelland and Taylor scheme was more obvious. The improvement of schemes considering dynamical roughness parameterization was more obvious in sea breeze condition.

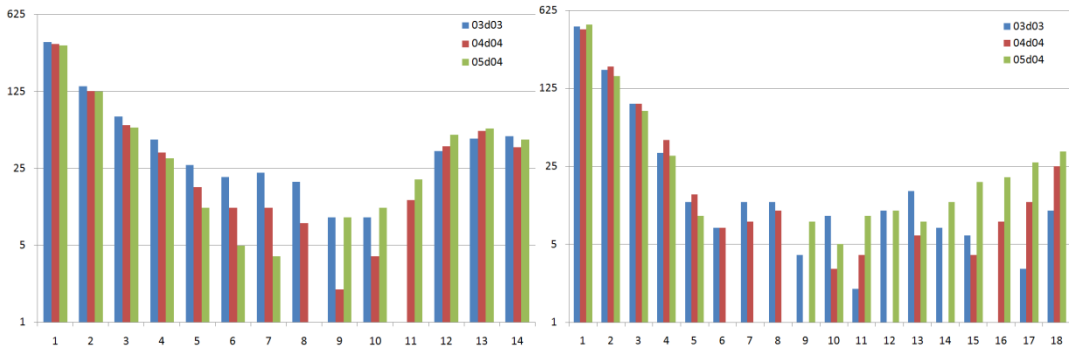

(a)58570 (b)58573

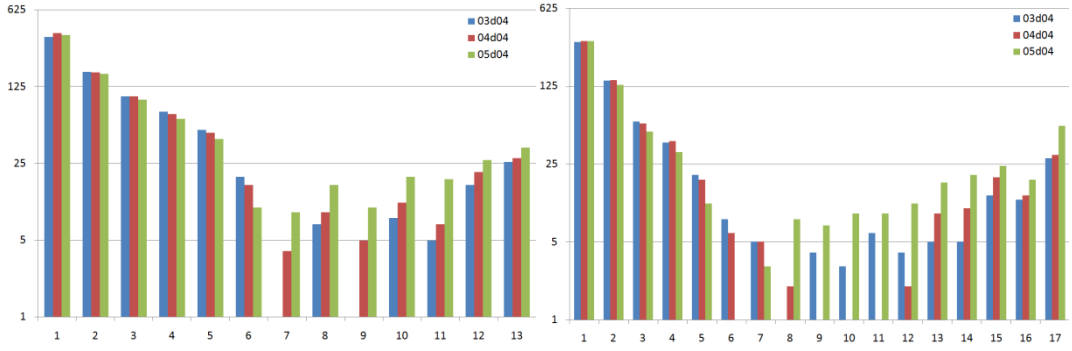

(c)11001 (d)11002

Fig 3 Relative error of wind speed in different wind speed segment

Figure 3 described relative error of average wind speed at different wind speed segment of 58570, 58573, 11001 and 11002. All simulation data was the result of domain D04 with 1km horizontal resolution. As indicated in figure 2, with all parameterization schemes, the relative error was decreased with wind speed increasing until wind speed ascended to about 8m/s, and then it increased with wind speed increasing. Hence, it was not well of wind speed on offshore and coastal areas in windy condition with all parameterization schemes of sea surface dynamical roughness. Among relative error of three schemes, when wind speed was less than about 8m/s, relative error of Yelland and Taylor scheme was lest and that of constant value scheme was biggest. While when wind speed was larger than about 8 m/s, relative error of Yelland and Taylor scheme was biggest and that of constant value scheme was lest. The error was bigger with parameterization scheme in windy condition because of that there was much waves foam, it made sea surface smooth and the dynamical roughness was descended. Therefore the real phenomenon in windy condition was not well described by parameterization scheme of sea surface dynamical roughness even with Yelland and Taylor scheme which considered the coeficient at different wind speed condition, and the simulation error of wind speed was big in windy condition on offshore and coastal areas.

5. Conclusions and discussions

The simulation of wind speed on offshore and coastal areas was influenced by parameterization scheme of sea surface dynamical roughness. Three methods were adopted to simulate wind field of offshore and coastal areas in Hangzhou Bay such as constant value of roughness, WRF model scheme, Yelland and Taylor scheme. The following conclusions were drawn by comparison between observations and simulation results as:

1) The simulated results of wind speed was improved on offshore and coastal areas with parameterization scheme of sea surface dynamical roughness, and that of Yelland and Taylor scheme was better than that of WRF model scheme.

2) With same parameterization scheme, the simulation results of 1km horizontal resolution was best, followed by that of 333.333m resolution. But the simulation results of Yelland and Taylor scheme with fine resolution was better than that of WRF model scheme with coarser resolution.

3) As indicated by relative error of wind speed simulation results at different wind direction of all observation stations: Yelland and Taylor scheme was best, and the simulation results of wind speed was improved obviously in sea breeze condition with parameterization scheme.

4) As shown by relative error of average wind speed at different wind speed segment with 3 schemes, when wind speed was less than about 8 m/s, the relative error decreased with wind speed increasing, the error of Yelland and Taylor scheme was lest, and that of constant value scheme was biggest. While when wind speed was bigger than about 8 m/s, the relative error increased with wind speed increasing, the error of Yelland and Taylor scheme was biggest, and that of constant value scheme was lest.

It was important that choosing suitable parameterization scheme of sea surface dynamical roughness to improve simulation results of wind speed in offshore and coastal areas. But the dynamical characteristic of sea surface in windy condition was not well described by parameterization schemes based on friction speed.

Reference

Charnock H, 1955, Wind stress on a water surface, Quart. J. Roy. Meteor. Soc, 81: 639-640

MMMD, NCAR, 2010, Weather Research and Forecast ARW Version 3 Modeling Systems User's Guide [EB/OL], http://www.mmm.ucar.edu/wrf/docs/user_guide_V3/SRWUsers-GuideV3.pdf

Oost W A, G J Komen, C M J Jacobs, et al, 2002, New evidence for a relation between wind stress and wave age from measurements during ASGAMAGE, Boundary-Layer Meteor, 103:409-438

Taylor P K, M J Yelland, 2001, The dependence of sea surface roughness on the height and steepness of the waves, J. Phys. Oceanogr, 31: 572-590

Yelland M, P K Taylor, 1996, Wind stress measurements from the open ocean, J. Phys. Oceanogr, 26:541-558

Mapping coastal wind field using wind-current transfer function analysis

Sung Yong Kim[1]
[1]Division of Ocean Systems Engineering
Korea Advanced Institute of Science and Technology
291 Daehak-ro, Guseong-dong, Yuseong-gu, Daejeon, 305-701, Republic of Korea
syongkim@kaist.ac.kr

ABSTRACT

This paper provides a technical description on the parameterization of two environmental variables (ocean surface currents and wind stress) to map the coastal surface wind field, based on empirically and analytically derived transfer functions. As the accuracy and dynamical consistency of transfer functions are crucial in the estimate of the coastal wind field, we compare the two transfer functions to quantify their uncertainty and signal-to-noise ratio and to interpret them in a dynamical framework. This analysis has potentials to design and locate the offshore wind farms and serves as a useful tool to analyze the offshore wind conditions and resources in a hindcast mode.

1 Introduction

Evaluation of wind energy resource is an important research question in planning and locating the near-shore and offshore wind farms [1]. The surveys for wind resource have conducted with available wind data collected, typically, from shore-based and buoy-mounted platforms as well as satellite remote sensing [2], numerical simulations, and data-assimilated products. In observations of the coastal wind field, their temporal resolution and spatial coverage have been a trade-off to capture the variability of wind. For instance, the point measurement of wind at a single station may guarantee high-density temporal sampling. On the other hand, the satellite-based measurements can be advantageous to cover a broad region. However, they may have limitations in covering the coastal areas within 100 km from the shoreline due to low signal-to-noise ratio of instruments and producing maps with high-temporal resolutions due to the orbital period.

The statistical relationships between wind stress and kinematic parameters derived from coastal ocean radars have been investigated to indirectly estimate the wind field [3, 4]. In particular, the wind field has been mapped using parameters in multi-frequency

coastal radars with statistical techniques such as multivariate linear regression and Kalman filter [5, 6, 7]. On the other hand, the synthetic aperture radar (SAR) imagery has been used to retrieve the surface wind velocity field [8, 9].

The novelty of this paper is to statistically parameterize two dynamic variables (wind stress and currents) in the governing equations of the wind-current system for mapping coastal wind field, which were not addressed in the previous work [5]. The transfer function and response function estimated from observed wind stress and surface currents are compared with those derived from the analytical model. In this short paper, we focus on providing a feasibility to map coastal wind field using the transfer function analysis and leave the full-scale comparison and validation for a companion paper. As the statistical and analytic derivations have been investigated in previous studies extensively [10, 11], their brief introduction will be given.

2 Observations

2.1 Surface currents

The high-frequency radar (HFR)-derived hourly and km-resolution surface current maps contain the upper ocean responses to geophysical driving forces of winds, tides, low frequency atmospheric and oceanic forces, and their interactions, varying from mesoscale to submesoscale [12]. The maximum extent of HFR varies from 50 to 150 km from shoreline where are potential locations of the near-shore and offshore wind farms, depending on the radar operating frequency. This shore-based radar network provides an operational near-real time monitoring system and can be used to estimate the coastal wind field resources. An example of observed surface currents off southern San Diego (1 km resolution) is shown in Figure 1, and their spatially averaged hourly time series are used in this paper.

2.2 Coastal winds

The wind observations off southern San Diego are collected from shore stations, offshore buoys, and quikscat satellite. In this paper, we use the shore-based wind observation at a single location in order to minimize complexity in regression and to compare the analytic and empirical transfer functions directly.

The decorrelation length scales of coastal wind field and surface currents can be an indicator to determine the density of samplings in space and time. Moreover, the spectral energy of winds can identify the primary frequency bands containing major variance.

3 Methods

3.1 Surface current mapping

Statistical formulations between wind stress (τ) and surface currents ($\mathbf{u}$) at a given location and depth ($\mathbf{x} = (x, y, z)$) are given in the frequency and time domains:

$$\hat{\mathbf{u}}(\mathbf{x}, \sigma) = \mathbf{H}^*(\mathbf{x}, \sigma)\hat{\tau}(\mathbf{x}, \sigma), \tag{1}$$

$$\mathbf{u}(\mathbf{x}, t) = \int_{t'} \mathbf{G}^*(\mathbf{x}, t - t')\tau(\mathbf{x}, t')\mathrm{d}t', \tag{2}$$

where $\mathbf{H}^*$ and $\mathbf{G}^*$ are the (current mapping) transfer function in the frequency domain and the response function (or Greens' function) in the time domain, respectively.

In coastal regions, the wind-current system can be anisotropic and asymmetric, which means the current response is a function of wind direction, differing from the isotropic response in the open ocean [13, 14, 10, 12]. The wind-driven currents can generate pressure gradients against the coastal boundaries, and the frictional balance due to bottom bathymetry can be anisotropic and asymmetric. In other words, the wind direction relative to the coastline can be a crucial factor to determine the wind-current system in the coastal areas [13]. Thus, the parameterization of vector quantities (equations 1 and 2) may reflect these physical constraints. For simplicity, we adapt the isotropic constraint ($\mathbf{u} = u + iv$, $\tau = \tau_x + \tau_y$) in this paper. The anisotropic analysis has been addressed elsewhere [10].

The current mapping transfer function can be also derived from the linearized momentum equations at a given depth (z) [13], which is consistent with the open ocean environment.

$$\mathbf{H}^*(z, \sigma) = \frac{e^{\lambda z}}{\rho \lambda \nu}, \tag{3}$$

where $\lambda = \sqrt{i(\sigma + f_c)/\nu}$, f_c is the Coriolis frequency and ν is the kinematic viscosity of sea water. The interpretation of wind transfer function and momentum balance in the context of coastal boundaries were examined in [15]. By definition, when the impulse of a delta function is applied to the system

$$\tau = \delta(t - \alpha), \tag{4}$$

the response ($\mathbf{u}$) is identical to the Greens' function ($\mathbf{G}^*$) of the system:

$$\mathbf{u}(\mathbf{x}, t) = \mathbf{G}^*(\mathbf{x}, t - \alpha). \tag{5}$$

3.2 Mapping coastal wind field

The wind field can be mapped using a similar parameterization:

$$\hat{\tau}(\mathbf{x},\sigma) = \mathbf{H}(\mathbf{x},\sigma)\hat{\mathbf{u}}(\mathbf{x},\sigma) \tag{6}$$

$$\tau(\mathbf{x},t) = \int_{t'} \mathbf{G}(\mathbf{x},t-t')\mathbf{u}(\mathbf{x},t')\mathrm{d}t'. \tag{7}$$

From the analytic model, the wind mapping transfer function ($\mathbf{H}$) at surface ($z = 0$) is presented as an inverse of the current mapping transfer function ($\mathbf{H}^*$) in equation 1:

$$\mathbf{H}(\sigma) = \frac{1}{\mathbf{H}^*(\sigma)} = \rho\sqrt{i(\sigma + f_c)\nu} \tag{8}$$

Note that the data-derived wind mapping transfer function should be estimated using the inverse method in frequency-by-frequency instead of simply inverting the current mapping transfer function. Particularly, the wind mapping and current mapping response functions ($\mathbf{G}$ and $\mathbf{G}^*$) may not have relevance, so their empirical estimation needs to be examined with care.

4 Results

4.1 Mapping currents with wind

The current mapping transfer function ($\mathbf{H}^*$) and response function ($\mathbf{G}^*$) estimated from observations and an analytic model (e.g., linearized momentum equations) are shown in Figure 2. The overall shapes of transfer functions are similar except for a peak at low frequency ($|\sigma| < 0.4$ cpd, Figures 2a and 2b). This mismatch is a result of the pressure setup of the wind-driven sea level near the coastal boundary because the analytic model does not include the coastal boundary conditions. The fluctuations of phase at high frequency ($|\sigma| > 3$ cpd) are nearly converged into $\pm 45^\circ$ (Figure 2b). Both response functions (Figures 2c and 2d) exhibit the temporal decay with inertial oscillations in the wind-current system, which shows how wind energy is dissipated as the response to a delta function-shaped wind impulse.

4.2 Wind mapping with currents

In a similar way, the wind mapping transfer function ($\mathbf{H}$) and its response function ($\mathbf{G}$) are shown in Figure 3. The upside down shapes of the magnitude and phase of transfer functions are well captured and comparable with the analytic model results (Figures 3a and 3b). The response function in the time domain decays rapidly and converges into zero within 12 hours without temporal fluctuations because most of variance is from high-frequency noise and the variance at the inertial frequency has the minimum (Figures 3c and 3d).

4.3 Uncertainty and dynamical consistency

The estimates in this paper are based on non-overlapped and evenly subsampled time series of wind stress and surface currents. The linear model is derived from the training data and applied to independent test data to compute the cross-validated error. Moreover, the mean and standard deviation of transfer functions and response functions across the subsamples are used to visualize the uncertainty and signal-to-noise ratio of estimates. In particular, the standard deviation and fluctuations of the transfer function become dominant [10].

The numerical simulations and extensive analysis for the current mapping transfer functions have been addressed elsewhere [10, 15].

4.4 Comparison with conventional approaches

The final outputs of the proposed analysis will be the wind field having equivalent resolutions to surface currents (e.g., km in space and hourly in time) at the elevation where the wind observations were sampled. The extrapolation of wind profiles using an assumption of the atmospheric boundary layer can be made to generate the wind climatology.

In-situ wind observations from multiple sources (e.g., ships, lighthouse, and buoys) in the coastal regions have been gridded with objective analysis and the data-assimilation technique with help of numerical models [16]. As the proposed analysis is a purely data-derived approach, the signal-to-noise ratio in the observations may affect the quality of final outputs.

5 Conclusion and discussion

This paper shows a feasibility to map coastal surface wind field based on empirically estimated transfer functions, computed from the high-frequency radar-derived surface currents and wind stress at a shore-based station. As the accuracy and dynamical consistency of transfer functions are crucial in this estimate, the analytic and empirical transfer functions are compared. In particular, these two transfer functions help to quantify the uncertainty in the data-derived model and to identify the frequency band having low signal-to-noise. The proposed work can be used to design and locate the offshore wind farms and serve as a useful tool to analyze the offshore wind conditions in a hindcast mode.

In the wind resource assessment using the transfer function analysis, the vertical profiles of wind and atmospheric turbulence may not be directly addressed. This statistical framework separates the wind-coherent and wind-incoherent signals and is applicable to map the coastal wind field from the observed surface currents.

References

[1] I. Karagali, M. Badger, A. N. Hahmann, A. Peña, C. B Hasager, and A. M. Sempreviva. Spatial and temporal variability of winds in the Northern European Seas. *Renewable Energy*, 57:200–210, 2013.

[2] I. Karagali, A. Peña, M. Badger, and C. B. Hasager. Wind characteristics in the north and baltic seas from the quikscat satellite. *Wind Energy*, 2012.

[3] P. E. Dexter and R. Casey. Ocean wind field mapping at long ranges with an HF radar. *Australian Meteorol. Mag*, 26:33–44, 1978.

[4] P. E. Dexter and S. Theodoridis. Surface wind speed extraction from HF skywave radar Doppler spectra. *Radio Science*, 17(3):643–652, 1982.

[5] J. Drake, J. F. Vesecky, F. K. Ludwing, D. Sinton, and J. Paduan. *Use of real-time high frequency radar observations to estimate winds that can be used as part of on-line objective analyses in California coastal regions*. 14th conference on Interactions of the Sea and Atmosphere, 2006.

[6] J. F. Vesecky, J. A. Drake, K. Laws, F. L. Ludwig, C. C. Teague, and L. A. Meadows. Using multifrequency HF radar to estimate ocean wind fields. In *Geoscience and Remote Sensing Symposium, 2004. IGARSS'04. Proceedings. 2004 IEEE International*, volume 2, pages 1167–1170. IEEE, 2004.

[7] A. Long and D. Trizna. Mapping of North Atlantic winds by HF radar sea backscatter interpretation. *Antennas and Propagation, IEEE Transactions on*, 21(5):680–685, 1973.

[8] E. Korsbakken, J. A. Johannessen, and O. M. Johannessen. Coastal wind field retrievals from ERS synthetic aperture radar images. *J. Geophys. Res.*, 103(C4):7857–7874, 1998.

[9] M. Badger, J. Badger, M. Nielsen, C. B. Hasager, and A. Peña. Wind class sampling of satellite SAR imagery for offshore wind resource mapping. *Journal of applied meteorology and climatology*, 49(12):2474–2491, 2010.

[10] S. Y. Kim, B. D. Cornuelle, and E. J. Terrill. Anisotropic response of surface currents to the wind in a coastal region. *J. Phys. Oceanogr.*, 39(6):1512–1533, 2009.

[11] S. Y. Kim, B. D. Cornuelle, and E. J. Terrill. Decomposing observations of high-frequency radar derived surface currents by their forcing mechanisms: Decomposition techniques and spatial structures of decomposed surface currents. *J. Geophys. Res.*, 115, 2010.

[12] S. Y. Kim, E. J. Terrill, B. D. Cornuelle, B. Jones, L. Washburn, M. A. Moline, J. D. Paduan, N. Garfield, J. L. Largier, G. Crawford, and P. M. Kosro. Mapping the

U.S. West Coast surface circulation: A multiyear analysis of high-frequency radar observations. *J. Geophys. Res.*, 116, 2011.

[13] V. W. Ekman. On the influence of the Earth's rotation on ocean-currents. *Ark. Mat. Astron. Fys.*, 2:1–53, 1905.

[14] J. Gonella. A rotary-component method for analysis in meteorological and oceanographic vector time series. *Deep Sea Res.*, 19:833–846, 1972.

[15] S. Y. Kim, G. Gopalakrishnan, B. D. Cornuelle, and A. Ponte. Interpretation of anisotropic wind transfer functions using momentum balance derived from an idealized numerical model. 2013. submitted.

[16] A. M. Sempreviva, R. J. Barthelmie, and S. C. Pryor. Review of methodologies for offshore wind resource assessment in european seas. *Surveys in Geophysics*, 29(6):471–497, 2008.

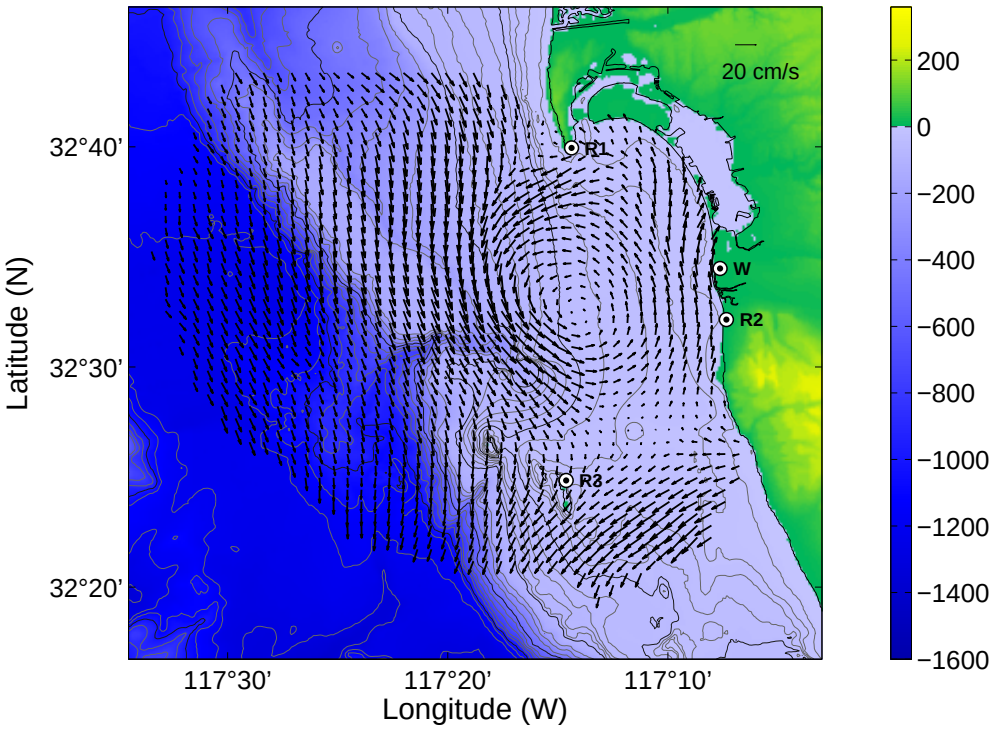

Figure 1: A study domain to estimate the wind mapping transfer function. Three HF radars [R1 (Point Loma), R2 (Imperial Beach), and R3 (Coronado Islands)] for surface currents, one station at the Tijuana River Valley (W, TJR). The bottom bathymetry contours are indicated by thin curves with 10 m ($0 < z < 100$ m) and 50 m ($100 < z < 1000$ m) contour intervals and thick curves at the 50, 100, 500, and 1000 m depths.

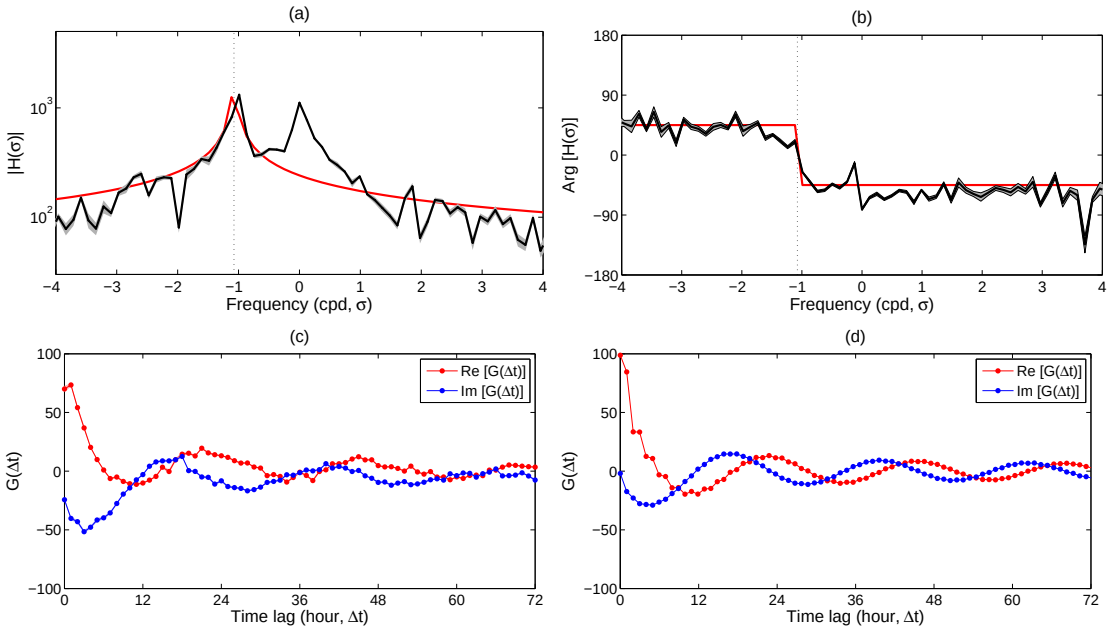

Figure 2: Comparison of isotropic current mapping transfer functions and response functions ($\mathbf{H}^*$ and $\mathbf{G}^*$). (a) Magnitudes of data-derived (black) and analytic-model-derived (red) transfer functions. (b) Phases of data-derived (black) and analytic-model-derived (red) transfer functions. Dotted vertical lines indicate the local inertial frequency ($f_c = 1.07$ cpd). (c) Amplitudes of the data-derived response function. (d) Amplitudes of the analytic-model-derived response function.

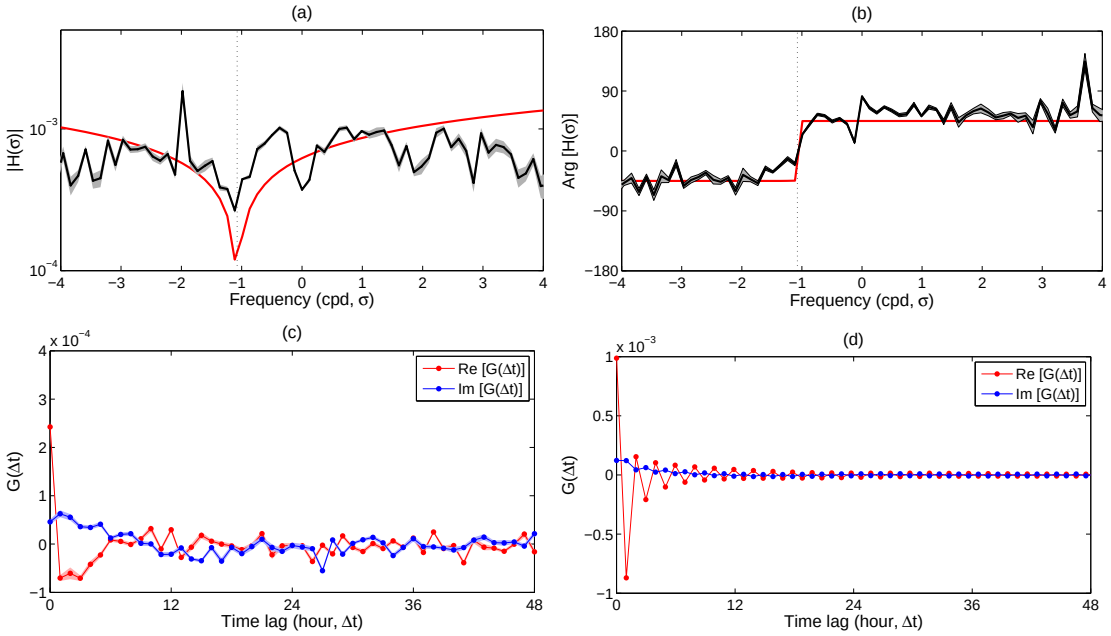

Figure 3: Comparison of isotropic wind mapping transfer functions and response functions (**H** and **G**). (a) Magnitudes of data-derived (black) and analytic-model-derived (red) transfer functions. (b) Phases of data-derived (black) and analytic-model-derived (red) transfer functions. Dotted vertical lines indicate the local inertial frequency ($f_c = 1.07$ cpd). (c) Amplitudes of the data-derived response function. (d) Amplitudes of the analytic-model-derived response function.

Simulation of neutral Wind flow over complex terrain with OpenFoam

X. Zhang[1], D. Zhang[2]
State Key Laboratory of Alternate Electrical Power System with Renewable Energy Sources(North China Electric Power University), Beijing 102206)
[1]zzxd@yeah.net
[2]zhangdesheng0068@126.com

ABSTRACT

The aim of the present project is to evaluate OpenFoam as a Computational Fluid Dynamics (CFD) solver for numerical simulation of neutral Atmospheric Boundary Layer (ABL) wind flow, especially the wind conditions over complex terrain, because nowadays, more and more wind farms are located at hilly or mountainous areas, especially in China. As an initial study, the existing solver simpleFoam is adopted to solve the Reynolds-Averaged Navier-Stokes (RANS) equations, along with modified standard k-ε turbulence model and wall functions. Wind flow over flat terrain is used as testing case, and the simulation results show that the CFD model is consistent with logarithmic wind profile. Then, the Bolund case is adopted for site simulation. The wind measurement campaign[1] performed at the Bolund peninsula in Denmark in the winter of 2007–2008 is important work for research of wind flow models, same is the Blind comparison[2] based on the measurement campaign. The Bolund island exhibiting a significantly steep escarpment in the main wind direction. The physical shape of Bolund represents, in a scaled-down form, a typical wind turbine site in complex terrain[1]. The overall CFD simulation error is around 13%, this is, in a way, acceptable result.

1. Methods

Meshing: The Bolund island is situated about 200m×150m of the region, with a height of 11 meters above sea level. The simulation domain is 800m×500m, with the coordinate origin locate at the center of the island horizontal projection. Average horizontal grid spacing is 7m×7m with refinement at steep terrain area (Figure 2). Average grid spacing is also 7m for vertical direction, but applying increment scheme, the first layer grid nodes are about 0.5 meter above ground (or sea lever).

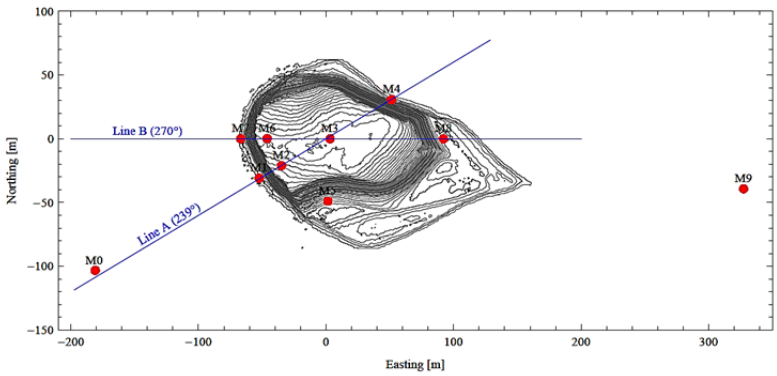

Figure 1 Bolund island and mast sites

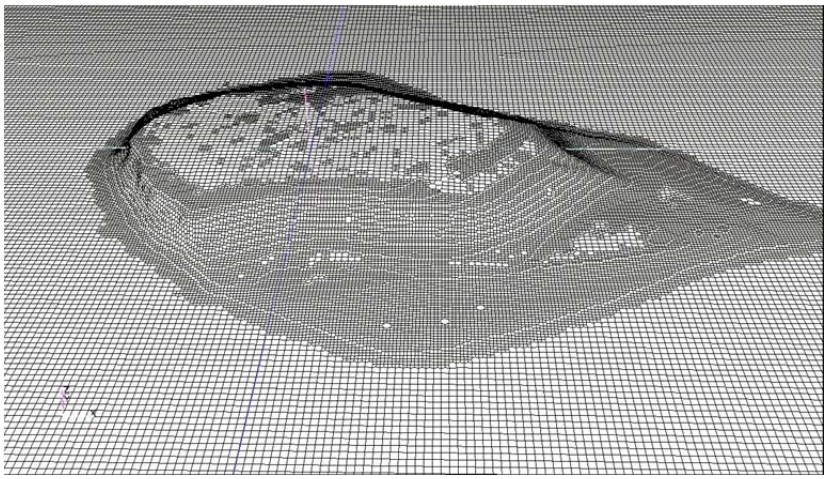

Figure 2: Meshing of the ground boundary, applying SnappyHexMesh

Wind conditions: There are totally 4 coming wind conditions simulated (Table 1). For case 1~3, wind direction are west or west southerly, the wind flowing from the sea with roughness length z_0=0.0003. For case 4, wind direction is east, the wind flowing from land with z_0=0.015.

Table 1 Simulated wind conditions

Case	Wind direction[°]	Roughness length, z_0[m]	TKE_0 / u_0^{*2}	u_0^* [m/s]
1	270	0.0003	5.8	0.4
2	255	0.0003	5.8	0.4
3	239	0.0003	5.8	0.4
4	90	0.015	5.8	0.5

The coming wind velocity is for full height ABL:

$$u = \frac{u^*}{\kappa}\left(\ln\frac{z}{z_0} + \frac{z}{L_M} - \frac{z}{H}\cdot\left(\frac{z}{2L_M}\right)\right) \tag{1}$$

where u^* is friction velocity, κ is the von Karman constant (approximately 0.4), H is height of ABL, given by[3]

$$H = u^*/(6f) \tag{2}$$

the coriolis parameter f is defined as

$$f = 2\Omega\sin(|\lambda|) \tag{3}$$

where Ω is the angular speed of the earth's rotation, and λ is the local geographical latitude. L_M is a the length scale for middle of ABL[4], given by

$$L_M = \frac{u^*}{f\left(55 - 2\ln\left(\frac{u^*}{fz_0}\right)\right)} \tag{4}$$

Turbulence model: The standard k-ε turbulence model, with modified model constants, has proven to be capable of correctly modeling the atmospheric boundary layer flows[5, 6]. The transport equations of turbulence kinetic energy k and its' dissipation rate ε are

$$\frac{\partial}{\partial x_i}(\rho k u_i) = \frac{\partial}{\partial x_j}\left[\left(\mu + \frac{\mu_t}{\sigma_k}\mu\right)\frac{\partial k}{\partial x_j}\right] + P_k - \rho\varepsilon \tag{5}$$

$$\frac{\partial}{\partial x_i}(\rho \varepsilon u_i) = \frac{\partial}{\partial x_j}\left[\left(\mu + \frac{\mu_t}{\sigma_\varepsilon}\right)\frac{\partial \varepsilon}{\partial x_j}\right] + C_{1\varepsilon}\frac{\varepsilon}{k}P_k - C_{2\varepsilon}\rho\frac{\varepsilon^2}{k} \tag{6}$$

where P_k is generation rate of turbulence kinetic energy,

$$P_k = -\rho\overline{u_i' u_j'}\frac{\partial u_j}{\partial x_i} \tag{7}$$

and then turbulence eddy viscosity μ_t is calculated from

$$\mu_t = \rho C_\mu \frac{k^2}{\varepsilon} \tag{8}$$

C_μ , σ_k, σ_ε, $C_{1\varepsilon}$, $C_{2\varepsilon}$ along with κ are model constant, consider atmospheric surface layer and steady, homogeneous, logarithmic wind flow, the model constants should satisfy the following equation[7]

$$\sigma_\varepsilon\left(C_{2\varepsilon} - C_{1\varepsilon}\right)\sqrt{C_\mu} = \kappa^2 \tag{9}$$

Most wind measurements suggested a model constant C_μ around 0.3, a site measurement in northwest China suggested a C_μ=0.36[8]. For Bolund case, C_μ=0.3 is adopted.

Table 2 k-ε turbulence model constants

C_μ	κ	σ_k	σ_ε,	$C_{1\varepsilon}$,	$C_{2\varepsilon}$
0.03	0.4	1.0	1.3	1.209	1.92

Turbulence of coming wind: The coming profiles of turbulence kinetic energy k and it's dissipation rate ε are proposed by Yang Yi, et al[9],

$$k = \frac{u^{*2}}{\sqrt{C_\mu}}\sqrt{C_1 \ln\frac{z}{z_0} + C_2} \tag{10}$$

$$\varepsilon = \frac{u^{*3}}{\kappa z}\sqrt{C_1 \ln\frac{z}{z_0} + C_2} \tag{11}$$

Constants C_1 and C_2 are derived as following: when $z=z_0$, $k = u^{*2} / \sqrt{C_\mu}$; when $z=H$, $k \to 0$, here $k=10^{-6}$ is used for $z \geq H$.

Wall functions: The simpleFoam solver use wall functions based on roughness height, K_s. Wind profile within the surface layer of ABL is always described with logarithmic function based on friction velocity and based on roughness length, z_0. To solve this problem, wall functions adopting roughness length could be used[10, 11], or use roughness height with the relationship $K_s=9.793z_0/C_s$[12], where C_s is roughness constant. The second scheme is adopted for current work.

Test case: A test simulation is carried out for homogeneous wind flow over flat terrain, the simulation domain is regular hexahedron, it's length is1200m, width is 200m and thickness is 700m. Roughness length of the terrain as well as the coming wind is 0.03. for wind velocity profile at inlet, x=500m and x=1000m, the maximum error is within 5% (Figure 3).

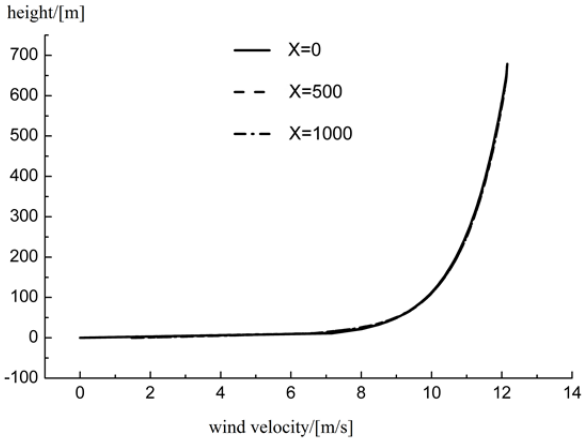

Figure 3: wind profile along flat terrain.

2. Results:

Figure 4 shows the measured and simulated velocity speedups along line B with wind direction of 270°. The simulated results at windward side three points at 5 meter's high are in agreement with measurement very well, but for 2 meter's high, the simulated result is lower than measurement at mast 7 and higher than measurement at mast 6. The simulated wind speed at lee side is higher than measurement. Figure 5 shows the measured and simulated velocity speedups along line B with wind direction of 255°, most CFD data agree with measured data very well, except mast 6 at 2 meter, where simulated wind speed is accelerating but measured wind speed is slowing down. The real flow structure at this point is unknown, we can image that there is a swirl motion at the front top location because of a steep cliff, but the CFD model cannot give accurate description. Because simulated results agree with measurements very well for front top 5 meter high point, we can image that the cliff induced swirl does not extend very high.

The simulated and measured wind data along line A with Wind direction of 239° is shown in Figure 6, in this case, mast 1 locates at front bottom of the cliff, and mast 2 locates at front top of the cliff. At 5 meter high, CFD results and measurements are consistent, at 2 meter

high, again, CFD result is lower at bottom and higher at top of the cliff, compare with measurements.

At lee side of the island, that is, mast 8 for wind direction of 270° and mast 4 for wind direction of 239°, the deviation of simulated results from measurement is a little larger. In case of 270° wind direction, simulated wind speed is higher than measurement, at both 5 and 2 meter high. In case of 239° wind direction, simulated wind speed is lower than measurement, at both 5 and 2 meter high.

Cases of 270°, 255° and 239° wind directions show that atmospheric boundary flow with windward cliff is very complicated, there will be swirl, reflux and separated flow in the flow field. When the wind is coming from 90° direction, the windward side of the island is gentle slope, and CFD results agree with measurements very well, as shown in Figure 7.

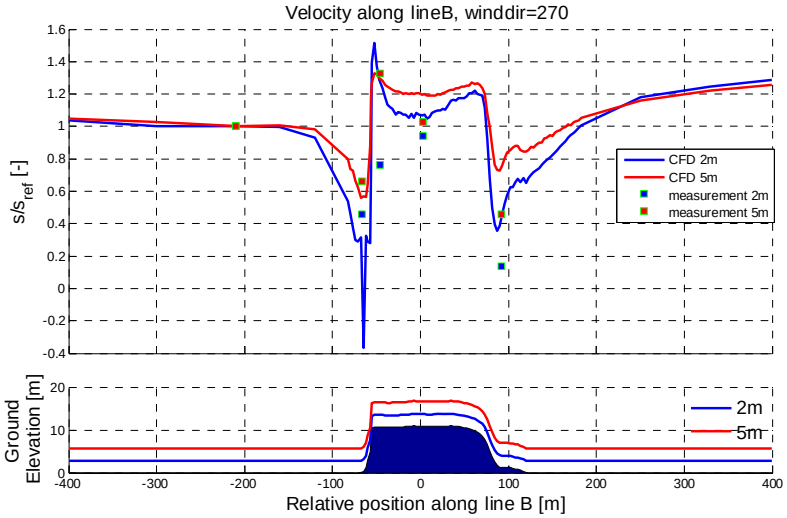

Figure 4: velocity speedups along Line B, wind direction is 270°

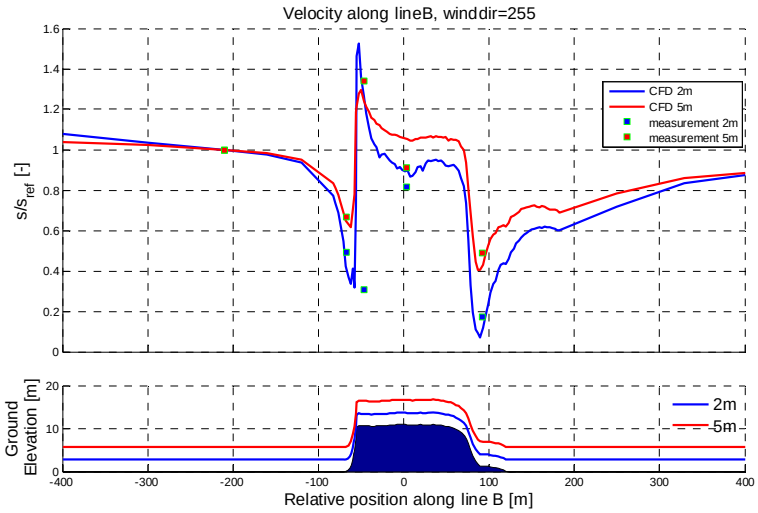

Figure 5: velocity speedups along Line B, wind direction is 255°

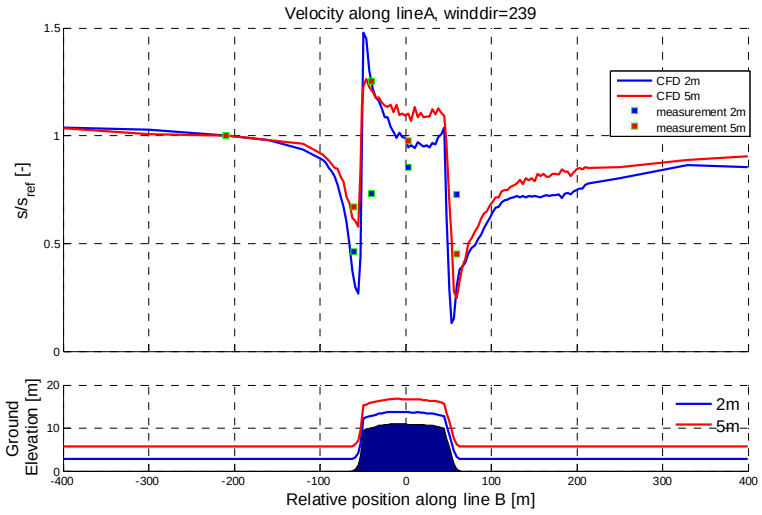

Figure 6: velocity speedups along Line A, wind direction is 239°

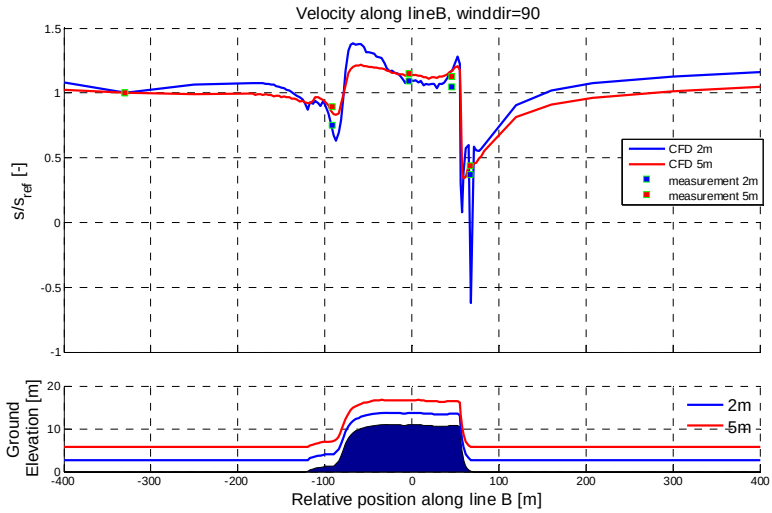

Figure 7: velocity speedups along Line A, wind direction is 90°

3. Conclusion:

CFD simulation based on RANS equations and *k-ε* turbulence model is relatively mature technique in industry application. For Atmospheric Boundary Layer, the case study shows that the simpleFoam solver provided in OpenFoam is suitable for simulation of neutral ABL flows over complex terrain. This is very attractive because OpenFoam is open source, free and much more open than some commercial CFD tools.

Acknowledgements The research is funded by International Science & Technology Cooperation Program of China.(2010DFA64600). We would like to express our gratitude to Mr. Andreas Bechmann for the measurement data and results processing codes.

REFERENCES

[1]J. Berg, J. Mann, A. Bechmann, M. S. Courtney, and H. E. Jørgensen, "The Bolund Experiment, Part I: Flow Over a Steep, Three-Dimensional Hill," *Boundary-Layer Meteorology,* vol. 141, pp. 219-243, 2011/11/01.
[2]A. Bechmann, N. N. Sørensen, J. Berg, J. Mann, and P. E. Réthoré, "The Bolund Experiment, Part II: Blind Comparison of Microscale Flow Models," *Boundary-Layer Meteorology,* vol. 141, pp. 245-271, 2011/11/01.
[3]T. Burton, *Wind Energy Handbook*: Wiley, 2001.
[4]S. Gryning, E. Batchvarova, B. Brümmer, H. Jørgensen, and S. Larsen, "On the extension of the wind profile over homogeneous terrain beyond the surface boundary layer," *Boundary-Layer Meteorology,* vol. 124, pp. 251-268, 2007.
[5]P. Brodeur and C. Masson, "Numerical site calibration over complex terrain," *Journal of Solar Energy Engineering-Transactions of the Asme,* vol. 130, Aug 2008.
[6]A. Bechmann, N. N. Sorensen, J. Johansen, S. Vinther, B. S. Nielsen, and P. Botha, "Hybrid RANS/LES method for high reynolds numbers, applied to atmospheric flow over complex terrain," in *Conference on the Science of Making Torque from Wind*, Lyngby, DENMARK, 2007.
[7]P. J. Richards and R. P. Hoxey, "APPROPRIATE BOUNDARY-CONDITIONS FOR COMPUTATIONAL WIND ENGINEERING MODELS USING THE KAPPA-EPSILON TURBULENCE MODEL," in *1st International Symp on Computational Wind Engineering (Cwe92)*, Tokyo, Japan, 1992, pp. 145-153.
[8]S. Liang, X. Zhang, and S. Kang, "Simulation Method of Flow Over Complex Terrain," *Journal of Engineering Thermophysics,* vol. Vol. 32, pp. 945-948, Jun. 2011.
[9]Y. Yang, M. Gu, S. Chen, and X. Jin, "New inflow boundary conditions for modelling the neutral equilibrium atmospheric boundary layer in computational wind engineering," *Journal of Wind Engineering and Industrial Aerodynamics,* vol. 97, pp. 88-95, 2009.
[10] X. Zhang, "CFD simulation of neutral ABL flows," Roskilde, Denmark, April 2009.
[11]M. Balogh, A. Parente, and C. Benocci, "RANS simulation of ABL flow over complex terrains applying an Enhanced k-ε model and wall function formulation: Implementation and comparison for fluent and OpenFOAM," *Journal of Wind Engineering and Industrial Aerodynamics,* vol. 104–106, pp. 360-368, 5// 2012.
[12]B. Blocken, T. Stathopoulos, and J. Carmeliet, "CFD simulation of the atmospheric boundary layer: wall function problems," *Atmospheric Environment,* vol. 41, pp. 238-252, Jan 2007.

The influence of static stability of the free atmosphere on the power extracted by a very large wind farm

Mahdi Abkar, Fernando Porté-Agel

École Polytechnique Fédérale de Lausanne (EPFL), Wind Engineering and Renewable Energy Laboratory (WIRE), ENAC-IIE-WIRE, CH-1015 Lausanne, Switzerland
mahdi.abkar@epfl.ch fernando.porte-agel@epfl.ch

Abstract

Large-eddy simulation is used to study the influence of free-atmosphere stratification on the structure of atmospheric boundary-layer flow inside and above very large wind farms, as well as the power extracted by the wind turbines. In the simulations, tuning-free Lagrangian scale-dependent dynamic models are used to model the subgrid-scale turbulent fluxes, while the turbine-induced forces are parameterized with an actuator-disk model. It is shown that for a given surface cover (with and without turbines) thermal stratification of the free atmosphere reduces the entrainment from the flow above compared with the unstratified case, leading to lower boundary-layer depth. Due to the fact that in very large wind farms vertical energy transport associated with turbulence is the only source of kinetic energy, lower entrainment leads to lower power production by the wind turbines. In particular, for the wind-turbine arrangements considered in the present work, the power output from the wind farms is reduced by about 35 percent when the potential temperature lapse rate in the free atmosphere increases from 1 to 10 K/km (within the range of values typically observed in the atmosphere). Moreover, it is shown that the presence of the turbines has significant effect on the growth of the boundary layer.

1. Introduction

Within a very large and sufficiently dense wind farm, the atmospheric boundary-layer (ABL) flow asymptotes to the fully-developed regime. In this regime, the performance of the wind turbines is not affected by the farm entrance region, and the power extraction from the wind farm is mainly due to the vertical energy transport from the flow above [1-3]. In other words, the kinetic energy must be entrained from the free atmosphere to balance that extracted by the farm, leading to an increased boundary-layer depth [4,5].

In the absence of wind turbines, entrainment and boundary-layer growth are controlled by different factors such as earth's rotation, surface momentum and buoyancy fluxes, and static stability of the free atmosphere immediately above the ABL. The shear at the surface and the positive surface buoyancy fluxes facilitate the growth of the boundary layer, while the Earth's rotation, the negative surface buoyancy fluxes, and the static stability of the free atmosphere limit the boundary-layer growth [6]. Since the power extracted by the turbines in very large wind farms is directly linked to the entrainment of kinetic energy from the external environment, it is of great importance to investigate how the above mentioned parameters (buoyancy fluxes, free-atmosphere stability, and earth's rotation) can affect the performance of wind farms.

Most of the previous numerical studies on the interaction between atmospheric boundary layer and wind farms, using computational fluid dynamics (CFD) [2,5] and one-dimensional models [1,3], have focused on the purely neutral ABL. In that case, the effect of surface buoyancy fluxes and free-atmosphere stratification can be ignored. However, it has been shown that the purely neutral ABLs are rarely observed in the atmosphere, and most of the real ABLs that are classified as neutral are almost always *conventionally neutral* [7]. *Conventionally neutral* ABLs are defined as neutrally-stratified ABLs capped by the stably-stratified free atmosphere. The main effect of the free-atmosphere stratification is to reduce the entrainment from the free atmosphere, leading to lower boundary-layer

depth. The smaller boundary-layer depth limits the size of the largest eddies, which have a relatively important contribution to the turbulent kinetic energy and fluxes. As a result, the free-atmosphere stability limits the turbulent transport away from the surface compared with the unstratified case [8-11].

In order to isolate the effects of free-atmosphere stratification on the turbulent flow through wind farms and the turbines performance, in this study we focus on the interaction between *conventionally neutral* ABLs and very large wind farms. In this regard, a suit of large-eddy simulations (LES) of fully-developed wind-farm ABL flow is performed including the effect of earth's rotation and free-atmosphere stability. Different values of the potential temperature lapse rate ($\Gamma = \frac{\partial \theta}{\partial z}$) in the free-atmosphere within the range of 1 to 10 K/km, typically observed in the atmosphere [12], are considered. In the simulations, tuning-free Lagrangian scale-dependent dynamic models [13] are used to model the subgrid-scale fluxes, while the turbine-induced forces are parameterized with an actuator disk model [14]. It should be highlighted that considering the Coriolis forces in the governing equations allows investigating how the wind direction changes inside and above the farm due to the presence of the turbines, which is not possible in the unidirectional boundary layer flow resulting from an imposed pressure gradient. Moreover, the important effect of the wind farm on the boundary-layer growth can be explicitly resolved and studied. In Section 2, the LES framework used in this work is described. In Section 3, the results obtained from the LES of ABLs over very large wind farms are presented. Finally, a summary and conclusions are provided in Section 5.

2. Large-eddy simulation framework

2.1. LES governing Equations

LES solves the filtered continuity equation, the filtered Navier-Stokes equations (written here using the Boussinesq approximation), and the filtered transport equation for potential temperature:

$$\frac{\partial \tilde{u}_i}{\partial x_i} = 0\,, \quad \frac{\partial \tilde{u}_i}{\partial t} + \tilde{u}_j \frac{\partial \tilde{u}_i}{\partial x_j} = -\frac{\partial \tilde{p}^*}{\partial x_i} - \frac{\partial \tau_{ij}^d}{\partial x_j} + \delta_{i3} g \frac{\tilde{\theta} - \langle \tilde{\theta} \rangle}{\theta_0} + f_c \varepsilon_{ij3} \tilde{u}_j + \mathcal{F}_i\,, \quad \frac{\partial \tilde{\theta}}{\partial t} + \tilde{u}_j \frac{\partial \tilde{\theta}}{\partial x_j} = -\frac{\partial q_j}{\partial x_j}\,, \quad (1)$$

where the tilde represents a spatial filtering at scale $\tilde{\Delta}$, t is time, $\tilde{u}_i$ is instantaneous resolved velocity in the i-direction (with $i = 1, 2, 3$ corresponding to the streamwise (x), spanwise (y) and vertical (z) direction, respectively), $\tilde{\theta}$ denotes the resolved potential temperature, θ_0 is the reference temperature, the angle brackets represent a horizontal average, g refers to the gravitational acceleration, f_c is the Coriolis parameter, δ_{ij} is the Kronecker delta, ε_{ijk} denotes the alternative unit tensor, $\tilde{p}^* = \tilde{p}/\rho + \frac{1}{3}\tau_{kk}$ is the effective pressure, $\mathcal{F}_i$ is a forcing term (e.g., wind-turbine induced forces), $q_j = \widetilde{u_j \theta} - \tilde{u}_j \tilde{\theta}$ denotes the SGS heat flux, $\tau_{ij} = \widetilde{u_i u_j} - \tilde{u}_i \tilde{u}_j$ represents the kinematic SGS stress, and τ_{ij}^d is its deviatoric part. Note that τ_{ij}^d and q_j are unknown and need to be parameterized as a function of filtered (resolved) fields. A common parameterization strategy in LES consists of computing the deviatoric part of the SGS stress with an eddy-viscosity model [15], $\tau_{ij}^d = \tau_{ij} - \frac{1}{3}\tau_{kk}\delta_{ij} = -2\tilde{\Delta}^2 C_S^2 |\tilde{S}| \tilde{S}_{ij}$, and the SGS heat flux with an eddy-diffusivity model, $q_j = -\tilde{\Delta}^2 C_S^2 Pr_{sgs}^{-1} |\tilde{S}| \frac{\partial \tilde{\theta}}{\partial x_j}$, where $\tilde{S}_{ij} = \left(\partial \tilde{u}_i / \partial x_j + \partial \tilde{u}_j / \partial x_i\right)/2$ is the resolved strain rate tensor and $\tilde{S} = \sqrt{2 \tilde{S}_{ij} \tilde{S}_{ij}}$ is the strain rate magnitude. C_s represents the Smagorinsky coefficient and $C_S^2 Pr_{sgs}^{-1}$ is the lumped coefficient, where Pr_{sgs} is the SGS Prandtl number. Here, we employ the scale-dependent Lagrangian dynamic models [13] to compute the local optimized value of the model coefficients without any ad hoc tuning. In contrast with the traditional dynamic models [16,17], the scale-dependent dynamic models compute dynamically not only the value of the model coefficients in the eddy-viscosity and eddy-diffusivity models, but also the dependence of these coefficients with scale. More details on the formulation of

scale-dependent dynamic models for the SGS stress and the SGS scalar fluxes can be found in Porté-Agel *et al*. [18], Porté-Agel [19] and Stoll and Porté-Agel [13].

2.2. Wind-turbine parameterization

To parameterize the turbine-induced forces, the actuator-disk model with rotation [14,24] is used. Through this model, the lift and drag forces acting on the turbines are parameterized using the blade element momentum (BEM) theory, and are distributed over the rotor area. Unlike the standard actuator-disk model, which assumes the loads are distributed uniformly over the rotor disk and acting only in the axial direction, the actuator-disk model with rotation includes the effect of turbine-induced flow rotation as well as the non-uniform force distribution. Fig. 1 shows a cross-sectional element of radius r in the (θ, x) plane, where x is the axial direction. Different forces, velocities and angles are shown in this figure. $V_x = V_x(r,\theta)$ and $V_\theta = V_\theta(r,\theta)$ are axial and tangential velocities of the incident flow at the blades, respectively, in the inertial frame of reference. The local velocity relative to the rotating blade is defined as $V_{rel} = (V_x, V_\theta + \Omega r)$, where Ω is the turbine angular velocity. The angle of attack is defined as $\alpha = \varphi - \gamma$, where $\varphi = \tan^{-1}(\frac{V_x}{V_\theta + \Omega r})$ is the angle between V_{rel} and the rotor plane and γ is the local pitch angle. The resulting force is given by:

$$f_{disk} = \frac{dF}{dA} = \frac{1}{2}\rho V_{rel}^2 \frac{Bc}{2\pi r}(C_L e_L + C_D e_D)\,, \tag{2}$$

where an annular area of differential size is $dA = 2\pi r dr$, B is the number of blades, $C_L = C_L(\alpha, Re)$ and $C_D = C_D(\alpha, Re)$ are lift and drag coefficient, respectively, c is the chord length, and e_L and e_D denote the unit vectors in the directions of the lift and the drag, respectively. Porté-Agel *et al*. [25] provided details of the SWT-2.3-2.9 wind turbine in a simulation of an operational wind farm.

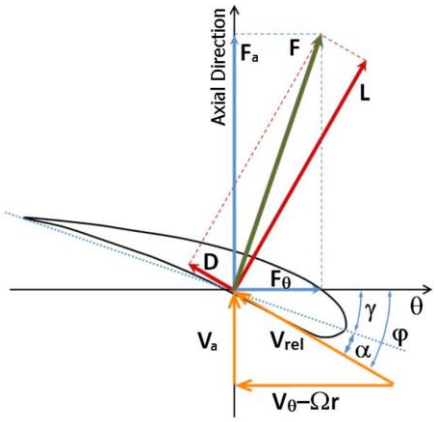

Figure 1: A cross-sectional aerofoil element.

2.3. Numerical Setup

The LES code used in this study is a modified version of the one described by Albertson and Parlange [26], Porté-Agel *et al*. [18], Stoll and Porté-Agel [13] and Wu and Porté-Agel [14]. In the simulations, tuning-free Lagrangian scale-dependent dynamic models are used to model the subgrid-scale turbulent fluxes, and the turbine-induced forces are parameterized using the above-mentioned actuator-disk model. Since the Reynolds number of the ABL is very high, no near-ground viscous processes are resolved, and the viscous term is neglected in the momentum equation. The vertical derivatives are approximated with second-order central differences and the horizontal directions are discretized pseudo-spectrally. Periodic boundary conditions are applied horizontally; as a result, a very large (infinite-size) wind farm is simulated. Full dealiasing of the nonlinear terms is obtained by padding and truncation according to the 3/2 rule [27]. The time advancement is carried out using a second-order-accurate Adams–Bashforth scheme [28]. The finite-difference scheme in the vertical direction

requires specification of boundary conditions at the top and bottom of the domain. The upper boundary condition consists of a stress-free/flux-free condition. A Rayleigh damping region is also used to limit gravity-wave reflection from the top of the domain. At the bottom surface, the standard formulation based on local application of Monin-Obukhov similarity theory [29] is used. Although this theory was developed for mean quantities, it is a common practice in LES of atmospheric flows to compute the instantaneous filtered surface momentum flux [30,31]. In this study, we focus on the *conventionally neutral* ABL and, therefore, the surface heat flux is set to zero.

The boundary layer is driven by an imposed uniform geostrophic wind (G) of 10 m/s; the Coriolis parameter is set to $f_c = 1 \times 10^{-4}$ rad/s. The initial mean vertical profiles are specified as linearly increasing potential temperature with a prescribed depth-constant temperature gradient Γ, and a constant wind velocity (equal to geostrophic wind magnitude) at all levels. The initial flow is laminar with imposed very small perturbations at the first 100m from the surface. It should be mentioned the angle of the geostrophic wind is set so that, when the flow reaches the quasi-steady state, the mean velocity direction is aligned with the turbine axes at the hub-height level. The code is run for a long-enough time to guarantee that quasi-steady conditions are reached. The domain is divided into N_x, N_y, and N_z uniformly spaced grid points in streamwise, spanwise and wall-normal directions, respectively. The grid planes are staggered in the vertical direction, with the first vertical velocity plane at a distance $\Delta_z = L_z/(N_z - 1)$ from the surface, and the first horizontal velocity plane $\Delta_z/2$ from the surface. The filter width is computed using the common formulation $\tilde{\Delta} = (\Delta_x \Delta_y \Delta_z)^{1/3}$, where $\Delta_x = L_x/N_x$ and $\Delta_y = L_y/N_y$. The Siemens SWT-2.3-93 wind turbines, with rotor diameter (D) of 93m and a hub-height (z_h) of 80m, are "immersed" in the flow. In order to investigate the layout effects, the framework is also applied to study several cases of aligned and staggered wind farms with different streamwise (s_x) and spanwise (s_y) spacings. The key parameters of the various LES cases are summarized in Table 1.

Table 1. Key parameters of the various LES cases.

Case	z_o (m)	Abbreviation	$\Gamma\left(\frac{K}{km}\right)$	Number of wind turbines ($N_{tx} \times N_{ty}$)	$s_x \times s_y$	Turbine arrangement	$L_x \times L_y \times L_z$ (m^3)	$N_x \times N_y \times N_z$
A1	0.1	$nt - \Gamma 1$	1	No farm	-	-	$3906 \times 3255 \times 1045$	$126 \times 175 \times 80$
A3	0.1	$nt - \Gamma 10$	10	No farm	-	-	$3906 \times 3255 \times 1045$	$126 \times 175 \times 80$
B1	0.1	$s5 \times 5 - \Gamma 1$	1	8×7	5×5	Staggered	$3720 \times 3255 \times 1687$	$120 \times 175 \times 128$
B2	0.1	$a5 \times 5 - \Gamma 1$	1	8×7	5×5	Aligned	$3720 \times 3255 \times 1687$	$120 \times 175 \times 128$
C1	0.1	$s5 \times 5 - \Gamma 10$	10	8×7	5×5	Staggered	$3720 \times 3255 \times 1045$	$120 \times 175 \times 80$
C2	0.1	$a5 \times 5 - \Gamma 10$	10	8×7	5×5	Aligned	$3720 \times 3255 \times 1045$	$120 \times 175 \times 80$
D1	0.1	$s7 \times 7 - \Gamma 1$	1	6×5	7×7	Staggered	$3906 \times 3255 \times 1687$	$126 \times 175 \times 128$
D2	0.1	$a7 \times 7 - \Gamma 1$	1	6×5	7×7	Aligned	$3906 \times 3255 \times 1687$	$126 \times 175 \times 128$
E1	0.1	$s7 \times 7 - \Gamma 10$	10	6×5	7×7	Staggered	$3906 \times 3255 \times 1045$	$126 \times 175 \times 80$
E2	0.1	$a7 \times 7 - \Gamma 10$	10	6×5	7×7	Aligned	$3906 \times 3255 \times 1045$	$126 \times 175 \times 80$

3. LES Results

Fig. 2 shows the vertical profiles of the horizontally-averaged velocity magnitude M and wind direction in very large wind farms for two different values for Γ. As expected, for a given surface cover (with and without turbines), the stronger stratification (i.e., larger value for Γ) leads to lower entrainment from the free atmosphere and, consequently, shallower boundary-layer depth. It is also evident that the presence of the turbines has significant effect on the growth of the boundary layer. It is also observed from Figure 6b that the ratio of the ageostrophic to geostrophic velocity component increases due to the presence of the wind turbines. In other words, the wind direction (arctangent of the ratio of the ageostrophic to the geostrophic velocity components) changes inside the wind farm due to the presence of the turbines. Recently, a similar trend was reported by Johnstone and Coleman [5]. They performed numerical simulation of the neutral turbulent Ekman layer over an infinite wind farm,

and showed that the Ekman spiral becomes more pronounced when the wind turbines are present. It is important to note that the Reynolds number used in the mentioned work was extremely small in comparison to that of the real atmospheric boundary layer.

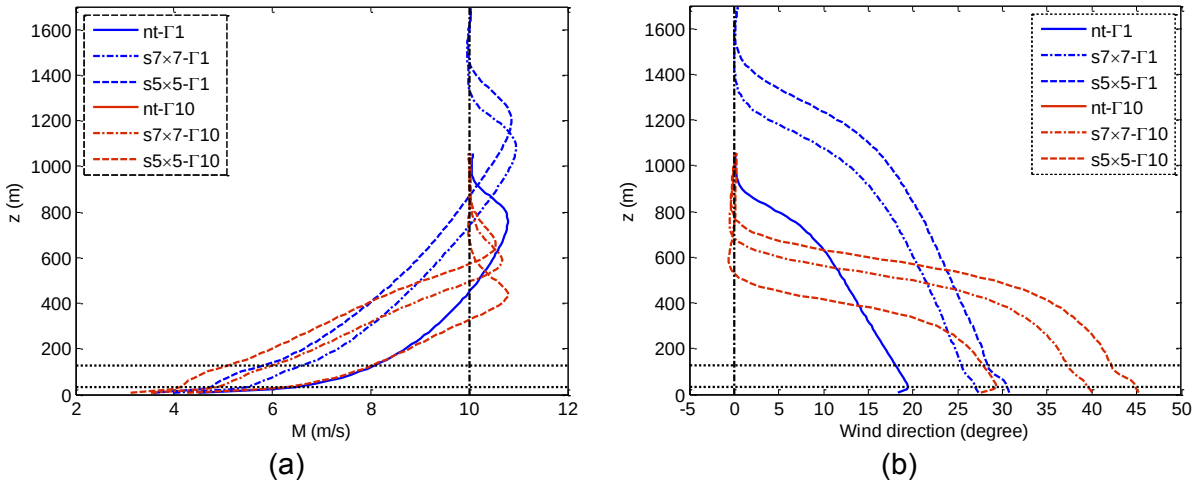

Figure 2. Vertical profile of (a) horizontally-averaged velocity magnitude M, and (b) wind direction inside the ABL for two different values of Γ with and without wind farm. The horizontal dotted lines show the top-tip and bottom-tip heights.

The vertical profiles of the total shear stress are presented in fig. 3. In the absence of turbines increasing the free-atmosphere stability reduces the surface momentum flux. This reduction of the surface shear stress is mainly due to the fact that the smaller boundary-layer depth limits the size of the largest eddies, which have an important contribution to the turbulent kinetic energy and fluxes [9]. In very large wind farms, as observed in this figure and also reported in previous studies [2,5,24], the surface shear stress decreases due to extraction of momentum by the turbines compared with the no-farm case. Besides, the total shear stress has a peak at the turbine-top level, where the strong wind shear occurs, and has a higher value compared with the surface shear stress in the absence of turbines. It should be mentioned that the previous studies were limited to the purely neutral condition, thus ignoring the influence of free-atmospheric stratification. As shown in fig. 3, applying the plane-averaged momentum balance between the top-tip and the bottom-tip heights shows that the extracted momentum by the farm increases when the static stability of the free atmosphere decreases. It can be concluded that more kinetic energy can be entrained from the flow above when the potential temperature lapse rate decreases, leading to higher power production by the farm.

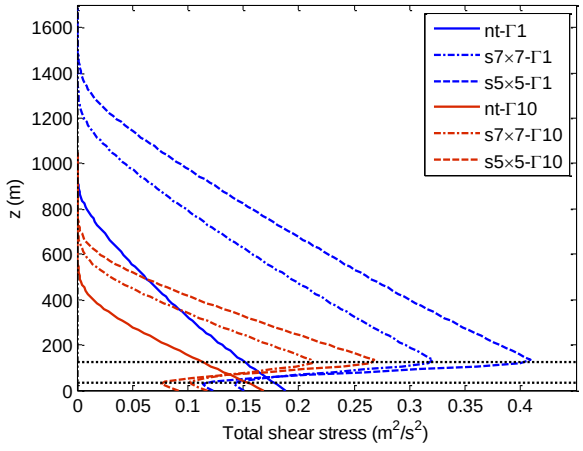

Figure 3: Vertical profile of total shear stress $\left(\sqrt{\tau_{xz}^2 + \tau_{yz}^2}\right)$ for two different values of Γ.

In this study, we also investigate the effect of wind farm layout (aligned vs. staggered) on the flow and the power extracted by the farm. Fig. 9 shows vertical profiles of the horizontally-averaged velocity and the total shear stress. Note that, above the wind-turbine region, the profiles are almost identical for different layouts. The main effect of configuration is found below the turbine region, where the staggered wind farms extract more momentum compared with the aligned ones. Using the plane-averaged momentum balance between the top-tip and the bottom-tip heights, one can show that the momentum and, consequently, the power extracted by the farm is higher when the layout changes from aligned to staggered. In particular, for the wind farms considered here, the power output from the staggered wind farms is about 10 percent higher than the aligned ones.

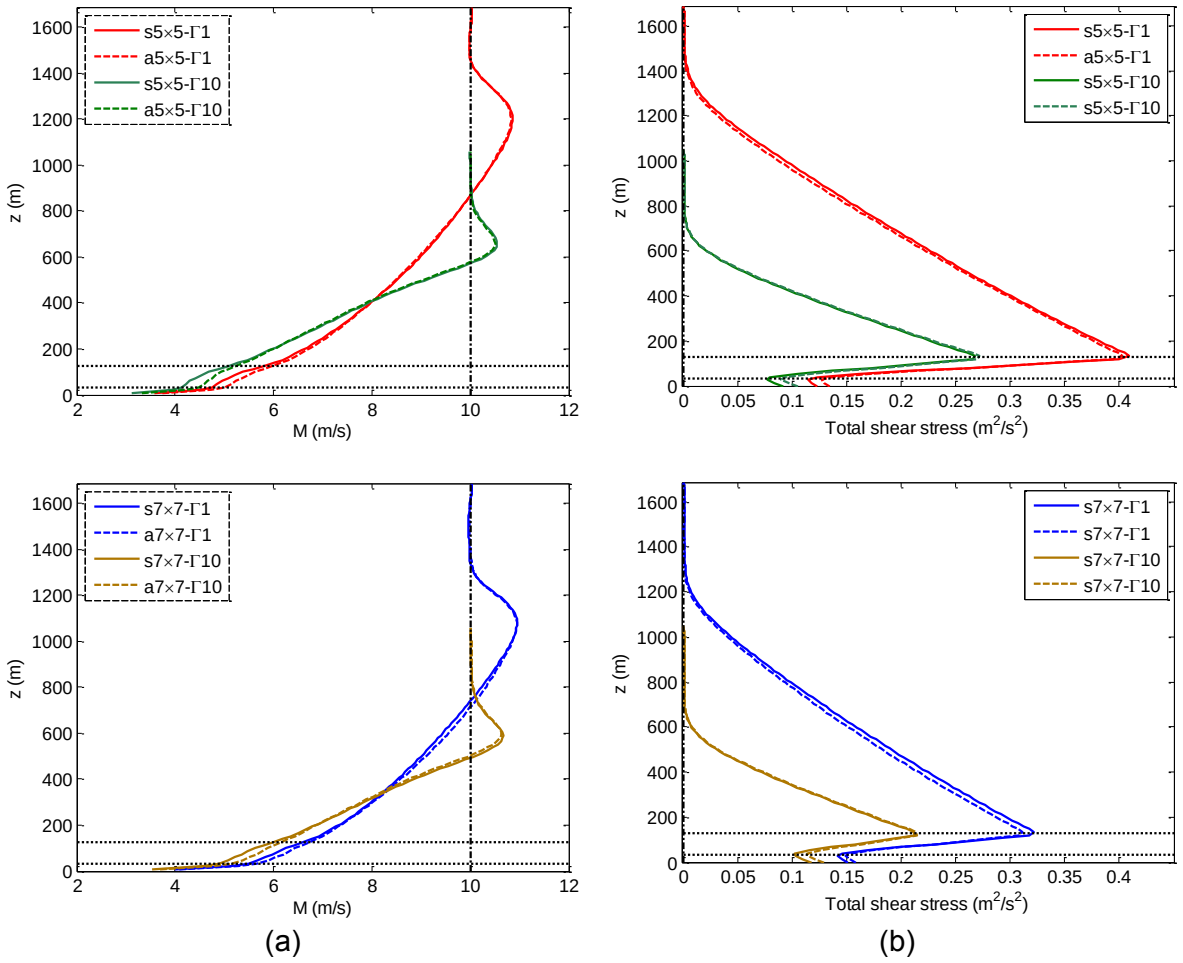

Figure 4: Vertical profile of (a) horizontally-averaged velocity magnitude M, and (b) total shear stress for two different values of Γ and two different layouts.

Fig. 5 displays the contour plots of mean and instantaneous streamwise velocity (at the hub-height level) for the aligned and staggered layout for $s = 7$. As shown in this figure, in aligned farms, the presence of high-speed "channels" between the turbine rows and low-speed regions along the turbine axes is clear. In contrast, in the staggered farm, the flow is more uniform in the spanwise direction and no high-speed channels are clearly visible. Similar flow pattern has been shown by Meyer and Meneveau [38], Markfort *et al*. [39] and Wu and Porté-Agel [24]. In addition, in the staggered farms, the turbine wakes have a longer distance to recover before the next downwind turbine, which results in a higher velocity at the turbines and, consequently, larger power output compared with the aligned counterparts. For this reason, although the power extracted by the staggered farms is higher compared with the aligned ones, the horizontally-averaged velocity is lower for the staggered cases (see fig. 4a).

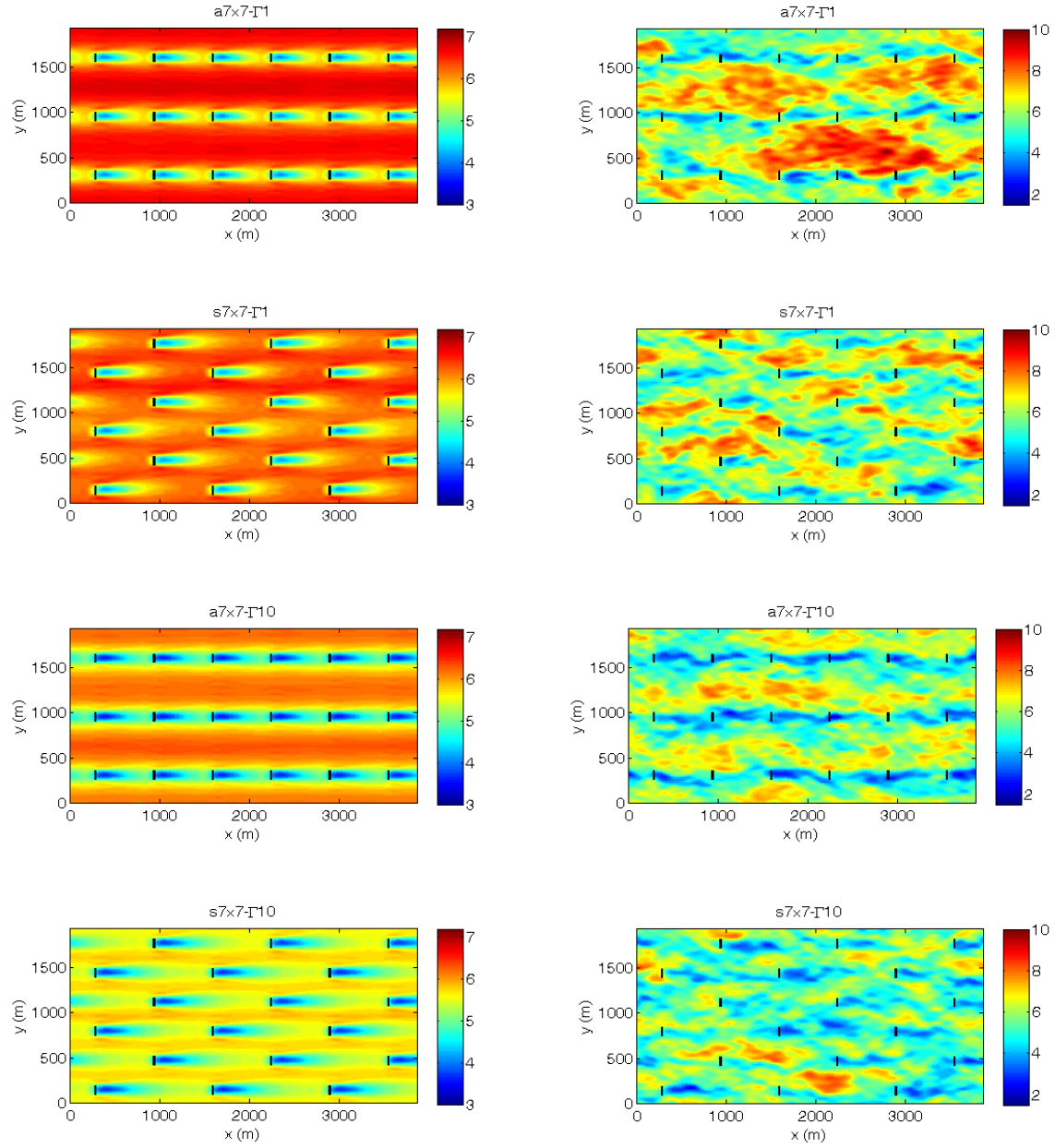

Figure 5: Contour of mean (left) and instantaneous (right) streamwise velocity (m/s) at the hub-height level for $s = 7$. Only a section of the domain is shown.

4. Mean kinetic energy budgets

In this study, the LES framework is also used to investigate the effect of free-atmosphere stability on all the terms in the budgets of mean kinetic energy inside and above infinite-size wind farms. This study can provide valuable insights to have better understanding about the relative significance of various physical processes that govern turbulent motions. By performing a time- and horizontal averaging on equation (1), one can have:

$$\frac{\partial\langle\bar{\tilde{u}}_i\rangle}{\partial t} + \langle\bar{\tilde{u}}_j\rangle\frac{\partial\langle\bar{\tilde{u}}_i\rangle}{\partial x_j} = -\frac{\partial\langle\bar{\tilde{p}}^*\rangle}{\partial x_i} + f_c\varepsilon_{ijk}\langle\bar{\tilde{u}}_j\rangle - \frac{\partial}{\partial x_j}\left(\langle\bar{\tau}_{ij}^d\rangle + \langle\overline{\tilde{u}_i''\tilde{u}_j''}\rangle\right) + \langle\bar{\mathcal{F}}_i\rangle \ , \tag{3}$$

where $\tilde{u}_i'' = \tilde{u}_i - \langle\bar{\tilde{u}}_i\rangle$, overbar and angle brackets denote temporal and horizontal averaging, respectively. The balance for the mean kinetic energy can be obtained by the product of equation (3) with $\langle\bar{\tilde{u}}_i\rangle$ as follows:

$$\frac{\partial\langle\bar{\tilde{K}}\rangle}{\partial t} + \langle\bar{\tilde{u}}_j\rangle\frac{\partial\langle\bar{\tilde{K}}\rangle}{\partial x_j} = W_G + T - P - W_t. \tag{4}$$

The terms in equation (4) are defined as follows:

$$\begin{gathered}\langle\bar{\tilde{K}}\rangle = \frac{1}{2}\langle\bar{\tilde{u}}_i\rangle\langle\bar{\tilde{u}}_i\rangle,\\ W_G = f_c.\left(-v_g\langle\bar{\tilde{u}}\rangle + u_g\langle\bar{\tilde{v}}\rangle\right),\\ T = \frac{\partial\Phi_j}{\partial x_j}, \quad \Phi_j = -\langle\bar{\tilde{u}}_i\rangle\left(\langle\bar{\tau}_{ij}^d\rangle + \langle\overline{\tilde{u}_i''\tilde{u}_j''}\rangle\right),\\ P = -\left(\langle\bar{\tau}_{ij}^d\rangle + \langle\overline{\tilde{u}_i''\tilde{u}_j''}\rangle\right)\frac{\partial\langle\bar{\tilde{u}}_i\rangle}{\partial x_j},\\ W_t = -\langle\bar{\tilde{u}}_i\rangle\langle\bar{\mathcal{F}}_i\rangle,\end{gathered} \tag{5}$$

where $\langle\bar{\tilde{K}}\rangle$ represents the kinetic energy of the mean flow, W_G is the work done on the boundary layer in maintaining the pressure gradient [5], u_g and v_g are the geostrophic wind components in streamwise and spanwise direction, respectively, T denotes the transport of the kinetic energy by turbulence, Φ_j is the total flux of kinetic energy in j direction, P is the production of turbulent kinetic energy and W_t is the work done by the turbines. In a fully-developed wind-farm ABL flow, equation (4) reduces to:

$$0 = W_G + T - P - W_t \tag{6}$$

where $W_G = f_c.\left(-v_g\langle\bar{\tilde{u}}\rangle + u_g\langle\bar{\tilde{v}}\rangle\right)$, $T = \frac{\partial\Phi_z}{\partial z}$, $\Phi_z = -\left[\langle\bar{\tilde{u}}\rangle\left(\langle\bar{\tau}_{xz}^d\rangle + \langle\overline{\tilde{u}''\tilde{w}''}\rangle\right) + \langle\bar{\tilde{v}}\rangle\left(\langle\bar{\tau}_{yz}^d\rangle + \langle\overline{\tilde{v}''\tilde{w}''}\rangle\right)\right]$, $P = -\left[\left(\langle\bar{\tau}_{xz}^d\rangle + \langle\overline{\tilde{u}''\tilde{w}''}\rangle\right)\frac{\partial\langle\bar{\tilde{u}}\rangle}{\partial z} + \left(\langle\bar{\tau}_{yz}^d\rangle + \langle\overline{\tilde{v}''\tilde{w}''}\rangle\right)\frac{\partial\langle\bar{\tilde{v}}\rangle}{\partial z}\right]$, and $W_t = -\left(\langle\bar{\tilde{u}}\rangle\langle\bar{\mathcal{F}}_x\rangle + \langle\bar{\tilde{v}}\rangle\langle\bar{\mathcal{F}}_y\rangle\right)$.

Fig. 6 shows the effect of free-atmosphere stability on the mean kinetic energy budgets in the absence of wind turbines. It is observed that the thermal stratification in the free atmosphere reduces the entrainment of kinetic energy from the flow above, leads to lower boundary layer depth.

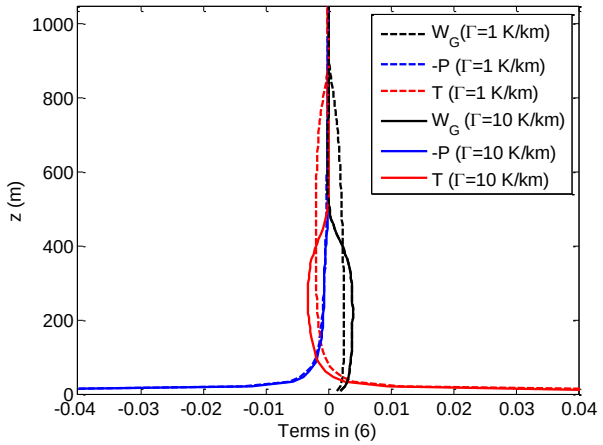

Figure 6: Mean kinetic energy budgets (m^2/s^3) for two different values for Γ.

The mean kinetic energy budget terms in Equation (6) for very large wind farms are displayed in fig. 7. It is observed that, with the presence of wind turbines, the work done by the pressure gradient increases due to in the growth of the boundary-layer depth. As mentioned before, in very large wind farms, the extracted energy by the turbines must be entrained from the external environment. For a

given surface cover, by decreasing the static stability of the free atmosphere higher amount of kinetic energy can be entrained from the external environment, leads to higher power output from the turbines. In addition, it is observed that the turbulent production has a peak at the turbine-top level, which is consistent with the fact that the peak shear stress also happens at this level, but its value near the surface decreases compared with no-farm case. This effect is also consistent with the observed trend in fig. 3 where the surface shear stress has lower value compared with the surface shear stress in the absence of the turbines. The influence of free-atmosphere stability on the reduction of kinetic energy entrainment and, consequently, the work done by the turbines is clear in this figure.

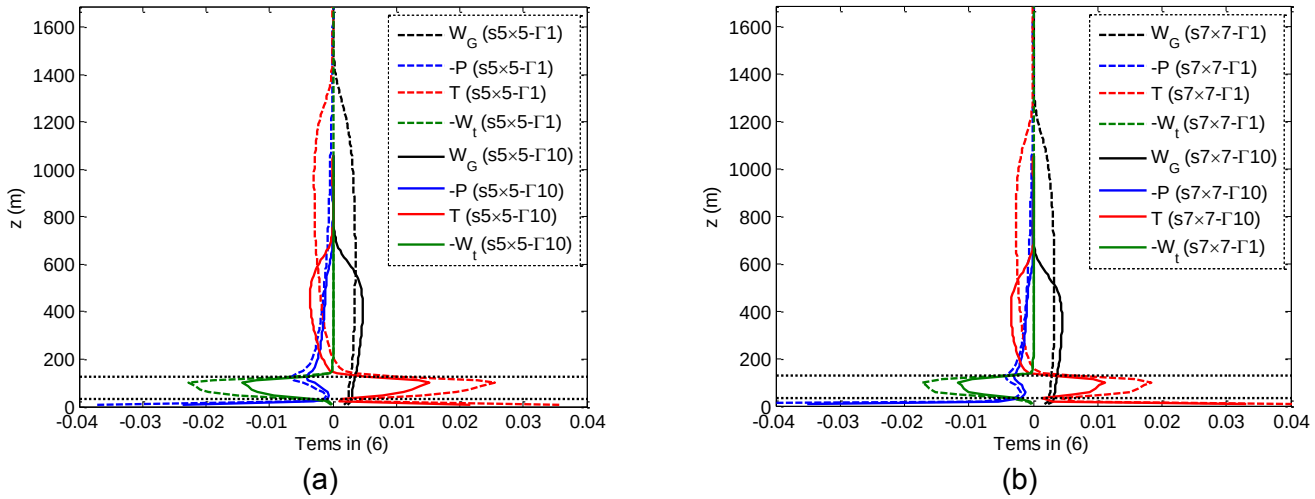

Figure 7: Mean kinetic energy budgets (m^2/s^3) for two different values of Γ: a) s = 5 and b) s = 7.

Fig. 8 shows the total flux of kinetic energy inside the ABL. It is observed that the turbulent energy flux has a peak at the turbine-top level and its value increases with decreasing the stratification in the free atmosphere. This figure shows that how the energy is transported from the flow above the turbine-top level to below that level. Applying the plane-averaged kinetic energy balance between the top-tip and the bottom-tip heights shows that more kinetic energy can be entrained from the flow above when the potential temperature lapse rate decreases, leading to higher power production by the farm.

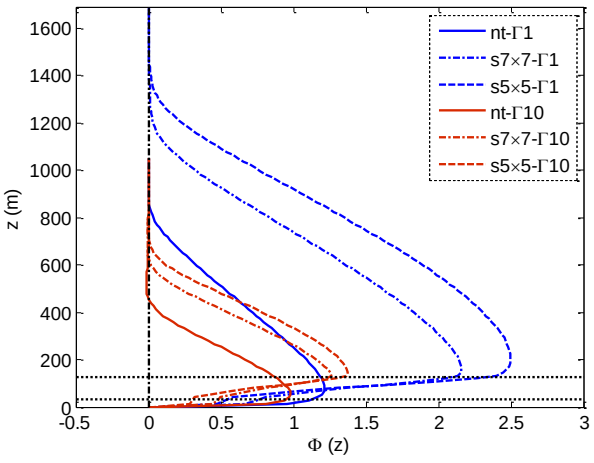

Figure 8: Vertical profile of turbulent energy flux (Φ_z) (m^3/s^3) inside the ABL.

5. Conclusion

The present work focuses on the influence of thermal stratification of the free atmosphere on the structure of ABL flow, as well as the power extracted by the wind turbines. A suite of large-eddy simulations of fully-developed wind-farm ABL flow has been performed including the effect of earth's rotation and free-atmosphere stability. In the simulations, tuning-free Lagrangian scale-dependent dynamic models [13] are used to model the subgrid-scale turbulent fluxes, while the turbine-induced forces are parameterized with the actuator disk model with rotation [14].

The large-eddy simulations performed in this study demonstrate that the presence of the turbines has a significant effect on the boundary-layer depth. In very large wind farms, the vertical energy transport associated with turbulence is the only source of kinetic energy. As a result, the kinetic energy must be entrained from the external environment, leading to an increase in the ABL height. On the other hand, the results presented here indicate that the thermal stratification of the free atmosphere reduces the growth of the boundary-layer height, leading to lower kinetic energy entrainment from the flow above and, consequently, lower power production by the turbines. In particular, for the wind-turbine arrangements considered in the present study, the power output from the wind farms is reduced by about 35 percent when the potential temperature lapse rate in the free atmosphere increases from 1 to 10 K/km.

Future research will focus on developing a similar model to include the effect of surface buoyancy fluxes in stable and convective boundary layers on the power production in large wind farms. Furthermore, the LES framework will also be used to investigate the effect of free-atmosphere stability on all the terms in the budgets of mean and turbulent kinetic energy inside and above infinite as well as finite-size wind farms.

Acknowledgments. This research was supported by the Swiss National Science Foundation (grant 200021-132122). Computing resources were provided by the Minnesota Supercomputing Institute (MSI) and the Swiss National Supercomputing Center (CSCS) under project ID s306.

References and Notes

[1] S. Frandsen, "On the wind speed reduction in the center of large clusters of wind turbines", J. Wind Eng. Ind. Aerodyn., vol. 39 (1992) pp. 251–265.
[2] M. Calaf, C. Meneveau, J. Meyers, "Large eddy simulation study of fully developed wind turbine array boundary layers", Phys. Fluids, vol. 22(2010) p. 015110.
[3] C. Meneveau, "The top-down model of wind farm boundary layers and its applications", J. Turbul., vol. 13 (2012) N7.
[4] H. Lu, F. Porté-Agel, "Large-eddy simulation of a very large wind farm in a stable atmospheric boundary layer", Phys. Fluids, vol. 23 (2011) p. 065101.
[5] R. Johnstone, G.N. Coleman, "The turbulent Ekman boundary layer over an infinite wind-turbine array", J.Wind Eng. Ind. Aerodyn., vol. 100 (2012) pp. 46-57.
[6] S. Zilitinkevich, I. Esau, A. Baklanov, "Further comments on the equilibrium height of neutral and stable planetary boundary layers", Q. J. R. Meteorol. Soc., vol. 133 (2007) pp. 265-271.
[7] S. Zilitinkevich, A. Baklanov, J. Rost, A. Smedman, V. Lykosov, P. Calanca, "Diagnostic and prognostic equations for the depth of the stably stratified Ekman boundary layer", Q. J. R. Meteorol. Soc., vol. 128 (2002) pp. 25-46.
[8] S. Zilitinkevich, I. Esau, "On integral measures of the neutral, barotropic planetary boundary layers", Bound. Layer Meteorol., vol. 104 (2002) pp. 371-379.
[9] I. Esau, "Parameterization of a surface drag coefficient in conventionally neutral planetary boundary layer", Annales Geophysicae, vol. 22 (2004) pp. 3353-3362.
[10] J. Taylor, S. Sarkar, V. Armenio, "Large eddy simulation of stably stratified open channel flow", Phys. Fluids, vol. 17 (2005), p. 116602.
[11] J. Taylor, S. Sarkar, "Direct and large eddy simulations of a bottom Ekman layer under an external stratification", Int. J. Heat and Fluid Flow, vol. 29 (2008) pp. 721-732.

[12] Z. Sorbjan, “Effects Caused by Varying the Strength of the Capping Inversion Based on a Large Eddy Simulation Model of the Shear-Free Convective Boundary Layer”, J. Atmos. Sci., vol. 53 (1996) pp. 2015-2024.
[13] R. Stoll, F. Porté-Agel, “Dynamic subgrid-scale models for momentum and scalar fluxes in large-eddy simulations of neutrally stratified atmospheric boundary layers over heterogeneous terrain”, Water Resour. Res., vol. 42 (2006) W01409.
[14] Y.-T. Wu, F. Porté-Agel, “LES of wind-turbine wakes: Evaluation of turbine parameterizations”, Bound. Layer Meteorol., vol. 138 (2011) pp. 345-366.
[15] J. Smagorinsky, “General circulation experiments with the primitive equations: I. The basic experiment”, Mon Weather Rev., vol. 91 (1963) pp. 99-164.
[16] M. Germano, U. Piomelli, P. Moin, “A dynamic subgrid-scale eddy viscosity model”, Phys. Fluids, vol. 7 (1991) pp. 1760-1765.
[17] P. Moin, K.D. Squires, S. Lee, “A dynamic subgrid-scale model for compressible turbulence and scalar transport”, Phys. Fluids, vol. 3 (1991) p. 2746.
[18] F. Porté-Agel, C. Meneveau, M.B. Parlange, “A scale-dependent dynamic model for large-eddy simulation: Application to a neutral atmospheric boundary layer”, J. Fluid Mech., vol. 415 (2000) pp. 261-284.
[19] F. Porté-Agel, “A scale-dependent dynamic model for scalar transport in large-eddy simulations of the atmospheric boundary layer”, Bound. Layer Meteorol., vol. 112 (2004) p. 81.
[20] R. Stoll, F. Porté-Agel, “Surface heterogeneity effects on regional-scale fluxes in stable boundary layers: surface temperature transitions”, J. Atmos. Sci., vol. 66 (2008) pp. 412-431.
[21] R. Stoll, F. Porté-Agel, “Large-eddy simulation of the stable atmospheric boundary layer using dynamic models with different averaging schemes”, Bound. Layer Meteorol., vol. 126 (2008) p.1.
[22] F. Wan, F. Porté-Agel, R. Stoll, “Evaluation of dynamic subgrid-scale models in large-eddy simulations of neutral turbulent flow over a two dimensional sinusoidal hill”, Atmos. Environ., vol. 41 (2007) pp. 2719-2728.
[23] F. Wan, F. Porté-Agel, “Large-eddy simulation of stably-stratified flow over a steep hill”, Bound. Layer Meteorol., vol. 138 (2011) pp. 367-384.
[24] Y.-T. Wu, F. Porté-Agel, “Simulation of Turbulent Flow Inside and Above Wind Farms: Model Validation and Layout Effects”, Bound. Layer Meteorol., vol. 146 (2013) pp. 181-205.
[25] F. Porté-Agel, Y.-T. Wu, H. Lu, “Conzemius, R.J. Large-eddy simulation of atmospheric boundary layer flow through wind turbines and wind farms”, J. Wind Eng. Ind. Aerodyn., vol. 99 (2011) pp. 154-168.
[26] J.D. Albertson, M.B. Parlange, “Natural integration of scalar fluxes from complex terrain”, Adv. Water Resour., vol. 23 (1999) p. 239.
[27] S.A. Orszag, “Transform method for calculation of vector coupled sums: Application to the spectral form of the vorticity equation”, J. Atmos. Sci., vol. 27 (1970) pp. 890-895.
[28] C. Canuto, M.Y. Hussaini, A. Quarteroni, T.A. Zang, “Spectral Methods in Fluid Dynamics”, Springer, 1988.
[29] A. Monin, M. Obukhov, “Basic laws of turbulent mixing in the ground layer of the atmosphere”, Trans. Geophys. Inst. Akad.Nauk., vol. 151 (1954) pp. 163-187.
[30] I. Marusic, G.J. Kunkel, F. Porté -Agel, “Experimental study of wall boundary conditions for large-eddy simulation”, J. Fluid. Mech., vol. 446 (2001) pp. 309-320.
[31] M. Abkar, F. Porté-Agel, “A new boundary condition for large-eddy simulation of boundary-layer flow over surface roughness transitions”, J. Turbul., vol. 13 (2012) pp. 1-18.
[32] C.G. Rossby, R.B. Montgomery, “The Layers of frictional influence in wind and ocean currents”, Phys. Oceanogr. Meteorol., vol. 3 (1935) pp. 1-101.
[33] S. Zilitinkevich, I. Esau, “The effect of baroclinicity on the depth of neutral and stable planetary boundary layers”, Q. J. R. Meteorol. Soc., vol. 129 (2003) pp. 3339-3356.
[34] A.K. Blackadar, “The vertical distribution of wind and turbulent exchange in a neutral atmosphere”, J. Geophys. Res., vol. 67 (1962) pp. 3095-3102.

[35] T. Holt, S. Raman, “A review and comparative evaluation of multilevel boundary layer parameterizations for first-order and turbulent kinetic energy closure schemes”, Rev. Geophys., vol. 26 (1988) pp. 761-780.
[36] P.J. Mason, D.J. Thompson, “Stochastic backscatter in large-eddy simulations of boundary layers”, J. Fluid Mech., vol. 242 (1992) pp. 51-78.
[37] S. Zilitinkevich, V. Perov, J. King, “Near-surface turbulent fluxes in stable stratification: Calculation for use in general circulation models”, Q. J. R. Meteorol. Soc., vol. 128 (2002) pp. 1571-1587.
[38] J. Meyers, C. Meneveau, “Large eddy simulations of large wind-turbine arrays in the atmospheric boundary layer”, In 48th AIAA Aerospace Sciences Meeting Including the New Horizons Forum and Aerospace Exposition, Orlando, Florida (2010), Art no. AIAA2010-827.
[39] C.D. Markfort, W. Zhang, F. Porté-Agel, “Turbulent flow and scalar transport through and over aligned and staggered wind farms”, J. Turbul., vol. 13 (2012) N33.

Effect of turbine alignment on the average power output of wind-farms

Richard J. A. M. Stevens[1,2], **Dennice F. Gayme**[1] **and Charles Meneveau**[1]
[1]Dept. of Mech. Engineering, Johns Hopkins University, Baltimore, Maryland 21218, USA
[2]Dept. of Physics, Mesa+ Institute, and J. M. Burgers Centre for Fluid Dynamics, University of Twente, 7500 AE Enschede, The Netherlands

Abstract

Using Large Eddy Simulation (LES), we investigate the influence of the alignment of successive turbine rows on the average power output of a finite length wind-farm with a stream-wise spacing between the turbines of $S_x = 7.85D$ and a span-wise spacing of $S_y = 5.23D$, where D is the turbine diameter. Different turbine alignments affect the extent to which wakes from upstream turbines interact with downstream turbines. We consider 13 turbine rows in the stream-wise direction and change the layout of the wind-farm by adjusting the angle $\psi = \arctan \frac{S_{dy}}{S_x}$ with respect to the incoming flow direction, where S_{dy} indicates the span-wise offset from one turbine row to the next. For the case considered here, $\psi = 0$ degrees corresponds to an aligned wind-farm, while a perfectly staggered configuration occurs at $\psi = \arctan[(5.23D/2)/7.85D] = 18.43$ degrees. We simulate the interaction between each wind-farm and the atmospheric boundary layer using a LES that uses a newly developed concurrent-precursor inflow method. For an aligned configuration we observe a nearly constant average turbine power output for the second and subsequent turbine rows, which is about 60% of the average power produced by the turbines in the first row. With increasing ψ the power loss in subsequent turbine rows is more gradual. We find that the highest average power output is not obtained for a staggered wind-farm ($\psi = 18.43$ degrees), but for an intermediate alignment of around $\psi = 12$ degrees. Such an intermediate alignment allows more turbines to be outside the wake of upstream turbines than in the staggered configuration in which turbines are directly in the wake of turbines placed two rows upstream.

Introduction

At the end of 2011 almost 3% of global electricity demand came from wind power (1) and various scenarios (2; 3) aim for this contribution to increase to 20% by 2030. Several countries have already achieved a relatively high usage of wind power in 2011, such as 26% in Denmark, and 16% in Portugal and Spain (4). To realize the worldwide targets for wind power production large wind-farms will be required.

The problem can be approached at many different spatial and temporal scales. From the perspective of atmospheric dynamics on large regional or global scales wind turbine arrays are often modeled as surface roughness elements or net drag coefficient. This parameterization leads to an increased roughness length that needs to be parameterized. This approach is useful,

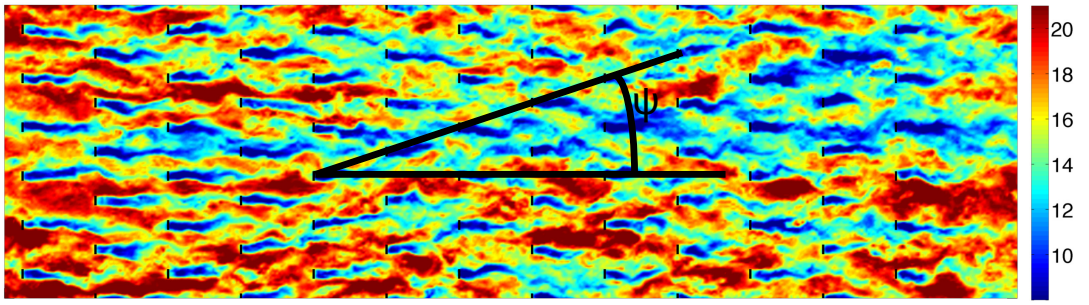

Figure 1: Snapshot of the stream-wise velocity at hub-height in a staggered wind-farm in which the stream-wise distance between the turbines is $S_x = 7.85D$ and the span-wise distance is $S_y = 5.23D$. The wind-farm layout is parameterized by the angle $\psi = \arctan \frac{S_{dy}}{S_x}$ with respect to the incoming flow direction, where S_{dy} indicates the span-wise displacement and S_x is the stream-wise distance between the subsequent rows, indicates the wind-farm layout. The color scale indicates u/u^*, the stream-wise wind velocity in units of friction velocity.

among others, in simulations in which the effect of large wind-farms at regional and global scales is considered. Examples are studies that aim to predict the effect of large wind turbine farms on the global climate (5; 6), regional meteorology (7), or short time weather patterns (8; 9). In such simulations, the horizontal computational resolution near the ground is often significantly coarser than the height of the Atmospheric Boundary Layer (ABL) and therefore insufficient to study the physical mechanisms that are important in large wind-farms. RANS (Reynolds-averaged Navier-Stokes) simulations have traditionally been the main tool to model large wind-parks (10; 11), but recently Large Eddy Simulations (LES) of the interaction between wind turbines and the turbulent ABL have become available (10).

There are several LES studies that model the interaction between one or two turbines and the ABL (12; 13; 14; 15; 16; 17; 18; 19; 20). However, only a limited number of LES have focused on large wind turbine parks. Ivanell (21) performed LES of two of the ten rows of the Horns Rev farm in Denmark and assumed periodic conditions in the span-wise direction to approximate the full plant aerodynamics. That work employed a power law profile for the mean wind inflow condition and a plane of fluctuating body forces parallel to and near the upstream boundary to create turbulence. In that study the wind inflow angle was varied by $\pm 15^\circ$ with respect to the alignment of the turbine rows. Churchfield et al. (22; 23; 24) used LES to model the Lillgrund wind-farm plant using a precursor simulation of an ABL to generate the turbulent inflow condition. The time-averaged power production of the turbines for their simulation of a wind-farm with aligned rows agrees well with field observations up to the sixth turbine row. Meyers and Meneveau (25) and Calaf et al. (26; 27) performed LES in a horizontally periodic domain in order to study infinitely long wind-farms. They looked at the effect of the spacing between the wind turbines on the total average power output and the scalar transport. Their results showed that in infinite wind-farms the total average power output is mainly determined by the vertical fluxes of kinetic energy in the wind-farm, which was confirmed in the wind tunnel experiments of Cal et al. (28). Later Yang et al. (29) showed that in infinite aligned wind-farms the stream-wise spacing has a stronger influence on the average power output than the span-wise

spacing. Wu and Porté-Agel's (30; 31) simulations of finite length wind-farms demonstrated that when successive turbine rows are staggered (i.e. turbines are aligned with those two rows ahead of them) the relatively longer separation between consecutive downwind turbines allows the wakes to recover more, thus exposing the turbines to higher local wind speeds and lower turbulence intensity levels compared to an aligned farm. Just as Churchfield et al. (22; 23; 24) they used a separate precursor simulation to obtain the turbulent inflow conditions.

Method

Here we discuss the influence of turbine alignment on the average power output of wind turbines in a finite length wind-farm in which the stream-wise distance between the turbines is $S_x = 7.85D$ and the span-wise spacing is $S_y = 5.23D$, where D is the turbine diameter. The diameter and hub-height of the considered turbines is 100m. The domain size we use is 12.57 km x 3.14 km x 2 km in the stream-wise, span-wise and vertical direction and we use a roughness height of $5 \times 10^{-5} L_z$ (where $L_z = 2km$ is the domain height) and a computational grid with $1024 \times 128 \times 256$ computational points. We consider a wind-farm with 13 turbine rows in the stream-wise direction and 6 turbines in the span-wise direction. We change the wind-farm layout by adjusting the angle $\psi = \arctan \frac{S_{dy}}{S_x}$ with respect to the incoming flow direction, where S_{dy} indicates the span-wise displacement of subsequent downstream turbine rows, as illustrated in figure 1. For the configuration specified above $\psi = 0$ degrees corresponds to an aligned wind-farm, while $\psi = \arctan[(5.23D/2)/7.85D] = 18.43$ degrees corresponds to a staggered on. In all of the studies considered herein, the area covered by our wind-farm remains constant, and we look at the influence of the layout of the wind-farm on the average power production.

We simulate the different finite length wind-farms with a recently developed concurrent-precursor method (32). This method considers two interacting computational domains simultaneously, i.e. in one domain a turbulent ABL is simulated in order to generate the turbulent inflow conditions for a second domain in which wind turbines are placed. In each domain we consider a neutral ABL and solve the filtered incompressible Navier-Stokes (NS) equations together with the continuity equation. This means that stratification effects and changes in the wind direction over time are not included. The dynamic Lagrangian scale-dependent Smagorinsky model is used to calculate the subgrid-scale stresses (33). In our code the skew-symmetric form of the NS equation is implemented, which uses a spectral discretization in the horizontal directions and a second-order finite differencing scheme in the vertical direction. A second-order accurate Adams-Bashforth scheme is used for the time integration. The top boundary uses zero vertical velocity and a zero shear stress boundary condition. At the bottom surface a classic imposed wall stress boundary condition relates the wall stress to the velocity at the first grid point and in the span-wise direction we use periodic boundary conditions. The turbines are modeled using an area average actuator disk method (12; 26; 27; 32).

In the remainder of this paper we first compare the current LES results with field measurements from Horns Rev and other model results, and then discuss the influence of the alignment of the turbine rows on the average power production of the wind-farm.

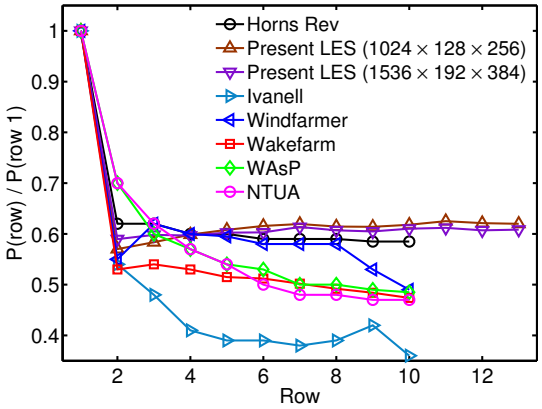

Figure 2: Comparison of the average power output as function of the downstream position between field measurements in Horns Rev, our LES, LES results from Ivanell (21), and several models. Adapted from figure 5 of Ref. (10). Note that the Wakefarm model results have been updated based on Fig. 11.13 of Ref. (37).

Comparison with other data

To evaluate the quality of the LES used in the present work we compare the average power output as function of the stream-wise position downstream of the first turbine position with field measurements fro Horns Rev. The span-wise and stream-wise distance between the turbines used in this study are comparable to the ones used in Horns Rev (34), but not exactly the same. These differences could have some influence on the absolute values, but presumably not on the observed trends. Figure 2 shows that our LES results compare very well with the Horns Rev field measurements. In particular, one can see that our LES correctly captures the nearly constant average power output as function of the downstream position for the second and subsequent rows. Note that such a behavior was also observed in wind tunnel studies by Wu and Porté Agel (31) as well as in their LES results. The average power output in the fully developed regime (as will be seen later, for most cases we approach a fully developed regime in our LES near the 10^{th} row) is likely to have some dependence on the model parameters. It should be noted that there is some uncertainty in the field measurements taken in Horns Rev. (35; 34; 10), which show variations in the average power output in the fully developed regime on the order of 6%, with a standard deviation of about 15%. Nevertheless, the trend observed in the mean power output data, i.e. the almost constant average power for the second and subsequent downstream, is similar in all reported measurements for aligned wind conditions and is well predicted by our LES.

This nearly constant average power as function of the down stream position is due to the complex interaction between the turbines and the ABL. The average power output of downstream turbines is mainly determined by the wake recovery, which depends on the vertical kinetic energy flux that is created by the turbine wakes. In order to capture this large scale phenomenon one needs to accurately model the properties of the ABL and our LES seem to capture these

processes well. Figure 2 shows some differences between the LES of Ivanell (21), who only simulated the two central columns, and the Horns Rev measurements. In Ref. (21), this effect is attributed to the sensitivity of the downstream average power production to the alignment of the wind with respect to the turbines and it is pointed out that there is a significant uncertainty in this alignment in the measurement data. However, they also use a different subgrid scale model and method to generate the turbulent inflow condition than we do in our simulations and this could also account for some of the observed differences.

A number of engineering models have also been proposed to capture the wake effects in large scale wind-farms. A comparison of different studies along with the Horns Rev data is presented in figure 5 of Sanderse et al. (10) and figure 6 of Ref. (36) and this information is also presented in figure 2 together with updated results from Ref. (37). A description of the main features of the models is given by Barthelmie et al. (34). The models vary in the level of detail (complexity) but in general they use some empirical relation for the interacting wakes and/or solve some form of the RANS equations with a $k-\varepsilon$ turbulence closure scheme. It is worth noting that considering the inherent uncertainties in experimental data the agreement between these engineering models and the field measurements is reasonably good. Averaging over wider wind angles significantly improves the results obtained by the models, for example the the Farmflow model shows excellent agreement with Horns Rev data when the wind directions are averaged over 255 to 285 degrees (37). Barthelmie et al. (34), who presented the comparison of these models with the Horns Rev data, mention that although standard models perform adequately for the prediction of wakes in small wind-farms the models seem to have difficulties in predicting the behavior in large multi-row wind-farms when standard parameters are used. They indicate that the interaction of turbulence generated by wind turbines wakes with the overlying atmosphere could be the reason for this. These interactions can be modeled better with LES than by RANS models as LES are better able to predict the unsteady, anisotropic turbulent atmosphere. In addition, the concurrent precursor method we use to generate the turbulent inflow condition is able to capture the time-evolving streaky structures that are natural in an ABL, but difficult to include in synthetic models or in statically swept spatial fields, which is important to accurately model the interaction between the ABL and a wind-farm (32). Therefore we consider LES to be a good research tool to obtain insights about the physical processes that are important in very large wind-farms. We remark on two important assumptions of the present study: it considers only neutral atmospheric conditions (no stratification), and the overall inflow velocity direction is held constant in time. Under realistic conditions, additional meandering of the overall inflow direction would be expected to generate some smearing over results covering a range of angles ψ. In the remainder of this paper we will use LES to consider the effects of wind turbine layout on the average power production in a finite length wind-farm.

Results

We study the effect of the turbine alignment with respect to the incoming flow on the average power output by adjusting the angle ψ, shown in figure 1. Note that changing the wind-farm layout in this way makes sure that the land area that is covered as well as the total number of turbines remains constant. The average power output is evaluated according to $P = \langle -FU_d \rangle$, where $F = -\frac{1}{2}C_T'\rho U_d^2 A$ is the local force used in the actuator disk model. Here U_d is the disk

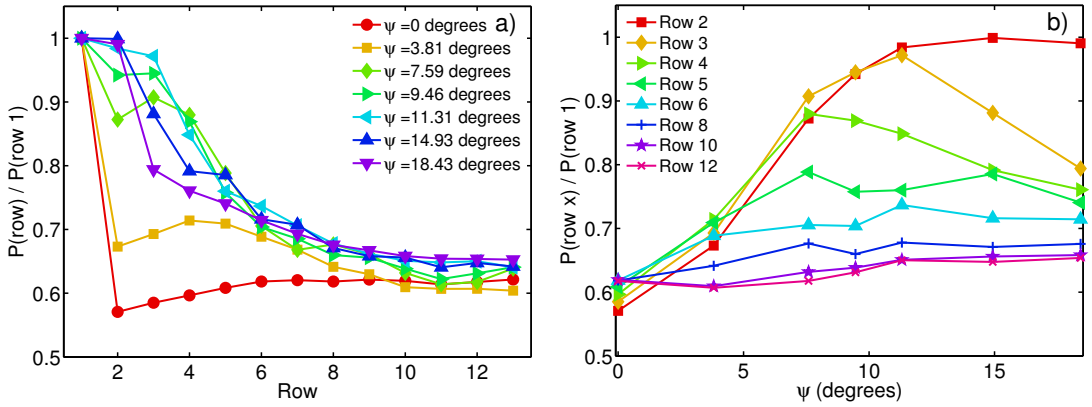

Figure 3: Panel a shows the average power output per turbine normalized by the average power output of turbines in the first row as function of the downstream position for different alignment angles ψ. Panel b shows the average power output in the different rows as function of the alignment angle ψ. Here $\psi = 0$ indicates that the turbines in the wind-farm are aligned and $\psi = 18.43$ corresponds to the fully staggered configuration

averaged velocity, $A = \pi D^2/4$ is the turbine rotor area, ρ is the density of the fluid, and $C_T^{'} = C_T/(1-a)^2$, where a is the axial induction factor. Using typical values $C_T = 4/3$ and $a = 1/4$ leads to $C_T^{'} = 4/3$ (26; 27; 38; 12; 39). Figure 3a shows the averaged normalized power output as function of the downstream position for the different alignments. This figure reveals that for an aligned wind-farm there is a very strong drop in the average power production at the second turbine row and then the average power output from each row remains nearly constant for subsequent downstream turbines. With increasing ψ the power loss in the first couple of rows is more gradual until we get to $\psi = 11.31$ degrees and then the slope begins to increase again. Thus, the staggered arrangement does not necessarily generate the highest average wind-farm power output.

In order to understand this effect it is helpful to look at the data in a different way. Figure 3b shows the normalized power output as function of the alignment angle ψ for the different turbine rows. For the second turbine row the figure reveals a significant power loss for the aligned or nearly aligned cases, while the average power output approaches the value of the first turbine row for the staggered configuration (18.43 degrees). It is important to note that an alignment angle of 11.31 degrees is already sufficient to make sure that the power production at the second row is not hindered by the wakes created by the turbines in the first row. Thus for a wind-farm with two turbine rows the power output will be the same for any alignment angles between 11.31 and $\psi = 18.43$ degrees. However, the alignment becomes much more important for longer wind-farms. The power output of the third turbine row as function of the alignment angle ψ reveals an optimum around $\psi \approx 11.31$ degrees. Interestingly the power output of the third turbine row is approximately equal to the power output of the second row when $0 < \psi \lesssim 11.31$ degrees, while the power output is significantly lower in the third row than at the second row when $\psi \gtrsim 11.31$ degrees.

In order to understand these observation we show the time-averaged stream-wise velocity

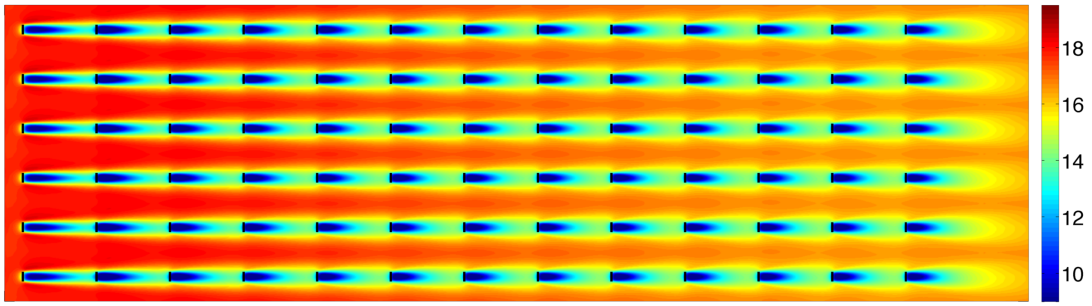

(a) 0 degrees (aligned)

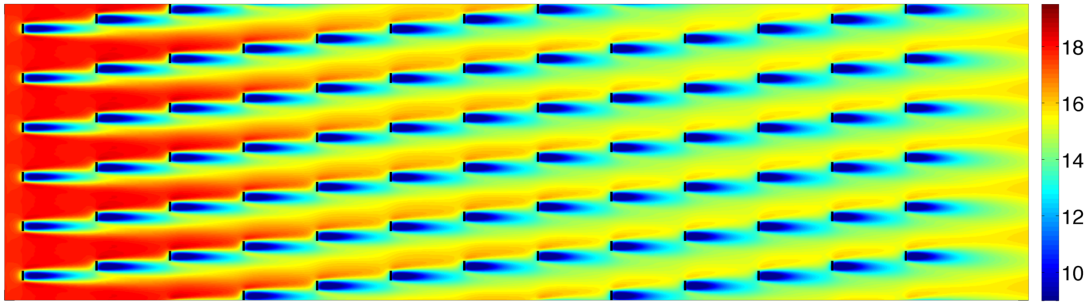

(b) 7.59 degrees (highest power output in fourth row)

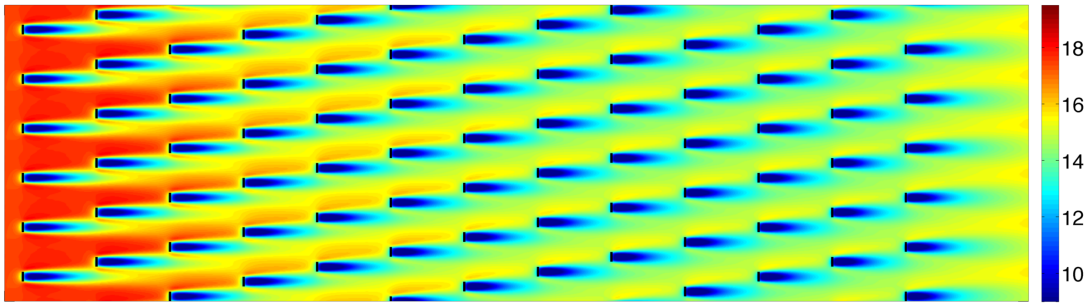

(c) 11.31 degrees (highest power output in third row)

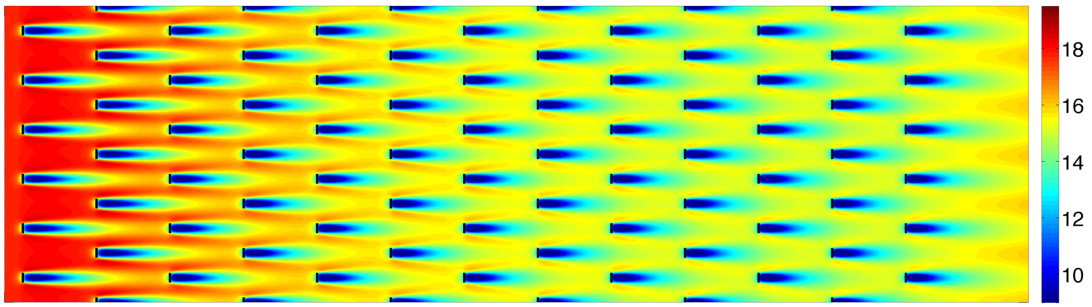

(d) 18.43 degrees (staggered)

Figure 4: The time-averaged stream-wise velocity at hub height for (a) $\psi = 0$ degrees (aligned) (b) $\psi = 7.59$ degrees (highest average power output in fourth row) (c) $\psi = 11.31$ degrees (highest average power output in the third row and for the entire wind-farm) and (d) $\psi = 18.43$ degrees (staggered). The color scale indicates u/u^*, the averaged stream-wise wind velocity in units of friction velocity.

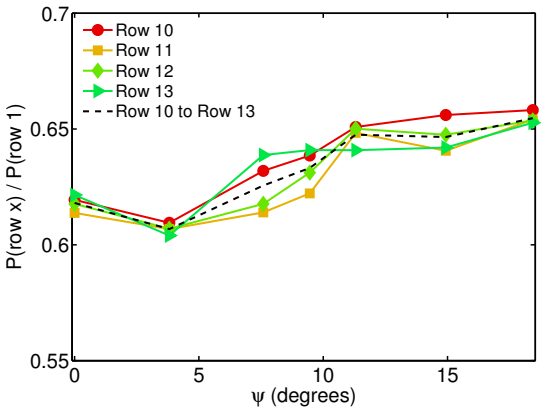

Figure 5: The normalized averaged turbine power output as function of the alignment angle ψ in the fully developed regime of the wind-farm.

at hub height for several cases in figure 4. As periodic boundary conditions in the span-wise direction are used all statistics are periodic in this direction. To improve the statistics we have therefore averaged the stream-wise velocity in $1/6^{th}$ of the original span-wise domain, i.e. the periodicity imposed by the turbines, and subsequently this averaged velocity profile is shown over the original span-wise domain (40). The figure reveals that for $\psi \lesssim 11.31$ degrees the turbines in the first three rows influenced only by the wakes created by turbines directly upstream. For the $\psi = 11.31$ degrees case, which gives the highest power output for turbines on the third row, one can see that both the turbines in the second and third row experience a nearly undisturbed inflow as the alignment angle ψ is sufficient to ensure that the wake of the upstream turbines do not influence them. For smaller alignment angles the turbines experience some negative effect of the expanding and meandering wakes of the upstream turbines. For $\psi \gtrsim 11.31$ the turbines in the third row are starting to encounter the wake created by the first turbine row and for the staggered configuration (18.43 degrees) the turbines in the third row are directly in the wake of those in the first turbine row, which limits the power production of these turbines.

Figure 3b reveals that the power output in the fourth turbine row is highest for an alignment angle of $\psi = 7.59$ degrees. Figure 4 shows that for $\psi = 11.31$ degrees the average power production in the fourth turbine row is limited due to the effect of the wake created by the first turbine row. With the more moderate $\psi = 7.59$ degrees the turbines in the fourth turbine row are not influenced by the wakes created by the turbines in the first row and only feel the meandering wake created by turbines in the third row. For further downstream turbine rows a small further reduction of the turbine power output is observed when $\psi > 0$ degrees. The reason is that the average kinetic energy that is available at hub height slowly decreases inside the wind-farm. Therefore the average wind speed that reaches the subsequent downstream turbines gradually decreases, as is seen in figure 4b and figure 4c, until the fully developed regime is reached. In this fully developed regime the vertical kinetic energy flux that is created by the turbine wakes supplies the power that is extracted by the turbines (26; 28) and the turbine power output seems nearly independent of the angle ψ, as seen in figure 3b. However, figure 5 shows that there are some small differences in this fully developed regime. This figure shows that the average power

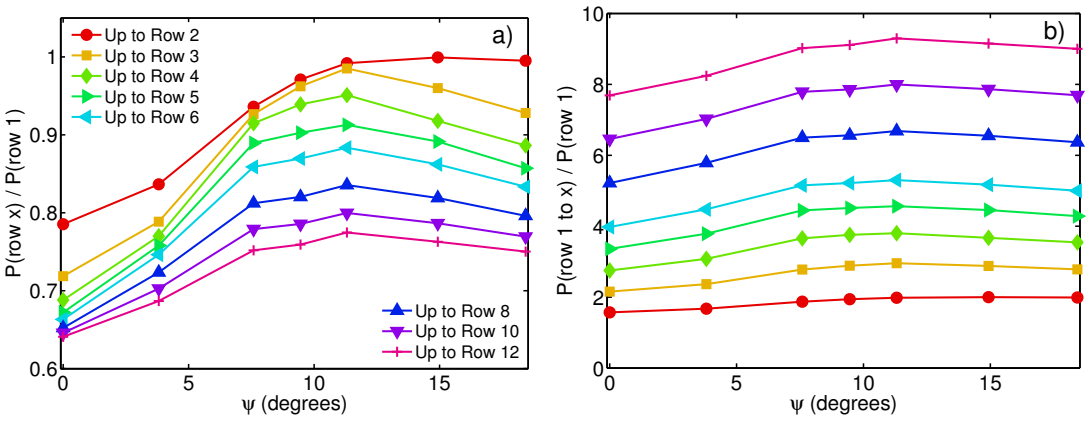

Figure 6: Panel a shows the average power output per turbine normalized by the average power output of turbines in the first row for different wind-farm lengths as function of the alignment angle ψ and panel b shows the total power output for different wind-farm lengths normalized by the power output of the first turbine row.

output is highest for the staggered case. As pointed out by Wu and Porté-Agel (31), this effect can be explained by the longer recovery length that is available for the wakes in the staggered case as compared to the aligned case.

So far we have seen that the highest power output that is found at a particular turbine row depends on the alignment. In particular, in the third row the highest power output is obtained with an alignment angle of $\psi = 11.31$ degrees, whereas the maximum occurs at $\psi = 7.59$ degrees in the fourth row, and in the fully developed regime for a staggered configuration ($\psi = 18.43$ degrees). Therefore one may wonder which wind-farm layout gives the highest power output for the whole wind-farm. Assuming that the power output of turbines is not influenced by downstream turbines we can calculate the average power output per turbine for different wind-farms lengths. Figure 6 shows the average power output per turbine normalized by the power produced by turbines on the first row for wind-farms ranging from 2 to 13 turbine rows as function of the alignment angle ψ. The highest average power output is obtained for the $\psi = 11.31$ degrees case. Figure 6a shows that for a wind-farm with 13 rows in the stream-wise direction the average turbine power output can range from approximately 60% up to about 75% of the power output of the first row. Figure 6b shows the corresponding total power output for different wind-farm lengths normalized by the power output of the first row.

Figure 7 shows the average power output per turbine for different wind-farm length normalized by the power output of an aligned wind-farm of the same length. It shows that the effect of the alignment is strongest for wind-farms with four turbine rows, where an increase in the power production of about 40% is observed for the $\psi = 11.31$ case with respect to the aligned case. For shorter wind-farms the relative increase is lower as a smaller percentage of wind turbines are affected by wake effects. For longer wind-farms the relative power output increase that can be obtained with respect to the aligned cases decreases as the power output in rows further downstream depends less on the orientation than in the first rows.

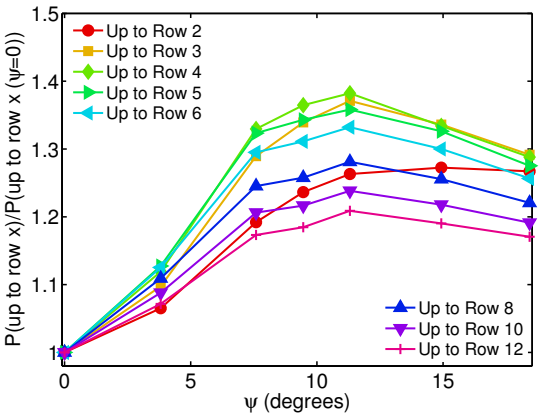

Figure 7: The averaged turbine power outputs for different wind-farm length normalized by the power output obtained by an aligned wind-farm of that length.

Conclusion

Here we discussed the use of Large Eddy Simulations (LES) to study finite length wind-farms. We have seen that the LES is capable of capturing the main trends observed in field experiments. The availability and flexibility of the simulations can therefore be exploited to study large wind-farms in more detail. We studied the effect of the wind-farm layout, parametrized by the alignment angle ψ with respect to the incoming flow, on the average power output of a wind-farm. With fixed land area our results show that under very specific circumstances and depending on the wind-farm length, the average power output of the wind-farm can reach values 40% higher than the power output of an aligned wind-farm. Interestingly the highest average power output is not necessarily obtained for a staggered wind-farm (18.43 degrees in this case), but for an intermediate angle of 11.31 degrees. It is important to stress that each of these results have been obtained using a single inflow direction. In realistic applications, one should average over different inflow directions, depending on the distribution of inflow angles. In future work we want to use the LES results to study the development of the vertical kinetic energy flux, which is crucial for the power production in the fully developed regime of the wind-farm (26) and want to compare the results with various engineering models.

Acknowledgements: This work is funded in part by the research program 'Fellowships for Young Energy Scientists' (YES!) of the Foundation for Fundamental Research on Matter (FOM) supported by the Netherlands Organization for Scientific Research (NWO), and in part by the US National Science Foundation, grants # CBET 1133800 and OISE 1243482. The computations have been performed on our local cluster and the LISA cluster of SARA in the Netherlands.

References

[1] Half-year report 2011. World Wind Energy Association. August 2011.

[2] Commission of the European Communities. *A European strategic energy technology plan - technology map*, 2007.

[3] U.S. Department of Energy. 20% *wind energy by 2030: increasing wind energy's contribution to U.S. electricity supply*, U.S. Department of Energy, 2008.

[4] Wind in Power, 2011 European statistics, The European wind energy association, February 2012.

[5] D. Keith, J. DeCarolis, D. Denkenberger, D. Lenschow, S. Malyshev, S. Pacala, and P. J. Rasch, *The influence of large-scale wind power on global climate*, Proc. Natl. Acad. Sci. U.S.A. **101**, 16115 (2004).

[6] C. Wang and R. G. Prinn, *Potential climatic impacts and reliability of very large-scale wind farms*, Atmos. Chem. Phys. **10**, 2053 (2010).

[7] S. Baidya-Roy, S. W. Pacala, and R. L. Walko, *Can large scale wind farms affect local meteorology?*, J. Geophys. Res. **109**, D19101 (2004).

[8] D. Barrie and D. Kirk-Davidoff, *Weather response to management of large wind turbine array*, Atmos. Chem. Phys. Discuss. **9**, 2917 (2009).

[9] L. Zhou, Y. Tian, S. Roy, C. Thorncroft, L. F. Bosart, and Y. Hu, *Impacts of wind farms on land surface temperature*, Nature Clim. Change **2**, 539 (2012).

[10] B. Sanderse, S. P. van der Pijl, and B. Koren, *Review of computational fluid dynamics for wind turbine wake aerodynamics*, Wind Energy **14**, 799 (2011).

[11] L. Vermeer, J. Sorensen, and A. Crespo, *Wind turbine wake aerodynamics*, Progress in Aerospace Sciences **39**, 467 (2003).

[12] A. Jimenez, A. Crespo, E. Migoya, and J. Garcia, *Large-eddy simulation of spectral coherence in a wind turbine wake*, Environ. Res. **3**, 015004 (2008).

[13] A. Jimenez, A. Crespo, and E. Migoya, *Application of a LES technique to characterize the wake deflection of a wind turbine in yaw*, Wind Energy **13**, 559 (2010).

[14] J.-O. Mo, A. Choudhry, M. Arjomandi, and Y. Lee, *Large eddy simulation of the wind turbine wake characteristics in the numerical wind tunnel model*, Journal of Wind Engineering and Industrial Aerodynamics **112**, 11 (2013).

[15] C. Li, S. Zhu, Y. Xu, and Y. Xiao, *2.5D large eddy simulation of vertical axis wind turbine in consideration of high angle of attack flow*, Renewable Energy **51**, 317 (2013).

[16] L. A. Martinez, S. Leonardi, M. Churchfield, and P. Moriarty, *A comparison of Actuator disk and actuator line wind turbine models and best practices for their use*, 50th AIAA Aerospace Sciences Meeting including the New Horizons Forum and Aerospace Exposition (2012).

[17] J. E. Cater, S. E. Norris, and R. C. Storey, *Comparison of Wind Turbine actuator methods using Large Eddy Simulation*, 18th Australasian Fluid Mechanics Conference Launceston, Australia 3-7 December 2012 (2012).

[18] N. Troldborg, J. Sorensen, and R. Mikkelsen, *Numerical simulations of wake characteristics of a wind turbine in uniform inflow*, Wind Energy **13**, 86 (2010).

[19] N. Troldborg, G. C. Larsen, H. A. Madsen, K. S. Hansen, J. N. Sorensen, and R. Mikkelsen,

Numerical simulations of wake interaction between two wind turbines at various inflow conditions, Wind Energy **14**, 859 (2011).

[20] R. C. Storey, S. E. Norris, K. A. Stol, and J. E. Cater, *Large eddy simulation of dynamically controlled wind turbines in an offshore environment*, Wind Energy **doi: 10.1002/we.1525**, (2012).

[21] S. Ivanell, Ph.D. thesis, Dept. of Mechanics, Gotland Univ., Stockholm, Sweden, 2010.

[22] M. J. Churchfield, S. Lee, P. J. Moriarty, L. A. Martinez, S. Leonardi, G. Vijayakumar, and J. G. Brasseur, *A Large-Eddy Simulation of Wind-Plant Aerodynamics*, 50th AIAA Aerospace Sciences Meeting including the New Horizons Forum and Aerospace Exposition AIAA 2012 (2012).

[23] M. J. Churchfield, S. Lee, J. Michalakes, and P. J. Moriarty, *A numerical study of the effects of atmospheric and wake turbulence on wind turbine dynamics*, Journal of Turbulence **13**, 132 (2012).

[24] S. Lee, M. Churchfield, P. Moriarty, J. Jonkman, and J. Michalakes, *Atmospheric and Wake Turbulence Impacts on Wind Turbine Fatigue Loadings*, 50th AIAA Aerospace Sciences Meeting AIAA 2012 (2012).

[25] J. Meyers and C. Meneveau, *Large eddy simulations of large wind-turbine arrays in the atmospheric boundary layer*, In 48th AIAA Aerospace Sciences Meeting Including the New Horizons Forum and Aerospace Exposition, Orlando, Florida Art. no. AIAA2010 (2010).

[26] M. Calaf, C. Meneveau, and J. Meyers, *Large eddy simulations of fully developed wind-turbine array boundary layers*, Phys. Fluids **22**, 015110 (2010).

[27] M. Calaf, M. B. Parlange, and C. Meneveau, *Large eddy simulation study of scalar transport in fully developed wind-turbine array boundary layers*, Phys. Fluids **23**, 126603 (2011).

[28] R. Cal, J. Lebrón, L. Castillo, H. Kang, and C. Meneveau, *Experimental study of the horizontally averaged flow structure in a model wind-turbine array boundary layer*, J. Renewable Sustainable Energy **2**, 013106 (2010).

[29] X. Yang, S. Kang, and F. Sotiropoulos, *Computational study and modeling of turbine spacing effects in infinite aligned wind farms*, Phys. Fluids **24**, 115107 (2012).

[30] Y.-T. Wu and F. Porté-Agel, *Large-Eddy Simulation of Wind-Turbine Wakes: Evaluation of Turbine Parametrisations*, Boundary-Layer Meteorol **138**, 345366 (2011).

[31] Y. T. W. and. F. Porté-Agel, *Simulation of Turbulent Flow Inside and Above Wind Farms: Model Validation and Layout Effects*, Boundary-Layer Meteorol **146**, 181 (2013).

[32] R. J. A. M. Stevens, J. Graham, and C. Meneveau, *A concurrent precursor inflow method for Large Eddy Simulations and applications to finite length wind farms*, submitted to Renewable Energy (2013).

[33] E. Bou-Zeid, C. Meneveau, and M. B. Parlange, *A scale-dependent Lagrangian dynamic model for large eddy simulation of complex turbulent flows*, Phys. Fluids **17**, 025105 (2005).

[34] R. J. Barthelmie, K. Hansen, S. T. Frandsen, O. Rathmann, J. G. Schepers, W. Schlez, J. Phillips, K. Rados, A. Zervos, E. S. Politis, and P. Chaviaropoulos, *Modelling and Measuring Flow and Wind Turbine Wakes in Large Wind Farms Offshore*, Wind Energy **12**, 431

(2009).

[35] R. Barthelmie, O. Rathmann, S. Frandsen, K. Hansen, E. Politis, J. Prospathopoulos, K. Rados, D. Cabezn, W. Schlez, J. Phillips, A. Neubert, J. Schepers, and S. van der Pijl, *Modelling and measurements of wakes in large wind farms*, Journal of Physics: Conference Series **75**, 012049 (2007).

[36] R. Barthelmie, S. Frandsen, O. Rathmann, K. Hansen, E. Politis, J. Prospathopoulos, J. Schepers, K. Rados, D. Cabezn, W. Schlez, A. Neubert, and M. Heath, *Measurement on a wind turbine wake: 3d effects and bluff body vortex shedding*, Report number Ris-R-1765(EN) (2011).

[37] J. G. Schepers, Ph.D. thesis, Delft University, 2012, doi:10.4233/uuid:92123c07-cc12-4945-973f-103bd744ec87

[38] J. Meyers and C. Meneveau, *Optimal turbine spacing in fully developed wind farm boundary layers*, Wind Energy **15**, 305317 (2011).

[39] T. Burton, D. Sharpe, N. Jenkins, and E. Bossanyi, *Wind Energy Handbook* (John Wiley & Sons, New York, 2001).

[40] R. J. A. M. Stevens, D. F. Gayme, and C. Meneveau, *Large Eddy Simulation studies of power output in large wind farms: effects of wind farm length and turbine placement*, to be submitted to J. Renewable Sustainable Energy (2013).

Optimization of Wind Farm Layout: A Refinement Method by Random Search

J. Feng, W.Z. Shen

Technical University of Denmark, Department of Wind Energy, DK-2800 Lyngby, Denmark

jufen@dtu.dk wzsh@dtu.dk

Abstract

Wind farm layout optimization is to find the optimal positions of wind turbines inside a wind farm, so as to maximize and/or minimize a single objective or multiple objectives, while satisfying certain constraints. Most of the works in the literature divide the wind farm into cells in which turbines can be placed, hence, simplifying the problem from with continuous variables to with discrete variables. In this paper, a refinement method, based on continuous formulation, by using random search is proposed to improve the optimization results based on discrete formulations. Two sets of optimization results of a widely studied test case are refined using the proposed method. One set of the results is from a published work using GA based on discrete formulation, the other set is the improved results using authors' own GA code. Steady improvements are obtained for both sets of results.

1. Introduction

Wind farm is a group of wind turbines located at a site to generate electricity, which is also called as "plant", "cluster", "array" and "park" in the literature. The world's first onshore wind farm was installed in 1980 on the shoulder of Crotched Mountain in southern New Hampshire, USA, with the capacity of 0.6 MW, consisting of 20 wind turbines rated at 30 kW each [1]. In 1991, the world's first offshore wind farm, Vindeby offshore wind farm was erected off the north coast of the Danish Island Lolland, which marked the beginning of offshore wind energy development. It had a total capacity of 4.95 MW and consisted of 11 Bonus 450 kW turbines [2]. Nowadays, the progress of technologies, such as power electronic [3], wind speed forecasting [4], coordinated control [5], together with the increased experience of wind farm construction and operation have enabled the development of modern wind farms, i.e., larger, smarter wind farms, which are typically consisted of hundreds of utility-scale (multi-MW sized) wind turbines and with a total capacity of hundreds MW. In parallel with this trend, the efforts for increasing the percentage of wind power of the total electricity consumption have led to the proliferation of modern wind farms.

Due to the multi-disciplinary nature and the evolution towards larger size, smarter control and more advanced capabilities, the development of wind farm is becoming a highly complex process which pursues multiple and in many cases conflicting objectives under different constraints. It involves different design and engineering tasks, which may come from technical, logistical, environmental, economical, legitimacy and even social considerations [6].

Among all these tasks, the optimization of wind farm layout is a critical one. In the literature, wind farm layout usually refers to the placements of wind turbines inside the wind farm. Therefore, wind farm layout optimization is to determine the positions of turbines inside the wind farm to maximize and/or minimize some objective functions, such as to maximize the energy production and minimize the cost, while meeting various constraints, which may include wind farm boundary, wind turbines proximity, noise emission level, initial investment limit, and so on. In the most general case, i.e., considering the selection of wind turbine number, different wind turbine types, discrete hub heights,

wind farm layout optimization is a multi-objective mixed integer-discrete-continuous nonlinear constrained optimization problem without analytical formulation. It is mathematically complex and can't be solved by using classical analytical optimization techniques.

In the last two decades, this complex problem has received more and more attentions. Different problem formulations have been proposed and various optimization algorithms have been used to tackle this problem. Previous works are based on various simplified formulations, which range from an array of equally spaced turbines [7,8], to an array of unequally spaced turbines [9], to aligned or staggered grid like (row-column) layout [10, 11], to pre-divided discrete grid points for possible turbine location [12], to continuous searching space for possible turbine positions [13,14]; using a range of algorithms, such as Monte Carlo [11,15], genetic algorithm (GA) [12,16], simulated annealing (SA) [14], (PSO) [17]; seeking different kinds of objectives, e.g., maximize the power [9], annual energy production (AEP) [14], profit [8,13], net present value (NPV) [11], minimize the cost of energy (CoE) [12, 15-17], levelized production cost (LPC) [18]. More comprehensive survey of published works can be found in several papers [19-21].

Most of the published works are using grid based discrete formulation, which simplifies the searching space of the optimization problem from continuous space to discrete space. By removing the grid and formulating the problem in the continuous space, the searching space will be enlarged and the potential to find better solutions will be increased. Considering this, a refinement method is proposed in this paper, which formulates the locations of turbines as continuous variables and tries to improve the optimization results from any other methods. This method is applied to a widely studied ideal test case. This case was first proposed and solved using GA by Mossetti et al. [12]. Later improved results were obtained by Grady et al. [16] also using GA. In order to verify the effectiveness of the method over different results, the same problem is also solved using a GA code developed by the authors, which obtains better results for two wind cases than Grady et al. [16]. These two sets of GA optimization results are then both refined by the proposed method, which both obtains steady improvement.

2. Problem formulation

In their seminal work in 1994, Mossetti et al. [12] proposed an ideal test case. This test case is set to find the optimal number and positions of wind turbines in a 50D×50D square field, where D=80m is the rotor diameter of wind turbine and the minimum distance between two turbines is 5D. The area is subdivided into 100 cells with same size. The center of each cell is a possible location for placing wind turbine, which makes the whole field with 100 possible locations and the searching space with 2^{100} possible layouts. The subdivided wind farm area is shown in Fig. 1, where solid lines represent the boundary of wind farm, dashed lines represent the effective boundary, i.e., the boundary of possible locations for wind turbines, and every cross at the center of each cell means a possible location.

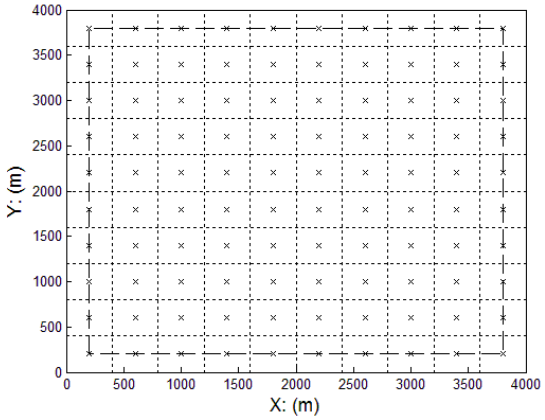

Fig. 1. Subdivided wind farm area.

In order to calculate the wind field in the wind farm, the wake effects between turbines have to been modeled appropriately. In Mossetti study, Jensen wake model [22] is used, which is developed by considering that momentum is conserved within the wake, and that the wake region expands linearly in the direction of wind flow. Fig. 2 shows the schematic of this model.

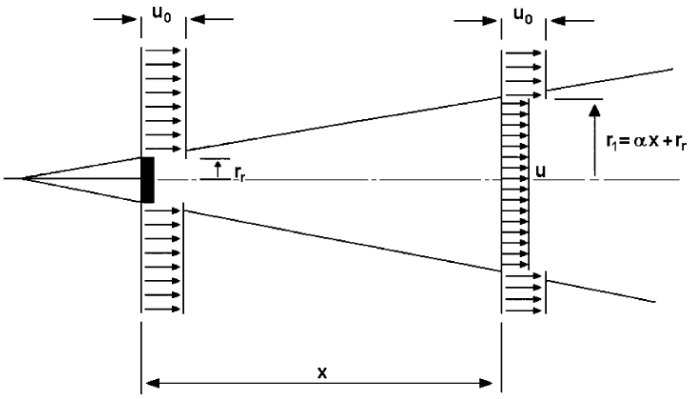

Fig. 2. Schematic of Jensen wake model.

The wind speed downstream of the turbine is governed by the following expression:

$$u = u_0 \left[1 - \frac{2a}{(1+\alpha(x/r_r))^2}\right], \tag{1}$$

where a is the axial induction factor, x is the distance downstream the turbine, r_r is the downstream rotor radius, which is related to rotor radius r_0 by the following expression:

$$r_r = r_0\sqrt{\frac{1-a}{1-2a}}, \tag{2}$$

and α is the entrainment constant, also known as the wake decay constant, which is empirically computed as

$$\alpha = \frac{0.5}{\ln(z/z_0)}, \tag{3}$$

where z is the hub height and z_0 is the surface roughness of the terrain. The axial induction factor a can be calculated from the turbine thrust coefficient C_T as

$$a = \frac{1-\sqrt{1-C_T}}{2}, \tag{4}$$

And the radius of the downstream wake is increased linearly with the distance as

$$r_1 = \alpha x + r_r, \tag{5}$$

For a wind turbine affected by multiple wakes and/or partial wakes, the effective wind speed it experienced is derived based on the kinetic energy deficit balance assumption, which is obtained as

$$\bar{u}_i = u_0\left[1 - \sqrt{\sum_{j=1,j\neq i}^{N}\frac{A_{ij}}{A_0}\left(1-\frac{u_{ij}}{u_0}\right)^2}\right], \tag{6}$$

where A_0 is the rotor area, A_{ij} is the part of the area of the *i*th turbine's rotor which is affected by the wake generated by the *j*th turbine (in the case the *i*th turbine is no effected by the wake of the *j*th turbine, $A_{ij} = 0$), and u_{ij} is the wind speed of the wake generated by the *j*th turbine at the position of the *i*th turbine , which can be determined by Eq. (1).

Using an ideal power curve [16], the total power extracted from the wind by a wind farm consisting of N wind turbines are given by

$$P_{tot} = \sum_{i=1}^{N} 0.3\bar{u}_i^3 \tag{7}$$

Then the wind farm efficiency can be defined as

$$\eta = \frac{P_{tot}}{N \cdot P_{iso}} \tag{8}$$

where P_{iso} is the power produced by an isolated wind turbine under the same wind condition.

The wind turbine properties used in this test case are listed in Table 1, and the surface roughness is assumed as $z_0 = 0.3$ m.

Table 1. Wind turbine properties

Hub height (h)	60 m
Rotor radius (r_0)	40 m
Rotor diameter (D)	80 m
Thrust coefficient (C_T)	0.88

The cost of wind farm is modeled by a simple function which only depends on the number of turbines. The total cost per year for the entire wind farm is expressed as follows [12]

$$\text{Cost} = N\left(\frac{2}{3} + \frac{1}{3}e^{-0.00174N^2}\right) \tag{9}$$

The following objective function, which represents the cost of per unit of energy produced, will be minimized

$$\text{CoE} = \text{Cost}/P_{tot} \tag{10}$$

Besides, there are constraints about the locations of turbines which are not explicitly stated but satisfied by the 5D width cells setting, which means that the minimal distance between any two turbines is 5D. The minimal distance constraints can be stated as

$$d_{ij} = \sqrt{\left(x_i^2 - x_j^2\right) + \left(y_i^2 - y_j^2\right)} \geq 5D, \quad \text{for } i, j = 1,2,\cdots N, \text{and } i \neq j \tag{11}$$

where d_{ij} is the distance between two turbines, x_i and y_i are the coordinates of the ith turbine.

Three wind cases are considered [12]: Case (a): uniform north wind with a speed of 12m/s; Case (b): Equally distributed (36 directions) wind with a speed of 12m/s; Case (c): Ununiformly distributed (36 directions) wind with speeds of 8, 12 and 17 m/s. The distribution of the wind case (c) is shown in Fig. 3.

The above problem formulation defines a complete ideal test case for wind farm layout optimization, which is especially suitable for algorithm study. It was first developed and solved with GA by Mossetti et al. [12], then Grady et al. [16] tackled this case with their improved GA and obtained better solutions, other algorithms, such as Monte Carlo [15], PSO [17] have also been applied to study this test case.

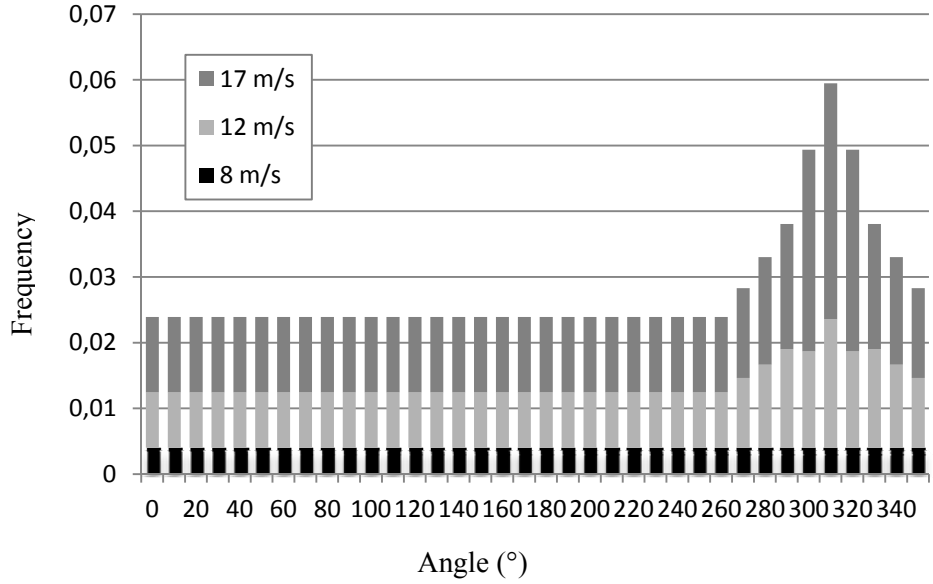

Fig. 3. Distribution of wind case (c): ununiformly distributed wind [16]

3. Refinement algorithm

Because of the discrete nature of the formulation stated in Section 2, it is very convenient to apply all kinds of discrete type meta-heuristics [23], such as the binary coded GA [12, 16]. In this test case, one solution, i.e., one possible layout can be represented by a 100 bit string consisting of 0 and 1, where 1 means that a turbine is located in the relative cell, and 0 means no turbine.

For a general wind farm layout optimization problem, if the number of turbines is not specified, the searching space for optimal solution is mixed integer-continuous type, where the number of turbines is represented by an integer and the locations of turbines are represented by continuous variables. By assuming that all turbines can only be placed in the center of the pre-divided cells, the searching space is simplified into a discrete type, by which solutions can be easily formulated as binary strings. Although this simplification is very important for the application of discrete type meta-heuristics, there are no physical constraints that the turbines have to be placed in the center of cells, and there are no real cells or grids in the actual wind farm field. Therefore by removing this grids and cells setting, the possible searching space for layout is largely increased, from discrete space to continuous space. This increase of searching space may be utilized by certain algorithms to find better solutions, i.e., to refine the optimization results based on the discrete searching space.

In this work, a simple method is proposed to find better solution, using the optimization results obtained from any discrete type of optimization methods. The algorithm is shown as follows:

Algorithm 1: Random search (RS) algorithm for optimization refinement of wind farm layout

---

Initialize:
Select initial solution ***s0*** *from the optimization result of an existing method*
Evaluate fitness value: $f0=f(s0)$

While *stop condition is not true:*

1. ***Random Move***
   Select a turbine randomly, move its position in a random direction with a random step: $s=s0+\Delta s$

2. ***Feasibility Check***
   Check feasibility of ***s*** *using constraints of the problem*
   If s *is not feasible:*
      repeat the Random Move (step ***1****)*
   end If

3. ***Fitness Evaluation***
   Calculate the fitness value of feasible solution ***s: f=f(s)***

   Optimal Solution Update
   If f<f0*:*
      set ***s0=s, f0=f***
   end If

End While
S0 *is the refined optimization solution*

It should be noticed that there is a *feasibility check* step in the algorithm, which deals with the constraints of the problem. As stated in Section 2, the minimal distance constraints, i.e., the requirements of locations of turbines governed by equation (11), also the effective boundary constraints (as shown in Fig. 1), are automatically satisfied by the cells setting of the problem formulation. Now, when the grids and cells are removed and the turbines are allowed to randomly move, these constraints have to be treated explicitly. So for every new solution introduced by random move, its feasibility has to be checked. Only when all the constraints are satisfied, the solution is considered to be feasible and the algorithm moves to next step.

The other feature needs to be pointed out is that the number of turbines is fixed in this algorithm, which stays the same as in the initial solution from any other optimization method.

This algorithm is simple, intuitive and easy to implement. It can be used as a last stage refinement tool to improve the results obtained by any other algorithms, especially for those based on discrete formulation.

4. Results and Comparisons

In this section the proposed refinement algorithm is used to improve the results obtained by Grady et al. [16], which are improved GA optimization results comparing to the original results presented in Mossetti study [12]. In order to verify the effectiveness of this algorithm, the test case in Section 2 is also solved by using a GA developed by the authors. Comparing to Grady study [16], our GA treats the same test case with the same problem formulation, but uses different crossover, mutation and selection methods, also adds an elitist strategy, which successes in finding the same optimal solution for wind case (a), and better solutions for wind cases (b) and (c).

These two sets of optimization results are both refined with the same refinement algorithm (RS), the numerical results presented in Table 2 show steady improvements for all wind cases.

It can be seen from Table 2 that the proposed refinement algorithm with RS can obtain steady improvement for both sets of GA optimization results. The greatest improvements are achieved for the wind case (a), in which the power and wind farm efficiency increases by more than 6%, and the cost of energy decreases by more than 5%. For the wind cases (b) and (c), improvements are also achieved for Grady GA results and present GA results. Comparing these two sets of GA results, it can be concluded that our own GA is able to find better layouts than the results in Grady study [16]. Based on the improved initial solutions, better refined results are also obtained for these two wind cases. The fact that the greatest improvements are for wind case (a) may be explained by the smallest number of turbines of this case, which means the wind farm field is less densely filled, thus the space for

improvement is also larger. The results in Table 2 suggest that the quality of initial solutions, which are the starting point of random evolution towards better results, is very important for the success of the proposed refinement method.

Table 2. Comparison of layout performance of GA optimization results and refined results

	Case (a)				Case (b)				Case (c)			
	N	CoE	P(kW)	η(%)	N	CoE	P(kW)	η(%)	N	CoE	P(kW)	η(%)
Grady GA Published	30	0.001544	14310	92.0	39	0.001567	17220	85.2	39	0.000803	32038	86.6
Grady GA Re-eval.	30	0.001545	14294	91.9	39	0.001578	17056	84.4	39	0.000859	31336	84.2
Discrepan--cy (%)	/	0.06	0.11	0.11	/	0.70	0.95	0.94	/	6.97	2.19	2.85
RS result	30	0.001454	15190	97.7	39	0.001558	17279	85.5	39	0.000840	32044	86.5
Exe. Time	36045 s				39479 s				48341 s			
Improve--ment (%)	/	-5.90	6.27	6.27	/	-1.29	1.31	1.31	/	-2.21	2.26	1.31
Present GA	The same as for Grady GA				41	0.001511	18572	87.4	39	0.000855	31478	85.0
Exe. Time					86420 s				345871 s			
RS Result					41	0.001462	19195	90.3	39	0.000837	32178	86.9
Exe. Time					39741 s				50403 s			
Improve--ment (%)					/	3.25	3.35	3.35	/	-2.18	2.22	2.22

Note: 1. The 'Grady GA Re-eval.' are re-evaluated results of the published Grady study, using our code, the discrepancy is introduced by the difference in detailed wake modeling, coding, computation, and especially the exact data of wind case (c) (this paper uses data extracted from the figure in [16]);
2. Improvement percentage is calculated based on re-evaluated results of Grady GA;
3. The improve percentage of CoE is negative, which means the CoE is minimized further;
4. 'Exe. Time' is the execution time using a personal computer with 2.33GHz CPU and 1.96GB RAM.

The optimal layouts for all wind cases, from the original and refined results of both the Grady and our own GA, are shown in Figs. 4-6.

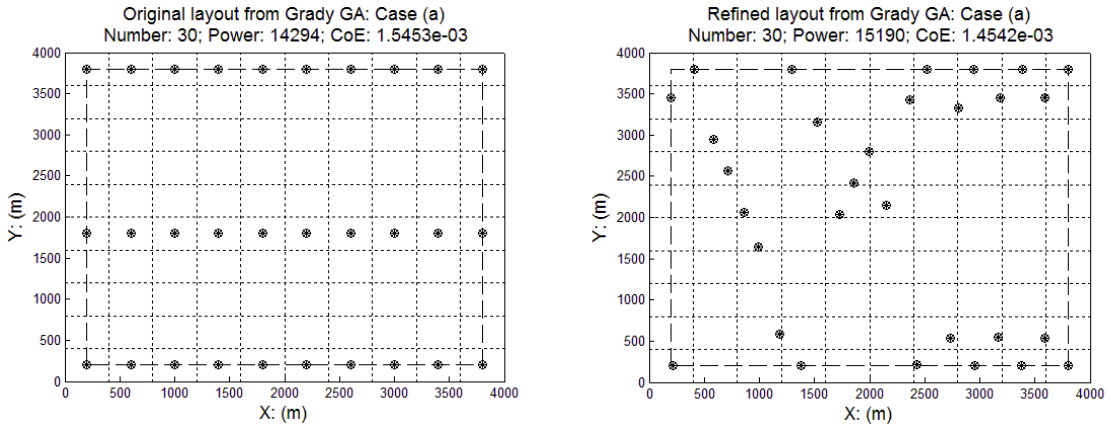

Fig. 4. Comparison of optimal layout for case (a)
(In this case, our own GA and Grady GA get the same solution.)

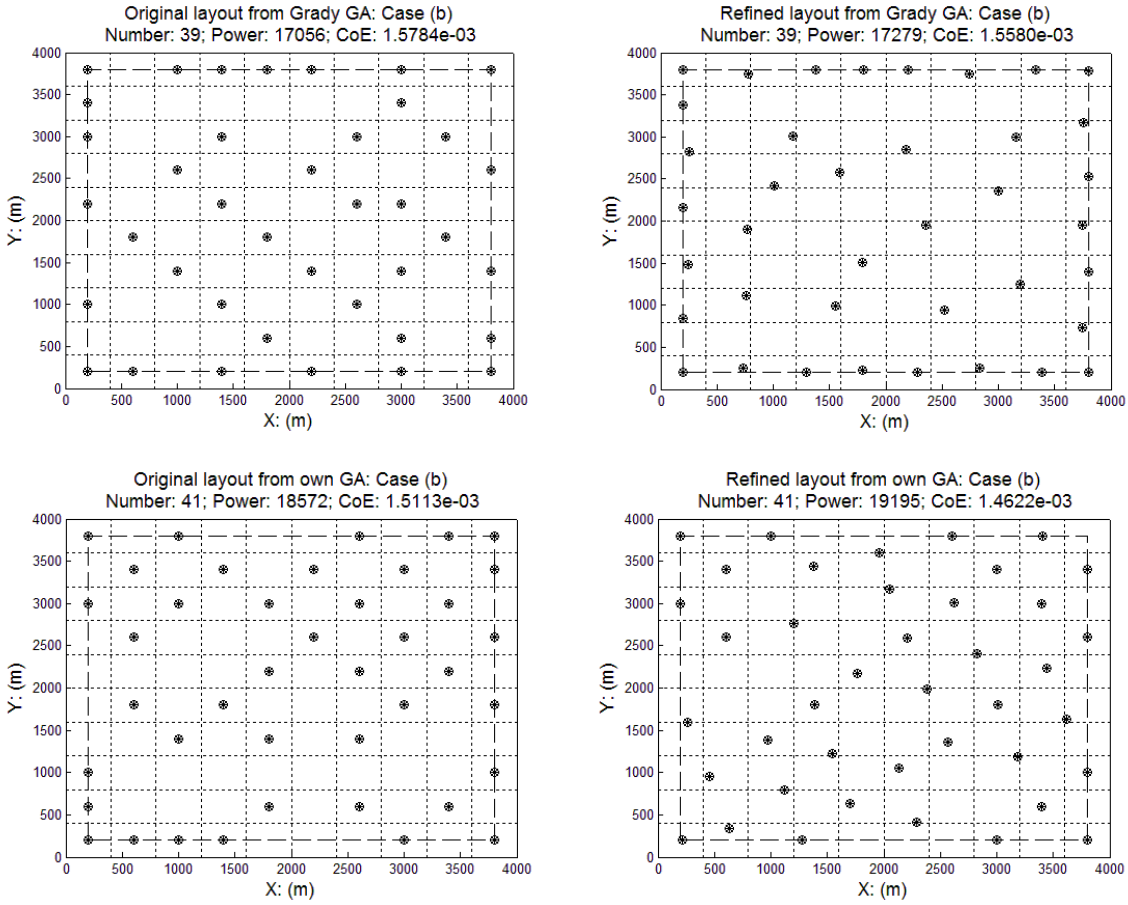

Fig. 5. Comparison of optimal layout for case (b)

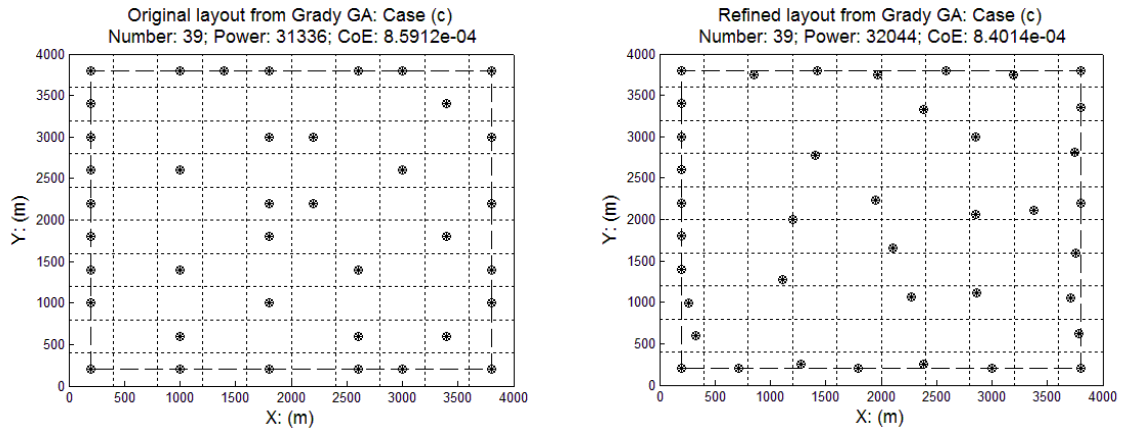

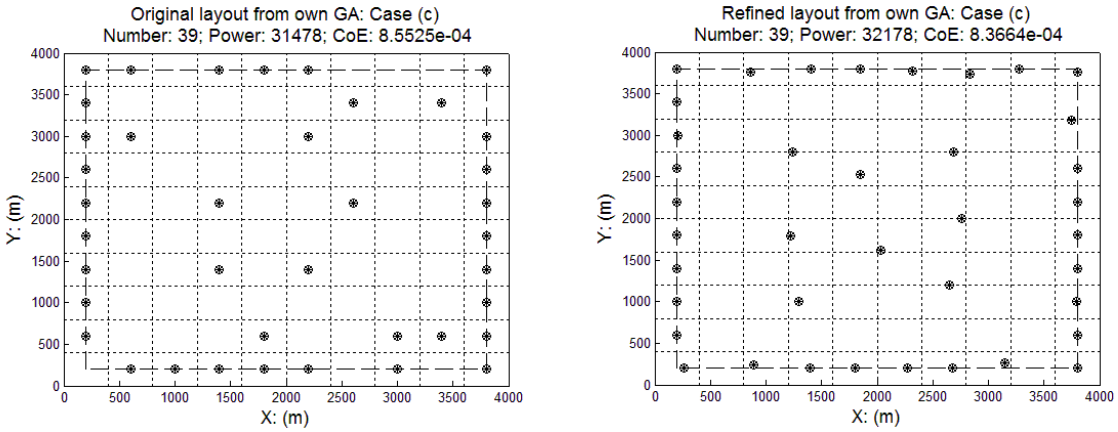

Fig. 6. Comparison of optimal layout for case (c)

5. Conclusions

In this paper, a refinement method by random search is developed. The algorithm is simple, intuitive and easy to implement, it has the ability of treating the constrained wind farm layout optimization in the continuous formulation. The application of this method to improve the optimization results from GA of a widely studied test case demonstrates its effectiveness. The performance of the algorithm is dependent on the quality of initial solutions, which may be obtained by other optimization methods. The results shown in this paper indicate that this algorithm can serve as a last stage refinement tool, by improving existing optimization results and obtaining better solutions. This algorithm could be further investigated and combined with other optimization methods, to tackle more realistic wind farm layout optimization in future study.

Acknowledgment

This work was supported by the international collaboration project (DSF Sagsnr. 10-094544) under Danish Research and Innovation Council for Strategic Research.

REFERENCES

[1] University of Massachusetts: Wind Energy Center, "Wind energy center alumni and the early wind Industry", available at: http://www.umass.edu/windenergy/about.history.alumni.php (accessed February 2013).
[2] SEAS-NVE, "Vindeby offshore wind farm", available at: http://www.seas-nve.dk/AboutSeasNve/Wind/References/Offshore/Vindeby.aspx (accessed February 2013).
[3] Z. Chen, J.M. Guerrero, F. Blaabjerg, "A review of the state of the art of power electronics for wind turbines", IEEE Transactions on Power Electronics, vol. 24(8) (2009) pp. 1859-75.
[4] L. Ma, S.Y. Luan, C.W. Jiang, H.L. Liu, Y. Zhang, "A review on the forecasting of wind speed and generated power", Renewable and Sustainable Energy Reviews, vol. 13 (2009) pp. 915-20.
[5] M. Popat, B. Wu, F.R. Liu, N. Zargari, "Coordinated control of cascaded current-source converter based offshore wind farm", IEEE Transactions on Sustainable Energy, vol. 3(3) (2012) pp. 557-65.
[6] P. Jain, *Wind Energy Engineering*, New York: The McGraw-Hill Companies, Inc. (2011).
[7] R.J. Templin, "An estimation of the interaction of windmills in widespread array", National Aeronautical Establishment, Laboratory Report LTR-LA-171, Otawa, Canada, (1974).

[8] P.A. Crosby, “Application of a Monte Carlo optimization technique to a cluster of wind turbines”, Journal of Solar Energy Engineering, Transactions of the ASME, vol. 109 (1987) pp. 330-6.
[9] F.C. Kaminsky, R.H. Kirchhoff, “Optimal spacing of wind turbines in a wind energy power plant”, Solar Energy, vol. 39(6) (1987) pp. 467-71.
[10] M.R. Patel, *Wind and Power Solar Systems*, Boca Raton, FL: CRC Press (1999).
[11] K. Atias, S.P. Ladany, “Optimal economic layout of turbines on windfarms”, Wind Engineering, vol. 30(2) (2006) pp. 141-51.
[12] S. G. Mosetti, C. Poloni, B. Diviacco, “Optimization of wind turbine positioning in large windfarms by means of a genetic algorithm”, Journal of Wind Engineering and Industrial Aerodynamics, vol. 51 (1994) pp. 105-16.
[13] U.A. Ozturk, B.A. Norman, “Heuristic methods for wind energy conversion system positioning”, Electric Power Systems Research, vol. 70 (2004) pp. 179-85.
[14] R.A. Rivas, J. Clausen, K.S. Hansen, L.E. Jensen, “Solving the turbine positioning problem for large offshore wind farms by simulated annealing”, Wind Engineering, vol. 33(3) (2009) pp. 287-98.
[15] G. Marmidis, S. Lazarou, E. Pyrgioti, “Optimal placement of wind turbines in a wind park using Monte Carlo simulation”, Renewable Energy, vol. 33 (2008) 1455-60.
[16] S.A. Grady, M.Y. Hussaini, M.M. Abdullah, “Placement of wind turbines using genetic algorithms”, Renewable Energy, vol.30 (2005) pp. 259-270.
[17] C.Q. Wan, J. Wang, G. Yang, X. Zhang, “Optimal micro-siting of wind farms by particle swarm optimization”, Advances in Swarm Intelligence, Springer Berlin Heidelberg (2010) pp. 198-205.
[18] C.N. Elkinton, J.E. Manwell, J.G. Mcgowan, “Optimizing the layout of offshore wind energy systems”, Marine Technology Society Journal, vol. 42(2) (2008) pp.19-27.
[19] P.-E. Réthoré, “State of the art in wind farm layout optimization”, Wind Energy Research (2010), available at: http://windenergyresearch.org/2010/10/state-of-the-art-in-wind-farm-layout-optimization/ (accessed February 2013).
[20] A. Tesauro, P.-E. Réthoré, G.C. Larsen, “State of the art of wind farm optimization”, Proceedings of EWEA 2012 – European Wind Energy Conference & Exhibition, Copenhagen, Denmark, (2012).
[21] S.A. Khan, S. Rehman, “Iterative non-deterministic algorithms in on-shore wind farm design: A brief survey”, Renewable and Sustainable Energy Reviews, vol. 19 (2013) pp. 370-84.
[22] I. Katic, J. Højstrup and N.O. Jensen, “A simple model for cluster efficiency”, Proceedings of the European Wind Energy Association Conference and Exhibition, Rome, Italy, (1986) pp.407-10.
[23] M. Gendreau, J.-Y. Potvin (Eds.), *Handbook of Metaheuristics* (2nd edition), Berlin: Springer (2010).

Modeling large offshore wind farms under different atmospheric stability regimes with the Park wake model

A. Peña[1], P.-E. Réthoré[1], O. Rathmann[1]

[1]DTU Wind Energy, Risø campus, Frederiksborgvej 399, 4000 Roskilde, DK, aldi@dtu.dk

ABSTRACT

Here, we evaluate a modified version of the Park wake model against power data from a west-east row in the middle of the Horns Rev I offshore wind farm. The evaluation is performed on data classified in four different atmospheric stability conditions, for a narrow wind speed range, and a wide range of westerly wind directions observed at the wind farm. Simulations (post-processed to partly account for the wind direction uncertainty) and observations show good agreement for all stability classes, being the simulations using a stability-dependent wake decay coefficient closer to the data for the last turbines and those using the WAsP recommended value closer to the data for the first turbines. It is generally seen that under stable and unstable atmospheric conditions the power deficits are the highest and lowest, respectively, but the wind conditions under both stability regimes are different. The simulations do not approach the limits of the infinite wind farm under any stability condition as winds are not parallel to the row.

INTRODUCTION

In the last years, investigation of the effect of atmospheric stability on the production of wind farms has gained attention, partly because it has been observed, particularly at large offshore wind farms, that under stable and unstable atmospheric conditions, the wind farms under- and over-perform, respectively, when compared to wind farm data under neutral conditions [1]. Most wake models do not account for stability conditions other than neutral and, thus, model under-performance–when compared to wind farm data–is sometimes attributed to the effect of atmospheric stability.

The Park wake model [2] used in the Wind Atlas Analysis and Application Program (WAsP) [3] is based on the model of Jensen [4], which makes use of the wake decay coefficient k_w to estimate the wind speed reduction for a given thrust coefficient, downstream distance, turbine diameter, and upstream wind speed. It is recommended in WAsP to use $k_w = 0.05$ for offshore wind farms (lower than the recommended value onshore of 0.075). This is because k_w is related to the entrainment of the wake in the atmosphere (it is in fact the slope of the expansion of the wake) and as such it is a function of the surface roughness z_o (the lower the roughness the less

wake expansion). Frandsen [5] by semi-empirical means suggested $k_w = 0.5/\ln(h/z_o)$, where h is the turbine's hub height, which generally translates into lower k_w values than the WAsP recommendations ($k_w = 0.039$ for a typical wind turbine offshore). Barthelmie and Jensen [6] found that using $k_w = 0.03$ adjusted well the results of the Park wake model at the Nysted wind farm when compared to data. Interestingly, at Nysted, i.e. in the South Baltic Sea, stable conditions are mostly observed.

Here, we present an analysis of wind farm data carried out at the Horns Rev I offshore wind farm, where we are able to classify wind turbine power data into different atmospheric stability classes. A set of simulations using a modified version of the Park wake model are performed using different k_w values correspondent to particular atmospheric stability conditions. The simulations are post-processed in order to partly take into account the wind direction uncertainty and compared to the data. Since Horns Rev I is a rather large wind farm, for the wind directions analyzed we might expect that some cases will approach the limits of an infinite wind farm. Therefore, we also present the results of the Park wake model evaluated to its infinite theoretical limits.

MODIFIED PARK WAKE MODEL

We implemented the Park wake model described in Katic et al. [2] in a Matlab script to run simulations for a wide variety of wind directions, wind speeds, wind farm layouts, wind turbine specifications, and k_w values. We refer to it as "modified" because in WAsP the model has been extended to account for the effect of ground-reflected wakes from upwind turbines and our version takes into account the wakes upwind (directly or sideways) only.

Peña and Rathmann [7] showed that adjusting k_w to match the wind speed reductions estimated by a stability dependent infinite wind farm boundary layer model (a totally different model based on the concept of Frandsen [5], which generally gives higher wind speed reductions in stable compared to unstable conditions) resulted in lower k_w values under stable compared to unstable conditions. The adjustment was performed evaluating the Park wake model for an infinite wind farm. Similar results were found when evaluating this 'infinite' Park wake (IPW) model assuming,

$$k_w = u_{*free}/u_{hfree} = \kappa/\left[\ln\left(h/z_o\right) - \psi_m(h/L)\right], \tag{1}$$

where u_{*free} and u_{hfree} are the undisturbed friction velocity and hub-height wind speed, respectively, $\kappa = 0.4$ is the von Kármán constant, and $\psi_m(h/L)$ is the extension to the logarithmic wind profile to account for stability and depends on the height (in this case the hub-height) and atmospheric stability by means of L (the Obukhov length). The expressions for ψ_m can be found in Peña [8]. Expressions for the IPW model are also given in Peña and Rathmann [7]. Since our Matlab implementation only accounts for upwind wakes, we use the expressions for the same type of wakes.

HORNS REV I WIND FARM

The Horns Rev I wind farm is located in the Danish North Sea at about 17 km west from the coast (from the wind farm's northwest corner). A layout of the wind farm showing the positions

of the 80 wind turbines (rows are named from A to H and columns from 1 to 10) and three meteorological (met) masts is shown in Fig. 1-left. The turbines are Vestas V80 2 MW machines of 80-m rotor diameter and 70-m hub height. Power and thrust-coefficient curves are illustrated in Fig. 1-right.

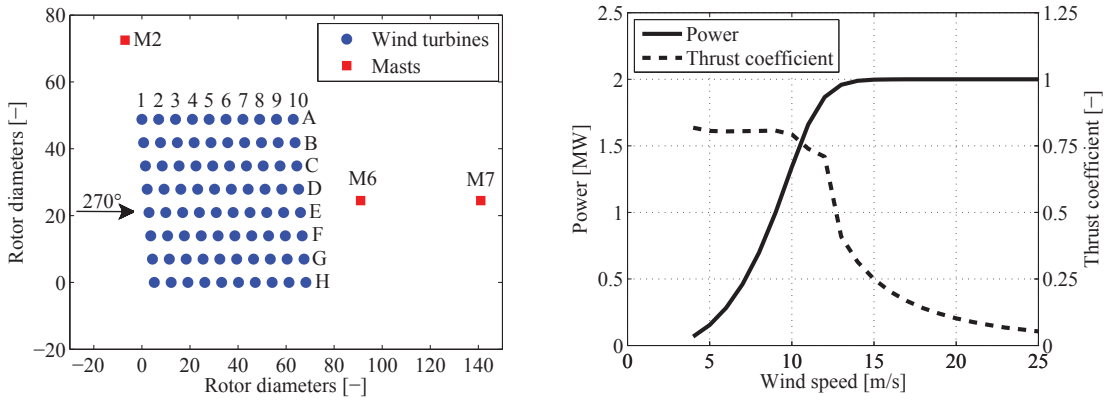

Figure 1: (left) The Horns Rev I offshore wind farm. (right) Power and thrust coefficients as function of wind speed for the Vestas V80 wind turbine (figures taken from [3])

A met mast (M2) is located about 2 km north from the northwest edge of the wind farm. Met data from this mast have been extensively analyzed for atmospheric stability studies (e.g. in Peña and Gryning [9], Peña et al. [10], and Peña and Hahmann [11]). Here we use measurements from the cup anemometers at 62 and 15 m above mean sea level (AMSL–all measurements are referred to AMSL hereafter unless otherwise stated), a wind vane at 43 m, temperature sensors at 13 and –4 m (the latter is below mean sea level), and humidity and pressure sensors at 13 and 55 m, respectively.

DATA TREATMENT

Concurrent 10-min data from the wind turbines and M2 are used. Data from the turbines include a power quality signal indicating the status of the turbine and the power signal (stopped, down-regulated, etc). We choose to use data when all turbines show status equal to 1 (i.e. a validated measurement where the turbine does not stop and there are no spikes or drop outs).

Atmospheric stability at the wind farm is assessed using the observations at M2. In order to filter data where the climate/conditions are not similar at the two places, we first analyze the wind direction observed at M2 and that at turbine 07 (row G, column 1). For the latter we use the nacelle position, which was found to be optimal for analyzing the wake effect for wind directions $270 \pm 60°$ [12]. Figure 2 shows a scatter plot between the two measurements where it is observed a very good correspondence for most cases. We select cases where the difference between both signals is lower than 15° and where the wind direction at turbine 07 is $270 \pm 60°$ (the latter criterion also ensures that no wakes affect the stability estimations at M2 and might allow us to study the array in the limits of the infinite wind farm).

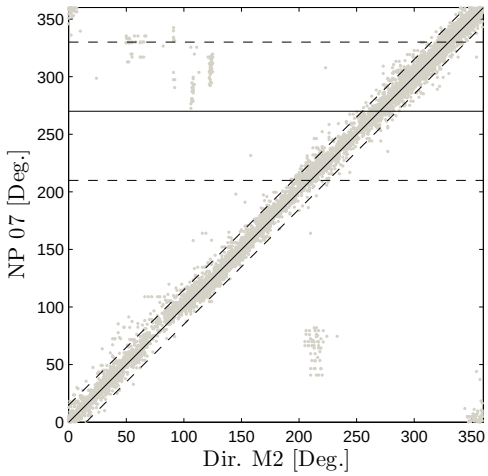

Figure 2: Wind direction observed at M2 at 43 m and the nacelle position (NP) of turbine 07. The lines illustrate the filtering criteria used for the data (see text)

We further study the agreement between the wind speeds observed at M2 at 62 m and the nacelle one at M7 at 70 m (Fig. 3-left). As illustrated both signals show very good agreement and so we use them to further filter data: we choose the wind speed range $5-10$ m s^{-1} (since the thrust coefficient is nearly constant within this range) and the difference between both signals needs to be lower than 1 m s^{-1}. Before this 'filtering' step, we check the power performance using the wind speed and power signals of turbine 07, which as seen in Fig. 3 compares well with the one provided by the manufacturer (slightly over and under-estimating the power below and above ~ 10 m s^{-1}, respectively).

Our analysis is focused on the wind speed deficits of row E and so we extract power data correspondent to the turbines on that row only. We use another filtering criterion based on the standard deviation of the power signal. It is noted a good amount of data with negative power values and we were advised to use values higher than 5 kW for the standard deviation of the power for the analysis (Kurt Hansen, personal communication). We increase the criterion to 12 kW. These final reduced dataset is then complemented with the concurrent measurements from M2 (atmospheric static stability is derived as in Peña and Hahmann [11], i.e. estimating the bulk Richardson number, which translates into a measure of L), and the nacelle position and wind speed of turbine 05 (row E, column 1). Figure 4-left shows the power performance of turbine 05 where a very similar behavior to that observed for turbine 07 is found (Fig. 3-left). For the rest of the analysis, we use the wind speed resulting from converting the power to wind speed of turbine 05 (through the power curve in Fig. 1-right) as a proxy for the undisturbed wind speed. For completeness, we illustrate in Fig. 4-right that the nacelle position of turbine 05 cannot be used for wake analysis since it is rather different to that of turbine 07.

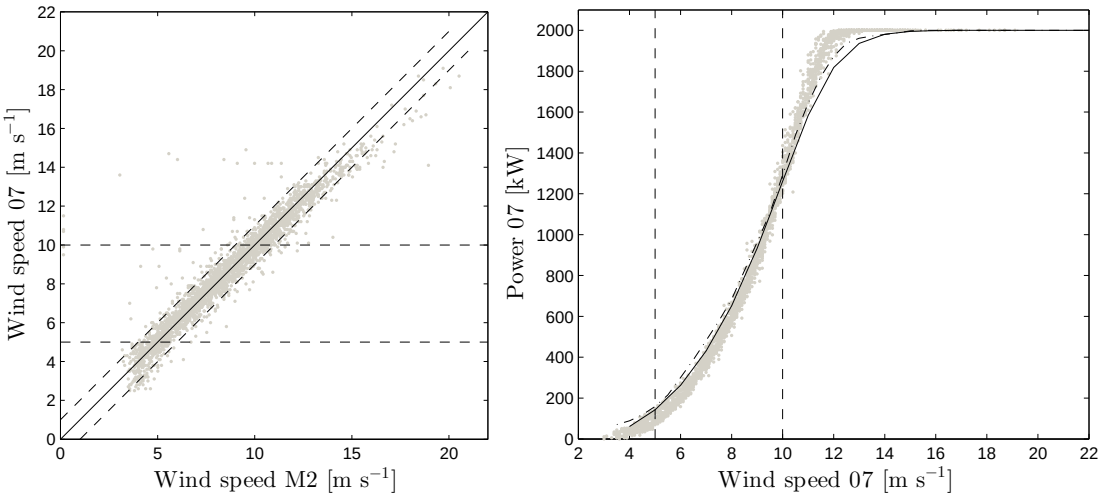

Figure 3: (left) Wind speeds at M2 at 62 m and that at the nacelle of turbine 07 at 70 m. The lines illustrate the filtering criteria used for the data (see text). (right) Power performance at turbine 07 based on its nacelle wind speed. The lines show two power curves: the one used in this study (solid line) and that from the offshore Vestas V80 wind generator in WAsP (dash-dotted line)

RESULTS

The final dataset results in 1525 10-min values. The data is classified in four stability classes: very unstable (-75 m $\leq L \leq -10$ m), unstable (-500 m $\leq L \leq -75$ m), neutral ($|L| \geq 500$ m), and stable (500 m $\geq L \geq 5$ m). Figure 5-left shows the ensemble average of power deficits of row E (normalized with the power of turbine 05) for the different stability classes. Although it is observed a general higher power reduction in stable compared to unstable conditions, this type of comparison is misleading, since the wind speed and direction conditions under each stability class are not the same. Figure-5-right illustrates the histograms of wind speed for the different stability conditions and is noticed that they show different distributions. We further narrow the analysis to wind speeds of 8.5 ± 0.5 m s^{-1} to reduce the variability of wind conditions maximizing the amount of data.

Although the reduction in the variability of power deficits, for each stability class the difference in the individual 10-min power deficit values is very large. One of the main reasons for this is that the observed wind direction range is rather broad and the distributions are different (Fig. 6). However we cannot narrow the range any further as we might find very few or no data: e.g. most very unstable and unstable conditions are seen within the range 290°–310°, whereas there are no data and nearly nothing for that range under neutral and stable conditions, respectively.

For each stability class we choose to run simulations using the Horns Rev I layout (thrust coefficient and power curves as in Fig.1) using the modified Park wake model for $u_{hfree} =$ 8.5 m s^{-1} and a wide undisturbed wind direction range of 180°–360° (at a resolution of 0.5°). This is performed for k_w values of 0.05, 0.0349, 0.0338, 0.0313, and 0.0231, which correspond,

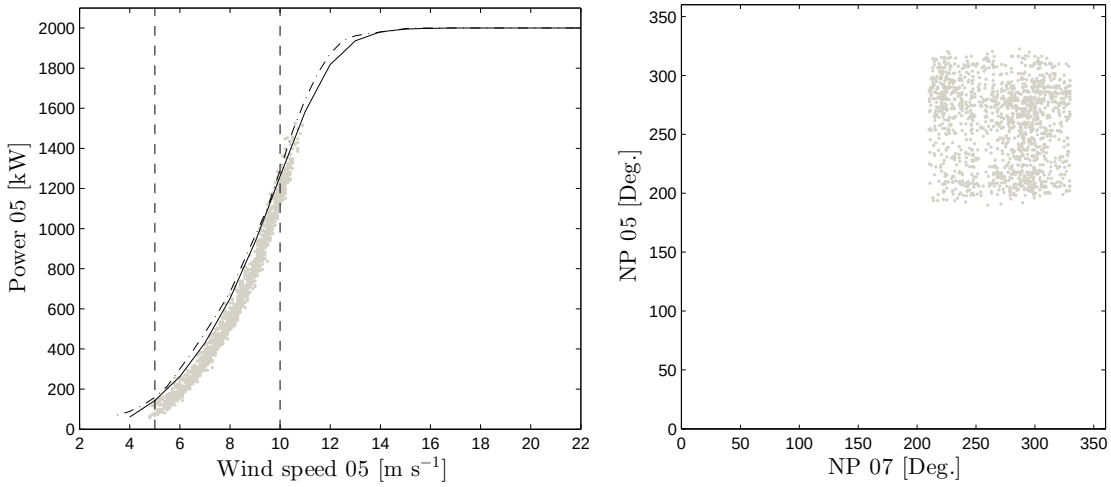

Figure 4: (left) As Fig. 3-right but for turbine 05. (right) Comparison of the nacelle position signals of turbines 05 and 07

respectively, to the WAsP recommended one, and those for very unstable, unstable, neutral, and stable conditions. For the estimation of these coefficients, we average the bulk Richardson number under each class, convert this average into a L value, estimate the ψ_m correction at hub height, and evaluate Eq. (1) assuming $z_o = 0.0002$ m.

The simulations are further post-processed to take into account part of the wind direction uncertainty as in Gaumond et al. [13], i.e. assuming that within a 10-min interval the wind direction distributes as a normal distribution with a given standard deviation σ (we use a value of 2.5°). The procedure is briefly as follows: for each observed 10-min wind direction θ under each atmospheric stability class, we extract the simulations correspondent to the range $[\theta - 3\sigma, \theta + 3\sigma]$. We then weight each simulation using the normal probability distribution function. For each observed 10-min wind direction and speed deficit, there is therefore a single simulated wind speed deficit (derived from 31 gaussian-weighted simulations).

Figures 7–10 show the results of the comparison of the observed 10-min power deficits and those simulated at row 5 for the different stability classes. They are not shown in the same figure as they correspond to observations/simulations under different wind direction conditions. The ensemble average of both simulations (with a stability-specific k_w value) and observations are also shown together with that of the simulations using $k_w = 0.05$. As the results of the simulations are wind speed deficits, we translate them into power deficits with the power curve in Fig. 1.

The results generally show a very good agreement between the ensemble averages of simulations and observations. For each stability condition the result using the stability-specific k_w value shows higher power reductions compared to that using $k_w = 0.05$, as a lower k_w value increases the wake effect. Particularly, under neutral stability conditions, the ensemble average of the simulations using both the stability-specific and WAsP recommended k_w values shows that the model predict higher power deficits than observed for all turbines in the row. This is very

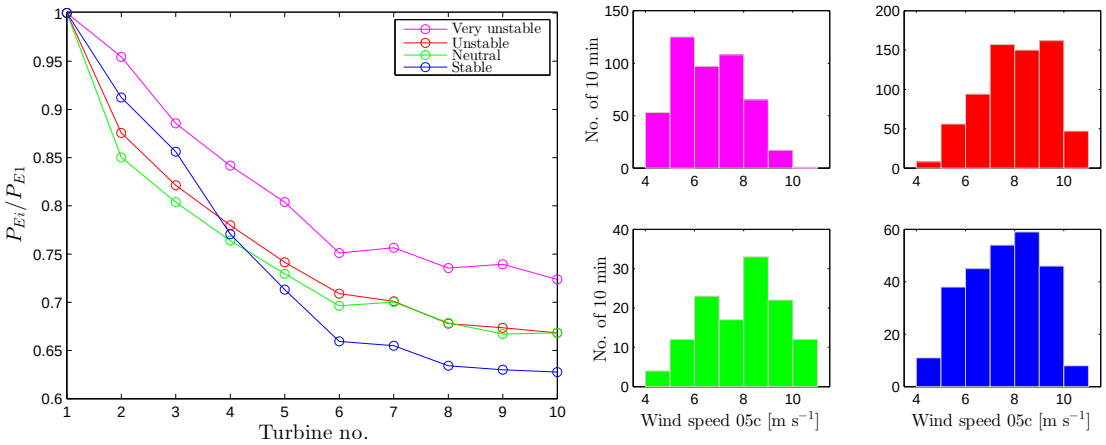

Figure 5: (left) Ensemble average power deficit of row E (normalized with the power of turbine 05 P_{E1}) for different atmospheric stability conditions. (right) Wind speed histograms (based on the power-converted value from turbine 05) for each stability condition

interesting because in most of the studies at Horns Rev I and at other large offshore wind farms where the Park wake model has been used, the results are normally the opposite: model under-prediction of the power deficits. This might be partly due to range of wind directions we use for our analysis and to the post-processing of the simulations accounting for the wind direction uncertainty.

Apart from the neutral case (which is the one with the less data), the simulation with the stability-dependent k_w fits better the power deficit at the last turbines in the row compared to the simulations using $k_w = 0.05$, which in turn generally fit well the results of the first turbines in the row. However, most of the outliers (i.e. the individual 10-min power deficits where $P_{Ei}/P_{E1} > 1$) are found at those first turbines in the row (there are fewer outliers at the last turbines). Removing such 'outliers' brings the ensemble average closer to the simulation but there is no good reason to remove them as they seem to be good observed data.

We can also note that the range of the results of the simulations and that of the observations for each stability class is well predicted (except for the clear outliers). The cloud of observations (and simulations) of power deficits for unstable conditions is clearly between 0.5 and 0.8 and for very unstable conditions between 0.6 and 0.8.

The largest power deficit drop is observed at turbine E2 (as expected) and appears in the neutral class (this is the one where most of the observed wind comes from 270°). The infinite limits of power reduction are 0.26, 0.15, 0.28, 0.30, and 0.44 for neutral, stable, unstable, very unstable, and the WAsP-recommended k_w-values, respectively; none of the ensemble observed power deficits seem to approach the infinite limits.

Also interestingly, under very unstable atmospheric conditions the ensemble average of power deficit (simulated and observed) at turbine E2 is very similar to that at turbine E1; as shown in Fig. 6 for this atmospheric stability condition, there are no observation of winds parallel to the row and winds mostly come from 300°. Turbine E2 is thus mostly affected by partial wakes from turbines E1 and D1.

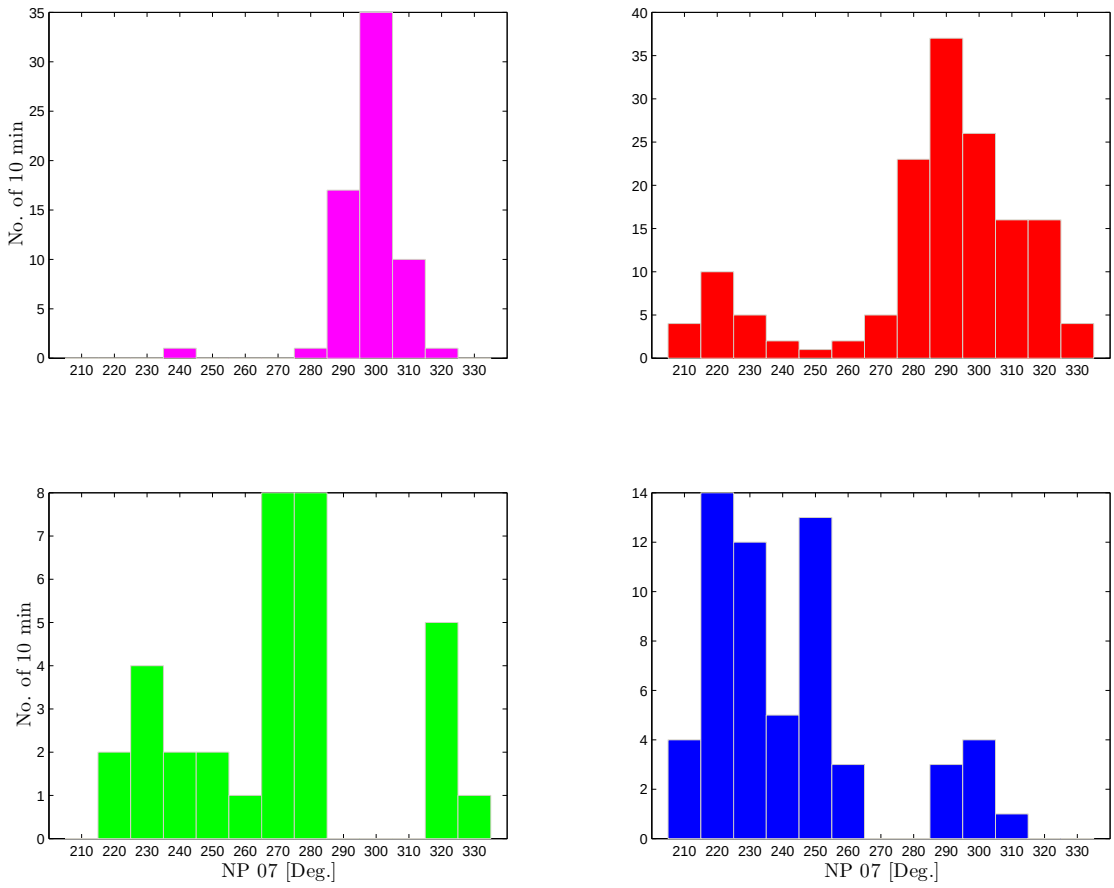

Figure 6: Wind direction histograms (based on the nacelle position of turbine 07) for each stability condition: very unstable (top left), unstable (top right), neutral (bottom left), and stable (bottom right)

CONCLUSIONS

Power deficit data from the Horns Rev I offshore wind farm are analyzed under different atmospheric stability conditions, a nearly constant undisturbed wind speed, and a wide range of westerly wind directions. The resulting dataset is compared with simulations using a modified version of the Park wake model and the limits of the Park wake model when evaluated as an infinite wind farm.

It is found a very good agreement between simulations and observations for a west-east row in the middle of the wind farm. The simulations using a stability-dependent k_w value are closer to the observations at the last turbines and those using the WAsP recommended k_w value of 0.05 closer to the observations at the first turbines on that row.

Due to the range of observed and simulated wind directions, it is difficult to conclude whether under stable or unstable atmospheric conditions the wind farm, respectively, under-

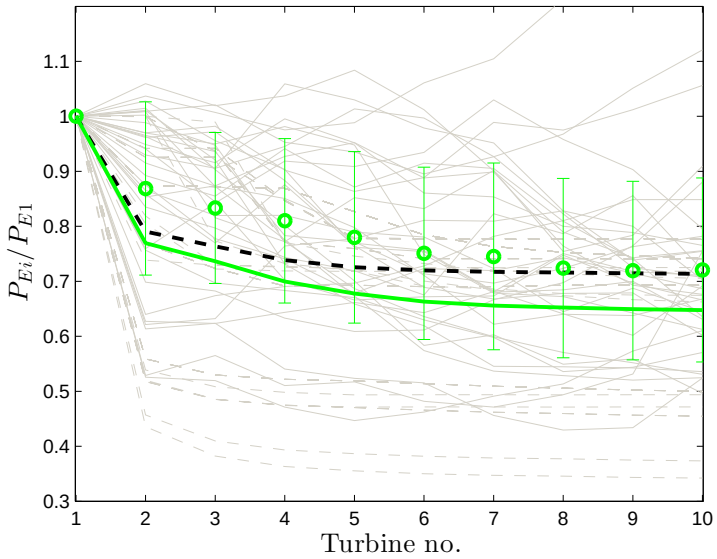

Figure 7: Power deficits of row E (normalized with the power of turbine 05 P_{E1}) for neutral conditions. The gray solid lines show the 10-min power deficits (in gray dashed lines for each simulation), the colored circles the ensemble average (error bars with $\pm$ the standard deviation), the solid colored line the ensemble average of the simulations with the stability-specific k_w value, and the black dashed line that of the simulations with $k_w = 0.05$

or over-performs. However, it is seen higher power reductions under stable than unstable atmospheric conditions. In none of the conditions, the observations seem to approach the limits of the infinite wind farm.

REFERENCES

[1] Jensen LE. Array efficiency at Horns Rev and the effect of atmospheric stability. *Proceedings of the European Wind Energy Association Conference & Exhibition*, Milano, 2007.

[2] Katic I, Højstrup J, Jensen NO. A simple model for cluster efficiency. *Proceedings of the European Wind Energy Association Conference & Exhibition*, Rome, 1986.

[3] Mortensen NG, Heathfield DN, Myllerup L, Landberg L, Rathmann O. Getting started with WAsP 9. *Technical Report Risø-I-2571(EN)*, Risø National Laboratory, Roskilde 2007.

[4] Jensen NO. A note on wind generator interaction. *Technical Report Risoe-M-2411(EN)*, Risø National Laboratory, Roskilde 1983.

[5] Frandsen S. On the wind speed reduction in the center of large clusters of wind turbines. *J. Wind Eng. Ind. Aerodyn.* 1992; **39**:251–265.

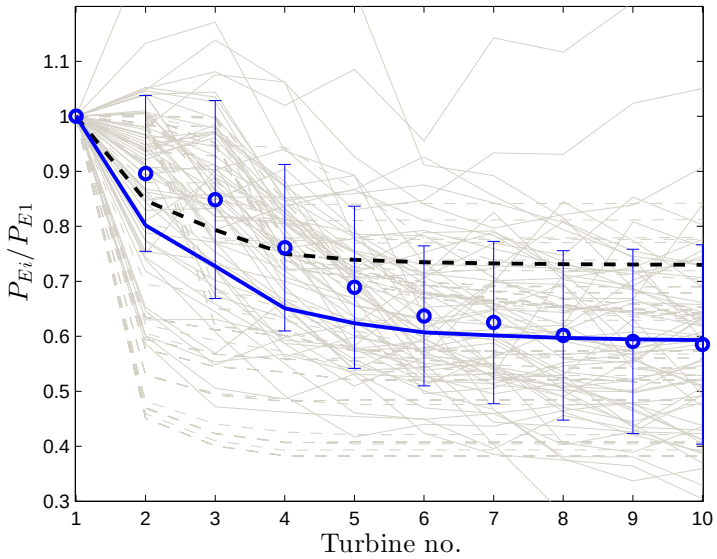

Figure 8: As Fig. 7 but for stable conditions

[6] Barthelmie R, Jensen LE. Evaluation of wind farm efficiency and wind turbine wakes at the Nysted offshore wind farm. *Wind Energy* 2010; **13**:573–586.

[7] Peña A, Rathmann O. Atmospheric stability dependent infinite wind farm models and the wake decay coefficient. *Wind Energy* 2013; In press.

[8] Peña A. Sensing the wind profile. *Technical Report Risø-PhD-45(EN)*, Risø DTU, Roskilde 2009.

[9] Peña A, Gryning SE. Charnock's roughness length model and non-dimensional wind profiles over the sea. *Bound.-Layer Meteorol.* 2008; **128**:191–203.

[10] Peña A, Gryning SE, Hasager CB. Measurements and modelling of the wind speed profile in the marine atmospheric boundary layer. *Bound.-Layer Meteorol.* 2008; **129**:479–495.

[11] Peña A, Hahmann AN. Atmospheric stability and turbulent fluxes at Horns Rev–an intercomparison of sonic, bulk and WRF model data. *Wind Energy* 2012; **15**:717–730.

[12] Hansen KS, Barthelmie RJ, Jensen LE, Sommer A. The impact of turbulent intensity and atmospheric stability on power deficits due to wind turbine wakes at horns rev wind farm. *Wind Energy* 2012; **15**:183–196.

[13] Gaumond M, Rethoré PE, Ott S, Peña A, Bechmann A, Hansen KS. Evaluation of the wind direction uncertainty and its impact on wake modelling at the horns rev offshore wind farm. *Wind Energy* 2013; In press.

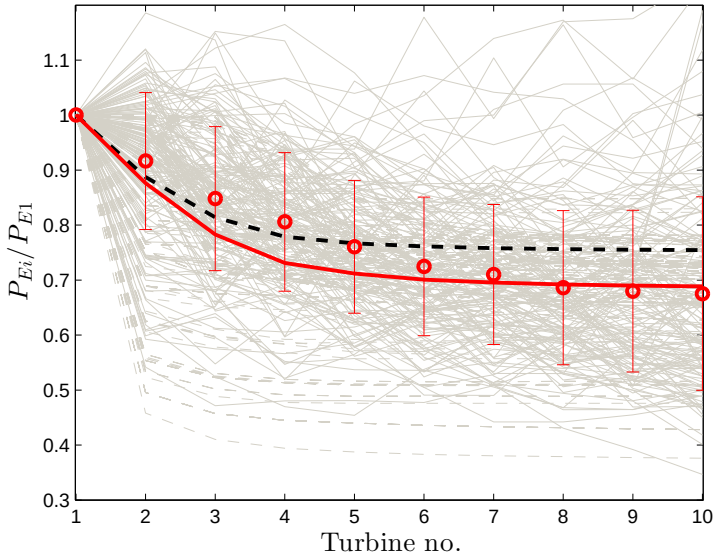

Figure 9: As Fig. 7 but for unstable conditions

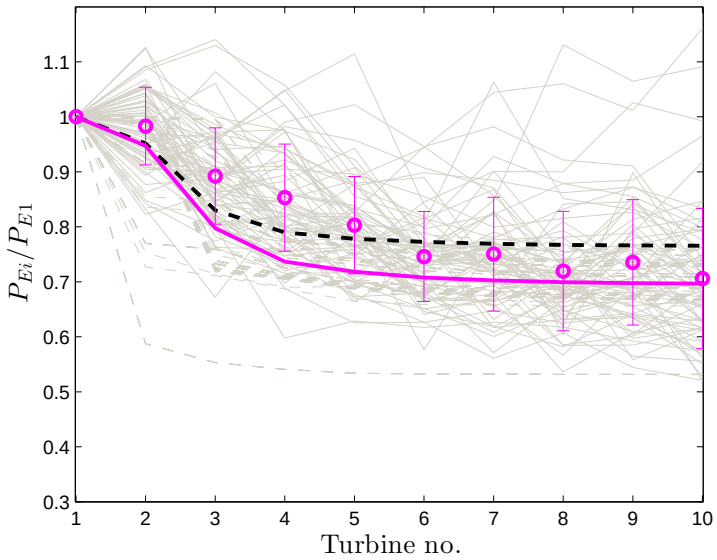

Figure 10: As Fig. 7 but for very unstable conditions

Wavelength Analysis of Wind Farm Energy Entrainment

Jensen Newman[1,2] & Luciano Castillo[1]

[1] National Wind Resource Center,Department of Mechanical Engineering, Texas Tech University, Box 41021, Lubbock TX, 79423 Email: luciano.castillo@ttu.edu
[2] Department of Mathematical Sciences, Rensselaer Polytechnic Institute, 110 Eighth St. Troy, NY 12180 Email: newmaa6@rpi.edu

ABSTRACT

A scaled down array 3 x 5 of wind turbine was analyzed to gain further understanding of how turbulent transport brings mean kinetic energy (MKE) into the array from the Turbulent Boundary Layer above. Particularly, it is of great interest to know which length scales contribute to the energy of the wind farm. This was examined by applying a Proper Orthogonal Decomposition (POD) to 2D particle image velocimetry (PIV) data and constructing modal expansions for the Reynolds stress terms *i.e.* $\langle u'v' \rangle$. A by-product of this analysis was a demonstration that POD modes of the Reynolds stress fields calculated using PIV data resolved at different times can still be used to give a modal expansion of these fields as if all PIV data were resolved simultaneously. It was also shown that a few modes carry the bulk of the Reynolds shear stress. Thus, 75% of the total Reynolds shear stress was carried by the first 13 modes. A high degree of correlation between a POD mode's Reynolds shear stress contribution and its contribution to the MKE entrainment was demonstrated in this study. Specifically, a methodology for defining a characterstic length for each Reynolds stress mode based on its MKE flux was developed. From this analysis it was shown that the modes fall into two catagories: 1) Idiosyncratic modes with characteristic length scales of O(D) (rotor diameter) and 2) smaller scales consisting of Fourier type modes. The idiosyncratic modes capture the inhomogeneity in the flow and account for much of the MKE entrainment. Therefore, the sum of the first 6 modes captures 45% of the MKE entrainment into the array. On the other hand, the higher mode numbers are related to the small scales of turbulence and homogeneity - their length scales decay as $1/n$ where n is mode number.

1 Introduction

For wind energy to become a prominent source of energy, advanced analysis tools are required to understand the interaction between the Atmospheric Boundary Layer (ABL) and the wind park. In the past, development of these tools has taken place by considering approaches

such as stream-tube analysis, 1-D wake models, Large Eddy Simulations (LES), blade element momentum theory, modeling turbines as roughness elements and using classical boundary layer theory [1-3] Recently focus has shifted to the physics of entire wind farms rather than a single turbine. In particular, recent studies by Cal *et al.* [4] and Calaf *et al.* [5] showed, using experimental and numerical methods respectively, that the most important term in the mean kinetic energy (MKE) equation was the vertical transport of MKE by the Reynolds shear stress: $-\langle U\rangle\langle u'v'\rangle$. Both studies showed that the energy entrainment due to this term was of the same order of magnitude as the power extracted by turbines in a wind farm. Thus, the Reynolds shear stress is a very important quantity in bringing energy into the wind farm from the ABL above. Also, there has been much recent development in fundamental turbulence using the concepts of large and very large scale motions (LSM, VLSM). These large structures are important in the current context because they have repeatedly been shown to carry large percentages of the Reynolds shear stress (33%-66%) [8-10]. Because of the importance of Reynolds shear stress mentioned above, it is anticipated that such turbulent structures will play a critical role in providing energy for the wind park. In terms of practical implications it is expected that identification of the length scales which are critcal in the entrainment of MKE will lead to better designed placement, and thus more effecient wind farms. The thought process being that one must first identify these length scales, then determine how wind farm parameters such as spacing, staggering, hub height, rotor diameter etc. influence the energy produced in the wind farm. Eventually, one would like to design a wind farm which acts like a band pass filter in wavenumber space which admits the energy containing range. However, these scales must be identified first and this requires spectral analysis be performed on the data.

Spectral analysis has been used in wind energy research dating back almost 30 years. Kristensen and Frandsen [9] developed a model to predict the power spectrum of the streamwise velocity which acounted for the rotation induced by the turbine and found good agreement between models and experiments. Hojstrup [10] studied spectral coherence in the wake of a wind turbine. He found that conventional coherence models work well in the wake case due to the fact that the seperations investigated were likely smaller than the characteristic length scales of the turbulence generated in the wake. Chamorro and Porté-Agel [11] used wind tunnel experiments to demonstrate that the spectral stucture of the flow around the top-tip height of the turbines is described well by the von Karman spectral formulation. Crespo and Hernandez [12] developed a wake spectrum law by modifying an expression commonly used in undisturbed atmospheric flow to use a non-linear combination of turbulent kinetic energy, and dissipation as a vertical length scale. More recently, Chamorro *et al.* [13] showed that different regions of the turbines amplify certain frequency ranges and that LSM and VLSM are dampend in the turbine wake. In these studies, the spectral analysis is done in the frequency domain due to difficulties in computing spatial correlations over large distances. Additionally, these studies did not examine the spectral characteristics of the physical mechanisms which bring MKE into the array.

Using the Proper Orthogonal Decomposition (POD) and a method developed herein, the MKE entrainment is decomposed in modes each of which has a characteristic length scale. In this way we are able to asses the spectral content of the MKE entrainment. Thus, the paper is organized as follows: The MKE equation and vertical entrainment terms are considered in §2.1, the POD is discussed in §2.2, the experimental setup is discussed in §3, modal contributions to

the Reynolds shear stress and MKE are examined in §4, characteristic length scales and spectral content are examined in §5 and lastly the conclusions are articulated in §6. The major questions we seek to address in this article are: (i) which scales of turbulence are responsible for energy entrainment into the wind park? and, (ii) how many modes are necessary to capture 75% of the energy entrainment?

2 Analysis

2.1 The Mean Kinetic Energy Equation

The conservation equation for the Mean Kinetic Energy, $\bar{E} = \frac{1}{2}\langle \mathbf{U} \rangle \cdot \langle \mathbf{U} \rangle$, can be written as follows, [14].

$$\frac{\bar{D}\bar{E}}{\bar{D}t} = -\nabla \cdot \bar{\mathbf{T}} - \mathscr{P} - \bar{\varepsilon}, \tag{1}$$

where

$$\frac{\bar{D}}{\bar{D}t} = \frac{\partial}{\partial t} + \langle \mathbf{U} \rangle \cdot \nabla \,,$$

$$\bar{\mathbf{T}}_i = \langle U_j \rangle \langle u_i u_j \rangle + \langle U_i \rangle \langle p \rangle / \rho - 2\nu \langle U_j \rangle \bar{S}_{ij},$$

$$\mathscr{P} = -\langle u_i u_j \rangle \frac{\partial \langle U_i \rangle}{\partial x_j},$$

$$\bar{\varepsilon} = 2\nu \bar{S}_{ij} \bar{S}_{ij},$$

$$\bar{S}_{ij} = \frac{1}{2}\left(\frac{\partial \langle U_i \rangle}{\partial x_j} + \frac{\partial \langle U_j \rangle}{\partial x_i} \right),$$

$\langle U_i \rangle$ and u_i are the i^{th} components of the mean and fluctuating velocity respectively, $\langle p \rangle$ is the mean pressure, ν is the kinematic viscosity, $\bar{S}_{ij}$ is the mean rate of strain tensor, $\mathscr{P}$ is the production of turbulence by the mean flow, $\langle u_i u_j \rangle$ is the Reynolds stress and $\bar{\varepsilon}$ is the mean flow dissipation. Furthermore, the term $\langle U \rangle \cdot \nabla$ represents the transport of MKE by the mean flow, $\langle U_j \rangle \langle u_i u_j \rangle$ represents transport of MKE by the turbulent fluctuations in the form of Reynolds stresses.

For the present study, we are interested in contributions from the first term in $\bar{T}_i$ that is $\langle U_j \rangle \langle u_i u_j \rangle$. Specifically, we want to examine MKE flux through a horizontal surface at the top tip height of the turbines: $y^* = y_h + \frac{D}{2}$ where y_h is the turbine hub height and D is the rotor diameter. Therefore, we consider taking a volume integral of Eqn. 1, and applying the divergence theorem to get a surface integral for the mean fluxes, this is then examined on a horizontal surface at y^* where $\hat{n} = \hat{e}_2$ to yield:

$$-\int_x \langle U \rangle \langle u'v' \rangle + \langle V \rangle \langle v'v' \rangle dx|_{y^*}. \tag{2}$$

In the current study we present results only for $\langle U \rangle \langle u'v' \rangle$, which is the flux of streamwise MKE through the horizontal surface due to the Reynolds shear stress. This becauase effects from the wall normal fluxes $\langle V \rangle \langle v'v' \rangle$ were found to be an order of magnitude smaller than those from $\langle U \rangle \langle u'v' \rangle$.

2.2 The POD

The POD results from attempting to find an orthonormal basis whose partial sums capture more turbulent kinetic energy than any other basis. The technique was first introduced in turbulence by Lumley [15] and has been used in innumerable studies of turbulence. Derivation of the equations is presented in [16] and it was shown here that the POD eigenfuctions are solutions of a homogeneous Fredholm integral equation of the 2^{nd} kind. Thus

$$\frac{1}{S}\int_S \langle u_i(\mathbf{x},t)\tilde{u}_j(\mathbf{x}',t)\rangle \phi_j^n(\mathbf{x}')d\mathbf{x}' = \lambda^n \phi_i^n(\mathbf{x}). \tag{3}$$

The factor of $\frac{1}{S}$ (the area of the integration domain) is included so that our eigenfunctions will be dimensionless and the eigenvalues will have the dimensions of velocity squared and can thus be representative of the modal TKE content (see [16]). In this section $\mathbf{x}$ denotes a vector whereas x denotes a component of a vector *i.e.* $\mathbf{x} = (x,y)$. An accent of $\tilde{}$ indicates a complex conjugate, though in the present analysis we will deal with only real quantities. Furthermore, the orthogonal eigenfuctions, ϕ, are normalized so that they satisfy,

$$\frac{1}{S}\int_S \phi_i^n \tilde{\phi}_i^m d\mathbf{x} = \delta_{nm}. \tag{4}$$

where δ_{nm} is the kronecker delta. Moreover, Eqn. 3 is most easily solved by writing the average of $u_i(\mathbf{x},t)u_j(\mathbf{x}',t)$ as $\frac{1}{N_t}\sum_{p=1}^{N_t} u_i(\mathbf{x},t_p)u_j(\mathbf{x}',t_p)$ and using the direct computation method (see for instance [17], [18]). Effectively, the POD modes are constructed as linear combinations of the N_t snapshots as follows:

$$\phi_i^n(\mathbf{x}) = \sum_{p=1}^{N_t} c_p^n u_i(\mathbf{x},t_p) \tag{5}$$

where c_p^n is the p^{th} component of the n^{th} eigenvector of the time correlation matrix between the velocity snapshots. This procedure produces an expansion for the fluctuating velocity field u_i in the form:

$$u_i(\mathbf{x},t) = \sum_{n=1}^{N_t} a^n(t)\phi_i^n(\mathbf{x}). \tag{6}$$

The time dependent coefficients $a^n(t)$ are determined from projections of the instantaneous fields onto the POD modes:

$$a^n(t) = \frac{1}{S}\int_S u_i(\mathbf{x},t)\phi_i^{n*}(\mathbf{x})d\mathbf{x} \tag{7}$$

At this point, important remarks about the POD modes that are computed from the PIV data must be made. First, from Figure 1, it can be seen that the domain being analyzed is comprised of separate PIV planes. Second, the fact that these data were shot at different times presents a problem in the POD analysis in that the two-point, one time correlation $R_{ij} = \langle u_i(x,y,t)u_j(x',y',t)\rangle$ cannot be computed between multiple planes of PIV data. Instead we have the following formulation:

$$\hat{R}_{ij}(\mathbf{x},\mathbf{x}') = \begin{cases} R_{ij}(\mathbf{x},\mathbf{x}') & \text{x, x' in the same plane (same time)} \\ \langle u_i(x,y,t)u_j(x',y',t+\triangle t)\rangle & \text{x, x' in different planes (different times)} \end{cases} \quad (8)$$

where R_{ij} is the standard two point correlation. The description of the kernel in eqn 8 is critical to the analysis that follows.

Most important is the fact that for certain values of x and x', the kernel that we have at our disposal is known to be the same as the kernel that would exist if all PIV data had been shot simultaneously. According to Hilbert-Schmidt theory [19], the solution of the integral equation is also used to give a diagonal decomposition of the kernel. Thus, for the case of all PIV data planes being shot simultaneously, this would yield:

$$R_{ij}(\mathbf{x},\mathbf{x}') = \sum_{n=1}^{N_t} \lambda^n \phi_i^n(\mathbf{x})\phi_j^n(\mathbf{x}'), \quad (9)$$

and similarly,

$$\hat{R}_{ij}(\mathbf{x},\mathbf{x}') = \sum_{n=1}^{N_t} \hat{\lambda}^n \hat{\phi}_i^{\,n}(\mathbf{x})\hat{\phi}_j^{\,n}(\mathbf{x}'), \quad (10)$$

where $\hat{\lambda}^n$ and $\hat{\phi}_i^{\,n}(\mathbf{x})$ are the eigenvalues and eigenfunctions resulting from solving the POD equation using the kernel $\hat{R}_{ij}(\mathbf{x},\mathbf{x}')$ as opposed to $R_{ij}(\mathbf{x},\mathbf{x}')$. For zero spatial separation *i.e.* $x = x'$ the two point correlation gives an expansion of the Reynolds stress in terms of the POD modes, namely:

$$R_{ij}(\mathbf{x},\mathbf{x}) = \langle u_i u_j\rangle(\mathbf{x}) = \sum_{n=1}^{N_t} \lambda^n \phi_i^n(\mathbf{x})\phi_j^n(\mathbf{x}). \quad (11)$$

Also, from equation 8 when $\hat{R}_{ij}$ has zero separation, x and x' are in the same domain so it is equal to R_{ij}. It follows that:

$$\hat{R}_{ij}(\mathbf{x},\mathbf{x}) = \sum_{n=t}^{N_t} \hat{\lambda}^n \hat{\phi}_i^{\,n}(\mathbf{x})\hat{\phi}_j^{\,n}(\mathbf{x}) = R_{ij}(\mathbf{x},\mathbf{x}) = \langle u_i u_j\rangle(\mathbf{x}). \quad (12)$$

Therefore, Eqn 12 is the key result of this analysis and it is crucial to understand very clearly what this equation shows. First, from eqn 12, it is clear that even though the PIV planes were not shot simultaneously, we may still use it to perfrom two important steps in our analysis: 1) we can compute the Reynolds stress field as if the PIV data *had* been shot simultaneously. This also follows from statistacal homogeneity. and 2) we are able to easily construct modal decompositions of the Reynolds stresses. Second, the $\hat{\phi}'s$ are the modes which we analyze here and a total of $N_t = 100$ uncorrelated snapshots were used to generate the modes. The analysis is performed on the domain S_t as shown in Figure 1. Notice that the PIV planes lie along the center - line of the scaled down array.

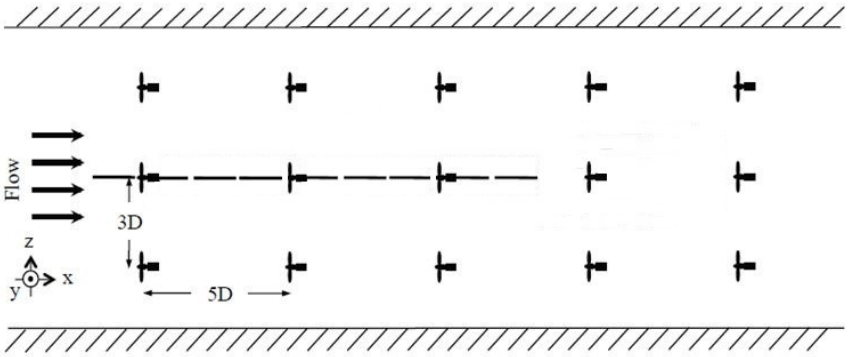

Figure 1: The scaled turbine array with streamwise analysis locations presented in the current study boxed in dotted lines. Solid black lines represent planes of PIV data collected in [1]. Only the planes analyzed in the current study were taken with turbines in place.

3 Brief Experimental Description

The experimental setup used in the current study is that of Lebron [1]. However, some details of the experimental set up are summarized here. Experiments were conducted at the Corrsin Wind Tunnel at Johns Hopkins University. This is a closed loop wind tunnel with primary and secondary contraction ratios of 25:1 and 1:1.27. Free stream turbulence of this facility has been shown to be less than 0.1%. Dimensions of the test section are 10 x 1.2 x 0.9 m (L x W x H). During the experiments, the free stream velocity was held constant at 8 m/s and measured using a pitot tube upstream of the array. This lead to a wind speed of 6.1 m/s at hub height at the inlet to the experimental domain.

Scaled turbines with rotor diameter (D) and hub height both equal to 12 cm were set up in a 3 x 5 wind turbine array with separations of 5D and 3D in the streamwise and spanwise directions respectively. Dimensions of the scaled down array are shown in Figures 1 and 2. Furthermore, dimensions of the experiment are approximately 1/830 scale of a real wind turbine array with rotor diameters and hub heights of 100 m with a tip speed ratio of 4. In order to approximate actual flows found in the atmospheric boundary layer under neutrally stable conditions, the inflow of the test section was conditioned using vertical strakes, the scaled array was set up on a flat plate and chains with roughness height 15mm were laid down perpendicular to x to simulate roughness (see Figure 2). From the PIV data collected in front of the array the maximum turbulence intensity resulting from these chains was found to be 0.33. Power measurements in watts were determined by the empirical equation

$$\bar{P}_{wt} = \bar{\omega}\bar{T}_{wt} = \bar{\omega}\,(0.27063 + 5.6824I)\,10^{-3}, \tag{13}$$

established by Kang and Meneveau [20] where $\bar{\omega}$, $\bar{T}_{wt}$ and I are respectively the rotor angular velocity (in 1/s), DC motor shaft torque (in $N-m$) and DC motor electric current (in Amperes). These measurements were averaged over each row of turbines and are presented in Table 1.

PIV measurements were collected using a TSI Stereoscopic PIV system at a sampling rate

Row	Power (W)
1	0.40
2	0.25
3	0.24
4	0.22
5	0.25

Table 1: Turbine power measurements in watts averaged over each row of turbines.

of 7 Hz and 3000 samples were collected. Three planes of data (like that shown in Figure 2) were collected along the centerline of the array between the turbines (*i.e.* the data planes are $x-y$ planes). These data planes are shown as black lines in Figure 1. The field of view of the PIV planes was 23 cm $\times$ 23 cm.

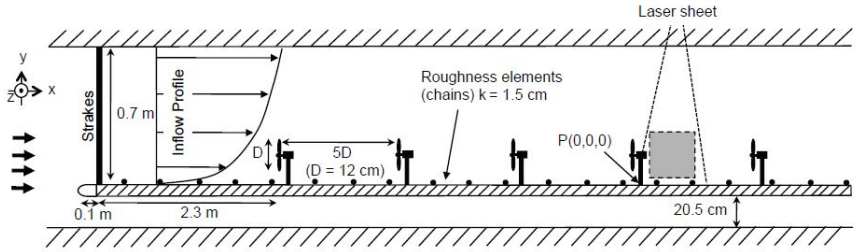

Figure 2: Elevation view of the experimental setup used in [1]

4 Modal distributions of Reynolds shear stress and MKE entrainment

Figure 3(a) shows that as expected, low order modes have large contributions to the Reynolds shear stress. Modal contributions to Reynolds stresses were evaluated from P_n^{ij}/P_T^{ij} where $P_n^{ij} = \int_{S_t} \hat{\lambda}^n \hat{\phi}_i^n \hat{\phi}_j^n d\mathbf{x}$ and $P_T^{ij} = \int_{S_t} \langle u_i u_j \rangle d\mathbf{x}$. P_T can be seen to be the total Reynolds shear stress content of the analysis domain. This type of behavior was also observed by [6] and it is very interesting to see similar qualitative behavior between the current study and those results in [6] since the data in the current study lack streamwise homogeneity. It may be noted that the decay is not strictly monotonic. Recalling that modes are ordered in terms of decreasing eigenvalue $\hat{\lambda}$, this effectively means that the eigenvalues $\hat{\lambda}$ are not strict indicators of a mode's contribution to Reynolds shear stress. Alternatively, the modes could have been ordered in terms of decreasing contribution to Reynolds shear stress, then the curve would have been strictly monotonic decaying and the eigenvalues would not have been.

Figure 3(b) shows graphs of the MKE fluxes, $-\langle U \rangle \langle u'v' \rangle$ as functions of wall-normal coordinate y/y^* as well as curves for the first 3 modes, and the sum of the first $N_{75\%}$ (number of modes necessary to recapture 75% Reynolds shear stress) modes. These plots were generated

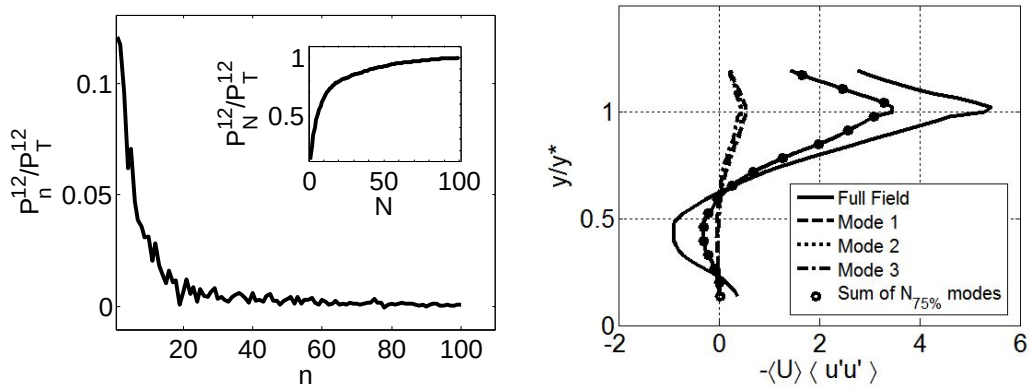

(a) Modal contributions to total Reynolds shear stress.

(b) $-\langle U\rangle\langle u'v'\rangle$ integrated in x.

Figure 3: (a) Modal contributions to total Reynolds shear stress. n indicates a single mode number, N indicates the sum of mode number N and lower. $P_n^{ij} = \int_{S_t} \hat{\lambda}^n \hat{\phi}_i^n \hat{\phi}_j^n d\mathbf{x}$, $P_T^{ij} = \int_{S_t} \langle u_i u_j \rangle d\mathbf{x}$. (b) Kinetic energy entrainment terms $-\langle U\rangle\langle u'v'\rangle$, first three modes and sum of first $N_{75\%}$ modes as a function y for S_t.

by integrating the fields in $x \in S_t$ at each y.

From Figure 3(b) it can be seen that $-\langle U\rangle\langle u'v'\rangle|_{y/y^*=1} > 0$ for data above the hub height and thus the net effect of Reynolds shear stress is to entrain MKE into the wind farm. Alternatively, it can be seen that at the bottom of the rotor ($y/y^* = 1/3$) energy is extracted from the array since $-\langle U\rangle\langle u'v'\rangle|_{y/y^*=1/3} < 0$. This shows that the effect of $-\langle U\rangle\langle u'v'\rangle$ averaged over the length of S_t is to move energy down from above the rotors and eject it below the rotors.

Values of the entrainment at y* from the first three modes and the sum of the first $N_{75\%}$ for each domain are summarized in table 2. This table shows that the first three modes decay monotonically in terms of their contribution the MKE entrainment. It can also be seen that there is a more significant change in the contribution from mode 1 to mode 2 than from mode 2 to mode 3.

In order to evaluate modal contributions to vertical entrainment, the quantity Q_n^{ij}/Q_T^{ij} where $Q_n^{ij} = \int_x \langle U_i(x,y^*)\rangle \hat{\lambda}^n \hat{\phi}_i^n(x,y^*)\hat{\phi}_j^n(x,y^*)dx$ and $Q_T^{ij} = \int_x \langle U_i(x,y^*)\rangle\langle u_i'(x,y^*)u_j'(x,y^*)\rangle dx$ (summation is not implied on repeated indicies here) is examined. Notice that Q_T is the MKE flux per unit spanwise width from the Reynolds stress $\langle u_i u_j\rangle$. Figure 4(a) shows modal behavior for Reynolds shear stress entrainment contributions which mirrors behavior of the modal contributions to the total Reynolds shear stress. That is, modes which contain a large amount of Reynolds shear stress also contribute substantially to MKE entrainment. The first mode of S_t contributes about 12%. Again, it may be observed that the modal contribution to the MKE entrainment is not decaying monotonically. Like the Reynolds shear stress this indicates that $\hat{\lambda}$ is not a perfect indicator of the modes contribution to the MKE entrainment.

Evidently, there are Reynolds shear stress modes which extract energy from the array, but modes which do have higher mode numbers *e.g.* ($n = 87$ in S_t) and thus, have a much more negligible effect in the entire energy exchange to and from the array.

5 Length Scales

The goal of the current section is to determine which length scales are dominant in adding or extracting MKE to the wind farm. So the question is: how should a length scale be related to the POD modes? Typical length scales in flows are associated with *coherent motions* or eddies [14]. Coherent motions are determined from the velocity field which is not available in the current analysis (c.f. §2.2). However, it is desired to know how these coherent motions bring MKE into the array; and thus the interest is really in *coherent energy transfers*. If the scales involved in these coherent energy transfers could be determined directly, the question of how coherent motions bring energy into the array could be answered. Consequently, a coherent energy transfer is defined as energy transfer into the array which occurs over an extended streamwise distance. The next question is: do such coherent energy transfers exist and if so, how do they differ between modes?

Figure 5 (a) shows the coherent energy transfer over S_t for mode 1 and Figure 5 (b) for mode 20. Clearly from Figure 5, such coherent energy transfers can be observed in the first mode. Thus, the current approach is to examine data of the type shown in Figure 5 for each mode and to determine the largest coherent transfer of energy for each mode. In this way, each mode may be characterized as coherently transferring energy on this length scale and smaller. The quantity L^n_{max} is defined as the length of the longest positive run of $\langle U \rangle \hat{\lambda}^n \hat{\phi}^n_1 \hat{\phi}^n_2$ and is calculated for each mode (*i.e* n = 1,2,3...). This approach is similar to that developed by [6] to associate length scales with the POD velocity modes in the inhomogeneous direction of a turbulent channel flow.

Figure 4(b) shows $\frac{L^n_{max}}{D}$ calculated in this way for each mode. The length scales of the first three modes and the sum of the first $N_{75\%}$ modes is shown in Table 2. From Figure 4(b), it is observed that lengths defined in this way have excellent modal decay properties. That is, low modes have larger coherent energy transfers than high modes. Furthermore, from Figure 4(b) one can observe that the largest L_{max} is 1.7D for S_t. The smallest scales found in the flow are, of course, the Nyquist cutoff of $2\triangle x = 0.007$ m or 0.058D. In addition, from Figure 4(b) , an interesting trend is also observed in the high order mode lengths. Here, a line with slope of $\frac{1}{n}$ is also plotted and it is seen that the higher order modes decay approximately as $\frac{1}{n}$. This Figure represents a key result of the current study as it demonstrates that Reynolds stress modes can be separated into 2 distinct categories: idiosyncratic modes (the first 6 modes) which capture the bulk of the flow inhomogeneity and Fourier type modes which are essentially homogeneous (their modal length decays like $\frac{1}{n}$). Further, it can be observed that the idiosyncratic modes are responsible for large transfers of MKE into the array - the sum of the first six modes captures 45% of the entrainment, and have length scale O(D). It may be observed that like the modal contributions to the Reynolds shear stress and the MKE entrainment, the decay of the modal length scales is not strictly monotonic. This shows that like the Reynolds shear stress and MKE entrainment contributions, the modal length scale is not strictly indicated by the eigenvalues. While not a strict indicator, the correlation between larger eigenvalues and larger length scales is still very good.

The tendency of higher order modes (for a turbulent channel and Rayleigh convection) to asymptote towards Fourier modes with period $\frac{L}{n\pi}$ was also observed by [21]. They found that approximately the first 5 modes did not follow this behavior. Clearly, from Figure 4(b) this

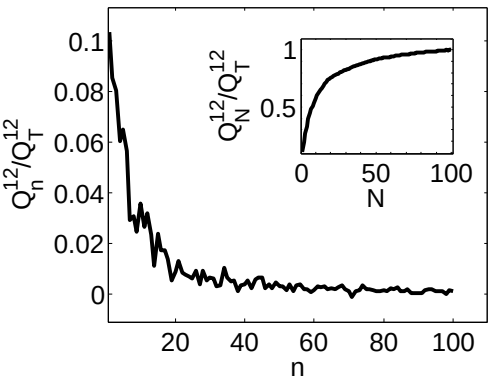

(a) Modal contributions to MKE entrainment.

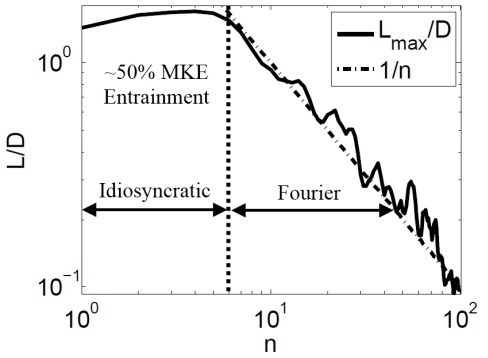

(b) Characteristic length scales for each mode, $\frac{L_{max}^n}{D}$

Figure 4: (a) Modal contributions to MKE entrainment by Reynolds shear. n indicates a single mode number, N indicates the sum of mode numbers N and lower. $Q_n^{ij} = \int_x \langle U_i(x,y^*)\rangle \hat{\lambda}^n \hat{\phi}_i^n(x,y^*)\hat{\phi}_j^n(x,y^*)dx$, $Q_T^{ij} = \int_x \langle U_i(x,y^*)\rangle \langle u_i(x,y^*)' u_j(x,y^*)'\rangle dx$ (Summation not implied on repeated indicies). (b) Comparison of $\frac{L_{max}}{D}$ for S_t with a $\frac{1}{n}$ slope.

Mode	$-\langle U\rangle\langle u'v'\rangle$ $\frac{m^3}{s^3}$	L_{max}/D
1	0.54	1.4
2	0.45	1.6
3	0.42	1.7
$N_{75\%}$	2.70	13

Table 2: Numerical values of the MKE entrainment terms $-\langle U\rangle\langle u'v'\rangle$ from the first three modes and from the sum of the first $N_{75\%}$ at y* and characterstic length scales for each.

behavior begins around n = 6. Furthermore, it is encouraging to see that this newly defined length scale obeys a similar trend as length scales associated with POD modes of velocities found in other studies.

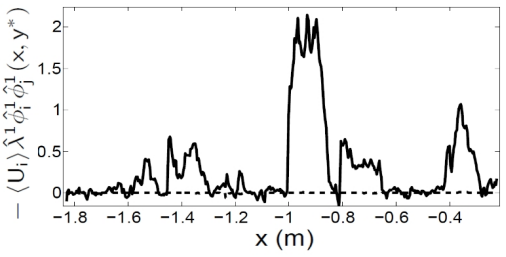

(a) S_t, n = 1

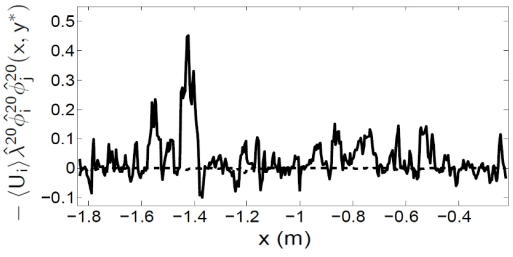

(b) S_t, n = 20

Figure 5: (a) $-\langle U_i\rangle\hat{\lambda}^1\hat{\phi}_i^1\hat{\phi}_j^1$. (b) $-\langle U_i\rangle\hat{\lambda}^{20}\hat{\phi}_i^{20}\hat{\phi}_j^{20}$. Solid lines are $i = 1$ $j = 2$, dashed lines are $i = j = 2$.

6 Conclusions

A POD analysis was performed on the 2D PIV data from a scaled 3 x 5 wind turbine array. This was done in order to examine modal contributions of the Reynolds stresses and mean kinetic energy (fluxes) entrainment and subsequently to establish over which length scales the bulk of the mean kinetic energy is entrained. In order to do this, it was necessary to establish what information could be extracted from 2D PIV data shot at different times. It was demonstrated that the full Reynolds stress field may still be computed and that a modal decomposition of these fields may be constructed.

In addition, from the modal expansions of the Reynolds stresses it was established that low order modes have large contributions to Reynolds shear stress . For instance, mode 1 contained 13% of the total Reynolds shear stress. From knowledge of the overall trend of stress transport, it was established that Reynolds shear stress mode 1 accounts for 12% of the total energy transfer.

Furthermore, the concept of coherent transfers of energy was introduced as entrainment of mean kinetic energy which occurs over an extended length in the streamwise direction. From this definition, length scales could be associated with each mode based on the length of its largest coherent energy transfer so that a particular mode could be taken to execute energy transfers at this length scale and below. From this concept length scales were introduced for each mode and it was established that the Reynolds shear stress modes fell into two distinct categories based on length scale. The first group were the idiosyncratic modes which had length scales O(D) (the largest being 1.7D), behaved in a non homogenoues manner and accounted for 45% of the entrainment of MKE. The second group were the Fourier type modes, which behave homegenously and individually contribute little to the MKE entriainment. These modes' length scales decay like $1/n$, similary to what was found in other studies for channel flow. Lastly it should be mentioned that the Reynolds number scaling of the Reynolds shear stress modes should be investigated so as to better elucidate how these results will apply to full scale turbines.

References

[1] J. Lebron, "PIV Measurements of a Scaled-Down Wind Farm Subject to Atmospheric Boundary Layer Conditions", Doctoral Thesis, Rensselaer Polytechnic Institute Dept. Mechanical Engineering (2011)

[2] C. Meneveau, "The top-down model of wind farm boundary layers and its applications", J. Turbulence vol. 13 (2012)

[3] J. Lebron, L. Castillo, C. Meneveau, "Experimental study of the kinetic energy budget in a wind turbine streamtube", J. Turbulence vol. 13 (2012)

[4] R., Cal, J. Lebron, L. Castillo, H. Kang, C. Meneveau, "Experimental Study in the horizontally averaged flow structure in a model wind-turbine array boundary layer", Journal of Renewable and Sustainable Energy, vol. 2 (2010)

[5] M. Calaf, C. Meneveau, J. Meyers, " Large eddy simulation study of fully developed wind-turbine array boundary layers", Physics of Fluids vol. 22 (2010) pp. 1-16

[6] Z. Liu, R. Adrian, T. Hanratty, "Large-scale modes of turbulent channel flow: transport and structure", J. Fluid Mechanics vol. 448 (2001)

[7] M. Guala, S. Hommema, R. Adrian, "Large-scale and very-large scale motions in turbulent pipe flow", J. Fluid Mechanics vol. 554 (2006)

[8] B. Balakumar, R. Adrian, " Large and very-large scale motions in channel and boundary-layer flows", Phil. Trans. R. Soc. A vol. 365 (2007) pp.665-681

[9] L. Kristensen, S. Frandsen, "Model for power spectra of the blade of a wind turbine measured from the moving frame of reference", J. Wind Eng. Ind. Aerodyn. vol. 10 (1982) pp. 249-262

[10] J. Højstrup, "Spectral coherence in wind turbine wakes", J. Wind Eng. Ind. Aerodyn. vol. 80 (1999) pp. 137-146

[11] L. Chamorro, F. Porté-Agel, "Effects of thermal stability and incoming boundary-layer flow characteristics on wind turbine wakes: A wind tunnel study", Boundary Layer Meteorology vol. 136 (2010) pp. 515-533

[12] A. Crespo, J. Hernandez, "Turbulence characteristics in wind turbine wakes", J. Wind Eng. Ind. Aerodyn., vol. 61 (1996) pp. 71-85

[13] L. Chamorro, M. Guala, R. Arndt, F. Sotiropoulos, "On the evolution of turbulent scales in the wake of a wind turbine model", J. Turbulence vol. 13, no. 27 (2012) pp.1-13

[14] S. Pope, "Turbulent Flows',' Cambridge University Press: Cambridge (2000)

[15] J. Lumley, "Coherent structures in turbulence',' In Transition and Turbulence ed. R.E. Meyer (1981) pp. 215-241

[16] P. Holmes, J. Lumley, G. Berkooz, "Turbulence, Coherent Structures, Dynamical Systems and Symmetry", Cambridge University Press: Cambridge (1997)

[17] M. Rahman, "Integral Equations and their Applications", WIT:Southampton (2007)

[18] Sirovich, L. Turbulence and the dynamics of coherent structures, Parts I-III. *Quarterly of Applied Mathematics* 1987; **XLV**: 561-590

[19] I. Stackgold, "Boundary Value Problem of Mathematical Physics", The Macmillan Company: New York (1967)

[20] Kang, H., Meneveau, C. Direct mechanical torque sensor for model wind turbines. *Measurement Sci. Tech.* 2010; **21**

[21] Baltzer, J., Adrian, R. Structure, scaling and synthesis of proper orthogonal decomposition modes of inhomogeneous turbulence. *Physics of Fluids* 2011; **23** DOI: 10.1063/1.3540663

LES study of the impact of various wind turbine actuator forcings on kinetic energy entrainment in large wind farms

C. VerHulst, C. Meneveau

Johns Hopkins University, Department of Mechanical Engineering and Center for Environmental and Applied Fluid Mechanics, Baltimore, MD
cverhul1@jhu.edu and meneveau@jhu.edu

ABSTRACT

Vertical entrainment of kinetic energy has been shown to be a limiting factor for performance of very large arrays of wind turbines. In this study, Large Eddy Simulations of fully-developed turbulent atmospheric flow over infinitely large wind farms modeled using actuator disks are used to analyze this vertical entrainment. Numerical experiments that attempt to enhance the transfer of kinetic energy from the high-velocity flow above the turbines down to the turbine level are performed using additional vertical forcing applied at the turbine disks. The vertical forcing chosen for the numerical experiments is taken to be proportional to the axial drag force the turbine exerts on the flow and is a function of the instantaneous disk-averaged velocity. The direction of the forcing (i.e. upward or downward) is dependent on the magnitude of the axial velocity at the disk: in one set of LES, a downward force is prescribed in conjunction with a high axial velocity, whereas a low axial velocity results in an upward force. Such additional forcing is found to have a discernible effect on the total power generated by the wind turbine array. Consistent with previous findings, the net kinetic energy flux to the level of the turbines is found to vary along with the total power produced by the wind turbine array. The most significant effect of the forcing at the turbine disks is found to be a change in the effective roughness of the wind turbine array which directly influences the availability of high-velocity flow at the turbine height.

INTRODUCTION

As offshore wind turbines are installed in increasingly large arrays, the need to better understand large-scale interactions between neighboring turbines and the atmospheric flow is motivating new research in the field. The relevant spatial scales range from millimeters to kilometers, making both experimentation and computation a challenge. Similarly, the range of time scales, variability of atmospheric conditions, thermal stratification, and non-trivial terrain effects serve to further increase the complexity. A significant amount of work has been directed toward the

design and understanding of a single wind turbine or a small number of wind turbines [1], but when turbines begin to interact with each other and the atmospheric boundary layer in large wind turbine arrays, their performance can drop quite dramatically [2, 3]. Understanding the mechanisms that cause this reduction in power is crucial for the design of future wind turbine arrays. Early analytical studies modeled these effects with a superposition of wakes that expand in a predefined manner [4, 5], but these provided no information about the dynamics of the flow. Similarly, RANS calculations provide limited insight into the dynamics, though they can be significantly cheaper than a time-resolved simulation [6]. In this study, Large Eddy Simulation (LES) [7] is used in conjunction with a wind turbine actuator disk model [8, 9, 10] to provide good temporal resolution of the flow's large-scale turbulent structures.

For wind turbines placed together in an array, it is well-known that the wake of upstream turbines reduces the available energy to downstream turbines. The power produced by subsequent rows has been shown to decrease, but often tends to level off [2, 3]. At some point, for very large arrays, the flow becomes fully-developed and there is a balance between the forcing of the atmospheric boundary layer and the resistance of the wind turbines. One relevant parameter for this analysis is the kinetic energy in the mean flow, given by $\frac{1}{2}\bar{u}_i\bar{u}_i$ where the overbar denotes an average in time. Vertical entrainment of this quantity from the high-velocity flow above the array must become an important factor in array performance when the flow reaches a fully-developed state. This entrainment of mean kinetic energy, and the means to modify it, is the focus of the present study.

The transport equation for mean kinetic energy in a flow driven by a mean pressure gradient dp_∞/dx is given by

$$0 = \underbrace{-\bar{u}_j\partial_j(\tfrac{1}{2}\bar{u}_i\bar{u}_i)}_{\text{advection}} \underbrace{-\partial_i(\bar{u}_i p/\rho)}_{\text{pressure flux}} + \underbrace{\nu\partial_j\partial_j(\tfrac{1}{2}\bar{u}_i\bar{u}_i)}_{\text{viscous diffusion}} \underbrace{-\nu\partial_j\bar{u}_i\partial_j\bar{u}_i}_{\text{pseudo-dissipation}} + \underbrace{\bar{u}_i\bar{f}_i}_{\text{power extraction by wind turbines}}$$
$$\underbrace{-\partial_j(\bar{u}_i\overline{u_i'u_j'})}_{\text{turbulent KE flux}} + \underbrace{\overline{u_i'u_j'}\partial_j\bar{u}_i}_{\text{turbulent KE dissipation}} \underbrace{-\bar{u}_1\partial_1(p_\infty/\rho).}_{\text{work done by mean pressure gradient}} \quad (1)$$

Previous analyses have shown that, for large wind turbine arrays, the horizontally-planar-averaged form of this mean kinetic energy energy, given by $\frac{1}{2}\langle\bar{u}_i\rangle\langle\bar{u}_i\rangle$ with spatial averaging denoted by the angle brackets, is primarily a function of two mechanisms at the level of the turbines: a decrease in energy by power extraction at the turbines and an increase in energy by turbulent kinetic energy flux [8, 11]. These results lead us to believe that increasing the kinetic energy flux to the level of the turbines could potentially improve the array efficiency, particularly in the far-downstream portion of the array. In the present work, we explore the question of whether modifications to individual wind turbine aerodynamic characteristics, represented here in a first exploratory attempt by additional vertical forcing at the disk, could affect the overall vertical kinetic energy flux in very large wind turbine arrays. The results are intended to provide information about the possibilities and inherent limitations of using modified rotor designs and/or control schemes to affect the entrainment of kinetic energy.

DESCRIPTION OF METHOD

Large Eddy Simulation code

The Large Eddy Simulation (LES) code used for this analysis solves the incompressible Navier-Stokes equations for pressure driven flow without thermal stratification (neutral):

$$\partial_i \tilde{u}_i = 0, \tag{2}$$

$$\partial_t \tilde{u}_i + \tilde{u}_j(\partial_j \tilde{u}_i - \partial_i \tilde{u}_j) = -\partial_i p^* + \tfrac{1}{Re}\partial_j\partial_j \tilde{u}_i + \tilde{f}_i - \partial_j \tau^d_{ij} - \partial_1 p_\infty \delta_{i1}, \tag{3}$$

with the deviatoric part of the subgrid-scale stress term and the modified pressure given by

$$\tau^d_{ij} = \widetilde{u_i u_j} - \tilde{u}_i\tilde{u}_j - \tfrac{1}{3}\delta_{ij}(\widetilde{u_k u_k} - \tilde{u}_k\tilde{u}_k) = -2(c_{s,\Delta}\Delta)^2|\tilde{S}|\tilde{S}_{ij}, \tag{4}$$

$$p^* = \tilde{p} + \tfrac{1}{2}\tilde{u}_j\tilde{u}_j + \tfrac{1}{3}(\widetilde{u_k u_k} - \tilde{u}_k\tilde{u}_k). \tag{5}$$

The variables are implicitly filtered by the coarse grid of LES and are non-dimensionalized by density, ρ, the height of the atmospheric boundary layer, H, and the friction velocity, $u_*=\sqrt{\frac{H}{\rho}\frac{dp_\infty}{dx}}$. The non-dimensionalization is implied for eqns. 2-9 but will be shown explicitly in the results section.

The flow is driven by a mean pressure gradient dp_∞/dx=1 (non-dimensional), and the turbines are represented by a drag force given by $\tilde{f}_i$. The Reynolds number is taken to be very high so the viscous term is neglected. The deviatoric part of the subgrid-scale stress term, τ^d_{ij}, is represented using the Lagrangian scale-dependent dynamic model [12]. The domain is periodic in the horizontal directions to allow for the use of a pseudo-spectral method. In the vertical direction a second-order finite difference approach is used. Time advancement is accomplished using a second-order Adams-Bashforth scheme.

The turbines are modeled as actuator disks [8, 9, 10] to avoid the need for high resolution in time and space. The effect of the turbine on the flow is represented by the drag force given by

$$F_t = -\frac{1}{2}\rho C'_T \left(u^T_d\right)^2 A \tag{6}$$

where C'_T is the modified thrust coefficient, u^T_d is the velocity averaged across the disk and smoothed in time, and A is the frontal area of the turbine disk. This total force is distributed onto the grid using a Gaussian-filtered indicator function, ϕ, which varies smoothly in space so as to avoid numerical errors during calculation of derivatives using the pseudo-spectral method. The force per unit mass at each gridpoint is given by

$$f_x = -\frac{1}{2}C'_T \left(u^T_d\right)^2 \phi/\Delta x \tag{7}$$

with Δx as the effective thickness of the turbine disk. For these simulations, the turbine diameter is given by D/H=0.1 and the hub height is given by z_h/H=0.1. In the fully-developed turbulent

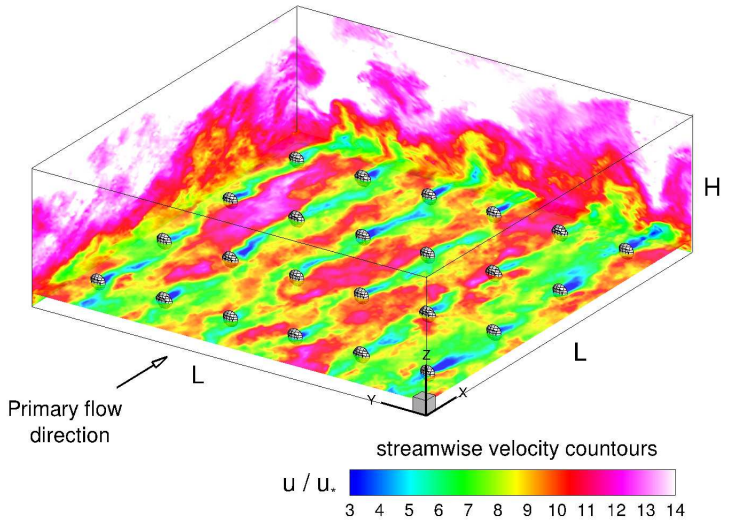

Figure 1: Instantaneous streamwise velocity contours are shown on three planes in the domain, and the turbines are indicated by the grey ellipsoids. A mean pressure gradient drives the flow in the x-direction.

flow around these wind turbines, an undisturbed upstream velocity, as is typically used to calculate the drag force, is not available, so the averaged velocity at the disk is used in its place and the thrust coefficient, C_T, is replaced by the modified thrust coefficient $C_T' = C_T/(1-a)^2$ [8] which is a function of the induction factor, a. For this analysis, the use of a=0.25 and C_T=0.75 lead to C_T'=1.33. The velocity u_d^T is averaged across the disk and smoothed in time using a one-sided exponential filter

$$u_d^T = \frac{1}{T}\int_{-\infty}^{t} u_d(t')\exp\left(-\frac{t-t'}{T}\right)dt' \tag{8}$$

which can be advanced in time as $(u_d^T)^{n+1} = (1-\varepsilon)(u_d^T)^n + \varepsilon(u_d)^n$ with $\varepsilon = \frac{\Delta t}{T}/\left(1+\frac{\Delta t}{T}\right)$ when discretized to first order. The time-scale of this filter was selected to be approximately T=10 seconds. This additional smoothing is required to justify the use of a constant C_T' which is consistent with the actuator disk approximation (i.e. the turbine model is only accurate in an average sense). Lastly, the instantaneous power produced by each turbine is approximated as the product of the drag force and the time-filtered disk averaged velocity,

$$P = F_t u_d^T. \tag{9}$$

An instantaneous snapshot of the domain is shown in fig. 1 with contours of streamwise velocity on three orthogonal planes. The streamwise direction is x, the spanwise direction is y, and the wall-normal direction is z. The turbine locations are indicated by grey ellipsoids, and they exert a drag force opposite the x-direction. The length of the domain in the horizontal directions is given by L and the height of the domain is given by H. For these simulations, a domain size ratio of L/H=π was used. Since the domain is periodic in the streamwise and spanwise

directions, the wind turbine array modeled here is infinite and the flow is fully-developed. The number of gridpoints used to discretize the domain is given by nx x ny x nz = 128 x 128 x 61. The boundary condition at z/H=1 is zero shear and zero vertical velocity. A standard log-law based wall-stress boundary condition is used (as in ref. [8]) to enforce no-slip at z/H=0, since the viscous term has been neglected and viscous sublayers are not being resolved.

Vertical forcing at the turbine disks

In an attempt to increase the net kinetic energy flux to the turbines, additional synthetic forcing is applied to the flow at the turbine disks. In our numerical experiments, this approach is meant to mimic the effects of fast-acting rotor control schemes that could generate net thrust components in the vertical directions (e.g. by suitably controlled angle-dependent pitch variations). Alternatively, such additional forcing could perhaps be caused by an active structure (e.g. some kind of stator blades) mounted on the turbine tower behind the blades so as to influence the flow without significantly decreasing the performance at the rotor. We stress that these are meant as numerical "what if" experiments and are not meant, as of yet, to represent the effects of any fully realistic device. The synthetic vertical force applied at the turbine disks is chosen to be a function of the disk-averaged velocity, u_d, and is given by

$$f_z = A\, f_x\, \mathrm{sign}(u_d/u_* - 7.2) \tag{10}$$

such that a high velocity at the disk coincides with a downward force for positive values of A (since $f_x < 0$ in the chosen coordinate system). This forcing scheme is shown in table 1 for easy reference. The mean value of the non-dimensional disk-averaged velocity was estimated to be approximately u_d/u_*=7.2 based on previous simulations. Since stronger winds imply higher f_x (and therefore higher f_z for a given A) we expect the net forcing to be in the downward direction for positive A. For this analysis, we chose a suite of values to be tested, i.e. A=[1, 1/2, 1/4, 1/10, 1/20, 0, -1/20, -1/10, -1/4, -1/2, -1].

Table 1: Direction of vertical forcing based on sign of A

$A > 0$	$A < 0$
high velocity $\rightarrow$ force downward	high velocity $\rightarrow$ force upward
low velocity $\rightarrow$ force upward	low velocity $\rightarrow$ force downward

The cases with large $|A|$ would likely be unrealistic to implement in practice, but they serve to accentuate the differences between cases so as to ensure that observed trends are not merely a result of noise in the calculations. Regardless, at this stage the investigation is primarily intended as a proof of concept to identify whether such additional forcing near the turbine disk could have an appreciable effect on the flow's rate of vertical entrainment of mean kinetic energy.

Rescaling from friction velocity to Geostrophic velocity

The LES results are non-dimensionalized by the friction velocity, $u_*=\sqrt{\frac{H}{\rho}\frac{dp_\infty}{dx}}$, which itself can vary between cases, so another velocity scale is needed for a fair comparison among cases. Since the Geostrophic velocity, G, acts as a measure of total available wind resource for a wind farm located on flat and homogeneous terrain, the results are rescaled to be a function of G rather than u_*. To accomplish this rescaling, the following implicit scaling law from ref. [13] is used:

$$\frac{G}{\hat{u}_*} = \frac{1}{\kappa}\sqrt{\left[\ln\left(Ro\frac{\hat{u}_*}{G}\right) - A\right]^2 + B^2} \tag{11}$$

where $Ro=G/(f\hat{z}_0)$ and the constants A=1.7 and B=4.5 are chosen to agree with the survey of ref. [14]. This formula was derived for a neutral boundary layer in the region where $\hat{z}_0 \ll z \ll H$ (recalling that $\hat{z}_0$ is the effective roughness height and H is the thickness of the boundary layer), but is applied to our results for the logarithmic region located above the wind turbines. The presence of such a logarithmic velocity region above the wind turbine array was first postulated by refs. [1, 4] and later demonstrated by LES of ref. [8].

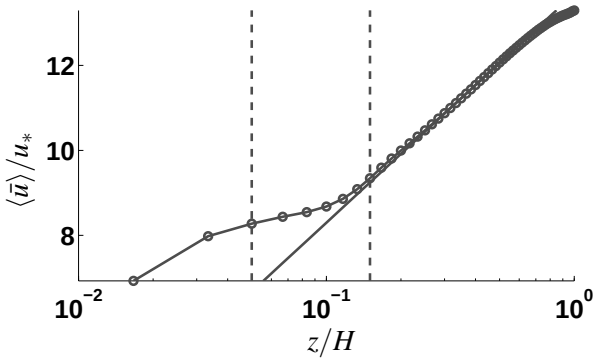

Figure 2: The effective roughness and friction velocity are calculated by fitting eqn. 12 to the logarithmic region above the wind turbines. The turbines are located in the region between the dashed lines.

To determine the effective roughness of the wind turbine array, $\hat{z}_0$, and the effective friction velocity, $\hat{u}_*$, for use in eqn. 11, we fit a log-law profile of $\langle\bar{u}\rangle/u_*$ vs. z/H (output from LES simulations) above the wind turbines to find the non-dimensional $\hat{z}_0/H$ and $\hat{u}_*/u_*$ according to the equation

$$\frac{\langle\bar{u}\rangle}{u_*} = \frac{\hat{u}_*}{u_*}\frac{1}{\kappa}\ln\left(\frac{z/H}{\hat{z}_0/H}\right). \tag{12}$$

The value of $\hat{z}_0/H$ is then used in eqn. 11 to find $\hat{u}_*/G$. Finally, $u_*/\hat{u}_*$ from eqn. 12 and $\hat{u}_*/G$ from eqn. 11 are combined to determine u_*/G which will be used to rescale the LES results.

The fit for the baseline case (A=0) is shown in fig. 2. For this analysis, the von Kármán constant is κ=0.41 and the Rossby number $Ro=G/(f\hat{z}_0)$ is calculated using G=20 m/s, $f=10^{-4}$

1/s, and $\hat{z}_0$ determined by the log-law fit. The use of eqn. 11 for rescaling of flow around a wind turbine array with pressure gradient forcing has also been described in ref. [15], and a discussion of the relationship between pressure forcing and Geostrophic velocity can also be found in the appendix of ref. [8].

RESULTS

Velocity profiles and log-law fits

For each of the cases considered here, a logarithmic region of mean streamwise velocity, $\langle\bar{u}\rangle/u_*$, was found to exist above the wind turbines. Fig. 3 shows the velocity profiles for the cases with the strongest forcing ($A = \pm 1$). In both of these cases, two distinctive logarithmic regions above the turbine array were identified (in addition to the logarithmic region below the turbines). Not surprisingly, the addition of strong vertical forcing increased the size of the 'inner' region that is directly affected by the turbines. The 'outer' region, the higher of the two logarithmic regions above the turbines, was chosen for the fit using eqn. 12. For the cases with weaker vertical forcing, the profiles were similar to the one shown in fig. 2 with only a single logarithmic region above the turbines, as in ref. [8]. The effective roughness and effective friction velocity from the log-law fit are given for each case in fig. 4. For positive values of A, the forcing decreases the apparent roughness of the wind turbine array. For a given driving pressure gradient, this would imply higher velocity throughout the boundary layer.

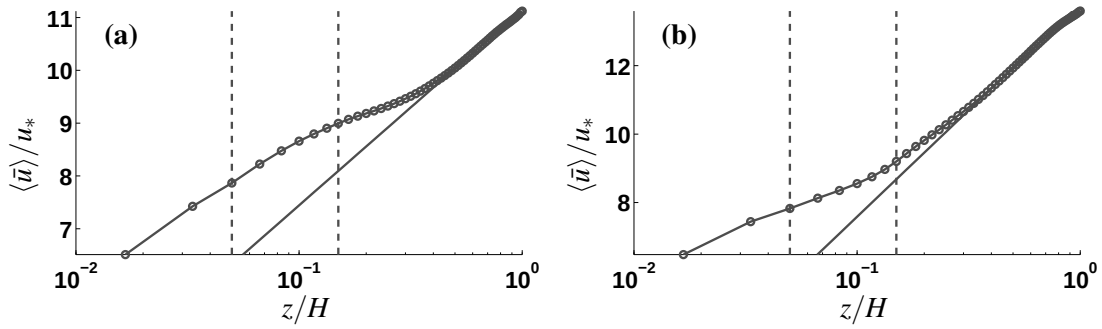

Figure 3: The streamwise velocity profiles are shown for the cases with (a) A=1 and (b) A=-1. A logarithmic region is present above the turbine array for both cases. The wind turbines are located in the region between the dashed lines.

The ratio of friction velocity to Geostrophic velocity, calculated from eqns. 11 and 12, is shown in fig. 5 for each case. Here, it is important to distinguish between the array's apparent friction velocity, $\hat{u}_*$, and the friction velocity used to non-dimensionalize the governing equations, $u_*=\sqrt{\frac{H}{\rho}\frac{dp_\infty}{dx}}$. The apparent friction velocity in fig. 5a is consistent with the effective roughness heights given in fig. 4a: an effective increase in roughness translates to an increase in the effective wall drag $\hat{\tau}_w = \sqrt{\rho\hat{u}_*^2}$. If the height of the boundary layer is taken to be constant, then an increase in roughness would necessitate an increase in the driving pressure gradient which would lead to an increase in u_* as is shown in fig. 5b.

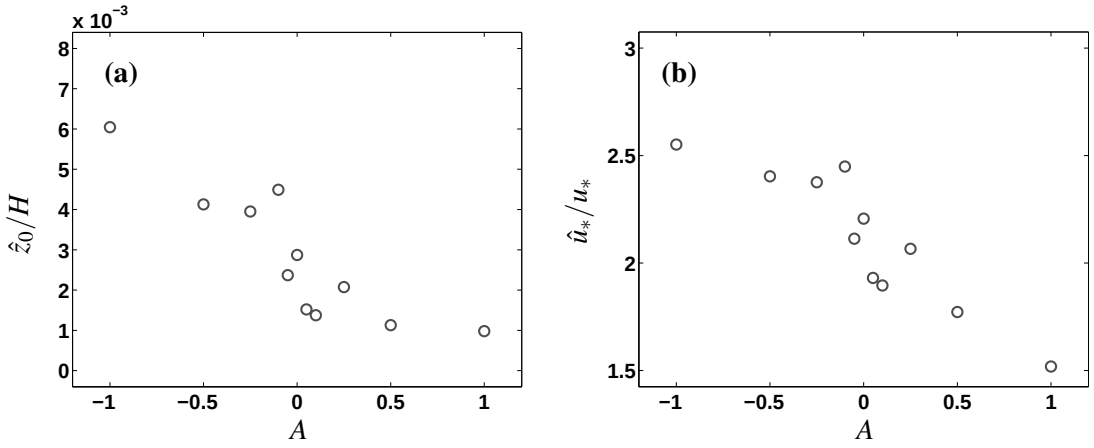

Figure 4: The ratios (a) $\hat{z}_0/H$ and (b) $\hat{u}_*/u_*$ from the log-law fit of velocity given by eqn. 12 are shown as a function of forcing magnitude.

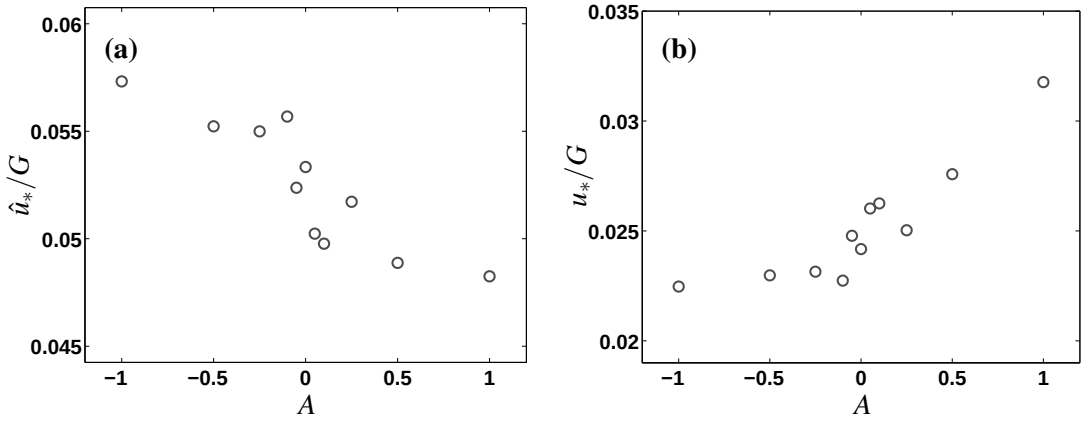

Figure 5: The ratios (a) $\hat{u}_*/G$ and (b) u_*/G are shown as a function of forcing magnitude.

The direction of the vertical forcing was determined by comparing the magnitude of the disk-averaged velocity to the value u_d/u_*=7.2, the mean value from previous simulations without vertical forcing. This approach was not ideal since there was no guarantee that the mean disk-averaged velocity would remain at this value once the additional forcing was applied. Surprisingly, the mean velocity remained quite close to 7.2 for all cases. Probability density functions (PDFs) of u_d/u_* are given for each case in fig. 6. Also, surprisingly, the vertical forcing had quite a strong effect on the distributions. For negative values of A the PDF tended to become more narrow with a large proportion of the velocities near the mean. For positive values of A a bimodal distribution was found with the highest probability for sub-mean velocities but with long tails for very high velocities. Examination of individual PDFs for each turbine show that this bimodal distribution is present for each turbine and is not merely a result of spanwise inhomogeneities.

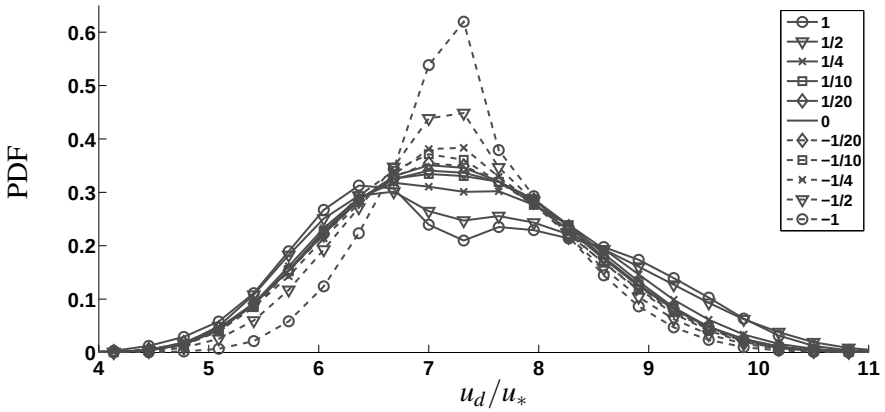

Figure 6: PDF of disk-averaged velocity for each case with A shown in the legend.

Applied vertical force

The magnitude of the vertical force, averaged in time and across horizontal planes, is shown in fig. 7 for each case. Since force is proportional to the square of velocity, the high-velocity forcing dominates the time-average. Hence, the net vertical forcing is downward for positive A and upward for negative A. This net force could also be estimated from the velocity histograms as proportional to $E[A\text{sign}(7.2-u_d/u_*)(u_d/u_*)^2]$ where $E[\cdot]$ denotes the expected value. The high-velocity long tails in the PDFs for strong positive A lead to an increase in the time-averaged vertical forcing compared to the strong negative A cases. As such, the effect of the forcing is expected to be more significant for the cases with $A > 0$.

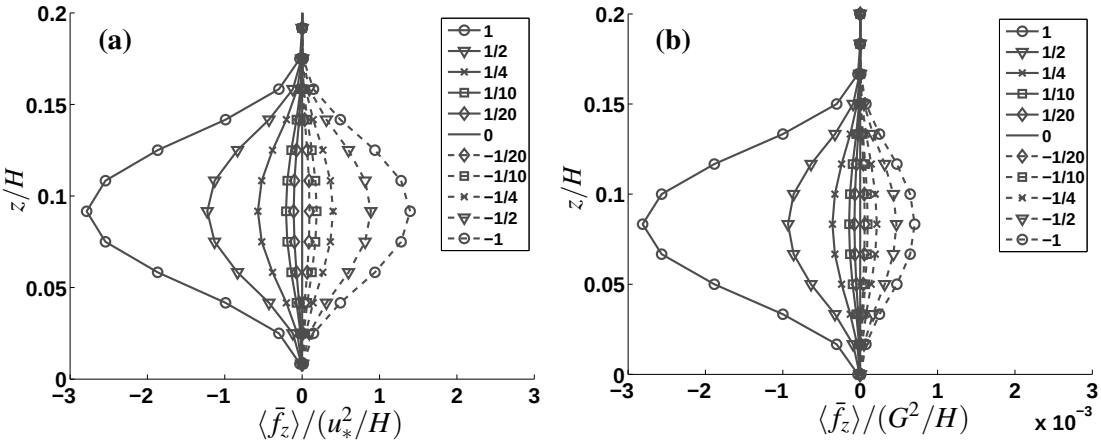

Figure 7: The horizontal average of the applied vertical force is shown for each case. The raw LES output in (a) is normalized by u_*, but has been rescaled to G in (b). The value of A is given in the legend.

Turbine power and turbulent kinetic energy flux

The intention of the additional vertical forcing scheme was to increase the net kinetic energy to the level of the turbines with the hope of increasing the power produced by the wind turbine array. The total power generated by the wind turbine array, estimated for each turbine according to eqn. 9 and then summed, is given in fig. 8a as a function of the forcing magnitude. The turbine power is highest for $A > 0$, largely due to the high values of u_*/G for these cases.

The net kinetic energy flux to the level of the turbines is given by

$$\Phi_T = \rho \int_0^L \int_0^L \int_{z_h-D/2}^{z_h+D/2} \left[-\partial_j(\bar{u}_i \overline{u_i' u_j'}) - \partial_j(\bar{u}_i \overline{\tau_{ij}^d}) \right] dz dy dx = \rho \int_0^L \int_0^L \left[-\bar{u}_i \overline{u_i' u_3'} - \bar{u}_i \overline{\tau_{i3}^d} \right]_{z_h-D/2}^{z_h+D/2} dy dx, \quad (13)$$

which simplifies due to the periodic boundary conditions in the x- and y-directions. The net kinetic energy flux to the turbine level is given in non-dimensional form in fig. 8b for all cases. There is a clear correlation between the power produced by the turbine array and the net kinetic energy flux to the turbine level. The increase in these quantities is strongest for highest values of $A > 0$ which corresponds to downward forcing for high-velocity flow. Note that the slightly larger power output at turbines compared to the integrated energy flux can be attributed to the work done by the pressure forcing which in the turbine region can slightly exceed the turbulent dissipation term (see eqn. 1). Table 2 shows the resulting trends for this analysis based on the sign of A.

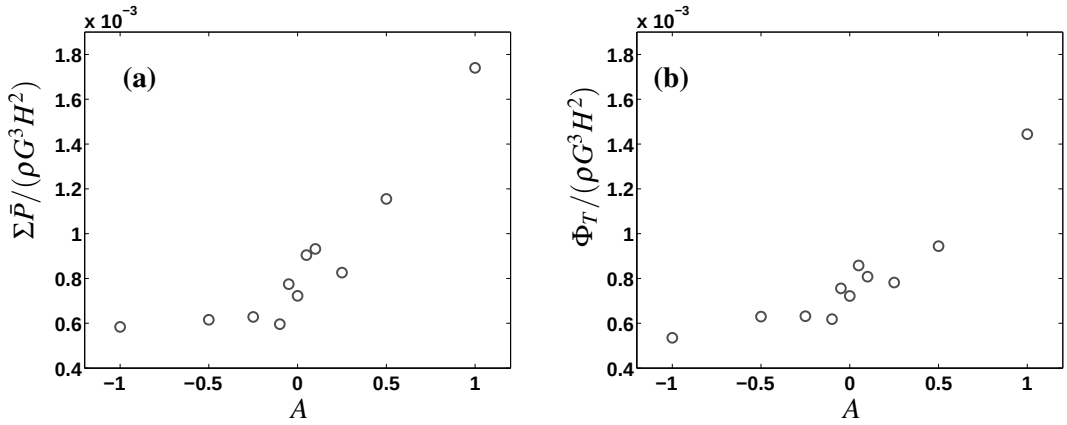

Figure 8: (a) Mean turbine array power and (b) net kinetic energy flux to the level of the turbines are shown as a function of forcing magnitude.

CONCLUSIONS

Based on the results of this study, it appears that additional vertical forcing at the turbines can have a significant effect on the rate of mean kinetic energy entrainment in a large wind turbine

Table 2: Summary of results based on sign of A

$A > 0$	$A < 0$
high velocity $\rightarrow$ force downward	high velocity $\rightarrow$ force upward
low velocity $\rightarrow$ force upward	low velocity $\rightarrow$ force downward
net force downward	net force upward
smaller effective roughness	larger effective roughness
higher turbine array power	lower turbine array power
higher mean KE flux to turbine level	lower mean KE flux to turbine level

array. When downward forcing corresponds with high velocities, the net drag force exerted on the atmospheric boundary layer by the wind turbine array is reduced, leading to higher velocities at the turbine disk for a given Geostrophic velocity. This increase lead to an improvement of turbine power and kinetic energy flux to the turbines. Interestingly, the vertical forcing also had an effect on the distribution of velocities at the disk which may be relevant to prediction of power generation and turbine operating regimes.

Clearly, the vertical forces imposed for the extreme cases in this study would be impractical or impossible to implement in practice. Also, no attempt was made to compare the net energy gain with the energy that would be required to impose this active forcing. Since only a small subset of possible forcing schemes were examined in this study, it appears possible that practically realizable and effective active forcing schemes could be developed. The analysis in this study also focused primarily on horizontally-averaged quantities in order to isolate variation in the vertical direction, but the mean kinetic energy field has a complex three-dimensional structure. It would be interesting to further examine the kinetic energy flux, along with the other terms in the mean kinetic energy balance equation, in a fully-three-dimensional sense. Also, future efforts can be focused on studying the coherent structures responsible for these fluxes, for instance using Proper Orthogonal Decomposition tools.

As wind turbine arrays continue to grow in size, it becomes increasingly important to develop innovative strategies to improve the performance of the wind turbines in the far downstream portion of the array. A design that enhances entrainment of kinetic energy could make that possible. With the aid of Large Eddy Simulation we now have the capability to experiment with designs and flow control concepts that would be difficult to test in physical experiments. While such numerical studies have their advantages in facilitating such initial "what if" experimentations, their inherent limitations must also be kept in mind, especially the further need for developing technically or economical feasible implementations.

ACKNOWLEDGEMENTS

This work was funded by NSF grants CBET-1157246 and OISE-1243482, and a NSF graduate research fellowship. Simulations were performed on the NCAR Yellowstone supercomputer.

REFERENCES

[1] S. Frandsen, R. Barthelmie, S. Pryor, O. Rathmann, S. Larsen, J. Hojstrup, and M. Thogersen, "Analytical modelling of wind speed deficit in large offshore wind farms," Wind Energy, vol.9 (2006) pp. 39.
[2] R. J. Barthelmie, S. C. Pryor, S. T. Frandsen, K. S. Hansen, J. G. Schepers, K. Rados, W. Schlez, A. Neubert, L. E. Jensen, and S. Neckelmann, "Quantifying the impact of wind turbine wakes on power output at offshore wind farms," Journal of Atmospheric and Oceanic Technology, vol.27 (2010) pp. 1302.
[3] R. J. Barthelmie, K. S. Hansen, S. T. Frandsen, O. Rathmann, J. G. Schepers, W. Schlez, J. Phillips, K. Rados, A. Zervos, E. S. Politis, and P. K. Chaviaropoulos, "Modelling and measuring flow and wind turbine wakes in large wind farms offshore," Wind Energy, vol.12 (2009).
[4] S. Frandsen, "On the wind speed reduction in the center of large clusters of wind turbines," J. Wind Eng. Ind. Aerodyn, vol.39 (1992) pp. 251.
[5] P. B. S. Lissaman, "Energy effectiveness of arbitrary arrays of wind turbines," Journal of Energy, vol.3 (1979).
[6] A. Crespo, J. Hernández, and S. Frandsen, "Survey of modelling methods for wind turbine wakes and wind farms," Wind Energy, vol.2 (1999).
[7] A. Jimenez, A. Crespo, E. Migoya, J. Garcia, "Advances in large-eddy simulation of a wind turbine wake," Journal of Physics: Conference Series, vol. 75 (2007).
[8] M. Calaf, C. Meneveau, and J. Meyers, "Large eddy simulation study of fully developed wind-turbine array boundary layers," Physics of Fluids, vol.22 (2010).
[9] R. Mikkelsen, "Actuator disk methods applied to wind turbines," PhD dissertation, Technical University of Denmark (2003).
[10] Y. Wu and F. Porté-Agel, "Large-Eddy Simulation of wind-turbine wakes: evaluation of turbine parametrisations," Boundary Layer Meteorology, vol.138 (2011) pp. 345.
[11] R. B. Cal, J. Lebrón, L. Castillo, H. S. Kang, and C. Meneveau, "Experimental study of the horizontally averaged flow structure in a model wind-turbine array boundary layer," Journal of Renewable and Sustainable Energy, vol.2 (2010).
[12] E. Bou-Zeid, C. Meneveau, and M. B. Parlange, "A scale-dependent Lagrangian dynamic model for large eddy simulation of complex turbulent flows," Physics of Fluids, vol.17 (2005).
[13] A. K. Blackadar and H. Tennekes, "Asymptotic Similarity in Neutral Barotropic Planetary Boundary Layers," Journal of the Atmospheric Sciences, vol.25 (1968) pp. 1015.
[14] S. S. Zilitinkevich, "Velocity profiles, the resistance law and the dissipation rate of mean flow kinetic energy in a neutrally and stably stratified planetary boundary layer," Boundary Layer Meteorology, vol.46 (1989) pp. 367.
[15] J. Meyers and C. Meneveau, "Effect of wind-turbine surface loading on power resources in LES of large wind farms," Direct and Large-Eddy Simulation VIII, vol.8 (2011) pp. 425.

A Research on Wind Farm Micro-sitting Optimization in Complex Terrain

Chang Xu[1], Jianchuan Yang[1], Chenqi Li[1], Wenzhong Shen[2], Yuan Zheng[1], Deyou Liu[1]

[1]Hohai University, College of Energy and Electrical Engineering, Nanjing, Jiangsu Province, 211100, China, zhuifengxu@hhu.edu.cn, yefeng1t@hhu.edu.cn

[2]Technical University of Denmark, Department of Wind Energy, Nils Koppels Alle, Building 403, 2800,Lyngby, Denmark, wzsh@dtu.dk

ABSTRACT

Wind farm layout optimization in complex terrain is a pretty difficult issue for onshore wind farm. In this article, a novel optimization method is proposed to optimize the layout for wind farms in complex terrain. This method utilized Lissaman and Jensen wake models for taking the terrain height and the wake loss from the upstream turbines into the wind turbine power output calculation. Wind direction is divided into sixteen sections, and the wind speed is processed using the Weibull distribution. The objective is to maximize the total wind farm power output and the free design variables are the wind turbines' park coordinates which subject to the boundary and minimum distance conditions between two wind turbines. A Cross Particle Swarm Optimization (CPSO) method is developed and applied to optimize the layout for a certain wind farm case. Compared with the uniform and experience method, results show that the CPSO method has a higher optimal value, and could be used to optimize the actual wind farm micro-sitting engineering projects.

Keywords: wind farm micro-sitting, complex terrain, wake model, probability density, cross particle swarm optimization (CPSO)

1 Introduction

In the past few years there is a growing energy demand with the worldwide economic development, where fossil fuel almost accounts for all of the energy consumption. It's well known that the fossil fuel is nonrenewable and could generate all kinds of emissions which pollute the environment as well as affect human's health [1]. Global people's minds are being awakened to develop and utilize renewable energy which covers wind energy, solar energy, wave energy, hydrogen energy, etc. Nevertheless, with the current technology status, wind energy is almost the lowest-cost in all the renewable energy utilization fields and can be installed on a large scale or distributed power. It is promising to be the third energy supply in addition to fossil energy and hydro energy in China.

During the last 10 years, the total installed wind turbines capacity in China has reached 65 000MW which is the top one position in the world, most of them are scaled wind farm utilizations and at the same time, are located on flat terrain with good wind energy resources. The zone in addition to flat terrain is called complex terrain. The next stage in wind farm development will be focused on complex terrain [2]. There are often a few advantages for the decision maker to exploit the wind energy resources in complex terrain on the lower land, operation and environment costs. At the same time this kind of projects often creates many high quality job opportunities and incents the local economic as well. However, it is difficult to predict the wind energy distribution and layout the wind farm due to the detouring flow in the complex terrain and the wakes in the wind farms are very hard to be modeled. Currently, how to make full use of the wind energy and lay out the wind farms are both academic and engineering issues.

Many factors will affect the wind power output of a wind farm, such as wind turbines selection, layout method, grid connection, etc. However, the layout of a wind farm is one of most effective ways to improve wind energy utilization efficiency [3-5].

There are some studies or software applied in the actual wind farm micro-sitting. Common software include WAsP, Windfarm, Windsim, Meteodyn WT, etc. WAsP from Danish Risø National Laboratory is the most widely used software up to now, however WAsP itself has some drawbacks, such as, WAsP can't optimize the placement of wind turbines independently without the help of other necessary techniques and is proved to be not accurate enough from the practical data in complex terrain [6]. The CFD can simulate the flow field in complex terrain accurately and the velocities in front of each wind turbine can be determined. On the other hand CFD computations are excessive computational costly, with a considerable long process runtime and it is unsuitable to implement in the practical use of the optimization issue [7]. Rasoul rahmani [8], Alireza Emami [9], C. Szafron [10] and Chunqiu Wan [11] presented a simplified wake model accompanied with Weibull wind speed distribution in their studies, but the model didn't consider the wind direction and elevation which had great influences on the turbine wake. Liu [12] applied the Genetic Algorithm (GA) to the wind farm layout optimization, but the efficiency of the overall algorithm was not discussed and the power calculation was too rough to predict accurately the energy production. Furthermore, the above mentioned methods are all based on the rectangular and flat topography. However, most of the wind farms are located on irregular and uneven topography which increases the difficulties in wind farm modeling and calculation of the optimal results.

In this paper, a novel methodology is used to optimize the wind turbines' park coordinates for maximizing the wind farm's power production in a specified irregular zone wind farm with knowing the number of turbines. In the proposed approach, Lissaman wake model and Jenson wake model are established that can be applied in complex terrain with different wind directions. The calculation of the power output based on the probability density method by wind speed Weibull distribution combined with wind speed-power curve. The CPSO algorithm is implemented for the optimization problem, and compared with uniform distribution method and experienced distribution method. The feasibilities and reliabilities are analyzed for the wind farm layout optimizations as well.

2 Mathematical Models

2.1 Wake model

Wind turbine in a wind farm extracts energy from atmosphere, reducing the wind velocity and producing swirling eddies behind the rotor which is called wind turbine wake [13]. The mean velocity and turbulence intensity in the wake zone are different from that in the free stream. If a turbine locates behind an upstream turbine in the wind direction, the turbine will be affected by the wake created by the upstream turbine, which will reduce its power output. The wind speed has the stochastic characters in both direction and magnitude [14]. In order to calculate wind power production under different speeds, different directions and different layouts in the wind farm should be transformed and wind speed distribution should be modeled.

In this paper, the wind directions are divided into 16 intervals with 22.5^{o} for each interval from 0^{o} to 360^{o}. The angular bisector of the interval can be deemed to the direction of each interval.

The statistical characteristic of the wind speed at a certain height has been approximated by the two-parameter Weibull distribution function which is proved to

be appropriate enough distribution pattern for the wind energy field [15-16]. For a given wind speed v in the direction interval θ_{iv}, with a shape parameter K_{iv} and a scale parameter C_{iv} of the Weibull distribution function, its frequency $g(v,\theta_{iv})$ can be calculated as:

$$g(v,\theta_{iv}) = \frac{K_{iv}}{C_{iv}}\left(\frac{v}{C_{iv}}\right)^{K_{iv}-1}\exp\left(-\left(\frac{v}{C_{iv}}\right)^{K_{iv}}\right)T(\theta_{iv}) \tag{1}$$

where $T(\theta_{iv})$ is the probability in the wind direction interval iv, iv is from 1 to n (n=16).

$$T(\theta_{iv}) = \frac{\varepsilon_{iv}}{\varepsilon_{sum}} \tag{2}$$

where ε_{iv} is the count statistics that the wind speed direction within the range of $(iv-1)*22.5^o$ and $iv*22.5^o$, ε_{sum} is the total count statistics of wind speed.

According to Lissaman wake model [17], wind speed varies with elevation by index relationship. Suppose that a set of wind data is measured at a certain height z_0 (*Fig.1*), the wind speeds at turbine i and j can be calculated by equations (3) ~ (4):

$$v_i = v_0\left(\frac{z(i)+h}{z_0}\right)^{\alpha} \tag{3}$$

$$v_j = v_0\left(\frac{z(j)+h}{z_0}\right)^{\alpha} \tag{4}$$

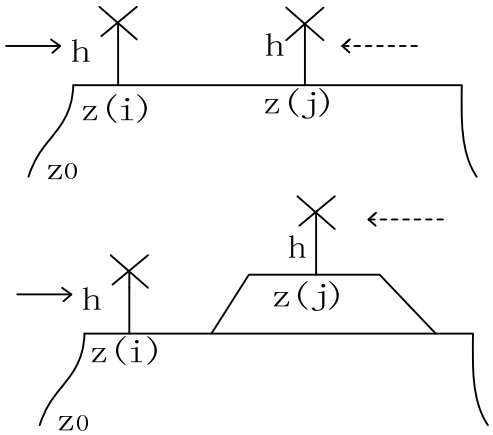

***Fig.1* Lissaman wake mode**

where $z(i)$ and $z(j)$ are the elevations of turbine i and turbine j, respectively, h is the wind turbine tower height, v_0 is the wind speed measured at z_0, and α is the friction coefficient which is determined by the terrain (α=1/7 for the paper) .the actual wind speeds of turbine i and j are:

$$v_i' = v_i(1-d_i) \tag{5}$$

$$v_j' = v_j(1-d_j) \tag{6}$$

Where d_i and d_j are wind speed deficits, in this paper, we apply Jenson wake model to calculate the value.

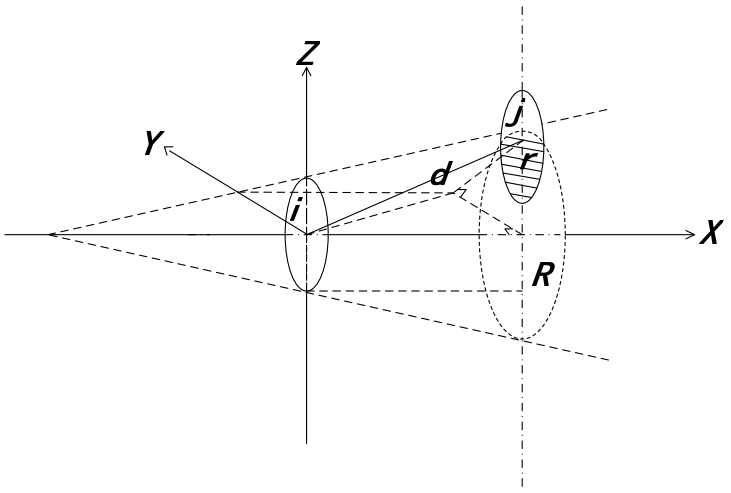

Fig.2 **Jenson wake mode**

When the wind blows from left to right, the turbine i is the upstream turbine,it will not be affected by any other turbine, so the speed deficit of two turbines are[12]:

$$d_i = 0 \tag{7}$$

$$d_{\mathrm{j}} = [1-(1-C_T)^{1/2}](\frac{r}{R})^2(\frac{h}{\mathrm{h}+\Delta Z})^{2\alpha_1}\frac{A_{\mathrm{w}}}{\pi r^2} \tag{8}$$

Where C_T thrust coefficient, r is the blade radius, R is the wake radius and A_w swept area of a turbine's rotor.

When the wind blows from right to left, the wind speed deficit of two turbines can be calculated as :

$$\mathrm{d_j} = 0 \tag{9}$$

$$d_{\mathrm{i}} = [1-(1-C_T)^{1/2}](\frac{r}{R})^2(\frac{h+\Delta Z}{\mathrm{h}})^{2\alpha_1}\frac{A_{\mathrm{w}}}{\pi r^2} \tag{10}$$

Suppose there are N turbines in a wind farm and the kinetic energy deficit keeps conservation due to all the wakes, the inlet velocity of a turbine for a certain wind speed and a wind direction interval can be obtained by equation (11):

$$v_i^{'} = \sqrt{v_i^2 + \sum_{\substack{j=1 \\ j\neq i}}^{N}[v_{\mathrm{ij}}^2 - v_i^2]} \tag{11}$$

Where v_{ij} represents the turbine i's inlet velocity after the effects of the turbines j.

2.2 Power model

The power that a turbine obtained from the wind is associated with the wind speed, and the power curve could be linearly approximated [18]:

$$f(v) = \begin{cases} 0, v < v_{in} \\ \lambda v + \eta, v_{in} \le v \le v_{rated} \\ p_{rated}, v_{rated} \le v \le v_{out} \end{cases} \tag{12}$$

Where v_{in}, v_{out} and v_{rated} are wind turbine's cut-in, cut-out and rated wind speeds respectively. P_{rated} is the rated power. λ and η are the coefficients of the wind turbine power curve.

Combined with the equation (1) and (12), a wind turbine power output can be calculated by:

$$E(p)=\sum_{iv=1}^{n}\int_{0}^{+\infty}\frac{360^{o}}{n}g(v,\theta_{iv})f(v)dv \tag{13}$$

The total power that all wind turbines produced the of the wind farm is:

$$E(P_{sum})=\sum_{l=1}^{N}E(P_l) \tag{14}$$

$E(P_l)$ is the power of function of turbine l and $E(P_{sum})$ is the power function of the total wind farm.

III Algorithms for the turbine placement optimization Cross Particle Swarm Optimization (CPSO) algorithm

In this paper, the target of the optimization issue is the maximization of the wind farm total power production, which means the minimization of the power loss due to wind direction and turbines coordinates. The objective function of an individual for the evolutionary algorithms is the logarithmic of total power production's multiplicative inverse:

$$f=ln(1/E(P_{sum})) \tag{15}$$

The fitness value of an individual for evolutionary algorithms is:

$$F=\frac{1}{f+\psi} \tag{16}$$

Where ψ is a small positive value to ensure the fitness value be a positive value.
The basic steps of standard PSO algorithm can be simplified as[19]:

$$x_i^{t+1}=x_i^t+v_i^{t+1} \tag{17}$$

$$v_i^{t+1}=\omega v_i^t+\beta_1 r_1(p_i-x_i^t)+\beta_2 r_2(p_g-x_i^t) \tag{18}$$

Where: v_i^{t+1} ,velocity of agent i at iteration t; ω, inertia weight; β_1, β_2, positive weighting constants; r_1, r_2, random number between 0 and 1; x_i^t, current position of individual at iteration t; p_i, local best of the individual i; p_g, global best of all the individuals.

The standard PSO algorithm would be easily traped into local optimal point compared with other population based algorithms for lacking of population diversities [20]. In this paper, some operators are designed to overcome this drawback. Firstly the strategy is inertia weight is gradually decreased. In the standard PSO, the inertia weight is a fixed constant, while the inertia weight ω is responsible for the searching area. A big ω means search the optimization solution in the large space , and A small ω means small local searching space [21]. Therefore, The big ω is efficient at the beginning of the iterations and the small ω will be better to get the optimization result at the later stage of the iterations. The inertia weight in the paper is defined:

$$\omega=\omega_{max}(\omega_{max}/\omega_{min})^{\frac{1}{1+10t/T_{sum}}} \tag{19}$$

Where $\omega_{\max}$ and $\omega_{\min}$ are max and min inertia weights, t is the current generation or inertia time and T_{sum} is the total generations or inertia times.

Secondly，the inferior particles will be eliminated. In the behavior of the swarm, there will always be some particles far from the optimal results,which affect the overall optimization efficiency. The improved algorithm introduces some new particles that

based on cross operator to replace the bad ones. The new particle's positions and corresponding speeds are:

$$x_r^t = q_1 x_g + (1-q_2)x_{b_1}^t \tag{20}$$

$$v_r^t = q_3 v_g + (1-q_4)v_{b_2}^t \tag{21}$$

Where t is the current generation, x_r^t and v_r^t are the inferior particle and its speed, x_g and v_g are the global best particle and its speed, x_{b1}^t and v_{b2}^t are random selected particle and speed from other particles respectively. q_1, q_2, q_3 and q_4 are random numbers from 0 to 1.

Thirdly, individual optimal position and global optimal position mutate. During the iteration, particles gradually approach the local optimal and global optimal，and the search efficiency may be trapped into stagnation. In order to keep the search ability at this time, individual optimal position and global position both mutate if the particles' position close to optimal over the limitation.

$$p_i' = c_1 p_i + (1-c_2 p_i) \tag{22}$$

$$\text{If} \quad |x_i - p_i| < \nabla$$

$$p_g' = c_3 p_g + (1-c_4 p_g) \tag{23}$$

$$\text{If} \quad |x_i - p_g| < \nabla_1$$

Where c_1, c_2, c_3, c_4 are random numbers from 0 to 1, $\nabla$and ∇_1 are the limitation constants.

4 Case study

4.1 Wind farm description

In order to compare the reliability and feasibility of the proposed method. The efficiencies of the three evolutionary algorithms are checked in the same wind farm of north China. The wind farm is the complex terrain shown as *Fig. 3*. The wind farm is an irregular graphic with *X*-axis and *Y*-axis both from 0 m to 7000 m , and elevation from 1337.5 m to 1517.5 m .

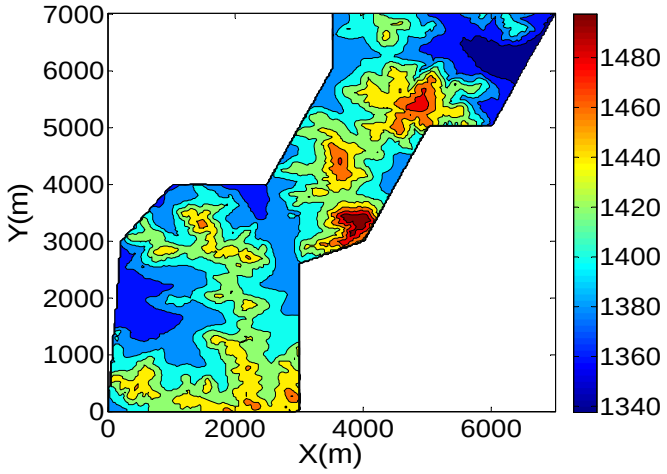

***Fig.3* Wind farm topographic contour**

The wind farm locates in the rich wind resource zone.*Fig.4* and *Fig.5* describe the wind's frequency and power density distribution. *Tab.1* shows the Weibull

distribution parameters，*K* value, *C* value，probability, and power density of 16 wind direction sections.

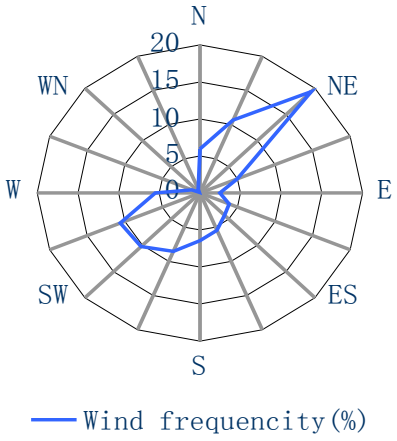

***Fig.4* Wind direction rose chart**

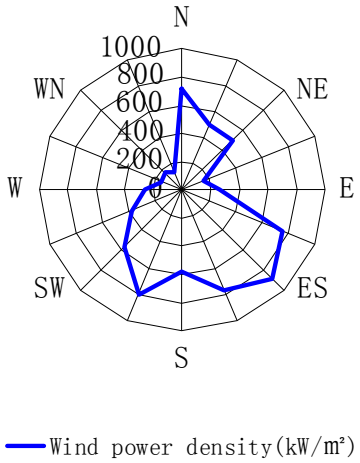

***Fig.5* Wind power density rose chart**

4.2 Results and analysis

Objective function convergence curves and optimal placement distributions are checked and analyzed for the three evolutionary algorithms applied in the wind farm layout optimization. Objective function convergence curve for CPSO is shown as *Fig.6*, Optimal placement distribution results for CPSO is shown as *Fig.7*.

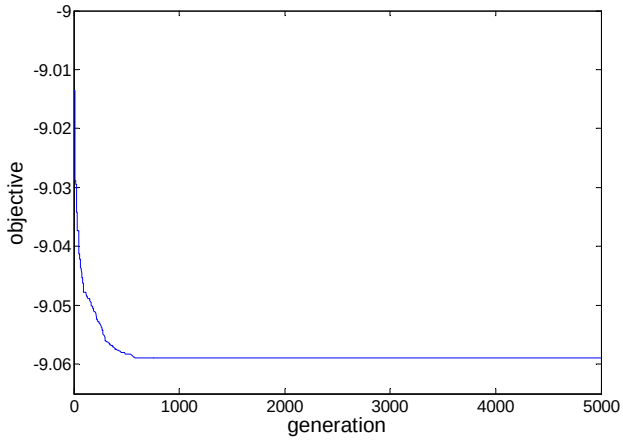

***Fig.6* Objective function convergence curve (CPSO)**

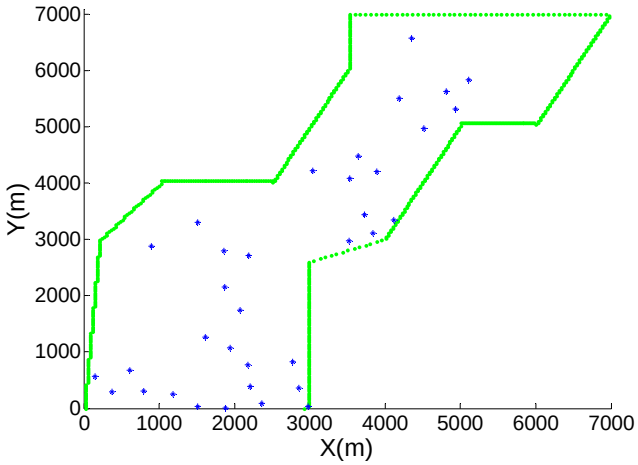

***Fig.7* Optimal placement distribution (CPSO)**

Wind turbine uniform layout scheme（Uniform distribution）is often applied for the flat terrain wind farm. Higher elevation positions with good wind energy resource are also usually chose to place the wind turbine by the experienced engineer for the complex terrain（Experience distribution). The regulations of these two schemes are the turbines are required to keep 5 to 9 diameters in the prevail direction and 3 to 5 diameters in the direction perpendicular to the prevail direction, and wind turbines configurate plum blossom [22].Uniform layout scheme for the wind farm is shown as *Fig.7*. Distribution scheme by choosing high elevation is shown as *Fig.8* for the complex terrain wind farm. Data of wind speeds, wind directions, topography and wind turbine parameters can be loaded into WAsP, and WAsP can exports wind turbines power outputs for these two layout methods [23].

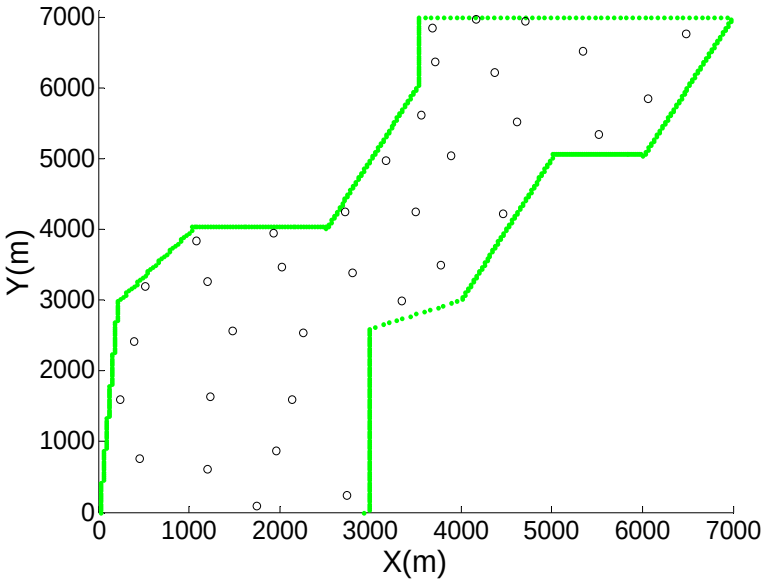

***Fig.7* Placement of uniform distribution**

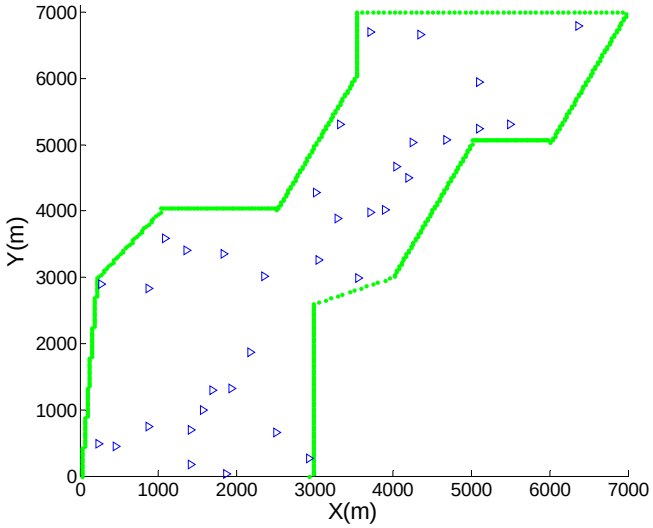

***Fig.8* Optimal placement of experience distribution**

The result comparisons of the five layout methods are shown as in Tab.1, where the power is wind farm annual average power production for all turbines.

***Tab.1* Optimization results comparison**

	Optimal objective	Power(kW)	Converge Time(h)
Uniform distribution	-9.0141	8218.3	2.1
Experience distribution	-9.0346	8388.4	2.1
CPSO	-9.0589	8594.7	7.2

From the Tab.3, the uniform distribution and experience distribution methods get the lower power production and the lower time than the three proposed evolutionary algorithms because of no optimization computation process. After testing, the coordinate distributions of the three algorithms meet the requirements of distance and boundary restrictions at the same time. The layouts of the three optimization algorithms concentrate on the high position (compare the layout with the wind farm topographic contour in *Fig.2*) where the power density is higher than the others. The CPSO have improved the total power production by 2.46% compare with the experience distribution method. The uniform distribution and experience distribution methods concentrate on the prevail wind direction and distance from each other, without considering the effect of elevation and optimizing distribution, so the schemes of these two methods are both not competent.

5. Conclusion

In this paper, a wake model was established which could be implemented in calculating wind farm power output of the complex terrain. The wake model utilized the Lissaman model and Jensen model which process the wind speeds of different elevation in the wind farm , and consider the effect of the wake intersection area with the rotor on the wind turbine power output. The wind direction was divided into 16 sections and the wind speed was processed by Weibull distribution. The probability density of each section was used to calculate of wind turbine power output. A optimization algorithm called CPSO is proposed in the paper. Results from the CPSO optimization were compared with the uniform and experience method. Results show the CPSO optimization methods perform better than the uniform and experience method in the wind farm layout optimization. CPSO proposed by the paper shows the

best performance in the distribution problem and can be used to optimize the wind farm layout engineering issue.

Acknowledgements: This paper is partially supported by the National Key Basic Research Development Program of China (973),project number is 2010CB227102-1); the Scientific Research Foundation for the Returned Overseas Chinese Scholars from State Education Ministry, project number is 2012-940;and the Six Personnel Field Peak Projects in Jiangsu Province, project number is 2012-XNY-12.

References:

（1）Carlos M. Ituarte-Villarreal and Jose F. Espiritu. Wind turbine placement in a wind farm using a visual based optimization algorithm [J]. Computers and Industrial Engineering, 2008 (41):672-677.

（2）Han, X. Guo, J. Wan, p. Adequacy study of a wind farm considering terrain and wake effect [J]. Journals and Magazines.2012, 10(06):1001-1008.

（3）Li ling, Zeng Xiang Jun, Zhang Ping.Wind farms reactive power optimization using genetic/tabu hybrid algorithm[C].Chang'sha, China, ICICTA, 2008:1272-1276.

（4）J.M. Morales, R.Minguez, A.J. Conejo. A methodology to generate statistically dependent wind speed scenarios [J]. Applied Energy, 2010(87):843-855.

（5）Zhang Changshui, Hou Guangdong, Wang Jun. A fast algorithm based on the submodular property for optimization of wind turbine positioning [J]. Renewable Energy, 2011(36): 2951-2958.

（6）Xu Guobin，Peng Xiufang，Wang Haijun．Micro-siting of Complex Terrain for Wind Power Station [J] .Water Resources and Power，2010，28(4)：157-160.

（7）Rajai Aghabi Rivas, Jens Clausen, Kurt S.Hansen, et al.Solving the turbine position problem for large offshore wind farms by simulated annealing [J]. Wind Engineering, 2009,3(33):287-298.

（8）Rasoul Rahmani, A.Khairuddin, Sam M.Cherati, et al. A novel method for optimal placing wind turbines in a wind farm using particle swarm optimization (PSO) [C]. Johor, Malaysia,IEEE,2010:134-139.

（9）Alireza Emami, Pirooz Noghreh. New approach on optimization in placement of wind turbines within wind farm by genetic algorithms [J].Renewable Energy, 2010,35:1559-1564.

（10）C.Szafron. Off shore wind farm layout optimization[C]. Janiszewskiego, Poland, EEEIC, 2010:542-545.

（11）Chunqiu Wan, Jun Wang, Geng Yang, et al. Optimal micro-siting of wind turbines by genetic algorithms based on improved wind and turbine models[C]. Shang'hai,China, IEEE, 2009:5092-5096.

（12）Feng-Jiao Liu, Pai-Hsun Chen, Shyi-Shium Kuo. Wind characterization analysis incorporating genetic algorithm: A case study in Taiwan Strait[J].Energy, 2011(36):2611-2619.

（13）Moskalenko, N. Otto-von-Guericke-Univ, Magdeburg, et al. Study of wake effects for offshore wind farm planning[C]. Magdeburg, Germany,MEPS, 2010:1-7.

（14）Yunus Eroglu, Serap Ulusam Seckiner. Design of wind farm layout using ant colony algorithm[J]. Renewable Energy.2012(44):53-62.

（15）Mathaba. T, Mpholo. M, Letuma. M. Velocity and power density analysis of the wind at Lefseng-la-terae in Lesotho[J].Renewable Energy, 2012(46):210-217.

（16）Shi. LB, Wang. C, Yao, LZ. Optimal power flow solution incorporating wind power[J]. IEEE Systems Journal.2011(6)233-241.

（17）Tai-Her Yeh, Li Wang, Senior Member. A study on generator capacity for wind turbines under various tower heights and rated wind speeds using Weibull distribution [C].Tainan, China, Energy Conversion, IEEE,2008,2(23):592-602.

（18）C. Kongnam, S. Nuchprayoon. Decision analysis on generation capacity of a wind park[J]. Renewable and Sustainable Energy Reviews,2009,8(13): 2126- 2133.

（19）Marcela Martinez-Rojas, Andreas Sumper, Oriol Gomis-Bellmunt, et al. Reactive power dispatch in wind farms using particle swarm optimization technique and feasible solutions search[J]. Applied Energy 2011(88)4678-4686.
（20）Chunqiu Wan, Jun Wang, Geng Yang, et al. Wind farm micro-sitting by Gaussian particle swarm optimization with local search strate``gy[J].Renewable Energy,2012 (48) 276-288.
（21）Chen Guo-Chu, Yang Wei, Zhang Yan-chi, et al. Simplified classification PSO and its application in wind farm modeling[J].Control and decision,2011,3(26):381-386.
(22) WU Qing-yuan, He De-xin, Sun Ru-lin, Wu Yun-dong. Wind powerengineering technical manual[M], Beijing: Machinery industry press, 2004.
(23) Dunsic, Zeijko, Mikulovic,et al. A model for vertical wind speed data extrapolation for improving wind resource assessment using WAsP [J] .Renewable Energy,2011 (41):407-411. 8.1031e+03